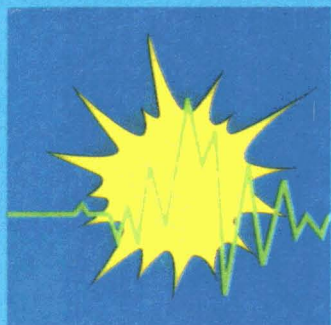


Non-Nuclear Energy
(JOULE) Programme



The Underground
Disposal of CO₂



FINAL REPORT OF
JOULE II PROJECT NO. CT92-0031

**THE UNDERGROUND DISPOSAL OF
CARBON DIOXIDE**

THE UNDERGROUND DISPOSAL OF CARBON DIOXIDE

Edited by S Holloway

BRITISH GEOLOGICAL SURVEY

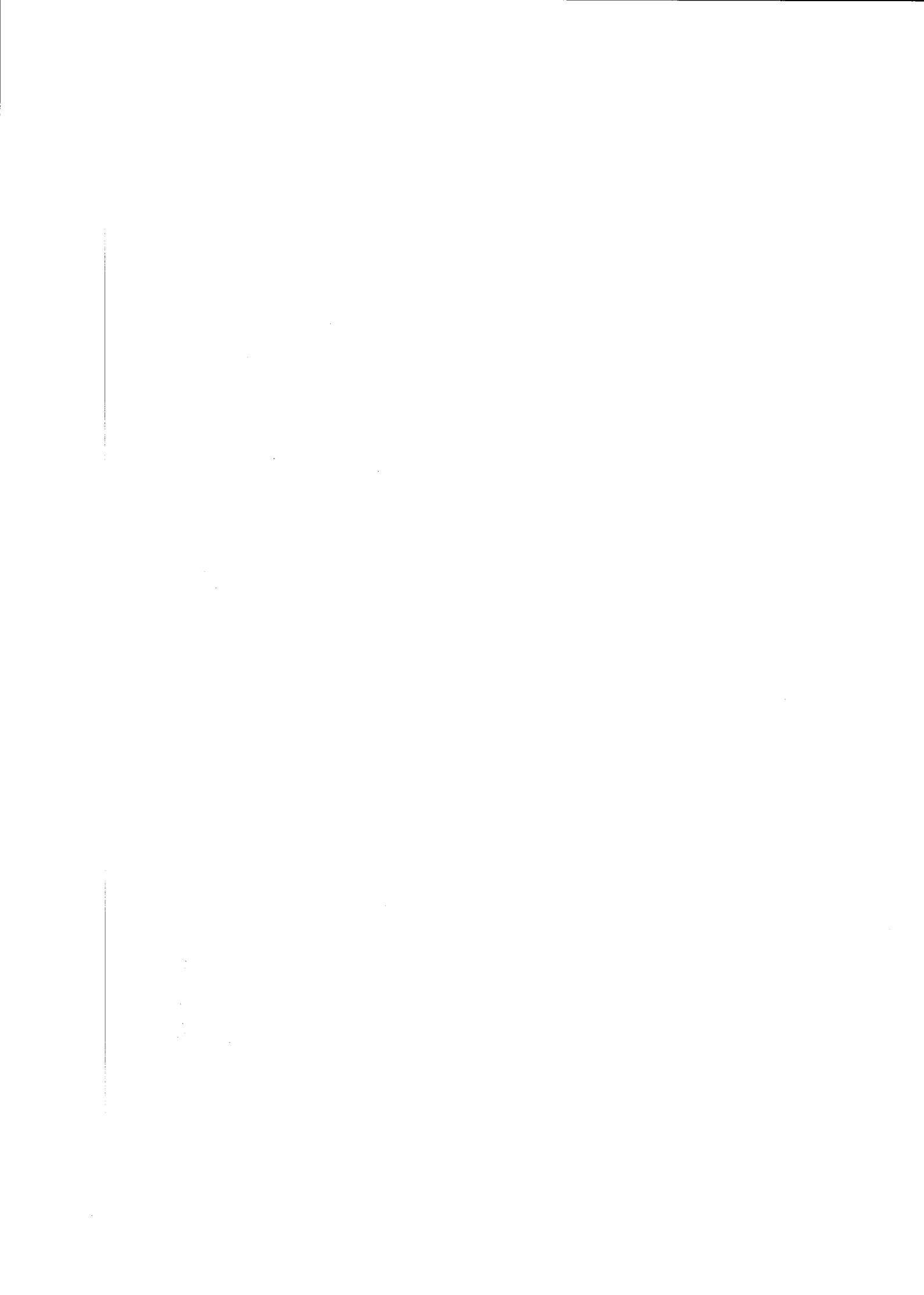
Contract No JOU2 CT92-0031

FINAL REPORT

Research funded in part by
THE COMMISSION OF THE EUROPEAN COMMUNITIES
in the framework of the
JOULE Programme
Sub-Programme
Non Nuclear Energy

ISBN 0 85272 280 X

Date: February 1996



FOREWORD

This report gives the detailed results, conclusions and recommendations of Joule II project No. CT92-0031: 'The Underground Disposal of Carbon Dioxide'. A summary of the results of the project is given in the Summary

Report of the project, which was compiled on 28 February 1995.

The addresses of the organisations participating in the project are given below:

PARTICIPATING ORGANISATIONS

British Geological Survey
Keyworth
Nottingham
NG12 5GG
United Kingdom

CRE Group Ltd
Stoke Orchard
Cheltenham
Gloucester
GL52 4RZ
United Kingdom

RWE Aktiengesellschaft
Kruppstrasse 5
PO Box 10 30 61
45030 Essen
Germany

TNO Institute of Applied Geoscience
Schoemakerstraat 97
PO Box 6012
2600 J A Delft
The Netherlands

BRGM
Avenue de Concyr
B.P. 6009
45060 Orleans Cedex 2
France

IKU Petroleum Research
N-7034 Trondheim
Norway

Statoil
Ranheimsveien 10
Postuttak
N-7004 Trondheim
Norway

University of Sunderland
Renewable Energy Centre
Priestman Building
Ryhope Road
Sunderland
United Kingdom

AUTHORS

The following authors have contributed to the report:

BRITISH GEOLOGICAL SURVEY

S Holloway, C A Rochelle, K Bateman, J M Pearce,
H E Baily, R Metcalfe

BRGM

I Czernichowski-Lauriol, B Sanjuan, J Barbier, H Fabriol

CRE GROUP LTD

I R Summerfield

IKU PETROLEUM RESEARCH

E Lindeberg

RWE AG

T Schwarzkopf

RWE ENERGIE AG

J Putter, M Krumbeck

RWE-DEA AG

H Moller, K A Gaida

STATOIL

O Kaarstad, B Berger

TNO INSTITUTE OF APPLIED GEOSCIENCE

J P Heederik, L G H van der Meer, R van der Straaten,
E Elewaut, D Koelewijn, H Cox

UNIVERSITY OF SUNDERLAND

R Harrison, P Doherty

ACKNOWLEDGEMENTS

The British Geological Survey and CRE Group Ltd gratefully acknowledge the support of the UK Department of Trade and Industry Environment Division, through their Energy and the Environment Programme. The TNO Institute of Applied Geoscience gratefully acknowledges the support of Novem, the Netherlands Agency for Energy and the Environment. BRGM gratefully acknowledge the his contribution of the French Ministry of Industry. BGS would also like to thank Dr Chris Franklin of ETSU for contribution to the project, and all participants wish to thank Dr David Savage who was so instrumental in bringing the group together.

The opinions expressed in this report are those of the authors and not necessarily those of the UK Department of Trade and Industry or ETSU.

CONTENTS

CHAPTER 1 – INTRODUCTION 1

- 1.1 The aim of the project 1
- 1.2 Structure of the project 1
- 1.3 Abstract 1

CHAPTER 2 – BACKGROUND 3

- 2.1 An introduction to the greenhouse effect 3
- 2.2 The role of anthropogenic CO₂ in the green-house effect 3
- 2.3 Future CO₂ emission scenarios and future atmospheric CO₂ concentrations 4
- 2.4 Some aspects of the global carbon cycle and its balance 4
- 2.5 Purpose of the study 5
- 2.6 References 5

CHAPTER 3 – QUANTITIES AND QUALITY OF CO₂ WHICH MAY BECOME AVAILABLE FOR DISPOSAL FROM FOSSIL FUEL FIRED POWER PLANT IN THE EUROPEAN UNION AND NORWAY 6

- 3.1 Objectives 6
- 3.2 Most promising power generation options 6
- 3.3 Quantities of CO₂ and location of sources 6
- 3.4 Future predictions 8
- 3.5 CO₂ quality 11
- 3.6 References 13

CHAPTER 4 – INVENTORY OF THE CO₂ STORAGE CAPACITY OF THE EUROPEAN UNION AND NORWAY 16

- 4.1 Introduction 16
- 4.2 Calculating the CO₂ storage capacity 19
- 4.3 The CO₂ storage capacity of Belgium 32
- 4.4 The CO₂ storage capacity of Denmark 35
- 4.5 The CO₂ storage capacity of France 41
- 4.6 The CO₂ storage capacity of Germany 47
- 4.7 The CO₂ storage capacity of Greece 54
- 4.8 The CO₂ storage capacity of Ireland 57
- 4.9 The CO₂ storage capacity of Italy 60
- 4.10 The CO₂ storage capacity of Luxembourg 67
- 4.11 The CO₂ storage capacity of the Netherlands 67
- 4.12 The CO₂ storage capacity of Norway 79
- 4.13 The CO₂ storage capacity of Portugal 85
- 4.14 The CO₂ storage capacity of Spain 85
- 4.15 The CO₂ storage capacity of the United Kingdom 92
- 4.16 Results and conclusions 105

CHAPTER 5 – SAFETY AND STABILITY OF STORAGE 116

- 5.1 Introduction 116
- 5.2 Effects 118
- 5.3 Surface and injection installations 120
- 5.4 The storage reservoir 124
- 5.5 CO₂ leakage and potable groundwater supply 139
- 5.6 Subsurface retention time of escaping CO₂ 151
- 5.7 References 160

CHAPTER 6 – RESERVOIR MODELLING AND ENHANCED OIL RECOVERY (EOR) 163

- 6.1 Objective 163
- 6.2 Background 163
- 6.3 Basic mechanisms for CO₂ disposal in geological formations 163
- 6.4 Reservoir modelling 167
- 6.5 Literature on aquifer disposal 174
- 6.6 Literature on CO₂ injection in oil and gas reservoirs 180
- 6.7 Conclusion and recommendations 181
- 6.8 References 182

CHAPTER 7 – INORGANIC GEOCHEMISTRY 183

- 7.1 Introduction 183
- 7.2 Literature review of inorganic geochemical aspects of the underground disposal of carbon dioxide 183
- 7.3 Construction of dedicated experimental devices and numerical simulators 186
- 7.4 Interpretation of the experiments 205
- 7.5 The Bravo Dome CO₂ field (USA): A natural analogue of carbon dioxide disposal 254
- 7.6 Reservoir-wide predictions 259
- 7.7 Conclusions and recommendations 264
- 7.8 References 272

CHAPTER 8 – TECHNO-ECONOMIC MODELLING OF THE UNDERGROUND DISPOSAL OF CARBON DIOXIDE 00

- 8.1. Introduction 277
- 8.2 Economic methodology 277
- 8.3 Carbon dioxide recovery at the power station 277
- 8.4 Costs of CO₂ avoided at power stations 286
- 8.5 CO₂ transport 290
- 8.6 CO₂ underground disposal 291
- 8.7 Simulation of enhanced oil recovery 293
- 8.8 CO₂ disposal test cases and sensitivity studies 294
- 8.9 Conclusions 298
- 8.10 References 298

Appendix 8A – Economic cost modelling case studies 302

CHAPTER 9 – CONCLUSIONS AND RECOMMENDATIONS 320

- 9.1 Conclusions 320
- 9.2 Recommendations 321

APPENDIX A – TECHNICAL AND ECONOMIC OPTIMIZATION OF CO₂ REMOVED IN AN IGCC POWER PLANT 323

CHAPTER 1

Introduction and abstract

1.1 THE AIM OF THE PROJECT

The purpose of Joule II Project Number CT92-0031 'The Underground Disposal of Carbon Dioxide' is to examine the potential for reducing CO₂ emissions to the Earth's atmosphere from fossil fuel fired power plant by disposing of this CO₂ underground. The report discusses whether this could be done practically, safely and economically, with minimal long term effects on man or the global environment. The report concentrates on the CO₂ disposal process but also includes a detailed study of the technical and economic optimisation of CO₂-removal in a lignite-fired IGCC power plant.

1.2 THE STRUCTURE OF THE PROJECT

The project was structured into six work areas:

Area 1 — Quality and quantity of CO₂ which might become available for disposal in the EU and Norway — led by Mr Iain Summerfield of CRE Group Ltd.

Area 2 — Inventory of CO₂ storage capacity — led by Dr Riex van der Straaten of TNO Institute of Applied Geoscience

Area 3 — Safety and stability of storage — led by Dr Bert van der Meer and Dr Jan Pict Heederik of TNO Institute of Applied Geoscience

Area 4 — Reservoir modelling and enhanced oil recovery — led by Dr Erik Lindeberg of IKU Petroleum Research

Area 5 — Inorganic geochemistry — led by Dr Isabelle Czernichowski-Lauriol of BRGM

Area 6 — Techno-economic modelling — led by Prof. Bob Harrison of Sunderland University

The results of the work in these areas are given in Chapters 3 to 8. Appendix A comprises the detailed study of the technical and economic optimisation of CO₂-removal in a lignite-fired IGCC power plant.

The links between the partners in the production of this report are described below.

Chapter 1 was compiled by BGS from the contributions of all participating organisations. Chapter 2 was written by BGS. Chapter 3 was written by CRE Group Ltd from contributions by CRE Group Ltd, RWE AG and Statoil. Chapter 4 was written mainly by TNO and includes contributions on individual countries by TNO, BRGM, RWE DEA AG, IKU Petroleum Research and BGS. Chapter 5 was written by TNO, with contributions by BGS and BRGM. Chapter 6 was compiled by IKU Petroleum Research from work by IKU Petroleum Research and TNO. Chapter 7 was compiled by BRGM from work by BRGM and BGS. Chapter 8 was written by the University of Sunderland. The project was coordinated by Dr Sam Holloway of the British Geological Survey.

Plenary meetings of all participants, with presentations from each work area, were held at six monthly intervals in order to exchange information between areas and ensure a common approach to all problems. Further meetings of smaller groups were held on a regular basis.

1.3 ABSTRACT

Underground disposal is a perfectly feasible method of disposing of very large quantities of carbon dioxide, such as are produced by fossil fuel fired power plant. All the necessary technological steps are commercially proven. Furthermore, the study of large naturally occurring CO₂ accumulations indicates that CO₂ can be retained in underground reservoirs for millions of years.

The concept is so well established that large scale commercial underground CO₂ disposal will begin in 1996, when Statoil start to dispose of approximately 1 million tonnes of CO₂ a year into the Utsira Formation aquifer above the Sleipner Vest gas field in the centre of the North Sea.

In 1990, approximately 950 million tonnes of carbon dioxide were emitted to the atmosphere from power plant in the European Union and Norway.

Flue gas from today's power plant contains a maximum of about 16% CO₂. It would be both undesirable and impractical to dispose of this flue gas in an untreated state. Firstly, the available storage space would not be big enough to cope with the vast quantities of untreated flue gas. Secondly, it would be undesirable to dispose of the harmless or beneficial atmospheric components, such as nitrogen, which is the largest component by volume of flue gas. Thirdly, there is an overriding thermodynamic argument which prohibits the deep underground storage of untreated flue gas — the work needed to compress it would be a minimum of around 65% of the total work which could be obtained from the power plant. Therefore CO₂ would have to be separated from, or concentrated in, the flue gas.

The energy required to separate CO₂ from power station flue gas decreases the efficiency of power generation. This means that more fuel is used, and therefore more CO₂ is produced, in order to generate the same amount of electricity. So if 90% of the CO₂ generated by a power plant which incorporated CO₂ separation could be captured and disposed of underground, there would be a net CO₂ avoidance of around 85% of the emissions of an equivalent plant without CO₂ separation.

Shallow subsurface storage of CO₂ as a gas or liquid is considered impractical. There is insufficient gas-tight man made void space to store significant quantities of CO₂. The alternative method of storage, disposing of the CO₂ in traps in shallow porous and permeable reservoir rocks, is not practical because they generally have a more important use — for groundwater supply.

Storage in deep porous and permeable reservoir rocks, capped by very low permeability seals, such as clays or shales, is practical. These reservoirs have few uses and, at

typical subsurface conditions, free CO₂ would be in a dense, supercritical phase at depths of around 800 m or more. This would vastly increase the storage per unit volume of reservoir rock compared to storage at shallow depths. Storage could take place in structural or stratigraphic traps, but modelling suggests these would not be necessary; the CO₂ could simply be injected into certain large, thick, essentially horizontal aquifers, for example in the centre of the North Sea, where, on a geological time scale, it would dissolve into the surrounding formation water before it migrated more than a few kilometres towards the basin margins.

We estimate that there is space available in the European Union and Norway to store approximately 800 Gt CO₂. This estimate is highly provisional — in reality the storage capacity of each reservoir is case specific and requires individual modelling. Only gross generalisations can be made for the European Union and Norway as a whole. Nonetheless, it is clear that there is adequate storage space to cope with CO₂ supply from power generation in Europe for the foreseeable future. The bulk of this storage space is offshore, mostly in the North Sea.

There are some risks to man and the environment attached to the underground disposal of CO₂. These could be minimised by appropriate design and monitoring of all stages of the CO₂ transport and disposal process, using best oilfield practice. Pipeline ruptures, or leaks from surface facilities, are possible, although CO₂ is classed as a low hazard material for pipeline transport in the USA today. The other main risks are associated with the storage reservoir. A slow but persistent leak from an unidentified migration pathway out of a storage reservoir is a possibility. This could be a danger or pollutant at the point where the leak reached the surface, or could pollute potable water above or updip from the storage reservoir. There might be a danger of asphyxiation from the highly unlikely event of a catastrophic release of CO₂ from a storage reservoir. Risks associated with the storage reservoir would be much reduced if storage took place offshore.

The injection of CO₂ into a carbonate reservoir will lead to the dissolution of carbonate minerals in the vicinity of the injection wells and the formation water thereabouts will become saturated with respect to carbonate. As the formation water moves away from the injection wells, carbonates could be precipitated as pressure reduces or temperature changes. Thus permeability is likely to be increased significantly around the injection site, but may decrease further away, towards the reservoir margins. There is the possibility that dissolution of carbonate by prolonged injection of CO₂ into a limestone reservoir could eventually cause subsidence around the injection site, particularly when the reservoir pressure around the injection well declines. Injection of CO₂ into sandstone reservoirs is unlikely to cause subsidence. Absidence will not occur providing the reservoir pressure is not allowed to approach or exceed the geostatic pressure.

Injection of CO₂ into a sandstone reservoir will cause dissolution of feldspars and subsequent precipitation of clays, carbonates and quartz (or another silica phase). The buffering power of aluminosilicate reactions will favour CO₂ uptake in the formation water by the formation of bicarbonate ions and complexes. Calcite precipitation could ensure (permanent) fixing of carbon via reaction of CO₂ with Ca-rich minerals or formation fluids.

Shale and anhydrite caprocks sealing the storage reservoirs are not likely to be greatly affected by CO₂/water/rock reactions.

The underground storage of CO₂ may result in the mobilisation of trace elements from oils or heavy minerals encountered in the reservoir, due to the complexing power of bicarbonate and thiocarbonate and to the solvent properties of supercritical CO₂.

The costs of CO₂ separation are between 25 and 65 Ecu per tonne of CO₂ avoided, depending on the type of power plant selected. CO₂ recovery from a purpose built integrated gasification combined cycle (IGCC) plant with CO₂ separation is the least expensive option. The costs of CO₂ transport are variable depending principally on the length and diameter of the pipeline selected. They range up to about 14.5 Ecu/tonne of CO₂ avoided in our modelled scenarios. The costs of the underground disposal process alone are around 1 to 2.25 Ecu per tonne of CO₂ avoided. Modelling of CO₂ disposal combined with enhanced oil recovery indicates that if large volumes of CO₂ can be used to recover oil which would otherwise be produced in other locations, then cost credits from the sale of the produced oil could totally defray the costs of CO₂ recovery at power stations, resulting in CO₂ avoidance at near zero cost.

The next major step in implementing CO₂ disposal from power plant should be the demonstration of the disposal process. Any demonstration project which started from scratch would be extremely expensive. The Sleipner Vest and Natuna Sea commercial CO₂ disposal projects are essentially large scale demonstrations of the practicality of the underground disposal of carbon dioxide. As such they present an unparalleled opportunity for further research into underground disposal. Any form of collaborative research with the operators of the above schemes would be extremely valuable scientifically and a cost-effective way to verify the findings of this report.

Our primary recommendation is that the European Commission should approach Statoil and Exxon with a view to collaborating scientifically on the Sleipner Vest and Natuna Sea CO₂ disposal projects respectively.

Additionally we believe further research is required in the following areas:

1. Geochemical modelling and reservoir simulation of the disposal of carbon dioxide into offshore formations, preferably in the North Sea, without the need for a conventional fluid trap. This would require detailed geological data from the chosen formations. It would lead to a refined estimate of the storage potential of the North Sea and a more detailed concept of disposal into such formations.
2. Further geochemical experiments and modelling to determine more precisely the effects of CO₂ on the permeability, porosity and stability of reservoir and cap rocks.
3. Construction of a two-phase flow reaction-transport reservoir simulator. This could be achieved by coupling a two phase flow reservoir simulator with the geochemical reaction-transport simulator developed for this project. It would enable simulation of the migration of supercritical CO₂ and water through a carbonate or sandstone reservoir and prediction of the geochemical changes that will occur with their effect on porosity and permeability. This will allow us to predict, for example, the amount of CO₂ which will dissolve in the formation water of the modelled reservoir and the amount of CO₂ which will be fixed by carbonate-precipitating CO₂/water/rock reactions. Such a code should also enable optimisation of the design and operating conditions of the disposal operations.

CHAPTER 2

Background

S Holloway, British Geological Survey

2.1 AN INTRODUCTION TO THE GREENHOUSE EFFECT

Our planet is warmed by a natural greenhouse effect. The Earth's surface absorbs incoming short wavelength solar radiation in the visible spectrum and, in response, emits longer wavelength infra red radiation. Trace gases in the atmosphere, known as greenhouse gases, absorb certain frequencies of this infra red and reradiate it. The downward component of this radiation warms the Earth's lower atmosphere and surface, whilst the upward component is lost into space. This effect has been demonstrated by satellite observations of the outgoing radiation from the Earth and by the observed relationships between the surface temperatures and atmospheric compositions of Venus and Mars (Thurlow, 1990). Without this natural greenhouse effect the mean annual temperature on Earth would be about -6°C instead of about $+15^{\circ}\text{C}$ (Houghton, 1994).

CO_2 is a greenhouse gas. Man-made CO_2 emissions thus contribute to an anthropogenic, or enhanced, greenhouse effect. Physically, there is no doubt that if all other factors remained equal, the increased levels of CO_2 in the atmosphere which result from man's activities would increase the natural radiative heating of the Earth's surface and lower atmosphere. Indeed the physical effect on the Earth's radiative balance of increasing the CO_2 content of the atmosphere can readily be calculated. For example, the direct effect of a doubling of atmospheric levels of CO_2 would be a warming of just over 1°C at the Earth's surface (Thurlow, 1990). Thus the key question is not whether man-made CO_2 emissions will cause an enhanced greenhouse effect, but how will this affect the Earth? Will natural negative feedback mechanisms ameliorate or counteract the anthropogenic greenhouse effect, or will climatic warming occur — perhaps reinforced by positive feedback mechanisms?

Both positive and negative feedback mechanisms are known to operate in today's climate. But their existing complex inter-relationships could alter in a warmer world, and new feedback mechanisms could be triggered (see Leggett, 1990 for a summary). As a single example, the water vapour feedback mechanism, which operates in today's climate, is likely to be enhanced in a warmer world. Higher temperatures mean an increase in evaporation, which leads to an increase in water vapour in the atmosphere. All other factors being equal, this will produce an additional greenhouse effect which has been calculated to enhance the direct physical effect of a doubling of atmospheric CO_2 levels by anything between 0.5°C and 3.5°C (Thurlow, 1990). However, the relationship between increased water vapour in the atmosphere and changes in cloud cover, cloud type, cloud altitude and precipitation is poorly understood. At present, clouds have a net cooling effect on the lower atmosphere; they reflect more heat than they trap. But the balance between their warming and cooling properties varies with cloud type and altitude, which could alter as temperature rises. Such unknowns

mean that, as yet, climate modelling does not provide conclusive evidence that the addition of anthropogenic greenhouse gases to the atmosphere is causing, or will cause, climatic warming.

For these and other reasons, predictions of the climatic warming which could be caused by the increased concentrations of anthropogenic greenhouse gases in the atmosphere contain a large degree of uncertainty. However, the scientific assessment of the International Panel on Climate Change (WMO/UNEP, 1990) is that in a business as usual scenario, global mean temperature is likely to be about 1°C higher in 2025 than now and about 3°C higher than now by the end of the 21st century. In other words, they believe that anthropogenic greenhouse gases *will* cause a historically unprecedented global warming in the next century.

Global temperatures have already risen by 0.3 to 0.6°C this century. Whilst this is consistent with anthropogenically induced global warming, it is also within the bounds of normal climate variability. At present we cannot separate the two effects with certainty. Nonetheless, 1990 was the warmest year since records began in 1860, and all but one of the 11 warmest years on record have occurred since 1980.

It is beyond the scope of this report to speculate as to the likely implications of an unprecedented global warming. However, Woodwell (1990) suggests that the single most important implication of anthropogenic global warming is that the predicted climate change could occur an order of magnitude faster than the most rapid climate changes of the recent geological past. This may have profound consequences on the ability of organisms and ecosystems to respond. Many ecosystems may change fundamentally. The response of animals to adverse climate change is, initially, to migrate to more favourable climates (Huntley, 1990). In the past this was possible for man, but in the future it is quite possible that national borders, now commonly heavily defended, will be closed to climate refugees, possibly with disastrous implications for the affected populations.

2.2 THE ROLE OF ANTHROPOGENIC CO_2 IN THE GREENHOUSE EFFECT

Most of the natural greenhouse effect is known to be caused by water vapour and carbon dioxide in the atmosphere (Schonwiese, 1992). However, water vapour is not classed as an anthropogenic greenhouse gas. The amount of water vapour in the atmosphere depends essentially on its temperature.

This is not the case with CO_2 however. As a result of man's activities, the concentration of CO_2 in the atmosphere had risen from a relatively stable level around 275 ppmv in the pre-industrial era to about 315 ppmv when measurements started at Mauna Loa in Hawaii in 1958. Since then it has risen to about 355 ppmv (Houghton, 1994). It continues to rise, currently at rates of about 1.8 ppmv per year.

CO₂ emissions are conventionally expressed as tonnes of carbon as CO₂. However, in this study we have expressed them as tonnes of CO₂ as the report deals mainly with the disposal of carbon dioxide, rather than directly with the greenhouse effect. One tonne of CO₂ contains approximately 0.273 tonnes of carbon. Annual anthropogenic emissions of CO₂ are currently thought to be about 6.43 gigatonnes (= Gt, = 10⁹ tonnes) of carbon as CO₂ (Subak et al., 1993), equivalent to about 23.5 Gt CO₂. Approximately 19.8 Gt CO₂ (85% of net CO₂ release) comes from energy, 13% from land use changes and 2% from cement manufacture (Subak et al., 1993). The major contributor is fossil fuel combustion, which, in 1984, contributed some 18.7 Gt (Smith, 1988; Thurlow, 1990) or approximately 80% of the anthropogenic atmospheric CO₂.

Although, molecule for molecule, carbon dioxide is one of the least powerful anthropogenic greenhouse gases (Smith, 1988), it has the greatest global warming potential because it is emitted to the atmosphere in such vast quantities. It is probably responsible for about 56% of the anthropogenic greenhouse effect at present (Smith, 1988). The other main contributors are, in descending order, CFC's, methane, nitrous oxide and ozone. It has been estimated that a reduction of at least 60% in CO₂ emissions would be required to stabilise global atmospheric CO₂ at today's levels (WMO/UNEP, 1990).

2.3 FUTURE CO₂ EMISSION SCENARIOS AND FUTURE CO₂ CONCENTRATIONS IN THE ATMOSPHERE

It is impossible to be certain what the major sources of CO₂ emissions will be in the medium term future (say in the year 2020). This is because they depend largely on unpredictable political, technical and sociological developments. However, the investment which has been made in existing infrastructure means that the most likely scenario is that fossil fuels will be supplying the major part of the world's energy needs well into the next century (Smith, 1988). As fossil fuels continue to be exploited at high rates, CO₂ levels in the atmosphere will continue to rise — unless we take action on emissions.

Forecasts of global energy demand and supply and future CO₂ emissions into the distant future (i.e. 2050 and beyond) are less certain still. However, on the positive side, the presence of uncertainty in the forecasts is largely due to the fact that we have the freedom to choose between different strategies for energy supply (Smith, 1988). We are not committed to a fossil fuel fired world in the long term.

Despite these caveats, long term forecasts of future CO₂ concentrations in the atmosphere have been made. They indicate that CO₂ concentrations are unlikely to reach double the pre-industrial level before the middle of the next century, and may not double until after the year 2100 (Smith, 1988).

2.4 SOME ASPECTS OF THE GLOBAL CARBON CYCLE AND ITS BALANCE

Carbon is cycled around the globe between the geosphere (rocks and unconsolidated sediments), the terrestrial biosphere (plants, animals, soils), the atmosphere, and the oceans. It is the *balance* between the amounts of carbon in

these domains which determines the amount of CO₂ in the atmosphere.

The geosphere contains 99.94% of all the carbon on Earth. This is largely as carbonate and carbonaceous rocks (e.g. limestone, carbonaceous shales and, in much smaller quantities, fossil fuels). A proportion of this carbon is slowly cycled between the geosphere and the atmosphere and oceans as a result of the processes of weathering and erosion, which remove carbon from the atmosphere, and vulcanicity, which adds it to the atmosphere. As the vast bulk of all the carbon on Earth is in the geosphere, a small change in the balance between weathering and erosion and vulcanicity can have a large effect on the levels of carbon in the atmosphere.

During weathering, atmospheric carbon dioxide reacts with atmospheric water to produce a weak carbonic acid. This falls as rain, which reacts with the siliciclastic minerals in rocks to produce bicarbonate ions, which are then transported by rivers into the ocean. Thus an increase in the rate of weathering and erosion relative to volcanic outgassing of carbon gases from the Earth's interior will lower carbon dioxide levels in the atmosphere. This may be a very significant process over what are, in human terms, very long, but in geological terms, intermediate, timescales. Raymo et al. (1988) have proposed that increasing rates of uplift in the Himalayas, Andes and Tibetan Plateau have led to a significant increase in the global rate of chemical weathering since late Miocene times. Raymo (1991) suggests that this has lowered atmospheric CO₂ concentrations and could have triggered the appearance of the ice ages which have affected the northern hemisphere since Pliocene times.

In the terrestrial biosphere, exchange of carbon with the atmosphere occurs as a result of biomass growth and decay. The net sedimentation of organic matter to produce fossil fuels, principally coal, gradually withdraws carbon from the atmosphere, via the terrestrial biosphere into the geosphere. Changes in land use affect the amount of carbon stored in the terrestrial biosphere at any one time. Deforestation and the ploughing of virgin land both release CO₂ to the atmosphere. Afforestation has the opposite effect.

The concentration of CO₂ in the atmosphere equilibrates readily with that in the surface layers of the ocean, and their CO₂ levels can be regarded as being in equilibrium. However, the deep ocean is undersaturated with CO₂ compared to the atmosphere. It represents a huge potential sink, sufficient to absorb all anthropogenic CO₂ emissions. However, since there is only very slow exchange of surface waters and deep waters within the ocean, it is the rate of exchange between the surface and deep waters of the ocean which dictates the pace at which atmosphere - whole ocean equilibration occurs (Wilson, 1992).

The circulation of the world's oceans is characterised by the sinking at high latitudes of surface water which has become denser by cooling as it flows towards the poles. This water is then circulated throughout the interconnected deep ocean basins. Upward mixing of this circulating water occurs as a result of upwelling currents, which mostly originate at intermediate depths in low latitudes. Assuming that this circulation system remains essentially unaltered, the carbon pools of the ocean and atmosphere will become mixed on a timescale appropriate to this circulation. This timescale is thought to be in the order of a thousand years (Wilson, 1992).

Thus, all other factors being equal, and assuming the fossil fuel consumption proceeds at high rates until fossil

fuels are no longer competitive in price, the burning of fossil fuel reserves will produce a transient peak in atmospheric CO₂ levels. This will probably reach a maximum in the next couple of centuries (this being the period when we are most likely to burn the bulk of our fossil fuel reserves), and then fall over a period of several hundred years, before a new (higher than pre-industrial) level of equilibrium is reached as a result of ocean-atmosphere re-equilibration.

It is not possible to determine the likely post-fossil fuel equilibrium level of atmospheric CO₂ because of the feedbacks that may be involved. Global sources and sinks of carbon are themselves liable to be affected by climate change and increases in global carbon fluxes. For example, the warming of the surface layers of the world's oceans will decrease their capacity to take up CO₂. Conversely, the lowering of pH of oceanic waters is very likely to cause dissolution of calcite on the sea bed. This will lower the CO₂ concentration in the ocean, which is likely to decrease significantly the final equilibrium level of CO₂ in the atmosphere (Wilson, 1992).

Man has already intervened in the natural carbon cycle, largely by burning fossil fuels from the geosphere, causing CO₂ levels to rise in the atmosphere. Clearly, there is potential for man to intervene again and deposit anthropogenic CO₂ in the other domains of the planet; the geosphere, terrestrial biosphere or oceans, instead of the atmosphere.

2.5 PURPOSE OF THE STUDY

Although we realise that there is potential for a greenhouse crisis, we do not know for certain that it will occur, how grave it will be, or how it would rate amongst global priorities when at its height. However, if we want to stabilise global levels of atmospheric CO₂, we need to make plans now to take action in the near future, rather than wait for levels to rise further. The inertia of the system means that we are always committed to a greater warming potential than at the point where emissions are reduced. We therefore need to research ways in which CO₂ emissions realistically could be mitigated; i.e. without profound changes to our way of life.

Given the global drive to raise living standards, and the projected rise in the world's population, it is likely that global energy demand will continue to rise for the foreseeable future. Current uncertainties about nuclear power, the low global market share of renewable energy, and the existing power generation infrastructure, suggest that in the next few decades at least, a high proportion of the demand for electricity will be satisfied by fossil fuel fired power generation. One way of reducing CO₂ emissions without radically altering our use of fossil fuels for power generation could be to dispose of CO₂ from power station flue

gases underground. This would return the CO₂ to the geosphere rather than emitting it to the atmosphere. The purpose of this study is to determine whether this could be done practically, safely and economically, with minimal long term effects on man or the global environment.

Electricity generation contributes about 30% of global emissions from fossil fuel consumption (Thurlow, 1990) and thus about 24% of total global anthropogenic CO₂ emissions. So CO₂ disposal from thermal power plant could make significant inroads into anthropogenic CO₂ emissions.

The study focuses on the possibilities for the underground disposal of CO₂ from power plant in Europe as the necessary detailed information on the geology, power supply and emissions is available for this area. However, many of the principles outlined are generic rather than area specific, and have global application.

2.6 REFERENCES

- HOUGHTON, J T. 1994. *Global warming: the complete briefing*. Lion Publishing plc, Oxford, England.
- HUNTLEY, B. 1990. Lessons from climates of the past, 133–148 in: LEGGETT, J K (editor) *Global Warming — The Greenpeace Report*. Oxford University Press, Oxford, UK, 554pp.
- LEGGETT, J K. 1990. The Nature of the Greenhouse Threat, pp.14–43 in: LEGGETT, J K (editor) *Global Warming — The Greenpeace Report*. Oxford University Press, Oxford, UK, 554pp.
- RAYMO, M E. 1991. Geochemical evidence supporting T C Chamberlin's theory of glaciation. *Geology*, **19** (4), 344–347.
- RAYMO, M E, RUDDIMAN, W F, and FROELICH, P N. 1988. Influence of late Cenozoic mountain building on ocean geochemical cycles. *Geology*, **16** (7), 649–653.
- SCHONWIESE, C-D. 1992. Recent developments in scientific knowledge on climate change. *Energy Conversion and Management*, **33** (5-8), 297–304.
- SUBAK, S, RASKIN, P, and Von HIPPEL, D. 1993. National greenhouse gas accounts: Current anthropogenic sources and sinks. 15–57.
- THURLOW, G (editor). 1990. *Technological responses to the Greenhouse Effect*. Watt Committee Report No. 23, Elsevier, London, 98pp.
- WMO/UNEP. 1990. *Scientific Assessment of Climate Change*. Working Group 1 Report of the Intergovernmental Panel on Climate Change, WNO, Geneva.
- WILSON, T R S. 1992. The deep ocean disposal of carbon dioxide. *Energy Conversion and Management*, **33** (5-8), 627–634.
- WOODWELL, G M. 1990. The effects of Global Warming, pp.116–132 in: LEGGETT, J K (editor) *Global Warming — The Greenpeace Report*. Oxford University Press, Oxford, UK, 554pp.

CHAPTER 3

Area 1 Quantities and quality of CO₂ which may become available for disposal from fossil fuel fired plant in the European Union and Norway

Iain Summerfield (CRE Group Ltd)
Jochen Putter (RWE Energie AG)
Olav Kaarstad, Bjorn Berger (Statoil)
Thomas Schwarzkopf (RWE AG)

3.1 OBJECTIVES

This chapter of the report determines the quantity of CO₂ produced from European fossil fuel fired power plant and the general geographical location of European fossil fuelled power plant. It estimates how these CO₂ emission sources may change over the period 1990–2020 and it determines the likely trace contaminants in the CO₂ which could be separated from power plant flue gas streams. Thus it gives an indication of the current and possible future scale of the CO₂ disposal issue in the European Union and Norway. It also provides data on the amounts of CO₂ which are likely to be made available for disposal from both existing fossil fuel fired power plant and power plant which are either under development or at the concept stage.

3.2 MOST PROMISING POWER GENERATION OPTIONS

The thermal efficiency of a number of coal-fired power systems was estimated using CRE Group Ltd's ARACHNE process simulation system to determine the reduction in efficiency which would occur if a CO₂ separation stage was introduced to remove 90% of the CO₂. This allowed the selection of the most promising options for follow-on costing studies and cost comparison with natural gas-fired plant. For the purposes of this comparison a consistent set of assumptions had to be made. It was assumed that state of the art sulphur recovery would be included in the power plant, in addition to other environmentally necessary features. It was also assumed that the CO₂ product would be as a liquid at 10°C and 136 bar (2000 psi). These conditions were adopted so that the energy required to prepare CO₂ for disposal would be included in the efficiency calculations.

The coal fired power generation technologies into which the integration of CO₂ recovery has been considered, include:

- conventional pulverised fuel (PF) combustion to drive a steam turbine;
- a novel process in which coal is burnt in oxygen and recycled flue gas to raise steam for a turbine;
- an Integrated Gasification Combined Cycle (IGCC) scheme.

The gas-fired technology considered was a natural gas combined cycle plant.

The results of this analysis showed that, among the coal-fired schemes, the IGCC plant had the highest power generation efficiency and therefore the lowest cost. Because of this, it is likely that CO₂ separation would be applied to this type of power plant first. IGCC was first demonstrated in the early 1980's in California. IGCC technology is being seriously considered in 21 countries and 8 of these countries have plans to build a total of 18 IGCC plants. Whilst the individual components of an IGCC with CO₂ removal have been demonstrated at commercial scale, the overall system has not. A fuller analysis of IGCC with CO₂ removal has been carried out as part of this study and is described in Appendix A.

3.3 QUANTITIES OF CO₂ EMISSIONS AND LOCATION OF SOURCES

In 1990 the energy-related emissions of CO₂ from the European Community (EC) totalled 3042 million tonnes. Table 3.1 shows that a total of 950.6 million tonnes of that CO₂ emission — the largest proportion at 31.2% — is from power generation sources. Furthermore, the inherent nature of power generation leads to a relatively small number of very large localised sources of CO₂ emission. Therefore, power plant are the obvious choice for the consideration of CO₂ separation and disposal.

The quantity of CO₂ produced in 1990 from thermal power plants throughout the then twelve member states of the EC (Belgium, Denmark, France, Germany, Greece, Italy, Ireland, Luxembourg, Netherlands, Portugal, Spain and UK) and Norway has been estimated from published data. This was derived from the known fuel use in power generation for each country, assuming that the total carbon content of the fuel is converted to CO₂. It should be noted that separating and disposing of CO₂ results in increased

Table 3.1 European Community CO₂ Emissions by Sector in 1990.

	Million Tonnes CO ₂	%
Power Generation	950.6	31.2
Energy Sector	129.5	4.3
Industry	601.1	19.8
Transport	707.5	23.3
Domestic & Tertiary	653.6	21.5
Total	3042.3	100.0

energy use in the power plant. For an IGCC, this results in an increase in fuel use of 25 to 30%, and a consequent increase in CO₂ emissions. These increased CO₂ emissions are not included in Table 3.1.

Published and in-house data were used to determine the geographical location of fossil fuel fired power plant in Europe. These data were used in conjunction with data from other parts of the programme to determine the most likely locations for CO₂ removal and disposal. It should be noted that, as most of these power plants use pulverised coal technology, they are not the most suitable for the integration of CO₂ removal and disposal. However, it can be assumed that if new IGCC plants were built to replace these plants, the locations chosen would be close to the plants that they were replacing.

A number of ground rules were set to ensure that the emissions assessments were carried out on a consistent basis. The ground rules are:

Year of estimate	1990
Power plant size	>100 MW _e
European Countries	Belgium, Denmark, France, Germany, Greece, Italy, Ireland, Luxembourg, Netherlands, Norway, Portugal, Spain, UK
Power plant fuels	Coal, oil, natural gas
Emission factors	— brown coal 1.18 kg CO ₂ /kWh — hard coal 0.97 kg CO ₂ /kWh — oil 0.85 kg CO ₂ /kWh — natural gas 0.53 kg CO ₂ /kWh

The data on power generation and associated CO₂ emissions for the 13 European countries in 1990 are summarised in Table 3.2. The data are also shown graphically in Figures 3.1 and 3.2, and superimposed onto a map of Europe in Figure 3.3. From these figures it can be seen that the three largest emitters of CO₂ from power plant are Germany, United Kingdom and Italy. Whilst France is the second greatest power producer in Europe, its large nuclear capacity means that French CO₂ emissions from electricity production are relatively low.

Despite giving an accurate estimate of the total CO₂ emission from power generation sources (i.e. fossil fuel power plant) for the countries in question, this data does not provide the geographical distribution of those CO₂ emission sources. The first step in determining the geographical distribution was to pinpoint the location of each power plant to identify those close to potential CO₂ disposal sites. The second step was to estimate the CO₂ emission from each power plant to complete the picture of CO₂ emission quantity and location. This was achieved using the known electrical output and assumed efficiency for each power plant.

Figure 3.1 European Power Production 1990.

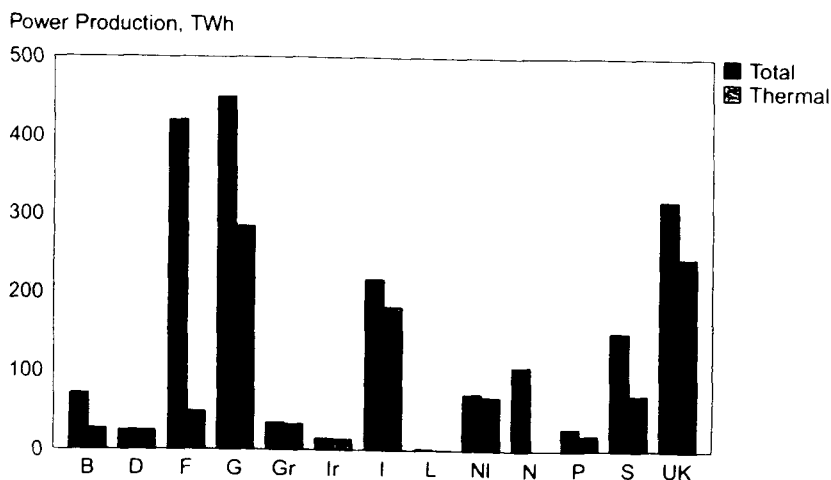


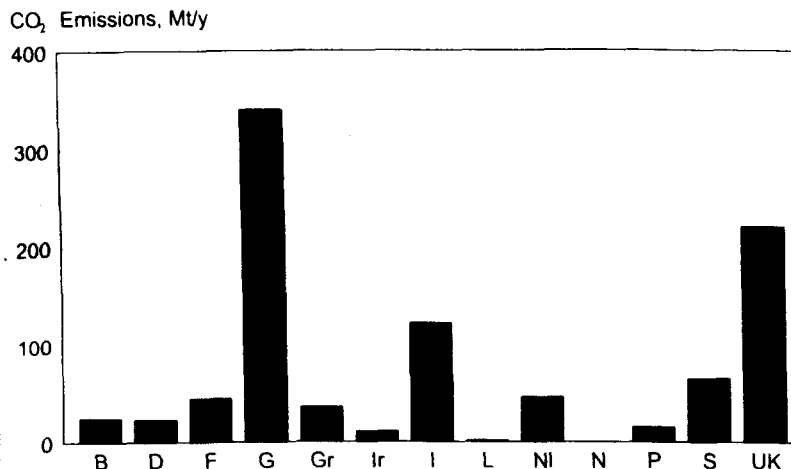
Table 3.2 CO₂ Emissions from Power Generation in 1990.

Country	Electricity Production TWh	Thermal Power Production TWh	CO ₂ Emissions MtCO ₂ (1990)
Belgium	70.85	27.21	24.6
Denmark	25.75	25.08	23.0
France	420.16	48.14	44.4
Germany	449.49	283.92	340.6
Greece	35.00	33.00	35.8
Ireland	14.52	13.53	11.0
Italy	216.89	181.78	122.7
Luxembourg	1.38	0.56	1.5
Netherlands	71.87	68.19	45.8
Norway	106.00	—	0.1
Portugal	28.50	19.20	15.2
Spain	150.62	70.17	64.4
United Kingdom	318.98	246.13	220.9
EC (Total)	1803.99	1016.91	950.0

The use of an assumed plant efficiency makes this method less accurate than using fuel conversion data - which is far more difficult to ascertain on an individual plant basis. Also, the omission of power plant of less than 100 MW size from that part of the study (as CO₂ removal would be less viable and more costly for smaller power plant) inevitably leads to an underestimate of total CO₂ emissions from power plants. Therefore, the national fuel conversion figures should be used for a more accurate estimate of the total CO₂ emissions, and the power plant figures to give a better indication of the geographical distribution of actual emission sources.

Published data have been used to determine the geographical location of fossil fuel fired power plant in Europe. Maps of power station locations have been prepared for each country (Figures 3.4 to 3.12), and they were collated onto a map of the region as a whole (Figure 3.13). The location maps are complete for Denmark, Germany, Greece, Netherlands, Spain and UK and include at least the coal-fired plant for the other countries. In addition, estimated CO₂ emissions for each power station are provided for Germany, Greece, Netherlands and Spain (Table 3.3)^{5,6,7,8}. A provisional list of power plant in the remaining nine countries has also been prepared based on information from International Energy Data 1992. These are shown in Table 3.4.

Figure 3.2 European CO₂ Emissions from Power Production 1990.



3.4 FUTURE PREDICTIONS

Projections for changes to the electricity generating sector to 2020 are not readily available. Even shorter term predictions (e.g. 2000, 2005 or 2010) are surrounded by a considerable degree of uncertainty. This uncertainty is increased by a number of factors:

- The uncertainties in predicting the economic growth rate, and hence energy demand. There will also be local variations within and between the countries in question, with a corresponding effect on the fuel (and hence CO₂ emission) used for the increased power generation.
- Energy efficiency. Even if economic growth increases, the demand for energy can decrease if energy efficiency measures are widely adopted.
- Fuel mix uncertainties. These include the continuing uncertainty over the future of nuclear power, the potential rise in renewable energy, and the switch from coal to natural gas in response to a carbon tax or other environmental/cost pressures.
- The effect of changes in CO₂ emissions from other sources, such as transport. The total emission of CO₂ is the important factor in determining its effect on the environment, not its source. Therefore, there could be more urgent calls for CO₂ reduction from power generation in response to a rise in the total CO₂ emissions, irrespective of the contribution of power generation CO₂ to the total (due to the small number of large plant required to be modified to make a significant reduction in emissions).
- The imposition of government regulations to limit CO₂ emissions. In signing the Framework Convention on Climatic Change at the United Nations Conference for Environment and Development (UNCED) in Rio de Janeiro, the EU and its member states made a commitment to stabilise CO₂ emissions by 2000 at 1990 level in the Union as a whole¹.

Following the signing of the Framework Convention, the EU proposed a number of initiatives to limit CO₂ emissions and to improve energy efficiency. These are listed below:

- The promotion of renewable energy sources (ALTENER programme).
- The improvement of energy efficiency (SAVE programme).
- A monitoring mechanism for CO₂ and other greenhouse gases.
- A tax on carbon dioxide emissions and energy.
- The prospect of government intervention in the energy market for domestic reasons (for example through support of indigenous coal industries).

Table 3.3 Fossil Fuel-Fired Power Stations In Europe.

Plant Name	Fuel Type	Gross Capacity (MW)
GERMANY (1991 figures)		
1	Boxberg	Brown Coal 3520
2	Buschhaus	Brown Coal 350
3	Chemnitz-Nord 2	Brown Coal 177
4	Dresden	Brown Coal 110
5	Finkenheerd	Brown Coal 109
6	Frimmersdorf	Brown Coal 2400
7	Goldenberg	Brown Coal 530
8	Hagenwerder	Brown Coal 1200
9	Hirschfelde	Brown Coal 155
10	Janschwalde	Brown Coal 3000
11	Klingenberg	Brown Coal 180
12	Lippendorf	Brown Coal 600
13	Lübbenau	Brown Coal 1300
14	Neurath	Brown Coal 2100
15	Niederaussem	Brown Coal 2700
16	Offleben	Brown Coal 525
17	Schwandorf	Brown Coal 500
18	Thierbach	Brown Coal 840
19	Vetschau	Brown Coal 1200
20	Weisweiler	Brown Coal 2200
21	Aschaffenburg	Hard Coal 300
22	Bergkamen	Hard Coal 743
23	Bexbach	Hard Coal 750
24	Datteln	Hard Coal 290
25	Ensdorf	Hard Coal 532
26	Farge	Hard Coal 356
27	Flensburg	Hard Coal 170
28	Flingern	Hard Coal 120
29	Frankfurt	Hard Coal 139
30	Hannover	Hard Coal 292
31	Heyden	Hard Coal 800
32	Ibbenbüren	Hard Coal 745
33	Kellermann	Hard Coal 200
34	Kiel (Förde)	Hard Coal 350
35	Knepper	Hard Coal 370
36	Lübeck-Siems	Hard Coal 125
37	Mainz I	Hard Coal 285
38	Moabit	Hard Coal 155
39	Rauxel	Hard Coal 175
40	Reuter	Hard Coal 832
41	Rudow	Hard Coal 175
42	Shamrock	Hard Coal 142
43	Tiefstack	Hard Coal 187
44	Voerde	Hard Coal 1420
45	Wedel	Hard Coal 481
46	Wehrden	Hard Coal 112

Table 3.3 Continued.

Plant Name	Fuel Type	Gross Capacity (MW)
47 Westerholt	Hard Coal	300
48 Westfalen	Hard Coal	672
49 Ahrensfelde	Gas	114
50 Barmen	Gas	106
51 Ermden	Gas	450
52 Ermsland	Gas	840
53 Gaisburg	Gas	195
54 Gersteinwerk	Gas	840
55 Hagen-Kabel	Gas	220
56 Herrenhausen	Gas	100
57 HKW Merkenich	Gas	141
58 Huckingen	Gas	600
59 Huntorf	Gas	292
60 Kirchlengern	Gas	162
61 Linden	Gas	165
62 Meppen	Gas	600
63 Mittelsbüren	Gas	258
64 Müchen-Freimann	Gas	162
65 Niederrad	Gas	128
66 Niehl	Gas	315
67 Robert Frank	Gas	820
68 Thyrow	Gas	300
69 Brunsbüttel	Oil	272
70 Gera-Nord	Oil	150
71 Hausham	Oil	100
72 Ingolstadt	Oil	1100
73 Irsching	Oil	930
74 Marbach	Oil	320
75 Pleinting	Oil	725
76 Vockerode	Oil	546
77 Wilmersdorf	Oil	280
78 Afferde	Mixed	129
79 Altbach	Mixed	990
80 Arzberg	Mixed	457
81 Charlottenburg	Mixed	385
82 Dettingen	Mixed	100
83 Duisburg	Mixed	479
84 Elberfeld	Mixed	102
85 Franken	Mixed	1243
86 Hafen	Mixed	657
87 Hastedt	Mixed	300
88 Heilbronn	Mixed	1278
89 HKW Süd/Nord/West	Mixed	641
90 HKW West	Mixed	122
91 Lausward	Mixed	907
92 Leiningerwerk	Mixed	500
93 Lichterfelde	Mixed	450
94 Mannheim	Mixed	1830
95 Mehrum	Mixed	912
96 Moorburg	Mixed	1133
97 München Süd	Mixed	530
98 Nord	Mixed	350
99 Oberhavel	Mixed	200
100 Rheinhafen	Mixed	1010
101 Römerbrücke	Mixed	120
102 Sandreuth	Mixed	110
103 Scholven	Mixed	3648
104 Staudinger	Mixed	1550
105 Stuttgart-Münster	Mixed	170
106 Veltheim	Mixed	860
107 Walheim	Mixed	387
108 Werdohl-Elverlingsen	Mixed	721
109 Werne	Mixed	765
110 Wilhelmshaven	Mixed	770
111 Zschornewitz	Mixed	487

SPAIN (1990 figures)			
1 Escucha		Brown Coal	175
2 Meirama		Brown Coal	550
3 Puentes		Brown Coal	1400
4 Serch		Brown Coal	175
5 Teruel		Brown Coal	1050
6 Abono		Hard Coal	903
7 Anllares		Hard Coal	350
8 Compostilla		Hard Coal	1312
9 Guardo		Hard Coal	498
10 La Robla		Hard Coal	625
11 Lada		Hard Coal	505
12 Litoral de Almeria		Hard Coal	550
13 Los Barrios		Hard Coal	550
14 Narcea		Hard Coal	569
15 Pasajes		Hard Coal	214
16 Puente Nuero		Hard Coal	388
17 Soto de Ribera		Hard Coal	672
18 Aceca		Oil	327
19 Algeciras		Oil	753
20 Badalona		Oil	344
21 Cadiz		Oil	138
22 Besos		Oil	450
23 Candelaria		Oil	332
24 Castellon		Oil	1083
25 Cristoba		Oil	378
26 Escombreras		Oil	858
27 Ibiza		Oil	110
28 Jinaman		Oil	416
29 Malaga		Oil	122
30 Almeira		Oil	113
31 Sabon		Oil	470
32 San Andrian		Oil	1050
33 San Juan de Dios		Oil	195
34 Santurce		Oil	936
35 Akudia		Mixed	325
36 Foix		Mixed	520
37 Puertollano		Mixed	220
GREECE (1990 figures)			
1 Amyntaion		Brown Coal	600
2 Kardia		Brown Coal	1200
3 Megalopolis		Brown Coal	850
4 Ptolemais		Brown Coal	620
5 Demetrius		Brown Coal	1200
NETHERLAND (1991 figures)			
1 Bergum		Gas	664
2 Clauscentrale		Gas	1278
3 Diemen		Gas	368
4 Donge		Gas	121
5 Dordrecht		Gas	317
6 Ecms, Emshven		Gas	695
7 Flevo		Gas	884
8 Galoleistraat		Gas	370
9 Harculo		Gas	689
10 Hemweg		Gas	866
11 Hengelo		Gas	102
12 Hunze		Gas	517
13 Lage Weide		Gas	394
14 Merwedekanaal		Gas	426
15 Velsen		Gas	846
16 Waalhaven		Gas	664
17 Amer		Mixed	1919
18 Borcula		Mixed	870
19 Gelderland		Mixed	602
20 Maascentrale		Mixed	400
21 Maasvlakte		Mixed	1036

Figure 3.3 European Thermal Power Production and resulting CO₂ Emission 1990.

Clearly, these factors make predictions difficult, particularly for longer terms. In DG XVII's 1990 report "Major Themes in Energy Revisited", four alternative scenarios were used to show the effect of a number of alternative strategies on the prediction of energy use and CO₂ emission to 2010.

The scenarios were:

Scenario 1 — Business As Usual. This includes the integration of the European market and "conventional wisdom" on economic growth and oil prices, but no major policy changes.

Scenario 2 — Increased Economic Growth. In this scenario, the economic growth rate was increased from 2.7% to 3.5% between 1990 and 2000 to reflect a more favourable international situation and the benefits derived from the completion of the internal market in Europe.

Scenario 3 — Protecting the Environment. The aim of this scenario was to reconcile the competing objectives of sustaining high economic growth, secure supplies of moderately priced energy and protecting the environment. This was to be achieved by a rapid increase in energy efficiency after the turn of the century accompanied by a significant increase in nuclear power and gas-fired units substituting for coal-fired plants.

Scenario 4 — Protecting the Environment, with more moderate growth. The same efficiency gains as scenario 3 combined with a more moderate economic growth and higher end user prices.

The results of the projections based on these four scenarios are shown in Figure 3.14. This shows a very large variation of predictions, particularly for the year 2010. The CO₂ emissions predictions for 2010 (compared with 1990 levels) vary from 26% increase for scenario 2, through 14% increase for scenario 1 and 13% decrease for scenario 3, to 23% decrease for scenario 4. Therefore, it is apparent that predictions can only be made once the most likely assumptions have been established and stated.

Despite these uncertainties, predictions of future electricity demand and fuel mix have been made, based on figures provided by DG XVII of the EC. These estimates are shown in Table 3.5. Also shown in this table are estimates of national CO₂ emissions from electricity production. Figure 3.15 shows a comparison between 1990 CO₂ emissions and 2005 predictions. Although the predictions follow the same ranking as the 1990 figures, there is a large variation in the national increases in CO₂ emissions. As a consequence, the gap between the highest and lowest emitters of CO₂ is not as pronounced as in 1990. Notably, the United Kingdom shows no significant increase in CO₂ emissions between 1990 and 2005. This is because of a

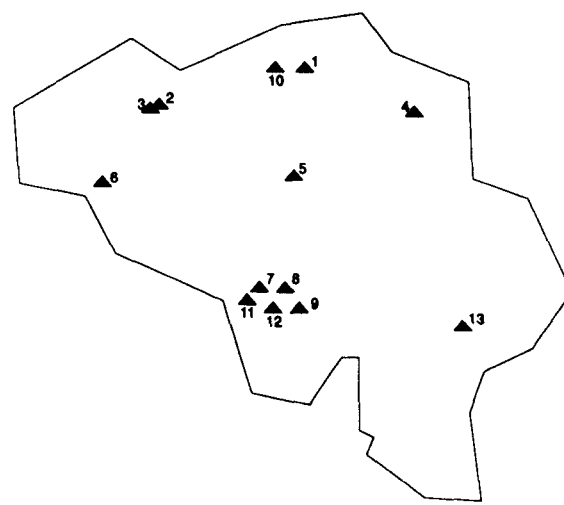
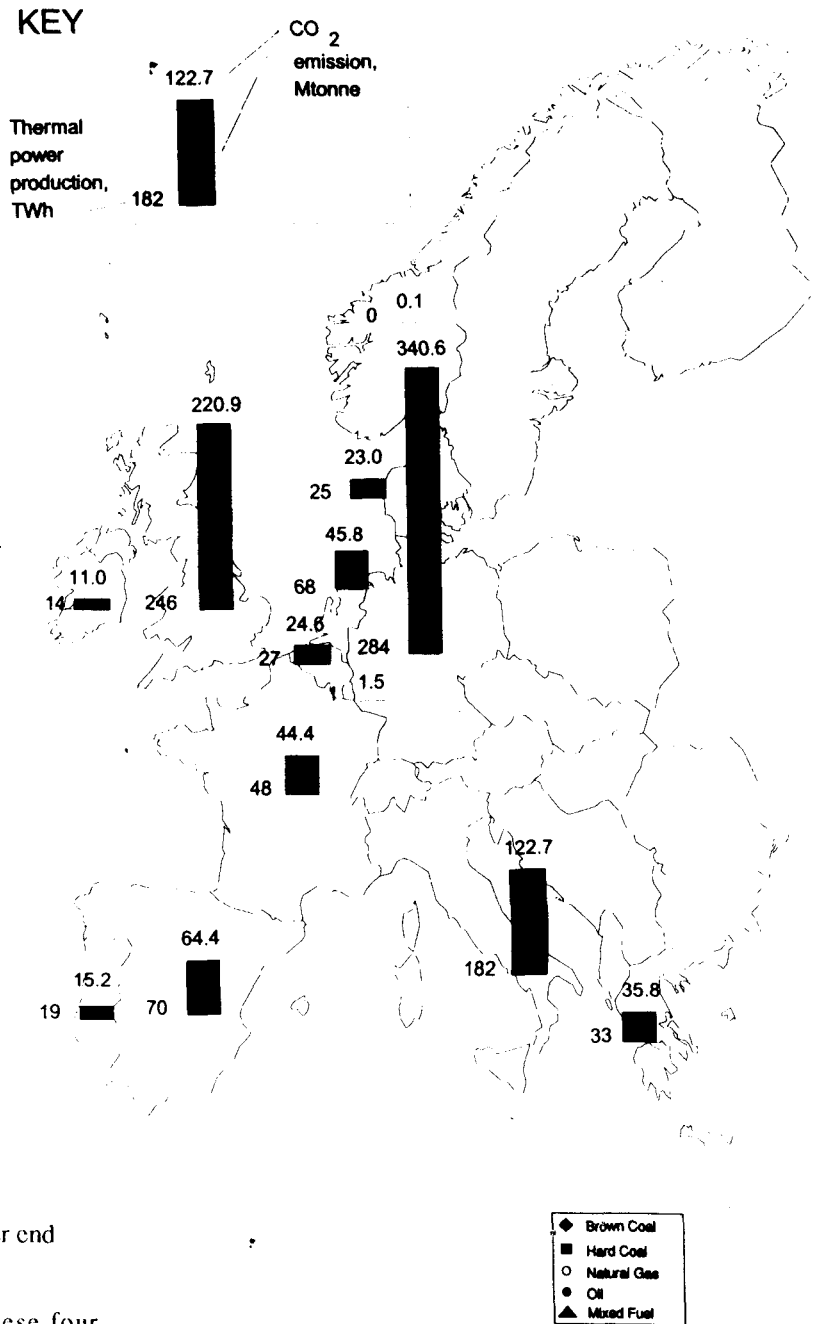


Figure 3.4 Location of Thermal Power Plants in Belgium.

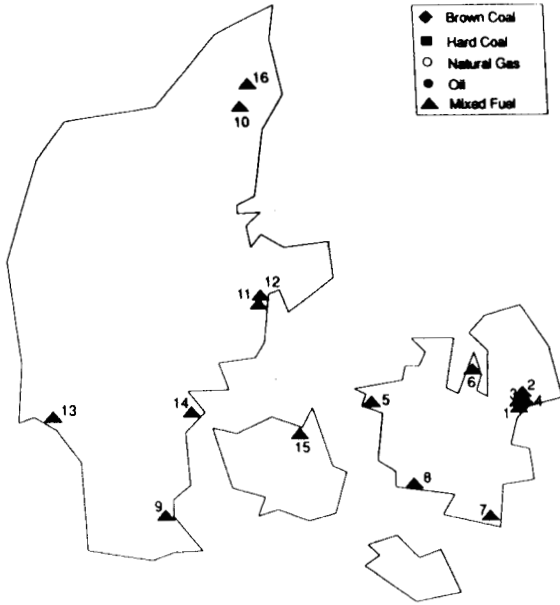


Figure 3.5 Location of Thermal Power Plants in Denmark.

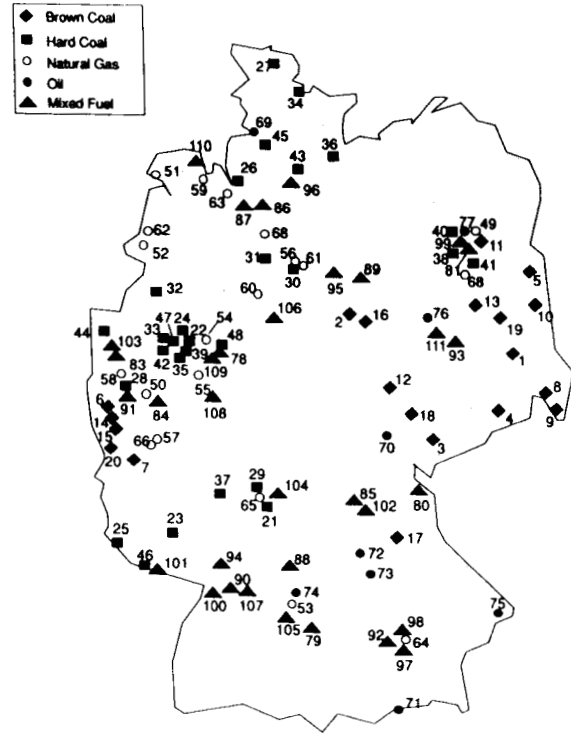


Figure 3.7 Location of Thermal Power Plants in Germany.

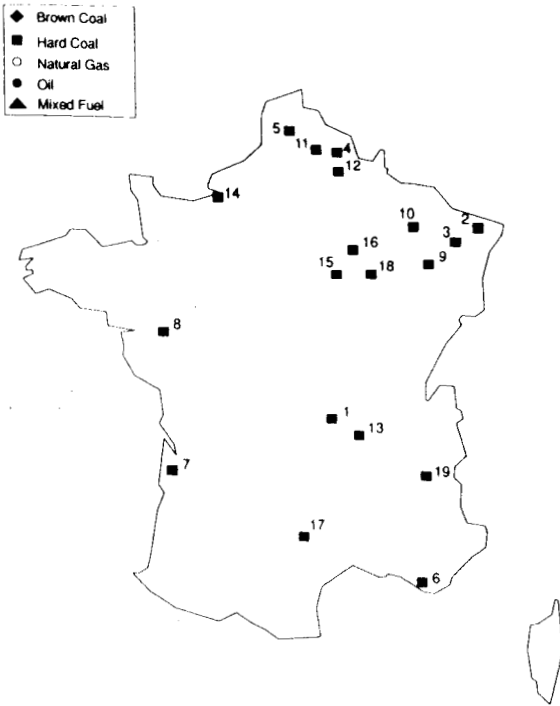


Figure 3.6 Location of Thermal Power Plants in France.



Figure 3.8 Location of Thermal Plants in Greece.

significant shift from coal firing to natural gas fired combined cycle plant with higher efficiencies and a lower CO₂ emission factor.

To conclude, predictions of the CO₂ emissions for 2020 are not readily available. Predictions for 2005 are available for the 13 countries of the study. In the main, these show an increase of CO₂ emissions across Europe, with the main sources being relatively unchanged (i.e. Germany, United Kingdom and Italy). However, these projections should be treated with caution, as the assumptions (and policy, etc. they are based on) can radically alter the predictions, as shown in Figure 3.14.

3.5 CO₂ QUALITY

The quality of the CO₂ produced from power plant systems is dependent on the power generation process and the CO₂ removal process. In principal, the CO₂ can be cleaned to any level of trace contamination, however the lower the con-

Table 3.4 Coal-fired Power Stations in Europe existing on 31 December 1990.

centration of contaminants, the higher the cost of processing. Therefore a number of minimum standards have been set which aim to minimise the cost of CO₂ processing whilst producing CO₂ of a quality which is suitable for piping to the disposal point and underground injection. These standards are summarised below:

- High concentration of permanent gases in a fluid which is to be pumped lead to increased energy use in the pumps. Therefore, concentrations of permanent gases, e.g. N₂, O₂, should be low in order to minimise the energy required for CO₂ compression and pumping. This would be achieved by proper design and operation of the CO₂ separation process.
- High concentrations of water in the CO₂ may lead to pipeline corrosion problems or the formation of CO₂ hydrates. The presence of water in the CO₂ may also cause problems due to ice formation in the low temperature CO₂ liquefaction process. The CO₂ separated from the power plant would therefore need to be dehydrated in order to minimise the water content and prevent these problems. It should be noted that when the CO₂ is injected underground, it will contact water in the rock formation. The effects of this are considered in Chapter 7, Inorganic Geochemistry.
- The concentrations of other contaminants, e.g. SO₂, NO₂, H₂S, CO, are all likely to be low and are unlikely to have any effects on the operation of the pipeline or underground injection systems.

Based on these standards, the trace contaminant compositions have been estimated from in-house data on power plant/separation plant combinations. Three cases have been considered; CO₂ removal from a flue gas, CO₂ removal from synthesis gas, and CO₂ removal from a recycled flue gas system. In each case the trace contaminants are different, although there are some species in common. The CO₂ quality for each case is summarised below.

1. CO₂ from a Pulverised Fuel Plant with Flue Gas Desulphurisation and Amine CO₂ Scrubbing
~99% CO₂, 0.01% O₂, 0.2% N₂, <10 ppm SO₂, <1 ppm NO_x
Dried to meet CO₂ liquefaction and disposal requirements.

Country	Plant name	Fuel type	Net capacity (MW)
BELGIUM			
1. Anvers	Mol (11-12)	coal-oil-gas	260
2. Flandre Orientale	Langerbrugg (19)	coal-oil-gas	124
3. Flandre Orientale	Rodenhuize (1,4)	coal-oil-gas	418
4. Limbourg	Langerlo (1-2)	coal-oil-gas	560
5. Brabant	Pont-Brule (2-3)	coal-oil-gas	255
6. Flandre Orientale	Ruien (1-5)	coal-oil	681
7. Hainaut	Baudour	coal-oil-gas	116
8. Hainaut	Bressoux (7-8)	coal-oil-gas	110
9. Hainaut	Marchienne	coal-oil-gas	118
10. Anvers	Schelle (31-32)	coal-oil-gas	272
11. Hainaut	Amercoeur (1-2)	coal-oil-gas	272
12. Hainaut	Peronnes	coal-oil-gas	115
13. Liege	Awirs (3-4)	coal-oil-gas	250
DENMARK (Of the total capacity shown here, 11 % is solely based on oil)			
1. Avedoere	Avedoerevaerket	coal-oil	250
2. Copenhagen	Amagervaerket	coal-oil	506
3. Copenhagen	H C Orestedvaerket	coal-oil-gas	111
4. Copenhagen	Svanemollevaerket	coal-oil-gas	106
5. Kalundborg	Asnaesvaerket	coal-oil	1500
6. Kyndby	Kyndbyvaerket	coal-oil-gas	865
7. Masnedoe	Masnedoevaerket	coal-oil	145
8. Stigsnaes	Stigsnaesvaerket	coal-oil	413
9. Aabenraa/Ensted	Enstedvaerket (7-8)	coal-oil	444
10. Aalborg	Nordkraft (5-6,8)	coal-oil	379
11. Aarhus	Aarhusvaerket (1-2)	coal-oil	140
12. Aarhus	Studstrupvaerket	coal-oil	1114
13. Esbjerg	Vestkraft (5-7)	coal-oil	440
14. Fredericia	Skaerbaekvaerket	coal-oil	369
15. Odense	Fynsvaerket (2-4,6)	coal-oil-gas	537
16. Vorskov	Vendsysselvaerket	coal-oil	440
FRANCE			
1. Blanzly	Lucy (3)	hard coal	247
2. Moselle	Emile Huchet (6)	hard coal	588
3. Moselle	HBL A	hard coal	330
4. Nord	Hornaing (3)	hard coal	235
5. Pas-de-Calais	Courrieres (1)	hard coal	150
6. Provence	Gardanne (4-5)	hard coal	818
7. Landes	Arjuzanx (3)	lignite	117
8. Loire Atlantique	Cordemais (1,4,5)	hard coal	1745
9. Meurthe et Moselle	Blenod (1-4)	hard coal	1000
10. Moselle	La Maxe (1-2)	hard coal	500
11. Nord	Bouchain (1-2)	hard coal	500
12. Nord	Pont-sur-Sambre (3)	hard coal	250
13. Rhone	Loire-sur-Rhone (1-2)	hard coal	500
14. Seine Maritime	Le Havre (1,2,4)	hard coal	1415
15. Seine et Marne	Montereau (3-4)	hard coal	500
16. Seine et Mame	Vaires (1-2)	hard coal	480
17. Tarn	Albi (1)	hard coal	250
18. Val de Marne	Vitry (1-4)	hard coal	1040
19. Val d'Oise	Champagne (1-2)	hard coal	490
IRELAND (Including all fuels)			
1. Co Clare	Moneypoint (1-3)	hard coal	915
2.	Aghada	gas/oil	525
3.	Poolbeg	gas/oil	510
4.	Tarbert	oil	500
5.	Great Island	oil	120
6.	North Wall	gas	250
7.	Marina	gas	115

Table 3.4 Continued.

A typical 500 MW_e plant, retrofitted as described to remove 90% of the CO₂, would yield 600 tonne/h of CO₂

2. CO₂ from an Integrated Gasification Combined Cycle producing Hydrogen via Shift Reaction and Physical Solvent Scrubbing

~99% CO₂, <1% H₂, 0.02% CO, 0.02% N₂ and <10 ppm H₂S.

Dried to meet CO₂ liquefaction and disposal requirements.

This is an example of a purpose built, advanced 'clean coal plant'. A 500 MW_e plant, removing 90% of the CO₂, would yield 450 tonne/h of CO₂.

3. CO₂ from a Pulverised Fuel Plant with Flue Gas Recycle

~97% CO₂, 1% O₂, 1% N₂, 0.8% SO₂, <10 ppm NO_x

Dried to meet CO₂ liquefaction and disposal requirements.

A typical 500 MW_e plant, retrofitted as described, would yield 530 tonne/h of CO₂.

3.6 REFERENCES

1. SUMMERFIELD, I R, GOLDTHORPE, and S H, BOWER, C J. 1993. Proc. IMechE, Part A Journal of Power and Energy, Vol. 207, 81-88.
2. EPRI Journal. 6-15, July/August 1994.
3. Energy in Europe, Annual Energy Review (December 1992). Commission of the European Communities, Directorate General for Energy.
4. Energy in Europe, Annual Energy Review (December 1991). Commission of the European Communities, Directorate General for Energy.
5. VDEW Statistic (1991).
6. Eurostat, monthly statistics (12/1992).
7. VGB Tatigkeitsbericht (1991/92).
8. Electriciteit in Nederland (1992).
9. International Energy Data (1992). World Energy Council Report, London.
10. Energy in Europe, Special Issue — Energy for a New Century: The European Perspective (July 1990). Commission of the European Communities, Directorate General for Energy.

Country	Plant name	Fuel type	Net capacity (MW)
ITALY			
1. Friuli-Venezia Giulia	Monfalcone (1-2)	coal-oil	320
2. Liguria	Genova (3,4,6)	coal-oil	281
3. Liguria	La Spezia (1-4)	coal-oil	1791
4. Liguria	Vado Ligure (1-4)	coal-oil-gas	1242
5. Puglia	Brindisi Nord(1-4)	coal-oil	1206
6. Sardegna	Sulcis (1-3)	coal-oil	684
7. Toscana	S Barbara (1-2)	lignite-oil	234
8. Veneto	Fusina (1-4)	coal-oil-gas	920
9. Veneto	Porto Marghers (2-3)	coal-oil	133
PORTUGAL			
1. Godonmar	Tapada do Outeiro (1-3)	domestic coal-oil	135
2. Sines	Sines (1-4)	hard coal	1136
UNITED KINGDOM (Including all fuels)			
1. Midlands	Ironbridge	hard coal	950
2. Midlands	Rugeley (A-B)	hard coal	1526
3. Midlands	Staythorpe	hard coal	336
4. Midlands	West Burton	hard coal	1920
5. Midlands	Willington (A-B)	hard coal	768
6. North East	Blyth (A-B)	hard coal	1548
7. North East	Drax (1-6)	hard coal	3750
8. North East	Eggborough	hard coal	1720
9. North East	Skelton Grange	hard coal	448
10. North East	Thorpe Marsh	hard coal	942
11. North West	Agecroft	hard coal	232
12. North West	Padiham	hard coal	112
13. South East	Tilbury	coal-oil	1344
14. South East	West Thurrock	coal-oil	1052
15. South West	Aberthaw (A-B)	hard coal	1726
16. South West	Didcot	hard coal	1900
17. South West	Uskmouth	hard coal	336
18. N Ireland	Belfast West	hard coal	229
19. N Ireland	Kilroot (I)	coal-oil	360
20. Midlands	Castle Donnington	hard coal	564
21. Midlands	Cottam	hard coal	1920
22. Midlands	Drakelow (B-C)	hard coal	1358
23. Midlands	Hams Hall	coal-gas	366
24. Midlands	High Marnham	hard coal	930
25. Midlands	Ratcliffe-on-Soar	hard coal	1940
26. North East	Ferrybridge (B-C)	hard coal	2214
27. North West	Fiddler's Ferry	hard coal	1880
28. South East	Kingsnorth	coal-oil	1920
29. South Scotland	Cockenzie	hard coal	1152
30. South Scotland	Kincardine	hard coal	375
31. South Scotland	Longannet (1-4)	hard coal	2304
32. North West	Ince	oil	1050
33. South East	Grain	oil	2756
34. South East	Littlebrook	oil	2115
35. South East	Richborough	oil	120
36. South West	Fawley	oil	2000
37. South West	Pembroke	oil	2000

Table 3.5 Predicted Power Generation Capacity in 2005.

Country	Electricity Production TWh (2005)	Thermal Power Production TWh (2005)	Estimated CO ₂ Emissions, MtCO ₂
Belgium	84.87	40.90	29.8
Denmark	43.35	41.57	32.0
France	582.94	108.53	75.9
Germany*	553.45	385.75	302.4
Greece	59.14	55.45	56.7
Ireland	21.08	20.21	13.3
Italy	333.62	272.08	163.2
Luxembourg	0.95	0.83	2.2
Netherlands	98.48	95.56	60.9
Norway	116.70	0.40	0.4
Portugal	49.83	36.63	25.7
Spain	219.64	132.79	99.4
United Kingdom	380.66	311.00	222.4
Total	2544.69	1501.75	1083.9

* Excluding former GDR.



Figure 3.9 Location of Thermal Power Plants in Italy.

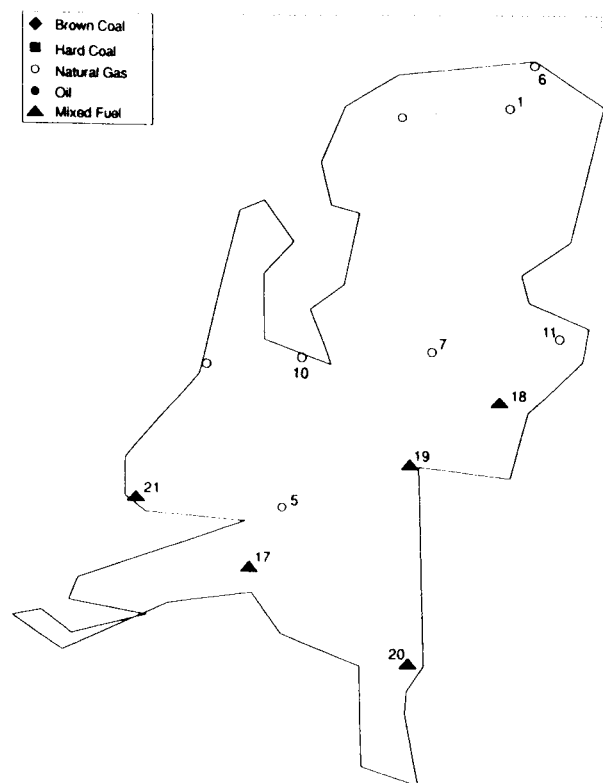


Figure 3.10 Location of Thermal Power Plants in the Netherlands.

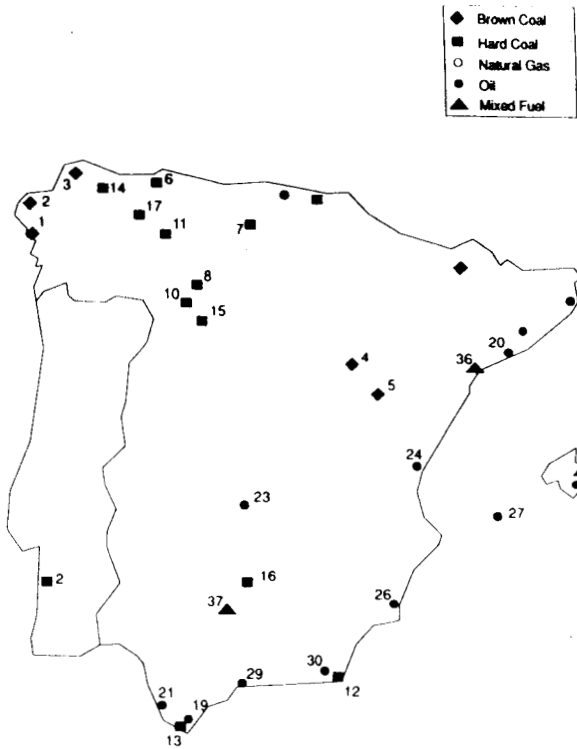


Figure 3.11 Location of Thermal Power Plants in Spain and Portugal.

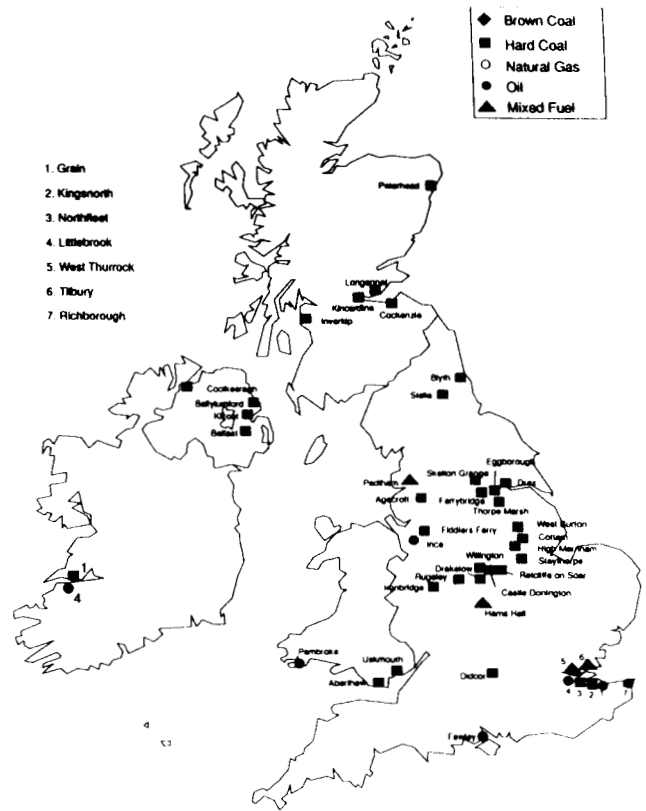


Figure 3.12 Location of Thermal Power Plants in the UK and Ireland.



Figure 3.13 Location of Thermal Power Plants in the EU and Norway.

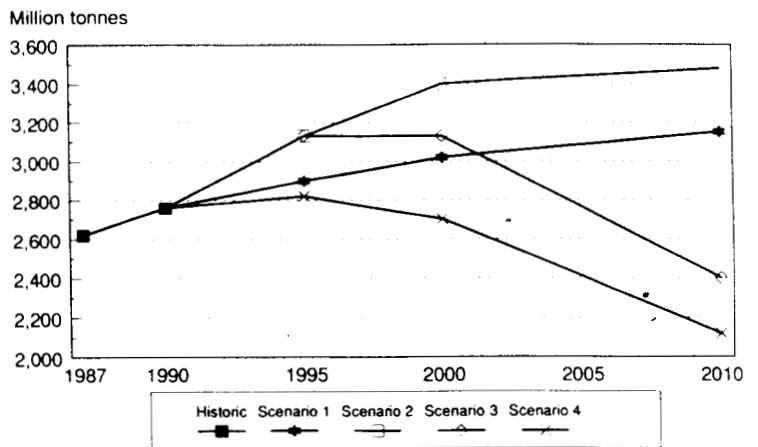
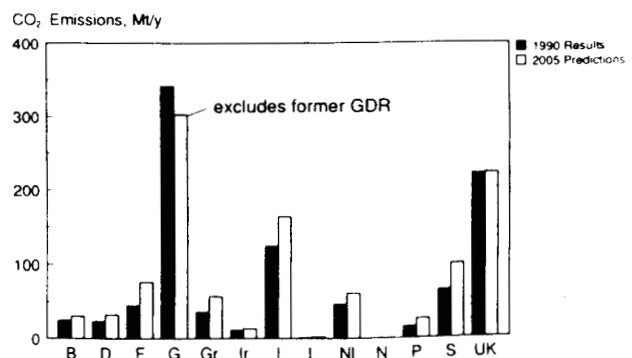


Figure 3.14 Prediction of Carbon Dioxide Emissions.

Figure 3.15 European CO₂ Emissions from Power Production.



CHAPTER 4

Area 2 Inventory of the Theoretical CO₂ Storage Capacity of the European Union and Norway

Emile Elewaut, D Koelewijn and Rieks van der Straaten (TNO)

Heather Baily and Sam Holloway (BGS)

Jean Barbier (BRGM)

Erik Lindeberg (IKU)

H Möller and K H Gaida (RWE-DEA AG)

4.1 INTRODUCTION

Rieks van der Straaten

4.1.1 The objective of area 2

The objective of Area 2 of the JOULE II project is to give for the European Union and Norway an assessment of the theoretical carbon dioxide (CO₂) storage capacity of the deeper subsurface, i.e. of deep-seated aquifers or depleted hydrocarbon fields. An inventory of this capacity is presented in the following sections, country by country.

In the first JOULE II interim report (JOULE II, 1993), a preliminary inventory was made. As was to be expected, for each country different criteria were used to define a suitable CO₂ storage site and different methods were applied to calculate the CO₂ storage capacity. This made it very difficult to compare one country to another and it was almost impossible to get an overall picture of the storage capacity for the European Union. Assumptions, criteria and the method of storage calculation therefore needed standardisation before an inventory could be made. The standard method to establish the CO₂ storage capacity is discussed in section 4.2.

During the last few years several attempts have been made to assess the storage capacity of the subsurface in Europe, i.e. the storage potential of the deep-seated aquifers and/or hydrocarbon reservoirs. These estimates vary greatly, as shown in Table 4.1.1. The wide range of values can be attributed to different assumptions and constraints, such as whether or not the storage should be confined to a trap, the fraction of the reservoir to be filled with CO₂, the average CO₂ reservoir density, and the area of aquifers suitable for disposal (see discussion in Hendriks and Blok, 1993).

4.1.2 The scope of the inventory

It should be emphasised that the storage capacity estimates presented in the following sections are incomplete and contain major uncertainties.

The inventory is incomplete because in some areas little or no information on the deeper subsurface is available. For most countries the offshore domain is poorly known. The offshore aquifers of Denmark, France, Germany, Greece, Ireland, the Netherlands and Portugal are not included in the inventory, and only a very limited part of the offshore area of Spain and Italy is taken into consideration. The North Sea Basin is the largest sedimentary basin of Europe (see Figure 4.1.1). With respect to the offshore section of this basin, only the United Kingdom and Norway are considered, which means that a considerable volume of potential reservoir rocks is kept out of the inventory.

The accuracy of the capacity estimates will be low, because the reservoir properties, such as distribution, trap volume, net thickness, porosity, permeability, pressure and temperature, are only known to a limited extent. In many cases, they have to be assessed by using average values that may deviate considerably from the reservoir specific ones. For the hydrocarbon fields, a complete understanding of the material balance and the production history is required to establish an accurate estimate of the storage potential. This information is not accessible and the capacity estimates are generally based on publically available data on (commercial) production and expected reserves.

Another very large uncertainty is introduced by the question of whether or not CO₂ storage should be restricted to geological traps. Because on average only 3% of the aquifer volume will be in a trap, the CO₂ storage capacity of the entire aquifer will be more than thirty times the capacity of its trapped fraction. Many aquifers have top

Table 4.1.1 Estimates of the CO₂ storage capacity of Western Europe (EU), from various sources. The storage capacities are in Gigatonnes CO₂.

	Oil & Gas Fields	Aquifers	Source
European Union	28	13.6	Koide et al. 1992
	1.0–34.6	102–407	Mot et al. 1993*
	28		Van der Meer & Van der Straaten 1993
	21.8	326.6	Hendriks & Blok 1993**
	40–85	10–2500	JOULE II 1993@
	33	30–770	Hendriks 1994+
			this report@

* Gas fields only,

+ Western Europe,

@ EU and Norway; the low figure refers to storage in traps, the high figure to storage not confined by traps

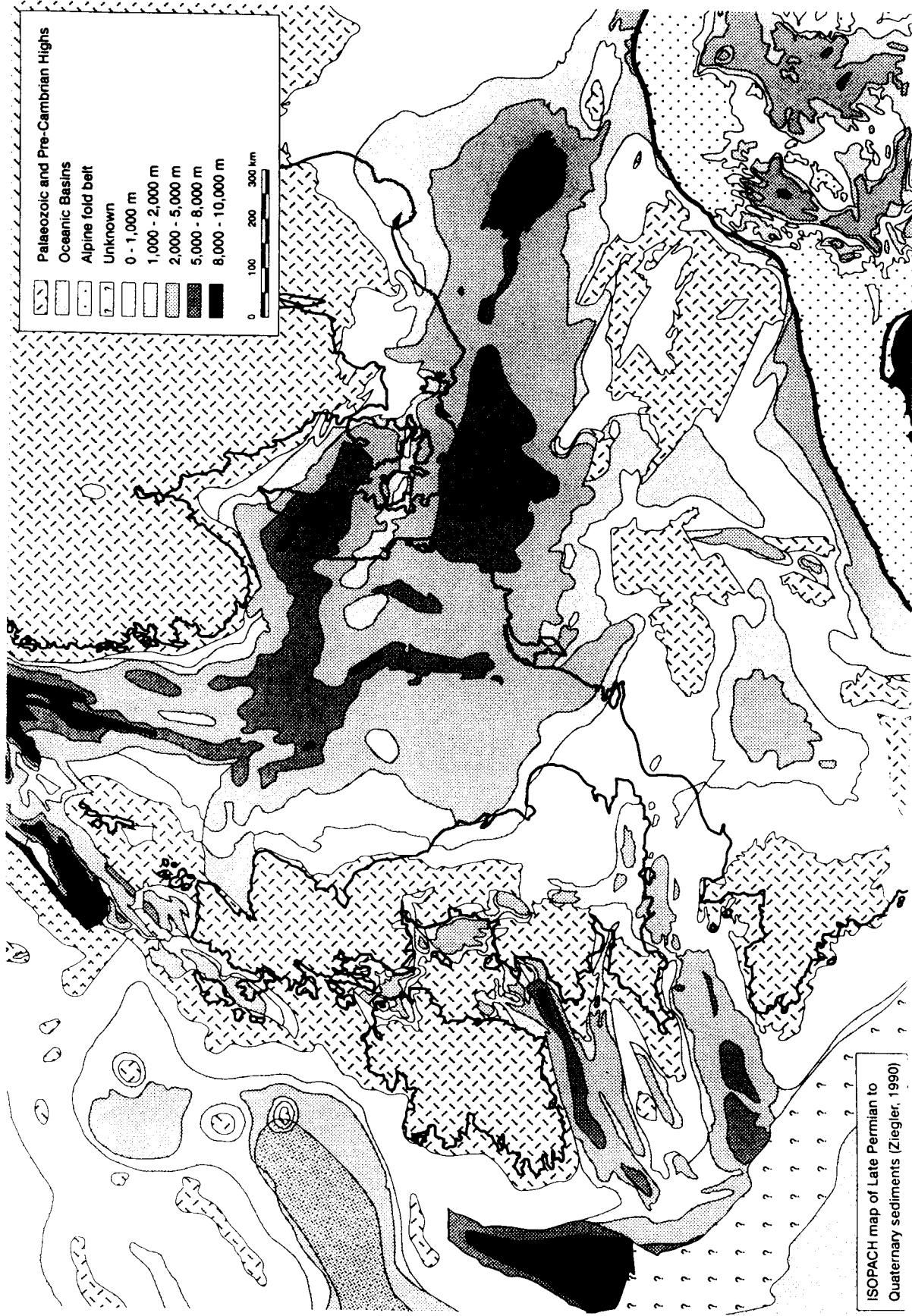


Figure 4.1.1 Isopach map of Late Permian to Cenozoic Series in Northwestern Europe (after Ziegler 1990, Encl. 43).

seals with a limited range, are in communication with shallow formations that may contain valuable fresh water resources, and/or crop out somewhere. For these aquifers, usage of the entire aquifer volume for CO₂ storage may cause a serious environmental hazard and any CO₂ injected should therefore be confined by traps. Some unused aquifers, however, are entirely sealed off from neighbouring formations or have an effective top seal which extends over a very large area. In these cases, the risk of CO₂ escaping from these aquifers may be considered to be negligible, even if the non-trapped part is used for CO₂ disposal. In the inventories that follow, the 'default' storage capacities of aquifers are those of the trapped fraction. These figures are presented in standardised tables. In the text, however, the aquifer's suitability for CO₂ storage in the entire aquifer (not confined to traps) will be discussed. If an aquifer is considered to be appropriate for this storage concept, a rough estimate of the capacity of the entire aquifer volume will be given. A major uncertainty is additionally formed by the 'storage efficiency', i.e. the percentage of the pore volumes of aquifers and hydrocarbon reservoirs that can actually be filled by CO₂. For aquifers it is assumed that 2–6% of the reservoir's pore volume can be filled, depending on the nature of the reservoir (see discussion in section 4.2).

In the case of hydrocarbon fields, the actual pore volume of the reservoir remains unknown and capacity estimates are based on the assumption that the total reservoir volume of recoverable hydrocarbons can be entirely replaced by CO₂. Although this assumption may be an oversimplification, at present it is considered to be the best option to estimate the storage potential of the oil and gas fields (see discussion in section 4.2).

The estimates for the CO₂ storage capacities per country are extensively discussed in the sections 4.3 to 4.15 (the twelve EU countries and Norway). Each section includes a summary, a concise overview of the geology of the country, a section about aquifers and a section about oil and gas fields. The capacity estimates are mostly based on the assumptions, constraints and calculation methods discussed in section 4.2. For several countries, however, the data are such that some adjustments had to be made to the general guidelines given in this section. The results are presented in tables and are discussed in the text. Distinction is made between onshore and offshore, and oil and gas fields. The sections end with some comments on the results.

4.1.3 The concept of underground CO₂ disposal

The general idea of CO₂ disposal underground is to store the gas in a reservoir (porous and permeable rock) in the deeper subsurface almost completely shut off from the atmosphere, retaining the CO₂ for a very long period. In geological terms, however, the actual requirements for the time of CO₂ underground are fairly short. Peak levels of atmospheric CO₂ are expected in the next few centuries when fossil fuel reserves are being utilised to their economic limits. A time lag of a few thousands years before the CO₂ re-enters the atmosphere would thus be sufficient to prevent it contributing to peak radiative heating of the earth's surface. This objective can be fulfilled relatively easily by any subsurface disposal concept.

CO₂ Disposal in Aquifers

There are two main concepts for CO₂ disposal in aquifers. The first requires a subsurface trap for buoyant fluids with

defined lateral boundaries (spill point) and a closed structure, in analogue to oil or gas fields. In the second concept, CO₂ is disposed of directly into aquifers without the need for further confinement to traps. In both cases, the storage reservoir requires a cap rock to prevent vertical migration of CO₂ to the surface and sufficient permeability to allow the injection of great quantities of CO₂. From natural CO₂ reservoirs and modelling results we know that the migration behaviour of CO₂ is fairly similar to that of natural gas. Thus, in practical terms, if confined by cap rocks similar to those present above hydrocarbon accumulations, CO₂ would almost certainly be retained for millions of years underground, far longer than necessary to prevent it contributing to likely peak levels of global warming.

The concept of disposal of CO₂ into a closed structure is likely to apply in onshore Europe, where the sedimentary basins are mainly small. Some of the aquifers in the deeper parts of these basins may be in direct connection with nearby outcrops. These aquifers may have other uses at shallow depth, for example water supply. Thus environmental constraints in the onshore area are likely to prevent the injection of CO₂ into an aquifer unless it is confined in a trap which will prevent it contaminating the useful parts of the aquifer. However, there may be some aquifers onshore which have no uses and are not connected to the surface onshore.

The second concept, that of disposal into aquifers without the need for a closed structure to confine the CO₂, may be most widely applicable in large sedimentary basins where the aquifers have no current uses, for example the North Sea basins. Here CO₂ could be injected into an aquifer with only a top seal. If it was injected sufficiently far from the basin margins, reactions with the host rock and the surrounding formation water as it moved along any flow path within the aquifer would ensure that it did not emerge at the land surface or sea bed. Another candidate for the concept in which the entire aquifer volume is used for CO₂ disposal would be a deep-seated aquifer that is entirely sealed off from its neighbouring formations (a 'closed' aquifer). Examples of such aquifers are those underlying most oil fields in the North Sea.

As long as the main objective is fulfilled, i.e. to prevent CO₂ from re-entering the atmosphere for more than several thousands of years, both disposal concepts are valid. However, quantifying the potential for unconfined disposal poses difficulties. This report and the inventory focuses on underground CO₂ disposal into closed structures with defined lateral boundaries, either abandoned hydrocarbon reservoirs or traps on aquifers, simply because the CO₂ storage potential can be calculated relatively straightforwardly. The capacity is in that case the amount of CO₂ needed to fill the structure.

So, the estimate of the storage capacity of aquifers is primarily focused on the trapped proportion. This estimate will be very conservative because it disregards the enormous storage potential of aquifers beside that of closed structures. An example of an unconfined CO₂ reservoir would be a sandstone formation several tens of meters thick with an adequate topseal and a range of several hundreds of square kilometres, but with undefined lateral boundaries and without structural traps. In that case, the question of whether this aquifer is a suitable storage site depends on the time it would take for the CO₂ to get from the injection point to the point where it would interact with the atmosphere, e.g. the

surface or the shallow ground water. This time will be determined by the injection rate, the migration velocity, the length of the flow path, and all physical and chemical processes taking place along this path. Calculating the enormous theoretical storage capacity of such aquifers can therefore be expressed in terms of injection rates only and will be highly reservoir specific, which makes any generalisation very difficult. A reliable estimate can only be given by a detailed evaluation of an individual reservoir.

In the following sections only the storage capacity of closed structures on aquifers will be included in the 'default' tables that give an overview of the storage capacity. If enough information is available, the suitability of the reservoir for storage 'not confined by traps' will be discussed. For an aquifer that is considered appropriate for this disposal concept, a rough estimate of its storage capacity will be presented. However, one should realise that the data set on the subsurface is too poor and too incomplete to give an exact quantification or to prove that applying the entire (non-trapped) volume for CO₂ disposal will be without risks. In addition, it will be largely a political decision whether only traps or the entire aquifer volume will be used to store CO₂.

CO₂ Disposal in Oil and Gas Fields

The basic concept of CO₂ disposal in depleted oil or gas reservoirs is that the amount of CO₂ that can be stored in a reservoir is directly related to the amount of hydrocarbons that has been recovered from it. In this study, it is assumed that the reservoir volume of ultimately recoverable hydrocarbons can entirely be replaced by CO₂. Arguments for this assumption will be given in section 4.2.

The major difference between CO₂ storage in aquifers and storage in hydrocarbon fields is that in the latter case a substantial volume of fluids or gases has been subtracted from the reservoir, which enhances the storage capacity greatly. Additional benefits are that the hydrocarbon traps have a proved capability to retain fluids and gases underground for thousands to millions of years and that the reservoir is better understood because of the knowledge gathered during hydrocarbon exploration and production. Moreover, some of the infrastructure used during the hydrocarbon production may be re-used for the CO₂ injection venture. Although CO₂ disposal into hydrocarbon reservoirs represents a special case of disposal into traps on aquifers, the approach of estimating the storage capacity will be quite different. The storage capacity of aquifers is based on the available pore volume, and the CO₂ storage efficiency (i.e. the proportion of the pore volume that can be filled with CO₂) in a fully water saturated reservoir with a hydrostatic pore pressure. However, data on the pore volumes of the hydrocarbon reservoir are generally not publically available. In addition, the storage efficiency in oil and gas fields will be larger than in aquifers, because of the withdrawal of hydrocarbons.

Given the large commercial interests, most information on hydrocarbon reservoirs is kept confidential by the oil industry. The only information that is well documented are hydrocarbon production and reserve figures. In order to be able to give a broad inventory of the CO₂ storage capacities of most oil and gas fields, the inventory has been based on these accessible figures.

4.2 CALCULATING THE CO₂ STORAGE CAPACITY

Rieks van der Straaten

4.2.1 Introduction

This section deals with the way in which the CO₂ storage capacities of the individual countries of the European Union and Norway are estimated. It discusses the method of calculation, the assumptions on which the calculation is based and the criteria that define an appropriate CO₂ storage site. Attention will largely be focused on the general aspects of CO₂ storage underground and the storage efficiency of CO₂ in an aquifer or depleted hydrocarbon field. Three types of potential CO₂ reservoirs are recognised: 1) gasfields, 2) oil fields, and 3) aquifers. For each of these three types, the criteria that define a potential CO₂ reservoir will be discussed and a standard method will be proposed to calculate the CO₂ storage capacity of the reservoir. Distinction will be made between onshore and offshore reservoirs, and between 'open' and 'closed' reservoirs.

The calculation is based on several assumptions. To be able to validate the inventory of the CO₂ storage capacity, it is essential to focus on these assumptions, because they largely determine whether the results give a reliable estimate of the storage potential. The nature of the assumptions depends on the data that are available. In the case of a rich data set of good quality, less speculative assumptions have to be made. In contrast, in areas where little data are at hand, the storage calculation will be based on average values and unproven presumptions about the reservoir. Which assumptions will be made and for what reason, requires therefore careful discussion.

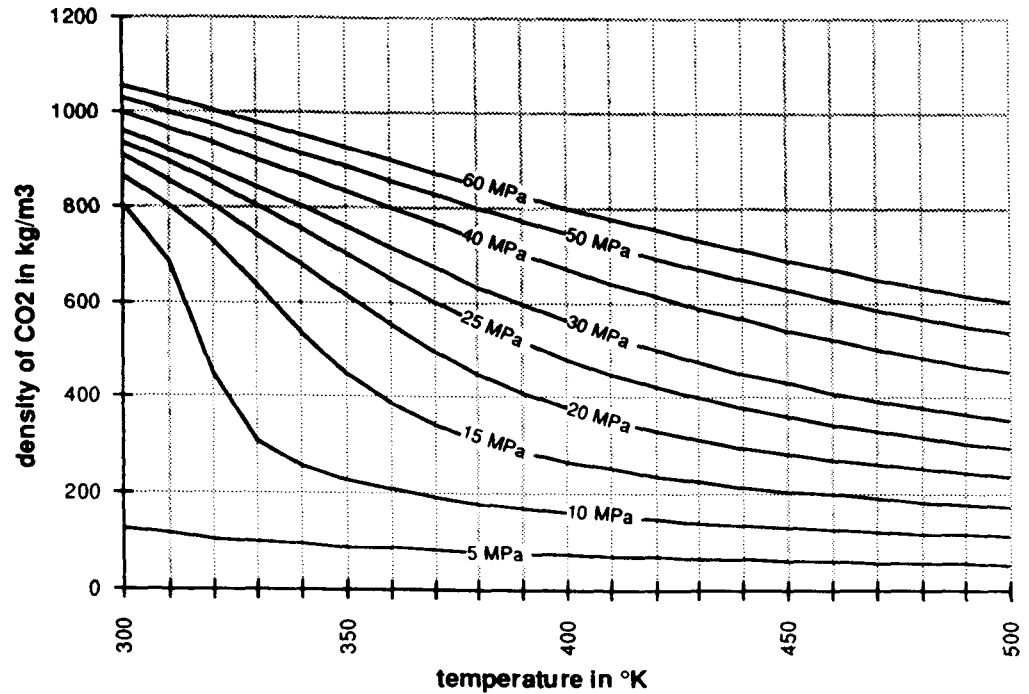
The accessibility and the nature of the data on the deeper subsurface varies country by country. In some countries a dense data grid on the deeper subsurface is publicly accessible, whereas in other countries little is known about the deeper subsurface. Much information stems from oil and gas exploration activities. However, a large part of this information is held in confidence by oil companies. We were therefore not able to obtain the necessary data to determine the storage capacity for all individual fields. In some countries, a country-wide study has been carried out on potential geothermal resources, which led to an inventory of the deep-seated aquifers onshore. Other sources of information are scientific articles and reports or publications provided by state geological surveys and the ministries of economic affairs.

4.2.2 General Aspects of underground CO₂ disposal

4.2.2.1 SUBSURFACE CONDITIONS

The CO₂ in the underground reservoir must be in its supercritical state, i.e. at a temperature *or* pressure above the critical point of CO₂. The purpose of this constraint is that the underground CO₂ must have a high density to dispose of large quantities of CO₂ in the subsurface in a practical way. An ideal CO₂ storage site has a high pressure and a low temperature, because under these conditions the CO₂ is the most dense (Figure 4.2.1.). So, if the pressure is high enough (well above the critical pressure of CO₂), the temperature may be subcritical. However, supercritical pressures *and* temperatures are preferable, because these conditions ensure that the underground CO₂ remains in one phase, which prevents problems arising from two-phase flow behaviour.

Figure 4.2.1 The density of CO₂ as a function of temperature and pressure (data from Van der Sluijs 1991).



The critical pressure of CO₂ is 7.38 MPa (73.8 bar). The average underground hydrostatic pressure increases with depth by ca 10.5 MPa/km for aquifers that are in open communication with the surface water (Tissot and Welte, 1984).^[1] Applying this average gradient, the critical pressure of CO₂ will be reached at a depth of around 690 m. However, aquifers or hydrocarbon reservoirs that are sealed off from the rest of the subsurface may be under- or overpressured. Rapid burial of sediments which does not allow pore fluids to dissipate during compaction ('*disequilibrium compaction*' of Gaarenstroom et al., 1993) can lead to overpressured aquifers. Other processes that will generate anomalously high pressures are a rise in temperature, the transformation of organic matter into hydrocarbons, and the cracking of oil into gas, because during these processes the volume of the pore fluids will increase significantly (Tissot and Welte, 1984; Gaarenstroom et al., 1993). In addition, vertical tectonic movements may also lead to abnormal fluid pressures. Depleted gas fields generally are strongly underpressured.

The critical temperature of CO₂ is 31.1°C (304.2 K). The average geothermal gradient is approximately 25°C/km. If an average surface temperature of 10°C is assumed, the critical temperature will be reached at a depth of 840 m. The Geothermal Atlas of Europe (Haenel and Staroste, 1988) shows, however, a considerable variation in the geothermal gradients and subsurface temperatures at a depth of 1000 m ranges from 20 to 75°C, with locally temperatures of more than 200° in volcanic areas. The major

[1] According to Archer & Wall (1992), hydrostatic gradients are commonly between 10 and 12 MPa/km and a gradient of 11 MPa/km may be used to predict the pore fluid pressure in reservoirs at a depth between 2000 and 4000 m. Since pore water at more shallow depths will be less saline and therefore less dense, the hydrostatic pressure in the highest part of the subsurface (<2000 m) will be less than 11 MPa/km.

[2] Archer & Wall (1992) state that in many petroliferous basins the geothermal gradient is around 29°C/km. In one of their examples they apply this gradient for the North Sea, assuming a mean sea water temperature of 4.5°C. With these values, the supercritical temperature under the North Sea occurs below a depth of 920 m (ignoring water depth).

sedimentary basin of Western Europe, the North Sea Basin, shows onshore a temperature of about 40°C at a depth of 1000 m, which corresponds with a geothermal gradient of ca 30°C/km, implying supercritical temperatures below a depth of 700 m.^[2]

In establishing the underground CO₂ storage capacity, a minimum depth of 800 m has been used as cutoff value. This means that a reservoir has only been considered as a potential CO₂ storage site if it is below this depth. In addition, an average geothermal gradient of 30°/km and a hydrostatic gradient of 10.5 MPa/km (105 bar/km) will be applied, if no local temperature and pressure data are available.

4.2.2.2 DENSITY OF CO₂ UNDER RESERVOIR CONDITIONS

The density of CO₂ is a function of pressure and temperature, as shown in Figure 4.2.1. At subsurface conditions below a depth of 1500 m, corresponding to a geothermal gradient of 25–35°C/km and a hydrostatic pressure of 10.5 MPa/km, the density of supercritical CO₂ remains re-

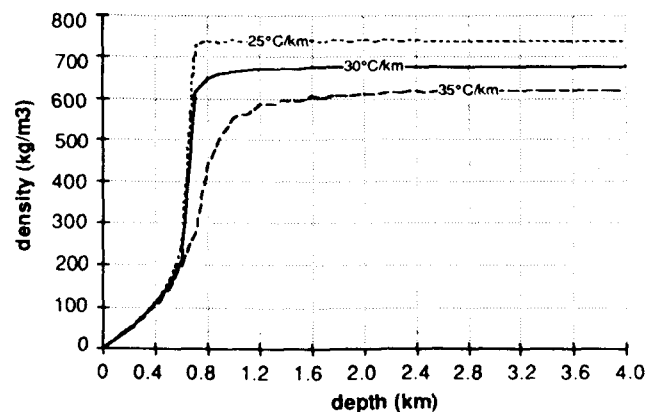


Figure 4.2.2 The density of CO₂ as a function of depth, assuming a hydrostatic gradient of 10.5 MPa/km and geothermal gradients ranging from 25 to 35°C/km (data from Van der Sluijs 1991).

markedly constant with depth and varies between 600 and 740 kg/m³ (Figure 4.2.2.). The CO₂ density at a depth of 800 m (= 8.5 MPa) will be ca 440 and 740 kg/m³, for gradients of 35 and 25°C/km respectively. Under the initial reservoir conditions of most oil and gas fields (P/T data presented in sections 4.6, 4.12 and 4.15), CO₂ will have a density of about 730 kg/m³ (660–800 kg/m³). This may be due to some overpressure caused by the generation of the hydrocarbons. If the reservoir is underpressured, if the geothermal gradient is anomalously high, or if the CO₂ is contaminated (with e.g. CH₄), the density may be considerably lower.

It is concluded that the average density of CO₂ will be around 700 kg/m³ at depths below 800 m, for 'normal' hydrostatic and geothermal gradients.

4.2.2.3 CO₂ STORAGE MECHANISMS

CO₂ injected into the pores of water saturated reservoir rocks may occur in three forms (pers. com. Eric Lindeberg):

- As free CO₂, i.e. in a CO₂ rich dense phase that may contain some water.
- In an aqueous phase: either as CO₂ dissolved in the brine or as dissolved bicarbonate ions (HCO₃⁻) liberated by CO₂ dissolving carbonate minerals.
- In solid minerals resulting from CO₂ reacting with minerals in the reservoir rock.

Partly based on these different forms of occurrence, four mechanisms can be distinguished that play an important role in the storage of CO₂ in a defined water-saturated reservoir (either a depleted and water flooded hydrocarbon reservoir or a trap on an aquifer):

- Volumetric sweep efficiency of CO₂, i.e. the displacement of formation water by free CO₂.
- Dissolution of CO₂ in the formation brine.
- Chemical reactions between CO₂ and minerals or pore fluids of the reservoir rocks.
- Pressure build-up in the reservoir.

Volumetric Sweep Efficiency of CO₂

An underground reservoir is generally formed by a porous rock with pores filled with fluids, usually consisting of salt water. If CO₂ is to be stored in such a reservoir, it has to displace these fluids. The displaced proportion of fluids is called the 'sweep efficiency' of CO₂. If the process is considered in three dimensions and displaced volumes are taken into account, it will be referred to as 'volumetric sweep efficiency'.

If an reservoir is 'closed', i.e. sealed off from the remainder of the subsurface by impermeable rock, the amount of CO₂ that can be stored will be determined by the pressure increase caused by the CO₂ injection (discussed below). If the reservoir is 'open', i.e. in hydraulic communication with neighbouring rocks, the volumetric sweep efficiency will determine the volume of CO₂ that can be stored. Any pressure increase due to CO₂ injection in these reservoirs will be compensated by interstitial fluids flowing out of the reservoir into adjacent formations.

Hence, continued CO₂ injection will ultimately result in CO₂ being spilled at the boundaries of the reservoir. The volumetric sweep efficiency corresponds to the fraction of the pore volume that can be filled with CO₂ before this gas reaches the boundaries of the reservoir.

The ability of CO₂ to displace water is low. This is largely caused by the low density of CO₂ relative to water, its high mobility, and rock heterogeneity. If CO₂ is injected into a reservoir it will float on the formation water (gravitational segregation), because of its lower underground density. In addition, because of its lower viscosity, it will move through the intergranular pores much more quickly than the formation water. Instead of displacing the water, the CO₂ largely by-passes the water and forms (multiple) low-viscosity fingers. Viscous fingering will be important in a homogeneous reservoir. However, this mechanism will usually be overshadowed by a preferential flow path of the CO₂ due to the heterogeneity of the reservoir ('channeling'). The combined effect of these processes is that once the CO₂ is injected into a geological trap, it tends to rise to the ceiling of the structure and to spread out in viscous fingers or channels. Hence, only a small proportion of the pore volume can be filled before CO₂ is spilled at the edges of an 'open' reservoir.

The volumetric sweep efficiency of CO₂ in an 'open' reservoir will be reservoir specific and will depend of various factors, such as relative permeabilities, densities and mobilities of the fluids, the injection scheme, reservoir dip, and rock heterogeneity (e.g. the ratio between vertical and horizontal permeability). Although extensive reservoir modelling has been done to quantify the CO₂ sweep efficiency, there is still some controversy about which percentage will be representative for the 'average' aquifer, especially because it is not well known how such an average aquifer will look like.

Van der Meer (in press) modelled an 'open' reservoir consisting of a dome-shaped trap on an 'open' aquifer. In order to extrapolate the results of the 2D-model to a 3D-reservoir, a horizontal sweep efficiency of 50% was applied. Dissolution was not taken into account. The modelling indicated a storage efficiency of 1 to 8%, depending on rock heterogeneity, reservoir dip, and the CO₂ injection rate. He defined the storage efficiency^[3] as the ratio between the CO₂ surface volume that could be stored in his simulation model and the CO₂ surface volume required to fill the entire pore volume of the reservoir under a maximum (geostatic) pressure. For an open reservoir at hydrostatic pressure, these percentages will correspond to an volumetric sweep efficiency of about 2 to 11%. These values are more or less in agreement with the modelling performed by Lindeberg (pers. com. 1994) on a similar reservoir which indicated a volumetric sweep efficiency of about 6%.

Dissolution of CO₂

On average, about 50 kg CO₂ can be dissolved in one cubic metre of water under subsurface conditions (30–150°C, 10–40 MPa). However, this value may vary by 50%, depending on the temperature, pressure and salinity of the formation water. The higher the pressure and the lower the salinity, the more CO₂ can dissolve. This effect is much more pronounced above 100°C. The relation

[3] The term storage efficiency refers in this inventory only to the fraction of the reservoir pore volume that can be filled with CO₂, irrespective of pressure.

between temperature and CO₂ solubility is more complex (see Chapter 7).

After injecting CO₂ into the subsurface, dissolution of CO₂ occurs at the interface of the bubble of free CO₂ and the formation water. The amount of dissolved CO₂ will be proportional to the total area of the CO₂-water contact. If the CO₂ mobility is relatively high, the displacement of the water by the CO₂ is entirely dominated by multiple viscous fingering. Strong fingering will create a relative large area between brine and CO₂ and thus favours the uptake of CO₂ into the brine by dissolution and diffusion. This will both be a sink for CO₂ and will possibly improve macroscopic sweep efficiency. A similar effect may be brought about by channelling in a heterogeneous reservoir. Dissolution because of molecular diffusion is only 10 cm/year, but may be much faster due to dispersion.

Some reservoir models are based on the presumption that about 20–30% of the injected CO₂ will dissolve in a relatively short time (Gunter et al., 1993, Korhøi, in press). Reservoir simulations by Lindeberg (pers. com. 1994) suggested during an injection period of about 5 years dissolution of 10% of the total amount of disposed CO₂. According to Van der Meer (pers. com. 1994), dissolution will not be so efficient and will be confined to a thin shell around the expanding bubble of free CO₂. He believes that it does not significantly contribute to the storage efficiency. Modelling of CO₂ storage in aquifers by Holt et al. (in press) also suggests that the amount of CO₂ dissolved in the formation brine will be insignificant compared to the amount of CO₂ stored as a free phase. However, it is commonly believed that when time passes the CO₂ will dissolve and ultimately all free CO₂ will go into solution (e.g. Gunter et al., 1993). The occurrence of natural CO₂ pools in the subsurface similar to hydrocarbon reservoirs, some of which may be more than *ca* 65 million years old (Studlick et al., 1989), indicates that this process is extremely slow and that dissolution will play an insignificant role after migration.

The processes discussed above largely apply to reservoir rocks with a primary permeability, such as sandstone formations. In rock with a secondary permeability due to fracturing, such as fractured Chalk Formation, the uptake of CO₂ will be very different because of extreme channelling. The fracture system, which typically occupies 0.3 to 1% of the volume (Selvig and Kosack, 1991), will be rapidly filled with CO₂ which will propagate far out through the formation. The displacement of brine from the matrix will be small due to low matrix permeability and high capillary pressure between CO₂ and brine. CO₂ will, however, diffuse into the matrix until the matrix brine has been saturated with approximately 50 kg CO₂ per m³ brine (cf. the uptake of oxygen from the branching air distribution system in lungs). The time that elapses before a solubility equilibrium is reached, will be in the order of months for the typical block sizes found in North Sea Chalk reservoirs. In the case of a CO₂ disposal project that lasts for several years, a significant amount of CO₂ will be stored dissolved in the matrix brine. A saturation of 50 kg CO₂/m³ brine corresponds to a filling of the pore volume with free CO₂ by approximately 7%. Brine swelling will be negligible. This mechanism for uptake of CO₂ into the matrix should be subject to further investigation. In the inventories that follow, fractured Chalk is assumed to have a storage efficiency of 6%.

Dissolved CO₂ will be important as a 'permanent' sink, but the role of dissolution during the injection process remains ambiguous. At present, it is believed that the

major control on the filling of most reservoirs will be the expanding bubble of free CO₂. Dissolution is thought to be restricted to a thin zone around the bubble and to be a slow process relative to the flow velocity of free CO₂. Any CO₂ that gets into solution is expected to be overrun by the moving front of the bubble. The most important parameter to compute the storage capacity is therefore expected to be the macroscopic, volumetric sweep efficiency of free CO₂.

Chemical Reactions

Although this remains to be confirmed by experiments, free supercritical CO₂ is generally considered to be relatively non-reactive. If CO₂ is dissolved in the formation water, however, it may react with the rock minerals. The chemical reactions that will take place will greatly depend on the mineralogy and texture of the rock, the composition of the formation water, the temperature and pressure in the reservoir, flow rates and the timing of the reactions (see Chapter 7). As with dissolution into formation water, CO₂ deposition in solid minerals is a mechanism that will possibly be important to provide a permanent sink in the long term.

The general ultimate effect of chemical reactions on the CO₂ storage capacity is not clear. The interactions between CO₂, water and rock are too reservoir specific and too complex to quantify their effect on the storage capacity. They are therefore not taken into account in the inventory of the underground CO₂ storage capacity of the European Union and Norway.

Pressure Build-Up

If CO₂ is injected with sufficient pressure into an aquifer which is in open communication with the surface (an 'open' aquifer), the CO₂ is able to push away the formation water. Displaced formation water may eventually flow into surface waters, which may be oceans, lakes or phreatic groundwater. The pressure will be hydrostatic again when the conditions in the aquifer have reached equilibrium after CO₂ injection. In reservoirs connected to an aquifer system that does not communicate with the surface (a 'closed' system), water displacement by CO₂ must be accommodated by compression of rock and interstitial water. If the reservoir volume is insignificantly small compared to the volume of the connected aquifer system, formation water flowing out of the reservoir into the aquifer system will lead to a negligible increase of the reservoir pressure. The pressure will increase significantly if the reservoir itself is 'closed'.

If CO₂ is intended to be injected into an aquifer, CO₂ must be able to permeate the aquifer at a reasonable rate with limited pressure losses^[4]. Based on modelling of the radial pressure behaviour of CO₂ injected into an 'open' aquifer at a depth of 800 m and 1800 m, Van der Meer et al. (1992) concluded that with permeabilities smaller than 50 mD ($\approx 0.050 \mu\text{m}^2$), unacceptable pressure losses occurred. CO₂ injection under these conditions was not workable. Between 50 and 100 mD, CO₂ injection is only feasible if wells are used that have a negative skin factor, i.e. an improved flow performance at the bottom hole injection point. Van der Meer et al. (1992) therefore suggest a cut-off level of 50–100 mD.^[5]

In the case of a 'closed' aquifer (system), the volume of CO₂ injected must be accommodated by compression of the reservoir. In a relatively small reservoir the pressure build-up near the bottom hole injection point will be very large (Van der Meer, in press). The compressibility of both the formation water and the rock will be of importance.

The most practical parameter for estimating how the pressure increases due to injection is the pore volume compressibility (c_p), which is believed to be a function of the porosity (Hall, 1953)^[6] and/or net overburden pressure (Fatt, 1958). The compressibility of the formation water (c_w) is well characterised as a function of temperature, pressure and salinity (Numbere et al., 1977).

Archer and Wall (1992) give the following typical compressibility values for the formation brine, for the pore volume of consolidated and unconsolidated sand, and for hydrocarbons:

— formation brine	4.35·10 ⁻⁵	bar ⁻¹
— consolidated sand at 400 bar	3.63·10 ⁻⁵	bar ⁻¹
— unconsolidated sand at 400 bar	1.43·10 ⁻⁴	bar ⁻¹
— undersaturated black oil	2.47·10 ⁻⁴	bar ⁻¹
— gas at 400 bar	2.51·10 ⁻³	bar ⁻¹

If the pressure is increased by 10 MPa (100 bar), the pore water and formation is compressed by 0.8% for consolidated sand and by 1.9% for unconsolidated sand, leading to an 'extra' pore volume that can be occupied by CO₂. The above compressibility values illustrate that if the aquifers contain hydrocarbons, this surplus volume will be larger.

For typical North Sea conditions, the pore volume compressibility will be 1.5·10⁻⁴ bar⁻¹ on average, with an uncertainty of about 50% (Hall, 1953, Fatt, 1958). The compressibility of formation water for North Sea aquifers will vary only between 3.9·10⁻⁵ bar⁻¹ and 4.5·10⁻⁵ bar⁻¹. Hence, a reasonable estimate of the total compressibility of the reservoir (c_r), i.e. the sum of the water and the pore compressibility, will be 1.9·10⁻⁴ bar⁻¹ (1.5·10⁻⁴ bar⁻¹ + 0.41·10⁻⁴ bar⁻¹). This implies that if 2% of the reservoir pore volume is filled, the pressure will increase by 10.5 MPa (105 bar), assuming a 100% efficiency of the compression during the injection operation.

It is concluded that only aquifers with an average permeability larger than 100 mD ($\approx 0.1 \mu\text{m}^2$) can constitute suitable CO₂ reservoirs. In the inventories below, this permeability value has been used as a cut-off. The filling of a 'closed' aquifer with CO₂ by 2% of the pore volume will

[4] The CO₂ flow from the bottom hole injection point into the aquifer is given by the following equation:

$$Q = \Delta P \cdot k \cdot h / (\mu \cdot T \cdot z \cdot \ln(r)) \cdot \text{factor}$$

where: Q	=	flow rate at distance r
ΔP	=	pressure drop at distance r
k	=	permeability
h	=	height of formation
μ	=	gas viscosity (function of pressure!)
r	=	distance from bottom hole injection point
z	=	gas deviation factor (function of pressure!)
factor:	=	includes the unit conversion constant, well radius, and the skin factor

[5] It should be noted that these relatively high permeabilities are solely required near the bottom-hole well. Since the CO₂ disperse radially, the amount of CO₂ that must be squeezed through the intergranular pores, decreases exponentially away from the injection point. Hence, farther away from this point, smaller pores can accommodate an equal rate of CO₂ injection.

[6] $c_p = - (1/V_p) \cdot (dV_p/dp)$, where c_p = pore volume compressibility, V_p = pore volume and p = internal pressure.

result in a pressure increase in the order of 10.5 MPa (105 bar). So, if the reservoir can withstand this pressure increase, this fraction of the entire pore volume of a 'closed' aquifer could be filled. The pressure underground and the strength of the reservoir are, however, unknown for most aquifers. Moreover, in most cases it will be very difficult to demonstrate that an aquifer is actually 'closed'.

4.2.3 Aquifers

4.2.3.1 DEFINITIONS

'Open' and 'Closed' Aquifers

A broad definition of an aquifer is: 'a water-bearing stratum or bed' (Visser 1980). A more restricted definition is: 'a body of permeable rock that is capable of storing significant quantities of water, is underlain by impermeable material, and through which groundwater moves' (Allaby and Allaby, 1990). An additional criterion may be that the aquifer is 'capable of producing water as from a well' (American Geological Institute, 1974). A confined aquifer is sealed above by impervious material (Visser, 1980, Allaby and Allaby, 1990). We will use the term 'aquifer' for a permeable and porous rock body in the subsurface sealed above by an impervious layer. Laterally, the aquifer may be open or sealed. It is assumed that all aquifers are water-saturated.

Two kinds of aquifers can be distinguished: an 'open' aquifer and a 'closed' aquifer. An 'open' aquifer is an aquifer sealed by an impervious layer at the top, but with lateral boundaries that are at some point in open communication with the ground surface. A 'closed' aquifer (or aquifer system) is an aquifer which is completely sealed off from adjacent formations by impervious layers. One should realise that entirely 'open' and entirely 'closed' aquifers are hypothetical end members of a wide spectrum of possible situations. Note that in a 'closed' aquifer moving formation water will be unlikely. In the case of an 'open' aquifer, the fluid pressure will correspond to the hydrostatic one.

Seals and Caprocks

Seal and caprock are terms used by petroleum geologists to refer to rock layers that are impermeable to hydrocarbons, or strictly speaking, to horizons which will reduce the vertical migration of hydrocarbons in the subsurface. Visser (1980) defines a 'seal' or 'sealing formation' as 'rocks impermeable to hydrocarbons and, in consequence, capable of forming a trap or a permeability barrier in a reservoir', and a 'cap rock' as 'rock, essentially impervious to hydrocarbons, covering the reservoir'. One should bear in mind that 'impermeable' is here not used as an absolute concept, since all sedimentary rocks, apart from salt, are to some degree permeable over time. Hence, a more accurate definition of a seal would be: 'horizons which do not allow hydrocarbons arriving in an adjacent carrier rock at a given rate to leave the carrier rock at the same rate'. However, we will use the term 'seal' in a broader sense: it will be used for horizons impermeable not only to hydrocarbons, but also to other fluids and gases that tend to escape from a carrier rock, such as formation water and (free) CO₂. A 'cap rock' will refer to a seal immediately above an aquifer or reservoir.

Fluids and gases will in the long term escape from the reservoir by e.g. diffusion, even from a reservoir with a perfect seal. This is, however, a very slow process. For example, under stable tectonic conditions the half-life (i.e.

the time taken for half the petroleum to leak away from a particular accumulation) of most reservoirs in the North Sea is in the order of several millions of years. The existence of natural CO₂ reservoirs, some of them formed more than 65 million years ago, illustrates that the retention time of CO₂ in similar subsurface reservoirs will be in the same order of magnitude.

The migration behaviour of CO₂ in natural CO₂ reservoirs is fairly similar to that of natural gas (CH₄), although the permeability of cap rocks to CO₂ is slightly different, and the efficiency of certain cap rocks may be adversely affected by geochemical reactions with CO₂. Given these caveats, it is assumed that knowledge of the migration behaviour of natural gas could be applied to future CO₂ disposal sites. Thus, in practical terms, if confined to cap rocks known to seal hydrocarbon accumulations, CO₂ would almost certainly be retained for millions of years underground, far longer than necessary to prevent it contributing to likely peak levels of global warming. This statement is substantiated by our knowledge of the geological history of natural CO₂ fields (see Studlick et al., 1989).

Evaporites form an important cap rock for various major aquifers in Europe (e.g. Zechstein above Rotliegend, Keuper above older Triassic aquifers). These evaporites usually contain anhydrite. Chemical analysis revealed that CO₂ may dissolve anhydrite (Chapter 5). However, a major natural CO₂ reservoir is capped by anhydrite, which suggests that anhydrite may form an effective seal for CO₂ (Smackover reservoir capped by anhydrite of the Buckner Formation, Studlick et al., 1989).

Structural and Stratigraphic Traps

A trap is defined as: 'The configuration of rocks, impermeable to hydrocarbons, partly enveloping the reservoir, so as to prevent escape of accumulating, or accumulated, hydrocarbons' (Visser 1980). In a broader sense, the term can be used for structures that are capable of holding fluids or gases underground which are lighter than the formation water. In the case of CO₂ storage, the term refers to a rock configuration that can retain the CO₂ in the reservoir, so 'hydrocarbons' in the definition of Visser (1980) should be replaced by CO₂. According to Allaby and Allaby (1990), the following types of traps are distinguished:

- **structural traps:** traps formed by deformation of porous and non-porous rocks, such as:
 - *anticlinal trap:* a fold structure with an arc of non-porous rock overlying porous rock, providing a trap in which oil, gas or water may accumulate.
 - *fault trap:* a structure in which water, oil, or gas may be trapped on one side of a fault plane by an impervious horizon thrown above it by a fault
 - *unconformity trap:* [7] a structure in which folding, uplift and erosion of porous strata has been followed by deposition of later beds which act as a seal
- **stratigraphic trap:** a trap resulting from lithological variation, such as:
 - *sand pinch-out traps:* discontinuous lenses of sand and silt embedded in impervious sediments, e.g. in

a fluvial or delta environment, or closures on the margins of sand bodies

- *reef traps:* porous reef limestones surrounded by impervious rock

Structural traps are commonly referred to as 'closed structures'. In the storage inventory of aquifers, as presented in the following section, traps have generally been identified on structural contour maps. Hence, the traps recognised will be structural traps or stratigraphic traps at the limit of a reservoir formation. Definition of other forms of stratigraphic traps requires detailed information on the lithological variation underground. These data were generally not available.

Traps on aquifers may form 'open' or 'closed' reservoirs. An 'open' trap refers to a trap with a spill point and is in hydraulic communication with the underlying aquifer (e.g. anticlinal and unconformity traps and some dipping fault traps). A 'closed' trap has no spillpoints. It is completely sealed off and does not communicate with the remainder of the aquifer (e.g. traps caused by intra-formational facies changes, faulted blocks). In the inventory, the term 'trap' will be used for structures on *part* of an aquifer. A 'closed' aquifer, as defined above, will not be regarded as a trap on an aquifer, although it will be enclosed by a large stratigraphic or structural trap.

Storage Efficiency

The term 'CO₂ storage efficiency' is used in this inventory for the expected maximum volume of CO₂ that can be stored in a reservoir, expressed as a percentage of the total reservoir pore volume. Hence, the term simply refers to the fraction of the reservoir pore volume that can be filled with CO₂.

4.2.3.2 STORAGE IN AQUIFERS

In view of CO₂ storage in aquifers, several topics have to be addressed for individual cases. Firstly, the pressure build-up in the aquifer will be a point of concern. In 'open' reservoirs, the increased pressure at the injection site will be compensated by pore water moving along the pressure gradient towards levels of lower pressure. In 'closed' reservoirs, where formation water cannot flow out of the reservoir, CO₂ injection will result in a high reservoir pressure. Regional and temporal pressure changes in the aquifer and the accompanying movement of fluids have to be investigated. In addition, the strength of seals and reservoir rocks should be established to determine if the storage site can withstand these pressures. Secondly, due to the nature of CO₂ flow by viscous fingering, channelling and gravitational segregation, the most critical issue is the migration and regional distribution of injected CO₂ over time. Only those aquifers where a re-entering of stored CO₂ to the atmosphere can be excluded for several thousands of years are suitable. In most cases the time-lag will be far greater. If storage and migration of CO₂ over thousands to millions of years is considered, other factors such as dissolution, diffusion and mineral reaction come into play, which for simplification reasons have not been considered in the storage calculations presented in the inventory below.

So, underground storage of CO₂ will be highly reservoir specific. Nevertheless, options for CO₂ disposal in aquifers fall naturally in three categories:

1. Storage in traps on 'open' aquifers. Two kind of traps can be distinguished: 'open' and 'closed' traps. In the

[7] It is not clear whether an unconformity trap is a stratigraphic or a structural trap, since it contains elements of both.

case of an 'open' trap, CO₂ injection will be stopped as the CO₂ reaches the spill point of the trap (cf. category 2). 'Closed' traps form reservoirs that are entirely sealed off from other porous rocks by structural or stratigraphic permeability barriers. Injection in these traps will be determined by the pressure build-up (cf. category 3).

2. Storage outside traps in aquifers with 'open' lateral boundaries. The restriction that the CO₂ should be confined to a trap is released in this option and the entire aquifer will be available for CO₂ disposal as long as the CO₂ does not reach the limits of the top seal.
3. Storage in 'closed' aquifers. Since a 'closed' aquifer does not communicate with other formations, the whole pore volume of the aquifer will be available for CO₂ disposal. The amount of CO₂ that can be injected will be determined by the pressure build-up and the strength of the reservoir. The pressure increase will be considerable, especially around the injection point.

It will be apparent that the reservoir subdivision into traps on an aquifer and the entire aquifer is rather ambiguous and is largely a matter of scale. A 'closed' aquifer can be considered as an aquifer enclosed by a large 'closed' trap, and an 'open' aquifer which can be largely filled without CO₂ escaping from it, can be regarded as a special kind of (composite) 'open' trap. With respect to the technical aspects of assessing the CO₂ storage capacity of an aquifer reservoir, there will be no fundamental difference between traps and aquifers, and it will probably only be relevant whether the reservoir (either a trap on a small part of the aquifer or the entire aquifer) is 'open' or 'closed'.

The local pressure build-up forms an important drawback of CO₂ injection into 'closed' reservoir, since it may endanger the integrity of the reservoir. The pressure increase due to the surplus volume of CO₂ stored in the reservoir must be accommodated by compression of the rock and its interstitial fluids. In the following inventories it is assumed that 'closed' reservoirs can be filled with CO₂ by 2% of the reservoir pore volume (see section 4.2.2.3), i.e. a CO₂ storage efficiency of 2%. When injecting CO₂ in an 'open' reservoir, the pressure build-up will not be a problem. The major concern will be to prevent CO₂ from being spilled at the open boundaries of the reservoir (spill-point). The reservoir volume of CO₂ that can be stored corresponds with the volume of formation water flowing out of the reservoir before CO₂ reaches these boundaries. Hence, the fraction of the pore volume in the reservoir that can be filled with CO₂ corresponds with the volumetric sweep efficiency of CO₂ (see section 4.2.2.3), which is estimated to be around 6% on average. This value will be used in following inventories for 'open' reservoirs.

The standard approach of the inventory is to present the estimated storage capacity of the trapped fraction of the aquifers, irrespective whether these aquifers are 'open' or 'closed'. This is done because the application of the entire volume of either an 'open' or 'closed' aquifer for storage purposes will pose major uncertainties. The data set on the subsurface is generally poor and incomplete, so that it will be very difficult to gather all information necessary to predict accurately what will happen to the CO₂ along its entire flow path if the entire aquifer is used for disposal purposes. It will be impossible to give an exact estimate of the storage potential. Over an extensive range, it will generally be very difficult to determine if a reservoir is actually

'closed' or if the quality of the seal, the stability of the reservoir rock and yield strength of faults and fractures is sufficient to withstand the increased pressures. In the case of a 'closed' aquifer, the filling of the aquifer by 2% of its entire pore volume will generate a pressure that may endanger the stability of the reservoir. This problem will not arise if storage will be restricted to traps on a small proportion of the aquifer. In the case of an 'open' aquifer, CO₂ will spread over a very large area in the subsurface, which is only known to a limited extent. This will complicate the safeguarding of reservoir integrity and reduce the controllability of the CO₂ stored underground.

In some cases, however, the storage capacity will be discussed for CO₂ disposal in the entire aquifer. This will be done if enough information on the subsurface is available and aquifers can be identified that are entirely sealed ('closed') and so deeply buried below a thick package of impermeable rock, that the risk of CO₂ escaping from them is considered to be negligible (category 3). Other candidates are deep aquifers that have 'open' lateral boundaries but an appropriate top seal with a very large range, and that will not be used for geothermal heat recovery, potable water supply or any other purpose. The range should be so large that the disposed CO₂ will not reach the margins of the basin or the limits of the top seal (category 2).

Storage in Traps on 'Open' Aquifers

'Open' aquifers are characterised by direct communication between the fluids in the aquifer and the surface at some point in the basin, e.g. where the aquifer crops out at the edge of the basin. Consequently, the disposed CO₂ may ultimately escape from the reservoir and reach the surface, probably after a period in the order of thousands to ten thousands of years. So, a structural trap will be required if the CO₂ is intended to be held underground permanently at a fixed location. A reason to restrict CO₂ storage to traps may additionally be the recoverability of the stored CO₂. CO₂ storage in traps is likely to apply in onshore Europe, where the sedimentary basins are usually small. CO₂ will therefore reach the boundaries of the seal after a relatively short period. Moreover, some of the aquifers may outcrop nearby or may be used for water supply, geothermal heat recovery or storage of natural gas.

The pressure in a 'open' aquifer is directly related to the column of formation water above the aquifer. Hence, the average hydrostatic pressure of 10.5 MPa/km (105 bar/km) can be applied to calculate the underground pressure. The thus calculated pressure will, however, not be valid if the formation water shows anomalous salinities or if the aquifer is at a great depth (>3000 m). Under 'normal' underground conditions, i.e. with a hydrostatic gradient of 10.5 MPa/km and a geothermal gradient of 25–35°C/km, the density of free CO₂ will typically be between 600 and 740 kg/m³. To calculate the CO₂ storage capacity of the aquifer, a CO₂ density of 700 kg/m³ should therefore provide a reliable estimate (section 4.2.2.2).

Storage in 'open' traps implies that the viscous fingering (or preferential channelling due to reservoir heterogeneity) and gravitational segregation of CO₂ determines the fraction of the trapped pore volume that can be filled. The effect of dissolution of CO₂ and possible chemical reactions is considered to be insignificant. For this inventory, it is assumed that the storage efficiency of 'open' traps is 6%, i.e. after filling of 6% of the trapped pore volume CO₂ will be spilled at the edges of the trap and the injection operation will be stopped. One should realise, however, that at this moment the pressure gradient in the aquifer will

be the highest. CO₂ will therefore continue to expand after injection until a pressure equilibrium is reached. This will cause an overspill. The time between cessation of injection and pressure equilibrium will be in the order of the injection period (pers. com. Van der Meer 1994). The density of the CO₂ stored will be determined by the initial pressure and temperature of the aquifer.

For a 'closed' trap, it is assumed that 2% of the trapped pore volume can be filled with CO₂ (see storage in 'closed' aquifer, discussed below), which means a CO₂ storage efficiency of 2%. Although the density of CO₂ will be larger than under the initial reservoir conditions due to the pressure increase caused by the CO₂ injection, the estimated storage capacity will be based on a CO₂ density at initial temperature and pressure.

In most cases, however, the storage capacity is based on the total trapped fraction of one or more aquifers, including both 'open' and 'closed' traps. In that case, it is assumed that 4% of the trapped pore volume can be filled with CO₂.

Storage in 'Open' Aquifers Outside Traps

In large sedimentary basins where the aquifers are currently regarded as useless (mostly offshore), the restriction that CO₂ should be stored in a trap may be ignored and (a part of) the entire aquifer volume could be used for CO₂ disposal. CO₂ could be injected into an aquifer with only a top seal, as long as CO₂ does not reach the boundaries of the basin or the limits of the top seal. In theory, the injection would have to be stopped before CO₂ is predicted to eventually arrive at the boundaries of the basin or the limits of the seal. There is, however, a possibility that this moment will never occur in aquifers with a very large range, because along the flow path through the aquifer, CO₂ may dissolve or reprecipitate before it arrives at the limits of the aquifer. To what extent this will happen depends on the specific reservoir characteristics and the injection rate. It will therefore be impossible to give a reliable estimate of the CO₂ storage capacity in general terms. If aquifers are believed to be appropriate for this type of disposal, an arbitrary estimate of its theoretical maximum storage capacity is given (see below).

There are several indications that even if CO₂ escapes from the reservoir, it will take a very long time before it reaches the surface. For the Netherlands, it would take at least five thousand years before a large bubble of free CO₂ released at a depth of 1000 m would reach the surface (Chapter 5). Modelling by Weir et al. (1994) indicates that free CO₂ escaping from a reservoir will dissolve in the water after few thousands years. Buoyancy will never bring this carbonated water to the surface if it is fresh water, because it will be denser than the surrounding CO₂-free water. Koide et al. (1994) state that a 'self-trapping' mechanism will retain free CO₂ underground in outcropping aquifers for offshore areas with a water depth of several hundreds of meters and a maximum temperature of 10°C. The 'self-trapping' mechanism is induced by the formation of CO₂-hydrates under the cool formation temperature and the pressure of the water column. A similar mechanism may apply to the shallow subsurface onshore.

Van der Meer (in press) modelled the above disposal concept. In the model, 274 Mt CO₂ is injected over a period of 50 years into a quasi-infinite aquifer of 55 m thick ($f = 20\%$, $K_h = 200$ mD, $K_h/K_v = 0.1$). The simulation, which did not consider dissolution, revealed that the injected CO₂ will rise to the top of the aquifer and spread out, forming a flat bubble of free CO₂ below the top seal. Directly after injection, the CO₂ will occupy an area of

about 200 km² (radius of *ca* 8 km). This area will continue to expand afterwards until a pressure equilibrium is reached. Thereafter, the CO₂ will not expand any more and will be relatively stable. The only CO₂ movements will be those due to buoyancy (if the aquifer is inclined), diffusion and flowing groundwater, all in the order of a few centimetres to tens of centimetres per year. When pressure equilibrium is reached, about 100 years after the injection has stopped, the CO₂ will occupy an area of about 250 km² (radius of *ca* 9 km). The aquifer pore volume below this area is 2.8 km³, which leads, in this specific example, to a CO₂ occupation of about 14% of the total pore volume, with a horizontal sweep efficiency of 100% and a CO₂ reservoir density of 700 kg/m³. The CO₂ occupation will be 7% with a horizontal sweep efficiency of 50%. However, the storage capacity will be related to the area of the aquifer rather than the volume of the aquifer, because the CO₂ will immediately rise to the ceiling of the reservoir and is not confined by any trap, which implies that only the pore volume in the upper part of the aquifer will play a significant role. For the storage calculation in this inventory, it is assumed that 6% of the entire pore volume of an 'open' aquifer can be filled with CO₂ (i.e. a storage efficiency of 6%) if the aquifer is considered to be suitable for storage outside traps.

A major disadvantage of this disposal concept is that the uncertainties about the integrity of the reservoir will be large and that the controllability of the CO₂ storage site will be small, because the area occupied by CO₂ will be extensive. Since CO₂ will not remain fixed to a trap, it will be able to invade a large part the aquifer and the uncertainties about what could happen along the entire flow path will be difficult to predict. Much information for the entire range of the aquifer must be available before CO₂ storage can be considered. Some of the aquifer properties that should be known are: quality of the top seal, yield strength of faults and fractures, mechanical and chemical stability of the reservoir rock, underground pressure, orientation and magnitude of tectonic stresses, flow pattern and velocity of the formation water, and depth of the boundary between fresh, potable water and useless brine. Within the area that could be invaded by CO₂, the integrity of the reservoir should be sufficient to guarantee a safe CO₂ retention time of at least thousands of years. In addition, one should be certain that disposed CO₂ (or formation brine displaced by the CO₂) will not pollute ground or surface water. Hence, it will generally be very problematic to differentiate between aquifers that need traps for CO₂ storage and those that do not need traps, since this requires information that is generally not available.

Storage in 'Closed' Aquifers

A 'closed' aquifer is entirely enclosed by impermeable rock, e.g. a sand lens enclosed by mudstones or an aquifer confined to a faulted block. So, the entire aquifer can be considered to be within a stratigraphic or structural trap and there is no reason to restrict the CO₂ storage to closed structures on parts of the aquifer. Since pore fluids and gases cannot flow out of the aquifer, CO₂ injection will result in a considerable pressure increase, and the underground volume occupied by the disposed CO₂ has to be accommodated by compression of the reservoir rock and its interstitial fluids. For the typical rock and brine compressibility found in the North Sea, the filling of the total pore volume with CO₂ by 2% will increase the pressure by 10.5 MPa (see section 4.2.2.3). Assuming that such an rise in pressure is acceptable, an estimate of the storage capacity of 'closed' aquifers can be based on a CO₂ storage efficiency of 2%.

Temperature and pressure control CO₂ density. Since 'closed' aquifers do not communicate with the surface, they may be under- or overpressured. However, a 'closed' aquifer will most probably be overpressured (> hydrostatic pressure) after CO₂ injection, which means that the reservoir density of CO₂ will be larger than 700 kg/m³, because this density will only be valid for average hydrostatic conditions. In spite of CO₂ injection increasing the pressure, the estimate of the storage capacity will be based on a CO₂ density under initial reservoir conditions. If no reservoir specific data are available, average geothermal and hydrostatic gradients will be assumed (30°C/km and 10.5 MPa/km). On the one hand, the storage estimate will be conservative because it will be based on a CO₂ density that will be lower than the actual one. On the other hand, the estimate will be optimistic because it remains uncertain whether the reservoir can withstand the rise in pressure associated with the 2% CO₂ occupation (see below).

In the above section, the aquifer is assumed to be 'closed' in absolute terms, but the extent to which the seal is impervious to pore fluids or gases depends on the fluid pressure in the aquifer. If this pressure is increased enough, the seal will leak and pore fluids will migrate into adjacent aquifers with lower pressures. Hence, in a reservoir the pressure can be increased by pumping CO₂ into it up to the point where this 'leaking pressure' is reached. Gaarenstroom et al. (1993) discuss overpressured pre-Cretaceous aquifers, forming a fault-bounded reservoir complex sealed off from the overburden formations by impervious Late Cretaceous and younger strata. The complex consists of a number of cells that are in pressure equilibrium. Most cells are at the brink of leaking: any substantial pressure increase will cause one cell to leak into another through its faulted boundaries. If the pressure decreases, the leak will close again. The retention capacity of the system as a whole, i.e. the difference between the fluid pressure in the reservoir and the expected leakage pressure of the top seal, varies for these reservoirs from ca 1 to 14 MPa (average 7.3 MPa). For the average compressibility mentioned in section 4.2.2.3, this would mean that 0.2 to 2.8% (average 1.5%) of the pore volume can be filled with CO₂.

The results from reservoir modelling suggest that the pressure build-up close to the well could be very high (Van der Meer pers. com. 1994). In those cases, the possibility of the leaking of seals or the re-activation or opening of faults has to be considered. An unacceptable high pressure near the injection well may develop if ca 2% of the entire pore space of a closed system is filled. In the case of CO₂ injection at shallow depth, the pore pressure may locally even become larger than the overburden pressure. This implies that the pressure is so large that the overlying formations will be lifted, a situation which should be prevented at any time.

The data on the subsurface are discontinuous: only where wells have been drilled and cores have been sampled is actual lithological information at hand. It will therefore be very difficult to demonstrate if an aquifer is actually 'closed'. Only a guess can be made about the probability that an aquifer is entirely sealed off from other formations. An anomalous fluid pressure significantly deviating from the hydrostatic one, may indicate that the aquifer is 'closed', but as discussed above, its seal may easily yield under increased pressure.

4.2.3.3 OFFSHORE VERSUS ONSHORE

In the inventories that follow, a strict distinction has been made between offshore and onshore aquifers. This is not

done because the aquifers differ so much, but because it was felt that it should be possible to evaluate the different technical, economic and ecological conditions for CO₂ disposal onshore and offshore. Examples are differences in drilling and transport costs or in environmental legislation. Another reason is the difference in the availability of data. Published data on the subsurface below the sea are scarce and very limited for most countries. Hence, the quantification of the CO₂ storage potential of offshore aquifers is highly restricted.

An additional argument for this subdivision is that the likelihood of coming upon a 'closed' aquifer offshore will be larger than onshore, because the sedimentary basins below the sea tend to be larger and thicker. They are therefore more likely to contain deep-seated aquifers which are entirely overlain by impervious rocks. In addition, coarse and therefore permeable sequences predominate at the basin margins, whereas in the basin centre finer grained sediments prevail that may constitute suitable cap rocks. Useless aquifers with a very extensive range will be candidates for CO₂ disposal not confined to traps. These aquifers will also be more abundant offshore than onshore, because offshore the basins are generally larger and most aquifers are not being used. However, the distinction between onshore and offshore aquifers is far from unambiguous, because a large part of the land area of The Netherlands, Germany and Denmark can be considered as an onshore continuation of the North Sea Basin.^[8]

4.2.3.4 STORAGE CALCULATION FOR AQUIFERS

Aquifers have only been included in the inventory of potential CO₂ reservoirs if it was possible to quantify their storage capacity. This means that the storage calculation is primarily focused on the CO₂ storage in traps and that the large potential for CO₂ disposal in aquifers outside traps is only considered if enough data on the subsurface are available. Other constraints that should be fulfilled are an average permeability of at least 100 mD ($\approx 0.1 \mu\text{m}^2$) and a depth of 800 m (see section 4.2.2). Most storage inventories that follow conform to these constraints. If not, this will be mentioned explicitly. In some cases the nature of the data dictates other restrictions, e.g. in France and Germany, where the inventory has been based on geothermal reports that used other criteria to define 'good' reservoir rocks. A storage capacity for each individual trap will not be given, since in most cases individual traps cannot be identified. Instead, the likely volume of the aquifer confined to traps is estimated as a percentage of the total aquifer volume. This percentage is based on the results from basins for which structural contour maps exist. If insufficient permeability measurements are available, the storage capacity has not been presented, because the appropriateness of the aquifer is questionable.

If it is apparent from the available data that major unused aquifers are most probably 'closed' or have a good top seal extending over a very large area, the concept of using the entire pore volume of the aquifer for CO₂ disposal (storage outside traps) will be discussed. When these aquifers are considered to be appropriate for this concept, a rough estimate of the storage capacity for the entire aquifer will be presented. This is done to give an impression of the large

[8] On a geological time scale, i.e. over a period of ten thousand years, the distinction between offshore and onshore becomes even less substantial, because shallow seas may emerge or coastal lowlands may be inundated as a result of eustatic sea-level changes.

capacity of the entire pore volume of these aquifers that would be totally disregarded if only the potential of traps would be mentioned. However, these estimates give only an order of magnitude of the storage potential and are generally based on information that is insufficient to give an accurate value. The uncertainties involved will be very large. Whether the entire aquifer can actually be used for CO₂ disposal, or an accurate prediction of the capacity, can only be established by a detailed evaluation of the individual reservoirs, which is beyond the scope of this inventory.

The storage capacity can be calculated for two situations: for the entire aquifer pore volume and for the pore volume confined by traps. The latter is the 'default' capacity given in the inventories that follow and is presented in standardised tables. In both situations, for storage in and outside traps, the storage capacity of the reservoir is calculated by multiplying the reservoir pore volume by the CO₂ storage efficiency. For 'closed' reservoirs this efficiency is assumed to be 2% and in 'open' reservoirs 6% (see previous sections); an intermediate percentage of 4% is used if it is not clear whether the reservoir is 'open' or 'closed' (Table 4.2.1). The above calculation will result in the reservoir volume of the expected amount of CO₂ that can be stored in the reservoir. Subsequently, the reservoir volume is multiplied by the CO₂ density under initial reservoir conditions (P, T) in order to convert the volumetric units into weight units. This is done because weight will give a better impression of an amount of gas (independent of P and T).

Table 4.2.1 CO₂ storage efficiency, i.e. the fraction of the reservoir pore volume that can be filled with CO₂.

RESERVOIR TYPE	
'closed' aquifer or 'closed' trap	2%
'open' aquifer or 'open' trap	6%
aquifers or traps from which it is unclear if they are open' or 'closed'	4%

* Fractured Chalk is an exception and is assumed to have a storage capacity of 6%.

The storage capacity of the trapped fraction of an aquifer is calculated as follows:

$$Q_{\text{trap}} = V_p \cdot h_{st} \cdot \text{TRAPPED}\% \cdot \rho_{CO_2}$$

where:

$$V_p = V_b \cdot \text{Net:Gross} \cdot \phi$$

$$Q_{\text{trap}} = \text{storage capacity confined to traps [Mt CO}_2\text{]}$$

$$\phi = \text{porosity [\%]}$$

$$V_p = \text{total pore volume of the aquifer below 800 m [km}^3\text{]}$$

$$h_{st} = \text{storage efficiency, i.e. fraction of the pore volume that can be filled with CO}_2 \text{ (see Table 4.2.1) [\%]}$$

$$V_b = \text{bulk volume of the aquifer below 800 m [km}^3\text{]}$$

$$\text{Net:Gross} = \text{percentage of porous, permeable rock [\%]}$$

$$\text{TRAPPED}\% = \text{percentage of aquifer being in a trap [\%]}$$

$$\rho_{CO_2} = \text{CO}_2 \text{ density at initial reservoir conditions [kg/m}^3\text{]}$$

The storage capacity for a concept in which the entire pore volume of an aquifer is used for CO₂ disposal is calculated as follows:

$$Q_{\text{aqui}} = V_p \cdot h_{st} \cdot \rho_{CO_2}$$

where:

$$Q_{\text{aqui}} = \text{storage capacity of entire aquifer [Mt CO}_2\text{]}$$

$$V_p = \text{total pore volume of an aquifer (>800 m) [km}^3\text{]}$$

$$h_{st} = \text{storage efficiency, i.e. fraction of the pore volume that can be filled with CO}_2 \text{ (see Table 4.2.1) [\%]}$$

$$\rho_{CO_2} = \text{CO}_2 \text{ density at initial reservoir conditions [kg/m}^3\text{]}$$

Determination of the Bulk Volume of an Aquifer (V_b)

The bulk volume of the aquifers is established in two ways:

- 1) multiplying the distribution area by the average thickness
- 2) integrating the isopach lines on the contour map

If no volumetric information is available, no estimate of the storage capacity can be made. Only the part of the aquifer will be considered that is below a depth of 800 m. In the case that CO₂ is stored outside traps, the entire aquifer should be below 800 m.

Determination of the Trapped Proportion of an Aquifer (TRAPPED%)

Closed structures are identified on structural contour maps. The percentage by area of the distribution of these structures is taken as a measure for the trapped part of the aquifer. The contour lines are of an appropriate horizon, of the aquifer itself or of a surface stratigraphically conformable and close to the aquifer.

The trapped aquifer volume is calculated by taking the product of the surface area of the closed structures and the (average) thickness of the aquifer. Although the thus calculated volume will not correspond to the actual trapped part in the case of shallow structures on aquifers that are homogeneous throughout (where the spill point will be higher than the base of the aquifer), we will use this calculation because the CO₂ storage efficiency is based on this volume.

If no traps can be defined, e.g. if no structural contour maps are available, 3% of the aquifer is assumed to be in a trap.

Determination of the CO₂ Density

The CO₂ density is established from the temperature and pressure in the aquifer, which are either based on actual measurements or inferred from local geothermal and hydrostatic gradients. If these data are not available, a density of 700 kg/m³ will be used, based on average gradients of 30°C/km and 10.5 MPa/km (see section 4.2.2.2). Note that the CO₂ reservoir density in 'closed' aquifers will be considerably larger, because of the high pressure induced by CO₂ injection.

4.2.4 Hydrocarbon reservoirs

4.2.4.1 ASSUMPTIONS AND DEFINITIONS

In this study, the storage capacity of a hydrocarbon reservoir has been calculated from the underground volume of

the ultimately recoverable oil and gas. The ultimate oil and gas recovery refers to the cumulative *commercial* production added to the *proven* reserves. As synonym for ultimate recovery the term 'initial reserves' will be used as well. The calculation goes out from the presumption that all recoverable hydrocarbons can be replaced by CO₂. Since data on the total material balance are rare, the amount of produced water, flared gas, and injected fluids or gases are all ignored.

A hydrocarbon reservoir is defined as 'that portion of a trap which contains oil and/or gas as a single hydraulically connected system' (Craft and Hawkins, 1991). Many hydrocarbon reservoirs may be hydraulically connected to various rock volumes outside the trap and they may share a common aquifer. A hydrocarbon field may comprise several reservoirs at different stratigraphic horizons or in different pressure regimes (Archer and Wall, 1992).

Reserves refer to 'estimated volumes of hydrocarbons anticipated to be commercially recoverable and marketable from a given date forward, under existing economic conditions, by established operating practices, and under current government regulations' (after Coleman et al. in Craft and Hawkins, 1991). Proven reserves have a 90% probability of recovery (Archer and Wall, 1992). In the inventory, proven oil reserves will be assumed to include primary and secondary recovery (e.g. water injection), but to exclude the amount of oil that can be retrieved by tertiary recovery techniques such as gas (CO₂) injection.

To calculate the underground volume of the hydrocarbons recovered, the formation volume factors for oil and gas (B_o and B_g , respectively) have been used. The formation volume factor is the ratio between a volume of fluid at reservoir temperature and pressure and its volume at standard conditions^[9]: (volume at reservoir conditions)/(volume at standard conditions). The factor is dimensionless and varies with the temperature and the pressure in the reservoir. Hence, the factor will not be constant during production and will be different for each reservoir.

In the case of an oil reservoir, the formation volume factor (B_o or FVF) will also involve the solution gas: 'the factor will be the volume in barrels that one stock tank barrel occupies in the formation (reservoir) at reservoir temperature and with the solution gas which can be held in the oil at that pressure' (Coleman et al. in Craft and Hawkins, 1991). Because the oil, being a liquid, is difficult to compress and because both, the increased temperature and the presence of solution gas increase the volume of the oil, the factor will always be greater than 1.

The volume of produced condensate is included in the gas volume factor, which means that the combined volume of gas and gas condensate in the reservoir is calculated from the standard volume of gas only. Since gas is easily compressible, the factor is largely determined by the pressure in the reservoir. Under the high reservoir pressure the gas occupies a volume that is much smaller than that under standard conditions. The factor is therefore always much smaller than 1. The gas expansion factor E (or GEF) is the reciprocal of the gas formation factor B_g ($E = B_g^{-1}$). A plot of expansion factor E against reservoir pressure P is linear over small pressure ranges (Archer and Wall, 1992).

In the case of an reservoir in which hydrocarbons occur in two phases, as a liquid and as a gas, establishing the formation volume factor will be more complicated and distinction should be made between reservoir conditions above and below bubble point pressure. However, this information is generally not publically available and has not been done in this inventory.

If no oil formation volume factors are known, it is assumed that the underground volumes of oil and gas are additive. Hence, all surface gas is considered to be a gas underground also, i.e. not dissolved in the oil. Condensate is treated as if it was oil, unless the condensate production was taken care of in the gas expansion factor.

4.2.4.2 STORAGE IN DEPLETED OIL AND GAS FIELDS

The basic idea of CO₂ disposal in depleted oil and gas reservoirs is that the recovery of hydrocarbons creates room in the subsurface to store CO₂. So, the storage capacity of an oil or gas field is directly related to the expected amount of hydrocarbons that will be produced from the field. In this study, it is assumed that the *entire* underground volume of the ultimately recoverable hydrocarbons can be replaced by CO₂.

To allow the accumulation of hydrocarbons in the trap, the trap must be open at its lower limits.^[10] So, the pore fluids in the reservoir are generally in pressure communication with the fluids outside the reservoir. In consequence, the pressure drop created by the hydrocarbon recovery will be compensated by fluids flowing from outside the trap into the underpressured reservoir, thus restoring the initial pressure. It may take, however, many years before the initial pressure is restored, depending on how easily the reservoir can be invaded by water^[11]. Hence, the hydrocarbon field may remain underpressured for a long period after abandonment.

Oil reservoirs

The pressure in a depleted oil reservoir is largely determined by the nature of the oil production. A very important producing mechanism during primary oil recovery comes from water influx into the reservoir. The water influx brings the oil to the well and ensures that the pressure in the reservoir is maintained. After depletion the reservoir will be water-saturated and pressurised. For most other producing mechanisms, such as gas cap drive, solution gas drive or depletion drive, the water inflow is much slower, the pressure restoration is not 'instantaneous', and the reservoir will be significantly underpressured after primary production. When CO₂ is injected, the volume once occupied by the oil can be replaced with CO₂ until the initial reservoir pressure is restored. However, most oil fields are subject to water injection to improve the oil recovery (secondary production). These fields will after depletion be pressurised and water-saturated, irrespective of their primary production mechanisms.

Most of the oil is generally still in place after primary production. The efficiency of primary oil recovery varies from less than 5 to 75% of the original oil in place (OOIP),

[9] The standard conditions for the cubic feet (SCF) or standard barrel of fluid (BBL) and cubic meters (SCM or sm³) are slightly different. SCF and BBL are at a temperature of 60°F (15.6°C) and a pressure of 1 atmosphere (0.101325 MPa) and SCM is at 15°C and 1 bar (0.100 MPa). The most commonly used units in the oil industry are BBL and SCF. Standard conditions for barrels are also referred to as stock tank conditions.

[10] The generation of hydrocarbons is accompanied by volume changes. This can lead to high local pressures and may initiate microfractures providing an escape route into the reservoir. These microfractures are believed to heal as pressures are dissipated (Archer & Wall, 1986). This mechanism explains the occurrence of hydrocarbons in entirely confined traps.

[11] Another mechanism that is able to restore or maintain the initial reservoir pressure is compaction.

depending on the type of drive mechanism. Water or gas may be injected to continue the recovery of hydrocarbons when the natural drive of an oil reservoir is no longer sufficient to produce the oil. The procedure is designed to increase or maintain the reservoir pressure and to sweep the oil to the well. Water and gas injection are well known secondary recovery methods. They are common practice in the oil industry and can be regarded as conventional oil production techniques. The average oil recovery by these conventional methods world-wide is around 35% OOIP (Boberg, 1988).

When the production of additional oil is not economically possible by secondary methods, it may for some fields be attractive to apply tertiary techniques. Enhanced Oil Recovery (EOR) usually involves such a tertiary production. Miscible fluid displacement methods are counted among the EOR techniques and have been developed to recover more of the original oil in place than with conventional water or gas injection methods. Because of the miscibility between the displacing fluid and the oil, only a small residual oil saturation is left behind after flooding. CO₂ is used as miscible fluid. Although CO₂ is not first-contact miscible with reservoir oils at normal reservoir pressures, dynamic miscible displacement is possible above a Minimum Miscibility Pressure. The volumetric sweep of CO₂ is generally poor. To overcome this problem the injection of CO₂ is usually alternated with that of water, a production method known as the water-alternated-with-gas scheme (WAG). CO₂ is used to dissolve the oil and water to displace the oil. A major disadvantage of CO₂ injection is that it is very expensive. Hence, oil fields that were abandoned because EOR was too expensive, will produce oil again if 'free' CO₂ becomes available. The owner of the oil field will therefore be very reluctant to use such an oil field solely for CO₂ storage, and CO₂ storage in abandoned oil fields will generally have to be combined with EOR.

EOR examples from the USA and Canada show that the surplus of oil that can be produced by CO₂ injection is approximately 13% OOIP, ranging from 7 to 21% (Todd and Grant, 1993, Holt et al., in press). The reservoir volume of CO₂ disposed of during EOR is on average 2.3 times the reservoir volume of incremental oil. This means that the average volume occupied by the disposed CO₂ is 30 vol% OOIP (Figure 4.2.3), which approximately corresponds to the average oil recovery by conventional methods of 35%. The amount of CO₂ that can be stored is so large because all oil from EOR is replaced by CO₂, the net water saturation is reduced and CO₂ will additionally occupy some of the volume of oil which is produced, but not defined as incremental (Holt et al., in press). Modelling of 25 years of tertiary CO₂ injection into a Norwegian water-flooded oil field reveals that the amount of CO₂ that can be stored in the reservoir will be 63 vol% OOIP, which corresponds in this specific case to 133% of the reservoir volume of the initial oil reserves. The CO₂ storage efficiency is larger than the US and Canadian examples, because CO₂ injection was not alternated with water injection, which is an scheme that would be appropriate for any future combination of EOR and CO₂ disposal. Hence, our basic assumption that the underground volume of the ultimately recoverable oil can be replaced by CO₂ is a reasonable one, even in case of entirely water-flooded, pressurised reservoirs.

In this inventory all oil reservoirs that have been abandoned will be regarded as water-flooded reservoirs with a pressure close to the initial one. If CO₂ injection is not

coupled to tertiary oil recovery, these reservoirs will have a CO₂ storage capacity comparable to that of a trap on an aquifer, which means that only 2% of the trapped pore volume can be filled. Hence, CO₂ disposal in oil fields will only be considered in combination with EOR. We assume that the underground volume of CO₂ disposed during EOR equals the underground volume of oil recovered before, i.e. during primary and secondary production. This assumption is based on an average oil recovery by conventional methods of 35% OOIP, and an average CO₂ disposal of at least 30 vol% OOIP (discussed above). We additionally assume that the currently published figures on the initial oil reserves do not include tertiary recovery. This means that the reservoir volume of CO₂ that can be stored corresponds to the reservoir volume of the published ultimately oil recovery. This estimate will be conservative, because ultimate oil recovery is based on *proven* reserves, which are usually smaller than the actual reserves, and because some oil fields will be underpressured, which will permit the storage of some additional CO₂.

Gas Reservoirs

Gas reservoirs differ from oil reservoirs in that they show a primary recovery efficiency in excess of 80%, commonly up to 95%. The gas is highly mobile, which enables it to travel easily through the rock, and the energy stored in the compressed gas is usually sufficient to get most of the underground gas to the surface (Giuliano 1981). There are essentially two types of gas fields: 1) a 'closed' reservoir in which the gas is brought to the surface by the expansion of the gas (depletion drive); and 2) an 'open' reservoir in which the pressure is maintained by the inflow of water from an adjacent aquifer (water drive). In the 'closed' reservoir the influx of water is insignificant and pressure after production will be very low, as low as a few tens of bars; enough to maintain the pressure in the distribution network. Such reservoirs are quite common, because gas moves far more quickly through the pores than the formation brine and the local high pressures generated by the gas generation may have opened fractures that healed after pressure dissipation. For example, the 'Indefatigable Gas Field' in the North Sea derives most of its depletion

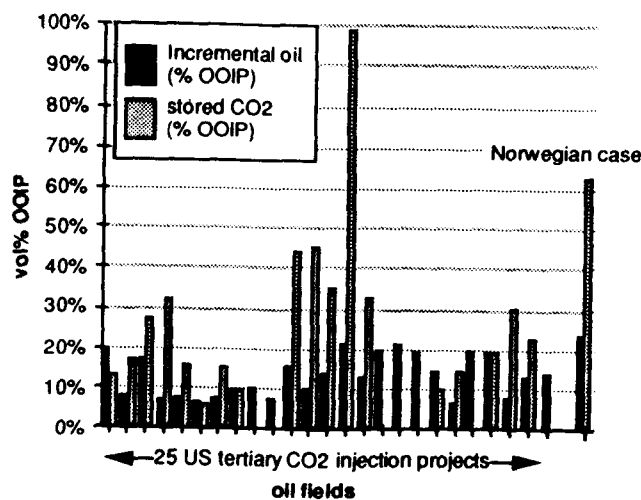


Figure 4.2.3 Incremental oil recovery and CO₂ storage during EOR by tertiary CO₂ injection for 25 US projects and one Norwegian reservoir model (data from Holt et al., in press). OOIP refers to original oil in place.

energy from expansion of the gas in the reservoir and less than 2% of the energy comes from water drive and compression of the reservoir matrix (Pearson et al., 1991).

In the case of a 'closed' (or 'volumetric') gas reservoir, the reservoir volume of initial gas reserves will be a good measure for the CO₂ storage capacity, because the depleted gas reservoir can be considered as an 'empty' container, i.e. no pore water or water invasion, little gas left in the reservoir and a very low pore pressure. The reservoir volume of the gas that has been produced can be entirely replaced by CO₂, since the displacement of methane by CO₂ is unconditionally stable (Mot et al. 1992). Craft and Hawkins (1991) state that 'Experience with volumetric gas reservoirs indicates that recoveries will range from 80 to 90%' and 'Some gas pipeline companies use an abandonment pressure of 100 psi per 1000 ft of depth', which corresponds to 2.3 MPa per 1000 m depth. The Dutch gas fields are expected to have abandonment pressures as low as 1 MPa, or even less (pers. com. Dutch Geological Service, 1994). Craft and Hawkins (1991) further state in their section on storage of natural gas that: 'Verification of the inventory simply means knowing the storage capacity of the reservoir as a function of pressure. This suggests that a p/z plot or some other measure of material balance be known for the reservoir of interest', and '..., it is apparent that a good candidate for a storage reservoir would be a depleted volumetric gas reservoir. With a depleted volumetric reservoir, the p/z [≈ pressure] versus G_p [total reservoir gas production] curve is usually known and water influx is not a problem'. This suggests that the assumptions previously made probably are justified.

The permeabilities of 'closed' gas reservoirs may be very low (a few mD), which could make CO₂ injection difficult. This will, however, not be a serious problem, since this disadvantage will be overcome by the extreme underpressure and the lack of water in the depleted gas reservoir. A high permeability is especially needed in water-saturated reservoirs for displacing the formation water. Since the gas reservoir can be considered as being 'empty' and the CO₂ will not have to displace any water, we only have to consider the injectivity for CO₂. The injectivity for CO₂ is much higher than that for formation water because of the difference between the viscosity of CO₂ (0.02 to 0.55 cP) and formation water (0.761 to 1.443 cP, varying with salinity) at reservoir conditions. Anyway, it will be impossible to differentiate in this inventory between low- and high-permeability gas fields, because for most fields this property remains unknown.

A water-saturated gas reservoir can be considered as a trap on an underpressured aquifer. Although fully water-saturated fields will be rare, all gas fields will be subject to water-flooding to some degree, which will decrease the 'empty' pore volume available for CO₂ storage. The simplest way to establish the storage capacity of gas fields in which water-influx has been substantial, is to subtract the volume of water that invaded the reservoir from the reservoir volume of initial gas reserves. A measure for the importance of water influx would be the pressure history of the fields (Craft and Hawkins, 1991). However, this information will generally not be available. For the storage calculation, we will therefore assume that the entire underground volume of gas can be replaced by CO₂, i.e. all gas reservoirs are regarded as being 'closed'.

When the CO₂ enters the depleted gas reservoir it will blend with the natural gas that is left behind. Contamination with natural gas, largely composed of methane

(CH₄), will decrease the density of CO₂ (e.g. IEA, 1993b). Under 'normal' reservoir conditions, the density of CO₂ contaminated with 10 Molar % CH₄ is about 70 to 90% of the density of pure CO₂ (Figure 4.2.4), depending on the depth of the reservoir. However, the excess molar volume of this CO₂/CH₄ mixture will only be 3%, i.e. the volume occupied by the mixture will be 3% larger than the added volumes of the two gases in separate phases (Reamer et al. 1944). This reduction of the CO₂ reservoir density due to CH₄ contamination will be insignificant compared to the other uncertainties in the storage calculation and will therefore be ignored.

4.2.4.3 STORAGE CALCULATION FOR HYDROCARBON FIELDS

The inventory of the storage capacity of hydrocarbon fields is restricted to those reservoirs where the initial pressure and temperature are above the critical point of CO₂, or to reservoirs below a depth of 800 m if pressure and temperature are unknown. If no depth values for the reservoirs are available at all, it will be assumed that 20% of the oil and gas fields is too shallow for CO₂ storage, i.e. above a depth of 800 m (cf. Tissot and Welte, 1984). A further restriction is that the abandoned hydrocarbon field is only considered as a potential CO₂ reservoir if it has a minimum storage capacity of 10 Mt. If the cumulative capacity of the smaller fields is substantial, their ultimate recoveries have been presented. This is done to give some idea of their capacity, in case it proves feasible to use smaller reservoirs.^[12]

Although hydrocarbon fields may show very low permeabilities, no constraints on this property have been introduced, since the permeability of the reservoir rock remains unknown for most of the hydrocarbon fields.

If the above restrictions are taken into account, the CO₂ storage capacity of a hydrocarbon field can be simply calculated as follows:

$$\begin{aligned} V_{Uoil} &= V_{oil(st)} \cdot B_o / 1000 \\ V_{Ugas} &= V_{gas(st)} \cdot B_g \\ Q_{CO_2} &= (V_{Uoil} + V_{Ugas}) \cdot \rho_{CO_2} \end{aligned}$$

Where:

V_U	=	Underground Volume of oil or gas [billion m ³]
$V_{oil(st)}$	=	Volume of oil at standard conditions [million sm ³] ^[13]
$V_{gas(st)}$	=	Volume of gas at standard conditions [billion sm ³]
B_o	=	oil formation volume factor (FVF)
B_g	=	gas formation volume factor (= E ⁻¹) ^[14]
ρ_{CO_2}	=	density of CO ₂ at reservoir conditions [kg/m ³]
Q_{CO_2}	=	CO ₂ Storage Capacity [Mt]

[12] If the number of these field is large, they have been lumped under the heading 'smaller fields'.

[13] Standard conditions are at 15°C and 0.1 MPa (1 bar). Oil production is often presented in Megatons. Assuming an average crude oil density of 850 kg/m³ at standard surface conditions, this figure can be converted to a volume of oil in million m³ (also at surface conditions) by dividing the Megatons by 0.85.

[14] 'E' or 'GEF' is the gas expansion factor.

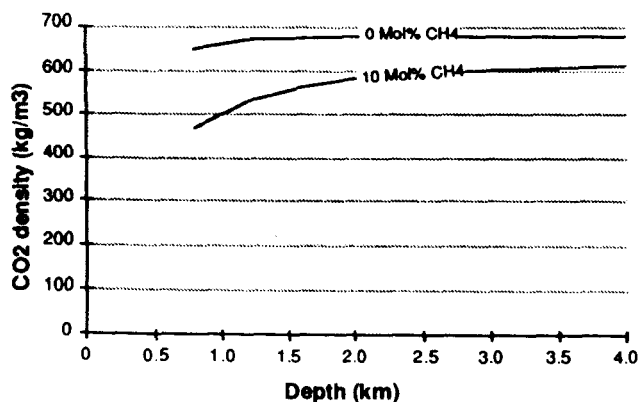


Figure 4.2.4 Density of pure CO₂ and CO₂ contaminated with 10 Molar% CH₄, under reservoir conditions that match a geothermal and hydrostatic gradient of 30°C/km and 10.5 MPa/km, respectively (data from Van der Sluijs 1991).

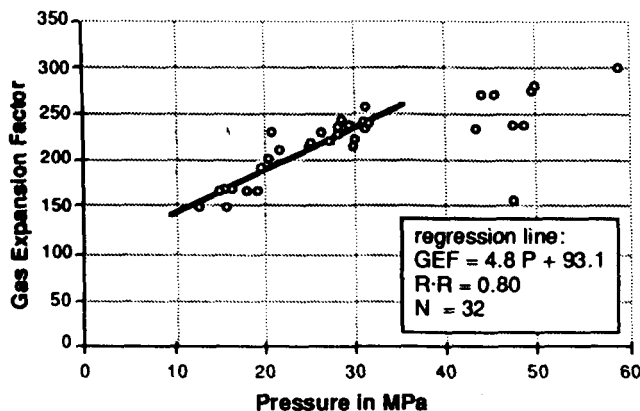


Figure 4.2.5 The Gas Expansion Factor plotted against pressure. The data are from British and Norwegian gas fields. The regression line only applies to gas fields with no or little condensate and with an initial pressure below 35 MPa.

Determination of the Underground Volume of Oil (V_{Uoil})

In many cases, the underground volume of oil has been established by multiplying the ultimate oil recovery by the formation volume factor (FVF) for a certain reservoir. This factor also accounts for the underground volume occupied by the solution gas, so the volume of solution gas should have been subtracted from the ultimate gas recovery. However, this has not been done, because in most cases it is not clear how much gas was originally dissolved in the oil. The solution gas will therefore be treated as if it originated from a gas cap. If no reservoir specific FVF is known, a FVF of 1.2 will be used (based on the average FVF of 64 British oil fields that do not produce gas; see section 4.15).

Determination of the Underground Volume of Natural Gas (V_{Ugas})

The underground volume of gas is determined in a similar way by dividing the ultimate gas recovery by the gas expansion factor E ($= GEF = B_g^{-1}$) for a specific reservoir. Note that this factor also accounts for the underground volume of condensate and that the ultimate condensate recovery should therefore be excluded from the storage calculation. The gas expansion factor (E) is largely controlled by pressure. If no reservoir specific expansion factors are available, E can be assessed from the reservoir pressure by the following linear relation (based on 32 British and Norwegian well data, see Figure 4.2.5): $E = 4.8 P + 93.1$, where P is the reservoir pressure in MPa. This equation will only be valid if the reservoir pressure is between 10 and 35 MPa, which approximately corresponds to gas fields shallower than 3 km.

If no pressure data are at hand, a local hydrostatic gradient or a gradient of 10.5 MPa/km will be applied to calculate the pressure from depth. An average gas expansion factor of 200 will be used if no depth data are available either.

If the gas expansion factor has been derived from the plot in Figure 4.2.5 or if an average value of 200 is used, the volume of ultimately recoverable condensate has been added to the ultimate oil recovery. This was done because the gas fields in the plot produce little condensate and the application of the derived expansion factors will therefore not account for the underground volume of condensate that may have been produced.

Determination of the CO₂ Density (ρ_{CO_2})

The CO₂ density has been established from the initial temperature and pressure in the reservoir. These P/T data are either based on actual measurements or inferred from local geothermal and hydrostatic gradients. If none of these data were available, a density of 700 kg/m³ has been used, based on average gradients of 30°C/km and 10.5 MPa/km (see section 4.2.2.2). Note that in entirely 'closed' reservoirs the pressure after production may be considerably lower than the initial one and that after CO₂ injection the pressure may be higher. This increased pressure may lead to CO₂ densities higher than those used in the calculation.

4.2.4.4 DEPLETION

A rough indication of the lifetime of a gas or oil field can be obtained by dividing the proven reserves by the current annual production. In the case that there are no lifetimes of the individual fields accessible, this ratio has been presented as an estimate of the date of depletion.

On the one hand, this method will lead to a conservative estimate of the lifetime, because the true reserves will be larger than the proven ones. On the other hand, the estimated lifetime calculated in this way will be too large, because it is not realistic to assume that the present rate of gas and oil production will not grow. The IEA (1993a) predicts that the world oil demand will increase modestly by 1.7% per year. Gas consumption, however, will grow rapidly by ca 2.5% per year in the industrialised world, and is expected to almost triple before 2010 in the 'developing countries'.

4.3 THE CO₂ STORAGE CAPACITY OF BELGIUM

Emile Elewaut and Rieks van der Straaten

4.3.1 Summary

The entire offshore area of Belgium and the major part of the land area is occupied by the 'London-Brabant Massif'. The metamorphic rocks of the massif have no porosity and are therefore unsuitable for CO₂ disposal. In the north-east corner of Belgium, however, the metamorphic basement is down faulted and here some Carboniferous and Permo-

Triassic sediments may include aquifers suitable for CO₂ disposal. The presence of traps, however, is questionable. Though complicated by folds and faults, the small basins directly south of the 'London-Brabant Massif' may also contain some potential reservoirs. In the Condruz Synclinorium of the Variscan Ardennes orogen, south-east of the massif, possible reservoirs are formed by Devonian sandstones and limestones, but because of the total absence of data on the deeper subsurface in this area, no estimates of the storage potential could be made.

On the basis of the data on the deeper subsurface to which we had access, no reservoirs appear to be suitable for disposing of CO₂. Most deeper sediments show a low permeability and/or do not have structures to retain the CO₂.

Belgium has no hydrocarbon fields.

4.3.2 Geological overview

Belgian geology, both onshore and offshore, is dominated by the presence of the London-Brabant Massif (Figure 4.3.1). The massif is a basement high that runs from the Belgian North Sea in the west to the Ardennes in the east. It consists of dense, metamorphic rocks with neither porosity nor primary permeability. The massif is covered to the north and south by younger rocks.

Offshore, in the Belgian part of the North Sea, a shallow sediment cover overlies the London-Brabant Massif. The sediments are too shallow for CO₂ storage.

In the northern part of the land area, the sediments covering the London-Brabant Massif form the southernmost border of the North Sea Basin (the Campine Basin, Figure 4.3.1). The thickness of this younger cover varies between 50 to 100 m in the south to slightly more than 1000 m in the north. Most of these sediments are too shallow for CO₂ storage. In the north-eastern corner of the country, however, the marginal North Sea Basin is down faulted in the Roermond Graben and deepens towards the north-east. There, some aquifers are present at depths suitable for CO₂ storage.

Directly south of the London-Brabant Massif, in the small basins between the massif and the Ardennes, the geological setting is structurally complicated by the presence of faults and folds. Namurian sandstones and Dinantian limestones in this area may eventually be shown to have storage potential.

The area south-east of the London-Brabant Massif is occupied by the Ardennes which are part of the Variscan orogen (Variscan Externides). Here, the Condruz Synclinorium (Figure 4.3.1) forms an intensively folded and very large structure that extends to a depth of up to 4000–5000 m. Although the area is well known from a geological point of view, this knowledge does not extend beyond the outcrops or the shallow subsurface. No data at all are available on the deeper subsurface. In the southernmost part of Belgium marginal sediments of the Mesozoic Paris Basin are exposed. They are too shallow for CO₂ storage (see the chapter on Luxembourg, section 4.10.2).

4.3.3 Aquifers

4.3.3.1 ONSHORE AQUIFERS

Constraints

The basic information has been provided by:

- A geological overview of the post Palaeozoic rocks of North-eastern Belgium by Demyttenaere & Laga

(1988) and Demyttenaere (1989), including depth and isopach maps of Mesozoic and Cenozoic units, seismic profiles and well logs.

- A feasibility study intended for the 'Belgische Geologische Dienst' on the underground storage of natural gas in the Henegouwen area and in the Campine Basin, in central and north-eastern Belgium, respectively (TGO, 1989, 1990).
- Well data from North-eastern Belgium (Gulinck 1956, Melchior, 1956).
- Results of the 'Belgian geotransverse' (Bouckaert et al., 1986).
- Seismic data from Northern Belgium (Vandenberghe et al., 1986).
- The geothermal atlas of the European Community edited by Haenel and Staroste (1988).

The literature gives a good impression of the Campine Basin, the Roermond Graben, and the small basins south of the London-Brabant Massif in the Henegouwen area. We had insufficient information on the deeper subsurface of the Ardennes.

North of the London-Brabant Massif (Campine Basin/Roermond Graben)

Dinantian (Lower Carboniferous) Carbonates

The top of the Dinantian calcareous rocks is intensely karstified. The porosity is high but variable, ranging from 4 to 20%. Permeability is high as well, values of several Darcy's have been measured. The burial depth varies from 1000 to 3000 m. To the north of Antwerp, the karstified layers are being used for storage of natural gas. A number of closed structures has been defined. However, we did not have access to the seismic data that have been acquired to define possible locations for natural gas storage.

Westphalian (Upper Carboniferous) Sandstones

The Westphalian D consists of the Neeroeteren Sandstone, the only Westphalian rock unit with some porosity. A shale layer of some 10 m divides the Neeroeteren Sandstone into a lower and an upper sandstone unit. The thickness of the sandstone unit varies between 30 and 150 m at a depth of up to 3000 m in the Roermond Graben. The average porosity is ca 15 %, the average permeability amounts to 35 mD. The maximum values are 20% and 200 mD. The sandstones are covered in the north-east by Permo-Triassic shales that are considered impervious. However, in the south they are overlain by Cretaceous permeable sandstones. The presence of a permeable cover makes the Neeroeteren Sandstones unsuitable for CO₂ storage, at least to the south-east of their range. To the north-east, the Permo-Triassic shales may constitute an adequate seal and the sandstone may become closed by faults in places. Since the seismic data of that area were not accessible, the position of any traps could not be defined.

Although the average permeability is low, the Neeroeteren Sandstone may show CO₂ storage potential because it contains high-permeability layers and is relatively thick, which will facilitate the injection of CO₂. However, the sandstone is considered to be unfit for the storage of natural gas (TGO 1989), so it is probably unsuitable for CO₂ disposal also.

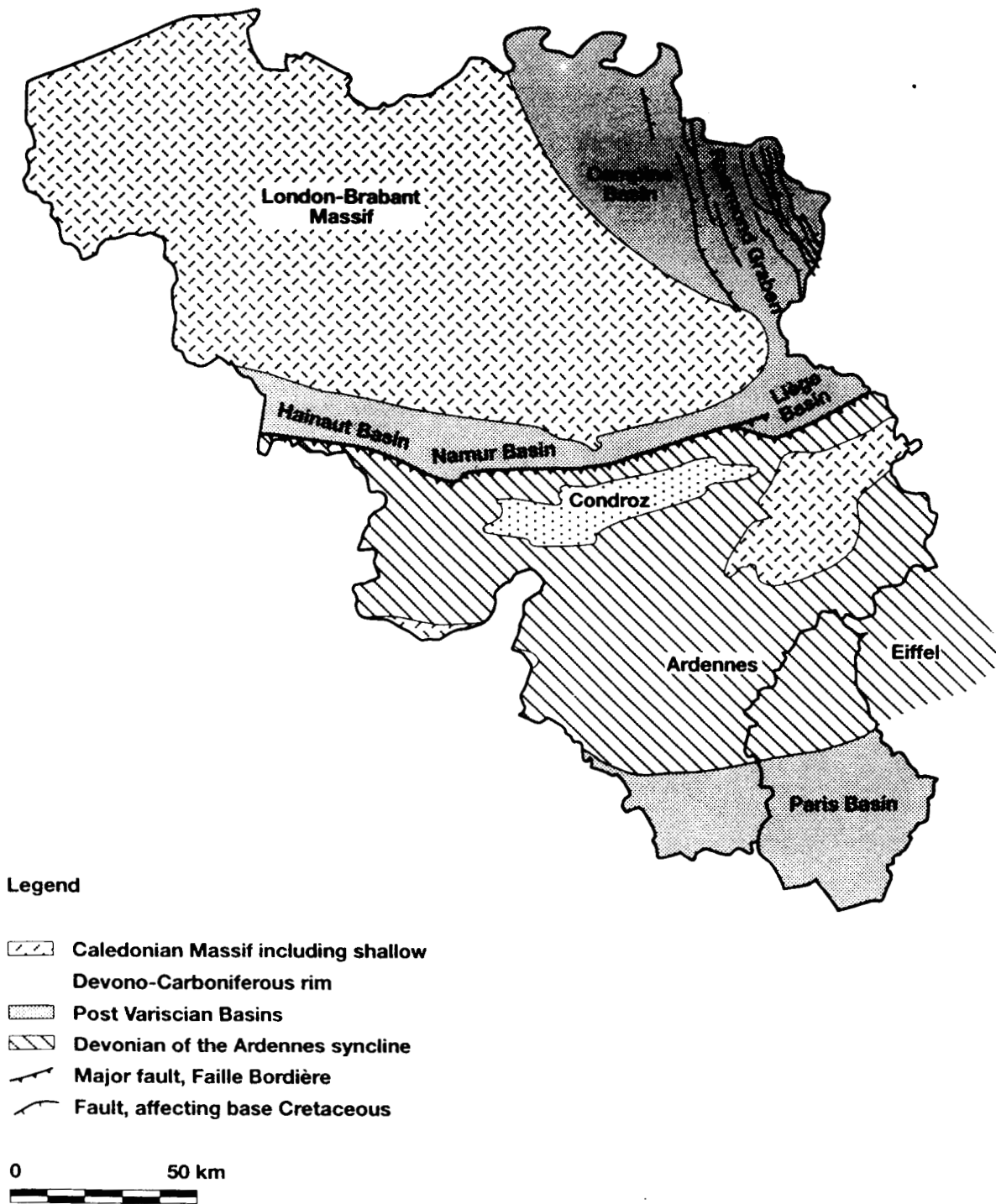


Figure 4.3.1 Major geologic features of Belgium and Luxemburg (after Harnl & Staroste, 1988).

Permo-Triassic Sediments

The Permo-Triassic succession in northern Belgium does not include the Rotliegend Formation that is so prominently present to the north-west, in The Netherlands and in the North Sea Basin. The Middle Buntsandstein has a thickness of about 200 to 250 m and may include some beds with good reservoir properties, but can only be regarded as an appropriate reservoir rock in those areas where it is covered by the argillaceous sediments of Muschelkalk, Keuper or Jurassic. The porosity varies between 5 and 19 %. One test showed a water injectivity of 1.3 m³/h/bar. Based on data

from the southern Netherlands (section 4.11), most sediments of the Middle Buntsandstein are expected to have unfavourable reservoir characteristics (low permeability). The data available do not permit us to define closed structures. Any closed structure would be related to faults.

South of the London-Brabant Massif (Hainaut / Namur Basin)

Namurian Sandstones

The Namurian coal-bearing strata contain some lenticular sandstone bodies with large areal extent. Their thickness is

limited and the porosity is in the order of a few percent (3.8% for the Gres d'Ardenne). They are expected to have bad reservoir properties.

Dinantian Limestones

The Dinantian limestones are intensely karstified at certain levels. The karst zones are thin (5 to 20 m). Although the Dinantian itself, with its evaporitic layers, can be considered a suitable cap rock, there is ample evidence for intense groundwater circulation, possibly along faults. Although most reservoir rocks occur at depths unsuitable for CO₂ injection, some deeper structures may occur. Quantification of the total storage capacity is highly problematic.

Southeast of the London-Brabant Massif (Condroz Synclinorium Of The Ardennes)

Possible reservoir rocks could be Devonian sandstones and limestones showing paleokarst. For the deeper sandstones, porosity estimates of 3% can be considered optimistic. The paleokarst layers are thin and irregularly distributed. The area does contain a large number of closed structures, but quantification is absolutely impossible due to the complete absence of data.

Storage Capacity

Apart from the Condroz Synclinorium in the Ardennes, the confidential reports by TGO (1990 a,b) cover the entire area where deep-seated sediments occur. As far as we had access to the data on the deeper subsurface, we could not define reservoirs suited for CO₂ disposal, as indicated above. Most deeper sediments show less favourable reservoir properties and/or do not have structures to retain the CO₂ underground. In some areas there is some storage capacity, but a quantification is impossible because of the lack of data.

The karstified Dinantian limestones have a high permeability and there are locally some traps, so they have CO₂ storage potential. The data are, however, insufficient to establish the lateral distribution of the karst horizon or to define any traps. Mot et al. (1992) estimate that the Dinantian karst limestones have a storage capacity of 0.18 Gt CO₂, based on potential geothermal resources in Belgium given by Haenel and Staroste (1988). Since Mot et al. assume that 1 ton CO₂ occupies 1.4 m³ of pore space under reservoir conditions, this amount corresponds with a bulk pore volume of 0.25 km³. Using the storage calculation method presented in section 4.2 and assuming that 4% of the pore volume can be filled with CO₂ and 3% of this volume is in a trap, the storage potential of the limestones amounts to only 0.2 Mt CO₂. Although the data are too poor to evaluate the aquifer's suitability for using its entire volume for CO₂ storage, this disposal concept would result in a storage capacity of 7 Mt CO₂.

4.3.3.2 OFFSHORE AQUIFERS

The sediments opposite to the Belgian coastline are too shallow for CO₂ storage.

4.3.4 Hydrocarbon Fields

No hydrocarbon fields have been found to date in the Belgium, either offshore or onshore.

4.4 THE CO₂ STORAGE CAPACITY OF DENMARK

Rieks van der Straaten

4.4.1 Summary

The major part of onshore Denmark is occupied by the 'Danish Basin', a WNW-ESE tectonic depression bordered by the Scandinavian crystalline basement in the north and by the Ringkøbing-Fyn High in the south. The Permian and younger sediments in this depression reach a thickness of up to 9000 m and include a large volume of porous rocks which form a potential reservoir for CO₂ disposal. Suitable traps to retain the CO₂ are domes created by salt diapirism. The storage capacity of the onshore aquifers is estimated to be ca 5600 Mt CO₂, assuming that CO₂ disposal will be in traps and that 6% of the trapped pore volume can be filled with CO₂. Data on the offshore aquifers are not available and are therefore excluded from the inventory.

Denmark has offshore oil and gas fields in the Danish Central Graben, located in the North Sea about 250 km from the Danish west coast. The storage capacity of these fields is estimated to be about 590 Mt CO₂. There are no hydrocarbon fields on land.

4.4.2 Geological Overview

The following general outline of the major geological features of Denmark is largely based on Andersen and Doyle (1990) and is illustrated in Figure 4.4.1.

The Danish Basin occupies the major portion of onshore Denmark and is part of the Norwegian-Danish Basin, an WNW-ESE trending depression bounded by normal faults. The Danish Basin has a fill of Permian and younger sediments up to 9000 m thick. It is bordered in the north by the Fenno-Scandian Shield, a Pre Cambrian high of crystalline basement. In the south, the basin is bounded by the Ringkøbing-Fyn High, an upthrown basement block with a relatively thin sediment cover of less than 2500 m. The Ringkøbing-Fyn High is transected by several N-S trending graben-like features, and dips gently towards the south into the marginal parts of the North German Basin that occupies the southernmost part of Denmark.

The offshore area of Denmark shows two major basins: the Danish Basin in the North and the Danish Central Graben in the west. The Danish Central Graben, located about 250 km from the Danish west coast, is a complex rifted basin trending N-S to NW-SE. The Graben is bounded in the east by the Ringkøbing-Fyn High. Major rifting occurred in Mid to Late Jurassic times during which more than 4000 m of sediments accumulated. By the Late Cretaceous differential subsidence ceased and a general subsidence followed. An additional 2000-3000 m of Cenozoic sediments were deposited. The Central Graben contains all known hydrocarbon fields of Denmark.

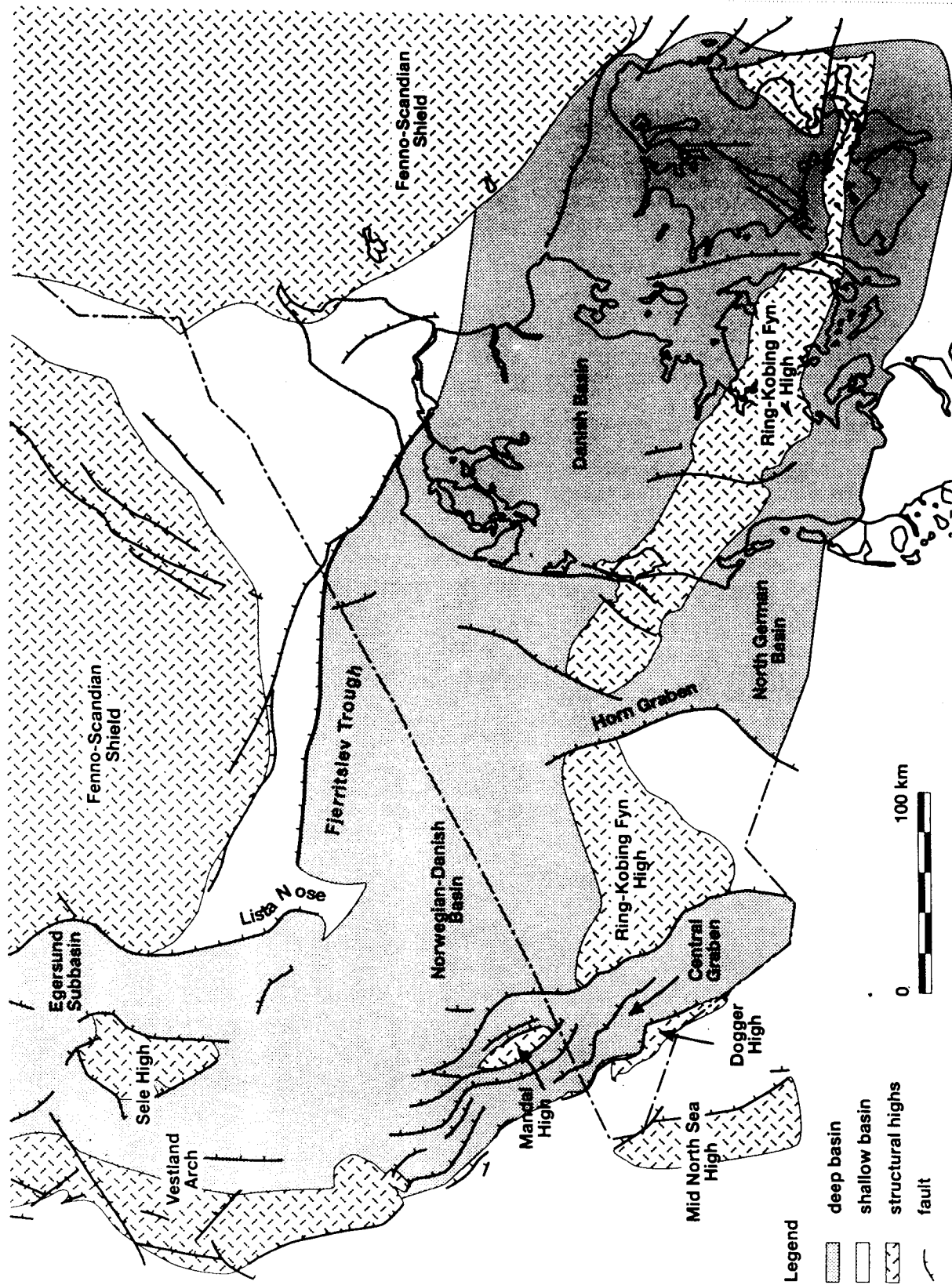
4.4.3 Aquifers

4.4.3.1 ONSHORE AQUIFERS

Constraints

The inventory of the CO₂ storage potential of the Danish onshore aquifers is based on geological maps of the Danish

Figure 4.4.1
Generalised geology
of Denmark.



Basin (DGU 1991a,b,c) and a report on potential geothermal reservoirs (DGU 1981), both provided by the Danish Geological Survey. The geological maps cover the largest part of the mainland (Jylland), the area from 8°00'E to 11°00'E and from 57°30'N to 55°30'N. The geothermal report deals with the entire land area of Denmark (except for Bornhold).

The inventory is further restricted by the burial depth of the potential reservoirs. Only deeply buried sediments form a potential CO₂ storage site, because the pressure and temperature in the subsurface must be high enough to retain the CO₂ in a dense, supercritical state. According to the Geothermal Map of Europe (Haenel and Staroste, 1988), the temperature of the Danish subsurface ranges between 30 and 40°C at a depth of 1000 m. To make sure that the pressure is high enough and that the critical temperature of CO₂ (31.1°C) is reached, a cutoff-level of 1000 m below mean sea-level is used. That means that only sediments below a depth of 1000 m are considered, thus excluding the Upper Cretaceous (the Chalk Group) and the Tertiary sediments. The pre-Mesozoic Permian deposits (the sandstones of the Rotliegende Group), situated at a depth between 1000 and 9000 m (DGU, 1991c), are not considered either, though they may provide suitable CO₂ reservoirs [15].

Triassic

The Triassic deposits of Denmark are 500 to 7 500 m thick. They reach their largest thickness in the central area of the Danish Basin. The top of the Triassic is situated at a depth of about 400 to 1000 m outside this depression, and is buried under a sediment cover up to 4000 m thick in the centre of it. The total rock volume of the Triassic on the Danish mainland below a depth of 1000 m, amounts to approximately 90 672 km³ (in the area mapped by the DGU, 1991c).

The main Triassic aquifers are contained in the Bunter Sandstone, the Tønder and the Gassum Formation (DGU, 1981). The aquifers consist of sandy deposits and are generally sealed by clay or evaporites. Based on the isopach maps and porosity measurements from the DGU, (1981), the total pore volume is estimated to be 3018 km³.

Bunter Sandstone Formation

The Bunter Sandstone Formation has a Lower Triassic age and consists of fine grained sandstones, siltstones and claystones, locally with a high content of carbonate, anhydrite and mica. In the Danish Basin coarse grained sandstones are present. The formation is generally less than 300 m thick, but reaches in the central Danish Basin a thickness of more than 900 m. On the Ringkøbing-Fyn High the formation is thin or locally absent. Net sand thicknesses are variable. Porosity and permeability decrease with depth. Porosity varies from 20–30% at 1000–2000 m to less than 15% below 3000 m. The highest permeability to air is ca. 1000 mD. The Bunter Sandstone Formation is sealed by evaporites and claystones of the Ørslev Formation, which cover nearly the entire land area of Denmark.

Tønder Formation

The Tønder Formation has a Mid Triassic age and consists of silty claystones with interbeds of fine grained sandstone. To the north in the Danish Basin, the volume of sand

increases, but the sand beds become thinner and less sorted. The average thickness of the formation is between 100 and 300 m. The net sand thickness is 20 to 40 m on average, but up to 100 m in the Danish Basin. Depth to the top of the formation varies from 800–1000 m on the Ringkøbing-Fyn High to more than 3500 m in the Danish Basin. On this high the formation is locally absent. Porosity varies greatly, from 30–40% at 1000 m to 10% at 3500 m. One bed with a porosity of 28% showed a permeability to air of 1000 mD. In less porous beds the permeability may be significantly smaller.

Gassum Formation

The formation is diachronous and its age ranges from Upper Triassic in the central parts of the Danish Basin to Lower Jurassic at the marginal parts. The lithology consists of fine to medium grained sandstones with interbeds of claystone and siltstone, and shows a southward fining trend. With few exceptions, the formation is only present in the Danish Basin, where it reaches a thickness of 100 to 200 m. Net sand thickness generally exceeds 50 m in the central basin. Depth to the top of the formation varies from more than 2500 m in the central parts of the basin to 500–1000 m in the marginal parts. Down to 1 500 m the porosity is 30–40%, at 2000 m ca 25%, and at 3000 m ca 12%. Brine permeability varies from 8 mD at 3200 m to 300 mD at 1500 m, but there are exceptions to this general trend. Average permeability to air is approximately 700 mD. Both the Gassum Formation and the Tønder Formation are sealed off from the shallow subsurface by the thick clay package of the Lower Jurassic Fjerritslev Formation.

Jurassic and Lower Cretaceous

Outside the Danish Basin, the Jurassic and Lower Cretaceous show a thickness of 200 to 400 m and the top of the Lower Cretaceous is situated at a depth between 200 and 1000 m. These deposits are left out of the inventory, because they are considered to be too shallow for CO₂ disposal. The Jurassic and Lower Cretaceous deposits inside the Danish Basin are situated at a depth below 1000 m, and fall therefore within the scope of the inventory. In the centre of this depression, they are generally restricted to a depth below 1500 m and reach a thickness up to 3500 m. These deeper deposits show a total rock volume of 16 800 km³ (in the area mapped by the DGU, 1991b).

The two major aquifers of Jurassic to Lower Cretaceous age are the Haldager Sand Formation and the Frederikshavn Member of the Bream Formation. They occur solely in the northern part of Denmark. Both are sandwiched between clay packages. Based on the isopach maps and the porosity measurements of these aquifers (DGU, 1981), their combined rock volume below a depth of 1000 m approximates 3600 km³ and their total pore volume is estimated to be ca 300 km³.

The Haldager Sand Formation

The Haldager Sand Formation has a Mid Jurassic age. Its lithology consists of siltstones and fine to medium grained sandstones with thin claystone intercalations. The formation is restricted to the Danish Basin where it reaches a maximum thickness of ca 150 m in the southeastern part. In the central and northeastern parts it shows a general thickness of 25–30 m. The depth to the top of the formation ranges between 1000–2000 m in the marginal parts of the basin, to more than 3000 m in the more central parts. Porosity decreases with depth from 30% at 1500 m to 20%

[15] Because the Rotliegende sandstones are deeply buried and have experienced severe diagenesis, they have a small permeability (ca 4 mD). They are therefore assumed to form inferior reservoirs. However, data are scarce.

at 2500 m. Three measurements reveal a permeability to air of 500 mD at 21% porosity and 2000 mD at 33% porosity.

Frederikshavn Member (Bream Formation)

The Frederikshavn Member has a Upper Jurassic to Lower Cretaceous age and consists of siltstones and fine grained sandstones with interbeds of silty clay. Some sandstones are clayey or contain mica, pyrite, or glauconite, which influences their reservoir properties in a negative way. The grain size, thickness and number of sandstone beds increase towards the northeast. The member is restricted to the Danish Basin below the Danish mainland (Jylland). The thickness ranges from 50 to 250 m; net sand thickness from 5–35 m to 70 m. Porosity is between 15–20% and 25–35% at a depth of 2000 m and 1000 m, respectively. For high porosities, the permeability to air is assumed to vary between 400 and 1000 mD.

Closed Structures

The Danish Basin is characterised by salt diapirism and normal faulting. Possible traps for CO₂ are predominantly formed by salt domes or salt piercements, forming 'open' reservoirs.

The contour maps of the top of the Lower Cretaceous (DGU 1991a) and of the Triassic (DGU 1991b), reveal that about 4% of the area is occupied by closed structures. Only structures were considered where the top of the mapped horizon is below a depth of 1000 m. On both contour maps, about half of the closures shows an amplitude of more than 300 m.

The application of a minimum depth of 1000 m implies that the Triassic deposits in a major dome in north-western Denmark (below Thisted, 8°60'E–57°00'N) are excluded from the inventory.

Storage Capacity

The total storage capacity in traps on the Triassic to Lower Cretaceous aquifers of the Danish onshore is estimated to be approximately 5.6 Gt CO₂ (Table 4.4.1). The storage calculation conforms to the method presented in section 4.2, and is based on an average CO₂ reservoir density of 700 kg/m³ and a trapped pore volume of 4%. Since most traps are formed by 'open' anticlinal (dome shaped) structures, it is assumed that 6% of this volume can be filled with CO₂. The storage capacity is restricted to the trapped portion of the aquifers below a depth of 1000 m.

The above storage estimate does not include the storage capacity of the large dome near Thisted because the top of the structure is too shallow (ca 600 m). The structure has a total area of about 1700 km², of which about 1100 km² is below a depth of 1000 m. Only a small part is onshore (30% by area). Although its top is too shallow for the youngest

Triassic aquifer (the Gassum Formation), the structure may form a suitable trap for the Tønder and the Bunter Sandstone Formations, situated at the middle and lower part of the Triassic, respectively. Although the Tønder and Bunter Formations show at this location a low permeability, they have an enormous net sand thickness, in the order of 1 km, which allows CO₂ injection at a large scale. For these two formations the storage capacity of the dome is estimated to be about 4.2 Gt CO₂ (with a 6% CO₂ storage efficiency and a CO₂ reservoir density of 700 kg/m³).

The Danish Basin, which is a structural basin bounded by normal faults, contains most of the aquifers considered above. The Triassic to Lower Cretaceous aquifers in this basin are deeply buried under a thick package of predominantly impervious rocks of Cretaceous age (silt, clay, marl and chalk). The Triassic is covered by a very thick sequence of Jurassic clay. The largest part of the land area of Denmark is occupied by the Danish Basin and the North German Basin and can be regarded as a geological continuation of the North Sea Basin, which is a 'juvenile' basin with a compaction-induced excess hydrostatic head (see section 4.11). Hence, the aquifers in the Danish deeper subsurface are expected to be overpressured and completely sealed off from the overburden formations. This will especially apply for the Triassic aquifers. Although some of the deeper aquifers in the Danish Basin may communicate to some extent with their lateral counterparts outside the basin (above a depth of 1000 m), they are considered to be largely 'closed'.^[16] The constraint that the CO₂ storage must be in traps, could therefore be released. In that case, the entire pore volume becomes available for CO₂ disposal and the storage capacity would be ca 47 Gt CO₂ (Triassic: 42.3 Gt, Jurassic: 4.4 Gt), assuming that 2% of the pore volume can be filled. The expected overpressure and isolation may, however, complicate CO₂ injection.

4.4.3.2 OFFSHORE AQUIFERS

The offshore aquifers are not considered here, because data on these aquifers are not available. The information on the offshore area is very limited and largely confidential, because of the hydrocarbon recovery in this area.

4.4.4 Hydrocarbon fields

4.4.4.1 ONSHORE HYDROCARBON FIELDS

There are no Danish hydrocarbon fields onshore. Although a number of oil shows have been reported from Zechstein

[16] The nature of the lower boundary of the Bunter Formation is largely unknown. At this boundary the formation may communicate with older formations.

Table 4.4.1 Potential CO₂ storage capacity of traps on the major onshore aquifers of Denmark, below a depth of 1000 m. The storage calculation is based on a trapped proportion of the aquifers of 4%. Because the traps form 'open' reservoirs, it is assumed that 6% of the pore volume can be filled with CO₂. The underground CO₂ density has been taken as 700 kg/m³.

Onshore Aquifers	Age	Total rock volume (km ³)	Average porosity (%)	Average net/gross ratio (%)	Total pore volume (km ³)	Storage capacity (Mt CO ₂)
Bunter	Triassic	20 650	22	38	1726	2 900
Tønder	Triassic	8809	30	22	581	977
Gassum	Triassic/Jurassic	8230	24	36	711	1195
Haldager	Jurassic	1230	25	63	194	325
Frederikshavn	Jurassic/Cretaceous	2356	24	21	119	199
Total		41 275			3331	5597

carbonate prospects in southern Jylland, no commercial fields have been discovered on land to date (Andersen and Doyle, 1990; Danish Energy Agency, 1992).

4.4.4.2 OFFSHORE HYDROCARBON FIELDS

Constraints

To assess the CO₂ storage capacity of the Danish oil- and gasfields, data from a report on the oil and gas production in Denmark published by the Danish Energy Agency (1992) were used. The figures are confined to commercial production, cumulative up to 1991, and recoverable reserve estimates from January 1, 1992. The reserves consist of the expected on-going, approved and planned recovery. Possible recovery has been excluded. Data on the complete material balance, including all produced or injected fluids and gases, were not available. The well data are restricted and information on temperature, pressure and the properties of the oil and gas are lacking.

Oil and Gas Fields

Six hydrocarbon fields are presently on production, and the development of eleven additional fields is planned in the near future (Figure 4.4.2). All fields are located in the Danish Central Graben, in the North Sea ca 250 km west of Jylland (between 3°40'E–5°30'E and 55°15'N–55°30'N). Danian to Maastrichtian Chalk reservoirs at a depth of about 2000 m predominate. These reservoirs are characterised by a porosity up to 45% and an original matrix permeability of 10 mD or less. The high porosity is attributed to overpressuring and presumed early hydrocarbon invasion, inhibiting normal compaction. The original matrix permeability is very low, but tectonically induced fracturing has in places considerably increased the effective permeability. Hydrocarbon traps are constituted by broad closures created by Tertiary inversion, domal

anticlines above salt pillows, salt piercements, and intra-chalk angular unconformities. Tertiary shale or impervious Chalk form the seals of the reservoirs.

The production in 1991 amounted to 6.1 milliard m³ gas and 8.3 million m³ oil. At January 1992, the cumulative production was 35 milliard m³ gas and 51 million m³ oil. Remaining gas reserves were at that date estimated to be 113 milliard m³, and the remaining oil reserves 116 million m³. So, the total ultimate recovery will approximately be 148 milliard m³ gas and 167 million m³ oil. However, about 15 milliard m³ of the gas produced has been re-injected, which yields a net ultimate gas recovery of 133 milliard m³. The ultimate hydrocarbon recovery of each field is listed in Table 4.4.2. The values for gas have been converted from normal cubic metres to standard cubic meters, using a factor of 1.055.

Storage Capacity

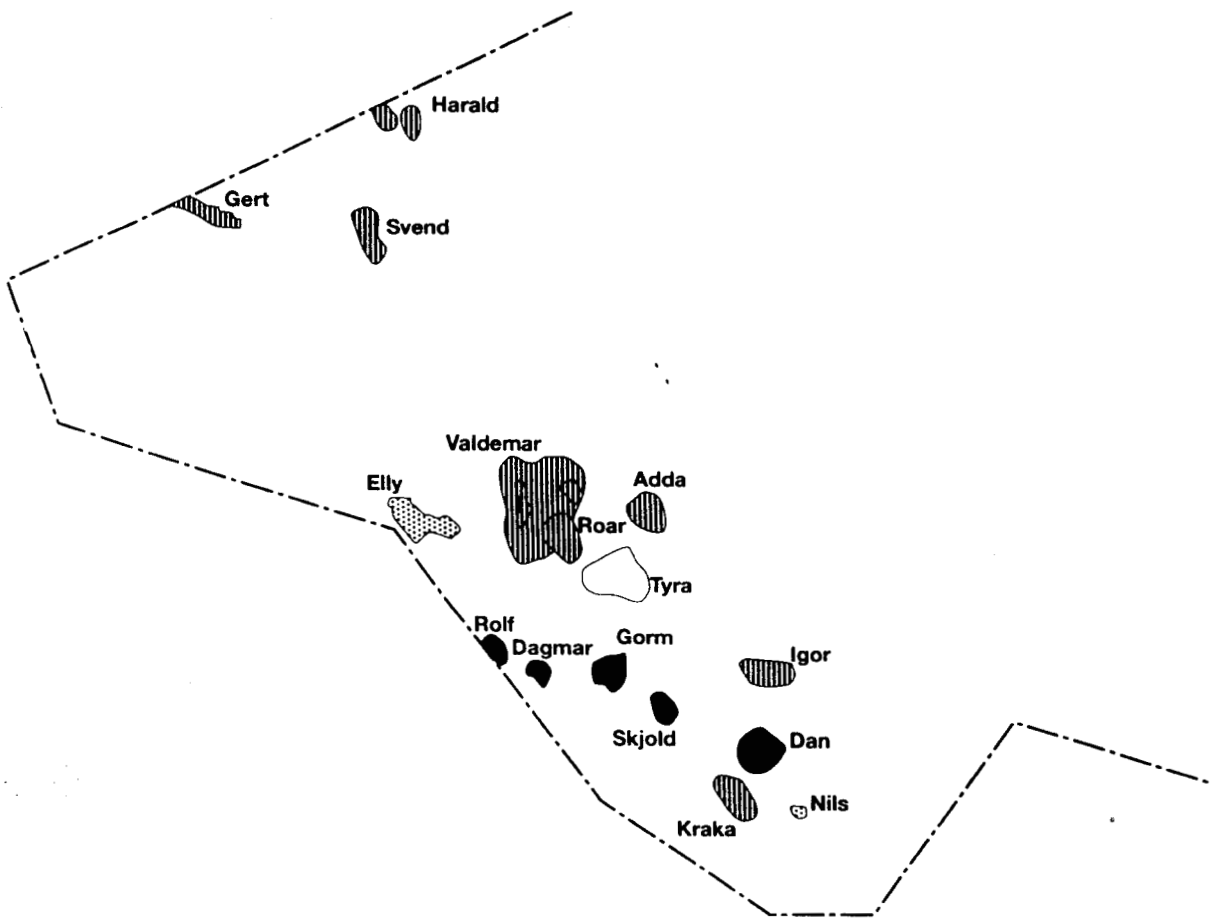
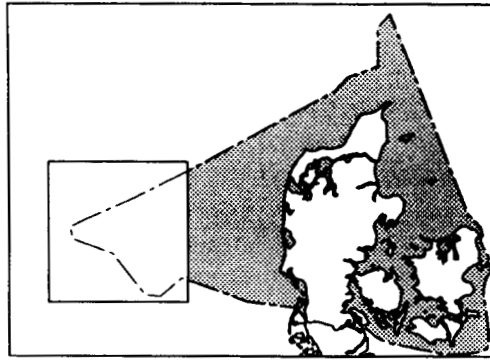
The storage capacity of all Danish oil and gas fields is estimated to be approximately 590 Mt CO₂ (see Table 4.4.2). The storage capacity has been calculated by multiplying the reservoir volume of the ultimately recoverable hydrocarbons with the CO₂ density under subsurface conditions, conforming to the method described in section 4.2. The calculation is based on a CO₂ reservoir density of 700 kg/m³ and an oil formation volume factor of 1.2. The gas expansion factor has been derived from the reservoir pressure, which, in turn, has been inferred from the reservoir depth by using a hydrostatic gradient of 10.5 MPa/km. If the reservoir depth is unknown, an average value of 1900 m has been used.

Depletion

There are at present no depleted hydrocarbon fields. All Danish fields are in production or will be developed in the near future. Based on the ratio between the estimated

Table 4.4.2 Potential CO₂ storage capacity of the offshore hydrocarbon fields of Denmark. Pressure (P) is based on reservoir depth and a hydrostatic gradient of 10.5 MPa/km. If depth is unknown, an average pressure of 20.6 MPa has been used. The gas expansion factor (GEF) is inferred from P. The CO₂ reservoir density is assumed to be 700 kg/m³. The ultimate gas recovery includes net gas production, i.e. the amount of re-injected gas has been subtracted from gross gas production.

OFFSHORE FIELDS			OIL & CONDENSATE			GAS TOTAL				
Name	Depth	P	Ultimate recovery	Life time	Storage capacity	Ultimate recovery	Life time	GEF	Storage capacity	Storage capacity
	m	MPa	10 ⁶ m ³	years	Mt CO ₂	10 ⁹ m ³	years		Mt CO ₂	Mt CO ₂
Adda	?	20.6	1.0			1.1		192		
Dagmar	1400	14.7	3.5	6		0.3	5	164		
Dan	1850	19.4	54.4	24	45.7	21.9	34	186	82.4	128.1
Elly	?	20.6	0.1		0.1	3.2		192	11.5	11.6
Gert	?	20.6	2.0			0.1		192		
Gorm	2200	23.1	40.3	16	33.8	10.5	12	204	36.1	69.9
Harald	?	20.6	5.0		4.2	26.4		192	96.2	100.4
Igor	?	20.6	0.1			2.1		192		
Kraka	1800	18.9	4.1	29	3.5	2.1	55	184	8.2	11.6
Regnar	?	20.6	0.1			0.1		192		
Roar	?	20.6	2.0		1.7	12.7		192	46.2	47.8
Rolf	1800	18.9	4.5	7		0.2	16	184		
Skjold	1600	16.8	28.1	5	23.6	1.7	7	174	6.9	30.5
Svend	?	20.6	7.0		5.9	2.1		192	7.7	13.6
Tyra	2000	21.0	13.3	5	11.2	46.3	15	194	167.1	178.3
Valdemar	2300	24.2	2.0			2.1		209		
Total			167.5	14	129.7	132.8	31		462.3	591.9



Legend

- oil field
- gas field
- ▨ field in development
- ◻ commercial discovery



Figure 4.4.2 Distribution of the hydrocarbon fields in the Danish Graben.

recoverable reserves and the current rate of (net) production, the hydrocarbon fields will become exhausted in 5 to 55 years (Table 4.4.2). However, this ratio provides only a rough indication of the date of depletion.

4.4.5 Concluding Remarks

In this inventory the storage capacity of traps on the Danish aquifers onshore has been estimated to amount to 5.6 Gt CO₂. Probably most of the deep-seated aquifers considered here are effectively sealed off from shallow subsurface and the surface. Because the risk of CO₂ escaping from these aquifers is expected to be low, they seem to be appropriate for a storage concept in which the entire pore volume of the aquifers is used for CO₂ disposal. In that case, the total capacity will be in the order of 47 Gt CO₂.

There is still great uncertainty about the actual underground pore volume in aquifers available for CO₂ disposal, which is largely due to the poor control on lateral variations in lithology and the scarceness of borehole measurements. A major problem is the availability of reliable permeability values. In this inventory permeabilities for air are used, which are considerably higher than those for the formation brine. The Danish Geological Survey (DGU, 1981) considered the brine permeability for the major Danish aquifers to vary between 15 and 100 mD. So, if a 100 mD cut-off level is used, Denmark may possess no potential for underground CO₂ disposal at all.

Reservoirs for geothermal energy and for CO₂ disposal have to meet more or less the same requirements. Both types of reservoir must be porous, permeable, and deep-seated. The DGU (1981) concluded that in Denmark a pore volume of 412 km³ can be used for geothermal energy. That is only 12 % of the pore volume in deep-seated aquifers assumed to be present by this inventory. The difference is partly due to the fact that the DGU has only considered aquifers between depths of 2000 and 3000 m and has excluded the Frederikshavn Member from their inventory because of its poor geothermal reservoir characteristics.

The present study did not discuss the storage capacity of the aquifers below the Danish North Sea, because the required data were not available. Yet, it is obvious that the Danish Central Graben will have a large CO₂ storage potential, possibly of the same order as the capacity on land.

4.5 THE CO₂ STORAGE CAPACITY OF FRANCE

Jean Barbier

4.5.1 Summary

One third of the land area of France is underlain by sedimentary basins that could contain aquifers suitable for CO₂ storage. The storage capacity of the trapped fraction of all these aquifers is estimated to amount to approximately 1530 Mt CO₂. In order of decreasing area, the basins in France are as follows:

- The *Paris Basin*: is located in the northern half of the country and contains a sedimentary succession more than 2 000 m thick. The cumulative thickness of Triassic and Jurassic aquifers exceeds 100 m. Traps are formed by large open folds.
- The *Aquitaine Basin*: in the southwestern part of France is filled by a sedimentary succession of 5000 m

thick. Traps are also formed by large open folds. The basin contains deep Triassic-Eocene aquifers. Upper Jurassic carbonates form oil and gas reservoirs, but seals and traps are of limited extent. The carbonates are therefore considered to be unsuitable for CO₂ storage. Upper Lias clays occur over large areas and seal porous Lower Jurassic dolomite and Triassic sandstone. The dolomite and sandstone are poorly known, but may form suitable CO₂ reservoirs.

- The *Rhône Valley Basin* in the southeast of the country is structurally very complex, because it has been affected by the Alpine orogeny. The basin is therefore excluded from the inventory.
- The *Alsace Basin*: in the northeast of France is unsuitable for CO₂ storage, because here permeability is largely due to fracturing and is therefore highly variable.

All French hydrocarbon fields are onshore. The gas fields are located in the Aquitaine Basin, and their ultimate gas recovery is estimated at some 322 milliard m³. The oil fields are very small and mostly occur in the Paris Basin. Their ultimate recovery is estimated at ca 100 Mt oil. The total CO₂ storage capacity of the oil and gas fields is estimated to be ca 930 Mt, 50 Mt in oil fields and 880 Mt in gas fields.

4.5.2 Geological Overview

Sedimentary basins underlie some two thirds of the French mainland. Excluding regions of intense folding and sequences less than 800 m thick, areas liable to contain deep-seated aquifers amount to one third of the country. These areas comprise six basins (Figure 4.5.1). In order of decreasing size, these are: the Paris Basin, the Aquitaine Basin, the Rhône Valley Basin, the coastal Mediterranean Basin, and finally the Limagne and Alsace basins. In northern France, there is another potential zone in Devonian limestones, though information about this possible aquifer and its associated seals is sparse.

These basins have different geological settings, affecting the hydrocarbon resources, aquifer type and trap structures to be expected. The Paris and Aquitaine basins are epicontinental shelf basins; the Alsace Basin is a graben, the Limagne Basin an intracratonic depression; the Rhône valley is a combination of continental depression and orogenic foredeep, while the coastal Mediterranean Basin is largely a passive continental margin.

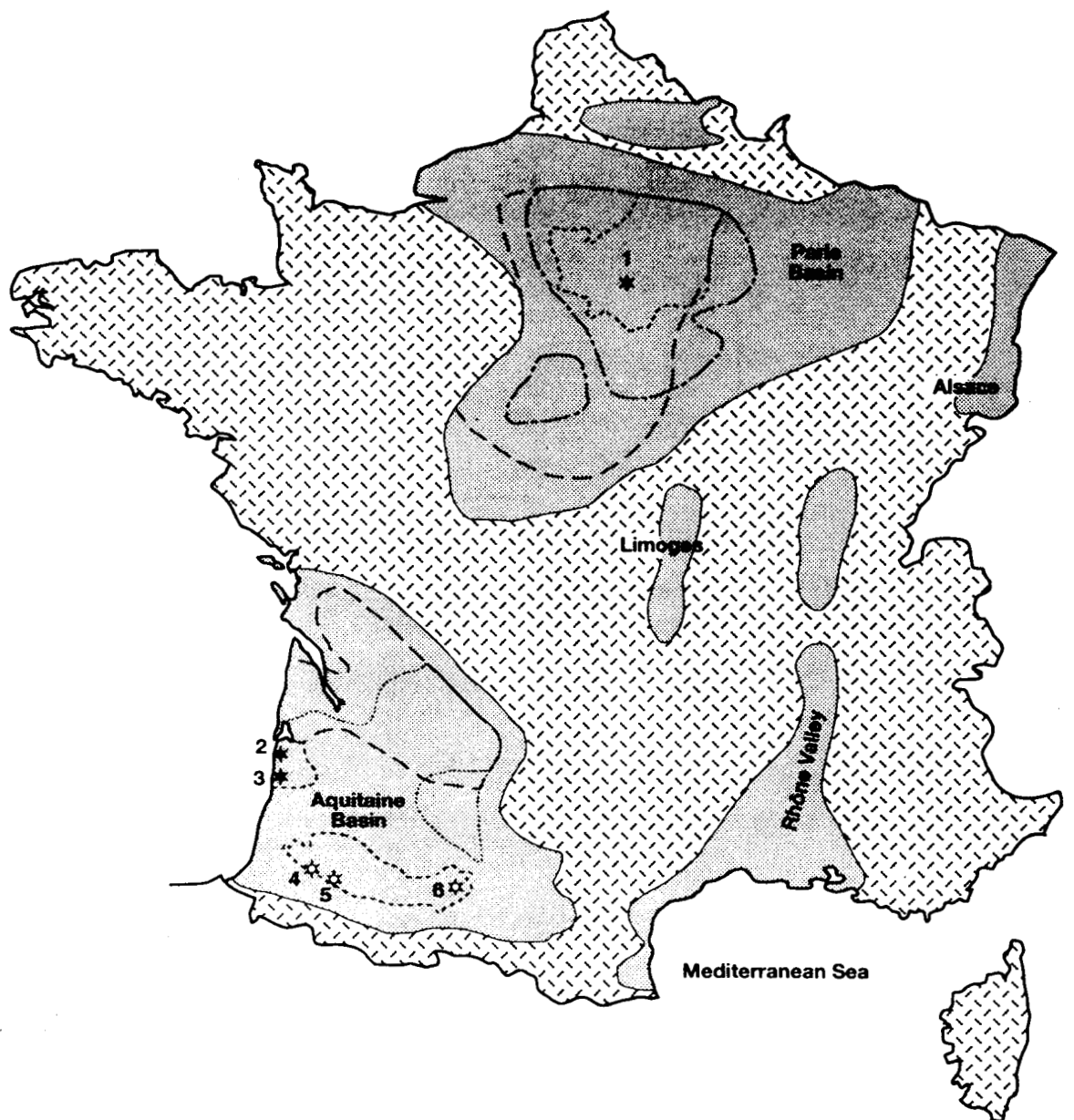
4.5.2.1 EPICONTINENTAL BASINS

The epicontinental basins are large, contain mostly marine sediments, and underwent mild deformation. They contain oil and natural gas. Aquifers are extensive and potential traps have large volumes.

The sedimentary succession in the Paris Basin reaches a total thickness of over 2000 m. The main aquifers are more than 100 m thick and comprise Triassic sandstone, Middle Jurassic/Dogger limestone and Upper Jurassic limestone. In the Aquitaine Basin, the succession thickens from the northeast (at the edge of the Massif Central mountains) towards the southwest, where it reaches a thickness of 5000 m. Aquifers occur throughout the sequence, but are thicker in the deeper part of the basin, i.e. in the southwest.

4.5.2.2 OTHER BASINS

The Alsace Basin is a graben formed during the Tertiary. Potential aquifers in this basin are the same as those in the



Legend

-  sedimentary series more than 1000m thick
-  Hercynian basement, with margins (folded or with shallow depth)
-  oil field
-  gas field

-  Triassic
-  Lias
-  Dogger
-  Upper Jurassic

Oil and gas fields

- (1) Chaunoy
- (2) Cazaux
- (3) Parentis
- (4) Lacq
- (5) Meillon
- (6) St. Marcet



Figure 4.5.1 Location of the main hydrocarbon fields and deep aquifers in France (after Maget, 1983).

eastern Paris Basin, namely Triassic sandstone, Dogger and Lusitanian limestone. The basin is, however, tectonically complex and the aquifers are cut by numerous faults. Permeability is largely due to fracturing, and is thus highly variable.

In contrast to basins discussed above, the Limagne Basin is filled with fluvial clays and sandstones, generally with low permeabilities. Total thickness seldom exceeds 800 m and the basin is therefore considered to be unsuitable for CO₂ storage.

The Rhône Valley Basin and Mediterranean Basin are extremely complex tectonically, as they have been affected by the Alpine orogeny. They are not further discussed in this study as it is difficult to define extensive aquifers in these strongly faulted basins. In addition, inadequate sealing capacity of faults is likely to cause problems.

4.5.3 Aquifers

4.5.3.1 ONSHORE AQUIFERS

Constraints

The inventory of the CO₂ storage potential of the French onshore aquifers is based on two unpublished reports on potential geothermal reservoirs (Housse and Maget, 1976, 1977). These reports were written in co-operation with a major oil company, and later formed the basis of a geothermal review of Europe (Haenel and Staroste, 1988). The review presents maps of the main aquifer thicknesses, as well as maps of transmissibilities. As a convention, a 1 D.m ($\approx \mu\text{m}^2$) boundary was used to delimit these aquifers, and to calculate the total pore volume. Some basins were not taken into account, due to their tectonic complexity (Mediterranean margin) or their low porosity (Rhône Valley, Alsace). Likewise, shallow fresh water aquifers (TDS < 1 g/l) of any depth were not taken into account, because of their economic importance. Reservoir porosity values, when given, are taken from the yearly hydrocarbon accumulation report of the French Ministry of Industry (Anonymous 1993). Such values represent rather sporadic data at basin scale. For the storage calculation, the author therefore followed Haenel and Staroste (1988) and assumed an average porosity of 10%.

Paris Basin

The Paris Basin constitutes a wide depression with a central diameter of 300 km. It is broadly tabular, and deformation is limited to broad undulations and rare low-throw faults. Lateral facies variations are abundant as the sedimentary succession is fluvial or epicontinental in origin. Oil and geothermal exploration have identified three main aquifers: the Triassic (Keuper), the Dogger, and the Upper Jurassic (Lusitanian). The Triassic and the Dogger are reservoir rocks for small hydrocarbon fields. The Rhaetian (Lower Lias) is also a petroleum-bearing unit and an aquifer, though altogether smaller, with a thickness of only 10–20 m.

Triassic (Bunter Sandstone Facies)

Two main reservoirs are found in the Triassic: one in the central and southern parts, the other in the eastern part. Both are composed of fluvial sandstones. The eastern reservoir outcrops over more than 100 km, and generally constitutes an excellent aquifer and an important much used fresh water resource. This aquifer will therefore not be considered as a potential CO₂ storage reservoir. The other reservoir is deeper (more than 3000 m deep in

places), and less well known. It features two zones defined by a transmissivity greater than 1 D.m: one in the Paris area, the other farther south. Their net thickness is 50–300 m and they extend over 20 000 km². In the southernmost and shallowest part of the aquifer, a trap near Chemery is used for natural gas storage.

Lower Jurassic

Two minor aquifers occur in the Lower Jurassic: Rhaetian sandstone in the eastern part of the basin, and Hettangian limestone/dolomite in the western part. Their average thicknesses are about 15 m, and transmissivity rarely reaches a value of 1 D.m. These reservoirs are therefore only mentioned in passing and will not be further considered in the inventory. The Rhaetian sandstones contain several minor oil accumulations.

Middle Jurassic (Dogger)

This aquifer is well known for two reasons. Firstly, because the Dogger contains the small oil fields of Coulommès and Villeperdueis and is a target for oil exploration. Secondly, the Dogger locally shows high permeability and high temperature (60°–85°C), and is therefore highly valued as geothermal resource in the Paris region.^[17]

The aquifer consists of oolitic limestone; accompanying facies consist of micritic limestone or chalk with a low permeability. The reservoir extends over some 15 000 km² in the central part of the basin, and is more than 100 m thick (Maget and Housse, 1976). Transmissivity is high, reaching 10–40 D.m in the central part of the aquifer, as documented by bottom-hole tests, calibrated by actual flow rates measured in geothermal boreholes. The reservoir is shown in Figure 4.5.1, to the extent of the 1 D.m limit. The Dogger limestone is overlain by Callovian-Oxfordian clay and marl, which form an effective seal.

Upper Jurassic

Several aquifers occur in the Upper Jurassic. The main one consists of an oolitic carbonate unit, with a reservoir thickness of 50–100 m and an areal extent of 15 000 km². In spite of the seal provided by the Kimmeridgian marl, the reservoir does not contain any known hydrocarbon resources.

Aquitaine Basin

The Aquitaine Basin consists of Triassic to Quaternary sediments, is more complex than the Paris Basin, and is markedly asymmetrical. Schematically, it can be described as a tabular stable platform in the north, grading into a subsiding area to the south. The latter is folded, and features salt tectonics near the Pyrenees mountains.

Several aquifers are known in the area. The shallower ones are used for fresh water production, and are thus not considered to represent a potential CO₂ reservoir. The dissolved salt content increases with depth and only the deepest aquifers are of interest to this study. These occur in the Triassic to basal Lias of the platform area and in the Jurassic-Lower Cretaceous of the subsiding area. They will be further discussed below.

[17] Note that CO₂ storage may interfere with geothermal operations. At present, in areas of 2000 km² the Dogger is used as geothermal reservoir.

Platform Region

The deeper aquifers consist of sandstone (Triassic-Lias) and dolomite (Lower Lias). The two reservoirs are generally separated by an impermeable clay layer, but communicate directly in the southeastern part of the platform area. Towards the south, Triassic sandstone grades into impermeable clay, and the Liassic sandstone and dolomite grade into compact dolomite, which is also impermeable.

The permeability of these reservoirs is not precisely known. The limits of the aquifers shown in Figure 4.5.1 were derived from flow rate tests, porosity values computed from logs, and a few measurements from cores. The gross thickness of Lias reservoirs ranges from 50 m (Carcans dolomite) to 80 m (sandstone facies). The thickness of the basal Triassic reservoir varies more widely between 10 and 100 m. For CO₂ storage calculations, it has been assumed that the combined Triassic-Lias shows an average thickness of 100 m and an areal extent of 16 000 km².

The middle Lias contains a small reservoir with a lateral range of some 12 000 km², consisting of oolitic carbonate and dolomite. Its thickness is approximately 50 m. This reservoir is overlain by middle Lias clay, which is laterally very consistent and most likely to provide an effective seal.

Reservoirs higher in the sequence than those discussed above, contain fresh water and are too shallow for CO₂ disposal (above a depth of 800 m). These will therefore not be further mentioned in the context of CO₂ storage.

Subsiding Region

This area can be subdivided into two subbasins: one located near the Atlantic (Parentis) and the other along the northern margin of the Pyrenees mountains. The shallower aquifers (here Upper Cretaceous and Eocene) contain fresh water, while the deeper aquifers (here Upper Jurassic to Lower Cretaceous) contain salt water. The older formations are poorly known, for example the Middle Lias is more than 2500 m deep to the north of the Parentis Basin and 3000 m deep near the Pyrenees.

In the Parentis Subbasin, the deepest reservoir is found in the Mano Dolomite (uppermost Jurassic), disregarding the older, middle Lias dolomitic limestone that only has a limited range. The eastern part of the Mano Dolomite contains fresh water, while the western part contains salt water associated with oil accumulations (Lucats). The reservoir produces water that is used as injection fluid to improve hydrocarbon recovery. The average gross thickness is 200 m. Porosity ranges between 10 and 20% and is partly due to fracturing.

Water in the Mano Dolomite communicates in many places with water in overlying sandstone and limestone aquifers (Lower Cretaceous), which form a complex aquifer. In the eastern part of the basin, it is shallow (less than 1000 m) and contains fresh water. In the western part, it contains salt water and several oil fields (Parentis, Cazaux) as well as indications of natural gas. The Lower Cretaceous varies in thickness (250–1000 m). Permeability is well known from oil exploration, and amounts to 1000 mD in the carbonate facies.

In the Pyrenees Range Margin, the deepest reservoir known is contained in an Upper Jurassic dolomite (Dogger-Kimmeridgian). In the shallower part of the stratigraphic succession, the Mano dolomite reservoir (Purbeckian-Portlandian) is some 200 m thick. The Upper Jurassic contains fresh water, with the exception of the southernmost part of the basin, where the reservoir con-

tains gas fields (Lacq, Rouse, Meillon). The Upper Jurassic communicates with the overlying Lower Cretaceous aquifer. The salt content varies as described in the Mano Dolomite above: the reservoir contains fresh water except in the vicinity of hydrocarbon fields. Gas fields in the Portlandian-Barremian sequence, in the extreme south of the Aquitaine Basin, have low porosities (2–7%). In other parts of the reservoirs, away from these fields, permeability and porosity are poorly known.

Over the whole of the subsiding region (Parentis Subbasin and Pyrenees margin), the part of the Jurassic-Lower Cretaceous reservoir containing no fresh water has an areal extent of roughly 5000 km². In this part CO₂ storage can be considered.

Overpressure in the reservoirs of the Aquitaine Basin has been mentioned by Housse and Maget (1977): '*... in the southern Aquitaine pressure values (for the Upper Jurassic) are biased by the occurrence of natural gas and correspond to very high values*'.

Closed Structures

Maps of the aquifer tops, published at the scale of 1:1 000 000 (Haenel and Staroste, 1988), are not sufficiently detailed for identification of trap structures. The following description of traps is based on the traps found in hydrocarbon fields (Schroeder and Schoeneich, 1986; Anonymous, 1993).

Paris Basin

There are about 40 small oil accumulations in the Paris Subbasin, which demonstrates the existence of effective traps and seals. Indeed, several impermeable layers are known, two of which are laterally very consistent. These are the marls of the Liassic (Toarcian) and Upper Jurassic (Callovian-Oxfordian). The uppermost Keuper and lower Liassic clays provide a seal for deposits in the Keuper and Rhaetian. The Callovian-Oxfordian marls provide one for deposits in the Dogger. The traps are mostly anticlines with very small closures; some are a combination of structural and stratigraphic traps, including pinch-out structures.

Aquitaine Basin

As was noted in the platform region (northern part of the basin), the aquifers most promising for CO₂ storage are likely to be Triassic sandstones, as well as the sandstone-dolomite of the lower Lias. These aquifers are overlain by a clay caprock (late Liassic), which is virtually continuous over the entire basin. The potential for CO₂ storage thus depends on local structures (anticlines, folds), yet to be identified.

In the subsiding region, trap structures are more common and of variable nature, as demonstrated by numerous accumulations or indicators of hydrocarbons. Traps consist of salt diapirs, anticlines, or permeability barriers (Schroeder and Schoeneich, 1986). Seals may be provided by anhydrite^[18], massive carbonate or marl.

Storage Capacity

Table 4.5.1 shows the storage capacity of traps on deep aquifers (Triassic to Upper Jurassic). As mentioned above, porosity values for the aquifers are from Haenel and Staroste (1988). The storage calculation (see section 4.2) is based on the assumption that 3% of the aquifer volume are

[18] Geothermal experiments showed that anhydrite may be leached by CO₂-water mixture (see section 4.2.3.1 and Chapter 5).

Table 4.5.1 Theoretical CO₂ storage capacity of traps on major deep aquifers in onshore France. The storage calculation is based on the assumption that 3% of the aquifers are in a trap and that 6% of the trapped pore volume can be filled with CO₂. For all aquifers an average porosity of 10% has been inferred. A CO₂ reservoir density of 700 kg/m³ has been used.

Basin	Aquifer age	Range	Average net thickness	Total pore volume	Storage capacity in traps
		(km ²)	(m)	(km ³)	(Mt CO ₂)
Paris Basin	Upper Jurassic	10 000	50	50	63
	Mid Jurassic *	15 000	100	150	189
	Lower Jurassic	11 000	20	22	28
	Triassic	21 000	200	420	529
North Aquitanian Basin (platform)	Mid Lias	12 000	50	60	76
	Triassic-Lias	16 000	100	160	202
South Aquitanian Basin (subsiding)	Jurassic to Lower Cretaceous	5000	700	350	441
Total				1212	1527

* including the area that is used for geothermal operations (2000 km²)

in a trap. Since most traps are anticlinal structures that form 'open' reservoirs, a storage efficiency of 6% is used, which means that 6% of the trapped pore volume can be filled with CO₂. It is further presumed that the CO₂ has an average density of 700 kg/m³ under reservoir conditions. If these assumptions are taken in consideration, the storage potential of the French onshore aquifers is about 1530 Mt CO₂.

Unused deep aquifers that are effectively sealed off from the shallow subsurface or that have a high-quality topseal with a very large distribution may be suitable candidates for a concept in which CO₂ storage is not restricted to traps and the CO₂ is allowed to invade the largest part of the aquifer as long as it does not escape from the aquifer. Deep aquifers in the Paris Basin are used for storage of natural gas (Triassic) or geothermal heat recovery (Mid Jurassic). The Upper Jurassic aquifer in the Paris Basin is unused, but the quality of its top seal may locally be questionable because the aquifer does not contain any hydrocarbons. The aquifers in the Paris Basin are therefore considered to be inappropriate for storage 'outside traps'. Aquifers in the South Aquitaine Basin (Subsiding Region) are also expected to be unsuitable. They either communicate with overlying sandstones or contain fresh water. The only potential candidates for storage 'outside' traps are probably the Triassic and Jurassic aquifers in the North Aquitaine Basin (Platform Region). They are overlain by Mid Lias clay that is laterally very consistent. It is expected to provide an effective seal. Laterally the aquifers grade into impermeable rock. The aquifers may therefore be 'closed'. If 2% of the entire aquifer pore volume can be filled, these aquifers have an estimated CO₂ storage capacity of 3.1 Gt.

4.5.3.2 OFFSHORE AQUIFERS

The Paris Basin and the Aquitaine Basin both extend offshore. The continental shelf (English Channel, Atlantic), however, did not prove favourable for hydrocarbon accumulation. Oil and gas exploration, therefore, were not very extensive. Potential aquifers are hardly known. Most of the information available is derived from seismic sections.

According to the geological map of the French continental margins (BRGM/CNEXO, 1982), a graben exists between France and the British Isles. In its central part, the sedimentary succession may be 1000 m thick. Detrital Triassic sediments at the base of the sequence could constitute an aquifer, as is the case in the Paris Basin. The eastern Channel contains the extension of the Hampshire Basin: the Cenozoic series there is 500 m thick. It is pos-

sible that aquifers occur in the basal part of the basin, in the Lower Cretaceous.

In the Bay of Biscay (Gulf of Aquitaine), the geological structure is far more complex, and the sedimentary sequence is thicker. Detrital Triassic sediments are documented 100 km from the Aquitaine coastline, where they form a thick sequence. Probably, this sequence also occurs off the coast of Brittany, where seismic lines have shown the presence of diapir-like structures within a sedimentary sequence of 5000 m thick (Derégnaucourt and Boillot, 1982). The Upper Jurassic contains a bio-detrital carbonate facies, which could represent a reservoir. The Upper Cretaceous contains pelagic facies (marls), and may provide an effective seal.

The only precise data regarding offshore aquifers relate, in Aquitaine, to the western extension of the Arcachon-Parentis Subbasin (Housse and Maget, 1977). This was studied over some 20 km offshore, and is not significant in the context of this study.

4.5.4 Hydrocarbon Fields

4.5.4.1 CONSTRAINTS

The present estimate is based on two sources: 1) the annual report on hydrocarbon fields by the French Ministry of Industry (Anonymous, 1993), and 2) the World-wide Production Report of the Oil & Gas Journal (1993). The method of calculating the storage capacity has been described in section 4.2.

Data on the ultimate recovery for each field are not available, because the proved reserves are unknown. There is only an estimate for the reserves of the whole of France (see below). Based on these general reserve estimates, the remaining oil reserves in the individual fields have been assessed by taking 27% of the cumulative oil production, the remaining gas reserves by taking 14% of the cumulative gas production.

The lithological characteristics of reservoirs, such as porosity, depth to top of formation, geological stage, API gravity of the oil, are listed in the yearly report of the Ministry of Industry. The gas reservoir volume was computed by assuming a hydrostatic pressure gradient of 10.5 MPa/km. This may lead in some cases to an overestimation of the reservoir volume, as overpressures are noted in hydrocarbon fields of the Aquitaine Basin. Figures for actual field pressures could not be obtained. The oil 'volume in place' was computed from the volume pro-

duced, the API gravity, and a value of 1.2 for the formation volume factor.

The distribution of French oil and gas fields is shown in Figure 4.5.1. Table 4.5.2 lists the inferred ultimate hydrocarbon recovery and the corresponding estimate of the CO₂ storage capacity of the hydrocarbon fields.

4.5.4.2 OIL FIELDS

Total oil production before 1993 amounts to 83 Mt. The proved reserves at the beginning of 1993 totalled 20 Mt of oil, with an additional 2.5 Mt associated with natural gas fields. The ultimate oil recovery is thus approximately 105 Mt in 1993.

Onshore Oil Fields

Most oil fields are very small^[19]. The only exceptions are: the Parentis and Cazaux fields (with a combined cumulative production of 44.8 million m³) in the Aquitaine basin, and the Chaunoy field (with a cumulative production of 7.0 million m³) in the Paris Basin. The Parentis reservoir consists of Lower Cretaceous limestones and dolomites, the Cazaux reservoir consists of uppermost Jurassic to Lower Cretaceous sandstones, and the Chaunoy reservoir consists of Keuper sandstones.

Offshore Oil Fields

There are no offshore oil fields.

4.5.4.3 GAS FIELDS

With the exception of a small field in the Paris Basin (Trois-Fontaines), the gas fields are located exclusively in the Aquitaine Basin. At the beginning of 1993, cumulative gas production totalled 283 milliard m³, corresponding to a commercial production of 195 milliard m³. The estimated remaining reserves are about 40 milliard m³ (or 1296 Bscf), and 28 milliard m³ after purification.

Onshore Gas Fields

By far, the largest gas field is the giant Lacq-profond field (Lacq deep). The reservoir occurs in limestone and dolomite of Upper Jurassic to Lower Cretaceous age, and extends over 110 km². Its porosity is very low, about 3.5%. Other major gas fields are Meillon (the reservoir extends over 50 km²), St Marcet and Rousse. As the Lacq field, they have also carbonate reservoirs, consisting of dolomite (Meillon), Upper Jurassic limestone and dolomite (Rousse), or Upper Jurassic to Lower Cretaceous marl-limestone (St Marcet). Porosity values are low, generally 3–4%, except for St Marcet where porosity reaches 7%.

Offshore Gas Fields

There are no known offshore gas fields. Isolated gas indicators are present in the offshore extension of the Parentis Subbasin.

4.5.4.4 STORAGE CAPACITY

The storage potential has been estimated using a CO₂ density of 700 kg/m³. The corresponding capacity values are given in Table 4.5.2. Small fields, with a capacity of less than 10 Mt CO₂, have not been taken into account. This yields a list of only six potential storage locations, all located in the Aquitaine Basin: the Parentis and Cazaux oil

fields, and the Lacq, St Marcet, Meillon and Auzas gas fields. Apart from these six, the Chaunoy oil field in the Paris Basin may be a future candidate if its reserves are larger than average. The current capacity of the Chaunoy field (based on cumulative production) is 6.6 Mt CO₂; the field has an annual production of 0.8 million m³, which yields an augmented CO₂ storage capacity of 0.7 Mt per year.

The total theoretical CO₂ storage in depleted hydrocarbon fields is thus estimated to be around 930 Mt, of which ca 690 Mt corresponds to the giant Lacq gas field, and ca 240 Mt to five other sites. Some doubt exists about the feasibility of CO₂ disposal in the Lacq and other gas fields, given the low reservoir porosity value of 3–4%.

It should be emphasised that the corresponding storage capacities are located in the extreme southwest of the country, i.e. removed from the major centres of industry.

4.5.4.5 DEPLETION

The only near-depleted field is the St Marcet gas field, which is currently producing only 0.01 milliard m³ per year. The other important fields are all operating at a constant or slowly declining rate, and no other cases of depletion are therefore expected in the near future.

Proved reserves are not known for individual fields. It is thus impossible to compute their remaining life expectancy as a function of current production. Hydrocarbon fields in France have a very long production life: St Marcet has been in production for 50 years, Parentis for 40 years, and Lacq for more than 35 years. It is thus rather unlikely that — besides fields already depleted — any of the hydrocarbon fields in France will become available for CO₂ storage in the short term.

4.5.5 Conclusions

The theoretical CO₂ storage capacity was calculated according to methods described in section 4.2, yielding the following values: ca 1 530 Mt in aquifers and ca 930 Mt in hydrocarbon fields. Several points, however, need to be considered.

Most of the storage potential computed in hydrocarbon fields is provided by the Lacq gas field alone. The gas fields (Lacq, Meillon and even St Marcet), however, occur in low-porosity reservoirs. It is therefore uncertain if supercritical CO₂ could be injected without any problems.

It will be several years yet before the hydrocarbon fields currently under production are entirely depleted. At present, of all the potential CO₂ storage sites reviewed, the St Marcet gas field is the only one nearing depletion.

Hydrocarbon fields currently represent the only clearly identified storage sites in France, but injection of CO₂ into gas fields may prove difficult, and oil fields are rather small. Therefore aquifers, having a total potential CO₂ capacity of 1530 Mt, provide the most likely storage sites in the short or medium term. However, the deeper aquifers in the Aquitaine Basin (away from the gas fields) are expected to be overpressured, which will complicate CO₂ injection in this region.

Another consideration stems from economics and supports the expectation that in the near future CO₂ storage will be restricted to aquifers: all potential sites associated with hydrocarbon fields (with one possible exception) are located in the Aquitaine Basin, i.e. remote from most French industrial centres. Conversely, potential aquifer storage sites, mainly in the Paris Basin, are much more central to the country and closer to the numerous CO₂ production sites.

[19] The annual report of the French 'Ministère de l'Industrie' lists more than 50 producing oil fields, of which only 15 have a cumulative production of more than 1 million m³.

Table 4.5.2 Potential storage capacity of the main hydrocarbon fields of onshore France. Ultimate recovery per field has been assessed by taking 127% (#) and 114% (*) of the cumulative production, for oil and gas respectively. The CO₂ reservoir density is assumed to be 700 kg/m³, the oil formation volume factor 1.2. The gas expansion factor is derived from initial reservoir pressure, which is inferred from reservoir depth, using a hydrostatic pressure of 10.5 MPa/km.

ONSHORE FIELDS		OIL		GAS		TOTAL
Name and Basin	Depth (m)	Ultimate Recovery # (million m ³)	Storage capacity (Mt CO ₂)	Ultimate Recovery * (milliard m ³)	Storage capacity (Mt CO ₂)	Storage capacity (Mt CO ₂)
Paris Basin						
Vert	1800	1.2				
Chaunoy	2450	8.9				
Coulommes	2150	2.8				
St Martin	1250	1.8				
Villeperdue	1630	6.3				
Trois-Font	1420			0.91		
Aquitaine Basin: North-Pyrenees						
St Marcet	840			7.98	41.1	41.1
Lacq prof.	3100			246.92	691.9	691.9
Lacq sup.	483	5.5				
Meillon	3700			55.97	139.9	139.9
Proupriary	1495			0.23		
Auzas	1600			0.57		
Rousse	4230			4.56	10.4	10.4
Ucha	4460			1.94		
Ger	?			0.11		
Pécorade	2320	2.5		0.46		
Vic Bihl	1900	4.5		0.57		
Lanot	4150			1.25		
	4530			0.11		
Lagrave	1590	2.7				
Aquitaine Basin: Parentis						
Cazaux	2400	15.4	13.0		13.0	
Lavergne	3190	2.6				
Mothes	2350	1.6				
Lugos	1480	2.2				
Parentis	1980	41.4	34.8	0.34	1.2	36.1
Ledeuix	2230			0.11		
Total		99.5	47.8	322.0	884.5	932.3

Gas reserves are estimated to be 14% of the cumulative gas production

* Oil reserves are estimated to be 27% of cumulative oil production

4.6 THE CO₂ STORAGE CAPACITY OF GERMANY

K.H. Gaida and H. Möller

4.6.1 Summary

The major German sedimentary basins are the Molasse Basin (south), the Upper Rhine Graben (west) and the North German Basin (north). Suitable aquifers in the Molasse Basin are predominantly formed by Tertiary sandstones. The Upper Rhine Graben is excluded from the inventory, because its aquifers show low porosity and crop out at the margins, the net thicknesses are unknown, and the basin is intensively block faulted. The North German Basin has Triassic, Jurassic and Cretaceous aquifers (mainly sandstones) and is characterised by traps generated by block tectonics and halokinetics. Especially the aquifers in the western part of this basin are not well known. The available data are rather incomplete and not representative. According to the sparse base data, the estimation of CO₂ storage capacity in German aquifers is unrealistically low (about 470 Mt CO₂ in traps).

The CO₂ storage capacity of the German onshore gas fields is estimated to be 2 340 Mt CO₂. Suitable offshore hydrocarbon fields do not exist. The capacities of the individual oil fields onshore are low. The major onshore oil

fields have an estimated storage capacity of ca 60 Mt CO₂.

4.6.2 Geological Overview

Three major sedimentary basins are developed in Germany (see Figure 4.6.1.):

- the Molasse Basin in the south,
- the Upper Rhine Graben in the southwest, and
- the North German Basin in the north.

Each of these basins is characterised by a specific geological history that is related to different tectonic regimes.

The German Molasse Basin is part of the Tertiary fore-deep in front of the Alps. It is about 300 km long and has a maximum width of about 100–120 km. The northern border of the basin is the erosional limit of Tertiary sediments. The southern border is tectonically controlled and characterised by steep dipping strata. The Molasse Basin can be subdivided into an undeformed northern part and an intensively folded southern part. The sediments of the Molasse basin are predominantly erosional products of the uplifting Alps during Tertiary times. To the south, the sediments reach a thickness up to 5000 m.

The Upper Rhine Graben is part of a NNE-SSW striking tectonic zone extending through the whole of Western Europe. The basin has a length of about 300 km and a maximum width of about 40 km. The development of the Upper Rhine Graben started in Tertiary times and is related to the emplacement of a very large subcrustal magma pillow resulting in stretching and consequent downfaulting of the overlying crust. The basin is filled with Tertiary sediments that have a maximum thickness of about 4000 m.

The North German Basin is part of a very large tectonic depression extending from the North Sea to Poland. During Permian to Tertiary times sediments up to 8 000 m thick accumulated. The development of the North German Basin started in the Permian. At this time the basin was bordered in the north by the Fenno-Scandian Shield, and in the south and southwest by the Bohemian Massif, the Rhenish Massif and the London-Brabant Massif.

From a petroleum geology point of view the sedimentary fill of the North German Basin can be subdivided into deep seated (2000–5000 m) gas bearing strata (Upper Carboniferous, Early Permian and Early Triassic) and relatively shallow (600–1500 m) oil bearing strata (Triassic, Jurassic, Lower Cretaceous). The major processes influencing the structural pattern and the sediment distribution within the North German Basin are block tectonics and halokinetics. Especially due to movements of the Zechstein salt, smaller sedimentary troughs developed, frequently striking in NNE-SSW direction.

A less important sedimentary basin is the Thuringian Basin situated in the eastern part of Germany. This basin is characterised by hydrocarbon occurrences in Zechstein carbonates.

4.6.3 Aquifers

4.6.3.1 ONSHORE AQUIFERS

Constraints

Published data on the regional distribution, quality, geological characteristics and petrophysical properties of aquifers in Germany are sparse. The data compiled within the following text were gathered mainly from geothermal inventory studies.

The data on aquifers of the Molasse Basin, the Upper Rhine Graben and the description of two aquifers in the western part of the North German Basin are taken from Haenel and Staroste (1988). This information contains a number of uncertainties, e.g. unknown facies changes, extrapolated porosity and permeability values. This will affect the accuracy of our estimate of the theoretical CO₂ storage potential.

Investigations of suitable aquifers for geothermal use in the western part of the North German Basin are currently in progress. Results were not available in time for this study. Maps of suitable Mesozoic aquifers to a scale of 1:200 000 covering the eastern part of the North German Basin (the former GDR territory) have been generated in the years 1988–1992. The total set of these maps was available for this compilation.

Western Molasse Basin

Aquitain Sandstones (Tertiary)

The Aquitain sandstones are of fluvial to limnogenic origin. West of the river Iller, Aquitain and Chatt sandstones are known as 'Untere Süßwassermolasse'. Both sandstone intervals are separated by a more clayey sedi-

ment. Little is known about the porosity. Values between 12 and 20%, decreasing with depth, are probable. No permeability values are available.

Chatt Sandstones (Tertiary)

The depositional environment of the Chatt sandstones is comparable to that of the Aquitain sandstones. The net thicknesses are variable and uncertain. Porosities vary between 2 and 26%, with an average of about 20%.

Baustein Beds (Tertiary)

The Baustein beds were deposited on prograding deltas. They are of minor importance in the western part of the Molasse Basin. The net thicknesses are low. Porosities are around 20%. Permeabilities of less than 100 mD can be expected at depths below 800 m.

Malm Carbonates (Late Jurassic)

The Malm consists of several hundred metres thick limestone and dolomite formations that are locally intensively karstified. The karstification extends down to 200–300 m below the top of the Malm. This karstified interval is considered to be an unsuitable CO₂ storage reservoir because it is connected to the surface. The average porosity of the carbonates is assumed to be 2.5%.

Trigonodusdolomit (Upper Muschelkalk, Triassic)

The Trigonodusdolomit consists of cavernous limestones and dolomites. On a regional scale, a mean porosity of only 2.5% has been assumed. Therefore this aquifer is considered to have little potential for CO₂ storage.

Eastern Molasse Basin

Burdigal Sandstones (Tertiary)

The sediments of the Burdigalian result from a marine transgression. They are limited to the southeastern part of the Wasserburg Trough and characterised by an alternation of clayey marls and sandy layers. The porosities of most sandstone layers vary between 25 and 28%. Permeabilities of 500–1000 mD are indicated in the literature. However, borehole data give values of only 100–200 mD, so an average permeability of 200 mD is assumed on a regional scale.

Aquitain Sandstones (Tertiary)

The Aquitainian sediments are characterised by an alternation of sandy beds and clayey marls. They were deposited in a fluvial environment to the west and a shallow marine environment to the east. Due to frequent facies changes, the distribution of the net thicknesses is very uncertain. Little is known about porosity and permeability. Porosities of about 20% and permeabilities of about 100 mD are assumed to be average values on a regional scale.

Chatt Sandstones (Tertiary)

The Chatt sandstones mainly are of fluvial origin. The porosities of 25–28% that have been measured, are not expected to be representative.

Baustein Beds (Tertiary)

The Baustein Beds originate from deltas that prograded to the north. Average porosities of 22% and average permeabilities of 200 mD have been determined.

Ampfingen Beds And Priabonian Basal Sandstone (Tertiary)

The Ampfingen beds and Priabonian basal sandstone, which are certainly not connected hydraulically, originate from a marine transgression of Eocene age. The Ampfingen

beds are assumed to be slightly younger than the Priabonian basal sandstone. The distribution of the latter is restricted to the southern and southwestern part of the eastern Molasse Basin. An average porosity of about 20% and an average permeability of 600 mD is indicated for the Ampfingen beds. The corresponding values for the Priabonian basal sandstone are 8–18% and about 200 mD. The Priabonian basal sandstone is considered to have no significant CO₂ storage potential, because its net thickness is low.

Cenomanian And Gault Sandstones (Cretaceous)

The Cenomanian and Gault sandstones originate from a marine transgression at the transition from Early to Late Cretaceous, and are very similar in lithology. They are regionally separated by the Landshut-Neuöttinger anticline. Porosities of ca 20% and permeabilities of about 100–1000 mD are thought to be representative for both sandstones.

Malm Carbonates (Late Jurassic)

As described above the karstified Malm carbonates are considered to be unsuitable for CO₂ storage.

Upper Rhine Graben

In the Upper Rhine Graben three aquifers were investigated by Haenel and Staroste (1988) with respect to possible recovery of geothermal energy:

- Upper Muschelkalk (Triassic)
- Bunter sandstone (Early Triassic)
- Hauptrogenstein (Dogger, Middle Jurassic).

These aquifers are not considered to be suitable for CO₂ storage because

- effective porosities are very low (1–2%)
- net thicknesses are not well known
- some of the formations outcrop at the margins of the Graben
- the whole Graben area is very intensively block faulted.

Aquifers Of The Eastern North German Basin

With respect to a possible recovery of geothermal energy, the Mesozoic aquifers of the eastern part of the North German Basin were studied in detail during the years 1988–1992. Maps to a scale of 1:200 000 that show the distribution and quality of aquifers and that cover the total area, were elaborated by Diener et al. (1988–1990), Brückner et al. (1990) and Diener et al. (1990–1992). Summary maps to a scale of 1:500 000 are currently being drawn.

As described by Wormbs (1992), the main Mesozoic aquifers are:

- Middle Bunter sandstones (Triassic).
- Rätkeuper-Liassic sandstones (boundary Triassic/Jurassic)
- Aalenian sandstones (Dogger, Mid Jurassic)
- Lower Cretaceous sandstones

The studies mentioned above also contain information on the distribution and quality of the Triassic Schilf-sandstein (Keuper) that shows rapid lateral facies changes.

Each Mesozoic aquifer shows a strong variation in quality over the area investigated. The Middle Bunter sandstone for example is more important in the north than in the south due to facies changes. The good quality aquifers are generally concentrated in the central part of the basin. Normally, the sandstones mapped alternate with shales and thick (up to 100 m), and massive sandstones (without intercalated shales) are only developed locally. The average depth of the Mesozoic aquifers is about 1 500 m. The eastern North German Basin is structurally mainly determined by block tectonics and halokinetics. These processes have influenced the facies distribution, i.e. the distribution of the sandstones and shales.

Western North German Basin

Data on aquifers of the western North German Basin are very rare. Investigations of suitable aquifers for the recovery of geothermal energy are currently in progress, but results are not yet published. Therefore, information on only four, more or less locally developed aquifers were available:

- Bentheimer sandstone (Lower Cretaceous)
- Valendis sandstone (Lower Cretaceous)
- Mittelrhät main sandstone (Keuper, Triassic)
- Solling sandstone (Bunter, Triassic).

The data of the Bentheimer and Valendis sandstones are taken from Haenel and Staroste (1988). The data on the Mittelrhät main sandstone and the Solling sandstone are taken from Beutler et al. (1992).

Bentheimer Sandstone (Lower Cretaceous)

The Bentheimer sandstone consists of sand bars that developed in a coastal shelf environment. It is one of the most important oil reservoirs in Germany. Oil fields are mainly located in anticlines. The average porosity of the sandstones is about 25%, permeability values vary between 1000 and 4000 mD.

Valendis Sandstone (Lower Cretaceous)

The Valendis sandstone is also an important oil reservoir. Porosities vary from 22 to 29% and permeabilities from 500 to 1000 mD. An average porosity of 25% is assumed.

Mittelrhät Main Sandstone (Keuper, Triassic)

These sandstones were deposited in a deltaic environment. Due to a high degree of reworking, these sandstones are very mature, showing quartz contents up to 90–95%. The sediments were mainly transported in channels, the orientation of which is influenced by halokinetic structures. The distribution of sandstones suitable for CO₂ disposal is therefore very complex. Net thicknesses of up to 100 m are possible. An average porosity of 20% is assumed in the areas investigated.

Solling Sandstone (Middle Bunter, Triassic)

Within the basal part of the Solling Formation, a massive sandstone with a thickness up to 80 m is locally developed. The sandstone, possibly a sand bar, occurs in a relatively narrow zone extending from the western Emsland to an

area north of Hanover. Average thicknesses of 20–30 m and an average porosity of 20% are indicated.

Storage Capacity

The total storage capacity of the trapped part of the aquifers onshore is estimated to amount to ca 470 Mt CO₂ (Table 4.6.1). Considering the incompleteness of the base data, the statements on CO₂ aquifer storage capacity in Germany are rough estimates only, indicating a minimum rather than a maximum value.

Our storage estimates are based on maps called 'Karten der Gesamtperspektivität'. These maps show the distribution of aquifers that meet the following requirements:

- temperatures above 40°C
- thicknesses higher than 20 m
- porosities higher than 20%.

These requirements form the boundary conditions of our estimate of the CO₂ storage capacity.

No information was available on the regional occurrence and frequency of structural traps on the aquifers mentioned above. It is therefore assumed that about 3% of the aquifer volume is within traps. It is further assumed that only 4% of the trapped pore volume can be filled with CO₂. In addition, the storage calculation is based on a CO₂ reservoir density of 700 kg/m³ (see section 4.2).

If the German part of the North German Basin is similar to the Dutch part, the deepest investigated aquifers in this

basin, the Triassic aquifers, are expected to be 'closed' and effectively sealed off from the shallow subsurface ('*' in Table 4.6.1). The restriction that CO₂ should be confined by traps could therefore be released and 2% of the total aquifer pore volume could be used for CO₂ disposal (see section 4.2 and 4.11). This leads to a total storage capacity of 2.24 Gt CO₂.

Since the aquifers in the Molasse Basin are likely to crop out in the north (erosional northern margin), a storage concept in which CO₂ must be confined by traps seems appropriate.

4.6.3.2 OFFSHORE AQUIFERS

The German offshore aquifers are not included in this inventory because data on their distribution and quality are not available.

4.6.4 Hydrocarbon Fields

This chapter only deals with hydrocarbon fields onshore Germany. Offshore fields do not exist, although a number of oil and gas shows have been reported from offshore wells.

At January 1 1993, total numbers of 134 producing gas fields and 100 producing oil fields have been reported. At this date the cumulative production was about 657 milliard m³ gas and about 257 million m³ oil. Remaining gas reserves at that date were estimated to be 365 milliard m³ gas and 63 million m³ oil. So, the total ultimate recovery in Germany will approximately be 1 022 milliard m³ gas and 320 million m³ oil.

Table 4.6.1 Theoretical storage potential of the trapped fraction of the German aquifers onshore. Only aquifers that are thicker than 20 m and below a depth of 800 m have been considered. The storage calculation is based on the assumption that 4% of the trapped aquifer pore volume can be filled with CO₂ and that 3% of the aquifer volume is in a trap. An underground CO₂ density of 700 kg/m³ has been used.

ONSHORE AQUIFERS IN GERMANY			Net volume (km ³)	Average porosity (%)	Average permeability (Darcy)	Total pore volume (km ³)	Storage capacity in traps (Mt CO ₂)
Basin	Formation name	Age					
MOLASSE BASIN							
western part	Aquitain sandstone	Tertiary	63	12%	?	7.6	6.35
	Chatt sandstone	Tertiary	299	20%	?	59.8	50.23
	Baustein beds	Tertiary	41	20%	ca. 0.1	8.2	6.89
eastern part	Burdigal sandstone	Tertiary	5	25%	0.2	1.3	1.05
	Aquitain sandstone	Tertiary	29	20%	ca. 0.1	5.8	4.87
	Chatt sandstone	Tertiary	352	25%	?	88.0	73.92
	Baustein beds	Tertiary	62	22%	0.2	13.6	11.46
	Ampfingen beds	Cretaceous	4	20%	0.6	0.8	0.67
	Cenomanian/Gault sandstone	Cretaceous	41	20%	> 0.1	8.2	6.89
NORTH GERMAN BASIN							
eastern part	Lower Cretaceous sandstone	Cretaceous	133	20%	> 0.1	26.6	22.34
	Aalenian sandstone	Jurassic	261	20%	> 0.1	52.2	43.85
	Liassic/Rätkeuper sandstone	Triassic/Jurassic	636	20%	> 0.1	127.2	106.85
	Schilfsandstein *	Triassic	121	20%	> 0.1	24.2	20.33
	Middle Bunter sandstone *	Triassic	63	20%	> 0.1	12.6	10.58
western part	Bentheimer sandstone	Cretaceous	9	25%	> 1.0	2.3	1.89
	Valendis sandstone	Cretaceous	4	25%	0.5–1.0	1.0	0.84
	Mittelrät sandstone *	Triassic	564	20%	> 0.1	112.8	94.75
	Solling sandstone *	Triassic	51	20%	> 0.1	10.2	8.57
Total			2738			562.3	472

* aquifers that are expected to be 'closed' and entirely below a depth of 800 m

The statements in the following text and tables are largely based on published data taken from the journal 'Erdöl und Kohle' (years 1967–1984), the journal 'Erdöl Erdgas Zeitschrift' (years 1965–1979), the annual reports of the WEG (years 1971–1992), the 1992 report of the 'Niedersächsisches Landesamt für Bodenforschung' and Boigk (1981).

4.6.4.1 ONSHORE GAS FIELDS

Constraints

To assess the CO₂ storage capacity of the German gas fields, the volumes of already produced and still recoverable approved and probable reserves were added^[20]. It is assumed that these volumes of hydrocarbons can be replaced by equivalent volumes of CO₂. The field data are restricted and often some basic data (e.g. initial pressure, temperature) are not available. In these cases the missing data were calculated by making regional comparisons with neighbouring fields or using standardised equations (e.g. for temperature calculations; see section 4.2).

Description

The main natural gas reservoir formations in Germany are Rotliegend sandstones and Zechstein carbonates. In some areas Upper Carboniferous strata and Bunter sandstones also are productive.

Gas reservoirs in Germany are mainly located within the North German Basin. Additionally, some bigger reservoirs were discovered in the Molasse Basin and the Thuringian Basin (see Figure 4.6.1.). Due to the scale of Figure 4.6.1, the locations of the single gas fields are not shown. However, the figure shows the areas in which neighbouring gas fields are situated. Table 4.6.2. shows a list of the major German onshore gas fields and basic field data. The column 'AREA' in Table 4.6.2. refers to the areas indicated on Figure 4.6.1.

Storage Capacity

The total storage capacity of the major German gas fields is estimated to amount to 2 340 Mt CO₂ (Table 4.6.2). The capacity is calculated by multiplying the underground volume of ultimately recoverable gas with the CO₂ density under subsurface conditions. The underground volume of ultimately recoverable gas is calculated by dividing the ultimate recovery values by the gas expansion factor (GEF). The GEF was determined by using a company owned computer program based on the equations of Yarborough and Hall (1974). This program takes pressure, temperature, and gas composition into account. Gas composition is an essential parameter for calculating a GEF, because it varies considerably in German natural gases (e.g. up to 25% H₂S in Zechstein reservoirs, up to 80% N₂ in Rotliegend reservoirs).

Depletion

There are at present no depleted major gas fields in Germany. Based on the ratio of estimated reserves / 1992 production, the gas fields will become exhausted in 6 to 24 years (Table 4.6.2). However, this ratio provides only a rough indication of the date of completion. It should be noticed that the theoretical storage capacity mentioned above will certainly be reduced by installing gas storage plants after depletion of some of the fields.

4.6.4.2 ONSHORE OIL FIELDS

Constraints

As described above, the ultimate recovery of the major German oil fields were estimated by adding the cumulative production up to 1992 and the recoverable (approved and probable) reserve estimates at January 1, 1993. It is assumed that these volumes of oil can be replaced by equivalent volumes of CO₂ (see section 4.2).

Most of the German oil reservoirs contain heavy to medium-density oil. Thus, an average oil density of 900 kg/m³ and an average oil formation volume factor (FVF) of 1.1 are assumed. In Germany production values or reserve estimates are normally given in million tonnes. These values have been converted into million m³ by using the average oil density of 900 kg/m³.

Description

The main oil reservoir formations in Germany are Mid Jurassic and Lower Cretaceous sandstones. The major German oil fields are located in a certain part of the North German Basin, known as the 'Lower Saxony Basin'. In this basin, very thick Mesozoic sediments accumulated, the distribution of which is often influenced by movements of the Zechstein salt.

Table 4.6.3. shows a list of the major German onshore oil fields and their ultimate recovery values. The geographic location of these fields is marked on Figure 4.6.2.

Storage Capacity

The storage capacity is calculated by multiplying the reservoir volume of ultimately recoverable oil with the CO₂ density under subsurface conditions. The reservoir volume of ultimately recoverable oil is calculated by taking the product of the ultimate recovery values and the average formation-volume-factor of 1.1.

Taking the standardised cut off values of 10 Mt CO₂ (minimum storage capacity) and reservoir depth below 800 m into account, the total estimated storage capacity of German onshore oil fields is very low and amounts to 60 Mt CO₂. The total storage capacity and the capacity of the individual fields is presented in Table 4.6.3.

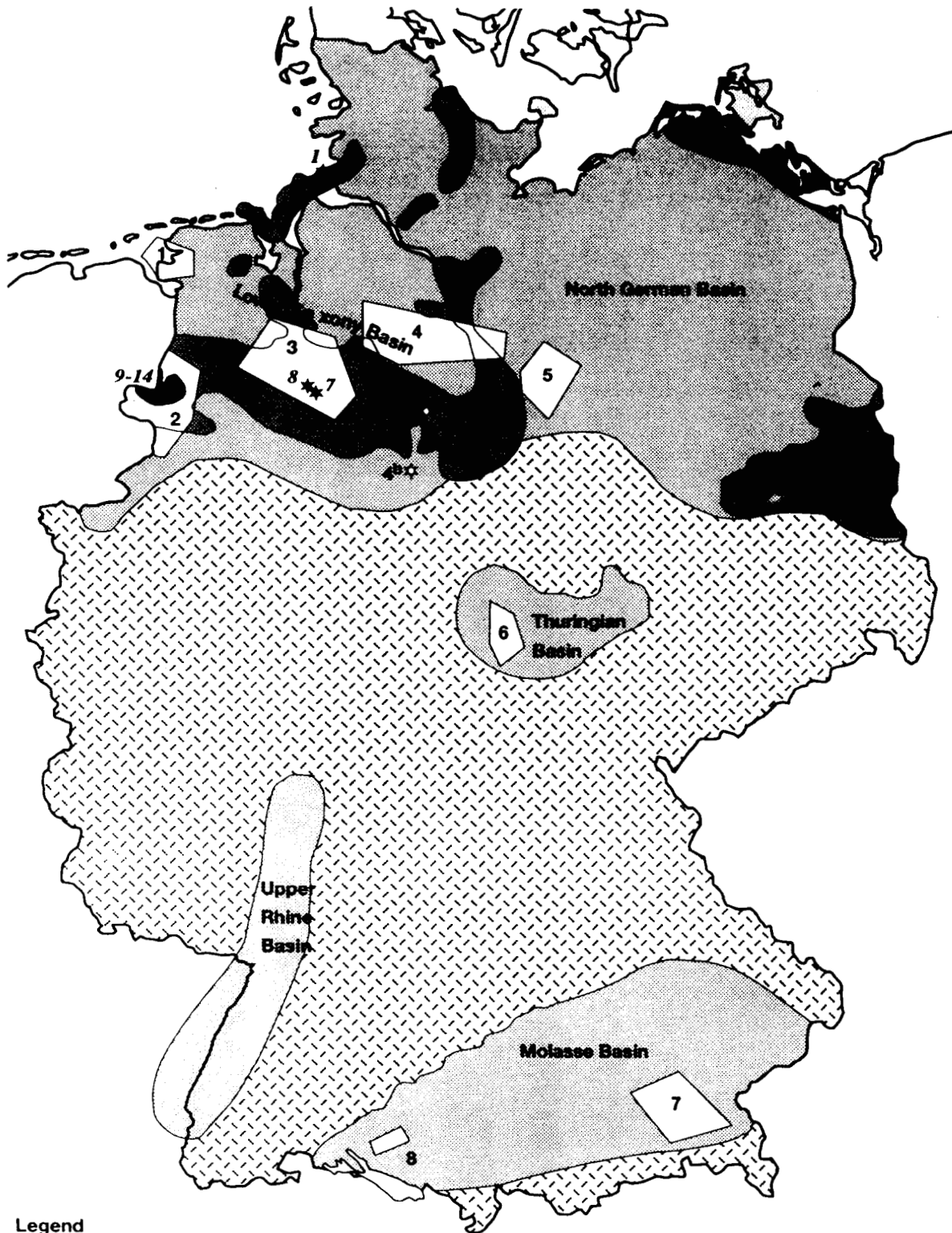
Depletion

There are at present no depleted major oil fields in Germany. Based on the ratio of estimated reserves/1992 production, the oil fields will become depleted in 7 to 51 years (Table 4.6.3). As mentioned before, this ratio provides only a very rough indication of the date of depletion.

4.6.5 Remarks

The revised storage capacity values presented in the above text differ significantly from the results of the preliminary study of the German underground CO₂ storage capacity (Progress Report No. 1, January to June 1993). The differences mainly result from applying a standardised method of calculation (see chapter 4.2), with other constraints and assumptions, that was not available during the preliminary study.

The estimate of the CO₂ storage capacity in German onshore aquifers of ca 470 Mt CO₂ is low and presumably too conservative. This is primarily due to the fact that data on German aquifers are sparse and very incomplete.



Legend

- major sedimentary basins
 - major oil bearing sedimentary basins
 - 3 regionally adjoining gas fields
 - regionally adjoining oil fields
 - 4^a ☆ gas reservoir
 - 8 ☆ oil reservoir
- 0 150 km
-

Figure 4.6.1 Major sedimentary basins in Germany, with gas plays and major oil fields (see for the names of gas plays and oil fields Tables 4.6.2 and 4.6.3, respectively).

Table 4.6.2 Theoretical storage potential of the onshore gas fields in Germany. Reservoir temperature (T) is inferred from a geothermal gradient of 30°C/km. Initial reservoir pressures (P) are measured values, except for the figures between brackets, which are extrapolated from nearby fields. The CO₂ reservoir density is established by using the computer program of Van der Sluijs (1991). The gas expansion factor (GEF) is calculated by a company owned computer program based on the equations of Yarborough & Hall (1974). Ultimate recovery is cumulative production (Dec. 1992) added to approved and probable reserves. Life time is remaining reserves divided by 1992 production. The 'Area' numbers refer to Figure 4.6.1.

GAS FIELDS		Average depth (m)	T (°C)	P (MPa)	GEF	CO ₂ density (kg/m ³)	Ultimate ⁺ recovery (10 ⁹ m ³)	Reservoir volume (10 ⁶ m ³)	Storage* capacity (Mt CO ₂)	Life time (years)
Area	Name									
1	Greetsiel	3720	122	44.6	283	722	2.20	7.78		
	Grenzbereich	3500	115	(42)	277	722	62.86	226.56	163.65	0
	Groothusen	3180	105	38.5	269	726	10.88	40.46	29.36	16
2	Apeldorn	2200	76	(29)	216	752	6.88	31.83	23.93	16
	Adorf-Dalum	2445	83	(32)	257	752	3.53	13.73	10.32	6
	Bentheim	1500	55	(20)	193	752	3.74	19.36	14.56	6
	Emlichheim	2875	96	(38)	275	751	7.94	28.84	21.66	6
	Fehndorf	2700	91	(35)	262	751	1.90	7.25		
	Itterbeck/Getelo	1975	69	(26)	233	752	6.37	27.33	20.56	6
	Kalle	3000	100	(39)	281	751	4.03	14.38	10.79	6
	Ratzel	2425	83	(32)	258	752	1.35	5.20		
	Rütenbrock	3500	115	(46)	290	750	3.13	10.78		
	Uelsen	1775	63	(23)	213	752	1.85	8.67		
Wielen	2110	73	(28)	242	752	3.51	14.52	10.92	6	
3	Bahrenborstel	2675	90	(35)	275	751	7.22	26.23	19.70	16
	Barenburg	2925	98	38.1	279	749	12.14	43.59	32.65	16
	Barrien	2500	85	40.8	291	812	16.79	57.67	46.81	16
	Buchhorst	2950	99	43	309	782	13.72	44.39	34.70	16
	Cappeln	3740	122	49.3	306	751	10.79	35.26	26.49	16
	Deblinghausen	3300	109	(43)	301	750	3.07	10.23		
	Dötlingen	3735	122	46.4	313	733	25.69	81.99	60.10	16
	Goldenstedt/Oythe	3550	117	46.4	309	749	17.89	57.88	43.36	16
	Hemmelte (Zechst.)	3400	112	45.2	304	754	14.52	47.77	36.04	16
	Hengstlage	2500	85	38	315	793	69.19	219.35	174.02	16
	Hengstlage-Nord	3930	128	48.7	317	708	10.50	33.18	23.48	16
	Hesterberg	3075	102	42.7	301	768	5.62	18.70	14.36	16
	Kirchhatten	3590	118	48.9	326	761	2.22	6.81		
	Klosterseele	4230	137	51.3	318	725	8.13	25.61	18.55	16
	Löningen-Menslage	1075	42	12.4	134	707	2.85	21.24	15.02	11
	Neerstedt	3980	129	47.9	312	723	9.01	28.84	20.84	16
	Quaadmoor	3745	122	46.3	318	731	4.50	14.18	10.37	16
	Rehden	1975	69	(26)	234	752	19.57	83.57	62.88	16
	Sage	3925	128	48.7	317	732	1.98	6.25		
	Sagermeer + Süd	3800	124	48.5	319	741	14.40	45.20	33.51	16
	Siedenburg	3400	112	(45)	299	750	46.98	157.35	117.98	16
	Staffhorst + Nord	3150	105	38.1	271	725	15.05	55.51	40.27	16
	Uchte	2540	86	(33)	256	752	6.40	24.98	18.77	16
Vahren	3660	120	46.4	295	740	8.80	29.79	22.03	16	
Varnhorn	3890	127	48.3	315	733	13.72	43.49	31.86	16	
Visbek	3265	108	42.7	298	750	40.84	137.29	102.93	16	
Wietingsmoor	3630	119	44.8	284	731	4.79	16.89	12.35	16	
Wöstendöllen	3750	123	46.4	318	732	5.43	17.10	12.51	16	
4	Halm./Wietzend./Mu.-SW	4445	143	54.8	301	729	14.15	47.05	34.32	22
	Hemsbünde	4660	150	(58)	309	733	20.97	67.85	49.75	22
	Munster+Lintzel	4450	144	55.8	303	735	12.05	39.81	29.26	22
	Munster-Nord	4450	144	54.5	299	727	4.13	13.85	10.07	22
	Schmarbeck	4450	144	55	300	730	3.12	10.42		
	Söhlingen	4800	154	58.7	306	726	47.64	155.72	113.12	22
	Soltau	4547	146	56.1	304	730	5.55	18.27	13.33	22
	4a Thönse	1915	67	21.7	210	704	3.55	16.91	11.91	12
4b Alfeld/Elze/Hil.Wald	1380	51	(16)	151	702	3.05	20.25	14.21	22	
5	Altensalzwedel	3300	109	(42)	260	741	11.51	44.36	32.88	8
	Heidberg-Mellin	3300	109	(42)	261	741	41.09	157.70	116.90	8
	Riebau	3300	109	(42)	257	741	14.17	55.04	40.80	8
	Salzwedel-Peckensen	3300	109	(42)	261	741	152.83	586.50	434.78	8
	Winkelstedt	3300	109	(42)	257	741	4.49	17.45	12.94	8
Wustrow	3300	109	42	264	741	13.88	52.62	39.01	22	

Table 4.6.2 *Continued.*

GAS FIELDS		Average depth (m)	T (°C)	P (MPa)	GEF	CO ₂ density (kg/m ³)	Ultimate* recovery (10 ⁹ m ³)	Reservoir volume (10 ⁶ m ³)	Storage* capacity (Mt CO ₂)	Life time (years)
Area	Name									
6	Behringen Mühlhausen	700	31	(9)	96	748	3.38	35.24	26.37	24
		700	31	(9)	93	748	1.58	16.98	12.71	24
7/8	Albaching-Rechtmehr.	1920	68	(21)	195	693	1.33	6.80	10.78	7
	Breitbrunn-Eggstätt	1525	56	(17)	167	692	2.60	15.57		
	Weitermühle-Steink.	1350	51	(15)	152	692	1.59	10.48		
	Fronhofen	1050	42	(12)	136	687	1.82	13.35		
Total		896.50						2340.4		

* Storage capacity is restricted to the fields that are below a depth of 800 m and can retain more than 10 Mt CO₂.

+ Normal cubic metres are converted to standard cubic metres by using a conversion factor of 1.055.

Table 4.6.3 Major German onshore oil fields. The reservoir CO₂ density is calculated from temperature and pressure using the computer program by Van der Sluijs (1991). The initial reservoir pressure (P) and temperature (T) are calculated from gradients of 11.5 MPa/km (regional gradient) and 30°C/km respectively. To establish the reservoir oil volume, a formation volume factor of 1.1 and a surface oil density of 900 kg/m³ are used. Ultimate recovery is cumulative production (Dec. 1992) added to approved and probable reserves. Lifetime is reserves divided by 1992 production.

OIL FIELD		Age of reservoir rock	Depth (m)	T (°C)	P (MPa)	CO ₂ density (kg/m ³)	Ultimate oil recovery (10 ⁶ m ³)	Reservoir volume (10 ⁶ m ³)	Storage* Capacity (Mt CO ₂)	Lifetime (years)
No	Name									
1	Mittelplate	Juras/Creta	2600	88	29.90	710	16.99	18.69	13.27	51
2	Plön-Ost	Jurassic	2400	82	27.60	710	8.09	8.90	—	—
3	Reitbrook	Juras/Creta	1200	46	13.80	709	7.02	7.72	—	—
4	Hankensbüttel	Jurassic	1400	52	16.10	710	16.23	17.85	12.67	7
5	Hohne	Trias/Juras	1500	55	17.25	710	6.56	7.22	—	—
6	Nienhagen	Juras/Creta	1000	40	11.50	707	9.53	10.49	—	—
7	Barenburg	Juras/Creta	650	30	7.48	674	8.41	9.25	—	—
8	Düste	Cretaceous	1000	40	11.50	707	6.77	7.45	—	—
9	Bramberge	Cretaceous	900	37	10.35	705	22.57	24.82	17.49	19
10	Emlichheim	Cretaceous	850	36	9.78	694	12.22	13.44	—	—
11	Georgsdorf	Cretaceous	800	34	9.20	702	20.81	22.89	16.06	13
12	Lingen	Juras/Creta	950	39	10.93	698	2.66	2.92	—	—
13	Rühle	Juras/Creta	700	31	8.05	696	44.91	49.40	—	—
14	Scheerhorn	Juras/Creta	1060	42	12.19	705	11.26	12.38	—	22
Total		194.01						59.50		

* Storage capacity is restricted to the fields that are below a depth of 800 m and can retain more than 10 Mt CO₂.

4.7 THE CO₂ STORAGE CAPACITY OF GREECE

Jean Barbier

4.7.1 Summary

Greece has been strongly affected by the Alpine orogeny and is intensely folded and (thrust) faulted. The northeastern part of Greece mainly consists of crystalline rocks without any CO₂ storage potential. Sedimentary rocks predominate in the southwest of the country. They consist of Mio-Pliocene flysch underlain by Mesozoic to Oligocene limestones. A thick but localised fill of intramontane 'molassic' basins is also present in various parts of the country. Although deltaic reservoirs have been found in these intramontane basins at a depth of 2 000 m, no aquifers have been defined precisely. In addition, the deltaic reservoirs are expected to be discontinuous. Therefore, the CO₂ storage potential of the Greek aquifers could not be established.

Exploitable quantities of oil and gas are found only offshore in the Prinos oil field and the South-Kavala gas field. Ultimate gas recovery of these two fields is expected to be 5.4 milliard m³; the cumulative oil production of the Prinos field approximates 14 million m³, and the total corresponding CO₂ storage capacity is estimated at 34 Mt.

4.7.2 Geological Overview

Greece can be divided into several NNW-SSE structural zones with a tectonic style characterised by folds and nappes. As far as deep reservoirs are concerned, three main geological units can be distinguished:

- sedimentary rocks in the southwest
- crystalline and igneous rocks in the northeast
- detrital graben-fill successions of Miocene to Quaternary age in various parts of the country

These three main geological units are shown in Figure 4.7.1.

The Southwestern Sedimentary Succession

The stratigraphy of the southwestern sedimentary succession begins with the Lower Triassic consisting of evaporites near the Ionian Sea that grade towards the northwest into siliciclastic deposits. The Lower Triassic is overlain by Upper Triassic to Eocene limestones and dolomites, followed by a clastic succession in flysch facies. The passage from carbonate to clastic deposition took place diachronously: according to the structural zones, earliest in the east, where it occurred in the Eocene (locally even as early as Middle Cretaceous), and later in the west, at the end of the Oligocene (Schroeder and Schoeneich, 1986). The major structures found onshore can be traced offshore in the Adriatic Sea (Monopolis and Bruneton, 1982).

The Northeastern Basement and Cover

This area is occupied by a Precambrian to Palaeozoic crystalline basement with a cover of lightly metamorphosed Mesozoic carbonates and pelites accompanied by some granite intrusions. These are all overlain by Cretaceous limestones of marine origin and younger, Late Cretaceous flysch-type sediments.

The Grabens

Two types of graben can be distinguished, intramontane molasse basins and fault basins. The former are the larger and are represented by the Mesohellenic Trough (Grevena Basin, Figure 4.7.1), the Vardar Trough, which opens into the Gulf of Salonika (Thermaikos Kolpos), and the extremity of the Thracian Basin, which is mainly in Turkey. Sedimentation in these basins started in the Eocene with conglomerates and marine limestones, continuing during the Oligocene with conglomerates and lacustrine clays. The presence of marine deposits has led to the exploration of these basins for hydrocarbons.

The fault basins (Strymon, Xanthi, and basins in the coastal area of Western Greece) are smaller and younger (Late Miocene to Pliocene). The basin sediments are essentially lacustrine, consisting of marl, sand and interbeds of platy limestone containing brown coal.

4.7.3 Aquifers

Of the three basic geological units mentioned above, only the southwestern sedimentary succession, and the grabens are likely to contain major aquifers.

4.7.3.1 ONSHORE AQUIFERS

The geothermal exploration described by Haenel and Staroste (1988) gives little information on deep aquifers. As numerous occurrences of hot and warm water were found at relatively shallow depth, the search for deep aquifers below a depth of 800 m was not very seriously pursued. For the deeper reservoirs that were found, exploitation of geothermal energy may interfere with CO₂ storage.

Oil exploration has tested two kinds of possible reservoirs, the Mesozoic and Eocene carbonates, and the sand intercalations expected in the graben-fill (Schroeder and Schoeneich 1986). No deep reservoirs have apparently been found among the carbonates: *'In addition the Eocene limestone did not show favourable reservoir characteristics'* (id., p.73). However, the unconformity between the carbonates and the younger clastic succession locally shows karstification and the development of a secondary

porosity. In fact, the transition from the limestones to the Tertiary clastic deposits is in places accompanied by oil accumulations, e.g. the offshore Katakolon field and the hydrocarbon occurrences on the island of Zante in the Ionian Sea (Schroeder and Schoeneich, 1986). This porous zone along the unconformity constitutes in these areas a geothermal reservoir, as does a similar karst zone at the contact between the carbonates and the overlying conglomerates in the Nestos delta at a depth of about 700–1000 m (Haenel and Staroste, 1988).

In the Neogene clastic deposits, possible reservoirs are present in the Vardar Trough, where hydrocarbon occurrences were found in *'five or six gas-condensate pays in Miocene sands, each 5 to 15 m thick'* (Schroeder and Schoeneich, 1986).

In the Strymon graben in the north of the country, a reservoir has been detected at a depth of 2000 m (BRGM/IGME, 1982). Reinterpretation of oil exploration documents shows porosities of 15% over cumulative thicknesses from 50 to 200 m, and transmissivities in excess of 3 Dm. The upper part of the sedimentary succession is made up of clay but whether the clay forms an efficient seal is not known. Given the deltaic origin of the sediments, it is likely that the aquifers are discontinuous, and Ungemach (1984) considers exploration in such reservoirs somewhat hazardous.

4.7.3.2 OFFSHORE AQUIFERS

Potential aquifers offshore comprise the same stratigraphic levels as onshore. The Katakolon hydrocarbon field is situated in the Mesozoic and Tertiary carbonates, and the Prinos and South-Kavala fields in Miocene sands. The extent of the aquifers that contain the hydrocarbon reservoirs is not known.

4.7.4 Hydrocarbon Fields

4.7.4.1 ONSHORE HYDROCARBON FIELDS

No oil reserves are known onshore. A few gas occurrences have been found in the Nestos delta and the Strymon basin, but they are of no economic interest.

4.7.4.2 OFFSHORE HYDROCARBON FIELDS

The only exploited hydrocarbon fields are in the Gulf of Thrace, in the northeast of the country (Prinos and South-Kavala). The Oil & Gas Journal (1992) estimates their oil reserves at 41 million barrels (6.5 million m³), whereas World Oil (August 1993) gives an estimate of only 28 million barrels (4.5 million m³). Gas reserves are estimated by the Oil & Gas Journal (1992) at 300 milliard ft³ (8.5 milliard m³), whereas World Oil estimates gas reserves at 12 milliard ft³ (0.34 milliard m³).

Constraints

Data for gas are taken from the compilation of Schroeder and Schoeneich (1986), and those for oil from the Oil & Gas Journal (1992).

Oil fields

A small oil field is known at Katakolon, in the northwestern Peloponnese. The field is situated in the Mesozoic and Tertiary limestones beneath a Pliocene-Quaternary clay seal, but is currently not producing. The only oil production is from the Prinos field, which has a sand reservoir. At the beginning of 1993, its cumulative production amounted to 86.5 million barrels or 13.8 million m³ (Oil & Gas Journal 1992). An agreement has been signed in 1992 to continue production until 1999, which should enable exploitation of



Figure 4.7.1 Major geological units of Greece and locations of hydrocarbon fields.

a further 3.3 million m³ (World Oil 1993), bringing the ultimate recovery of Prinos to about 17.1 million m³. However, production from Prinos oil field is decreasing, and maintenance costs are high. It is therefore uncertain how long production will continue, despite the agreement for production to continue until 1999.

Gas fields

Small quantities of gas have been found in Miocene sands in the Gulf of Thermaikos. A gas cap is present in the

Katakolon oil field. The Prinos field also contains some natural gas; its ultimate recovery is expected to be 0.8 milliard m³. Much more important are the initial reserves of 4.6 milliard m³ in the South-Kavala field, in an anticline in Miocene sandstone.

Storage capacity

The potential CO₂ storage capacity in Greece related to hydrocarbon deposits amounts to 34 Mt, as shown in Table 4.7.2. The storage potential is restricted to the offshore

Table 4.7.1 Theoretical storage capacity in the offshore hydrocarbon fields of Greece. The storage calculation is based on a CO₂ reservoir density of 700 kg/m³, and an oil formation volume factor of 1.2. The gas expansion factor has been derived from the reservoir pressure, which, in turn, has been calculated from the depth of the reservoir, using a hydrostatic gradient of 10.5 MPa/km.

OFFSHORE FIELDS		OIL		GAS		TOTAL
Name	Depth (m)	Ultimate recovery (million m ³)	Storage capacity (Mt CO ₂)	Ultimate recovery (billion m ³)	Storage capacity (Mt CO ₂)	Storage capacity (Mt CO ₂)
Prinos	1700	16.93	14.22	0.80	3.1	17.3
Kavala	2000			4.60	16.6	16.6
TOTAL		16.93		5.40		33.91

* Oil data from World Oil, August 1993.

+ Data from Schroeder & Schoeneich (1986). The estimates of the reserves, however, vary greatly (see text).

area and is distributed almost equally between the Prinos oil field and the South-Kavala gas field. The storage estimate for the Prinos oil field is based on its cumulative production.

Depletion

It is uncertain if the production of the Prinos oil field will continue for very much longer. The reserves at South-Kavala, at the present rate of production of 90 million m³ per year (World Oil, August 1993), could last another five years.

4.7.5 Conclusions

Potential storage capacity in the two offshore hydrocarbon fields of Greece is appreciable. The life of these fields will not be very long.

No storage capacity has been identified in aquifers, for more than one reason: part of the country is underlain by crystalline basement in which no deep reservoirs exist, and part of the folded sedimentary succession in the west of the country includes no units with aquifer characteristics. The main known reservoirs are offshore in Miocene to Quaternary sands. The corresponding onshore deposits show geothermal potential in their shallower parts, and are poorly known in the deeper parts of the graben that they occupy.

To conclude, the potential CO₂ storage capacity of Greece can be estimated at 34 Mt, related to offshore hydrocarbon deposits that will soon be exhausted.

4.8 THE CO₂ STORAGE CAPACITY OF IRELAND

H.E. Baily

4.8.1 Summary

The Republic of Ireland was emergent during post-Variscan times and therefore is almost devoid of Mesozoic and Tertiary rocks onshore. An exception is the Permo-Triassic Kingscourt Outlier which is, however, too shallow for CO₂ storage. Data available for Palaeozoic onshore aquifers, such as the Namurian sandstones or late Devonian Kiltorcan Sandstone, indicate that they too are not suitable as CO₂ reservoirs. There are no onshore oil or gas fields in Ireland.

Ireland is ringed by a series of Mesozoic basins which are likely to contain promising reservoirs. Hydrocarbons have been recovered from several of these basins. Exploration data are sparse so it is not possible to quantify the storage potential of offshore aquifers at present. The Kinsale Head Gas Field in the South Celtic Sea is estimated to have a storage capacity of 160 Mt CO₂.

4.8.2 Geological Overview

The sedimentary basins of Ireland can be divided into two groups: the Carboniferous basins which correspond to those onshore and the Mesozoic basins which lie offshore. The Carboniferous basins are filled mainly with limestones, which are frequently argillaceous, but also contain clastic sediments. The fill of these basins is somewhat folded in the south of the country but deformation becomes less intense northwards. Some hydrocarbon exploration has been undertaken in these onshore basins, particularly in the Northwest Basin. Poor reservoir characteristics and the fact that many Carboniferous rocks crop out at surface preclude them from detailed consideration for CO₂ storage. The offshore basins contain variable thicknesses of Mesozoic and Tertiary rocks. These basins have been subjected to much more hydrocarbon exploration than the onshore basins, with the most extensively drilled being the Celtic Sea Basins.

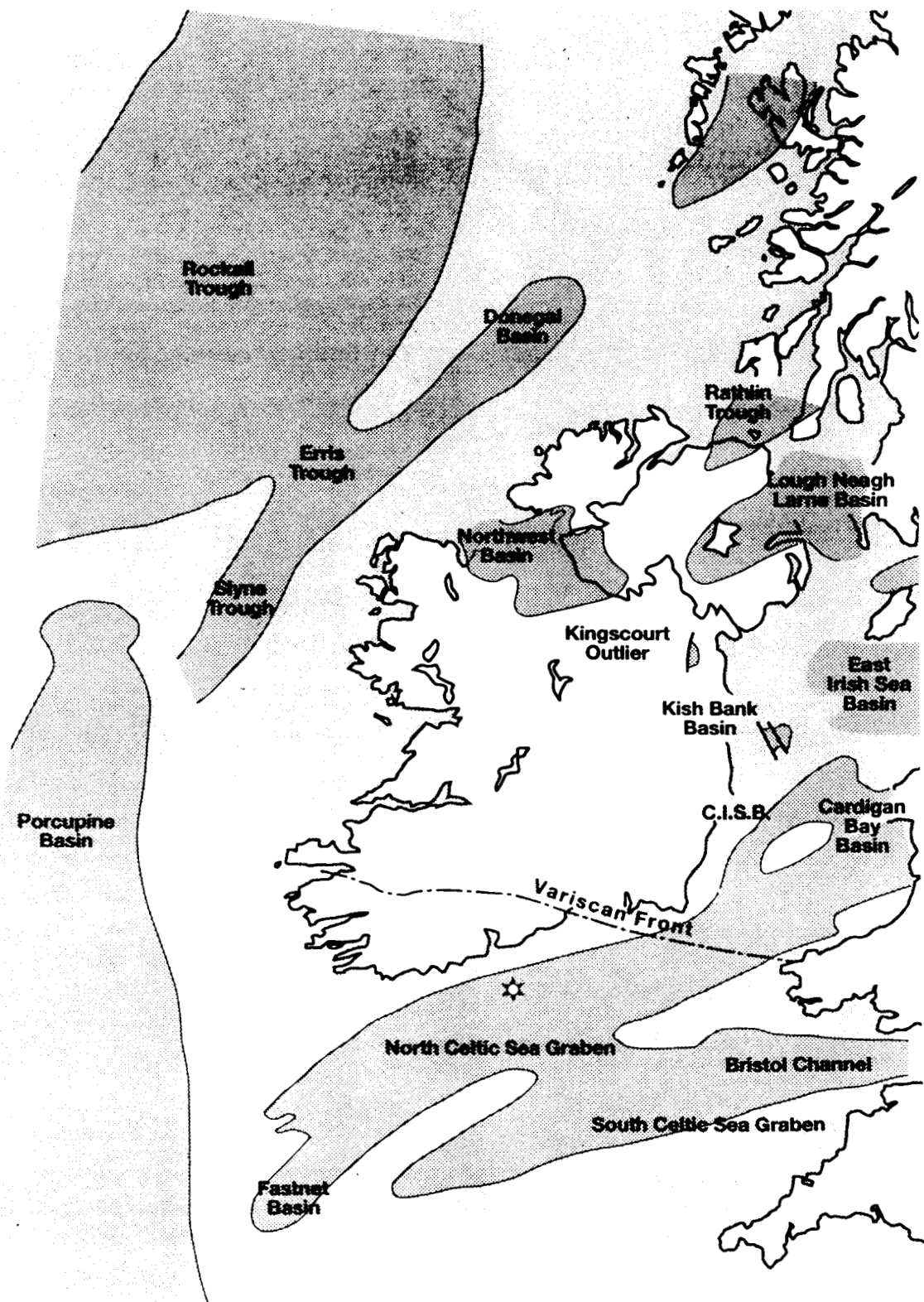
4.8.3 Aquifers

The major Irish sedimentary basins are shown in Figure 4.8.1. The majority of onshore aquifers in Ireland are of Carboniferous age, while those offshore range in age from Permian to Cretaceous. Cambrian, Ordovician and Silurian rocks onshore Ireland generally are considered to have very little primary porosity.

4.8.3.1 ONSHORE AQUIFERS

Most Carboniferous rocks of the Republic of Ireland are believed to be poor reservoirs although there are some notable exceptions which are recognised as important aquifers (Table 4.8.1).

The most important bedrock aquifers in Ireland are the Dinantian limestones in the synclines of southern Ireland, especially where dolomitised, north of the so-called Variscan Front (Daly 1993). They are not likely to be



Legend

- deep basins
- ☆ Kinsale Head gas field



Figure 4.8.1 Permian, Mesozoic and younger deep sedimentary basins of Ireland (after Shannon, 1991a). C.I.S.B. is the Central Irish Sea Basin.

Table 4.8.1 Summary of the characteristics of the Irish onshore aquifers.

Location	Formation	Age	Thickness m	Porosity %	Permeability mD
Kingscourt	Carricleck Sandstone	Carboniferous	30–60	10–20	250–500
Kilkenny	Kiltorcan Sandstone	Carboniferous		5–10	0–80
S. Ireland	Dinantian limestones	Carboniferous		2–5	0.5–10

suitable disposal sites for CO₂ as they frequently crop out at surface and permeability is irregular and unpredictable. The Kiltorcan Sandstone and Carricleck Sandstones are both important aquifers but their lateral extent below 800 m is unknown and consequently, they cannot be considered a potential storage site for CO₂.

4.8.3.2 OFFSHORE AQUIFERS

The characteristics of offshore aquifers are outlined in Table 4.8.2.

Celtic Sea Basin

The Celtic Sea Basin is well known; more than 60 hydrocarbon exploration wells have been drilled in the Irish sector of the Celtic Sea. A Cretaceous to Quaternary succession, with no Tertiary rocks, has been proven by drilling. There is no published information on the porosity or permeability of the Chalk in this area, however, it is likely to have no potential for storage of CO₂ as its top is less than 800 m below OD and it is not sealed. Triassic fluvial and aeolian sandstones occur over much of the Celtic Sea but are untested. Shannon (1991b) also noted that there are many small early Triassic rift basins likely to be lithologically highly variable from one to the next. These potential reservoir rocks may have potential for CO₂ storage but due to the current lack of data it is impossible to estimate their capacity.

Fastnet Basin

The Triassic to Tertiary succession of the Fastnet Basin has been recorded by Robinson et al. (1981) in which they recognised three intervals of important reservoirs, namely: Greensand/ Wealden fluvial and alluvial sandstones, early Jurassic deltaic sandstones and Triassic. Neither the current depth of these reservoir intervals nor their lateral extent is clear. While the Fastnet Basin may have suitable reservoir rocks for the storage of CO₂ it is impossible at the present time to estimate the storage capacity of such reservoirs.

Slyne Trough, Erris Trough And Donegal Basin

Few exploration wells have been drilled in the Slyne Trough, Erris Trough and Donegal Basin area to date and consequently the geology is poorly known. Murphy and Croker (1992) have recorded excellent quality reservoir rocks in both the Slyne and Erris Troughs (Table 4.8.2).

Porcupine Basin

Unlike many of the Irish offshore basins the Porcupine Basin lies on thinned crust, and contains up to 5 km of post-Palaeozoic fill (Naylor and Shannon, 1982). It can be subdivided into the North and Main Porcupine Basins. This study is only concerned with the former as the water depths in the latter are too deep to be considered realistically as a potential storage site for CO₂. The Porcupine Basin as a whole is an underexplored region with only twenty-five hydrocarbon exploration wells drilled to date, largely in the shallower marginal areas of the basin.

Potential aquifers in the Porcupine basin are summarised in Table 4.8.2 based on information from Naylor and Shannon (1982) and Croker and Shannon (1987). Little is known about hydrocarbon bearing structures in the North Porcupine Basin, but they are likely to be structurally complex and of small to moderate size. It is quite possible that there is some potential for CO₂ storage in the Porcupine Basin, but at the present time the limited data available for this area mean that an estimation of the storage capacity of possible reservoirs is not possible.

Central Irish Sea Basin

The Central Irish Sea is also a poorly explored region (Shannon 1991a) of dominantly Permo-Triassic rocks (Table 4.8.2). Because of the lack of data, it cannot be considered as a potential site for storage of CO₂.

Kish Bank Basin

The stratigraphical sequence in the Kish Bank Basin consists of Permo-Triassic to Liassic age rocks overlying a Carboniferous succession (Naylor and Shannon, 1982). Seismic interpretation indicates a sequence up to 3 km thick of probable Permo-Triassic rocks (Jenner, 1981), with the greatest thickness developed against the faults controlling the half-graben.

Although likely to be shallower in some parts of the basin, all the thick Permo-Triassic sandstones where proven in released wells, are currently at a depth of more than 800 m. Localised closures have been proven by drilling and seals in the form of mudstones and evaporites are common. The Kish Bank Basin has been considered in the past as a potential site for the storage of natural gas and it may well have storage potential for CO₂ given the favourably high porosities of the sandstones, relatively shallow water and proximity to the coast. It is impossible, however, given the paucity of released and published data, to estimate the capacity of the reservoirs for this purpose.

4.8.4 Hydrocarbon fields

Estimates of CO₂ storage potential of the Main Porcupine Basin and Rockall Trough (Fig. 4.8.1) have been excluded from this study because of the great depth of water in these two areas and their remoteness from major areas of CO₂ production. Published and released data on these basins are limited in quantity and any consequent estimate of storage capacity is therefore also limited in accuracy.

4.8.4.1 ONSHORE HYDROCARBON FIELDS

There are no onshore hydrocarbon fields in Ireland.

4.8.4.2 OFFSHORE HYDROCARBON FIELDS

Celtic Sea

The Celtic Sea Basin is composed of a pair of east-northeast trending grabens, separated by a narrow basement high. Ireland's major gas fields, the Kinsale Head and the Ballycotton Gas Fields, are located in the North Graben of the

Table 4.8.2
Summary of the characteristics of the Irish offshore aquifers. C.I.S.B. is the Central Irish Sea Basin.

Basin	Formation	Age	Thickness m	Porosity %	Permeability mD
Celtic Sea	Gault/Greensand Eq.	Triassic	50	20	420
Celtic Sea		Jurassic			
Celtic Sea		Cretaceous			
Fastnet Basin	Greensand/Wealden	Triassic	25-50	13	
Fastnet Basin		Jurassic	11-70	19-38	
Fastnet Basin		Cretaceous	50-140	10-40	
Erris Trough	Sherwood Sandstone	Carboniferous	thick	20	
Erris Trough		Triassic		<30	
Erris Trough		Lower Cretaceous		14-35	
Slyne Trough		Middle Jurassic		18	
N. Porcupine		Carboniferous		5-20	
N. Porcupine		Triassic		150	
N. Porcupine		Jurassic		17-22	10-100's
N. Porcupine		Cretaceous		94-366	25-33
C.I.S.B.		Sherwood Sandstone		Triassic	1200
Kish Bank Basin	Keuper Sandstone Eq.	Triassic	200	3-30	?-1000
Kish Bank Basin	St. Bees Sandstone Eq.	Triassic			
Kish Bank Basin	Collyhurst Sandstone	Triassic	>100	8-20	

Table 4.8.3 Theoretical CO₂ storage capacity of the Irish offshore hydrocarbon fields. Main Porcupine Basin and Rockall Trough are excluded. Note that the temperature of the Kinsale Head A is below the critical temperature for CO₂. The gas expansion factor has been calculated from the reservoir pressure, which in turn is inferred from depth (see section 4.2).

Gasfield	Basin	Ultimate recovery 10 ⁹ m ³ (st)	Depth m	T C	P MPa	CO ₂ density kg/m ³	GEF *	Storage capacity Mt CO ₂	Year of Depletion
Kinsale Head A	Celtic Sea	28.32	860	29	9.1	772	137	159.60	1999
Kinsale Head B	Celtic Sea			32					1999
Ballycotton	Celtic Sea								
TOTAL		28.32						159.60	

Celtic Sea Basin. There are no published data available for the Ballycotton Gas Field.

Kinsale Head Gas Field

The Kinsale Head Gas Field is Ireland's primary producer of natural gas (Figure 4.8.1). The main reservoir rocks are lithologically comparable with the Lower Cretaceous Wealden, Gault and Greensand sequence of southwest England. The Gault and Greensand Equivalents are Aptian to late Albian in age and consist of several sandstones separated by glauconitic claystones. The 'A' Sand, the main reservoir, is up to 48 m thick and depth to the formation top averages 836 m (Colley et al. 1981). Mean porosity is 20% with mean permeability of 420 mD. Average reservoir temperature for the 'A' Sand is just over 29°C. Seal to the reservoir sands is provided by the overlying Gault Clay. Colley et al. (1981) estimated recoverable reserves of gas as 28.32 milliard m³ and noted that methane made up more than 99% of the gas in the reservoir.

The underlying Upper Wealden sand ('B' sand of Colley et al. 1981) is up to 4 m thick and provides a minor reservoir. Average porosity of the Upper Wealden sand is 22%, average permeability 280 mD and average reservoir temperature is 32°C.

Estimates of CO₂ storage potential of the Kinsale Head Gas Field are given in Table 4.8.3. The Kinsale Head Gas Field is likely to be depleted by 1999 (Shannon 1991b). Its proven reservoir and cap rocks, known closure, existing

infrastructure, relatively shallow water depths, and relative proximity to the shore mean that it may have considerable potential for storage of CO₂. Much data on the Kinsale Head Gas Field remain confidential, so a more accurate estimate of its storage capacity will be possible in the future when these data are released.

4.9 THE CO₂ STORAGE CAPACITY OF ITALY

Jean Barbier

4.9.1 Summary

Italy was strongly affected by the Alpine orogeny, and most rocks are intensely folded and faulted. A foredeep trends N-S between the Apennine fold-and-thrust belt and the Adriatic foreland, running along the east coast of Italy. This depression is filled by detritus from the Apennines.

Two types of aquifers occur: one in Mesozoic carbonates, the other in Miocene-Quaternary clastic sediments. The former include the reservoirs of the geothermal fields of Tuscany. The latter have been studied in detail in the Po Valley. They also exist offshore, though their extent is poorly defined. As far as deep aquifers could be defined, their overall storage capacity is estimated to be in the order of ca 440 Mt CO₂, 353 Mt onshore and 84 Mt offshore.

Hydrocarbon fields are found in the foredeep, both onshore and offshore. Some of the fields are located near

major industrial centres. The ultimate hydrocarbon recovery is estimated to be ca 720–830 milliard m³ of natural gas, and ca 190–200 million m³ of oil. Three oil fields, two onshore and one offshore, and at least fifteen gas fields are theoretically liable to have a storage capacity of more than 10 Mt CO₂. The cumulative storage capacity of the hydrocarbon fields has been estimated to be at least 1790 Mt CO₂, more or less equally divided between onshore and offshore fields. A majority of these hydrocarbon fields, however, occur in reservoirs with very low porosity.

4.9.2 Geological Overview

The geological history of Italy can be subdivided into two periods: 1) a period of epicontinental deposition with mainly carbonate sediments (Triassic-Cretaceous), followed by 2) an orogenic period marked by the deposition of a thick detrital series (Neogene-Quaternary). The epicontinental stage reflects two successive environments: a carbonate platform similar to the present-day Bahamas, and a pelagic environment with carbonate, chert, and shale deposition. In theory, the Mesozoic sequence therefore consists of shallow-marine carbonates overlain by pelagic facies. The carbonates often are quite porous and constitute aquifers and reservoir rocks for some oil accumulations. The pelagic facies are characterised by very low porosity and permeability (compact limestone, shale) and form caprocks for the underlying reservoirs. The Neogene-Quaternary clastic series unconformably overlies the Mesozoic sediments. It includes sand reservoirs separated by low-permeability beds that may act as seals (Mattavelli et al., 1993).

Two broad structural zones are distinct on either side of a large overthrust (Figure 4.9.1). In the foreland, to the east of the overthrust, the carbonate units are tabular and are unconformably overlain by Pliocene-Quaternary clastic sediments (Adriatic region). To the west of the overthrust, the Apennine fold-and-thrust belt is present. Here, the carbonate units are unconformably overlain by a Miocene flysch and the combined sequence is intensely folded and faulted (Apennine region). In the foredeep depression, which stretches alongside the Apennines, the Pliocene-Quaternary detrital sequence is several thousands of metres thick, thinning to the east (Pieri and Mattavelli, 1986).

4.9.3 Aquifers

Aquifers occur in two broad units: one in the Mesozoic carbonate platform unit, the other in the Tertiary-Quaternary detrital sequence (Oligocene-Miocene flysch and Pliocene-Quaternary turbidites and continental clastics).

4.9.3.1 ONSHORE AQUIFERS

Constraints

Information regarding the deep aquifers is only available from oil industry data. The published particulars of hydrocarbon fields often include detailed data on the porosity or permeability of the reservoirs. Such data are, however, difficult to extrapolate laterally. For the purpose of geothermal exploration, all available data were reviewed in order to delineate deep aquifers of large areal extent. This work was supported by the EC, and concerned two broad geological regions: the Mesozoic carbonates (report EUR 99-19), and the Pliocene-Quaternary clastic sequence of the Piedmont region in northern Italy (contract EN3G-0031-I). The former publication is out of print and unavailable, but is quoted in Hanel and Staroste, 1988 (Cavalli et

al., 1988). The second publication was condensed into a brief review (Ghezzi et al., 1989), to which this study refers.

Mesozoic Platform Carbonates

The Mesozoic platform carbonate sequence contains an aquifer known across all the Italian peninsula. For this reason, it was mapped over the entire country. The aquifer is the reservoir of the main geothermal fields in Tuscany (Cavalli et al., 1988). The geological map and sections from Pieri and Mattavelli (1986, p.108, 117) show the presence of this carbonate facies, in the subsurface or at depth, across the southern half of the country, from Rome to Sicily, i.e. an area of about 50 000 km². To the north of Rome, the facies hardly crops out and is known from geothermal development boreholes. The facies also exists in the north of Italy, forming the Cavone oil field (3500 m deep) and the Malossa gas field (4300–6000 m deep). According to profiles by Cavalli et al. (1988), this reservoir in Tuscany has a highly variable gross thickness ranging from 200 to 1000 m. It is filled with fresh water near outcrops and recharging areas, but at depth, the water turns brackish or even saline. Several authors suggest that the porosity is low in many places.

According to Ghezzi et al. (1989), in the Po Valley carbonate sequence the reservoir corresponds to a discontinuous aquifer system, with an highly variable permeability. The average porosity at the Malossa field is 2–3% (Mattavelli and Margarucci, 1986). In the Adriatic fields of Emilia and Emma, the carbonate reservoir also shows low porosities and permeabilities (Mattavelli et al., 1993). The Taormina Formation, host to the Gela and Ragusa oil fields, has a 4% porosity (Pieri and Mattavelli, 1986). The original porosity of the Costa Molina oil reservoir was 2%. The only significant porosity in carbonate formations is described in the Siracusa Formation (Vega oil field), where it is as high as 11–16% (Mattavelli et al., 1993).

Tertiary-Quaternary Detrital Sequence

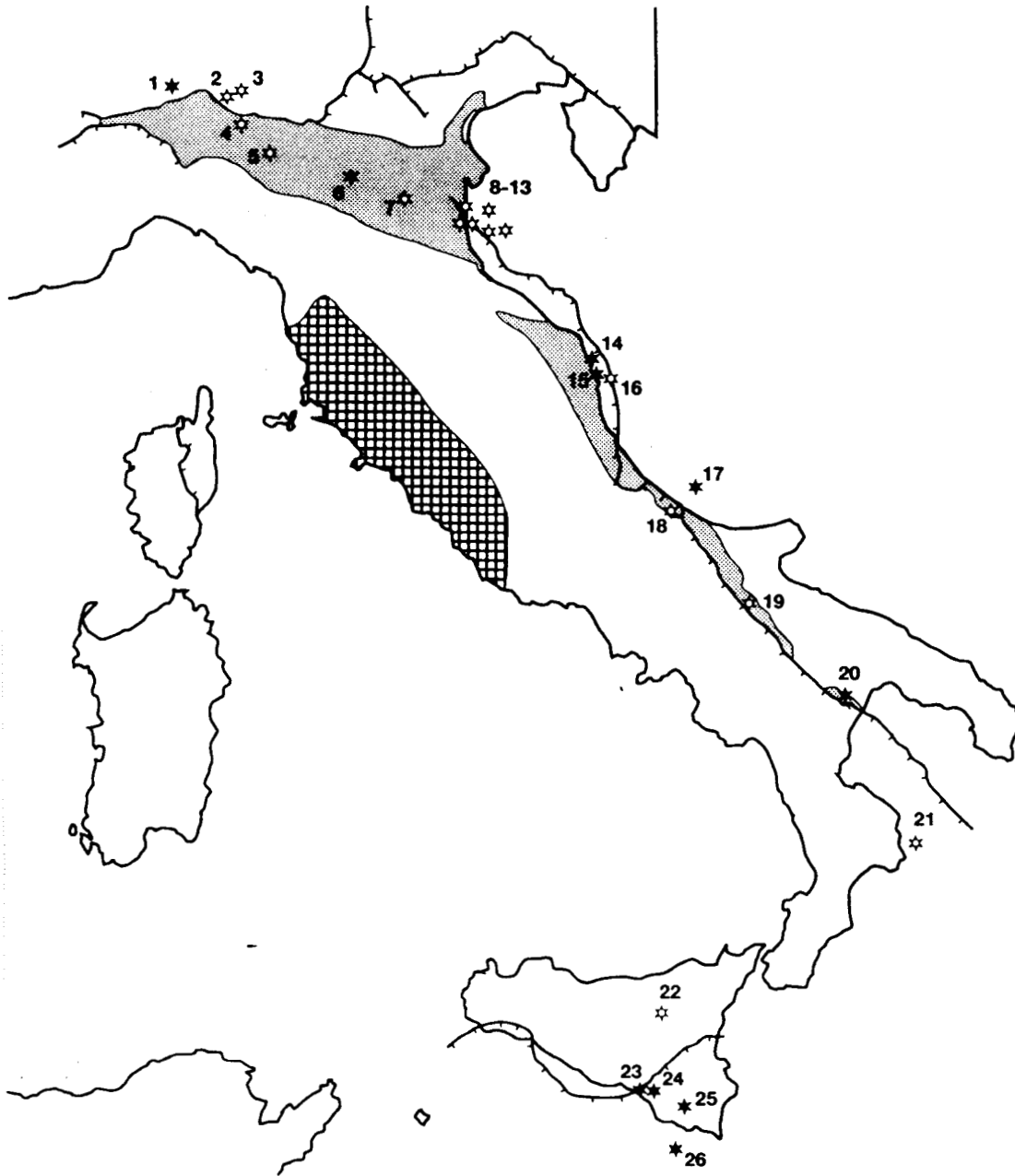
The best-documented aquifers in the Tertiary-Quaternary detrital sequence are continental sands found in Lombardy, in the Po Valley. Baglioni et al. (1988) distinguish four large potential reservoirs. The Desana Sand Formation and the Caviaga Sand Formation (Early Pliocene) extend over some 5000 km² to the south of Milan. Their cumulative gross thickness may be 800 m. The Sartirana Formation and Sergnano Gravel Formation are Messinian (late Miocene) in age, and are also detrital reservoirs, though with a lower gross thickness (300 m). They probably also extend over some 5000 km². Ghezzi et al. (1989) describe twenty reservoirs in a more detailed study, and additionally list a few porosity and permeability values for these aquifers (e.g. 20% porosity in the Sergnano Gravel Formation).

Traps

The potential traps vary according to their structural settings, and are well understood as a result of petroleum exploration. In the foreland area structural traps are faulted blocks or faulted anticlines, traps in the foredeep area are low-relief anticlines or stratigraphic traps due to facies variations, and thrust anticlines form the traps in the thrust belt (Mattavelli et al., 1993). Two types of seals occur: certain detrital units (e.g. Miocene flysch), and pelagic carbonates or shales of various ages.

Storage Capacity

The trapped storage capacities of known deep aquifers are listed in Table 4.9.1.



Legend

- zones with depth of the base of clastic series more than 1000m
 - carbonate reservoir of Tuscany
 - oil field
 - gas field
 - main overthrust, fault
- 0 200 km
-

Oil and gas fields

- | | |
|-----------------------------|------------------------|
| (1) Villafortuna-Trecale | (14) Sarago |
| (2) Settala | (15) Santa Maria aMare |
| (3) Maiossa | (16) David |
| (4) Caviaga | (17) Rosps Mare |
| (5) Cortemaggiore | (18) San Salvo Cupello |
| (6) Cavone | (19) Candela Palino |
| (7) Selva-Minerbio | (20) Pisticci |
| (8) Dosso degli Angeli | (21) Luna |
| (9) Porto Corsini Terra | (22) Gagliano |
| (10) Porto Corsini Mare | (23) Gela |
| (11) Porto Corsini Mare Est | (24) Ponte Dirillo |
| (12) Agostino-Poto Gribaldi | (25) Ragusa |
| (13) Amelia | (26) Vega |

Figure 4.9.1 Location of the deep aquifers and the main oil and gas fields in Italy, after Schroeder & Schoeneich (1986), Pieri & Mattavelli (1986), Mattavelli et al. (1993).

Capacities are only presented for a small portion of the Mesozoic platform carbonates, because no precise data are available and in most of these rocks porosity and permeability values are low, as noted earlier. Nevertheless, permeability in Tuscany, where this aquifer is best described, is sufficient for the operation of geothermal fields, to the point that fluid injection is considered to maintain flow rates. Several gas caps filled with pure CO₂ are known there, demonstrating that the presence of CO₂ does not hinder geothermal energy development. We have therefore limited the calculation of theoretical CO₂ storage capacity to Tuscany alone, and used the following assumptions:

- 3% of the aquifer volume is in a trap (see section 4.2)
- 4% of this trapped pore volume is available for CO₂ storage
- an average underground CO₂ density of 700 kg/m³

For the Mesozoic carbonate reservoir, the storage calculation is further based on an estimated range of 16 000 km² and a conservative net thickness estimate of 200 m (Baldi et al., 1988, Bertini et al., 1988, in Haenel and Staroste, 1988, plates 79–81). It has additionally been assumed that the average porosity is 10%. These figures yield a CO₂ storage capacity of about 269 Mt.

From the Tertiary deposits, only the well-known detrital series of the Po Valley were considered (Figure 4.9.1). Although the shallowest intervals contain fresh water, at depths suitable for CO₂ storage (>800 m) the water is generally saline (Ghezzi et al., 1989). So, there will be no conflict between CO₂ storage and fresh water production. However, CO₂ storage might be difficult if the aquifers are utilised for low-enthalpy geothermal production.

Baglioni et al. (1988) distinguish four Tertiary aquifer units. Their areal extent is probably in the order of 5000 km². Their thicknesses and porosities are difficult to estimate. The thicknesses given by various authors vary greatly. The Sergnano Gravel Formation for example, is attributed a maximum gross thickness of 500 m by Baglioni et al. (1988), while Ghezzi et al. (1989) mention a net thickness of only 80 m. The porosity of the Sergnano Gravel Formation may be 20%; that of the Settala sands may be 27% (Mattavelli et al., 1993). There are, however, many clayey sand layers with a much lower porosity.

Storage calculations for the Tertiary deposits are based on a range of 5000 km², and an assumed 100 m net thickness with an average porosity of 20%. The additional assumptions are equal to those for the Mesozoic platform carbonates, mentioned above. This yields a storage capacity of 84 Mt CO₂.

Table 4.9.1 Theoretical CO₂ storage capacity in traps on the major deep aquifers of Italy. The storage calculation is based on the assumption that 3% of the aquifer volume is in a trap and that 4% of the trapped pore volume can be filled with CO₂. The underground CO₂ density has been taken as 700 kg/m³.

Aquifer	Range (km ²)	Average net thickness (m)	Average porosity (%)	Total pore volume (km ³)	Storage capacity (Mt CO ₂)
Onshore					
Mesozoic carbonates (Tuscany)	16 000	200	10 (?)	320	269
Miocene and Pliocene (Po Valley)	5 000	100	20	100	84
Offshore					
Mesozoic carbonates (Tuscany)	5 000	200	10 (?)	100	84
Total				520	437

4.9.3.2 OFFSHORE AQUIFERS

The aquifers onshore, as described above, extend offshore, where they form the reservoirs of several hydrocarbon accumulations, in Mesozoic platform carbonates (Vega oil field, offshore Sicily; Rospo Mare oil field in the Adriatic) and in Tertiary–Quaternary clastics (Barbara, Luna, Agostino-Porto Garibaldi gas fields, etc.).

Constraints

For obvious reasons, no geothermal review was carried out from oil exploration data, as was the case for onshore aquifers. The only data compilation available is a map of the top of the carbonate aquifer in Tuscany, which covers a narrow domain extending 30 km offshore. There is thus very little documentation about the offshore aquifers, apart from some oil field descriptions, which are of limited interest for the complete understanding of the aquifers.

Mesozoic Platform Carbonates

The Mesozoic carbonate platform extends into the Adriatic Sea (Apulian platform), subcropping Miocene and Pliocene-Quaternary sediments. The corresponding unconformity is accompanied at Rospo Mare by karstified carbonates (André and Doucet, 1991), a related increased porosity, and the presence of carbonate reservoirs. Since the unconformity can be distinguished across most of Italy, a secondary reservoir may have developed by karstification in many places (cf. the Amposta and Casablanca oil fields in Spain, Seemann et al. 1986). Unfortunately, the areal extent of this feature is unknown. A carbonate aquifer is present in the Tyrrhenian area, offshore Tuscany. Its porosity is unknown (Cavalli et al., 1988).

Tertiary–Quaternary Detrital Sequence

In the Tertiary–Quaternary detrital sequence, reservoirs are formed by sand layers interbedded in clays. The lithology, in turbidite or flysch facies, is characterised by poor lateral continuity (Roveri et al., 1992). The sand layers are therefore discontinuous: they are totally absent at Rospo Mare (André and Doucet, 1991), and more than 60 sand layers have been found in a 1600 m thick section at Agostino-Porto Garibaldi (Mattavelli et al., 1993). At best, the sand layers can be assigned a likelihood of occurrence in a given area.

Traps

Various types of traps occur in different areas, be it the Adriatic Sea, the Tyrrhenian Sea or the southeast of the Italian peninsula, because these areas have different structural characters.

The Adriatic Sea area belongs to the foreland region, where traps occur in faulted blocks or anticlines. The areas

in the north of the country belong to the foredeep region. Traps are here formed by large anticlines. In the foreland carbonates of Sicily lateral facies changes are common, which constitute stratigraphic traps (Mattavelli et al., 1993). The structural context of the Tyrrhenian Sea is probably similar to that of Tuscany, with thrusts and faulted anticlines (Pieri and Mattavelli, 1986).

Storage Capacity

This discussion will be restricted to the Mesozoic platform carbonates, because data on the offshore clastic sequence is too fragmentary. Offshore Tuscany, the carbonate aquifer was studied over limited area of some 5000 km². A theoretical CO₂ storage capacity of 84 Mt is calculated for this region alone, using the same assumptions as for onshore storage calculations.

The offshore aquifer laterally passes into an onshore aquifer, which crops out in places. Therefore, this study opts to consider this reservoir as an 'open' aquifer that requires CO₂ storage in traps.

It must be noted that other carbonate reservoirs are known offshore, such as the Vega oil reservoir in Sicily. In addition, there is no reason why the deep karst at Rospo, as described above, is limited to the range of the oil field. Although its lateral extent is unknown, the karst is expected to occur over a (much) wider area.

4.9.4 Hydrocarbon Fields

According to Mattavelli et al. (1993), about 160 Mt (\approx 190 million m³) of oil and 720 milliard m³ of gas have been discovered onshore and offshore Italy. The oil figures are consistent with those published by the Oil & Gas Journal (1992): the estimated proved reserves were 747 million barrels (*ca* 119 million m³), and the cumulative production was about 496 million barrels (or 79 million m³), by the end of 1991. According to this estimate, the ultimate oil recovery should thus amount to 198 million m³. For gas, Schroeder and Schoeneich (1986) indicate a production of 343 milliard m³ cumulative to the year 1986. According to the World Energy Map (1993), the average annual production over the period 1987–1991 was approximately 19.4 milliard m³. According to the Oil & Gas Journal (1992), proved reserves in 1992 were expected to be about 13 000 milliard cubic feet (or 368 milliard m³). This leads to an ultimate gas recovery figure of 827 milliard m³, somewhat higher than the figure of 720 milliard m³ of gas given by Mattavelli et al. (1993).

4.9.4.1 CONSTRAINTS

Data regarding the ultimate recovery or proved reserves are not available for all hydrocarbon fields. Oil field production statistics are published yearly in the Oil & Gas Journal, but figures for reserves are not given for individual fields. With respect to gas, conversely, the International Map of Natural Gas Fields in Europe (Schroeder and Schoeneich, 1986) lists order-of-magnitude figures for remaining reserves, but no production data for individual fields. This study attempts to fill in these gaps with other published data. The main hydrocarbon fields referenced are shown in Figure 4.9.1.

4.9.4.2 OIL FIELDS

Mattavelli and Novelli (1990) identify six main oil fields: Villafortuna, Rospo, Gela, Ragusa, Vega and Nilde; the condensate production of the Malossa gas field must be added to the list. According to the Oil & Gas Journal, some 20 fields were in production in 1992. The most sig-

nificant ones, by far, are those in the Vega Basin on Sicily.

Onshore Oil Fields

All onshore oil fields are located in Triassic or Mesozoic carbonate reservoirs. In Sicily, the Gela and Ragusa fields had each in 1992 a cumulative production of approximately 130 million barrels (*ca* 20 million m³). According to Schramm and Livraga (1986), the ultimate oil recovery of other onshore fields in the Vega Basin is much smaller: 2.2 million m³ for Mila; 1.1 million m³ for Perla; and Ponte Dirillo has produced about 2 million m³ to date. Major fields on the mainland are the Malossa condensate field and Villafortuna-Trecate oil field. The cumulative condensate production by the end of 1991 of Malossa is in the order of 4 million m³. Villafortuna-Trecate has a more modest total production (up to 1991) of 2.7 million m³ of light oil (46°API). Other fields each have a low cumulative production of less than 2 million m³ oil.

Offshore Oil Fields

According to the Oil & Gas Journal (1992), the most significant offshore producer is located at Rospo Mare in the Adriatic, with an ultimate recovery of 15 million m³ (André and Doucet, 1991). This oil field is found in a karstified carbonate reservoir, at the unconformity between Miocene and Lower Cretaceous units. The cumulative production of Vega in Sicily (about 5 million m³) is at present smaller than that of the neighbouring Ragusa and Gela fields, though Schramm and Livraga (1986) estimate that the Vega field may contain 160 million m³ (1000 million barrels) of heavy crude, of which 30–50% may be recoverable. The Vega oil field is listed by Carmalt and St John (1986) in their review of giant fields. They quote 'recoverable reserves' (ultimate recovery) of 100 million m³. The Vega reservoir also consists of carbonate rock (Lower Lias).

Other oil fields are smaller, such as Santa Maria a Mare and Sarago Mare, each with a cumulative production of less than 3 million m³. No figures are given for Nilde, though Mattavelli and Novelli (1990) consider it to be a major oil field. The total production for each of the other fields is less than 1 million m³.

4.9.4.3 GAS FIELDS

With respect to gas production and reserves, two very approximate estimates are available. Mattavelli et al. (1993) identified some thirty gas fields of over 3.5 million tons of oil equivalent; this equates to *ca* 4 milliard m³, using the conversion of Carmalt and St John (1984). The International Map of Natural Gas Fields in Europe (Schroeder and Schoeneich, 1986) mentions the following: two fields with remaining reserves (in 1985) of more than 30 milliard m³ (Malossa and Agostino-Porto Garibaldi), twelve fields in the range of 10–30 milliard m³, and some 150 fields with reserves of less than 10 milliard m³. These schematic classifications gain some precision from occasional figures quoted in the literature, as mentioned below.

Regarding major gas fields, Mattavelli et al. (1993) classify Agostino-Porto Garibaldi as a field of over 100 milliard m³. Ultimate recovery in the Malossa field is estimated to amount to 50 milliard m³ ('recoverable reserves' of Carmalt and St John, 1986). It may well be, however, that these figures include possible rather than proved reserves, as was the case for the Vega oil field.

In the class of fields with reserves of 10–30 milliard m³ (Schroeder and Schoeneich, 1986), the Candela gas field had a cumulative production of 12.5 milliard m³ in 1987

and an annual production of 0.5 milliard m³ (Casnedi 1988). The Luna gas field had in 1992 a cumulative production of 19 milliard m³ of gas, maintains a productivity of 1.2 milliard m³ per year, and shows no signs of decline (Roveri et al., 1992). According to Sestini and Flores (1986), the Gagliano field may have initial reserves of up to 20 milliard m³. Although the Cortemaggiore field is not included in the major field review of Schroeder and Schoeneich (1986), it has an ultimate gas recovery of 15 milliard m³ (Pieri 1992).

Onshore Gas Fields

The review by Schroeder and Schoeneich (1986) includes seven entries in a list of major onshore fields with 10–30 milliard m³ gas reserves, in addition to the giant Malossa field. These are: Selva-Minerbio, San Salvo-Cupello, Candela-Palino, Gagliano, Caviaga, Porto Corsini Terra, Dosso degli Angeli. Apart from the latter three, these gas fields and their geological context are described in reviews by Pieri and Mattavelli (1986) and Mattavelli et al. (1993). As mentioned earlier, the Cortemaggiore gas field needs to be added to the list.

The Malossa reservoir consists of dolomite and limestone dated to the Triassic-Liassic boundary. The reservoirs of all other fields listed above are formed by Miocene-Pliocene sandstones, in flysch (Gagliano), in turbidite (San Salvo-Cupello, Candela-Palino, Selva-Minerbio), or in continental sequences (Cortemaggiore, Settala). Porosities and permeabilities of the continental deposits are generally high: at Cortemaggiore, reservoir porosity is 25–30% and permeability is 80–180 mD (Pieri 1992). In the Settala reservoir porosity is 27% (Mattavelli et al., 1993). The sand interbeds of the flysch at Gagliano have a porosity of 6–15% (Sestini and Flores, 1986), though Pieri and Mattavelli (1986) quote an average porosity of 6%.

Offshore Gas Fields

The main offshore gas fields identified by Schroeder and Schoeneich (1986) are located largely in the marine extension of the Po Valley Basin: Porto Corsini Mare East, Amelia, Porto Corsini Mare and Agostino-Porto Garibaldi. The David gas field is slightly further south, and the Luna field occurs at the southeastern point of the Italian peninsula.

For the majority of the onshore gas fields, reservoirs are predominantly formed by the sand interbeds of the Miocene-Pliocene turbidite sequence. Typical traps are low-relief anticlines.

4.9.4.4 STORAGE CAPACITY

Calculations of potential storage capacity are gross estimates, since the ultimate recovery figures are only known very approximately. These estimates are presented in Table 4.9.2.

A minimum CO₂ storage capacity of 10 Mt has been used to establish the storage capacity of the gas fields (see section 4.2). This amount corresponds to a gas reservoir volume of roughly 15 million m³. Given an average gas expansion factor of 200, this represents around 3 milliard m³ at surface conditions. This volume matches fairly closely to the cutoff value of 3.5 Mt toe (tons of oil equivalent; ≈ 4 milliard m³ gas) proposed by Mattavelli et al. (1993), to describe some 30 gas fields. Unfortunately, these fields could not always be identified precisely, given the scale of the published maps and the general unavailability of data on their reserves. For these reasons, this study preferred to follow the classification of Schroeder and Schoeneich (1986), retaining a nominal 15 fields of more

than 10 milliard m³. The Settala gas field, described by Mattavelli et al. (1993), was added to the list (Table 4.9.2). Settala represents a rare instance of high porosity reservoir (27%), which is significant in regard to potential CO₂ injection. Table 4.9.2 features a final entry (total of 80 milliard m³), labelled 'Unclassified fields'. This is done to avoid an underestimation of the CO₂ storage potential, by grouping 16 smaller fields with remaining reserves of around 5 milliard m³ each. The cumulative volume of ultimately recoverable gas calculated for the main fields is about 500 milliard m³, probably a reasonable estimate considering the total of 720–830 milliard m³ mentioned earlier.

Where no reserves figures could be found for individual gas fields in the 10–30 milliard m³ class, as listed by Schroeder and Schoeneich (1986), an arbitrary value of 20 milliard m³ was used. The margin of error for any single field is not very significant, and the cumulative error over a group of some 15 fields is probably rather low (Table 4.9.1). The calculation of the underground volume of gas has been based on a gas expansion factor derived from the pressure in the reservoir, using the formula given in section 4.2. The pressure has been inferred from the depth of the field where it is known (Pieri and Mattavelli, 1986, Mattavelli et al., 1993), using a hydrostatic gradient of 10.5 MPa/km. Where the depth of the field is unknown, a gas expansion factor of 200 has been assumed.

Storage calculations for oil fields made use of the cumulative production figure, as reserve figures are generally unknown. In the exceptional case of the Vega oil field, an arbitrary ultimate oil recovery of 50 Mt was used, i.e. 50% of the possible reserves according to Schramm and Livraga (1986). The oil formation volume factor was assumed to be 1.2 (see section 4.2).

The calculation yields a theoretical CO₂ storage capacity of at least 1790 Mt (Table 4.9.2), of which 105 Mt is expected in oil fields and 1685 Mt in gas fields. These figures have a high uncertainty factor, as ultimate recovery figures themselves are not generally known with any accuracy. Moreover, it should be noted that many gas or oil fields have low, even very low, porosity values. For example, the porosity in the Malossa gas field averages 2.5–3%, with a permeability of 50 mD (Mattavelli and Margarucci 1992), and the porosity in the Ragusa and Gela oil fields is 4% (Pieri and Mattavelli, 1986). CO₂ injection in such conditions could prove very difficult, and is not certain to be possible in all fields listed on Table 4.9.2. Considering only the fields with a porosity of more than 10% (Cortemaggiore, Vettala, Vega, Gagliano...), the theoretical storage capacity could nevertheless be as high as 200 Mt.

4.9.4.5 DEPLETION

Among the fields with an expected capacity of more than 10 Mt CO₂, only the Cortemaggiore field is depleted. This field is, however, currently used for storage of natural gas (Pieri, 1986) and thus will not be available for CO₂ disposal in the near future. The Vega oil field will not be depleted for several decades, assuming initial reserves of 50 Mt and a productivity of 0.5 Mt per year. Conversely, Schroeder and Schoeneich (1986) state that several small gas fields (with reserves of less than 10 milliard m³) may already be depleted. The storage capacities of these are unknown, though probably quite small.

4.9.5 Conclusions

Using the data and methods stated above, the theoretical CO₂ storage capacity has been estimated to amount to

Table 4.9.2 Theoretical storage capacity of the hydrocarbon fields of Italy.

Figures *in italics* (*) are based on cumulative hydrocarbon production figures; other figures are based on ultimate recovery estimates. The storage calculation is based on a CO₂ reservoir density of 700 kg/m³, and an oil formation volume factor of 1.2. The gas expansion factor has been derived from the reservoir pressure, which, in turn, has been calculated from the depth of the reservoir, using a hydrostatic gradient of 10.5 MPa/km. If no depth values were available a gas expansion factor of 200 has been used. The storage capacity of fields with a capacity of less than 10 Mt have been excluded.

ONSHORE FIELDS		OIL		GAS		TOTAL
Name	Depth (m)	Reserves [#] (million m ³)	Storage capacity (Mt CO ₂)	Reserves (milliard m ³)	Storage capacity (Mt CO ₂)	Storage capacity (Mt CO ₂)
Perla	2600	1.1				
Mila	3500	2.2				
Ragusa*	1500	<i>21.11</i>	<i>17.73</i>			<i>17.7</i>
Gela*	3400	<i>19.77</i>	<i>16.61</i>			<i>16.6</i>
Villafortuna*	6200	2.67				
Pisticci*	2300	1.45				
Ponte Dirillo*	3100	2.07				
Cavone*	3200	1.59				
Cortemaggiore	1700	1.23		1.03	15	58.6
Malossa*	5800	4.19		3.52	50	90.7
Gagliano	2000			(?)20		72.0
Candela	1000			15		72.9
Caviaga				(?)20		70.0
San Salvo	1000			(?)20		97.2
Selva	1500			(?)20		82.8
Dosso d. A.				(?)20		70.0
Porto C. Terra				(?)20		70.0
Settala	1100			(?)5		23.5
Total onshore		58	39	205	708	747
ONSHORE FIELDS		OIL		GAS		TOTAL
Name	Depth (m)	Reserves [#] (million m ³)	Storage capacity (Mt CO ₂)	Reserves (milliard m ³)	Storage capacity (Mt CO ₂)	Storage capacity (Mt CO ₂)
Rospo Mare	1500	14.9	12.55			12.6
Santa Maria *	2600	2.9				
Sarago *	1700	2.2				
Vega	2800	63.6	53.42			53.4
Agostino	3300			100	269.3	269.3
Barbara	1300			(?)20	88.0	88.0
Porto Corsini				(?)20	70.0	70.0
Luna *	1700			20	78.1	78.1
Porto Corsini E	3500			(?)20	51.9	51.9
Amelia				(?)20	70.0	70.0
David				(?)20	70.0	70.0
Total offshore		84	66	220	697	763
ONSHORE FIELDS		OIL		GAS		TOTAL
Name	Depth (m)	Reserves [#] (million m ³)	Storage capacity (Mt CO ₂)	Reserves (milliard m ³)	Storage capacity (Mt CO ₂)	Storage capacity (Mt CO ₂)
16 fields with 5·10 ⁹ m ³ gas each	?			80	280.0	280.0
Total on- & offshore		141	105	505	1685	1790

'Reserves' refers to cumulative production (font in italics) or ultimate recovery (normal font)

* remaining reserves unknown and therefore excluded.

437 Mt in aquifers, 105 Mt in oil fields and 1685 Mt in gas fields. One should bear in mind that a large part of the Italian aquifers remained unexamined due to the limited availability of data on the deeper subsurface. This estimate does not take into account the very low porosity and accordingly the very low permeability in most of the gas fields. Injection of CO₂ might therefore be quite difficult. Considering only sites known to have a porosity of more

than 10%, the CO₂ storage capacities are reduced to 60 Mt in aquifers (Pliocene-Quaternary in Lombardy), 50 Mt in oil fields (Vega) and 150 Mt in gas fields. In the short term, only aquifers might provide a CO₂ storage reservoir, as the hydrocarbon reservoirs (gas fields) that are currently depleted, are too small to offer a significant volume or are used for storage of natural gas (Cortemaggiore Field).

4.10 THE CO₂ STORAGE CAPACITY OF LUXEMBOURG

Emile Elewaut and Rieks van der Straaten

4.10.1 Summary

The subsurface of Luxembourg has no CO₂ storage capacity. The northern part of the country is occupied by metamorphic Cambro-Silurian basement. Sediments occur only in the southern and southwestern part of the country. They are too shallow for CO₂ disposal. There are no hydrocarbon fields in Luxembourg.

4.10.2 Geological Overview

Luxembourg shows two natural regions: the Oesling region in the north and northwest, which is part of the Ardennes (see Figure 4.3.1.), and the Gutland region in the south and southwest, which is part of the gently undulating countryside of the Lorraine.

In Oesling region, Cambro-Silurian basement outcrops in the Givonne Massif, the Rocroi Massif, the Serpont Massif and the Stavelot Massif. These Cambro-Silurian rocks are mainly metamorphic schists, slates and quartzites. The Wiltz syncline consists of lower Devonian rocks with predominantly shaly sediments. The depth to the Cambro-Silurian basement is here less than 800 m, which makes the Devonian sediments unsuitable for CO₂ disposal.

The southern Gutland region forms the northern, marginal part of the Paris Basin (see Figure 4.3.1.). The succession starts off with some 250 m of Buntsandstein sandstones, passing upward into the Muschel Sandstone (50 m) which forms the lower part of the Muschelkalk. These sandstones are overlain by the limestones of the Muschelkalk and shales, marls and dolomites of Keuper age. The sedimentary sequence continues with predominantly shaly sediments of Jurassic age. The cumulative thickness of these strata does not exceed 800 m. Therefore, none of them is suitable for CO₂ disposal.

The geological overview presented above is largely based on Waterlot et al. (1973).

4.10.3 Aquifers

4.10.3.1 ONSHORE AQUIFERS

All Luxembourgian sediments are too shallow for CO₂ storage.

4.10.3.2 OFFSHORE AQUIFERS

Luxembourg is surrounded by land, so there are no offshore aquifers.

4.10.4 Hydrocarbon Fields

There are no hydrocarbon fields in Luxembourg.

4.11 THE CO₂ STORAGE CAPACITY OF THE NETHERLANDS

D. Koelewijn and Rieks van der Straaten

4.11.1 Summary

This study evaluates the CO₂ storage capacity of individual traps in aquifers in the Dutch subsurface. As data on the

deeper subsurface are scarce, only parts of the Netherlands could be studied in such detail. From the slightly more than hundred structures examined, fifty are potential CO₂ reservoirs. These fifty traps have a total estimated pore volume of about 16 km³. Extrapolation to the entire Dutch onshore leads to a total trapped pore volume of ca 36 km³ which corresponds to a storage capacity of 1000 Mt CO₂. Data needed to evaluate the CO₂ storage capacity of the Dutch offshore were not available.

The Dutch hydrocarbon fields have a total storage potential of approximately 9.3 Gt CO₂. The giant Groningen Gas Field can contain 7440 Mt CO₂. The remaining gas fields are good for a total of ca 1840 Mt CO₂, 1020 Mt onshore and 820 Mt offshore. The largest oil field, the onshore Schoonebeek Field, can retain 34 Mt CO₂. However, it may be too shallow for CO₂ disposal (760 m). All other oil fields, both onshore and offshore, are considered too small for CO₂ storage and are therefore excluded from the inventory.

4.11.2 Geological overview

An outline of the major structural elements of the Netherlands is given in Figure 4.11.1. The figure is from Petroleum Geological Circle (1993) and RGD-TNO (1985b); the geological overview is largely based on Van der Meer et al. (1992) and Ziegler (1990). For more information on the geological history of the Netherlands the reader is referred to Van Staaldin et al. (1979). The Quaternary sediments will not be discussed, because they are too shallow for CO₂ disposal (see Zagwijn, 1989).

The Netherlands is located in the south-eastern, marginal part of the Cenozoic North Sea Basin. The basin is bordered in the east by the Rhenish Massif and in the south by the London-Brabant Massif. The far largest part of the Dutch surface is occupied by Quaternary rocks consisting of shallow marine and continental deposits. Outcrops of Tertiary or older rocks are rare. The southeast of the country is affected by a NW trending, Cenozoic fault system. The faults created a series of fault ridges and troughs and are still active.

Little is known about the oldest sediments in the Dutch subsurface. Rocks older than the Carboniferous have only once been penetrated by wells. The top of the Dinantian (Lower Carboniferous) is formed by the Visé limestone ('Kohlenkalk'), which is present beneath almost the entire Netherlands, generally at depths of more than 4000 m. The sedimentary sequence below the Visé limestone is virtually unknown.

During the Late Carboniferous paralic sediments accumulated in the Variscan Foredeep Basin which extended from Poland to Ireland and covered a large part of Northwestern Europe, including the Netherlands. The sediments were uplifted and deformed by a late Variscan orogenic phase. Erosion led to an extensive peneplain on which the Southern Permian Basin developed. The basin occupied the area between Poland and Britain, and was bordered in the south by Variscan structural highs, the London-Brabant Massif and the Rhenish Massif. The Southern Permian Basin was initially filled with the desert sandstones of the Rotliegend Group and was later flooded by the Zechstein Sea from which a thick sequence of evaporites precipitated. The southern limits of the Permian Basin are found in the southernmost part of the Netherlands. At present, the Zechstein evaporites are restricted to the north-eastern Netherlands and a narrow NW-SE belt running through the central part of the country.

During the Early Triassic the North Sea Basin was filled with continental siliciclastics. The London-Brabant Massif still was a topographic high that had a profound effect on the sedimentation. Close to this high, in the southern Netherlands, the sandstones, siltstones and shales of the Bunter Group were deposited. Elsewhere in the basin, in the rest of the Netherlands, the Lower Germanic Triassic Group accumulated, consisting of an alternation of shales and sandstones. The continental conditions were followed by a basin-wide transgression at the end of the Triassic, resulting in a thick series of Early Jurassic shales.

During the Late Jurassic to Early Cretaceous, sedimentation was controlled by rifting. Differential block movements and halokinesis of the Zechstein salt resulted in the uplift and erosion of some parts of the southern North Sea Basin, whereas other parts subsided (Figure 4.11.1). This generated small, isolated basins in the Dutch on- and offshore: the Central North Sea Graben, the Vlieland Basin, the Broad Fourteen's Basin, the Central Netherlands Basin, the Lower Saxony Basin, the West Netherlands Basin and the Roer Valley Graben. These basins were bounded by structural highs, such as the Texel-IJsselmeer High, the Peel Horst, and the London-Brabant Massif. The post Carboniferous sediments on some of these highs (e.g. Texel-IJsselmeer High) were entirely removed by erosion.

At the end of the Cretaceous transpressional tectonics prevailed. This led to uplift, erosion and a major inversion of the Mesozoic basins. Differential subsidence resumed in the Tertiary, generating a pattern of structural highs and lows (Figure 4.11.1). The northern part of the Netherlands was occupied by the Vlieland Zuiderzee Basin, the southern part by the West Nederland Basin and the 'Centrale Slenk' fault trough. These northern and southern depressions were separated by a WNW trending fault ridge, the 'Mid Nederland Hoog'. In the southernmost part the London-Brabant Massif remained a structural high. The depressions were filled by shallow marine and continental deposits.

4.11.3 Aquifers

The inventory of the CO₂ storage capacity of the Dutch aquifers is focused on the land area, because the available data on the subsurface of the Dutch offshore are too poor to give an estimate of its storage capacity. Essential data to quantify the storage capacity offshore, such as porosity, permeability and the rock volume in traps, were not available. However, the sedimentary basins in the Dutch North Sea (Broad Fourteen's Basin and Central Graben) contain a Mesozoic sequence several kilometres thick, which is expected to include sediments and structures well suited for CO₂ disposal.

4.11.3.1 ONSHORE AQUIFERS

The approach of this section is as follows. In a limited area where enough data are available to enable a detailed inventory of the aquifers and the geological structures, the CO₂ storage capacity of each trap on an aquifer considered suitable for CO₂ injection will be assessed. This will lead to a relatively accurate estimate for a part of the Dutch land area. Next, these figures will be extrapolated to the entire Netherlands onshore.

Constraints

In this study porous rocks in the subsurface are considered to form a potential CO₂ storage site if they fulfil the following constraints (see section 4.2): a permeability of at

least 100 mD, a minimum depth of 800 m, the presence of an impervious layer covering and sealing the reservoir rock, and the confinement to a geological trap.

The inventory of the CO₂ storage capacity of the onshore aquifers was brought about in the following way. Lithostratigraphic notes were studied to define reservoir characteristics of possible aquifers. Next, available depth maps of suitable aquifers, or a concordant horizon, were searched for trapping structures. The height and the areal extent of the traps were picked on these maps. Assumptions had to be made about the lateral distribution and the thickness of the aquifers, because these properties are generally only known on a regional scale. Porosity and permeability values of aquifers were extrapolated from known well data. From these data the pore volume of a suitable aquifer was calculated in each trap that had been identified. Finally, the storage capacities in the study areas were assessed and extrapolated to the entire Dutch onshore.

Subsurface maps of the Netherlands are scarce. The 'Geologische Atlas van de Diepe Ondergrond van Nederland' (RGD 1991a,b), presenting depth maps with a scale of 1:250 000 and contours of 50 or 100 m, is currently in press. At present, only parts 1 and 2 are available, covering the northern part of the province Friesland. Since these maps cover only a small part of the Netherlands, maps that were prepared for various other purposes were additionally used. At this moment only a small part of the deeper, Mesozoic subsurface could be studied in detail (e.g. RGD, 1983b, RIVM, 1989). All major Tertiary aquifers are, however, well documented by RGD-TNO (1983, 1984, 1985a).

Inventory of the Onshore Aquifers

Carboniferous

The Dinantian Visé limestone is generally located at depths of more than 4000 m and is assumed to be present beneath the entire Netherlands, with the exception of the Friesland-Gelderland area, where the Dinantian mainly consists of shale (NAM-RGD 1980). The limestone may have a secondary porosity due to karstification. The overlying shales of the Limburg Group are well suited as caprock.

The Late Carboniferous sediments are known as the Limburg Group, which consists of shales with coal and sand beds. The Limburg Group is present in the entire Dutch underground. The sand beds could well be suitable aquifers and are adequately sealed by the shales in which they are embedded. For the northern part of the Netherlands, sand units with a maximum thickness of 9 m to several tens of metres have been found (RGD, 1991 a,b). Since drilling generally stopped after reaching the top of the Carboniferous, no information is available about the lateral distribution or correlation of these units, or their porosity and permeability. In the eastern Netherlands, a locally developed, thick sand unit is present, referred to as the Tubberger Sandstone. It consists of sandstones beds alternating with subordinate shales and coal beds and contains gas (NAM-RGD, 1980).

Permian

The Upper Rotliegend Group is present underneath the entire Netherlands below a depth of 1500 m, except for the southern and the easternmost parts. Aquifers from this group are the Lower and Upper Slochteren Formation, consisting of sandstones and conglomerates. The Slochteren Formation shows an average net thickness of 140–200 m; it thickens towards the NW (Haenel and Staroste, 1988). The formation possesses good reservoir characteristics and is gas bearing in the northern and the

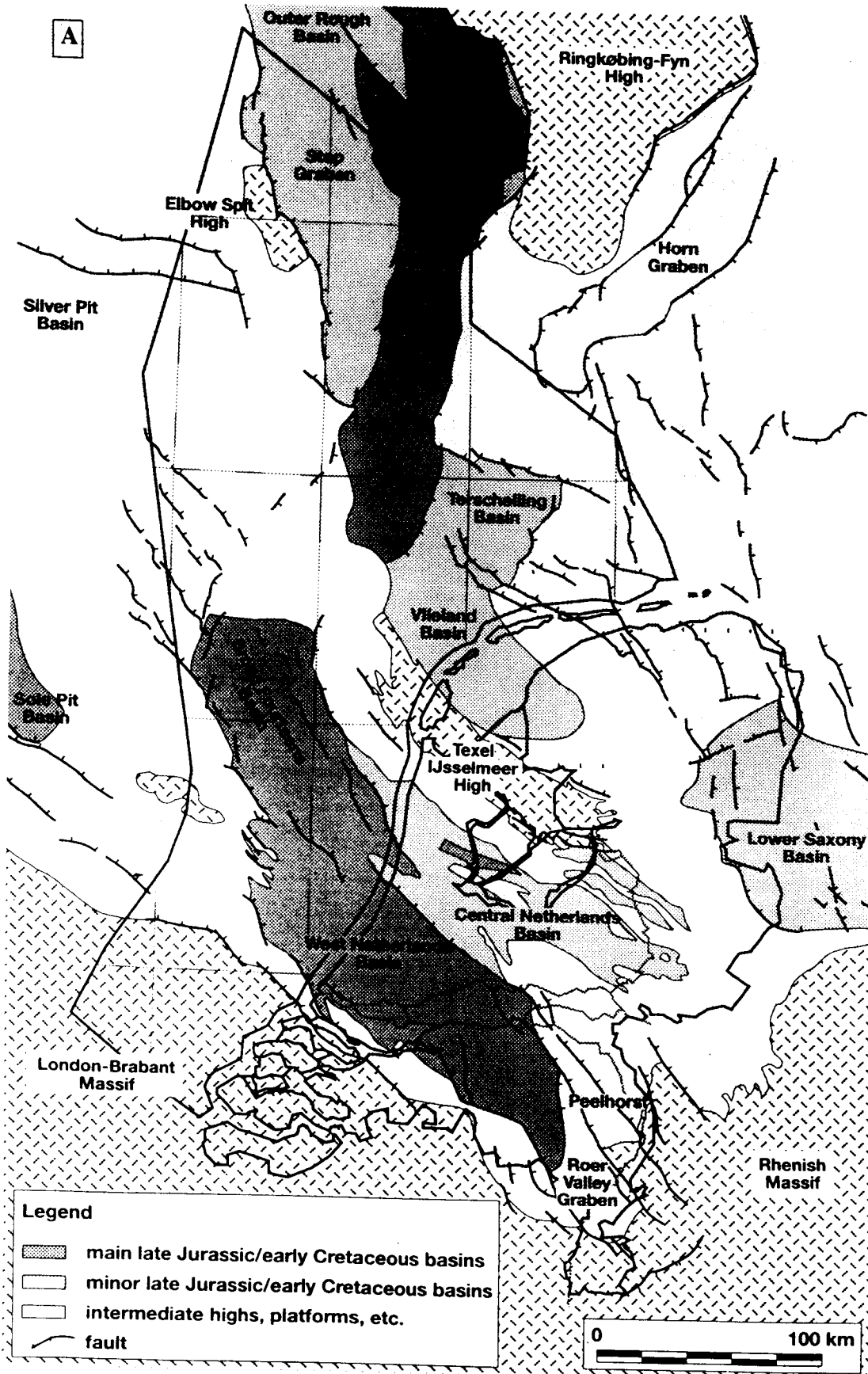
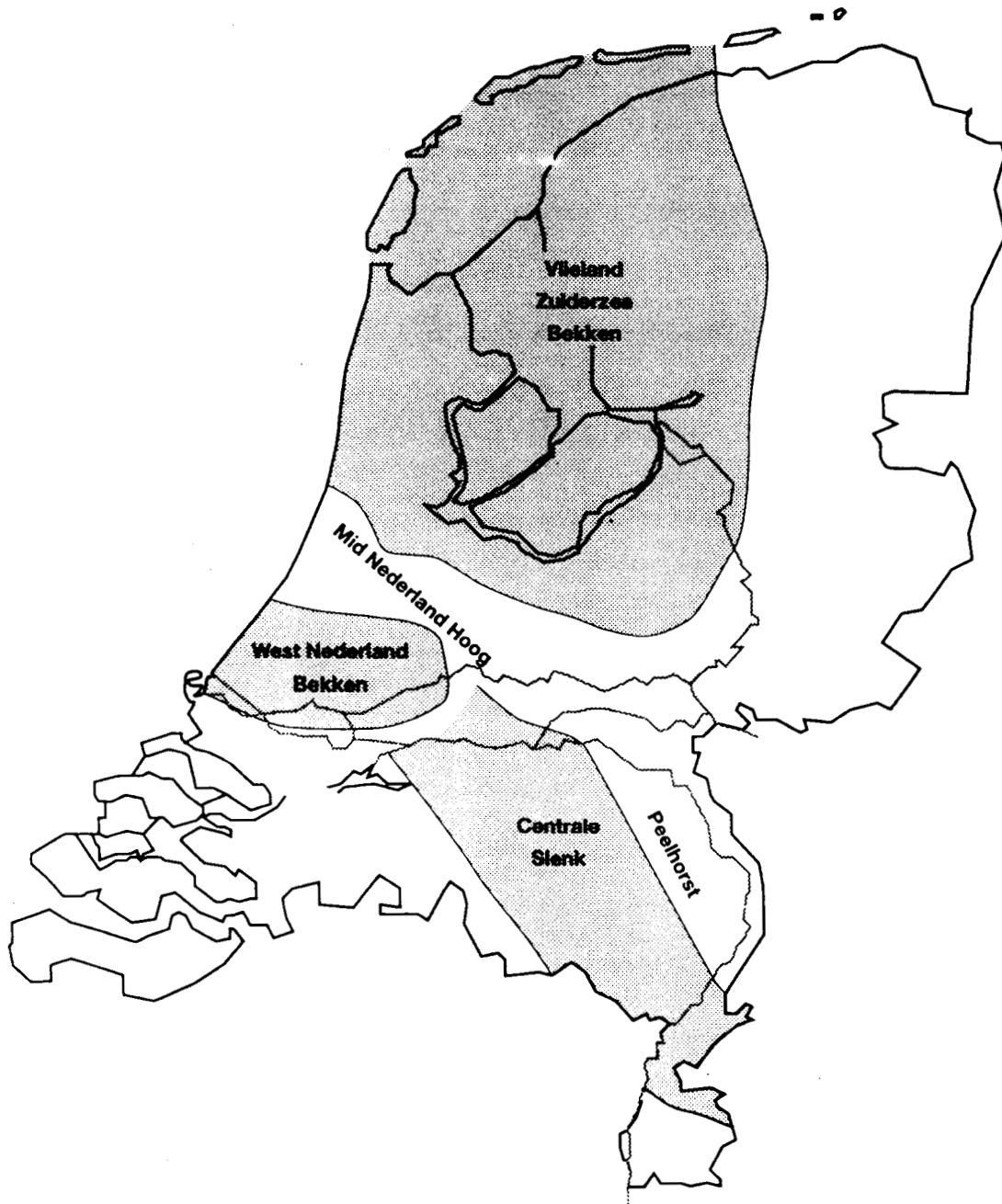


Figure 4.11.1 Generalised geology of the Netherlands. A) Mesozoic Basins (from Petroleum Geological Circle 1993), B) Cenozoic Basins (RGD-TNO 1985b).

B



Legend

 Tertiary and early Quaternary basin



Figure 4.11.1 *Continued.*

north-western part of the Netherlands. Porosity and permeability measurements are scarce and vary from 16% and 30–600 mD in the west, and 29 % and 25–290 mD in the north, to 9–15% and less than 10 mD in the east (RGD, 1983, 1991a, 1991b, Haenel and Staroste, 1988). RGD (1987) reports for the province Noord-Holland a net reservoir thickness of 150–200 m, an average porosity of 20–23% and an average permeability of 100–150 mD, and for the province Friesland a net thickness of ca 140 m, an average porosity of 19–22% (10–25%) and an average permeability of less than 50 mD (0.3–250 mD). They further show that in Friesland permeabilities larger than 100 mD are restricted to layers with porosities above 22%. Possible caprocks are the Ameland Claystone, the Ten Boer Claystone, the Silverpit Formation and the Zechstein Group^[21].

Some carbonate members of the Zechstein Group (the 'Hauptdolomite' and the 'Plattendolomite') locally possess reservoir properties. These carbonates are gas bearing in the eastern and north-western part of the Netherlands. However, not enough information is at hand to include these carbonates in the inventory.

Triassic

The Lower Germanic Triassic Group consists of an alternation of shales and sands originally deposited in the northern half of Netherlands, but largely removed by post-Triassic erosion in the north-western part of the country. The group is situated below depths ranging from ca 1000 to 4000 m and has been subdivided into the Lower and Main Buntsandstein Formation. The only aquifer in the Lower Buntsandstein is the Basal Buntsandstein, which is considered a bad reservoir because of clay and anhydrite cementation.^[22] In the Main Buntsandstein Formation three sandstone members have been recognised (RGD, 1982):

- The *Volpriehausen Sandstone Member* occurs in the (north)eastern and mid-western parts of the Netherlands. In the east, the member shows a thickness of 14–19 m and an average porosity of 14 to 23%. Measurement from one single well yielded permeabilities from 12 to 1670 mD (average of 600 mD) at an average porosity of 22%. In the west, the member consists of a 'massive' sandstone ca 40 m thick, of which only the upper 15–25 m has good reservoir characteristics. The average porosity varies from 8 to 21% and the permeability is 300–400 mD in high-porosity layers.
- The *Deifurth Sandstone Member* only occurs in the (north)eastern Netherlands and consists of two sandstone beds, an upper bed of 4–15 m and a lower bed of 10–20 m. The sandstone beds are separated by a claystone of about 8 m thick. In one single well the mean porosity is 13–18% and the average permeability 585 mD.
- The *Hardeggen Member* consists of an alternation of generally thin sandstones and silty shales. The member does not possess good reservoir properties.

[21] The Zechstein seal may be affected by CO₂, because anhydrite may dissolve into a CO₂-water mixture (see Chapter 5).

[22] In spite of its low permeability, injection into the Basal Buntsandstein may be possible because the anhydritic cement may partly dissolve into carbonate water (see Chapter 5).

In the southern Netherlands the Lower Triassic is developed as a uniform sandstone package which has not been subdivided (Bunter Group). Many claystone and clayey sand intercalations and cementation by anhydrite and dolomite make the sandstones bad reservoirs. RGD (1982) assumes average values for the porosity and a permeability in the sandstones in the order of 15% and 50 mD, and states that several levels with 'good' reservoir properties have been found, e.g. near Rijswijk and Spijkenisse. RGD (1987) mentions one core sample with a permeability of 200 mD.

The Mid and Late Triassic rocks predominantly consist of claystones, carbonates and evaporites. They have bad reservoir characteristics.

Jurassic

The Early and Mid Jurassic rocks largely consist of shales and marly limestones, with some clastic intercalations. The only Late Jurassic aquifer onshore is the Basal Weiteveen Clastics of the Niedersachsen Group deposited in the Lower Saxony Basin. It consists of conglomerates, sandstones and shales, and is overlain by limestones and evaporites.

The Late Jurassic to Early Cretaceous Delfland Formation contains in the area covered by RGD (1991a,b) several sand layers only a few metres thick, but no information on the lateral distribution and structure of the sandstones is available. Porosity ranges between 14.2 and 19.7% (exceptionally 35.2%) for the uppermost sand unit of the Delfland Formation (RGD 1991a).

Cretaceous

The Early Cretaceous Vlieland Formation contains several sandstone members, especially in the Vlieland Basin, the Lower Saxony Basin and the West Netherlands Basin:

- The *Vlieland Sandstone Member* in the Vlieland Basin consists of a fine to medium grained, glauconic sandstone up to 160 m thick with porosities of 11.4–16.7% (RGD, 1991b). The sandstone is gas bearing and locally conglomeratic. Permeabilities do not exceed 30 mD (Cottençon et al., 1975).
- The Lower Saxony Basin contains two sandstone bodies that penetrate the Vlieland Shale from the east. It is not always possible to separate these two sandstones. Especially at the edge of the basin they merge into one conglomeratic sandstone, referred to as the *Vlieland Sandstone* (NAM-RGD, 1980; RGD, 1991c). The two sandstone bodies are:
 - the *Bentheim Sandstone Member*: fine to medium grained, well sorted barrier sand with a net thickness of about 40 m. The sand forms the reservoir of the Schoonebeek oil field (RGD, 1983b). Although the Bentheim Sandstone may have good reservoir characteristics (TNO, 1986), it cannot be included in this inventory, because data on its distribution and its petrophysical properties are unavailable.
 - the *Gildehaus Sandstone Member*: a coarse grained to conglomeratic sandstone with clay flakes, coal and glauconite. The Gildehaus Sandstone is considered to have bad reservoir properties (RGD, 1983b, TNO, 1986).
- In the West Netherlands Basin, four sandstone wedges penetrate the Vlieland Shale from the south:

- the *Rijswijk Sandstone Member*: a generally fine to medium, but locally very coarse grained sandstone with minor shale intercalations. According to RGD, (1983b), the thickness ranges from 0 to 60 m (average 25–30 m), the porosity varies from 20 to 28%, and the average permeability amounts to 500 mD, with maximum values up to 5 Darcy. Both thickness and permeability are highly variable. Van der Meer et al. (1994) report for the south-western part of the basin less favourable reservoir characteristics: an average porosity of 16%, an average permeability of 330 mD and a net thickness of 24 m.
- the *Berkel Sand-Shale Member*: an alternation of fine sandstones, siltstones and shales with a maximum thickness of about 100 m (RGD, 1983b). The member contains at one location sandstone beds with a cumulative thickness of 60 m, an average porosity of 14% and an average permeability of 125 mD (Van der Meer et al., 1994).
- the *Berkel Sandstone Member*: a fine to medium grained sandstone with shale and conglomerate interbeds. The member is 40–100 m thick and has a porosity of 12–38% and a permeability ranging from 3 to 1300 mD (Visser et al., 1993). It shows near well Gaag-1 a porosity of 16%, a permeability of 330 mD and a net thickness of 40 m (Van der Meer et al., 1994).
- the *IJsselmonde Sandstone Member*: a complex of well-stratified, fine to medium grained sandstones with clay intercalations. Haenel & Staroste (1988) state that the sandstones of the member are excellent reservoirs, with gross thicknesses between 70 and 300 m, porosities between 20 and 30%, and permeabilities between 500 and 1000 mD, locally even more than 10 Darcy.
- the *De Lier Sand-Shale*: an alternation of thin sandstones and sandy shales, both glauconitic. The sandstones contain much clay and are therefore bad reservoirs (RGD, 1987).

During the late Early–Late Cretaceous, predominantly marls and marly shales were deposited, but in the West Netherlands Basin and the Roer Valley Graben two glauconitic sand units are distinguished:

- the *Holland Greensand Member*: a fine grained sandstone to siltstone on the southern basin margin rapidly shaling out to the north.
- the *Texel Greensand Member*: a fine grained calcareous sandstone

During the Late Cretaceous no siliciclastic sedimentation took place. The Ommelanden Chalk, originally a massive and impervious limestone, locally shows a secondary porosity due to fracturing (RGD, 1991a,b). The Upper Krijtkalk contains a gas field near Harlingen.

Tertiary

The Tertiary of the Netherlands is characterised by siliciclastics and has been subdivided into the Lower, Middle and Upper North Sea Group. The aquifers of the Lower North Sea Group are:

- *Heers Sand*: a glauconitic, calcareous sand with clay beds, at the base of the Lower North Sea Group. The clay content is very high and the reservoir quality is expected to be poor (RGD-TNO, 1984, 1985b).
- *Basal Dongen Sand*: a generally fine grained and silty sand distributed below the southern part of the Netherlands, south of the ‘Mid Nederland Hoog’, at a depth between 350 and 1800 m. The net thickness of the member generally varies from 10 to 30 m. In the ‘Centrale Slenk’ east of Tilburg, however, a thickness of 100 m is reached. The upper part of the member is here coarse grained, shows little silt and permeabilities up to 500 mD have been inferred. Elsewhere, the Basal Dongen Sand shows permeabilities that are estimated to be less than 100 mD (RGD-TNO, 1985a, TNO 1986). The Clay of Ieper (100–300 m thick) forms the caprock in most areas, but locally the clay has been eroded and the Basal Dongen Sand is overlain by the Berg Sand. North of the ‘Mid Nederland Hoog’, the member is called the Basal Dongen Tuffite. It shows here a different lithology, with less sand, more clay and numerous tuffite layers. The Basal Dongen Tuffite is considered to have poor reservoir characteristics (TNO, 1986). Core measurements from a single well in the north-eastern Netherlands showed a maximum permeability of only 8 mD (RGD-TNO, 1983, 1984).
- *Brussels Sand*: a very fine, calcareous and glauconitic sand. Porosities range between 30 and 35 %, permeabilities between 400 and 600 mD (RGD-TNO, 1983, 1984, 1985a). In the southern Netherlands the member is situated at depths ranging from 100 to 700 m (RGD-TNO, 1985a, TNO, 1986), which is too shallow for CO₂ disposal. In the northern Netherlands the member occurs at a depth of 0–1200 m and has a maximum thickness of 100–120 m, including some clayey intervals. Porosity is about 15–35% and permeabilities vary from 50–60 mD in clayey sand to 400–1000 mD in ‘clean’ sand (RGD, 1983, 1984, TNO, 1986). The Brussels Sand has locally been eroded due to halokinesis. The Clay of Asse (up to 160 m thick) forms the caprock, except where the clay has been eroded. There the Brussels Sand may be overlain by the Berg Sand which is sealed by the Boom Clay, or may be covered by the Breda Formation.

The aquifers of the Middle North Sea Group are:

- *Berg Sand Member*: a fine grained sand, with in the eastern Netherlands a basal gravel layer. Porosities range from 25 to 30%, (maximum?) permeabilities from 200 to 300 mD (RGD-TNO 1982, 1983, 1984). In the regions of Zwolle and Breda, however, permeability generally does not exceed 100 mD, although some layers show values in the order of 200–400 mD (TNO 1986). Towards the north-west, the member becomes thinner and contains more clay, and the grain-size and sorting of the sandstones decreases. The thickness varies from 20–30 m in the south to 0–15 m in the north and west. The Berg Sand outcrops in the southwest corner of the Netherlands and reaches a depth of more than 1800 m in the ‘Centrale Slenk’, being the only place where traps occur below a depth of 800 m. Caprock is formed by the Boom Clay, which has a thickness of 30–150 m (RGD-TNO 1985a, TNO 1986).

— *Voort Sand Member* is present in the south-eastern Netherlands and grades upwards and north-westwards into the Veldhoven Clay. The Voort Sand shows a maximum thickness of 200 m in the 'Centrale Slenk' and becomes thinner towards the north-west where it has a thickness of 15–20 m. The Voort Sand occurs at depths varying from 150 m on the 'Peel Horst' to about 1400 m in the 'Centrale Slenk', which is the only location where the sand is at the right depth for CO₂ disposal. Clayey sand layers generally have a permeability of less than 100 mD, but sands free of clay or silt may show values up to 1000 mD (Breda region, TNO, 1986). The member is overlain by the Breda Formation. Although this formation largely consists of clay, it cannot be regarded as an appropriate seal in the 'Centrale Slenk', because here the Voort Sand merges with the overlying sand bodies of the Breda Formation.

The Upper North Sea Group (Breda Formation) also contains sand bodies that may have good reservoir properties, but these are largely situated at a depth too shallow for CO₂ disposal (TNO, 1986).

Traps and Storage Capacity

This section focuses on the CO₂ storage capacity of the trapped portion of the onshore aquifers. Only those aquifers that have reservoir characteristics appropriate for CO₂ injection are considered (see section 4.2). Beside the storage capacity per aquifer, some aspects of the aquifers will be discussed that relate to their suitability for CO₂ injection.

We identified slightly more than hundred traps in those parts of the Netherlands where suitable depth maps of the subsurface were available. Only fifty traps are potentially suited for CO₂ disposal. The remaining traps are either too shallow or contain aquifers with poor reservoir characteristics. Generally, not enough information was available to define stratigraphic traps. Very large structures, extending beyond the area of the map sheet, could not be detected either. The pore volume of the individual trap has been calculated by multiplying the area of the structure by the net thickness of the aquifer and the estimated average porosity.

The total pore volume of the 50 traps in the study area is ca 16.2 km³, of which 2.3 km³ contains oil or gas. Extrapolation of these results to the entire Dutch onshore leads

to a total trapped aquifer pore volume of about 36.2 km³ (Table 4.11.1).

The storage calculation is restricted to the trapped portion of the aquifers and has been based on an average CO₂ reservoir density of 700 kg/m³. It is further assumed that 4% of the trapped pore volume can be filled with CO₂, since both 'open' and 'closed' traps have been found in the investigated area (see section 4.2). The estimated storage capacities of the onshore aquifers are shown in Table 4.11.1. They amount to ca 1000 Mt CO₂. However, most structures are small and from the fifty traps in the study areas that are appropriate for CO₂ disposal, only sixteen have a storage capacity that exceeds 10 Mt CO₂. The pore volumes of these sixteen larger structures add up to 13.7 km³ (84 vol%). If extrapolated to the entire Dutch onshore, this implies that about 850 Mt CO₂ could be stored in structures with a capacity of more than 10 Mt CO₂.

Slochteren Formation (Permian)

Potential traps on the Slochteren Formation have been identified on depth maps of the base of the Zechstein Group from the north-west corner of The Netherlands (RGD, 1991a,b). The aquifer range in the study area is about 3340 km² and the closed structures that have been recognised occupy some 260 km² (7.8% by area). The total trapped pore space in the study area is estimated to amount to ca 4.0 km³, of which 2.0 km³ is filled with natural gas. Only five structures are large enough to contain more than 10 Mt CO₂. Two of these larger structures contain gas. Most traps are fault blocks or faulted anticlines and the same type of traps can be expected everywhere underneath the Netherlands where the Slochteren Formation is present.

If only deposits with a net thickness of more than 100 m are considered, thus excluding the low-permeability development in the eastern Netherlands, the Slochteren Formation shows a distribution of ca 12 630 km², an average net thickness of 150 m and an average porosity of 16% (based on RGD, 1983a). This leads to a total pore volume of about 304 km³. Assuming that the above percentage of closures can be extrapolated to the entire Netherlands, the total trapped pore volume will be about 24 km³, which corresponds to a storage capacity of about 670 Mt CO₂ (Table 4.11.1). It should be noted that in the study area 50% of the trapped pore volume is filled with gas. So, the storage

Table 4.11.1 The CO₂ storage capacity of traps on the onshore aquifers in The Netherlands. The aquifers of the Main Buntsandstein considered are the Volpriehausen and the Detfurth sandstones. The storage calculation has been based on the assumption that 4% of the trapped pore volume can be filled with CO₂ that has a reservoir density of 700 kg/m³. Figures in italics have been estimated.

Aquifer	Age	Range (km ²)	Net Thickness (m)	Porosity (%)	Area of Traps (%)	Pore Volume		Storage Capacity (Mt CO ₂)
						Total (km ³)	in Traps (km ³)	
Slochteren	Permian	12 632	150	16	7.8%	304.04	23.81	666.59
M. Buntsandstein	Triassic	5 931	24	16	4.0%	22.71	0.91	25.43
Rijswijk Sand	Cretaceous	752	25	25	3.8%	4.70	0.18	4.99
Berkel Sand	Cretaceous	144	40	25	0.0%	1.44	0.00	0.00
IJsselmonde Sand	Cretaceous	97	100	25	4.9%	2.43	0.12	3.29
Basal Dongen Sand	Tertiary	—	61	25	—	—	6.51	182.14
Brussels Sand	Tertiary	—	81	25	—	—	2.79	78.14
Berg Sand	Tertiary	—	25	28	—	—	1.90	53.29
TOTAL							36.21	1014

— *Voort Sand Member* is present in the south-eastern Netherlands and grades upwards and north-westwards into the Veldhoven Clay. The Voort Sand shows a maximum thickness of 200 m in the 'Centrale Slenk' and becomes thinner towards the north-west where it has a thickness of 15–20 m. The Voort Sand occurs at depths varying from 150 m on the 'Peel Horst' to about 1400 m in the 'Centrale Slenk', which is the only location where the sand is at the right depth for CO₂ disposal. Clayey sand layers generally have a permeability of less than 100 mD, but sands free of clay or silt may show values up to 1000 mD (Breda region, TNO, 1986). The member is overlain by the Breda Formation. Although this formation largely consists of clay, it cannot be regarded as an appropriate seal in the 'Centrale Slenk', because here the Voort Sand merges with the overlying sand bodies of the Breda Formation.

The Upper North Sea Group (Breda Formation) also contains sand bodies that may have good reservoir properties, but these are largely situated at a depth too shallow for CO₂ disposal (TNO, 1986).

Traps and Storage Capacity

This section focuses on the CO₂ storage capacity of the trapped portion of the onshore aquifers. Only those aquifers that have reservoir characteristics appropriate for CO₂ injection are considered (see section 4.2). Beside the storage capacity per aquifer, some aspects of the aquifers will be discussed that relate to their suitability for CO₂ injection.

We identified slightly more than hundred traps in those parts of the Netherlands where suitable depth maps of the subsurface were available. Only fifty traps are potentially suited for CO₂ disposal. The remaining traps are either too shallow or contain aquifers with poor reservoir characteristics. Generally, not enough information was available to define stratigraphic traps. Very large structures, extending beyond the area of the map sheet, could not be detected either. The pore volume of the individual trap has been calculated by multiplying the area of the structure by the net thickness of the aquifer and the estimated average porosity.

The total pore volume of the 50 traps in the study area is *ca* 16.2 km³, of which 2.3 km³ contains oil or gas. Extrapolation of these results to the entire Dutch onshore leads

to a total trapped aquifer pore volume of about 36.2 km³ (Table 4.11.1).

The storage calculation is restricted to the trapped portion of the aquifers and has been based on an average CO₂ reservoir density of 700 kg/m³. It is further assumed that 4% of the trapped pore volume can be filled with CO₂, since both 'open' and 'closed' traps have been found in the investigated area (see section 4.2). The estimated storage capacities of the onshore aquifers are shown in Table 4.11.1. They amount to *ca* 1000 Mt CO₂. However, most structures are small and from the fifty traps in the study areas that are appropriate for CO₂ disposal, only sixteen have a storage capacity that exceeds 10 Mt CO₂. The pore volumes of these sixteen larger structures add up to 13.7 km³ (84 vol%). If extrapolated to the entire Dutch onshore, this implies that about 850 Mt CO₂ could be stored in structures with a capacity of more than 10 Mt CO₂.

Slochteren Formation (Permian)

Potential traps on the Slochteren Formation have been identified on depth maps of the base of the Zechstein Group from the north-west corner of The Netherlands (RGD, 1991a,b). The aquifer range in the study area is about 3340 km² and the closed structures that have been recognised occupy some 260 km² (7.8% by area). The total trapped pore space in the study area is estimated to amount to *ca* 4.0 km³, of which 2.0 km³ is filled with natural gas. Only five structures are large enough to contain more than 10 Mt CO₂. Two of these larger structures contain gas. Most traps are fault blocks or faulted anticlines and the same type of traps can be expected everywhere underneath the Netherlands where the Slochteren Formation is present.

If only deposits with a net thickness of more than 100 m are considered, thus excluding the low-permeability development in the eastern Netherlands, the Slochteren Formation shows a distribution of *ca* 12 630 km², an average net thickness of 150 m and an average porosity of 16% (based on RGD, 1983a). This leads to a total pore volume of about 304 km³. Assuming that the above percentage of closures can be extrapolated to the entire Netherlands, the total trapped pore volume will be about 24 km³, which corresponds to a storage capacity of about 670 Mt CO₂ (Table 4.11.1). It should be noted that in the study area 50% of the trapped pore volume is filled with gas. So, the storage

Table 4.11.1 The CO₂ storage capacity of traps on the onshore aquifers in The Netherlands. The aquifers of the Main Buntsandstein considered are the Volprichausen and the Detsfurth sandstones. The storage calculation has been based on the assumption that 4% of the trapped pore volume can be filled with CO₂ that has a reservoir density of 700 kg/m³. Figures in italics have been estimated.

Aquifer	Age	Range (km ²)	Net Thickness (m)	Porosity (%)	Area of Traps (%)	Pore Volume		Storage Capacity (Mt CO ₂)
						Total (km ³)	in Traps (km ³)	
Slochteren	Permian	12 632	150	16	7.8%	304.04	23.81	666.59
M. Buntsandstein	Triassic	5 931	24	16	4.0%	22.71	0.91	25.43
Rijswijk Sand	Cretaceous	752	25	25	3.8%	4.70	0.18	4.99
Berkel Sand	Cretaceous	144	40	25	0.0%	1.44	0.00	0.00
IJsselmonde Sand	Cretaceous	97	100	25	4.9%	2.43	0.12	3.29
Basal Dongen Sand	Tertiary	—	61	25	—	—	6.51	182.14
Brussels Sand	Tertiary	—	81	25	—	—	2.79	78.14
Berg Sand	Tertiary	—	25	28	—	—	1.90	53.29
TOTAL							36.21	1014

capacity calculated for aquifers and hydrocarbon fields will partly overlap.

The profiles presented by Van Staalduinen et al. (1979) and the Petroleum Geological Circle (1993) illustrate that the Slochteren formation is buried under a thick package of impervious rocks and is underlain by the Late Carboniferous Limburg Group, mainly consisting of shales. The profiles further suggest that the formation occurs in fault blocks with an approximate width of 10 to 100 km (the length may be considerably greater). It is not clear, however, whether or not the large fault blocks form 'closed' traps, because they generally extend beyond the area of the individual depth maps. Anyway, the Slochteren Formation is expected to be entirely sealed off from shallower overburden formations.

According to Cousteau et al. (in Tissot and Welte, 1984), the North Sea Basin represents a 'juvenile' basin with a compaction-induced excess hydrostatic head and a centrifugal, lateral water movement towards the margins of the basin. Since the major part of the Dutch land area can be regarded as an onshore continuation of the North Sea, overpressured aquifers with a lateral water movement are expected in the deeper subsurface of the Netherlands.

In view of the above considerations, the Slochteren Formation probably forms an overpressured and 'closed' aquifer, isolated from the surface and the shallow subsurface. Because of this isolation, the restriction of CO₂ storage to the trapped pore volume may not be essential. If this restriction is dropped and the entire pore volume becomes available for CO₂ disposal, the storage capacity of the Slochteren Formation would amount to approximately 4.3 Gt CO₂, assuming that only 2% of the pore volume can be filled with CO₂. However, the expected overpressure and 'closed' fault blocks may be a serious problem because of the rapid pressure build-up during CO₂ injection.

Main Buntsandstein Formation (Triassic)

The Triassic aquifers that are potentially suitable for CO₂ storage are the Volpriehausen and the Detfurth sandstones of the Main Buntsandstein Formation. Traps on these aquifers have been picked from a depth map of the top of the Main Buntsandstein in the north-eastern Netherlands (RGD, 1991c). The range of Triassic aquifers in the investigated area is about 4 750 km². The traps identified have a pore volume of ca 0.7 km³ and occupy about 190 km², i.e. 4.0% by area. The structures are small and have a maximum storage potential of less than 6 Mt CO₂. They have been formed by halokinesis, which complicates an extrapolation to the remainder of the Netherlands, where the traps will be fault related. Extrapolation of the trapped pore volume in the study area to the remainder of the Dutch onshore, will be based on the assumption that fault related traps are as frequent as traps related to halokinesis.

Although the distribution of the Main Buntsandstein Formation is not known exactly, the profiles and maps provided by RGD (1982) suggest that the formation is restricted to the area north of the Haarlem-Tiel-Haaksbergen axis, with an estimated range of about 5900 km². Assuming an average net thickness of 24 m and a mean porosity of 16 % (based on RGD 1982), the total pore volume of the Volpriehausen and the Detfurth sandstones amounts to ca 23 km³. Extrapolation of the trapped fraction found in the study area to the entire Netherlands leads to a total trapped pore volume of 0.91 km³ (Table 4.11.1) and a storage capacity of 25 Mt CO₂.

For reasons similar to those presented in the above section on the Slochteren Formation, the Triassic is

expected to contain 'closed' aquifers that are isolated from the shallow subsurface. Hence, it may prove possible to use the entire aquifer as a reservoir for CO₂ storage. In that case, the storage capacity would be about 0.3 Gt CO₂. As for the Slochteren Formation, overpressure and the occurrence of 'closed' traps on parts of the aquifers, will possibly make CO₂ injection problematic.

Vlieland Formation (Early Cretaceous)

The Cretaceous aquifers of the Dutch onshore that are potential CO₂ reservoirs belong to the Vlieland Formation of the Early Cretaceous Rinland Group. Although the Bentheim Sand in the Lower Saxony Basin could not be evaluated because of the lack of data, the aquifers suitable for CO₂ disposal are probably restricted to the West Netherlands Basin, which are: the Rijswijk Sandstone, the Berkel Sandstone and the IJsselmonde Sandstone. Based on a distribution map of these aquifers and a depth map of the top of the Delfland Formation (\approx base Vlieland Formation) (RGD, 1983b), three traps have been distinguished: two in the Rijswijk Sandstone and one in the IJsselmonde Sandstone. The three aquifers have a total pore volume of 8.6 km³, of which 0.3 km³ is in traps (Table 4.11.1). It should be noted that all of these traps contain oil and that injection of CO₂ in these aquifers is more likely to be combined with enhanced oil recovery. It is unclear to what extent the Cretaceous aquifers are in communication with the surface or the shallow subsurface.

Tertiary

Tertiary aquifers that are expected to possess good reservoir characteristics are:

- Basal Dongen Sand Member (upper part of member in eastern 'Centrale Slenk')
- Brussels Sand Member ('clean sands' north of 'Mid Nederland Hoog')
- Berg Sand Member ('clean sands' in 'Centrale Slenk')

Traps are formed by fault blocks, (faulted) anticlines, and unconformities. The total trapped pore volume of the investigated Tertiary aquifers is estimated to be 11.2 km³. As most of the Tertiary aquifers have been studied, this value probably is representative for the whole Netherlands.

The Tertiary consists of an irregular complex of locally developed sand bodies embedded in silt and clay. Moreover, the Tertiary aquifers mostly occur at shallow depth and generally do not have a continuous top seal over their entire range, due to regional erosion. They are therefore expected to be to some extent in hydraulic communication with the surface waters. So, the concept of filling the aquifers beyond the limits of the traps will not be appropriate for the Tertiary.

Other Aquifers

No data are available for the Carboniferous sandstones. These sandstones occur at great depths beneath the entire Netherlands and they can be good reservoirs. The non-studied Mesozoic aquifers (Weiteveen Clastics, 'Mid' Cretaceous greensands) all have a very limited distribution and their potential storage capacity is therefore considered to be low. All Quaternary strata are too shallow for underground CO₂ disposal. According to Zagwijn (1989) the maximum thickness of the Quaternary of the Dutch onshore is ca 500 m.

4.11.3.2 OFFSHORE AQUIFERS

The limited data on the subsurface of the Dutch North Sea do not allow a quantitative evaluation of the storage capacity of the offshore aquifers. Yet, the literature provides enough information to give a rough indication of the volumetric dimensions of the fill of the two sedimentary basins in the Dutch offshore: the Broad Fourteen's Basin in the south and the Central North Sea Graben in the north.

Broad Fourteen's Basin

The Broad Fourteen's Basin occupies an area of roughly 5400 km² (Figure 4.11.1). At its deepest part the basin contains about 6 km post Carboniferous fill. The Jurassic sequence is up to 1.5 km thick. (Petroleum Geological Circle, 1993).

Central North Sea Graben

The Dutch Central North Sea Graben extends over an area of roughly 6000 km² (Figure 4.11.1) and has a maximum post Carboniferous fill of more than 8 km (Petroleum Geological Circle 1993). The Jurassic is up to 2 km thick. Jurassic reservoirs suitable for CO₂ storage may be found among the following sandstone units (Herngreen and Wong, 1993):

- *Lower Graben Sandstone Formation* (Callovian): very fine to fine, well sorted fluvial (braided river) sandstones in beds generally less than 10 m thick, with intercalations of thin silty to sandy shales. Its thickness ranges from 40 m to 562 m. The formation shows a lateral distribution of about 3 500 km², and is conformably overlain by the Middle Graben Shale Formation.
- *Middle Graben Sand Member* (Oxfordian): a single thick sandstone unit embedded in the Middle Graben Shale Formation. The bed consists of fine to medium grained, moderately sorted barrier or mouth bar sandstone and is up to 20 m thick. The sandstone has a calcareous cement and a high carbonaceous content. It occurs over an area of about 900 km².
- *Upper Graben Sandstone Formation* (Oxfordian): two intervals of very fine to fine grained, carbonaceous sandstone, separated by a package of silty shales. The formation attains a maximum thickness of 123 m, shows a lateral distribution of about 900 km², and pinches out in, and is overlain by the Kimmeridge Clay Formation. The deposits are considered to represent deltaic or coastal bars developed in a paralic environment.
- *Delfland Formation* (Oxfordian-Ryazanian): a delta plain sequence of rapidly alternating sands, siltstones and shales. The formation has a thickness of 100 to 600 m and is present in an area of about 3000 km².
- *Scruff Greensand Formation*. (Portlandian-Ryazanian): a very glauconitic, very fine to fine grained, well sorted, massive, shallow marine sandstone. It shows variable amounts of clay. The formation is approximately 30 to 370 m thick, shows a lateral distribution of about 3000 km², and is covered by the sediments of the Clay Deep Formation or the Rijnland Group.

These sandy units all contain oil and gas. The three 'Graben Formations' are restricted to the Central Graben

(Herngreen and Wong, 1989). Beside the Jurassic, older sandstones have been found that form oil or gas reservoirs, such as sandstones in the upper part of the Carboniferous Limburg Group, the Rotliegend Slochteren Sandstone, and Lower Triassic sandstones. These sandy units may also be suitable for CO₂ storage.

4.11.4 Hydrocarbon Fields

4.11.4.1 CONSTRAINTS

To assess the storage capacity of depleted hydrocarbon fields the reservoir characteristics, recovery and the hydrocarbon properties are of great importance. These data were not available for the individual fields. Assumptions have therefore been made about the temperature, pressure and oil formation volume factor or gas expansion factor of the average reservoir (see Table 4.11.2). Temperature and pressure were inferred from the estimated depth of the fields, assuming a hydrostatic pressure gradient of 10.5 MPa/km and geothermal gradient of 30°/km. An exception is the Groningen Gas Field, of which reservoir temperature and pressure are known. The way in which the storage capacity has been calculated is described in section 4.2.

Most publications on the Dutch oil and gas fields only give general structural overviews and geological settings, and are relatively old. Van Lith (1983), Roos et al. (1983), Van Adrichem Boogaert and Burgers (1983), Van den Bosch (1983), Gdula (1983) are all from the conference on the south-eastern North Sea in 1982. More recent data are found in Doornhof (1992) and De Jong and Dusar (1992), although these articles dealt with other aspects of the reservoirs. A recent, but very concise overview of the petroleum geology of the Netherlands is given by Petroleum Geological Circle (1993). The major source of information we used was the annual report on hydrocarbon production and estimated reserves issued by the Ministry of Economic Affairs (EZ, 1994). This report differentiates between oil and gas and between onshore and offshore fields, but does not provide information on the individual hydrocarbon fields. The data on production and reserves are therefore lumped into four categories: 1) onshore oil, 2) offshore oil, 3) onshore gas and 4) offshore gas.

The distribution of the Dutch oil and gas fields is shown in Figure 4.11.2. Table 4.11.2 lists the ultimate recovery and the estimated CO₂ storage capacity of the hydrocarbon fields.

4.11.4.2 OIL FIELDS

At the end of 1993, the total volume of ultimately recoverable oil was assessed to be 119 million m³, 81 million m³ onshore and 38 million m³ offshore (EZ, 1994).

Onshore Oil Fields

The cumulative oil production onshore amounted to 73 million m³ at the end of 1993. The proved reserves were at that time estimated to be 8 million m³ (EZ, 1994).

The major oil field onshore is the Schoonebeek field in the north-eastern part of the Netherlands (Figure 4.11.2). At the beginning of 1994, the field had produced some 40 million m³ oil and its proved reserves were estimated to be about 1 million m³ (EZ, 1994)^[23]. Reservoir rock is formed by Lower Cretaceous sandstones deposited in the Lower Saxony Basin (RGD, 1988, Petroleum Geological

[23] The expected reserves of the Schoonebeek field are, however, as high as 21 million m³ oil.

Figure 4.11.2
Distribution map of the
Dutch oil and gas fields
(from Petroleum
Geological Circle 1993).

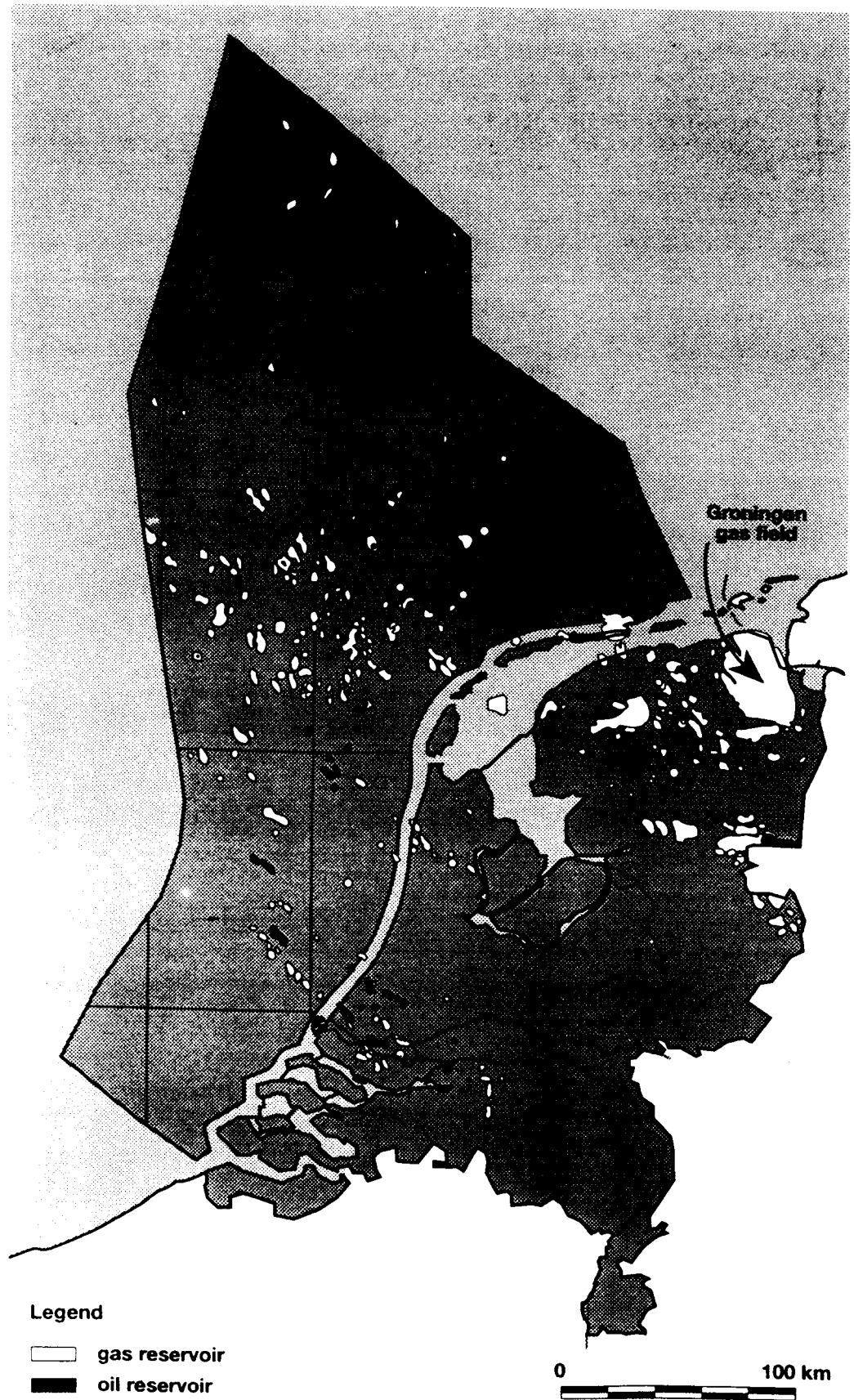


Table 4.11.2 The CO₂ storage capacity of the Dutch hydrocarbon fields. The data on the gas and oil production and reserves are from EZ (1994). The storage calculation conforms to the method described in section 4.2. The CO₂ reservoir density is assumed to be 700 kg/m³. The gas expansion factor has been inferred from the reservoir pressure, which in turn, has been derived from the reservoir depth by applying a hydrostatic gradient of 10.5 kPa/m. The Groningen Gas Field is an exception, showing a CO₂ reservoir density of 690 kg/m³ and a gas expansion factor of 250. Figures in italics are estimated average values.

HYDROCARBON FIELDS	OIL			GAS		TOTAL
	Depth	Ultimate recovery	Storage [#] capacity	Ultimate recovery	Storage [#] capacity	Storage [#] capacity
	(m)	(10 ⁶ m ³)	(Mt CO ₂)	(10 ⁹ m ³)	(Mt CO ₂)	(Mt CO ₂)
Groningen Gas Field*	2800	—	—	2697	7443	7443
Schoonebeek Oil Field	760	40.5	34.0	—	—	34
other 'smaller' onshore fields +	2000	40.2	—	89	—	—
other 'larger' onshore fields +	2000	—	—	284	1021	1021
total onshore		80.7	34.0	3069	8464	8498
'smaller' offshore fields	3000	38.2	—	141	—	—
'larger' offshore fields	3000	—	—	285	816	816
total offshore		38.2	0.0	426	816	816
TOTAL		118.9	34.0	3495	9279	9313

+ 'smaller' gas fields have an ultimate recovery of less than 3 milliard m³; 'larger' fields have greater capacities.

* The Groningen Field has an initial reservoir temperature of 107 °C and an initial reservoir pressure of 35 MPa.

Circle 1993). The field has very thick oil with difficult production. It was abandoned in 1994.

The other onshore oil fields are in the West Netherlands Basin ('Rijswijk Concession'). At the beginning of 1994, the total cumulative production in this area amounted to 33 million m³ oil and the proved reserves were estimated to be about 7 million m³ (EZ 1994). The source rock is formed by the Lower Jurassic, marine Posidonia Shale, which is restricted to the rift basins in the Dutch North Sea (the West Netherlands, the Broad Fourteen's, and the Central North Sea Graben). Upper Jurassic and Lower Cretaceous sandstones form the oil reservoirs (Petroleum Geological Circle 1993). The distribution map of the oil and gas fields in EZ (1994) suggests that the West Netherlands Basin contains onshore at least 11 oil fields (see Figure 4.11.2).

Offshore Oil Fields

At the end of 1993, the total cumulative oil production of the offshore fields amounted to 28 million m³ and the total proved oil reserves were estimated to be 10 million m³ (EZ 1994). This leads to an ultimate oil recovery of 38 million m³ for all fields on the Dutch Continental Shelf.

The offshore oil fields are located in the Central North Sea Graben, the Broad Fourteen's Basin and the offshore part of the West Netherlands Basin. As in the onshore West Netherlands Basin, the oil-prone Posidonia Shales (Lower Jurassic) charge Upper Jurassic and Lower Cretaceous sandstones. The distribution map of the oil and gas reservoirs in EZ (1994) suggests that the offshore oil is divided over more than 20 fields (Figure 4.11.2).

4.11.4.3 GAS FIELDS

At the beginning of 1994, the total ultimate gas recovery amounted to 3495 milliard m³, 3069 onshore and 426 milliard m³ offshore. The volume of produced condensate has been ignored. To give a rough indication of this

volume, the total production in 1993 amounted to 0.76 million m³ condensate.

For both the onshore and the offshore gas fields, the Carboniferous coal measures are the main source rock and the desert sandstones of the Permian Rotliegend form the far most important reservoir rocks. These reservoirs are sealed by a thick series of Zechstein evaporites. In the eastern Netherlands gas also occurs in Carboniferous sandstones and Zechstein limestones. Only where the Zechstein salt is absent or breached, the Carboniferous gas can migrate to higher levels, such as Triassic, Upper Jurassic or Lower Cretaceous sandstone reservoirs. (Petroleum Geological Circle 1993).

Onshore Gas Fields

At the beginning of 1994, the proved reserves of all onshore gas fields were estimated to be 1386 milliard m³ and their total cumulative production was 1683 milliard m³ gas (EZ, 1994). The major onshore gas reservoir is the Groningen Gas Field, a giant field with an expected ultimate recovery of 2700 milliard m³. At the end of 1993, 1420 milliard m³ gas had been produced and the proved reserves amounted to 1280 milliard m³ (Petroleum Geological Circle 1993, EZ 1994).

The reservoir rock of the Groningen Gas Field is a sandstone of the Rotliegend Group (Slochteren Formation) *ca* 90 m thick in the south, up to 200 m in the north, at a depth of *ca* 2800 m. The gas field consists of a single reservoir formed by a shallow, dome-shaped structure of 30 × 40 km. The surface area of the gas-filled part is about 800 to 900 km². The structure is transected by numerous NW-SE faults, but these faults do not affect the overlying Zechstein salt. Initial reservoir pressure is 35 MPa and initial reservoir temperature is 107 °C (see Dozy, 1975; Van Staalduinen et al., 1979; De Jong and Dusar, 1992).

Apart from the Groningen Gas Field there are many other, but considerably smaller gas fields underneath the

Dutch onshore (Figure 4.11.2). EZ (1994) summarises the size distribution of the 132 onshore gas fields in the Netherlands. Most are very small fields: 91 fields show an ultimate gas recovery of less than 3 milliard m³ and only 15 contain more than 10 milliard m³ gas.

Offshore Gas Fields

The 154 offshore gas fields showed at the beginning of 1994 a total cumulative production of 248 milliard m³ and their proved reserves were at that time estimated to be 178 milliard m³ (EZ, 1994). Most are small also: 102 fields have an initial volume of gas of less than 3 milliard m³ and only 12 fields contain more than 10 milliard m³.

The offshore gas fields are predominately in the Broad Fourteen's Basin, but small gas fields occur also in the offshore part of the West Netherlands Basin and in the Dutch Central North Sea Graben.

4.11.4.4 STORAGE CAPACITY

The storage capacity is presented in Table 4.11.2 and is calculated as proposed in section 4.2. To calculate temperature and hydrostatic pressure underground, using average geothermal and hydrostatic gradients (30°C/km and 10.5 MPa/km), the following assumptions had to be made about the depth of the gas reservoirs:

- an average depth of 2000 m for all gas fields onshore, except for the Groningen Field
- an average depth of 3000 m for the gas fields offshore

The reservoir conditions of the Groningen Gas Field are known and gas expansion and CO₂ density are therefore based on the actual temperature and pressure in the reservoir.

For each hydrocarbon field, a minimum storage capacity of 10 Mt CO₂ is required to allow CO₂ injection at a reasonable rate over a longer period. This value will be used as a cut-off level. Because the data on each individual hydrocarbon field are lacking, except for the Groningen and the Schoonebeek fields, we do not know which fields are large enough to contain more than 10 Mt CO₂. However, the field size distribution in EZ (1994) indicates that 91 onshore and 102 offshore gas fields are too small (< 3 milliard m³(st) initial gas), which corresponds with a volume of ultimately recoverable gas of ca 90 and 140 milliard m³, respectively.

The storage capacity of the average oil field (Schoonebeek excluded) is estimated to be less than 5 Mt CO₂. All but the Schoonebeek field are therefore considered to be too small. The Schoonebeek field is, however, situated at a depth of slightly less than 800 m (ca 760 m, 2500 ft), so it remains questionable whether the reservoir will be suitable for CO₂ injection.

If a minimum storage capacity of 10 Mt CO₂ is taken into account, the Dutch hydrocarbon fields have a total storage capacity of 9 313 Mt CO₂ (Table 4.11.2).

4.11.4.5 DEPLETION

The Schoonebeek oil field was abandoned in 1994. A rough indication of the overall lifetime of the other Dutch hydrocarbon fields can be obtained by dividing the proved reserves by the annual production. The gas production in 1993 was about 84 milliard m³, 66 milliard m³ onshore and 18 milliard m³ offshore. Apart from the Schoonebeek field, the Dutch oil fields are too small for CO₂ storage, so they will not be further considered.

In combination with the proved reserves presented above, these figures lead to the following lifetimes:

- onshore gas fields 21 years
(including Groningen)
- offshore gas fields 10 years

One should realise that these general figures say little about when an individual hydrocarbon field becomes available for CO₂ disposal. Some fields may become depleted earlier, other may produce longer. The applied method assumes that the proved reserves correspond with the actual ones and that the rate of production will not grow. These assumptions are obviously not true and will make the predicted date of depletion highly uncertain. In addition, governmental decisions and the world oil and gas price are of great influence on when a field is considered to be depleted.

In the case of Dutch government, it should be noted that the current policy is to spare the Groningen Gas Field and to produce as much as possible from the other gas fields. The Gasunie, the organisation that sells the gas, states that there is enough gas to maintain the current rate of production for more than 25 years. After this period there will remain 550 milliard m³ gas, which is intended to be recovered over a period of 10 to 15 years, at a strongly reduced rate (Het Parool, November 10, 1993). This not only suggests that the Gasunie foresees gas reserves of ca 2.6·10¹² m³, but it also implies that the Groningen field will not become available before the year 2028.

4.11.5 Concluding Remarks

Previous studies on CO₂ disposal in the onshore aquifers of the Netherlands give total storage capacities of 40–82 Gt (Van Engelenburg and Blok, 1991), 2.5–10 Gt (Huurdeeman 1992), and 1.2 Gt CO₂ (Van der Meer et al., 1992). In the present study the storage capacity of traps on the onshore aquifers is estimated to be ca 1.0 Gt CO₂. This capacity is low, even compared to the study by Van der Meer et al., (1992). Apart from different basic assumptions, the low capacity in this present study can be ascribed to a much more conservative attitude by using severe constraints on the quality of the aquifers.

For the Dutch onshore, it is concluded that the CO₂ storage capacity of most traps on aquifers is very limited. If a minimum capacity of 10 Mt CO₂ is required, most reservoirs will be too small and a specific site has to be selected where the total pore volume of a combination of traps and aquifers is large enough to retain more than 10 Mt CO₂. One should realise, however, that the method we applied only considers structural traps confined to the boundaries of the studied map sheets. We may therefore have overlooked closed structures extending beyond the map boundaries. For example, the Groningen Gas Field extends over an area of 800–900 km² and shows a Permian reservoir of 90–200 m thick. The gas produced in this area has the same pressure and composition, which indicates that the gas originates from one large reservoir with an estimated pore volume of ca 20 km³ (850*0.15*16%). This means that the Groningen Gas Field alone shows a pore volume that is as large as the total estimated trapped pore volume of all Permian onshore aquifers in the Dutch subsurface. In addition, the storage capacity of 1.0 Gt CO₂ does not include the potential of very large reservoirs formed by porous rocks completely sealed off from other

formations, such as large fault blocks or even entire aquifers.

The estimate of the storage potential of the Dutch hydrocarbon fields is more optimistic. We estimated that the onshore fields can contain some 8.5 Gt CO₂, which is in sharp contrast to the capacity of the aquifers of only 1.0 Gt. At first sight, these figures seem irreconcilable, since the hydrocarbon fields are contained in the aquifers. The difference can be explained by the following aspects of the method we used to assess the storage capacity:

- For aquifers only 4% of the trapped pore volume is available for CO₂ disposal, whereas for oil or gas reservoirs the entire pore volume initially occupied by (recoverable) hydrocarbons can be filled with CO₂.
- Hydrocarbon reservoirs often show a permeability that is large enough to produce oil or gas, but that is insufficient to inject CO₂ if the reservoir is water-saturated (e.g. the gas bearing Vlieland Sandstone).
- Hydrocarbon reservoirs are not restricted to small-scale structural traps, but may extend over larger areas, not recognised on the depth maps available (e.g. the Groningen Gas Field).

4.12 THE CO₂ STORAGE CAPACITY OF NORWAY

Erik Lindeberg

4.12.1 Summary

Most of the Norwegian onshore consists of crystalline basement that has no CO₂ storage potential. The scarce sediments onshore are unsuitable for CO₂ storage also, because they are too shallow. All hydrocarbon fields and deep-seated aquifers are situated offshore, mainly in three sedimentary basins in the Norwegian North Sea, the Viking Graben, the Central Graben and the Norwegian-Danish Basin. The latter basin and the offshore basins north of the 62° Northern Latitude are not included in the inventory, although they are expected to have formations suitable for CO₂ storage.

The Norwegian aquifers have an estimated CO₂ storage capacity of about 475 Gt when storage is not restricted to traps. The CO₂ storage capacity of geological traps on the aquifers (analogous to hydrocarbon traps) is estimated to be about 10.9 Gt CO₂. The total CO₂ storage potential of the hydrocarbon fields is estimated to amount to approximately 10 300 Mt CO₂, 7200 Mt in gas reservoirs and 3100 Mt in oil reservoirs. Based on the predicted commercial abandonment date for the individual fields, it is expected that an injection rate of 50 to 180 Mt CO₂ per year can be maintained from the end of this century to at least 2070.

It must be emphasised that this is a gross estimate of the theoretical potential of CO₂ storage only. No economical constraints have been put on the storage potential, neither do the estimates for the various sites include any technical or economical relative rating for which storage sites are the most promising.

4.12.2 Geological Overview

The Norwegian onshore is part of the Fenno-Scandian Shield, a basement high consisting of crystalline metamor-

phic and igneous rocks of Palaeozoic and Pre Cambrian age. The only significant amounts of sediment occur in the Oslo Graben, but even in this structural basin the sediments are too shallow for CO₂ disposal (above a depth of 1000 m). However, sediments are abundant offshore, in the Norwegian part of the North Sea, especially in the Viking Graben, the Central Graben and the Norwegian-Danish Basin (see Fig. 4.12.1). The Viking Graben and the Central Graben contain a series of post-Permian sediments about 5 to 10 km thick.

With respect to the Late Jurassic to Early Cretaceous rifting stage, the main hydrocarbon plays can be classified into pre-, syn-, and post-rift plays. From the UK sector to northern Norway, the pre-rift play is the most successful. This play has tilted fault block traps, Jurassic and older reservoirs and adjacent Late Jurassic source rocks. The total recoverable hydrocarbon resources are between 2000 and 3000 m³ oil equivalent.

4.12.3 Aquifers

4.12.3.1 ONSHORE AQUIFERS

The Norwegian onshore has no CO₂ storage potential, because sediments are scarce and too shallow for CO₂ disposal.

4.12.3.2 OFFSHORE AQUIFERS

Constraints

For aquifers that are shared between Norway and the United Kingdom, or between Norway and Denmark, only the part of the formation in the Norwegian sector has been considered. Only the major formations with more favourable reservoir properties have been included. The inventory is further restricted to aquifers south of the 62° Northern Latitude. The Haltenbanken, Norland, Barents Sea (close to industrial areas in Russia) and the Skagerak area in the Norwegian-Danish Basin are not included in the study.

Formations that contain hydrocarbons are well documented. For the formations that do not carry oil or gas, there is less information available. For the least accurately described formations some extrapolations on the basis of porosity/depth and permeability/porosity correlation, in combination with available qualitative descriptions of the lithology have been applied to get estimates of the porosity, permeability and net/gross ratio.

The background data for estimating the storage capacity of Norwegian aquifers have been collected from various sources (e.g. Vollset and Dore, 1984; Spencer, 1985, 1987; Isaken and Tonstadt, 1989; Norsk Hydro, 1992).

Storage Capacity

To estimate the CO₂ storage capacity for the offshore aquifers the total formation volumes are first determined. Average thicknesses are taken from available well data and the area distribution is obtained from geological maps. The pore volumes are next computed by multiplying the total volume with the net/gross ratio and porosity. The trapped proportion of the aquifers is assumed to be 3% of their entire volume. The Tertiary and Cretaceous show structural and stratigraphic traps. The Jurassic traps are formed by tilted, eroded fault blocks.

The estimated CO₂ storage capacity in traps on the Norwegian aquifers is based on a storage efficiency of 4%. Hence, the pore volume available for CO₂ storage is established by taking 4% of the trapped pore volume and the

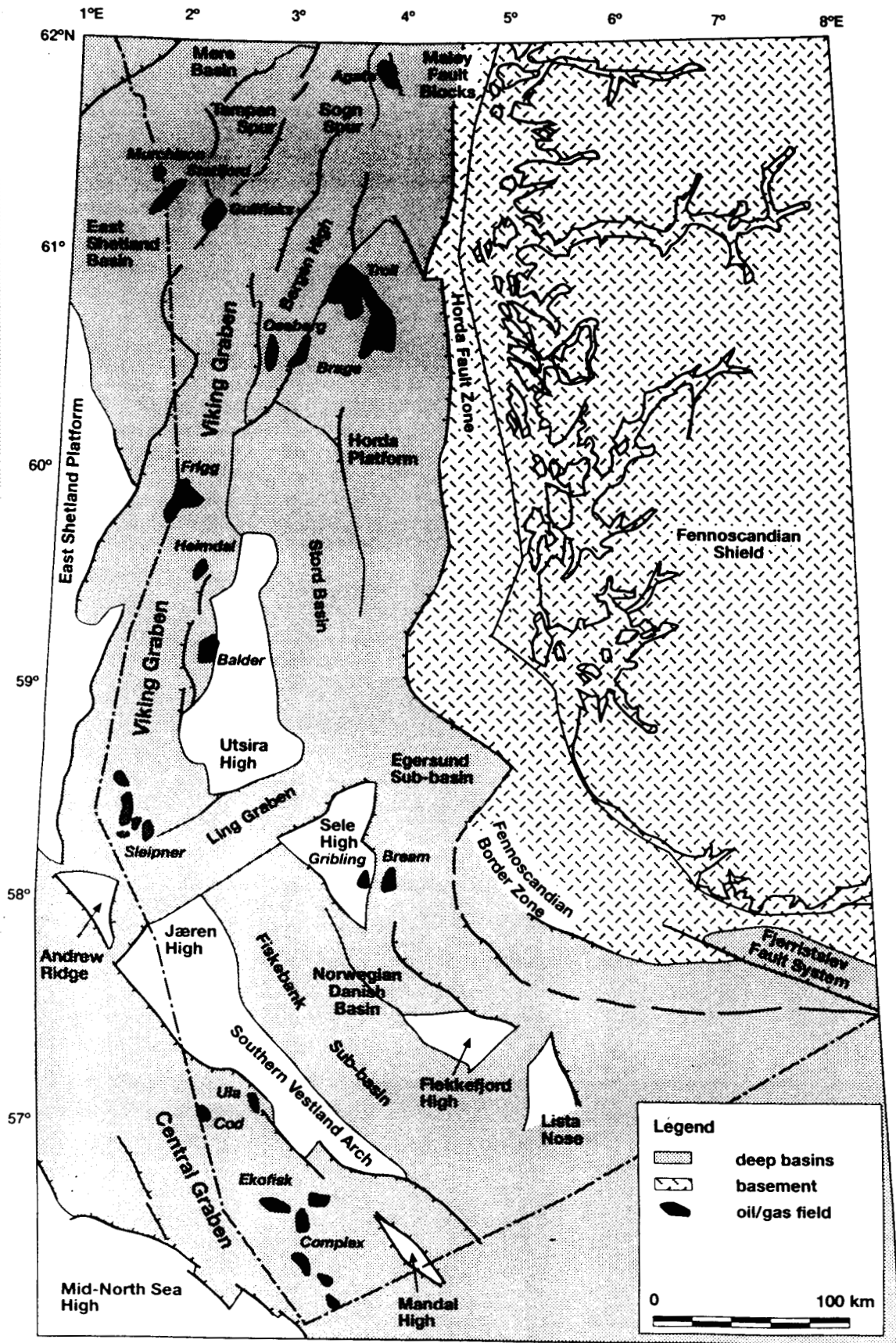


Figure 4.12.1 Map of the Norwegian offshore (south of 62°N) showing sedimentary basins and major hydrocarbon fields.

capacity is calculated by multiplying this available pore volume by the reservoir density of CO₂ (see section 4.2). The reservoir data for computing the storage capacity of CO₂ in aquifers and the results are presented in Table 4.12.1. The overall storage capacity of the trapped proportion of the aquifers amounts to ca 10 850 Mt CO₂.

The application of this method implies that the limitation of injection is when CO₂ reaches the spill point of the trap. The only aquifers where this model may be applied are Grid, Skade, Vade and Utsira, which are relatively shallow aquifers where the formation water is in direct communication with the surface water. Vade is insignificant in size, but Skade and Grid are large. Any CO₂ from Grid and Skade will, however, be trapped in Utsira, because Utsira completely covers Grid and Skade. The key point is therefore the integrity of the Utsira seal, which is considered to be high. For deeper formations CO₂ transport beyond the spill point will typically mean that CO₂ will only enter an other sealed formation which can be considered as a permanent storage. Hence, the trapped storage capacity must be considered to be very conservative and storage 'outside traps', involving the entire volume of the aquifers, will provide a far more realistic impression of the maximum technical storage capacity of the Norwegian aquifers (discussed below).

Currently, the deeper aquifers of the Norwegian offshore are not used for other purposes than hydrocarbon recovery. The aquifers have a large lateral distribution and are overlain by thick layers of impervious rocks. These cap rocks effectively seal off the aquifers from the shallow subsurface. Most aquifers considered in this inventory are below oil and gas fields which have proven seals. The youngest aquifer, the Utsira Formation, is present almost in the whole Norwegian sector of the North Sea and is sealed over its entire range by a claystone that is typically more than 100 m thick (Isaksen and Tonstadt, 1989). The quality of this seal is also indicated by the chemical composition of the Utsira formation water. In contrast to sea water, it contains no detectable amounts of sulphate (Rokke and Ofstad, 1994).

Because the Norwegian aquifers are effectively sealed off from the shallow subsurface, there is no reason why stored CO₂ should be confined by traps. If this constraint is released, the entire aquifer range becomes available for CO₂ disposal. The total storage capacity would then amount to about 475 Gt (Table 4.12.1). This estimate is based on same assumption that has been used to establish the storage capacity of the aquifers in the UK sector of the North Sea (section 4.15.3.2), i.e. the Tertiary aquifers are considered to be 'open' and have a storage efficiency of

Table 4.12.1 Theoretical CO₂ storage potential of the trapped proportion of the Norwegian aquifers offshore. The calculation is based on the assumption that 4% of the trapped pore volume can be filled with CO₂ and that 3% of the aquifer volume is in a trap. The table additionally includes an estimate of the storage capacity of the entire aquifer (not restricted to traps) in a separate column. This estimate is based on a storage efficiency of 6% for the Tertiary aquifers and the Chalk (*), and 2% for the Mesozoic aquifers other than the Chalk.

Aquifer	Age	Range (km ²)	Average Thickness m	Net:Gross	Porosity	Pore Volume (km ³)	Reservoir Density of CO ₂ (kg/m ³)	Storage Capacity in Traps (Mt CO ₂)	Storage Capacity of Entire Aquifer (Mt CO ₂)
Utsira	Miocene	32 000	150	0.65	0.35	1092	769	1008	50 385
Skade	Oligocene	13 000	120	0.65	0.32	324	719	280	13 998
Vade	Oligocene	1000	70	0.65	0.28	13	676	10	517
Grid	Eocene	10 000	137	0.65	0.28	249	623	186	9 320
Frigg @	Eocene	7500	180	0.95	0.29	372	695	310	15 509
Heimdal @	Paleocene	13 000	180	0.65	0.28	426	652	333	16 660
Hermod	Paleocene	1300	100	0.70	0.20	18	658	14	719
Ty	Paleocene	3700	180	0.70	0.20	93	664	74	3715
Vidar	Paleocene	2400	55	0.70	0.30	28	725	24	1206
Forties	Paleocene	500	120	0.70	0.25	11	716	9	451
Agat	Cretaceous	600	320	0.54	0.20	21	694	17	288
Ekofisk*	Cretaceous	32 000	150	0.85	0.35	1428	737	1263	63 146
Tor*	Cretaceous	32 000	300	0.85	0.35	2856	712	2440	122 008
Hod*	Cretaceous	32 000	300	1.00	0.35	3360	700	2822	141 120
Hidra*	Cretaceous	9000	50	0.65	0.30	88	719	76	3786
Brent+	Jurassic	15 000	303	0.75	0.28	955	742	851	14 176
Cook+	Jurassic	5000	218	0.40	0.25	109	749	98	1 631
Statfjord+	Jurassic	15 000	592	0.58	0.22	1134	761	1035	17 252
Skagerak#	Jurassic	4000	200	0.70	0.18	101	647	(78)	(1304)
Total						12 576		10 852	475 887

@ Frigg and Heimdal are connected to a large system. Frigg includes the Codd sand. Frigg's volume is not based on thickness and area figures, but is based on a internal ELF report. Range and thickness of Heimdal comes from a personal communication with ELF.

* Fractured Chalk with a low matrix permeability. The high fracture permeability, however, makes these aquifers suitable for gas injection and even large scale water injection, which both are tested.

+ The aquifer volumes are not calculated from thickness and area figures, but are based on more accurate 3-dimensional contour maps available at IKU. Average thicknesses have been derived from the aquifer volumes.

Skagerak is not included in the total revenue because of the permeability criterion, but is listed because it was considered to be a (less attractive) alternative to Utsira for deposition of Sleipner CO₂.

6% and the Mesozoic aquifers are considered to be 'closed' and have a storage efficiency of 2% except for the fractured Chalk formations (Ekofisk, Tor, Hod and Hidra). These Chalk formations are assumed to have a storage efficiency of 6%, because in these aquifers dissolution of CO₂ is expected to be the dominant storage mechanism (see section 4.2.2.3).

Deeper aquifers may communicate with producing oil and gas field. This can have either a negative or a positive effect on the hydrocarbon production. CO₂ may contaminate natural gas if it reaches a production well, or it may increase the water influx in reservoirs that have water drive. Storage of CO₂ in a shallow formation directly on top of producing reservoirs may cause corrosion of the wells penetrating the formation. This may lead to CO₂ leaking through the corroded wells, which could be a potential problem.

4.12.4 Hydrocarbon Fields

4.12.4.1 ONSHORE HYDROCARBON FIELDS

There are no Norwegian hydrocarbon fields onshore.

4.12.4.2 OFFSHORE HYDROCARBON FIELDS

All Norwegian hydrocarbon fields are situated offshore. Most fields are situated in the Viking Graben and the Central Graben. Some additional fields occur on the Norwegian Shelf north of 62°, offshore Trondheim and Hammerfest.

Constraints

The reserves in some oil and gas reservoirs are shared between Norway and UK. If a major part of the reservoir belongs to Norway, the whole reservoir is included in the inventory (Frigg and Statfjord fields). If a major part the reservoir belongs to UK, its storage capacity is not included in this inventory, but its whole storage capacity will be found on the UK inventory (Murchison field).

Storage Capacity

For the Norwegian gas reservoirs the CO₂ storage capacity is relatively easy to estimate on the basis of the recoverable hydrocarbons. The initial reservoir volume of the gas is computed from the expected ultimate recovery and the gas expansion factor (GEF). It is assumed that this volume will be available for CO₂ disposal. The reservoir temperature and initial pressure are used to calculate the density of CO₂ from an equation of state (Duan et al., 1992). See for the calculation method section 4.2.

The background data for estimating the storage capacity in Norwegian gas reservoirs has been collected from various sources (NPD, 1993, Skjæveland and Kleppe, 1992, Norsk Hydro, 1992, NED, 1993) and the results are presented in Table 4.12.2.

Oil reservoirs form more complex CO₂ storage sites, because they show a wide range of possible production histories. Combinations of various CO₂ injections schemes can be applied, but for simplicity only the two most important scenarios for the Norwegian oil fields will be

Table 4.12.2 Theoretical CO₂ storage capacity of the Norwegian gas fields and the related reservoir properties. The gas expansion factor (GEF) also accounts for the associated volume of condensate that will be produced, which is therefore kept out of the storage calculation. Starting and termination years between parentheses denote the production periods of fields in development for which final decisions are still pending.

OFFSHORE GAS FIELDS				ULTIMATE RECOVERY			PRODUCTION PERIOD		
Name	P (MPa)	T (°C)	CO ₂ density	Gas (10 ⁹ m ³)	Associated oil/cond. (10 ⁶ m ³)	GEF	Start year	End	Storage Capacity (Mt CO ₂)
Frigg	19.8	61	717	184.0	0.6	194	1977	1996	680
Odin	20.6	65	705	29.3	0.2	202	1984	1997	102
Nord-Øst Frigg	20.1	62	718	11.8	0.1	197	1983	1993	43
Øst Frigg	19.7	63	702	8.2		193	1988	1995	30
Lille-Frigg	20.0	63	708	7.0	2.7	196	1993	1999	25
Heimdal	21.7	76	658	35.6	4.2	211	1986	1997	111
Tommeliten Gam.	48.7	130	729	8.5	4.2	238	1988	1995	26
Tommeliten Alfa	48.7	130	729	7.8	4	238	1997	2005	24
Cod	59.0	161	717	7.4	2.9	300	1978	1995	18
Albueskjell	50.0	138	717	20.0	9	280	1979	2000	51
Sleipner Øst	30.0	104	648	50.0	30.3	213	1993	2002	152
Sleipner Vest	44.0	123	716	135.0	36	271	1996	2013	357
Loke	30.0	104	648	8.0	4.1	213	1994	2002	24
30/6 Gamma Nord	30.0	100	723	6.2	1.1	222	1991	2017	20
Midgard	25.1	90	641	87.0	14.3	214	(2002)	(2015)	261
Agat	45.5	118	741	43.0		271	(2005)	(2017)	118
Smørbukk	47.4	153	662	95.0	37	238	(2010)	(2022)	264
Smørbukk Sør	43.6	142	661	24.0	31	232	(2010)	(2022)	68
Troll Øst	15.8	68	565	825.0	19.2	151	1996	(2032)	3087
Troll Vest (gas)	15.8	68	565	463.0	10.8	151	(2020)	(2050)	1733
Total				2055.8	211.7				7194

mentioned here. The two most important CO₂ injection scenarios for oil fields are:

- CO₂ injection into reservoirs where the pressure is maintained by water injection. Most Norwegian oil fields are pressure maintained by water flooding. After the oil production has ceased there will still be 50–75% of the original oil in place left in the reservoir. Some of this oil can be produced by gas injection (tertiary production), during which a significant amount of water will be produced. This is unfavourable for the oil production because of the requirement of a high water processing capacity, but favourable for CO₂ storage.
- Some reservoirs are more or less pressure maintained by gas injection using hydrocarbon gas. The reservoir will therefore be converted into a gas reservoir. After many years of injection, the gas will partly be produced by pressure depletion. First after this artificial gas reservoir will be exhausted, CO₂ can be stored.

Pressure maintenance by water injection applies for most of the Norwegian oil fields, and gas injection applies for the main reservoirs of the Oseberg Field and the Statfjord Field. The other major reservoir of the Statfjord field (Brent Formation) is being water flooded.

The storage potential of CO₂ depends on the individual reservoir and what production strategy has been chosen. The estimate of the storage capacity of the reservoir is based on the assumption that the underground space available for CO₂ storage equals the reservoir volume of the ultimately produced hydrocarbons (see section 4.2).

The reservoir volume of the oil is calculated by multiplying the ultimate oil recovery by its Formation Volume Factor (B_o or FVF). If the reservoir has a gas cap, the underground gas volume is established by dividing the ultimate gas recovery by the Gas Expansion Factor ($GEF = 1/B_g$). The reservoir volumes of oil and gas are assumed to be additive. Initial temperature and pressure are used to compute the final CO₂ density at reservoir conditions. The most uncertain factor for this calculation is the estimate of the ultimate recovery.

Table 4.12.3 gives an overview of the storage capacities of the individual Norwegian oil fields. It additionally lists related reservoir properties and ultimate recovery figures. The data sources are the same as for the gas fields discussed above.

For gas and oil reservoirs, a forecast has been made for when the storage capacity technically can be available without interfering with ongoing petroleum production. This means that CO₂ injection starts after the production of hydrocarbons has ended. The forecast is based on the assumptions that each reservoir is used for a period of 15 years and that the injection will be continuous. The results are given in Figure 4.12.2. The figures for the availability for year 2032 and later (storage in Troll) are very uncertain.

For all reservoirs, CO₂ injection starts after pressure depletion or when water flooding is completed. If the injection is combined with enhanced oil recovery in water flooded oil fields, it will in some cases be useful to start CO₂ injection before the oil production has declined to much in order to minimise the long period of high water production. This could shift the injection profile somewhat forward in time. However, the possibility to store CO₂ may be postponed and the storage capacity increased, due to the experience that many reservoirs, during its production

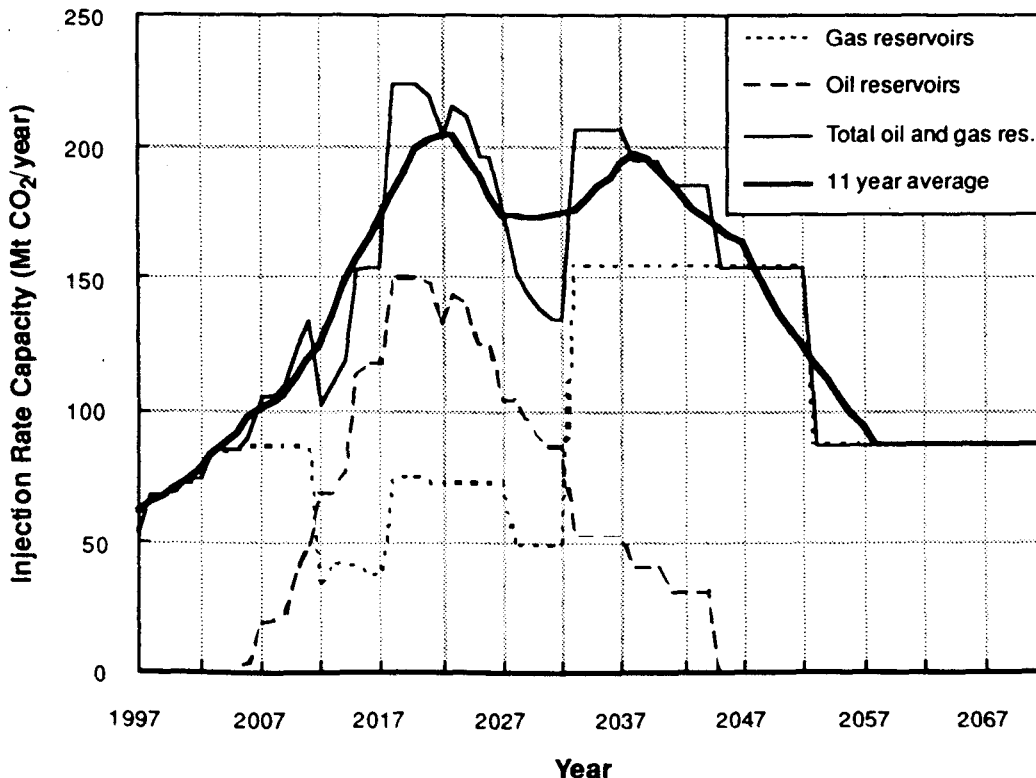


Figure 4.12.2 Estimated availability profiles for CO₂ storage in Norwegian oil and gas reservoirs.

Table 4.12.3 Theoretical CO₂ storage potential of the Norwegian oil fields. For some oil reservoirs (*) the underground volume of CO₂ corresponding to the storage capacity is larger than the underground volume of recoverable oil, because these reservoirs have large gas caps and the volume of these gas gaps are included in the storage estimate.

OFFSHORE OIL FIELDS				ULTIMATE RECOVERY			PRODUCTION PERIOD		
Name	P (MPa)	T (°C)	CO ₂ density	Oil & Condensate (10 ⁶ m ³)	FVF	Associated Gas (10 ⁹ m ³)	Start year	End	Storage Capacity (Mt CO ₂)
Ekofisk	48.5	131	725	360.0	1.78	151.0	1971	2030	465
Eldfisk	47.0	119	748	79.0	2.35	56.5	1979	2025	139
Tor	49.2	136	717	25.7	1.85	14.3	1978	2005	34
West Ekofisk	49.8	131	733	12.7	1.37	28.6	1977	2000	13
Valhall	45.2	90	822	79.6	1.65	19.0	1982	2013	108
Gullfaks	31.7	76	778	233.3	1.30	16.0	1986	2006	236
Statfjord (Brent)	40.4	100	760	465.0	1.58	52.1	1979	2009	558
Statfjord (Statfj.)	38.3	89	782	152.5	1.58	17.1	1979	2009	188
Gyda	59.4	154	734	32.0	1.69	4.2	1990	2010	40
Murchison	44.4	110	757	13.1	1.28	0.3	1980	1997	13
Snorre	38.3	92	771	133.3	1.38	6.7	1992	2011	142
Ula	49.1	143	698	71.8	1.35	4.3	1986	2009	68
Veslefrikk	32.1	122	608	45.2	1.50	3.5	1989	2008	41
Brage	21.0	86	585	47.2	1.27	1.7	1994	2010	35
Frøy	20.6	65	705	14.0	1.30	3.0	1995	2010	13
Statfjord Nord	39.8	98	756	31.0	1.28	2.5	1994	2015	30
Statfjord Øst	39.8	98	756	13.4	1.28	2.0	1994	2010	13
Tordis	40.0	95	773	19.3	1.30	1.2	1994	2007	19
Draugen	16.5	71	564	68.0	1.19	3.0	1993	2010	46
Heidrun *	25.2	85	667	87.3	1.28	37.8	1996	2011	169
Oseberg *	28.1	100	638	288.6	1.43	81.0	1988	2017	496
Balder	17.7	77	724	32.2	1.60	0.0	(2005)	(2021)	37
Gullfaks Sør *	46.0	125	724	25.6	1.60	56.1	(2005)	(2021)	162
Njord	39.0	116	698	35.0	1.59	7.2	2002	2015	39
Total				2342.3		566.6			3103

* Oil fields with large gas caps. The storage calculation is based on a gas expansion factor of 200 for Heidrun and 280 for Oseberg and Gullfaks.

period, prove to have more recoverable oil than the originally estimated. The recoverable resources of the reservoirs which were in production 10 years ago or which were decided to be developed at that time, have been increased with 30%.

From the details in Figure 4.12.2 major eras can be identified. The first era (between 1997 and 2012) is when the storage capacity is dominated by the first depleted gas fields in the area around Frigg. The next era (between 2012 and 2032) is dominated by the storage in the first depleted oil fields. The third era (from 2032 on) is dominated by storage in the Troll field.

4.12.5 Concluding Remarks

The most favourable storage sites in Norway are:

1) generally all water flooded oil reservoirs because they can give CO₂ a positive economic value.

2) almost depleted gas fields and their underlying aquifers, because they will soon be available for injection without interfering with hydrocarbon production.

3) aquifers above the hydrocarbon fields, because they are available immediately.

The oil fields are prospective candidates for tertiary CO₂ injection early in the next decade. Depleted gas fields and associated aquifers in the Heimdal and Frigg region are very attractive reservoirs considering that two platforms are already abandoned and that the production of the others will stop within a few years. There will then still be an infrastructure that could be used for CO₂ injection. Finally, the large Utsira Formation, present almost in the whole Norwegian North Sea, is a most promising candidate for CO₂ storage. Injection of 1 Mt CO₂ per year into Utsira will start in 1996.

4.13 THE CO₂ STORAGE CAPACITY OF PORTUGAL

Jean Barbier

4.13.1 Summary

Portugal is largely made up of Hercynian basement that shows no CO₂ storage potential. The only sedimentary basin is the Tagus Basin in the west of the country. Although the basin is relatively small, it contains a 5000 m thick succession of Triassic to Jurassic sediments, consisting of evaporites, carbonates, marls and sandstones. The Tagus Basin probably contains porous sediments with suitable reservoir properties and possible traps may have been generated by salt tectonics, but the quality of the seals seems to be poor, which is obviously unfavourable for CO₂ disposal. Offshore, where the succession is thicker, the conditions may be better. However, no structures are presently known that are suitable for underground storage of CO₂.

No significant accumulations of oil or gas have been discovered to date.

4.13.2 Geological Overview

Most of Portugal is composed of the Hercynian basement of the Iberian Meseta (Figure 4.14.1). The only areas that are likely to be of interest for CO₂ storage are the Tagus Basin, or Lusitanian Trough, and the Algarve Basin, which is the continuation of the Guadalquivir Basin in Spain.

The Tagus Basin is a graben containing a sedimentary succession 5000 m thick (Schroeder and Schoeneich, 1986). The most important feature of the basin is the presence of salt tectonic structures related to Triassic evaporites. The structures have been formed from the Liassic to the present (Ferreira 1971) and caused pre-Cretaceous erosion, which led to a great variance in the thickness of the Jurassic. The succession begins with Triassic and Lower Liassic evaporites, including rock salt, with marl and dolomite. The dolomite is in places cavernous (the 'Coimbra dolomite'). The overlying Upper Liassic-Dogger consists of marine carbonates. The Malm to Paleogene rocks comprise continental conglomerates and sandstones with intercalated marine limestones. The Oligocene and Miocene consist of lacustrine continental clay, sandstone and limestone. The succession ends with Pliocene arkose and shale. The same graben-fill and salt tectonic characteristics are found in the offshore continuation of the basin, but there the succession is even thicker.

The Algarve Basin is developed mainly offshore, and the stratigraphy of the basin-fill is similar to that of the Tagus Basin (Schroeder and Schoeneich, 1986).

4.13.3 Aquifers

In view of the considerable thickness of the Tagus Basin, it is very likely that the basin contains aquifers. The presence of closed structures is also probable, since the basin is dominated by salt tectonic structures. The crucial question concerns the seals. Oil exploration indicated poor sealing in the anticlines created by the rising salt (Ferreira, 1971), obviously an unfavourable characteristic for CO₂ storage. However, offshore, where the succession is thicker, it cannot be excluded that traps exist that have adequate seals. Seismic prospecting indicates the presence of dome struc-

tures in the sedimentary succession offshore (Montadert et al., 1975).

4.13.3.1 ONSHORE AQUIFERS

Inventory

Certain Mesozoic carbonates, such as the lower Lias, possess reservoir characteristics. Alves (1971, p.112) considers the Malm limestones in general as impermeable; the associated sandstones have porosities of the order of 10%, but their permeabilities are too low (<100 mD, and generally in the order of 10 mD) to constitute a potential reservoir for CO₂ storage.

In the exploration for deep aquifers, the Cretaceous continental sandstones have received the most attention (Haenel and Staroste, 1988). The investigated area is rather small, less than 300 km², and is situated around Lisbon, to the south of the Tagus Basin. The Aptian-Albian and Valanginian sandstones have porosities of about 15%, but contain reserves of fresh water, which poses a problem for any future CO₂ injection venture.

Storage Capacity

The Lower Cretaceous sandstones, in the Lisbon area, have a net thickness of 200 m. Over the 300 km² in which they have been studied, the pore volume corresponding to a porosity of 15% is 9 km³. The theoretical storage capacity in the trapped part of the aquifer is 7.6 Mt, assuming a proportion of traps of 3%, a storage efficiency of 4% and a CO₂ reservoir density of 700 kg/m³ (see section 4.2).

4.13.3.2 OFFSHORE AQUIFERS

No offshore aquifer is known with certainty.

4.13.4 Hydrocarbon Fields

Although in the Tagus Basin many showings of oil and gas have been discovered, no significant accumulations have been found. The absence of commercial amounts of oil or gas is possibly caused by the escape of hydrocarbons from poorly sealed diapirs, many of which have been truncated by erosion during Cretaceous and recent times. The only possible additional accumulation sites are on the flanks of the diapirs which, in any case, would only amount to modest quantities of oil or gas (Ferreira, 1971, Schroeder and Schoeneich, 1986).

4.13.5 Conclusion

The greater part of Portuguese onshore territory lacks deep reservoirs. Consequently, in our present state of knowledge, the CO₂ storage capacity is very small, only in the order of 8 Mt. However the sedimentological and structural nature of some areas, particularly offshore, show characteristics that indicate that additional storage capacity should not be ruled out.

4.14 THE CO₂ STORAGE CAPACITY OF SPAIN

Jean Barbier

4.14.1 Summary

Most of the Iberian Peninsula comprises a Hercynian basement overlain by a thin sedimentary cover, known as the

'Meseta'. North and south of the Meseta are strongly folded and faulted mountain ranges, in the north the Pyrenees and in the south the Betic Cordillera. The sedimentary basins are concentrated in the eastern part of the peninsula. The major Spanish basins are:

- *The Castilla Vieja Basin (Duero Basin)* This basin has been filled by terrestrial deposits that reach a maximum thickness of 2000 m.
- *The Castilla Nueva Basin (Cuenca-Albacete Basin)*
- *The Ebro Basin* The Ebro Basin is located in north-eastern Spain and contains Tertiary continental and marine sediments more than 3000 m thick.
- *The Guadalquivir Foredeep Basin* The Guadalquivir Foredeep Basin is located between the Meseta and the Betic Cordillera and contains an Eocene-Miocene limestone succession more than 4000 m thick, overlain by continental deposits.
- *The Pyrenean Basins* The tectonically highly complex Pyrenean Basins along the southern margin of the Pyrenees locally contain more than 8000 m of sedimentary rock; this anomalous thickness is due to overthrusting.

Most oil and gas is recovered from fields in the offshore extensions of these basins. Ultimate hydrocarbon recovery is approximately 40 million m³ oil and 31 milliard m³ gas.

The potential CO₂ storage capacity is estimated to be about 1 470 Mt in aquifers (in traps) and 50 Mt in hydrocarbon fields.

4.14.2 Geological Overview

The Iberian peninsula consists of a Hercynian basement overlain by a Triassic to Quaternary epicontinental sedimentary cover. The cover in the centre is very different from that at the margins of the peninsula. The former comprises thin, little-folded lacustrine successions on the 'Meseta', while the latter consists of the thick, largely marine successions of the Pyrenees, the Betic Cordillera and the Gulf of Valencia (Schroeder and Schoeneich, 1986).

The Centre Of The Peninsula

In the centre of the peninsula, most of the Hercynian basement is outcropping or overlain by a thin sediment cover. This cover is more than 1000 m thick in only three basins: the Castilla Vieja Basin, the Castilla Nueva Basin and the Ebro Basin (Figure 4.14.1).

The Castilla La Nueva Basin (The Cuenca-Albacete Basin)

The stratigraphy of the Castilla la Nueva Basin starts with a Germanic-type Triassic with marly Keuper, thin Muschelkalk and clay-sandstone Buntsandstein, all containing anhydrite. In the east of the basin, the Keuper and the base of the Lias contain a thick evaporite succession. The Jurassic is represented by a 500 m thick sequence of marine limestones and dolomites. The Cretaceous consists of carbonate, dolomite and anhydritic deposits above a thin continental sequence of sandstone and clay. The Cretaceous is capped by a Tertiary succession less than 200 m thick.

The Castilla La Vieja Basin (The Duero Basin)

Three sedimentary units can be distinguished in the Castilla la Vieja Basin. The units are bounded by major unconformities. The Triassic is thin and mostly detrital and Muschelkalk carbonates are absent. The Jurassic, where it exists, consists of platform carbonates (Casas-Sainz, 1993). The top of the Triassic-Jurassic was locally eroded before the Albian. The Jurassic is unconformably overlain by Lower Cretaceous fluvio-deltaic conglomerates, sandstones and siltstones, followed by Upper Cretaceous marine limestones. The thickness of the Cretaceous is variable. The Tertiary comprises continental clays, limestones and evaporites. It is separated from the Cretaceous by a second unconformity.

The Ebro Basin

The Ebro Basin is a foreland basin at the foot of the Pyrenees. The largely Tertiary sedimentary succession is several kilometres thick and consists of predominantly continental deposits.

In the western part of the basin, the Oligocene is made up of red clastic deposits of conglomerate, sandstone and siltstone. The Miocene, around 400 m thick, shows a similar lithology but includes intercalations of 'playa-type' evaporites with gypsum and halite (Casas-Sainz, 1993; Salvany et al., 1994). The southern limit of the western basin is formed by a large overthrust. The Mesozoic has here been thrust over Tertiary molasse deposits, which increased the thickness of the sediment pile considerably. Rocks older than the Oligocene are unknown because of the thickness of the succession.

In the eastern part of the basin, the Cretaceous is missing and a Tertiary succession similar to that described above lies unconformably on Jurassic or Triassic rock. The Jurassic is composed of marine limestones or marls (Lanaja 1987). The Triassic is of the Germanic type, with an evaporite facies (including the Rhaetian) that is locally more than 500 m thick.

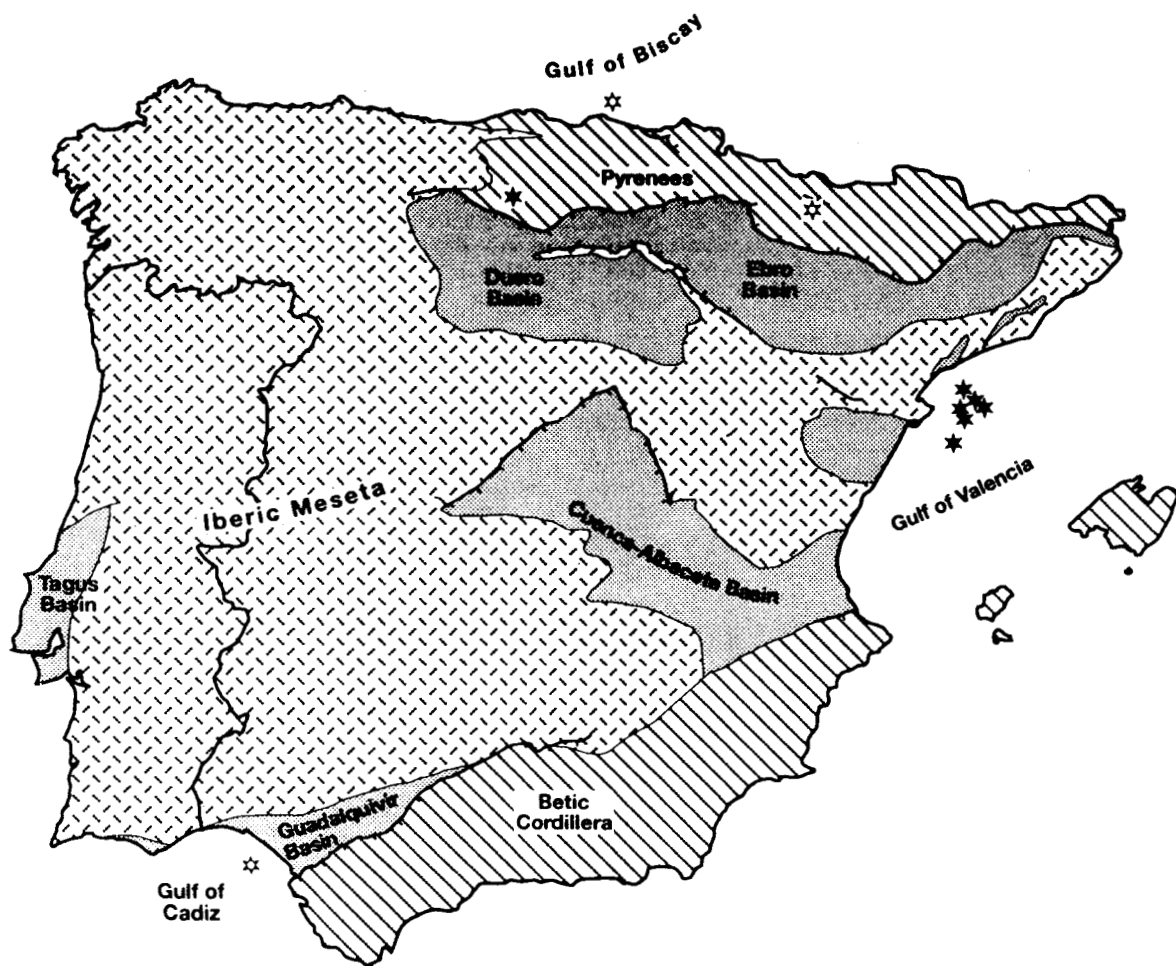
The Margins Of The Peninsula

There are two types of margin: active, folded margins located onshore (the Pyrenees and the Betic Cordillera) or even offshore (Gulf of Gascony) and passive margins taking the form of depressions or graben, located offshore.

Active Margins: the Pyrenees and Betic Cordilleras

The Duero and Ebro Basins pass in the northeast into the Pyrenean domain, which is as a fold-and-thrust belt with a 'double overthrust', meaning that both the French Aquitanian Basin on one side and the Spanish Ebro Basin on the other side, are overthrust by the Pyrenean chain (Ziegler, 1988, p.128). The structure continues offshore into the Gulf of Biscaye, where the continental shelf has been thrust over the trench (Derégnaucourt and Boillot, 1992, p.162). In tectonic terms this region is therefore extremely complex.

The stratigraphy of the Pyrenean domain is characterised by: marine Upper Cretaceous and Eocene in flysch or carbonate facies, pre-Cretaceous erosion that removed a large part of the Jurassic, and a thick detrital Buntsandstein facies in the Triassic (Lanaja, 1987). Nappe stacking resulted in a very thick sedimentary succession. In the western part of the Pyrenees, for example, the Cretaceous succession alone reaches a thickness of more than 8000 m (Brinkman and Loegters, 1968).



Legend

-  sedimentary basins more than 1000m thick
-  folded succession of the Pyrenees and the Betic cordillera
-  oil field
-  gas field
-  fault

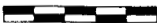
0 100 km


Figure 4.14.1 Sketch map showing the sedimentary basins in Spain and Portugal that are potentially suited for underground CO₂ storage.

In the southern part of Spain, the Guadalquivir Basin is an orogenic foredeep located between the Iberian Meseta to the north (foreland), and the Betic Cordillera (fold-and-thrust belt) to the south. Because the Betic Cordillera has overthrust the Iberian Meseta, this region is tectonically also extremely complex. A schematic section of the area can be found in Fontboté and Estevez (1980).

Passive Margins: the Gulf of Valencia

The Gulf of Valencia is a zone which extends offshore from Valencia to Barcelona. It is a graben formed during the Miocene (Ziegler, 1988, p.126), of which certain NE-SW structures continue onshore in Catalonia (Clavell and Berastegui, 1991). The Mio-Pliocene sedimentary succession reaches a thickness of 3 km. These sediments rest unconformably on platform carbonates of Jurassic to Lower Cretaceous age and a Germanic Triassic. The carbonates are karstified beneath the Miocene unconformity and there are several hydrocarbon fields in the corresponding reservoir.

4.14.3 Aquifers

4.14.3.1 CONSTRAINTS

For the study of the Spanish aquifers, there are two principal data sources: 1) reservoir descriptions from the geothermal review of Haenel and Staroste (1988), and 2) logs of oil wells supplied by Lanaja (1987). Haenel and Staroste (1988) unfortunately give detailed information on only three reservoirs. The well logs can be used to map potential reservoirs (sandstone or carbonate) but do not indicate whether these levels are in fact permeable. Yet, an approximate estimation of the reservoir potential of the deep aquifers can be obtained by combining the two data sources.

For the offshore area, there has been, of course, no geothermal prospecting. The data sources for the offshore aquifers are the well logs from Lanaja (1987), complemented by a compilation of seismic data on the Gulfs of Biscaye, Valencia and Cadiz.

4.14.3.2 ONSHORE AQUIFERS

In addition to the epicontinental basins, we have also considered the folded regions, the Pyrenees and the Betic Cordillera. The presence of hydrocarbon fields in highly folded and faulted regions prove that not only the epicontinental basins, but also the fold belts may contain suitable traps.

Inventory

The Castilla La Vieja Basin (the Duero Basin)

Haenel and Staroste (1988) classify the Upper Cretaceous marine limestones of the Castilla la Vieja Basin as aquifers. At the northeast boundary of the basin, near Vitoria, these rocks are known as the Subijana limestone. Mud losses were recorded during oil drilling and geothermal production tests of the reservoir were positive. There may also be reservoirs in the sandstone and conglomerate directly underneath, but the continuity of these fluvio-deltaic deposits would be more difficult to establish than that of the marine limestones.

The Castilla La Nueva Basin (the Cuenca-Albacete Basin)

In the Castilla la Nueva Basin, a thick Jurassic limestone, which is overlain by Cretaceous sandstones and clay (see

section 4.14.2), forms a large potential reservoir. In addition, a zone of highly porous Tertiary sand has been identified in the extreme west of the basin, north of Madrid (Lanaja, 1987). The zone is situated at a depth of 500 to 1100 m and shows reservoir characteristics over a range of about 700 km². The transmissivity here is high, ranging from 20 to 35 Dm (Haenel and Staroste, 1988).

The Ebro Basin

The aquifers of the Ebro Basin identified in places by Haenel and Staroste (1988) can be defined a little more precisely using the oil well logs of Lanaja (1987). The geothermal reservoir in the Jurassic limestone and dolomite near Huesca probably corresponds to the Upper Lias and Dogger carbonates. These carbonates are known from Lerida to Saragossa, over an area of around 5000 km². To the southeast and the northwest, they were removed during pre-Tertiary erosion and the Oligocene lies directly on the Triassic. This pre-Tertiary erosion horizon therefore determines the thickness of the carbonate reservoir, which reaches a maximum thickness of 400 m at the westernmost part of its known range.

During drilling in Lerida, potential sandstone and carbonate reservoirs of Triassic age were encountered. The Triassic carbonates mainly consist of Muschelkalk dolomite facies found between Lerida and Saragossa. The dolomite is generally 100 to 200 m thick, but locally absent. On the edges of the basin, the Tertiary lies directly on a 300 m thick package of Buntsandstein. The Buntsandstein consists of sandstones and conglomerates and might constitute a potential aquifer. Its extent, however, is unknown.

The Southern Margin of the Pyrenees

The Upper Cretaceous and the Eocene at the southern margin of the Pyrenees include marine carbonates several hundreds of metres thick (Lanaja, 1987) that constitute aquifers, at least locally. Sappenfeld and Schroeder (1968) reported an influx of salt water into a Cretaceous succession 2000 m thick during oil tests. Aquifers have also been reported in the Cretaceous and Eocene limestones in Jaca, at a depth of around 3000 m (Schroeder and Schoeneich, 1986; Haenel and Staroste, 1988).

The Guadalquivir Basin and Betic Cordillera

In the Guadalquivir Basin, as in the Betic Cordillera, a highly permeable dolomite covered by Tertiary clays and siltstones, is considered by Haenel and Staroste (1988) to be a possible geothermal target. Unfortunately, only few boreholes have penetrated the dolomite, so that its range is still unknown. The corresponding series is a very thick (1–2 km), marine succession of Lias to Lower Cretaceous carbonates.

Locally, in the Murcia region for example, the Triassic limestones and dolomites are thick enough (≥ 1 km) to represent a possible reservoir.

The Catalonia Grabens

The Catalonia Grabens are an onshore continuation of the Gulf of Valencia Graben. They are known for their thermal activity (Haenel and Staroste, 1988), but the circulation is generally along faults and the reservoirs are small. The largest graben, the Valles Graben, covers an area of less than 1000 km². In the Olot Graben, there is a limestone reservoir about 300 m thick beneath a thick evaporite seal (Haenel and Staroste, 1988).

Storage Capacity

The storage potential of the trapped part of the identified deep-seated aquifers is given in Table 4.14.1. The storage calculation is based on: 1) an inferred porosity of 10%, 2) a proportion of trapped volume of 3%, 3) a CO₂ storage efficiency of 4%, and 4) a CO₂ reservoir density of 700 kg/m³ (see section 4.2). The aquifers selected are described below.

The Castilla La Vieja Basin (The Duero Basin)

The Upper Cretaceous marine limestone in the Castilla La Vieja Basin (including the Subijana limestone) covers an area of at least 16 000 km². Its average thickness is estimated at 200 m, based on the Lanaja (1987) logs. This value is lower than the average of 500 m given by Haenel and Staroste (1988), which probably refers to all Cretaceous rocks and not only to the Upper Cretaceous carbonate facies. A thickness of 200 m is, nevertheless, a conservative estimate. The corresponding pore volume is 320 km³, giving a theoretical CO₂ storage capacity of 269 Mt.

The Castilla La Nueva Basin (The Cuenca-Albacete Basin)

The Jurassic of the Castilla Nueva Basin (Cuenca-Albacete Basin) covers an area of 10 000 km² and has an average net thickness of 500 m. This leads to a calculated pore volume of 500 km³ and a CO₂ storage capacity of 420 Mt. To these figures we should add the pore volume and storage capacity of the Tertiary of the Madrid region, being 18 km³ and 15 Mt CO₂ respectively.

The Ebro Basin

With a range of 5000 km² and an estimated average thickness of 200 m, the pore volume of the Lower Jurassic carbonates in the Ebro Basin will be 100 km³, which means a storage capacity of 84 Mt CO₂. The Muschelkalk limestone and dolomite have a comparable range but are generally thinner (*ca* 100 m). Their potential pore volume is consequently estimated at 50 km³ and the CO₂ storage capacity at 42 Mt.

The Southern Margin Of The Pyrenees

The Upper Jurassic to Eocene carbonate series (Lanaja 1987) are as much as 1000 to 2000 m thick in the region of the southern margin of the Pyrenees. They are present in an area of approximately 250 by 60 km (15 000 km²). By attributing an average net thickness of 500 m, the pore volume will be 750 km³, implying that the storage capacity is 630 Mt.

4.14.3.3 OFFSHORE AQUIFERS

Inventory

In the Gulf of Biscaye, the continental shelf is very narrow. The first 2000 m of the shelf consists of Upper Cretaceous to Eocene marls and clays, though locally the Upper Cretaceous is developed as a limestone. This limestone includes the Gaviota gas field (Schroeder and Schoeneich, 1986, Lanaja, 1987). Porosity and areal extent of this reservoir are unknown.

The Gulf of Valencia (the offshore Ebro Basin) also includes a thick sedimentary succession. The Eocene is here more than 2000 m thick, and the Mio-Pliocene more than 3000 m. The succession starts with Triassic in Germanic facies, which probably includes high-permeability sandstones. Clavell and Berastegui (1992) state that Lower Muschelkalk platform carbonates have favourable reservoir properties and that the Lias carbonates are good potential reservoirs as well. They give, however, no indications of porosities. Karstified Upper Jurassic and Upper Cretaceous carbonates below the Mesozoic-Tertiary unconformity include the reservoirs of several oil fields, e.g. Casablanca, Amposta, Dorada, and Tarraco.

The succession found in the Gulf of Cadiz consists mainly of clay. It is more than 2000 m thick. Nevertheless, several hundred metres of Lias-Dogger or Palaeocene-Eocene carbonates are locally present, for example in the onshore Guadalquivir Basin. The geographical range of these carbonates, though still undetermined, will be small.

Table 4.14.1 Theoretical CO₂ storage capacity of traps on deep Spanish aquifers. The storage calculation is based on a proportion of trapped volume of 3%, a storage efficiency of 4%, and a CO₂ reservoir density of 700 kg/m³.

Basin	Age	Range (km ³)	Average net thickness (m)	Inferred average porosity (%)	Total pore volume (km ³)	Storage capacity in traps (Mt CO ₂)
Onshore Duero	Upper Cretaceous	16 000	200	10	320	269
Cuenca-Albacete	Jurassic (Detritical) Tertiary	10 000	500	10	500	420
		700	250	10	18	15
Ebro	Jurassic Muschelkalk	5000	200	10	100	84
		5000	100	10	50	42
Pyrenean Margin	Upper Jurassic-Eocene	15 000	500	10	750	630
Offshore Gulf of Valencia		1000	50	15	8	6
	Total				1745	1466

Storage Capacity

Apart from the inferred porosities, the storage calculation for the offshore and onshore aquifers is based on the same assumptions.

Of the aquifers mentioned above, only the karst zone in the Mesozoic carbonates, corresponding to the oil fields of the Gulf of Valencia, could be defined precisely. Hence, the estimate of the offshore storage capacity will be restricted to this single aquifer. Clavell and Berastegui (1991) proposed a simple genetic hypothesis according to which the karst zone would have a thickness of about 50 m, and a porosity of 10–20%. The surface area covered by all of the oil fields, from Dorada in the north to Amposta in the south, is around 1000 km²; Amposta covers 9 km² of this area (Seemann et al., 1986). Based on these figures, the pore volume of the karst zone amounts to 7.5 km³ and its estimated CO₂ storage potential to 6 Mt.

4.14.4 Hydrocarbon Fields

4.14.4.1 CONSTRAINTS

Data concerning ultimate oil recovery are taken from the Oil & Gas Journal (1993). They correspond to data published by Seemann et al. (1986) and Clavell and Berastegui (1991) with the exception of the fields which are still in production, such as the Casablanca, the Salmonete and the Angula fields. For these fields the cumulative production figures from the Oil & Gas Journal have been used.

The proved gas reserves are those compiled by Schroeder and Schoeneich (1986) for the International Map of Natural Gas in Europe, which has been updated with information from the Oil & Gas Journal (1993) and Petroconsultants (1993). Since few fields are exploited, it is possible to estimate production and reserves of some of these fields by cross-checking.

4.14.4.2 OIL FIELDS

According to the Oil & Gas Journal (1993), the cumulative oil production at the end of 1992 was 35.9 million m³ of oil, and the reserves were only 3.6 million m³. Production is almost exclusively offshore.

Onshore Oil Fields

The only oil field onshore is the small field of Ayuolengo, which was discovered in 1964 and had a cumulative oil production of 2.5 million m³ up to 1992. Since annual production fell from 100 000 m³ in the early 80's to 20 000 m³ in 1992, this field may be considered to be nearly depleted.

Offshore Oil Fields

The oil producing zone is essentially at the mouth of the Ebro River in the offshore extension of the Ebro Basin. There are several fields, the largest of which is the Casablanca field. The others are the Amposta, Dorada, Tarraco, Salmonete and Angula fields (Figure 4.14.1). Casablanca's estimated cumulative production is about 115 million barrels of oil with an API gravity of 33° (≈ 17 million m³). The ultimate recovery of the almost depleted Amposta is 8.8 million m³ (Seemann et al. 1986). The Angula and Salmonete fields are in production since 1992, but their remaining reserves are unknown. The Dorada and Tarraco fields have been abandoned after having produced 2.8 and 2.3 million m³ oil, respectively.

In the Gulf of Biscay, the Gaviota field produces a small amount of condensate, the cumulative production being 0.6 million m³.

4.14.4.3 GAS FIELDS

According to Petroconsultants (1993), the total ultimate gas recovery at the end of 1992 was 30.6 milliard m³, 3.6 milliard m³ onshore and 27 milliard m³ offshore. These figures correspond to a cumulative production of 10 milliard m³ (1.6 onshore and 8.4 offshore) and estimated reserves of 20.6 milliard m³ (2.1 onshore and 18.5 offshore). This last figure is lower than the 25 milliard m³ (700 milliard ft³) given by the Oil & Gas Journal (1993) for proven reserves in January 1993.

Onshore Gas Fields

Near Seville, in the Guadalquivir Basin, there are many small fields less than 1000 m deep (Schroeder and Schoeneich, 1986). Marismas-3 is very shallow (300 m) with proved reserves of 0.7 milliard m³. The trap is stratigraphic, formed by sand bodies embedded in Miocene clays. These fields are mentioned only in passing, and they are not included in the estimations of CO₂ storage capacity because of their modest reserves. The Castillo field in the southern margin of the Pyrenees is too small for CO₂ disposal also. It produced only 0.03 milliard m³ from a Cretaceous limestone reservoir.

The Serrablo field (Jaca, Pyrenees), the largest onshore gas field in Spain, is hosted in fractured Eocene limestone. Production began in 1984 at a rate of 0.8 million m³ per day. Ultimate gas recovery was initially estimated at 2.5 milliard m³ (Schroeder and Schoeneich, 1986). This field is, however, listed by Carmalt and St. John (1986) in their review of giant fields as having 'recoverable reserves' of 3500 milliard ft³ (100 milliard m³). The difference from the previous figure is not explained, although it may refer in one case to commercial production and in the other to gross reserves.

Offshore Gas Fields

There are two gas producing zones, in the Gulf of Cadiz, in the continuation of the Guadalquivir Basin, and especially in the Gulf of Biscaye. Several small fields are known in the Gulf of Cadiz, the largest of which is Atlantida with 1.2 milliard m³ of ultimately recoverable gas. The total ultimately gas recovery in the Gulf of Cadiz is estimated to amount to 3 milliard m³. The reservoirs are in Miocene sandstone the top of which is at a depth of 1500 m.

The Gaviota gas field in the Gulf of Biscay is the largest known in Spain. The pay horizon is located in a Upper Cretaceous limestone at a depth of 2500 m. The Albatros field, which should enter into production in 1995, is located 18 km from Gaviota. The initial reserves of the Gaviota-Albatros field have been estimated at 12 milliard m³, but cross-checking with recent data make it possible to suggest a different figure of 24 milliard m³. According to Petroconsultants (1993), the total initial reserves discovered offshore (in Gaviota, Albatros and in the Gulf of Cadiz) are 755 milliard ft³ or 27 milliard m³. Hence, if we disregard the small fields known in the Gulf of Cadiz, the total Gaviota-Albatros field will have an ultimate gas recovery of 24 milliard m³.

A small amount of gas is present in the Miocene sand lenses around the Amposta oil field. Injection of this gas into the Amposta oil reservoir was attempted in order to maintain production (Seemann et al., 1986).

Table 4.14.2 Theoretical storage capacity of the major Spanish hydrocarbon fields onshore and offshore. Oil reserves are unknown and the storage estimate for oil is therefore confined to the volume of cumulative oil production. The storage calculation is based on a CO₂ reservoir density of 700 kg/m³, and an oil formation volume factor of 1.2. The gas expansion factor has been derived from the reservoir pressure, which, in turn, has been calculated from the depth of the reservoir, using a hydrostatic gradient of 10.5 MPa/km. If no depth values were available a gas expansion factor of 200 has been used. Storage capacities of fields with a capacity of less than 10 Mt have been excluded.

FIELDS		OIL		GAS		TOTAL
Name	Depth (m)	Cumulative production (million m ³)	Storage capacity (Mt CO ₂)	Ultimate recovery (billion m ³)	Storage capacity (Mt CO ₂)	Storage capacity (Mt CO ₂)
ONSHORE						
Ayoluengo*	1600?	2.5				
Serrablo	3000			2.5		
OFFSHORE						
Amposta*	3050?	8.8				
Atlantida	?			1.2		
Cadix	1450			1.5		
Casablanca	2700?	17.0	14.3			14.3
Dorada#	2040?	2.8				
Gaviota/Albatros	2500	0.6		12.0	38.3	38.8
Tarraco#	2750?	2.3				
TOTAL		34.0	14.3	17.2	38.3	53.0

* almost depleted

abandoned

4.14.4.4 STORAGE CAPACITY

The CO₂ storage capacity of the Spanish oil and gas fields is calculated as proposed in section 4.2 (see Table 4.14.2). The density of CO₂ at reservoir conditions is assumed to be 700 kg/m³. The reservoir volume of oil was calculated using a formation volume factor (FVF) of 1.20. The gas expansion factor (GEF) was deduced from the reservoir pressure which was, in turn, inferred from the reservoir depth by using an average hydrostatic gradient of 10.5 MPa/km (see section 4.2). The depth of the various gas fields is from Schroeder and Schoeneich (1986).

To establish the storage capacity of the hydrocarbon fields, only sites with a capacity of more than 10 Mt CO₂ have been taken into consideration (section 4.2). Only the Gaviota gas field and the Casablanca oil field satisfy this condition. They have a total estimated storage capacity of 53 Mt CO₂. Nevertheless, it should be noted that the Serrablo and the Amposta Marino oil fields and the gas fields in the Gulf of Cadiz all have significant theoretical capacities of more than 5 Mt CO₂.

4.14.4.5 DEPLETION

The Amposta Marino field, discovered in 1970, had an annual oil production of 0.09 million m³ in the early 80's, but no production figures are available for 1991 and 1992. It is therefore probably depleted, but its CO₂ storage potential is somewhat lower than 10 Mt. The same is true for the smaller fields of Dorada and Tarraco and the onshore field in Ayoluengo. Their current production is very low (0.02 million m³ per year).

The hydrocarbon fields that are currently depleted are all oil fields but their storage capacity is small.

4.14.5 Conclusion

Based on currently available information, the theoretical storage capacity in Spain could be around 1470 Mt for aquifers (in traps) and 50 Mt for hydrocarbon fields. These figures are only relative, for two reasons.

With respect to the aquifers, the most well-known zones are those of Vitoria (Subijana), Madrid, Burgos (Duero Basin) and the offshore Gulf of Valencia. The corresponding storage potential is around 280 Mt (the areal extent of the Madrid Tertiary and the Subijana limestone is small compared to that of the Upper Cretaceous Duero unit), but probably represents only a small part of the real potential of the sedimentary basins.

For the hydrocarbon fields, several factors might affect the value of the calculated storage capacities. Factors which could increase this figure are: 1) the ultimate recovery of the Gaviota-Albatros group which could be much larger than the 12 billion m³ used in this study, and 2) taking into account the smaller fields such as Amposta Marino, of which the ultimate recovery is just below the cutoff value of 10 Mt CO₂. A factor which might decrease the storage capacity is the permeability of the Gaviota and Albatros reservoirs, which might be insufficient for injecting CO₂.

The only hydrocarbon deposits which will be depleted in the near future are small. Consequently, no CO₂ storage reservoir with a capacity greater than 10 Mt can be expected among them. On the basis of current knowledge, the only large potentialities in the short term are those of the most well-known deep aquifers, the Cretaceous in the Duero Basin and those of the Mesozoic karst reservoir in the Gulf of Valencia.

4.15 THE CO₂ STORAGE CAPACITY OF THE UNITED KINGDOM

S. Holloway and H. E. Baily

4.15.1 Summary

Amongst the major deep aquifers of onshore Britain, only the Portland Sandstone, Sherwood Sandstone and Permian Sandstones are sufficiently permeable to have significant CO₂ storage potential. The total storage capacity of the traps on these onshore aquifers is estimated to be around 250 Mt CO₂. There are unlikely to be any traps that have sufficient capacity to store the CO₂ from a single 500 MW power station with a 25 year lifetime.

Offshore aquifers of the UK continental shelf are vast in both number and size. However, in many offshore areas the absence of data makes it impossible to quantify accurately their storage capacity. The capacity of the entire pore volume of the North Sea aquifers is estimated to amount to ca 240 Gt CO₂ ('non-trapped' capacity). The storage capacity of the trapped fraction is estimated to be around 8.6 Gt CO₂.

The onshore oil fields are estimated to have total storage potential of about 40 Mt CO₂ and the offshore oil and gas fields of ca 7500 Mt CO₂.

The surface geology of Northern Ireland is dominated by an 800 m thick layer of Tertiary basalts which covers an area of roughly 4000 km². Consequently, the pre-Tertiary geology of the region is poorly constrained. Some Mesozoic rocks are preserved in a series of concealed, deep basins, known as the Ulster Basins. The Triassic Sherwood Sandstone in these basins is believed to have good reservoir properties, but as it contains no definite closed structures it may be unsuitable for CO₂ storage. Northern Ireland does not have any onshore oil or gas fields.

4.15.2 Geological Overview

UK Mainland: Onshore Area

The sedimentary basins of the mainland UK onshore area can be divided into four groups: Lower Palaeozoic basins, Upper Palaeozoic basins, Permian and Mesozoic basins, and Tertiary basins.

Over most of the country the Lower Palaeozoic basins were intensely folded during the Caledonian Orogeny. Very little is known about Lower Palaeozoic rocks at depth, but near the surface they have very low porosity and permeability and there is no reason to suppose that their aquifer properties will improve at depth. For this reason they do not appear to have potential for the underground disposal of CO₂.

The pre-Permian Upper Palaeozoic basins of Britain have been affected by compression and folding during the Variscan Orogeny. They are better explored than the Lower Palaeozoic basins as hydrocarbons have been found in Carboniferous rocks in the East Midlands and further data are available from geothermal and coal exploration. However, CO₂ injection trials and reservoir data from the East Midlands hydrocarbon fields indicate that Upper Palaeozoic aquifers have no significant storage potential for CO₂, because of their relatively poor porosity and permeability. Injection trials indicated that only 11.5 tonnes/day of CO₂ could be injected into the Egmont oil field without fracturing the reservoir rock.

Permian and Triassic reservoirs with significant storage potential occur in several areas: the Wessex Basin, the Worcester Basin, the Cheshire Basin, West Lancashire (the onshore eastern margin of the East Irish Sea Basin), the Solway Basin and, towards the east coast beneath parts of East Yorkshire, Lincolnshire and Norfolk (the onshore western margin of the Southern North Sea Basin). One Jurassic reservoir has storage potential in the Wessex Basin.

In the UK onshore area, Tertiary rocks are not buried deeply enough to have any CO₂ storage capacity.

Northern Ireland: Onshore Area

Over much of Northern Ireland a succession of Tertiary basalts, up to 800 m thick, is overlain by thin Quaternary rocks. The basalts unconformably overlie rocks of Cretaceous to Palaeozoic age and, in the west of the country, still older rocks outcrop. Little is known about the Cretaceous and older rocks at depth as there are few released deep wells. Nearly all data comes from where they outcrop around the margins of the basalts, mainly in the west of Northern Ireland. Here the Sherwood Sandstone Group has good reservoir properties. The Palaeozoic and older rocks which outcrop in the west of Northern Ireland have no reservoir potential for CO₂ disposal.

UK Offshore Area

The UK Continental Shelf (UKCS) can be divided into two parts: the well studied North Sea Basins, which contain vast hydrocarbon reserves, and the less well known basins to the south, west and north of the country, many of which also contain hydrocarbons, although to date, these have been discovered in lesser quantities. The geology of some of these basins, for example the English Channel and East Irish Sea Basins, is fairly well known, but the geology of others, for example the Rockall Trough, is insufficiently known to estimate their CO₂ storage capacity. Throughout the UKCS, highly permeable reservoir formations are generally of Permian and younger age. The permeability of older rocks has been adversely affected by deep burial and/or compression during the Variscan and/or Caledonian orogenies.

The North Sea

The UK sector of the North Sea contains parts of four major basins; the Southern North Sea Basin, the Central Graben, the Witch Ground Graben and the Viking Graben.

The Southern North Sea Basin contains Carboniferous rocks overlain by a Permian and Mesozoic succession which reservoirs the gas sourced from the Carboniferous coals. The main reservoirs of interest for CO₂ storage are the Rotliegend Sandstone and the Bunter Sandstone. These are sealed by Zechstein mudstones and evaporites and the Mercia Mudstone Group respectively. The margins of the Southern North Sea Basin are exposed on land, in the UK to the west and in Holland and Germany to the east. The Southern North Sea Basin is sometimes known as the Southern Gas Basin as it contains exclusively gas fields. It is separated from the Central Graben by the Mid North Sea High, an area of thin Permian and Mesozoic rocks.

The Rotliegend Sandstone and the Bunter Sandstone both appear to be hydrostatically pressured throughout the Southern North Sea. They are assumed to be part of hydraulic systems connected, albeit tortuously, to outcrop at the basin margins.

The Central Graben, Witch Ground Graben and the Viking Graben are connected Mesozoic extensional basins overlain by a thick, largely unfaulted, Cretaceous and Tertiary succession. Tertiary rocks alone are more than 3 km thick in the centre of the Central Graben. Together with their margins, the Central Graben and Witch Ground Graben (in the Outer Moray Firth) occupy the area known as the Central North Sea. The Viking Graben, together with its margins, occupies the Northern North Sea. All three contain major reservoirs and hydrocarbon resources in Jurassic, Cretaceous and Tertiary rocks. These comprise both oil and gas fields, sourced principally from the Jurassic to earliest Cretaceous age Kimmeridge Clay Formation.

There is considerable pressure variation in the Central Graben, Witch Ground Graben and Viking Graben aquifers. The vast majority of the hydrocarbon fields showed an original overpressure, although this varied considerably, depending mainly on their depth and their distance from the margins of the basin. In general terms the Cretaceous, Jurassic and older reservoirs of the Central Graben, Viking Graben and Witch Ground graben are highly overpressured, whereas on their margins (for example in the East Shetland Basin, west of the North Viking Graben) these reservoirs become less overpressured as the limits of the basin are neared and the thickness of overlying strata decreases. If large parts of the Cretaceous and older aquifers are too highly pressured to inject CO₂ into safely, then this will have a dramatic effect on the storage capacity.

The English Channel

The English Channel is the offshore extension of the Wessex Basin in onshore England and the Paris Basin in onshore France. The only significant reservoir for CO₂ storage is the Bunter Sandstone, which is confined to the western end of the Basin. It has similar properties to the Sherwood Sandstone (the name of the Bunter onshore) in the Wessex Basin onshore.

It is not known whether the aquifers are normally pressured.

The East Irish Sea Basin

The East Irish Sea Basin consists of Permo-Triassic rocks overlain by small patches of Lower Jurassic strata and underlain by Carboniferous rocks which form the source of its oil and gas resources. Permian Sandstones and the Bunter Sandstone form the reservoirs with sufficient permeability for CO₂ storage. However, the fact that all the hydrocarbon discoveries in these rocks to date are in the Bunter Sandstone suggests that the Permian sandstones are not sealed and only the Bunter Sandstone has CO₂ storage potential.

Other UKCS Basins

Other UK offshore Basins are considered to have insufficient published data to assess their potential for CO₂ storage at present. Thus they have been omitted from this geological overview.

4.15.3 Aquifers

4.15.3.1 ONSHORE AQUIFERS

Summaries of the characteristics of the UK aquifers with CO₂ storage potential are given in Table 4.15.1. Their distribution is shown in Figure 4.15.1.

As mentioned above, only Permian and Mesozoic reservoirs have any potential for CO₂ storage in the UK onshore area. A brief review of UK onshore deep aquifers is given below, to explain the reasons why many of them have been ruled out for CO₂ storage.

Cretaceous Aquifers

The Chalk is one of Britain and Northern Ireland's most important sources of potable ground water, with most water derived from fissures rather than intergranular permeability. Unless it has internal seals, the Chalk is not regarded here as having any CO₂ storage potential as its top lies at less than 800 m throughout the country.

The underlying Upper and Lower Greensand are also unlikely to be potential CO₂ stores even in areas where they are buried deeper than 800 m, in the Wessex Basin, as they are hydraulically connected to the Chalk and are usually described as a single aquifer (e.g. Downing and Penn, 1991).

The top of the Wealden Beds (Lower Cretaceous) are nowhere buried to depths of more than 800 m below OD and they therefore have no potential for the underground storage or disposal of CO₂.

Cretaceous/Jurassic Aquifers

The Purbeck Beds consist predominantly of limestones and mudstones interbedded with a few thin sandstones. A widespread anhydrite bed occurs near the base of the Purbeck Beds. They are buried to depths of more than 800 m in two areas: the centre of the Weald Basin and the southern part of the Isle of Wight. Potential for disposal in these areas is nil as no sandstones have been proven in the Purbeck Beds in the centre of the Weald Basin or on the Isle of Wight.

Jurassic Aquifers

The Portland Sandstones occur around the southern and western margin of the London Platform. They thin steadily to the south and southeast and pass laterally into mudstones of the Kimmeridge Clay Formation. To the southwest they pass laterally into fine grained limestones known as the Portland Stone. Gas and oil discoveries have been made in the Portland Sands, proving that they are sealed by the mudstones and/or anhydrite of the overlying Purbeck Beds. The Portland Sands are at depths of more than 800 m in the centre of the Weald Basin and in the southern half of the Isle of Wight. Permeability probably averages around 100 mD, so they have potential for CO₂ disposal. The sandstone is essentially clean, with no internal impermeable layers. Only very small outcrops of the Portland Sandstone occur on the SW and W margins of the Wessex Basin, but it is in hydraulic contact with the Lower Greensand on the northern margin of the basin and thus connected to outcrop. It appears to be normally pressured and thus part of a hydraulic system which is connected to the surface rather than being completely sealed.

The Corallian Beds occur at depths of more than 800 m over much of the eastern and central Wessex Basin. They are sealed by the overlying Kimmeridge Clay Formation. Permeability is too low for consideration as a potential CO₂ reservoir. However, a thin upper sandstone unit has some potential as an oil or gas reservoir on the north side of the Weald Basin, where it forms the reservoir of the Palmers Wood oil field. A lower limestone unit has some hydrocarbon potential in the west part of the Wessex Basin.

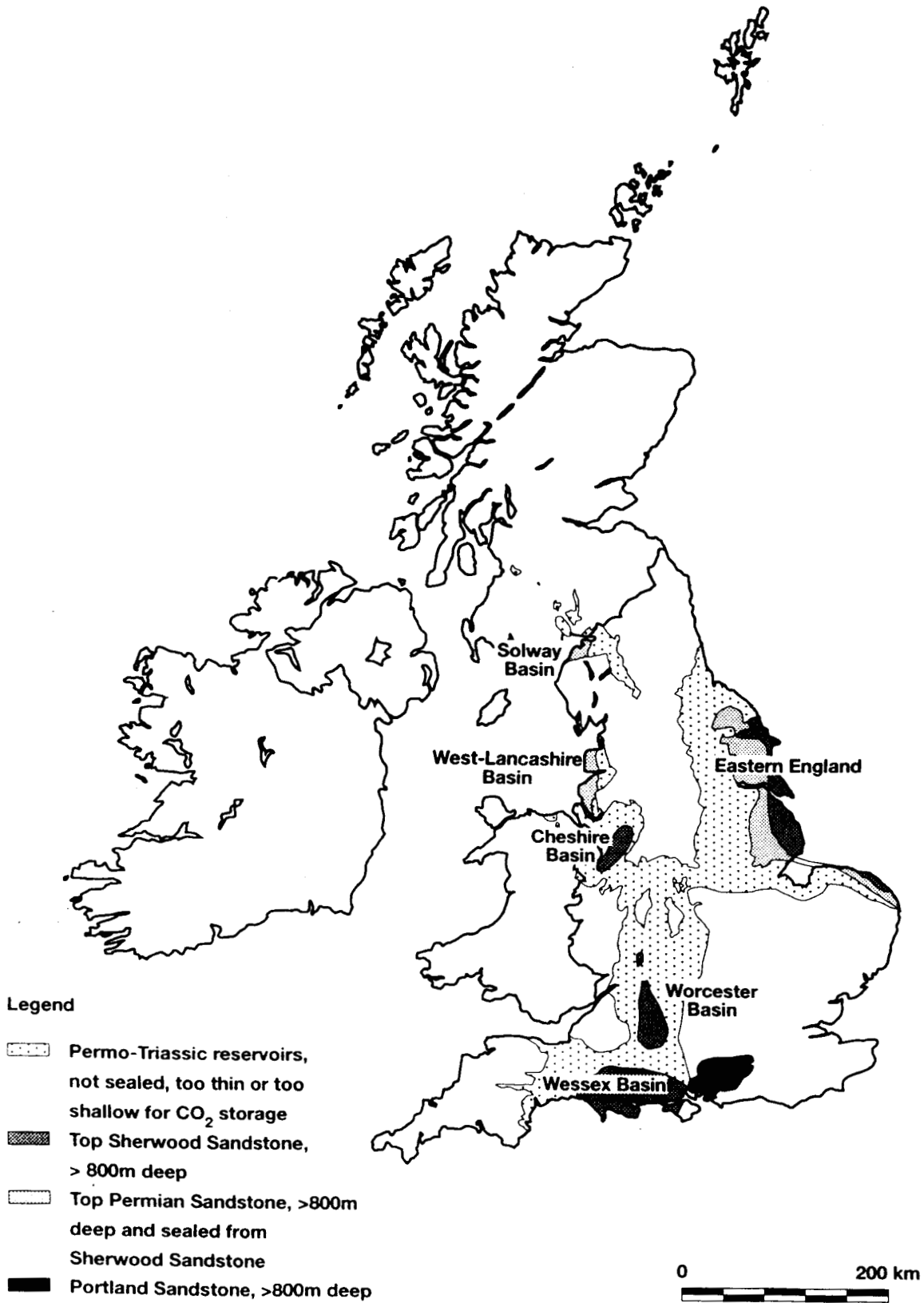


Figure 4.15.1 Location of possible areas onshore for CO₂ disposal in the UK (after Whittaker 1985).

The Great Oolite Group forms the reservoir in the Humbly Grove oil field and in numerous other (mostly small) hydrocarbon accumulations in the Weald Basin. This proves seal by the overlying Oxford Clay. Reservoir quality is best around the margins of the Weald Basin, decreasing in the basin centre due to the greater depth of burial (Penn et al., 1987). Porosity varies between 21% and less than 5% in the grainstones that form the best reservoir horizons. Primary porosity is the greatest contributor to the effective porosity, secondary porosity in the grainstones and microporosity in micrites do not contribute significantly (McLimans and Videtich, 1987). Permeability is too low for inclusion as a potential CO₂ reservoir in this study. However, the reservoir could perhaps be hydrofractured.

The Inferior Oolite Group is normally subdivided into three lithostratigraphical units, the Lower, Middle and Upper Inferior Oolite. The Lower and Middle Inferior Oolite are lithologically similar, comprising grey, sporadically ferruginous grainstones and packstones with interbedded mudstones and sandy, muddy limestones. The Upper Inferior Oolite is composed mainly of rubbly argillaceous limestones and bioclastic grainstones. The Inferior Oolite is up to 170 m thick in the centre of the Weald Basin and is sealed by the mudstones of the overlying Fuller's Earth Formation. Its permeability is too low to have CO₂ storage potential.

The Bridport Sands occur in the west of the Wessex Basin. To the east and northeast they pass laterally into ironstones and ferruginous limestones with no reservoir potential. The sandstones may have porosities of up to 30% in the clean intervals, but in some wells they contain moderate to high proportions of clay (Knox et al., 1981). The cemented horizons have porosities of less than 15% and permeabilities of less than 1 mD. Mean horizontal permeability of the Bridport Sands in a representative well, Winterborne Kingston, is 14 mD (Burgess, 1981). This is too low for inclusion as a CO₂ reservoir in this study. They are sealed either by tight limestones of the Inferior Oolite or the mudstones of the Fuller's Earth Formation, which overlies the Inferior Oolite. Seal is proven as they form one of the oil reservoirs in the Wytch Farm oil field. The Bridport Sands are buried to depths of more than 800 m in a small area in the southwest of the Wessex Basin.

Triassic Aquifers

The British Triassic can be divided lithostratigraphically into three broad groups. At the base is the Sherwood Sandstone Group, which is overlain by the Mercia Mudstone Group. The Mercia Mudstone Group is overlain by the Penarth Group, which is entirely of Rhaetian age. Neither the Mercia Mudstone Group nor the Penarth Group have significant reservoir potential on a regional scale.

By far the most important Triassic reservoir in Great Britain and Northern Ireland is the Sherwood Sandstone Group. It occurs in all the Mesozoic basins and consists of a thick succession of feldspathic sandstones which have excellent reservoir properties at depth. It is sealed by the overlying Mercia Mudstone Group. The Mercia Mudstone Group contains significant halite and both interstitial and bedded anhydrite at certain horizons.

The Sherwood Sandstone is buried to depths of more than 800 m beneath a small part of the Central Somerset Basin, large parts of the Wessex Basin, the southern Worcester Basin, the Cheshire Basin and parts of east Yorkshire, Lincolnshire and Norfolk, and also the Ulster

basins in Northern Ireland. It has very significant CO₂ storage capacity - more than half the total for the onshore UK. The Sherwood Sandstone outcrops around the margins of all these basins and appears to be normally pressured throughout the UK onshore area. Thus it is assumed to be part of a hydraulic system directly connected to the surface.

Lithologically the Group consists largely of regular fining upwards cycles of sandstone up to about 3 m thick, thought to represent continental braid plain or playa margin deposits. These commonly consist of coarse or medium grained feldspathic sandstones, variably cemented with calcite, silica and/or anhydrite, sometimes with conglomerates at their bases and thin mudstone horizons at their tops. In the southern half of the country, a conglomerate formation containing coarse, predominantly quartzite, pebbles occurs at the base of the succession, beneath the sandstone cycles. The rocks which make up the group can nevertheless be regarded as essentially clean sandstones which contain no large internal impermeable layers which might provide internal seals on a local scale.

Wessex Basin

Detailed descriptions of the lithology, petrology and distribution of the Sherwood Sandstone in the Wessex Basin are given by Knox et al. (1984), Lott and Strong (1982) and Holloway et al. (1989). In the Wessex Basin the Sherwood Sandstone forms the larger of the two reservoirs in the Wytch Farm oil field in south Dorset. According to Dranfield et al. (1987), the production capacity of the Sherwood Sandstone in Wytch Farm is about 60 000 bopd (ca 9500 m³/day). It also forms the reservoir of the Marchwood low enthalpy geothermal scheme.

Worcester Basin

In the Worcester Basin, although the Kidderminster Formation at the base of the Sherwood Sandstone has relatively low permeability, it cannot be regarded as an efficient gas-tight seal. So for gas disposal purposes, the Sherwood Sandstone is in hydraulic continuity with the underlying Permian Bridgnorth Sandstone, and the two can be treated as a single aquifer. Porosity in the Kidderminster Formation is less than 15% at depth. Porosity in the remainder of the Sherwood Sandstone is between 20–30%.

Cheshire Basin

In the Cheshire Basin the Sherwood Sandstone is also best regarded as in hydraulic continuity with the underlying Permian sandstones, although in the north of the Basin the two are separated by a variably sandy mudstone unit known as the Manchester Marl. A possible problem with gas disposal into the Permo-Triassic aquifer in the Cheshire basin is that brine is extracted from salt deposits in the sealing horizon, the Mercia Mudstone Group, by both pillar and stall methods and solution mining. It is not known how this affects the strength of the Mercia Mudstone Group.

Eastern England Basin

In East Yorkshire and Lincolnshire the Sherwood Sandstone reaches a maximum thickness of over 500 m. Over much of the area below 800 m the porosity of the Sherwood Sandstone exceeds 20%. The recent geothermal well at Cleethorpes proved 397 m of sandstone with an average porosity of about 20%. The average permeability is likely to exceed 200 mD (Downing and Gray, 1986).

Ulster Basins

The Sherwood Sandstone is believed to be thickest in the Lough Neagh-Larne Basin and the Rathlin Trough. Thickness varies from about 150 m to more than 800 m and it occurs below a depth of 800 m over much of Northern Ireland. The sandstones within the Group have been recorded as visibly porous at outcrop (Illing and Griffith, 1986) and provide good aquifers in the Belfast region. Permeability of the Sherwood Sandstone increases from west to east across the Lough Neagh-Larne Basin, probably due to better sorting and increase in grain size eastwards. Porosity and permeability are both primary (intergranular) and secondary (fissure) in origin, with fissure flow dominating in the aquifers. Intergranular porosity of the Sherwood Sandstone in Northern Ireland is generally lower than in other parts of the UK. Seal to the Sherwood Sandstone in Northern Ireland is provided by the overlying Mercia Mudstone Group, which consists of thick claystones and halites. CO₂ storage potential of the Sherwood Sandstone is likely to decrease westwards due to reduction in permeability and to the absence of bedded salt west of Lough Neagh.

The configuration of the sandstones at depth is highly debatable; seismic and gravity surveys so far have done little to elucidate the situation and consequently any estimate of the total volume of Sherwood Sandstone in Northern Ireland is somewhat tentative. It is also unclear as to what effect any Tertiary intrusions would have on the storage potential of the Sherwood Sandstone Group.

Permian Aquifers

Permian sandstones occur at depths of more than 800 m in the Worcester Basin, the Cheshire Basin, parts of west Lancashire, the Solway Basin, and the Eastern England Basin. Permian rocks beneath the Wessex Basin comprise mainly mudstones with thin breccias at the base; these have no proven reservoir potential and are not considered further here.

Worcester Basin

Thick Permian sandstones, known as the Bridgnorth Sandstone occur at depth. They are directly overlain by conglomerates of the Sherwood Sandstone. These conglomerates do not seal the Bridgnorth Sandstone, which is therefore considered to have CO₂ storage capacity only as the lower part of a Permo-Triassic aquifer which includes the Sherwood Sandstone (see above).

Cheshire Basin

Thick Permian sandstones occur at depth in the Cheshire Basin, but in the south they are not sealed from the overlying Sherwood Sandstone Group. In the northern half of the basin they are overlain by the Permian Manchester Marl. The sealing capacity of the Manchester Marl is unknown and for this reason they are considered to have no CO₂ storage capacity except as the lower part of a combined Permo-Triassic aquifer which includes the Sherwood Sandstone. Therefore no separate storage capacity estimates have been included in the tables.

West Lancashire

In West Lancashire, Lower Permian sandstones were proved as 715 m thick in the Formby-1 well. They are overlain by a thick sequence of Upper Permian mudstones, the St. Bees Shales, which are likely to form an excellent seal. The thickness of Lower Permian sandstone is poorly

known away from this one well, but seismic data suggest it is very variable in this area. An average thickness of 100 m has been assumed for volumetric purposes. The sandstones do not crop out in West Lancashire and their pressure conditions are not known.

Solway Basin

In the Solway Basin the Lower Permian Penrith Sandstone is overlain by the St. Bees Shale, which probably seals it. It is up to about 380 m thick (Silloth-1 borehole). The top 150 m has an average porosity of 15% and the lower 230 m about 8%. The downwards reduction in porosity is due to an increase in anhydrite cement (Downing and Gray, 1986). The sandstone does not crop out in the Solway Basin and it is not known whether it is connected to outcrops in the adjacent Vale of Eden. Pressure conditions are unknown.

Eastern England Basin

In East Yorkshire and Lincolnshire, relatively thin Lower Permian sands and breccias, known as the Yellow Sands, are sealed at depth by thick overlying Zechstein mudstones and evaporites. Sandstones are very thin or absent in many marginal parts of the Basin and they only consistently exceed 30 m in thickness in east Lincolnshire. The sandstones in the subsurface are thought to be connected to those at outcrop on the western margin of the basin and pressure conditions are hydrostatic.

The Yellow Sands are the lateral equivalents of the Rotliegend sandstones which form the reservoir of many of the UK gas fields in the Southern North Sea Basin. They are of variable and somewhat unpredictable lithology. They contain clean sandstones (dune sands) and also mixed conglomeratic and sandy lithologies (wadi deposits) which are often more heavily cemented. The clean sandstones commonly have permeabilities of at least 100 mD and the mixed lithologies have permeabilities of around 10 mD (Downing and Gray, 1986). Only the area which is mostly sandstone, as opposed to the less permeable breccia, has been used for volumetric purposes.

Ulster Basins

The Lower Permian Sandstone is known to be a useful aquifer around the margins of the Ulster Basins. Its distribution is variable but may be restricted to the Lough Neagh-Larne Basin. It is known to be laterally impersistent in certain areas. While the porosities and permeabilities of these sandstones seem favourable, the lack of data on their distribution means that it is impossible to calculate their CO₂ storage potential.

Carboniferous Aquifers

The Devonian and Carboniferous rocks in the UK are considered below in terms of the reservoir potential of their main geological formations. Those rocks occurring south of the Variscan thrust front (for the most part beneath the Wessex Basin) have been excluded from this discussion. They are poorly known and very heavily deformed and are so impermeable that they form the economic basement for hydrocarbon exploration in southern Britain.

Coal Measures are extremely widespread in Britain. In most areas up to about 25% of the succession may be sandstone, although higher proportions occur in the Upper Coal Measures. The sandstones in the Coal Measures have widely variable porosities and permeabilities, but porosity rarely exceeds 15% and permeabilities

average around 13 mD. The Coal Measures of all the English coal fields have been exploited by deep mining and the possibility of CO₂ leaking up dip into active, or even abandoned, coal mines is clearly a safety hazard. Furthermore, the recent surge in applications for licences to exploit coalbed methane in areas down dip from the deep mines may limit CO₂ disposal in coal fields covered by coalbed methane exploration licences. CO₂ storage potential of the Westphalian Coal Measures must be regarded as nil at present.

The main areas of occurrence of Namurian sandstones at depth are: South Wales, the East Midlands, Northwest England and Scotland. Those in northern England are for the most part too shallow to have any storage potential. In the East Midlands, many closures are proved by the presence of small oil fields in basal Westphalian and top-most Namurian sandstone reservoirs. However, it has been estimated by Bardon et al. (1993) that only 11.5 tonnes/day of CO₂ per well could be injected into these oil fields without the fracture pressure of the reservoir rock being exceeded. Therefore they have no CO₂ storage potential.

The Dinantian rocks of Britain and Northern Ireland consist overwhelmingly of limestones and shales which have very little porosity at depth. Deep groundwater does circulate through these limestones in certain areas. However, as in The Netherlands, the Dinantian limestones and shales are not likely to be considered for CO₂ storage in the near future, as more suitable and better known reservoirs are available.

Devonian Aquifers

Reservoir properties of the Old Red Sandstone in the UK are very difficult to assess, as little information is available from deep boreholes. Too little is known about its reservoir characteristics and distribution at depth to estimate its storage capacity, but the general picture seems to be that local areas of reasonable reservoir characteristics may exist.

Storage Capacity

Theoretical trapped storage capacities of the main UK aquifers onshore have been estimated to amount to about 245 Mt CO₂ and are given in Table 4.15.1.

The storage estimate is based on the following parameters and assumptions:

- cutoff 100 mD average permeability
- minimum depth of top of storage reservoir 800 m
- 1% of the aquifer volume is in a trap
- 6% of the trapped pore volume can be filled with CO₂
- average density of CO₂ at reservoir conditions of 700 kg/m³.

The rock volume of the aquifers was calculated from published maps showing the depths and thicknesses of the main reservoir formations (mainly from Whittaker, 1985, Downing and Gray, 1986 and Penn et al., 1987). Porosity and permeability values were derived from well logs and published data (Downing and Gray, 1986; Penn et al., 1987). Net:Gross ratios were estimated from well logs.

The traps on the aquifers onshore are mostly fault related structures that have a spill point much higher than the base of the aquifer. Therefore, the estimated trapped fraction of the aquifer volume has not been calculated by multiplying the surface area of the structure by the average thickness of the reservoir (as proposed in section 4.2), but is an assessment of the trapped volume above the spill point. Because the traps form 'open' reservoirs, it is assumed that 6% of the trapped pore volume can be filled with CO₂ (see section 4.2).

4.15.3.2 Offshore Aquifers

The offshore aquifers of the UK Continental Shelf are vast in both number and size. In the North Sea, Irish Sea and English Channel, reservoir characteristics and distribution of aquifers are relatively well known. However, they are comparatively poorly known in the Southwest Approaches, UK Celtic Sea and areas off the north and west coasts of Scotland (Figure 4.15.2). These areas lack producing oil and gas fields and the associated infrastructure (pipelines, platforms, etc.), and many of them contain few wells. They are considered less likely to be of interest for underground storage of CO₂ in the near future, simply because of the costs of installing infrastructure and reducing geological uncertainties by exploration. The same applies to the English Channel, although there are some data on the (generally poor) reservoir quality for this area.

Table 4.15.1 Theoretical CO₂ storage capacity of the trapped proportion of the main aquifers in the UK onshore. The storage calculation is based on the assumption that 6% of the trapped pore volume can be filled and that 1% of the aquifer volume is in a trap. An average CO₂ reservoir density of 700 kg/m³ has been used. All aquifers listed are at hydrostatic pressure.

Aquifer	Age	Range km ²	Thickness m	Net:Gross	Porosity	Pore Volume km ³	Storage Capacity* Mt CO ₂
Portland Sands	Jurassic	1 778	70	0.56	0.17	11.85	4.98
Sherwood Sandstone 1	Triassic	8 877	298	0.90	0.20	476.16	199.99
Sherwood Sandstone 2	Triassic	1 000	200	0.90	0.15	27.00	11.34
Permian Sandstone*	Permian	7 642	50	0.90	0.20	68.78	28.89
TOTAL						583.79	245.19

Sherwood Sandstone 1 is estimated from Britain (using average thickness of 298m).

Sherwood Sandstone 2 is estimated from Northern Ireland.

* Excludes where Permian Sandstones are hydraulically connected to the Sherwood Sandstone in the Worcester and Cheshire basins.

This report concentrates on the North Sea and East Irish Sea Basin (Figure 4.15.2), which are likely to be the main areas of interest. It should thus be noted that the storage capacity for the UK is actually likely to be much greater than recorded here for the North Sea and East Irish Sea alone.

The main source used here for the distribution of reservoir rocks in the North Sea is the UKOOA-sponsored Lithostratigraphic Revision of the UK North Sea (Knox and Cordey, 1992, 1993 and in prep.).

In the Northern and Central North Sea, Neogene and Palaeogene reservoirs are mostly hydrostatically pressured, the exceptions being in the deepest fields in the Central North Sea. Apart from the Utsira, Skade and Mousa Formations, they all occur below depths of 800 m over much, if not all, of their mapped range. Beneath updip parts of the East Shetland Platform and Western Platform sands may be essentially continuous to the sea bed. These areas (which, in any case, lack infrastructure) are not recommended for CO₂ storage.

Neogene Aquifers

The Utsira Formation is largely above 800 m depth in the UK sector and will not be considered for CO₂ disposal, although it probably has some potential in the South Viking Graben on the UK side of the UK/Norway median line (Figure 4.15.2). CO₂ from the Sleipner Vest field (Norwegian sector) is to be disposed of at a depth of 1000 m into the Utsira Formation, which is 250 m thick.

Palaeogene Aquifers

The Stronsay Group contains several important reservoirs including the Grid, Frigg and Tay Members. The Grid Sandstone Member consists mainly of fine to medium grained sandstone interbedded with variably silty mudstone. Total sand thickness rarely exceeds 100 m. It occurs over much of the Viking Graben, Central Graben and Witch Ground Graben. It may occur at depths greater than 800 m in about 40 UK blocks. It is sealed by the overlying Lark Formation but is connected updip to the Mousa Formation and, probably, eventually to the sea bed.

The Frigg Sandstone is a submarine fan sandstone found in the centre of the Viking Graben where it forms the reservoir of the Frigg gas field. It covers an area of about 6 blocks in the UK sector and ranges up to more than 300 m thick, although average thickness is nearer 100 m. The Skroo Sandstone Member is a lateral equivalent of the Frigg Sandstone found in the South Viking Graben but it is unlikely to be considered for CO₂ disposal, as it is too poorly developed.

The Tay Sandstone Member is a submarine fan sandstone restricted to southern parts of Quadrants 21 and 22. It is more than 200 m thick in some wells, though it contains significant proportions of mudstone.

Thick fan sandstones occur within the Balder Formation of the Moray Group in UK Quadrants 9 and 16, but their distribution is poorly known in detail. In Quadrant 9 the sandstones reservoir hydrocarbons in the Forth and Gryphon fields, where net:gross values may approach 100% in individual wells. However, the geometry of individual sand bodies in these fields is very complex and hard to predict. The disposal potential of these sands may be confined largely to the existing fields, which are at an early stage of development. The Dornoch Sandstone of similar age is likely to have good potential as a CO₂ store.

All members of the Sele Formation: the Cromarty, Flugga, Forties, Hermod, Skadan and Teal Sandstones, are

believed to be submarine sandstones and their reservoir characteristics are summarised in Table 4.15.2.

The Heimdal Sandstone Member of the Montrose Group is a submarine fan complex which occurs in the Viking Graben. It covers an area of about 40 blocks and reaches thicknesses of over 400 m. The Mey Sandstone Member is a slope apron complex consisting mainly of submarine fan sands, but including shallow marine sands at its updip limit. It is confined to the Central North Sea and Moray Firth where it is at depths of more than 800 m in about 100 blocks. The Maureen Formation consists of a submarine fan complex which occurs in both the central and northern North Sea. Its thickness is highly variable, reaching over 400 m in the sand-rich successions in parts of the Viking Graben and Moray Firth (Figure 4.15.2). On average it probably contains nearer 50 m of sand.

Cretaceous Aquifers

Porous, but low permeability, limestones of the Chalk Group are extremely widespread, occurring throughout the Southern and Central North Sea and over much of the South Viking Graben. They form oil reservoirs in the Norwegian sector (Ekofisk area) and the Danish sector of the Central Graben. This indicates that they are adequately sealed for CO₂ storage over at least parts of their distribution.

In addition to the Chalk, the Cromer Knoll Group also contains important Cretaceous reservoirs, especially the Britannia (Bosun) and Scapa Sands. The Britannia Sands form the reservoir in the Britannia gas field in the Witch Ground Graben. Sandstones of approximately the same age occur, mainly at great depth, in the Magnus Trough in the Northern North Sea. The Scapa Sands form the reservoir of the Scapa field in Quadrant 14. They are turbidite sands with average porosity of around 18% and average permeabilities of around 110 mD.

Jurassic Aquifers

The Brae Formation of the Humber Group consists of mixed conglomerates and sandstones interbedded with grey and dark grey mudstones. It is Upper Jurassic in age. It covers an area of equivalent to about 4 blocks along the western margin of the South Viking Graben. It is up to a kilometre thick in the Central Brae oil field. The Emerald Formation, which forms the reservoir in the Emerald oil field, is a thin (<30 m) sandstone which occurs on the western margin of the Viking Graben.

The Fulmar Formation is a transgressive shelf sandstone found at the base of the Humber Group in the Central Graben, where it covers an area of about 70 blocks and acts as the reservoir in the Fulmar Field. The Bruce Sandstone (reservoir of the Bruce condensate field), Birch, Burns and Claymore Members are all submarine fan sandstones, with the latter three found within the Kimmeridge Clay Formation.

The oldest two units of the Humber Group are the Magnus Member and Piper Formation which are located in the North Viking Graben and Moray Firth/Witch Ground Graben respectively.

The Beatrice and Hugin Formations of the Fladen Group are both shallow marine sandstones of Mid Jurassic age found in the Inner Moray Firth and South Viking Graben/Beryl Embankment respectively. The Pentland Formation is a prograding coastal plain deposit which mainly consists of mixed sandstones, mudstones and coals. It occurs over a wide area of the South Viking Graben, Outer Moray Firth and Central Graben. It has some reservoir potential, but

this is very hard to assess due to its variable thickness and lithology.

The Brent Group is a prograding coastal plain to deltaic sandstone of Mid Jurassic age found in the North Viking Graben and East Shetland Basin. It forms the reservoir to the major oil fields in these areas. Average permeability is about 650 mD.

The Mains and Orrin Formations of the Dunrobin Bay Group are Lower Jurassic sandstones found in the Moray Firth, while the Nansen and Statfjord Formations of the Banks group of similar age, form reservoirs in the Statfjord oil field. Average permeability in the Statfjord reservoir is 500 mD.

In the Southern North Sea Basin the main hydrocarbon reservoirs are the Lower Permian Rotliegend Sandstones and the Triassic Bunter Sandstone. In the southern and central parts of the basin, Zechstein evaporites and mudstones seal the Rotliegend reservoir, so that the higher

Bunter Sandstone reservoir does not commonly contain gas. However, it does contain some very large closures which overlie Zechstein salt swells. These are likely to be sealed by the overlying Mercia Mudstone Group and many of them may be accessible from the existing gas production platforms.

Storage Capacity

Storage in Traps

Theoretical trapped storage capacities of the main aquifers in the North Sea have been estimated to amount to ca 8.6 Gt CO₂ and are given in Table 4.15.2.

To simplify volume calculations, it has been assumed that one UK licence block is 200 km² in area (this is slightly below average for the North Sea). Detailed isopach and depth maps for most North Sea aquifers are not publicly available. Distribution maps for all the Tertiary to Jurassic aquifers are shown at small scale in Knox and

Table 4.15.2 Theoretical CO₂ storage capacity of the trapped proportion of the main aquifers in the UK offshore. The storage calculation is based on the assumption that 4% of the trapped pore volume can be filled and that 3% of the aquifer volume is in a trap. An average CO₂ reservoir density of 700 kg/m³ has been used. The Triassic Bunter Sandstone forms an exception and is assumed to have a trapped fraction of 7.5% and a storage efficiency of 6%.

Aquifer	Age	Range (km ²)	Thickness m	Net:Gross	Porosity	Pore Volume (km ³)	Trapped Storage Capacity (Mt CO ₂)
Grid	Palaeogene	8000	100	0.50	0.30	120.00	100.80
Frigg	Palaeogene	120	100	0.95	0.30	3.42	2.87
Tay	Palaeogene	2000	100	0.50	0.30	30.00	25.20
Balder*	Palaeogene	400	50	0.50	0.30	3.00	2.52
Dornoch	Palaeogene	10 000	100	0.90	0.30	270.00	226.80
Cromarty	Palaeogene	1600	60	0.50	0.30	14.40	12.10
Flugga	Palaeogene	1400	50	0.50	0.30	10.50	8.82
Forties	Palaeogene	13 000	100	0.50	0.24	156.00	131.04
Hermod	Palaeogene	10	50	0.80	0.30	0.12	0.10
Skadan	Palaeogene	600	15	0.50	0.30	1.35	1.13
Teal	Palaeogene	1200	100	0.50	0.30	18.00	15.12
Heimdal	Palaeogene	8000	200	0.50	0.30	240.00	201.60
Mey	Palaeogene	20 000	250	0.50	0.25	625.00	525.00
Maureen	Palaeogene	25 000	50	0.50	0.22	134.38	112.88
Chalk	Cretaceous	150 000	350	0.25	0.28	3675.00	3087.00
Britannia	Cretaceous	1300	100	0.50	0.20	13.00	10.92
Scapa	Cretaceous	600	75	0.50	0.18	4.05	3.40
Brae	Upper Jurassic	800	250	0.75	0.12	17.25	14.49
Emerald	Upper Jurassic	400	15	0.95	0.29	1.62	1.36
Fulmar	Upper Jurassic	14 000	135	0.95	0.23	412.97	346.89
Bruce	Upper Jurassic	200	60	0.75	0.25	2.25	1.89
Birch	Upper Jurassic	100	30	0.75	0.20	0.45	0.38
Burns	Upper Jurassic	7000	400	0.50	0.20	280.00	235.20
Claymore	Upper Jurassic	1200	100	0.90	0.20	21.60	18.14
Magnus	Upper Jurassic	150	125	0.76	0.21	2.99	2.51
Piper	Upper Jurassic	7000	110	0.80	0.24	147.84	124.19
Beatrice	Middle Jurassic	2200	50	0.41	0.21	9.47	7.96
Hugin	Middle Jurassic	1500	150	0.65	0.15	21.94	18.43
Pentland	Middle Jurassic	14 000	100	0.25	0.10	35.00	29.40
Brent	Middle Jurassic	5600	150	0.80	0.20	134.40	112.90
Mains	Lower Jurassic	4000	30	0.40	0.20	9.60	8.06
Orrin	Lower Jurassic	1000	30	0.60	0.20	3.60	3.02
Nansen	Lower Jurassic	6000	30	0.95	0.24	41.04	34.47
Statfjord	Lower Jurassic	2500	260	0.60	0.23	89.70	75.35
Bunter**	Triassic	40 000	150	0.90	0.18	972.00	3061.80
TOTAL						7521.94	8563.75

* Storage capacity from Quadrant 16 only.

** Trapped fraction of 7.5%, storage efficiency of 6%.

Cordey (1992, 1993). Net:gross ratios and porosities have been taken from published figures for oil and gas fields (mostly Abbotts 1991). For formations which contain no fields they have been crudely estimated from lithology. The density of CO₂ at reservoir conditions is assumed to be 700 kg/m³, an average for the oil fields.

Since no depth maps are available, the abundance and nature of traps could not be established. An average trapped fraction of 3% and a storage efficiency of 4% will therefore be assumed (see section 4.2). The Triassic Bunter Sandstone, however, is an exception. A depth map of this aquifer in the Southern North Sea reveals large and pronounced domes above salt diapirs that occupy 7.5% (by area) of the aquifer's distribution. A trapped fraction of 7.5% and a storage efficiency of 6% will therefore be used for the Bunter Sandstone.

Many Palaeogene aquifers are submarine fan sandstones that contain hydrocarbons. The reservoirs of these hydrocarbons include sandstone lobes embedded in impermeable mudstones. These sandstone lobes may form large stratigraphic traps for CO₂ storage and the assumption that only 3% of the aquifers is in a trap might therefore be conservative.

Storage Outside Traps

The Triassic Bunter Sandstone in the Southern North Sea Basin outcrops onshore where it is widely used for water supply. CO₂ storage should therefore be restricted to traps. However, this restriction may be released if storage is considered in the other offshore aquifers. Most of these aquifers have a cap rock that extends over a very large area and forms an effective permeability barrier between the aquifer and the overburden formations. Possible outcrops will be open to sea, not to land. If CO₂ is injected far away from the boundaries of the top seal, the risk of CO₂ escaping from these aquifers will be low (see section 4.2). Hence, a concept in which CO₂ storage is not restricted to traps could be considered.

All Paleogene aquifers are at hydrostatic pressure. To some extent, they are expected to be in hydraulic communication with the shallow subsurface. The entire aquifer can therefore potentially be used as an 'open' reservoir for CO₂ disposal, as long as the injected CO₂ does not reach

the limits of the top seal. In this concept, the Paleogene aquifers would have a storage potential of 68.3 Gt CO₂, assuming a CO₂ occupation of 6% of the entire pore volume (see section 4.2).

The Mesozoic aquifers are expected to be 'closed', because they are generally overpressured and deeply buried in fault basins. These aquifers show a total capacity of 17.5 Gt CO₂ (Chalk and Triassic excluded), assuming that 2% of their entire pore volume can be filled with CO₂. The pressure increase during CO₂ injection in these 'closed' systems will be of major concern, especially because most aquifers are significantly overpressured and sealing faults and cap rocks are near the point of leaking (see section 4.2). Hence, CO₂ injection may lead to formation water escaping from the reservoir into neighbouring rocks. It is not clear whether this will be an advantage (pressure decrease due to leakage) or a disadvantage (reduction of reservoir stability).

Dissolution of CO₂ into the formation water is considered to be the dominant storage mechanism in the Chalk (see section 4.2). Assuming that the entire volume of formation water is involved and that the CO₂ uptake by dissolution is equivalent to a CO₂ occupation of 6% of the total pore volume, the storage capacity of the Chalk will be 154.4 Gt CO₂.

Major Storage Sites

If storage in traps is considered, the Bunter Sandstone in the Southern North Sea represents a major storage site. It has a total trapped storage capacity of about 3.1 Gt CO₂ (Table 4.15.2). If storage is not restricted to traps and the injected CO₂ is allowed to spread over the largest part of the aquifer's range, two other major storage sites can be distinguished in the UK offshore: the Viking Graben and the Central Graben (Table 4.15.3), with an estimated capacity of 46 Gt and 33 Gt CO₂ respectively.

4.15.4 Hydrocarbon Fields

4.15.4.1 ONSHORE HYDROCARBON FIELDS

The theoretical storage capacities of UK onshore oil and gas fields are listed in Table 4.15.4. This table excludes the Nocton and Langar oil fields, which produced 72 tonnes

Table 4.15.3 The estimated theoretical storage capacity of the Viking Graben and the Central Graben in the UK North Sea *not* restricted to traps (outside traps). The calculation is based on a CO₂ reservoir density of 700 kg/m³. Note that not all aquifers have been included.

Location	Aquifers	Reservoir Type	Storage efficiency (%)	Total Pore Volume (km ³)	Storage Capacity (Gt CO ₂)
Viking Graben UK *	Tertiary	open aquifers	6%	381	15.99
	Mesozoic (excl. Chalk)	closed aquifers	2%	325	4.55
	Chalk	dissolution	6%	613	25.73
	Total			1318	46.3
Central Graben UK **	Tertiary	open aquifers	6%	156	6.55
	Mesozoic (excl. Chalk)	closed aquifers	2%	876	12.26
	Chalk	dissolution	6%	343	14.41
	Total			1375	33.2

* Frigg, Balder, Heimdal, Maureen, Brae, Emerald, Bruce, Birch, Magnus, Hugin, Brent, Mains, Orrin, Nansen, Statfjord, and Chalk (see Table 4.15.2). The range of the Chalk in the Viking Graben is assumed to be about 25 000 km².

** Forties, Fulmar, Burns, Piper, Pentland and Chalk (see Table 4.15.2). The range of the Chalk in the Central Graben is assumed to be about 14 000 km².

and 85 tonnes of oil respectively. The oil and gas fields occur in two main areas; the East Midlands and the Wessex Basin. The Welton field accounts for 68% of East Midlands initially recoverable reserves while the Wytch Farm field accounts for 94% of Wessex Basin reserves.

Storage capacities calculated for the onshore hydrocarbon fields are based on the assumption that the volume available for CO₂ storage equals the total volume of recovered hydrocarbons at reservoir conditions. The oil formation volume factor (FVF), gas expansion factor (GEF) and reservoir pressure and temperature for most of these fields is not publically available and estimates have been used (see section 4.2).

The total storage capacity of the onshore oil and gas fields is estimated to be 42 Mt — less than a single years UK CO₂ production from coal fired power plants. Only Wytch Farm has a large enough storage capacity to be considered as a potential 'stand alone' storage area.

4.15.4.2 OFFSHORE HYDROCARBON FIELDS

In addition to the North Sea hydrocarbon fields, the reservoirs of which have been discussed briefly above, the East Irish Sea Basin also contains a major gas field, the Morecambe Bay Field (Figure 4.15.2). Some small oil fields have also been discovered in the south of the East Irish Sea Basin recently, but no reserve estimates are officially available yet.

Table 4.15.4 Theoretical CO₂ storage capacity of the UK hydrocarbon fields onshore. FVF stands for oil formation volume factor, GEF for gas expansion factor, P for initial reservoir pressure and T for reservoir temperature. A crude oil density of 850 kg/m³(st) has been used to convert tonnes into m³'s. The CO₂ reservoir density has been calculated using the JouleII.bas program or is 700 kg/m³ where no P/T data available. P/T data for E. Midlands (*) are based on Gair et al. (1980). All numbers in italics are based on the Joule II standards to be used when relevant data are not available. A minimal storage capacity of 10 Mt has been applied, i.e. the capacities of the smaller fields are excluded.

ONSHORE FIELDS				OIL		GAS			TOTAL	
Name	P (MPa)	T (°C)	CO ₂ Density	Ultimate Recovery (10 ⁶ m ³)	Storage capacity (Mt CO ₂)	FVF	Ultimate Recovery (10 ⁹ m ³)	Storage Capacity (Mt CO ₂)	GEF	Storage Capacity (Mt CO ₂)
Wytch Farm	<i>16.80</i>	52	722	48.235	41.79	1.2				41.79
Wareham			700	0.824		1.2				
Kimmeridge			700	0.365		1.2				
Humbly Grove			700	1.071		1.2				
Hordean			700	0.165		1.2				
Palmers Wood	<i>9.98</i>	28.5	700	0.494		1.2				
Singleton			700	0.235		1.2				
Stockbridge			700	0.327		1.2				
Beckingham W *	9.55	42.5	700	0.012		1.1				
Crosby Warren*	9.55	42.5	700	0.073		1.1	0.01		139	
Farleys Wood*	9.55	42.5	700	0.035		1.1				
Hatfield Moors			700				0.14		200	
Long Clawson*	9.55	42.5	700	0.424		1.1				
Nettleham*	9.55	42.5	700	0.271		1.1				
Rempstone*	9.55	42.5	700	0.424		1.1				
Scampton North*	9.55	42.5	700	0.235		1.1				
Stainton*	9.55	42.5	700	0.035		1.1				
Welton*	15.40	54.0	679	3.882		1.1				
West Firsby*	9.55	42.5	700	0.186		1.1				
Whisby*	9.55	42.5	700	0.141		1.1				
Eakring*+	9.55	42.5	700	0.329		1.1				
Dukes Wood*+	9.55	42.5	700	0.706		1.1				
Caunton*+	9.55	42.5	700	0.045		1.1				
Kelham Hills*+	9.55	42.5	700	0.344		1.1				
S Leverton*+Y	9.55	42.5	700	0.058		1.1				
Plungar*+	9.55	42.5	700	0.515		1.1				
Egmanton*+Y	9.55	42.5	700	0.509		1.1				
Bothamsall*+Y	9.55	42.5	700	0.391		1.1				
Corringham*+Y	9.55	42.5	700	0.055		1.1				
Beckingham*+Y	9.55	42.5	700	0.345		1.1				
Gainsborough*+Y	9.55	42.5	700	0.533		1.1				
Apley Head*+	9.55	42.5	700	0.004		1.1				
Torksey*+Y	9.55	42.5	700	0.008		1.1				
Glentworth*+Y	9.55	42.5	700	0.031		1.1				
Trumfleet*+	9.55	42.5	700							
Lockton										
Eskdale							0.02		200	
TOTAL				61.305	41.79	0.17	-			41.79
				<i>Total capacity of fields that can hold less than 10 Mt CO₂</i>						(10.83)

+ ceased production; Y production figures available to 1981 only.

Storage Capacity

The theoretical total storage capacity of the hydrocarbon fields in the UK offshore area is estimated to be 7496 Mt CO₂.

The theoretical storage capacity of individual offshore hydrocarbon fields has been calculated in the same way as for onshore fields, and is based on the projected recovery of hydrocarbons (Table 4.15.5). The estimates of initial recoverable reserves for the UK offshore oil and gas fields are taken from 'The Development of the Oil and Gas Resources of the United Kingdom' — otherwise known as the 'Brown Book' (Department of Trade and Industry 1993). Only the proven reserves have been taken into account. Some oil fields, e.g. Crawford, have already ceased production and other oil fields and some gas fields are also about to become available.

The Statfjord and Frigg fields, which cross the UK/Norway median line but are mostly in the Norwegian sector are included in the Norwegian calculations (section 4.12). The Murchison field, which is mainly in the UK sector is included in the UK calculations below.

Availability of Storage Capacity in the UK Offshore Hydrocarbon Fields

Assuming that an individual field will become available for CO₂ storage on its projected commercial abandonment date, the availability of storage capacity in each year can be calculated. This is shown graphically in Figure 4.15.3. The fields have been categorised as oil fields, gas fields and fields containing both oil and gas. Abandonment of the largest oil field (Forties) is predicted at 2009 and of the largest gas field (Leman) at 2011.

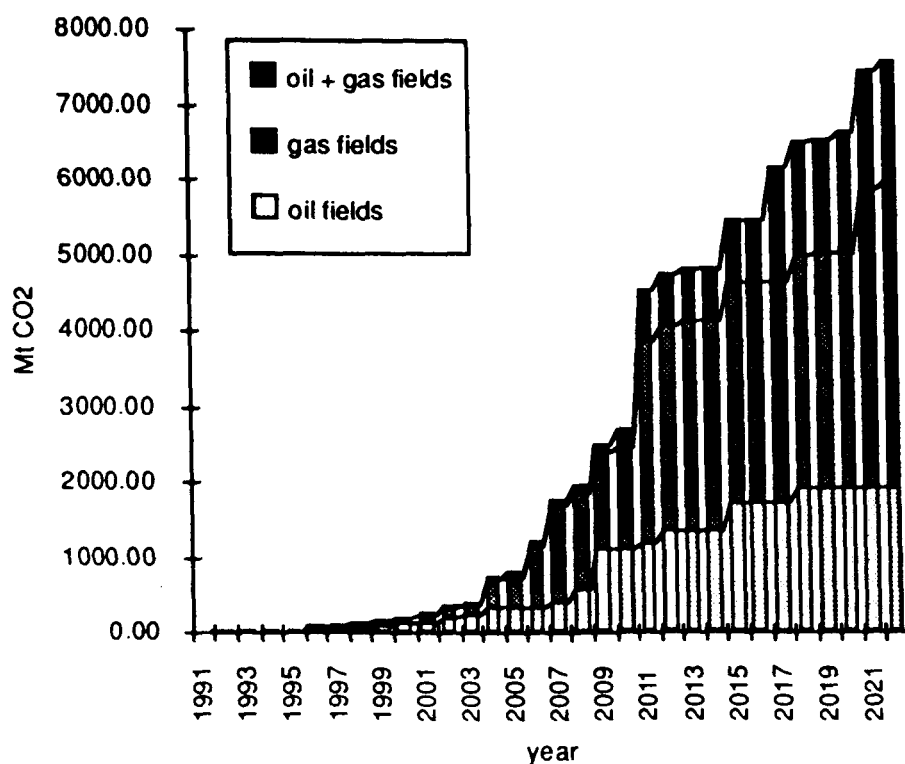
Table 4.15.5 Theoretical CO₂ storage capacity of the UK offshore hydrocarbon fields. Where gas expansion factor (GEF) not available, it is calculated from P/T data (see section 4.2). GEF values in italics are average values. A minimal storage capacity of 10 Mt has been applied, i.e. the capacities of smaller fields are excluded. See for further explanation Table 4.15.4.

OFFSHORE FIELDS				OIL			GAS			TOTAL
Name	P (MPa)	T (°C)	CO ₂ Density	Ultimate Recovery (10 ⁶ m ³)	Storage Capacity (Mt CO ₂)	FVF	Ultimate Recovery (10 ⁹ m ³)	Storage Capacity (Mt CO ₂)	GEF	Storage Capacity (Mt CO ₂)
Alba			700	59.67	50.12	1.20				50.12
Alwyn North	45	110	760	34.12	46.67	1.80				46.67
Alwyn North	49.6	120	761				26.70	73.89	275	73.89
Amethyst E & W	28.3	88	694				23.90	70.58	235	70.58
Anglia			700				6.70	23.45	200	23.45
Angus			700	1.36		1.20				—
Arbroath	25.5	118	525	17.29	12.08	1.33				12.08
Argyll			700	11.41		1.20				
Audrey			700	0.00			18.00	63.00	200	63.00
Auk	28	102	630	16.82	12.19	1.15				12.19
Balmoral	21.7	97	541	15.68	10.69	1.26				10.69
Barque	26.5	76	713				24.80	77.22	229	77.22
Beatrice	20	80	599	24.35	15.90	1.09				15.90
Beryl	33.8	97	716	149.41	181.86	1.70				181.86
Blair			700	0.10		1.20				
Brae N., S. & C.	48.9	121	754	87.80	115.85	1.75	55.00	126.43	328	242.29
Brae East			700	45.41	38.15	1.20	40.10	140.35	200	178.50
Brent	41	96	777	308.71	431.76	1.80				431.76
Bruce			700	28.24	23.72	1.20	78.00	273.00	200	296.72
Buchan	51.7	106	811	15.29	15.01	1.21				15.01
Camelot	19.6	66	681				6.20	21.11	200	21.11
Camelot NE.	19.6	66	681				0.90		192	
Chanter	26.1	77	718	1.18		1.10	0.80		218	
Claymore	27.1	77	729	90.82	72.83	1.10				72.83
Cleeton	28.6	79	737				7.90	25.31	230	25.31
Clipper	26.5	79	713				14.20	44.21	229	44.21
Clyde	44.5	147	655	20.82	16.91	1.24				16.91
Cormorant North	34.8	99	718	64.82	59.58	1.28				59.58
Cormorant South	34.8	99	718	32.00	29.41	1.28				29.41
Crawford	23.9	88	631	0.59		1.36				
Cyrus	23.6	111	517	2.00		1.19				
Della			700				1.70		200	
Deveron	34.5	104	697	3.18		1.12				
Don	49.8	129	738	4.94		1.36				
Donan			700	3.29		1.20				
Duncan			700	2.94		1.20				
Dunlin	41.5	99	771	57.76	50.33	1.13				50.33
Eider	34.6	107	688	15.65	12.38	1.15				12.38
Emerald	16.7	60	662	3.53		1.14				
Esmond	15.7	56	670				9.00	36.11	167	36.11
Everest			700	4.12	3.46	1.20	23.70	82.95	200	86.41

Table 4.15.5 Continued.

OFFSHORE FIELDS			OIL				GAS			TOTAL
Name	P (MPa)	T (°C)	CO ₂ Density	Ultimate Recovery (10 ⁶ m ³)	Storage Capacity (Mt CO ₂)	FVF	Ultimate Recovery (10 ⁹ m ³)	Storage Capacity (Mt CO ₂)	GEF	Storage Capacity (Mt CO ₂)
Forbes	19.3	67	669				1.40		167	
Forties	22.2	61	751	391.53	376.37	1.28				376.37
Fulmar	39.3	141	626	84.35	75.51	1.43	7.47	23.38	200	98.89
Gannet			700	24.59	20.65	1.20	3.90	13.65	200	34.30
Glamis	31.5	119	611	2.71		1.64				
Gordon	18	62	677				4.10	16.62	167	16.62
Hamish			700	0.39		1.20				
Heather	34.1	113	661	16.12	16.51	1.55				16.51
Hewett			700				115.00	402.50	200	402.50
Highlander	29.3	93	684	11.65		1.15				
Hutton	43.4	107	759	32.24	27.40	1.12				27.40
NW Hutton	51.3	118	776	18.24	19.81	1.40				19.81
Indefatigable	28.4	91	682				128.00	382.88	228	382.88
Innes			700	0.82		1.20				
Ivanhoe	24.2	79	682	9.51		1.22	0.18		209	
Kittiwake	45	117	740	7.88		1.20				
Leman	20.8	52	783				324.20	1108.51	229	1 108.51
Linnhe			700	0.12		1.20				
Lomond			700	2.00	1.68	1.20	14.20	49.70	200	51.38
Lyell			700	4.71		1.20				
Magnus	45.9	116	749	120.12	128.65	1.43				128.65
Maureen	26.1	117	539	32.94	21.31	1.20				21.31
Miller	50	121	761	37.65	56.44	1.97				56.44
Moira			700	0.71		1.20				
Montrose	25.8	125	504	15.41	11.73	1.51				11.73
Morecambe	12.8	32	802				152.00	818.15	149	818.15
Murchison (UK)	43.4	110	750	60.07	59.02	1.31				59.02
Nelson			700	66.71	56.03	1.20				56.03
Ness			700	5.65		1.20				
Ninian	44.7	102	782	184.71	173.33	1.20				173.33
Osprey	41.4	101	764	11.06		1.09				
Petronella	23.8	71	718	5.18		1.70				
Pickerill			700				22.90	80.15	200	80.15
Piper	25.5	79	700	159.53	140.70	1.26				140.70
Ravenspur N.	31.3	104	664				35.10	98.76	236	98.76
Ravenspur S.	31	93	703				18.00	52.73	240	52.73
Rob Roy	24.2	79	682	10.41	8.66	1.22	0.63	2.06	209	10.72
Rough	31.3	92	711				10.20	28.33	256	28.33
Saltire			700	22.00	18.48	1.20				18.48
Scapa	23.3	85	636	13.76	10.16	1.16				10.16
Scott			700	70.94	59.59	1.20				59.59
Sean N. & S.	27.2	92	662				16.40	49.13	221	49.13
Staffa			700	0.99		1.20	0.04		200	
Strathspey			700	13.18	11.07	1.20	9.50	33.25	200	44.32
Tartan	32.1	102	680	17.65	22.20	1.85				22.20
Tern	24.7	93	620	33.06	23.16	1.13				23.16
Thames, Yare, Bure & Wensum	25.6	78	706				8.95	29.25	216	29.25
Thistle	41.8	104	757	70.94	63.37	1.18			200	63.37
Tiffany			700	19.75	16.59	1.20			200	16.59
Toni			700	6.24		1.20			200	—
Valiant N.	25.2	160	397				7.80	14.08	220	14.08
Valliant S.	25.2	160	397				7.50	13.53	220	13.53
Vanguard	25.2	160	397				2.60		220	—
Victor	27.9	89	685				26.00	78.46	227	78.46
Viking	30.1	85	727				80.10	244.68	238	244.68
Vulcan			700				25.50	89.25	200	89.25
Welland			700				8.60	30.10	200	30.10
West Sole	29.4	85	719				53.80	161.85	239	161.85
TOTAL				2708.79	2617.32		1421.67	4878.59		7495.91
									<i>Total capacity of fields that can hold less than 10 Mt CO₂</i> (110.42)	

Figure 4.15.3 The availability of CO₂ storage capacity in UK offshore hydrocarbon fields (source of abandonment data: Arthur Andersen).



4.16 RESULTS AND CONCLUSIONS

Rieks van der Straaten

4.16.1 The results of the inventory

Table 4.16.1 and Figure 4.16.1 give an overview of the estimated CO₂ storage capacity in geological traps for each country of the European Union and Norway. The estimates are restricted by the calculation methods and the limitations of the data set, which are described in detail in the previous sections. The column '25 years CO₂ emissions by power plants' was added to the table to give an impression of the order of magnitude of the CO₂ sources, i.e. the fossil fuel based power stations. A direct comparison between CO₂ sources and possible CO₂ sinks underground (in aquifers and abandoned hydrocarbon reservoirs) will be unrealistic because future developments in power generation were not taken into account and power plants equipped with the technology to capture CO₂ from the flue gases do not exist today. As mentioned in Chapter 3, the number of these technologically advanced power plants are expected to be low before the year 2020. So, by that time the available storage capacity will be greater than the volume of captured CO₂ by orders of magnitude.

The European (EU and Norway) cumulative CO₂ storage capacity in geological traps amounts to 63 Gt CO₂, 30 Gt in aquifers and 33 Gt in hydrocarbon fields. This amount is in the order of 67 times the entire EU power plant CO₂ emission in 1990. It should be noted that the Danish, Dutch, and German North Sea are excluded from the inventory, because for these countries the information on the offshore area was insufficient to establish a storage estimate. This part of the North Sea is expected to show a substantial CO₂ storage potential, probably in the order of several gigatonnes. In addition, the offshore domains of the United Kingdom, France, Italy, Spain, Portugal and Greece will have more storage potential than listed in Table 4.16.1.

One should further bear in mind that the storage potential of aquifers in this table is based on the concept that CO₂ disposal is confined to traps. The storage capacity of the aquifers is expected to be 25 times larger (770 Gt CO₂) if the entire aquifer pore volume is taken into consideration, i.e. if CO₂ disposal in aquifers is not confined to traps (see Table 4.16.2).

4.16.2 Favourable Storage Sites

Seventeen favourable storage sites have been selected from the inventories presented in sections 4.3 to 4.15 (Table 4.16.3): two sites formed by geological traps on Triassic aquifers (Nr 1–2), seven Permian to Miocene aquifers (or aquifer systems) which are assumed to be appropriate for CO₂ disposal outside traps (Nr 3–9), and eight gas fields (Nr 10–17). Storage in oil fields has not been considered, since it will be combined with enhanced oil recovery and is therefore too reservoir specific. The choice of the favourable storage sites is largely determined by the magnitude of their capacity (>0.5 Gt). The distance to CO₂ production areas is not taken into account, because the costs of CO₂ transport will be low compared to other costs involved (see Chapter 8). The choice is neither based on the strength and stability of the reservoir, because these properties are largely unknown and can only be established by a detailed study on the individual reservoirs.

4.16.2.1 AQUIFERS

In selecting favourable aquifer reservoirs, not only the trapped fraction of aquifers has been considered (as in Table 4.16.1), but also the aquifer volume outside traps, assuming that in some cases the entire aquifer pore volume can be applied for CO₂ disposal (Table 4.16.2). This leads to a much larger estimate of the storage potential. For example, the potential of the aquifers in the Viking and Central Graben is in the order of 600 Gt CO₂ if the entire aquifer volume is available for CO₂ storage. This amount

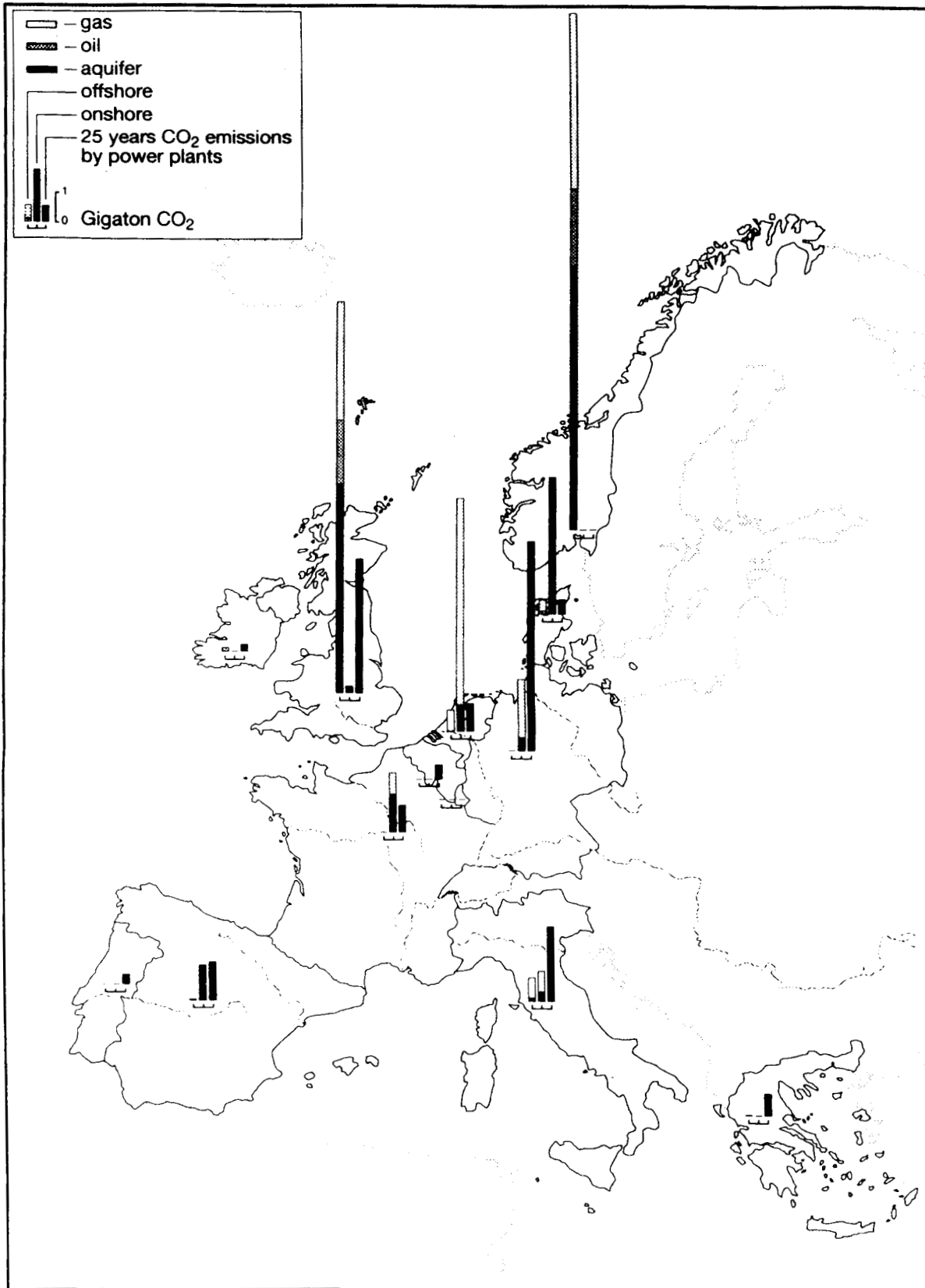


Figure 4.16.1 CO₂ storage capacity in geological traps for the EU countries and Norway. The figure additionally includes 25 years of CO₂ emissions by power plants (data from 1990; see Chapter 3). All figures are in Gt CO₂ (= Gigatonne = 1012kg). See Table 4.16.1.

Table 4.16.1 CO₂ storage capacity in geological traps for the EU countries and Norway. The table additionally includes 25 years of CO₂ emissions by power plants based on the emissions in 1990. All figures are in Gt CO₂ (= Gigatonne = 1012 kg). Fields with question marks denote that the data were insufficient to give an estimate of the storage capacity. See sections 4.3 to 4.15 for the way in which the storage capacity estimates have been established. Note that the storage capacity for aquifers is restricted to the fraction in traps.

COUNTRY	OFFSHORE				ONSHORE				TOTAL offshore & onshore	25 years CO ₂ EMISSIONS by power plants
	gas	oil	trapped aquifers	total offshore	gas	oil	trapped aquifers	total onshore		
Belgium	0.00	0.00	0.00	0.00	0.00	0.00	0.00	0.00	0.00	0.62
Denmark	0.46	0.13	?	0.59	0.00	0.00	5.60	5.60	6.19	0.58
France	0.00	0.00	?	0.00	0.88	0.05	1.53	2.46	2.46	1.11
Germany	0.00	0.00	?	0.00	2.34	0.06	0.47	2.87	2.87	8.52
Greece	0.02	0.01	?	0.03	0.00	0.00	?	0.00	0.03	0.90
Ireland	0.16	0.00	?	0.16	0.00	0.00	?	0.00	0.16	0.28
Italy	0.84	0.07	0.08	0.99	0.85	0.04	0.35	1.24	2.23	3.07
Luxembourg	0.00	0.00	0.00	0.00	0.00	0.00	0.00	0.00	0.00	0.04
Netherlands	0.82	0.00	?	0.82	8.46	0.03	1.01	9.51	10.33	1.15
Norway	7.19	3.10	10.85	21.15	0.00	0.00	0.00	0.00	21.15	0.00
Portugal	0.00	0.00	?	0.00	0.00	0.00	0.01	0.01	0.01	0.38
Spain	0.04	0.01	0.01	0.06	0.00	0.00	1.46	1.46	1.52	1.61
U. Kingdom	4.88	2.62	8.56	16.06	0.00	0.04	0.25	0.29	16.35	5.52
Total	14.40	5.94	19.51	39.86	12.54	0.22	10.67	23.43	63.29	23.75

Excluding the storage potential of the Thisted Dome (about 4.2 Gt CO₂).

Table 4.16.2 CO₂ storage capacity in aquifers not confined to traps. The table lists deep-seated aquifers that are considered to be suitable for a concept in which CO₂ storage is not confined to traps and in which CO₂ is allowed to spread over the largest part of the entire aquifer range. One should realise that the judgement on an aquifer's suitability for this type of disposal is based on a poor and incomplete data set. The storage efficiency is 2% for 'closed' aquifers and 6% for 'open' aquifers. If it remains unclear whether an aquifer is open or closed a storage efficiency of 4% has been applied.

STORAGE IN AQUIFERS NOT CONFINED TO TRAPS (IN GIGATONNES CO ₂)			
COUNTRY	OFFSHORE	ONSHORE	TOTAL
Belgium	0	0	0
Denmark	?	47	47
France	?	3	3
Germany	?	2	2
Greece	?	?	0
Ireland	?	?	0
Italy	?	0	0
Luxembourg	0	0	0
Netherlands	?	5	5
Norway	476	0	476
Portugal	?	0	0
Spain	?	?	0
U. Kingdom	240	0	240
Total	716	57	773

is about ten times the storage estimate of the trapped proportion of all European aquifers investigated. Storage in traps contributes in a marginal way to the total capacity of the major storage sites. Only one structure, the Danish 'Thisted Dome', is considered to be large enough to form one single reservoir where CO₂ can be stored in an economic way (note that the 'Thisted Dome' is not included in the storage estimate of Denmark, because the structure is too shallow). The major part of the capacity originates from aquifers that are believed to be appropriate for CO₂ disposal 'outside traps', either because the aquifers are considered to be entirely sealed off from other formations ('closed' aquifers) or because their lateral extent is so large that the risk of CO₂ escaping from the reservoir is expected to be low (see section 4.2).

Table 4.16.3 includes a column in which a rough estimate of the potential of the individual major storage sites is given. Note that some of these individual storage sites are still very large (entire sedimentary basins). Most aquifers in the table are deep-seated aquifers that are expected to be 'closed' and (slightly) overpressured. So, the pressure build-up during CO₂ injection will be a major concern and some reservoirs may not be able to withstand the pressure induced by the filling of this fraction of the pore volume^[24]. However, the storage capacity of fractured Chalk Formation (Table 4.16.3, included in Nrs 7-9) is expected to be larger because of the increased CO₂ uptake of the matrix by dissolution, which probably is equivalent to a CO₂ occupation of ca 7% of the pore volume (see section 4.2). The Tertiary aquifers in the Viking Graben (Norway and UK) and in the Central Graben (UK) are expected to form 'open' reservoirs.

Table 4.16.3 Individual major CO₂ storage sites in the European Union and Norway (discussed in sections 4.3 to 4.15). The aquifer capacities show large uncertainties. Because the storage capacity of the entire pore volume of some aquifers is taken into account, the values in this table are considerably higher than in Table 4.16.1. Note that the storage capacities of the reservoirs are not additive, because some overlap (e.g. the Permian aquifer of the Netherlands and the Groningen Field).

Nr	Aquifers		Location	Age (Formation)	Country	Storage (Gt CO ₂)
1 [†]	single trap	onshore	Thisted	Triassic	DK	4
2	in traps	offshore	Southern North Sea	Triassic (Bunter)	GB	3
3	not in traps	onshore	N. German Basin [‡]	Permian /Triassic	NL	5
4	not in traps	onshore	Danish Subbasin	Triassic/Jurassic	DK	47
5	not in traps	onshore	N. German Basin	Triassic	D	2
6	not in traps	onshore	Aquitania Basin	Triassic/Liassic	F	3
7 [#]	not in traps	offshore	Vik./Centr. Graben	Mesozoic-Cenozoic	N	476
8	not in traps	offshore	Viking Graben	Mesozoic-Cenozoic	GB	46
9	not in traps	offshore	Central Graben	Mesozoic-Cenozoic	GB	33

Nr	Gas Fields		Location	Field Name	Country	Storage (Gt CO ₂)
10	gas	onshore	N. German Basin	Groningen	NL	7.4
11	gas	onshore	Aquitania Basin	Lacq	F	0.7
12	gas	onshore	N. German Basin	cluster 3	D	1.0
13	gas	onshore	N. German Basin	cluster 5	D	0.7
14	gas	offshore	Southern North Sea	Leman	GB	1.1
15	gas	offshore	E. Irish Sea	Morecambe	GB	0.8
16	gas	offshore	Horda Platform	Troll (E.&W.)	N	4.8
17	gas	offshore	Viking Graben	Frigg	N	0.7

[†] does not conform to selection criteria (too shallow) and is partly onshore and partly offshore

[‡] North German Basin + Southern North Sea Basin = Northwest European Basin
= Southern Permian Basin

[#] total capacity of the investigated Norwegian sector of the North Sea; the largest volume of the Norwegian aquifers is confined to the Viking and the Central Graben.

The storage estimates for the reservoirs 'not in traps' in Table 4.16.3 are based on the filling of a certain fraction (storage efficiency) of the entire pore volume of the aquifer. In many cases, an aquifer does not form a single reservoir, but will consist of several faulted blocks that poorly communicate with each other. Examples are the Permian in the Netherlands and the Mesozoic aquifers in the North Sea Grabens. So, the amount of CO₂ corresponding to the storage capacity cannot be injected from one location because an aquifer will generally contain a number of separate reservoirs. Aquifers that don't have this compartmentalisation probably are the Bunter Sandstone in the Southern North Sea, the Triassic-Jurassic of the Danish Basin (?) and most Tertiary aquifers.

4.16.2.2 GAS FIELDS

Only the largest gas fields have been selected as favourable storage sites (Table 4.16.3). These fields will not become available in the short term. The major German fields will produce gas for another 16 to 22 years, the Groningen Field for at least 35 years, and the Troll fields even for more than 50 years. The largest UK gas field (Leman) is expected to be abandoned in the year 2011. The storage estimate of the gas fields is based on their ultimate recovery. On the one hand, the estimate will be conservative, because only the proved reserves are taken into account and the actual reserves will probably be significantly larger. On the other

hand, the estimate will be optimistic, because the water inflow into the reservoir has been neglected. However, in spite of these uncertainties the storage estimate will be accurate compared to that of the aquifers.

4.16.2.3 OIL FIELDS

As stated above, CO₂ storage in oil fields will be combined with Enhanced Oil Recovery (EOR) and the question of whether an oil field will be used for CO₂ disposal will be determined by its suitability for EOR. This will be highly reservoir specific. Hence, storage in oil fields will only be considered if the associated EOR profits exceed the costs of CO₂ injection. The size of the reservoirs is therefore less important in deciding whether CO₂ storage is economically attractive. Although little is publically available on the policy of the oil companies, we know from one major oil field in the UK, the Forties Oil Field, that it is currently considered as potential candidate for EOR. The Forties Oil Field is the largest oil field in the UK offshore and is one of the nearest to land. The oil field is located in the Central North Sea and has a Palaeocene sandstone reservoir (Forties Sandstone, Sele Formation). Its date of abandonment is predicted to be 2009 and its CO₂ storage capacity is estimated to amount to 0.38 Gt CO₂. For Norway, all oil fields are expected to be prospective candidates for tertiary CO₂ injection (pers com. Erik Lindeberg 1995). More oil fields may be considered for EOR if free CO₂ becomes available.

4.16.2.4 FUTURE REQUIREMENTS

Although huge reservoirs will be required for large-scale, economic CO₂ disposal (see Chapter 8), it is expected that

[24] In overpressured aquifers the CO₂ reservoir density will be larger, which will increase the storage capacity.

in the short term no large volumes of CO₂ will be captured from power station flue gases and that all CO₂ injection ventures will be demonstration projects at a small scale. These demonstration projects have to be carried out to get a better knowledge of the CO₂ disposal process. It is expected that these projects require small, manageable storage sites near a modest CO₂ capture installation, rather than larger but less controllable reservoirs. Hence, in the near future small 'confined' reservoirs onshore, such as currently depleted gas fields and traps on aquifers, are more attractive than large reservoirs that will be either 'unconfined' (entire volume of large aquifers, largely offshore) or not available for a long time (giant gas fields). Such small storage sites are abundant in most countries that have any significant CO₂ storage potential onshore (Table 4.16.1). However, selection of these reservoirs will be highly case specific and will be impossible in the context of this broad inventory.

4.16.3 Sources and Sinks

In this section the magnitude and location of CO₂ sources and CO₂ sinks are compared. CO₂ sources are fossil fuel based power stations and CO₂ sinks are underground reservoirs formed by depleted hydrocarbon fields or aquifers. With respect to the sinks, this section focuses on the major storage sites, as presented in Table 4.16.3. Note that the aquifer capacities in this table should be regarded as maximum values. All data on power generation and CO₂ emission are from 1990 (see Chapter 3). If 'Europe' is used, it refers to the countries that are involved in this project, i.e. the twelve countries of the European Union^[25] and Norway.

4.16.3.1 THE NORTH SEA COUNTRIES^[26]

Given cumulative trapped storage capacities per country (Figure 4.16.1) and the distribution of major storage sites (Table 4.16.3), it is evident that the North Sea countries have the largest CO₂ storage potential of Europe. An exception is Belgium that has no potential at all. A conservative estimate of the storage capacity (storage in traps) of the North Sea countries amounts to 57 Gt CO₂ (Table 4.16.1), which is 90% of the European total. In addition, all major storage sites, apart from the northern Aquitanian Basin, are clustered in and around the North Sea. This large storage potential is obviously related to the enormous volume of sediments that accumulated in the North Sea Basin (see Figure 4.1.1). The area directly south of the North Sea is densely populated, which results in a large CO₂ production. In 1990, the cumulative CO₂ emissions by power plants of the North Sea countries amounted to 660 Mt CO₂ (i.e. 69% European emissions), of which the largest part stemmed from power plants in Germany (341 Mt) and the UK (221 Mt). So, there is the fortunate situation that the area with the largest CO₂ emissions coincides with the area with the largest storage potential.

The major concentrations of power generation in the UK are in the London area, the Midlands, and Northeast England. About half of the thermal power is generated in the Midlands and Northeast England. Hard coal is used here as fuel. The nearest potential CO₂ storage sites are offshore: the Bunter Sandstone (about 3 Gt CO₂) and the Leman Gas Field (1.1 Gt CO₂) in the Southern North Sea Basin, and the Morecambe Gas Field in the East Irish Sea Basin (0.8 Gt CO₂). These major reservoirs are all within a range of 200 km.

In Germany, 39% of the total power production is located in the northern part of the country (north of the Münster-Dresden axis) and 33% in the Ruhr area. Power stations here are mostly fuelled with lignite (brown coal) or hard coal. Many of them are associated with nearby coal mining areas, e.g. between Cologne and Aachen (lignite), Lausitz (lignite), and the Ruhr area (hard coal). Potential storage sites for CO₂ are located in Mesozoic aquifers and Palaeozoic gas reservoirs of the North German Basin (Table 4.16.3), which extends from the Netherlands to Poland. The storage potential in the North German Basin could be very high, but is largely unknown because of limited data on the subsurface. In southern Germany the geology is unfavourable for underground disposal of CO₂ and no large storage sites could be defined.

4.16.3.2 SOUTHERN EUROPE^[27]

The storage potential of Southern Europe is very limited. A conservative estimate of the cumulative storage capacity (in traps) is about 6 Gt CO₂ (Table 4.16.1), which is about 10% of European total. Large storage sites are restricted to the Aquitanian Basin in southern France (Table 4.16.3): Triassic-Lias aquifers in the northern part of the basin (ca 3 Gt CO₂) and the Lacq Gas Field (ca 0.7 Gt CO₂). However, it should be noted that only a small fraction of the offshore aquifers has been considered and that the offshore aquifers that remained unexamined will most certainly provide a significant surplus of storage capacity.

In Southern Europe, the amount of CO₂ emitted by thermal power stations is 283 Mt CO₂, which is 30% of the total European emissions. Although the power generation in France is the second largest in Europe, thermal power generation is very limited and produces only 44 Mt CO₂. So, the potential of the Aquitanian Basin is expected to be sufficient to store the CO₂ from French power plants for a considerable time. The largest CO₂ producers in Southern Europe are Italy (123 Mt CO₂/yr) and Spain (64 Mt CO₂/yr). The total CO₂ storage capacity in geological traps is estimated to amount to 2.3 Gt for Italy, and 1.5 Gt for Spain. No major storage sites have been found in these countries and the size of the individual CO₂ reservoirs are expected to be too small to justify a CO₂ capture and injection venture at a large scale. In Italy, application of the entire volume of the major Mesozoic aquifer onshore for disposal purposes (storage outside traps) seems inappropriate because it crops out at various places and is currently being used for geothermal heat recovery and water supply. However, it might be possible to store CO₂ outside traps in the offshore domain. It is unclear to what extent the aquifers in Spain are suitable for a CO₂ disposal scheme in which the entire aquifer volume will be available for CO₂ disposal.

4.16.4 Conclusions

For the European Union and Norway, the total theoretical storage capacity of the subsurface in geological traps is estimated to amount to at least 63 Gt CO₂, 30 Gt in traps

[25] Belgium, Denmark, France, Germany, Greece, Ireland, Italy, Luxembourg, The Netherlands, Portugal, Spain, and The United Kingdom.

[26] Belgium, Denmark, Germany, The Netherlands, Norway, and The United Kingdom.

[27] France, Spain, Italy, Greece and Portugal.

on aquifers, 6 Gt in oil fields and 27 Gt in gas fields. This is roughly 70 times the cumulative CO₂ production from power plants in the year 1990. However, various major aquifers are considered to be suitable for CO₂ disposal not restricted to traps, because they are either entirely sealed off from the overburden formation or have such a large distribution that the risk of CO₂ escaping from the aquifer is negligible. The total storage capacity of these major, 'non-trapped' aquifer reservoirs amounts to about 770 Gt.

Major storage sites are concentrated in and around the North Sea, which facilitates CO₂ disposal in northern Europe and complicates CO₂ disposal in southern Europe. The storage capacity of most individual hydrocarbon fields and most traps on aquifers is very small, too small to use these reservoirs for a large-scale CO₂ disposal scheme. The applicability of oil fields will largely depend on the profitability of an EOR (enhanced oil recovery) venture.

The inventory of the underground CO₂ storage capacity includes major uncertainties. Establishing the total CO₂ storage capacity for aquifers is the most problematic, because the inventory is incomplete, and the storage processes and the reservoir properties of the 'average aquifer' are not yet understood well enough to provide an accurate estimate. A large proportion of the offshore aquifers were not included in the inventory, because for most countries the offshore data are very limited. The offshore aquifers that remained unexamined will certainly have a substantial storage potential. Depending on the type of reservoir, the injection scheme and the model presumptions, it is expected that roughly 2 to 10% of the aquifer's pore volume can be filled with CO₂ and that the CO₂ reservoir density may vary between 500 and 1000 kg/m³. Hence, the storage capacity may range in the various aquifers from approximately 10 to 100 kg CO₂/m³ pore volume. A low storage capacity (10 kg CO₂/m³ pore volume) may, for example, be encountered in a hot and 'closed' aquifer, whereas a cold and 'open' aquifer may show a high storage capacity (100 kg CO₂/m³). In addition, it is not clear to what extent storage should be restricted to traps.

Taking the limitations of the subsurface data into account, the total pore volume of aquifers in the European Union and Norway potentially suitable for CO₂ storage is estimated to amount to about 30 000 km³. Roughly 1000 km³ of this pore volume (≈3%) is assumed to be confined by traps. The total CO₂ storage capacity of aquifers will largely depend on the disposal concept. Major factors controlling the storage capacity are the fraction of the pore volume that can be filled with CO₂ and whether or not the CO₂ storage should be confined to traps. A very conservative estimate of the storage capacity will be a CO₂ occupation of 2% of the *trapped* aquifer pore volume, which leads to a value of approximately 13 Gt CO₂^[28]. A very optimistic (and unrealistic) estimate will be a 6% occupation of the *entire* pore volume of all aquifers considered, which corresponds to ca 1200 Gt.

Although the CO₂ storage estimates for the hydrocarbon fields also contain some uncertainties, they are considered to be far more accurate. The storage estimates are based on the assumption that the entire reservoir volume of ultimately recoverable hydrocarbons (cumulative production added to proven reserves) can be replaced by CO₂. The most important uncertainties are expected to originate from:

- the estimated proven reserves, which are generally significantly smaller than the volumes that will actually be produced
- the application of commercial hydrocarbon production and the neglecting of other fluids either produced or injected
- natural water invasion in gas fields
- the suitability of oil fields for EOR.

If CO₂ disposal is combined with Enhanced Oil Recovery, the oil fields are estimated to have a total storage capacity of about 6 Gt CO₂. Major oil fields are situated in the Norwegian and British North Sea. Gas fields are estimated to have a total storage capacity of about 27 Gt. Major gas fields are situated in the Norwegian and British North Sea and in the onshore area of the northern parts of the Netherlands and Germany.

4.17 REFERENCES

- ABBOTS, I L. 1991. United Kingdom Oil and Gas Fields, 25 Years Commemorative Volume. *Memoir of the Geological Society, London, Volume 16*.
- ALLABY, A, and ALLABY, M (editors). 1990. *The concise Oxford Dictionary of earth sciences*. Oxford University Press, Oxford, 410pp.
- ALLEN, D J, and HOLLOWAY, S. 1984. The Wessex Basin. *Investigation of the geothermal potential of the UK*. British Geological Survey, Keyworth.
- ALVES, A M. 1971. O Lusitania da parte sul da Bacia Cenozoica ocidental Portuguesa e as suas características petrolíferas. I. Congresso Hispano-Luso-Americano de Geologia Economica, Madrid and Lisbon, 99–108.
- ANDERSEN, C, and DOYLE, C. 1990. Review of hydrocarbon exploration and production in Denmark. *First Break*, 8, 155–165.
- ANDRÉ, P, and DOULCET, A. 1991. Rospo Mare field, Italy, Apulian platform, Adriatic Sea. In: BEAUMONT, E.A, and FOSTER, N H (editors) *Atlas of Oil and Gas Fields, Structural Traps VII*, *Am. Assoc. Petrol. Geol. Treatise Petrol. Geol.*, 29–53.
- ANONYMOUS. 1993. *France: recherche et production pétrolières, 1992*. Ministère de l'Industrie, Direction des Hydrocarbures, Service de conservation des gisements d'hydrocarbures.
- ARCHER, J S, and WALL, P G. 1992. *Petroleum Engineering: principles and practice*. Graham & Trotman, London, 362pp.
- AMERICAN GEOLOGICAL INSTITUTE. 1974. *Dictionary of Geological terms*. Anchor Press, New York, 545pp.
- BAGLIONI, A, PEROTTO, G, BISON, P, LA TORRACE, F. 1988. Potential Geothermal Reservoirs — Region of Lombardy. In HAENEL, R, and STAROSTE, E (editors) 1988. *Atlas of Geothermal Resources in the European Community, Austria and Switzerland*. Commission of the European Community, p.37.
- BALDI, P, BUONASORTE, G, CAMELI, G M, CECCARELLI, A, RIDOLFI, A, GRASSI, S, SQUARCI, P, and TAFI, L. 1988. Potential Geothermal Reservoirs -Tuscany-Latium Geothermal Province. In HAENEL, R, and STAROSTE, (editors) 1988. *Atlas of Geothermal Resources in the European Community, Austria and Switzerland*. Commission of the European Community, p.38.
- BARDON, C, WOODHEAD, I A, and GRIST, D M. 1993. Enhanced oil recovery from the Egmont Oil field by Carbon Dioxide miscible flooding. *Proceedings of the European Offshore Petroleum Conference*. 6pp.

[28] Assuming a CO₂ reservoir density of 700 kg/m³.

- BERTINI, G, CASTELLUCCI, P, CECCARELLI, A, MINISALE, A, RIDOLFI, A, CALORE, C, CELATI, R, SQUARCI, P, TAFFI, L. 1988. Potential Geothermal Reservoirs — Larderello, Travale and Monte Amiata geothermal fields. In HAENEL, R, and STAROSTE, E (editors) 1988. Atlas of Geothermal Resources in the European Community, Austria and Switzerland. Commission of the European Community, p.37
- BEUTLER, G, ROCKEL, W, RÖHLING, H-G, SCHULZ, R, and WERNER, K-H. 1992. Regionale Untersuchungen von geothermischen Reservaten und Ressourcen in Nordwestdeutschland. Geothermal Energy Symposium 1992. Tagungsband. 301–310. Forum für Zukunftsenergien e.V. Geothermische Vereinigung e.V.
- BRAUSTEIN, J, and O'BRIEN, G D. 1968. Diapirism and Diapirs. AAPG Memoir no. 8, pp.275–292.
- BRGM/IGME. 1982. Etude de faisabilité d'un projet géothermique à Serres (Grèce). Partie I, étude sous-sol. BRGM report no. 82 SGN 801 GTH.
- BRGM and CNEOX. 1982. Carte géologique de la marge continentale Française. Notice explicative. Bureau de Recherches Géologiques et Minières & Centre National pour l'Exploitation des Océans.
- BRINKMAN, R, and LOEGTERS, H. 1968. Diapirs in western Pyrenees and foreland, Spain. In Diapirism and Diapirs, (Eds. J. Braustein & G. D. O'Brien), AAPG Memoir no. 8, pp. 275–292.
- BOIGK, H. 1981. Erdöl und Erdgas in der Bundesrepublik Deutschland. 330pp. Enke Verlag. Stuttgart.
- BOUCKAERT, J, FOCK, W, and VANDENBERGHE, N. 1988. First results of the Belgian geotransverse 1986. Annales de la société géologique de Belgique, III: 269–290.
- BRÜCKNER, W, and WORMBS, J. 1990. Geothermische Ressourcen im Nordteil der DDR: Blatt Wittenberge. Geologische Forschung und Erkundung. Schwerin.
- BURGESS, W G. 1981. Hydraulic characteristics of the Triassic Sherwood Sandstone and the Lower Jurassic Bridport Sands intervals, as derived from drill stem tests, geophysical logs and laboratory tests. In: RHYS, G H, LOTT, G K, and CALVER, M A. (editors). The Winterborne Kingston borehole, Dorset, England. Report of the Institute of Geological Sciences, No. 81/3, 164–175.
- CASNEDI, R. 1988. Subsurface Basin Analysis of Fault-Controlled Turbidite System in Bradano Through, Southern Adriatic foredeep, Italy. Am. Assoc. Petrol. Geol. Bull, V. 72, no. 11, pp.1370–1380.
- CARMALT, S W, and ST JOHN, B. 1986. Giant oil and Gas Fields In: Future Petroleum Provinces of the World (Ed. M. T. Halbowy), Am. Assoc. Petrol. Geol. Mem. no. 40, pp.13–54.
- CASAS-SANZ, A M. 1993. Oblique tectonic inversion and basement thrusting in the Cameros Massif (Northern Spain). Geodinamica Acta, vol. 6, no. 3, pp. 202–216.
- CAVALLI, G, GHEZZI, G, MARCHETTI, M P. 1988. Potential Geothermal Reservoirs - Main reservoir. In HAENEL, R, and STAROSTE, E (editors) 1988. Atlas of Geothermal Resources in the European Community, Austria and Switzerland. Commission of the European Community, p.37
- CLAVELL, E, and BERASTEGUI, X. 1992. Petroleum Geology of the Gulf of València. In Generation, accumulation and production of Europe's hydrocarbons (ed. A M. Spencer), Spec. Pub. of the European Petroleum Geoscientists no. 1, pp.335–368.
- COLLEY, M G, MCWILLIAMS, A S F, and MYERS, R C. 1981. Geology of the Kinsale Head Gas Field, Celtic Sea, Ireland. In ILLING, L V, and HODSON, G D (editors). Petroleum Geology of the Continental Shelf of North-West Europe. 504–510.
- COTTENÇON, A, PARANT, B, and FLACELIÈRE, G. 1975. Lower Cretaceous gas fields in Holland. In: WOODLAND, A W. (editor): Petroleum and the Continental Shelf of North West Europe. Applied Science Publishers.
- CROKER, P F, and SHANNON, P M. 1987. The evolution and hydrocarbon prospectivity of the Porcupine Basin, Offshore Ireland. In J BROOKS, and K GLENNIE (editors). Petroleum Geology of North West Europe. 633–642.
- DALY, E P. 1993. Hydrogeology of the Dolomite Aquifer in Southeast Ireland. Geological Survey of Ireland Report No. GW93/5.
- DANISH ENERGY AGENCY. 1992. Oil and Gas Production in Denmark, 1991. Ministry of Energy. København.
- DE JONG, M G G, AND DUSAR, M. 1992. Reservoir Modelling of the Vlieland sandstone of the Kotter field (block K18b), offshore, the Netherlands. Geologie en Mijnbouw 71: 173–188.
- DEMYTTENAERE, R. 1989. The post-Paleozoic geological history of north-eastern Belgium. Mededelingen Kon. Academie voor Wetenschappen, Letteren en Schone Kunsten België. No 4, Jaargang 51. Leuven, Belgium.
- DEMYTTENAERE, R, AND LAGA, P. 1988. Breuken- en isohypsenkaarten van het Belgische gedeelte van de Roerdal Slenk; eerste resultaten van een seismisch onderzoek op het gebied van Poppel–Lommel–Maaseik. Ministerie van Economische Zaken–Administratie der Mijnen–Geologische Dienst van België. Professional Paper 1988/4, Nr 234, 20pp.
- DEPARTMENT OF TRADE AND INDUSTRY. 1993. Development of the Oil and Gas Resources of the United Kingdom. HMSO, London.
- DEREGNAUCOURT, D, and BOILLLOT, G. 1982. Structure géologique du Golfe de Gascogne. Bull. BRGM (2), I, no. 3, pp.149–178.
- DGU. 1981. Kortlaegning af potentielle geotermiske reservoirer i Danmark.. Geological Survey of Denmark, Series B, no 5.
- DGU. 1991a. Geological map of Denmark. 1:400,000. The Danish Basin: 'Base Chalk and the Chalk Group'. Geological Survey of Denmark. Map series no. 29.
- DGU. 1991b. Geological map of Denmark. 1:400,000. The Danish Basin: 'Top Triassic' and the Jurassic-Lower Cretaceous. Geological Survey of Denmark. Map series no. 30.
- DGU. 1991c. Geological map of Denmark. 1:400,000. The Danish Basin: 'Top Zechstein' and the Triassic. Geological Survey of Denmark. Map series no. 31.
- DIENER, I, WORMBS, J. et al. 1988–1990. Kartenwerk Geothermie 1:200 000: Geothermische Ressourcen im Nordteil der DDR.
- Blatt Neuruppin 1988. ZGI. Berlin.
- Blatt Güstrow 1988. ZGI. Berlin.
- Blatt Schwerin/Doberan 1989. ZGI. Berlin.
- Blatt Neubrandenburg/Torgelow 1989. ZGI. Berlin.
- Blatt Eberswalde/Bad Freienwalde 1990. ZGI. Berlin.
- DIENER, I, WORMBS, J. et al. 1990–1992. Geologische Grundlagen für die Geothermienutzung in Nordost-Deutschland.
- Blatt Berlin/Frankfurt (o) 1990. UWG. Berlin.
- Blatt Magdeburg/Brandenburg 1991. UWG. Berlin.
- Blatt Salzwedel 1992. UWG. Berlin.
- Blatt Cottbus 1992. UWG. Berlin.
- Blatt Rostock/Stralsund 1992. UWG. Berlin.
- DOORNHOF, D. 1992. Surface subsidence in the Netherlands: the Groningen gas field. Geologie en Mijnbouw 71: 119–130.
- DOWNING, R A, and GRAY, D A (editors). 1986. Geothermal Energy — The potential in the United Kingdom. HMSO, London.
- DOWNING, R A, and PENN, I E. 1991. Groundwater flow during the development of the Wessex Basin and its bearing on hydrocarbon and mineral resources. British Geological Survey Hydrogeology Series Research Report SD/91/1. BGS, Keyworth.
- DOZY, J.J. 1975. Geologie, aardolie en aardgas van Noordwest-Europa. Mijnbouwkunde, Vakgroep Toegepaste Geologie en Exploratie Technieken, Technische Hogeschool Delft
- DRANFIELD, P, BEGG, S H, and CARTER, R R. 1987. Wytch Farm Oil field: reservoir characterisation of the Sherwood

- Sandstone for input into reservoir simulation studies. *Petroleum Geology of North West Europe, Proceedings of the third Conference*, Volume 1, pp.149–160.
- DUAN, Z, MØLLER, N, and WEARE, J H. 1992. An equation of state for the CH₄-CO₂-H₂O system: I. Pure systems from 0 to 1000°C and 0 to 8000 bar. *Geochimica and Cosmochimica Acta*, 56, 2605–2617.
- ERDÖL ERDGAS ZEITSCHRIFT. 1965–1979. 82. - 95. Jahrgang.
- ERDÖL UND KOHLE. 1967–1984. 18. - 37. Jahrgang.
- EZ. 1994. *Olie en Gas in Nederland — opsporing en winning 1993*. Ministerie van Economische Zaken. 's Gravenhagen, The Netherlands.
- FATT, I. 1958. Pore Volume Compressibilities of Sandstone Reservoir Rocks, *J. Petrol. Technol.* March 1958.
- FERREIRA, G C. 1971. I. Bacia de Monte Real. Influencia do diapirismo e da erosao antecretacica no seu potencial petrolifero. I. Congreso Hispano-Luso-Americano de Geologia economica, Madrid and Lisbon, pp.123–141
- FONTBOTE, J M, and ESTEVEZ, A. 1980. Geologia de la Cordillera Bética. Bol. Geol. y Minero, T. XCI-II, pp.249–292. 26th International Geological Congress, Espagna, Tomo II.
- GAARENSTROOM, L, TROMP, R A J, DE JONG, M C, and BRANDENBURG, A M. 1993. Overpressures in the Central North Sea: implications for trap integrity and drilling safety. In: PARKER, J R. (editor), *Petroleum Geology of Northwest Europe: Proceedings of the 4th Conference. Petroleum Geology*, The Geological Society, London, pp.1305–1313.
- GAIR, D J, GRIST, D M, and MITCHELL, R W. 1980. The East Midlands additional oil project. *Proceedings of the European Offshore Petroleum Conference, London*.
- GDULA, J E. 1983. Reservoir geology, structural framework and petrophysical aspects of the De Wijk gas field. *Geologie en Mijnbouw* 62: 191–202.
- GHEZZI, G, GHEZZI, R, and MARCHETTI, M P. 1989. Assessment of the Low Enthalpy Geothermal resources of the Pò Valley Plain — Italy. In LOUWRIER, STAROSTE, and GARNISH (editors), *European Geothermal Update*, Commission of the European Communities.
- GIULIANO, F A (editor). 1981. *Introduction to oil and gas technology*. Second edition. Intercomp Resource Development and Engineering, Inc. Houston, Texas.195pp.
- GULINCK, M. 1956. Caracteristiques hydrogeologiques de sondage de Turnhout. *Communications de l'observations royal de Belgique* Nr 108, serie geophysique Nr 37: 1–6.
- GUNTER, W D, PERKINS, E H, and MCCANN, T J. 1993. Aquifer disposal of CO₂-rich gases: reaction design for added capacity. In: RIEMER, P W F (editor), *Proceedings of the International Energy Agency carbon dioxide symposium*, Oxford March 1993. *Energy Convers. Mgmt* 34, pp.941–948.
- HAENEL, R, and STAROSTE, E (editors). 1988. *Atlas of Geothermal Resources in the European Community and Austria and Switzerland*. Commission of the European Community.
- HALBOUTY, M T. 1986. Future Petroleum Provinces of the World. Am. Assoc. Petrol. Geol. Mem. no. 40.
- HALL, H N. 1953. Compressibility of Reservoir Rocks. *Trans. AIME*, p.309.
- HENDRIKS, C. 1994. *Carbon Dioxide Removal from Coal-Fired Power Plants*. PhD thesis, University of Utrecht, Department of Science, Technology and Society, 259pp.
- HENDRIKS, C A, and BLOK, K. 1993. Underground storage of carbon dioxide. In: RIEMER, P W F (editor), *Proceedings of the International Energy Agency carbon dioxide symposium*, Oxford March 1993. *Energy Convers. Mgmt*, Vol. 34, pp.949–958.
- HERNGREEN, G F W, and WONG, TH E. 1989. Revision of the 'Late Jurassic' stratigraphy of the central Dutch North Sea Graben. *Geologie en Mijnbouw* 68: 73–106.
- HOLLWAY, S, MILODOWSKI, A E, STRONG, G E, and WARRINGTON, G. 1989. The Sherwood Sandstone Group (Triassic) of the Wessex Basin, southern England. *Proceedings of the Geological Association* 100 (3), 383–394.
- HOLT, T, JENSEN, J-I, and LINDBERG, E. In press. Underground storage of CO₂ in aquifers and oil reservoirs. *Proceedings Second International Conference on Carbon Dioxide Removal, Kyoto 24–27 October 1994*.
- HOUSSE, B, and MAGET, Ph. 1976. *Potentiel géothermique du Bassin Parisien*. Rapport BRGM-SNEA, contrat DGRST 74-7-0990, 125p.
- HOUSSE, B, and MAGET, Ph. 1977. *Potentiel géothermique du Bassin Aquitain*. Rapport BRGM/SNEA, contrat DGRST 76-7-1332.
- HURDEMAN, A J M. 1992. *Injection of CO₂ into the subsurface*. In: E. Mot (Ed), *Confining abating CO₂ from fossil fuel burning - a feasible option ? (revised edition)*. TNO report 91-250 on behalf of the Commission of the European Communities.
- IEA. 1993a. *World Energy Outlook*. International Energy Agency.
- IEA. 1993b. *Carbon Dioxide Disposal in Aquifers*. IEA report OE14 by Stanley Industrial Consultance. IEA Greenhouse Gas R&D Programme. International Energy Agency.
- ILLING, L V, and GRIFFITH, A E. 1986. Gas prospects in the 'Midland Valley' of Northern Ireland. pp.73–84. in BROOKS, J., GOFF, J C, and VAN HOORN, B (editors). *Habitat of Palaeozoic gas in Northwest Europe*. Geological Society Special Publication, 23.
- ISAKSEN, D, and TONSTADT, K. 1989. A revised Cretaceous and Tertiary lithostratigraphic nomenclature for the Norwegian North Sea. *NPD Bulletin* 5, Stavanger.
- JENNER, J K. 1981. The Structure and Stratigraphy of the Kish Bank Basin. In ILLING, L V, and HOBSON, G D (editors) *Petroleum Geology of the Continental shelf of North-west Europe*. 426–431.
- JOULE II. 1993. *The underground disposal of carbon dioxide. First Interim Report of JOULE II Project No. CT92-0031*, 232 pp.
- KNOX, R W O'B, and CORDEY, G (editors). 1992–1994. *Lithostratigraphic Nomenclature of the UK North Sea*. British Geological Survey, Keyworth, Nottingham.
- KNOX, R W O'B, MORTON, A C, and LOTT, G K. 1981. Petrology of the Bridport Sands in the Winterborne Kingston borehole, Dorset. Pp.107–121 in RHYS, G H, LOTT, G K, and CALVER, M A (editors). *The Winterborne Kingston borehole, Dorset, England. Report of the Institute of Geological Sciences*, No. 81/3.
- KNOX, R W O'B, BURGESS, W G, WILSON, K S, and BATH, A H. 1984. Diagenetic influences on the aquifer properties of the Sherwood Sandstone in the Marchwood Geothermal Borehole, Southampton, England. *Investigation of the geothermal potential of the UK*. British Geological Survey, Keyworth, Nottingham.
- KOIDE, H G, TAZAKI, Y, NOGUCHI, Y, NAKAYAMA, S, IJIMA, M, ITO, K, and SHINDO, Y. 1992. Subterranean containment and long-term storage of carbon dioxide in unused aquifers and in depleted natural gas reservoirs. In: BLOK, K, TURKENBURG, W C, HENDRIKS, C A, and STEINBERG, M (editors), *Proceedings of the first international conference on carbon dioxide removal*, Amsterdam March 1992, *Energy Convers. Mgmt Vol. 33*, p.619–626.
- KOIDE, H, TAKAHASHI, M, and TSUKAMOTO, H. 1994. Self-trapping mechanisms of carbon dioxide in the aquifer disposal. Book of Abstracts, *Second International Conference on Carbon Dioxide Removal, Kyoto 24–27 October 1994*, p.50.
- KORBØL, R. In press. Sleipner Vest CO₂ disposal, injection of extracted CO₂ into the Utsira formation. *Proceedings Second International Conference on Carbon Dioxide Removal, Kyoto 24–27 October 1994*.
- LANAJA, J M. 1987. Contribucion de la exploration petrolifera al conocimiento de la geologia de Espana. IGME (Instituto Geologico y Minero de Espana), Madrid, 465p.

- LOTT, G K, and STRONG, G E. 1982. The petrology and petrography of the Sherwood Sandstone (?Middle Triassic of the Winterborne Kingston Borehole, Dorset. *Rep. Institute of Geological Sciences*. No. 81/3 pp.135–142.
- LOUWRIER, K., STAROSTE, E., GARNISH, J. D. 1989. European Geothermal Update, Commission of the European Communities. Kluwer Academic Publishers, Dordrecht, Boston, London.
- MAGET, Ph. 1983. *Potentiel géothermique "Basse température" en France*. Rapport BRGM 83 SGN 375 SPG, 319p.
- MATTEVELLI, L. and MARGARUCCI, V. (1986) - Malossa Field, Italy, Po Basin. In: *Atlas of Oil and Gas Fields, Structural Traps VII*, (Eds. E. A; Beaumont & N. H. Foster), *Am. Assoc. Petrol. Geol. Treatise Petrol. Geol.*, pp.119–137.
- MATTEVELLI, L. and NOVELLI, L. 1990. Geochemistry and Habitat of Oils in Italy. *AAPG Bull.* vol. 74 no. 10, pp.1623–1639.
- MATTEVELLI, L., PIERI, M. and GROPPI, G. 1993. Petroleum exploration in Italy: a review. *Marine and Petroleum Geology*. 10, 410–425.
- MCLIMANS, R K, and VIDETICH, P. E. 1987. Reservoir diagenesis and oil migration: Middle Jurassic Great Oolite Limestone, Wealden Basin, Southern England. *Petroleum Geology of North West Europe, Proceedings of the third Conference*, Volume 1, pp.119–128.
- MELCHIOR, P. 1956. Sur l'effet des marées terrestres dans les variations de niveau observées dans les puits en particulier au sondage de Turnhout. *Communications de l'observations royal de Belgique* Nr 108, serie geophysique Nr 37: 7–28.
- MONOPOLIS, D, and BRUNETON, A. 1982. Ionian Sea (Western Greece): its structural outline deduced from drilling and geophysical data. *Tectonophysics*, 83, pp.227–242.
- MONADERT, L, WINNOCK, E, DELTIEL, R, GRAU, G. 1975. Continental margins of the Galicia–Portugal and Bay of Biscay. *The Geology of Continental Margins*, Springer ed., pp.323–342.
- MOT, E, DE BAAR, H J W, BARTELDIS, H, ESSER, P M, HUURDEMAN, A J M, VAN DE LAAK, P J A, MICHON, S G L, and NIELEN, R J. 1992. *Confining abating CO2 from fossil fuel burning — a feasible option ? (revised edition)*. TNO report on behalf of the Commission of the European Communities DG XI., 153pp.
- MURPHY, N J, and CROKER, P F. 1992. Many play concepts seen over wide area in Erris, Slyne troughs off Ireland. *Oil and Gas Journal*, 14 September. 92–97.
- NAM–RGD. 1980. Stratigraphic Nomenclature of the Netherlands. Nederlandse Aardolie Maatschappij & Rijks Geologische Dienst. Verh. K.N.G.M.G. 32.
- NAYLOR, D. 1992. The post-Variscan history of Ireland. In PARNELL, J (editor). *Basins on the Atlantic Seaboard*. Geological Society Special Publication No. 62, 255–275.
- NAYLOR, D, and SHANNON, P M. 1982. *Geology of Offshore Ireland and West Britain*. Graham & Trotman, London. 161pp.
- NED. 1993. *Norsk petroleumsvirksomhet. Faktaheftet for 1993*. Norwegian Royal Ministry for Trade and Energy.
- NIEDERSÄCHSISCHES LANDESAMT FÜR BODENFORSCHUNG. 1992. *Erdöl und Erdgas in der Bundesrepublik Deutschland 1992*. 38 pp. Hannover.
- NORSK HYDRO. 1992. *Facts of Norwegian Oil and Gas Fields*. Informasjon og Samfunnskontakt; Norsk Hydro, July 1992.
- NPD. 1993. *Årsberetning for 1992*. Norwegian Petroleum Directory
- NUMBERE, D, BRIGHAM, W E, and STANDING, M B. 1977. *Correlation for Physical Properties of Petroleum Reservoir Brines*. Petroleum Research Institute, Stanford University, November 1977, p.17.
- OIL & GAS JOURNAL. December 28, 1992. Worldwide production report.
- OIL & GAS JOURNAL. Decembre 27, 1993. Worldwide production report.
- PARK, R S. 1991. A preliminary estimate of the storage capacity of UK oil and gas fields for the storage of carbon dioxide. Unpublished report for British Coal, Coal Research Establishment, Stoke Orchard, Cheltenham, UK.
- PEARSON, J F S, YOUNG, R A, and SMITH, A. 1991. The Indefatigable Field, Blocks 48/18, 48/19, 48/23, 48/24, UK North Sea. In: ABBOTS, I L (editor). United Kingdom Oil and Gas Fields, 25 Years Commemorative Volume. *Memoir of the Geological Society, London*, 14, pp.443–450
- PENN, I E, CHADWICK, R A, HOLLOWAY, S, ROBERTS, G, PHARAOH, T C, ALLSOP, J M, HULBERT, A G, and BURNS, I M. 1987. *Principal features of the hydrocarbon prospectivity of the Wessex-Channel Basin, UK*. Pp109–118 in BROOKS, J, and GLENNIE, K W (editors) *Petroleum Geology of North West Europe*, Graham & Trotman, London.
- PETROCONSULTANTS. 1993. World Production and Reserves Statistics 1993.
- PETROLEUM GEOLOGICAL CIRCLE. 1993. *Synopsis: Petroleum geology of the Netherlands — 1993*. Preprint AAPG Conference 17-20 October 1993, The Hague, the Netherlands. Geologie en Mijnbouw. 20pp.
- PIERI, M. 1986. Cortemaggiore field. In: *Atlas of Oil and Gas Fields, Structural Traps VII*, (Eds. E A; Beaumont & N H. Foster), *Am. Assoc. Petrol. Geol. Treatise Petrol. Geol.*, pp.99–118.
- PIERI, M, and MATTAVELLI, L. 1986. Geological Framework of Italian Petroleum Resources. *AAPG Bull.* vol. 70 no. 2, pp.103–130.
- REAMER, H H, OLDS, R H, SAGE, B H, and LACEY, W N. 1944. Methane - Carbon dioxide in the gaseous region. *Ind. Eng. Chem.* 36/1, 88–90.
- RGD. 1982. *Inventarisatie van de Lower Trias Group in Nederland t.b.v de winning van aardwarmte*. (1982) Rijks Geologische Dienst. Report no. 82DS21
- RGD. 1983a. *Inventarisatie van de Upper Rotliegend Group (Stochteren Sandstone Formation) in Nederland t.b.v de winning van aardwarmte*. Rijks Geologische Dienst. Report no. 83DS05EX
- RGD. 1983b. *Inventarisatie van de Rijnland Group (Vlieland Formation) in Nederland t.b.v de winning van aardwarmte*. Rijks Geologische Dienst. Report no. 83KA11EX.
- RGD. 1987. *Diepe Geothermie in Nederland - Nadere Reservoirkarakterisering en technische–en economische aspecten van hergebruik van verlaten putten*. Rijks Geologische Dienst. Report no. 87KAR08.
- RGD. 1988. *Geologie van Nederland, Deel 2. Delfstoffen en samenleving*. Rijks Geologische Dienst. SDU Uitgeverij, 's Gravenhage. 83pp.
- RGD. 1991a. *Geologische Atlas van de Diepe Ondergrond van Nederland — Blad I: Vlieland-Terschelling*. Rijks Geologische Dienst.
- RGD. 1991b. *Geologische Atlas van de Diepe Ondergrond van Nederland — Blad II: Ameland-Leeuwarden*. Rijks Geologische Dienst.
- RGD. 1991c. *Optimalisatie van bestaande (hydro)geologische databestanden op basis van gegevens uit het onderzoeksgebied Noordoost Nederland*. Rijks Geologische Dienst. Report no. 30102/TR/A2.
- RGD–TNO. 1983. *Geologische en Hydrogeologische Inventarisatie van Tertiaire en Onder-Kwartaire Afzettingen in Midden-Nederland t.b.v. Ondergrondse Opslag en Winning van warm water*. Rijks Geologische Dienst & TNO Dienst Grondwaterverkenning. Report no. 83KAZ20EX.
- RGD–TNO. 1984. *Geologische en Hydrogeologische Inventarisatie van Tertiaire en Onder-Kwartaire Afzettingen in Noord-Nederland t.b.v. Ondergrondse Opslag en Winning van warm water*. Rijks Geologische Dienst & TNO Dienst Grondwaterverkenning. Report no. 84KAR08EX.

- RGD-TNO. 1985a. *Geologische en Hydrogeologische Inventarisatie van Tertiaire en Onder-Kwartaire Afzettingen in Zuid-Nederland t.b.v. Ondergrondse Opslag en Winning van warm water*. Rijks Geologische Dienst & TNO Dienst Grondwaterverkenning. Report no. 82DS22.
- RGD-TNO 1985b. *Aardwarmtewinning en Grootschalige Warmteopslag in Tertiaire en Kwartaire Afzettingen*. Rijks Geologische Dienst & TNO Dienst Grondwaterverkenning.
- RIVM. 1989. *Inventarisatie en evaluatie van geohydrologische gegevens van Noordoost en Oost Nederland ten behoeve van het onderzoek naar de opberging van radioactief afval in zoutformaties*. Rijksinstituut voor Volksgezondheid en Milieuhygiëne. Report no. 728512005.
- ROBINSON, K W, SHANNON, P M, and YOUNG, D G. 1981. The Fastnet Basin: An Integrated Analysis. In ILLING, L V, and HOBSON, G D (editors). *Petroleum Geology of the Continental Shelf of North-west Europe*. 444-454.
- ROOKE, E, and OFSTAD, D R. 1994. *Utsira Formation: An Alternative Source for Injection Water in the Oseberg Syd Reservoir*. NPF Conference on Reservoir Management.
- ROOS, B M, and SMITS, B J. 1983. Rotliegend and Main Buntsandstein gas fields in block K/13 — A case history. *Geologie en Mijnbouw* 62. 75-82
- ROVERI, M, BERNASCONI, A, ROSSI, M E, and VISENTIN, C. 1992. Sedimentary Evolution of the Luna Field Area, Calabria, Southern Italy. In: *Generation, Accumulation and Production of Europe's Hydrocarbons II*, A. M. Spencer (editor), *Special Publication of the European Association of Petroleum Geoscientists no. 2*. Springer Verlag Berlin Heidelberg, pp.217-224.
- SALVANY, J M, MUNOZ, A, PEREZ, A. 1994. Nonmarine evaporitic sedimentation and associated diagenetic processes of the southwestern margin of the Ebro Basin (Lower Miocene), Spain. *Journ. of Sedim. Research*, vol. A64, no. 2, pp.190-203.
- SAPPENFELD, L W, and SCHROEDER, E R. 1968. Iza, an unusual diapir in northern Spain. In *Diapirism and Diapirs*, (editors J. Braustein & G D. O'Brien), AAPG Memoir no. 8, pp.293-300.
- SCHRAMM, M W, and LIVRAGA, G. 1986. Vega field and the potential of the Ragusa Basin, offshore Sicily. In: *Future Petroleum Provinces of the World (editor M. T. Halbouty)*, *Am. Assoc. Petrol. Geol. Mem. no. 40*, pp.559-566.
- SCHROEDER, L, and SCHOENEICH, H. 1986. *International Map of Natural Gas Fields in Europe*. Explanatory Notes. Niedersächsisches Landesamt für Bodenforschung und Rohstoffe, Pfeiffer ed., Hannover, 175p.
- SEEMANN, U, PUMPIN, V F, and CASSON, N. 1986. Amposta Oil field. In: *Atlas of Oil and Gas Fields. Structural Traps II*, (editors E A; Beaumont and N H Foster), *Am. Assoc. Petrol. Geol. Treatise Petrol. Geol.*, pp.1-20.
- SELLWOOD, B W, SCOTT, J, MIKKELSEN, P, and ACKROYD, P. 1985. Stratigraphy and sedimentology of the Great Oolite Group in the Humbly Grove oil field. Hampshire. *Marine and Petroleum Geology* 2, 44-55.
- SELVIG, A, and KOSSACK, C A. 1991. North Sea Chalk Reservoirs: An Appealing Target for Horizontal Wells? SPE paper 22930.
- SESTINI, G, and FLORES, G. 1986. Petroleum Potential of the Thrust belt & Foretroughs of Sicily. In: *Future Petroleum Provinces of the World (editors M. T. Halbouty)*, *Am. Assoc. Petrol. Geol. Mem. no. 40*, pp.567-583.
- SHANNON, P M. 1991a. The development of Irish offshore sedimentary basins. *Journal of the Geological Society, London*, 148, 181-189.
- SHANNON, P M. 1991b. Tectonic framework and petroleum potential of the Celtic Sea, Ireland. *First Break*, 9, 107-122.
- SKJÆVELAND, S M, and KLEPPE, J. 1992. *Recent Advances in Improved Oil Recovery Methods for North Sea Sandstone Reservoirs*. SPOR Monograph, NPD, Stavanger.
- SPENCER, A M. 1985. *Habitat of Hydrocarbons on the Norwegian Continental Shelf*. Norwegian Petroleum Society, Graham and Trotman.
- SPENCER, A M. 1987. *Geology of the Norwegian Oil and Gas Fields*. Norwegian Petroleum Society, Graham and Trotman.
- STUDLICK, J R J, SHEW, R D, BASYE, G L, and RAY, J R. 1989. A giant carbon dioxide accumulation in the Norphlet Formation, Pisgah Anticline, Mississippi. In: BARWIS, J H, MCPHERSON, J G, and STUDLICK, J R J (editors). *Sandstone Petroleum Reservoirs*. Springer-Verlag, New York.
- TGO. 1989. *Evaluatie van de mogelijkheden voor gasstockage in de Kempen*. Confidential report by TGO for the Belgische Geologische Dienst.
- TGO. 1990. *Evaluatie van de mogelijkheden voor gasstockage in Henegouwen*. Confidential report TGO for the Belgische Geologische Dienst.
- TISSOT, B P, and WELTE, D H. 1984. *Petroleum Formation and Occurrence*. Springer Verlag, Berlin, 699pp.
- TNO. 1986. *Onderzoek naar Adiabatische Perslucht opslag in Nederland*. TNO Dienst Grondwaterverkenning. Report no. OS-86-43.
- TODD, M R, and GRAND, G W. 1993. Enhanced oil recovery using carbon dioxide. In: P.W.F. RIEMER (editor), *Proceedings of the International Energy Agency carbon dioxide symposium, Oxford March 1993*. *Energy Convers. Mgmt* 34, p.1157-1164.
- UNGEMACH, P. 1984. Les ressources géothermiques de la Communauté européenne. Etat de l'exploration — Perspectives de développement. *Bull. BRGM Hydrogéologie — Géologie de l'Ingénieur*, vol. 1, pp.11-42.
- VAN ADRICHEM BOOGAERT, H A, and BURGERS, W F J. 1983. The development of the Zechstein in the Netherlands. *Geologie en Mijnbouw* 62: 83-92.
- VANDENBERGHE, N, POGGIAGLIOLMI, E, and WATTS, G. 1986. Offset-dependent seismic amplitudes from karst limestones in Northern Belgium, *First Break Vol 4, Nr 5*: 9-27.
- VAN DEN BOSCH, W J. 1983. The Harlingen field, the only gas field in the Upper Cretaceous chalk of the Netherlands. *Geologie en Mijnbouw* 62: 145-156.
- VAN DER MEER, L G H. In press. The CO₂ storage efficiency of Aquifers. *Proceedings Second International Conference on Carbon Dioxide Removal, Kyoto 24-27 October 1994*.
- VAN DER MEER, L G H, GRIFFHOEN, J, and GEEL, C R. 1992. *Investigations regarding the storage of carbon dioxide in aquifers in the Netherlands*. TNO Applied Geoscience. TNO Report no OS 92-24-A.
- VAN DER MEER, B, and VAN DER STRAATEN, R. 1993. *Disposal of carbon dioxide arising from fossil fuel based power generation in exhausted oil and gas wells*. IEA report OE15. IEA Greenhouse Gas R&D Programme, International Energy Agency.
- VAN DER MEER, M, HEEDERIK, J P, and VAN DER STRAATEN, R. 1994. Geothermisch Doublet De Lier, Additioneel Onderzoek. TNO Report OS-94-35-B (concept).
- VAN DER SLUITS, J. 1991. *Interactive Thermodynamic Data Generator*. Based on the Enerpack routines by Evert Nieuwlaar. Department of Science Technology and Society, University of Utrecht, The Netherlands. Computer program.
- VAN ENGELENBURG, B, and BLOK, K. 1991. *Prospects for the disposal of carbon dioxide in aquifers*. Report G-91006, Vakgroep Natuurwetenschappen en Samenleving. University Utrecht (RUU), The Netherlands.
- VAN LITH, J G J. 1983. Gas fields of Bergen concession, the Netherlands. *Geologie en Mijnbouw*, 62: 63-74
- VAN STAALDUINEN, C J, VAN ADRICHEM BOOGAERT, H A, BLESS, M J M, DOPPERT, J W CHR, HARSVELDT, H M, VAN MONTFRANS, H M, OELE, E, WERMUTH, R A, and ZAGWIJN, W H. 1979. *The Geology of the Netherlands*. Med. RGD, vol 31-2.
- VISSER, W A (editor). 1980. *Geological Nomenclature*. Royal Geological and Mining Society of the Netherlands. Bohn,

- Scheltema & Holkema, Utrecht - Martinus Nijhoff, The Hague, 540pp.
- VISSER, C (editor). 1993. *Voorstudie geothermie De Lier*. TNO Applied Geoscience. TNO Report no OS 93-70-C.
- VOLLSET, J, and DORE, A G. 1984. *A revised Triassic and Jurassic lithostratigraphic nomenclature for the Norwegian North Sea*. NPD Bulletin No 3, Stavanger.
- WARRINGTON, G, AUDLEY-CHARLES, M G, ELLIOTT, R E, EVANS, W B, IVIMEY-COOK, H C, KENT, P E, ROBINSON, P L, SHOTTON, F W, and TAYLOR, F M. 1980. A correlation of Triassic rocks in the British Isles. *Special Report of the Geological Society, London, No. 13*, 78pp.
- WATERLOT, G, BEUGUIES, A, and BINTZ, J. 1973. Ardenne Luxembourg. Masson & Cie Eds.
- WEG. 1978-1992. Annual reports of the Wirtschaftsverband Erdöl- und Erdgasgewinnung e.V. Hannover.
- WEIR, G J, WHITE, S P, and KISSLING, W K. 1994. Reservoir storage and containment of greenhouse gases. Book of Abstracts, *Proceedings Second International Conference on Carbon Dioxide Removal, Kyoto 24-27 October 1994*, p.56.
- WHITTAKER, A. 1985. *Atlas of onshore sedimentary basins in England and Wales: Post-Carboniferous stratigraphy and tectonics*. Blackie, Glasgow.
- WORMBS, J. 1992. *Geologische Grundlagen für die Geothermienutzung in Nordost-Deutschland*. Geothermal Energy Symposium 1992. Tagungsband. 251-265. Forum für Zukunftsenergien e.V., Geothermische Vereinigung e.V.
- WORLD OIL. August 1993.
- YARBOROUGH, L, and HALL, K R. 1974. *How to solve equation of state for Z-factors*. The Oil and Gas Journal. February 18, 1974. 86-88.
- ZAGWIJN, W H. 1989. The Netherlands during the Tertiary and Quaternary: A case history of Coastal Lowland evolution. *Geologie en Mijnbouw* 68: 107-120.
- ZIEGLER, P A. 1988. Evolution of the Arctic-North Atlantic and the Western Tethys. *AAPG memoir* no. 43; 198pp.
- ZIEGLER, P A. 1990. Geological Atlas of Western and Central Europe. Shell International Petroleum Maatschappij B.V., 239pp.

CHAPTER 5

Area 3 Safety and Stability of Underground CO₂ Storage

Henk Cox, Jan Piet Heederik, Bert van der Meer and Rieks van der Straaten (TNO)

Sam Holloway and Richard Metcalfe (BGS)

Hubert Fabriol (BRGM)

Iain Summerfield (CRE)

5.1 INTRODUCTION

Jan Piet Heederik, Bert van der Meer and Rieks van der Straaten

The stability of an underground storage reservoir is fundamental for underground CO₂ disposal and the safety aspects of the injection activity are extremely important for the social acceptance of the implementation of such an enterprise. Basically, all issues related to CO₂ storage in the subsurface are known with the exception of the local environmental impact of the geochemical interaction between the injected CO₂ and the reservoir rocks. Analysis of reservoir rocks and cap rocks from natural CO₂ fields suggests that although the rocks have been affected, this interaction is not dramatic (see Chapter 7 of this report; Studlick et al., 1989).

CO₂ injection is not unprecedented. CO₂ is currently being injected in oil reservoirs to improve the mobility of oil with a low viscosity. The published research on the effects of subsurface injection of CO₂ is largely focused on the oil-CO₂ interaction and the volumes of CO₂ involved are much smaller than in a CO₂ disposal venture. In the case of Enhanced Oil Recovery (EOR), the idea is to inject a minimum of CO₂ to recover a maximum of oil. CO₂ injection is alternated with water injection to improve the oil sweep efficiency. Produced CO₂ is recycled. So, conceptually there is a large difference between the operation of a CO₂ storage project and CO₂ injection for EOR purposes. This difference is best illustrated if we consider the injection pressure. In the case of EOR, the rise in pressure due to CO₂ injection is offset by a pressure reduction due to production of fluids (oil, water, and produced CO₂). Since generally more fluids will be produced than injected, EOR will result in an average reservoir pressure reduction. CO₂ injection is not used for pressure maintenance. In the case of CO₂ storage in a water saturated reservoir, the space to store CO₂ only becomes available as a result of compression of the fluids and rock in the reservoir, or (long-distance) displacement of formation water into adjacent formations or to the surface. Hence, CO₂ storage will induce a (temporary) pressure increase in the reservoir. In particular this pressure build-up in the storage reservoir during the injection activity will have a large influence on the stability of the reservoir.

In the past, CO₂ injection into the subsurface by the oil industry has not attracted the attention of environmentalists or governmental control. As a result no relevant data are available in the EOR industry that relate to reservoir stability. This chapter provides a detailed description of all possible facts that have an influence of reservoir stability as a result of CO₂ injection. Furthermore, an estimation is made of the possible effects of CO₂ injection on the

subsurface environment and possible preventive measures are discussed.

The situation is different in the case of the surface and the injection system installation. Since the first production of hydrocarbons, wells have been drilled, and pipelines have been used to transport the product from the production location to the market. A wealth of data is available on operating experience with such installations, on the failure rate of all equipment used, and the impact on the environment in case of failure. This situation is clearly shown in the safety assessment of pipelines (section 5.3.2.1).

In all cases, engineers are capable of designing an installation in such a way that the safety risks of its individual components are almost eliminated. This reduction or elimination of safety risks is closely related to the economics of the whole activity. Evaluation of the circumstances that led to disasters reveals that many, usually improbable matters may go wrong. Generally, it is the combination of insignificant events that lead to the disaster and in many cases it was human failure in this chain of events. To quote Prof. Wagenaar: *'You are building in the risks of a disaster, if you introduce humans as an essential safety component in your system'*. The inevitable conclusion is that ultimately humans have to check the machine and that technology has to take human fallibility into account. The design of a control system for a CO₂ storage activity must therefore include a 'forward thinking logic'. If a control system is capable of predicting the consequence of an action as a result of human diagnostic activity, the chance of total system failure could be reduced. A good example of such a control system is the ABS system in modern cars. In normal operation it is not active, only if a driver makes an error, i.e. hard braking on a slippery road surface, the system takes corrective actions.

Criteria for underground injection of fluid waste

Underground CO₂ storage can be considered as a special kind of deep well injection of fluid waste. In the USA, industrial waste injection started with re-injection of brines that were produced in combination with oil. Injection of other types of waste started in the sixties. Their number grew from 30 wells in 1964 to 333 wells in 1974. Walker and Cox (1976) mention the beneficial and adverse effects of waste injection, which will be summarised below. The benefits of subsurface injection are that it will generally be an economic way to dispose of large quantities of fluid waste and that this waste is effectively removed from the earth's surface. Potential adverse effects are (Walker and Cox, 1976):

- *Contamination of (potential) natural resources*, e.g. hydrocarbon and groundwater reserves. An additional problem of subsurface pollution is its long term effect

and limited controllability. Waste stored underground should therefore be confined to rock layers not containing natural resources. Definition of such reservoirs will be problematic in areas with unregistered abandoned wells.

- **Pre-emption of subsurface storage space:** since a given geological formation has a finite capacity for accepting injected fluids, its use as a disposal reservoir can preclude use for other types of storage.
- **Subsurface pressure alterations:** fluid waste injection will generally result in an increase of the reservoir pressure. The most important potential effect of pressure increases is the stimulation of seismic activity. The significant factor appears to be a reduction in the friction existing at faults. Other effects are formation fracturing and migration of resident fluids with objectionable qualities. The effects of increased pressure travel at a faster rate and have a wider area of influence than the actual movement of the waste itself.
- **Chemical compatibility problems:** geochemical or biochemical interaction between waste and rock. One of the most obvious problems is mineral precipitation reducing or destroying the permeability of the reservoir. This may become an environmental hazard where contingency plans do not exist for waste handling in the event of well malfunction. Another compatibility problem is dissolution of rock by the injected waste, which may result in the subsidence or collapse the land surface. The probability of such an occurrence appears low where injection takes place at a considerable depth.

The US Environmental Protection Agency gives seven specific criteria to be used for the evaluation of injection proposals (in Walker and Cox, 1976):

- 1 *All reasonable alternative measures have been explored and found less satisfactory in terms of environmental protection;*
- 2 *Adequate pre-injection tests have been made for predicting the fate of materials injected;*
- 3 *There is conclusive technical evidence to demonstrate that such injection will not interfere with present and potential use of water resources or result in other environmental hazards;*
- 4 *The subsurface injection system has been designed and constructed to provide maximal environmental protection;*
- 5 *Provisions have been made for monitoring both the injection operation and the resulting effects on the environment;*
- 6 *Contingency plans that will obviate any environmental degradation have been prepared to cope with all well shut-ins or any well failures;*
- 7 *Provisions will be made for plugging injection wells when abandoned and for monitoring plugs to ensure their adequacy in providing continuous environmental protection.*

Although these criteria originate from twenty years ago, they appear to be still applicable for underground fluid waste injection. Similar criteria are expected to be used in the evaluation of a future CO₂ disposal project.

Scope of the safety and stability study

Chapter 5 is a compilation of work performed by the following persons:

Iain Summerfield	CRE	'Risk analysis of CO ₂ transport pipelines'
Richard Metcalfe	BGS	'Consequences of underground CO ₂ disposal on the quality of potable groundwater'
Henk Cox	TNO	'Geophysical techniques to define potential CO ₂ reservoirs'
Hubert Fabriol	BRGM	'Pre-feasibility of micro-seismic monitoring'
Bert van der Meer	TNO	'Subsurface retention time of escaping CO ₂ '

Each of the above contributions discusses different safety aspects of underground CO₂ disposal and have been written as 'stand-alone' reports. In this chapter they have been placed into the following framework:

- Possible effects of CO₂ disposal (section 5.2)
- The surface and injection installations (section 5.3)
- The storage reservoir (section 5.4)
- CO₂ leakage and its effect on groundwater quality (section 5.5)
- Subsurface Retention Time of Escaping CO₂ (section 5.6)

In the section on the surface and injection installation (section 5.3), design, safety aspects and CO₂ discharge in the case of a system failure are discussed. However, relatively little attention is paid to these parts of the storage system and the chapter is largely focused on the stability of the reservoir during and after CO₂ disposal. This is done because reservoir stability will be the most critical aspect of CO₂ disposal, whereas the safety aspects of transport and CO₂ injection are relatively well known and will largely correspond to the safety aspects of other fluid injection activities (e.g. by the oil industry).

The stability of an underground reservoir after injection of a large volume of CO₂ (section 5.4) is, however, an untested phenomenon that will pose several new problems that are less well understood. The major problems are expected to arise from the pressure build-up in the reservoir during injection, which may endanger the stability of the reservoir. The pressure increase may degenerate the sealing capacity of the cap rock, induce micro-seismicity, trigger faults or cause absidence of the ground surface. Because large-scale underground CO₂ storage is unprecedented, careful monitoring of the reservoir during the injection process will be required. Another point that

will be addressed is the question of what will happen if the reservoir is damaged and large volumes of CO₂ are able to escape from the reservoir into shallower formations or even to the surface. How does CO₂ leakage effect the quality of ground waters resources (section 5.5)? How long does it take before the CO₂ reaches the surface (section 5.6)?

5.2 EFFECTS

Jan Piet Heederik and Bert van der Meer

5.2.1 Introduction

When considering the safety and stability of injecting CO₂ into aquifers and depleted oil or gas fields we have to fall back on the knowledge and data gained from CO₂ injection projects, and the working practices used in these projects by the oil and gas industry. CO₂ injection for Enhanced Oil Recovery (EOR) is an everyday practice in the USA and other parts of the world.

Potential adverse effects in relation to safety and/or environmental damage can be categorised into five groups (see section 5.1):

- escape of CO₂ to the atmosphere
- CO₂ pollution of groundwater or other underground resources
- seismicity
- subsidence or absidence of the earth surface
- degradation of the storage reservoir underground

The total storage system is subdivided into three specific parts in order to evaluate the risks and safety measures associated with each individual part. We distinguished the following components: 1) the surface installations and equipment; 2) the injection system (i.e. mainly the injection wells); and 3) the storage reservoir. In the following sections a description will be given of causes of possible safety and environmental risks associated with underground CO₂ storage. Possible preventive measures will be discussed according to present knowledge and safety and environmental rules.

Escape of CO₂ to the atmosphere can occur in all parts of the of the storage system. For this reason the general effects and circumstances of CO₂ releases to the atmosphere are discussed in the following section. The individual releases of CO₂ from specific parts of the CO₂ storage system are covered by separate consecutive sections, which additionally include a description of the possible preventive measures to eliminate or minimise the risk of CO₂ releases to the environment.

5.2.2 Escape of CO₂ to the Atmosphere

A major risk formed by the leakage of large amounts of CO₂ to the surface is suffocation of human beings or animals. At surface conditions CO₂ is heavier than air, CO₂ tends to cling to the earth's surface, forming a blanket-like cloud that flows into and fills topographic depressions. In this way pools of CO₂ may develop in valleys from which all oxygen has been driven away. At

first, the danger of these clouds will not be noticed, because CO₂ is a colourless and odourless gas. Natural releases of large amounts of CO₂ occur in volcanic areas. The 1986 disaster in Cameroon caused by a sudden escape of large amounts of volcanic CO₂ from Lake Nyos, killing more than 1700 people, illustrates that CO₂ clouds may form a serious hazard (see Hendriks, 1994). Another example is the more modest escape of CO₂ after the 1947 eruption of the Hekla on Iceland that led to the death of animals that strayed into CO₂ pools accumulated in local depressions (Francis, 1976).

If we consider an amount of 100 Mt CO₂ stored underground (ca 25 years CO₂ production from a 500 MW coal fired power station) and assume that it is somehow possible that this stored amount could escape from the reservoir and reach the surface in a very short time, CO₂ release could result in a cloud of ca 50 km³, which may in the most unfortunate case (with a cloud thickness of 3 m) cover an area of roughly 18 000 km². The disastrous effect of such a cloud in populated areas is obvious, but the likelihood of such a disaster is very small. The escape of almost all CO₂ that has been injected over 20 years is impossible in a short time due to the limitation of the injection system. The effects of the burning Kuwait oil and gas wells have shown that the escaped volumes are controlled even in the absence of controlling safety valves. In the case of CO₂, a leak may be partly obstructed by the formation of dry ice, thus reducing the rate of release. However, the Cameroon case shows that modest CO₂ releases can be captured in deep lakes in which the amount of CO₂ may gradually build-up and that a sudden release of the thus accumulated CO₂ may have a disastrous effect. Fortunately, most lakes are confined to depressed areas and most CO₂ released will therefore stay above the lake.

Another risk related to CO₂ escape is instant freezing of plants, animals or human beings in the direct vicinity of the leak, due to the temperature drop caused by expansion of the liquid CO₂. The rapid CO₂ expansion may cause the formation of dry ice. Section 5.3 gives a more detailed report on the causes of CO₂ leakage to the atmosphere.

5.2.3 Groundwater pollution

Potable groundwater is generally found in the top 100–200 m of the subsurface. This fresh water could be contaminated by leakage of free CO₂ from either the injection system (i.e. injection wells) or the storage reservoir. In both cases, the CO₂ will be at a higher pressure than that of the formation and will have penetrated the surrounding strata. The subsequent de-compression will result in an expansion of the CO₂ volume and a reduction of the CO₂ density. The density of the free CO₂ will always be lower than the water density of the invaded zone resulting in a tendency of the CO₂ to move upwards. This tendency or gravity segregation will increase when the CO₂ comes closer to the Earth's surface. The time it will take CO₂ to reach the potable groundwater zone will largely depend on the depth of the actual leak, the volume of leaked CO₂ and the permeability and heterogeneity of the formations between the leak and the potable water zone. In the case of a well failure, CO₂ leakage can be controlled by a monitoring system in combination with a number of automatic check valves. The use of such a control system will reduce the potential amount of CO₂ escaping from the well to insignificant proportions. A full description of such a system is given in section 5.5. A CO₂ leakage from the storage reservoir is less controllable, making it rather

difficult to quantify the possible safety and environmental consequence of such an event. Section 5.4 reports on the stability aspects of CO₂ storage reservoirs while section 5.4.3. reports in particular on the possible consequences of groundwater pollution by leaked CO₂.

5.2.4 Seismicity

Underground disposal of CO₂ requires the control (if possible) of the physical and chemical modifications of the reservoir. This is essential for safety and long term disposal. It is well known that injection of large amounts of fluid into a sediment layer or fractured rock modifies its mechanical state. High pore-pressure gradients in or around the reservoir may induce micro-earthquakes and even damaging earthquakes. The process may be enhanced by contraction of the rock due to cooling by 'cold' injection fluids. Several examples are described in the literature. In the case of re-injection of waste fluid in the Rocky Mountain Arsenal well (Colorado, USA), three earthquakes with magnitudes larger than 5 were recorded in 1967. Oil and gas reservoirs may also be sources of reservoir-induced seismicity (RIS), generally when fluids are injected for enhanced oil recovery (EOR). In Cogdell (Texas, USA) and Rangely (Colorado, USA) seismicity was extensively studied and reservoir pressure was modelled to determine the minimum pressure needed for seismic failure. At Rangely, cycles of injection and backflow showed that seismicity was correlated with pressure changes in the reservoir. Microseismicity has also been observed around water injection wells of geothermal projects. Lastly, induced seismicity in gas storage reservoirs has been reported from two locations. Although the magnitudes are very low, micro-earthquakes can be recorded, and can be used as an aid in the study of the mechanical behaviour of reservoirs.

The study of induced seismicity has two aspects. The most important is seismic hazard assessment. The other aspect is in situ monitoring of the mechanical behaviour of the reservoir. The latter is not yet obligatory, as it needs more sophisticated technology and is still at an experimental stage. Both aspects require careful examination of the conditions at the disposal site, i.e. historical seismicity, structural study of the area, evaluation of the critical fluid pressure for failure, and pre-injection seismic monitoring of the area to define the 'zero state' seismicity. In addition, modifications of the reservoir state should be examined if it is a pre-exploited reservoir. During disposal operations a combined network of subsurface and downhole sensors can be installed to monitor induced seismicity. State-of-the-art seismological monitoring allows real-time determination of the location of hypocentres, with either a surface network for large events, or downhole sensors for microseismicity. The surface network is mainly designed to assess and prevent seismic hazards, the subsurface network to study reservoir processes in detail. The full results of a study of induced seismicity are reported in section 5.4.4.

5.2.5 Subsidence or Absidence of the Earth's Surface

It is possible that the earth's surface will sink or rise because of man-made pressure changes in the subsurface. Several cases of subsidence are well known and extensively documented. Examples are the Ekofisk oil field and the Groningen Gas field. For all these cases, the mech-

anism is well understood, but prediction of subsidence is found to be difficult. The data on absidence are limited, but it is understood that here the same theories can be applied as for subsidence.

The total pressure at any depth, resulting from the combined weight of the formation rock and fluids, is known as the overburden pressure. At a given depth, the overburden pressure is equal to the sum of the fluid pressure and the grain or matrix pressure acting between the individual rock particles. Since the total pressure remains constant at any particular depth, a reduction in the fluid pressure will lead to a corresponding increase in the grain pressure, and vice versa. It will be clear that the grain pressure will increase by fluid withdrawal, while the grain pressure will decrease by fluid injection. Whether this change in grain pressure is accommodated by the rock depends on the rock structure and characteristics. The pressure change can reach a level which the rock frame cannot withstand. When the grain pressure rises in an unconsolidated sandstone, the grains will initially regroup and eventually be crushed. This will reduce the pore space. In the case of injection, the grain pressure will eventually be reduced to zero. With a further increase of the fluid pressure, the grains will tend to float in the injected fluid. In the case of consolidated rock, rock failure depends on the strength of the matrix. The rock frame may collapse if the grain pressure becomes too large due to fluid withdrawal, while in the injection situation a negative grain pressure will fracture the matrix.

The main phenomenon of this rock transformation is the change in pore space. As a result, the earth's surface may sink or rise, depending on factors such as formation thickness, areal extent of the compaction, depth of the formation and the characteristics of the overburden. For CO₂ injection, only an increase of the fluid pressure needs to be considered. Subsidence due to pressure changes is therefore not expected. It is further not envisaged that absidence will take place in a CO₂ reservoir as long as the maximum storage pressure is kept below the geostatic pressure (= initial overburden pressure), implying that the incremental reservoir pressure will always be less than the original grain pressure and the grain pressure will remain positive. Regular monitoring of the surface level above the storage site can confirm this theory. However, in a reservoir that is under high tectonic stresses, any significant reduction of the grain pressure may trigger faults. This may lead to uplifting or down-faulting of the surface, depending of the nature of the tectonic regime.

Another cause for subsidence may be dissolution of the reservoir rock (chemical compaction). For example, in an underpressured gas reservoir the load of the overburden may be supported by the strength of the rock framework. If the rock framework is leached by aqueous CO₂, the reservoir may cave in under the weight of the overburden formation. Chemical compaction will particularly be a matter of concern in carbonate rocks with a high (secondary) porosity, but grain-to-grain pressure solution may also be enhanced by a decrease of the pH in siliclastic rocks. Moore. (1989) mentions some major factors that affect chemical compaction of carbonate rocks (Table 5.2.1). Considering these factors, it is obvious that if overpressured hydrocarbon bearing carbonate rocks become underpressured and saturated by carbonated water, they are likely to endure chemical compaction. The effect of CO₂ on the rock matrix, such as dissolution, will be discussed in Chapter 7.

Table 5.2.1 Factors affecting chemical compaction of carbonate rocks (after Moore, 1989).

Factors Enhancing Chemical Compaction	Factors Retarding Chemical Compaction
Metastable mineralogy (= aragonite)	Stable mineralogy (= calcite, dolomite)
Magnesium poor meteoric water in pores	Oil in pores (inhibits carbonate dissolution)
Insolubles such as clay, quartz and organics	Elevated pore pressure
Tectonic stress	Organic boundstones

5.3 SURFACE AND INJECTION INSTALLATIONS

Iain Summerfield and Bert van der Meer

5.3.1 Introduction

A CO₂ storage system will require a surface installation consisting of a CO₂ transmission pipeline, a CO₂ delivery station, a pipeline distribution network and a monitoring system. After being processed and compressed, the CO₂ output from a power plant will be brought through the CO₂ transmission pipeline to the central delivery station at the disposal site. At this station, the quality and quantity of the CO₂ must be controlled. Depending on the quality, some additional treatment may be necessary, such as filtering, introduction of inhibitors or re-compression. The pipeline distribution network will be needed to carry the CO₂ to the individual injection wells. The monitoring system will control pressure and flow during the CO₂ injection process.

5.3.2 CO₂ Transmission Pipelines

An analysis of pipeline design for CO₂ transport has been carried out. This analysis assumes that the output of CO₂ from a single power plant needs to be transported 75 km to the disposal site. Pipeline design and safety are considered in this section.

5.3.2.1 PIPELINE DESIGN

The use of carbon dioxide for injection into ageing oil wells to enhance oil production is established technology, widely practised in the USA. This technology typically involves transmission of liquid CO₂ by pipeline from natural CO₂ wells to oil wells. The total CO₂ transmission capacity in the USA is about 100 million Nm³/day. The longest CO₂ transmission pipeline in the USA is the Sheep Mountain CO₂ pipeline which is 656 km long and is in two segments with diameters of 500 and 610 mm.

For this analysis, it is assumed that liquid CO₂ at 100 bar and 10°C is to be transported from the power plant 75 km to a suitable disposal site. The required flow rate of CO₂ is 220 tonnes per hour. The pipeline is sized to ensure that the operating pressure of the pipeline does not drop below the local vapour pressure of CO₂. Vaporisation of the CO₂ in the pipeline would inhibit flow. A 250 mm diameter pipe would result in an overall pressure drop due to frictional losses of about 20 bar, thus giving a delivery pressure of about 80 bar. The vapour pressure of CO₂ at the ambient temperature of the pipeline would be about 50 bar. The critical pressure and temperature of CO₂ are 72.8 bar and 31°C. This size of pipeline therefore gives an adequate margin to allow for the expected range of temperature and elevation variations along the pipe.

Liquid carbon dioxide pipelines require a carbon steel pipe with the following characteristics:

- high impact toughness to resist crack propagation
- the ability to cope with low temperature conditions down to -20°C in normal operation
- the ability to cope with rapid temperature change caused by line depressurisation which could cause the temperature to fall as low as -78.5°C (solid sublimation temperature at atmospheric pressure).
- resistance to corrosion from mild carbonic acid which may result from the inclusion of small quantities of water in the CO₂ produced from the power plant.

For these characteristics impact tested API 5L carbon steel is specified. The other specifications of the pipeline are: a nominal diameter of 250 mm and a wall thickness of 16.5 mm with a corrosion allowance of 3.0 mm. The pipeline would be of fully-welded construction with an external cold-tar wrap for corrosion protection.

The pipeline would normally be buried 1 m deep, to the top of the pipe. Increases in depth of burying would be made to allow for land drains, crossings, peat and marsh areas, for security purposes etc. The pipeline trench would be back-filled with selected material from the original soils sequence and compacted to minimise settlement.

5.3.2.2 SAFETY ASPECTS OF CO₂ TRANSMISSION PIPELINES

Considering safety, the pipeline design is based upon the following considerations:

- the classification of CO₂ as a low-hazard material in existing pipeline codes
- the CO₂ transmission capacity of the 250 mm pipeline
- the discharge and dispersion consequences of pipeline ruptures.

CO₂ Discharge From a Pipeline Rupture

For consideration of CO₂ leaks from pipes the following definitions of types of pipe defect are adopted (Pipes and Pipelines International, 1988):

- pinhole or crack defects with a diameter up to 20 mm
- hole defects with a diameter from 20 mm to pipe radius (125 mm)
- rupture defects with a diameter larger than the pipe radius (125 mm)

For a CO₂ disposal pipe with a 250 mm diameter, the total amount of liquid CO₂ between two adjacent isolation valves would be about 3000 tonnes (ca 1 500 000 Nm³).

The 'pinhole' category of pipe failures has a largest hole size of 20 mm. CO₂ would escape at a rate up to about

6 kg/s through such a hole and it would take about 150 hours for the section of pipe to discharge all its CO₂. At this rate of loss the CO₂ would probably disperse into the surrounding air until the leak was identified and repaired.

Failures of the 'hole' type would result in defects with equivalent diameters ranging from 20 mm to 125 mm. The corresponding CO₂ release rates would range from 6 kg/s to 240 kg/s. Accordingly the CO₂ content of the pipe between two shut-off valves would be discharged in a period ranging from 150 to 3.5 hours.

Failures of the "rupture" type would involve effective hole diameters from 125 mm to 250 mm. The corresponding rate of CO₂ release would be up to 10 tonnes per second and the CO₂ from one pipe section could be discharged in 10 minutes. In such circumstance the liquid CO₂ would be subject to adiabatic expansion which would result in the release of 67% of the CO₂ in the vapour phase, 30% as solid CO₂ snow at the site of the rupture (occupying about 7400 m³) and 3% remaining as CO₂ snow inside the pipe. The temperature resulting from rapid adiabatic expansion of liquid CO₂ to atmospheric pressure would be -56°C.

CO₂ Dispersion

A series of simulations of CO₂ release from perforated pipelines was carried out based on an hole size of 10 mm in a 1 m diameter pipe (corresponding to 1.5 kg/s discharge rate) and wind speeds of 1 m/s and 10 m/s. These simulations determined a pattern of release to atmosphere and the corresponding CO₂ concentration maps. In these simulations the IDLH (Immediate Danger to Life and Health) figure for CO₂, in the region of 3 to 5% by volume in air, was reached at ground level only within 50 m of the source. This exercise showed that CO₂ losses from a small leak would result in ground level concentrations which would not constitute a significant risk to life. A similar theoretical simulation would need to be carried out to predict the dispersion of CO₂ from a large discharge.

Frequency Of Pipeline Failure

A group of six European natural gas transmission companies has collated information on pipeline incidents directly relevant to pipeline design and operation practices in Europe (Pipes and Pipelines International, 1988). The incidents are uniquely defined and restricted to gas transmission lines covering a length-time period of more than 970 000 km·years. A total of over 600 incidents, which all involved loss of gas, comprise the database for this analysis. The data are derived from records from 1970 to 1987 but refer to pipes dating from the 1950's onwards. The incidents are classified by size of failure and by cause.

The specific cause classifications used in this analysis are:

- **External interference:** breach of the transmission pipe by some external agency e.g. accident or agricultural activity
- **Hot tapping:** in advertent breaches of the pipe by utility workers mistaking the pipe for, say, a water pipe
- **Corrosion** (more prevalent in older pipes)
- **Construction defect** (including defects in materials); these failures are more prevalent in pipes constructed before 1970

- **Ground Movement;** only in areas of high geological activity

The Table 5.3.1 gives the historical data analysed by size and cause, as incident rates per million kilometre·years. Failures due to external interference are strongly dependent on pipe size, larger pipes being much less prone to damage by external interference. An analysis of the data available for the dependence of ruptures due to this cause on pipe diameter indicates the following relationship between frequency of ruptures due to external interference (*f*) and the pipe diameter in mm (*d*): $f = e^{10.3-1.12 \ln(D)}$ per 10⁶ km·year. For a 250 mm diameter pipe this relationship gives 60 ruptures per million km·years from external cause, i.e. 70% of the average value for ruptures from this cause based on the historical database.

To estimate the likelihood of the occurrence of a pipeline failure of sufficient magnitude to potentially create a hazardous cloud of CO₂, the following assumptions are made:

- all 'ruptures' cause large losses
- the largest 10% of 'holes' cause large losses
- the frequency of failure due to external cause for a 250 mm pipeline is 70% of the overall frequency of failure by external cause.
- experience in pipeline design, protection and siting means that the failure frequency of future pipelines is 10% of that of pipelines in the past.

On the basis of these assumptions the estimated frequencies of occurrence of large losses by defect size and cause, are listed in Table 5.3.2. These figures show a total estimated frequency of large losses of CO₂ to be about 11 per million kilometre·years. Therefore the estimated frequency of a major incident occurring involving large losses of CO₂ from a 75 km long pipeline is once every 1200 years.

5.3.3 Surface Equipment at the CO₂ Disposal Site

5.3.3.1 DESIGN OF THE SURFACE EQUIPMENT

On top of the CO₂ storage reservoir, a central CO₂ delivery station will be required to control the quality and quantity of the delivered CO₂. It should be sufficiently equipped to enable the operator to test and service the wells in normal

Table 5.3.1 Natural gas pipeline failures in Europe per million km·years during the period 1970–1987 (Pipes and Pipelines International, 1988).

Cause	Pinhole	Hole	Rupture	Total
External interference	70	170	89	329
Hot tapping	12	10	0	22
Corrosion	100	2	1	103
Construction defect	74	37	11	122
Ground movement	6	15	13	34
Other	44	4	6	54
Total	306	238	120	664

Table 5.3.2 Estimated frequency of occurrence of large losses by defect size and cause, in incidents per million kilometre-years.

Cause	Hole	Rupture	Total
External interference	1.2	6.25	7.45
Hot tapping	0.1	0	0.10
Corrosion	0.02	0.1	0.12
Construction defect	0.35	1.1	1.45
Ground movement	0.15	1.3	1.45
Other	0.04	0.6	0.64
Total	1.86	9.35	11.21

prevent well clogging), the introduction of inhibitors or re-compression. Apart from this delivery point, a pipeline distribution network will be needed to transport the CO₂ to the individual injection wells. A pressure and CO₂ flow monitoring system will additionally be required to control the CO₂ injection process.

The wellhead cluster principle should be used in order to minimise the environmental impact of the surface installation. This principle requires the drilling of deviated wells. The general layout of the surface facilities is shown in Figure 5.3.1. The pipeline distribution network at the wells will be equipped as shown in Figure 5.3.2.

A wellsite ESD (Emergency Safety Device) valve will provide protection in case of a failure. This valve may be activated either locally or remotely through the SCADA system (Supervisory Control and Data Acquisition). A filter, with 5 micron elements, will ensure that particles which could otherwise damage the well are removed from the CO₂ stream. A flow meter will measure the quantity of CO₂

operations without delay. Some additional treatment may be necessary, such as filtering (removal of solid particles to

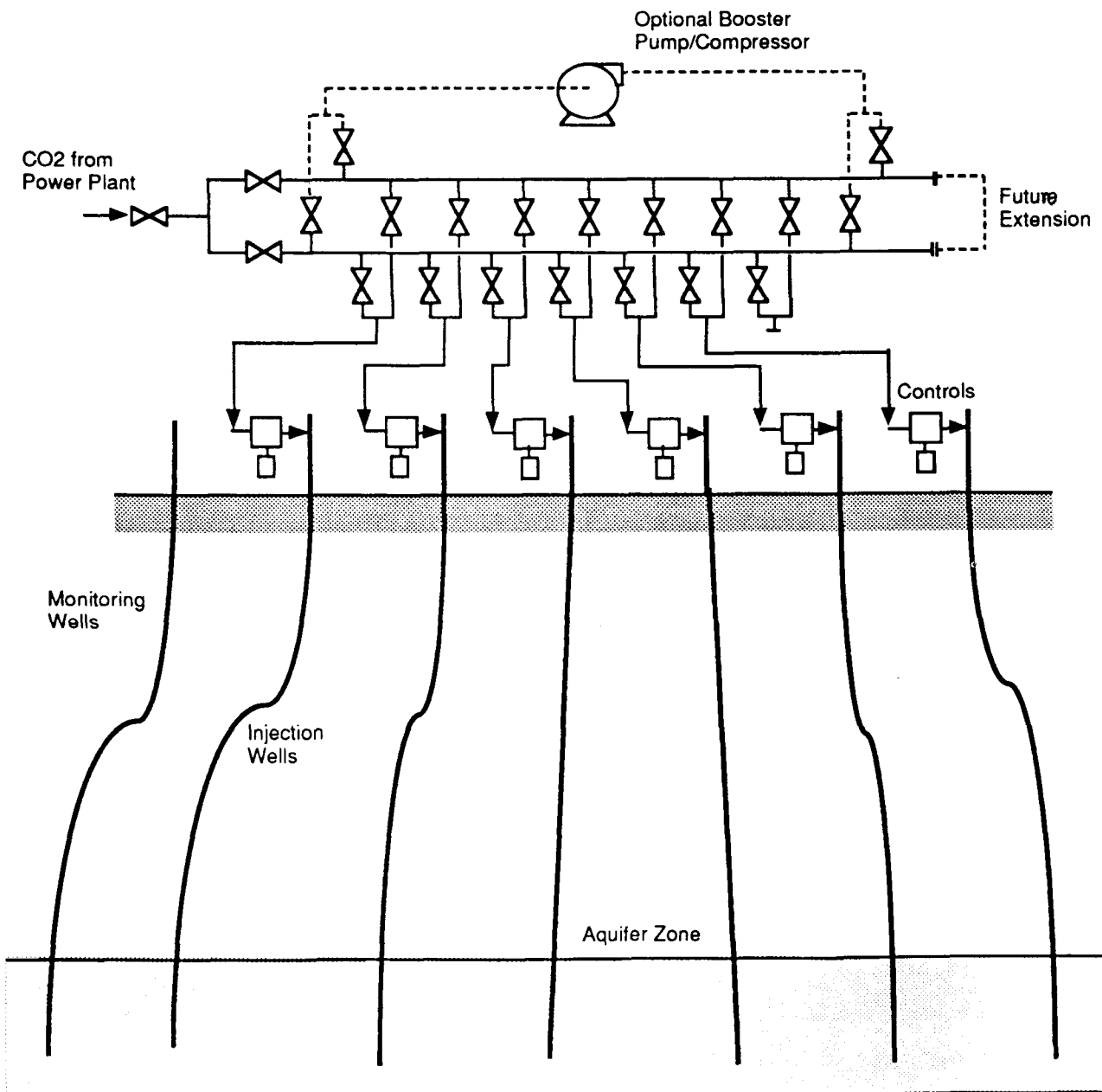


Figure 5.3.1 General layout of the surface facilities.

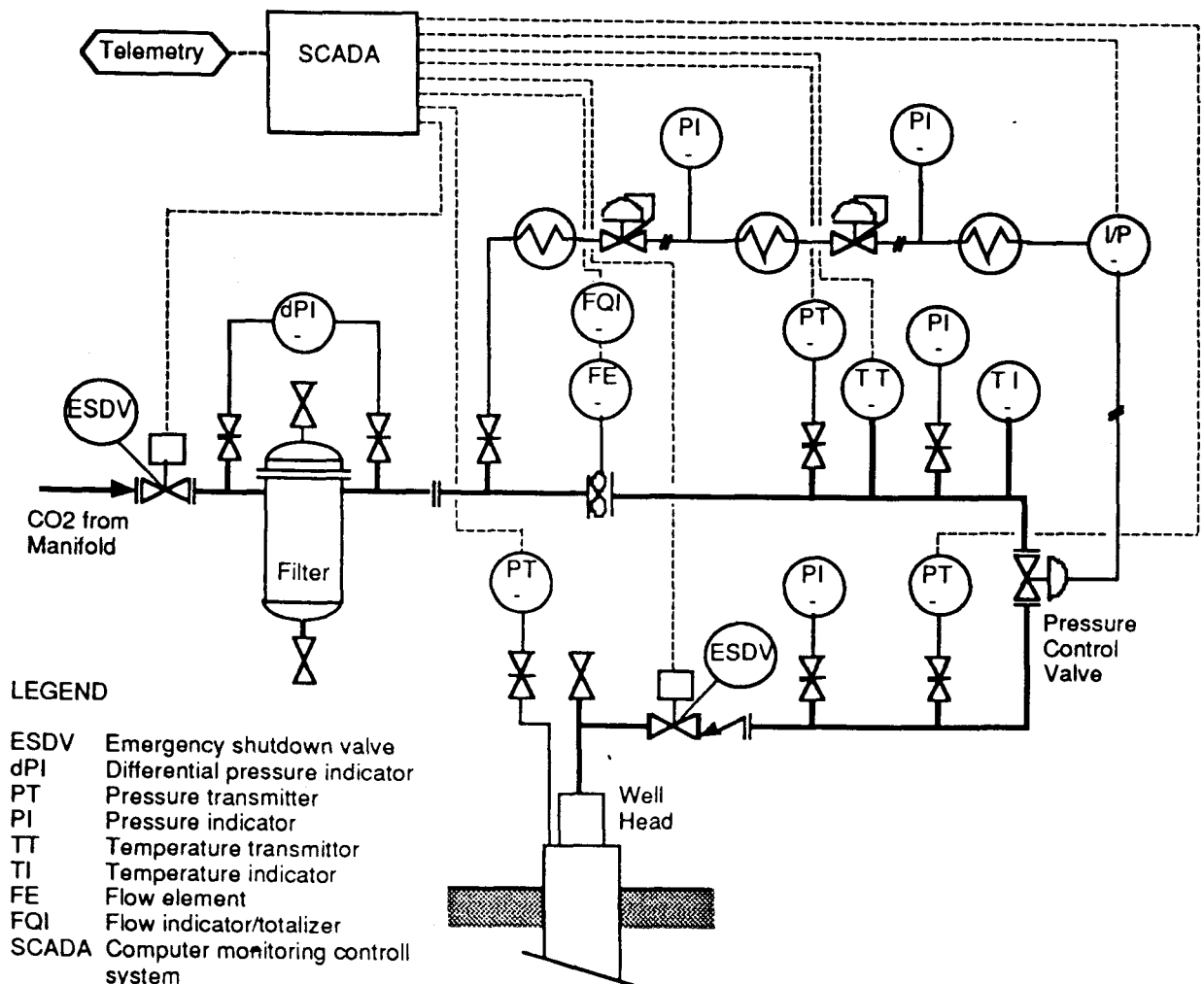


Figure 5.3.2 Well head surface piping and controls.

being injected, and, via the SCADA system, provides the means to record the material balance to check for any line breaks. Pressure and temperature sensors also form an integral part of the material balance instrumentation and monitor flowing conditions at the well. A control valve accepts signals via the SCADA system to apportion the total system flow to each well as required. This valve is also required for the start-up of the injection and to maintain a back-pressure for proper operation of the flow meter. A discharge check valve is provided for safety, to avoid back-flow production of previous injected CO₂ in an emergency situation. Local SCADA components and telemetry systems will be required, including a local emergency power supply.

5.3.3.2 SAFETY ASPECTS OF THE SURFACE EQUIPMENT

Malfunctioning of the surface system can cause CO₂ leakage to the atmosphere. Possible causes are:

- leaking connectors and appendages
- unsuitable and leaking materials
- unsuitable constructions and execution
- decay of materials through time
- external damage to pipelines caused by, for example, digging and/or building activities

Malfunctioning of the system can be reduced by rigorous maintenance and the use of suitable high quality materials. Dehydration of the CO₂ is the measure normally taken to control corrosion in the oilfield CO₂ distribution system. Special precautions against corrosion, such as internally coating the pipe or using special steel, do not appear to be common operating practice, except where high concentrations of H₂S are present. For this latter situation, one operator reported using stringent precautions to obtain satisfactory welds in addition to using a pipe with sufficiently low Rockwell-C hardness to resist sulphide stress cracking.

In the event of a destructive failure of the surface system, only a small quantity of CO₂ will be released to the atmosphere. Since the CO₂ will be at a relatively high pressure in the system, a failure will cause a rapid pressure drop in the distribution system. A simple additional device integrated in the pressure monitoring system could close off the failing subsystem. The amount of CO₂ released will thus be restricted to the contents of the failing subsystem (see section 5.3.2).

5.3.4 The Injection Installation

5.3.4.1 DESIGN OF THE INJECTION INSTALLATION

The injection installation will consist of a number of wells that have to be drilled in order to inject the CO₂ into the

underground reservoir. The location of the injection wells will be selected by geologists or geophysicists. With modern directional drilling techniques, the surface location does not have to be directly above the point where the drill hole penetrates the target formation. For practical and environmental reasons it is very attractive to keep the surface activities confined to a small area. So, if possible, all new wells should be drilled from the same location, i.e. from one drilling platform.

The injection well system will generally follow local high pressure gas practice, with additionally special attention for corrosion control. A basic injection well consists of a stove pipe or conductor pipe which is pushed into the upper part of the subsurface or soft sea floor before deeper drilling starts. This pipe has diameter between 25 to 50 cm. The rest of the hole is reinforced with intermediate casing strings, a series pipes decreasing in diameter. The individual length of each casing segment depends on the weight of the pipe (i.e. pipe thickness), the type of geological formation penetrated, and the drilling rig. The casing segments are attached to the penetrated formation with cement which is pumped down the inside of the pipe, followed by a plug that wipes the cement from the inside of the casing. Drilling mud is pumped in on top of the plug to displace the cement to the bottom and out into the space between the casing and the wellbore.

A cement evaluation tool (Cement Bond Log) must be used in the CO₂ injection well, because it is important to have an exact indication of the cement compressive strength, which is a function of the shear coupling between pipe, cement and formation. It is also important to have an indication of the cement distribution around the casing, in order to detect the presence of channels. The cement job has to be of a very high quality where the bottom casing segment passes through the cap rock, preventing any CO₂ from leaking from the reservoir to the overburden formation.

Injected CO₂ enters the reservoir rock via perforations made in the lower part of the bottom casing section. Injection will take place through an injection or tubing string that runs through the casing. The space between the tubing and casing is sealed off from the CO₂ with a packer. This space forms an important barrier between the CO₂ and the subsurface. Monitoring the pressure behaviour in this space will indicate CO₂ leakage from the injection string. At the top of the tubing, on the ground surface, a wellhead is installed. The technical lay-out of a typical CO₂ injection well is shown in Figure 5.3.3.

5.3.4.2 SAFETY ASPECTS OF THE INJECTION INSTALLATION

The following situations could lead to the failure of the well during injection and could subsequently cause the rocks above the storage reservoir to be contaminated by CO₂:

- unsuitable construction and/or execution
- leaking pipe connections
- defective materials
- collapse of the well
- human failure

Malfunctioning of the well injection system can be reduced by a high level of maintenance and the use of well selected materials. The constant quality of the casing

is crucial in preventing leaks. The state of the casing and the tubing have to be controlled by corrosion control tools (Pipe Analysis Log). Any leak in the well can be detected by monitoring the pressure in the space between the casing and the tubing ('annulus' in Figure 5.3.3.).

Wells that penetrate rock-salt need special attention. Due to its plastic behaviour, the salt could cause wellstrings to collapse. Earthquakes or ground movements may have the same effect and there have been many examples of casing collapse in oil and gas fields caused by shear along faults intersecting the well (see section 5.4.3.4). If the well fails, large amounts of CO₂ may escape. The CO₂ in the underground reservoir may escape until the in situ pore pressure equals the hydrostatic pressure on the formation. Leakage can be detected from the pressure/flow history of the well. Safety valves installed at regular intervals in the well, could limit the amount of escaping CO₂.

If CO₂ escapes from the injection system, the CO₂ will migrate upwards due to its relatively low density. Assuming a hydrostatic pressure distribution in the subsurface, the CO₂ density will decrease with depth. So, the escaping CO₂ will percolate upward with an increased velocity. CO₂ will go into solution where it is passing groundwater bearing formations. In the majority of well failure cases, the amount of CO₂ released will be very small, i.e. an amount equal to the content of the well tubing. In normal cases such a leak will be detected by the SCADA system due to a rapid pressure increase in the annulus, resulting in the closure of the back flow preventer and the emergency shutdown valve at the well head. In that case, most leaked CO₂ entering the rock formation will be absorbed by the formation water. Failure of the back flow preventer, the packer or the cement between the casing and the caprock will have a much greater impact. The first two problems may result in a well blow-out. High pressure CO₂ from the storage reservoir will find its way upwards to the casing and will expand due to increasing lower pressure. The wellhead construction must be designed in such a way that it is able to handle this pressure increase. Repair of such a mechanical problem is more simple than in case of an oil or gas well, because CO₂ is non-combustible and non-toxic. For the effects of a leaking caprock the reader is referred to sections 5.5 and 5.6, which cover CO₂ retention time and the effects of a leaking CO₂ reservoir on the quality of groundwater.

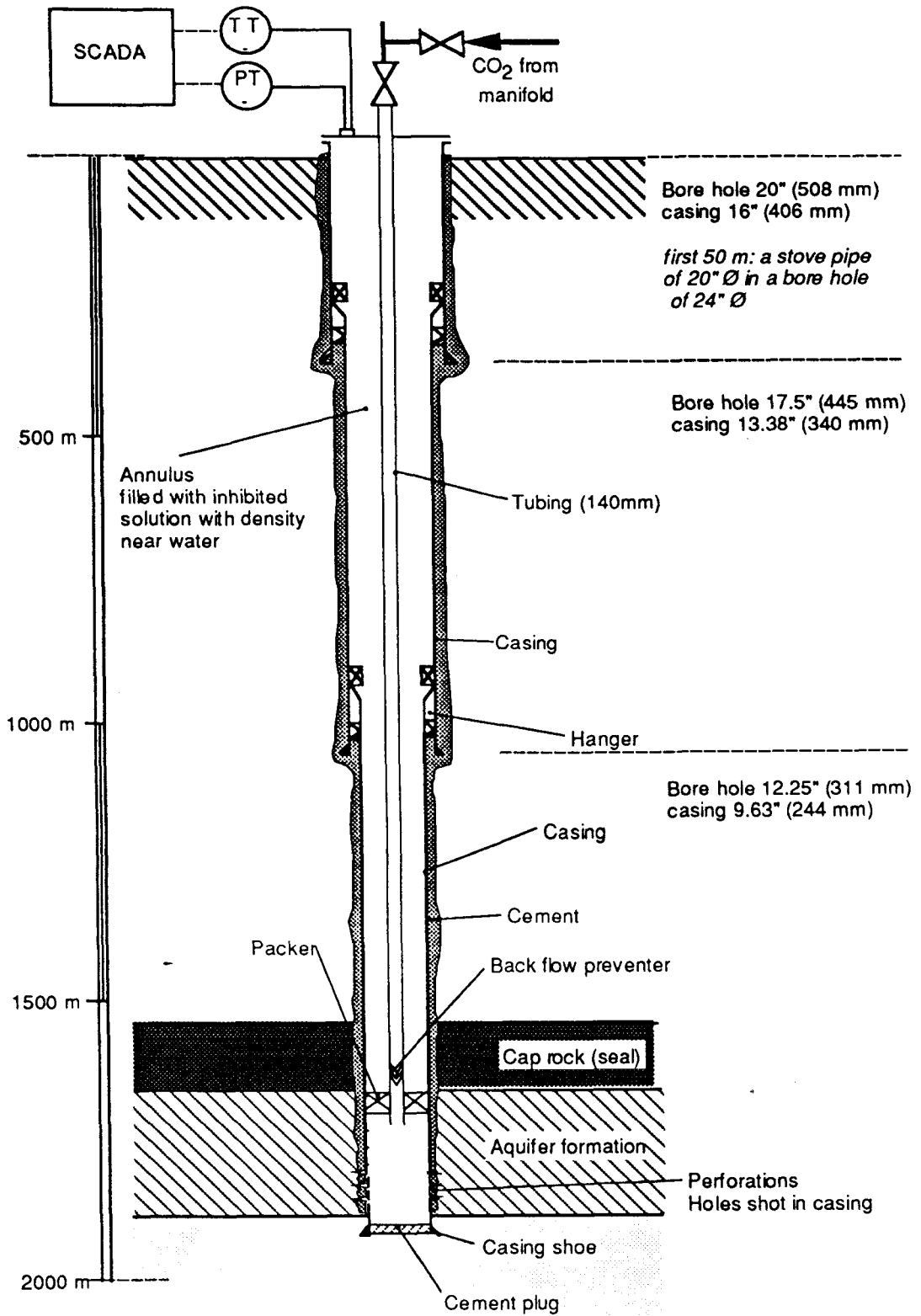
5.4 THE STORAGE RESERVOIR

Henk Cox, Hubert Fabriol and Bert van der Meer

5.4.1 Introduction

The basic principle of storage implies that the material that has been stored stays at a pre-defined storage location. In almost all storage cases, processes are taking place which are in conflict with this principle. If no special measures are taken, most materials degrade in time. These degradation processes are taking place in the material that is stored and in the storage container, and may be induced or enhanced by changes in temperature, pressure and volume. In all cases they have a negative effect on the storage integrity, i.e. the stability of the storage activity. In case of underground CO₂ storage the following processes can be identified:

Figure 5.3.3
Typical injection
well lay-out



- 1 Processes affecting the condition of the stored CO₂. Important factors are reservoir temperature, reservoir pressure, residual components and possible chemical influence of formation fluids and rock on CO₂.
 - 2 The interaction of the CO₂ on the rock and subsequently on the fluid flow parameters of the reservoir rock.
 - 3 Processes which have an influence on the storage boundaries, e.g. geochemical reactions influencing the sealing capacity of the caprock.
 - 4 Processes induced by movements of the earth crust such as tectonic activities and/or microseismic events.
 - 5 Processes which are a direct result of human activities. Examples of these processes are overfilling, hydraulic fracturing of the caprock, an incomplete understanding of the geological environment or topology, such as unobserved open faults or spillpoints.
- All above identified processes will have the effect that CO₂ could escape directly or indirectly from the storage reservoir. Normally, all known effects of CO₂ storage in

the subsurface will be taken into account in the design of a storage site. However, it will be impossible to reduce the risk of CO₂ leaking from the reservoir to zero. So, it is will be important to evaluate what will happen if CO₂ does leak into adjacent formations. In the following sections, we are evaluating the geological and reservoir engineering aspects in relation to the stability of the storage process (points 3–5). The geochemical aspects of CO₂ storage are discussed in the chapter 7 (points 1–2).

5.4.2 Reservoir Selection

5.4.2.1 GENERAL CONSIDERATIONS

Several factors must be considered if a CO₂ storage reservoir is selected. One of the most important is the extent and the quality of the seal of the proposed reservoir. For oil- or gas fields, the properties of the seal are already known. In the case of aquifer storage, the knowledge of the cap rock characteristics will generally be limited and an extensive survey will be needed to fill in this gap.

Another limiting factor will be future environmental legislation. Some specific criteria to be used for the evaluation of waste injection proposals in the USA have been mentioned in section 5.1. The criterion that will be relevant for reservoir selection is that there should be *'conclusive technical evidence to demonstrate that waste injection will not interfere with present and potential use of water resources or result in other environmental hazards'*. In the Netherlands, future environmental legislation is expected to permit underground CO₂ storage only if the process is reversible. This requires CO₂ confined to a fixed storage area, which implies a trap which stops fluid migration.

The main characteristic of a trap of a hydrocarbon reservoir is that it has an impermeable top, known as a caprock or seal. In most cases, the trap is open for fluid flow at the outer boundaries of the formations, which allowed the hydrocarbon fluid to migrate into the trap structure. In fluid storage terms we call these open sites

“spillpoints”. The structural highest spillpoint will determine the storage capacity of the structure. If the reservoir is overfilled or a spillpoint is overlooked, CO₂ may escape into the surrounding strata depending of the topology of the subsurface. Leakage may additionally occur through natural or man-made pathways that are overlooked and/or undefined.

5.4.2.2 GEOPHYSICAL TECHNIQUES TO DEFINE TRAPS

Onshore, the most suitable structures for storage of carbon dioxide are large closed structures on highly permeable aquifers at depths of 800 m or more. Such structures are almost identical to those sought in petroleum exploration. Since the problem of defining traps for petroleum exploration and CO₂ storage are almost identical, the exploration techniques used in the oil industry will be those suited for CO₂ disposal. Seismic reflection profiling is the standard and preferred technique used by the oil industry to delineate traps which might contain oil or gas. These profiles provide a 2-dimensional section through the earth, typically to depths of 5 km or more. Intersecting networks of 2-D profiles are commonly acquired, in order that a 3-D interpretation of the subsurface structure can be made. Other geophysical techniques, such as gravity, magnetic and electrical conductivity surveying play a minor role under certain favourable circumstances. Exploration for CO₂ disposal sites will be concentrated in sedimentary rocks. With a few exceptions, such as salt deposits, these rocks don't show great differences in densities or electrical properties, and have little magnetic signature, reducing the value of these alternative geophysical methods. An overview of the fore-mentioned geophysical techniques is presented in Table 5.4.1.

2-D Seismic Data

Seismic reflection data is expensive to acquire. Onshore UK, the cost of 2-D data per line kilometre varies between ECU 6500 and ECU 50 000, depending on the area in which the survey is to be acquired, permit problems,

Table 5.4.1 Overview of the characteristics of geophysical techniques and their related parameters.

CHARACTERISTICS	GEOPHYSICAL TECHNIQUE				
	Gravity	Static Field Magnetic	GE	Diffuse Field EM	Propagating Field Seismic Methods
Mapped Parameter	density	magnetic susceptibility	electrical conductivity	electrical conductivity	medium scale: travel time velocity (depth) & seismo- stratigraphic behaviour small scale: acoustic impedance
Resolution	strong decrease with depth			strong decrease with depth	slight decrease with depth
Detectability	large contrasts on large scale			large contrasts on large scale	small to large contrasts on small scale
Uniqueness	—	—			medium scale: + small scale: —

GE = Geo-Electrical, EM = ElectroMagnetic

mobilisation costs for the equipment and crew, etc. This is likely to be higher than in mainland Europe, as at times there are no crews actually based in the UK. Even within the UK, most surveys are towards the lower end of this cost range. In the North Sea, the cost of 2-D seismic acquisition was around ECU 350–500 per line kilometre in 1992, and could have decreased slightly since then. This excludes allowances for weather problems (add say 30% in summer, up to 70% in northern waters in winter). However, most of the world's sedimentary basins now have at least a few seismic profiles across them. It is cheaper to purchase existing seismic data than to acquire new data.

Grids of two-dimensional seismic data acquired for oil and gas exploration vary widely in their line spacing. The density of the existing seismic grid will depend on the hydrocarbon prospectivity of a particular sedimentary basin. A typical line spacing is 1.5 to 3 km. Such a density of data would be adequate to define the presence and approximate size of closures in a basin, but more data would be required to establish the exact size of a trap and to define its spill points.

3-D Seismic Data

Shooting a 3-D seismic survey over a potential closed structure is likely to be the best way to obtain an accurate picture of its volume and spill points. 3-D seismic data essentially consists of a very dense grid of 2-D seismic data, acquired in a single programme, which can be processed and migrated in three dimensions. Line spacing generally is 12–25 m as opposed to 1.5 to 3 km in 2-D surveys. 3-D migration has a distinct advantage over 2-D migration in that it enables data from dipping strata or other surfaces out of the plane of a 2-D profile to be returned to its correct position in three dimensions. Therefore it can provide a relatively accurate image of layer boundaries in the subsurface.

3-D seismic interpretation is computer-based and carried out at a workstation. 3-D data allows the interpreter to work directly with volumes, rather than making a spatial interpretation from the widely spaced grids of observations that make up intersecting networks of 2-D profiles. One can look at slices at any angle through the modelled subsurface, for example time slices (horizontal plane), or horizon slices (single reflection surface). Weak anomalies may be enhanced by using colour to display reflection strength or amplitude.

A major drawback of 3-D seismic data is that they are expensive to acquire. In 1991 the average costs of a 3-D land survey varied between 9000 and 30 000 ECU per km² (The Leading Edge, November 1993, p.1096). In the past 3-D has been used mainly to delineate accurately the structure and stratigraphy of hydrocarbon discoveries. However, 3-D surveys for exploration purposes are now commonplace in major oil provinces offshore, for example in the North Sea. 3D coverage onshore is less common than offshore, due to the higher costs of seismic acquisition and the lower costs of drilling.

Non-Seismic Geophysical Techniques

The three geophysical techniques considered relevant here are gravity, magnetic and electrical conductivity surveying. Their major advantages are low costs and simple data acquisition. They generally provide, however, data that are less detailed than seismic data and should therefore be considered as complementary to seismic survey. Despite the dominant role of seismic reflection methods, gravity and magnetic methods continue to find an application in

hydrocarbon exploration. Electrical techniques are widely used in groundwater investigations. Although seismic data are capable of providing much superior resolution, particularly in the depth range of interest, they may not always be available or of sufficient quality in the areas concerned. An example of resolution will be a 50 m thick reservoir at a depth of 800 m. This reservoir will remain invisible with non-seismic techniques, but can be properly detected with seismic techniques.

The application of such geophysical techniques to the location of CO₂ disposal sites will be largely determined by the amount of existing information from other sources. They are not capable of defining the details of aquifer and cap rock characteristics or structure, but they can be effective in the assessment of unexplored ground and in augmenting the results of other studies to establish the structural framework.

Gravity methods

Many countries have regional gravity data which are adequate for picking out major structural elements. For example, there is systematic coverage throughout the UK and its continental shelf. There is usually no basic problem in increasing the number of stations locally to improve the definition of target anomalies as surveys can be undertaken in built-up areas, or over water. Excessive vibration and very severe topography are the only factors which restrict useful data acquisition.

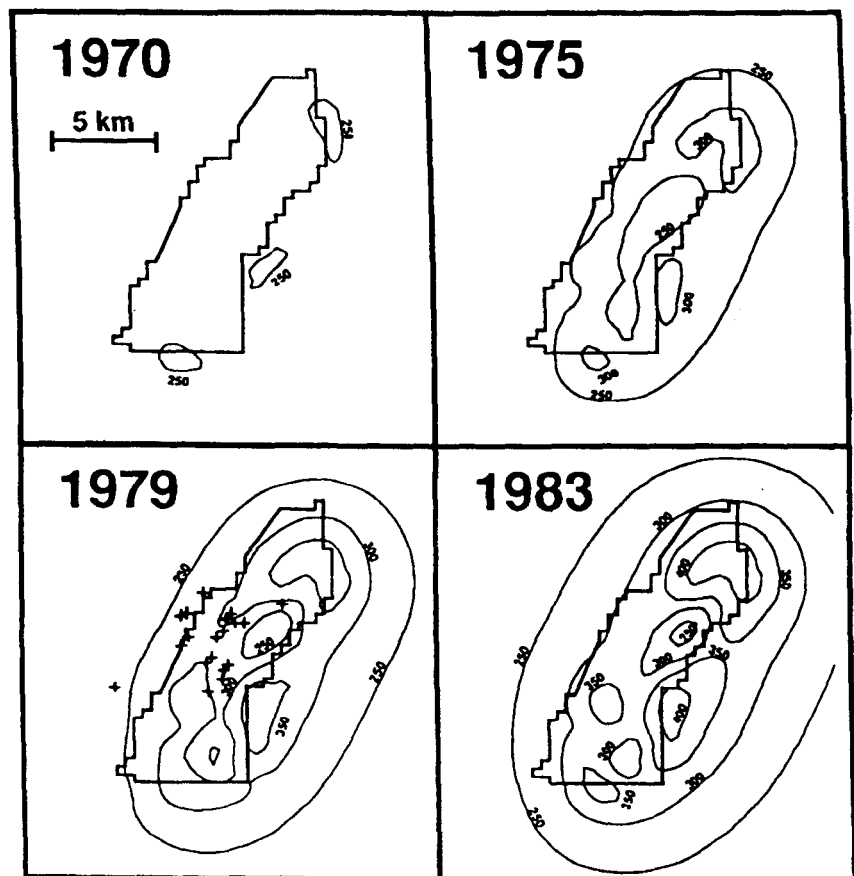
Porous sedimentary rocks are generally characterised by relatively low densities and, if present in sufficient thickness and areal extent, they will be expressed as gravity lows. Other features such as structural highs and major basic or granitic intrusions, are often identified by distinct density contrasts, as are the effects of faults. Computer processing and display of a gravity data grid provide the basis for a lineament analysis and a qualitative structural interpretation. Shaded relief images can be used to visualise subtle anomaly gradients associated with e.g. faults, which are not apparent on contour maps. Colour and variable contour scaling highlights small amplitude anomalies in areas of slack gradient whilst preserving information on larger anomalies. Techniques for distinguishing gravity anomalies at different depths include wavelength filtered, derivative, continuation and residual maps. Gravity anomalies can be modelled quantitatively in two or three dimensions to determine the shape of the causative bodies. The reliability of such interpretations depends on a number of factors such as the ability to differentiate the anomaly of interest from surrounding effects, and knowledge of formation densities, depths and thicknesses.

The identification of Permian salt structures, which in the Southern North sea are commonly associated with closures in the overlying Sherwood Sandstone, is a specific example of the possible application of gravity surveying to locating sites for CO₂ disposal. Halokinesis leads to marked changes in the thickness of halite, which has a low density of about 2160 kg/m³, whereas Triassic sandstones and marls typically have densities of around 350 and 2450 kg/m³, respectively. Salt bodies are often ill-defined on seismic profiles and gravity data can help in discriminating between alternative interpretations.

Magnetic methods

Magnetic data are efficiently collected by means of airborne surveys. Helicopters permit detailed surveying at low levels (to about 50 m above ground level) and ground traverses can be used to provide additional control over

Figure 5.4.3 Calculated fluid pressures (in bars) in the Cogdell oil field for the years indicated. Crosses represent micro-earthquakes (from Davis and Pennington, 1989).



increases in pressures from the initial hydrostatic pressure were equivalent to the shear strength of sedimentary rocks (around 10 to 20 MPa). They then calculated the stress loading on selected sections of the field caused by aseismic slip on a neighbouring part. They concluded that both fluid pressures and loading stress control the deformation in the field. At first, high pressures from injection occur along the boundary of the field, causing aseismic failure. As deformation continues, stresses accumulate in a region where slip has not yet occurred. In the later years of injection, seismicity occurs in a region of high strength, due to low fluid-pressure related to fluid extraction, and of high stress due to loading by neighbouring aseismic deformation.

Water Injection into the Rangely Oil Field (Colorado, USA)

The Rangely structure consists of an anticline of Mesozoic and Palaeozoic sedimentary rocks 350 m thick, which form the principal oil reservoir at about 1700 m depth. There is little evidence of faulting, except for a single NE-SW fault which intersects the anticline. This fault is the main seismically active structure, as shown by epicentre locations. Development of the field started in 1945 and waterflooding in 1957. An unverified report indicates that felt earthquakes occurred in the area before fluid injection.

Although this case has some points in common with the previous examples, it is important since it was the first study in which a specific seismic monitoring was carried out at the same time as pressure tests were performed (Raleigh et al., 1976). These authors attempted to prove the applicability of the Mohr-Coulomb criterion and to control the seismic activity in a part of the field. Instrumental records began in 1962 and continuous recording in 1969. It was therefore impossible to establish any correlation between the initiation of waterflooding and the onset of seismic activity at Rangely. An initial 10-day seismic survey had shown that earthquakes occurred in a high pressure area generated by waterflooding. Monitoring and modelling of reservoir fluid pressure showed that seismicity occurred in the highest pressure zone and that the NE-SW fault zone rapidly transmitted adjustments in pressure from the injecting wells towards the southwest, into the seismic zone. The permeability of the northwest part of the fault was not unusually high and seismicity was almost non-existent.

Stress-state measurements, along with laboratory measurements of strength on cores, gave 25.7 MPa as the critical fluid pressure required to trigger earthquakes. From October 1969 to November 1970, injection in four wells raised the bottomhole pressure in the vicinity from 23.5 to 27.5 MPa. During that time, more than 900 earthquakes occurred in the field (Figure 5.4.4), 367 of them within

1 km of the bottom of the injecting wells, at an average depth of 3.5 km below the surface. Local magnitudes ranged from -0.5 to 3.1. The negative cut-off magnitude explains the large number of earthquakes. After this period of injection, the four wells were shut-in and back-flowed during 6 months, decreasing pressures from 27.5 MPa to 20.3 MPa. Seismic activity also decreased, from 28 to about one earthquake per month. When injection was re-initiated at 26.5 MPa, the seismic activity near the wells remained at less than one earthquake per month. This effect is well-known in hydraulic fracturing, no micro-seismicity appears in a rock initially fractured until the last injection pressure reached in the prior injecting period is exceeded. Figure 5.4.4 shows that the frequency of seismic events correlates with the injection pressure, and that there is a pressure threshold critical for earthquake occurrence.

The Geothermal The Geysers Field (California, USA)

The Geysers geothermal area is located 130 km north of San Francisco and is by far the largest geothermal field in the world, since its 26 power plants generate more than 2000 MW of electric power (Oppenheimer 1986). Steam is extracted directly from the reservoir. The reservoir rock is massive graywacke with low-permeability matrix and a fracture porosity of 1–3%. Steam is produced from more than 200 wells which penetrate the steam-filled, open fracture network from 0.8 to 3.0-km depth. Seismicity in The Geysers area was reported in 1969 and has been carefully recorded and studied ever since. Up to now, more than 100 000 earthquakes (magnitude threshold of 0) have been recorded all over the production area, the highest magnitude being 4.0.

Although it has been demonstrated that the earthquake frequency increased with the geothermal production, no

specific targets. Interference from man-made sources of magnetism can be a problem in the more populated areas.

Rock magnetisation is usually determined by relatively small proportions of one of a limited number of minerals (most commonly magnetite). As there is no direct relation between density and magnetisation, the gravity and magnetic data tend to be complementary, relating to different parts of the sequence. Typically, the main density contrasts occur at shallower depths while the magnetic anomaly pattern often relates to deeper sources within the basement, because sedimentary rocks show usually a low magnetic signal. Similar techniques are adopted for the interpretation of both gravity and magnetic data and, in the case of 2-D profile modelling, the fields are best considered simultaneously.

The presence of volcanic rocks and igneous intrusions is often indicated by their magnetic response. Volcanic rocks such as dykes and sills can form important local barriers to fluid flow. Faulting is often expressed by the juxtaposition of units with different magnetisation or by the presence of intrusions along the line of faulting.

Conductivity Methods

Conductivity survey techniques provide data which can be interpreted in terms of resistivity and unit thickness within a layered sequence. Traversing records lateral thickness variations and 3-D models can be developed if sufficient data are collected on a grid pattern.

Two conventional geo-electrical survey techniques are distinguished: 1) *Horizontal Electrical Profiling* (HEP), and 2) *Vertical Electrical Sounding* (VES). The resistivity of the subsurface is measured by moving current electrodes across the surface, usually along a straight line. In HEP the electrodes are kept at a fixed distance to study one specific (not-well defined) depth interval. VES is performed by increasing the distance between the electrodes. This causes the current to traverse progressively deeper layers, of which the electrical characteristics increasingly contribute to the potential differences observed at the earth's surface. The *Time ElectroMagnetic* (TEM) method is also sensitive for underground resistivity variations. TEM uses a large transmitter loop and a small receiver coil. A direct current running through the transmitter loop is sharply disrupted, which causes a change in the electromagnetic field. This change induces currents in the subsurface (Faraday's Law). The variation in the secondary magnetic field generated by these currents are measured by the receiver coil.

Resistivity and electromagnetic (EM) surveys are widely applied in groundwater studies to locate aquifers. Formation resistivity generally decreases if the water content or the fluid salinity increases. Most aquifers in the shallow subsurface (above a depth of 400 m) can be identified as layers with a relatively high resistivity, and clay (generally with 50 vol% water) as layers with a relatively low resistivity. For deeper layers (below a depth of 800 m) the situation will be more complex because of water salinity, compaction and dehydration of clays, and poor resolution.

5.4.3 Reservoir Seismicity

5.4.3.1 INTRODUCTION

Underground withdrawal or injection of large amounts of fluid modify the mechanical state of the porous and possibly fractured media concerned. This generally induces local, small-scale modifications which do not alter the reservoir permeability significantly and are not percep-

tible from the surface. Nevertheless, important effects have been observed in some cases. These effects are of two kinds:

- 1 Surface effects, due to slow deformation related either to reservoir compaction (subsidence) or to the re-injection of fluids (abscidence).
- 2 Underground effects, such as reduction in permeability, consequences of reservoir compaction, or induced seismicity, due to sudden ruptures along pre-existing faults or weak joints and even well-collapse due to fault shearing.

Examples of Reservoir Induced Seismicity (RIS) are common in the literature, in fields as various as rock withdrawal in mines, artificial reservoir impoundments (e.g. dams), hydrocarbon extraction in oil or gas fields, deep-well fluid waste injection or re-injection of geothermal production. Some of the earthquakes reported were destructive, including some with a magnitude larger than 5. Seismicity can be induced by withdrawal or injection of fluids. Although the mechanisms are not identical, they are based in both cases on the same rock mechanics: poro-elasticity and mass transfer.

The re-use of abandoned oil or gas reservoirs for fluid or gas storage must take these possible types of damage into account, even if the abandoned reservoir has not previously shown any anomalous behaviour. As far as we know, there are only two examples of induced seismicity in the case of underground storage of natural gas. This is because the injection pressure is quite low (2 to 3 MPa above the hydrostatic pressure), and because few monitoring experiments with high sensitivity sensors have been carried out around a gas injection site. Nevertheless, the seismic hazard related to induced seismicity must be carefully assessed, insofar as damaging earthquakes have been detected in and around hydrocarbon reservoirs after some tens of years of exploitation. Even if the final evaluation of the seismic hazard shows that the induced seismicity is an irrelevant side effect of the injection, the long-term aspects of the storage must not be neglected.

5.4.3.2 FAULTING AND FRACTURING

Faults and Fractures

Fractures are, in the geological context, planes along which a rock lost its cohesion. Distinction is made between fractures with or without offset by shearing along the fracture surface. Faults are fractures along which there is visible offset. Basically, three types of faults are recognised based on the direction of the displacement: 1) normal faults, 2) reverse faults, and 3) strike-slip faults. Faulting takes place under compressive stresses. Normal faults are formed in a 'extensional' tectonic regime in which the largest compressive stress is vertical (sediment loading) and the smallest compressive stress horizontal (extension). Reverse faults are formed in a 'compressive' tectonic regime in which the largest compressive stress is horizontal (orogenic forces) and the smallest compressive stress vertical (sediment loading).

Joints are fracture surfaces along which there has been imperceptible movement. Frequently, the faces of the joint have moved apart, i.e. a separation by movements perpendicular to the surface of a joint known as dilational separation. Such dilational joints are generated by tensional stresses, from e.g. rock shrinkage due to dehydration (cf. mud cracks) or cooling. Open, unfilled dilational joints

are called fissures. These fractures play a role in exogenic processes, since they represent paths along which surface water can penetrate the formation. Fissures may be filled by rock particles. Under natural circumstances, however, fissures will generally not be formed in the deeper subsurface. Joints will also be referred to as 'fractures'.

Hydraulic fracturing

If the injection pressure is too high, the host formation may fracture. The high-pressure fluid opens pre-existing fractures and faults or creates new dilational joints. This feature is known as hydraulic fracturing and is frequently used by the oil industry to improve the inflow performance of an oil or gas well. If the fractures propagate only through the CO₂ storage formation no overruling argument can be found to restrict the maximum injection below the formation fracture pressure. Only if the integrity of the caprock is affected, limitation must be set for the injection pressure. Important in this matter is in-situ stress contrast. An in-situ stress profile is a plot of depth vs. the minimum pressure required to create a hydraulic fracture. The fracture stress contrast between the CO₂ storage formation and the caprock (stress in caprock minus stress in storage formation) determines the degree of vertical confinement, i.e. a large value of in-situ stress contrast will confine the fracture height and induce a longer fracture, a low stress contrast will result in significant height growth and a shorter fracture. At an early stage in the design of the storage system it will be necessary to determine the in-situ stress profile in order to predict and set the maximum injection pressure. To compute an in-situ stress profile economically, one must use primarily data from a log. A long-spaced sonic log or digital sonic log measures the compressional travel time and shear travel time through the various rock layers. These travel times determine the velocity ratio, Poisson's ratio, and minimum horizontal stress. Several publications (Holditch, 1988; Gidley et al., 1989; Roberson et al., 1991) describe the mechanics of performing these calculations. Despite the ability to estimate the in-situ stress profile from logs, one should calibrate the log with stress tests. Various correlations (Robinson et al., 1991) allow the engineer to calibrate the log data against the stress tests. Furthermore the lithology can provide a good indication of the in-situ stress. Magnitudes of earthquakes induced by hydraulic fracturing are never larger than one and negative magnitudes (on a logarithmic scale) are routinely recorded by downhole sensor arrays. The location of the microseismicity caused by hydraulic fracturing is used as a tool to map in real time the progression of the injected fluid front (Beauce et al., 1992).

The Mohr-Coulomb Law of Failure

The cause of seismicity most frequently mentioned is an increase of pore pressure due to fluid injection, which decreases the effective stress on pre-existing faults that are close to failure and consequently allows accumulated shear stresses to be released (discussed below). The injection of fluid can even trigger damaging earthquakes along faults which are moved to a critical state by principal regional stress loading. This means that the present tectonic context (tectonic stresses and related fault systems) is of fundamental importance. It is important to note that this is somewhat different from hydraulic fracturing, where the highly pressurised fluid either opens pre-existing fractures and joints, or creates new small-scale joints that propagate into the massive rock, generally parallel to the direction of maximum horizontal stress.

The strength of a rock to resist faulting is derived from two sources. One is the natural cohesive strength of the rock, the second is the internal frictional resistance to faulting. The stress required to fault a rock must be large enough to overcome cohesive strength, so that the rock may fracture. At the same time it must be large enough to overcome rock's internal resistance to faulting, so that movement can take place along the fracture. In contrast to the cohesive strength, the internal frictional resistance to faulting is not an intrinsic rock property, and varies both as a function of the coefficient of internal friction ($\tan \phi$), a measure of the shear friction (\approx roughness) of the fracture plane, and the level of normal stress acting (σ_N) on the potential plane of faulting. The relation between the critical shear stress required for faulting (σ_c), the natural cohesive strength of the rock (σ_0) and the internal frictional resistance to faulting is expressed by the Mohr-Coulomb law of failure (or the Mohr-Coulomb criterion) in the following way (see Davis, 1984):

$$\sigma_c = \sigma_0 + \tan \phi (\sigma_N)$$

Fluid injection will increase the fluid or pore pressure (σ) which will offset the magnitude of lithostatic normal stress (σ_N) acting on the plane of faulting. The effective stress ($\sigma_N - \sigma$) acting normal to a fault would equal the difference between the normal stress and the fluid pressure. With these concepts in mind, the Mohr-Coulomb law of failure can be modified as follows:

$$\sigma_c = \sigma_0 + \tan \phi (\sigma_N - \sigma)$$

From the above equation it is evident that an increased pore pressure can result in slip along pre-existing faults. This can be sketched on a Mohr's circle showing stress conditions at failure (Figure 5.4.1): the Mohr-Coulomb criterion predicts failure when the Mohr's circle intersects the failure envelope. σ_c and σ_N (in fact $\sigma_N - \sigma$) are deduced from the projection of the principal elements of the stress tensor into the slip direction and normal to the fault plane. This requires complete knowledge (absolute value and direction) of the stress tensor, which, in fact, is always approximate. In the presence of fluid, the effective stress level is reduced by the amount of fluid pressure which moves the Mohr circle to the left towards the failure envelope.

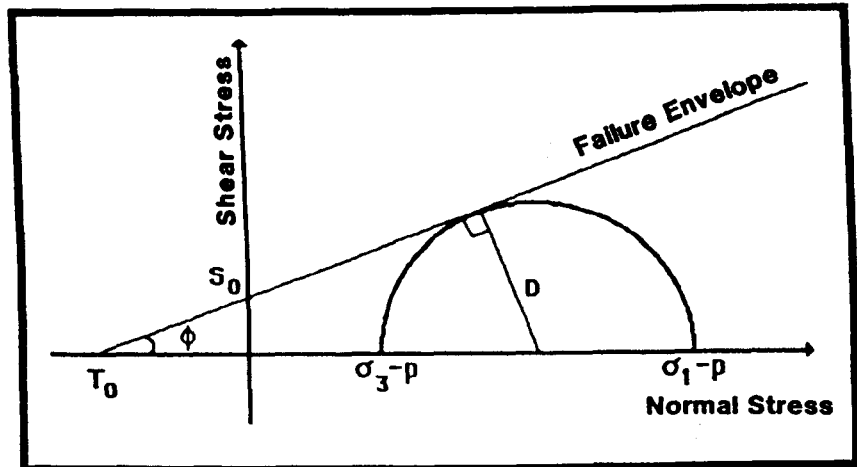
Faults and CO₂ Storage

In case of a potential CO₂ reservoir it is essential to have an in-depth knowledge of the occurrence of faults and fracture (joint) systems in the subsurface formation. Fracture systems can have an influence on the CO₂-water displacement front (permeability) while faults can have a deteriorating effect on the integrity of the storage reservoir. Especially fault systems which extend into the caprock are of importance. They can act as preferential pathways for CO₂, reducing the sealing capacity of the caprock.

In principle, fracturing of the reservoir rock will increase the average permeability, because the permeability along the fracture planes is generally greater than the original permeability of the rock. However, several geological processes could have reduced the permeability of the fault:

- **Clay-smearing:** fault movements may have smeared out clay along the fault plane. The extent to which this process may lead to a 'sealing' fault strongly depends on the clay content of the affected formations and the offset along the fault.

Figure 5.4.1 Mohr's circle shows stress conditions at failure. Its radius D is the deviatoric stress $(\sigma_1 - \sigma_3)/2$, where σ_1 and σ_3 are the maximum and the minimum principal components of the stress tensor. ϕ is the angle of internal friction. T_0 and S_0 are the tensile and shear rock strengths, respectively. An increase in fluid pressure p decreases the effective stress, thereby moving the circle towards the left, i.e. towards failure (from Davis and Pennington, 1989).



- **Cataclase** (grain-pulverisation) leading to the formation of gouge or mylonite (= milled rock), and thus substantially reducing the permeability in the fault zone. The magnitude of the normal (compressive) stress acting on the fault plane during faulting will determine the degree of pulverisation and the development of fault gouge. The relatively high normal stresses on reverse faults and strike-slip faults suggest a higher chance on sealing-faults than by normal faults. Mandl et al. (1977) concluded that cataclase only occurred in the initial stage of the fault development. Continuing fault off-setting is a result of gliding of blocks along the already developed gouge.
- **Mineral precipitation.** Cementation of secondary mineral deposits in the open pore space in the fault zone can make the fault plane impermeable. Open fractures that are filled are commonly known as veins.

Considering a potential CO_2 storage location, two facts will be of importance. Firstly, in existing gas or oil fields possible faults have already proven their sealing capacity for hydrocarbons. Secondly, it is difficult to determine the exact location of faults and to establish the sealing capacity of the entire fault plane. With present 3-D seismic data it is possible to locate faults on a scale of several meters. Core samples taken across the fault plane can give some information about the permeability within the fault plane but it will be difficult or even impossible to extrapolate a few permeability measurements to the entire fault plane.

Apart from faulting induced by an increased fluid pressure (discussed above), fluid injections may re-activate faults as a result of changes in the fluids contained in the fault zone. Given its low viscosity, the liquid CO_2 is likely to displace water at fractures and could lubricate faults. A substantial increase in the fluid pressure in the storage reservoir could alter the normal stress on a fault, and possible open the fault and increase the fault permeability. The combination of increased permeability and a large pressure differential across the fault plane could lead to leakage of CO_2 into overburden formations. The escaping CO_2 will migrate upwards due to its low density. The dispersion of the CO_2 will largely depend on the geological conditions of the rock or formations above the reservoir (see Chapter 6).

5.4.3.3 EXAMPLES OF RESERVOIR INDUCED SEISMICITY

Examples of reservoir induced seismicity for every type of reservoir have been reviewed in Gupta (1985), Gibowicz (1989) and Grasso (1992). The general impression is the

extreme variability of the experimental data concerning the magnitude (from non-sensible to damaging earthquakes), the delay between the start of injection and the seismic event (from a few days to several years), and the distance between the point of injection or impoundment and the hypocentres (up to some tens of kilometres). The complexity of the phenomena is increased when extraction and re-injection are carried out in the same reservoir, simultaneously or delayed in time, as for fluid injections into producing oil fields. In geothermal fields, fluid re-injection is used either to maintain reservoir pressure or to prevent formation brines contaminating the surface environment.

Five examples have been selected for this review, on the basis of the following criteria:

- Injection of fluid or gas in four different contexts: hydrocarbon fields, fluid waste injection, geothermal exploitation and storage of natural gas.
- Aquifer reservoirs, if possible.
- Existence of good records of the induced seismicity.
- Completeness of the investigations carried out after the appearance of seismicity, i.e. locations of hypocentres, reservoir pressure measurements, regional and local stress measurements, modelling of fluid pressure distribution, etc.

Four examples are taken from the United States; this is basically because the US Geological Survey was able to study the different cases and to publish the results. A brief description of each case is followed by a comparative table, including some characteristic parameters as the type of injection, the location of seismicity and the theory used to explain the seismicity occurrence.

Injection of Fluid Waste: the Denver Earthquakes

A total of 625 000 m^3 of fluid waste have been injected during discontinuous periods from 1962 to 1966 in a deep well drilled at the Rocky Mountain Arsenal (RMA), located northeast of Denver, Colorado, USA (Figure 5.4.2; Hsieh and Bredehoeft, 1981). Injection took place into a highly fractured Precambrian Gneiss at 3650 m depth. The last earthquake pre-dating injection had been in 1882 and showed a magnitude around 5. Between April 1962, shortly after the start of the injection programme and August 1967, more than 1500 earthquakes were recorded. Some of these exceeded magnitudes of 3–4, and in 1967 three major

earthquakes, each with a magnitude greater than 5, shook the Denver area and caused minor damage. By the mid-eighties the seismic activity had virtually disappeared.

The earthquakes were occurring in an elongate region about 10 km long and 3 km wide, centred on the well and at depths of 2 to 8 km. Two kinds of recording instrument were used, intermittent mobile arrays set up around the injection well and a permanent seismograph located 40 km from the seismic area. A comparison of earthquake frequency and average injection rate showed a convincing correlation (Figure 5.4.2). The earthquakes are considered to be related to movements along fractures in the Precambrian bedrock, triggered by the pore-pressure increase due to injection. The mechanism invoked was rock movement caused by a Mohr-Coulomb type failure in a fluid-filled rock environment. The earthquakes are confined to that part of the reservoir where pressure build-up exceeds 3.2 MPa. This critical value is interpreted as the pore pressure above which earthquakes occur. Such a small value suggests that the basement rock was already close to failure prior to injection, particularly as the three larger than 5 magnitude earthquakes occurred more than 5 km from the injection well and more than 14 months after injection ended. Grasso (1992) suggested a delayed stress transfer by propagation along the pre-existing fracture affected by the earliest seismic activity to an area where the pre-existing stress is high and near failure.

Water Injection into the Cogdell Oil Field (Texas, USA)

The Cogdell oil field is a typical example of seismicity induced by high-pressure water injection into a limestone oil reservoir for secondary recovery (Davis and Pennington, 1989). Salt water injection was initiated in 1956, seven years after the field was discovered. The first seismic events were felt in 1974 in a town about 20 km to the south of the field. The largest earthquakes occurred in 1978, with local magnitudes up to 5.3. The epicentres were located close to the centre of the field and depths ranged from 1.9 to 3 km,

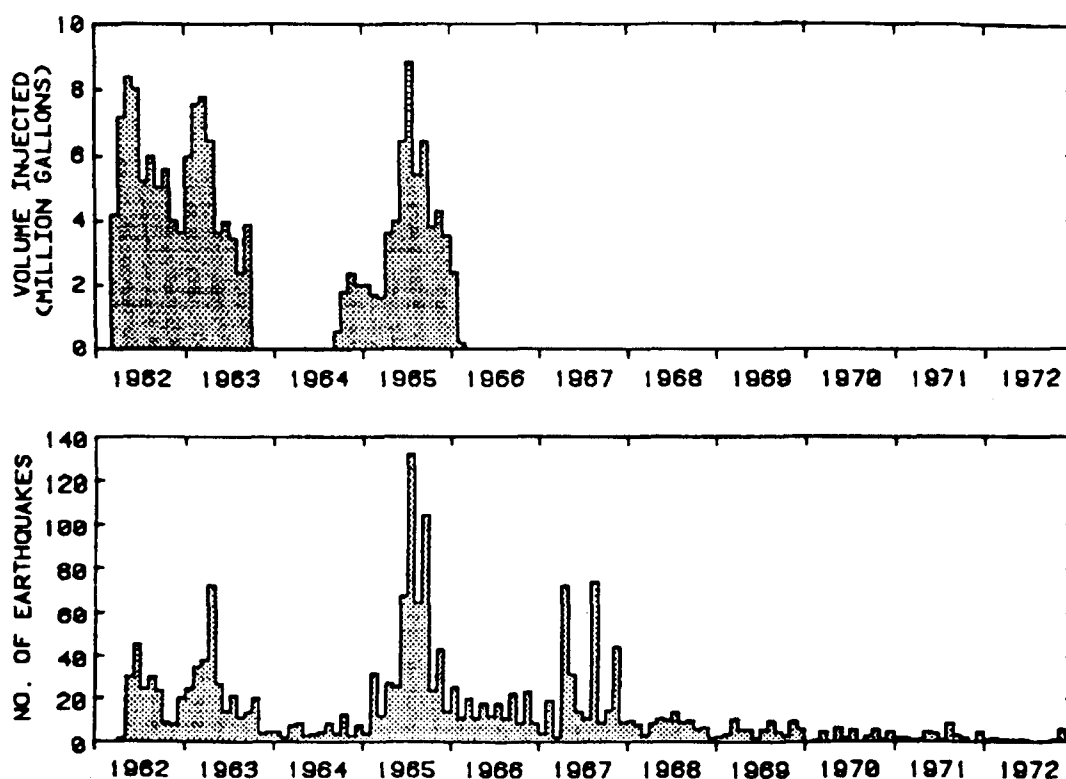
consistent with the injection depth of 2.1 km. From 1956 to 1983, 114 million m³ of water were injected through 119 injecting wells^[1], located around the perimeter of the field, leaving a net volume of 37 million m³ in the reservoir. The surface injection pressure was greater than 35 MPa.

Although the seismicity was not completely documented (only a local network was operated from 1979 to 1981 and the closest permanent seismograph was located at 110 km), the reservoir pressure history has been carefully recorded. Davis and Pennington (1989) examined both data sets using two models. The first model assumed that the deformation was exclusively seismic and controlled by changes in effective pressure, due to fluid injection only (see Mohr-Coulomb criterion discussed in section 5.4.3.2). The second model used fluid pressure and stress loading from aseismic (ductile) deformation to develop high-stress regions on a fault which failed seismically. According to the Mohr-Coulomb criterion, an injection pressure of about 6 MPa should be sufficient to induce failure, whereas injection pressures exceeded 38 MPa during 14 years prior to the first earthquake! Examining the injection pressure data of 2420 oil projects in Texas which inject at shallow depth, they found that 877 should be in failure. As only the Cogdell is known to be seismically active, it was concluded that shear failure probably occurs in many of these fields, but it may occur as either ductile deformation or as earthquakes below the detection threshold for the area. Consequently, another mechanism has to be invoked to explain the induced seismicity.

Davis and Pennington (1989) modelled the pressure distribution in the Cogdell reservoir using a simplified model of a homogeneous, isotropic aquifer of infinite areal extent, with no faults. They calculated the fluid pressures in the field for different years (Figure 5.4.3) and showed that

[1] Including five gas injectors that operated from 1967 to 1976. No information about their specific behaviour is available.

Figure 5.4.2
Comparison of fluid injected and the frequency of earthquakes at the Rocky Mountain Arsenal, near Denver. Upper graph: monthly volume of fluid injected in the disposal well. Lower graph: number of earthquakes per month (from Hsieh and Bredehoeft, 1981).



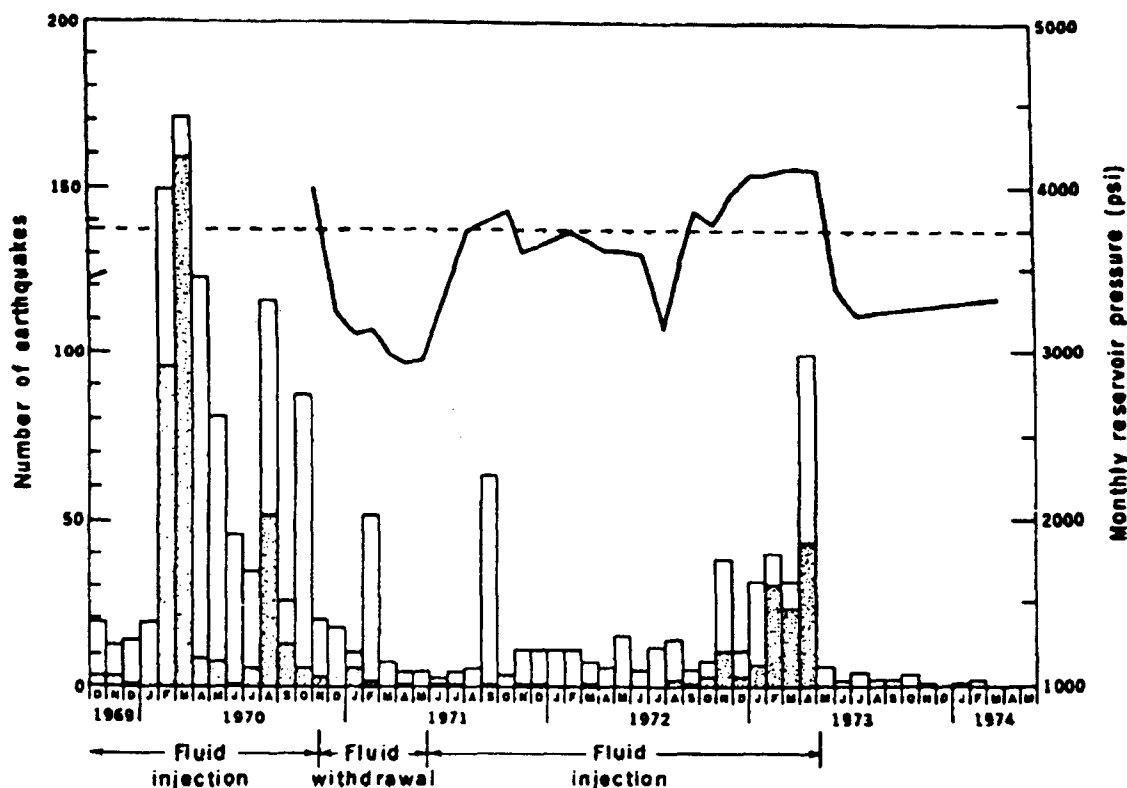


Figure 5.4.4 Frequency of earthquakes at Rangely, from 1969 to 1974. The lower parts of the bars indicate earthquakes within 1 km of the injecting wells. Pressure history in well Fee 69 is shown by the heavy line, predicted critical pressure is shown by the dashed line (from Raleigh et al., 1976).

obvious correlation between seismic activity and steam withdrawal has been found for steam wells that were more than seven years in production. Seismicity is generally considered not to be associated with any dominant fault system and seems to occur somewhat at random, clustered in the production region. Most of the seismicity originates from a depth shallower than 5 km.

Oppenheimer (1986) has studied the seismicity distribution, estimated the stress-field orientation from the inversion of 210 fault-plane solutions and compared it to geodetic data. The latter indicate a volumetric contraction of the reservoir, denoted by a subsidence rate of 3.4 cm/yr. The area of maximum subsidence correlates with the location of the maximum steam pressure decline. Faulting is driven by regional shear stresses which existed prior to the withdrawal of steam and which are larger than any induced shear stresses that may trigger earthquakes.

Two plausible mechanisms for seismicity induced by production are:

- 1 Volumetric contraction due to mass withdrawal may perturb the stress field and cause faulting in the reservoir rock, already near failure under the regional stress field.
- 2 Aseismic deformation due to the regional stress field may be converted to 'stick slip' by seismic deformation, owing to an friction increase along fault surfaces due to e.g. precipitation of dissolved silica.

In some places, earthquakes and steam condensate (water) injection correlate (Stark, 1990) and clusters of microseismic events appear around the bottom of the injection wells. These events are helpful for mapping the progression of the re-injected fluid (Figure 5.4.5). Although

injection is carried out under zero well-head pressure (i.e. by gravity), effective stress reduction by an increase of pore pressure could explain the induced seismicity, insofar as water is injected.

In conclusion, induced seismicity exists but it is mainly related to extraction in the case of the steam-filled area and is governed by the regional stress field, which is site-specific and will not follow a general rule. Seismicity related to injection is linked to water and not to steam. This is due to the fact that pore pressure in the latter case is low, since steam is highly compressible. Consequently the effective pressure is high and prevents movement along fractures in the steam-filled area (Majer et al., 1993). This explains why microseismic events are concentrated around the injection wells and are absent where all water has turned into steam.

Storage of Natural Gas in the New Haven Reservoir (central Michigan, USA)

The New Haven storage reservoir, north of Lansing (Michigan, USA), consists of a 10-m-thick 'stray' sandstone at an average depth of 320 m. Detailed microseismic monitoring of the site was carried out during 14 periods between July 1975 and April 1979. Despite the fact that technical specifications of the recording and computing systems may now appear quite obsolete, the network is undoubtedly appropriate, since it has five downhole sensors, including one at the top of the reservoir and one in the cap rock. The main conclusions of the study are:

- The structural stability of the reservoir is high, because high-magnitude events were rare.
- Most high-magnitude events were located in the central section of the reservoir.

Figure 5.4.5 Microseismicity recorded around injection wells in The Geysers geothermal field from November 1988 to August 1989. Epicentres of events deeper than 1000 m and with coda magnitude >0.7 are represented by dots. Open circles represent injection wells. The area of the circle is proportional to the volume injected during the same period. Numbered squares are selected power plants (from Stark, 1990).

— Over the pressure range studied (1.5 to 4.3 MPa at wellhead) the frequency of microseismic events was found to decrease with increasing wellhead pressure.

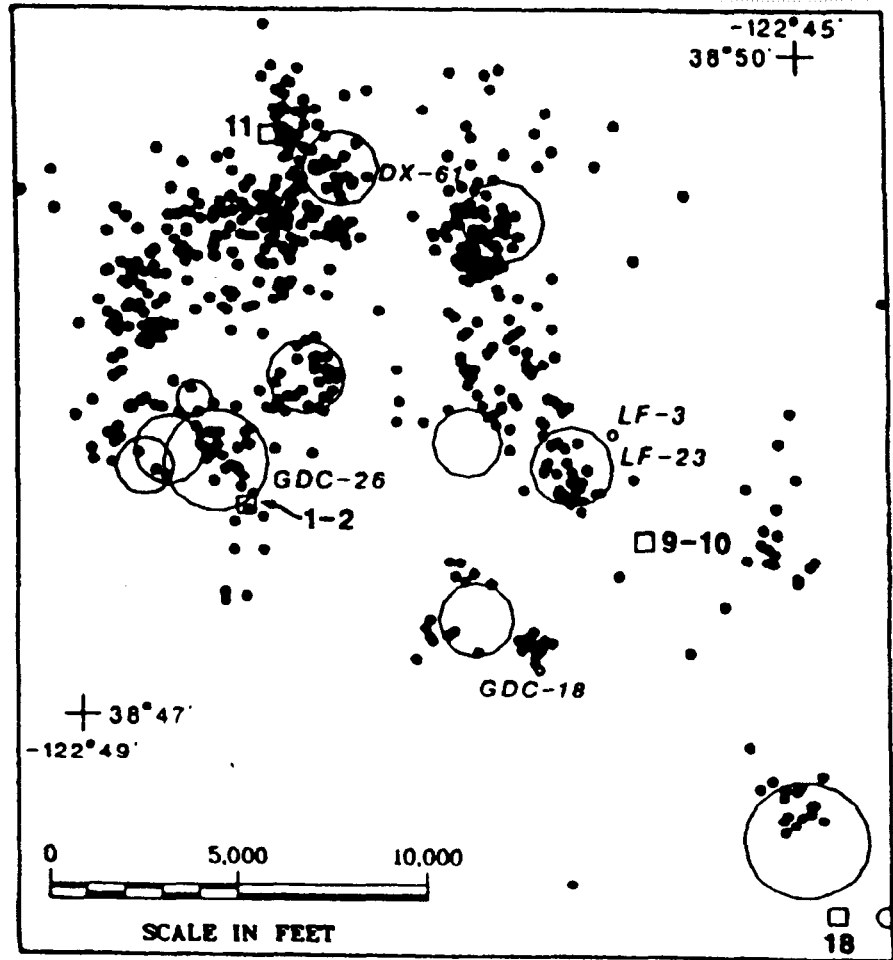
Storage of Natural Gas in the Germigny Reservoir (Paris Basin, France)

The second example of a natural gas storage reservoir is the Germigny Reservoir operated by Gaz de France (Deflandre et al., 1993), in the sedimentary Paris Basin. The reservoir consists of an anticline on a sandstone and a shaly sandstone. The reservoir top is at 750 m b.s.l. Injection started in 1983 and at present the total volume of gas stored varies from 1400 million m³ at winter-end to 2100 million m³ at autumn-end (injection takes place from March to November). Microseismic survey is characterised by the installation of three permanent geophones (3-axis) in a single observation hole, clamped to the casing wall between casing and tubing at depths of 783, 815 and 905 m. The sensor frequency range is appropriate to high frequency acoustic emissions (28 to 2000 Hz) and sensitivity and amplification gain are suitable for recording very low-level signals.

Only 27 events were recorded from November 1991 to April 1992 (Figure 5.4.6). This is because of:

- Low rock strength which undoubtedly permits aseismic (ductile) deformation.
- Low well-head injection pressure (<3 MPa) and high compressibility of gas.
- Relatively long distance (>1 km) between the seismic observation hole and the injection hole.
- Discontinuous monitoring, due to intermittent cathodic protection of the well, which impeded correct functioning of the seismic sensors (though no damage occurred).

Nevertheless, the microseismic activity would be expected to be more intense near to the injection wells, at the top of the anticline. Figure 5.4.6 shows clearly that micro-earthquakes are correlated to pressure changes in the vicinity of the observation well. With respect to the



location of events (Figure 5.4.7), seismicity is concentrated at less than 200 m from the well and at the top and the bottom of the reservoir, close to layers with a higher strength. A velocity model based on lithology and sonic logs ensures accurate location of the hypocentres in two dimensions, as the sensors are aligned vertically. As no fault has been detected either by drilling or by seismics, the mechanism of induced seismicity could be the reduction of effective stress and resulting slip along bedding planes.

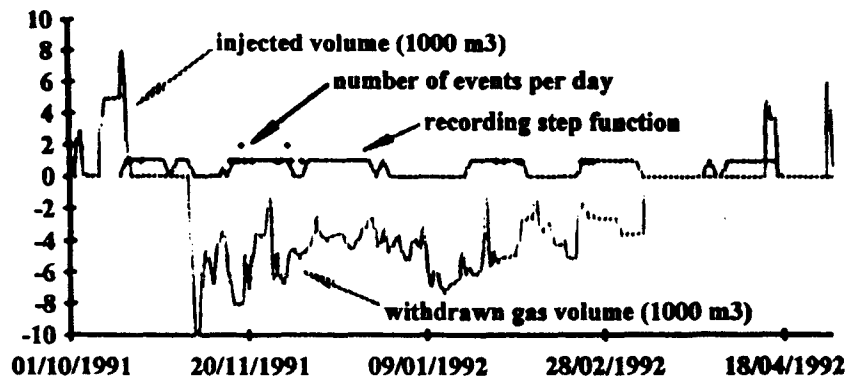
Synthesis of Case Histories

Relevant parameters for each of the five examples are listed in Table 5.4.2. The table shows that induced seismicity is generally shallow (<10 km depth), occurs in different lithologies, both close to the injection point and far away from it, either shortly after the start of injection or many years later, magnitudes range from negative values to more than 5 and inducing mechanisms are varied and complex. In the case of gas disposal in a non-depleted reservoir sited in a non-faulted sedimentary structure, it makes sense to expect a null seismic hazard at the surface. In any other case, different from this ideal situation, microseismicity could be expected and studies should be carried out prior to and during disposal operations, in order to assess induced seismicity hazard.

Preliminary studies to be carried out prior to starting gas disposal (section 5.4.3.4) together with the monitoring of surface deformation and seismicity during CO₂ injection form the basis for seismic hazard assessment. The mechanisms that could induce seismicity are:

Figure 5.4.6 Germigny underground gas storage. Crosses are number of events per day, the continuous line the volume of gas injected or withdrawn and the dashed line the recording periods (from Deflandre et al., 1993).

Germigny underground gas storage



1. **Reduction of effective pressure** due to an increase in pore pressure (Mohr-Coulomb criterion).
2. **Poro-elastic stresses** caused by changes in pore fluid distribution. This effect has not been mentioned in the examples cited above, mainly because it is more appropriate to the case of oil or gas extraction. Segall (1989) applies poro-elastic theory to the simulation of changes in horizontal normal stresses around the depleted reservoir, assuming that vertical contraction is accommodated by subsidence of the free surface. The main result is that stresses are generated where there are no changes in pore fluid content, i.e. in undrained pores outside the reservoir. Segall, like Grasso (1992), suggests that this mechanism could also apply to cases of fluid injection such as at Denver or Rangely.
3. **Change from aseismic deformation to seismic slip.** Two mechanisms are invoked:
 - a) **Stress loading.** At Cogdell, production decreases pore pressure and increases rock shear strength; the initial response to fluid injection is aseismic deformation at the periphery. This loads stress in the centre of the field which finally fails seismically.
 - b) **Increase in the coefficient of friction,** i.e. shear strength, following the deposition of exsolved silica onto fracture surfaces. This effect could be specific to high-temperature geothermal fields.
4. **Change in reservoir volume.** Shear stresses are increased because of reservoir compaction due to mass withdrawal. This generates compression near the centre and extension at the edges of the reservoir. The opposite effect would be observed in the case of injection in a non-depleted reservoir. Inflation should produce absidence over the reservoir, i.e. extension at the centre and compression on the edges. This feature has been observed in geothermal fields such as Heber in California.

5.4.3.4 ZERO STATE RESERVOIR EVALUATION

Initial studies, prior to gas disposal, are essential to assess the zero-state of the reservoir, in order to assess the various parameters related to induced seismicity. As demonstrated by the examples cited above, they should include historical seismicity, mechanical modifications of the reservoir (in the case of an old oil or gas field), structural framework, regional and local stress regime, modelling of pressure distribution in the reservoir and, if possible evaluation of critical pressure for failure, and monitoring of microseismicity. This section deals with these preliminary studies, which are presented in the order in which they should be performed.

Historical Seismicity

In case of CO₂ disposal in an abandoned hydrocarbon field, two questions need to be answered first. Was the area seismically active before oil or gas extraction?, and did any induced seismicity appear during exploitation (extraction and EOR)? It should be possible to find the answers to both questions in historical seismicity records (newspapers, libraries, etc.) and instrumental seismicity data (catalogues of national and international seismological networks). The important points to be noted concerning earthquakes are locations, as precise as possible, magnitudes (or intensity in case of historical seismicity), recurrence, any observed surface effects associated with fault rupture, and geological context. Concerning induced seismicity, local observations would be important if any anomalous vibrations were felt by site personnel or the local population.

Modifications of Reservoir State

Two other possible sources of information on the evolution of the mechanical state of the reservoir are subsidence and condition of the wells. Subsidence can be detected from minor damage at the surface such as cracks in buildings, fields or roads, changes in slope or the appearance of hollows etc. It can also be measured by geodetic levelling. This makes it possible to evaluate the strain regime over the field and is a way of investigating the compaction or later inflation of the reservoir.

The deformation of the open-hole walls from a circular to an oval section can give a measure of the existing stress regime. This gives information on the orientation of the horizontal components of the stress field, and may even show the presence of an active fault if there is a rupture in the well. The condition of the borehole can be observed on calliper logs or wall-imaging logging tools such as the Borehole Televiwer (BHTV). Ovalisation can also affect casing and tubing. There have been many examples of casing collapse in oil or gas fields caused by shear along faults intersecting the well, activated either by fluid injection during drilling or by reservoir compaction.

Structural Study of the Reservoir And its Regional Setting

As mentioned above, induced seismicity is closely related to pre-existing faults and the regional stress regime. Any faults detected in or around the reservoir either by surface observations or from wellbore information constitute weak surfaces along which stress modifications may be released,

Figure 5.4.7 Location on a vertical section of the seismic events recorded at the Germigny gas storage from November 1991 to April 1992. Depths are measured from surface, horizontal distances from the well axis. G1, G2 and G3 are the geophones (from Deflandre et al., 1993).

even if no seismicity has been observed before exploitation. It is recommended to extend the geological study beyond the immediate confines of the reservoir, which should be well known from geophysics and wellbore information, to a radius of 5–10 km in the surrounding region.

Significant geological features that should be surveyed are:

- Faults, whether active or not.
- Lithological changes, especially changes in mechanical rock properties which could act either as a barrier to failure propagation (region with a high cohesive strength) or as a boundary where accumulated stresses may be released seismically (region with a high critical shear stress).
- Structures such as horsts or grabens and all relevant information on past or present tectonics.

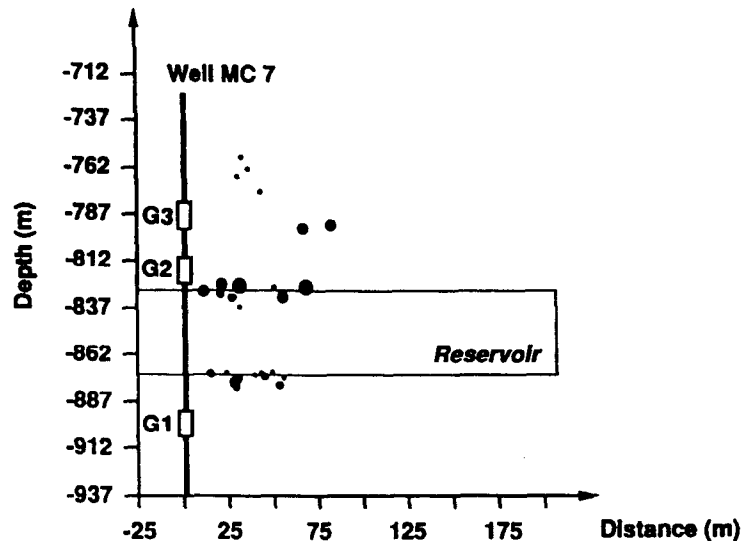
The methods most generally used for regional stress evaluation are inversion of focal mechanisms of regional earthquakes, overcoring measurements, wellbore breakouts, hydraulic fracturing and young fault slip studies. For example, the orientation of the principal stress components and the stress ratio ϕ ^[2], can be determined from a population of faults (Angelier, 1984). This method can also be applied to fractures observed in cores or on image logs. In Europe, maps of the spatial variation of the orientation of horizontal components can be consulted as a base for regional stress tensor evaluation (Müller et al., 1992). Local stress measurements are considered in the next section.

Evaluation of the Critical Fluid Pressure

Before starting gas injection, a theoretical value of the injection pressure required to induce shear failure in the reservoir can be predicted. Using the Mohr-Coulomb law of failure (see section 5.4.3.2), this critical pressure is a function of four parameters at least: cohesive strength of the rock (σ_0), the angle of internal friction (ϕ), and the absolute value and orientation of the principal components of the stress tensor ($\sigma_1, \sigma_2, \sigma_3$). As has been observed at Cogdell, injection pressures higher than critical pressure do not necessarily result in earthquakes. Shear failure probably occurs but stresses are released either by aseismic creep (ductile deformation) or by non-detectable microseismicity. Critical injection pressure will therefore be a significant, but not limiting, parameter to be taken into account in estimating the optimum storage pressure. Among other things, uncertainties in the estimations of the different parameters have to be taken into account.

[2] Stress ratio ϕ is a measure for the shape of the stress ellipsoid and is defined as: $\phi = (\sigma_2 - \sigma_3) / (\sigma_1 - \sigma_3)$.

Location of microseismic events



The methods used to evaluate the parameters are briefly:

- Strength and angle of internal friction of rocks are measured on cores in the laboratory during *tri-axial tests*, by evaluating the breakdown pressure under known stresses and different rates of fluid pressurisation.
- Normal and shear stresses are given by the projections of the principal components of the local stress tensors ($\sigma_1, \sigma_2, \sigma_3$). The most commonly used method is that of *Hydraulic Tests on Pre-existing Fractures (HTPF)*. Assuming certain simplifying hypotheses, this method gives direct measurements of the orientation and the absolute value of the three components. Other methods available are borehole breakouts (mentioned above), and drill core analyses such as *Anelastic Strain Recovery (ASR)*. Because the latter is based on the stress relief and needs freshly recovered cores, it must be planned in any drilling programme for new wells.
- Orientation of the plane of faulting with respect to the orientation of the stress tensor. There are three possible cases:
 - a Fault planes consistent with the stress tensor principal axes, i.e. the angle between the axes is equivalent to the angle of friction. This is the most favourable case, which requires the minimum critical pressure. Reality is not so simple and it is generally assumed that the planes of faulting contain the maximum horizontal stress direction.
 - b Fault planes not consistent with stress tensor principal axes, which means that faulting results from a tectonic phase older than the present one. The critical pressure would be higher than in (a), but the direction of failure should be along the fault plane as this is a zone of weakness.
 - c No faults detected in the high-stress region. In this case, the stress required to fault a rock must not only be large enough to overcome the rock's internal resistance to faulting, but also the natural cohesive strength of the rock (Mohr-Coulomb

Table 5.4.2. Synthesis of Case Histories.

Case History	Type of operation	Reservoir Lithology	Average depth of injection (km)	Total injected volume (million m ³)	Epicentral location of earthquakes (respect to bottom Hole)	Average depth of hypocenter (km)	Largest Magnitude	Delay between start of injection and onset of seismicity	Most plausible mechanism for inducing seismicity
Denver	Injection of fluid waste	Precambrian gneiss	3.65	0.625	0 to 10 km	2 to 8	5.5	< 1 month	decrease of effective pressure by increase of pore pressure, critical pressure for failure: 3.2 MPa deferred stress transfer to an area near to failure
Cogdell	Oil field, EOR	Reef limestone	2.1	114	On the boundaries of low pressure regions	1.9 to 3	5.3	18 to 20 years	conversion from aseismic deformation to seismic failure by stress loading in the center of the field
Rangely	Oil field, EOR	Weber sandstone	2.0	not known	On the southwest portion of a fault, 0 to 4 km	3.5	3.1	several days	reduction of effective pressure by increase in pore pressure, critical pressure for failure: 25.7 MPa
The Geysers	Geothermal field, extraction and reinjection	Massive Grauwacke	1 to 3	not known	Close to several injecting wells and the recent producing wells, elsewhere diffuse pattern	< 5 km	4.0	correlation in time with several injecting wells and in the early years of operation of producing wells	volumetric contraction of the reservoir conversion from aseismic deformation to stick-slip seismic failure by chemical processes
Germigny	Gas storage	Sands and shaly sandstones	0.75	1400 to 2100 (of gas)	Close to observation well (< 200 m)	< 0.9	< -2(?)	correlation with pressure changes (injection and production)	reduction of effective stress long strata of different lithology

criterion). It is generally assumed that the most probable direction of failure will be that of maximum horizontal stress. Another possibility could be the interface between two media of different strength, e.g. a bedding plane between two sedimentary facies (bedding slip).

Modelling Pressure And Stress Distribution

Once the value of critical pressure has been estimated, the distribution of fluid pressures in the reservoir can be examined to locate the zones most probably close to seismic failure. Pressure modelling will not be considered here, since this will be done in Chapter 6. From the induced seismicity point of view, it is important to obtain maps of the spatial distribution of fluid and gas pressure before and during injection in order to correlate fluid pressure and potential microseismicity. A correlation between high pressures and microseismicity will argue for an 'effective stress mechanism' for inducing failure (see section 5.4.3.2). In contrast, stress transfer or stress loading could be inferred from microseismicity in low pressure zones.

Stress distribution around the reservoir should also be modelled, for example using the Biot theory of poro-elasticity (Segall 1989) to determine where stress loading appears due to reservoir inflation, i.e. deformation induced by fluid injection. If no failure occurs in a high pressure region, it could mean that deformation is aseismic. The resulting stress loading onto peripheral portions of the reservoir could be modelled along pre-existing faults (e.g. Davis and Pennington, 1989) to detect points where stress accumulates (asperities) and could be released seismically.

Studying Seismicity

The knowledge of the seismicity of the field in its zero-state is as essential for reservoir engineering as it is from the induced seismicity point of view, in order to compare the dynamic behaviour of the reservoir with the conditions prevailing prior to gas injection. It would therefore be preferable to start seismic monitoring 4 to 6 months before the beginning of operations. Even if the network is not deployed completely, 3 or 4 stations (e.g. one downhole sensor and three surface stations) would be suitable to record and, if possible, locate any local seismicity, natural or induced by previous field exploitation. If one of the criteria for selecting the site was the lack of any seismicity, that would be checked by this initial monitoring.

If no seismicity is recorded before, but appears after injection, it would be normal to assume that it was related to injection and it would be easier to prevent damaging earthquakes. In contrast, if seismicity is recorded before injection, the first task would be to distinguish if it is reservoir induced or simply related to natural fault movements. In either case, further induced seismicity could be expected later on, during gas disposal.

5.4.4 Reservoir Monitoring

5.4.4.1 INTRODUCTION

Large-scale storage of CO₂ in the subsurface is an unprecedented enterprise. It will therefore be crucial to monitor the process carefully. The major task of monitoring is to record and control the stability of the reservoir and to observe the development of the expanding CO₂ bubble.

The stability of the reservoir can be monitored by looking at the seismicity. It will be important to understand the source of seismicity, because only then an effective

control on the seismicity can be achieved. The system must be able to monitor the reservoir in such a way that it is possible to pinpoint the hypocentre of a seismic event and to answer questions such as: 'Is the seismicity natural or reservoir induced? Does it originate from 'hydraulic fracturing', an 'effective stress' mechanism or from 'stress loading'? Does it correlate with the injection activity?'

It will be important to follow the development of the expanding CO₂ bubble to check if the preliminary injection models correspond with the real situation and to ensure that CO₂ remains in the reservoir and does not escape to the overburden formation where it may endanger potable ground water resources. Regular checking of reservoir simulations enables a continuous modification and fine-tuning of the models.

In the following section, we will first give an outline of the installation to monitor seismicity. Next, the possibilities are discussed to record the development of the CO₂ distribution in the reservoir.

5.4.4.2 MONITORING RESERVOIR INDUCED SEISMICITY

The various examples of induced seismicity have shown that although this appears commonly as a result of underground fluid injection, damaging earthquakes are not common. Each instance of reservoir-induced seismicity is a special case strongly dependent on local geological conditions. As far as underground gas storage is concerned, seismic hazard can be regarded as very low, since gas is highly compressible, injection pressures are low and the reservoir would be sited in a quiet tectonic environment. However, damaging induced earthquakes have been recorded in and around hydrocarbon reservoirs after some tens of years of exploitation, which justifies paying special attention to seismic monitoring prior to, during and after CO₂ disposal.

The state of the art of seismological instrumentation, downhole sensors and computers is such that it is now possible to design a combined downhole and subsurface network dedicated to producing real-time processing of seismic signals and location of micro-earthquakes. Even if the frequency of seismic events is low, this would quickly give information on mechanical modifications of the reservoir, i.e. the location of zones where the reservoir is becoming fractured and the critical pressure needed for failure and earthquake generation. Two options should be considered with regard to cost:

- The minimum cost network. This would involve subsurface sensors only, no more than four or five. It would be devoted to seismic hazard assessment first, since only earthquakes with positive magnitudes would be recorded. This information would give a general idea of the behaviour of the reservoir, but precise location of active zones would remain impossible, as would monitoring the gas front.
- The combined subsurface-downhole network. This would be useful for seismic hazard assessment as well as for monitoring the microseismicity generated within or close to the reservoir. It has been shown above that the total cost would be at least twice the cost of a minimum network. Nevertheless, the information yielded by low-level microseismicity is important since it could give an insight in real time onto the location of the gas front and the way in which the reservoir is deformed. Moreover, an increase in microseismic activity recorded by the downhole sensors, both in time distribution and in magnitude, is certainly important in

modifying the initial seismic hazard evaluation. Examples of underground gas storage are too scarce to predict that a null seismic hazard at the start of disposal would not be followed by an increase of seismic activity after long-term injection.

Lastly, to understand and interpret the results of reservoir-induced seismicity monitoring the occurrence of events, locations of hypocentres and determinations of the direction of displacement have to be related to wellbore active seismic surveys, geology, rock mechanics and reservoir engineering. Precise locations of microseismicity indicates zones where pressure gradients and rock rigidity are high and where the initial state of reservoir has been modified, i.e. fractures created by seismic failure which could increase permeability. This means that microseismic monitoring can be regarded as a complementary tool for reservoir assessment.

5.4.4.3 SEISMIC MONITORING OF THE CO₂ EXPANSION IN THE RESERVOIR

One method to monitor the progression of the injected CO₂ through the reservoir is by recording the sound (microseismicity) induced by the expanding CO₂ front by a network of downhole and surface geophones. This method has been discussed in section 5.4.4.2. An other method to visualise the development of the CO₂ bubble is by recording the reflection of artificial sound waves at the gas/water interface, i.e. shooting seismic lines across the storage site. This method will be briefly discussed below.

A CO₂ bubble in an underground reservoir behaves in many ways analogous to the bubble of natural gas (methane) in a gas storage scheme. The presence of natural gas (essentially methane) in the pore spaces of a reservoir, as opposed to water, can be detected by seismic methods, because gas and water have different densities and sonic velocities. This creates an impedance contrast between the two fluids, which partially reflects compressional (sound) waves and may generate a reflection at the gas/water interface. The effective impedance contrast increases with porosity, because in rocks with a high porosity the pore fluid occupies a greater proportion of the medium through which the sound waves are passing. However, even low levels of gas saturation are sometimes sufficient to create a reflection. In oil and gas exploration, these seismic reflections are considered to be reliable gas indicator.

The impedance contrast, and the reflection coefficient, at the fluid interfaces in a reservoir are a function of the density and acoustic velocity of the fluids and their rock matrix. The density of pure methane at reservoir conditions of 35°C and 10.6 MPa, corresponding to a depth of around 1000 m, is approximately 80 kg/m³, and the density of formation water is around 1050 kg/m³. However, the density of CO₂ at these reservoir conditions is about 700 kg/m³, nearly nine times that of methane, and much closer to that of formation water. Thus the impedance contrast between CO₂ and water will be smaller than between natural gas and water. This means that it will be more difficult to resolve a CO₂/water interface on seismic data. However, on the best quality modern 3D seismic data acquired over producing oilfields, even oil/water contacts are sometimes visible. Oil has a reservoir density of about 850 kg/m³. So, it might be technically possible to image the distribution of CO₂ in a storage reservoir using 3-D seismic, but it would be very expensive (see section 5.4.2). And if conditions were less than ideal, results might be poor. It would be sensible to acquire 2-D trial lines before attempting a 3-D seismic shoot.

5.5 CO₂ LEAKAGE AND POTABLE GROUNDWATER QUALITY

Richard Metcalfe

5.5.1 Introduction

The safety issues of CO₂ disposal in underground reservoirs have been considered in the previous sections of this chapter, which pointed out that apart from reservoir induced seismicity the major risk associated with CO₂ disposal arises from the possible leakage of CO₂ from the storage installation or the reservoir. The possibility that fresh groundwater supplies might be polluted by such leakage has been considered briefly in section 5.2. The purpose of this section is to consider the likely consequences of CO₂ leakage for potable water quality in more detail.

The likely effects of CO₂ leakage on potable water quality are complex. Within the time-scale of the present study, these effects cannot be investigated comprehensively. Therefore, the approach has been to consider firstly the nature of potable groundwater, and then secondly whether the addition of CO₂ to such water is likely to affect its potability.

Clearly, the effects of adding CO₂ to a groundwater will depend to a large degree upon the water/rock interactions. These will in turn vary widely, reflecting the wide range of lithologies which may act as groundwater aquifers. Therefore it is not possible, within the scope of this report, to consider the effects of CO₂ leakage in all types of aquifer. Thus, the report concentrates on the possible effects of CO₂ leakage into potable groundwaters in 'red bed' and chalk aquifers. Particular reference is made to the Permian-Triassic red bed and Cretaceous Chalk aquifers in the U.K., because they are the most important sources of groundwater for U.K. domestic consumption (together, these aquifers contribute ca 30% of potable water supplies). These reservoirs are also widespread through Northern Europe. By considering these aquifers, various underlying processes which are likely to affect potable water quality in carbonate and clastic rocks in general can be evaluated.

Having evaluated the nature of potable water, and Chalk and red bed aquifers in the U.K., the report aims to assess the likely importance of CO₂ leakage as a potential control of potable groundwater quality. Additionally, it is aimed to highlight those topics which must be researched more thoroughly before a complete understanding of the polluting potential of CO₂ can be made.

5.5.2 The Nature Of Potable Water

5.5.2.1 THE COMPOSITION OF POTABLE WATER

Potable groundwaters must be fresh, with a total dissolved solid (TDS) content of < ca 500 mg/l (based on maximum permissible levels of dissolved constituents: CEC Directive 80/778). However, in general there is a trend towards increasing salinities with increasing depths of abstraction. This is because, as the distances from the sites of recharge increase, the abstracted groundwaters usually contain progressively larger components of relatively old water. Typically, these latter will be saline, either because their primary salinity is preserved (for instance in the case of connate marine waters), or else because water/rock interactions (including evaporite dissolution) have been relatively extensive. For these reasons, potable groundwaters are generally abstracted from relatively shallow depths,

Figure 5.5.1 Trace elements in groundwater and their significance in terms of health and environmental protection. After Edmunds et al. (1989).

TRACE ELEMENTS					MAJOR ELEMENTS			
CONCENTRATION IN PARTS PER MILLION								
< 0.00001	0.00001-0.0001	0.0001-0.001	0.001-0.01	0.01-0.1	0.1-1.0	1.0-10	10-100	> 100
Nb	Cs	Rb	Li	P	Sr	Mg	Na	HCO ₃
Ru	Zr	La	Ba	B	F	K	Ca	
Rh	Mo	V	Cu	Br		Si	SO ₄	
Pd	Ag	Se	Mn	Fe			Cl	
In	Be	As	U	Zn			NO ₃	
Hf	Th	Cd	I					
Ta	Ce and REE	Co						
Re	Hg	Ni						
Os	Sc	Cr						
Ir	Sb	Pb						
Pt	Sn	Al						
Po	Te	Y						
Au	Tl							
	Bi							
	W							
	Ga							
	Ge							

Essential Elements	
Fe	Elements considered essential for human or animal health.
Sr	Elements probably essential for health.
Pb	Non-essential elements.
Toxic Elements	
Cd	Elements considered to be toxic or undesirable in excessive amounts and for which maximum admissible concentrations (MAC) have been set by the CEC.
V	Other elements considered undesirable in excess but for which no statutory limit has been set by the CEC.

Concentration in dilute, oxygenated groundwater at pH7

usually < ca 300 m. Accordingly, the temperatures of potable groundwaters are usually similar to surface temperatures, ≤ ca 25°C, and their pressures are typically < ca 30 bar.

Additionally, potable groundwaters, are usually geologically young. In the cases of the Permo- Triassic red beds and Cretaceous chalks of the U.K., most potable groundwaters appear to have been recharged in the Quaternary. For example, in the Chalk aquifers of the London Basin, groundwaters were recharged mainly in post-Pleistocene times (Edmunds et al., 1987, 1992), although Pleistocene groundwater older than 25 000 years are likely in the central part of the basin (Smith et al., 1976). Similarly, in the Triassic red bed aquifers of the English midlands, potable groundwaters seem to have been recharged in Pleistocene and more recent times (Bath et al., 1979; Jackson and Lloyd, 1983).

The chemical criteria which a groundwater must meet in order to be deemed potable are outlined in Edmunds et al. (1989). They pointed out that nine major species (HCO₃, Na, Ca, SO₄, Cl, NO₃, Mg, K and Si) usually account for ca 99% of the total solute content by weight, with the minor and trace elements (those at concentrations of less

than ca 1 mg/l) constituting the remaining 1%. The significance of the various constituents of groundwaters in terms of health and environmental protection are illustrated in Figure 5.5.1. This shows those elements which are considered essential for human health and those which are considered to be toxic to some extent.

The guideline concentrations (GL) and maximum admissible concentrations (MAC) for a number of common chemical constituents in potable groundwaters have been specified by both the Commission of the European Communities (CEC) and the World Health Organisation (WHO) (Table 5.5.1).

5.5.2.2 THE CHALK AQUIFERS OF THE U.K.

The nature of Chalk aquifers in the U.K. and the hydro-chemistry of the groundwaters they contain have been considered in detail in Edmunds et al. (1987, 1992). The main features of these investigations are summarised here.

The Chalk behaves as an aquifer as a result of its dual (or even multiple) porosity which is extremely high, in the range 20–45%. It is generally composed of very pure calcium carbonates, but Mg, Sr, Mn and Fe may be important minor constituents (Tables 5.5.2 and 5.5.3). The acetic

Table 5.5.1 Standards of water quality for human consumption.

		CEC GL* (mg/l)	MAC* (mg/l)	WHO GV* (mg/l)
Calcium	(Ca ²⁺)	100	—	—
Magnesium	(Mg ²⁺)	30	50	—
Sodium	(Na ⁺)†	20	150	200
Potassium	(K ⁺)	10	12	—
Chloride	(Cl ⁻)	25	—	250
Sulphate	(SO ₄ ²⁻)	25	250	400
Aluminium	(Al ³⁺)	0.05	0.5	0.2
Nitrate	(NO ₃ ⁻)†	25	50	45
	(as N)	5.65	11.3	10
Nitrite	(NO ₂ ⁻)†	—	0.1	—
Ammonium	(NH ₄ ⁺)	0.05	0.5	0.2
Iron	(Fe ³⁺)	0.05(FeT)	0.2(FeT);	0.3(FeT)
	(Fe ²⁺)	—	—	—
Manganese	(Mn ²⁺)	0.02	0.05	0.1
Copper	(Cu ²⁺)	3000	—	1000
Zinc	(Zn ²⁺)	5000	—	5000
Phosphate	(HPO ₄ ²⁻)	400	5000	—
Fluoride	(F ⁻)†	8–12°C	1500	1500
		25–30°C	700	—
Barium	(Ba ²⁺)	100	—	—
Silver	(Ag ⁺)	—	10	—
Arsenic	(As)†	—	50	50
Cadmium	(Cd ²⁺)†	—	5	5
Cyanide	(CN)†	—	50	100
Chromium	(Cr)†	—	50	50
Mercury	(Hg)†	—	1	1
Nickel	(Ni)	—	50	—
Lead	(Pb ²⁺)†	—	50	50
Antimony	(Sb)	—	10	—
Selenium	(Se)†	—	10	10
Pesticides	(Separately)	—	0.1	different for
	(Total)	—	0.5	each compound
Polycyclic Aromatic Hydrocarbons (PAH)	—	0.2	—	—
Carbon Tetrachloride (CTC)	—	—	3	—
Trichloroethene (TCE)	—	—	30	—
Temperature (°C)	12	25	—	—
pH	—	6.5–8.5	—	6.5–8.5
Conductivity (mS/cm at 20°C)	400	—	—	—

* CEC: Council of the European Communities Directive 80/778;

GL: Guide level; MAC: Maximum admissible concentration;

WHO: World Health Organisation. Guidelines for drinking water quality. 1984;

GV: Guide value

† Inorganic constituents of health significance (World Health Organisation 1984)

[additionally: asbestos, barium, beryllium, nickel, silver, — no guide value set].

acid insoluble (non-carbonate) residue of the Chalk is generally very low, with a maximum of *ca* 12% in Berkshire. In Berkshire, this non-carbonate fraction is in decreasing order: quartz > montmorillonite > white mica > apatite > palygorskite > feldspar > marcasite > cristobalite. Additionally, in the Lower Chalk only, kaolinite and mixed-layer clays are found. The Chalk may also contain small quantities of organic matter (humic materials and bitumen range from *ca* 0.01% to *ca* 0.2%: Pacey, 1989).

Table 5.5.2 Whole-rock analyses of Chalks, from Jarvis (1980).

Concentration in %	Soft white Chalk	Phosphatic Chalk
SiO ₂	1.200	0.740
Al ₂ O ₃	0.249	0.174
Fe ₂ O ₃	0.370	0.413
MnO	0.035	0.029
MgO	0.233	0.255
CaO	54.90	53.70
Na ₂ O	0.031	0.306
K ₂ O	0.047	0.045
P ₂ O ₅	0.300	10.10
Sr	0.059	0.113

Near to recharge zones^[3] congruent dissolution^[4] predominates and calcite saturation is rapidly approached. Therefore, in the (water) saturated zone, the groundwaters are all at or near to saturation with calcite.

Near to the zones of recharge Mg/Ca ratios in the waters are typically low. However, as the waters flow away from these zones, the molar Mg/Ca ratios increase gradually to *ca* 1, reflecting increases in dissolved Mg concentrations. Similarly, Sr, Mn and Fe concentrations also increase along groundwater flow paths. This is thought to be due to the incongruent dissolution of the aquifer carbonate. Relatively high Mg, Sr, Mn and Fe contents occur in those carbonates with chemical characteristics that were acquired in the marine depositional environment. As reactions with fresh water progress, these components partition into the aqueous phase and fractionally purer, low-Mg calcite forms. Thus Mg, Sr, Mn and Fe become increasingly important components of groundwaters as the duration of water/rock interactions increases with increasing groundwater residence

[3] The recharge zone is the area of an aquifer in which there is a downward water movement towards the water table.

[4] Congruent dissolution is the transition from a solid substance to an aqueous phase of the same composition.

Table 5.5.3 Trace element composition of the Chalk, after Edmunds et al. (1992).

Concentration in ppm	Geological subdivision of the Chalk				
	Campanian	Santonian	Coniacian	Turonian	Cenomanian
Sr	731	626	377	381	417
Mg	1530	1379	1379	2032	2303
K	41	64	58	84	192
Na	317	287	214	299	411
Mn	155	230	222	216	387
Fe	89	104	78	307	698
Zn	16	—	13	11	7

times. Hence, these components are present in the greatest concentrations in the deepest (oldest) waters. Additionally, with increasing depth in the London Basin there is a change in groundwater chemistry, from Ca-HCO₃ to Na(Mg)-HCO₃ type. The increase in Mg with depth is probably due to carbonate reactions, since the exchange of Mg with Ca in clay minerals would require a very high Mg/Ca ratio on the solid phase. However, cation exchange on clays was thought by Edmunds et al. (1992) to explain the increase in Na concentrations with depth. This increase cannot be explained solely by mixing with deep Na-Cl water since the increase in Na occurred *before* any increase in Cl concentrations.

Sulphate concentrations in unconfined aquifers (i.e. without a top seal) are similar to those of the unsaturated zone (ca 35 mg/l) and persist across the unsaturated zone. With progressively increasing depth beyond the unsaturated zone, the concentration of SO₄ reaches ca 50 mg/l. This is considered to be due to the local occurrence of trace amounts of gypsum in Chalk hard grounds (Edmunds et al., 1987).

However, the variations in groundwater chemistry in the Chalk are not all attributable to carbonate reactions, and trace occurrences of minerals such as gypsum. It seems that residual connate water is present in the matrix of the chalk and may contribute to increases in salinity with depth which are reflected in larger Na and Cl contents (Bath and Edmunds, 1981).

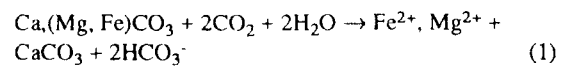
Trace element compositions of Chalk groundwaters have been presented in Edmunds et al. (1989) and analyses

Table 5.5.4 Maximum, median and minimum values of major, minor and trace elements in the Berkshire Chalk.

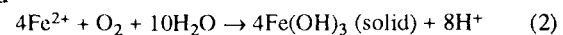
Parameter	Concentration, mg/l		
	Minimum	Median	Maximum
Na	5.1	14.8	170
K	0.60	3.5	10.2
Ca	34.7	85	148.
Mg	1.32	8.4	29.4
HCO ₃	263	301	341
SO ₄	2.5	20.7	137
Cl	10.4	17.7	183
NO ₃	1.6		7.8
Si	4.9	8.1	13.5
Sr	0.25	2.0	6.28
Ba	0.002	0.051	147
F	<0.100	0.740	2.4
Br	0.020	0.067	1.14
I	0.003	0.011	0.067
Li	0.0004	0.004	0.029
B	0.003	0.056	0.526
FeT	<0.003	0.098	0.810
Mn	<0.00003	0.003	0.139
Cu	<0.0002	0.0003	0.007
Zn	<0.002	0.010	0.918

of the Berkshire Chalk are summarised in Table 5.5.4. These workers found that in the Chalk, the concentrations of toxic metals are generally low due to the buffering of pH by carbonate.

Edmunds et al. (1992) highlighted the importance of redox buffering in the Chalk aquifer as an additional control on metal mobility. They noted that along flow paths away from outcrop there is a progressive decrease in EH, from +330 – +420 mV to < +160 mV at the point where oxygen disappears. They considered that Fe (II) release from carbonates is an important control on redox conditions, according to:



and



In Berkshire the concentration of Fe was found to increase from < 0.01 mg/l in the oxidised zone (prior to the removal of dissolved oxygen) to ca 1 mg/l in the anaerobic zone.

In comparison with mineral solubility controls, redox reactions, dispersion and cation exchange are considered to have only a limited importance in the Chalk compared with clastic sediments.

5.5.2.3 PERMO-TRIASSIC RED BED AQUIFERS OF THE U.K.

Red beds originate as first-cycle, immature sediments formed mainly by erosion of crystalline rocks (e.g. Turner, 1980; Frostick and Reid, 1987). They accumulate in continental settings and remain under oxidising conditions for relatively long periods following deposition. This leads to the breakdown of unstable detrital ferromagnesian constituents, such as olivine, pyroxene and amphibole, which produces hematite and imparts the characteristic red coloration. Arid climates are often conducive to the accumulation of red beds and hence evaporites are a characteristic feature of many red bed sequences. All these factors mean that in contrast to Chalk aquifers, red bed aquifers are usually chemically heterogeneous.

In the U.K. the Permo-Triassic red bed aquifers of the Sherwood Sandstone Group show geographical variations in mineralogical composition, with lithic and feldspar fragments being more abundant in the south than in the north (Burley 1984). Quartz and K-feldspar grains are generally the dominant detrital constituents, while kaolinites, illite, carbonate, quartz and feldspar are the dominant authigenic^[5] minerals. Carbonates may comprise up to 40 vol% of the rock (Burley 1984). Early diagenetic, intergranular, and replacive carbonates are characteristically

[5] Authigenic is applied to minerals that formed in the rock of which they are part during, or soon after, its deposition.

non-ferroan whereas later burial diagenetic carbonates may contain significant Fe (Burley, 1984; Bath et al., 1987; Strong and Milodowski, 1987).

The Triassic red beds in the U.K. may, in different places, host: 1) major oil and gas reservoirs (North Sea, Wessex and Irish Sea basins); 2) Cu-Pb-Zn mineralisation (Cheshire and Lincolnshire basins); 3) commercially valuable evaporites, including sylvite (Cleveland); 4) anhydrite (Cheshire, Cumbria and Nottinghamshire); and 5) halite (Cleveland, Cheshire). Additionally, these red beds may act as major potable water sources (Cheshire, Lancashire and Nottinghamshire), and geothermal reservoirs (Wessex Basin).

Red beds may contain a significant amount of heavy metals (Table 5.5.6), the remobilisation of which may give rise to ore deposits, particularly of Cu and U, but also of Pb, Zn and Ag (Gustafson & Williams 1981; Kimberley 1979; Durrance 1986). For example, whole-rock data in Wedepohl (1978) suggest that red bed sandstones have mean abundances of: Pb = 9.9 ppm; Cu = 10.0 ppm; and Zn = 30.9 ppm.

The chemical heterogeneity of red beds leads in turn to the development of a number of different formation water types. Calcium carbonate groundwaters may develop where meteoric waters weather silicate and carbonate minerals, but calcium sulphate and sodium chloride groundwaters may evolve where there is dissolution of evaporite minerals. For example, in the Sherwood Sandstone Group aquifers of the Cheshire Basin of northwest England, four main types of groundwaters can be discerned: Saline (TDS > 10 000 mg/l) Na-Cl dominated waters; brackish (TDS = 1000–10000 mg/l) Na-Cl dominated waters; fresh (TDS = <1000 mg/l) Na-Cl type waters; and fresh (TDS = <1000 mg/l) waters with a Ca-Na-HCO₃ chemistry. However, in general potable groundwaters from Triassic aquifers have chemistries which

Table 5.5.5 Maximum, median and minimum concentrations of trace elements in groundwaters from the Permo-Triassic sandstones of Lancashire and north Cheshire.

Parameter	Concentration, mg/l		
	Minimum	Median	Maximum
Na	8.7	14.2	46
K	1.6	2.0	4.3
Ca	36.4	61.5	114
Mg	7.2	21.9	30.3
HCO ₃ -lab	112	232	421
SO ₄	13.3	40.	96
Cl	15.5	26.5	99
NO ₃	<0.5	3.16	9.9
Si	4.0	5.2	8.5
Sr	0.045	0.131	0.504
Ba	0.01	0.088	0.640
F	<0.1	0.1	0.140
Br	0.048	0.080	0.190
I	0.0037	0.0040	0.0050
Li	0.003	0.007	0.01600
B	0.003	0.016	0.23400
Fe.TOTAL	<0.001	0.0034	3.91
Mn	<0.0002	0.0003	0.644
Cu	<0.0002	0.0016	0.012
Zn	<0.003	0.004	0.020
As	<0.001	0.001	0.057
V	<0.0002	<0.0006	0.0039
Al	<0.0003	—	0.012
Ni	<0.001	—	0.014

are dominantly controlled by equilibria involving carbonate cements (Edmunds et al., 1984, 1989; Bath et al., 1987; Lucey 1987). In contrast, deep groundwaters from red beds in the U.K. are generally highly saline and of Na-Cl type, reflecting a dominant salinity source in halite dissolution (Edmunds 1986). Salinities are highly variable, but may approach halite saturation (> 300 g/l TDS).

The trace element concentrations in a wide range of groundwaters from red bed aquifers in the U.K. have been presented in Edmunds et al. (1989) and analyses of waters from such aquifers in Lancashire and Cheshire are presented in Table 5.5.5. These workers pointed out that in these aquifers, concentrations of a number of transition metals tend to be higher than in Chalk aquifers (e.g. Mn, Cu, Fe; cf. Tables 5.5.4 and 5.5.5). They noted that in red bed aquifers, the concentrations of several metals (e.g. Al, Zn, Be, Co, Cr, Ni, V) increase as pH falls below ca 6.0.

In many potable groundwaters, however, variations in pH seem to reflect carbonate buffering, as in Chalk aquifers. For example, in the Sherwood Sandstone aquifer of the English Midlands, pH was found to increase from ca 7 to ca 8 at greater distances from the outcrop (Edmunds et al., 1984). These workers also found that at increasing distances from recharge zones, redox conditions varied in a similar fashion to those in Chalk aquifers. They further discovered that only the waters in the unconfined part of the aquifer are sufficiently oxidising to contain dissolved oxygen, and down dip from the outcrop, Fe²⁺ and then Fe³⁺ and HS⁻ become important in controlling redox potentials, as EH falls from +300 mV to 0 mV.

5.5.3 Factors Affecting Water Quality

A large number of factors must be considered when attempting to evaluate the potential effects of CO₂ leaks from disposal sites upon the quality of potable groundwaters. The most important processes are likely to be:

1. perturbation of groundwater flow regimes
2. migration of saline waters with CO₂
3. migration of dissolved organic matter with CO₂
4. mineral dissolution
5. co-precipitation of metals
6. sorption of metals
7. microbial activity
8. aqueous complexation of metals

Clearly, these processes will be interrelated. For example, aqueous complexation will influence (and be influenced by) the stability of the various minerals in an aquifer. This complicates the assessment of the likely impact of CO₂ leakage on groundwater quality, and consequently it is not possible to consider these processes in detail.

The analysis of the above aspects reveals that there are four basic underlying factors which must be considered when evaluating the significance of CO₂ disposal for the potability of groundwaters:

1. pH buffering
2. redox buffering
3. fluid flow
4. transport of pollutants (e.g. hydrocarbons).

Table 5.5.6 The mean contents of Cu, Pb, Zn and U in minerals found within immature red bed sediments. After Metcalfe et al. (1994); Data from Wedepohl (1978). 'N' denotes number of samples

Mineral	Cu (ppm)		Pb (ppm)		Zn (ppm)		U (ppm)	
	Mean	N	Mean	N	Mean	N	Mean	N
Pyroxene	130	95	6	20	248	28	3.6	n.r
Amphibole	81	39	16	76	823	60	7.9	n.r
Magnetite	80	251	<10	13	563	93	1-30	
Biotite	227	752	40	512	545	672	8.1	n.r
Muscovite	36	12	26	33	54	19	2-8	
Kaolinite	23	13	n.r	n.r	59	50	n.r	n.r
Plagioclase	71	108	19	61	17	23	2.7*	n.r
K-feldspar	<1-20	140	791	5	3	2.7*	n.r	
Allanite	n.r	n.r	n.r	n.r	n.r	n.r	200	n.r
Epidote	n.r	n.r	n.r	n.r	n.r	n.r	43	n.r
Apatite	n.r	n.r	n.r	n.r	n.r	n.r	65	n.r
Garnet	33	61	n.r	n.r	n.r	n.r	6-30	
Zircon	n.r	n.r	n.r	n.r	n.r	n.r	1330	n.r
Sphene	n.r	n.r	n.r	n.r	n.r	n.r	280	n.r
Monazite	n.r	n.r	n.r	n.r	n.r	n.r	3000.	n.r

n.r = not reported

* Value reported for a combination of K-feldspar and plagioclase

In particular, the effect of CO₂ addition on pH and redox conditions is likely to be a major control on groundwater quality.

The importance of pH and redox as major controls on water quality has been highlighted by Edmunds et al. (1989). They found that dissolved oxygen exerts a major control on the mobility of many elements. For example, Cu, V, U and Cr were found to be mobile under oxidising conditions, but to occur at very low concentrations under anaerobic conditions. However, other elements, such as Fe, are mobile only under reducing conditions at the pH of most groundwaters. Several elements, including Mn and Zn were found to be relatively insensitive to redox changes. Edmunds et al. (1989) found that the concentration of many trace elements in groundwaters increase with increasing acidity. However, because different lithologies have different chemical characteristics and pH buffering capacities, the behaviour of trace metals was found to depend to some extent upon the nature of the aquifer. For example, in carbonate aquifers most of the toxic metals were found to be buffered at low levels by the carbonate system, except for F, Sr, I, and B. In contrast, waters from sandstones tend to show higher concentration of many transition elements (e.g. Fe, Mn, Cu) than in waters from carbonate aquifers, regardless of the pH (cf. Tables 5.5.4 and 5.5.5). However, as pH decreases to < ca 6, dissolution of the sandstone matrix is inferred to cause significant increases in concentrations of metals such as Al, Zn, Be, Co, Cr, Ni and V.

5.5.3.1 PERTURBATION OF GROUNDWATER FLOW REGIMES

It is conceivable that the injection of CO₂ into an underground reservoir and the subsequent leakage of the CO₂ from that reservoir might perturb groundwater flow regimes. This in turn might affect the quality of potable waters in the vicinity of the CO₂ disposal site indirectly, for instance through influencing mixing between saline waters and fresher potable waters. Additionally, it is possible that CO₂ leakage into an aquifer which bears potable groundwater might be accompanied by a large volume increase. This is because the majority of potable groundwaters have in-situ temperatures and pressures which are below the critical point of CO₂ (31.2°C and 7.28 MPa). Thus, any CO₂ which enters a potable groundwater will tend to occur in a gaseous, rather than supercritical, state. Any expansion of CO₂ as a consequence of its transition from a supercritical fluid to a gas might in turn lead to perturbation of groundwater flow by a gas drive mechanism.

5.5.3.2 MIGRATION OF SALINE WATERS WITH CO₂

Migration of saline waters might be a consequence of CO₂ leakage affecting fluid flow regimes. In many aquifers from which groundwaters are abstracted, there is a transition from low-salinity potable waters, to higher salinity impotable waters. It can be envisaged that the perturbation of the saline transition zones as a result of CO₂ leakage might cause the salinity of the groundwaters to rise to a point where they are no longer potable. Any assessment of the importance of this process must take account of the effect of salinity upon the partitioning of CO₂ between supercritical, gaseous and aqueous phases. Apart from perturbation due to escaping CO₂, formation brine will be displaced by the injected CO₂ during 'regular' storage in open aquifers. These brines are driven out of the aquifer and may contaminate fresh water resources in the overburden formations.

5.5.3.3 MIGRATION OF DISSOLVED ORGANIC MATTER WITH CO₂

Supercritical carbon dioxide is an excellent solvent for many organic compounds. Therefore, especially in cases where hydrocarbon reservoirs are used for CO₂ disposal, it is possible that any CO₂ leakage into a potable groundwater might lead to contamination of groundwater supplies by organic matter. Any assessment of the importance of this process must take account of the likely variation in partitioning of organic matter between liquid petroleum-like phases moving with the CO₂, the aqueous phase, supercritical CO₂, and gaseous CO₂.

5.5.3.4 MINERAL DISSOLUTION

The addition of CO₂ to a potable groundwater might have a major effect on the stability of the mineral constituents of the host aquifer. Largely, this will be in response to a decrease in pH which will accompany the introduction of CO₂. In particular, a major consequence of this is likely to be carbonate dissolution. This might have serious implications for groundwater quality simply by increasing the hardness of the water. One aspect of the increase in hardness is that the concentrations of the major constituents of carbonates (notably Ca, Mg and Fe) might increase to levels which are greater than the CEC guideline levels/maximum acceptable levels. Additionally, trace elements which may occur in the structures of carbonates may be liberated to solution.

Veizer (1983) has presented data for the concentrations of trace elements in sedimentary carbonates. Average trace

element contents of sedimentary carbonates are given in Table 5.5.7. This illustrates that carbonates can accommodate significant amounts of potential pollutants such as heavy metals. Additionally, Edmunds et al. (1989) concluded that incongruent dissolution of carbonate leads to the concentrations of a number of trace elements (such as Sr, F, Li, B, I, Mn) to increase with increasing groundwater residence times. Thus, it is conceivable that dissolution of carbonate upon addition of CO₂ to an aquifer could liberate certain heavy metal pollutants to solution.

The stability of silicates may also be affected by pH changes, and CO₂ leakage might also lead to silicate dissolution and transformations. For example, Figure 5.5.2 illustrates that decreases in pH (increases in H⁺ concentrations) may lead to the kaolinitisation of feldspar. This might in turn cause the liberation of trace metals to solution. For example, K-feldspar may contain significant quantities of Pb (mean 140 mg/kg; Wedepohl, 1978) which could enter solution as a consequence of feldspar dissolution.

Additionally, the stability of any ore minerals which are present in an aquifer might also be affected by a decrease in pH. Such dissolution is likely to be particularly important in red bed aquifers, which may host ore deposits. For example, oxides and carbonates such as hematite (Fe₂O₃), cerussite (PbCO₃), smithsonite (ZnCO₃) and tenorite (CuO) may dissolve as conditions become more acidic (Figure 5.5.2). The addition of CO₂ to a water may perturb its redox state as well as its pH. The exact effect on redox potentials (EH) will depend upon what redox-buffering equilibria are established in the aquifer. However, CO₂ addition may lead to an increase of EH (oxidation). Figure 5.5.3 shows that this could lead to the dissolution of metal sulphides which may be present in the aquifer, such as chalcocite (Cu₂S), sphalerite (ZnS), and galena (PbS).

As mentioned previously, organic compounds are anticipated to migrate with supercritical CO₂ and these might exert an influence upon mineral stability. Organic acids may play an important role in this. This has been the subject of some debate, and it is uncertain, for example, whether the primary role of these acids is to increase reaction rates (e.g. Stoessel and Pittman, 1990), or whether metal-organic complexing enhances mineral dissolution (e.g. Surdam et al., 1984; Surdam et al., 1989). However, it seems that organic acids may buffer the pH and EH of fluids (e.g. Lundegard and Land, 1986; Shock, 1988; Huang and Longo, 1992). Thus, equilibria involving organic matter must be taken into account when assessing mineral stabilities in the presence of CO₂ which migrates from an underground disposal site.

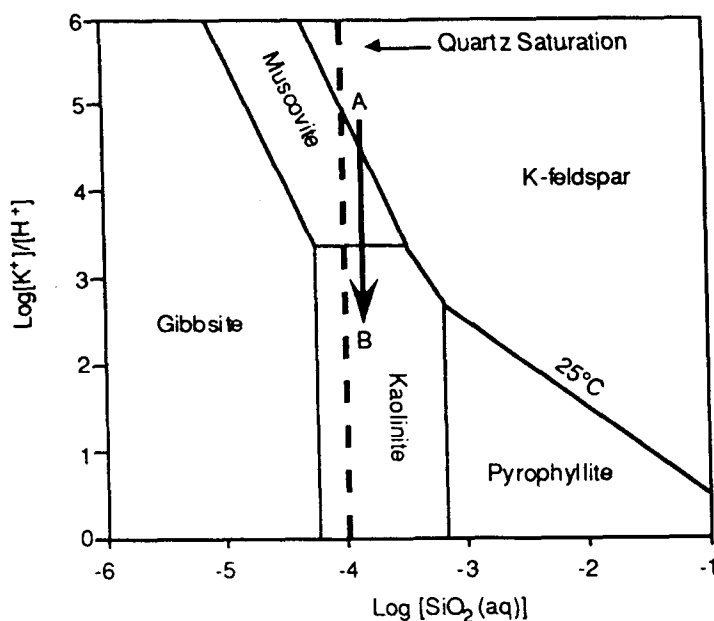
5.5.3.5 CO-PRECIPIATION OF METALS

In order to understand the potential of metals to pollute potable groundwaters in response to CO₂ leakage from a disposal site, it is necessary to understand how secondary mineral formation might affect metal mobility. As discussed in the previous section, CO₂ leakage into an aquifer might lead to mineral dissolution, and consequently release of metals to solution. However, it is also conceivable that CO₂ leakage might lead to mineral precipitation and/or recrystallisation. Such precipitation could effectively remove co-precipitated metals from solution. In most aquifers which bear potable groundwaters it is probable that carbonates and Fe-oxides might be particularly important in this respect. It might be envisaged that carbonates would precipitate in response to temperature fluctuations or where equilibria other than carbonate equilibria buffer pH, so that addition of CO₂ at constant pH would lead to carbonate formation. Additionally, the

Table 5.5.7 Mean trace element contents of sedimentary carbonates (in ppm). After Veizer (1983).

Element	Carbonates	Deep Sea Carbonates
Li	5	5
Be	0.x	0.x
B	20	55
F	330	540
Ne	400	2000
Mg	47000	4000
Al	4200	20000
Si	24000	32000
P	400	350
S	1200	1300
Cl	150	21000
K	2700	2900
Ca	302300	312400
Sc	1	2
Ti	400	770
V	20	20
Cr	11	11
Mn	1100	1000
Fe	3800	9000
Co	0.1	7
Ni	20	30
Cu	4	30
Zn	20	35
Ga	4	13
Ge	0.2	0.2
As	1	1
Se	0.08	0.17
Br	6.2	70
Rb	3	10
Sr	610	2000
Y	30	42
Zr	19	20
Nb	0.3	4.6
Mo	0.4	3
Ag	0.0x	0.0x
Cd	0.035	0.0x
In	0.0x	0.0x
Sn	0.x	0.x
Sb	0.2	0.15
I	1.2	0.05
Cs	0.x	0.4
Ba	10	190
La	x	10
Ce	11.5	35
Pr	1.1	3.3
Nd	4.7	14
Sm	1.3	3.8
Eu	0.2	0.6
Gd	1.3	3.8
Tb	0.2	0.6
Dy	0.9	2.7
Ho	0.3	0.8
Er	0.5	1.5
Tm	0.04	0.1
Yb	0.5	1.5
Lu	0.2	0.5
Hf	0.3	0.41
Ta	0.0x	0.0x
W	0.6	0.x
Au	0.00x	0.00x
Hg	0.04	0.0x
Tl	0.0x	0.16
Pb	9	9
Th	1.7	x
U	2.2	0.x

Figure 5.5.2 Logarithmic mineral stability diagram for the system $K_2O-SiO_2-Al_2O_3-H_2O$. This illustrates how variations in the activities of dissolved K^+ , $SiO_2(aq)$ and H^+ can be a major control on the stabilities of silicate minerals. It can be envisaged that a water which is equilibrated with K-feldspar at A might move into the kaolinite stability field at B as pH falls (H^+ rises) upon addition of CO_2 . Phase boundaries were calculated for $25^\circ C$ and 0.1 MPa using the SUPCRT92 computer code (Johnson et al., 1991).



behaviour of carbonate minerals and Fe-oxides might be coupled. For example, dissolution of ferroan calcite due to an influx of CO_2 might lead to the release of Fe^{2+} to solution. This Fe^{2+} might undergo oxidation and re-precipitate in Fe-oxides.

As described above, carbonates can accommodate ppm quantities of heavy metals in their structures (Table 5.5.6; Veizer, 1983). Thus, it is conceivable that precipitation or recrystallisation of carbonate could scavenge certain pollutants from solution.

Naturally, any precipitation of Fe-oxides will tend to remove polluting Fe from solution. However, it may also remove any metals which are co-precipitated with the Fe. Unfortunately there are at present insufficient data available to enable an assessment of the importance of co-precipitation in Fe-oxides. However, Gerth (1990) investigated the incorporation of heavy metals into goethite in highly alkaline (sodium hydroxide) solutions. He concluded that the proportion of incorporated metal decreases in the order $Cu = Co > Cd > Zn \gg Ni > Th \gg U$. Additionally, by conducting leaching experiments in which whole-rock samples were exposed to progressively more stringent chemical leaching agents, Zielinski et al. (1983) concluded that 10–63% of the metal content in the red beds is located in leachable sites on secondary Fe-oxides, and to some extent on minor Mn oxides, and clays. The abundances of metals on leachable sites were found to increase in the order: $Cr (10) < V (15) < Pb (\geq 20) < Zn (22) < U (27) < Fe (30) < Ni (41) < Cu (44) < Co (47) < Mn (63)$, where values in parentheses are average percentages of metals which are leachable. Taken together these results suggest that potentially, co-precipitation of metals with Fe-oxides may be an important control on water quality.

5.5.3.6 SORPTION OF METALS

Sorption is potentially a significant control on the mobility of heavy metals which might pollute a groundwater supply. The dominant sorbents in nature are the common hydrous oxides of Fe, Al, Mn and Si. Organic matter and clay minerals may act as important sorbents. Cation exchange reactions (including sorption) involving clay may exert a strong influence on the mobility of metal cations in solution (e.g. Bolt et al., 1981; Freedman et al., 1994). However, in many cases it is likely that metal complexation with organic materials will exert a relatively large influence on the water chemistry compared to sorption on these materials (see Bolt et al., 1981 for a description of these processes). Both cation exchange and complexation reactions will be pH dependent and any decreases in pH which are a consequence of CO_2 disposal could conceivably cause metals to be liberated to the solution. The prediction of such an effect would be complicated, because clay minerals and organic materials are compositionally and structurally variable. This leads to different mineral sorbing different

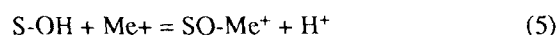
metals to varying degrees (Freedman et al., 1994).

Iron oxides are an important constituent of red beds, and also commonly form coatings on fractured walls in Chalk aquifers. Therefore, as an illustration of the possible effects of CO_2 leakage on the sorption of metals in aquifers, the present report concentrates on the sorption characteristics of Fe-oxides.

Sorption arises because of the existence of surface charges on solid phases. In particular, surfaces of oxides and hydroxides are capable of adsorbing or dissociating H^+ from surface OH^- groups, according to:



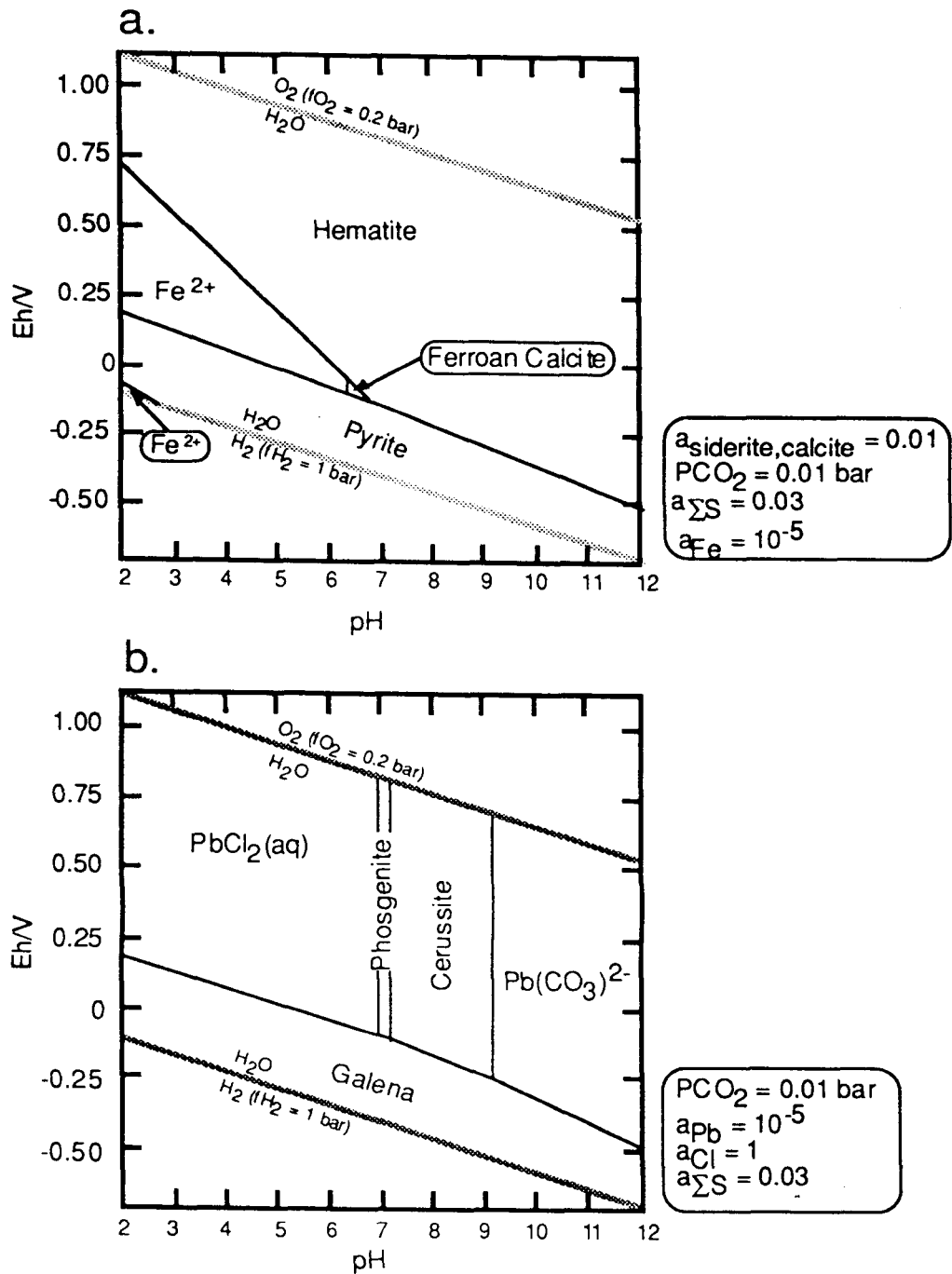
where S-OH indicates surface sites occupied by OH. This produces charged sites which affect the electrostatic attraction for other ions on or near the surface, and create sites for further reaction according to equilibria such as:



where Me^+ is a metal cation. When ions are not bound at any particular surface site sorption is said to be 'non-specific'. Conversely, when ions are bound at specific surface sites they are said to be 'specifically sorbed'. The abundance of these SOH_2^+ and SO^- charged sites depends upon the pH, and consequently the proportion of a metal cation which is specifically sorbed is also pH-dependent (Figure 5.5.4). The proportion of a cation which is specifically sorbed increases from zero to 100% as pH increases. This occurs over a relatively small range of pH to form an 'adsorption edge'.

Recently, the possible importance of sorption on Fe-oxides in red beds has been assessed by Metcalfe et al. (1994). Sorption edges for Cu, Pb, Zn, Co and Ag when these are sorbed by hydrous ferric oxide ($FeOOH$) were calculated. Figure 5.5.4 shows the calculated graphs for sorption of Pb, Cu, Zn, Co and Ag ($5 \times 10^{-7} M$) in 0.1 M NaCl onto goethite with surface areas of 53 400 and 53.4 m^2 per litre of solution. The position of the pH edge is partly dependent on the sorbate/sorbent ratio. Similar graphs are obtained in each case, but the adsorption edge is shifted up by about 1.5 pH units in the lower sorbate/sorbent ratio case (Figure 5.5.4a compared to Figure 5.5.4b).

Figure 5.5.3 EH-pH diagrams for Fe, Pb, Zn and Cu at 25°C and 0.1 MPa. a. and d. were constructed using the EQ3/6 thermodynamic database (Wolery and Daveler, 1992; Wolery, 1992a, b); b. and c. were adapted from Rose (1989). In general, metal mobility is favoured by relatively low pH and relatively oxidising conditions.



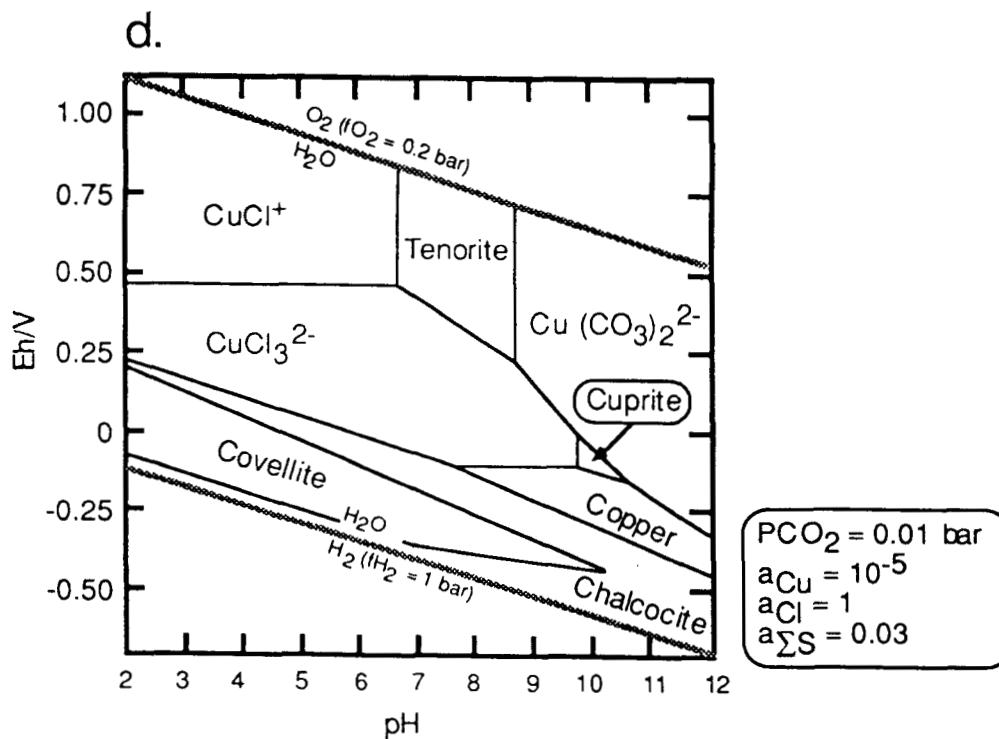
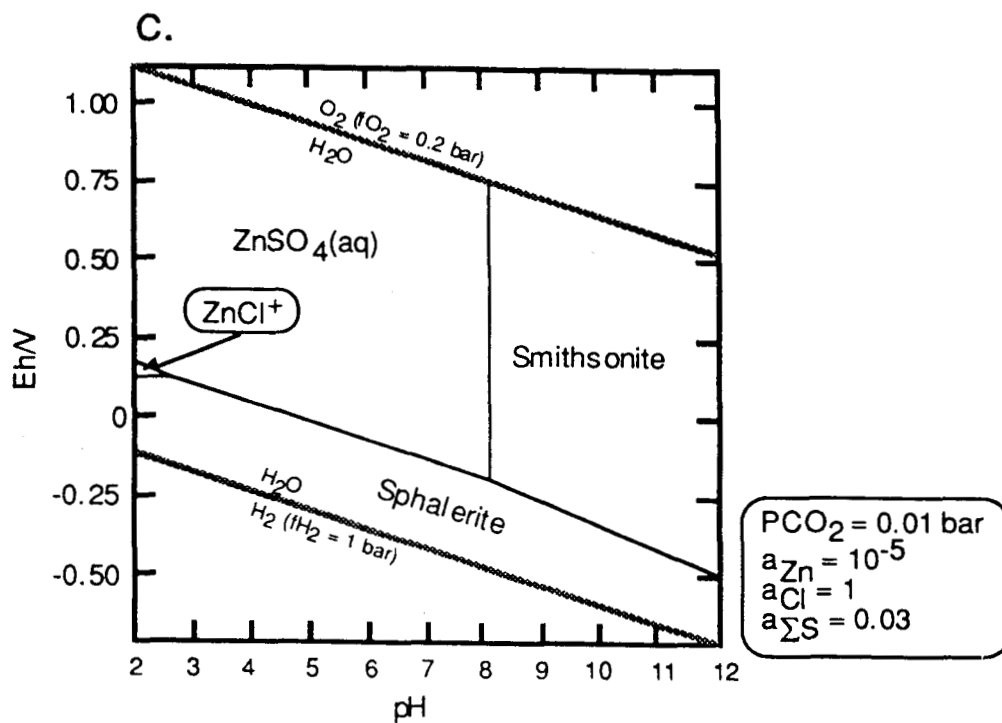
From Figure 5.5.4 it is clear that variations in pH due to CO_2 leakage could have a significant effect on the ability of Fe-oxides in aquifers to control the mobility of heavy metals. Decreases in pH due to the addition of CO_2 to an aquifer could lead to the partitioning of metals from Fe-oxides into the aqueous phase. This is likely to be particularly important in the case of red bed aquifers because their heavy metal contents and Fe-oxide contents are relatively large. However, at present experimental data are limited and it is not possible to make a thorough evaluation of the possible importance of sorption.

5.5.3.7 MICROBIAL ACTIVITY

It is being recognised increasingly that microbes are important mediators of chemical reactions in a wide range of extreme sub-surface environments, including deep

groundwaters (Brierley and Brierley, 1973; Marquis, 1976; Yayanos et al., 1979; Sherwood Lollar et al., 1993; Pedersen, 1993; Stetter et al., 1993); hydrothermal systems (Baross and Deming, 1983; Jannasch and Mottl, 1985; Wirsen et al., 1993); and deep boreholes (Pedersen, 1993; Stetter et al., 1993). Many bacteria in subsurface environments are chemolithotrophs ('rock eaters'), which can obtain their energy solely from inorganic sources. In doing this, these organisms metabolise inorganic constituents of rocks and groundwaters, such as H_2 , H_2S , Fe^{2+} , or NH_3 . Therefore, potentially, they can exert a significant effect upon the quality of potable groundwaters. Some chemolithotrophs are able to assimilate CO_2 as their sole carbon source (Chapelle, 1993) and therefore it is conceivable that CO_2 leakage may stimulate microbial activity. Such activity might in turn influence the pH and redox con-

Figure 5.5.3
Continued.



ditions of groundwater system and control the stability of minerals and aqueous species. The exact controls on groundwater chemistry which are exerted by microbial activity are likely to be complex.

5.5.3.8 AQUEOUS COMPLEXATION OF METALS

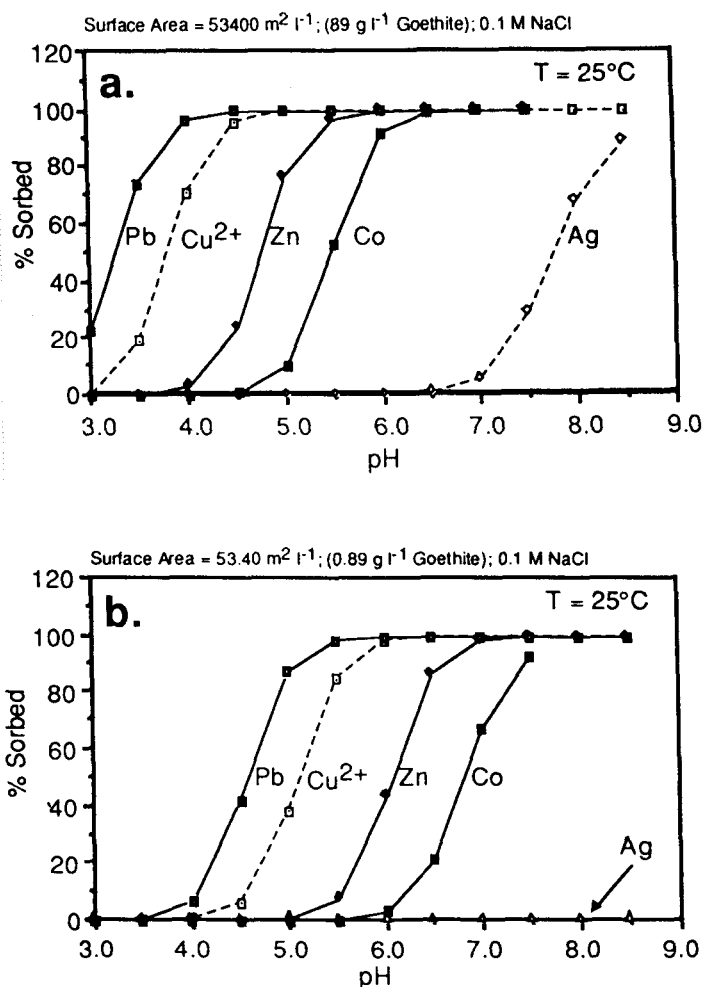
The aqueous complexation of metals in groundwaters will be a major control upon both metal mobility and water potability, since the formation of complexes will enhance the mobility of the metals. Thus, it is important to

evaluate the possible effects of CO_2 upon metal speciation^[6].

The characteristics of the waters required for the mobilisation of heavy metals in red beds have been evaluated by Rose and co-workers (Rose, 1976, 1989; Rose and Bianchi-Mosquera, 1985), Zielinski et al. (1983,

[6] 'Metal speciation' refers to the distribution of aqueous species (e.g. chloride complexes, hydroxide complexes etc.) of metals.

Figure 5.5.4 Modelled sorption 'edges' for a range of heavy metals when the sorbing phase is Fe-oxide. Sorption was modelled for Eh conditions consistent with Cu^{2+} stability; Cu^+ is considered likely to sorb in a similar fashion to Ag^+ . In a. the specific surface area of the sorbing Fe-oxide is 100 times greater than in b. A comparison between a. and b. illustrates that the sorption edges will move towards higher pH as specific surface areas become smaller. In the case of Fe-oxides such a decrease in specific surface areas will occur as the oxide 'ages' and becomes more crystalline. This highlights the need to understand the crystallographic character of Fe-oxides when assessing their capacity to sorb heavy metals. The sorption edges were calculated using the code HYDRAQL (Papelis et al., 1988) in conjunction with surface complexation data from Dzombak and Morel (1990). After Metcalfe et al. (1994).



1986), Eugster (1985), Sverjensky (1984, 1987, 1989), Nash et al. (1981), Durrance (1986), and Hofmann (1990, 1991, 1992).

In summary, the cuprous Cl-complexes (CuCl_2^- , CuCl_3^{2-}) are probably the most important Cu-transporting species over most of the range of redox conditions encountered during red bed diagenesis. However, complexes with oxalate, formate, acetate and fulvate may be important in organic-rich pore fluids. Additionally, the carbonate complexes, $\text{CuCO}_3(\text{aq})$ (pH 7.4–9.3), or $\text{Cu}(\text{CO}_3)_2^{2-}$ (pH > 9.3) may account for appreciable copper solubility in the presence of CO_2 . In contrast, Fe is insoluble as hematite under most conditions required for Cu mobility (Figure 5.5.3a), whereas Pb is soluble as $\text{PbCl}_2(\text{aq})$ (at pH < 7; Figure 5.5.3b), and Zn is soluble as $\text{ZnSO}_4(\text{aq})$ (at pH < 8.1; Figure 5.5.3c). Silver behaves differently in being soluble under only the most oxidising conditions as AgCl_2^- (Eh > 200 mV). Therefore, Ag-rich Cu deposits may only form under more oxidising conditions. Uranium mobility is similarly favoured by oxidising conditions, which allow formation of uranyl (UO_2^{2+}) complexes rather than uranous (U^{4+}) complexes. However, in contrast to Cu, Pb, Zn etc., the most common ligand involved in U transport is generally carbonate, particularly in the presence of meteoric waters, although phosphate, vanadate, fluoride and silicate complexes may also be important.

These observations suggest that the leakage of CO_2 into an aquifer might have a major effect on the speciation of heavy metals. Principally this will be a consequence of the pH and redox dependence of speciation (Figure 5.5.3). Additionally, certain metals (e.g. Cu and U) may form complexes with CO_3^{2-} . The mobility of such metals is likely to be enhanced by high partial pressures of CO_2 .

In addition, any CO_2 originating in a depleted hydrocarbon reservoir might transport organic matter. This might in turn exert a control on metal complexation in groundwaters. Increasingly, attention is being drawn to controls on cation mobility and secondary mineral stability by the organic components of natural waters (e.g. Surdam et al., 1984; Manning, 1986; Hennes et al., 1988; Thornton and Seyfried, 1987; Seewald et al., 1990). Liquid hydrocarbons may transport cations such as V, Ni, Cu and Zn, (Manning 1986), while Ca, Mg, Fe, Al, Sr, Mn, U, Th, Pb, Cu and Zn may be transported as complexes with light mono- and dicarboxylic acids (e.g. Giordano and Drummond, 1991;

Holm and Curtiss, 1990; Fein, 1991; Harrison and Thyne, 1992). Furthermore, it appears that the inorganic chemistry of aqueous solutions influences the behaviour of organic components, for example, high Ca concentrations leading to formation of Ca-oxalate and prevention of oxalate complexes transporting metal cations (Hennes et al., 1988; Huang and Longo, 1992).

5.5.4 CO_2 Leakage as a Control on Potable Water

The hydraulic regimes which operate in most likely sites for CO_2 disposal will be distinct from those in areas where potable groundwater is abstracted. For example, formation waters around depleted hydrocarbon reservoirs which are used for CO_2 disposal will generally be deep, highly saline, ancient and relatively slow moving. In contrast, potable groundwaters are mostly abstracted from relatively shallow sources, are of low salinity (typically fresh), relatively young (often recharged during the Pleistocene or Holocene) and rapidly moving. Additionally, where disposal sites are located in depleted offshore hydrocarbon reservoirs, usually they will be located a long way from sites of groundwater abstraction. Thus, in many cases it is unlikely that CO_2 leakage from disposal sites in hydrocarbon reservoirs will have a significant effect on groundwater quality. However, it is possible that leakage of CO_2 into potable groundwaters may occur from onshore hydrocarbon reservoirs or hydrocarbon reservoirs which lie only a short distance offshore. Additionally, the extraction of hydrocarbons from a reservoir, followed by injection of CO_2 to the reservoir, might conceivably alter the hydrogeological regime sufficiently to influence groundwater

quality indirectly. For instance, transition zones between shallow fresh, and deeper saline waters might move. Such hydraulic variations might themselves lead to CO₂ leakage.

The assessment of the possible importance of such perturbations to fluid flow will not be a trivial task. This is partly because in-situ fluid flow in deep formations cannot be measured directly, but must be evaluated by means of theoretical models. These utilise a knowledge of subsurface hydraulic head gradients and of the hydraulic properties of the rocks in the formations of interest. Such data are often difficult to acquire and may be sparse. Additionally, in attempting to evaluate fluid flow as a consequence of CO₂ disposal, further complexity arises because potentially there are a large number of phases which are involved in flow (e.g. supercritical CO₂, gaseous CO₂, liquid water, liquid hydrocarbons, and gaseous hydrocarbons).

Similarly, it will be difficult to assess accurately the likely impact on groundwater quality of pollutants which might migrate with leaking CO₂. This is because of the large number of factors which must be taken into account. Any assessment must consider the possible multi-phase nature of flow and the wide range of possible pollutants (e.g. trace metals, organic acids, petroleum, organic gases, and liquid petroleum). Nevertheless, it is possible to make some assessments of the likely chemical consequences of CO₂ leakage into an aquifer which bears potable water.

Edmunds et al. (1989) reported that in many U.K. groundwaters, a number of elements occur at natural concentrations above the CEC guideline values for drinking water (notably, Ba, Cu Mn, Al, Zn and Ni). Additionally, a number of elements, notably F, Fe, Mn, Al and As were found to occur at levels greater than the maximum admissible concentrations. This can be appreciated by comparing the data presented in Figure 5.5.1 and Tables 5.5.1, 5.5.4, and 5.5.5. Additionally, it can be appreciated from Tables 5.5.2, 5.5.3, 5.5.6 and 5.5.7 that the mineral constituents of Chalk and red bed aquifers might accommodate considerable quantities (up to 10s or 100s of ppm) of heavy metals. Taken together, these observations suggest that mineral dissolution as a consequence of CO₂ disposal might result in potable groundwaters acquiring heavy metal contents above the maximum admissible levels. It is important to note that, because many potable groundwaters have heavy metals near to the maximum admissible concentrations, only a relatively small addition of CO₂ may possibly be sufficient to render a water impotable.

In order to consider further the likely importance of the addition of CO₂ to potable groundwaters, some simple numerical simulations have been undertaken using the computer code EQ3/6 (Wolery, 1992a,b; Wolery and Daveler, 1993). As described above, carbonate is an important constituent of red bed aquifers as well as Chalk aquifers, and the compositions of groundwaters is typically controlled, at least partly, by carbonate equilibria. Therefore, the effects of adding CO₂ to pure water which is equilibrated with calcite have been investigated.

Only closed system conditions were considered. The initial water was assumed to be pure and was allowed to equilibrate with calcite at 25°C and 0.1 MPa, with CO₂ held at atmospheric levels (CO₂ fugacity = 3.16 × 10⁻⁵ MPa). The starting redox state was fixed at an E_H of -100 mV, which is similar to measured values in many natural groundwaters which are sampled from the reducing side of the redox boundary at which dissolved oxygen is consumed completely (e.g. Edmunds et al., 1984). This initial water had a pH of 8.3 and contained 20 mg/l Ca due to calcite dissolution.

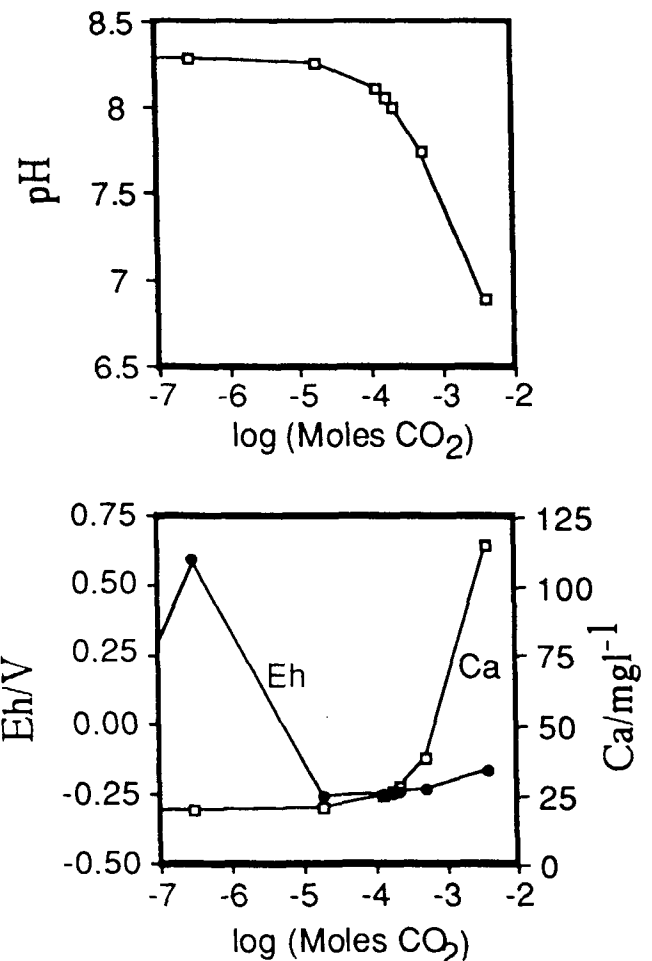


Figure 5.5.5 Theoretical plots which illustrate some chemical effects of adding CO₂ to fresh water which is equilibrated with calcite: a. variations in pH; and b. variations in Eh and dissolved Ca concentrations. A closed system in which 5 moles of CO₂ are available to react with 1 kg of pure water, in contact with excess calcite, is simulated. From a. it is apparent that significant decreases in pH are possible even in a carbonate-buffered system. b. illustrates that the addition of CO₂ to a carbonate-buffered fresh water will lead marked fluctuations in the redox state of the water and to increases in water hardness (represented by Ca concentrations) The plots were calculated for a temperature of 25°C and a pressure of 1 bar using the code EQ3/6 (Wolery and Daveler, 1992; Wolery, 1992a, b).

The addition of five moles of CO₂ at a temperature of 25°C and a pressure of 0.1 MPa was then simulated. This suggested that the addition of only very small quantities of CO₂ may produce significant changes in pH, E_H, and dissolved Ca concentrations (Figure 5.5.5). For example, the addition of 0.004 moles of CO₂ resulted in a simulated decrease in pH of 1.4 units, and an increase in dissolved Ca from 20 mg/l to 114 mg/l. Additionally, redox conditions fluctuated considerably during the simulation. There was a dramatic increase in EH, from -100 mV to 580 mV initially, followed by a sharp reduction to -270 mV and then a gradual increase to -170 mV. By comparing these variations in pH and EH with the fields of mineral stability in Figure 5.5.3, it can be appreciated that such changes in fluid conditions could conceivably result

in the release of heavy metals to solution by mineral dissolution. Additionally, a comparison of the simulated decrease in pH with the widths of the sorption edges illustrated in Figure 5.5.4 suggests that metals might also be released to solution as a consequence of a decrease in the sorbing capacities of mineral surfaces.

Another effect of the addition of even these small quantities of CO₂ to the solution causes Ca concentrations to rise above the guideline level of 100 mg/l recommended by the CEC (Table 5.5.1).

5.5.5 Conclusions and Recommendations

Although we could not evaluate all possible controls of CO₂ leakage upon potable water quality due to time constraints, it has been possible to draw the following tentative conclusions:

- The leakage of CO₂ into potable groundwater supplies is most likely to be a problem when CO₂ disposal takes place on land
- Carbonate minerals and Fe-oxides are likely to exert important controls on groundwater quality in both sandstone aquifers and carbonate aquifers
- It is possible that CO₂ leakage may transport heavy metal pollutants from ore deposits into nearby potable groundwater supplies
- Even small leaks of CO₂ from underground disposal sites may possibly cause significant deteriorations in the quality of potable groundwaters

Additionally, certain general topics which should be evaluated in more detail in the future are highlighted:

- pH buffering
- redox buffering
- fluid flow
- transport of pollutants (e.g. hydrocarbons)

More specifically, the following issues ought to be investigated in more detail:

- The stability of minerals in CO₂ rich atmospheres
- The role of sorption as a control on metal mobility
- The effect of CO₂ on microbial activity
- The kinetics of mineral dissolution and precipitation
- The consequences of the subsurface transition from super-critical CO₂ to gaseous CO₂
- Relationships between the various fluid phases which are likely to migrate with CO₂
- Partitioning of potential groundwater pollutants between different fluid phases which migrate with CO₂
- The nature of potential pollutants which might migrate with CO₂

- The consequences of CO₂ disposal for groundwater flow

Finally, any future assessment should consider the economic consequences of CO₂ disposal for the exploitation of potable groundwater sources. For example, the contamination of water by trace metals as a consequence of CO₂ migration may not be a problem if the metals are already removed from solution during routine processing procedures. Conversely, it may be the case that the addition of only small quantities of some pollutants may require considerable expenditure to remediate.

5.6 SUBSURFACE RETENTION TIME OF ESCAPING CO₂

Bert van der Meer

5.6.1 Introduction

The safety and stability aspects of CO₂ storage activities can be approached in two ways. One way is to consider all possible factors that have a negative influence on the stability of the storage activity. A second approach is to evaluate the effects of a breakdown of the stability of a storage reservoir and to study the related safety aspects. This section reports on the findings of a study that is conducted according to this last approach. The main goal of this work was to determine the effects of an uncontrolled release of CO₂ in the subsurface, i.e. how and when does this CO₂ reach the surface?

If CO₂ leaks from a structural or stratigraphic trap, or a 'hydraulic' trap, the CO₂ will move upwards because its density will be lower than the density of the formation water. In general, it can be assumed that the upwards movement of the injected or escaped CO₂ is much faster than the CO₂ propagation due to diffusion. So the free CO₂ front of the rising CO₂ bubble will overtake the CO₂-water interface generated by molecular diffusion.

5.6.2 Simulation Study

The objective of the simulation study was to estimate the subsurface retention time of CO₂ either injected into the subsurface without being confined to a trap, or leaking from a geological trap. Because the main direction of the CO₂ flow was expected to be vertically upwards, a model was defined with a large number of grid layers and a limited number of lateral grid blocks. The study area is represented by 86 grid layers. A radial grid model was used with only one 30° grid cell in the horizontal theta-direction, to minimise the total number of grid cells. 25 blocks were used in the horizontal radial-direction in order to minimise the possible boundary effects and to study the full development of the rising and expanding CO₂ bubble. The radial-direction grid size was set to 10 m in the middle section, with grid cell size increasing towards the outer boundary of the grid. The outer boundary of the model is located at a distance of 4750 m from the centre of the spillpoint.

The first 1000 m of the subsurface has been modelled, because this part of the subsurface was considered to be the most interesting. We positioned an injection well in the middle of grid layer 80 at a depth of 1000 m, to simulate a spillpoint of a trap or an 'uncontrolled' CO₂ injection. At this depth, the subsurface conditions are such that the CO₂

is in a supercritical state. For the 30° sector, a maximum injection rate of $0.485 \times 10^6 \text{ Nm}^3/\text{d}$ was used at a fixed maximum bottomhole pressure of 18 MPa. This injection rate corresponds to a total injection or spillage rate of $5.82 \times 10^6 \text{ Nm}^3/\text{d}$ for a fully 3-dimensional situation (360°).

Normally, pressure in the subsurface increases hydrostatically with depth. A CO₂ bubble that rises through the subsurface will change from a supercritical into a gaseous phase when it passes through the critical pressure of CO₂ (CO₂ critical conditions: 31°C, 7.38 MPa). This change in phase will result in a large expansion of the volume of CO₂. The SimBest II black-oil simulator marketed by Scientific Software-Intercomp was used to model the rising CO₂ bubble. This three-phase (gas, oil, water) simulator was used in the gas-water mode where the available gas phase was employed to simulate the CO₂. The simulator is isothermal and does not simulate viscous fingering effects, but does take full account of density differences and phase mobilities of the two phases. The two phases are completely separated, which means that there is no diffusion, dispersion or absorption of CO₂ into the water phase. These processes are assumed to have only an effect on a small scale, i.e. within one grid cell. The phase flow is controlled by a set of the relative permeability functions. By means of endpoint shifting it is possible to immobilise some of the CO₂ in the case of a CO₂ drainage situation. This enables the remaining CO₂ (or the CO₂ that dissolved in the water after the main CO₂ front/bubble has passed by) to be simulated. This modelling method does not take account of possible volumetric changes in the formation water caused by the CO₂ going into solution.

As indicated above, the model is based on a horizontal layering of the subsurface. Hence, vertical or oblique permeability anomalies caused by non-horizontal features transecting the sediment layers that may affect the flow path of the CO₂, such as faults, dykes or veins, are not considered in the model.

5.6.3 Results

5.6.3.1 BASE CASE REFERENCE MODEL

A base case model was created to be used as reference. It was constructed with all layers 12.5 m thick, to control the possible numerical dispersion in all other cases. All grid cells were assigned a constant permeability of $1 \mu\text{m}^2$ (Darcy) and a porosity of 35%. This high permeability was chosen with the aim of creating a worst case in relation to the expected retention time. It is debatable if it is a realistic level, especially in the Dutch situation, but one must realise that the Dutch subsurface contains geological layers with permeabilities in excess of $30 \mu\text{m}^2$.

Figure 5.6.1 shows the CO₂ concentration distribution over time, calculated for the base case. The plots are showing the cross-sectional area of the subsurface with a radius of 1560 m and a total depth of 1065 m. The topside of the plots represents the earth's surface. The first five plots have a contour interval of 5%. In the last three plots, with low CO₂ concentrations, contour intervals of 2.5% are used. The total CO₂ injection time is 365 days, with a total of $2.124 \times 10^9 \text{ Nm}^3$ CO₂ injected. Over time, the shape of the CO₂ bubble is mainly controlled by the relative permeability function. Strong CO₂ concentrations will be proportionally more mobile than weak concentrations (at the sides and bottom of the bubble), and therefore the CO₂ bubble will become ovoid. One possible shortcoming of the model is the lack of a free flow exit option at the

surface (surface venting). However, we believe that this shortcoming has little influence on the surface breakthrough time of the CO₂. For the base case we calculated a breakthrough time or CO₂ retention time of less than 731 days. The simulation results presented clearly show CO₂ remaining in the subsurface as residual or solution CO₂. This CO₂ is 4% of the effective pore space, as dictated by the endpoints set for the relative permeability function.

Analysis of the pressure behaviour of the subsurface fluid between the point of spill and the surface reveals only a small pressure increase at the start of the leakage. Figure 5.6.2 shows the fluid pressure above the spill point through time. The plot contains two reference pressure lines. The solid line shows the initial water pressure for a default hydrostatic gradient of 10.0 MPa/km; the dashed line shows the geostatic pressure against depth for a constant rock density of 2600 kg/m³. Apart from the 2 years time slice, all simulated time intervals show a reduction of the hydrostatic gradient caused by the inclusion of the lighter (residual) CO₂. The pressure behaviour for the 2 years time slice shows a substantial pressure increase in relation to the original hydrostatic pressure at a depth 200 m. The CO₂ saturation distribution map (Figure 5.6.1b) shows a high CO₂ concentration at this depth (150–220 m). The pressure increase can be explained by the expansion of this rising high-concentration area.

5.6.3.2 DUTCH SUBSURFACE MODEL

A more realistic model was created for the Dutch subsurface (northeastern part of the country), based on the permeability distribution shown in Figure 5.6.3. Individual layer thicknesses were used to reflect the probable geological stratigraphy. When selecting the layer thicknesses, we aimed to minimise numerical dispersion and to obtain the smoothest possible CO₂-water fronts. The minimum layer thickness was 7.5 m, the maximum was 20 m. The same CO₂ injection data were used as in the base case. In this case, however, the injection period had to be much longer (30 years) to inject the same amount of CO₂, because the injection block was much less permeable. The simulation results (Figure 5.6.4) show that the CO₂ is appreciably delayed by the low permeability of clay layers. The resulting breakthrough time for modelled Dutch subsurface is about 5500 years. It is clear that the retention time of CO₂ injected in the subsurface largely depends on the geological layer with the lowest permeability and the thickness of these layers.

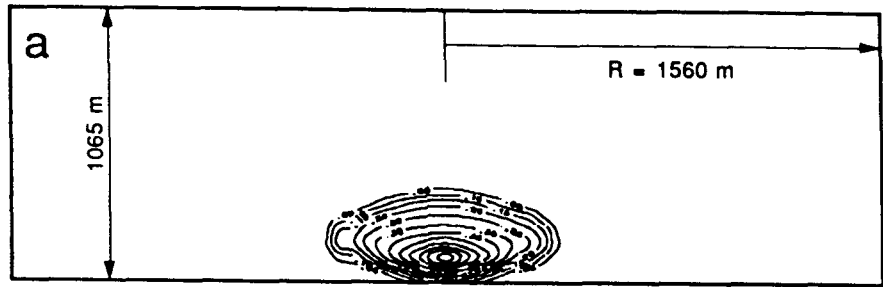
The fluid pressure profile (Figure 5.6.5) for the area above the spill point shows initially a large pressure increase as a result of the injection. This proves that a large pressure contrast is needed between the storage reservoir and the spillover area to maintain a substantial leak-off rate for a longer period in low-permeability areas. After the leakage has stopped (after the injection period of 30 years) a stable pressure profile is achieved. The pressure profile for 25 and 50 years show some pressure response as a result of the expansion of the rising CO₂ around the depth interval of 800 m.

5.6.4 Conclusions

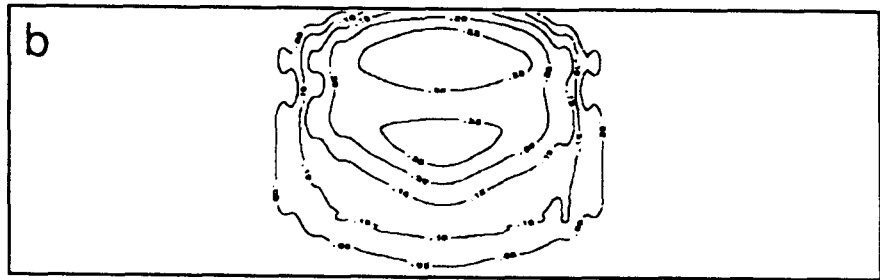
From the simulation work described above the following conclusions can be drawn:

1. The retention time of CO₂ injected in the subsurface depends on the thickness of the least permeable overlying geological layer.

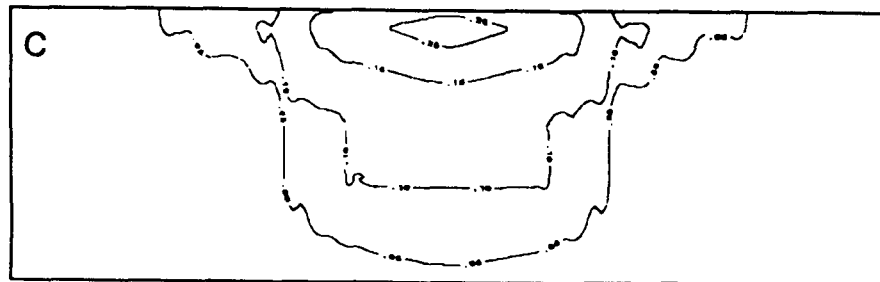
Figure 5.6.1 Underground CO₂ concentration in the base case model after 0.5 (a), 2 (b), 5 (c), 10 (d), 20 (e), 40 (f), 60 (g), and 80 years (h). Radius of the shown subsurface area is 1560 m, total depth is 1065 m. CO₂ is injected over a period of 365 days, leading to a total amount of injected (or spilled) CO₂ of $2.124 \cdot 10^9 \text{ Nm}^3$ (ca 4 Mt CO₂).



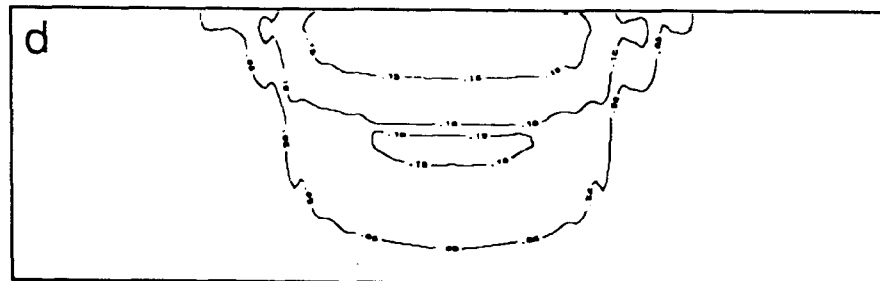
CO₂ Concentration at 0.5 year (5 % contour interval)



CO₂ Concentration at 2 years (5 % contour interval)



CO₂ Concentration at 5 years (5 % contour interval)



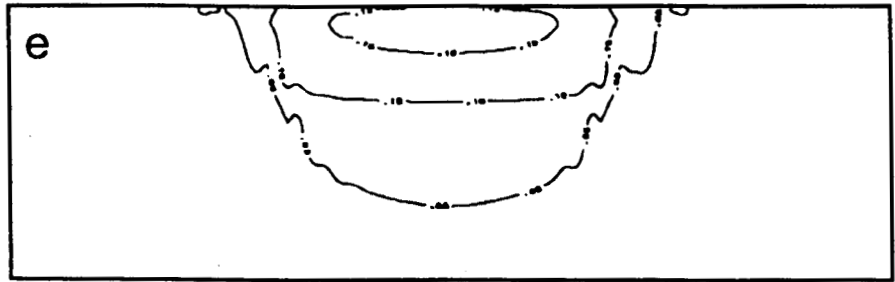
CO₂ Concentration at 10 years (5 % contour interval)

2. A reservoir simulator used to simulate hydrocarbon flow in the subsurface can be used to estimate the possible breakthrough time of CO₂ injected in the subsurface.
3. The simulations show that the breakthrough time of CO₂ released at 1000 m depth will be in the order of 2 years if the subsurface has an uniform permeability of

1000 mD. If the permeability is reduced to 1 mD in one or two geological layers, this time could be around 5000 years.

4. Harmonic averaging of the vertical permeability can not be used to calculate CO₂ subsurface retention times. For each possible storage location all geological layers must be considered in a simulation study.

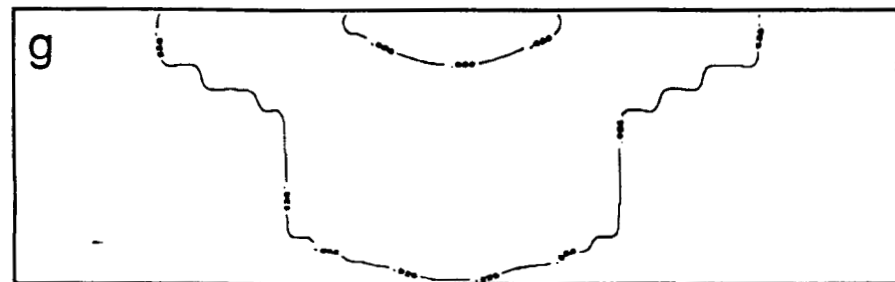
Figure 5.6.1 *Continued.*



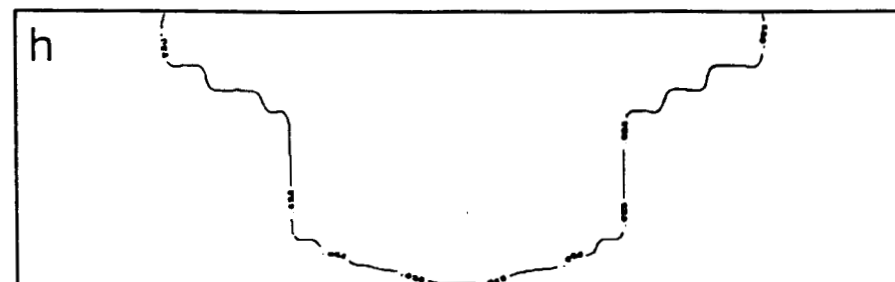
CO₂ Concentration at 20 years. (5 % contour interval)



CO₂ Concentration at 40 years. (2.5 % contour interval)

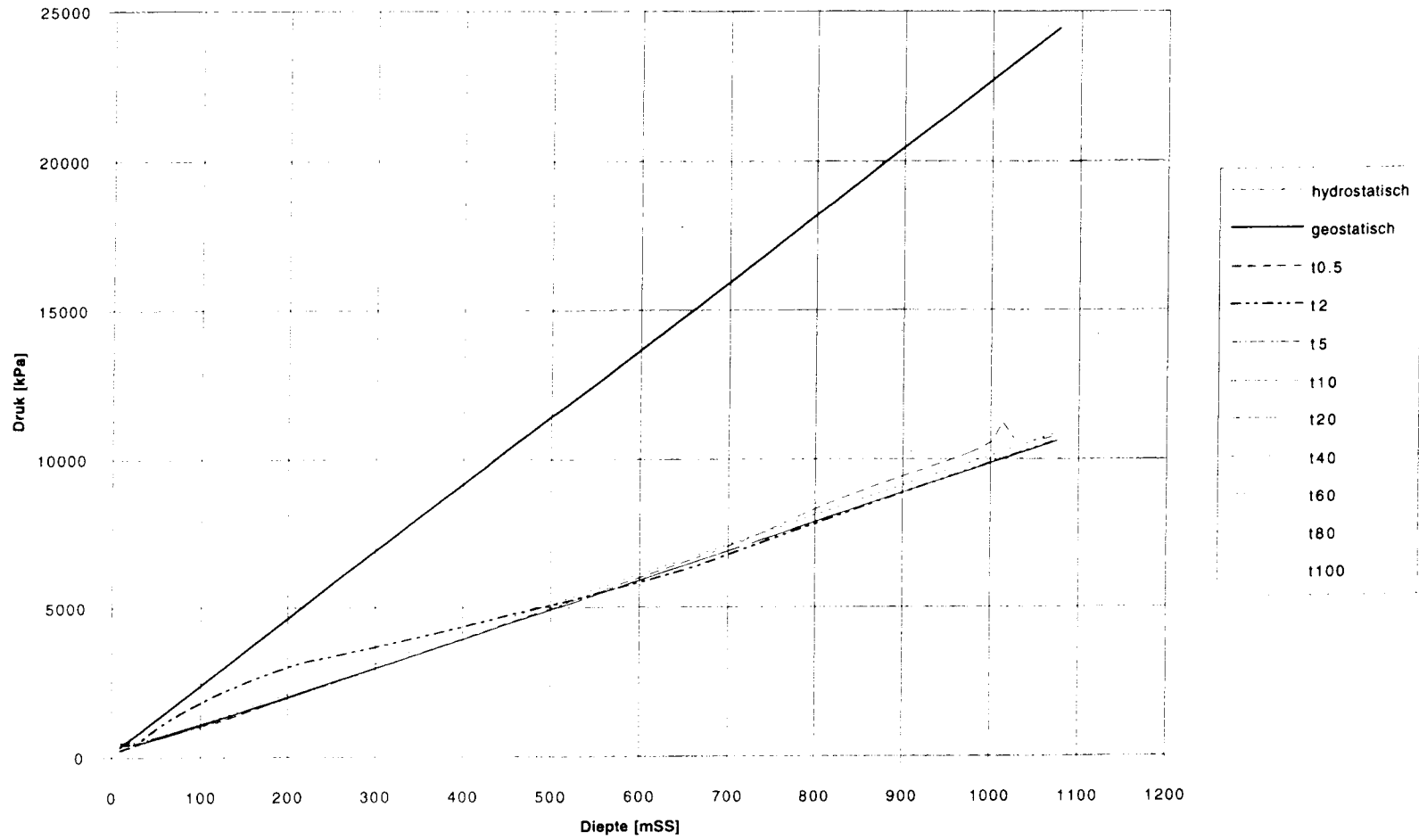


CO₂ Concentration at 60 years. (2.5 % contour interval)



CO₂ Concentration at 80 years. (2.5 % contour interval)

Figure 5.6.2 Profile of the fluid pressure above the injection (or spill) point in the base case model for the time slices presented in Figure 5.6.1.



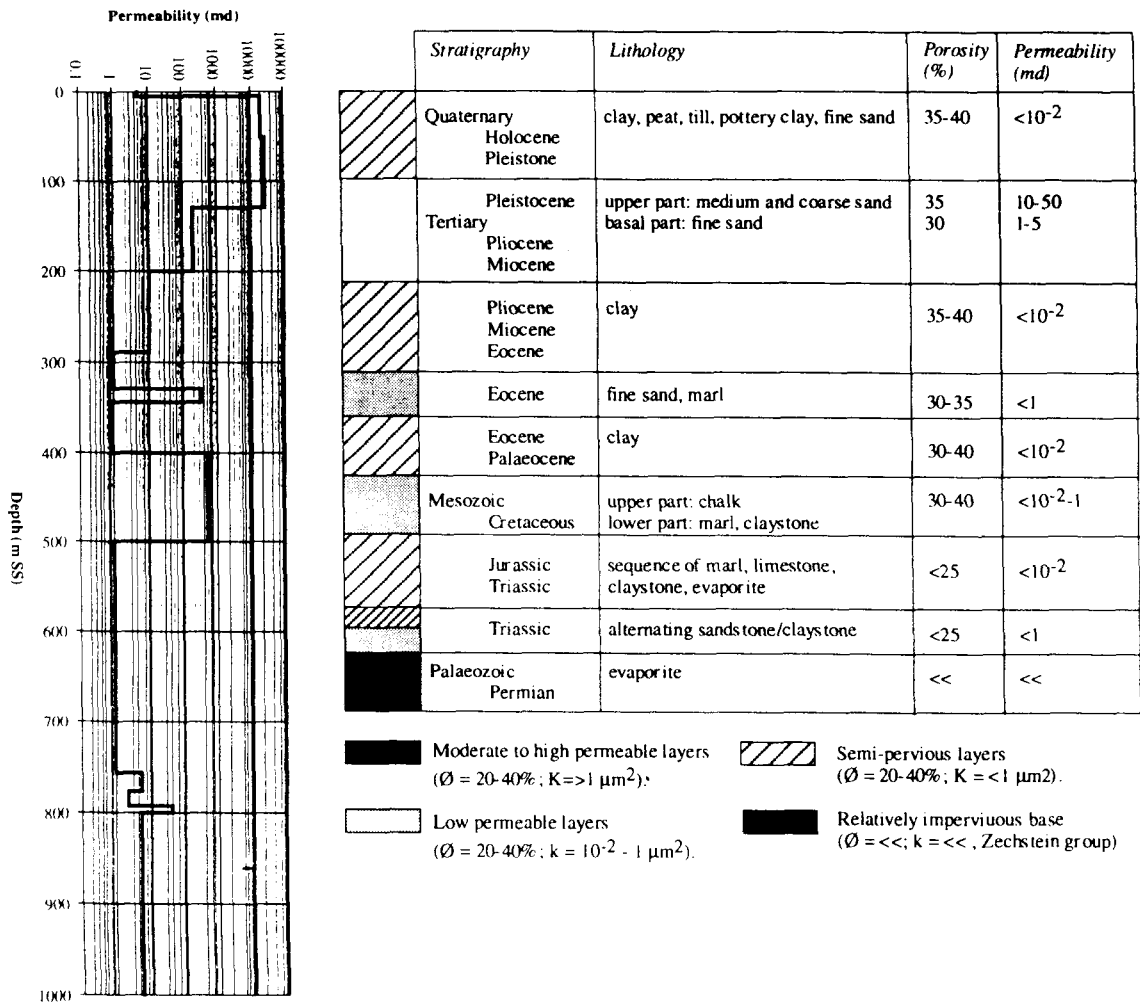
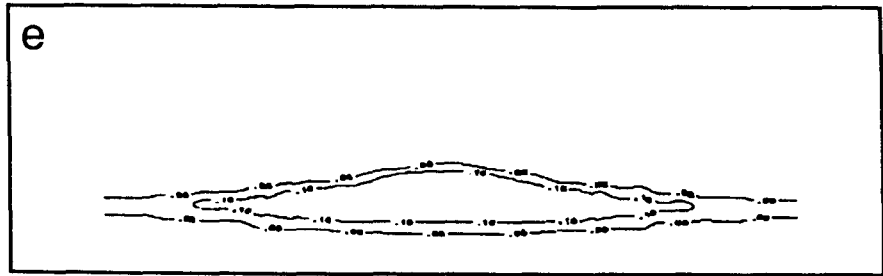
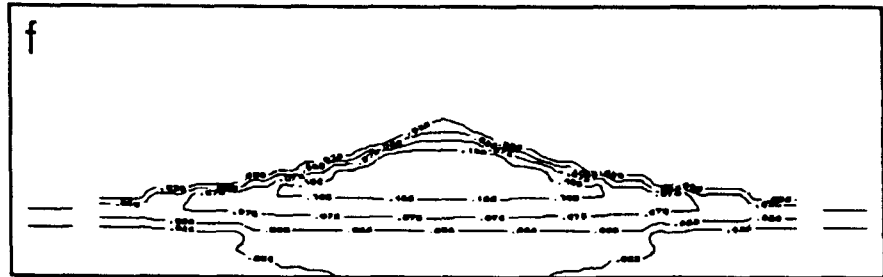


Figure 5.6.3 Schematised regional geology in the NE Netherlands: A) subsurface permeability distribution; B) stratigraphy, lithology and hydrogeological characteristics.

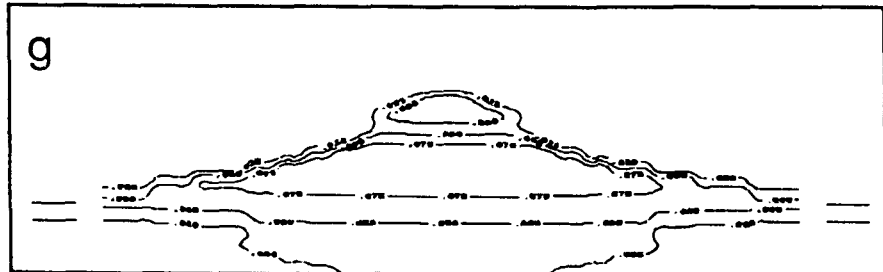
Figure 5.6.4 Continued.



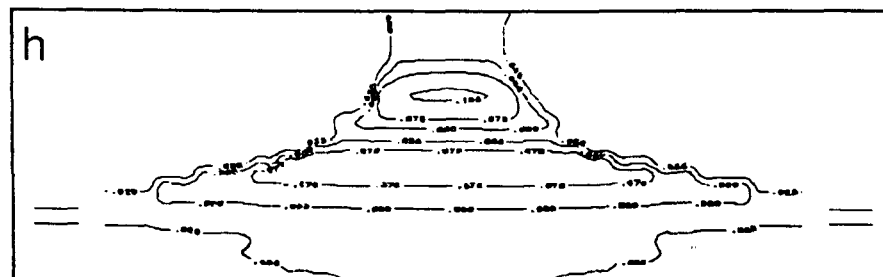
CO₂ Concentration at 1000 years (5 % contour interval)



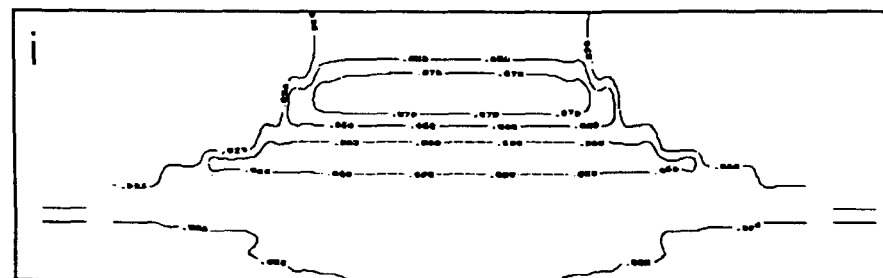
CO₂ Concentration at 2000 years (2.5 % contour interval)



CO₂ Concentration at 4000 years (2.5 % contour interval)

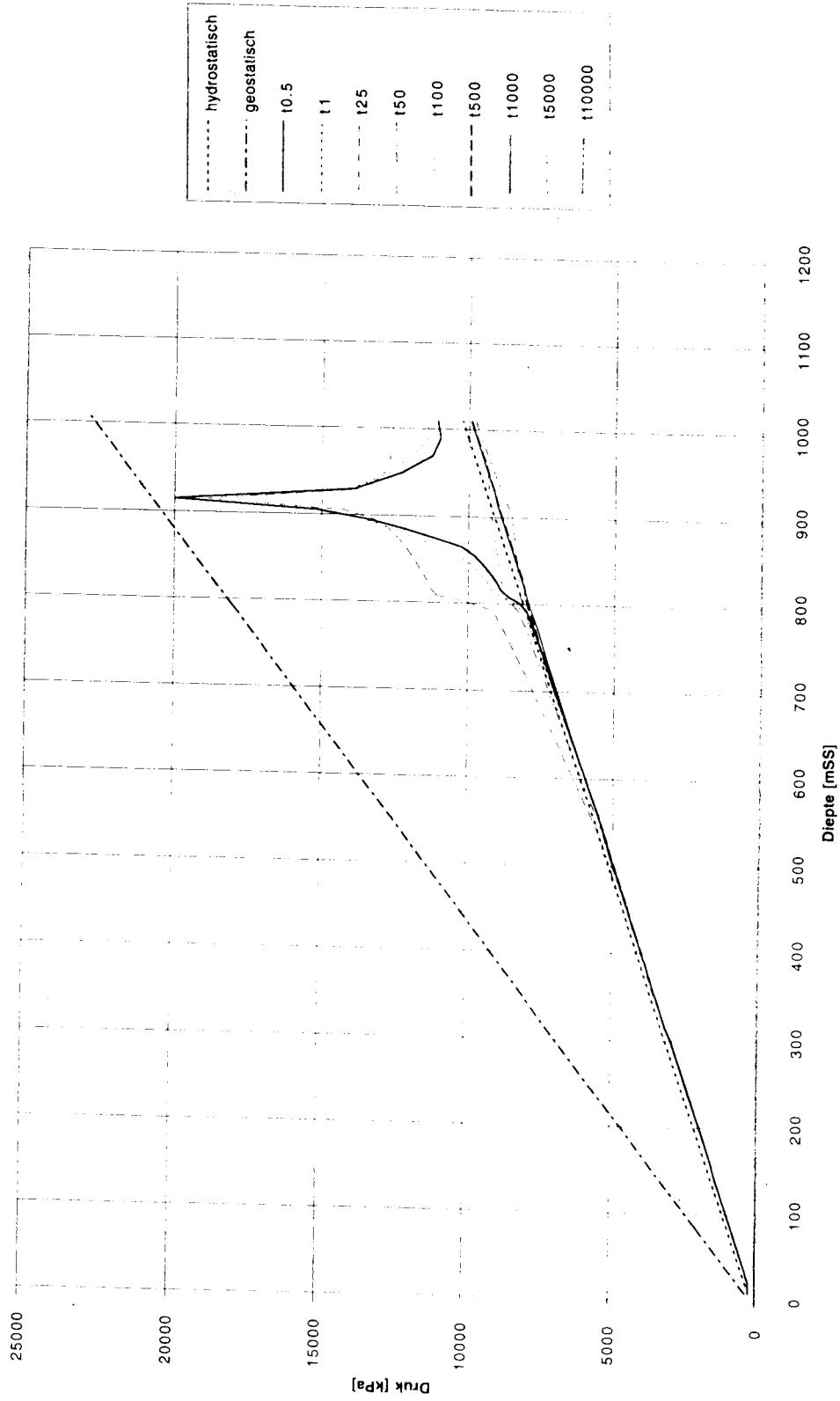


CO₂ Concentration at 6000 years (2.5 % contour interval)



CO₂ Concentration at 10000 years (2.5 % contour interval)

Figure 5.6.5 Profile of the fluid pressure above the injection (or spill) point in the Dutch subsurface model for the time slices presented in Figure 5.6.4.



5.7 REFERENCES

- ATKINS, P W. 1982. Physical Chemistry. Oxford University Press. 1095pp.
- ANGELIER, J. 1984. Tectonic Analysis of Fault Slip Data Sets. *J. Geophys. Res.*, **89**, 5835–5848.
- BAROSS, J A, and DEMING, J W 1983. Growth of 'black smoker' bacteria at temperatures of at least 250°C. *Nature*, **303**, 423–426.
- BATH, A H, and EDMUNDS, W M. 1981. Identification of connate water in interstitial solution of Chalk sediment. *Geochimica et Cosmochimica Acta*, **45**, 1449–1461.
- BATH, A H, EDMUNDS, W M, and ANDREWS, J N. 1979. Palaeoclimatic trends deduced from the hydrochemistry of a Triassic sandstone aquifer, United Kingdom. *In: Isotope Hydrology 1978*. IAEA, Vienna. 545–568. *Commission of the European Communities, 1980. The quality of water for human consumption. Directive 80/778*. CEC, Brussels, 13pp.
- BATH, A H., MIŁODOWSKI, A E, and STRONG, G E. 1987. Fluid flow and diagenesis in the East Midlands Triassic sandstone aquifer. *In: GOFF, J C, and WILLIAMS, B P J (editors) Fluid flow in sedimentary basins and aquifers. Geological Society Special Publication*, **34**, 127–140.
- BEAUCE, A, JONES, R, FABRIOL, H, TWOSE, C, and HULOT, C. 1992. Microseismic Monitoring of Hydraulic Experiments During Phase 2a of the Soultz HDR Project (Alsace, France). *17th Workshop on Geothermal Reservoir Engineering, Stanford USA, January 1992*.
- BOLT, G H, BRUGGEWERT, M G M, and KAMPHORST, A. 1981. Adsorption of cations by soil. *In: BOLT, G H, and BRUGGEWERT, M G M (editors) Soil chemistry A: Basic Elements*. Elsevier Scientific Publishing, New York, pp.84–90.
- BRIERLEY, C L, and BRIERLEY, J A. 1973. A chemoautotrophic and thermophilic micro-organism isolated from an acid hot spring. *Canadian Journal of Microbiology*, **19**, 183–188.
- BURLEY, S D. 1984. Patterns of diagenesis in the Sherwood Sandstone Group (Triassic), United Kingdom. *Clay Minerals*, **19**, 403–440.
- CHAPPELLE, F H. 1993. *Groundwater microbiology and geochemistry*. John Wiley & Sons Inc, New York. 424pp.
- DAVIS, G H. 1984. Structural Geology of Rocks and Regions. John Wiley & Sons, Inc. 492pp.
- DAVIS, D S, and PENNINGTON, W D. 1989. Induced Seismic Deformation in the Cogdell Oil Field of West Texas. *Bull. Seism. Soc. Am.*, **79**, 1477–1494.
- DEFLANDRE, J P, LAURENT, J, and BLONDIN, E. 1993. Use of Permanent Geophones for Microseismic Surveying of a Gas Storage Reservoir. *55th EAEG Meeting, Stavanger, Norway 7-1 June 1993*.
- DURRANCE, E M. 1986. *Radioactivity in Geology: principles and applications*. Chapter 6, The Geochemistry of uranium and thorium. Ellis Horwood, Chichester.
- DZOMBACK, D A, and MOREL, F M M. 1990. *Surface Complexation Modelling*. Wiley Interscience, New York.
- EDMUNDS, W M. 1986. Geochemistry of geothermal waters in the U.K. *In: DOWNING, R A, and GRAY, D A (editors) Geothermal energy: the potential in the United Kingdom. Her Majesty's Stationery Office, London*, 111–122.
- EDMUNDS, W M, MILES, D L, and COOK, J M. 1984. A comparative study of sequential redox processes in three British aquifers. *In: ERIKSSON, E (editor) Hydrochemical balances of freshwater systems. IAHS Publication*, **50**, 55–70.
- EDMUNDS, W M, COOK, J M, DARLING, W G, KINNIBURGH, D G, MILES, D L, BATH, A H, MORGAN-JONES, M, and ANDREWS, J N. 1987. Baseline geochemical conditions in the Chalk aquifer, Berkshire, U.K.: a basis for groundwater quality management. *Applied Geochemistry*, **2**, 251–274.
- EDMUNDS, W M, COOK, J M, KINNIBURGH, D G, MILES, D L, and TRAFFORD, J.M. 1989. *Trace-element occurrence in British groundwaters*. British Geological Survey Report, Hydrogeology Series, **SD/89/3**.
- EDMUNDS, W M, DARLING, W G, KINNIBURGH, D G, DEVER, L, and VACHIER, X X. 1992. *Chalk groundwater in England and France: hydrogeochemistry and water quality*. British Geological Survey Report, Hydrogeology Series, **SD/92/2**.
- EUGSTER, H P. 1985. Oil shales, evaporites and ore deposits. *Geochimica et Cosmochimica Acta*, **49**, 619–635.
- FEIN, J B. 1991. Experimental study of aluminium-, calcium- and magnesium- acetate complexing at 80°C. *Geochimica et Cosmochimica Acta*, **55**, 955–964.
- FRANCIS, P. 1976. *Volcanoes*. Penguin Books Ltd. Harmondsworth, England, 368pp.
- FREEDMAN, Y E, MAGARTZ, M, LONG, G L, and RONEN, D. 1994. Interaction of metals with mineral surfaces in a natural groundwater environment. *Chemical Geology*, **116**, 111–121.
- FROSTICK, L E, and REID, I. 1987. Tectonic control of desert sediments in rift basins ancient and modern. *In: FROSTICK, L, and REID, I (editors) Desert sediments: ancient and modern. Geological Society, London, Special Publication*, **35**, 53–68.
- GERTH, J. 1990. Unit cell dimensions of trace metal-associated goethites. *Geochimica et Cosmochimica Acta*, **54**, 363–371.
- GIBOWICZ, S J. 1989. *Seismicity in Mines 1989*. Birkhuser Verlag, 283pp.
- GIDLEY, J L. et al. (editors). 1989. Recent Advances in Hydraulic Fracturing. *Monograph Series*, SPE, Richardson, TX (1989), **12**, Chaps. 3–5,11.
- GIORDANO, T H, and DRUMMOND, S E. 1991. The potentiometric determination of stability constants for zinc acetate complexes in aqueous solutions to 295°C. *Geochimica et Cosmochimica Acta*, **55**, 2401–2415.
- GRASSO, J R. 1992. Mechanics of Seismic Instabilities Induced by the Recovery of Hydrocarbons. *PAGEOPH.*, Vol. **139**, n. 3/4.
- GUPTA, H K. 1985. The Present Status of Reservoir Induced Seismicity Investigations with Special Emphasis on Koyana Earthquakes. *Tectonophysics*, **118**, 275–279.
- GUSTAFSON, L B, and WILLIAMS, N. 1981. Sediment-hosted stratiform deposits of copper, lead and zinc. *Economic Geology, 75th Anniversary Volume*, 139–178.
- HARRISON, W J, and THYNE, G D. 1992. Predictions of diagenetic reactions in the presence of organic acids. *Geochimica et Cosmochimica Acta*, **56**, 565–586.
- HENDRIKS, C. 1994. *Carbon Dioxide Removal from Coal-Fired Power Plants*. PhD. Thesis, Universiteit Utrecht.
- HENNET, R J C, CRERAR, D A, and SCHWARTZ, J. 1988. Organic complexes in hydrothermal systems. *Economic Geology*, **83**, 742–764.
- HOFMANN, B A. 1990. Reduction spheroids from northern Switzerland: mineralogy, geochemistry and genetic models. *Chemical Geology*, **81**, 55–81.
- HOFMANN, B A. 1991. Mineralogy and geochemistry of reduction spheroids in red beds. *Mineralogy and Petrology*, **44**, 107–124.
- HOFMANN, B A. 1992. Isolated reduction phenomena in red beds: a result of porewater radiolysis? *In: KHARAKA, Y K, and MAEST, A S (editors) Water-Rock Interaction 7*. Balkema, Rotterdam, 503–506.
- HOLDITCH, S A. 1988. GRI Staged Field Experiment. *SPEFE (Sept. 1988)*, p.519.
- HOLM, T R, and CURTISS, C D. 1990. Copper complexation by natural organic matter in groundwater. *In: MELCHOIR, D C, and BASSETT, R L (editors) Chemical modelling in aqueous systems II. American Chemical Society, Washington D.C.*, 509–518.

- HSIEH, P A, and BREDEHOEFT, J D. 1981. A Reservoir Analysis of the Denver Earthquakes: a Case of Induced Seismicity. *J. Geophys. Res.*, **86**, 903–920.
- HUANG, W-L, and LONGO, J M. 1992. The effects of organics on feldspar dissolution and the development of secondary porosity. *Chemical Geology*, **98**, 271–292.
- JACKSON, D, and LLOYD, J W. 1983. Groundwater chemistry of the Birmingham Triassic sandstone aquifer and its relation to structure. *Quarterly Journal of Engineering Geology, London*, **16**, 135–142.
- JANNASCH, H W, and MOTTL, M J. 1985. Geomicrobiology of deep-sea hydrothermal vents. *Science*, **229**, 717–725.
- JARVIS, I. 1980. Geochemistry of phosphatic chalks and hard grounds from the Santonian to early Campanian (Cretaceous) of N. France. *Journal of the Geological Society of London*, **137**, 705–721.
- JOHNSON, J W, OELKERS, E H, and HELGESON, H C. 1991. *SUPCRT92: a software package for calculating the standard molal thermodynamic properties of minerals, gases, aqueous species, and reactions from 1 to 5000 bars and 0° to 1000°C*. University of California, Berkeley.
- KIMBERLEY, M M. 1979. Uranium geochemistry. In: KIMBERLEY, M M (editor) Short course in uranium deposits: their mineralogy and origin. *Mineralogical Association of Canada Short Course Handbook*, **3**, 339–375.
- LUCEY, P A. 1987. *The hydrochemistry of groundwaters in the West Cheshire Aquifer of N.W. England*. Unpublished M.Phil Thesis, University of Lancaster.
- LUNGEKARD, P D, and LAND, L S. 1986. Carbon dioxide and organic acids: their role in porosity enhancement and cementation, Palaeogene of the Texas Gulf Coast. In: GAUTIER, D L (editor): Roles of Organic matter in sediment diagenesis. *Society of Economic Palaeontologists and Mineralogists Special Publication*, **38**, 129–147.
- MAJER, E L, ROMERO, A, VASCO, D, KIRKPATRICK, A, PETERSON, J E, ZUCCZ, J J, HUTCHINGS, L J, and KASAMEYER, P W. 1993. *Seismic Monitoring at the Geysers*. Report LBL-34774, Lawrence Berkeley Laboratory.
- MANDL, G, DE JONG, L N J, and MALIHA, A. 1977. Shearzones in granular material. An experimental study of their structure and mechanical genesis. *Rock Mechanics*, **9**, 209–221.
- MANNING, D A C. 1986. Assessment of the role of organic matter in ore transport processes in low-temperature base-metal systems. *Transactions of the Institution of Mining and Metallurgy*, **95**, B195–B200.
- MARQUIS, R E. 1976. High pressure microbial physiology. In: ROSE, A H, and TEMPEST, D W (editors) *Advances in microbial physiology*, **14**. Academic Press, 159–241.
- METCALFE, R, ROCHELLE, C A, SAVAGE, D, and HIGGO, J J W. 1994. Fluid-rock interactions during continental red bed diagenesis: implications for theoretical models of mineralisation in sedimentary basins. In: PARNELL, J (editor) *Geofluids: Origin, migration, and evolution of fluids in sedimentary basins. Geological Society Special Publication*, **78**, in press.
- MOORE, C H. 1989. Carbonate Diagenesis and Porosity. *Developments in Sedimentology* **46**. Elsevier, Amsterdam, 338pp.
- MÜLLER, B, ZOBACK, M H, FUCHS, K, MASTIN, L, GREGERSEN, S, PAVONI, N, STEPHANSSON, O, and LJENGGREN, C. 1992. Regional Pattern of Tectonic Stress in Europe. *J. Geophys. Res.*, **97**, 11,783–11,803.
- NASH, J T, GRANGER, H C, and ADAMS, S S. 1981. Geology and concepts of genesis of important types of uranium deposits. *Economic Geology*, 75th Anniversary Volume, 63–116.
- OPPENHEIMER, D H. 1986. Extensional Tectonics at The Geysers Geothermal Area, California. *J. Geophys. Res.*, **91**, 11,463–11,476.
- PACEY, N R. 1989. Organic matter in Cretaceous chalks from Eastern England. *Chemical Geology*, **75**, 191–208.
- PAPELIS, C, HAYES, K, and LECKIE, J O. 1988. *HYDRAQL: A program for the computation of chemical equilibrium composition of aqueous batch systems including surface-complexation modelling of ion adsorption at the oxide/solution interface*. Department of Civil Engineering, Stanford University, Stanford, California. Technical Report No. 306.
- PEDERSEN, K. 1993. The deep subterranean biosphere. *Earth Science Reviews*, **34**, 243–260.
- PIPES AND PIPELINES INTERNATIONAL. 1988. Gas pipeline incidents — *A report of the European gas pipeline incident data group*, July-August 1988
- RALEIGH, C B, HEALY, J H, and BREDHOEFT, J D. 1976. An experiment in Earthquake control at Rangely, Colorado. *Science*, **191**, 1230–1237.
- ROBINSON, B M, HOLDITCH, S A, and PETERSEN, R E. 1991. Gas Research Institute's Second Staged Field Experiment: A Study of Hydraulic Fracturing. paper *SPE 21495 presented at the 1991 SPE Gas Technology Symposium*, Houston, Jan 22–24.
- ROBERSON, B M. et al. 1992. Hydraulic Fracturing Research in East Texas: Third GRI Staged Field Experiment," *JPT* (Jan. 1992), p.78.
- ROSE, A W. 1976. The effect of cuprous chloride complexes in the origin of red-bed copper and related deposits. *Economic Geology*, **71**, 1036–1048.
- ROSE, A W. 1989. Mobility of copper and other heavy metals in sedimentary environments. In: BOYLE, R W, BROWN, A C, JEFFERSON, C W, JOWETT, E C, and KIRKHAM, R V (editors) *Sediment-hosted stratiform copper deposits. Geological Association of Canada, Special Paper*, **38**, 97–110.
- ROSE, A W, and BIANCHI-MOSQUERA, G C. 1985. Adsorption of Cu, Ag and other metals on Fe-oxides as a control on elemental composition of stratiform and redbed copper deposits. *Geological Society of America, Abstracts with Programmes*, **17**, 702.
- SEEWALD, J S, SEYFRIED, W E, and THORNTON, E C. 1990. Organic-rich sediment alteration: an experimental and theoretical study at elevated temperatures and pressures. *Geochimica et Cosmochimica Acta*, **55**, 659–669.
- SEGALL, P. 1989. Earthquakes triggered by fluid extraction. *Geology*, **17**, 942–946.
- SHERWOOD LOLLAR, S, FRAPE, S K, FRITZ, P, MACKO, S A, WELHAN, J A, BLOMQUIST, R, and LAHERMO, P W. 1993. Evidence for bacterially generated hydrocarbon gas in Canadian Shield and Fennoscandian Shield rocks. *Geochimica et Cosmochimica Acta*, **57**, 5073–5085.
- SHOCK, E L. 1988. Organic acid metastability in sedimentary basins. *Geology*, **16**, 886–890.
- SMITH, D B, DOWNING, R A, MONKHOUSE, R A, OTLET, R L, and PEARSON, F J. 1976. The age of groundwater in the Chalk of the London Basin. *Water Resources Research*, **12**, 392–404.
- STARK, M A. 1990. Imaging Injected Water in the Geysers Reservoir using Microearthquake Data. *Geothermal Res. Council Transactions*, Vol. **14**, part II, 1697–1704.
- STETTER, K O, HUBER, R, BLOCHL, E, KURR, M, EDEN, R D, FIELDER, M, CASH, H, and VANCE, I. 1993. Hyperthermophilic archaea are thriving in deep North Sea and Alaskan oil reservoirs. *Nature*, **365**, 743–744.
- STOESSELL, R K, and PITTMAN, E D. 1990. Secondary porosity revisited: the chemistry of feldspar dissolution by carboxylic acids and anions. *American Association of Petroleum Geologists Bulletin*, **74**, 1795–1805.
- STRONG, G E, and MILODOWSKI, A E. 1987. Aspects of the diagenesis of the Sherwood sandstones of the Wessex Basin and their influence on reservoir characteristics. In: MARSHALL, J (editor) *Diagenesis of Sedimentary Sequences. Geological Society, London, Special Publication*, **36**, 325–337.
- STUDLICK, J R J, SHEW, R D, BASYE, G L, and RAY, J R. 1989. A giant carbon dioxide accumulation in the Norphlet Formation,

- Pisgah Anticline, Mississippi. In: BARWIS, J H, MCPHERSON, J G, and STDLICK, J R J (editors) *Sandstone Petroleum Reservoirs*. Springer-Verlag, New York.
- SURDAM, R C, BOESE, S W, and CROSSEY, L J. 1984. The chemistry of secondary porosity. *American Association of Petroleum Geologists Memoir*, **37**, 127–149.
- SURDAM, R C, CROSSEY, L J, HAGEN, E S, and HEASLER, H P. 1989. Organic-inorganic interactions and sandstone diagenesis. *American Association of Petroleum Geologists Bulletin*, **73**, 1–23.
- SVERJENSKY, D A. 1984. Oil field brines as ore-forming solutions. *Economic Geology*, **79**, 23–37.
- SVERJENSKY, D A. 1987. The role of migrating oil field brines in the formation of sediment-hosted Cu-rich deposits. *Economic Geology*, **82**, 1130–1141.
- SVERJENSKY, D A. 1989. Chemical evolution of basinal brines that formed sediment-hosted Cu-Pb-Zn deposits. In: BOYLE, R W, BROWN, A C, JEFFERSON, C W, JOWETT, E C, and KIRKHAM, R V (editors) *Sediment-hosted Stratiform Copper Deposits. Geological Association of Canada Special Paper*, **36**, 127–134.
- THORNTON, E C, and SEYFRIED, W E. 1987. Reactivity of organic-rich sediment in seawater at 350°C, 500 bars: experimental and theoretical constraints for the Guaymas Basin hydrothermal system. *Geochimica et Cosmochimica Acta*, **51**, 1997–2010.
- TURNER, P. 1980. Continental red beds. *Developments in Sedimentology*, **29**. Elsevier, Oxford.
- VEIZER, J. 1983. Trace elements and isotopes in sedimentary carbonates. In: REEDER, R J (editor) *Carbonates: mineralogy and chemistry. Reviews in Mineralogy*, **11**, 265–299.
- WALKER, W R, and COX, W E. 1976. *Deep Well Injection of Industrial Waste: Government Controls and Legal Constraints*. Virginia Water Resources Center Blacksburg, Virginia, USA.
- WEDEPOHL, K H (editor). 1978. *Handbook of geochemistry*. Springer-Verlag, Berlin.
- WIRSEN, C O, JANNASCH, H W, and MOLYNEAUX, S J. 1993. Chemosynthetic microbial activity at mid-Atlantic ridge hydrothermal vent sites. *Journal of Geophysical Research*, **98**, 9693–9703.
- WOLERY, T J. 1992a. *EQ3/6 package overview and installation guide*. Lawrence Livermore National Laboratory Report.
- WOLERY, T J. 1992b. *EQ3NR, Theoretical manual and user's guide*. Lawrence Livermore National Laboratory Report.
- WOLERY, T J, and DAVELER, S A. 1992. *EQ6 Theoretical manual and user's guide*. Lawrence Livermore National Laboratory Report.
- WORLD HEALTH ORGANISATION. 1984. *Guidelines for drinking water quality: volume 2, health criteria and other supporting information*. WHO Geneva.
- YAYANOS, A A, DIETA, A S, BOXTEL, R V. 1979. Isolation of a deep-sea barophilic bacterium and some of its growth characteristics. *Science*, **205**, 808–810.
- ZIELINSKI, R A, BLOCH, S, and WALKER, T R. 1983. The mobility and distribution of heavy metals during the formation of first cycle red beds. *Economic Geology*, **78**, 1574–1589.
- ZIELINSKI, R A, BLOCH, S, and WALKER, T R. 1986. Mobility and distribution of heavy metals during the formation of first cycle red beds. In: MUMPTON, F A (editor) *Studies in Diagenesis. United States Geological Survey, Bulletin*, **1578**, 52–59.

CHAPTER 6

Area 4 Reservoir modelling and enhanced oil recovery

E Lindeberg (IKU Petroleum Research — Norway)

L G H van der Meer (TNO Institute of Applied Geoscience — The Netherlands)

6.1 OBJECTIVE

The primary purpose of work area 4 of the project was to provide a basis on which to estimate the capacity of aquifers and oil reservoirs to store CO₂. A secondary purpose, which emerged during the project, was to develop the concepts of disposing of CO₂, both in conventional fluid traps and in large, essentially horizontal aquifers without the need for a conventional fluid trap. The work undertaken included the acquisition of new physical data and the production of new reservoir models and numerical simulations. It also included a review of the most important transport mechanisms, and published physical data, field experience, reservoir models and numerical simulations. The majority of the many simulations made during the course of the project have already been published elsewhere (Van der Meer, 1992, 1993, 1994; Holt, Jensen and Lindeberg, 1994; Lindeberg, 1995).

6.2 BACKGROUND

E Lindeberg

Compared to ocean disposal, the underground disposal of CO₂ is a relatively new concept for combating increased accumulation of anthropogenic CO₂ in the atmosphere. Specific literature on this topic is therefore sparse. On the other hand, closely related topics in the petroleum industry, e.g. gas storage in reservoirs, enhanced oil recovery (EOR) by gas injection, have not only been studied theoretically, but also applied in the field for decades. Although these topics are related to CO₂ disposal, there are important distinctions. In gas storage it is essential that as much as

possible of the injected gas can be recovered. Dispersed and dissolved gas will decrease the performance of the recovery. For CO₂ disposal in aquifers, the recovery of CO₂ is not an objective, and dissolved and dispersed CO₂ will improve the storage potential. In traditional EOR it is important to minimise the net use of CO₂ since the CO₂ has to be purchased for 0.04 to 0.10 ECU per Sm³. In EOR combined with disposal of excess CO₂, a quite different strategy for developing the field must be chosen. This strategy must combine dual motives: to get a cost effective recovery of extra oil *and* to leave as much CO₂ as possible in the reservoir when the project is completed.

In any study of underground CO₂ disposal, the basic physical knowledge of the mechanisms involved in multi-phase transport in porous media stems from the same scientific platform as that used in the petroleum industry. This platform is based on elements from reservoir engineering, geology and chemistry. The physical mechanisms described below are the main components modelled in reservoir simulations.

6.3 BASIC MECHANISMS FOR CO₂ DISPOSAL IN GEOLOGICAL FORMATIONS

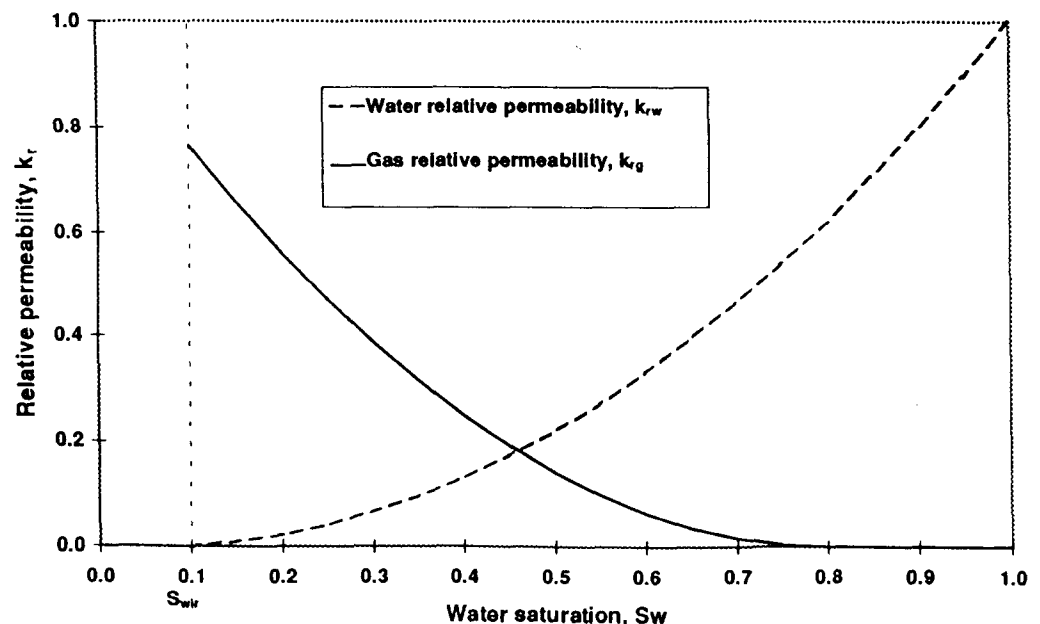
E Lindeberg

6.3.1 Viscous and gravity forces

Relative permeability

The Darcy equation, which describes the flow of fluids in a porous medium, relating the velocity of a fluid to the pressure gradient, is given in Equation 6.1 for flow in one (x) dimension.

Figure 6.1 Relative permeabilities in a gas/water system.



$$q_i = \frac{k_i}{\mu_i} \cdot \frac{dp_i}{dx} \quad (6.1)$$

where q_i is the volume flux of phase i , k_i is the permeability of phase i , dp_i/dx is the pressure gradient in phase i and μ_i is viscosity of phase i .

If more than one phase is flowing, each phase will have its individual fluxes based on its respective set of parameters. The permeability of each phase is a function of the saturation of the phase (= volume fraction of the phase). Examples of these functions are shown in Figure 6.1. Here the relative permeability, k_{ri} is defined as $k_{ri} = k_i / k'_i$ where k'_i is the permeability when only one phase is flowing.

In Figure 6.1 it can be seen that when gas (CO_2) is displacing water the saturation will never go below a certain value, the irreducible water saturation, S_{wir} . The relative permeabilities are best determined experimentally for each fluid system, but can be estimated from certain correlations.

Mobility ratio

If CO_2 is displacing water horizontally, the displacement is unstable because CO_2 gas is the less viscous and therefore the more mobile phase, and will tend to bypass the more viscous and less mobile phase (water). The mobility ratio is,

$$M = \frac{k'_g / \mu_g}{k'_w / \mu_w} \quad (6.2)$$

where k'_w is the permeability in the water zone ahead of the gas and k'_g is the permeability in the gas-contacted portion of the reservoir. M is a measure for the stability of the displacement.

The permeability ratio depends on rock properties and fluid/rock interactions, and does not depend strongly on pressure and temperature. The viscosity ratio, however, is entirely a fluid property and a direct function of pressure

and temperature and can therefore give some general information regarding the stability. In Figure 6.2 viscosity ratios from 63 different North Sea formations are shown.

The viscosity ratio increases from 4 at great depth to 17 in shallow aquifers. From this it can be concluded that the sweep efficiency will improve with depth, because a higher mobility ratio gives a less stable displacement (Craig, 1991).

Density

In the same figure the density of CO_2 is plotted, showing that there is a characteristic density difference between CO_2 and water of approximately 300 kg/m^3 , almost independent of reservoir conditions. This density difference is sufficient to cause injected CO_2 to flow upwards and accumulate above the water phase below the cap rock. If CO_2 is injected into horizontal structures this will cause a fast lateral spreading and poor vertical sweep (gravity override) as illustrated in Figure 6.3. However, if the CO_2 is injected into dipping structures this can be utilised to give a gravity stable CO_2 phase displacing the water below, giving an efficient sweep.

The ratio of viscous and gravity forces can be expressed as

$$R_v = \frac{q \cdot \mu_w}{k \cdot g \cdot \Delta \rho} \cdot \frac{L}{h} \quad (6.3)$$

where L and h are respectively length and height of the reservoir, g is acceleration of gravity and q is the volume flux. For a given homogenous reservoir, the injection rate is the only variable parameter. Due to injectivity limitations, the flow regime will typically be dominated by gravity override. In a heterogeneous reservoir with a highly permeable zone (thief zone) between zones with lower permeability it might well be possible to achieve viscous dominated flow regimes. The same will hold for thin reservoirs (h is small). An example of the importance

Figure 6.2 Viscosity ratios between water and CO_2 for 63 different North Sea formations. CO_2 densities at the same conditions are also illustrated.

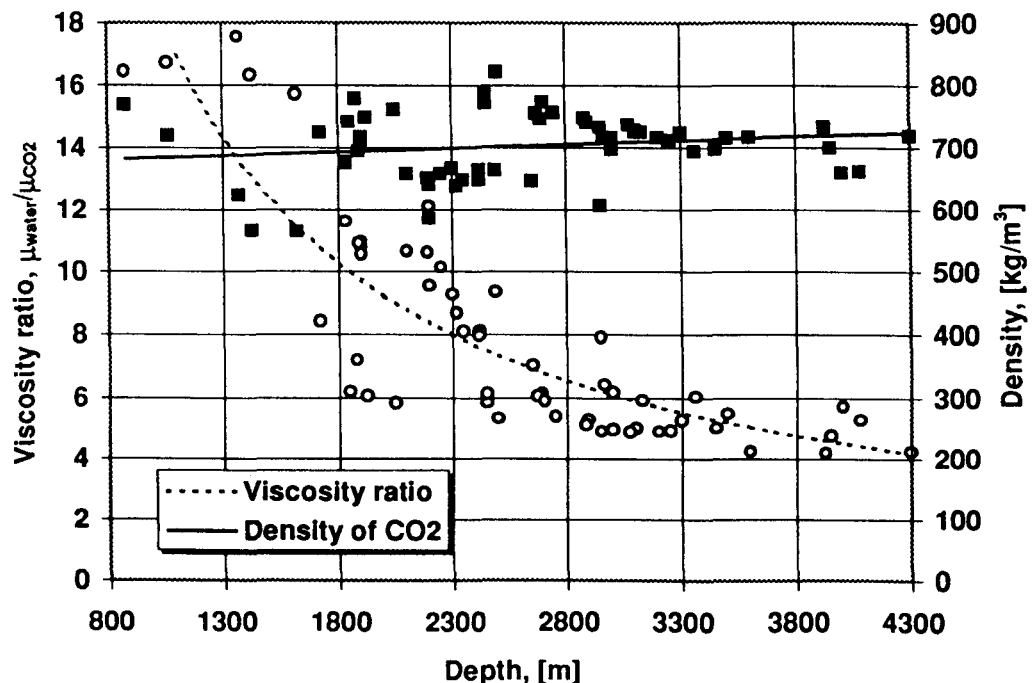
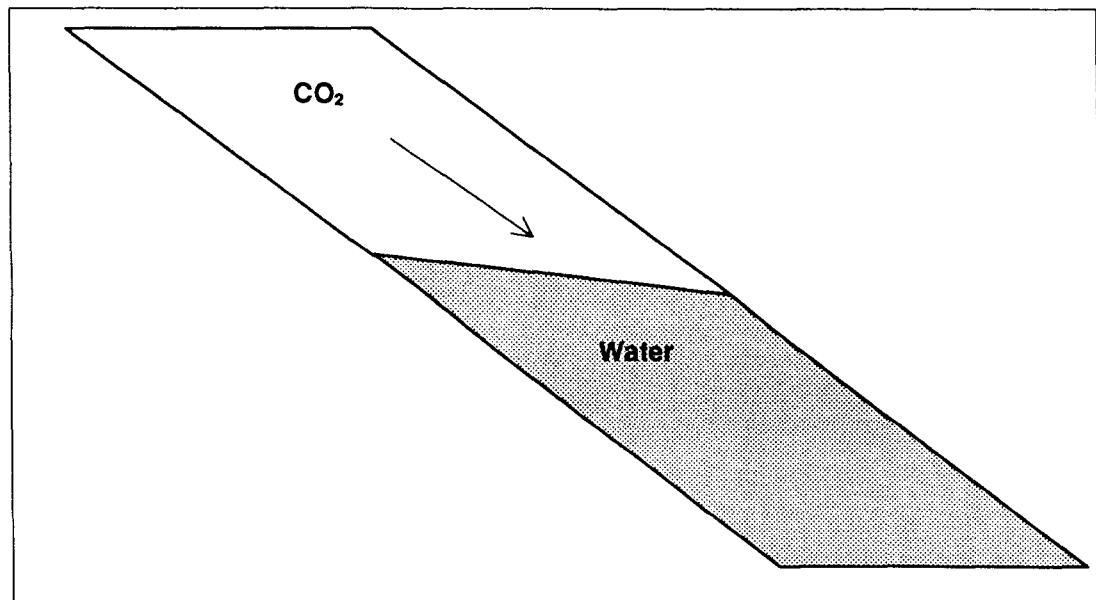
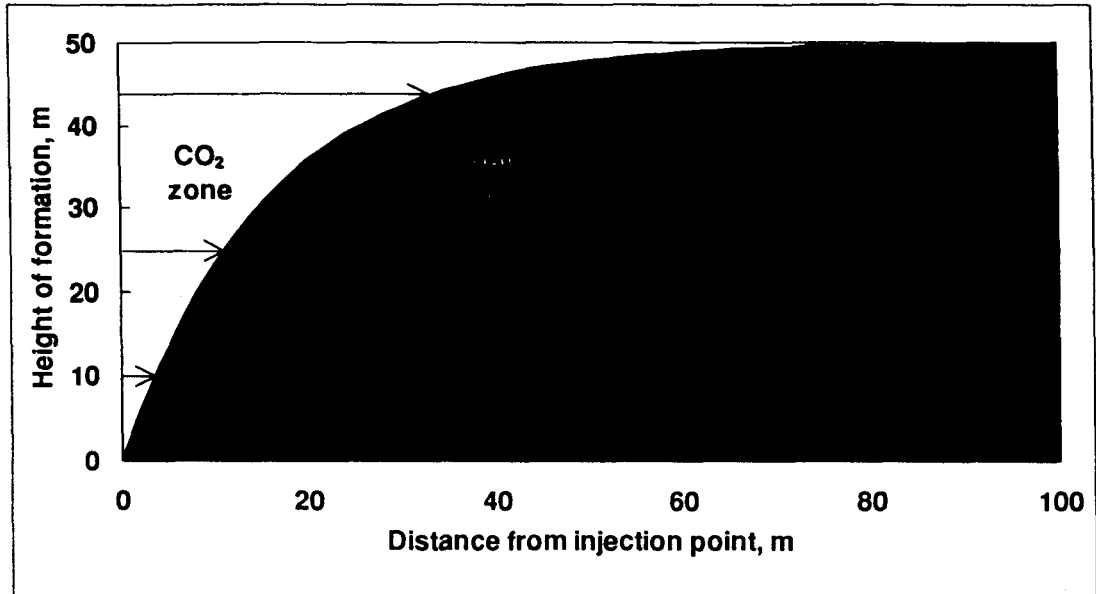


Figure 6.3
 Example of displacement processes dominated by gravity: in a horizontal reservoir (above) and in a dipping reservoir (below).



of viscous and gravity flow regimes will be reviewed in Section 6.5.

6.3.2 Phase properties of the CO₂/water systems

When water is contacted with CO₂ in the reservoir, some of the CO₂ gas will dissolve in the water. The maximum solubility of CO₂ in water depends on the temperature, pressure and salinity of the water. In Figure 6.5 experimental solubility data for CO₂ in pure water are plotted. The heavy curve indicates typical reservoir conditions at different depths at corresponding pressures and temperatures. The solubility will vary between 56 to 60 kg/m³ water. The solubility decreases with increased salinity. At a salinity of 3% the solubility is approximately 85% of the solubility of pure water (Enick and Klara, 1990) Taking this reduction in solubility into account, the solubility will vary between 47 and 51 kg/m³ corresponding to a reservoir volume of free CO₂ of 6.7 to 7.3% of the pore volume. This is a significant contribution to the storage potential if

a large fraction of the water becomes saturated with CO₂. The degree of dissolution will depend on the dispersion of CO₂ in water, on geometry (how large water surface is contacted with CO₂) and on the time scale.

6.3.3 Molecular diffusion

The transport of molecules in the absence of bulk flow is referred to as molecular diffusion. In one dimension the mass transport in moles per unit of time, $\delta n / \delta t$, due to diffusion can be expressed by Fick's law as:

$$\frac{\partial n}{\partial t} = -D_o \cdot A \cdot \frac{\partial C}{\partial x} \quad (6.4)$$

where D_o is the bulk diffusion coefficient, A is cross-sectional area, C is the concentration and x is the distance. Renner (1988) correlated the diffusion coefficient for CO₂ in

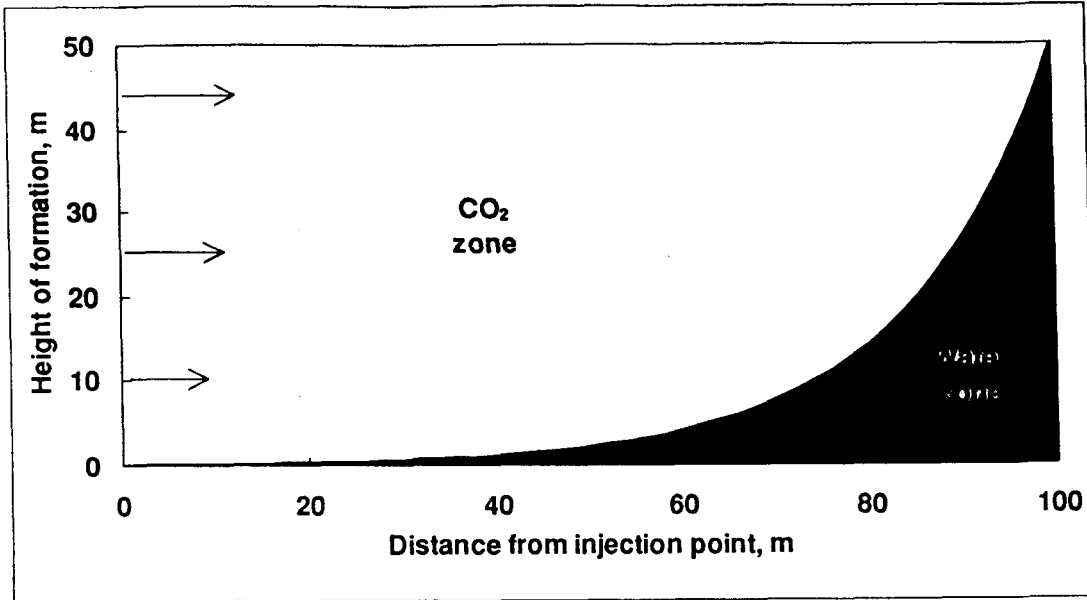
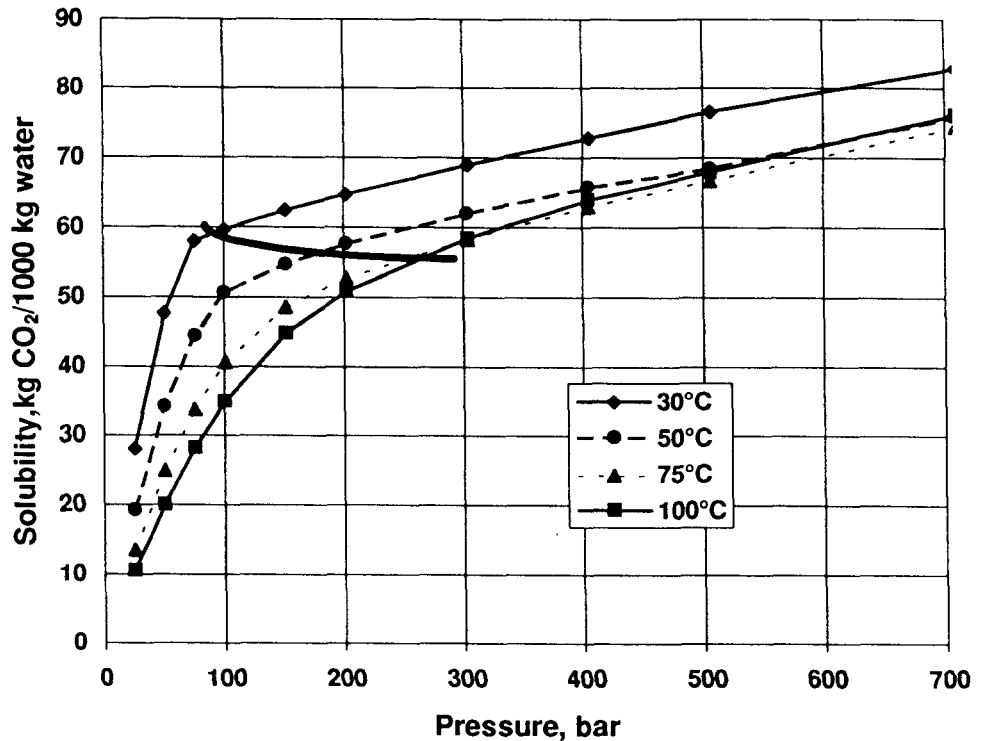


Figure 6.4 Example of displacement processes dominated by viscous forces in a horizontal reservoir. The more viscous dominated the flow is, the better sweep efficiency and larger storage potential can be expected.

Figure 6.5 Solubility of CO₂ in water at different pressures and temperatures.



water and brine with the viscosity of brine and the viscosity of CO₂. Other parameters, such as temperature and pressure, were not found to have a significant effect. The expression

$$D_o = 0.6391 \cdot \frac{\mu_g^{6.911}}{\mu_w^{0.1584}} \quad (6.5)$$

was fitted on the basis of both low and high pressure data (the unit of viscosity is cp). The viscosities of CO₂

(Michels et al., 1958) and brine (Numbere et al., 1977) as functions of pressure and temperature (and for brine also salinity), are well described.

Diffusion in a porous medium can be described by Equation 6.4 by replacing the diffusion coefficient with an effective diffusion coefficient, *D*, that depends on the structure of the porous medium. It can be argued that molecular diffusion is analogous to the conduction of electricity, that is, molecular concentration gradient, mass flux and diffusion coefficient are analogous to electrical potential, current and conductivity, respectively. The formation

factor, F , is defined as the ratio between the electrical resistivity of the porous medium saturated with brine to the electrical resistivity of the brine alone. The effective diffusion coefficient can be correlated to the formation factor by the expression

$$D = \frac{D_o}{F \cdot \phi} \quad (6.6)$$

where ϕ is the porosity. The factor $F \cdot \phi$, also called the tortuosity factor τ , is equal to 1 if all pores are straight and parallel to the transport direction. In real porous media it typically varies between 1.41 and 6 depending on the texture of the medium.

Diffusion is a slow process compared to other transport processes and can be ignored in many cases in reservoir engineering. However, in fractured reservoirs, when gas is flowing in the fractures between matrix blocks filled with brine, it can take less than a year to saturate the water in the matrix block with CO_2 by diffusion. Diffusion can also play an important role for reservoirs where zones of high and low permeability alternate.

6.3.4 Convective mixing

When one phase is displacing another in a porous medium they will create a mixing zone between them due to convection. The mixing zone will spread out both in the direction of displacement (longitudinal) and vertical to the direction of flow (transverse). This process can be described as quite similar to molecular diffusion, see Equation 6.4, but with a convective mixing coefficient instead of the diffusion constant. The combined effect of the two mechanisms is called dispersion.

6.3.5 Capillary pressure

When CO_2 displaces water in a water wetting porous medium there will be a pressure difference across the curved interface between the phases. This pressure difference is called the capillary pressure and is a function of the interfacial tension and the pore size. In a porous medium where all pores have the same diameter, r , the capillary pressure over the CO_2 /water interface will be

$$p_c = \frac{2 \cdot \sigma \cdot \cos\Theta}{r} \quad (6.7)$$

where σ is the interfacial tension between CO_2 and water, and Θ is the wetting angle measured through the water phase. In aquifers the rock/ CO_2 /water system will be strongly water wetting and therefore $\cos\Theta \approx 1$. The interfacial tension between CO_2 and water is typically 35 mN/m at reservoir conditions. A model from Kozeny (1927) can be used to estimate the grain size diameter in a porous medium,

$$D_p = \sqrt{\frac{k \cdot 150 \cdot (1 - \Phi)^2}{\Phi^3}} = \left(\frac{1}{\Phi} - 1\right) \cdot 12.2 \cdot \sqrt{\frac{k}{\Phi}} \quad (6.8)$$

if the permeability, k , and porosity, Φ is known. If the grains are monodispersed spheres in rhombohedral packing,

the smallest circular aperture the non-wetting phase will have to penetrate has a radius of 0.077 of the sphere diameter and the corresponding porosity is 26%. From Equation 6.7 and 6.8 a rock having a permeability of 1 Darcy will have a capillary pressure of 0.13 bar corresponding to a capillary height of 4 m in the CO_2 /water system. This effect can modify the simple distribution patterns illustrated in Figures 6.3 and 6.4. Due to capillary pressure, the sweep will increase in a horizontal reservoir in the gravity dominated flow regime and decrease in the viscous dominated flow regime.

6.3.6 CO_2 injection into oil reservoirs. Miscible displacement

All the mechanisms described above are also important when CO_2 injection into oil fields is simulated. Their relative importance might, however, be different. There is one special phase property in the CO_2 /oil system which is of particular importance and has no analogue in the CO_2 /water system. This is the ability for CO_2 and oil, under certain conditions, to produce miscible displacement.

When an injection fluid mixes directly and fully with reservoir oil, and the mixtures remain single phase, the fluids are said to be first-contact miscible. Other injection fluids form two phases when they are mixed with reservoir fluid. However, with these fluids, in-situ mass transfer of components between reservoir oil and injection fluid can form a displacing phase with a transition zone of fluid compositions that range from oil to injection fluid composition, and all compositions within the transition zone are contiguously miscible. Miscibility achieved by in-situ mass transfer of components resulting from repeated contact of oil and injection fluid is called multiple contact miscibility.

Compared to other injection gases, such as nitrogen or hydrocarbon gas, CO_2 will generally be more prone to form miscible displacement. Because only one phase results from mixtures of miscible fluids, there are no interfaces and consequently no interfacial tension, and there is no effect of relative permeability on the recovery efficiency. Residual oil can therefore be reduced to the lowest possible value in the parts of the reservoir which are swept by CO_2 .

6.4.1 Reservoir Modelling E Lindeberg

All the physical mechanisms described above can be modelled in modern numerical reservoir simulators which solve the flow equation when reservoir formation and flow data are provided. Convective mixing will, however, appear in the model due to numerical dispersion which is a function of the space resolution of the numerical model, and not as a function of the physical flow. By selecting a sufficiently fine grid, numerical dispersion can be minimised.

The solution of the flow equations at different time steps can be used to calculate how CO_2 distributes in a given reservoir formation. By varying boundary condition, rates, formation properties etc., the sensitivity of key parameters can be determined. In this way it is possible to obtain general information about the effect of CO_2 injection into the reservoir.

The most significant uncertainty when a specific injection project is simulated will usually be the physical description of the aquifer formation itself. Other input parameters for the relatively simple CO_2 /brine system are well described by most simulators.

6.4.2 Modelling Tools

L G H. van der Meer

Introduction

Computer modelling has become an increasingly important tool for predicting physical and chemical processes. The main problem is how to translate these processes into mathematical equations. In most cases the process is dynamic, with parameter dependencies in time, space and boundary conditions. Furthermore, it is necessary to use approximations and assumptions in order to describe a complete system. Great care has to be taken with the mathematical formulation of subparts of the system. The fluid displacement process in a porous medium consists of many subprocesses, each with its own scale. Some processes act on the millimetre scale whereas others act on a much larger scale, for instance over several metres. Care has to be taken to relate all subprocesses to the same scale.

When modelling fluid flow processes in the subsurface we generally use grid systems, in which the 3-dimensional space of the subsurface is represented by a number of cells. These grid cells have dimensions of 1 or 2 m to several hundreds of metres, depending on the size of the part of the subsurface to be modelled and the practical constraints to the number of grid cells to be used. With these kinds of grid cell dimensions it is impractical to model effects such as fluid interfaces (e.g. between CO₂ and water) which take place within the space of one grid cell. On the other hand, the geochemical influences of the fluids on the subsurface rock material can and must be modelled. Any possible changes in the permeability or porosity of subsurface rock, brought about by the injected fluid have to be modelled, because of the overall effect on the fluid displacement behaviour. Even though the process is active at pore scale, the results have large-scale implications. Proper modelling of any subsurface process requires an in-depth analysis of all active processes, and a scale classification of all the effects that influence the processes in relation to the simulation tools available.

Simulation models serve only as an aid to engineers and policy makers in making intelligent decisions regarding future reservoir operations. An engineer using a computerized simulation model to study a reservoir must exercise considerably more judgment than he would if no such model were employed. He must decide what type of model his questions and the reservoir warrants. The question is not whether to simulate but rather what tools to use in performing the simulation.

Reservoir Simulators

Webster's New Collegiate Dictionary defines "simulate" as "to assume the appearance of without reality". Simulation of CO₂ storage reservoir performance refers to the construction and operation of a model whose behaviour assumes the appearance of actual reservoir behaviour. The model itself is either physical (e.g. laboratory sandpack) or mathematical. A mathematical model is simply a set of equations which, subject to certain assumptions, describes the physical processes active in the reservoir. The mathematical models relevant here consist of a set of partial differential equations which express conservation of mass and/or energy. In addition, the models entail various phenomenological "laws" describing the rate of processes active in the reservoir. All commercially available reservoir simulators are based on Darcy's law, that relates the volumetric velocity to the pressure gradient and gravity force for single-phase flow in a porous medium.

The gridsystem used is based on the orthogonal principle. Each gridcell will represent a part of the reservoir. For each of these gridcells average reservoir properties are selected and projected to a point in the middle of the gridcell. The cell centred gridpoint enables fluid flow in the three main directions (x, y, and z). For each of these main directions the Darcy law can be written for a single fluid. The resulting volumetric velocity is also referred to as superficial or Darcy velocity. For multiphase fluid flow, for each fluid the Darcy equation is modified by relative permeability. Relative permeability is an experimentally determined rock property to relate volumetric velocity to pressure gradient when more than one phase is flowing. This relative permeability is in general a non-linear function of saturation (concentration). Extensive laboratory experiments in multiphase fluid flow have indicated insignificant sensitivity of the relative permeability versus saturation relation to viscosities of the flowing phases.

The resulting mathematical model is simply a set of equations (for each gridcell) which describe certain physical processes occurring in the reservoir. In nearly all cases these equations express conservation of some quantity which is flowing or being transported through the reservoir. Examples are conservation of mass of a flowing fluid and conservation of thermal energy in cases involving injection of hot fluids to enhance oil recovery. In general, the quantity one wishes to conserve is indicated by verbal statement of the problem. A general balance about the system, expressing the conservation of the flowing quantity over a small time increment Δt , can simply expressed as:

$$\text{IN} - \text{OUT} = \text{GAIN}$$

The term multiphase flow denotes the simultaneous movement of two or more immiscible phases through a porous medium. Obvious examples are gas-oil, gas-oil-water and CO₂-water. The equations describing this flow are simply the conservation written for each phase. In these equations the quantities to be conserved are important. Customary quantities (or units) are normal cubic metres (at surface conditions, Nm³) of water, oil, gas and CO₂. This volume unit is convertible to mass through densities at standard conditions. Gas exists in the reservoir both as free gas and as gas in solution in the oil. The relationship between surface (standard conditions) and reservoir conditions is laid down in a set of PVT functions. These PVT functions contain the formation volume factors for the three free phases (water, oil and gas) and a relation of the gas-oil-ratio, all as function of pressure.

So, a mathematical model consists of a set of differential equations for each gridcell which describe the conservation of mass and the superficial velocity for each of the phases (water, oil and gas). Via a finite difference presentation of these differential equations it is possible to solve the equations by means of a numerical solution technique.

In the above we have only talked about the 3 phase (water, oil and gas) simulators. More complex forms of simulators are the so called compositional reservoir simulators. In their most complex form these models simultaneously solve a set of mass and energy conservation equations and associated constraint equations for each of a number of gridcells representing a reservoir. A mass balance equation is written for each of the N_c components included in the process description, and an overall energy balance equation represents thermal effects. The constraint equations express the requirements that the saturations must sum to unity and that the mole fraction of com-

ponents in each phase must sum to unity. The mass and energy balance equation are written in finite-difference form in order to utilise the most numerically efficient and stable formulation.

These models also describe mass transport by Darcy flow, and incorporate gravity, viscous, and capillary forces. Furthermore, they allow any number and identities of components. Each component may partition among any of the four phases (water, oil, gas and solid) as dictated by the user-specified pressure and temperature dependent component K-values. The density and viscosity of each phase are a function of its composition, pressure, and temperature.

From the above we can conclude the following:

The transport of any phase in the simulator is controlled by its mobility in relation to other phases present. The phase mobility is largely dependent on the relative permeability of this phase. Relative permeability is an experimentally determined rock property which is determined on a relatively small portion (core plug, several cm³) of the reservoir. Two remarks can be made in relation to the laboratory experiment:

1. How representative is the data gathered in this experiment to phase flow on a reservoir scale?
2. Which macroscopic flow effects will be included in the relative permeability data?

Simulation on a reservoir scale will utilise relatively large dimension gridcells. Even with present computer technology there is a practical limit to the number of gridcells that can be used. In the case of a simple 3-D, 2 phase simulation over a period of 30 years we are limited to some 1 000 000 gridcells. In case of a multi-components simulation the limited come close to 25 000 gridcells. Even in these detailed simulations the gridcell dimensions are in the order of several tens of metres. All calculated results will be average values over the entire gridcell. Thus it is clear that at the present it is impossible to simulate small and even perhaps medium scale displacement effects on a reservoir basis.

In modern simulators, great care is take to ensure that no fluids are lost, or better that a mass balance is being preserved. So, if fluids are injected, nothing is being lost in the process. In some simulators it is possible to assign solubility of a component in another phase. The difference here is that there is a difference in tracking down the component which has no repercussion on the mass balance. In one simulation the simulator will calculate that all of one component is in a free state while the other will indicate that a portion of this component is in solution in another component. In the ultimate case it could have minor consequences on the density and viscosity of the mixed phase. Here again, the solubility in the simulator of one component in the other is controlled by user-specified pressure and temperature dependent component K-values. These equilibrium K-values are determined in laboratory experiments. At the start of any simulation the question has to be answered whether these laboratory data are representative for a process that takes place under reservoir conditions, because K-values have an absolute character and do not account for process or reaction timing.

Simulation of the CO₂ storage process

Two processes will dominate the CO₂-water displacement process: gravity segregation and viscous fingering. All available simulators are capable of properly simulating dif-

ferences in gravity of the flowing phases. Mainly because gravity segregation is a large scale effect it will not be restricted by the gridcell dimensions. This is in contrast with viscous fingering. Viscous fingering gets initiated on a pore scale and the use of large gridcells will eliminate the simulation of this process. Koval (1963) Todd and Longstaff (1972), Christie and Bond (1987), Frayers (1988) King et al. (1993) and recently Tchelepi (1994) have made important studies of the possibilities for numerical simulation of the viscous fingering process. Much of this work has been concentrated on special cases or isolated processes. Todd and Longstaff (1972) looked at viscous fingering in a homogeneous porous medium and developed an analytical model to predict the concentration distribution. Koval (1963) provided the calibration of the model based on experimental data derived by Blackball et al., Todd and Longstaff's fractional flow equations are:

$$\phi \frac{\partial C}{\partial t} + V \frac{\partial f(C)}{\partial x} = 0 \quad (6.9)$$

$$f(C) = \frac{C}{C + (1-C)/M_{\text{eff}}} \quad (6.10)$$

whose solution is given by

$$x = (Vt\phi) \frac{df(C)}{dC} \quad (6.11)$$

and the Koval correction is given by

$$M_{\text{eff}} = (0.78 + 0.22 M^{1/4})^4 \quad (6.12)$$

King et al (1993) performed detailed numerical simulation on this problem with a special adapted simulator (MISTRESS). As can be seen in Figures 6.6a and 6.6b excellent agreement between the prediction methods is demonstrated. Using the fractional flow theory we may predict the time to CO₂ breakthrough, the spread of the fingered region, and the concentration distribution. All of these quantities are completely determined once the mobility ratio is specified.

This analytical model is only valid for linear flow with a stable constant injection of displacing (solvent) fluid. In order to evaluate the concentration distribution in a CO₂ injection well drainage area, compensation has to be made for decreasing CO₂ front velocities in combination with volumetric gravity segregation effects. A prediction can be made of the frontal development via a simple engineering approach to compensate for these effects. Figure 6.7 shows the results for the outgrowing front (M=20). As can be seen, at a frontal radii of 1000 metres from the well the finger length can be estimated at 200 m.

King et al. (1993) ask: "What happens in a heterogeneous porous medium?". First of all, we have introduced Uncertainty. While we may construct detailed

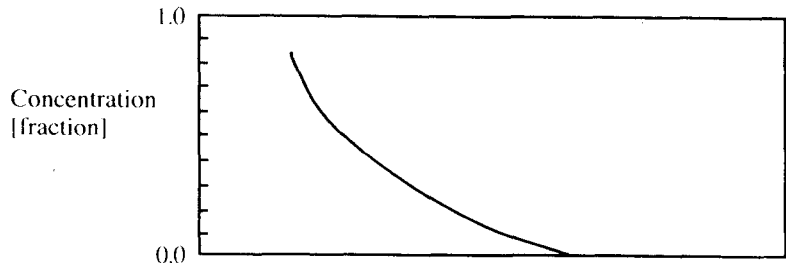
Figure 6.6 Miscible viscous fingering of solvent into oil in a horizontal homogeneous porous medium.



(a) Computed on a 500x200 fine grid using Flux Corrected Transport

descriptions of heterogeneity, their detailed intrawell spatial distribution is uncertain. One way to treat this uncertainty is to introduce multiple stochastic realisations, each to be considered a possible description of the reservoir. King et al (1993) generated four statistically identical permeability maps on a 250×100 grid, using Sequential Gaussian Simulation.

By using the same fine grid simulation techniques that successfully predicted the viscous fingering pattern of Figure 6.6a, they were able to predict the response of a miscible flood, as is shown in Figure 6.8. Each simulation was performed to 2.0 Pore Volume Injected (PVI), and cost approximately 20 Cray hours. They reported further that the predicted oil recovery varied between 59 and 72% for the four possible permeability distributions. In other words, after 80 Cray hours there is no ability pre-



(b) Predicted average solvent concentration profile using the Koval fractional flow

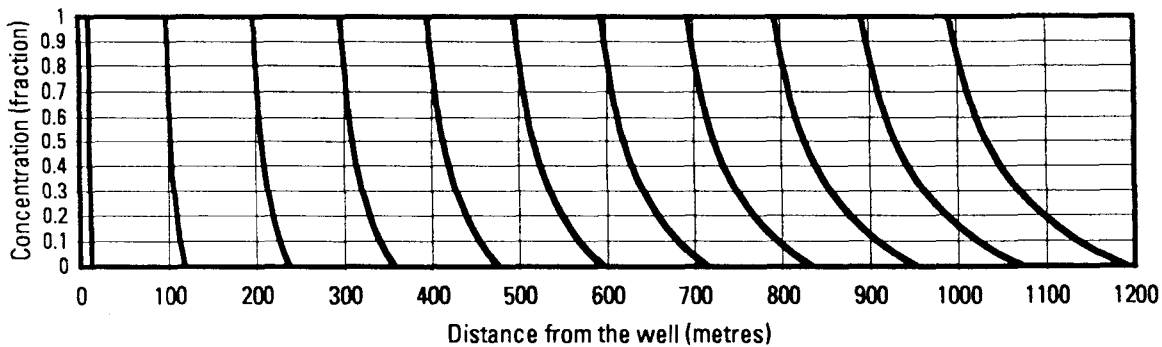
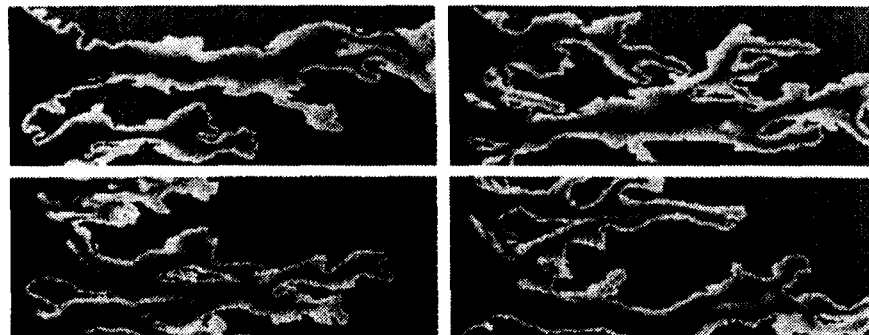


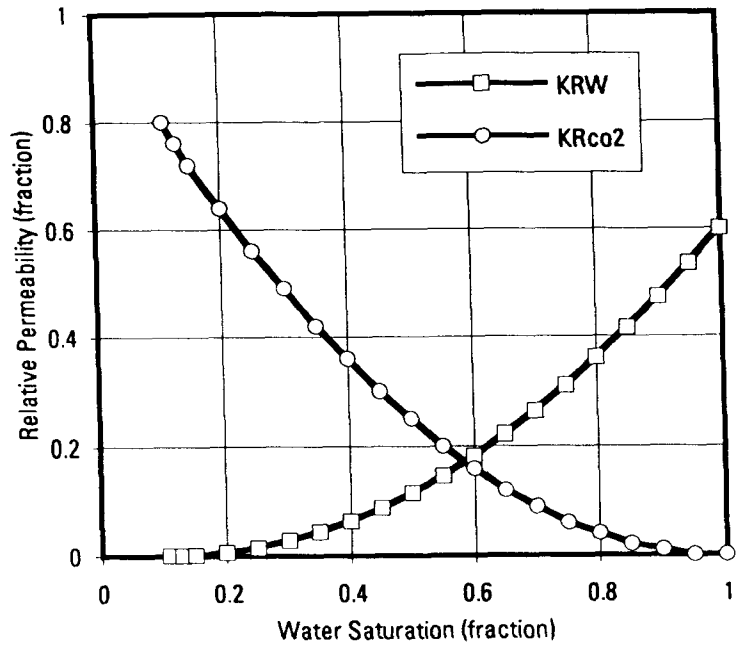
Figure 6.7 Predicted frontal development as a result of viscous fingering in a homogeneous porous medium.

Figure 6.8 Solvent concentration maps of gas displacing oil at 0.30 PVI, showing the interaction of viscous fingering and heterogeneity.



The flood is at an adverse mobility ratio of $M=10$, computed on statistically identical isotropic permeability maps. The permeability has a log-normal distribution ranging from 10^{-1} to 10^1 mDarcy, with a correlation length of 25 grid blocks. Each flood takes approximately 20 Cray hours.

Figure 6.9 Relative Permeability Curves for Water-CO₂ System.



dict to a fifth realisation, much less the response from a reservoir.

Kings work clearly shows that:

- i. Detailed modelling of miscible displacement process on reservoir scale is impractical.
- ii. Large uncertainties are introduced by the estimation of the heterogeneity of the intrawell permeability. It will be clear that this estimation is impossible in an undrilled formation.
- iii. Heterogeneity in permeability distribution will have a much larger effect on the CO₂ frontal movement than viscous fingering.

The above mentioned work has been concentrated on horizontal flow excluding gravity effects. TNO has attempted to predict the detailed vertical CO₂-water displacement process using a commercially available simulator to study the relevant processes. In the same manner as King et al (1993), a statistical generated permeability map was generated for a 100 × 100 grid.

Several attempts have been made to simulate CO₂-storage activities on a field scale, e.g. Gunter et al. (1993), Korbøll and Kaddour (1994) and van der Meer (1992, 1993, 1994). All used different approaches to take account of the solubility CO₂ in water. Nobody has a direct solution to the viscous fingering problem. All have used commercial available oil industry reservoir simulators. Gunter et al. (1993) used a four-phase, multi-component thermal STeam and Additive Reservoir Simulator (STAR) developed by the Computer Modelling Group in Calgary. In this model CO₂ was allowed to dissolve in water via user defined K-values. The K-values were estimated as:

$$\log K = -2.419 + 0.9838 \log P \quad (6.13)$$

Statoil (Korbøll and Kaddour, 1994) used a 3-dimensional, 3-phase (water, oil, and gas), and isothermal simulator (Intera ECLIPSE) to predict the effects of a CO₂-storage operation. In the normal use of this type of simulator it is not possible to simulate any absorption in the water phase. Statoil discarded the water phase. They used the oil phase to simulate the brine in an aquifer and the gas phase to simulate the CO₂ (E Lindeberge, pers. comm.). This approach enabled them to use the Gas Solution Ratio (Rs) function to model the CO₂ solubility in water. This Rs function normally defines the volume of gas dissolved in oil as function of pressure.

Van der Meer used the same type of simulator (SIMBEST II, SSI). He used the so-called Gas-Water option to simulate CO₂-storage. This option is a subset of the simulator which omits the oil phase. The gas and the water phases are immiscible.

If we compare the simulators used the following remarks can be made:

- a. All three simulators are based on the Darcy flow equation and consequently phase movement is controlled by relative permeability. The use of relative

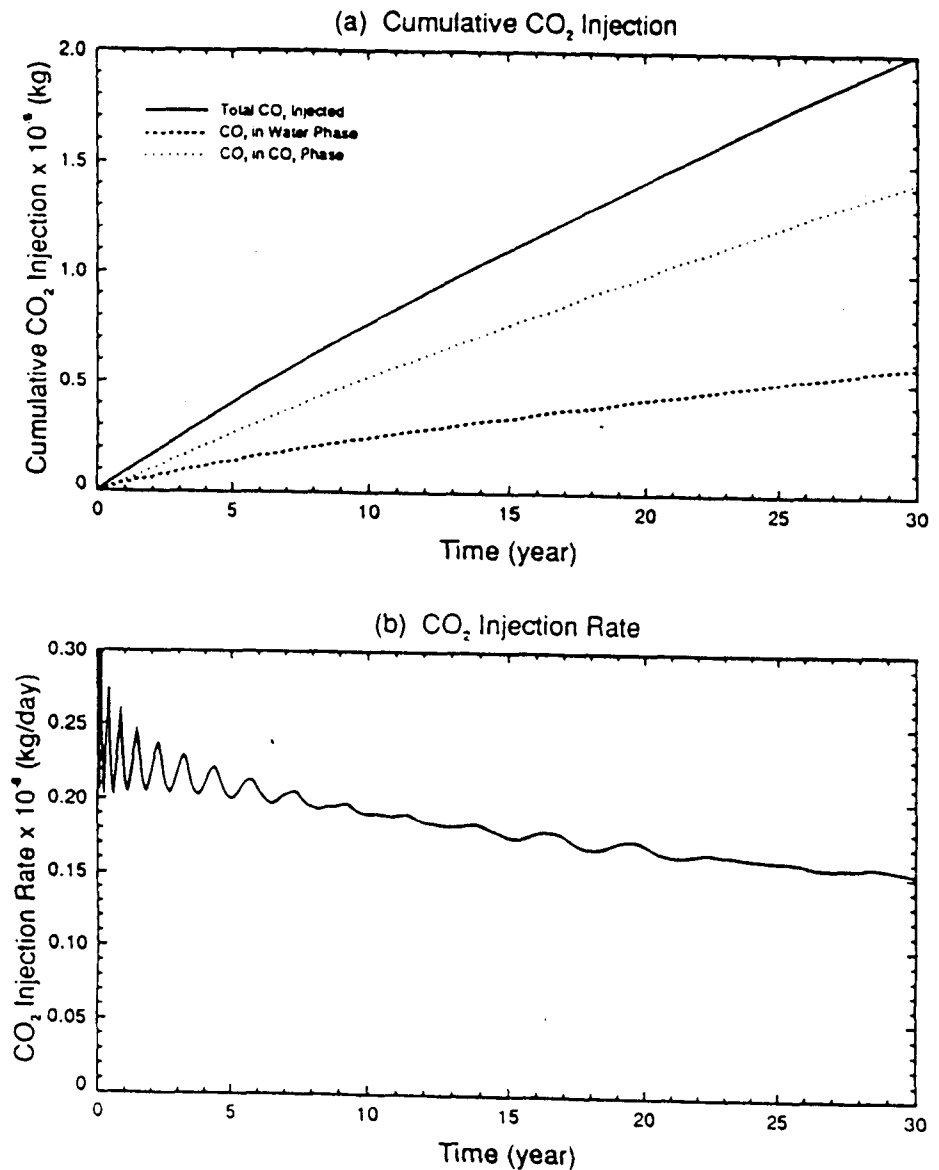
permeability will guarantee a distributed phase interface.

- b. None of the simulators are able to simulate viscous fingering on a reservoir scale. The main reason for this is the use of relatively large gridcells with average reservoir properties which represent corresponding large sections of the reservoir.
- c. The simulators were used for test problems of CO₂ injection in aquifers. At initial conditions the aquifers contained only water. In all three cases CO₂ injection is controlled either by well injection or a maximum injection rate.
- d. All injected fluid volumes were maintained in the reservoir. The only difference between the CO₂ volumes in the reservoir is the tracking method. Both Gunter et al (1993) and Korbøll and Kaddour (1994) subdivide the CO₂ in the reservoir into free CO₂ and CO₂ in solution in the water. Van der Meer is not able to make this distinction. But the total volumes of CO₂ in the reservoir are the same.

The best way to evaluate the differences in the prediction method is to use the different methods on a universal test problem. Dr W Gunter kindly made available his simulation input data deck and simulation results. In order to prevent the rerun of all cases it was decided to use his data and results as base case. His simulation model was set up in order to investigate the potential for subsurface disposal of CO₂ in Alberta. The aquifer selected was a Lower Mannville siliciclastic aquifer in the Wabamun Lake Area, Alberta.

The aquifer is located at a depth of 1450 m and has a thickness of 55 m. The absolute permeability in the horizontal and vertical direction are 1.3 and 0.39 mD, respectively, and the porosity is 12%. The pressure at the top of the reservoir is 11 300 kPa. The average temperature of the aquifer is 40°C, which was estimated based on a ground surface average temperature of 6°C and a geothermal gradient in the area of 23°C/Km. A compressibility of 4.7×10^{-7} 1/kPa was used for the sandstone in the num-

Figure 6.10 Injection Well Performance Plots (Gunter).



critical simulation. The fracture pressure at the top of the formation was 32 800 kPa which was estimated based on a gradient of 22.61 kPa/m that related the maximum principal stress to the weight of the overburden. The relative permeability curves used for the water-CO₂ system are given in Figure 6.9.

The carbon dioxide in the aquifer was in a supercritical condition and was treated as a single phase fluid in the Gunter et al. numerical simulation. The densities of CO₂ at 40°C varied from 638 kg/m³ at 10 000 kPa to 907.7 kg/m³ at 30 000 kPa. The viscosity of CO₂ at 40°C and 20 000 kPa was 0.077 cp. In his study the effects of pressure over the pressure range of 10 000 to 30 000 kPa on the viscosity of CO₂ was ignored. The CO₂ was allowed to dissolve in the water. The K-values for CO₂ in water varied from 0.0367 at 10 000 kPa to 0.1082 at 30 000 kPa. The density of the CO₂ in the water phase was set to the same density of the water.

A 2-D radial grid model with 140 (i=28, j=1, k=5) gridcells was used to represent a region of the aquifer with a radius of 0.65 km, around the injector. All five layers have a uniform thickness of 11 m. At the outer boundary of

the model a semi-analytical aquifer model was used to estimate the pressure build-up due to the boundary effects. Gunter reported that all simulation runs were performed on a SUN workstation, SPARC station 2 and that runs with 330 and 140 gridcells took approximately 6 and 2.5 CPU hours respectively (30 years, 65 sec./gridcell).

In the numerical simulation, 100% CO₂ at 40°C was injected at a constant injection pressure of 29 500 kPa (i.e. 90% of the fracture pressure). The vertical injection well was perforated over the entire thickness of the aquifer. The results of a 30 years CO₂ injection simulation is shown in Figures 6.10 and 6.11. As can be seen from the injection well performance plot, the cumulative injected amount of CO₂ is a little more than 2.0×10^9 kg. The average CO₂ injection rate is close to 182 600 kg/day. The calculated rate shows a slowly declining trend from an initial rate of approximately 240 000 kg/day. Furthermore the calculated initial rate exhibits an unrealistic fluctuating behaviour. The cumulative injection plot also includes the amounts of CO₂ in the water phase and the amount of free gas. The ratio between these amounts can be interpreted as stable. The figures F.11a to 6.11d are contour plots of the cross-

Figure 6.11 Cross sectional CO₂ concentration maps (Gunter).

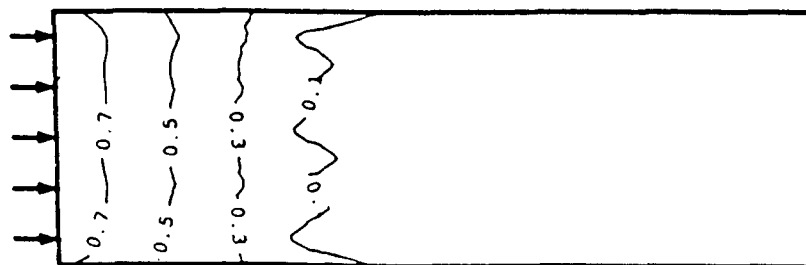
sectional CO₂ saturation distribution for 4 time periods. The first 10 years show a near vertical displacement front with a CO₂-water transition zone of some 250 m in length. In the last 10 years a slowly overhanging front controlled by gravity effects is observed.

As part of this project, van der Meer reproduced the above simulation with a 3-D, 2 phase simulator without any phase interaction. The original STAR dataset was translated into data acceptable by the SIMBEST II simulator with exception of the CO₂ PVT data. From initial test runs it was learned that it was not possible to reproduce the STAR analytical aquifer behaviour with one available in SIMBEST II. In order to get a similar behaviour the gridsystem was extended in the radial direction with 20 extra gridcells with a constant ΔR of 500 m, totally representing a 10 km ring of the reservoir. The SIMBEST II runs were made on a IBM, RS6000 - 320H workstation. The average running time for a 30 year simulation was 19.5 CPU seconds (0.08125 sec./gridcell).

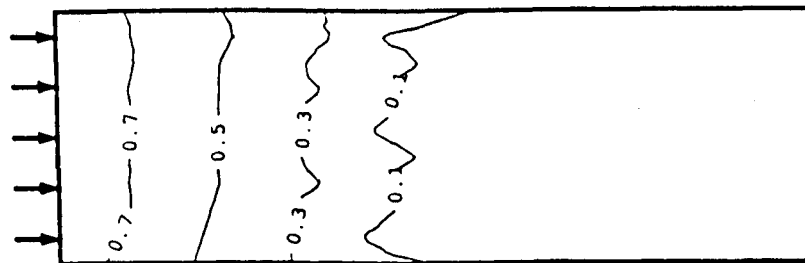
As can be seen from the well results (Figure 6.12) the 2-phase simulator calculates the same type of results.

Cumulative CO₂ injection is 2.006×10^9 kg giving an average rate of 183 200 kg/day. The plot shows a good radial rate development at the start of the injection followed by a semi-steady state behaviour. If we look at the cross-sectional CO₂ saturation distribution results (Figure 6.13) for 4 time periods for this simulation we see a steadily increasing CO₂ front which in the later part of the simulation gets influenced by CO₂ gravity effects. The plots are showing some contouring instabilities for the 20 and 30 year time slices at the start of the front. This problem is caused by the relatively large gridcell dimensions at the outer boundary of the original model. Decrease of the gridcell dimensions in this area, which effectively increases the number of data points, would cure this problem. The size of the gridcells used in both simulation exercises is clearly seen on these contour plots. The contour lines on the van der Meer simulation represent the saturation distribution for all CO₂ injected into the model, whereas those on the Gunter et al. simulation are for free CO₂ only.

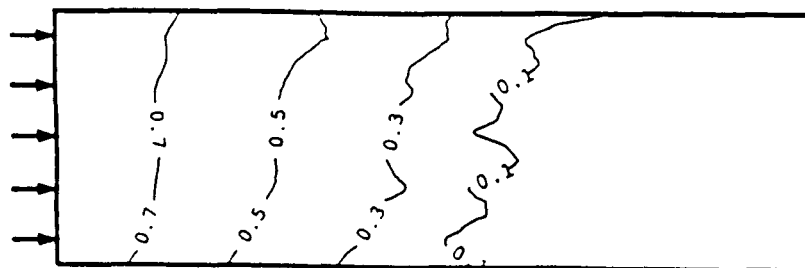
There is good agreement between the results from both simulators. Predicted injection well performance is the same. The differences in daily injection rate development through time is mainly controlled by the pressure response from the aquifer boundaries. There are arguments to justify the use of the extra gridcells to generate a proper aquifer



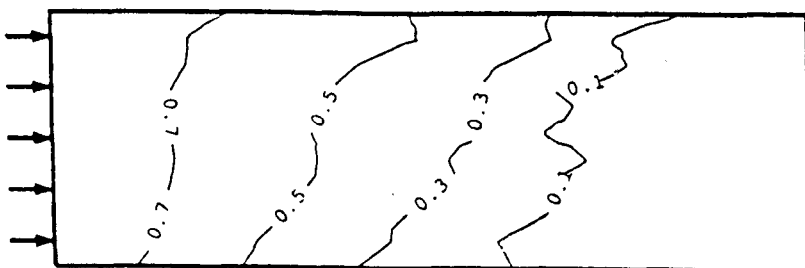
(a) after 5 years



(b) after 10 years



(c) after 20 years

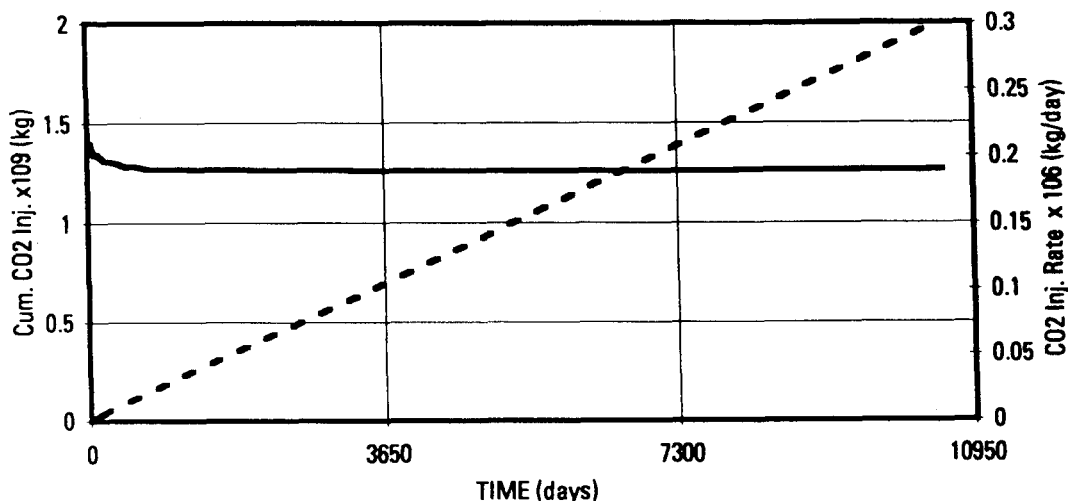


(d) after 30 years

response (spatial modelling of geological properties). But it is sensible to restrict the number of gridcells when using a complex simulator, in order to keep the processing time down, especially if the incremental gridcells serve only a single function such as pressure support.

A comparison of the contour maps (Figure 6.14) of the two simulation activities reveals that the free CO₂ front of Gunter et al. is closer to the well than the free plus dissolved CO₂ front of van der Meer. In case of the Gunter et al. contours, CO₂ undersaturated gridcells at the leading

Figure 6.12
Predicted well
performance plot.



edge of the CO₂-water front and are preventing the development of free CO₂. At this front the solubility rule (K-value) has to be satisfied first before free CO₂ will show up in that gridcell. So, if we look at Figure 6.14d, and specifically at the right side of the 0.1 contour, the relatively large gridcells there will be filled up with CO₂ until the K-value function is satisfied. This effect is clearly seen if we compare the shape of the 0.1 and 0.5 contour line in the 30 year plot. At the top of the formation the 0.1 contour line is not showing up the gravity effect properly. A portion of the faster moving CO₂ at the top is going into solution in the larger boundary gridcells. The Gunter et al. plots are showing an underestimation of the CO₂-water displacement process, which will serve to reduce the differences between the results of the two models.

Closer to the well the differences become much smaller and this effect is directly related to the decrease of water saturation. This decrease will effectively increase the free CO₂ portion in the Gunter et al. simulation results.

In conclusion it can be stated that:

- i. Both the miscible and immiscible simulator approaches gave similar results.
- ii. Although the miscible simulation suggested that there was less free CO₂ in the reservoir, this was only partly because CO₂ had dissolved in the formation water, and partly because the compositional simulation underestimated the free CO₂ saturation distribution at the leading edge of the displacement front.
- iii. In the areas with low residual water saturation the CO₂ saturation prediction for both methods is nearly the same.
- iv. Both simulators predicted the same well performance.

6.5 LITERATURE ON AQUIFER DISPOSAL

E. Lindeberg

6.5.1 Introduction

Carbon dioxide can be trapped underground in three main ways. Firstly it may be confined, principally as a free gas phase, within a fluid trap directly analogous to an oil or gas trap; the gas is confined by its own buoyancy in a structure such as a dome, beneath a cap rock or seal. In practice, the

factor limiting the storage capacity of the trap is the distribution of CO₂ within it. It is assumed that once CO₂ reaches the spill point injection must cease. All published simulations agree that at the end of the injection period the majority of the CO₂ will be in a free phase and little CO₂ will be dissolved in the formation water. Therefore the difference in storage capacity between approaches which assume miscibility between CO₂ and water and those which assume immiscibility is likely to be small. However, the miscible approach might produce a slightly higher storage capacity than the immiscible approach.

Secondly, CO₂ may be trapped in two ways when injected into large, essentially horizontal aquifers. Part of the CO₂ will be trapped by dissolving in the formation water. In this case, if there is a sealing horizon above the aquifer, the CO₂-rich formation water will remain trapped as long as there are no forces causing it to flow to (shallower) points where the CO₂ will come out of solution. Such conditions may be approached in many offshore reservoirs, where there may be very little fluid flow at depth. However, in such a case, at the time injection ceases, there will be large amounts of free CO₂ present in the reservoir as well as dissolved CO₂. In the medium term, in a horizontal or sub-horizontal aquifer, this may be trapped hydrodynamically as a free phase. If there is no fluid flow, once the pressure difference between the free CO₂ and the surrounding formation water has equalised, the only force acting on the CO₂ which might cause it to migrate is its own buoyancy. All simulations of the injection of CO₂ into large horizontal aquifers indicate that there will be only a slow redistribution of the free CO₂, implying that in the medium term, i.e. in a climate change perspective, the free CO₂ will remain in the reservoir provided it is not injected too close to the boundary.

A more controversial question is, will the free CO₂ eventually find its way to the surface or will it all dissolve before it reaches the edge of the reservoir, preferably close to the injection site? In practice, the rate of dissolution after injection ceases will depend on the characteristics of the reservoir, the salinity of the formation water, the temperature and pressure, and, most importantly, on the time frame considered and the way the CO₂ mixes with the water. This last factor will determine how much CO₂ comes into contact with formation water which is not saturated with CO₂ and thus how much CO₂ can dissolve. The simulations described below suggest that, with the right reservoir parameters, dissolution can and will be an important trapping mechanism. The problem is nonetheless highly

Figure 6.13 Cross sectional CO₂ concentration maps (TNO).

controversial and the subject of active research and debate. It is inappropriate to include this debate within the scope of this project and it will not be considered further here.

6.5.2 Literature review

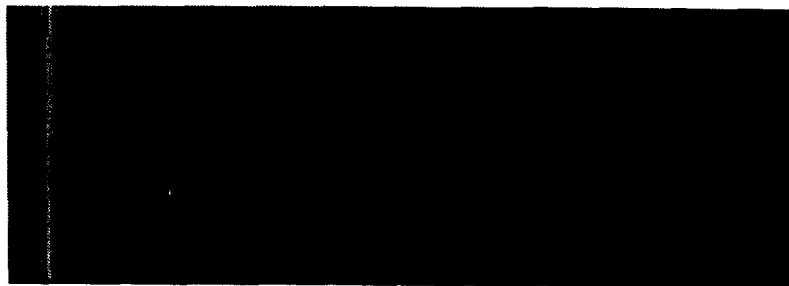
Only a few papers on aquifer disposal describe the specific storage mechanisms involved and can be used to further deduce expected storage potentials. Here only papers which use physical considerations or specific models for their estimates are reviewed. Papers on CO₂ reacting with minerals as storage mechanism are not discussed here and are included in Chapter 7.

6.5.3 Simulation of injection into a structural trap

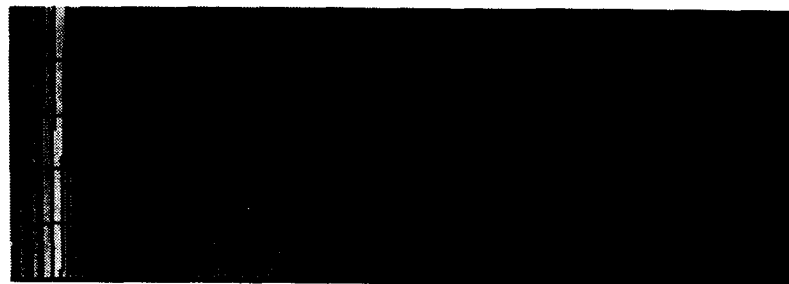
Van der Meer (1992) produced the first detailed simulation of CO₂ injection into an underground storage reservoir. The purpose of this simulation was to investigate the storage potential of a realistic reservoir when CO₂ from a thermal power plant was injected into it for a long period. The injection of CO₂ through six wells at a rate of 2500 tonnes (135 000 N m³) per well/per day was simulated. Injection was to stop when the CO₂ reached the spill point of the structure. Thus the distribution of CO₂ in the reservoir would determine the storage potential of the structure. An approach in which the injected CO₂ and the formation water were regarded as immiscible was used in the simulation.

The reservoir was a 50 m thick circular anticline with 2250 m radius and 1° dip with a spill point at the periphery. A radial geometry was used by selecting a 60° sector of the model and dividing it into a grid of 4 × 15 grid points. The storage potential was defined as the amount CO₂ injected when the gas reached the spill point. The dominant process controlling the distribution of the CO₂ was gravity override. The simulation gave a storage of 3% of the total pore volume. Due to the radial grid, the model was actually two dimensional and when an area sweep of 67% was applied, the resulting storage capacity was reduced to 2% of the pore volume.

In later work van der Meer (1994) performed several simulations on a similar model with a higher resolution of 1200 grid points (20 x 60). Sensitivity to injection rate, permeability distribution and dip angle was assessed in different simulations. Pressure boundary conditions were also varied. In one set of simulations the down dip pressure was kept constant (simulating hydraulic communication with the surface water). In another set a partial pressure increase was included (simulating an aquifer with



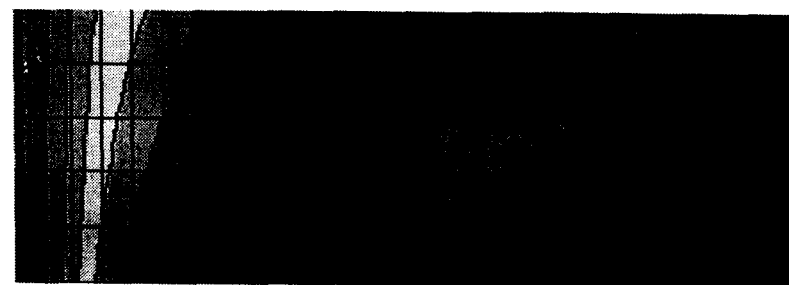
(a) after 5 years



(b) after 10 years



(c) after 20 years



(d) after 30 years

restricted communication with the surface). In the third set the full pressure increase due to injection into a sealed closure with no communication to the surface was applied. In such a case, the pressure increase will be determined only by the compressibility of the reservoir rock and the brine, as long as solubility of CO₂ in brine is ignored. The maximum allowed pressure increase, in this case up to the lithostatic pressure, will then determine the storage potential, and not the distribution of CO₂. The results showed that 1.7% of the pore volume could be utilised for disposal in this case. Results from the other

Figure 6.14 Comparison of Simulation Results.

two sets showed variation in the storage potential between 2.77 and 9.46% before correcting for the area sweep. The case with the doubled dip angle gave 15.71%. An areal sweep efficiency of 50% was assumed in these simulations, reducing the storage potentials above by half. Increased injection rate gave higher storage potential.

Holt, Jensen and Lindeberge (1994) simulated CO₂ injection into a dipping reservoir with large variations in horizontal permeability in its different layers. Pressure and temperature were set to 200 bars and 62C, respectively. CO₂ was injected through one well at the top of the reservoir.

The reservoir data were based on a real Norwegian offshore reservoir with 10° dip, consisting of a highly permeable sandstone with horizontal permeabilities typically in the range 100–2000 mD, with an average of 340 mD. The reservoir had three distinct zones with a highly permeable zone in the middle. The anisotropy is indicated by the ratios between average ratio between vertical and horizontal permeability for all grid blocks and the ratio between the average vertical and average horizontal permeability for all grid blocks:

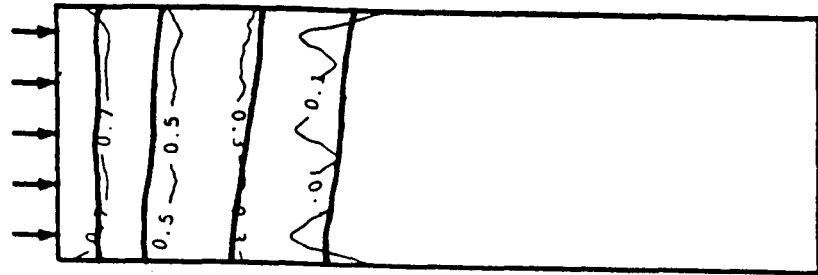
$$\left(\frac{k_{vert}}{k_{hor}}\right) = 0.02 \quad \frac{k_{vert}}{k_{hor}} = 0.045$$

and in more detail by the permeability distribution represented in the histogram in Figure 6.15.

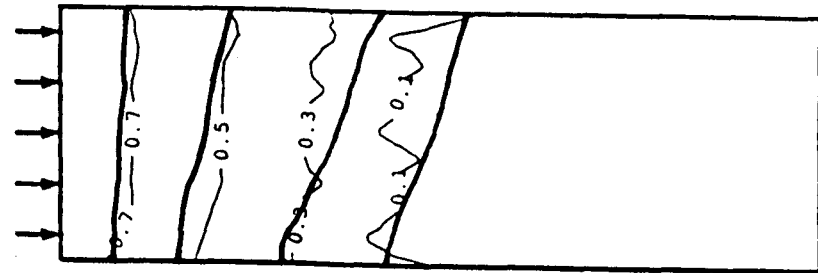
A three phase black oil simulator (Eclipse 100) was used, but since there was no possibility to include dissolution of gas in water in this simulator the “oil” phase was given the properties of the water phase and only two phases were used. In this way the solubility of water was included in the simulations. In the base case a 4800 grid point were used in three dimensional Cartesian model (12 × 10 × 40). The data for solubility of CO₂ in water were based on Enick and Klara (1990).

During the simulations the hydrostatic pressure gradient at the bottom end cross section was kept constant, and the injection was stopped when free CO₂ passed this plane. The relative permeability curves used are shown in Figure 6.15. Most of the data points are determined from core flood experiments where CO₂ displaced water in a 1.2 m core of Bentheimer sandstone at conditions corresponding to aquifer injection. Some of the data points are other IKU

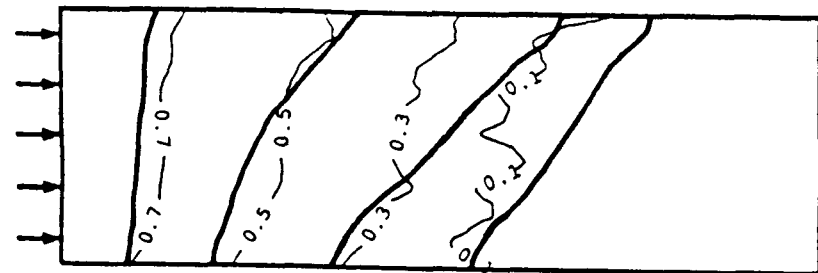
Petroleum Research measured gas and water relative permeabilities of the same rock, and are included based on



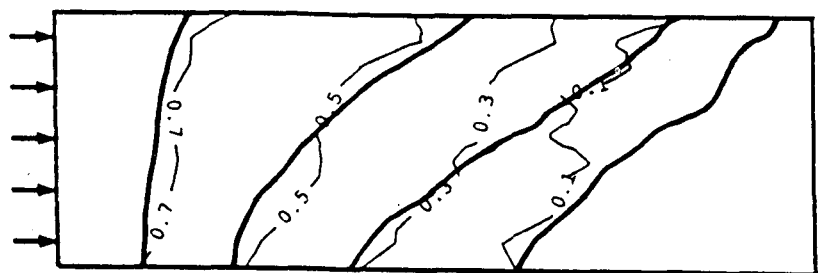
(a) after 5 years



(b) after 10 years



(c) after 20 years



(d) after 30 years

the assumption that these permeabilities are functions of own phase saturation only. A set of relative permeability data from a North Sea gas reservoir is also shown in the figure. This set was also used in the simulations for comparison.

In the base case simulation 1.6% PV/year or 3900 ton/day CO₂ was injected with the well perforated through all layers. The sensitivity to various process conditions and parameters was investigated, and the results are given in Figure 6.17 and Table 6.1. In the base case simulations the

Figure 6.15
Histogram of permeability distribution in horizontal and vertical direction.

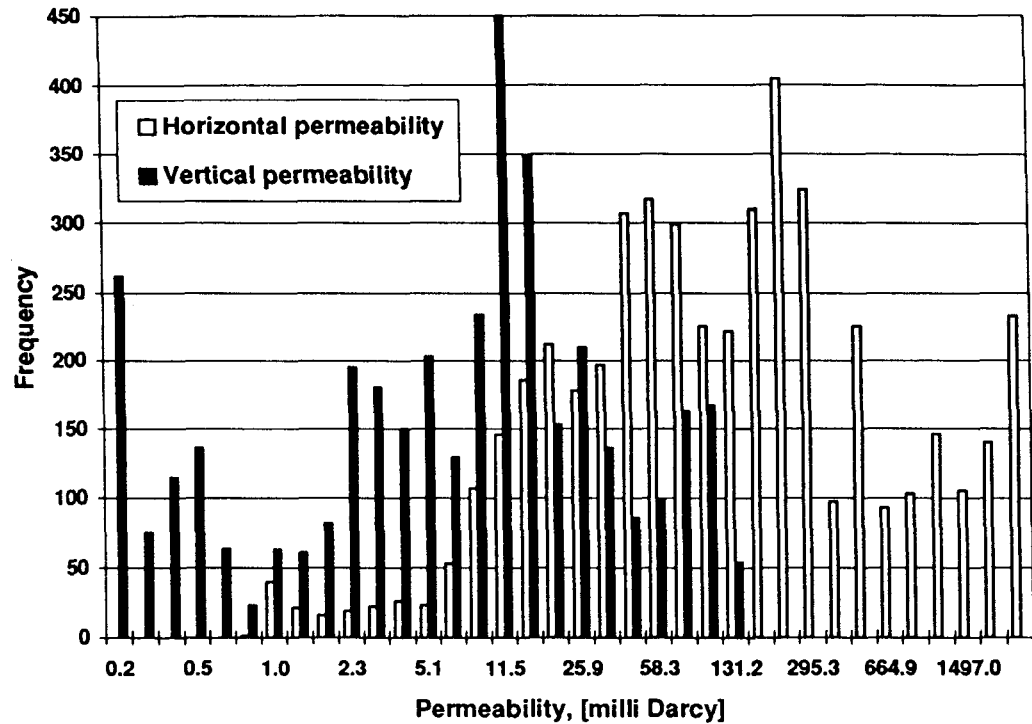


Figure 6.16 Relative permeability curves.

reservoir was divided into 4800 grid blocks, and the Bentheimer relative permeabilities were used.

As seen in Table 6.1 and Figure 6.17 the CO₂ storage capacity depends strongly on the injection rate. At high flow rates the displacement is dominated by viscous forces and CO₂ flows rapidly through the most permeable paths, and the storage capacity reaches a constant lower limit. At lower rates the flood becomes dominated by gravity forces. The displacement front becomes stabilised, and after-drainage of water increases the storage capacity further.

These results are in apparent contrast to the simulation results obtained by van der Meer (1994), reviewed above. He found the opposite relation; increased injection rate gave increased storage. This can, however, be explained by analysing the conditions for

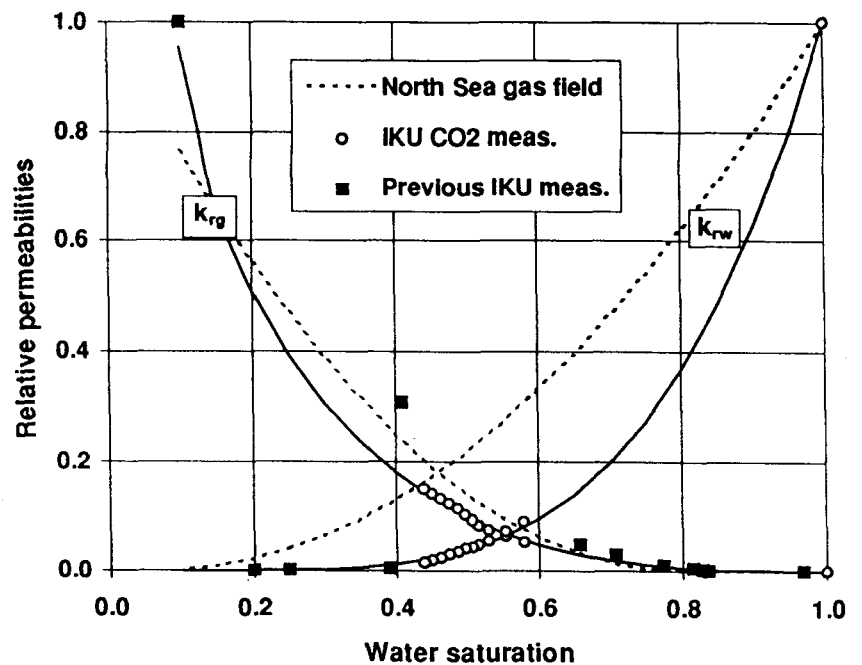
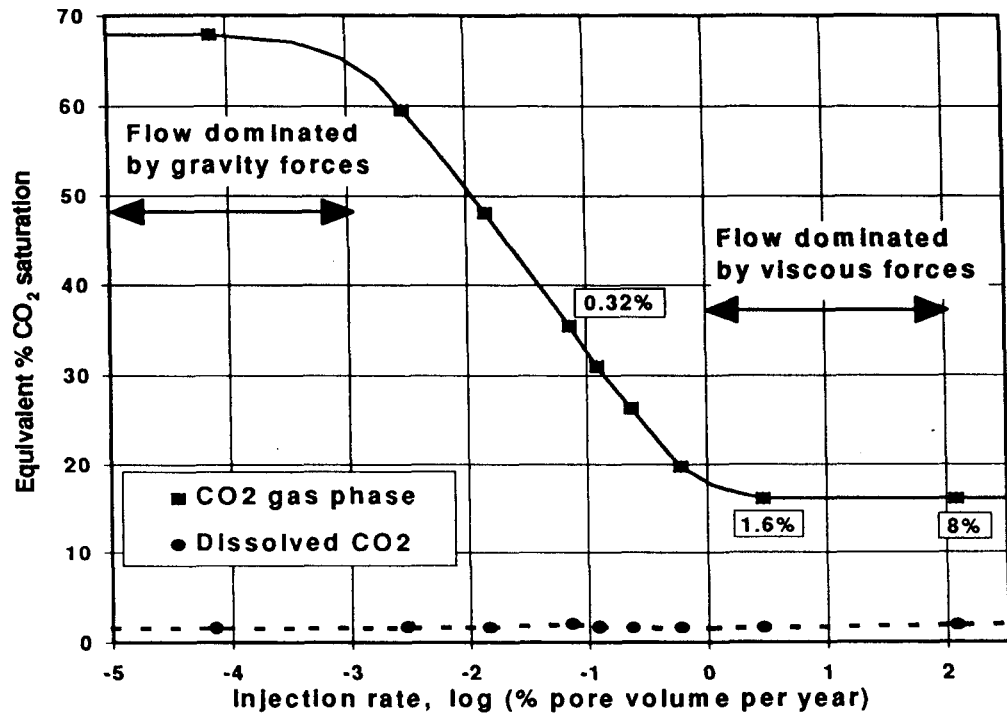


Table 6.1 Simulated CO₂ injection into aquifers.

Avg. perm.(mD)		Well perforation	CO ₂ stored (% PV)
kvertical	khorizontal		
15	340	all layers	16.1 ¹⁾
15	340	all layers	16.4 ²⁾
75	340	all layers	17.0
375	340	all layers	19.4
75	1700	all layers	26.1
15	340	all layers	12.9 ³⁾
15	340	top layer	18.8
15	340	bottom layer	17.4

1) base case
2) 13800 grid blocks
3) North Sea gas field rel.perm.

Figure 6.17 Storage capacity vs. injection rate.



the simulations. In van der Meer's almost horizontal aquifer the situation will correspond to the situation shown in the upper part of Figure 6.17. Increasing the injection rate will alter the flow regime towards the direction of stronger viscous flow and accordingly less gravity override (Figure 6.4). In the more dipping reservoir of Holt et al. (1994), the situation will almost reach the idealised situation shown in the lower part of Figure 6.17, when the rate gets low enough (gravity stabilised flow).

The CO₂ storage capacity is also sensitive to permeability. Well perforations had less influence on the storage capacity of CO₂. The CO₂ dissolved in brine is expressed in equivalent PV units in order to compare with the CO₂ stored as a free phase. The amounts of CO₂ dissolved are small compared to the total CO₂ stored as a free phase (3 to 11% of the total CO₂ injected).

6.5.4 Simulation of injection into large horizontal aquifers

Large, essentially horizontal reservoirs with only small variations in cap seal depth, constitute maybe the largest fraction of the total aquifers in the world, and are therefore also potentially the largest disposal site for CO₂.

Van der Meer (1994) simulated CO₂ injection into a quasi-infinite horizontal aquifer with a total thickness of 55 m. A model representing 30 × 30 km of the subsurface was constructed. The reservoir had a horizontal permeability of 200 mDarcy and a kv/kh ratio of 0.1. To simulate the quasi-infinity, an analytical infinite aquifer function was situated at the boundary of the model. 15 000 tonne CO₂/day was injected for 50 years followed by a shut-in period of 100 years. During the injection period the radius of the CO₂ bubble reached a diameter of 16 km, and grew to 18 km after the shut-in period. This corresponds to a storage efficiency of 9 volume % if wells are placed in a hexagonal pattern 18 km apart, and a porosity of 0.3 is assumed. Because of the similarities of the results obtained from the compositional simulation of Gunter et al. (1993) and its reproduction by van der Meer using an immiscible

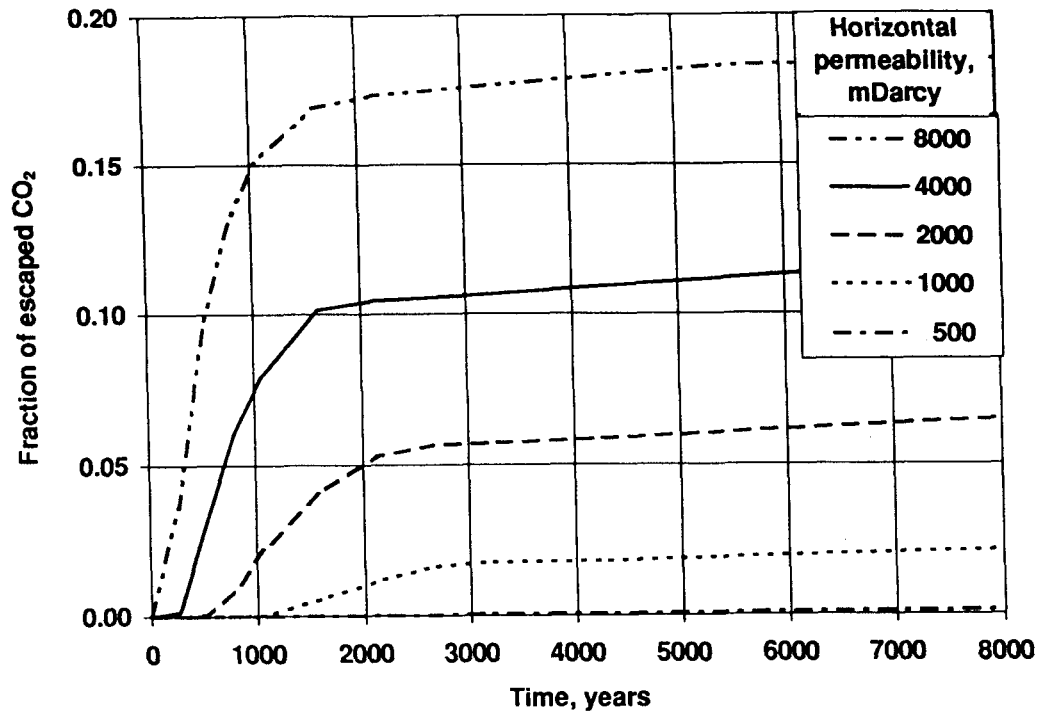
approach, an immiscible approach to the solubility of CO₂ in water was used.

Lindeberge (1995) also simulated CO₂ injection into a horizontal and large, but finite aquifer. The formation was 160 m thick and CO₂ was injected 8000 m from the boundary of the aquifer for a 25 year period at a rate of 15 000 tonnes/day. In the simulation, CO₂ accumulated under the seal over the reservoir brine, and after the injection period the CO₂ migrated slowly towards the edge of the aquifer. At the same time there was also a slow vertical diffusional and convectional transport of CO₂ bringing CO₂ into solution. It was assumed that any CO₂ reaching the boundary would escape into the atmosphere, and the result of the competing horizontal migration and vertical transport of CO₂ into the brine would determine how much and how fast CO₂ will escape from the reservoir.

The escape profiles were strongly dependent on the horizontal permeability as illustrated in Figure 6.18. After the injection period the migration path from the tip of the CO₂ tongue to the edge varied between 3000 and 4000 m in length. The different escape curves illustrate how the horizontal permeability affects the loss rate. At low permeabilities, below 1000 mD, the CO₂ reaches the edge after more than 1000 years and very little is lost because most of the CO₂ has already been dissolved in the aquifer during this period. A simulation with 250 mD horizontal permeability was also performed, and in this case the CO₂ never reached the boundary. For the higher permeabilities the CO₂ should probably be injected somewhat further away from the edge. In the worst case (8000 mD, 3000 m migration distance) approximately 17% of the injected CO₂ is lost during the first 2000 years while the rest remains in the reservoir as dissolved CO₂. The rapid migration period (2000 to 3000 years) is followed by a much slower transport of CO₂ out of the formation. This can be seen on the figure as the escape curves are not completely flat after 2000 to 3000 years. This transport is only due to diffusion and can probably be ignored from the perspective of contribution to climate change.

It must be emphasised that the term "Fraction lost" used in the graph does not refer the total amount CO₂ poten-

Figure 6.18 CO₂ escape curves from a horizontal aquifer when CO₂ is injected 8000 m from a spill boundary. The escape rate depends strongly on horizontal permeability. Vertical permeability is 200 mDarcy in all cases.



tially injected into the aquifer, but only to the loss from this borderline injector. If this is a large aquifer, there will be room for several injectors far from the border. The CO₂ injected in more remote wells will not be subject to spill as long as not more than 0.07 pore volume of CO₂ is injected — corresponding to the solubility of CO₂.

It can be concluded that CO₂ storage under large horizontal seals is a feasible concept even if the reservoir is in communication with the atmosphere at its boundary, particularly if injection takes place a long way from the boundary. If any anticlines exist on the otherwise horizontal cap rock surface, these will be filled, by gravity stable displacement, by migrating CO₂ up to the point of residual water saturation. This can give a large increase in the CO₂ disposal potential because the water will be drained down to its residual water saturation. This can give 60 to 90 volume % CO₂ saturation locally. Simulation with a small upward constant slope (1:1000) was also performed. This gave larger CO₂ loss, but did not alter the conclusion above.

In the Sleipner Vest gas field in the North Sea, one of the producing reservoirs contains hydrocarbon gas with up to 9% CO₂. This has to be removed to meet pipeline specifications before exporting the gas. The extracted CO₂ will be injected into the Utsira Formation, a thick, highly porous and permeable, essentially horizontal aquifer overlying the producing reservoirs. Injection will be at a rate of approximately 1 million tonnes/year for the life of the field, through a single well. Injection will start in the second half of 1996.

Korbøll and Kaddour (1994) simulated CO₂ injection into the Utsira Formation for the development of the Sleipner gas field. After injection of 1 million tonnes CO₂ per year for 20 years, the maximum extension of CO₂ in any direction in the layer with highest permeability was not more than 3000 m. In this particular aquifer the CO₂ swept area is almost negligible compared to the total area of the aquifer. In their (compositional) simulation, 18% of the injected CO₂ dissolved in the brine.

Wier et al. (1994) simulated CO₂ injection into a 3000 m thick fresh water aquifer at 2950 m depth. The aquifer was not a geological trap, but a continuous sand body reaching

all the way up to the surface. It was divided a lower zone consisting of a 100 m thick layer with 100 mD permeability and an upper 2900 m thick layer with 10 mD vertical permeability. This layer was in equilibrium with the atmosphere at the top. The two zones were separated by a shale layer with a permeability of 1 mD and porosity of 0.04. The simulation was based on Darcy's equation, including solubility of CO₂ in water, but diffusion was ignored and capillary pressure was set to zero. After injecting 31.5 million tons CO₂ over a ten year period the results showed that 12% of the CO₂ would escape into the atmosphere after 5000 years while the rest would be dissolved in approximately equal amounts in the upper and lower aquifer. This was the worst case scenario. If the permeabilities were chosen to allow the CO₂ to spread 1 km from the injection point laterally, all the injected CO₂ would dissolve completely during its migration towards the surface and no CO₂ would be lost.

It is questionable whether the capillary pressure should have been ignored in this simulation, and this is also mentioned by the authors. A 1 mD shale with a porosity of 0.04 would probably form an effective barrier due to large capillary forces and not allow any CO₂ to penetrate it as long as only buoyancy is the driving force. Also the simulation is something of a special case in that it involves injection into a thick fresh water aquifer. Most reservoirs contain saline formation water at depths of more than a few hundred metres.

On a slightly different topic, Koide et al (1992) attempted to estimate the world total underground storage potential for CO₂. They estimated that 1% of the volume of the world's sedimentary basins might be suitable for storing CO₂. For simplicity, they assumed the CO₂ would be trapped by dissolution in the formation water. In their calculations they assumed an average solubility of 41/kg CO₂/m³ formation water, and an average reservoir thickness of 300 m with 20% porosity. This gave a storage potential of 6.4% of the total pore volume. A 20% displacement efficiency was assumed. This reduced the storage potential to 1.3% of the total pore volume considered.

The advantage of such models is that they can easily provide estimates for storage potential in sedimentary basins. Similar methods have also been used by Hendriks et al. (1992) and Koide et al. (1993). However, it is difficult to estimate factors such as the average sweep efficiency and the percentage of the volume of the world's sedimentary basins which may be available for CO₂ storage. Although it may be possible to achieve a sweep efficiency of 20% in some injection projects, it is probably too high for a world average for CO₂. Furthermore, it is not realistic to assume that all the CO₂ will dissolve in the formation water with such a high displacement efficiency, so the presence of free CO₂ in a gas phase could not be ignored. To use a sweep efficiency to estimate the fraction of the reservoir being saturated does not reflect how non-miscible phases are flowing in a porous medium.

A refinement of this model to also include storage of free gas in anticlines was presented by Tanaka et al., 1994.

6.6 LITERATURE ON CO₂ INJECTION IN OIL AND GAS RESERVOIRS

E. Lindeberg

To improve oil recovery, CO₂ injection could either be applied instead of water injection (secondary production) or after water injection (tertiary production). Holt and Lindeberge (1993 and 1994) performed a laboratory study and field simulation on the performance of CO₂ injection compared to water injection. In this case they also tried to maximise both the oil recovery and the storage of CO₂.

A description of a Norwegian continental shelf oil reservoir was used in the study. The reservoir is a highly permeable sandstone with horizontal permeabilities typically in the range 100–2000 mD with an average permeability of 340 mD. The ratio between vertical and horizontal permeabilities is determined to be 0.004 as an average for all blocks, and to be 0.04 for the ratio of average vertical and average horizontal permeabilities. The reservoir has a dip of 10, and consists of three distinct zones with low permeability layers in between. While 43% of OOIP (original oil in place) could be recovered with water injection, 63% of OOIP could be recovered by injection of 0.75 hydrocarbon pore volumes of CO₂.

Most known oil fields have been, or are, under water flooding, either by water injection and/or by natural aquifers invading the oil zone during depletion. Tertiary gas injection is gas injection after water flooding. During this process large amounts of water will be co-produced with the recovered oil. In practical operations water is often injected with the gas, either to reduce gas mobility and improve volumetric sweep, or to minimise the volume of valuable injected gas. This may lower the storage potential as the gas saturation is reduced by water.

CO₂ is an attractive injection gas. This is demonstrated through a large number of field projects. Table 6.2 summarises the results of 25 US tertiary CO₂ injection projects (full field and pilots, terminated and ongoing). The performance of the ongoing projects is estimated by the operators.

Many of the projects are described by Brock and Bryan (1989) who give references to the original lit-

erature needed for the calculations performed here. Additional and/or newer data are given by Beliveau (1991), Burbank (1992), Davis (1994), Flanders and DePauw (1993), Stein et al. (1989) and Wackowski and Masoner (1994). The average incremental recovery of these projects is 13.2% of OOIP, and the average estimated disposal of CO₂ is 1080 Sm³/m³ stock tank oil. This agrees with data for some Canadian projects summarised by Todd and Grant (1993).

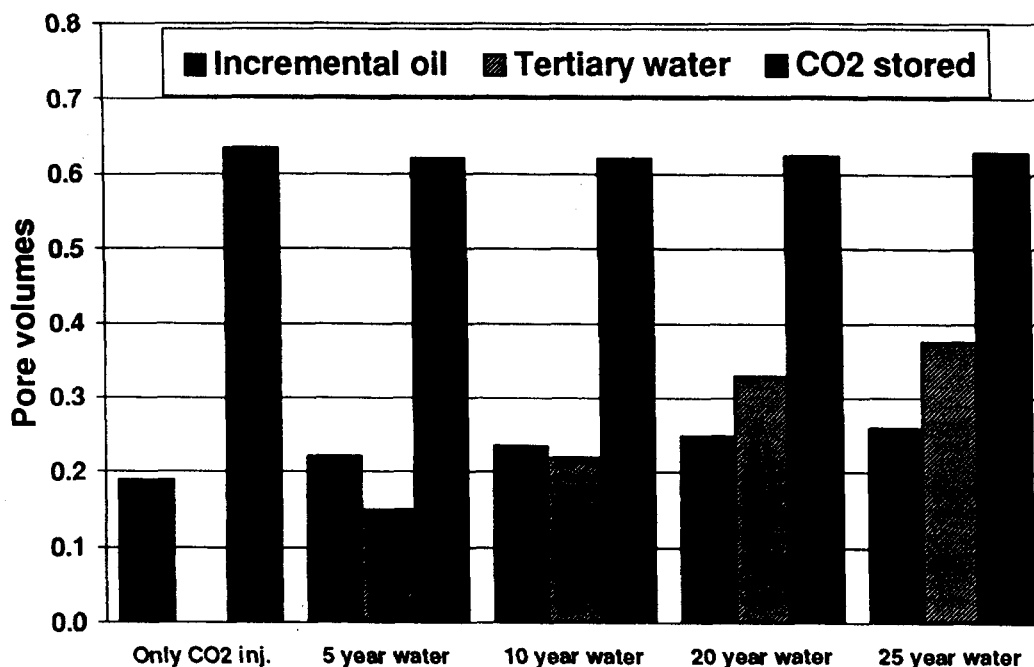
CO₂ disposed per volume of incremental oil is on average 2.3 reservoir m³/reservoir m³. This indicates a net reduction in the water saturation. The large amount of CO₂ stored is also due to oil recovered which is not defined as incremental. In the calculations underlying Table 6.2 it is assumed that all purchased CO₂ is retained in the reservoir, i.e. insignificant amounts are vented (if otherwise is not given). The figures above, taking into account that the connate water saturation typically is 20–30% pore volumes (PV), show that an amount of CO₂ corresponding to more than 20% of the reservoir PV is stored on average. Holt et al. (1994) used a similar reservoir to Holt and Lindeberge (1993 and 1994, see above) in the study of CO₂ injection after periods of water injection of variable lengths, using numerical simulations.

Various process combinations were simulated using a compositional reservoir simulator. These were 25 years of CO₂ injection and combinations of water and gas injection starting with 5, 10, 20 or 25 years of water followed by 25 years of CO₂. For all scenarios fluid was injected down dip with a reservoir rate corresponding to 3.8 volume % of OOIP per year. During CO₂ injection some of the layers had to be shut in due to restrictions on the produced gas/oil ratio (GOR). At the end of the simulations these layers were opened without restrictions on the GOR. Incremental oil is in the following defined as the oil produced at the end of the CO₂ injection minus the oil produced after 30 years of water-flooding (giving a final water cut of 90%).

Field	Incremental oil (%OOIP)	CO ₂ utilisation	
		MCF/STB	res. m ³ /res. m ³
Dollarhide	19	2.4	0.7
East Vacuum	8	6.3	2.1
Ford Geraldine	17	5	1.6
Means	7.1	11	4.5
Northeast Purdy	7.5	4.6	2.1
Rangely	6.8	2.4	0.9
Sacrock 17 patterns	7.5	6.5	2.0
Sacrock 4 patterns	9.8	3.2	1.0
S.Wasson Clearfork	10	—	—
South Welch	7.6	—	—
Twofreds-East	15.8	8	2.8
Wertz	10	10	4.5
Garber	14	6	2.5
Little Creek	21	12.6	4.7
Maljamar	13	8.4	2.5
Midale	20	3	—
North Coles Levee	21	—	—
Port Neches	19	—	—
Quarantine Bay	14.7	1.8	0.7
Rock Creek	7	7.1	2.1
Slaughter Estate	19.6	—	—
Weeks Island	19	3.3	1.0
West Sussex	8	10.3	3.8
Lick Creek	13.3	2.8	1.7
Wilmington	14	—	—

Table 6.2 Summary of 25 US CO₂ field projects.

Figure 6.19
Incremental oil,
produced water and
stored CO₂ in five
different water/CO₂
injection scenarios.



The results of the simulations are given in Figure 6.19. It is seen that all the process combinations involving CO₂ resulted in almost the same amount of stored CO₂ in the reservoir, approximately 63% hydrocarbon pore volume (HCPV). This corresponds to 66% of the injected CO₂. The amounts of incremental oil produced are slightly sensitive to the process combinations. With a recovery of 47.2% HCPV after 30 years of water injection, the total recovery of oil at the end of the processes varies from 69.3 to 73.1% of OOIP. These high oil recoveries indicate a favourable reservoir for CO₂ injection. The 63% HCPV of CO₂ stored corresponds to 50% PV, which is higher than the corresponding US reservoir values. The reason for this is the high oil recoveries, and most importantly, that CO₂ is not followed by water for the process combinations simulated in this study.

6.7 CONCLUSION AND RECOMMENDATIONS

E Lindeberg, L G H van der Meer

6.7.1 CO₂ disposal in aquifers

The CO₂ disposal capacity for a given aquifer formation can be predicted from simulation if sufficient reservoir information is available. From such predictions, the disposal capacity can be optimised and specially suitable aquifers can be selected. Depending on injection rate, injection point and reservoir properties, there will be strong variations in how much CO₂ that can be stored in an aquifer.

Much of the literature gives storage capacity as the fractional pore volume filled with CO₂. This is, however, an ambiguous parameter because some of the CO₂ will be in the free gas phase and some will be dissolved in the water. The amount of CO₂ stored is also a function of temperature and pressure. It is suggested that in the future the CO₂ storage capacities in aquifers are given as the average CO₂ density (kg CO₂/m³ pore volume).

Dipping reservoirs forming buoyancy traps due to faults or anticlines are well defined disposal sites for large scale CO₂ injection projects. Disposal capacities of 14 to 420 kg CO₂/m³ have been reported. For a given reservoir the dis-

posal potential is strongly dependent on the reservoir properties, dip angle and injection rate. Therefore it is difficult to give a typical value for this type of reservoir. It is recommended to use values in the range of 14 to 120 kg CO₂/m³ (2 to 17% on volume basis) for projects of practical size.

Horizontal reservoirs are likely, because of their abundance and large volumes, to be the most important disposal sites for CO₂. If they do not have a confining seal at their periphery, some of the CO₂ may eventually escape if the cap rock is perfectly horizontal or has a small upward dip towards a spill point. If injection too close to the periphery is avoided, these reservoirs can, however, be considered as permanent disposal sites in the perspective of a climate change. Even the smallest anticline on the cap rock under-surface would form a buoyancy trap which would be filled with CO₂. An estimate for the disposal potential in these reservoirs is 40 kg CO₂/m³ (or 6 volume %).

Reservoirs completely confined by seals can also be used for disposal. The disposal potential will be limited by the mechanical stability of the rock. 14 kg CO₂/m³ (or 2% on volume basis) can be expected if a pressure increase of 100 bar can be accepted.

The results are summarised in Table 6.3.

6.7.2 CO₂ injection in oil reservoirs

If the objective for a CO₂ injection project is both to improve oil recovery and to optimise CO₂ storage, the storage potential can be significantly larger than seen in CO₂ field projects where only high oil recovery and high utilisation was a target.

In a secondary injection project, the reservoir volume of stored CO₂ will closely correspond to the reservoir volume of total oil produced in the field.

In a tertiary injection process, CO₂ will displace significant amounts of both oil and water giving a large storage capacity for CO₂. As a simple rule, the total storage potential of CO₂ measured in reservoir volume is equal to the sum of the reservoir volume of oil produced during water flooding and tertiary CO₂ flooding.

Table 6.3 Disposal capacities in various aquifers recommended for use in screening estimates when detailed reservoir information is not available.

Aquifer type	Disposal potential		Comments
	kg CO ₂ /m ³	vol. %	
Dipping with spill point	14–120	2–17	depends on injection rate and dip angle
Large horizontal cap seal	40	6	depends on permeability
Fractured	40	6	solubility and diffusion controlled
Confined (closure)	14	2	depends on allowed pressure increase

6.8 REFERENCES

- BELIVEAU, D, and PAYNE, D A. 1991. Analysis of a Tertiary CO₂ Flood Pilot in a Naturally Fractured Reservoir. *Paper SPE 22947*, presented at the 66th Ann. Tech. Conf. and Exhib., Dallas, TX, October 6–9.
- BROCK, W R, and BRYAN, L A. 1989. Summary Results of CO₂ EOR Field Tests, 1972–1987. *Paper SPE 18977*, presented at the SPE Joint Rocky Mountain Regional/Low Permeability Reservoirs Symposium and Exhibition, Denver, Colorado, March 6–8.
- BURBANK, D E. 1992. Early CO₂ Flood Experience at the South Wasson Clearfork Unit. *Paper SPE/DOE 24160*, presented at the SPE/DOE 8th Symp. on Enhanced Oil Recovery, Tulsa, Oklahoma, April 22–24.
- CHRISTIE, M A, and BOND, D J. 1987. "Detailed Simulation of Unstable Processes in Miscible Flooding," *SPE/ERE (Nov. 1987)*, 514; *Trans., AIME*, 283.
- CRAIG, F F. 1971. *The Reservoir Engineering Aspects of waterflooding*. Monograph Vol. 3 of the Henry L Doherty Series, SPE, New York, 45–47.
- DAVIS, D W. 1994. Project Design of a CO₂ Miscible Flood in a Waterflooded Sandstone Reservoir. *Paper SPE/DOE 27758*, presented at the SPE/DOE 9th Symp. on Improved Oil Recovery, Tulsa, Oklahoma, April 17–20.
- ENICK, R M, and KLARA, S M. 1990. CO₂ Solubility in Water and Brine under Reservoir Conditions. *Chem. Eng. Comm.*, 90, 23–33.
- FAYERS, F J. 1988. "An Approximate Model With Physically Interpretable Parameters for Representing Miscible Viscous Fingering," *SPE/ERE (May 1988)*, 551.
- FLANDERS, W A, and DEPAUW, R M. 1993. Update Case History: Performance of the Twofreds Tertiary CO₂ Project. *Paper SPE 26614*, presented at the 68th Ann. Tech. Conf. and Exhib. of the Society of Petroleum Engineers, Houston, Texas, October 3–6.
- GUNTER, W D. et al.. 1993. "Aquifer Disposal of CO₂-Rich Gases", Alberta Research Council, March 1993, Report No.: C-1993-5.
- HOLT, T, JENSEN, J.-I, and LINDBERG, E. 1994. Underground Storage of CO₂ in Aquifers and Oil Reservoirs. Paper presented at ICCDR-2, October, Kyoto, Japan.
- HOLT, T, and LINDBERG, E. 1992. Thermal Power — Without Greenhouse Gases and with Improved Oil Recovery. *Energy Convers. Mgmt.*, Vol. 33, No. 5-8, 595–602.
- HOLT, T, and LINDBERG, E. 1993. CO₂ from Industrial Sources as Injection Gas in Oil Reservoirs. *Energy Convers. Mgmt.*, Vol. 34, No. 9-11, 1189–1196.
- KING, M J, BLUNT, M J, MANSFIELD, M, and CHRISTIE, M A. 1993. "Rapid Evaluation of the impact of Heterogeneity on Miscible Gas Injection," Paper presented at the 7th European IOR Symposium in Moscow, Russia, (Oct. 27–29, 1993).
- KOVAL, E J. 1963. "A Method for predicting the Performance of Unstable Miscible Displacement in Heterogeneous Media," *SPEJ (June 1963)*, 145; *Trans. AIME*, 228.
- LINDBERG, E. 1995. Escape of CO₂ from large horizontal aquifers confined only by a cap seal. Paper to be presented at the conference "Greenhouse Gases: Mitigation Options", August, London.
- LINDBERG, E, and HOLT, T. 1994. EOR by Miscible CO₂ Injection in the North Sea. *Paper SPE 27767*, presented at the SPE/DOE Ninth Symposium on Improved Oil Recovery, April 17–20, Tulsa, Oklahoma.
- NUMBERE, D, BRIGHAM, W E, and STANDING, M B. 1977. *Correlations for Physical Properties of Petroleum Reservoir Brines*, Petroleum Research Institute, Stanford University, November. p.8.
- STEIN, M H, FREY, D D, WALKER, R D, and PARIANI, G J. 1989. The Slaughter Estate Unit CO₂ Flood: A Comparison Between Pilot and Field-Scale Performance. *Paper SPE 19375*, presented at the SPE Production Technology Symposium, Lubbock, Texas, November 13–14.
- TANAKA, S, KOIDE, H, and SASAGAWA, A. 1994. Possibility of Underground CO₂ Sequestration in Japan. Paper presented at ICCDR-2, October, Kyoto, Japan.
- TCHELEPI, H A. 1994. "Viscous Fingering, Gravity Segregation and Permeability Heterogeneity in Two-Dimensional and Three-Dimensional Flow," Phd dissertation, Stanford University (March 1994).
- TODD, M R, and GRANT, G W. 1993. Enhanced Oil Recovery Using Carbon Dioxide. *Energy Convers. Mgmt.*, Vol. 34, 1157–1164.
- TODD, M R, and LONGSTAFF, W J. 1972. "The Development, Testing, and Application of a Numerical Simulator for Predicting Miscible Flood Performance," *JPT (July 1972)*, 874; *Trans. AIME*, 253.
- VAN DER MEER, L G H. 1992. Investigations Regarding the Storage of Carbon Dioxide in Aquifers in the Netherlands. *Energy Convers. Mgmt.*, Vol. 34, 611–618.
- VAN DER MEER, L G H. 1993. The Conditions Limiting CO₂ Storage in Aquifers. *Energy Convers. Mgmt.*, Vol. 34, 959–966.
- VAN DER MEER, L G H. 1995. The CO₂ Storage Efficiency of Aquifers. *Energy Convers. Mgmt.*, Vol. 36, No. 6-9, 513–518.
- WACKOWSKI, R K, and MASONER, L O. 1994. Rangely Weber Sand Unit CO₂ Project Update: Operating History. *Paper SPE/DOE 27755*, presented at the SPE/DOE 9th Symp. on Improved Oil Recovery, Tulsa, Oklahoma, 17–20 April.
- WEIR, G J, WHITE, S P, and KISSLING, W M. 1994. Reservoir Storage and Containment of Greenhouse Gases. Paper presented at ICCDR-2, October, Kyoto, Japan.

CHAPTER 7

Area 5 Inorganic Geochemistry

Isabelle Czernichowski-Lauriol, Bernard Sanjuan (BRGM — Orleans, France)

Chris Rochelle, Keith Bateman, Jonathan Pearce, Paul Blackwell (BGS — Keyworth, United Kingdom)

7.1 INTRODUCTION

The objective of Area 5 was to analyse the geochemical aspects of the underground disposal of CO₂ and to assess whether the chemical reactions between CO₂, formation water and rock can enhance the storage capacity or should guide the design of the storage operations.

Unlike methane, which is commonly stored underground as a gas engineering practise, CO₂ is an acidic reactive gas which will partially dissolve in water and cause mineral dissolution and precipitation, resulting in porosity-permeability variations. Depending on the nature and the scale of the chemical reactions, the reservoir-CO₂ interactions may have significant consequences on the CO₂ storage capacity, on the injection process, on fluid flow through the reservoir and on safety and stability aspects.

Work in Area 5 was structured round three different and complementary approaches. The first was an extensive literature review of natural and man made CO₂ occurrences, such as: natural CO₂ accumulations in sedimentary basins, enhanced oil recovery by CO₂ injection, natural gas storage, diagenesis linked to CO₂ generation by decarboxylation of organic matter, ore generation and metal transport by CO₂, and the use of supercritical (SC) CO₂ in chemical processing. The second approach consisted of laboratory experiments using potential reservoir rocks and caprocks, in order to study the mechanisms and rates of water-rock-CO₂ reactions. The third approach was numerical modelling which was used to interpret experiments and give reservoir-wide predictions. The following paragraphs detail the methods and results for these three approaches and try to combine them to give a good assessment of the consequences of CO₂ reactivity within a host formation.

However, as emphasized in research area 2 (Chapter 4) concerning calculation of storage capacity in Europe, only general trends can be given. This is because the chemical reactions that can take place in any host formation will be highly reservoir specific, and will depend on the mineralogy and texture of the rock, the temperature and pressure in the reservoir, flow rates and the timing of the reactions.

7.2 LITERATURE REVIEW OF THE INORGANIC GEOCHEMICAL ASPECTS OF THE UNDERGROUND DISPOSAL OF CARBON DIOXIDE

An extensive literature review has been carried out in order to highlight the chemical processes that are expected to occur and to focus the experimental and modelling studies on problems perceived to be of major importance. A comprehensive report is included in the first JOULE II interim report (Holloway et al., 1993).

7.2.1 Studies of enhanced oil recovery by CO₂ injection

During the 1980s, carbon dioxide injection became an important technique in the petroleum industry's tertiary

recovery effort. However, there is little in the literature regarding the effects of CO₂ injection on reservoir rocks. Of the few relevant studies, reduced injectivity has been observed in some reservoirs (Ross et al., 1982) and concern about the possible increased scaling tendency of the produced water (Bowker and Shuler, 1991) has led some scientists to study the inorganic geochemical aspects of CO₂-reservoir interactions. These were studied by means of core-flood experiments and analyses of changing brine chemistry at the wellheads of production wells. However, only the fate of carbonate minerals was examined, although Bowker and Shuler (1991) recognized that the changes in water composition could be a consequence of the alteration of other minerals (e.g. feldspars and clays) beside carbonates. In these previous studies the sandstone samples used for experiments were chosen for their high carbonate content (>10%).

For carbonate reservoirs, various experiments have shown that CO₂ injection can cause an increase in permeability due to the dissolution of carbonate minerals. Ross et al. (1981) briefly described an experiment with a limestone core sample where carbonated water was injected at a temperature of 80°C and pressure of 100 bars. Holm (1959) reports experiments where supercritical CO₂, followed by carbonated water, were injected through cores saturated with oil, in the pressure range of 62 to 180 bars and temperature range of 35° to 74°C. Although the objective of these experiments was to evaluate the oil recovery efficiency of the process, he noted that permeability was enhanced and that in field application, this would occur in the immediate vicinity of the injection wells. More recent experiments by Omole and Osoba (1983) were conducted on dolomite rocks at pressures varying from 70 to 172 bars while the temperature was maintained at 27°C. They confirmed the previous experimental results but showed that reduction in permeability by carbonate precipitation occurred when the pressure drawdown across the core was significant. This was because the solubility in water of both CO₂ and calcite decreases with decreasing pressure. They concluded that CO₂ injection would dissolve carbonate rocks and increase permeability near the injection well, but that carbonate minerals would precipitate along the flow path as the pressure reduced, resulting in a decrease in permeability. Pressure drawdown between injection and production wells should not be excessive to avoid problems during CO₂ flooding of carbonate reservoirs.

For sandstone reservoirs, there is no consensus on the effect of CO₂ injection on reservoir rocks. Previous laboratory experiments and field studies have shown that increases or decreases in permeability and injectivity were recorded. The response of the reservoir to CO₂ injection was found to be highly dependent on the mineralogical and textural properties of the sandstone. The quartz-carbonate sandstones studied by Ross et al. (1981, 1982) had a behaviour similar to that of carbonate rocks. Carbonate dissolution leads to an increase in permeability and

injectivity. For typical sandstones containing quartz, feldspars, clays and carbonates considered by Sayegh et al. (1990) and Bowker and Shuler (1991), permeability and injectivity are either reduced or unchanged. This was attributed to competition between two antagonistic effects; enhancement of permeability along preferential bands of more poorly cemented rock through the dissolution of carbonate cements, and reduction of permeability because of the migration of fines. Unfortunately, the behaviour of aluminosilicate minerals was not studied, whereas their dissolution, suspected by Bowker and Shuler (1991) during field tests, could have an effect on a wide range of mineralogical reactions.

Therefore, in general, evidence from enhanced oil recovery shows that the effect of CO₂ flooding on the mineralogical and petrophysical properties of the reservoir will depend on many factors such as, rock mineralogy, rock texture, flow rate, reservoir temperature and pressure, timing of mineral reactions, etc. Sayegh et al. (1990) conclude that the net effect of these factors will be reservoir specific, and possibly site specific within a single reservoir depending on its heterogeneities.

7.2.2 Studies of Diagenesis Linked to Thermal Maturation of Organic Matter

Useful information can be obtained from previous studies on the diagenesis of oil-bearing sedimentary basins, where thermal decarboxylation of kerogen between 80 and 140°C has generated CO₂. Fluids can then become enriched in carbon dioxide and, under specific hydrologic conditions, may even achieve saturation with CO₂ in the case of geopressured sediments (Capuano, 1990). The subsequent effects of CO₂-rich fluids on reservoir rocks have been discussed at length because of their controversial role in the development of secondary porosity in sandstone reservoirs. In many basins this is the dominant type of porosity (e.g. Lundegard and Land, 1986), and study of the characteristic suite of authigenic mineral assemblages could be a useful petroleum-exploration guide by providing information on fluid flow during petroleum generation (Capuano, 1990).

In the past, conventional wisdom held that secondary porosity in sandstones was caused by carbonic acid dissolution of feldspars and carbonate minerals (e.g. Schmidt and McDonald, 1979). Initially, it may be thought that increased CO₂ concentration would cause a decrease in pH, that in turn results in the dissolution of carbonates. However, in clastic reservoirs, the pH is not controlled by carbonate species but by aluminosilicate equilibria. With the pH thus fixed independently, increased CO₂ concentration cannot result in decreased pH, but must result in elimination of excess CO₂ by carbonate precipitation (Smith and Ehrenberg, 1989).

Capuano (1990) also noted that the CO₂ enrichment of geopressured fluids led to feldspar dissolution and kaolinite-carbonate precipitation. This author also pointed out that once the source of CO₂ is exhausted, continued burial of the sediments results in continued feldspar dissolution and increase in pH. This would shift the solution equilibrium towards illite, and ultimately albite saturation, resulting in illite-carbonate and albite-carbonate precipitation. Smith and Ehrenberg (1989) noted that at temperatures higher than 110–140°C, kaolinite becomes unstable and is replaced by illite, or illite and chlorite. The porewater pH is then controlled by equilibria between mineral pairs such as feldspar-illite, kaolinite-illite or kaolinite-chlorite.

McGowan and Surdam (1990) have suggested that carboxylic acid anions, resulting from the thermal maturation of kerogen between 80 and 140°C, may be abundant in some formation waters and can also buffer the pH, thus participating in the control of carbonate mineral stability. The conclusion that addition of CO₂ to silicate-buffered or carboxylic-buffered formation waters will, in general, cause precipitation of carbonates is now shared by various authors, among them Smith and Ehrenberg (1989), Capuano (1990) and McGowan and Surdam (1990). This compares favorably with observed relationships in hydrocarbon reservoirs.

Smith and Ehrenberg (1989) concluded that the CO₂ partial pressure versus temperature correlation in clastic hydrocarbon reservoirs from the US Gulf Coast and from the Norwegian continental shelf, was the result of inorganic chemical equilibria between feldspar, clay and carbonate minerals. Lundegard and Land (1986) reported that in sandstones from the Texas Gulf, petrographic observations show authigenic kaolinite, sometimes filling secondary pores, and occurrences of undissolved calcite adjacent to skeletal feldspars. Capuano (1990) reported observed alteration assemblages in the kerogen-rich geopressured sediments of the Frio Formation from the Texas Gulf Coast, which were first studied by Loucks et al. (1984) and Milliken et al. (1981). The precipitation of carbonates during and after the development of secondary porosity has been described by Loucks et al. (1984). This would support the idea of carbonate mineral precipitation as a result of feldspar dissolution by CO₂-rich fluids. The association of this zone of secondary porosity with hydrocarbon maturation and the production of CO₂ has been well established (e.g. Siebert et al., 1984; Franks and Forester, 1984). Kaolinite precipitation, albitization and smectite/illite transition have all been associated with the development of this zone (Capuano, 1990).

7.2.3 Natural Occurrences of Carbon Dioxide

Natural occurrences of large amounts of high purity CO₂ (>90%) are found in many parts of the world, e.g. in the United States, South Australia, Libya, Hungary, Turkey, Japan, China, Germany, Norway, Canada and southeast British Columbia. They originate from igneous emanations (volcanic activity) and/or subsequent thermal metamorphism of intruded carbonate rocks (Farmer, 1965; Studlick et al., 1990). These accumulations are generally found in deep formations, in both carbonate and sandstone reservoirs.

Most of the natural accumulations of CO₂ in the United States were discovered while searching for natural gas or oil. They are the main source of CO₂ used for flooding oil reservoirs in enhanced oil recovery processes (Angino, 1984; Mathews, 1989; Bondor, 1992). Advantages of the underground reservoirs include their high purity, and large volume. This explains the recent interest in this type of natural accumulation.

Unfortunately, few detailed mineralogical and chemical studies on natural CO₂ fields have been carried out. As far as the authors of this paper are aware, there are no comparative studies between the mineralogy of CO₂ reservoir rocks and parts of the same formation unaffected by CO₂. The most detailed description comes from the study by Studlick et al. (1990) on the geopressured carbon dioxide accumulation in the Norphlet formation of Pisgah Anticline (Central Mississippi). The reservoir temperature was not specified but must be near to, or greater than,

130°C, while the depth was about 5000 m. Dissolution of feldspars and precipitation of clays (kaolinite or illite), quartz and carbonates have been observed throughout the Norphlet formation both onshore and in the Gulf of Mexico. The sediments had excellent original primary porosity, estimated at 40–45%, but the average porosity is now 12%. The majority of reduction in porosity and permeability is related to pervasive fibrous illite that completely fills some pores and porethroats. Studlick et al. (1990) conclude that the most important variable controlling reservoir quality and productivity is diagenetic alteration of sandstone fabrics and that the main reason for vertical zonation in reservoir quality is the presence of locally pervasive illite. However, the introduction of CO₂ into the Pisgah anticline did not directly result in extensive clay precipitation, since illite and chlorite also occur in most of the Norphlet which has not been subjected to CO₂ migration.

Formation water analyses are available for only two CO₂ occurrences: the Caroline field in south Australia (Mulready, 1977), and the Isobe-Machi field in Japan (Motojima, 1957). The waters are enriched in bicarbonate and sodium, and contain traces of calcium, magnesium and sulfate.

Natural accumulations prove that CO₂ is stable and can be trapped in aquifers over geological periods of time. In the case of the Pisgah Anticline, the geopressed high purity CO₂ originated through thermal metamorphism of Jurassic carbonates by the Jackson Dome igneous intrusion, which probably occurred during the Late Cretaceous.

Further investigations on natural CO₂ accumulations would be highly relevant as analogues for CO₂ disposal. For this reason, it was decided to conduct a more detailed study on one of the CO₂ fields, the Bravo Dome field in New Mexico. This study is presented in section 7.5.

7.2.4 Studies of Ore Generation and Metal Transport by CO₂

Investigations into the role of CO₂-rich fluids in hydrothermal mineralisation and the formation of economic mineral deposits provide considerable evidence for the mobilisation and transport of trace metals such as Pb, Zn, Au, Pt, Pd, Ni and Hg (Kay and Strong, 1983; Haynes and Kesler, 1986; Hennem et al., 1988). Mobilisation occurs as a result of the formation of bicarbonate and possibly thio-carbonate complexes. The formation of such complexes may allow the extensive transport of heavy metals. Such transport may be relatively fast in a CO₂ disposal reservoir due to the rapid fingering of CO₂-rich fluids along more permeable pathways. Deposition of these base metals appears to occur predominantly as a result of CO₂ degassing. Hence the CO₂-rich front in a disposal reservoir may be a site of heavy metal precipitation.

Mobilisation of trace metals can also result from the well-known solvent properties of SC CO₂ with respect to bitumens, which are rich in such elements. For example, many studies have identified the important role of bitumen in the formation of certain uranium deposits (e.g. Curiale et al., 1983; Parnell, 1985; Parnell and Eakin, 1987; Parnell and Eakin, 1989), and Hg and Au deposits (Peabody and Einaudi, 1992; Gize and Macdonald, 1993). Residual oils within a disposal reservoir could thus be a readily available source of trace elements.

The solvent properties of SC CO₂ are widely used in analytical chemistry and process chemical engineering (Williams, 1981; McHugh and Krukoni, 1986; Haw-

thorne, 1990; Wenclawiak, 1992). Compared to liquid solvents SC CO₂ has similar solvating strength, but there are two other properties which have distinct advantages in chemical applications:

- i) SC CO₂ has diffusivities an order of magnitude higher than liquid solvents and viscosities an order of magnitude lower giving much better mass transfer capabilities. This results in very fast extraction of target compounds typically 10-60 minutes compared to several hours or even days using conventional methods.
- ii) The solvent strength of liquid solvents is essentially fixed, but the solvent strength of SC CO₂ can be changed by altering temperature and pressure. Using this control, extraction can be optimised for a particular class of compounds.

Although the phase behaviour and solubility of different compounds in SC CO₂ can be predicted, or if necessary measured, the actual behaviour of SC CO₂ in natural systems is highly dependent on the matrix with which the SC CO₂ is interacting (Wenclawiak, 1992). The general theme of many previous studies is that the effects of matrix interaction cannot be predicted accurately, and in order to characterise them accurately, experiments using the specific matrix under study must be made. There is also some dispute as to whether the solvent properties of SC CO₂ are enhanced or reduced in the presence of water. Although water is only soluble to approximately 0.1% in SC CO₂ (Hedrick and Taylor, 1990), it can greatly effect the apparent solvent strength.

7.2.5 Discussion

Disposing of carbon dioxide underground seems to be a valid concept, as:

- (i) natural accumulations prove that CO₂ is stable and can be trapped in aquifers over geological periods of time,
- (ii) gas storage, although concerning natural gas, is a common engineering practise,
- (iii) injection of supercritical CO₂ into oil reservoirs is a technique used for enhanced oil recovery.

The technical feasibility of the underground disposal of carbon dioxide will depend on the chemical reactions that occur between formation water, minerals and supercritical CO₂. Although these reactions will be highly reservoir specific, general trends can be drawn for carbonate and sandstone reservoirs guided by the review above.

Injection of CO₂ into a carbonate reservoir will lead to the dissolution of carbonate minerals. Gunter et al. (1993a) have calculated that, for a closed carbonate aquifer system, reaction between mineralogy and formation water does not significantly increase CO₂ uptake. However, when considering the dynamics of the storage process, the behaviour of carbonate reservoirs is likely to be more complex. In the vicinity of the injection wells, carbonate minerals will dissolve and the formation water will become saturated with respect to these. As the formation water moves away from the injection wells, carbonate minerals could precipitate as the pressure is reduced, or if the temperature is

increased. Thus porosity and permeability should be enhanced in the vicinity of the injection wells, but could be farther altered by precipitation of carbonates due to local variations of pressure and temperature in the reservoir. Temperature and pressure are thus crucial parameters to monitor in order to optimize the storage process in a carbonate reservoir, especially as the kinetics of carbonate mineral dissolution and precipitation are relatively fast compared to silicate minerals.

Injection of CO₂ into a sandstone reservoir will cause dissolution of feldspars and subsequent precipitation of clays, carbonates and quartz (or another silica phase). Where CO₂ leaching is the most intense, i.e. in the central storage zone or within fingers of CO₂-rich fluids moving along more permeable pathways, the clays would consist of kaolinite. However, they would consist of illite or chlorite if the temperature was above 110–140°C or where leaching was less intense, i.e. at the edges of the storage zone or between the CO₂-rich fingers. Albite could also precipitate instead of clay where leaching is less intense. The expected precipitation of carbonates, resulting from a complex set of mineral reactions, led Gunter et al. (1993a) to the conclusion that sandstone aquifers containing basic silicate minerals could absorb more CO₂ than other aquifers. Observations of natural CO₂ reservoirs (e.g. Bravo Dome field) indicate that a decrease in permeability may result from these mineral transformations, due to the formation of authigenic minerals. It should be stressed however, that diagenetic alteration caused by CO₂ migration into natural reservoirs has not been studied in detail and reactions have only been inferred on the basis of very limited data. Little information can be learnt from many previous core-flood experiments in enhanced oil recovery studies because the samples were especially chosen for their high carbonate content and low, or zero, feldspar content. As a consequence, carbonates had a dominant effect on the CO₂-water-rock interactions. However, the experiments reported by Bowker and Shuler (1991) on CO₂-flooding provide interesting information as the samples contained equal amounts of feldspars and carbonates (about 10%). They observed that carbonate minerals dissolved along channels, corresponding to preferential bands of more poorly cemented rock. Therefore, depending on the rock texture and mineral kinetics, carbonate minerals may tend to dissolve initially, either in the vicinity of the injection well, or locally in the reservoir.

The underground storage of CO₂ may result in the mobilization of trace elements from residual oils or heavy minerals encountered in the reservoir, due to the complexing power of bicarbonate and thiocarbonate and to the solvent properties of supercritical CO₂. However, deposition of base metals is likely to occur at the edges of the reservoir due to CO₂ degassing when the pressure is reduced.

7.3 CONSTRUCTION OF DEDICATED EXPERIMENTAL DEVICES AND NUMERICAL SIMULATORS

In order to investigate in detail the geochemical interactions between supercritical CO₂, formation water and reservoir rocks, specific experimental devices and computer codes were constructed.

For the experiments, materials were selected in order to minimise corrosion by CO₂-rich fluids. The high pressure of the experiments (20 MPa) required specific vessels, valves and measurement techniques, with the types of

experiment chosen so as to reproduce conditions as closely as possible of those in potential reservoirs.

With respect to the numerical modelling, a geochemical simulator of the CO₂-reservoir interactions was constructed using a code generator, which represents a very new approach to geochemical modelling (Fabriol and Czernichowski-Lauriol, 1992). The main advantages of this approach (compared to classical codes for water-rock interaction) are the efficiency of the calculations and the suitability for coupling with other codes such as transport and flow models. A coupled chemistry and transport code was developed, taking into account a significant and representative set of chemical elements, chemical species and minerals.

In parallel with the use of the new tailor-made geochemical simulator, the EQ3/6 geochemical code was intensively used (Wolery, 1992a). It is currently one of the most complete and powerful codes for modelling water-rock interactions. As a reference code, it was used both for code-to-code verification of the geochemical simulator, and for general modelling of the geochemical reactions occurring during the experiments.

7.3.1 Description of the Experiments

In order to focus the experimental programme, factors such as, potential host lithology, in-situ conditions, porefluid composition and experimental design had to be considered. The underlying experimental approach was to provide a wide coverage of qualitative data using many experiments, and a narrower range of quantitative data on specific areas necessary for successful computer modelling. As a consequence, four basic types of experiment were chosen:

- i) Long term, low maintenance batch experiments that reacted a wide range of small rock samples with water and SC CO₂.
- ii) Experiments flooding samples of wet sandstone with dry SC CO₂, and water previously equilibrated with SC CO₂.
- iii) Obtaining thermodynamic and kinetic data for the dissolution of SC CO₂ into water.
- iv) Obtaining kinetic data for the dissolution of key aquifer minerals.

Types (i) and (ii) should provide qualitative data on types of phases undergoing dissolution and precipitation, and be useful test cases for modelling. However, the rates of certain reactions may be important and it is the quantitative data from (iii) and (iv) that will be used to assess these. For example, the rate of reaction between two fluids is likely to be much faster than that between a fluid and a solid. Consequently, the reactions between SC CO₂ and formation water could be very important initially as a sink for CO₂. However, over longer timescales fluid-mineral reactions such as those proposed by Gunter et al. (1993a) will also be an important sink for CO₂.

Chapter 4 has identified Permo Triassic red bed sequences under the North Sea as having the largest potential for CO₂ disposal close to Europe. As well as being large aquifers, they also contain significant quantities of hydrocarbons confirming the presence of closures. Therefore, samples were obtained from onshore equivalents of these lithologies; Sherwood Sandstone for the host lithology, Mercia Mud-

stone for the caprock, and anhydrite which is commonly present.

To select appropriate conditions of temperature and pressure, data were studied for the southern North Sea gas fields (Abbotts, 1991). From this, and our knowledge on underground aquifers, 80°C and 200 bars pressure appear to be both representative, and attainable with the experimental equipment available and were used in all experiments. Although some experiments involve the use of de-ionised water, the majority use NaCl solution of seawater salinity (approximately 0.55 molar Cl).

Prior to performing the experiments, it was necessary to design and construct equipment that would perform well. Although dry SC CO₂ is relatively inert, in the presence of water or NaCl solution it is much more reactive. Previous studies (Schremp and Roberson, 1975) have shown that steel will corrode and standard O-ring seals will blister and fail. To minimise both corrosion and experimental failure, exposed surfaces were chosen so as to be as inert as practicable. Therefore, steel vessels (316 stainless steel) were generally lined with PTFE (polytetrafluoroethylene), high pressure tubing made of steel was replaced by that of nickel, O-ring seals were made of viton, and pressurised sampling containers were made of titanium.

7.3.1.1 THE SOLUBILITY AND KINETICS OF DISSOLUTION OF SUPERCRITICAL CO₂ INTO WATER AND SYNTHETIC SEAWATER

The underground disposal of CO₂ will result in both SC CO₂ filling a region of the host lithology and CO₂ dissolved in groundwater within that lithology. In order to enhance the accuracy of storage calculations (i.e. to account for both CO₂ as a SC phase and dissolved in groundwater), and to construct accurate computer models of SC CO₂/host formation water/host formation mineralogy interactions, it is necessary to have data on the solubility and rate of reaction of SC CO₂ and water. Therefore, a series of experiments were performed to assess these factors under conditions relevant to the disposal of CO₂.

Literature data for the solubility of CO₂ into water is limited over the range of pressure and temperature of relevance to the underground disposal of CO₂. Previous studies at greater than 1 atmosphere pressure (Ellis and Golding, 1963; Stewart and Munjal, 1970) concentrated on pressures (1–90 bars) that are lower than those of relevance to this study, but did cover a range of temperatures up to 330°C. However, these studies did indicate that equilibrium can be obtained in under 24 hours. The study by Kuk and Montagna (1983) assimilated data from their study with that of Wiebe and Gaddy (1941) to give CO₂ solubilities at 100 and 150 atmospheres pressure, and over a temperature range of 30–80°C. Extrapolation of the data from the above studies to 80°C and 200 bars pressure, indicates that the solubility of CO₂ is likely to be in the order of 55 g for every kilogram of de-ionised water, and that solubility decreases with increasing salinity. Other studies (van Eldik and Palmer, 1982), albeit at relatively

low pressures, have also shown that 99% of dissolved CO₂ is as the dissolved gas rather than true carbonic acid. Thus, the reaction of primary interest, for which rate data are needed, is:



The studies mentioned above typically used de-ionised water in solubility measurements. However, in potential host lithologies the SC CO₂ will be in contact with saline fluids. In order to provide data that are; comparable with previous studies, applicable to the other experiments, and applicable to actual disposal conditions, experiments were performed on both de-ionised water and a synthetic seawater (0.55 M NaCl solution) at 80°C and 200 bars pressure. A few more minor experiments were also performed to investigate how solubility of SC CO₂ varied with temperature at 200 bars pressure. A summary of the experiments conducted is given in Table 7.1.

Apparatus and experimental methodology

As a consequence of the relatively fast reaction between de-ionised water and SC CO₂, it was necessary to develop a simple high pressure reactor that would allow extraction of fluid over relatively short, time intervals. In this way, a series of experiments of increasing timescales would provide information on how the system reacted and came to equilibrium. The equipment used is shown in Figure 7.1. A known quantity of the continuously stirred aqueous phase partly filled a stainless steel reactor of known internal diameter (5.1 cm) at 80°C. This temperature was controlled to within ± 1°C by use of a fan-assisted oven. The stirring rate was kept constant at 300 rpm (± 5 rpm) by use of a magnetic stirrer. This was the fastest rotation rate that did not result in formation of a 'vortex cone' at the surface of the aqueous phase. Dye tracer tests showed that this was mixed in under 5 seconds. Rapid mixing is desirable so that concentration gradients do not develop at the surface of the aqueous phase due to the rapid solution of CO₂. By keeping the surface of the aqueous phase planar, a constant and easily calculable surface area is maintained.

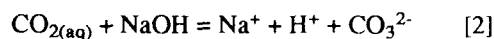
Once the equipment was at the desired temperature, 200 bars pressure of CO₂ was applied above the surface of the aqueous phase as rapidly as possible. The system was then allowed to react for a set period of time before a sample of the aqueous phase was withdrawn by means of a 'dip tube' (of external diameter 0.318 cm). The method of CO₂ collection was into a previously weighed 'floating piston' sampling vessel that contained a known quantity of 4M NaOH solution (see Figure 7.1). Just prior to collection of the sample, the pipework was flushed out with some of the CO₂-rich fluid. Previous studies (Kuk and Montagna, 1983) indicate that CO₂ is more soluble at 25°C compared to 80°C. Consequently, sampling could be performed outside the oven without causing degassing (as long as the

Table 7.1 Summary of SC CO₂ solubility experiments.

Run numbers	Starting fluid	Experimental conditions		
		Temperature (°C)	Pressure (bar)	Duration
358–404, 454	De-ionised water	80	200	0–24 hours
457–459, 461–462				
405–452, 455–456	Synthetic seawater	80	200	0–26 hours
460–463	De-ionised water	80	200	24.5 hours
464, 465	De-ionised water	80	200	24 hours

Figure 7.1 Schematic diagram of the apparatus used for the SC CO₂ solubility experiments.

pressure was kept constant). Stabilisation of the dissolved CO₂ was achieved by reacting it with 4M NaOH solution at 200 bars pressure:



As long as the NaOH is present in excess, the CO₃²⁻ will remain stable and allow for analysis. However, great care had to be taken on sampling to prevent pressure reduction and hence degassing. Degassing would result in the formation of bubbles that may cause the floating piston sampler to not fill completely with liquid. A consequence, a smaller than expected sample would be taken, which would result in an underestimation of the quantity of CO₂ in solution.

Once a sample had been collected, the sampling vessel was reweighed and the sample allowed to react with the NaOH solution for a few minutes. After this time, the pressure could be reduced and a subsample taken for analysis without degassing occurring. Analysis was performed by straightforward carbonate titration. The results were then corrected for dilution with the 4M NaOH solution. A plot of changing concentration over time was then constructed, revealing equilibrium and non-equilibrium conditions. For non-equilibrium conditions, calculation of dissolution rate was straightforward as the fluid chemistry, reacting surface area, and time interval over which the sample was taken, were all known.

The resulting data could then be used to address two main issues:

- (i) the solubility of SC CO₂ (using de-ionised water and synthetic seawater).
- (ii) the kinetics of dissolution of SC CO₂ (using de-ionised water only).

Analytical procedure

* Instrumentation

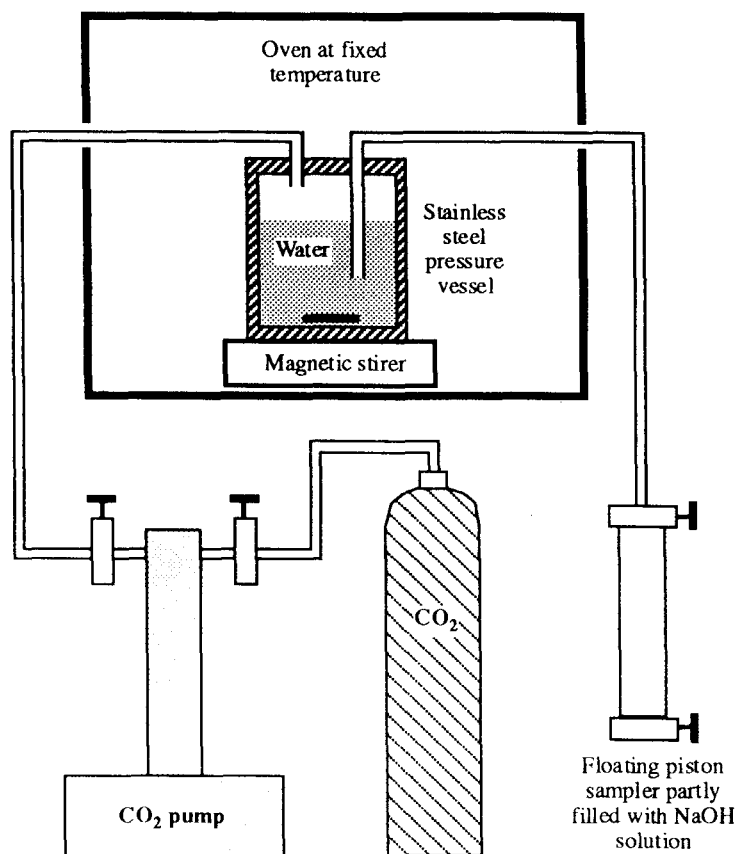
Analyses were performed by titration on a Radiometer VIT90 Video Titrator with ABU93 Triburette and SAM90 Sample Station. Measurements of pH were made using a Radiometer pHG200 pH electrode with a REF200 reference electrode.

* Calibration of pH

Calibration was performed using Whatman high resolution pH buffers at pH 7 and pH 10. The ambient laboratory temperature was measured using a mercury in glass thermometer and the exact pH at that temperature was manually entered immediately prior to calibration. A response slope of better than 94% was achieved in all analytical runs.

* Titration

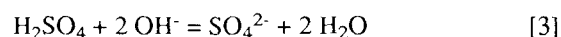
0.5 mol.l⁻¹ (1N) Sulphuric acid was used as titrant against 2.0 ml of sample or 1.0 ml of sodium hydroxide blank. The pH of the analytical sample was monitored as a function of volume of titrant added and the titration was allowed to



proceed until a pH of less than 2 was achieved. Equivalence points (EPs) were automatically calculated using the first derivative of the titration curve.

* Results

For the samples three equivalence points were observed. The first, at pH ~11.5, represents neutralisation of hydroxyl ions:



The second at pH ~8 represents the carbonate/hydrogen carbonate end point:



The third at pH ~4.5 represents the hydrogen carbonate/carbonic acid end point:



Overall, equations [4] and [5] represent:



At the high pH values of the samples, all the carbonate present will be in the CO₃²⁻ form (Hem, 1985) therefore, as there is no carbonate speciation in the samples, the volume of titrant required for equation [4] should be identical to the volume required for equation [5]. If the total volume of titrant added to each of the three equivalence points is designated as V₁, V₂ and V₃, and given that the sample volume is 2 ml and the titrant concentration is 0.5 mol.l⁻¹, the concentration of hydroxyl ions (M_{OH⁻}) and

carbonate ions ($M_{\text{CO}_3^{2-}}$) present in the sample may be calculated by simple equivalence (Vogel, 1978).

$$M_{\text{OH}^-} = (2^Y \times 0.5 \times V_1) / 2 \quad [7]$$

where: Y = Stoichiometric factor.

$$M_{\text{CO}_3^{2-}} = (0.5 \times (V_2 - V_1)) / 2 \quad [8]$$

or

$$M_{\text{CO}_3^{2-}} = (0.5 \times (V_3 - V_2)) / 2 \quad [9]$$

In practice an average of V_2 and V_3 was used to calculate $M_{\text{CO}_3^{2-}}$.

For the blanks, either one or two equivalence points were observed. Where only one equivalence point was observed the carbonate concentration was assumed to be less than the detection limit which is estimated to be 0.005 mol.l^{-1} . Where two equivalence points were observed the first is a combined hydroxyl/carbonate end point and the second is the hydrogen carbonate/carbonic acid end point. Again the concentration of hydroxyl ions and carbonate ions may be calculated by equivalence, given a sample volume of 1 ml and a titrant concentration of 0.5 mol.l^{-1} .

$$M_{\text{OH}^-} = V_2 - 2 \times (V_2 - V_1) \quad [10]$$

$$M_{\text{CO}_3^{2-}} = V_2 - V_1 \quad [11]$$

* Quality Control

A quality control standard, containing 2.00 mol.l^{-1} of hydroxyl ions and $0.5000 \text{ mol.l}^{-1}$ of carbonate ions, was prepared by dissolving 40.00 g of BDH AnalaR sodium hydroxide and 26.4472 g of BDH AnalaR sodium carbonate in 500 ml of deionised water. This standard was analysed at the start and finish of the analytical run and after not more than every ten samples. Results are tabulated in Table 7.2.

7.3.1.2 BATCH EXPERIMENTS

In order to obtain a better understanding of rock-water- CO_2 interactions, long-term batch experiments have been performed. The rock types used in such experiments were chosen so as to be typical of lithologies expected in the vicinity of any CO_2 disposal site. These include samples of sandstones (the most likely host lithology), mudstones (typical cap rocks) and anhydrite (typically found as both caprock and as a cement in the sandstones). The long duration of the experiments will allow for increased reaction, and as a result, will facilitate observations of the mineralogical changes. Fluid chemical data have also been obtained from the experiments and are used to confirm the mineralogical observations. Such observations are used to reinforce the conclusions about which reaction mechanisms have been operating and be compared with previous studies (e.g. Gunter et al., 1993a). Data from studies such as this will then be useful in highlighting ways in which CO_2 can

be permanently fixed into the deep subsurface (i.e. incorporated into secondary minerals).

Experimental methodology

Due to their long duration, the experiments performed in this part of the study needed to be both reliable and requiring minimal maintenance. Such experiments are ideally suited to using simple batch apparatus (see below). Details of the experiments conducted are given in Table 7.3. Unreacted cores are described in section 7.3.1.7. At the start of an experiment both solid (a small block approximately 2 cm in diameter and 5 cm long) and liquid (25 ml) were placed in a pressure vessel, heated and a pressure of CO_2 applied. Temperature and pressure were checked regularly and kept constant throughout the experiments. After a given length of time the apparatus was allowed to cool then depressurised over several hours. The relatively slow depressurisation was intended to minimise rapid degassing and hence limit damage to the rock samples and any delicate secondary minerals. On opening the pressure vessel a sample of the fluid was taken for chemical analysis (see section 7.3.1.5). The solid phase was carefully removed and rapidly frozen by immersion in liquid nitrogen before analysis (see section 7.3.1.6).

Apparatus

The equipment employed in this investigation were 100 ml, PTFE-lined, stainless steel pressure vessels. These were well-suited for carrying out long term experiments as, being lined with PTFE, were inert to the reactive saline CO_2 -rich fluids used. A reaction vessel is shown in Figure 7.2. A maximum of 16 vessels (at any one time) were connected together in a thermostatically-controlled oven at 80°C . This allowed for all experiments to be kept at 200 bars pressure of CO_2 via a single pump. The CO_2 input lines were placed at the top of the vessels so that aqueous fluids could not move between vessels.

Table 7.2 Quality control information for the analytical procedure used in the SC CO_2 solubility experiments (see text).

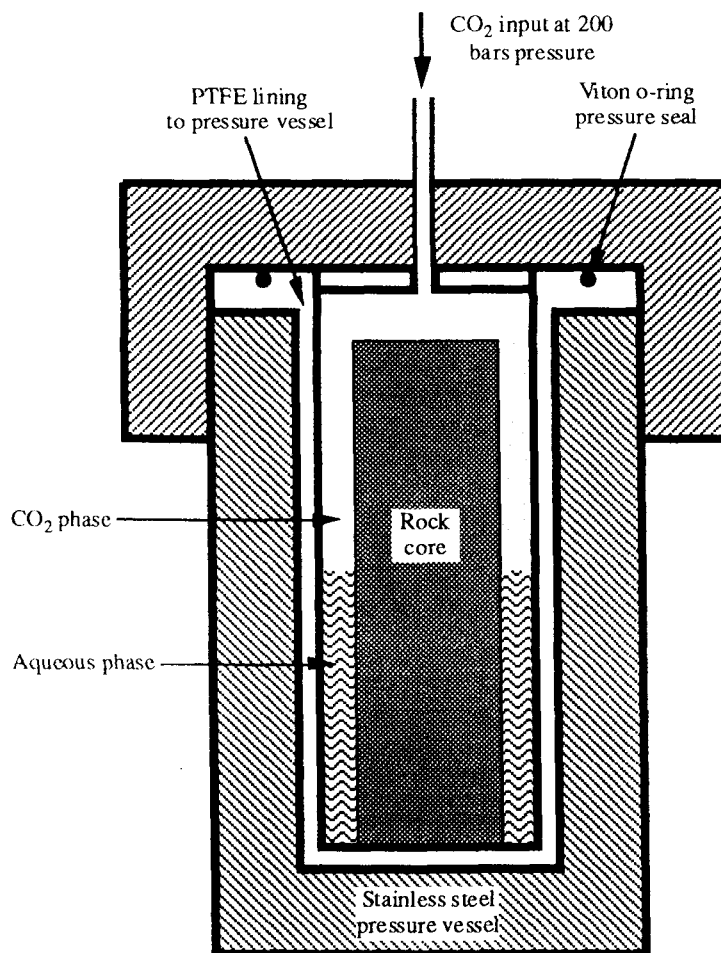
	EP1 OH^- mol.l^{-1}	EP2 CO_3^{2-} mol.l^{-1}	EP3 CO_3^{2-} mol.l^{-1}	Average of EP2 & EP3 CO_3^{2-} mol.l^{-1}
	1.9307	0.5088	0.5099	0.5094
	1.9198	0.5329	0.5035	0.5182
	1.9313	0.5273	0.5135	0.5204
	1.8870	0.5047	0.5118	0.5083
	1.9143	0.5007	0.5059	0.5033
	1.8894	0.5183	0.5101	0.5142
	1.7596	0.4838	0.4751	0.4795
	1.7527	0.4768	0.4716	0.4742
	1.7492	0.4772	0.4700	0.4736
	1.8987	0.5263	0.5066	0.5165
	1.9251	0.5116	0.4769	0.4943
	1.9085	0.4980	0.4852	0.4916
	1.9154	0.4939	0.4877	0.4908
	1.8825	0.5098	0.5080	0.5089
	1.8828	0.4826	0.4842	0.4839
	1.9007	0.4878	0.4830	0.4854
	1.8842	0.5114	0.5091	0.5103
	EP1 OH^-	EP2 CO_3^{2-}	EP3 CO_3^{2-}	Average of EP2 & EP3 CO_3^{2-}
Mean (mol.l^{-1})	1.8783	0.5031	0.4948	0.4990
RSD (%)	3.2811	3.4889	3.2246	3.1679
Accuracy (%)	-6.0826	0.6224	-1.0341	-0.2059

Table 7.3 Summary of batch experimental runs and appropriate sample codes (all experiments were performed at 80°C and 200 bars pressure of CO₂).

Sample code (reacted solid)	Run number	Starting material	Description of fluid	Experiment duration
JMP24	Run 373	JMP1 Mudstone	SSW + CO ₂	109 days
JMP25	Run 377	JMP4 Anhydrite	SSW + CO ₂	111 days
JMP26	Run 378	None Blank	SSW + CO ₂	109 days
JMP27	Run 383	JMP11 Subarkose	SSW + CO ₂	109 days
JMP28	Run 371	JMP4 Anhydrite	SSW + CO ₂	232 days
JMP29	Run 372	JMP4 Anhydrite	DIW + CO ₂	232 days
JMP30	Run 399	JMP1 Mudstone	SC CO ₂ only	92 days
JMP31	Run 374	JMP2 Mudstone	SSW + CO ₂	232 days
JMP32	Run 375	JMP3 Mudstone	SSW + CO ₂	232 days
JMP33	Run 376	JMP3 Mudstone	DIW + CO ₂	232 days
JMP34	Run 379	JMP8E Subarkose	SSW + CO ₂	232 days
JMP35	Run 380	JMP8E Subarkose	DIW + CO ₂	232 days
JMP36	Run 381	JMP12 Arkosic arenite	SSW + CO ₂	232 days
JMP37	Run 382	JMP12 Arkosic arenite	DIW + CO ₂	232 days
JMP38	Run 384	JMP10 Sandstone	SSW + CO ₂	232 days
JMP40	Run 385	JMP13 Arkosic arenite	SSW + CO ₂	232 days
JMP41	Run 400	n/a Fullers' Earth	SC CO ₂ only	92 days
JMP42	Run 401	n/a Fullers' Earth	SSW + CO ₂	92 days

SSW = Synthetic seawater
DIW = De-ionised water

Figure 7.2 Schematic diagram of the apparatus used for the batch experiments.



7.3.1.3 CORE FLOODING EXPERIMENTS

In order to construct a system more representative of the situation that will occur during the injection of supercritical CO₂ into a host lithology, experiments flooding sandstone cores have been performed. They should also provide well characterised examples which could be used as test cases for numerical modelling. Two different experiments were performed on sandstone cores saturated with 0.55 M NaCl solution: a core flushed once with dry supercritical CO₂; and a core flushed with a 0.55 M NaCl solution that has been equilibrated with supercritical CO₂. Thus the two extremes of the water-supercritical CO₂ system have been covered. Both experiments utilised the same 0.55 M NaCl solution, the same temperature and pressure conditions (80°C, 200 bar) and the same Wilmslow Sandstone cores that were used in the batch experiments (Table 7.4). Unreacted cores are described in section 7.3.1.7.

Apparatus and experimental methodology

The apparatus (Figure 7.3) consisted of a sandstone core (45 mm diameter by 150 mm length) tightly held within a PTFE sheath. The sheathed core was exposed to a higher external pressure compared to that inside so that the PTFE deformed to fit tightly round the core (a pressure differential of ≈ 50 bar was used). The reactant fluid was passed down the core with the pressure differential ensuring that there was no preferential fluid flow

Table 7.4 Summary of core-flooding experiments performed (both experiments were performed at 80°C and 200 bars pressure of CO₂).

Run number	Starting material	Description of fluid	Experiment duration
Run 370	Sandstone (JMP8)	SC CO ₂ only	41 days
Run 409	Sandstone (JMP8D)	SSW + CO ₂	61 days

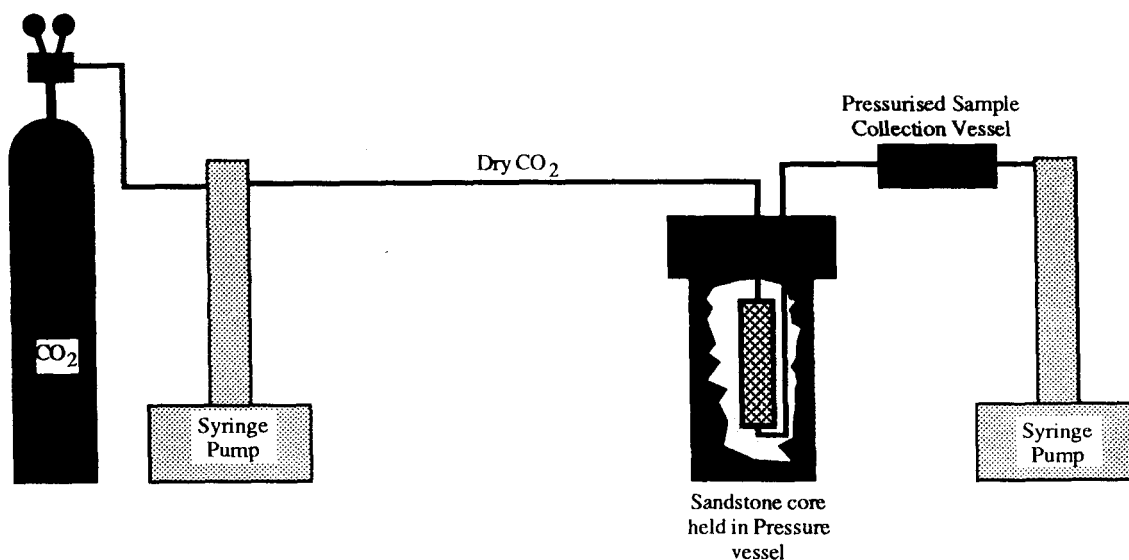


Figure 7.3 Schematic diagram of the core flood equipment. Setup for Run 370 using dry SC CO₂ only.

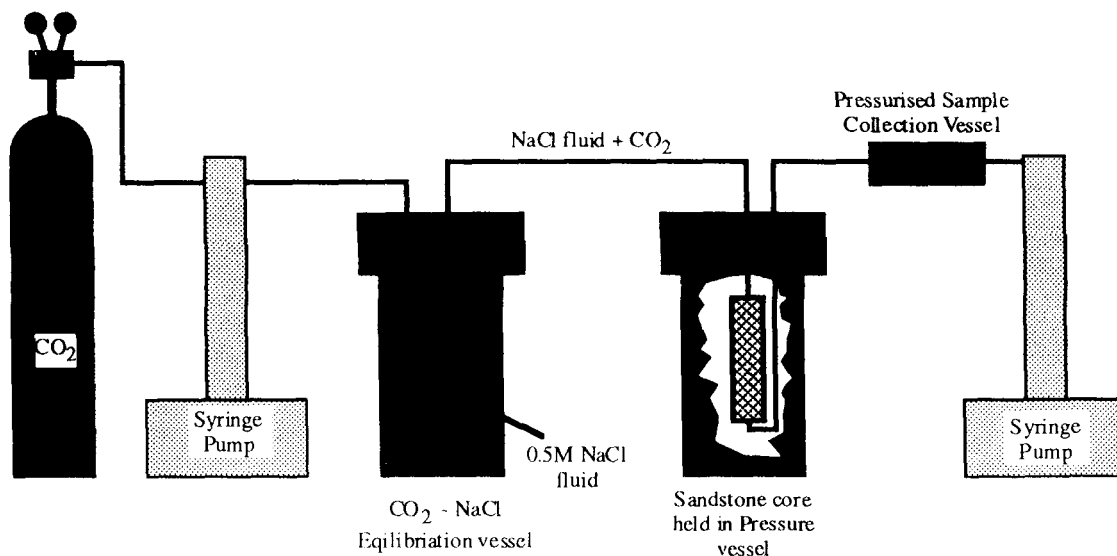


Figure 7.3 Continued. Schematic diagram of the core flood equipment. Setup for Run 409 using NaCl solution equilibrated with SC CO₂.

between core and PTFE sheath. The fluid expelled from the sandstone cores was collected at pressure, using the pressurised sample vessels, each had a nominal capacity of 20 cm³. When full, the sample vessel was removed and replaced by an empty vessel. Once removed, the full sample vessel was then slowly depressurised and degased, and the sample fluids sent for analyses. After reaction the cores were recovered and subjected to mineralogical examination. Tracer tests before the commencement of experiments gave an indication of porosity and were combined with data on porosity changes that were gathered during mineralogical analysis. Detailed mineralogical observations identified key reacting phases. Samples of fluid extracted during the flooding were also used to identify mineral dissolution.

* *Tracer tests and residence time distributions*

Flow behaviour in chemical reactors is conventionally interpreted by means of the 'stimulus-response' method of

analysis (Levenspiel and Bischoff, 1963; Levenspiel, 1972). Essentially, this involves the injection of a tracer into the reactor under typical operating conditions and subsequent analysis of the tracer distribution in the effluent. This type of test provides 'residence time distribution' (RTD) information about the fluid in the vessel (Levenspiel, 1972). A tracer may be introduced to the input fluid as a discrete 'spike' or as a step change in concentration. The theory is dealt with in great detail in Levenspiel (1972). The variance of a tracer residence time distribution may be used to determine the non-ideal flow characteristics of the sandstone core (see below).

* *Dispersion model*

The residence time information may be used to evaluate the dispersion characteristics of a sandstone core. We may consider that dispersion in a sandstone core, such as that employed in the experiments described here, occurs by the

differential flow properties of packets of fluid within the core, and by molecular and turbulent diffusion. If we assume that the principle component of dispersion is axial rather than radial (not unreasonable, given the length/width ratio of the sandstone core), and that perfect plug flow occurs at the boundaries of the vessel, then the following equation yields the vessel dispersion parameter, D_a/uL (where L = length of sandstone core), such that as $D_a/uL \rightarrow 0$ dispersion becomes negligible, and as $D_a/uL \rightarrow \infty$ dispersion becomes large (mixed flow) (Levenspiel, 1972):

$$\sigma_{\theta}^2 = \frac{\sigma^2}{t^{*2}} = 2 \frac{D_a}{uL} - 2 \left(\frac{D_a}{uL} \right)^2 (1 - e^{-uL/D_a}) \quad [12]$$

where:

- σ^2 = variance of the tracer residence time distribution,
- σ^2 = variance expressed as dimensionless time,
- t^* = mean residence time of autoclave (s),
- u = linear flow velocity ($m \cdot s^{-1}$),
- D_a = axial dispersion coefficient ($m^2 \cdot s^{-1}$),
- L = length of autoclave core tube (m).

The vessel dispersion parameter, D_a/uL may be derived from the variance of the tracer residence time distribution obtained by an inert tracer test within the sandstone core.

* Assessment of autoclave non-ideal flow behaviour via tracer tests

An assessment of autoclave flow behaviour has been carried out via inert tracer tests under fluid flow conditions analogous to the flow through experiments. Tracer tests were carried out at the experimental temperature (80°C) and pressure (200 bar) using Na-fluorescein as the inert tracer.

If dispersion is small ($D_a/uL < 0.01$) the vessel dispersion parameter D_a/uL may be derived as follows:

$$\sigma_{\theta}^2 = \frac{\sigma^2}{t^{*2}} = 2 \frac{D_a}{uL} \quad [13]$$

The variance of the RTD is most easily calculated from a step increase in tracer concentration or 'F' curve (Levenspiel, 1972). If D_a/uL is small (< 0.01), then the C curve approaches Gaussian, and the F curve when plotted on probability paper, lies on a straight line. The properties of a Gaussian distribution are such that one standard deviation, either side of the mean includes 68% of the area under the curve. Consequently, if we take the 16th and 84th percentile points of the F curve, then these are two standard deviations apart. These features are illustrated in Figure 7.4.

The tracer tests have revealed that departures from ideal plug flow behaviour are minimal under the conditions of experiment. The calculations are presented below.

Run 370

From Figure 7.4 equation of straight line is: $\min = 1478.9 + (80.639 \times \text{'prob'})$

Corrected for tubing length: $\min = 285 + (80.639 \times \text{'prob'})$

Difference between 16th and 84th percentiles is 2σ .

16% 'prob' = -0.7032 $\therefore \min = 228.3$
 84% 'prob' = 0.7032 $\therefore \min = 341.7$
 which gives $\sigma = 56.7 \text{ min}$

50% 'prob' = 0 $\therefore \min = 285.0 = t^*$ (mean residence time)
 @ pump rate = 10 ml.hr⁻¹ (=10/60 ml.min⁻¹)

$$\sigma^2 = (\sigma/t^*)^2 = (56.7/285)^2 = 0.04 \text{ (variance)}$$

The dispersion is $D_a/uL = \sigma^2/2 = 0.02$

Volume of core is = 238.5 cm³

Porosity = mean residence time (t^*) x mean flow rate = 47.5 ml

as a percentage of volume of the core
 = (porosity/volume of core) x 100% = 19.9%

Run 409

From Figure 7.4 equation of straight line is: $\min = 6328.9 + (87.421 \times \text{'prob'})$
 Corrected for tubing length: $\min = 305 + (87.421 \times \text{'prob'})$

Difference between 16th and 84th percentiles is 2σ .

16% 'prob' = -0.7032 $\therefore \min = 243.5$
 84% 'prob' = 0.7032 $\therefore \min = 366.5$

which gives $\sigma = 61.5 \text{ min}$

50% 'prob' = 0 $\therefore \min = 305.0 = t^*$ (mean residence time)
 @ pump rate = 10 ml.hr⁻¹ (=10/60ml.min⁻¹)

$$\sigma^2 = (\sigma/t^*)^2 = (61.5/305)^2 = 0.04 \text{ (variance)}$$

The dispersion is $D_a/uL = \sigma^2/2 = 0.02$

Volume of core is = 238.5 cm³

Porosity = mean residence time (t^*) x mean flow rate = 47.5 ml

as a percentage of volume of the core
 = (porosity/volume of core) x 100% = 21.3%

7.3.1.4 THE KINETICS OF MINERAL DISSOLUTION

In order to better understand rock-water-CO₂ interactions, a series of flow experiments have been conducted to investigate the dissolution behaviour of key aquifer minerals. These include anhydrite, (typically found as both a caprock and as a cement in sandstones) as well as quartz, albite and microcline, (major constituents of the sandstones). The experiments conducted are summarized in Table 7.5. Details on the preparation of such minerals and surface area determinations are given in section 7.3.1.7. All the experiments utilised the same 0.55M NaCl starting fluid used in the Batch Experiments. This fluid was pre-saturated with supercritical CO₂ at the experimental pressure and temperature conditions before reacting with the crushed mineral samples. Fluid chemistry data from these experiments can be used to obtain kinetic information for the dissolution of key aquifer minerals, which can then be

Figure 7.4 Time versus probability plot for tracer tests on the sandstone cores used for the core flooding experiments. (Prob = probability).

Top: Run 370
Bottom: Run 409

used as input data to geochemical models of a CO₂ disposal site.

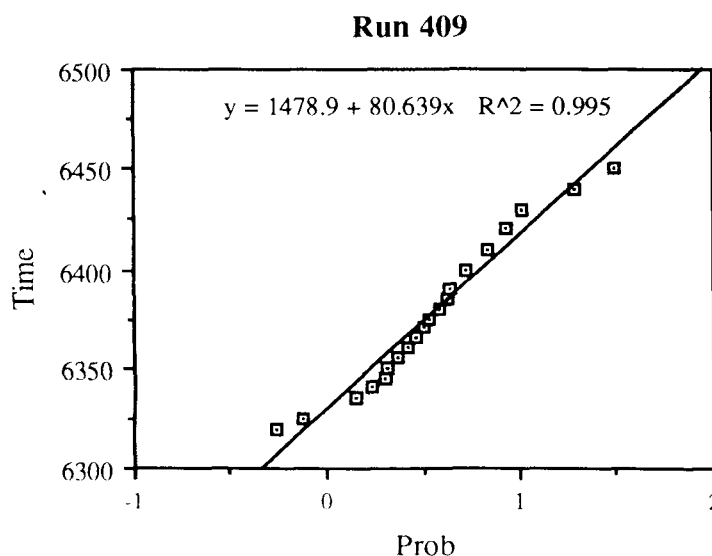
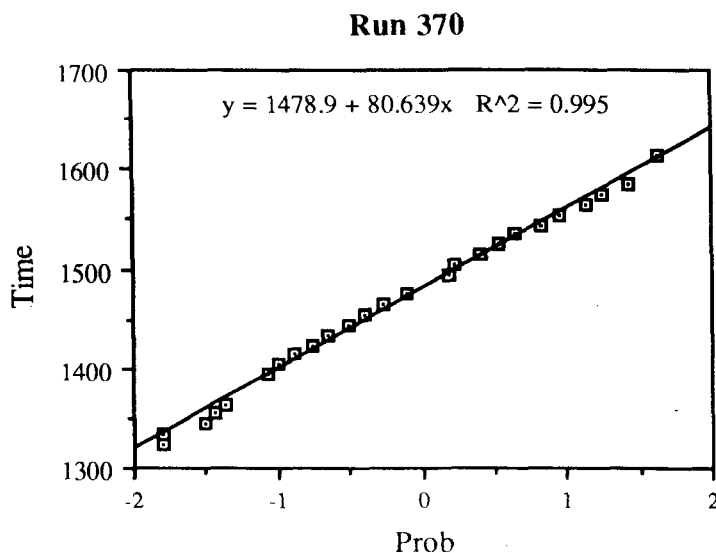
Experimental apparatus and methodology

The equipment used in these dissolution studies can be described as a simple plug flow reactor. The fundamentals of the flow reactor design are illustrated in Figure 7.5. In principle, this apparatus is well-suited to dissolution studies upon disaggregated rock and mineral grains under hydrothermal conditions. The rate of mineral dissolution will proceed much more slowly than dissolution of supercritical CO₂ (see section 7.3.1.1). Consequently, the experimental determination of dissolution rates under 'far from equilibrium conditions' was straightforward. The experimental equipment involved equilibrating the fluid with supercritical CO₂ prior to it reacting with a particular mineral. The latter was in the form of a specific grain size of known surface area, free of fines, and packed into a small tubular reactor made from PEEK (polyethyleneterephthalate) which is inert to attack by supercritical CO₂ and most chemical reagents. All materials were selected in order to minimise corrosion and experimental failure (see section 7.3.1). The equilibrated fluid was then passed through this reactor with far from equilibrium conditions (with respect to the mineral) being maintained by ensuring a high enough flow rate. The pressure and flow rate in the reactor was controlled by means of a single piston syringe pump and a back pressure regulator/sample collector. Calculation of dissolution rate was straightforward as fluid chemistry, reacting surface area, and time interval over which the sample was taken are all known.

Plug-flow reactors

In these reactors, solid reactants are maintained within a packed bed inside a tubular autoclave whilst fluid is passed through at a measured flow rate. Such reactors have been used for geochemical applications by Charles (1978), Charles and Bayhurst (1983), Potter (1981), Dibble and Potter (1982), Pohl and Liou (1983), Ponader and Liou (1985), Potter and Dibble (1986), Lane et al. (1986) and Posey-Dowty et al. (1986). The advantages of plug-flow reactors relate to; the ease of maintenance of far from equilibrium conditions for dissolution studies, the ease of variation of input fluid chemistry to investigate dependencies of reaction rate upon fluid composition, and the continuous output of fluid chemical data with time. Disadvantages relate to; the interpretation of the hydrodynamic behaviour of such reactors (few reactors behave ideally, so that data must be corrected for dispersion and non-ideal fluid flow characteristics); the technical complexity (and expense) of maintaining temperature, pressure and constant fluid flow rates under hydrothermal conditions; and the need to use integral functions of rate laws to derive kinetic data.

Much of the theory relating to the operation and analysis of behaviour of tubular reactors is present in the chemical engineering literature. Levenspiel (1972) and Hill (1977) give comprehensive descriptions and discussion of these



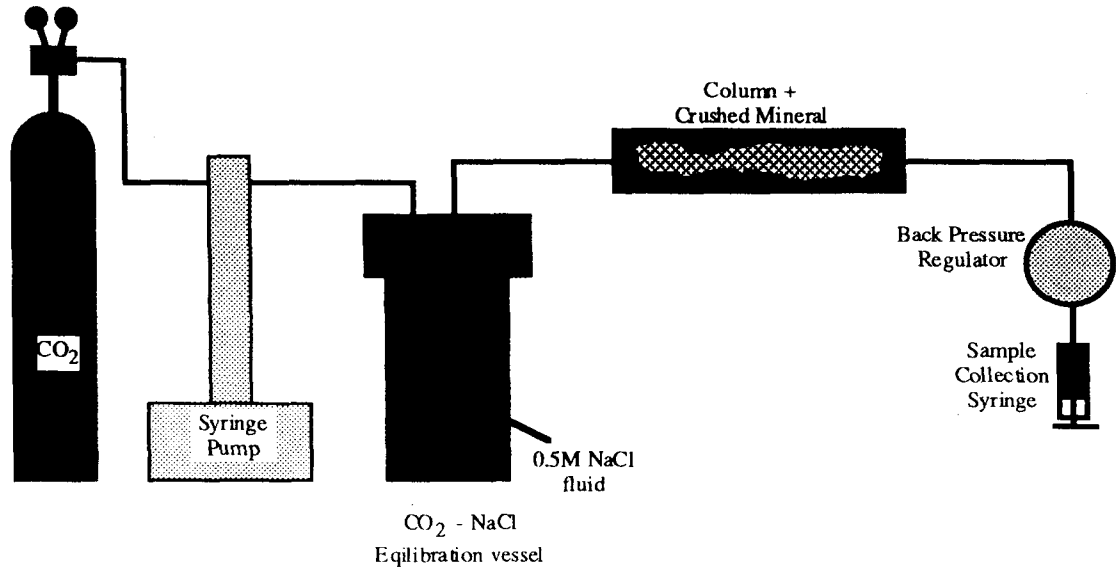
applications. Recently, applications of this technology and theory to geochemical problems have been presented by Posey-Dowty et al. (1986), Hellmann and Crerar (1986), and Rimstidt and Dove (1986).

For the tubular reactor described above, under ideal conditions of fluid flow, one may envisage that 'plug flow' conditions operate, i.e. fluid moves through the system in 'single file' without overtaking or mixing occurring. In reality, channelling of flow or eddying through the packed column means that tubular reactors may only approximate

Table 7.5 Summary of mineral kinetics experiments performed (all experiments were performed at 80°C and 200 bars pressure of CO₂).

Run number	Starting material of fluid	Description duration	Experiment
Run 423	Anhydrite	SSW + CO ₂	1 week
Run 446	Quartz	SSW + CO ₂	2 weeks
Run 447	Microcline	SSW + CO ₂	2 weeks
Run 449	Albite	SSW + CO ₂	2 weeks

Figure 7.5
Schematic diagram of the flow reactor used for the mineral kinetic experiments.



ideal plug flow. Thus the dispersion characteristics of a tubular flow reactor have to be taken into account when interpreting kinetic data from such equipment.

We may consider that dispersion in a tubular flow reactor such as that employed in this study occurs by the differential flow properties of packets of fluid within the reactor and by molecular and turbulent diffusion. If we assume that the principle component of dispersion is axial rather than radial (which is reasonable given the length/width ratio of the reactor), and that perfect plug flow occurs at the boundaries of the vessel, then the following differential equation describes one dimensional axial dispersion (Levenspiel, 1972):

$$\frac{\delta C}{\delta t} = D_a \frac{\delta^2 C}{\delta x^2} - u \frac{\delta C}{\delta x} \quad [14]$$

where:

- u = linear flow velocity ($m \cdot s^{-1}$),
- D_a = axial dispersion coefficient ($m^2 \cdot s^{-1}$),
- C = concentration ($mol \cdot m^{-3}$).

The rate of a mineral-fluid reaction may be regarded as being controlled by a zero-order, surface controlled process at constant temperature, pressure and fluid composition, under conditions far from chemical equilibrium (e.g. Helgeson et al, 1984; Lasaga, 1984). An empirical rate law describing rock/mineral dissolution under conditions far from equilibrium and at constant fluid composition may be represented as follows (Lasaga, 1981):

$$\frac{\delta C_i}{\delta t} = \frac{A_\theta}{V} \cdot k_\theta \cdot \chi_{i,\theta} \quad [15]$$

where:

- A is the exposed surface area of mineral θ ,
- V is the fluid volume,
- k is the rate constant of mineral θ ,
- i is the stoichiometric content of i in θ .

The rate of reaction is described by the rate of change of concentration of some chemical component i in the fluid phase due to the dissolution of its host mineral phase, θ .

Integrating equation [15] we have:

$$C_i - C_o = \frac{A_\theta}{V} \cdot k_\theta \cdot t \cdot \chi_{i,\theta} \quad [16]$$

where:

- C_o = initial concentration of i in the fluid phase,
- t = time.

Equation [16] thus allows us to relate fluid phase concentrations, mineral surface area, mineral composition, the rate constant for dissolution, and in a dynamic system, the fluid flow rate ($t/V = 1/\text{flow rate}$).

Incorporating the above into the dispersion model is as follows:

$$\frac{\delta C_i}{\delta t} = D_a \frac{\delta^2 C_i}{\delta x^2} - u \frac{\delta C_i}{\delta x} + \frac{A_\theta}{V} \cdot k_\theta \cdot \chi_{i,\theta} \quad [17]$$

At steady-state, $C_i/t = 0$, and for a continuous input solution at a fixed concentration, the following boundary conditions are relevant:

$$\left[-D_a \frac{\delta C_i}{\delta w} + uC \right]_{x=0} = uC_o$$

$$\frac{\delta C_i}{\delta x} (\infty) = \text{finite}$$

Equation (17) may be solved analytically (e.g. van Genuchten and Alves, 1982) as follows:

$$C_{i,x} = C_o + \frac{\chi \cdot k_\theta \cdot A_\theta \cdot (ux + D_a)}{u^2 \cdot V} \quad [18]$$

where:

- $C_{i,x}$ = concentration at distance x ,
- C_o = initial concentration.

Equation [18] may be re-arranged as follows:

$$k_{\theta} = \frac{u^2 \cdot V \cdot (C_{ix} - C_o)}{\chi A_{\theta} \cdot (ux + D_a)} \quad [19]$$

Under ideal plug flow conditions $D_a = 0$ and equation [18] becomes:

$$k_{\theta} = \frac{u \cdot a \cdot (C_{ix} - C_o)}{\chi A_{\theta} \cdot x} \quad [20]$$

If a = cross-sectional area of the reactor core tube (m^2), then $x = V/a$ (volume/area).

Substituting for x in equation [18] gives:

$$k_{\theta} = \frac{u \cdot a \cdot (C_{ix} - C_o)}{\chi A_{\theta}} \quad [21]$$

Note that this expression is identical to the following:

$$k_{\theta} = \frac{q \cdot (C_{ix} - C_o)}{\chi A_{\theta}} \quad [22]$$

given that $q = u \cdot a$, where q = volumetric flow rate ($m^3 \cdot s^{-1}$).

Previous studies using similar tubular reactors packed with crushed mineral samples have shown the deviation from ideal flow conditions to be small (Savage et al., 1989) therefore rate constants for dissolution quoted in this report derived from the experiments conducted in the tubular reactor have been calculated using equation [22].

7.3.1.5 METHODS OF WATER ANALYSIS

Samples of the initial and reacted fluids collected from the experiments were analysed for major cations using Inductively-Coupled Plasma - Optical Emission Spectroscopy (ICP-OES); for anions using Ion Chromatography (IC); for pH using an Orion® 520A pH meter calibrated using Whatman® NBS traceable buffers at pH 4, 7 and 10.

7.3.1.6 METHODS OF MINERALOGICAL ANALYSIS

Scanning electron microscopy

All samples of solid starting materials were considered dry before preparation and no further specialist drying techniques were used. Reacted samples, however, were rapidly frozen in liquid nitrogen before being freeze-dried in an Edward's Modulyo freeze drier. Specimens of freshly exposed surfaces were produced to include all possible experimental environments and were mounted on an aluminium pin-type stub. Specimens were coated in a layer of carbon to an approximate thickness of 25 nm in an Edward's E306A evaporation coater. This produced a conductive layer on the sample and prevented sample charging that caused image deterioration. Specimens were examined in a Cambridge Instruments Stereoscan S250 Scanning Electron Microscope (SEM) operating an accelerating voltage of 20 kV.

SEM involves the 'imaging' of electrons produced in, or returned from, material surfaces when a primary electron beam impinges upon that surface (Goldstein et al., 1981). The interaction of this beam with the electrons of atoms in the material's surface results in the emission of several

radiation types, including low energy secondary electrons. In SEM, the electron beam is scanned across an area of the sample. The resultant secondary electrons are detected and the signal obtained is displayed on a synchronously rastered TV monitor. In this way an image of the surface morphology is constructed. The image brightness or shadowing is dependent upon the orientation of the surfaces in relation to the secondary electron detector.

In addition to secondary electron radiation, X-rays are also produced. The energy of the X-rays emitted is characteristic of the atoms from which the X-rays were produced. The spectrum of X-rays produced is detected and recorded with a Link Systems 860 Microanalyser Energy Dispersive X-ray microanalyser using a Si (Li) solid state detector. Hence, by characterisation of the X-ray signal, qualitative information about the elemental components in the analysed phase can be obtained. The scanning electron microscope is calibrated at a range of magnifications using SIRA test samples that have themselves been calibrated against National Physics Laboratory standards. The X-ray microanalysis system is calibrated using a cobalt metal laboratory standard.

Samples were also prepared as blue-dyed polished thin sections. Polished thin sections were examined by back-scattered scanning electron microscopy (BSEM). The sections were coated with a thin layer of carbon, approximately 25 nm thick, prior to examination, in order to make the surfaces electrically conductive. BSEM observations were made using the SEM equipped with a KE-Developments 4-element solid-state backscattered electron detector. Mineral identification was made by qualitative examination of the energy dispersive X-ray (EDXA) spectra. Observations were made at a 20 kV accelerating voltage. In BSEM mode the image obtained from the polished thin section is related to the composition of the material being examined. Image brightness is proportional to the average atomic number of the material and its density, thus allowing the distribution of different minerals to be determined on the basis of their chemical composition. BSEM was also used for detailed point counting analyses. BSEM was used instead of more traditional optical microscopy since it was felt that the greater magnification and accurate stage positioning would enable subtle changes to be detected. Approximately 400 points were counted for each sample with some samples being split into two areas - above and below the CO₂-water interface. Photomicrographs were taken and a grid constructed over each photomicrograph, allowing systematic counting on a grid network.

Surface area analysis

Small subsamples of unreacted and reacted material were prepared by degassing in a vacuum oven at 60°C for a minimum of 24 hours to remove water vapour and adsorbed gases prior to analysis. Surface area analyses were obtained by a nitrogen adsorption technique based upon the BET adsorption/desorption isotherm model (Brunauer et al., 1938) using a Micromeritics Flowsorb II 2300 analyser. Surface area data was obtained by cycling the sample from room temperature to liquid nitrogen temperature ($\approx -196^\circ\text{C}$) whilst immersed in a 30:70 molar ratio stream of nitrogen and helium. Analyses were repeated until three consistent results were obtained. The manufacturer's stated error associated with each measurement is $\pm 3\%$.

Liquid resaturation porosimetry

The porosities of selected samples were determined by a propanol resaturation method (Bloomfield and Williams,

1994). The sample to be tested was weighed and then saturated with propanol. The sample was allowed to saturate for at least 24 hours before re-weighing. The sample was first weighed below propanol and then in air. The sample's dry bulk grain density and effective porosity were determined from these values according to the following formulae. The effective error for this technique is approximately $\pm 0.5\%$ (Bloomfield and Williams, 1994).

$$\rho_b = \frac{(w \rho_f)}{(S_1 - S_2)} \quad \text{g.cm}^{-3} \quad [23]$$

$$\rho_g = \frac{(w \rho_f)}{(w - S_2)} \quad \text{g.cm}^{-3} \quad [24]$$

$$\emptyset = 100 \frac{(S_1 - w)}{(S_1 - S_2)} \quad \% \quad [25]$$

where:

- w = dry sample weight (g),
- S₁ = saturated sample weight in air (g),
- S₂ = saturated sample weight under propanol (g),
- ρ_b = dry bulk density (g. cm⁻³),
- ρ_g = grain density (g. cm⁻³),
- \emptyset = effective porosity (%),
- ρ_f = density of propanol (g. cm⁻³).

Gas permeametry

Gas permeability was determined on right-cylindrical plugs approximately 24.5 mm in diameter and approximately 27.5 mm in length. These were oven dried at 60°C for at least 24 hours prior to testing (Bloomfield and Williams, 1994). The sample was sealed in a Hassler-type core holder and a nitrogen flow established through the core. The stabilised rate of nitrogen outflow was measured and the gas permeability was determined by the following equation:

$$K_g = 20,000 \mu Q L \frac{[P_o]}{[A(P_i^2 - P_o^2)]} \quad \text{mD} \quad [26]$$

$$P_j = P_o + P_g \quad \text{abs.atm} \quad [27]$$

where:

- K_g = measured gas permeability,
- L = specimen length (mm),
- A = specimen cross-sectional area (mm²),
- μ = gas viscosity (cP),
- Q = flow rate (cm³ s⁻¹),
- P_g = regulated nitrogen supply pressure (gauge, atmospheres),
- P_o = atmospheric pressure (absolute, atmospheres).

The errors associated with this technique are most effectively expressed in terms of significant figures. Consequently permeability data are rounded to one significant figure below a permeability of 1 mD and to 2 significant figures above a permeability of 1 mD (Bloomfield and Williams, 1994). Liquid equivalent permeabilities are based on an empirical correction of the gas permeability,

and hydraulic conductivity is calculated from the liquid equivalent permeability assuming a temperature of 20°C.

7.3.1.7 Starting materials

Fluids

Three fluids were used in the experiments: supercritical CO₂, de-ionised water and synthetic seawater.

* Supercritical CO₂

The SC CO₂ was produced by compressing high purity liquid CO₂. This liquid CO₂ was obtained in a cylinder fitted with a dip tube and pressurised with helium.

* De-ionised water

De-ionised water was used in some experiments to represent the most dilute water that any rock type could possibly encounter. It also has the highest solubility of SC CO₂ (see section 7.4.1) compared to saline fluids.

* Synthetic seawater

Finally, a synthetic seawater (0.55 M NaCl solution) was used in the majority of the experiments. Porewaters within deep aquifers or associated with hydrocarbon fields (Abbotts, 1991) are usually saline, though the degree of salinity varies. In order that the results from different experiments could be compared directly, it was necessary to use just one salinity, and a synthetic seawater was chosen to be representative. However, it is recognised that salinities in many aquifers/hydrocarbon fields are higher than this. The effect of higher salinity would be to lower the concentration of dissolved CO₂ in solution (see section 7.4.1) and hence be likely to reduce the degree of CO₂/rock reaction. For this study, it was felt that any such reduction in reaction would not be advantageous due to the relatively short (on a geological timescale) duration of the experiments.

Solids

* Individual minerals

Samples of anhydrite, quartz, albite and microcline were obtained and crushed to 125–250 μ m and with the fines carefully removed. The surface area of the unreacted minerals were determined by nitrogen adsorption BET. Table 7.6 gives a summary of surface area determinations performed on the crushed samples.

* Unreacted Mercia Mudstone (JMP1)

This sample was taken from the British Gypsum Audlem 15 borehole in Audlem, Staffordshire, UK, depth 86.30–86.50 m (Table 7.7). In hand specimen the sample consisted of an orange-red, massive mudstone with sub-millimetre reduction spots.

Petrographic analysis by SEM and BSEM revealed that the mudstone comprised predominant angular, subequant quartz grains up to $\sim 20 \mu$ m in diameter with tabular, angular, fresh K-feldspar. Muscovite and biotite flakes

Table 7.6 Summary of surface area determinations for the mineral kinetics experiments.

Mineral	Surface Area (m ² .g ⁻¹)
Anhydrite	0.9792
Quartz	0.0824
Albite	0.1674
Microcline	0.1519

Table 7.7 Summary of starting materials with locations and brief descriptions.

Sample Code	Borehole	Grid Reference	Sheet Number	Box	Core N°/ Run	Depth Interval	Sample Description
JMP1	Audlem 15	(3)66946 (3)40550	SJ64SE/10	10	25	86.30 - 86.50	Red-brown, massive mudstone, <1 mm reduction spots. Sample in 2 portions.
JMP2	Audlem 15	(3)66946 (3)40550	SJ64SE/10	11	25	88.20 - 88.45	Brown, massive mudstone, <1 mm to 10 mm reduction spots. High angle, <1 mm vein - ?unmineralised.
JMP3	Audlem 15	(3)66946 (3)40550	SJ64SE/10	12	26	91.61 - 91.86	Red-brown, massive mudstone, <1 mm reduction spots. Sample in 2 portions.
JMP4	Audlem 15	(3)66946 (3)40550	SJ64SE/10	14	28	97.78 - 97.90	Massive, cream anhydrite with cm- scale mudstone lamella and mudstone inclusions <5 cm across.
JMP5	Audlem 15	(3)66946 (3)40550	SJ64SE/10	14	29	99.57 - 99.81	Massive, cream anhydrite with fractured mudstone inclusions <5 cm across.
JMP6	Bewsey	(3)59260 (3)89480	SJ58NE/55	56	45	~1.53 - 1.88	Depths measured from top of each stick. Medium, orange-red sandstone.
JMP7	Bewsey	(3)59260 (3)89480	SJ58NE/55	72	57	0.00 - 0.49	Depths measured from top of each stick. Medium, orange-red sandstone.
JMP8	Bewsey	(3)59260 (3)89480	SJ58NE/55	81	63	0.12 - 0.74	Depths measured from top of each stick. Medium, orange-red sandstone.
JMP9	Bewsey	(3)59260 (3)89480	SJ58NE/55	73	58	~0.48 - 0.98	Depths measured from top of each stick. Medium, orange-red sandstone.
JMP10	Cleethorpes	????	Unknown	?	?	1116.4	
JMP11	Cleethorpes	????	Unknown	?	?	1303.96 - 1304.00	
JMP12	Cleethorpes	????	Unknown	?	?	1306.17 - 1306.27	Fine, well-sorted sandstone with little framework grain dissolution. Laminae of fine silty sand. Dolomite cement.
JMP13	Marchwood	SU 3991 1118	Unknown	?	?	1693.54 - 1693.67	Well sorted, quartz feldspathic sandstone. 2° porosity in K-feldspar. Euhedral K-Feldspar overgrowths. Calcite cement plus minor barite.
JMP14	Bewsey	(3)59260 (3)89480	SJ58NE/55	81	63	3.5 - 25.5	From JMP8B. Approximate depths measured from top of sample.
JMP15	Bewsey	(3)59260 (3)89480	SJ58NE/55	81	63	29.5 - 49.5	From JMP8D. Approximate depths measured from top of sample.
JMP16	Bewsey	(3)59260 (3)89480	SJ58NE/55	72	57	0.0 - 20.0	From JMP7. Approximate depths measured from top of sample.

were present with muscovite dominating over biotite. Although generally fresh, occasional micas were deformed by compaction. They were occasionally observed to have been altered with splaying along the basal cleavages and precipitation of structureless kaolinite and submicron hematite inclusions in the resultant secondary porosity. Occasional coarser biotite flakes had altered to a more chloritic phase along outer margins. Minor, angular, very slightly ferroan-manganous dolomite grains were generally fresh but occasionally displayed slight corrosion. Rare, composite grains of plagioclase and alkali feldspar were possibly small, angular lithic clasts. Accessory phases detected by BSEM included zircon, rutile, ilmenite — typically exsolved, anatase, hematite, rare apatite and rare celestite and/or barite. All accessory phases were less than 10 μm in diameter except for occasional authigenic rutile grains. Rare authigenic, anhedral monazite crystals were less than 5 μm in diameter.

The detrital grains described above were enclosed in a clay to fine silt-grade matrix consisting of very fine grained detrital grains, micas and illite-smectite clay. The clay consisted of irregular flakes less than 5 μm in diameter (Plate 1). The fabric was matrix supported with moderate alignment of mica flakes (Plate 2). Intergranular porosity, occurring between the mica flakes, typically formed elongate pores up to 4 μm long and with submicron thickness. Chlorite formed irregular and intermittent lenses or pods up to 20 μm thick within which chlorite flakes were oriented with the mudstone fabric. These chlorite patches contained higher porosity than the rest of the matrix. Porosimetry analysis of JMP3, a very similar mudstone sample adjacent to JMP1, indicated the porosity of this mudstone was 3.74% (Table 7.8). The measured surface area is given in Table 7.9.

** Unreacted Sherwood Sandstone*

JMP10

This sample of Sherwood Sandstone was taken from the Cleethorpes No. 1 borehole (TA 30237 07090) at a depth of 1116.4 ft (Table 7.7). The sample was a red, slightly friable,

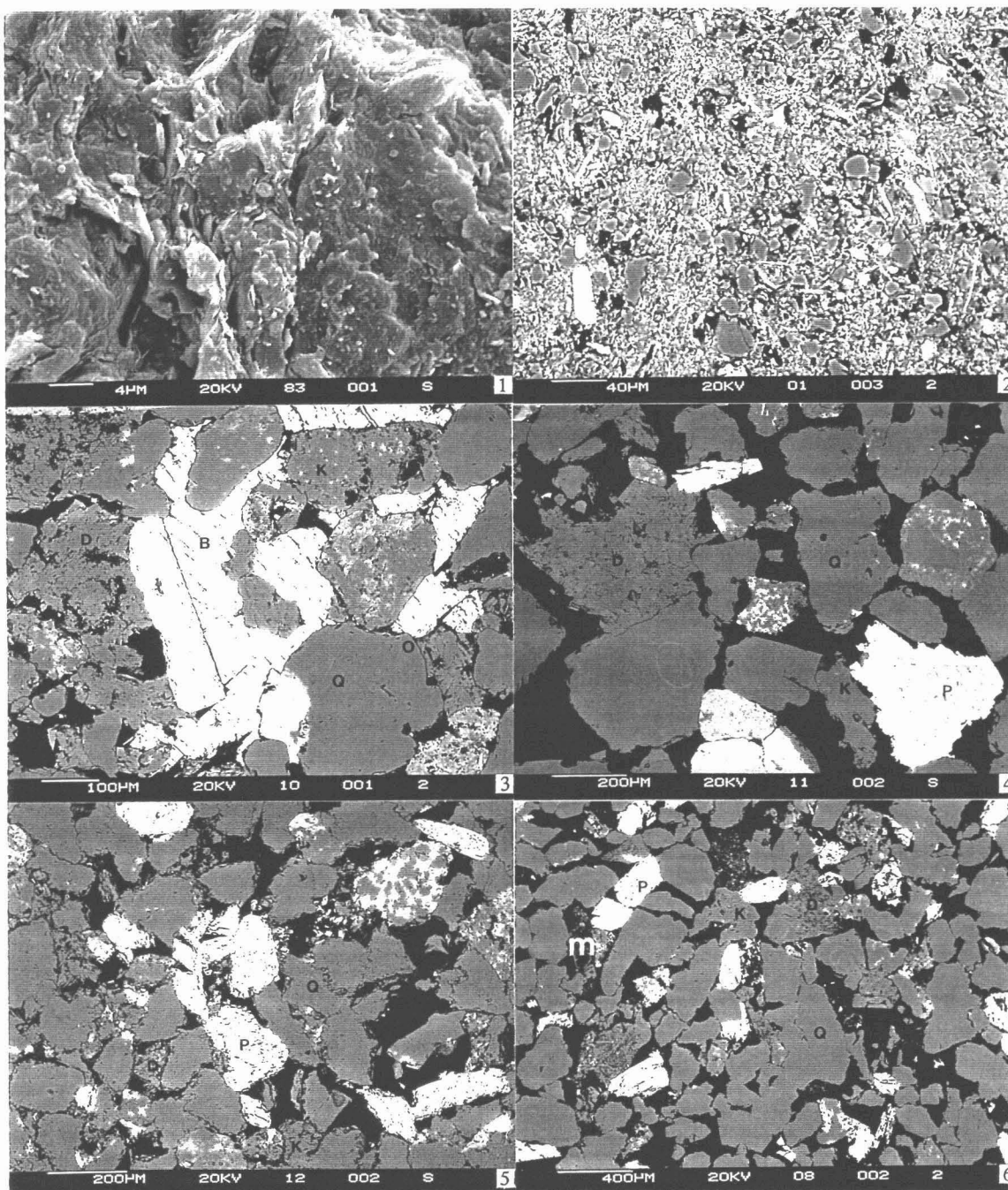
medium to fine grained, laminated, moderately sorted sandstone. Petrographic examination indicated that it consisted of predominantly subangular to subrounded detrital quartz, minor, subangular K-feldspar, plagioclase grains and rare micas. Heavy mineral bands comprising ilmenite, magnetite, zircons and rare xenotimes occurred at submillimetre intervals throughout the sample. Certain laminae were initially cemented by an expansive, poikiloplastic dolomite cement. This was enclosed by later anhydrite. Rare expansive patches of barite, up to 1 mm across, with a radiating fabric may represent pseudomorphed anhydrite (Plate 3). Occasionally, euhedral quartz overgrowths developed. The rare micas were deformed due to compaction and were typically splayed along basal cleavage with trace amounts of hematite precipitating between individual plates. The primary intergranular porosity was modified significantly by corrosion of dolomite and anhydrite cements as well as dissolution of K-feldspars and quartz overgrowths. The porosity was spatially controlled by the lamination with porosity reaching up to approximately 50% locally along certain laminae but typically around 10% in other areas. The extensive dissolution of both K-feldspars and cements has produced a high proportion of secondary, moldic, oversized and minus cement porosity.

JMP11

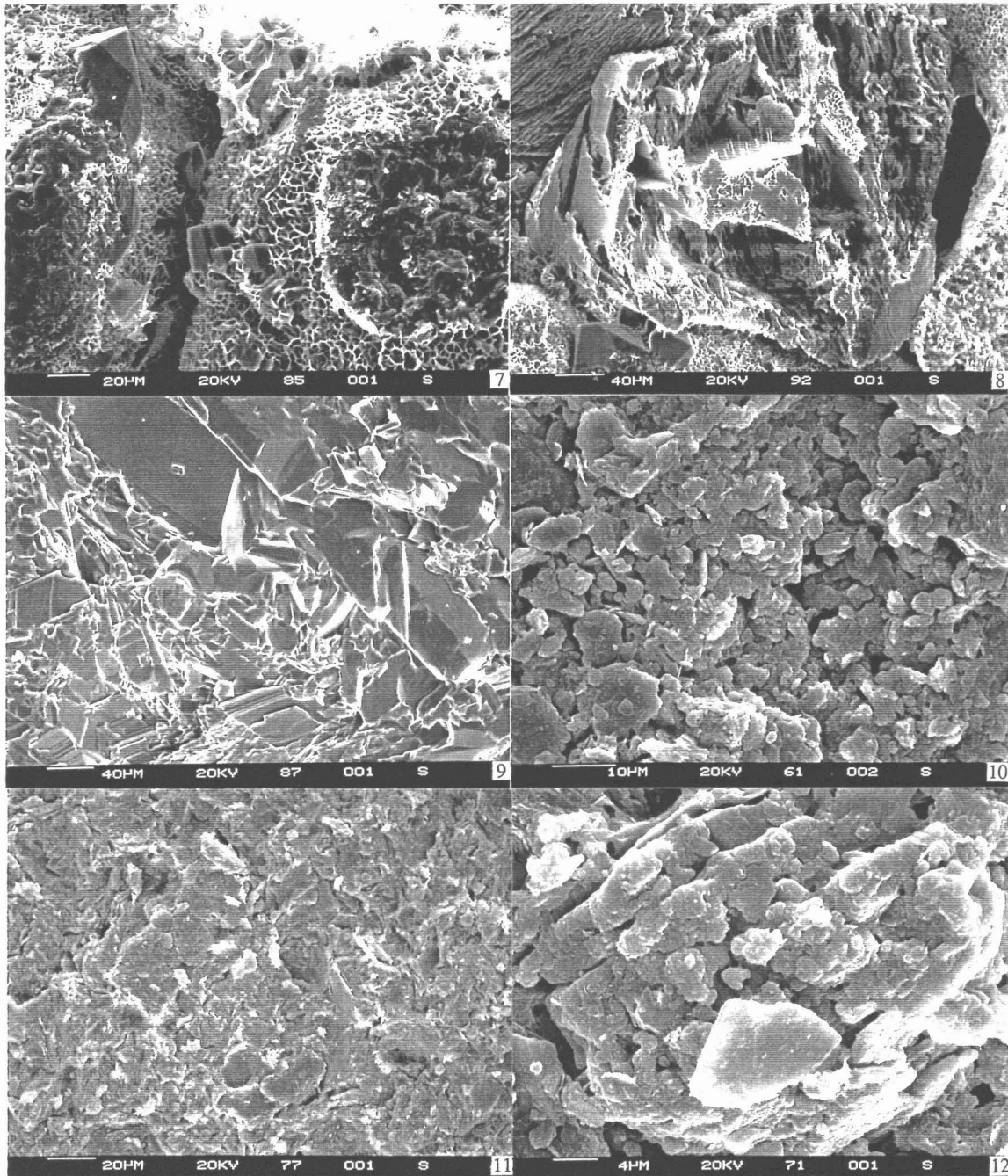
This sample of Sherwood Sandstone was taken from the Cleethorpes No. 1 borehole (TA 30237 07090) at a depth of 1303.96–1304.00 ft (Table 7.7). The sample was a red, slightly friable and medium grained subarkose with faint cross-lamination. Petrographic examination revealed the well-sorted sandstone to comprise predominantly subrounded to subangular, medium grained quartz, angular, K-feldspars, minor lithic fragments consisting predominantly of K-feldspar and plagioclase and trace ilmenite. This sample had very well developed intergranular porosity that was well connected (on removal of the sample from the experiment it was observed to be completely saturated throughout the whole of the sample). K-feldspars were observed to be superficially corroded. Diagenetic modification of the primary porosity had occurred with the

Table 7.8 Porosity, permeability and hydraulic conductivity data for a selection of unreacted and reacted samples used for the batch and core-flooding experiments.

Starting material	Reaction product	Porosity (%)	Permeability (mD)	Hydraulic conductivity (m/d)
JMP3		3.741		
JMP8A		21.582	1202.485	0.773
JMP8B	JMP14A	20.497		
JMP8B	JMP14B	20.614		
JMP8C		21.674	827.160	0.532
JMP8D	JMP15A	21.409		
JMP8D	JMP15B	21.568		
JMP8E		21.925	1151.936	0.741
	JMP34 base	20.911		
	JMP34 top	20.263		
		21.159		
JMP10		17.251		
	JMP38	18.880		
JMP11		24.210		
	JMP36	12.854		
	JMP37	12.924		
	JMP40	21.704		



- Plate 1 Secondary electron SEM photomicrograph of typical Mercia Mudstone micaceous matrix with elongate intergranular pores up to 5 μm long and 1 μm wide. Sample JMP1.
- Plate 2 Backscattered electron SEM photomicrograph of typical Mercia Mudstone detrital quartz, feldspar and mica grains in a micaceous matrix. Note porosity is bimodal with submicron intergranular porosity and isolated minor pores up to 10 μm in diameter. Sample JMP1.
- Plate 3 Backscattered electron SEM photomicrograph of typical Sherwood Sandstone starting material with detrital quartz (Q) and minor quartz overgrowths (O), detrital K-feldspars (K) with intragranular secondary porosity, severely corroded dolomite (D) cement and barite (B) cement possibly after anhydrite. Black is porosity. Sample JMP10.
- Plate 4 Backscattered electron SEM photomicrograph of unreacted Sherwood Sandstone. Quartz (Q) and K-feldspar (K), plagioclase (P), dolomite (D) and porosity (black). Compare with Plate 29 of reacted sandstone. Sample JMP11.
- Plate 5 Backscattered electron SEM photomicrograph of unreacted Sherwood Sandstone. Quartz (Q) and K-feldspar (K), plagioclase (P), dolomite (D) and secondary porosity (black). Sample JMP12.
- Plate 6 Backscattered electron SEM photomicrograph of unreacted Wilmslow Sandstone. Quartz (Q) and K-feldspar (K) typically corroded, plagioclase (P), dolomite (D) and secondary porosity (black) typically oversized. Note moldic porosity (M). Sample JMP8.



- Plate 7 Secondary electron SEM photomicrograph of detrital quartz surfaces coated in authigenic boxwork illite-smectite and euhedral quartz overgrowths. Note poorly developed fibrous illite at top right of photo. Sample JMP8.
- Plate 8 Secondary electron SEM photomicrograph of skeletal K-feldspar grain. Note lack of authigenic clay lining secondary porosity. Sample JMP8.
- Plate 9 Secondary electron SEM photomicrograph of unreacted anhydrite. Sample JMP5.
- Plate 10 Secondary electron SEM photomicrograph showing detail of enhanced porosity on the external surface submerged in seawater of Mercia Mudstone. Sample JMP24, reaction with CO₂-saturated synthetic seawater for one month.
- Plate 11 Secondary electron SEM photomicrograph of internal, freshly exposed surface of Mercia Mudstone from above seawater-CO₂ interface showing no alteration has taken place. Sample JMP24, reaction with CO₂-saturated synthetic seawater for 109 days.
- Plate 12 Secondary electron SEM photomicrograph showing detail of corroded dolomite grain resulting in considerable local increase in porosity. Sample JMP24, reaction with CO₂-saturated synthetic seawater for 109 days.



Table 7.9 Surface area data for starting materials and reaction products. Standard deviations are quoted as a guide for comparison with usually applied errors of $\pm 3\%$.

Run Number	Sample	Starting Material	Description	Specific Surface area m^2g^{-1}	Error $\pm 3\%$	Standard Deviation
n/a	n/a	JMP1	Mudstone starting material	21.1	0.63	0.20
n/a	n/a	JMP12	Arkosic arenite starting material	3.63	0.11	0.01
n/a	n/a	JMP13	Sandstone starting material	0.94	0.03	0.01
n/a	n/a	JMP11	Subarkose starting material	0.94	0.03	0.02
n/a	n/a	JMP3	Mudstone starting material	24.53	0.74	0.05
373	JMP24	JMP1	Mudstone, seawater+CO ₂ 3 months reaction	20.47	0.61	0.39
383	JMP27	JMP11	Subarkose, seawater+CO ₂ 3 months reaction	1.03	0.03	0.03
375	JMP32	JMP3	Mudstone, seawater+CO ₂ 8 months reaction	23.57	0.71	0.46
376	JMP33	JMP3	Mudstone, DIW+CO ₂ 8 months reaction	27.18	0.82	0.06
381	JMP36	JMP12	Arkosic arenite, seawater+CO ₂ 8 months reaction	4.31	0.13	0.08
382	JMP37	JMP12	Arkosic arenite, DIW+CO ₂ 8 months reaction	4.06	0.12	0.10
385	JMP40	JMP13	Sandstone, seawater+CO ₂ 8 months reaction	1.58	0.05	0.12
399	JMP30	JMP1	Mudstone, supercritical CO ₂ 8 months reaction	20.74	0.62	0.34

formation of minor, patchily developed quartz overgrowths and dolomite cement that infilled occasional pore spaces. No quartz overgrowths were observed enclosed by the dolomite, suggesting that the dolomite may pre-date quartz overgrowths. The dolomite was partially corroded in many places and may have originally been more extensive (Plate 4). Rare mica flakes were splayed along basal cleavage allowing precipitation of hematite within the resultant secondary porosity. Liquid resaturation porosity analysis indicated porosity of this sample was 24.21%. This value is in good agreement with the value obtained by point counting of 24.8% and helps to add some confidence to the validity of the point counting data (Table 7.10). The measured surface area is given in Table 7.9.

JMP12

This sample was taken from the Cleethorpes No. 1 borehole (TA 30237 07090) at a depth of 1306.17–1306.27 ft (Table 7.7). It was a red, fine grained, moderately well sorted and compacted sandstone. Although texturally and mineralogically similar to JMP11, point counting indicated that this sandstone was an arkosic arenite due to a slightly higher proportion of K-feldspar. It comprised angular, irregular detrital quartz, angular K-feldspars and minor angular plagioclase grains. Rare detrital hematite grains and rounded lithic, volcanic clasts were also present together with a trace of mica. The mica flakes were splayed along basal cleavage allowing precipitation of occasional authigenic hematite in the secondary porosity formed. Minor, clay-rich, patchy matrix occurred locally throughout the sample. The sandstone had a well-connected network of intergranular primary porosity. This had been substantially modified locally by the precipitation of euhedral quartz overgrowths, euhedral K-feldspar overgrowths and patchy dolomite cement. Authigenic, very poorly developed, ragged flaky illite-smectite flakes lined some pore walls, possibly post-dating the quartz cement. Secondary porosity developed as a result of extensive quartz overgrowth dissolution, minor K-feldspar corrosion, more significant plagioclase dissolution and insignificant

alteration of micas (Plate 5). In addition, the dolomite cement was also corroded. Hence, much of the porosity in this sample was therefore less than cement porosity (6.5% by point counting) with some areas of oversized and moldic voids (4.5% by point counting). Total porosity was determined by point counting to be 14.7% (Table 7.10). The measured surface area is given in Table 7.9.

JMP8

This sample of Wilmslow Sandstone was taken from the Bewsey borehole (Table 7.7). Several small splits were taken from this material for the batch experiments. For comparative purposes, poroperm analyses were completed on three samples of unreacted sandstone that were taken above the core samples (JMP8A), between them (JMP8C) and below them (JMP8E). This sandstone was a medium grained, orange-red, moderately well sorted, subarkose consisting of subrounded to subangular detrital quartz and K-feldspar grains, with minor lithic clasts, mud clasts and trace mica (Table 7.10, Plate 6). Detrital surfaces were extensively coated in well developed, authigenic, boxwork illite-smectite clay, up to 5 μm thick (Plate 7). EDXA indicated that the clay contained predominant K but also minor Mg and Fe, suggesting that minor amount of chlorite may be intimately admixed. Post-dating the authigenic clay were euhedral quartz overgrowths. Euhedral K-feldspar overgrowths developed on detrital K-feldspar grains and occasionally developed minor corrosion. Minor, fibrous illite developed from the boxwork illite-smectite clay but post-dated the quartz cement. Minor dolomite with post-dating calcite cement was also patchily distributed and possibly post-dated the quartz cement. Relationship to fibrous illite was unclear. Many K-feldspars were attacked to varying degrees from superficial corrosion to development of skeletal grains and moldic porosity (Plate 8). In some cases alteration to a possible illite-smectite clay occurred in areas of corrosion. Lithic clasts typically had well-developed intragranular porosity due to removal of plagioclase. The sandstone was generally poorly cemented. Liquid resaturation porosimetry determined porosities of

Table 7.10 Results of point counting based on approximately 400 counts per sample by BSEM-Batch and core flood experiments.

Run	Sample	Quartz	K-feldspar	Plagioclase	Lithics	Mica	Barite	Clay matrix	Quartz cement	K-feldspar cement	Calcite cement	Dolomite cement	llite	Total porosity
Starting material	JMP12	38.2%	15.7%	3.7%	4.0%	0.0%		4.7%	12.5%	0.0%	0.0%	2.5%	4.0%	14.7%
381	JMP36 base	42.8%	14.3%	0.5%	6.3%	0.3%		2.3%	8.5%	0.3%	0.0%	1.8%	4.3%	19.0%
381	JMP36 top	44.5%	12.8%	4.0%	4.3%	0.8%		2.5%	5.0%	0.0%	0.0%	1.3%	3.5%	21.5%
382	JMP37 base	49.3%	15.0%	2.5%	6.0%	0.0%		3.3%	4.0%	0.0%	0.0%	4.3%	2.5%	16.0%
382	JMP37 top	49.9%	14.8%	4.3%	4.3%	0.0%		0.5%	3.8%	0.0%	0.0%	4.3%	1.5%	16.4%
Starting material	JMP8	39.0%	9.3%	0.0%	4.5%	0.5%		5.0%	8.3%	0.5%	1.0%	3.5%	3.8%	24.8%
379	JMP34	42.5%	6.3%	0.0%	7.3%	0.3%		3.3%	10.0%	0.0%	0.0%	1.5%	9.8%	19.3%
380	JMP35	46.8%	5.8%	0.5%	6.8%	0.0%		1.8%	7.5%	0.0%	0.0%	0.8%	7.5%	22.8%
370 inlet	JMP14A	43.3%	5.8%	0.0%	6.5%	1.3%		4.5%	11.3%	0.5%	0.8%	1.8%	4.3%	20.3%
370 outlet	JMP14B	42.2%	7.1%	0.0%	5.1%	1.2%		2.9%	8.8%	0.2%	0.7%	1.7%	8.8%	21.1%
Starting material	JMP8D	56.3%	9.5%	0.5%	2.8%	0.3%		3.0%	0.0%	0.0%	0.0%	4.0%	4.3%	19.5%
409 inlet	JMP15A	57.0%	5.5%	2.3%	4.3%	0.5%		3.0%	0.0%	0.0%	0.0%	3.3%	1.5%	22.8%
409 outlet	JMP15B	59.1%	7.0%	2.8%	2.0%	0.3%		1.5%	0.0%	0.0%	1.3%	1.5%	1.0%	23.6%
Starting material	JMP13	43.3%	26.3%	0.8%	1.8%		0.5%	3.8%	0.0%	0.0%	5.0%	0.0%	2.8%	16.0%
385	JMP40	39.0%	24.3%	0.8%	0.3%		0.5%	2.0%	0.0%	0.0%	4.0%	0.0%	0.3%	29.0%
Starting material	JMP11	39.8%	11.0%	0.0%	5.3%	0.8%		1.8%	9.0%	0.0%	0.0%	7.5%	0.3%	24.8%
383	JMP27 base	45.3%	9.3%	0.8%	5.0%	0.0%		1.3%	5.0%	0.0%	0.0%	4.8%	2.3%	26.5%
383	JMP27 top	47.5%	6.8%	0.5%	5.3%	0.3%		0.8%	6.5%	0.5%	0.0%	6.5%	0.3%	25.3%

Table 7.10 *Continued.* Percentage change after reaction (value quoted is absolute difference between starting material and reaction product, i.e. for JMP36 base quartz value is 42.8-38.2 = 4.6).

Starting material	Run product	Quartz	K-feldspar	Plagioclase	Lithics	Barite	Mica	Clay matrix	Quartz cement	K-feldspar cement	Calcite cement	Dolomite cement	llite	Total porosity
JMP12	JMP36 base	4.6%	-1.5%	-3.2%	2.3%	0.3%		-2.5%	-4.0%	0.3%	0.0%	-0.7%	0.3%	4.3%
JMP12	JMP36 top	6.3%	-3.0%	0.3%	0.3%	0.8%		-2.2%	-7.5%	0.0%	0.0%	-1.2%	-0.5%	6.8%
JMP12	JMP37 base	11.1%	-0.7%	-1.2%	2.0%	0.0%		-1.5%	-8.5%	0.0%	0.0%	-1.0%	-1.5%	1.3%
JMP12	JMP37 top	11.7%	-0.9%	0.6%	0.4%	0.0%		-4.2%	-8.6%	0.0%	0.0%	1.9%	-2.5%	1.7%
JMP8B	JMP34	3.5%	-3.0%	0.0%	2.8%	-0.3%		-1.8%	1.8%	-0.5%	-1.0%	-2.0%	6.0%	-5.5%
JMP8B	JMP35	7.8%	-3.5%	0.5%	2.3%	-0.5%		-3.3%	-0.8%	-0.5%	-1.0%	-2.8%	3.8%	-2.0%
JMP8B	JMP14A	4.3%	-3.5%	0.0%	2.0%	0.8%		-0.5%	3.0%	0.0%	-0.3%	-1.8%	0.5%	-4.5%
JMP8B	JMP14B	3.2%	-2.1%	0.0%	0.6%	0.7%		-2.1%	0.6%	-0.3%	-0.3%	-1.8%	5.1%	-3.7%
JMP8D	JMP15A	0.7%	-4.0%	1.8%	1.5%	0.3%		0.0%	0.0%	0.0%	0.0%	-0.8%	-2.8%	3.3%
JMP8D	JMP15B	2.9%	-2.5%	2.3%	-0.7%	0.0%		-1.5%	0.0%	0.0%	1.3%	-2.5%	-3.2%	4.1%
JMP13	JMP40	-4.3%	2.0%	0.0%	-1.5%		0.0%	0.0%	-1.8%	0.0%	0.0%	-1.0%	-2.5%	13.0%
JMP11	JMP27 base	5.5%	-1.8%	0.8%	-0.3%	-0.8%		-0.5%	-4.0%	0.0%	0.0%	-2.8%	2.0%	1.8%
JMP11	JMP27 top	7.8%	-4.3%	0.5%	0.0%	-0.5%		-1.0%	-2.5%	0.5%	0.0%	-1.0%	0.0%	0.5%



between 21.58% and 21.93% (samples JMP8A and JMP8E respectively, Table 7.8) comprising mainly secondary porosity (secondary intergranular, moldic, oversized and minus cement) due to dissolution of K-feldspars and removal of a cement phase. The point counting analyses (~25%, Table 7.10) are in general agreement with these porosities and have broadly similar magnitudes. The differences are probably due to the poor preservation of authigenic clay textures in polished thin sections resulting in a higher value. Permeability will be significantly modified and reduced by authigenic clays blocking pore throats. Permeability of the unreacted sandstone was determined to be between 827.16 mD and 1202.49 mD (samples JMP8C and JMP8A respectively). Variations in permeability are likely to be controlled by the relative proportions of authigenic clays found in each sample since the porosities are similar and these authigenic clays will only slightly affect the pore volume but will greatly affect the permeability. Unfortunately, surface areas were not determined.

JMP13

This Sherwood Sandstone sample of arkosic arenite was taken from the Marchwood borehole (SU 3991 1118) from a depth of 1693.54 to 1693.67 feet (Table 7.7). Although most of the sandstone at this depth is generally well sorted, the sample taken was poorly sorted with coarse and medium grained laminae in millimetre-scale upward fining cycles. The sandstone consisted of angular to subrounded quartz and K-feldspar grains with rare, subrounded mudstone pellets, micas and plagioclase grains. Micas were deformed during compaction and slightly splayed along basal cleavage. Rare authigenic rutiles, up to 40 μm across, lined pore-walls and post-dated K-feldspar overgrowths. Ferro-magnesian heavy minerals were typically replaced by ilmenite. Quartz and K-feldspar overgrowths developed to a limited extent in this sample. The sandstone was very patchily cemented by a calcite cement. At least two calcite generations were recognised; an earlier Fe-rich, euhedral, sparry calcite developed from pore walls into open voids and a later Fe-poor poikilotopic calcite that enclosed the earlier calcite. The later calcite cement infills oversized pores up to 400 μm across (possibly indicating an expansive fabric or replacing a previous cement with an expansive fabric). Pre-dating the calcite were rare plates of barite and celestite. The sample had a well-connected pore network with approximately 16 % porosity determined by point counting (Table 7.10). This porosity was mainly secondary intergranular moldic and oversized voids. This was due to often severe corrosion of K-feldspars. Dissolution of feldspars post-dated calcite cement precipitation and sometimes resulted in moldic pores outlined by relict K-feldspar overgrowths and enclosed in calcite. The measured surface area is given in Table 7.9.

* Unreacted anhydrite (JMP5)

This sample of anhydrite was obtained from the British Gypsum Audlem 15 borehole in Audlem, Staffordshire, UK., depth 99.57–99.81 m (Table 7.7). It was a massive, orange to cream, anhydrite with very irregular lenses of faulted and highly brecciated mudstone. Petrographically the anhydrite consisted of interlocking fresh, massive crystals (Plate 9). The anhydrite contained inclusions of celestite as euhedral authigenic crystals up to 20 μm across. Also present were subhedral to euhedral, slightly ferroan dolomite patches up to several millimetres across composed of crystals up to 10 μm in diameter. These crystals were slightly corroded. The mudstone lenses con-

sisted of fine grained quartz, feldspar and mica in a clay-rich matrix. They had been extensively cemented and partially replaced by anhydrite.

* Unreacted fullers' earth mudstone

A sample of fullers' earth mudstone was obtained from near Woburn, UK, and is of Lower Greensand (Lower Cretaceous) age. The unreacted sample was green in colour, formed predominantly of smectite (variety Ca-montmorillonite), and consisted of clay-sized particles in a massive habit. Individual particles were too fine grained to resolve by SEM.

7.3.2 Description of the numerical simulators

Two kinds of simulator have been constructed, a geochemical simulator and a one-dimensional coupled reaction-transport code.

The first simulator calculates water solute speciation, and water-rock- CO_2 interactions as a function of time. It can be used by itself to simulate closed systems, such as the batch experiments or the mineral grain/residual water system within the CO_2 -dominated part of the reservoir, but it is also dedicated to be a subroutine of the coupled reaction-transport code.

The second code simulates the migration of dissolved CO_2 and other dissolved species in the water phase combined with their chemical interaction with the rock, assuming a constant flow velocity. This coupled reaction-transport code enables interpretation of the core flood experiments and the simulation of CO_2 -rich water migration through a reservoir. Such a situation may be encountered when the conditions of injection and the characteristics of the reservoir are such that all the injected CO_2 is able to dissolve into the formation water. It is a first step towards the simulation of open systems which is an absolute necessity for making reservoir-wide predictions concerning both the injection zone and further into the reservoir, i.e. to assess both the short term and the long term effects of CO_2 disposal.

A second step would be to achieve a higher degree of coupling by linking the reaction-transport code to a two phase flow model. This would enable the simulation of spatial and temporal changes in flow velocity and would allow the construction of SC CO_2 saturation profiles. Such a flow model was used in chapter 6, but the effective coupling with the reaction-transport code would have required effort in excess of the time frame of this project. However, the combination of the results from chapters 6 and 7 should allow for consideration of a more typical CO_2 injection scenario.

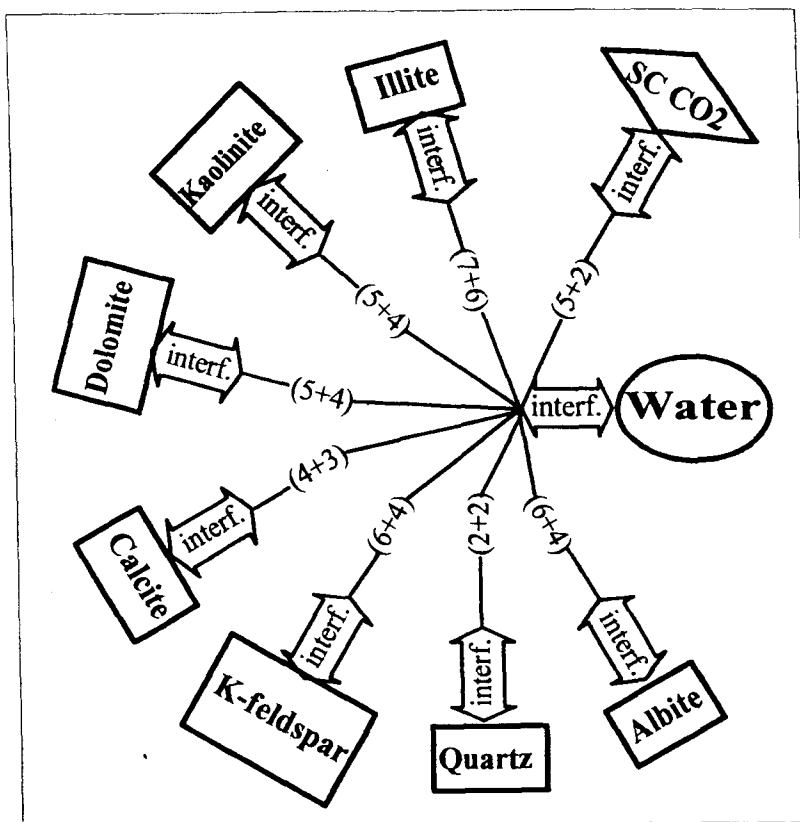
More details on these simulators are given below.

7.3.2.1 THE CO2ROCK GEOCHEMICAL SIMULATOR

The chemical simulator CO2ROCK calculates the speciation of water solutes and water-rock- CO_2 interactions as a function of time. It represents a multiphase system with a water phase, 7 mineral phases and a supercritical CO_2 phase (Figure 7.6). This simulator was built with a code generator, NEPTUNIX, combined with a graphic software package, ALLANTM, in accordance with a new approach to geochemical modelling that frees the model designer from data processing and numerical administrative detail (Czernichowski-Lauriol and Fabriol, 1992; Fabriol and Czernichowski-Lauriol, 1992). Once all the mathematical equations describing the chemical processes are provided (conservation of mass equations, laws of mass action, kinetic laws, aqueous solution model),

Figure 7.6 The CO2ROCK geochemical simulator.

It was developed using the ALLANTM/NEPTUNIX code generator software package (see text). A multiphase system is represented by a compound model. Each phase (liquid, solid, gas) is described by a simple model and represented by its associated icon. The simple models are graphically linked through ALLANTM to build the compound model. The numbers between brackets denote the number of intensive (temperature, activities) and extensive (mole variation per chemical element) variables exchanged.



NEPTUNIX automatically builds the FORTRAN code and the executable module (i.e. the simulator). ALLANTM provides a userfriendly interface for these operations and operates post-processing of the results from the simulation in the form of graphs.

The geochemical simulator takes into account eleven main chemical elements considered important in subsurface formations: O, H, Na, K, Ca, Mg, Al, Si, S, C, Cl. Their speciation in water was calculated according to 47 simple and complex species. Seven minerals were considered: Quartz (SiO_2), K-feldspar (KAlSi_3O_8), Albite ($\text{NaAlSi}_3\text{O}_8$), Kaolinite ($\text{Al}_2\text{Si}_2\text{O}_5(\text{OH})_4$), Illite ($\text{K}_{0.6}\text{Mg}_{0.25}\text{Al}_{2.3}\text{Si}_{3.5}\text{O}_{10}(\text{OH})_2$), Calcite (CaCO_3) and a disordered Dolomite ($\text{CaMg}(\text{CO}_3)_2$). All the thermodynamic data used came from the DATA0.COM.R10 database of the EQ3/6 geochemical software package (Wolery, 1992a). For the 11 elements used in this system, this database is consistent with the SUPCRT92 data, a reference software package for calculating the standard molal thermodynamic properties of minerals, gases, aqueous species and reactions (Johnson et al., 1991). The slight effect of pressure on the thermodynamic constants was not taken into account.

The aqueous solution model used in the water model of the simulator was based on an extensive Debye-Hückel formalism, similar to version 7.0 of EQ3/6 (Wolery, 1992b; Daveler and Wolery, 1992). The activity coefficients of charged species were calculated using the B-dot equation, the activity coefficient of aqueous CO_2 was computed from an expression after Drummond (1981) (though the sign error in version 7.0 was fixed, as per the changes in version 7.2), the same value was assigned to the activity coefficients of neutral non-polar species, while the activity coefficients of neutral and polar species were set to unity. The activity of water was calculated by an expression which was quasi-consistent with the B-dot equation (Wolery, 1992b). Note that the extended Debye-Hückel

formulation is valid for dilute solutions up to ionic strengths of 1 molal at most. For more accuracy, other semi-empirical formulations, such as the Pitzer type equations (Pitzer, 1973), should be used above the salinity of seawater (0.5 molal). However, formulations that would take into account the 11 chemical elements considered in this study, and the effects of temperature, are still under development. Changes in the amount of solvent water throughout the simulation were accounted for in the water model through the mass balance equations for each chemical element (O and H in this case). Laws of mass action expressed thermodynamic equilibrium between all aqueous species.

The simple models for each mineral contained a kinetic dissolution/precipitation law function of apparent kinetic constants ($\text{mol}\cdot\text{s}^{-1}$), and the thermodynamic affinity of the reaction. This was a simplified expression for dealing with kinetics, as mechanisms, rates and reactive surface areas are still poorly known.

The simple model for supercritical CO_2 also contained a kinetic law, a function of an apparent kinetic constant for dissolution ($\text{mol}\cdot\text{s}^{-1}$), and the ratio between CO_2 partial pressure and the total pressure of the system. Thus, no more dissolution occurred when the partial pressure of CO_2 reached the total pressure. The fugacity of CO_2 was computed from the partial pressure, using the fugacity coefficients given by Duan et al. (1992).

The CO2ROCK simulator could be run by constructing different sets of operating instructions, depending on the mineralogical composition of the reservoir. For example, one was dedicated to carbonate formations, with the masses of silicate and aluminosilicate minerals fixed to zero, others had a greater number of minerals and were dedicated to sandstone formations. A particular set was dedicated to the $\text{SC CO}_2/\text{H}_2\text{O}$ system by 'deactivating' all the minerals.

Compared to classic geochemical codes, the CO2ROCK simulator is well suited to coupling with other simulators

because of its computational efficiency, appropriate management of input/output parameters and efficient numerical treatment of kinetic equations. It is also tailor-made to represent only the chemical phenomena which are considered critical for the study involved. It is easy to modify the form of an equation or to add other simple models, such as new minerals. Its flexibility facilitates later coupling, or improvement of the conceptual chemical model, once greater knowledge on either the theoretical geochemistry, or site characterization has been obtained.

7.3.2.2 THE CATCO2 COUPLED CHEMISTRY AND TRANSPORT SIMULATOR

The coupled chemistry and transport code (CATCO2) consisted of sequential calls to the transport and chemistry subroutines for each time step in each grid block (Fabriol et al., 1993; Kervévan et al., 1994). The transport module was based on a random walk algorithm and accounted for the movement of dissolved species by advection, dispersion and diffusion. The chemistry module was the CO2ROCK simulator.

7.4 INTERPRETATION OF THE EXPERIMENTS

7.4.1 The solubility and kinetics of dissolution of supercritical CO₂ into water and synthetic seawater

7.4.1.1 DESCRIPTION OF THE RESULTS

The full set of experimental data are presented in Table 7.11. Careful observation of the data revealed that some samples had much less CO₂ in them than had been expected, whilst others had excess CO₂ in them. As mentioned in

section 7.3.1.1, an apparent reduction in CO₂ concentration can easily happen if pressure reduction occurred during sampling. As some of the valves on the experimental apparatus were beginning to show wear towards the end of the experimental programme, they became more difficult to control and hence there was an increase in spurious results. These have been identified in Table 7.11 and have been excluded from the reported results. However, the experiments showing excess concentrations of CO₂ can not be explained by valve failure, and will be treated later in this section. The errors assumed for the data were set at $\pm 0.05 \text{ mol.l}^{-1}$. These are much larger than the analytical errors, but were set so as to account for minor variations during sampling. Larger variations caused by obvious sampling problems were apparent from trends in the data, and caused the rejection of the data.

Solubility of SC CO₂ in de-ionised water at 80 °C and 200 bars pressure

Figure 7.7 shows the data for experiments at timescales up to 18 hours. Other data were also collected, but as noted above, were disregarded due to problems encountered during sampling. The data taken from experiments shorter than 2 hours duration show a rapid approach to equilibrium, which appears to be complete in about 4 hours. The value used for the solubility of SC CO₂ was the average of the four datapoints taken between 4 and 18 hours. This solubility of SC CO₂ in de-ionised water at 80°C and 200 bars pressure was measured, and found to be 1.153 mol.l^{-1} .

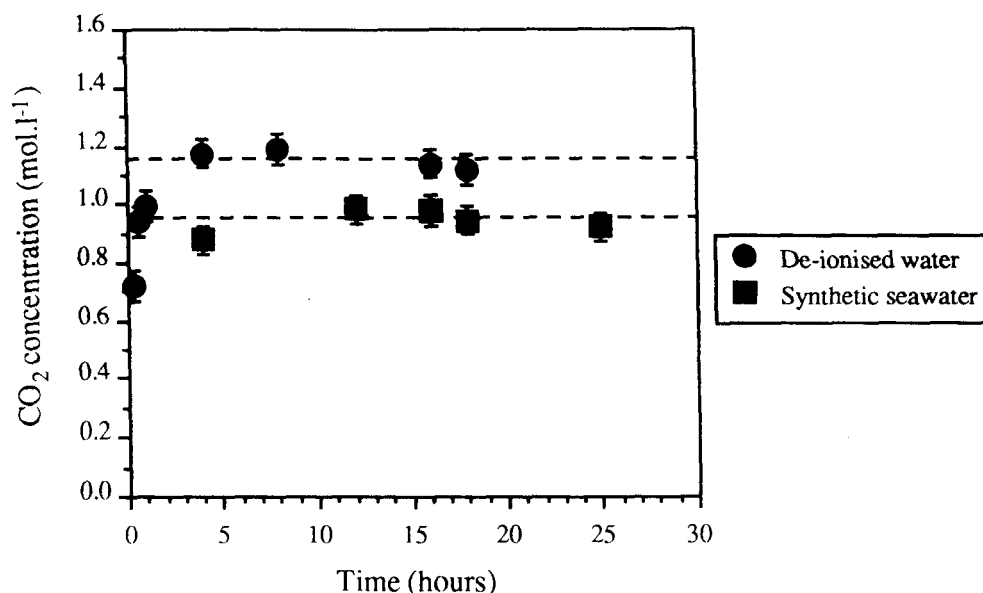
However, this value has not been corrected for changes in solution volume or density due to addition of CO₂, or in-situ pressure and temperature conditions. The data from Weast (1972/1973) indicate that the effects of isothermal

Table 7.11 Information on the SC CO₂ solubility experiments performed.

DIW = De-ionised water, SSW = Synthetic seawater, BD = Below detection.

Experimental run number	Fluid	Duration (hours)	Temperature (°C)	CO ₂ concentration (mol.l ⁻¹)	Data plotted (Y or N)
358	DIW	0.25	80	0.720	Y
359	DIW	0.083	80	0.349	Y
360	DIW	0.167	80	0.551	Y
361	DIW	0.5	80	0.941	Y
363	DIW	0.033	80	0.422	Y
364	DIW	0.05	80	0.475	Y
387	DIW	BLANK	25	0.014	Y
392	DIW	1	80	0.992	Y
393	DIW	8	80	1.186	Y
394	DIW	16	80	1.138	Y
395	DIW	0.042	80	0.535	Y
404	DIW	24	80	0.981	N
405	SSW	16	80	0.976	Y
406	SSW	25	80	0.921	Y
407	SSW	BLANK	25	BD	N
408	SSW	8	80	0.822	N
451	SSW	18	80	0.944	Y
452	SSW	26	80	0.751	N
454	DIW	18	80	1.118	Y
455	SSW	4	80	0.877	Y
456	SSW	12	80	0.981	Y
457	DIW	4	80	1.172	Y
459	DIW	22	80	1.041	N
460	DIW	16.5	60	0.987	N
461	DIW	2	80	0.915	N
462	DIW	13	80	0.862	N
463	DIW	24.5	60	1.086	N
464	DIW	24	40	0.986	N
465	DIW	16	40	0.577	N

Figure 7.7 Results of solubility experiments for SC CO₂ dissolving into de-ionised water and synthetic seawater.



compressibility and isobaric expansivity approximately cancel each other out in going from 25°C and 1 bar, to 80°C and 200 bars. The change in solution volume would be less than 2% which is considered smaller than the experimental error. The change in density of the solution due to dissolved CO₂ was measured (1.058 g.cm⁻³ at 25°C and 200 bars, or 1.046 g.cm⁻³ at 80°C and 200 bars). This can be used to calculate the amount of CO₂ dissolved in 1 kg of water rather than 1 litre of solution. The resulting value is 1.158 mol.kg⁻¹ of H₂O, or 5.10 g of CO₂ per 100 g of de-ionised water.

This data fits well into data reported in Kuk and Montagna (1983), and Wiebe (1941) (Figure 7.8). However, the failure of the experiments at 40°C and 60°C (see Table 7.11) does not allow for a more detailed comparison of the data from this study and those of previous workers.

Solubility of SC CO₂ in synthetic seawater at 80°C and 200 bars pressure

Figure 7.7 shows the data for experiments at timescales up to 25 hours. Other data were also collected, but as noted above, were disregarded due to problems encountered during sampling. Information about the approach to equilibrium were not collected as rate calculations will be calculated from the de-ionised water data. The value used for the solubility of SC CO₂ was the average of the four data-points taken between 12 and 25 hours. This solubility of SC CO₂ in synthetic seawater (0.55M NaCl) at 80°C and 200 bars pressure was measured, and found to be 0.971 mol.l⁻¹.

Corrections for changes in solution volume or density can be applied in a similar manner to the experiments using de-ionised water. The change in density of the solution due to dissolved CO₂ was measured (1.080 g.cm⁻³ at 25°C and 200 bars, or 1.069 g.cm⁻³ at 80°C and 200 bars). This was used to calculate the amount of CO₂ dissolved in 1 kg of water rather than 1 litre of solution. The resulting value is 0.977 mol.kg⁻¹ of H₂O, or 4.30 g of CO₂ per 100 g of de-ionised water.

The rate of dissolution of SC CO₂ into de-ionised water at 80°C and 200 bars pressure

Figure 7.9 shows the data for experiments at timescales up to 60 minutes. In general, the data show an initial rapid

increase in concentration, which falls off towards equilibrium. However, for data obtained from experiments of less than 5 minutes duration there appears to be an excess of CO₂. This is thought to be an experimental artefact caused by the rapid input of CO₂ into the pressure vessel. It is suspected that the rapid expansion of compressed CO₂ caused a localised drop in temperature resulting in the formation of clathrates. Only once the system had stabilised and the clathrates had disappeared, could useful data be obtained. Therefore, data on the 'far from equilibrium' dissolution rate of SC CO₂ into water were obtained by extrapolating to shorter timescales from data taken from experiments between 5 and 60 minutes.

The gradient of the initial CO₂ concentration increase represents the rate of dissolution. However, corrections have to be applied to account for the area over which de-ionised water and SC CO₂ were in contact. The contact area was calculated to be 20.358 cm² (surface area of the aqueous phase minus the cross sectional area of the dip tube). The data in Figure 7.9 indicate that 0.2 moles of CO₂ dissolved into de-ionised water in 150 seconds under far from equilibrium conditions. Therefore, the 'far from equilibrium' dissolution rate of SC CO₂ into water is calculated to be 6.55×10^{-5} mol.cm⁻².s⁻¹.

7.4.1.2 INTERPRETATION

The CO2ROCK simulator was run using the following specific set of operating conditions:

- temperature: 80°C
- pressure: 20 MPa (200 bar)
- CO₂ fugacity coefficient: 0.55 (data from Duan et al., 1992)
- experimental kinetic parameters:
 - * dissolution rate constant: $6.6 \cdot 10^{-5}$ mol.cm⁻².s⁻¹
 - * contact surface between SC CO₂ and water: 20.36 cm²
 - > apparent dissolution rate constant (vd): $1.34 \cdot 10^{-3}$ mol.s⁻¹

Figure 7.8
Solubility of CO₂ in de-ionised water using data from this study, and that reported by Kuk and Montagna (1983) and Wiebe (1941).

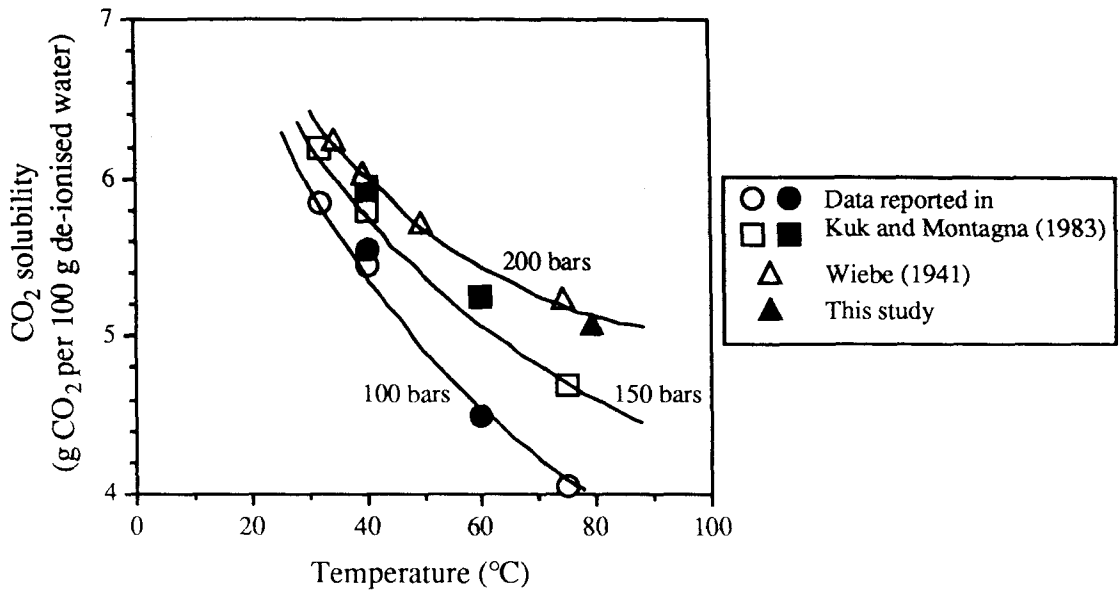
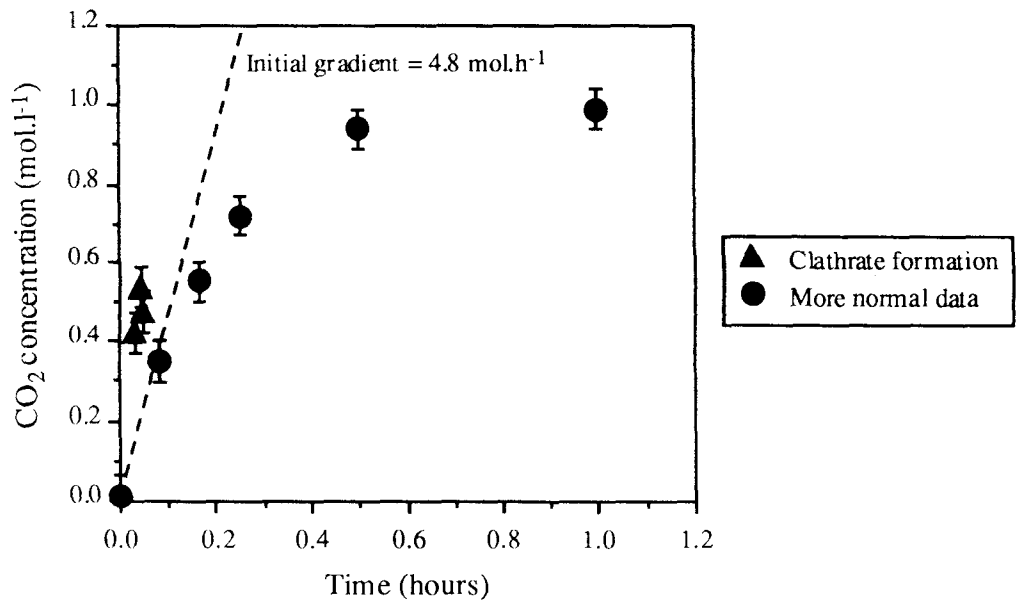


Figure 7.9 Results of kinetic experiments for SC CO₂ dissolution into de-ionised water and synthetic seawater.



* rate law: $d(SC\ CO_2) / dt = -vd * (1 - pCO_2/P)$

— initial water compositions:

* pure water

* 0.55 M NaCl solution

— no mineral reactions

The results of the calculations are the following:

* calculated solubility in pure water: 1.41 mol.kg⁻¹ H₂O

* calculated solubility in 0.55 M NaCl: 1.26 mol.kg⁻¹ H₂O

The calculated curves of CO₂ molalities (mol.kg⁻¹ H₂O) function of time are presented in Figure 7.10. For the kinetics of CO₂ dissolution, there is a good correlation with the experimental values. However, calculated values

at thermodynamic equilibrium are slightly higher than the measured ones. As well as uncertainties due to experimental procedure and conversions between mass and volume units, this slight discrepancy could be explained by the uncertainties on thermodynamic data. Consideration of the slight effect of pressure on thermodynamic constants and revision of the values of fugacity coefficient and activity coefficient of aqueous CO₂, might lead to a better fit between calculated and measured solubility data.

7.4.2 Batch experiments

7.4.2.1 DESCRIPTION OF THE RESULTS

All the fluid chemical data are presented on Table 7.12. No analyses are available for run 374 (SSW/JMP2 mudstone, 8 month duration) as no liquid was observed on opening the vessel. Conversely, some liquid was recovered from run 375 (SSW/JMP3 mudstone, 8 month duration), though the amount of it was greatly reduced from the 25 ml originally added.

Table 7.12 Chemical analyses of water samples from batch experiments (major elements).

Experiment	Run number	Starting material	Starting fluid	Duration days	pH		Ca		Mg		Na		K		Alk. (as HCO ₃)		Cl		SO ₄		SiO ₂	
					(1)	(2)	mg/l	mmol/l	mg/l	mmol/l	mg/l	mmol/l	mg/l	mmol/l	mg/l	meq/l	mg/l	mmol/l	mg/l	mmol/l	mg/l	mmol/l
Anhydrite	377	JMP4	SSW	111	6.54	7.22	1560	38.92	290	11.93	12700	552.42	24.2	0.62	1160	19.01	19400	547.20	3760	39.14	76.8	1.28
	371	JMP4	SSW	232	6.27	7.72	1640	40.92	448	18.43	13100	569.82	46.0	1.18	226	3.70	22000	620.54	3770	39.25	79.8	1.33
	372	JMP4	DIW	232	6.45	7.78	753	18.79	373	15.35	157	6.83	31.2	0.80	474	7.77	87.2	2.46	2260	23.53	111.2	1.85
Mudstone	373	JMP1	SSW	109	6.79	7.40	136	3.39	1150	47.32	12300	535.02	207	5.29	1810	29.66	20300	572.59	848	8.83	46.6	0.78
	375	JMP3	SSW	232	7.60	n/d	42	1.05	1860	76.53	11300	491.52	114	2.92	n/d	n/d	22300	629.00	872	9.08	37.4	0.62
	376	JMP3	DIW	232	7.10	8.84	12	0.30	561	23.08	1640	71.34	54.5	1.39	4400	72.11	1280	36.10	814	8.47	57.1	0.95
Sandstone	383	JMP11	SSW	109	7.01	7.94	183	4.57	252	10.37	11900	517.62	4950	126.59	2050	33.60	24300	685.41	207	2.15	38.9	0.65
	379	JMP8E	SSW	232	6.53	8.4	275	6.86	196	8.06	13500	587.22	85.8	2.19	1480	24.26	21900	617.72	65.4	0.68	72.3	1.20
	381	JMP12	SSW	232	6.48	8.46	289	7.21	474	19.50	15700	682.91	996	25.47	1570	25.73	25200	710.80	410	4.27	48.3	0.80
	384	JMP10	SSW	232	6.39	7.65	862	21.51	280	11.52	13600	591.57	3120	79.79	509	8.34	25400	716.44	1350	14.05	41.5	0.69
	385	JMP13	SSW	232	6.37	8.28	404	10.08	136	5.60	13300	578.52	107	2.74	1050	17.21	22600	637.46	738	7.68	56.9	0.95
	380	JMP8E	DIW	232	6.92	8.86	66	1.65	63	2.59	3820	166.16	43	1.10	3060	50.15	4380	123.54	101	1.05	79.6	1.32
	382	JMP12	DIW	232	6.60	8.15	174	4.34	310	12.75	2770	120.49	749	19.16	1910	31.30	2300	64.87	422	4.39	55.4	0.92
	378	Blank	SSW	109	4.31	3.68	<0.01	<0.0002	<0.01	<0.0004	12900	561.12	<10	<0.26	n/d	n/d	20300	572.59	<100	<1.04	<2.14	<0.04
	398	Blank	SSW	92	4.04	4.27	<1	<0.02	<1	<0.04	12200	530.67	<10	<0.26	n/d	n/d	21300	600.80	<5	<0.05	2.8	0.05
386	Blank	DIW	232	3.64	3.21	<1	<0.02	<1	<0.04	<2	<0.09	<2	<0.05	n/d	n/d	1.94	0.05	6.53	0.07	3.9	0.06	

pH (1): values were taken just after sampling at room temperature

pH (2): values were taken during alkalinity determination at room temperature

DIW: de-ionised water

SSW: synthetic seawater

n/d: not determined

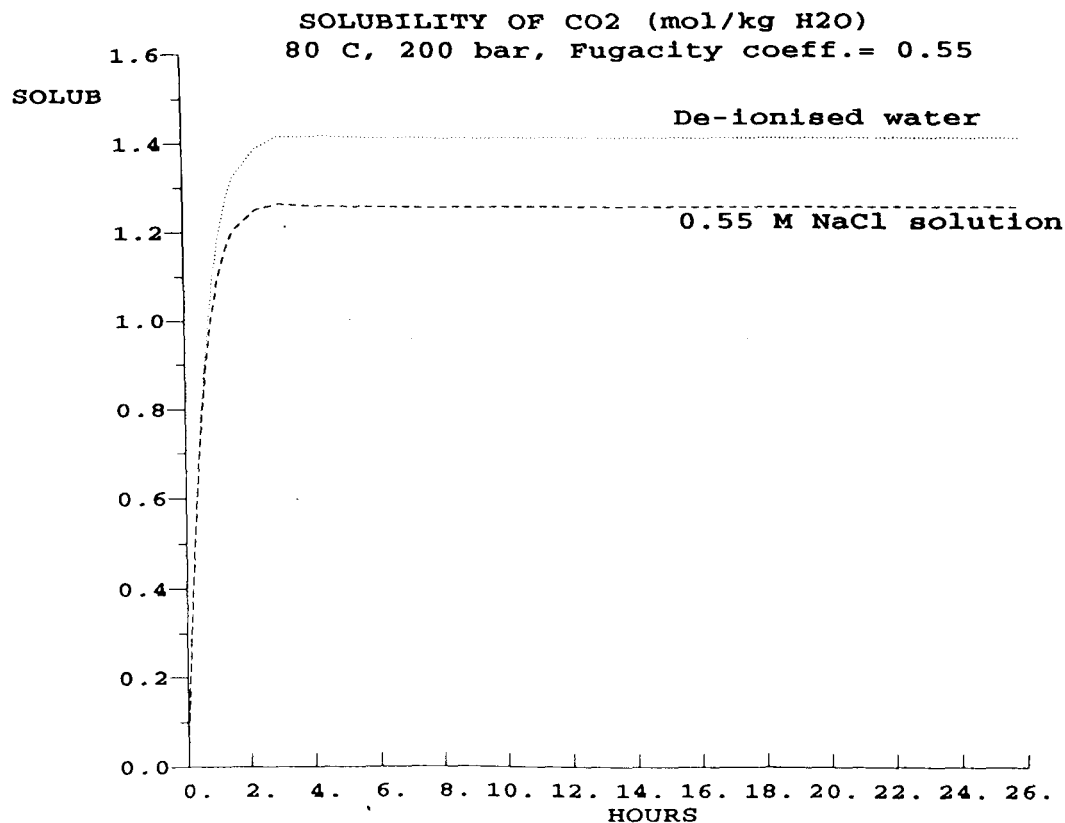
<: below state detection limits

Table 7.12 Continued. Chemical analyses of water samples from batch experiments (minor elements).

Experiment	Run number	Starting material	Starting fluid	Duration days	Ba		Sr		Mn		B		Tot. Fe		Al		Li	
					mg/l	mmol/l	mg/l	mmol/l	mg/l	mmol/l	mg/l	mmol/l	mg/l	mmol/l	mg/l	mmol/l	mg/l	mmol/l
Anhydrite	377	JMP4	SSW	111	0.021	1.53E-04	20.50	2.34E-01	0.824	1.50E-02	2.98	0.28	0.38	6.80E-03	<0.20	<7.41E-03	n/d	n/d
	371	JMP4	SSW	232	0.026	1.89E-04	20.40	2.33E-01	0.702	1.28E-02	5.40	0.50	0.47	8.42E-03	0.60	2.22E-02	0.49	7.06E-02
	372	JMP4	DIW	232	0.014	1.02E-04	8.16	9.31E-02	0.186	3.39E-03	3.00	0.28	0.09	1.61E-03	0.24	8.89E-03	0.39	5.62E-02
Mudstone	373	JMP1	SSW	109	0.351	2.56E-03	41.60	4.75E-01	< 0.005	<9.10E-05	31.90	2.95	<0.01	<1.79E-04	<0.20	<7.41E-03	n/d	n/d
	375	JMP3	SSW	232	0.270	1.97E-03	33.10	3.78E-01	<0.02	<3.64E-04	18.00	1.66	<0.20	<3.58E-03	<0.40	<0.015	4.28	6.17E-01
	376	JMP3	DIW	232	0.096	6.99E-04	9.46	1.08E-01	< 0.005	<9.10E-05	24.10	2.23	<0.05	<8.95E-04	<0.10	<3.71E-03	2.74	3.95E-01
Sandstone	383	JMP11	SSW	109	1.060	7.72E-03	1.36	1.55E-02	< 0.005	<9.10E-05	0.90	0.08	<0.01	<1.79E-04	<0.20	<7.41E-03	n/d	n/d
	379	JMP8E	SSW	232	2.160	1.57E-02	5.03	5.74E-02	0.070	1.27E-03	<1.00	<0.092	<0.20	<3.58E-03	<0.40	<0.015	0.58	8.36E-02
	381	JMP12	SSW	232	0.311	2.26E-03	7.64	8.72E-02	0.284	5.17E-03	2.00	0.18	<0.20	<3.58E-03	<0.40	<0.015	0.85	1.22E-01
	384	JMP10	SSW	232	0.131	9.54E-04	6.78	7.74E-02	0.278	5.06E-03	<1.00	<0.092	<0.20	<3.58E-03	<0.40	<0.015	0.32	4.61E-02
	385	JMP13	SSW	232	0.224	1.63E-03	10.30	1.18E-01	0.243	4.42E-03	2.00	0.18	6.64	1.19E-01	<0.40	<0.015	1.67	2.41E-01
	380	JMP8E	DIW	232	0.430	3.13E-03	1.06	1.21E-02	0.030	5.46E-04	<1.00	<0.092	<0.20	<3.58E-03	<0.40	<0.015	0.51	7.35E-02
	382	JMP12	DIW	232	0.142	1.03E-03	4.71	5.38E-02	0.136	2.48E-03	1.96	0.18	<0.20	<3.58E-03	<0.40	<0.015	0.74	1.07E-01
	378	Blank	SSW	109	0.086	6.26E-04	<0.02	<2.28E-04	0.006	1.09E-04	<0.50	<0.05	0.03	5.37E-04	1.94	7.19E-02	n/d	n/d
	398	Blank	SSW	92	0.137	9.98E-04	<0.02	<2.28E-04	0.025	4.55E-04	<1.00	<0.092	2.04	3.65E-02	<0.40	<0.015	<0.10	<0.014
	386	Blank	DIW	232	0.022	1.60E-04	<0.005	<5.71E-05	1.730	3.15E-02	0.35	0.03	5.66	1.01E-01	1.88	6.97E-02	<0.001	<1.44E-04

DIW: de-ionised water
SSW: synthetic seawater
n/d: not determined
<: below stated detection limits

Figure 7.10 Modelling of the dissolution of SC CO₂ into de-ionised water and synthetic seawater, using the CO2ROCK geochemical simulator.



Mineralogical and petrographical observations are presented below according to the three rock types used. The term seawater is used as an abbreviation of synthetic seawater (0.55 M NaCl solution).

Mudstone

** Three month reaction*

Mudstone + CO₂-saturated seawater (Run 373)

On opening of the reaction vessel, the mudstone sample (sample JMP24) had fragmented severely along curved surfaces, which were not present before the experiment. No differences were observed between air-dried and freeze-dried samples in state of preservation or the nature of textures. The external surface of the mudstone was characterised by an increase in the porosity in the lower half of the sample that was submerged in CO₂-saturated seawater (Plate 10). Pores formed during reaction were typically around 10 µm in diameter (up to 20 µm maximum) and were distributed ubiquitously across the surface of the lower half of the sample. Secondary porosity was widespread and, in some areas, porosity was further developed to leave a porous area up to 50 µm across. The depth of these voids varied up to approximately 10 µm. In the upper half, exposed to supercritical CO₂ only, no significant differences were present between the unreacted and reacted mudstone samples (Plate 11).

This increased porosity was a result of dolomite dissolution. Limited evidence was observed for corrosion of dolomite (Plate 12) from SEM analysis of the outer mudstone block surface. This was confirmed by BSEM examination. In polished thin section, the coarse, angular dolomite crystals present in the starting material were extensively removed at the margins of the mudstone (Plate 13). The zone of dolomite dissolution was well defined to a depth of approximately 2.5 mm. Towards the centre of the sample dolomite grains were generally fresh and corrosion

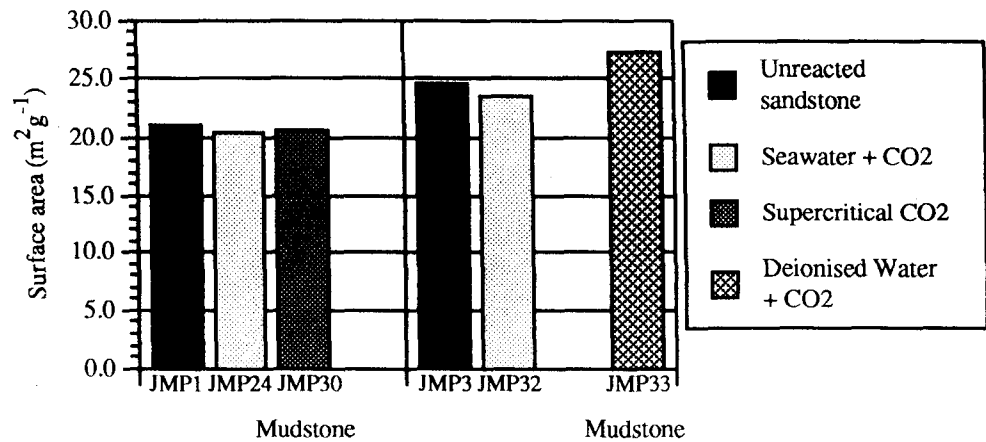
was rare although voids due to dolomite removal were detected with increasing rarity throughout the whole sample. The porosity resulting from dolomite dissolution was typically very irregular in morphology and variable in size, from 10–100 µm (Plate 14). Detailed examination of sinuous fractures within the mudstone indicated that these fractures probably formed by mechanical deformation since, in general, opposite fracture faces are symmetrical and can be matched together. However, in some areas, the fracture faces have been modified by chemical reaction since opposite faces can not be matched and enlargement of the fracture has taken place. This was due to dissolution of dolomite along the fracture face. In addition very rare, possible secondary precipitates of a Mg, Fe(±K) aluminium silicate were present in a few areas on the mudstone surface below the seawater/CO₂ interface (Plate 15). EDXA indicated it was of 'chloritic' composition. It formed poorly developed rosettes of irregular plates up to 10 µm across. This phase was very rare and it was not possible to determine definitively whether it was a reaction product. Its low concentration also prevented identification by XRD. The surface area of this sample was the same as the unreacted mudstone (Figure 7.11, Table 7.9) within experimental errors. This is surprising since the enhanced porosity and possible secondary clay should have produced an increase in surface area. However, the surface area sample was taken from within the central area of the core where reaction was much reduced.

** Eight month reaction*

Mudstone + supercritical CO₂ (Run 399)

One sample of red-brown, massive Mercia Mudstone was reacted with supercritical CO₂ only (JMP30). The mudstone remained intact on opening the reaction vessel and no fluid was apparent. Very little reaction was observed on this sample. Freshly exposed internal surfaces in both the

Figure 7.11 Nitrogen BET surface areas for mudstone starting materials and reacted samples JMP24 (Run 373), JMP30 (Run 399), JMP32 (Run 375) and JMP33 (Run 376).



lower and upper halves of the block were examined by SEM. The matrix and silt-sized particles were fresh. No increase in secondary porosity was observed. Similarly, the external surface, both at the base and top half of the block, appeared to have undergone very little reaction when examined by SEM. The surface area of this sample (Figure 7.11, Table 7.9) was identical to the unreacted mudstone within experimental errors.

Mudstone + CO₂-saturated seawater (Runs 374 and 375)

Two samples of red-brown, massive, Mercia Mudstone were reacted with CO₂-saturated seawater. On opening the reaction vessel the mudstone block in Run 374 (sample JMP31) had disintegrated into several fragments. Dolomite cement was significantly corroded both at the sample base which had been submerged in CO₂-saturated seawater and in the top half of the mudstone block which was above the CO₂-seawater interface. This corrosion resulted in locally enhanced secondary porosity and 'skeletal' grains (Plate 16). This corrosion, however, will only produce a very small increase in porosity in the sample as a whole. The bulk of the porosity was intergranular, between 1–10 µm in diameter, within the clay matrix. Generally, no corrosion occurred on the fine sand-sized quartz or most of the K-feldspar grains. However in the middle to lower region of the block, up to the CO₂-seawater interface, very minor corrosion of K-feldspar occurred forming submicron pits. Again, the increase in secondary porosity resulting from this minor K-feldspar dissolution was minimal. No secondary clay precipitates were observed associated with the K-feldspar dissolution.

The reacted mudstone block from Run 375 (sample JMP32) was very similar to that from Run 374. On opening the reaction vessel the mudstone block had disintegrated into many small fragments. Minor dissolution of dolomite occurred throughout the block, even above the CO₂-seawater interface although most dissolution occurred below the CO₂-seawater interface. Occasionally dolomite corrosion produced poorly defined rhombic, moldic pores (Plate 17). In these areas of local secondary porosity, Ca was detected by EDXA possibly suggesting the presence of secondary calcite following dissolution of dolomite. However, no calcite was directly observed. As in Run 374, K-feldspar dissolution appeared to be more spatially controlled with dissolution features only developing at, or below, the CO₂-seawater interface. As in the case of the mudstone reacted for three months (Run 373, sample JMP24) the surface area of this sample was within experimental error of the unreacted mudstone (Figure 7.11, Table 7.9).

Mudstone + CO₂-saturated de-ionised water (Run 376)

One sample (JMP33) of mudstone was reacted with CO₂-saturated de-ionised water. On opening of the reaction vessel, the mudstone had broken up - particularly the lower half of the block which had disintegrated into many small fragments. Generally the clay matrix remained unchanged during reaction. However, the coarser K-feldspar and dolomite grains were significantly corroded and in some cases completely removed to leave secondary moldic pores. These pores were generally rare and isolated. However, this dissolution lead to a significant increase in surface area from the unreacted mudstone (Figure 7.11, Table 7.9). No secondary clays developed in association with the K-feldspar dissolution.

Anhydrite

** Three month reaction*

Anhydrite + CO₂-saturated seawater (Run 377)

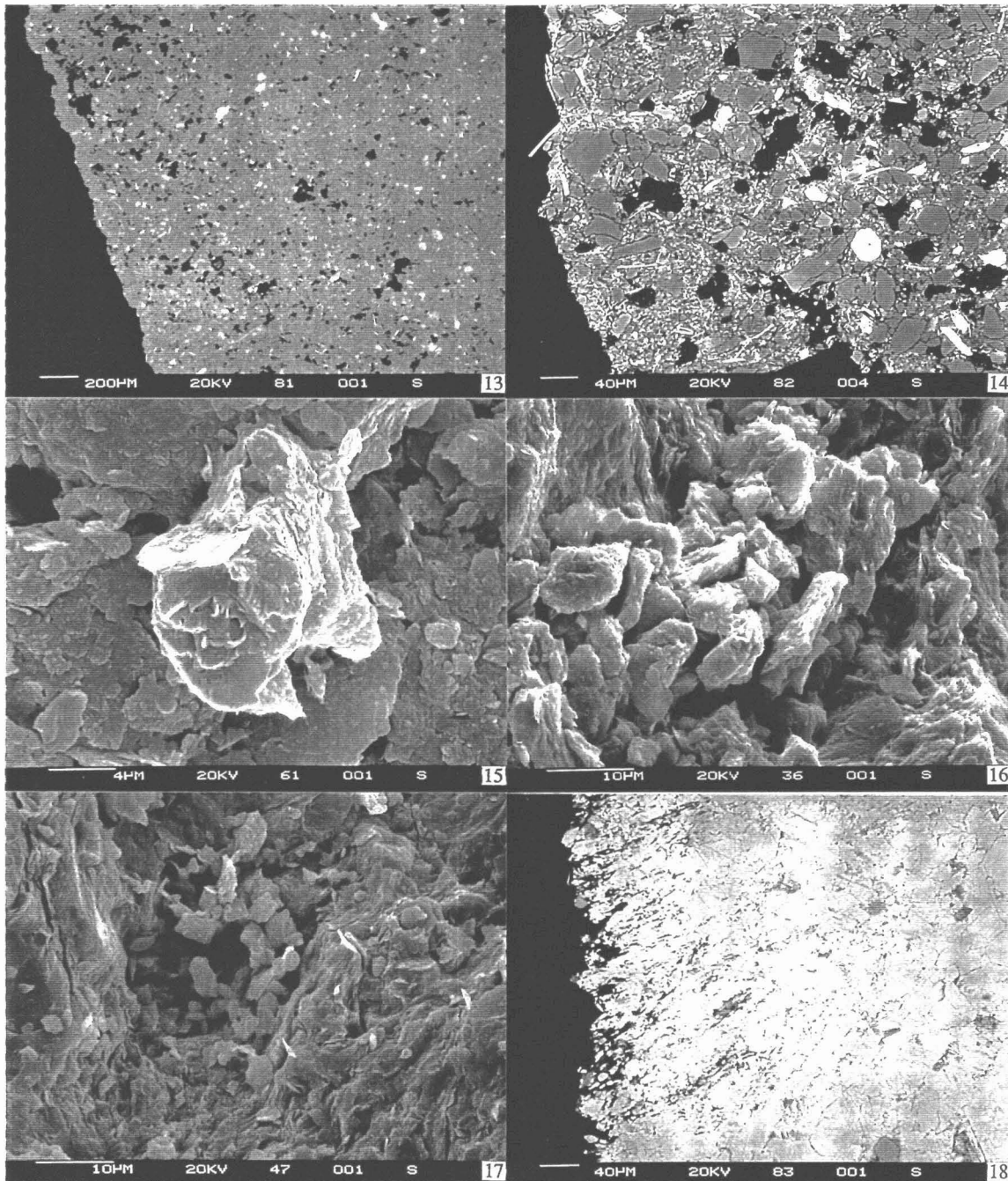
The submerged lower half of the anhydrite block (sample JMP25) was significantly corroded to a depth of approximately 160 µm (Plate 18). The corrosion appears to have been initiated along crystal boundaries roughly perpendicular to the outer surface of the block. The porosity had an elongate morphology and appeared to be well connected with the outer surface of the block. The dissolution was not evenly distributed across the whole surface of the sample but was confined to areas up to several millimetres across.

Along the CO₂-seawater interface extensive calcite and minor, later anhydrite precipitated (Plate 19). The calcite formed aggregates of radiating elongate, stubby crystals of trigonal symmetry (Plate 20). In some areas the calcite formed a dense matting with the underlying anhydrite being almost completely obscured. Post-dating the calcite were rare and isolated accumulations of anhydrite. The anhydrite occurred in bundles of radiating acicular crystals, typically up to 15 µm across (Plate 21). Above the CO₂-seawater interface the anhydrite remained unaltered with no evidence for dissolution being observed.

** Eight month reaction*

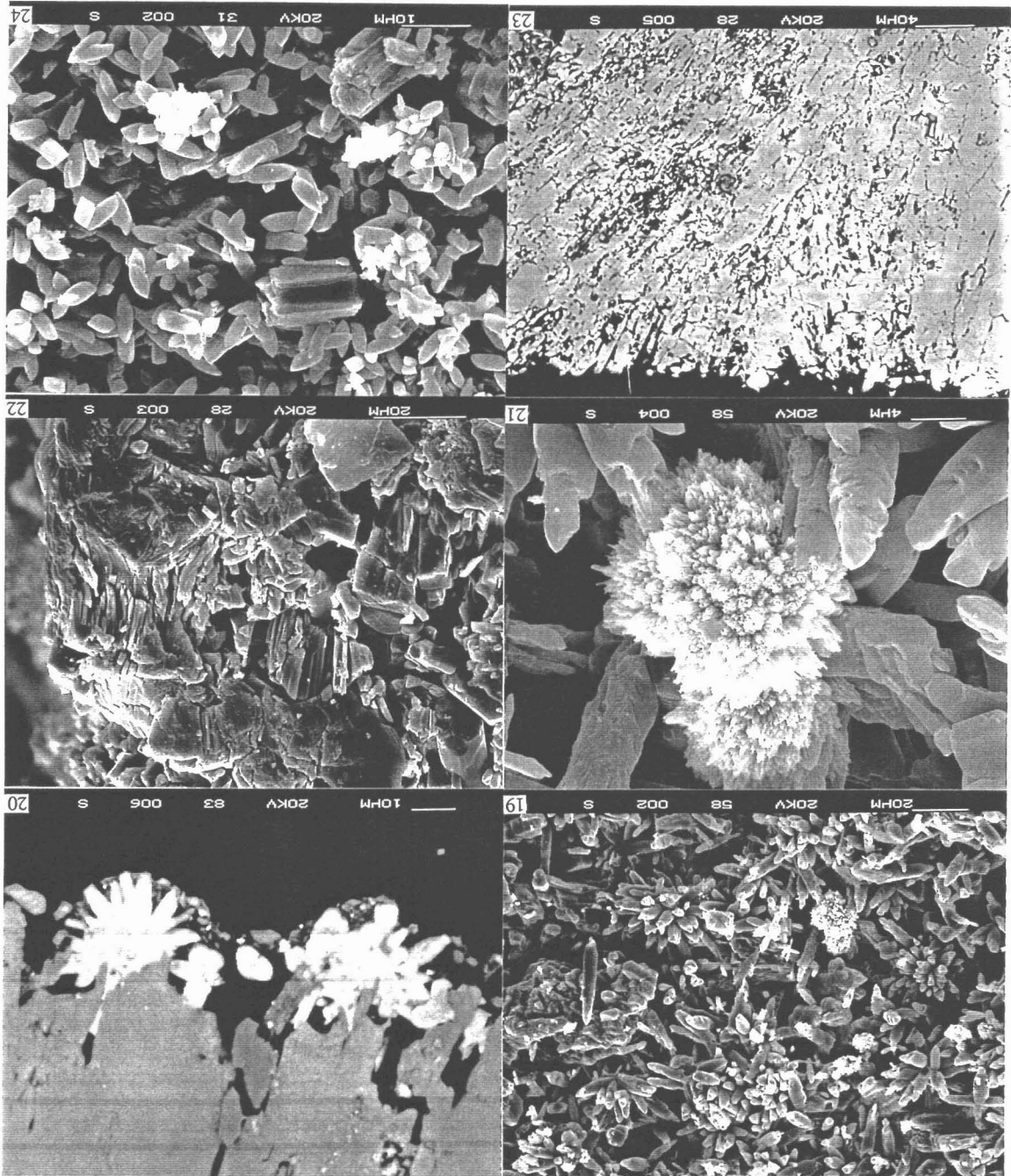
Anhydrite + CO₂-saturated seawater (Run 371)

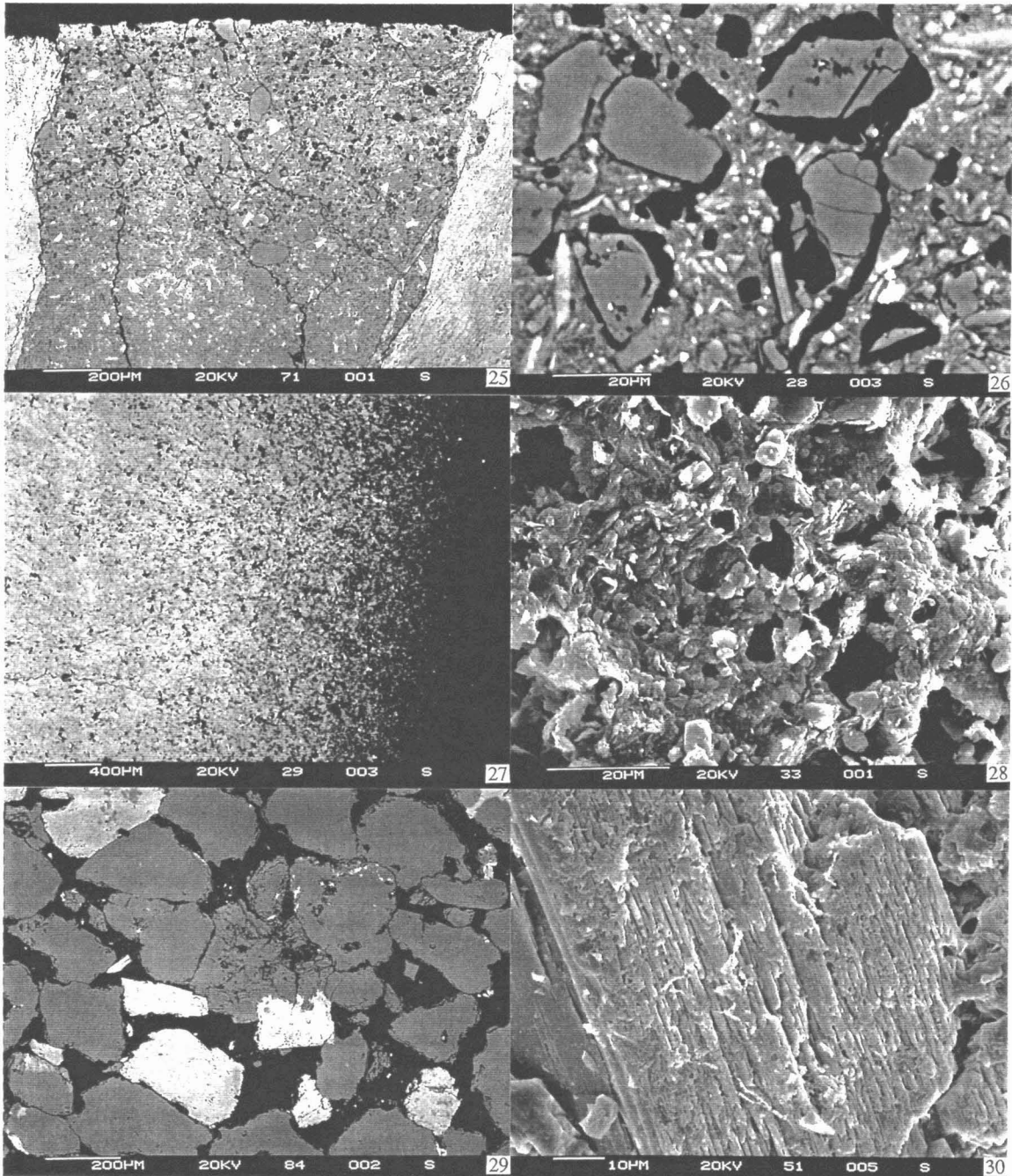
The anhydrite block (JMP28) consisted of interlocking subhedral crystals of varying size, from less than 10 µm to greater than 40 µm. Pores were typically less than 5 µm in diameter and the degree of connectivity was low. Examination of freshly exposed, internal surfaces revealed that the bulk of the sample remained fresh. In the lower half of the block, within 150 µm of the outer edge, minor amounts



- Plate 13 Backscattered electron SEM photomicrograph of reacted Mercia Mudstone sample showing development of porosity along outer zone of block to a depth of approximately 2.5 mm. Sample JMP24, reaction with CO₂-saturated synthetic seawater for 109 days.
- Plate 14 Backscattered electron SEM photomicrograph of reacted Mercia Mudstone sample showing development of porosity at outer surface of block. Note irregular pore morphology. Sample JMP24, reaction with CO₂-saturated synthetic seawater for 109 days.
- Plate 15 Secondary electron SEM photomicrograph of reacted Mercia Mudstone sample showing rare, secondary precipitate of 'chloritic' material. Sample JMP24, reaction with CO₂-saturated synthetic seawater for 109 days.
- Plate 16 Secondary electron SEM photomicrograph of corroded dolomite cement in mudstone reacted with CO₂-saturated seawater. Sample JMP31, run 374.
- Plate 17 Secondary electron SEM photomicrograph of moldic pore after corroded dolomite in mudstone reacted with CO₂-saturated seawater. Sample JMP32, run 375.
- Plate 18 Backscattered electron SEM photomicrograph of base of reacted anhydrite block with dissolution occurring to a depth of ~160 μm. Sample JMP25, reaction with CO₂-saturated synthetic seawater for 111 days.

- Plate 19 Secondary electron SEM photomicrograph of reacted anhydrite at the CO₂-seawater interface with extensive precipitation of radiating calcite and minor anhydrite (centre left). Sample JMP25, reaction with CO₂-saturated synthetic seawater for 111 days.
- Plate 20 Backscattered electron SEM photomicrograph of base of reacted anhydrite block showing secondary calcite precipitate. Anhydrite is mid-grey, calcite light grey and resin black. Sample JMP25, reaction with CO₂-saturated synthetic seawater for 111 days.
- Plate 21 Secondary electron SEM photomicrograph of upper half of reacted anhydrite block. Sample JMP25, reaction with CO₂-saturated synthetic seawater for 111 days.
- Plate 22 Secondary electron SEM photomicrograph of secondary pore due to anhydrite corrosion during reaction with CO₂-saturated seawater. Sample JMP28, run 375.
- Plate 23 Backscattered SEM photomicrograph of secondary porosity due to anhydrite corrosion during reaction with CO₂-saturated seawater. Sample JMP28, run 375.
- Plate 24 Secondary electron SEM photomicrograph of external surface of anhydrite block coated in elongate calcite and irregular calcite blocks with hexagonal cross-sections. Anhydrite reacted with CO₂-saturated seawater. Sample JMP28, run 375.





- Plate 25 Backscattered SEM photomicrograph of secondary porosity due to dolomite corrosion during reaction with CO₂-saturated seawater. Sample JMP28, run 375.
- Plate 26 Backscattered SEM photomicrograph of corroded dolomite rhombs following reaction with CO₂-saturated seawater. Sample JMP28, run 375.
- Plate 27 Backscattered SEM photomicrograph of secondary porosity due to anhydrite corrosion during reaction with CO₂-saturated de-ionised water. Sample JMP29, run 372.
- Plate 28 Secondary electron SEM photomicrograph of external surface of anhydrite block in an area of mudstone with relatively coarse secondary moldic pores developed due to dissolution of dolomite cement. Sample JMP29, run 372.
- Plate 29 Backscattered electron SEM photomicrograph of unreacted Sherwood Sandstone. Quartz and K-feldspar (mid-grey), plagioclase (light grey), dolomite (mid-grey) and porosity (black). Compare with Plate 12 of unreacted sandstone. Sample JMP27, reaction with CO₂-saturated synthetic seawater for 109 days.
- Plate 30 Secondary electron SEM photomicrograph of reacted Sherwood Sandstone showing corroded K-feldspar. Sample JMP27, reaction with CO₂-saturated synthetic seawater for 109 days.

of secondary corrosion were observed by SEM, resulting in isolated secondary pores (Plate 22 and 23). No secondary phases developed in these pores. No corrosion was observed in the upper half of the core.

The outer surface of the anhydrite block, below the CO₂-seawater interface, was extensively covered in secondary calcite. The calcite occurred as stubby, elongate crystals up to 10 µm long and occasionally formed radiating clusters although these were not as well developed as those present on the anhydrite block reacted for three months (Run 377, JMP25). In addition to these predominant, elongate crystals, calcite also occurred as blocky crystals with a poorly developed hexagonal cross-section (Plate 24). Although some corrosion of the anhydrite was observed, much of the surface was obscured by later calcite. Where corrosion was observed, it developed along crystal boundaries and along cleavage planes to a limited extent.

Mudstone lenses within the anhydrite suffered significant dissolution with porosity enhancement to a depth of up to 0.8 mm (Plate 25). This resulted in a visually-estimated increase in porosity to 15% locally within these areas. The increased porosity resulted from dissolution and removal of dolomite (Plate 26). The K-feldspars remained relatively uncorroded. In addition, porosity was enhanced adjacent to the mudstone lenses within the anhydrite.

Anhydrite + CO₂-saturated de-ionised water (Run 372)

SEM examination of a freshly exposed surface within the anhydrite block (JMP29) indicated it remained fresh with no evidence of reaction. Porosity was typically up to 10 µm in diameter and consisted of primary intercrystalline voids. Below the CO₂-de-ionised water interface, dissolution was significant. Although SEM examination of the outer surface indicated that porosity enhancement was only slight, BSEM analysis indicated that the depth of reaction and area of increased secondary porosity was up to 5 mm (Plate 27). Dissolution was particularly extensive to a depth of 1 to 2 mm with secondary porosity forming up to 50% of the volume in this band. Individual pores were up to 100 µm in diameter and of irregular morphology. In addition, reaction also occurred along cracks within the block to a depth of up to 100 µm from the fissure wall. No calcite was observed on the outer surface, in contrast to the extensive precipitate which developed in the seawater-reacted sample (Run 371).

A mudstone layer within the anhydrite block, and exposed on the outer block surface, contained significant secondary porosity due to the complete removal of a specific phase (Plate 28). The formation of this secondary porosity is limited to a depth of 3 mm, below which no dissolution was observed. Evidence from other experiments would suggest that the dissolved phase was probably dolomite although no evidence for this was found in this sample. In addition, BSEM examination indicated that the mudstone lenses were cracked possibly due to sodium exchange with calcium in swelling smectite clays causing swelling of the clay matrix and fragmentation.

Sandstone

** Three month reaction*

Sandstone + CO₂-saturated seawater (Run 383)

Within the lower half of the sandstone block (sample JMP27), submerged within the CO₂-saturated synthetic seawater, little reaction was observed (Plate 29). Since K-feldspar grains were already corroded, it proved difficult to

establish if further corrosion (as suggested by the high potassium concentration determined in the fluid at the end of the experiment) had taken place. Experimental corrosion of the K-feldspar may tentatively be identified as many grains appeared to be more severely corroded than observed in the unreacted sample (Plate 30). However, it was not possible to establish this definitively. Secondary porosity developed along feldspar cleavage to an approximate depth of 10 µm. Quartz overgrowths and most of the dolomite cement remained fresh with no evidence of corrosion detected (Plate 31). Dolomite was only occasionally corroded with pits and small channels typically less than 10 µm across.

At the CO₂-seawater interface rare calcite developed on some grain surfaces as euhedral to subhedral interlocking crystals, up to 10 µm in diameter (Plate 32). This calcite is thought to be a secondary precipitate as it was not observed on the starting materials. However, it was very rare and was not present on the polished thin section prepared from this sample.

Above the CO₂-seawater interface the exterior of the sandstone block was very heavily encrusted with halite (Plate 33).

Point counting analyses were performed on the unreacted and reacted sandstone from this experiment (Figure 7.12, Table 7.10). Two areas, below and above the CO₂-seawater interface, were quantified by this method. Differences were observed between many components. A large difference occurred for detrital quartz and quartz cement in both upper and lower halves of the reacted core (Figure 7.12). The detrital quartz component increased by 6–8% and the quartz cement component decreased by 3–4%. However, no evidence was found during SEM examination for either significant quartz precipitation or dissolution following reaction. These changes in quartz abundance may therefore reflect an underlying variation in the sandstone mineralogy from the unreacted to reacted samples. In addition, by combining the increase in detrital quartz with the decrease in quartz cement, the change in total quartz reflects an overall increase of 2–4%. This may suggest therefore that the assignment of quartz as either detrital or cement may have been inconsistent during point counting. This is possible since they have identical backscatter coefficients and are hence distinguished on petrographic relationships alone. The assignment may thus be somewhat arbitrary when both detrital grains and overgrowths have irregular outlines, and no boundaries between them are visible. Nevertheless if the differences in quartz components are genuinely a result of 'background' mineralogical variations, similar variations may also occur for other components. It is therefore considered that a difference of ±1% is probably not significant without corroborating petrographic observations.

The detrital K-feldspar component decreased below the CO₂-seawater interface by 2% and by 4% above the CO₂-seawater interface (Figure 7.12). This decrease in K-feldspar corroborates petrographic observations that K-feldspar had suffered further corrosion during reaction. Dolomite cement also decreased by 3% below the CO₂-seawater interface and by only 1% above the CO₂-seawater interface (Figure 7.12). This again substantiates SEM observations that dolomite was corroded, although only slightly, during reaction. A greater decrease in dolomite below the CO₂-seawater interface suggests that more dolomite was dissolved where the sandstone block was completely saturated. No halite or secondary calcite were detected during point counting. This confirms that these reaction products were concentrated on

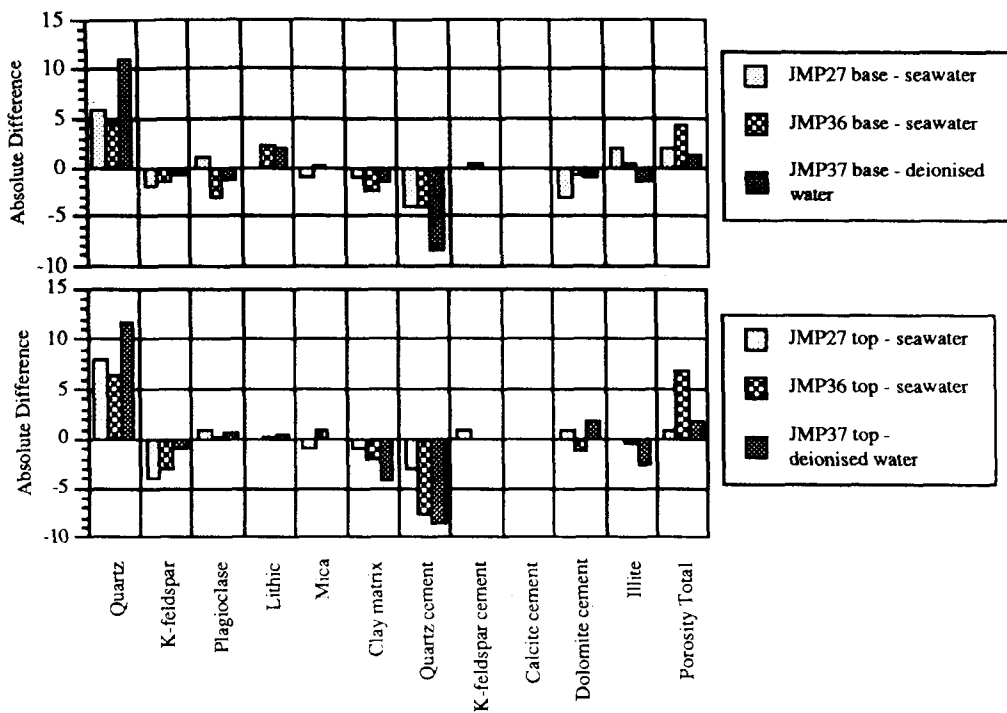


Figure 7.12 Differences in absolute percentage terms between unreacted and reacted sandstone samples on the basis of point counting data. For example, value plotted for total porosity in JMP36 base is 19.0% - 14.7% = 4.3%.

JMP27 from Run 383: Seawater + SC CO₂ reacted for 3 months.
 JMP36 from Run 381: Seawater + SC CO₂ reacted for 8 months.
 JMP37 from Run 382: De-ionised water + SC CO₂ reacted for 8 months.

the outer surface of the block. Halite was only developed above the CO₂-seawater interface on the external surface and not observed internally. Calcite developed at the CO₂-seawater interface. The outer edge of the block was avoided during point counting due to the difficulty of establishing the proportion of porosity in these areas.

The proportion of total porosity increased slightly in the reacted sandstone block. Below the CO₂-seawater interface total porosity increased by 2%, and above the interface by 1%. This would apparently correlate with the dissolution of K-feldspar and dolomite. The reduced amount of dolomite determined below the CO₂-seawater interface may account for the slight increase in total porosity. This is confirmed by a slight increase in surface area from the unreacted sandstone (Figure 7.13, Table 7.9).

** Eight month reaction*

Sandstone + CO₂-saturated seawater (Runs 379, 381, 384 and 385)

Run 379

In general, most of this sandstone remained fresh and unreacted. The detrital and authigenic quartz and, in most cases, K-feldspar overgrowths were fresh with no evidence for corrosion. The ubiquitous, authigenic and well-developed, boxwork illite-smectite clay was well-preserved throughout the sample. However, it was found that occasional K-feldspar grains and overgrowths were locally severely corroded. This corrosion was occasionally restricted to certain grain faces indicating that corrosion was highly localised. A detailed comparison of the lower half and upper half of the sandstone block suggested that the proportion of detrital K-feldspar and overgrowths in

the lower half of the block was slightly reduced. Point counting analyses indicated that a reduction of K-feldspar by 3.5% (Figure 7.14, Table 7.10) occurred following reaction in the lower half of the core. No comparative data for the upper half of the core was obtained, but this does indicate that significant K-feldspar dissolution took place. In addition, rare moldic pores were observed in the lower half of the block which were not present in the starting material. These pores were outlined by a relict K-feldspar overgrowth (Plate 34) and/or an authigenic boxwork illite-smectite coating (Plate 35). The pores may have resulted from complete removal of K-feldspar, although no specific evidence as to the nature of the lost phase was present. Occasionally associated with corroded K-feldspar overgrowths were poorly developed, ragged flaky illite-smectite flakes (Plate 36). The identification of this clay was based solely on SEM observation and qualitative EDXA analyses. XRD analysis was not possible due to the very small amount present in the sample. This clay was also observed by BSEM in a polished thin section of this sample. EDXA indicated it was an iron-rich, potassium aluminium silicate — probably illite-smectite. This clay was also associated with alteration of lithic casts in the samples.

In addition to corrosion of K-feldspar, detailed examination of the dolomite cement indicated that this was pitted by secondary dissolution. The pits and secondary voids varied in size from 5 µm up to channels 30 µm long and 5 µm wide (Plate 37). The depth of corrosion was up to 10 µm. Point counting analysis (Figure 7.14) indicated that a reduction in the proportion of porosity had occurred after reaction. Rare, subhedral to euhedral, equant calcite crystals up to 20 µm across, possibly of secondary origin

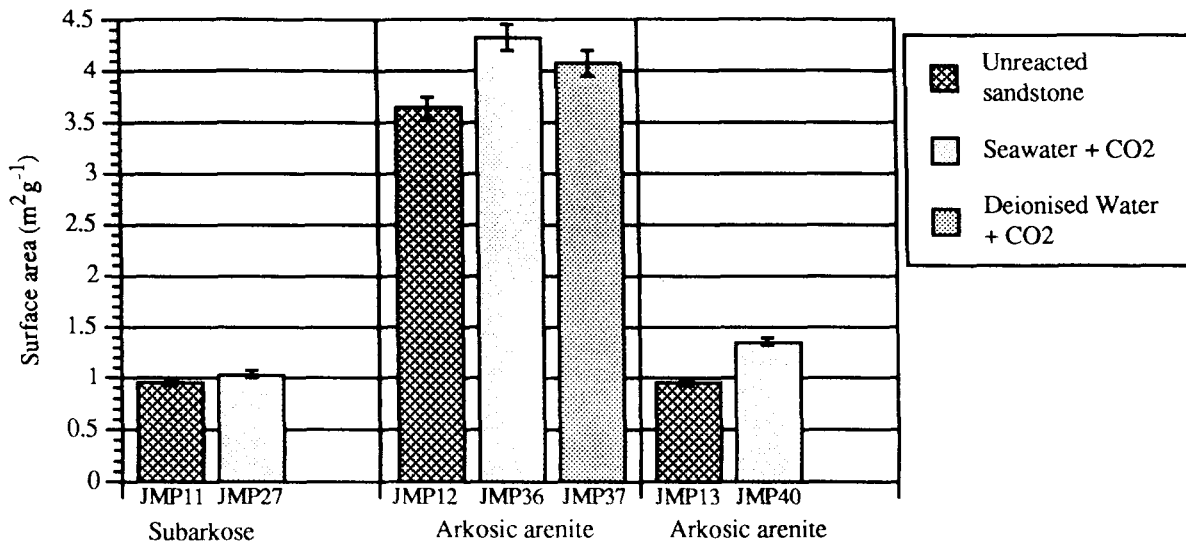
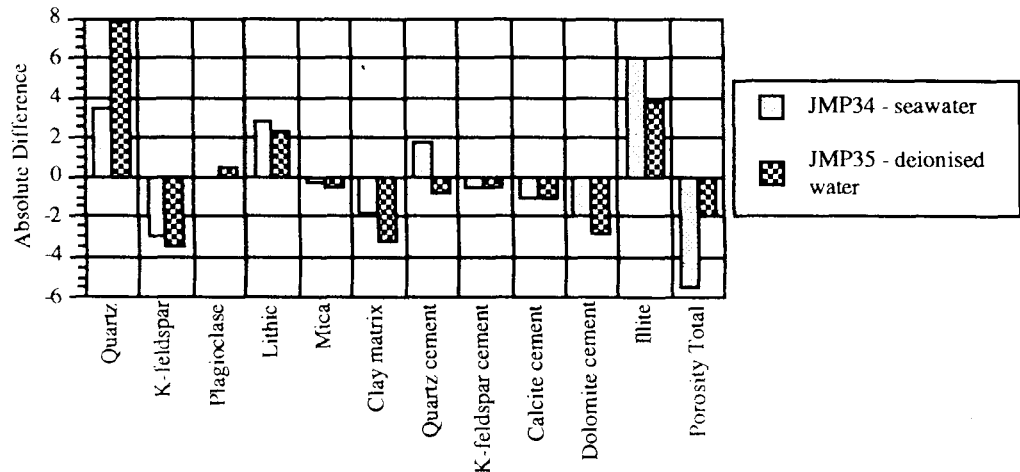


Figure 7.13 Nitrogen BET surface areas for sandstone starting materials and reacted samples JMP27 (Run 383), JMP36 (Run 381), JMP37 (Run 382) and JMP40 (Run 385).

Figure 7.14 Differences in absolute percentage terms between unreacted and reacted sandstone samples on the basis of point counting data (Table 7.10). For example, value plotted for total porosity in JMP34 is 19.3–24.8% = -5.5%.



JMP34 from Run 379: Seawater + SC CO₂ reacted for 8 months.
 JMP35 from Run 380: De-ionised water + SC CO₂ reacted for 8 months.

were finely disseminated on some pore walls. These crystals post-dated the boxwork illite-smectite clay (Plate 38). However, point counting analyses indicated a decrease in calcite cement (Table 7.10, Figure 7.14). EDXA analysis indicated that a significant proportion of the clay contained Na. This was probably due to ionic exchange between sodium in the synthetic seawater and the potassium present in the clay structure.

Similar secondary features to those present within the sandstone were observed on the outer surface. K-feldspar grains were corroded and were occasionally coated in structureless to very poorly developed, micron-scale flakes of a Na,K-clay — possibly smectite. The very small amounts of this material prevented identification by XRD. Careful EDXA detected no Cl indicating that the Na occurred within the clay and was not present as halite contamination. Minor, secondary, euhedral, equant calcite crystals (Plate 39) occurred across the external surface below the CO₂-seawater interface. The external surface above the CO₂-seawater interface was coated in more halite than the lower half. No calcite developed on the upper half. The amount of K-feldspar corrosion developed in the upper half of the block was much lower than that on the lower

half. Where corrosion of K-feldspar was observed in the upper half of the block, it was probably attributable to dissolution prior to reaction in the experiment. In addition, the authigenic boxwork illite-smectite clay was slightly better preserved in the upper half of the block. No obvious changes in the proportion of porosity from the block edge to the centre were noted by BSEM and no changes were noted between lower and upper halves.

Interestingly, both point count analyses (Table 7.10) and liquid resaturation porosimetry (Table 7.8) indicated an overall reduction in porosity for this sample. Although the porosity values obtained for the starting material by the two methods were slightly different, porosity values for the reaction products were in close agreement. This suggests that the increase in porosity caused by dissolution of K-feldspar and dolomite was more than compensated for by the precipitation of illite and quartz.

Run 381

The sandstone block in this sample contained similar secondary reaction features to those described for Run 379. K-feldspars again showed secondary corrosion. Point counting analysis confirmed this with decreases being

detected both below and above the CO₂-seawater interface, with the greatest decrease above the CO₂-seawater interface. However, no secondary Na,K-clays were observed by SEM, but were tentatively identified by BSEM examination of the polished thin section. An insignificant increase below and an insignificant decrease in clay above the CO₂-seawater interface were detected by point counting. The dolomite cement was also corroded. This was again confirmed by point counting analysis which detected slight decreases in the proportion of dolomite. Interestingly however, it appears from this data (Figure 7.13, Table 7.10) that there was a slightly greater decrease in the proportion of dolomite above the CO₂-seawater interface than below it. The external surface of this sample, particularly the lower half, was obscured by extensive halite. The halite texture was poorly developed and largely consisted of micron-scale, anhedral crystals. This is in contrast to the well developed halite textures observed in the three month experiment, and in this sample was probably an artifact of specimen preparation (Run 383). In addition to halite, secondary, euhedral, equant calcite crystals (Plate 40), up to 10 µm in diameter, developed across the external surface — both above and below the CO₂-seawater interface. Since the external surface of the sample was deliberately avoided during the point counting this was not detected by this method.

The total porosity determined by liquid resaturation porosimetry was 12.85% (Table 7.8) but was determined as 19.0% below and 21.5% above the CO₂-seawater interface by point counting (Figure 7.12). The porosity of the starting material was determined as 14.7% by point counting (Table 7.10). Although porosity measurements by point counting and porosimetry are in reasonable agreement for the starting material, porosity values for the reacted samples do not agree. Reasons for this are unclear but the poor preservation of clays in the polished thin section may account for the discrepancy. Surface area analyses confirm that dissolution of K-feldspar occurred, since a significant increase in surface area was detected (Figure 7.13, Table 7.9).

Run 384

The reaction features in this sample were very similar to those described above for Runs 379 and 381. However, the amount of secondary K-feldspar corrosion was reduced and highly localised. Dolomite and plagioclase corrosion were more extensive than in the samples described above. However, the corrosion was highly localised with some corroded dolomite crystals situated adjacent to fresh,

uncorroded dolomite. Trace amounts of secondary, generally poorly developed, anhedral, micron-scale calcite occurred throughout the sample and was also present on the external surface below the CO₂-seawater interface. No secondary clays were observed associated with corroded K-feldspar grains, either internally or externally. The external surface was largely obscured by halite both above and below the CO₂-seawater interface. Liquid resaturation porosimetry indicated a slight increase in porosity from 17.25% in the starting material to 18.88% in the reaction product. This reflected the dissolution of K-feldspar and dolomite and the lack of secondary clay formation observed by SEM. BSEM analysis also suggested a slight increase in pore space and an increase in the proportion of oversized porosity due to dolomite corrosion. The anhydrite cement was not corroded in this sample. In addition, major porosity enhancement occurred along a crack that may have developed as result of CO₂-rock interaction.

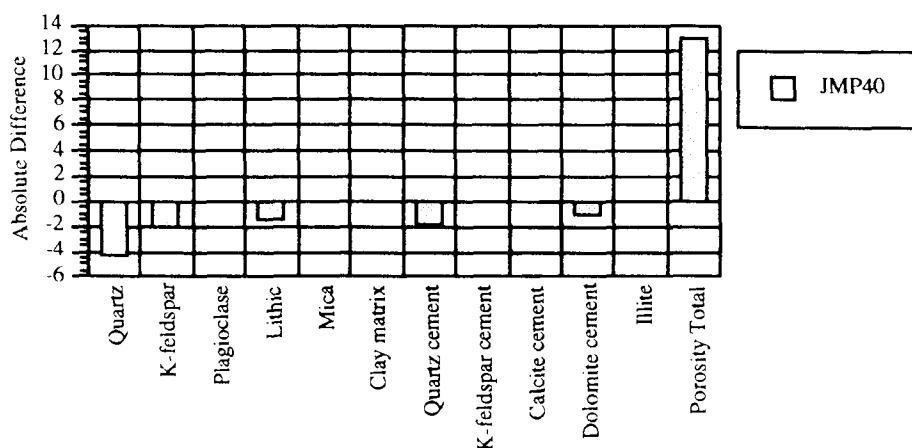
Run 385

This sandstone sample again contained corroded K-feldspar grains. Since these were corroded prior to reaction it was difficult to determine how much dissolution occurred during reaction. A slight decrease in the proportion of K-feldspar from 26.3% in the starting material to 24.3% in the lower half of the reacted block, below the CO₂-seawater interface, was detected by point counting. However, the strongly layered fabric, bimodal size distributions and patchy variable porosity in this sandstone made point counting data very difficult to interpret. Corrosion during reaction must have taken place on already existing corroded surfaces as many faces were still fresh after reaction. This again suggests that corrosion was very localised. Associated with most of the corroded K-feldspar grains was a poorly developed, irregular flaky clay (Plate 41). EDXA indicated it may be a Ca(K)-smectite although the very small amounts present prevented confirmation of this by XRD. This clay also occurred in the upper half of the sample but was most prevalent in the lower half. Although mainly associated with corroded K-feldspar grains it was also observed on other pore walls. However, point counting data indicated that the proportion of clays appeared to decrease (Figure 7.15, Table 7.10). The calcite cement in this sandstone was fresh in all areas. The external surface, both above and below the CO₂-seawater interface, was completely obscured by secondary halite.

A very significant increase in porosity (Plate 42), from 16.0% to 29.0% was detected by point counting (Figure

Figure 7.15 Differences in absolute percentage terms between unreacted and reacted sandstone samples on the basis of point counting data (Table 7.10). For example, value plotted for total porosity in JMP40 is 29.0–16.0% = 13.0%.

JMP40 from Run 385: Seawater + SC CO₂ reacted for 8 months.



7.15) although the sample heterogeneity makes comparison very difficult. The porosity in the lower half of the sample was determined by porosimetry to be 21.7% (Table 7.8). This value is more likely to reflect a truer average value for the porosity. An increase in porosity is also reflected in an increase in the surface area of the lower half of the sandstone (Figure 7.13, Table 7.9).

Sandstone + CO₂-saturated de-ionised water (Runs 380 and 382)

Run 380

In general, the reacted sandstone block appeared very similar to the unreacted sample. The detrital quartz grains and quartz cement were fresh with no evidence of corrosion. The minor K-feldspar present consisted of both grains that were fresh and those that were severely corroded. In some cases corrosion was limited to specific faces on a single crystal. No secondary clays were observed lining the intergranular porosity within the corroded feldspar. However, point count analyses (Figure 7.14) indicated a twofold increase in the proportion of illitic clay from 3.8% to 7.5% throughout the sample. Hence precipitation of this clay was not restricted to areas close to the dissolving K-feldspars. The rare dolomite cement was pitted and associated with secondary, sub-micron, euhedral calcite crystals which were seeded onto it (Plate 43). Point counting data (Figure 7.14, Table 7.10) suggested that the proportion of dolomite decreased fourfold from 3.5% to 0.8%. The calcite occurred throughout the sample — both above and below the CO₂-de-ionised water interface. These calcite crystals were much smaller than those present on the seawater reacted sandstones. The external surface of the sandstone block was also coated in euhedral, equant calcite crystals which were typically seeded onto corroded dolomite cement. The calcite on the external surface was generally coarser, being up to 10 µm in diameter, than on internal pore walls. There was possibly more calcite present on the external surface of the CO₂-de-ionised water sample compared to the CO₂-seawater sample. As for the CO₂-seawater sample, point counting indicated a slight drop in calcite content. However, most of the secondary calcite was concentrated on the external surface of the block and, to avoid problems of determining pore spaces, this was avoided during the point counting. Hence the calcite detected within the block was more likely to be primary calcite present before reaction. Above the CO₂-de-ionised water interface, ridges of Ca,K-smectite post-date the secondary calcite precipitate (Plate 44). This clay formed an extensive crust in large patches up to tens of microns across but probably <10 µm thick. The very small amounts present prevented confirmation of the clay mineralogy by XRD.

Both liquid resaturation porosimetry measurements and point counting analysis indicated a reduction in the proportion of porosity, relative to the starting material. However, the amount of reduction was not as great as in the CO₂-seawater experiments. Porosimetry indicated a drop of only 0.7% and point counting indicated a drop of 2.2%. Porosity values determined by the two techniques were comparable; 22.8% by point counting (Table 7.10) and 21.16% by porosimetry (Table 7.8). The reduction in porosity (Figure 7.14) may result from precipitation of secondary illitic clays, although other background variations may also account for this. For example, the proportion of quartz is significantly higher in the reaction product but there is no other evidence to suggest that this is of secondary origin.

Run 382

The reaction features in this sample were similar to those in Run 380 with minor secondary corrosion of K-feldspar and dolomite. Point counting analyses indicated that a reduction in K-feldspar of less than 1% occurred during reaction. BSEM analyses revealed that plagioclase was typically severely corroded and point count analysis indicated that a decrease of 1.3% occurred below the CO₂-fluid interface (Table 7.10). Results of point counting for dolomite were, however, more confusing with a decrease of 1.0% at the base of the sample below the CO₂-seawater interface but an apparent increase of 1.9% above the CO₂-seawater interface (Figure 7.12). No evidence for secondary precipitation of dolomite was obtained by SEM and this must be regarded with scepticism. However, SEM examination of this sample indicated that there was a general reduction in the proportion of authigenic clay present in the lower half of the sample, relative to the unreacted starting material. Where clay was still present, it was poorly preserved, possibly suggesting that reaction of the clay with the CO₂-saturated de-ionised water had taken place. Above the CO₂-de-ionised water interface, more authigenic clay was present and fibrous illite was also preserved. It had not been observed in the lower half of the block. Point counting data suggests that a slight decrease in the proportion of authigenic clays occurred, even above the CO₂-seawater interface.

The external surface of this block was coated in equant, subhedral calcite crystals up to 5 µm in diameter (Plate 45). Above the CO₂-de-ionised water interface no calcite developed. Calcite was not detected by point counting indicating that the calcite precipitated on the external surface of the block only since this was excluded during point counting. In addition, above the CO₂-de-ionised water interface the external surface was coated in a minor amount of debris from block preparation. This was not present below the CO₂-de-ionised water interface suggesting it was either washed off, or dissolved due to its higher surface area. Point counting data again indicated an increase in detrital quartz and a decrease in authigenic quartz of slightly less magnitude. No evidence of these changes was observed by SEM and, as in other analyses above, these changes are probably due to inconsistent differentiation of authigenic and detrital quartz during point counting.

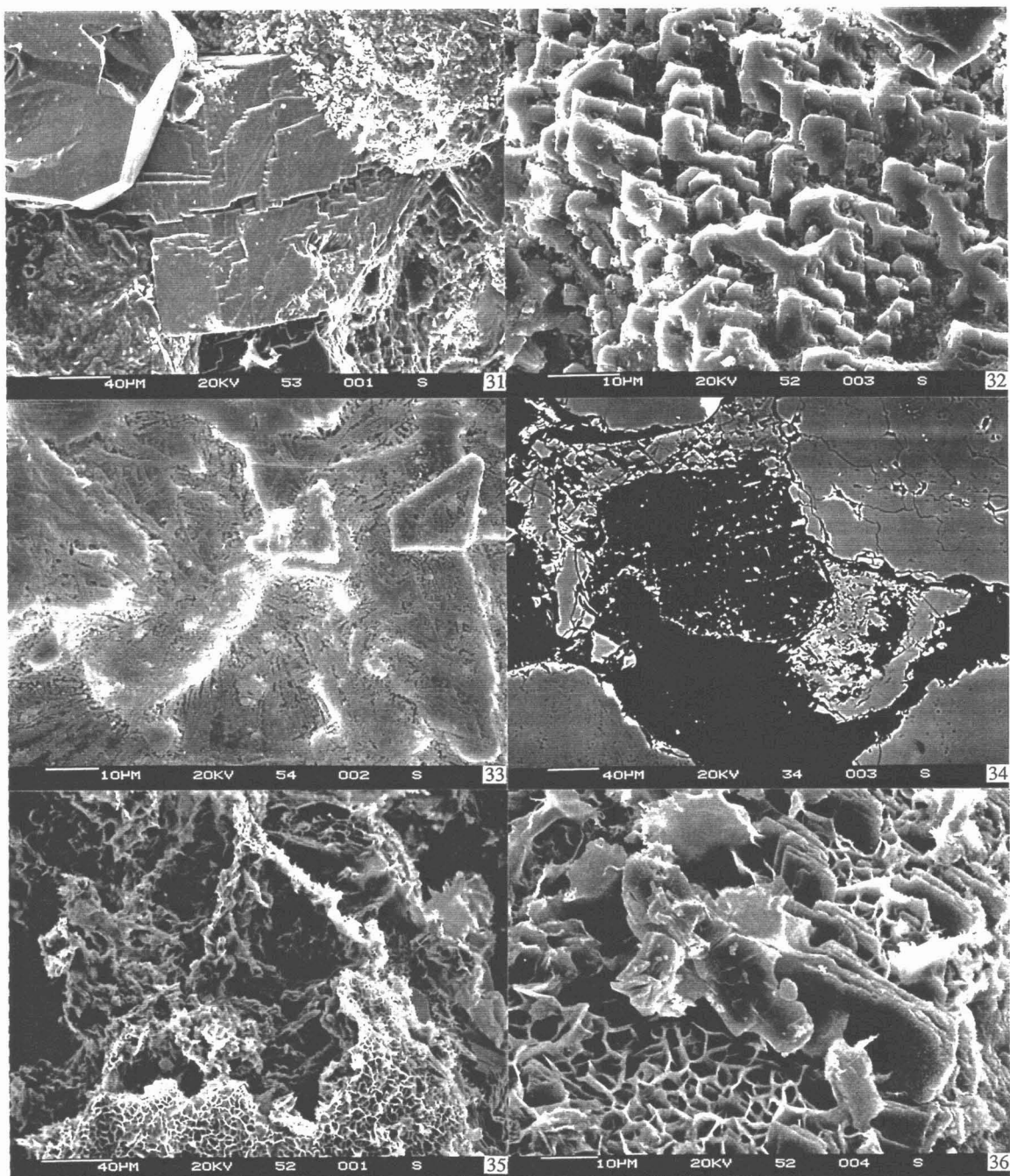
The porosity of the lower half of the reacted sandstone block was determined as 12.92% by liquid resaturation porosimetry (Table 7.8), compared to 16.0% by point counting (Table 7.10). No porosimetry analyses were conducted on the starting material, but comparison of point counting data suggested that an increase in porosity occurred in this sample due to the corrosion of K-feldspar and dolomite and the lack of clay precipitation (Figure 7.12). This was confirmed by a significant increase in surface area relative to the unreacted starting material (Figure 7.13).

Fullers' Earth

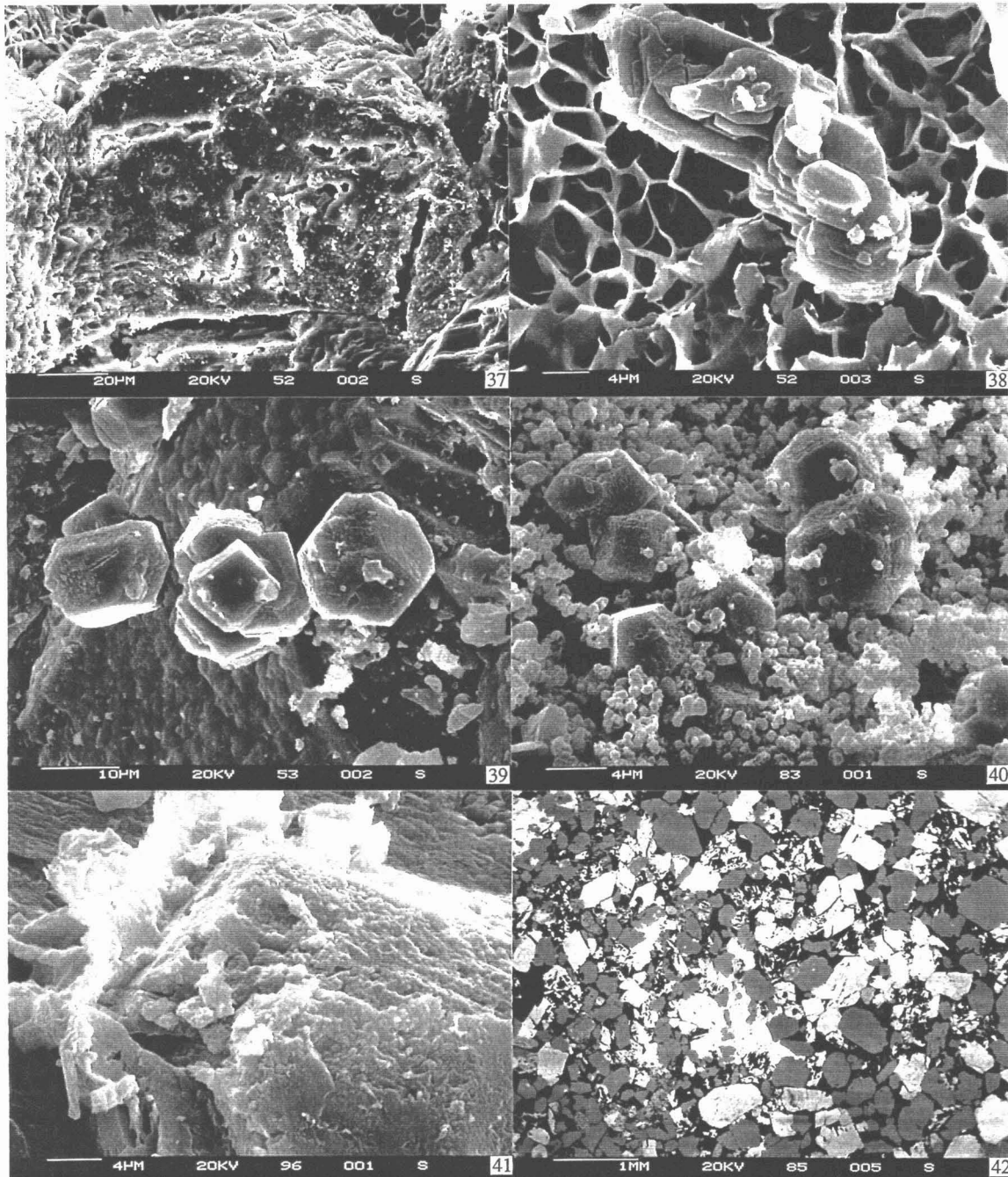
** Fullers' earth + supercritical CO₂ (Run 400)*

The fullers' earth sample fragmented slightly into several irregular blocks. SEM examination indicated that no significant alteration had occurred mineralogically although structurally it is likely that the clay had expanded considerably.

No aqueous fluid sample was available from this experiment.



- Plate 31 Secondary electron SEM photomicrograph of reacted Sherwood Sandstone showing fresh quartz overgrowths and dolomite cement. Sample JMP27, reaction with CO₂-saturated synthetic seawater for 109 days.
- Plate 32 Secondary electron SEM photomicrograph of reacted Sherwood Sandstone showing precipitation of rare calcite at the CO₂-seawater interface. Sample JMP27, reaction with CO₂-saturated synthetic seawater for 109 days.
- Plate 33 Secondary electron SEM photomicrograph of reacted Sherwood Sandstone showing extensive halite encrusting outer surface of block above the CO₂-seawater interface - note the well developed texture. Sample JMP27, reaction with CO₂-saturated synthetic seawater for 109 days.
- Plate 34 Backscattered SEM photomicrograph of moldic porosity due to K-feldspar dissolution, outlined by relict K-feldspar overgrowth. Sandstone reacted with CO₂-saturated seawater. Sample JMP34, run 379.
- Plate 35 Secondary electron SEM photomicrograph of moldic pore outlined by relict coating of authigenic boxwork illite-smectite. Sandstone reacted with CO₂-saturated seawater. Sample JMP34, run 379.
- Plate 36 Secondary electron SEM photomicrograph of possible secondary illite-smectite ragged flakes associated with corroded K-feldspar grains.



- Plate 37 Secondary electron SEM photomicrograph of secondary corrosion on dolomite cement. Sandstone reacted with CO₂-saturated seawater. Sample JMP34, run 379.
- Plate 38 Secondary electron SEM photomicrograph of possible secondary calcite. Sandstone reacted with CO₂-saturated seawater. Sample JMP34, run 379.
- Plate 39 Secondary electron SEM photomicrograph of possible secondary calcite on sandstone block external surface. Sandstone reacted with CO₂-saturated seawater. Sample JMP34, run 379.
- Plate 40 Secondary electron SEM photomicrograph of possible secondary calcite on sandstone block external surface partially coated in halite. Sandstone reacted with CO₂-saturated seawater. Sample JMP36, run 381.
- Plate 41 Secondary electron SEM photomicrograph of possible secondary Ca(K)-clay associated with corroded K-feldspar. Sandstone reacted with CO₂-saturated seawater. Sample JMP40, run 385.
- Plate 42 Backscattered SEM photomicrograph of extensive secondary porosity due to K-feldspar dissolution, outlined by relict K-feldspar overgrowths, and dolomite corrosion. Sandstone reacted with CO₂-saturated seawater. Sample JMP40, run 385.

* *Fullers' earth + CO₂-saturated seawater (Run 401)*

On opening the reaction vessel, it was found that the sample had disintegrated into many small irregular fragments. SEM examination revealed no mineralogical changes had taken place. The swelling was caused by sodium exchanging for calcium in the cation exchangeable interlayer. This will change the fullers' earth at least partially into a Na-bentonite which has much greater swelling characteristics, thereby causing its disintegration.

No aqueous fluid sample was available from this experiment as the fullers' earth appeared to have disintegrated and absorbed the fluid completely.

7.4.2.2 INTERPRETATION

For each set of experiments, the interpretation is based upon a combination of:

- the mineralogical data (X-ray diffraction) and petrographical observations (scanning electron microscopy: SEM and BSEM) carried out on the rock samples.
- the chemical analyses of the water samples (Table 7.12).

The main tools chosen for interpretation are the various chemical geothermometers described in the literature and the EQ3/6 geochemical code with the DATA0.COM.R10 database (Wolery, 1992; see section 7.3.2.1.). Using this code, chemical speciation of water samples and saturation indices (SI) for various minerals were calculated at 80°C and 1 bar pressure. [SI=log(IAP/K) where IAP is the ion activity product and K is the equilibrium constant for the corresponding reaction]. However, saturation indices for aluminosilicate minerals were not calculated because aqueous Al concentrations and pH measurements were not reliable. Analytical uncertainties on fluid composition was significant for some of the runs (372, 382, 383, 385, 398) as the ionic balance exceeded 5%. This was probably due either to uncertainties on the concentrations of the major ions Na and Cl, or to unreliable alkalinity measurements.

Except for CO₂ fugacity, the influence of pressure (200 bars) was not taken into account, as it was considered to have a negligible effect on equilibrium constants up to pressures of 300 bars. The CO₂ fugacity coefficient at 80°C and 200 bars (≈ 0.55) was deduced from Duan et al. (1992) data. Activity coefficients were calculated from the extended Debye-Hückel equation rather than from the theory of Pitzer (1973). For the 0.55 M NaCl solutions (synthetic sea water), the use of this equation represents the upper boundary of its field of application.

Anhydrite

The main reactions that were deduced from the mineralogical and petrographical observations on reacted and unreacted samples were (see section 7.4.2.1.):

- superficial dissolution of anhydrite on the lower half of the sample that was submerged in water.
- extensive precipitation of calcite: along the CO₂-synthetic seawater interface for the three month duration experiment, with minor, later anhydrite; over the entire surface of the lower half of the sample for the eight month experiment. However, no secondary calcite was observed using de-ionised water.

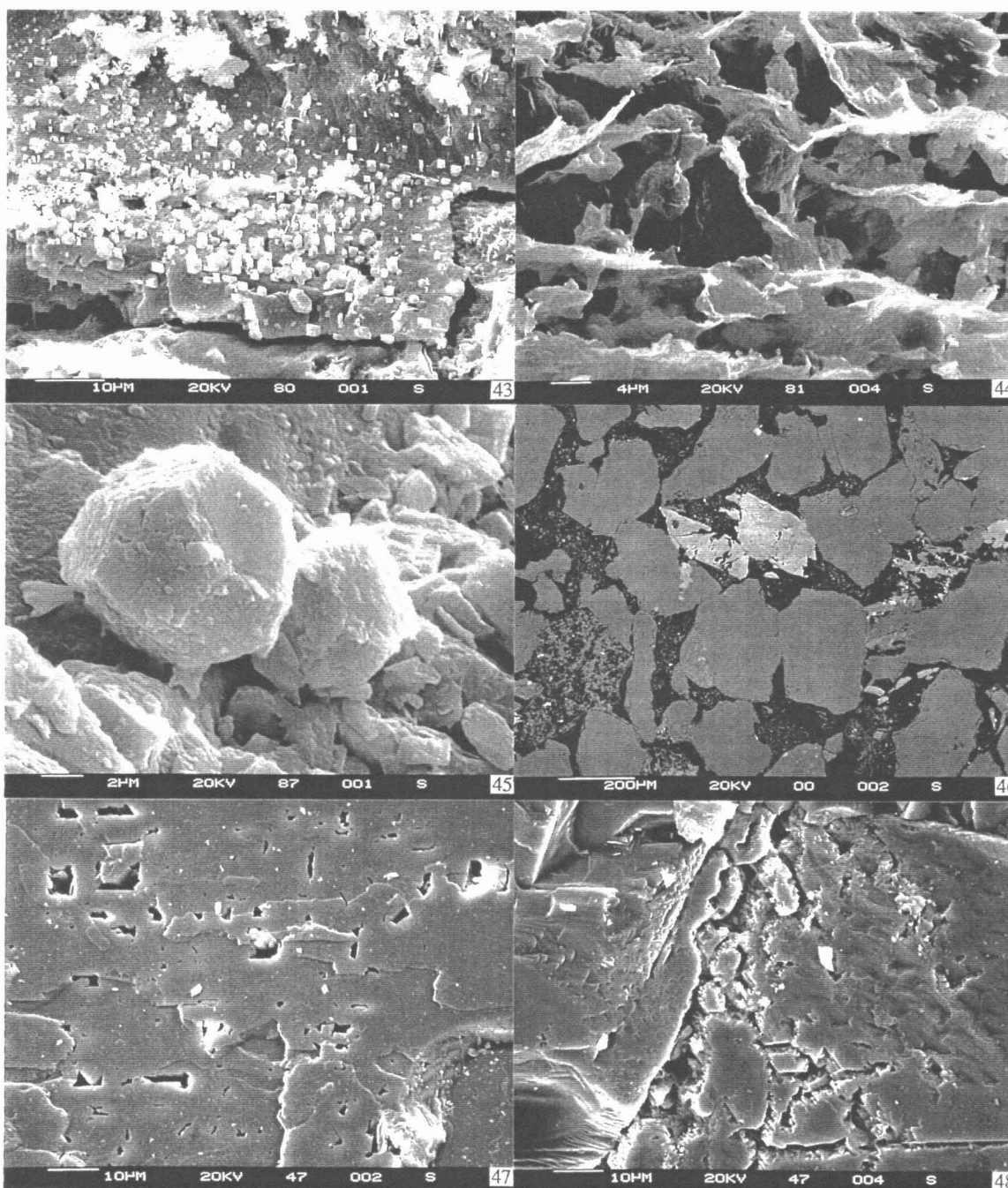
- significant dissolution of mudstone lenses for the eight month experiment, with an increase in porosity to 15% locally within these areas due to the removal of dolomite. In addition, porosity was enhanced adjacent to the mudstone lenses within the anhydrite.
- anhydrite remained unaltered in contact with supercritical CO₂.

The fluid chemistry (Table 7.12) confirmed the above mineralogical observations. High SO₄ and Ca concentrations resulted from extensive anhydrite dissolution. Ca and SO₄ concentrations in the synthetic seawater from the eight month experiment were almost identical to those in the shorter experiment. This suggests that equilibrium between CO₂-seawater-anhydrite was attained within the duration of the shorter experiment. However, concentrations of Mg and K approximately doubled relative to the shorter experiment and probably reflect greater dolomite, clay and K-feldspar dissolution (though mineralogical observations did not reveal dissolution of the latter). This is in agreement with the slower kinetics of aluminosilicate dissolution.

The solubility of minerals such as anhydrite or gypsum in NaCl solutions of various molality and at different temperatures has previously been extensively studied (Bock, 1961; Marshall et al., 1964; Blount and Dickson, 1969, 1973; Briggs, 1978; Harvie and Weare, 1980; Moller, 1988). The lower Ca and SO₄ concentrations in de-ionised water confirm that anhydrite is more soluble in the saline waters than in dilute waters under the experimental conditions. Approximately 5.3 g of anhydrite were dissolved at 80°C per litre of 0.55 M NaCl solution compared to 3.2 g.l⁻¹ in de-ionised water (approximately twice as much). Considering the experimental conditions (94.47 g of anhydrite and 25 ml of water), these values correspond to about 0.14% and 0.08% in mass of dissolved anhydrite relative to the rock sample, respectively.

Thermodynamic calculations using the EQ3/6 geochemical code were carried out for the three experiments. They confirm that water samples were saturated with respect to anhydrite in each experiment. The effect of abundant CO₂ gas on the solubility of anhydrite is not significant. Calculations performed with the same data but with much lower CO₂ fugacity (atmospheric CO₂ pressure) and at neutral pH (pH=7) give slightly lower solubilities because of the decrease in concentration of the Ca-HCO₃ complex.

It is difficult to assess whether the water has reached equilibrium with respect to calcite because equilibrium is strongly dependent on pH, alkalinity values or total carbonate concentrations at the conditions of the experiments (80°C, 200 bar). Total carbonate concentrations and pH have to be estimated from the measured pH and alkalinity measurements at 25°C and 1 bar once the fluids have cooled and degassed. The best approach is to use the previously measured, or calculated, CO₂ solubility data (see section 7.4.1.) to fix the CO₂ fugacity/total carbonate concentration since the experimental conditions (temperature, pressure and salinity) are the same for the anhydrite batch experiments and the CO₂ solubility experiments. The results of the EQ3/6 calculations show that whatever experiment or CO₂ solubility data are considered (accounting for the discrepancy between measured and calculated data), the water is undersaturated with respect to calcite if the measured alkalinity values are used. Alkalinity values would need to be at least twice those measured at room temperature and pressure in order to achieve water-



- Plate 43 Secondary electron SEM photomicrograph of possible secondary calcite crystals seeded onto slightly corroded dolomite cement. Sandstone reacted with CO₂-saturated de-ionised water. Sample JMP35, run 380.
- Plate 44 Secondary electron SEM photomicrograph of possible secondary flaky Ca,K-clay which post-dates secondary calcite on the external surface of the sandstone block. Sandstone reacted with CO₂-saturated de-ionised water. Sample JMP35, run 380.
- Plate 45 Secondary electron SEM photomicrograph of possible secondary calcite on sandstone block external surface. Sandstone reacted with CO₂-saturated de-ionised water. Sample JMP37, run 382.
- Plate 46 Backscattered electron SEM photomicrograph of fine grained sandstone 'rubble' infilling pore spaces at the outlet end of the core. Sandstone core reacted with CO₂-saturated seawater. Run 409.
- Plate 47 Secondary electron SEM photomicrograph of corrosion pits on microcline at inlet end of dissolution column. Run 447.
- Plate 48 Secondary electron SEM photomicrograph of extensive channelling from corrosion of microcline at inlet end of dissolution column. Run 447.

calcite equilibrium. Such a discrepancy could result from changing alkalinity of the sample, due to re-equilibration in going from 80°C and 200 bars to 25°C and 1 bar.

As Ca and SO₄ concentrations are roughly stoichiometric in the experiments using seawater (anhydrite dissolution), the precipitation of calcite is again potentially problematic because it should have removed some calcium from the solution. However some extra calcium needed to form the calcite could have come from dissolution of dolomite in mudstone lenses, which was observed in the mineralogical study. If we assume that most of the aqueous Mg in the 8 month experiment with synthetic seawater was released by this dissolution reaction, and that this element was not incorporated into other minerals, we can evaluate the quantities of dissolved dolomite and precipitated calcite in relation to the rock sample (about 0.09% and 0.05%, respectively). Such calculations would have given higher figures if part of the aqueous magnesium had been incorporated into other minerals. However, they would have been much lower if aqueous Mg was released by aluminosilicate (chlorite, illite) dissolution.

In the experiment using de-ionised water, the Ca concentration was lower than the SO₄ concentration. This could be linked to the precipitation of calcite, although this was not observed experimentally. Since CO₂ solubility is higher in de-ionised water compared to saline water, saturation with calcite can be achieved with lower calcium concentrations. However, the lower calcium concentration could also result from cation exchange for sodium within clay phases. According to Michard (1989), clays preferentially trap calcium and magnesium from dilute aqueous solutions, while alkali cations are preferentially trapped from more saline solutions.

Saturation calculations involving aluminosilicates were not considered because the analysed aqueous Al concentrations were excessively high, and because mineralogical observations of reacted samples revealed that such phases were scarce. Major comments are:

- Dissolution of aluminosilicates (and perhaps cation exchange) did occur: Si, Na, K, Li, B, Fe and probably a small part of Ca and Mg were released into solution

by such reactions. However, chemical geothermometers and molar Na/K ratios (Tables 7.13 and 7.14) showed that water remained far from equilibrium with respect to Na-Mg aluminosilicate minerals and that their reactions were minor. However, the Na/K/Ca and Ca/K geothermometers gave temperature values close to 80°C which suggests that a reaction involving K-feldspar, Ca-smectite and silica did occur, or some ion exchange within smectites (K-smectite + 0.165 Ca²⁺ = Ca-smectite + 0.33 K⁺).

- Silica concentrations were controlled by chalcedony (Table 7.14 and EQ3/6 calculations) or cristobalite (EQ3/6 calculations). As the solubility of these minerals decreases with increasing salinity, the silica concentrations were lower in the experiments with synthetic seawater.

Mudstone

The main reactions deduced from petrographical and mineralogical observations on the reacted and unreacted samples of mudstone were (see section 7.4.2.1.):

- disintegration of the mudstone samples into several fragments or many small fragments.
- significant dissolution of dolomite, especially below the water/CO₂ interface. In the three month experiment, dissolution of dolomite was only observed at the external surface while dolomite grains were generally fresh towards the centre of the samples. An increase in porosity was noted but there was no significant difference between the surface areas of reacted and unreacted samples, except for the experiment using de-ionised water where an increase was observed.
- minor dissolution of K-feldspar below the water/CO₂ interface. No secondary clay precipitates were observed associated with the K-feldspar dissolution.
- possible secondary precipitation of a Mg, Fe, K aluminium silicate below the water/CO₂ interface (observed only for the 3 month experiment with

Table 7.13 Na/K and Ca/Mg molar ratios of batch water samples compared to those concerning the equilibria: albite/K-feldspar, calcite/dolomite and calcite/disordered dolomite, at 80°C.

Experiment	Run number	Starting material	Starting fluid	log Na/K	log Ca/Mg
Anhydrite	377	JMP4	SSW	2.95	0.51
	371	JMP4	SSW	2.69	0.35
	372	JMP4	DIW	0.93	0.09
Mudstone	373	JMP1	SSW	2.00	-1.14
	375	JMP3	SSW	2.23	-1.86
	376	JMP3	DIW	1.71	-1.89
Sandstone	JMP11	JMP11	SSW	0.61	-0.36
	JMP8E	JMP8E	SSW	2.43	-0.07
	JMP12	JMP12	SSW	1.43	-0.43
	JMP10	JMP10	SSW	0.87	0.27
	JMP13	JMP13	SSW	2.33	0.26
	JMP8E	JMP8E	DIW	2.18	-0.20
	JMP12	JMP12	DIW	0.80	-0.47
Equilibrium constant (EQ3/6 database)				2.30	1.39/0.18
Equilibrium constant (Michard, 1983)				2.02	1.37/0.54

(SSW = Synthetic seawater, DIW = De-ionised water).

Table 7.14 Calculated temperatures (°C) from chemical geothermometers.

Experiment	Run number	T _{Na/K} (1)	T (2)	T (3)	T _{Na/K/Ca} =1/3	T =4/3	T _{Ca/K}	T _{K/Mg}	T _{Qz}	T _{cd}	T _{Na/Li} (4)	T (5)	T _{Mg/Li}	T _{Sr/K}	T _{Mn/K}
Anhydrite	377	-24	16	38		85	66	49	123	63	n/d	n/d	n/d	66	39
	371	-5	36	58	72	108	87	58	125	65	43	58	36	94	62
	372	283	283	294	62	87	52	143	82	133	194	52	98	71	
Mudstone	373	62	100	121	147		230	82	99	41	n/d	n/d	n/d	159	n/d
	375	37	76	98	131		229	62	89	31	158	104	67	129	n/d
	376	104	137	157	167		221	59	108	49	106	171	70	123	n/d
Sandstone	383	419	378	379	371		619	217	91	33	n/d	n/d	n/d	1445	n/d
	379	17	57	79	102		154	82	120	60	48	35	48	171	135
	381	153	180	198	216		335	140	100	42	57	41	47	413	247
	384	305	299	308	293		405	193	93	36	27	20	33	697	361
	385	27	67	88	109		155	92	108	49	94	65	75	161	115
	380	42	81	103	118		155	79	125	65	-5	67	57	177	122
	382	333	319	326	285		331	137	107	48	18	91	48	406	253

Na/K geothermometer: (1) Michard (1979) (2) Fournier (1979) (3) Giggenbach (1988)

Na/K/Ca geothermometer: Fournier and Truesdell (1973)

Ca/K geothermometer: Michard (1990)

K/Mg geothermometer: Giggenbach (1988)

Silica geothermometer

(Quartz and Chalcedony): Fournier and Rowe (1966)

Na/Li geothermometer: (4) Fouillac and Michard (1981) (5) Kharaka et al. (1982)

Mg/Li geothermometer: Kharaka and Mariner (1989)

Sr/K geothermometer: Michard (1990)

Mn/K geothermometer: Michard (1990)

synthetic seawater). EDXA indicated it was of 'chloritic' composition. This phase was very rare and mineralogical composition could not be determined exactly.

- possible presence of secondary calcite following dissolution of dolomite (Ca detection by EDXA). However, no calcite was directly observed.
- when exposed to supercritical CO₂ (either completely or just the upper half of the sample), mudstone samples did not show significant differences compared to the unreacted samples.

Consideration of the fluid chemical data (Table 7.12) supports the above observation of dolomite dissolution. Compared to the experimental blank (run 378) there were large increases in Ca and Mg. However, these were not in equimolar proportions as would be expected for stoichiometric dolomite dissolution. The high SO₄ concentrations suggest the presence of some anhydrite (or gypsum) in the mudstone which had undergone dissolution. This phase was not detected by mineralogical analysis because of either, it was a trace component, or because it was present initially in the pores of the samples as a result of pore-water evaporation (original fluid or drilling fluid) during the drying of the samples.

As Ca molalities were significantly lower than SO₄ molalities and far lower than Mg molalities, there must have been a reaction that removed Ca from solution and another that provided a source of Mg. The latter was probably linked to the dissolution of clay minerals. This could have been chlorite, as it was observed during mineralogical studies. The high aqueous Li concentrations (the highest for all the batch experiments, Table 7.12) can be related to the dissolution of this mineral. Moreover, the Mg/Li geothermometer gave temperature values in

reasonable agreement with the experimental value (Table 7.14).

The sink for calcium could have been calcite precipitation. However, there was no direct evidence for this from mineralogical observations, though the Na/K/Ca and Ca/K geothermometers (Table 7.14) indicate that aqueous calcium was not controlled by an aluminosilicate mineral. As for the anhydrite experiment, it was not possible to calculate accurately the degree of saturation with respect to calcite from pH and alkalinity measurements. Another explanation could be cation exchange with clays.

Na molalities were significantly lower than Cl molalities for both experiments involving seawater, while the reverse was true for the experiment involving de-ionised water. In the latter experiment, there was 35.2 mmol.l⁻¹ extra Na compared to Cl, while the sum of Mg and SO₄ was 31.6 mmol.l⁻¹. This suggests that the calcium released by dolomite and anhydrite dissolution was trapped within smectites by ion exchange with sodium. These reactions could have been the main ones occurring in the experiment involving de-ionised water. Albite and chlorite dissolution providing some Na and Mg could have been additional minor reactions, together with calcite precipitation trapping some Ca. This could explain the higher Mg molalities compared to Ca as both elements should have a similar behaviour in ion exchange reactions. In the experiments with seawater, the lower Na molalities compared to Cl suggest that Na was exchanged with Ca and Mg in smectites. However, the uncertainties in the blank analyses prevent to do some mass balance calculations. Chlorite and albite dissolution, together with calcite precipitation could have been additional reactions that controlled the behaviour of Mg, Na and Ca.

Dissolution of K-feldspar and albite might have proceeded to equilibrium with water for the experiments involving seawater. The values of the molar Na/K ratios were close to those representative of albite/K-feldspar

equilibrium (Table 7.13), while the average estimated temperatures from the Na/K geothermometer are in general agreement with the experimental temperature (Table 7.14). For the experiment involving de-ionised water, this equilibrium reaction appears to have not been reached.

For runs 383, 379 and 380, saturation of the aqueous phase with respect to K-feldspar and Mg-aluminosilicates must have almost been achieved because the K/Mg geothermometer (Table 7.14) yielded temperature values close to 80°C (although slightly underestimated). The high dissolved B concentrations (much higher than in the other batch experiments, Table 7.12) can be associated with muscovite dissolution. This mineral was described during mineralogical observations and is known to be a potential source of B in some environments. Aqueous K, supplied by K-feldspar and muscovite dissolution, probably reprecipitated into the undefined Mg, Fe, K aluminium silicate detected during mineralogical observations.

The aqueous silica concentrations were lower than in the experiments with anhydrite (Table 7.12). A less soluble silicate mineral appears to have controlled these concentrations. Saturation calculations using the EQ3/6 code indicated that this mineral could be chalcedony or quartz (instead of cristobalite or chalcedony for the experiments involving anhydrite). At 80°C, previous studies have shown that chalcedony (rather than quartz) precipitates (Michard, 1979; Nicholson, 1993). Using thermodynamic data from Helgeson et al. (1978), the following expression was applied to chalcedony:

$$t (^{\circ}\text{C}) = 1210 / (0.35 - \log(\text{SiO}_2)) - 273.15 \text{ (aqueous SiO}_2 \text{ concentration is in mol.l}^{-1}\text{)}$$

The temperatures estimated with this geothermometer (77, 67 and 86°C, respectively) are in better agreement with the experimental value (80°C). Similar observations for the 10–80°C temperature range have already been carried out by Michard (1990). As previously noted for the anhydrite experiments, the higher solubility of silica minerals in dilute waters compared to saline waters is confirmed by the measured Si concentrations.

The disintegration of the mudstone samples was probably due to mechanical deformation and swelling of the smectite clays present in the clay matrix. As the mudstone samples used for the experiments were dry, the smectites recovered part of their original water content when rewetted with de-ionised water or synthetic seawater. This interlayer or interparticle hydration led to an increase in volume which disrupted the mudstone fabric and caused fragmentation. This disintegration was intense in the eight month experiments with de-ionised water and synthetic seawater. Although the swelling potential of Ca-smectites (these probably formed in the DIW experiment) is much lower than that of Na-smectites (these are suspected to have formed in the SSW experiment), the salinity of the water is known to reduce the swelling potential of Na-smectites via the effect on ionic strength and activity of water (Ben Rhaiem et al., 1986 and 1987).

Sandstone

Several samples of Sherwood sandstone were selected for batch experiments. Mineralogical examination on unreacted samples always revealed the presence of detrital quartz and K-feldspar with minor plagioclase feldspars and rare micas. Dolomite cement was present in most samples. For JMP10 sandstone used in run 384, some anhydrite cement was also detected. For JMP11 subarkose and

JMP12 arkosic arenite samples, which were used in runs 383 and 381/382 respectively, rare mica and illite/smectite flakes were observed. In JMP8 subarkose sample (runs 379 and 380), well-developed illite-smectite clay with minor amounts of chlorite (suggested by Mg and Fe analyses) and some calcite cement post-dating dolomite cement were detected. JMP13 sandstone sample (run 385) contained at least two generations of calcite cement, without dolomite, plus minor barite. The main reactions which were deduced from petrographical and mineralogical observations on the reacted and unreacted samples were (see section 7.4.2.1.):

- dissolution of K-feldspar both below and above the SC CO₂-water interface, with the greatest dissolution in the upper half (within the SC CO₂).
- dissolution of dolomite cement both below and above the SC CO₂-water interface.
- minor formation of secondary calcite crystals at the SC CO₂-water interface and occasionally over the rest of the external surface. Only very rarely was secondary calcite observed to have developed within a sandstone block (run 384).
- extensive precipitation of halite on the external surfaces of the sandstones reacted with seawater, especially on the upper half of the sample in contact with SC CO₂.
- tentative identification of secondary clay precipitation in some of the eight month experiments. This clay was a poorly developed Na,K,Ca-aluminium silicate associated with corroded K-feldspar. Such a clay was described within the whole sample of the reacted SSW/JMP13 sample (run 385), associated mainly with corroded K-feldspar but also observed on other pore walls. Illitic clay formation was described for the subarkose sample (JMP8) reacted with both seawater and de-ionised water (run 379 and 380).
- slight increases in porosity for most samples except for the JMP8 subarkose samples reacted with both seawater and de-ionised water, where a slight decrease was observed.

One of the most notable observations was the extensive precipitation of halite on the external surfaces of sandstones reacted with seawater, especially on the upper part in contact with SC CO₂. It is considered unlikely that the halite formed as an efflorescence on the surface of the block during drying after the end of the experiments. Great care was taken to instantaneously freeze the sample in liquid nitrogen on immediate removal from the reaction vessel. In addition, much less halite was present on the lower part of the core, which was submerged in seawater, where it would be anticipated that most of the halite would form if uncontrolled drying had taken place. The very well developed halite textures (Plate 20) are not consistent with previous experience of salt drying as a surface efflorescence. It is suggested therefore that halite formed in situ during the experiments, as a result of drying of seawater on the block surface in the SC CO₂ atmosphere. It was noted on opening the reaction vessels that the whole of the block was moist. This was probably due to capillary action drawing up the seawater from the lower part of the vessel. It is thought that as the sandstone became saturated above the seawater surface, the SC CO₂ led to evaporation of the

water and halite precipitation. The halite formed an extensive crust over the whole block surface in the upper part of the core, obliterating the underlying sand grains. Hence no primary sandstone surfaces were examined. However, this halite crust was not preserved in the corresponding polished thin sections indicating that the crust was a superficial deposit where the seawater was directly exposed to SC CO₂. This was not observed in the mudstone and anhydrite experiments since capillary action was not possible due to the low porosities and permeabilities (caprock properties).

Prior to discussing the fluid chemical data (Table 7.12), consideration should be given to possible contamination by NaCl and KCl salts. These were probably present in the pores of the samples used for experiments as a result of pore-water evaporation (original fluid or drilling fluid) during the original drying of these samples. The salinities of the host formation fluids range from 35 to 80 g.l⁻¹ with 12g.l⁻¹ Na, 18-43 g.l⁻¹ Cl and 12 g.l⁻¹ K according to

analyses carried out after pump tests (Downing et al., 1985). Figure 7.16 shows that contamination by NaCl was observed for all the water samples, except perhaps for run 383. Contamination with KCl also occurred in runs 381, 383 and 384 (Figure 7.16). The scale of mineral reactions seems to have been affected by such contamination since K-feldspar corrosion was reduced where excess K was present. The extensive halite precipitation in run 381, and its poorly developed texture in contrast to the well developed halite textures observed in the other experiments, is probably linked to the very large contamination by NaCl for this run. As a general rule, extensive halite precipitation occurred for contaminated samples.

Ion exchange reactions between Na and Ca may have also occurred but were difficult to assess because of the contamination by residual salts and the analytical uncertainties on Na and Cl determinations. However, Na molalities are systematically lower than Cl molalities in the experiments that involved synthetic seawater whereas they are systematically higher than Cl molalities in the experiments that involved de-ionised water. In the experiments with de-ionised water, the higher Na content compared to Cl (Figure 7.16) could be linked to an exchange with calcium released by dolomite dissolution. Illite-smectite clays were described in the unreacted samples, and Ca-K smectite was tentatively identified in the reacted samples (run 380). In the experiment that reacted synthetic seawater with JMP8 subarkose containing illite-smectite clays (run 379), SEM-EDXA analysis revealed that some exchange of sodium (from the seawater) with calcium (in the exchangeable sites of the smectite interlayers) had occurred.

SO₄ concentrations were sometimes much higher than for the experimental blank, and the SO₄ versus Ca plot on Figure 7.17 shows that dissolved SO₄ and a significant part of aqueous Ca can be explained by anhydrite (or gypsum) dissolution. Thermodynamic calculations using the EQ3/6 code showed that the waters were undersaturated with respect to these minerals. However, anhydrite cement was only described in the JMP10 sandstone sample which actually corresponds to the highest quantity of dissolved calcium sulphate (run 384). Anhydrite was not observed in the other samples, but may have been present in trace amounts in cements, or as a residual salt due to pore-water evaporation during previous drying of the samples. Also in Figure 7.17, aqueous Sr appears to have been supplied to the solution by the dissolution of anhydrite, except for run 384.

Apart from for runs 384 and 385, aqueous Ca and Mg concentrations can be approximated to a linear regression through the origin (Figure 7.17). For runs 384 and 385, if aqueous Ca concentrations are corrected by eliminating Ca supplied by anhydrite dissolution, the water samples would then be close to the linear regression. Such a relationship would be consistent with the dolomite dissolution observed by petrographical examination. Molar Ca/Mg ratios show that disordered dolomite-calcite equilibrium seems to be almost achieved in runs 379, 380, 384 and 385 (Table 7.13). Indeed, calcite cement had been observed in the unreacted samples of three of these runs (379, 380, 385). In run 384, no calcite cement was present initially, but dissolution of anhydrite cement led to calcite precipitation. In the unreacted samples of the other runs (381, 382, 383), only dolomite cement had been found. For the runs without excess K (runs 379, 380 and 385), the Na/K/Ca and Ca/K geothermometers (Table 7.14) indicate that aqueous Ca did not react to any appreciable amount with silicate minerals. However, for these three runs, the similar temperature values obtained from the Ca/K and Sr/K geothermometers

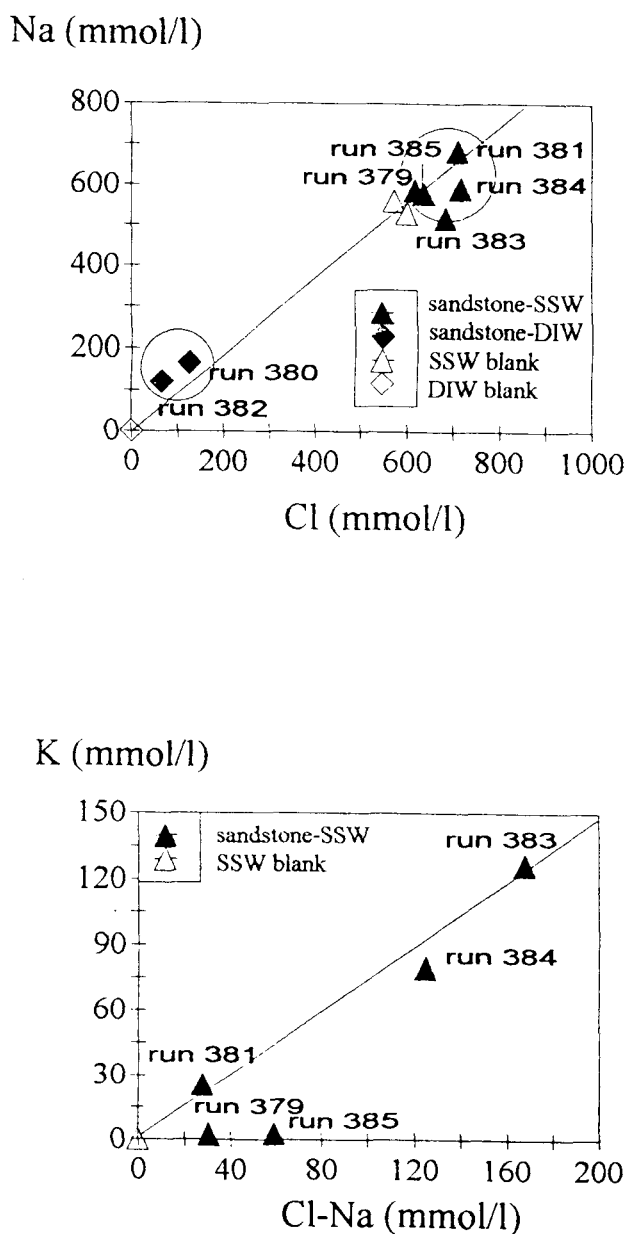
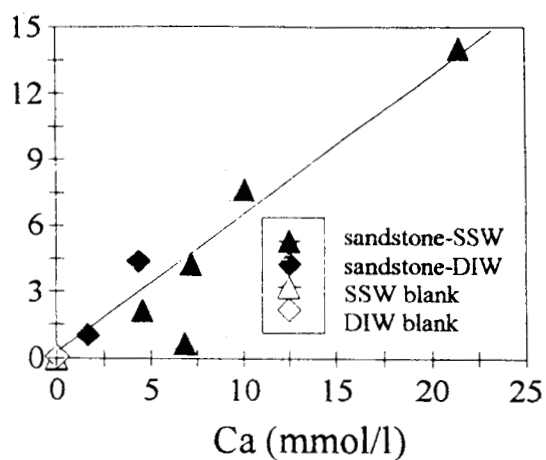
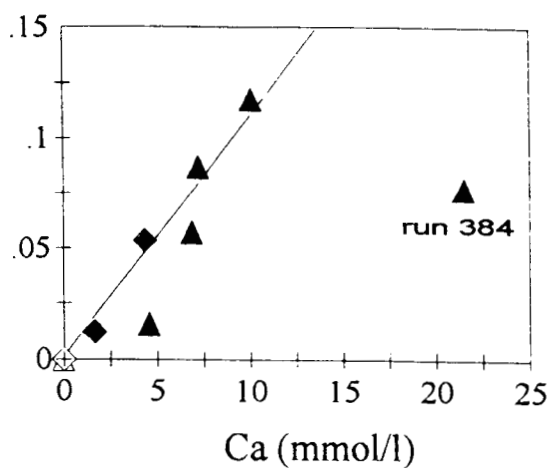


Figure 7.16 Diagrams Na versus Cl and K versus Cl-Na-Sandstone batch experiments.

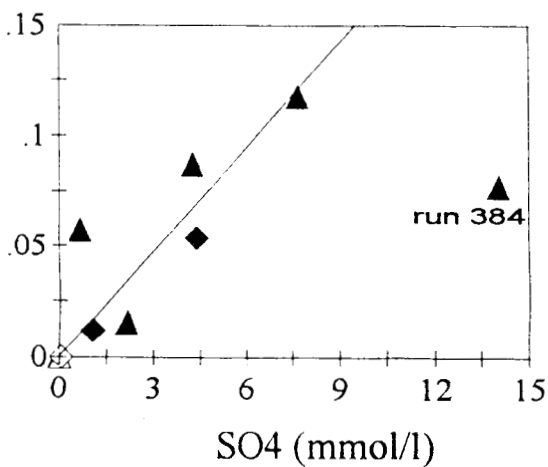
SO₄ (mmol/l)



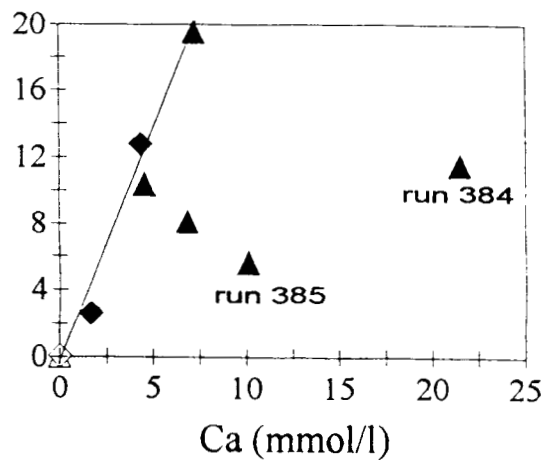
Sr (mmol/l)



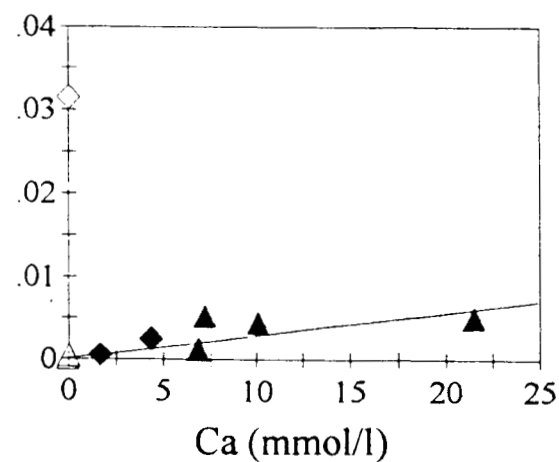
Sr (mmol/l)



Mg (mmol/l)



Mn (mmol/l)



log Ba (mol/l)

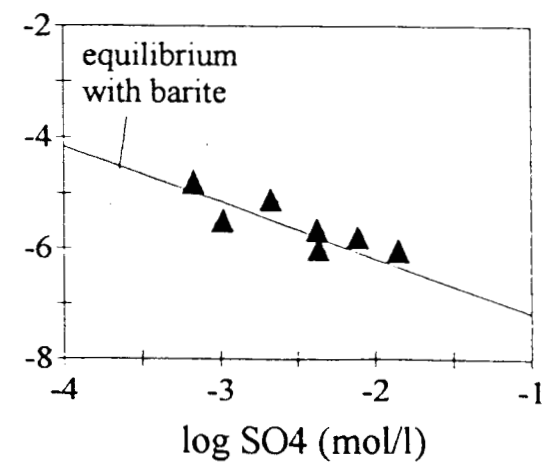


Figure 7.17 Concentration diagrams — Sandstone batch experiments.

(Table 7.14) indicate that these elements were probably controlled by the same reactions.

Aqueous Mn was probably released by dolomite dissolution (Figure 7.17). For runs 379, 380 and 385 (without excess K), the Mn/K geothermometer yields slightly overestimated temperature values (Table 7.14). The behaviour of dissolved Ba (Figure 7.17) appears to be controlled by a precipitation/equilibrium mechanism rather than by dissolution. It is suspected that precipitation of barite is the controlling mechanism.

For most of the runs, silica concentrations appear to be controlled by either chalcedony (Table 7.14, EQ3/6 calculations) or quartz (EQ3/6 calculations). If equilibrium is assumed, it is likely that any silica precipitate would be chalcedony rather than quartz. For runs 379 and 380 (sample JMP8), the silica concentrations were slightly higher than for the above. Chalcedony or cristobalite would then be the minerals that controlled these concentrations (if equilibrium is assumed).

For the runs without excess K (runs 379, 380 and 385), the temperatures estimated from the K/Mg geothermometer (Table 7.14) are in good agreement with the experimental temperature. In these runs, equilibrium between K- and Mg-bearing aluminosilicate minerals appears to have been achieved. It is worth noting that illite and other poorly identified aluminosilicate minerals were identified in these experiments. Although chlorite was detected in sample JMP8 (runs 379 and 380), it is likely that the influence of this mineral on Mg concentrations was limited. Dissolution of K-feldspar and disordered dolomite, together with illite precipitation seem to have been the main reactions.

The Fournier (1979) and Giggenbach (1988) Na/K geothermometers yielded temperature values close to 80°C, but only for runs without excess K (Table 7.14). Corresponding molar Na/K ratios were also similar to those representative of albite/K-feldspar equilibrium (Table 7.13). Therefore in these runs, it would appear that equilibrium was being approached.

Li concentrations show a similar behaviour to those of K concentrations in the runs without excess K (Figure 7.18). For these runs, the temperatures calculated from the Na/Li and Mg/Li geothermometers were slight underestimates (Table 7.14), showing that equilibrium between these elements had not been achieved.

7.4.2.3 CONCLUSIONS

The following sections describe the main conclusions of the experiments based on mineralogical and fluid chemical changes as a result of fluid/rock interaction.

Anhydrite

Anhydrite remained unaltered in contact with supercritical CO₂ alone. However, below the SC CO₂-water interface, anhydrite was severely corroded as a result of anhydrite solubility in water. Dissolution was greatest in the experiment using de-ionised water since the solubility of anhydrite is higher in dilute solutions than in saline solutions. Thermodynamic calculations have shown that the effect of CO₂ on the anhydrite dissolution mechanism is negligible. Secondary calcite precipitation at the outer surface of the anhydrite blocks was only observed for the experiments using synthetic seawater. Although mineralogical observations indicate that calcite precipitation was a direct result of anhydrite dissolution, thermodynamic calculations suggest that the fluids were undersaturated with respect to calcite. However, CO₂ had an effect on the

mudstone lenses included within the anhydrite, with some dissolution of dolomite and aluminosilicates, possible ion exchange within smectite clays and the appearance of cracks in the mudstone.

Therefore, it would appear that the caprock properties of anhydrite would not be altered by supercritical CO₂ injection. Evidence from natural CO₂ fields in the US indicates that CO₂ can be adequately capped by anhydrite on geological timescales (see section 7.5). However, irregularities within the anhydrite, such as mudstone lenses, could be effected and would be worthy of future investigation.

Mudstone

When exposed to supercritical CO₂ alone (either completely, or just the upper half of the sample), the mudstone samples did not show significant differences to the unreacted samples.

The most significant reaction between mudstones and CO₂-saturated fluids was the dissolution, and often complete removal, of dolomite. This resulted in locally enhanced secondary porosity. The precipitation of calcite

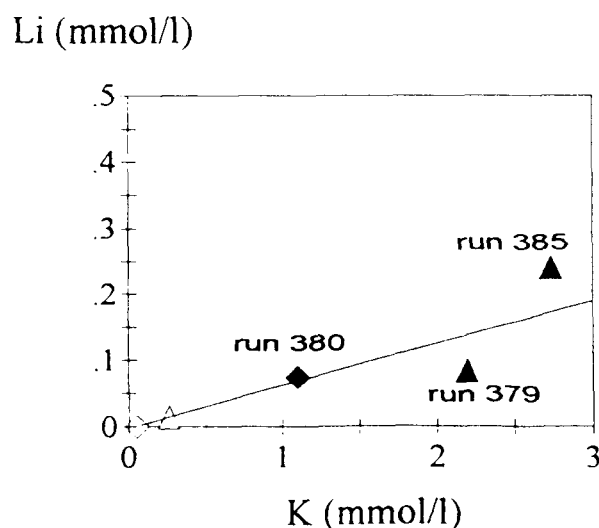
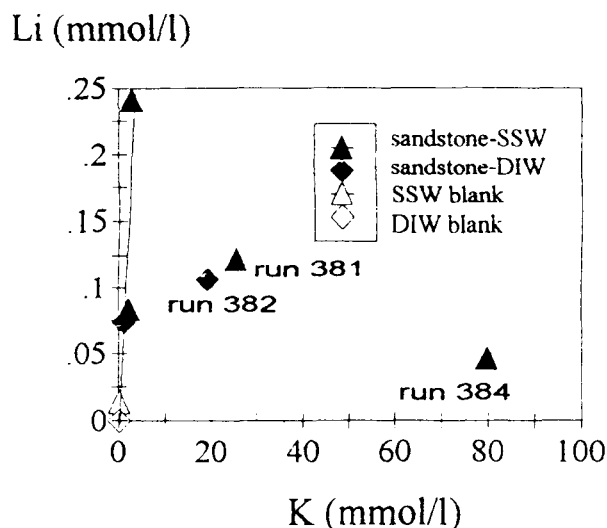


Figure 7.18 Diagram Li versus K — Sandstone batch experiments.

was only tentatively identified in some areas in association with dolomite removal. K-feldspar dissolution was also observed, with local enhancement of secondary porosity. However, these changes were often too small to allow for detailed comparisons to be made between the samples reacted for three or eight months. Only mudstone appeared to show appreciable reaction with CO₂-saturated de-ionised water, with an increase in surface area compared to the unreacted material. The surface areas of mudstone samples reacted with synthetic seawater did not change within experimental error.

In many of the experiments, it was found that reaction caused many of the mudstone blocks to disintegrate into several, or many small fragments. This may have been caused by the swelling properties of the smectite clays present in the clay matrix. However, this may not be a direct result of the effect of CO₂, but could be an effect of immersing dry samples in dilute or saline waters.

Therefore, it would appear that the caprock properties of mudstones would not be altered greatly by the injection of supercritical CO₂. Mudstones appear inert when in contact with supercritical CO₂ alone (gas cap). However, corrosion could occur at the edges of the reservoir where CO₂-saturated waters are in direct contact with the mudstones. Though it appears that large CO₂-rich water/rock ratios would be needed to cause intensive alteration of the mudstone caprock. The presence of natural CO₂ fields, together with large-scale enhanced oil recovery schemes using supercritical CO₂, suggest that mudstones are not severely affected.

Sandstone

The reactions between sandstone and CO₂-saturated fluids, whether seawater or de-ionised water, resulted in several changes common to most of the experiments conducted in this study. They occurred both below and above the SC CO₂-water interface as a result of capillary action drawing up the water from the lower half of the vessel. The most obvious change was corrosion of K-feldspar. This was observed in all reacted sandstones, though the type and quantity of corrosion varied between samples. In particular it appeared that where K-feldspar had already been corroded prior to these experiments, then corrosion continued at these corroded sites. This made identification of corrosion resulting from interaction with CO₂-saturated fluids difficult. However, point counting analyses indicated that the proportion of K-feldspar did indeed decrease. The exception to this was the arkosic arenite JMP13 reacted with seawater (run 385). As mentioned previously, point counting analysis of this sample was problematic due to its very heterogeneous nature, patchy porosity and poor sorting. Associated with the corrosion of K-feldspar was the tentative identification of secondary clay precipitation which was noted in most reacted sandstones. It must be stressed that the identification of such phases is very tentative, based only on SEM-EDXA observations. The very small amounts present prevented positive identification by XRD. This clay was observed by SEM as a poorly developed Na,K,Ca-aluminium silicate associated with corroded K-feldspars. Point counting analyses were somewhat variable, with some analyses giving an increase and others a decrease, in overall clay content. The best evidence for illitic clay precipitation came from the JMP8 subarkose sample in experiments using both seawater and de-ionised water (runs 379 and 380).

It should be noted that most of the samples used in the experiments appear to have been contaminated by NaCl

(and KCl) present in the pores as a result of pore-water evaporation during the original drying of these samples. This had an effect on the extent of the aluminosilicate reactions, with possible reductions in K-feldspar dissolution and clay precipitation. Such reactions appeared to be greatest with the JMP8 subarkose samples, the only samples that did not contain excess Na and K (runs 379 and 380).

In addition, most sandstones contained varying amounts of dolomite cement. In all cases, except run 382 (arkosic arenite + de-ionised water for 8 months), corrosion of dolomite during the experiments was observed by SEM. Point counting analyses of reacted sandstones also indicated a decrease in the proportion of dolomite.

Secondary precipitates are typically confined to the external surfaces of the reacted sandstone blocks. Secondary calcite formed a minor coating at the CO₂-water interface and occasionally over the rest of the external surface. Only very rarely was secondary calcite observed developing within a sandstone block (as was the case in the experiment using the JMP10 sandstone where some anhydrite cement had previously been detected). Generally however, secondary calcite was not detected by point counting which deliberately avoided the external surfaces of the blocks. Halite was also an extensive precipitate on the external surfaces of those sandstones reacted with synthetic seawater, especially for the samples contaminated by excess NaCl. The well-developed textures of the halite, and lack of halite below the CO₂-seawater interface, suggested that it had developed as an efflorescence during reaction. Seawater was drawn up through the block by capillary action, and then dried at the block surface in the supercritical CO₂ atmosphere.

Variations in porosity were not systematic throughout the series of experiments with most showing slight increases. Interestingly, reacted samples of the uncontaminated JMP8 subarkose showed slight decreases in porosity. Decreases in porosity were also noted by point counting in the core flood experiment using dry supercritical CO₂ (see section 7.4.3.) and very similar material. Such changes probably result from slightly larger decreases in K-feldspar and dolomite content, and larger increases in clay content.

Two major differences were noted between the sandstones reacted with seawater and those reacted with de-ionised water. The most obvious difference was the precipitation of extensive halite efflorescences from the seawater on the external surfaces of the sandstone blocks. This has already been discussed in previous sections. The second difference was the apparent interaction between seawater and clay minerals present in the sandstones. SEM-EDXA analysis revealed that, for samples containing authigenic illite-smectite clays, some exchange of sodium from the seawater with calcium present in the exchangeable sites of the smectite interlayers had occurred. This was difficult to confirm using the fluid chemical analyses because of the contamination by residual NaCl (and KCl) in the pores of many samples. However, these ion exchange reactions may have occurred because the sandstone samples used for the experiments were dried and did not represent *in situ* samples. As a result, the role of CO₂ in such reactions is not obvious. However, for samples reacted with de-ionised water, it is likely that some exchange occurred, between calcium (released by dolomite dissolution) and sodium (present in the exchangeable sites of the smectite interlayers).

For potential host formations, the main consequences of ion exchange reactions between CO₂-saturated water and

smectite clays present in the sandstones would be the following. In the case of saline host formation waters, it is not obvious that the addition of CO₂ would favor ion exchange reactions, because the percent increase of Na content in water (due to feldspar dissolution) would be low. However, the pH may have an important role. More investigations on ion exchange reactions are needed to determine whether Na-smectites would develop. If they do, two effects would be expected. Firstly, release of calcium into solution which might then contribute to the precipitation of calcite. Secondly, the formation of Na-smectites which have much greater swelling characteristics (Odom, 1984). If this process would occur extensively, greater swelling characteristics might result in blocked pore throats and a reduction in permeability (Kemp, 1992), particularly if combined with the precipitation of secondary clays as a result of feldspar dissolution. In the case of dilute host formation waters, the increase of their Ca content (due to dolomite dissolution) should favor ion exchange with sodium within smectite clays, so providing sodium to solution. However, Ca-smectites have much lower swelling characteristics, and permeability is less likely to be reduced.

In the types of reaction mechanism proposed in the theoretical study by Gunter et al. (1993a), Ca-feldspar reacts with CO₂ to form calcite and kaolinite. However, in the sandstones used in this study, Ca-feldspar was not present to any appreciable degree, and K-feldspar was the main silicate phase undergoing dissolution. Reactions involving K-feldspar and CO₂ do not result in calcite precipitation directly. Dedolomitisation reactions did appear to cause some precipitation of calcite, though it was neither obvious or large. Host sandstone formations are unlikely to contain appreciable Ca-feldspar as these are easily altered during rock diagenesis. The present study has shown that an increase of CO₂ uptake through mineral trapping could be achieved in sandstones rich in anhydrite cement, as anhydrite dissolution followed by calcite precipitation will occur. Ion exchange reactions within clays could also lead to calcite precipitation, but confirmation of this would require further investigation.

The experiments carried out in this study have also shown that some reactions will occur in that part of the reservoir filled with supercritical CO₂ (i.e. the 'gas cap'). This will be due to the presence of either residual water, or that drawn up by capillary action.

7.4.3 Core flooding experiments

7.4.3.1 DESCRIPTION OF THE RESULTS

Run 370, Dry supercritical CO₂

In this experiment the sandstone core (JMP8A) was first saturated with 0.55 M NaCl solution, then flushed once with dry SC CO₂. Thus the first samples obtained were of fluid only. As the experiment progressed, the samples contained increasing amounts of SC CO₂ until after 3 samples the volume of aqueous phase collected was negligible. For the final two samples taken, the pressurised sample vessels were filled with exactly 10 cm³ of de-ionised water and the exiting gas stream was allowed to dissolve into the de-ionised water, in order to assess the potential for the reaction of wet SC CO₂ with the sandstone core. The fluid chemical data are presented on Table 7.15.

Figure 7.19 shows a plot of pressure and flow variations during the experiment. The variations in pressure seen increasingly towards the end of the experiment, represent the recovery times of the system following the change over

of the sample vessels. This takes increasingly longer as the volume of SC CO₂ in the system increases with time.

Two samples were taken from the reacted sandstone core (one at the inlet end and one close to the outlet end) and compared with samples of unreacted sandstone taken from the same depth. K-feldspars close to the inlet were more severely corroded than in the unreacted sandstone. In some cases, corrosion produced moldic pores with relict authigenic illite-smectite coatings. Corroded K-feldspar grains were also noted at the outlet end but the amount of corrosion did not appear to be significantly increased above that observed in the unreacted sandstone. K-feldspar overgrowths were corroded to a depth of 10 µm in places. No secondary clays were present in association with the corroded feldspars. Both the boxwork illite-smectite, and fibrous illite, were preserved throughout the reacted core. However, the degree of fibrous illite preservation at the inlet may have been slightly reduced, with some fibres appearing flattened, possibly as a result of a passing fluid. Interestingly, it was noted that pore walls lined by quartz overgrowths, which were clean at the inlet end, were generally covered in fragments of clay at the outlet end.

Although little dolomite was observed in the unreacted sandstone, where present was locally corroded throughout the core. The degree of corrosion varied from fresh dolomite to severely corroded crystals. This localised corrosion suggests that fluid flow may have been along certain preferential routes. No secondary calcite was present within the sample, although authigenic calcite cement was observed as a very minor phase in both the unreacted and reacted sandstone. No dissolution features developed on this calcite as a result of reaction.

Point count analyses partially confirm the SEM observations described above (Table 7.10, Figure 7.19). As in the sandstone batch experiment (Run 383), total quartz increases in the reaction products. The increases in the core flood are 7% at the inlet and 4% at the outlet (Figure 7.20). As discussed above for run 383, such an increase may be attributable to changes in natural background mineralogy. No evidence for secondary quartz precipitation was found during SEM analysis. However, the original spatial proxi-

Table 7.15 Chemical analytical data for the core-flooding experiment using dry SC CO₂ (all concentrations quoted as mg.l⁻¹).

RUN 370 : 80 °C, 20MPa Sandstone Core — dry SC CO ₂					
Sample Time (hours)	370/blk 0.0	370/1 67.5	370/2 162.5	370/9 671.5	370/10 712.3
pH	6.51	6.29	7.12	4.97	5.25
Ca	0.70	51.4	363	5.46	7.92
Mg	<0.50	6.61	61.0	6.73	8.78
Na	14900	14800	16500	42.2	95.1
K	<2.00	23.6	36.3	<1.00	<1.00
Si	0.24	16.3	38.1	0.38	0.49
SiO ₂	0.51	34.9	81.5	0.81	1.05
Ba	<0.004	0.097	0.805	0.454	0.687
Sr	0.009	0.168	0.622	0.024	0.037
Mn	<0.004	4.71	6.27	0.047	0.064
Total Fe	<0.05	<0.05	0.07	0.38	0.98
Al	<0.20	<0.20	0.23	0.50	0.39
B	<0.20	0.79	0.65	<0.05	<0.05
Cl	19400	19300	19100	50.5	109
SO ₄	<100	<100	<100	<2.00	<10.0

Figure 7.19 Plot of outlet pressure and inlet flow rate over time for the core flood experiment using dry SC CO₂ only.

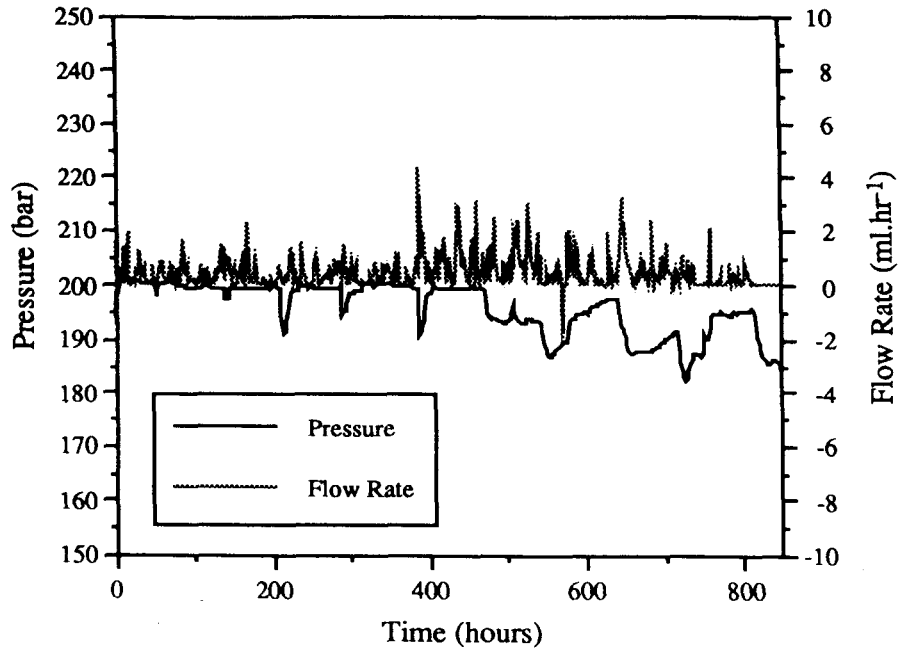
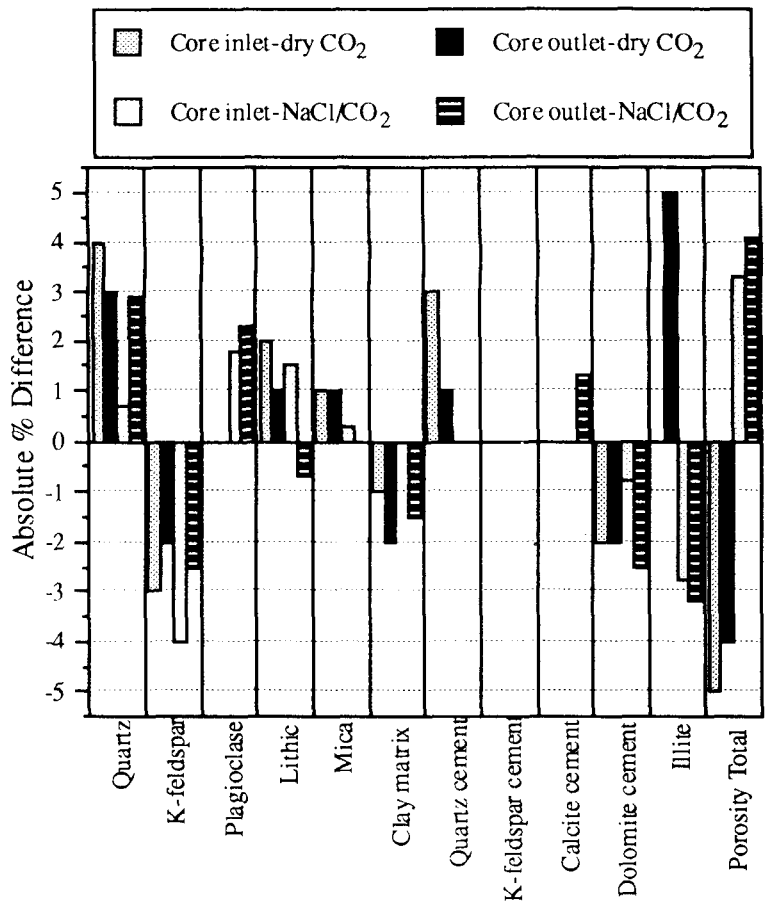


Figure 7.20 Differences in absolute percentage terms between unreacted and reacted sandstone samples on the basis of point counting data (Table 7.10).

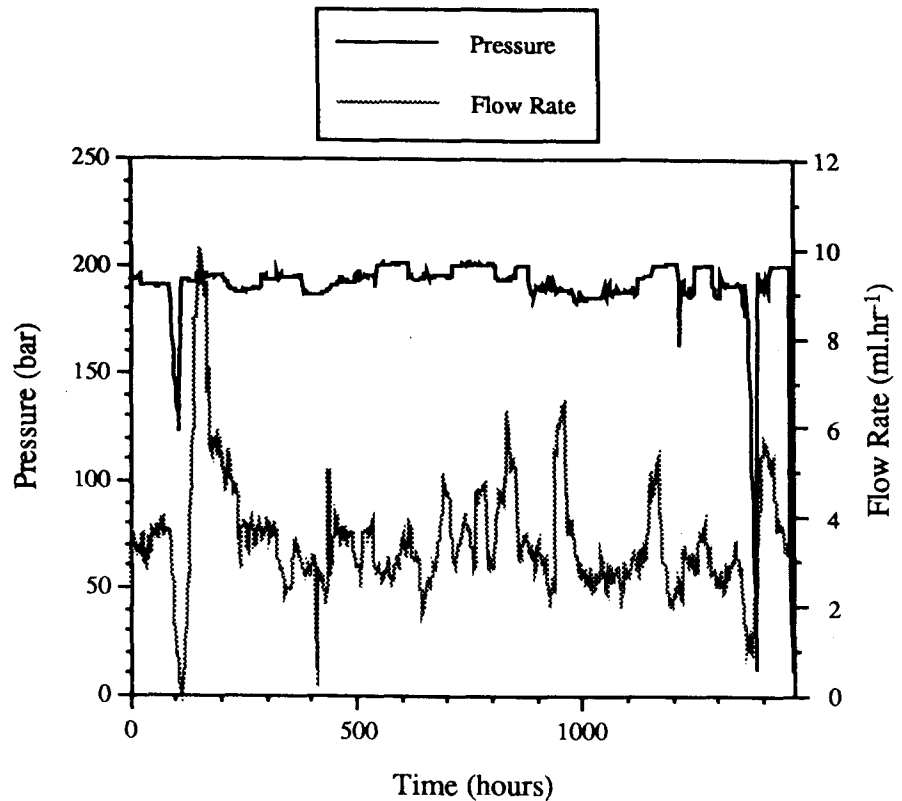
Core inlet and core outlet dry CO₂ from Run 370: Dry SC CO₂ only.
 Core inlet and core outlet NaCl/CO₂ from Run 409: NaCl equilibrated with SC CO₂.



mity of the unreacted and reacted samples was very close, and would require that mineralogical variations took place on the centimetre scale. Such variations are probably also reflected by variations in the proportion of lithic clasts. It is therefore important to reiterate that any variations detected by the point counting method may result from natural variations in mineralogy and not necessarily from reaction with CO₂-saturated seawater. Nevertheless, the point counting results do appear to confirm the SEM observations. Detrital K-feldspar decreased by 3% in the inlet sample and by 2% in the outlet sample (Figure 7.20). These decreases confirm the loss of K-feldspar throughout the column and that, as would be expected, the loss was greater at the inlet end of the column. The proportion of dolomite cement decreased by 2% in both the inlet and outlet samples (Figure 7.20). Furthermore, an increase in the proportion of 'mica' by 5% (EDXA indicated this was dominated by authigenic illite-smectite clay) in the outlet sample also apparently confirms the SEM observation that quartz overgrowths were coated in clay fragments. The total porosity however, decreased by 5% and 4% from inlet to outlet end respectively, relative to the unreacted sandstone (Table 7.10, Figure 7.20). This decrease probably reflected an increase in total quartz, 'mica' and illite, and is consistent with the decrease in porosity observed in the batch experiments using the same type of sample. Both porosi-

metry (Table 7.8) and point counting (Table 7.10) analyses indicated a decrease in porosity. The starting material porosity was 24.8% by point counting and 21.58% by porosimetry. The decrease observed by point counting was 4.5% at the starting end and 3.7% at the outlet end. However, that determined by porosimetry is much less, with a 1.1% reduction at the inlet end and 1.0% at the outlet end.

Figure 7.21 Plot of outlet pressure and inlet flow rate over time for the core flood experiment using 0.55 M NaCl solution equilibrated with SC CO₂.



Run 409, 0.55 M NaCl solution equilibrated with supercritical CO₂

In this experiment the sandstone core (JMP8D) was first saturated with 0.55 M NaCl solution and then flushed once with 0.55 M NaCl solution that had been equilibrated with supercritical CO₂. Therefore, all the samples obtained in this experiment were of reacted fluid. The fluid chemical data are presented in Table 7.16.

Figure 7.21 shows a plot of the pressure and flow variations with time. The variations in pressure represent the recovery times of the system following the change over of the pressurised sample vessels.

The sample used in this experiment was taken directly below that used in run 370. Two subsamples, one from the inlet end and one from the outlet end, were again prepared for SEM examination (stubs and polished thin sections). Generally the samples were very similar to the starting material (JMP8D) with well sorted, subrounded to angular quartz and angular K-feldspar grains, poorly cemented with a well-connected, secondary pore network. Rare micas had well developed splaying along basal cleavage with poorly developed fibrous, Fe-rich illitic clay between mica plates. Rare hematite and minor anatase occasionally developed within the mica plates.

Rare moldic secondary pores resulted from dissolution of detrital K-feldspar. The pores were outlined by relict K-feldspar overgrowths. This was confirmed by point counting analyses which showed an increase in porosity for both the inlet and outlet samples (Table 7.10, Figure 7.20). The dolomite cement, patchily developed in the unreacted sandstone, was corroded following reaction, particularly close to the inlet end. However, point counting analyses indicated that dolomite decreased slightly throughout the column and was particularly corroded at the outlet end (Figure 7.20). The corrosion occurred as superficial pitting. Occasional moldic rhomb-shaped pores deve-

loped within the dolomite cement, as a result of earlier dolomite dissolution while later dolomite was unaffected. Calcite precipitation was also detected by point counting at the outlet end of the column. This occurred as a minor, pore-filling cement which may have formed after reaction, during sample depressurisation. The calcite enclosed, and therefore post-dated, the authigenic clay which lined pore walls.

Many pore walls were lined by a layer of authigenic, Fe-rich, illitic clay. This developed from primary detrital grain surfaces and occurred up to 5 µm thick. In addition to this authigenic clay which was present in the unreacted sandstone, occasional aggregates of secondary clay were also developed up to 20 µm across. EDXA indicated that these were of illite-smectite composition although specific clay mineral identification was not possible. Secondary illitic clay also developed occasionally within secondary intragranular porosity within corroded K-feldspar grains. Although point counting indicated that a decrease in the proportion of clay occurred during reaction, careful SEM examination of the inlet and outlet ends indicated that secondary clay had developed, particularly at the inlet end. This apparent discrepancy is probably due to variable preservation during thin section preparation.

The most significant difference between the inlet and outlet samples was the proportion of fine grained, silty rubble that partially infilled many pores in the outlet sample (Plate 46). This may suggest that the silty matrix present in some areas had been washed towards the outlet end of the core and concentrated there. The rubble comprised silt-sized clasts of predominantly quartz, K-feldspar and clay-rich matrix. Approximately 50% of pores were at least partially filled and up to 70% of pore-throats were constricted by this silty matrix.

Based on point counting analyses, the total porosity increased by 3% and 4% from inlet to outlet end respectively, relative to the unreacted sandstone (Table 7.10,

Table 7.16 Chemical analyses of water samples (major elements) from core flooding experiments (sandstone-SSW interactions).

BGS code	Sample code	pH	Time h	Ca		Mg		Na		K		Cl		SO4		SiO2	
				mg/l	mmol/l	mg/l	mmol/l	mg/l	mmol/l	mg/l	mmol/l	mg/l	mmol/l	mg/l	mmol/l	mg/l	mmol/l
7218	Run 409/0		0.00	335	8.36	76.4	3.14	12700	552.42	47.2	1.21	20200	569.77	80	0.83	7.2	0.12
7219	Run 409/1	6.9	26.33	186	4.64	42.4	1.74	13100	569.82	40.2	1.03	19800	558.49	<20.0	<0.21	100.0	1.66
7220	Run 409/2	6.4	114.50	287	7.16	56.3	2.32	13500	587.22	45.1	1.15	20000	564.13	<20.0	<0.21	127.0	2.11
7221	Run 409/3	6.3	217.42	361	9.01	60.3	2.48	13200	574.17	44.8	1.15	19500	550.02	<20.0	<0.21	100.0	1.66
7222	Run 409/4	6.2	290.92	431	10.75	62.2	2.56	13000	565.47	38.7	0.99	19800	558.49	<20.0	<0.21	99.3	1.65
7223	Run 409/5	6.2	386.50	441	11.00	61.4	2.53	12900	561.12	41.9	1.07	19600	552.84	<20.0	<0.21	97.9	1.63
7224	Run 409/6	6.1	466.67	436	10.88	60.5	2.49	13000	565.47	39.5	1.01	19600	552.84	<20.0	<0.21	95.3	1.59
7225	Run 409/7	6.2	545.33	446	11.13	55.9	2.30	12700	552.42	36.5	0.93	19700	555.67	<20.0	<0.21	90.4	1.50
7226	Run 409/8	6.2	619.83	468	11.68	53.8	2.21	13200	574.17	35.7	0.91	19600	552.84	<20.0	<0.21	82.0	1.36
7227	Run 409/9	6.2	717.25	491	12.25	46.3	1.90	13100	569.82	35.2	0.90	19600	552.84	<20.0	<0.21	80.4	1.34
7228	Run 409/10	6.0	811.17	499	12.45	37.9	1.56	13000	565.47	33.6	0.86	19500	550.02	<20.0	<0.21	77.1	1.28
7229	Run 409/11	6.1	887.92	526	13.12	32.4	1.33	12900	561.12	31.8	0.81	19800	558.49	<20.0	<0.21	76.7	1.28
7230	Run 409/12	5.9	981.17	542	13.52	30.2	1.24	12700	552.42	30.9	0.79	19800	558.49	<20.0	<0.21	77.2	1.28
7231	Run 409/13	6.3	1053.00	531	13.25	28.9	1.19	11900	517.62	30.1	0.77	19500	550.02	<20.0	<0.21	72.7	1.21
7232	Run 409/14	6.2	1129.58	534	13.32	28.8	1.18	11800	513.27	32.3	0.83	19000	535.92	<20.0	<0.21	72.2	1.20
7233	Run 409/15	6.2	1223.25	586	14.62	32.8	1.35	12800	556.77	30.7	0.79	19500	550.02	<20.0	<0.21	78.4	1.30
7234	Run 409/16	6.0	1295.42	584	14.57	33.2	1.37	13000	565.47	29.8	0.76	19400	547.20	<20.0	<0.21	75.6	1.26
7235	Run 409/17	6.4	1394.58	605	15.09	30.2	1.24	13200	574.17	26.4	0.68	19300	544.38	<20.0	<0.21	71.0	1.18
7236	Run 409/18	6.3	1464.42	709	17.69	29.2	1.20	12800	556.77	27.0	0.69	19700	555.67	<20.0	<0.21	70.3	1.17

pH: values were taken just after sampling at room temperature.

Table 7.16 *Continued.* Chemical analyses of water samples (minor elements) from core flooding experiments (sandstone-SSW interactions).

BGS code	Sample code	pH	Time h	Ba		Sr		Mn		Total Fe		Al		Li		B	
				mg/l	mmol/l	mg/l	mmol/l	mg/l	mmol/l	mg/l	mmol/l	mg/l	mmol/l	mg/l	mmol/l	mg/l	mmol/l
7218	Run 409/0		0.00	0.17	1.24E-03	3.56	4.06E-02	0.27	4.91E-03	<0.20	<3.58E-03	<0.40	<0.015	0.14	2.02E-02	<1.00	<0.092
7219	Run 409/1	6.9	26.33	1.92	1.40E-02	1.07	1.22E-02	4.87	8.86E-02	<0.20	<3.58E-03	<0.40	<0.015	0.15	2.16E-02	<1.00	<0.092
7220	Run 409/2	6.4	114.50	2.25	1.64E-02	1.23	1.40E-02	4.05	7.37E-02	36.00	6.45E-01	<0.40	<0.015	0.11	1.59E-02	<1.00	<0.092
7221	Run 409/3	6.3	217.42	1.62	1.18E-02	1.18	1.35E-02	4.15	7.55E-02	16.40	2.94E-01	<0.40	<0.015	0.14	2.02E-02	<1.00	<0.092
7222	Run 409/4	6.2	290.92	2.42	1.76E-02	1.10	1.26E-02	6.57	1.20E-01	9.48	1.70E-01	<0.40	<0.015	0.15	2.16E-02	<1.00	<0.092
7223	Run 409/5	6.2	386.50	1.40	1.02E-02	0.91	1.04E-02	6.87	1.25E-01	11.10	1.99E-01	<0.40	<0.015	0.15	2.16E-02	<1.00	<0.092
7224	Run 409/6	6.1	466.67	3.27	2.38E-02	0.76	8.67E-03	7.08	1.29E-01	11.00	1.97E-01	<0.40	<0.015	0.16	2.31E-02	<1.00	<0.092
7225	Run 409/7	6.2	545.33	1.96	1.43E-02	0.62	7.08E-03	7.31	1.33E-01	8.99	1.61E-01	<0.40	<0.015	0.14	2.02E-02	<1.00	<0.092
7226	Run 409/8	6.2	619.83	2.72	1.98E-02	0.49	5.59E-03	8.42	1.53E-01	5.59	1.00E-01	<0.40	<0.015	0.12	1.73E-02	<1.00	<0.092
7227	Run 409/9	6.2	717.25	2.39	1.74E-02	0.37	4.22E-03	10.20	1.86E-01	3.78	6.77E-02	<0.40	<0.015	<0.10	<1.44E-02	<1.00	<0.092
7228	Run 409/10	6.0	811.17	3.04	2.21E-02	0.29	3.31E-03	13.20	2.40E-01	3.24	5.80E-02	<0.40	<0.015	0.13	1.87E-02	<1.00	<0.092
7229	Run 409/11	6.1	887.92	3.00	2.18E-02	0.24	2.74E-03	16.70	3.04E-01	2.52	4.51E-02	<0.40	<0.015	<0.10	<1.44E-02	<1.00	<0.092
7230	Run 409/12	5.9	981.17	5.61	4.08E-02	0.24	2.74E-03	19.10	3.48E-01	2.25	4.03E-02	<0.40	<0.015	<0.10	<1.44E-02	<1.00	<0.092
7231	Run 409/13	6.3	1053.00	3.02	2.20E-02	0.19	2.17E-03	20.50	3.73E-01	<0.20	<3.58E-03	<0.40	<0.015	<0.10	<1.44E-02	<1.00	<0.092
7232	Run 409/14	6.2	1129.58	4.59	3.34E-02	0.19	2.17E-03	22.10	4.02E-01	1.38	2.47E-02	<0.40	<0.015	<0.10	<1.44E-02	<1.00	<0.092
7233	Run 409/15	6.2	1223.25	1.62	1.18E-02	0.15	1.71E-03	25.60	4.66E-01	1.24	2.22E-02	<0.40	<0.015	<0.10	<1.44E-02	<1.00	<0.092
7234	Run 409/16	6.0	1295.42	3.42	2.49E-02	0.18	2.05E-03	25.70	4.68E-01	1.04	1.86E-02	<0.40	<0.015	0.14	2.02E-02	<1.00	<0.092
7235	Run 409/17	6.4	1394.58	3.23	2.35E-02	0.16	1.83E-03	22.30	4.06E-01	0.58	1.04E-02	<0.40	<0.015	<0.10	<1.44E-02	<1.00	<0.092
7236	Run 409/18	6.3	1464.42	1.77	1.29E-02	0.14	1.60E-03	22.70	4.13E-01	1.10	1.97E-02	<0.40	<0.015	<0.10	<1.44E-02	<1.00	<0.092

pH: values were taken just after sampling at room temperature.

Figure 7.20). However, there are three problems with such an observation; (i) point counting was questionable with respect to illite behaviour (see above), (ii) there was less evidence for this based on porosimetry (Table 7.8), and (iii) this increase was not consistent with the decrease in porosity observed in the batch experiments with the same type of sample.

7.4.3.2 INTERPRETATION

Run 370, Dry supercritical CO₂

Figure 7.22 shows the variation of pH and Na and Cl concentrations for the samples taken. There was little change in pH or in Na and Cl concentrations for the first three samples. The final two samples were of wet SC CO₂ being allowed to dissolve in a known volume of de-ionised water. It can be seen that not all the NaCl fluid had been removed from the sandstone core even after it had been flushed with dry SC CO₂ for ≈700 hours, as there was appreciable Na and Cl in the output stream. The source for these elements was the original NaCl fluid that was used to presaturate the sandstone core before flushing with dry SC CO₂.

Figure 7.23 shows the variation of Ca, Mg, K and SiO₂ concentrations for the samples taken. The starting fluid contained very little Ca, but the levels increased in the first two samples to a maximum of 360 mg.l⁻¹. Even the two 'de-ionised water' samples had a ten fold increase in Ca concentration. Possible sources for the increase in Ca were dissolution of the calcite and dolomite cements. Indeed, results of SEM point counting (Table 7.10) would seem to confirm this, but no dissolution features on calcite were observed in the reacted sample. A similar pattern was seen for Mg, K and SiO₂, but their overall concentrations were not as high as Ca. Possible sources were the dissolution of the dolomite cements (Mg) and K-feldspar (K and SiO₂). Again, the results of SEM point counting (Table 7.10) would seem to confirm the dissolution of these two minerals. Evidence for this also came from the mineralogical observations. Figure 7.24 shows the variation of Mn and Fe concentrations. These two elements show a similar pattern to that seen for Ca, Mg, K and SiO₂, but their

concentrations are much lower ([Mn] maximum = 6 mg.l⁻¹ and [Fe] maximum = 1 mg.l⁻¹). As Mn and Fe were at, or close to, their detection limits in the original NaCl starting fluid, the increase must be a result of interaction with one of the minor constituents of the sandstone core, possibly with the dolomite or illitic clay.

From mineralogical observations and fluid chemical analyses, it appears that the main reactions that took place during the sandstone core flooding experiment with dry supercritical CO₂ were the dissolution of feldspars and dolomite, with consequent precipitation of illite and a silica phase (probably chalcedony). However, calcite seems to have been stable as no dissolution features developed on the authigenic calcite, though no secondary cal-

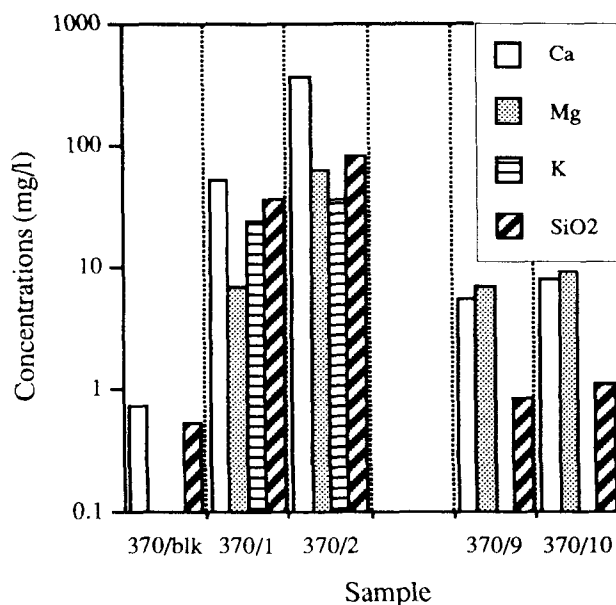


Figure 7.23 Plot of Ca, Mg, K and SiO₂ concentrations for the core flood experiment using dry SC CO₂ only.

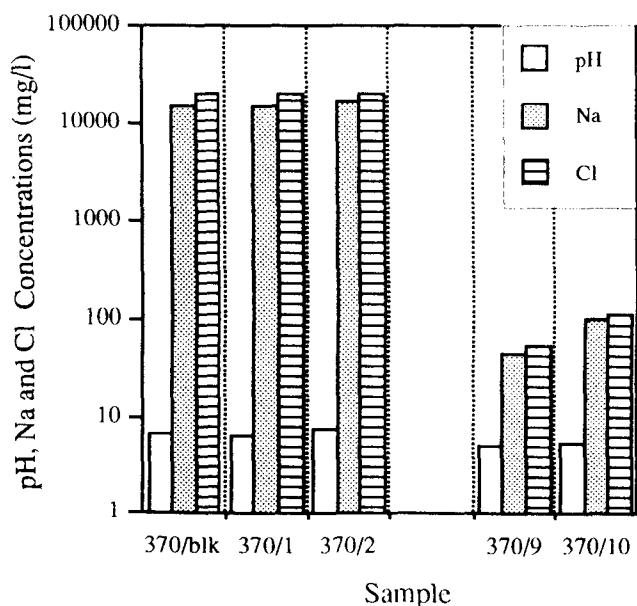


Figure 7.22 Plot of pH and Na and Cl concentrations for the core flood experiment using dry SC CO₂ only.

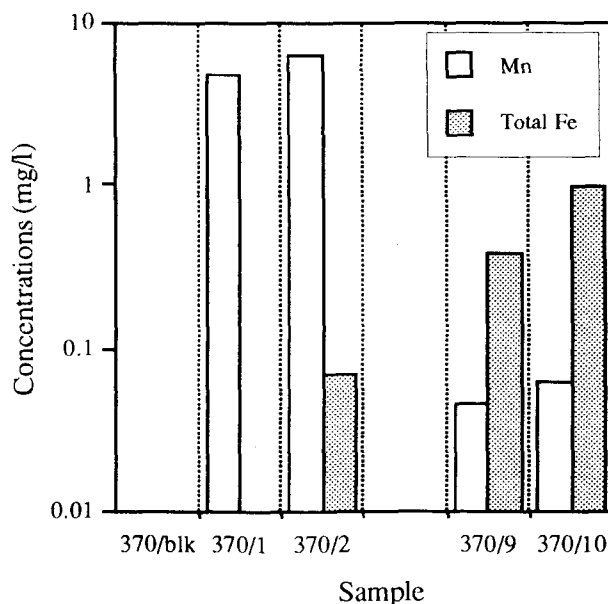


Figure 7.24 Plot of Mn and Fe concentrations for the core flood experiment using dry SC CO₂ only.

cite was observed. The overall decrease in porosity as determined by point counting and porosimetry, was probably due to the precipitation of secondary clays which were detected during point counting.

Run 409, 0.55 M NaCl solution equilibrated with supercritical CO₂

Figure 7.25 shows plots of concentrations over the experiment. A significant decrease in concentration with time occurs for K, Mg, Si, Fe and Sr. Conversely, Ca and Mn concentrations increase. Stable concentrations of Mg, Sr and Fe concentrations seem to occur over the duration of the experiment, but the concentrations of the other elements continue to change. Consequently, after nearly 1500 hours (about 61 days), steady state dissolution of minerals at 80°C had still not been achieved.

Cl concentrations were constant and close to the blank value (0.55 M). However, the slight increase at the beginning of the experiment may be explained by the experiment stabilising, or by the leaching of a small quantity of salts (essentially CaCl₂, MgCl₂ and KCl with minor proportions of SO₄, Sr and Li salts), possibly formed by evaporation of the original sandstone pore-water during the drying of the sample. Despite some variations in analytical uncertainty, Na concentrations are relatively constant. A general trend towards a slight increase with respect to the blank value (0.55 M) is noted. This excess with respect to the blank might be due to the dissolution of albite or clay minerals (smectite, montmorillonite, etc.).

The unusual behaviour of Ca, Mg, K and Sr from the blank initial sample to the first sample also suggest similar mechanisms to those described above.

The interpretation of variation in concentration over time is not straightforward as the system is not closed. Concentrations result from both mineral reaction kinetics, and flow and transport in the aqueous phase. However, the following deductions can be made.

The increase in calcium and magnesium concentrations in the first 300 hours is linked to dolomite dissolution and possibly to some calcite dissolution, as Ca concentrations are much higher than Mg concentrations (Figure 7.26b). However only dolomite corrosion was described during the mineralogical investigations possibly because the quantity

of calcite cement was too low to be detected. The further continuous decrease in Mg concentrations after 300 hours, with Ca release appearing to slow considerably (Figures 7.25 and 7.26b), suggests the formation of clays (possibly illite), as similar falls in SiO₂ and K concentrations were noted. Otherwise K concentrations would have been expected to rise as dissolution of K-feldspars was confirmed by the mineralogical analyses. Evidence for secondary clay precipitation was found during mineralogical analysis. The lower rate of Ca release after 300 hours reaction suggests that a Ca-bearing mineral such as Ca-smectite (smectite was observed) was forming or that some ion exchange reactions occurred. At the end of the experiment, the Ca/K geothermometer (Michard, 1990) gave a temperature of 83°C and the Na/K/Ca geothermometer (Fournier and Truesdell, 1973) gave temperatures of 60–108°C for the last sample. These values are close to 80°C, suggesting that water was close to equilibrium with respect to the controlling Ca-bearing aluminosilicate mineral. In the last samples, the values of the molar Ca/Mg product and Ca/Mg ratio become very similar (Table 7.17) suggesting that the fluid was tending towards steady state, and possible equilibrium with dolomite, calcite and illite.

The increase in SiO₂ concentrations in the first 114 hours was probably mainly due to the dissolution of K-feldspar grains. Although quartz was a major constituent of the sandstone there was little evidence from the mineralogical analysis for its dissolution. The following slight decrease in silica concentrations was probably associated with the formation of secondary clays and control by chalcedony precipitation.

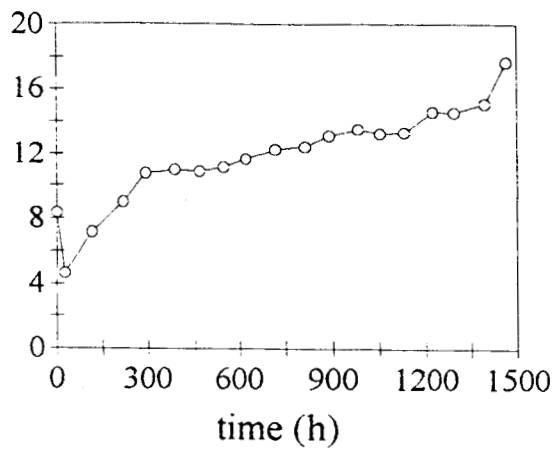
Molar Na/K ratios (Table 7.17) are higher than that expected for albite/K-feldspar equilibrium (Table 7.13). Moreover, the temperature estimated for the last sample (19°C using the Na/K geothermometer of Fournier (1979)) is much lower than 80°C, and even lower than the temperatures estimated for the previous samples. It would appear that both minerals were dissolving, but that the kinetics of dissolution compared to the velocity of the fluid was not high enough to achieve saturation in water.

The complex evolution of fluid chemistry at the core outlet is illustrated in Figures 7.26a,b,c and seems to

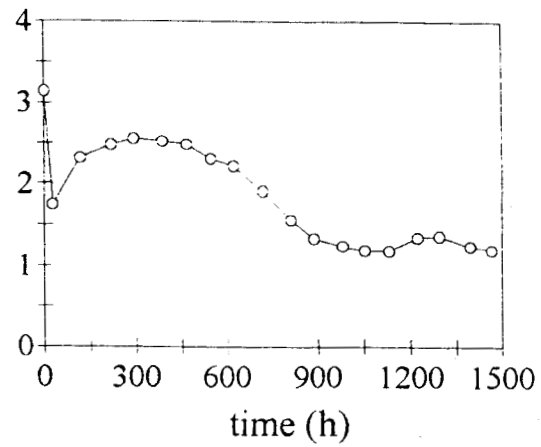
Table 7.17 Molar Na/K, Mg/K, Ca/Mg ratios and Ca.Mg product of the water samples from the core-flooding experiment using 0.55 M NaCl solution equilibrated with SC CO₂.

BGS code	Sample code	Time hours	log (Na/K)	Mg/K	log (Ca.Mg)	log (Ca/Mg)
7218	Run 409/0	0.00	2.66	2.60	1.42	0.42
7219	Run 409/1	26.33	2.74	1.70	0.91	0.42
7220	Run 409/2	114.50	2.71	2.01	1.22	0.49
7221	Run 409/3	217.42	2.70	2.17	1.35	0.56
7222	Run 409/4	290.92	2.76	2.59	1.44	0.62
7223	Run 409/5	386.50	2.72	2.36	1.44	0.64
7224	Run 409/6	466.67	2.75	2.46	1.43	0.64
7225	Run 409/7	545.33	2.77	2.46	1.41	0.68
7226	Run 409/8	619.83	2.80	2.42	1.41	0.72
7227	Run 409/9	717.25	2.80	2.12	1.37	0.81
7228	Run 409/10	811.17	2.82	1.81	1.29	0.90
7229	Run 409/11	887.92	2.84	1.64	1.24	0.99
7230	Run 409/12	981.17	2.84	1.57	1.23	1.04
7231	Run 409/13	1053.00	2.83	1.54	1.20	1.05
7232	Run 409/14	1129.58	2.79	1.43	1.20	1.05
7233	Run 409/15	1223.25	2.85	1.72	1.30	1.03
7234	Run 409/16	1295.42	2.87	1.79	1.30	1.03
7235	Run 409/17	1394.58	2.93	1.84	1.27	1.08
7236	Run 409/18	1464.42	2.91	1.74	1.33	1.17

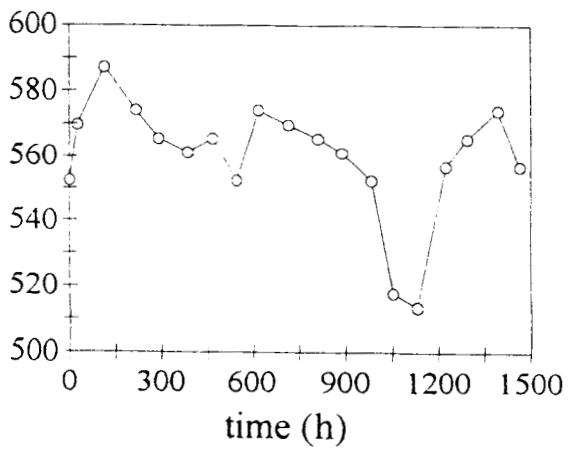
Ca (mmol/l)



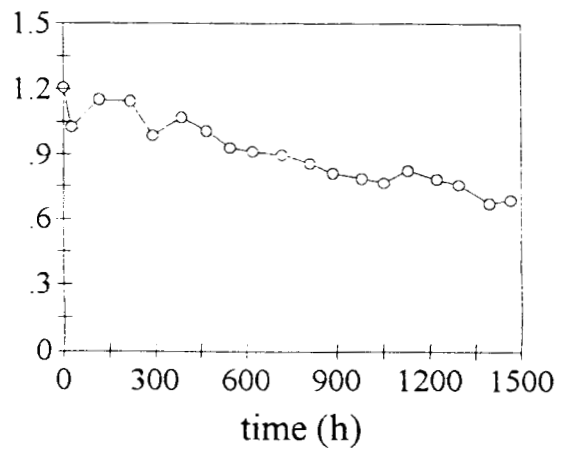
Mg (mmol/l)



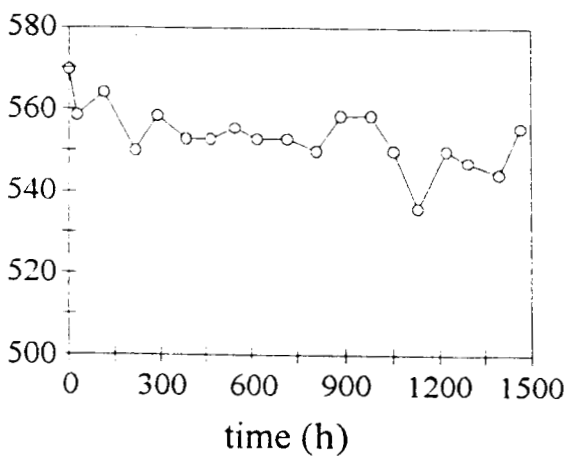
Na (mmol/l)



K (mmol/l)



Cl (mmol/l)



SiO2 (mmol/l)

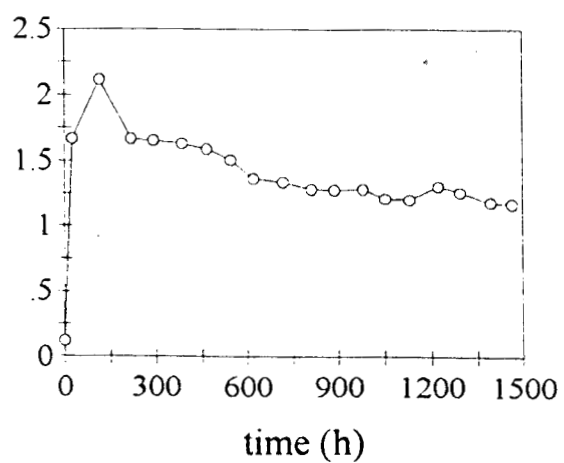
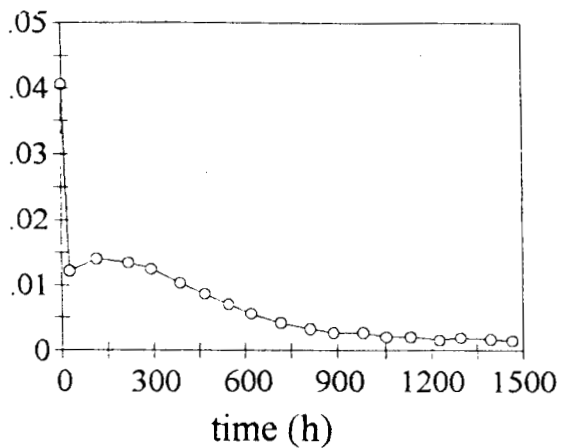
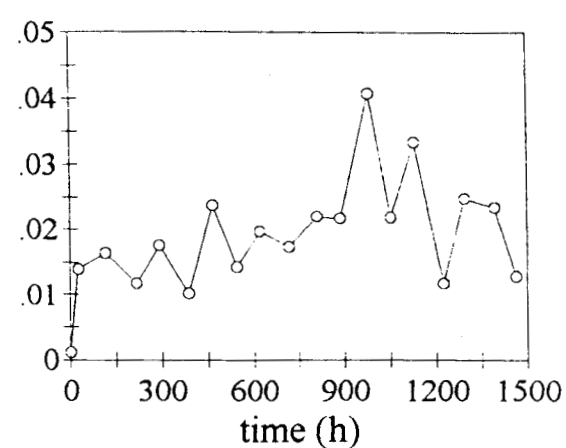


Figure 7.25 Plots of concentrations versus time (major elements) for the core flood experiment using 0.55 M NaCl solution equilibrated with SC CO₂.

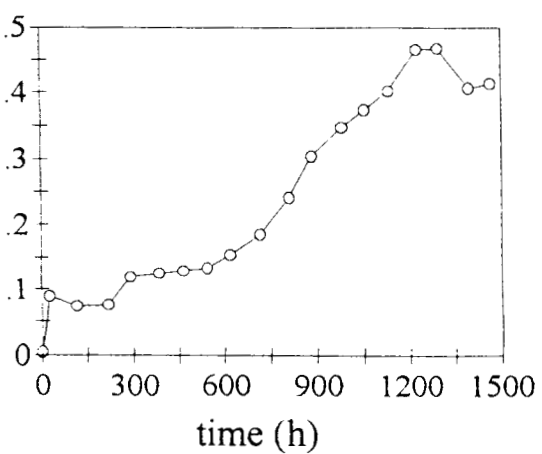
Sr (mmol/l)



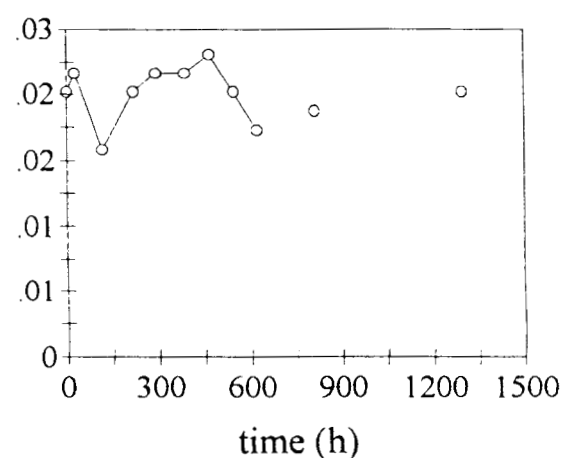
Ba (mmol/l)



Mn (mmol/l)



Li (mmol/l)



Fe (mmol/l)

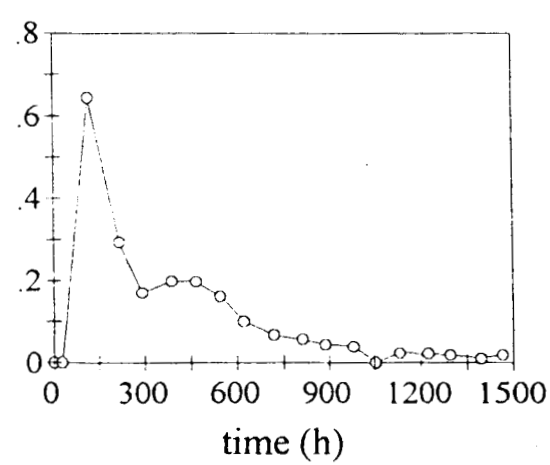
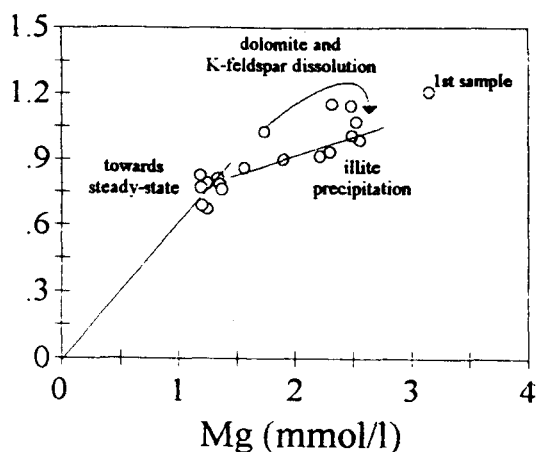
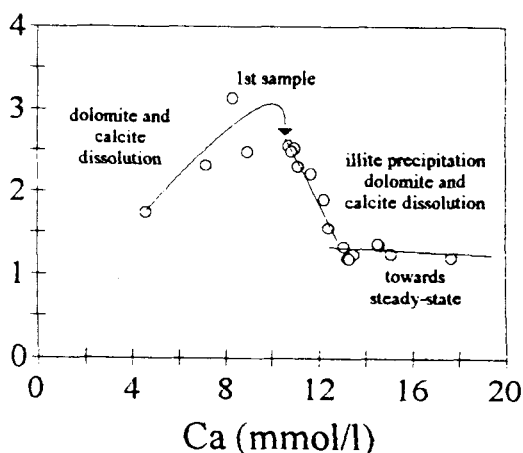


Figure 7.25 Continued. Plots of concentrations versus time (minor elements) for the core flood experiment using 0.55 M NaCl solution equilibrated with SC CO₂.

K (mmol/l)



Mg (mmol/l)



K (mmol/l)

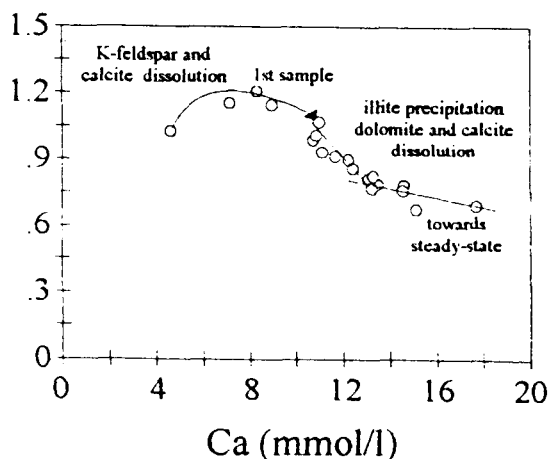


Figure 7.26 Plots of concentrations for the core flood experiment using 0.55 M NaCl solution equilibrated with SC CO₂.

- a- K versus Mg
- b- Mg versus Ca
- c- K versus Ca

involve the dissolution of K-feldspar, dolomite and calcite with the latter precipitation of illite and possibly some Ca-smectite.

The behaviour of aqueous Sr (Figures 7.25 and 7.27) was similar to that of aqueous Mg (Figures 7.25 and 7.27). Therefore, the source of the Sr was probably the dolomite, although K-feldspar may have also supplied some Sr to solution. The drop in Sr concentration later in the experiment could have been the result of its incorporation into secondary clays. As illite is not known to incorporate Sr, this element was probably trapped by another aluminosilicate such as Ca-smectite, either by precipitation or by cation exchange.

Mn (Figure 7.25) exhibits similar behaviour to Ca in that the concentrations rose throughout the experiment. It was probably released during the dissolution of carbonates, but appears to have not been precipitated as a secondary phase.

Fe (Figure 7.25) shows an unusual pattern of release with an initially high release falling to a minima at ≈300 hours followed by a slight rise in concentration over the next 200 hours till ≈500 hours when the concentrations start to decrease again. There are a number of possible sources for Fe in the output fluids. The initially high concentrations are possibly the result of the physical process of flushing the core, leading to the mobilisation of particulate iron, possibly as colloids. The later increase in Fe concentration seems to follow that of Mg which would suggest that some of the Fe was being released from dolomite. The subsequent tailing off of iron concentrations in the output fluids was probably a combination of the removal of particulate iron, and incorporation into secondary clays. For the last sample, the temperature was estimated to be 79°C using the Fe/K geothermometer described by Michard (1990). The mathematical expression for this is:

$$t (^{\circ}\text{C}) = 1220 / (\log (\sqrt{\text{Fe}/\text{K}}) + 2.66) - 273.15$$

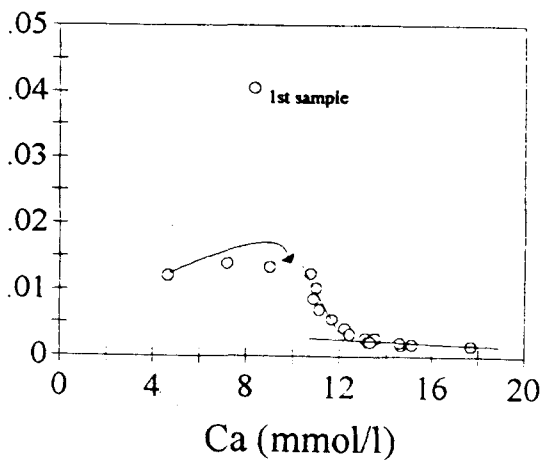
(aqueous Fe and K concentrations are in mol.l⁻¹).

Such an expression suggests control of Fe by equilibrium between water and a mineral. This mineral could be an Fe-rich illitic clay, which was identified during mineralogical analysis. This tends to be confirmed by the K/Mg geothermometer which yields a temperature of 77°C and by molar Mg/K ratios after 717 hours which range from 1.43 to 1.84 (Table 7.17). These values suggest that the water was saturated with respect to dolomite and the Fe-rich illitic clay.

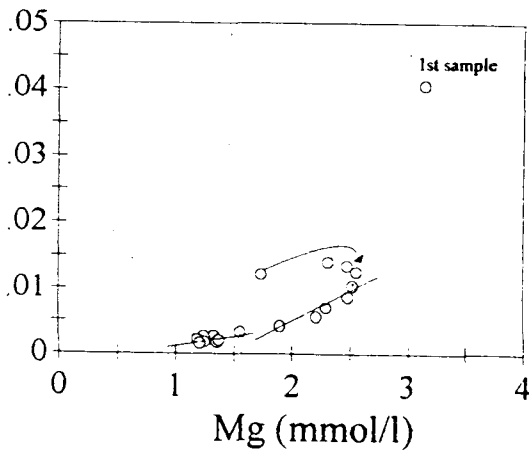
Al and Li concentrations remained low throughout the experiments. Given that Al is a major constituent of the K-feldspar thought to be undergoing dissolution, it is most likely that the formation of secondary clays are acting as a sink for the released Al. Except for the first samples (possible contamination by the sandstone pore water), aqueous Li concentrations are possibly linked to those of dissolved K (Figure 7.27c). The behaviour of aqueous Ba was very irregular, although an increase in concentration of this element was noted.

In summary, the main reactions that took place during the sandstone core flooding experiment using a 0.55 M NaCl solution saturated with supercritical CO₂ were the dissolution of feldspars and dolomite, and the precipitation of an Fe-rich illite, a Ca-smectite and a silica phase (probably chalcedony). At the end of the experiment, several elements appeared to be close to steady-state, with possible approach to equilibrium with respect to illite, Ca-smectite, chalcedony and dolomite. However, non-equilibrium

Sr (mmol/l)



Sr (mmol/l)



Li (mmol/l)

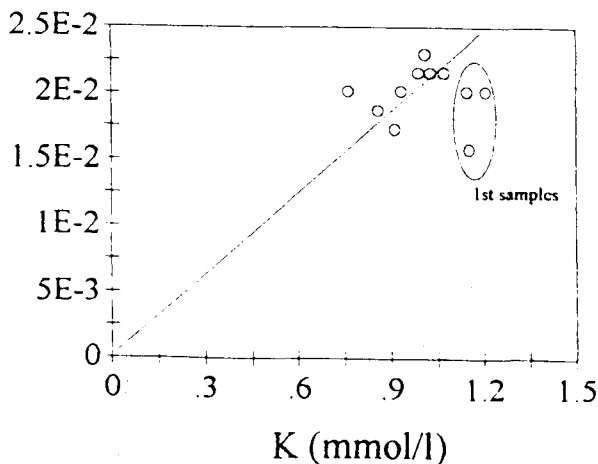


Figure 7.27 Plots of concentrations for the core flood experiment using 0.55 M NaCl solution equilibrated with SC CO₂.

- a- Sr versus Ca
- b- Sr versus Mg
- c- Li versus K

conditions existed with respect to K-feldspar and albite. The low quantity of calcite cement prevented detailed observations of it. The observation of a calcite precipitate

at the outlet end of the core possibly developed after reaction, as an artefact due to degassing. The net effect of the above mineral reactions on porosity was not clear (see section 7.4.3.1.).

A computer representation of these first conclusions was attempted through coupled modelling using the CATCO2 reaction-transport code (see section 7.3.2.2.). The simulated core sample (45 mm diameter by 150 mm length) was divided into 20 cells of 75 mm long and 45 mm diameter. Simulated injection of a 0.55 M NaCl solution, saturated with supercritical CO₂ at 80°C and 200 bars, at the inlet end of the core was modelled, at the experimental flow rate of 4.8 ml.d⁻¹. The dissolved CO₂ concentration within the injected fluid was 1.26 mol.kg⁻¹ H₂O, which was the calculated solubility of CO₂ under such temperature and pressure conditions (see section 7.4.1.2.). The darcy velocity of the fluid was calculated to be $0.349 \times 10^{-7} \text{ m.s}^{-1}$, based on the flow rate and the cross sectional area of the core. The dispersion was set to 0.02 m, based on results from tracer test experiments (see section 7.3.1.3.). The porosity and mineralogical composition were based on results from the point counting study (see Table 7.10). The time step (0.485 day) was calculated so that the Courant number was equal to 1. Minerals included in this simulation were the six minerals that constituted the CO2ROCK geochemical simulator, i.e. calcite, disordered dolomite, K-feldspar, albite, illite and quartz. Kaolinite was inactivated as this mineral was not described during the experiment. Prior to simulated injection, it was assumed that thermodynamic equilibrium was reached within the core between the six minerals and a 0.55 M NaCl solution. Table 7.18 summarizes the number of moles of each mineral used in the simulation, together with surface area data and kinetic data.

The kinetic behaviour of minerals is highly complex as the rates depend both on the mechanisms of dissolution and precipitation reactions, and on the reactive surface area between the fluid and each mineral. In general, both of these are still poorly known and dealing with kinetics is presently a major concern within the geochemical community. As kinetic effects are important within the time frame of laboratory experiments, the following simplifying assumptions were made. The intrinsic dissolution rates were taken from the experimental study described in section 7.4.4. and from previous studies under appropriate conditions (acidic pH range and temperature corrections). The nitrogen BET surface area of the rock was not experimentally determined for the Wilmslow sandstones but was assumed to be equal to the mean surface area of the Sherwood sandstones, i.e. 2 m².g⁻¹ (see Figure 7.12). The nitrogen BET surface area for each mineral was initially assumed to be proportional to its mass. However, BET techniques give physical surface areas and are known to overestimate the actual surface areas that interact with solutions by one to three orders-of-magnitude (Delany, 1985; White and Peterson, 1990; Azaroual, 1994). In our simulation the reactive surface areas were assumed to be 1% of the measured physical surface area, except for phyllosilicates (illite). Precipitation rates were assumed to be equal to dissolution rates.

The results of the calculations are plotted on Figures 7.28 to 7.32. The calculated Na and Cl concentrations at the outlet end of the core remained fairly constant. However, the concentrations of Ca, Mg, K and Si (Figure 7.28) were strongly dependent on mineral reactions and calculated values can be compared to measured values at the outlet end of the core (see Figure 7.25). Initial concen-

Table 7.18 Summary of the data used for the simulation of the core flood experiment with a synthetic seawater solution equilibrated with SC CO₂.

Minerals	Vol. %	Mole mol.kg ⁻¹ H ₂ O	Mass g.kg ⁻¹ H ₂ O	BET surface area (2) cm ² .kg ⁻¹ H ₂ O	k _{dissol} (3) mol.cm ⁻² .s ⁻¹	Active surface area (10) cm ² .kg ⁻¹ H ₂ O	Dissol. rate mol.s ⁻¹ .kg ⁻¹ H ₂ O	Precip. rate (11) mol.s ⁻¹ .kg ⁻¹ H ₂ O
Quartz	56.3	127.3	7649	1.5 10 ⁺⁸	10 ^{-15.3} (4)	1.5 10 ⁺⁶	8. 10 ⁻¹⁰	8. 10 ⁻¹⁰
K-feldspar	9.5	4.5	1252	2.5 10 ⁺⁷	10 ^{-14.5} (5)	2.5 10 ⁺⁵	8. 10 ⁻¹⁰	8. 10 ⁻¹⁰
Albite	0.5	0.3	79	1.6 10 ⁺⁶	10 ^{-14.9} (6)	1.6 10 ⁺⁴	2. 10 ⁻¹¹	2. 10 ⁻¹¹
Illite (+clay)	7.3	2.7	1037	2.1 10 ⁺⁷	10 ^{-16.3} (7)	2.1 10 ⁺⁷	1. 10 ⁻⁹	1. 10 ⁻⁹
Calcite	0.5 ⁽¹⁾	0.7	69	1.4 10 ⁺⁶	10 ⁻⁹ (8)	1.4 10 ⁺⁴	1. 10 ⁻⁵	1. 10 ⁻⁵
Dolomite	4.0	3.2	590	1.2 10 ⁺⁷	10 ⁻⁹ (9)	1.2 10 ⁺⁵	1. 10 ⁻⁴	1. 10 ⁻⁴
Lithics-Mica	3.0							
Porosity	19.5							

- (1) a trace amount of calcite was considered in the simulation
- (2) total surface area in contact with the fluid, estimated from the bulk surface area of the rock ($\approx 2 \text{ m}^2/\text{g}$)
- (3) intrinsic dissolution rate constants
- (4) from Rimstidt and Barnes (1980) — see section 7.4.4.2.
- (5) from Helgeson et al. (1984) combined with Murphy and Helgeson (1987) — see section 7.4.4.3.
- (6) from Knauss and Wolery (1986) — see section 7.4.4.4.
- (7) from Knauss and Wolery (1989) combined with Lasaga (1981)
- (8) estimated from Talman et al. (1990)
- (9) estimated from Talman and Gunter (1992)
- (10) active surface area was assumed to be 1% of total surface area, except for illite
- (11) precipitation rates were assumed to be equal to dissolution rates

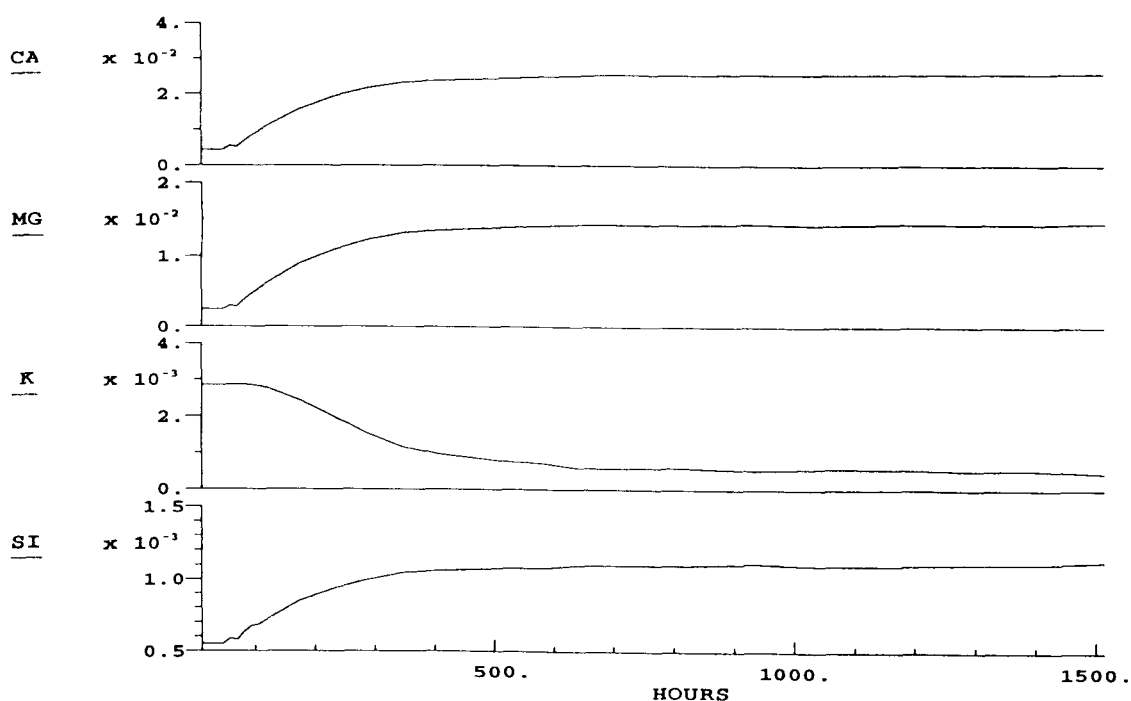


Figure 7.28 Calculated total concentrations (mol.kg⁻¹ H₂O) at core outlet during the simulation of the core flood experiment using 0.55 M NaCl solution equilibrated with SC CO₂.

trations of these four elements were close to the measured ones (especially if we remember that the first fluid sample would need to be corrected for any contaminating salts (see above)). Therefore, the fluid could be initially considered to be close to equilibrium with the six selected minerals. However, the K concentration was somewhat higher than that measured, which may have been a function of the set of minerals chosen, the thermodynamic data used, or slight deviation of the system from equilibrium.

The simulated Ca and K concentrations showed similar trends to the measured ones, and were within the same

range of values. However, the Mg and Si concentrations did increase with time, but the model failed to predict their further decrease as observed in the experiment. The addition of another Mg-silicate mineral to the CO₂ROCK simulator could be one way to improve the modelling. Note that the precipitation of a smectitic clay had been invoked above.

In the calculations the water chemistry reached a steady state after 50 iterations (i.e. 582 hours), whereas this was not the case in the experimental run even after 1500 hours. This discrepancy is probably linked to the difficulty in

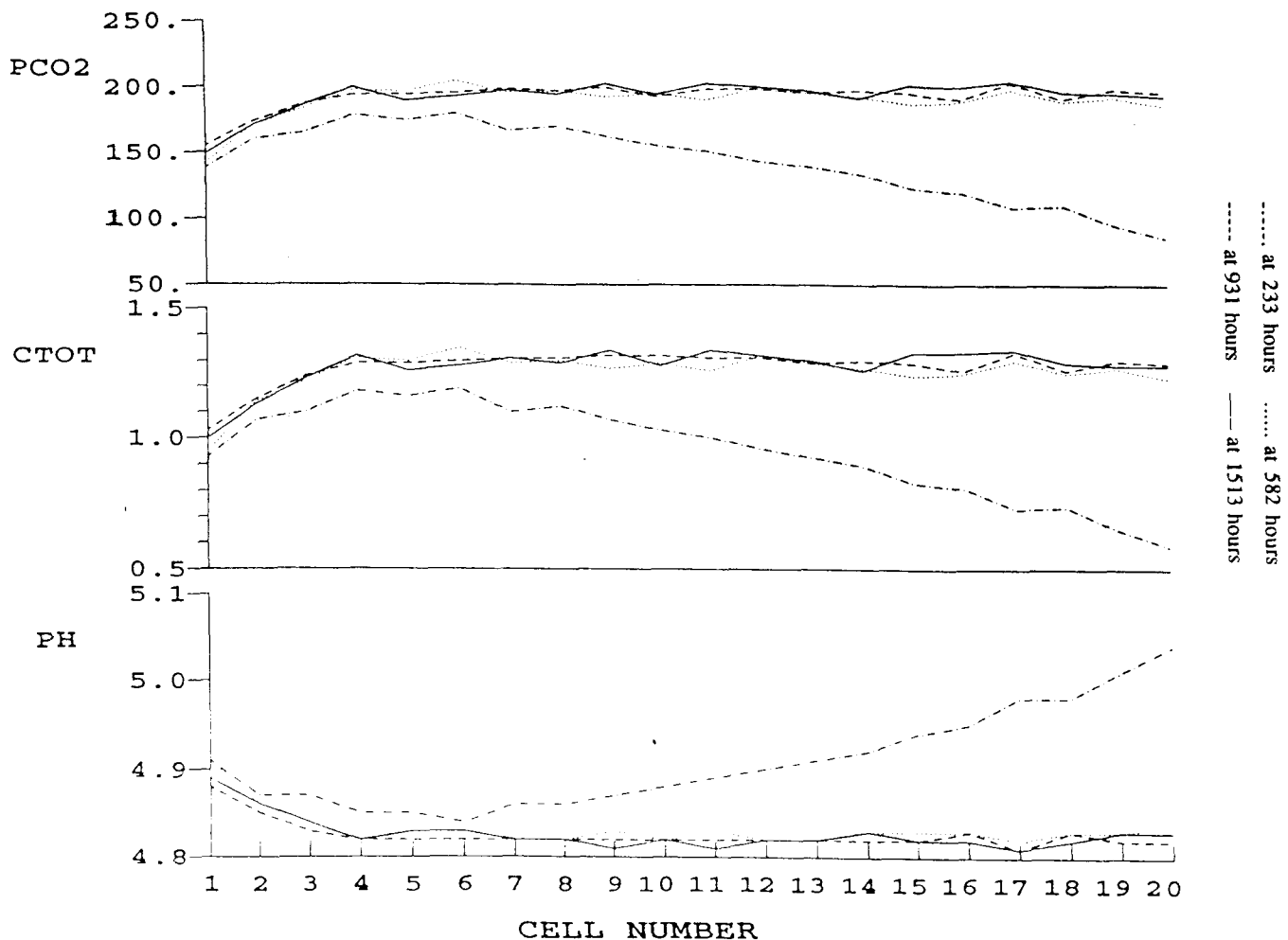


Figure 7.29 Progression of the fronts of CO₂ partial pressure (PCO₂, bar), total dissolved carbon (CTOT, mol.kg⁻¹ H₂O) and pH within the core, during the simulation of the core flood experiment using 0.55 M NaCl solution equilibrated with SC CO₂.

applying kinetic rates determined in laboratory to complex real systems. Discrepancies of up to four orders-of-magnitude between field estimates and laboratory measurements of reaction rates have been observed in various studies (i.e. Brantley, 1992). Such discrepancies could result from factors such as; inaccuracies in reactive surface area estimation, temperature variation, or differences in solution chemistry.

The fronts of simulated CO₂ partial pressure and total dissolved carbon progress through the core with time and reach final values equivalent to those of the injected fluid (Figure 7.29). The pH decreased progressively throughout the core as a result of increasing dissolved CO₂ and mineral reactions.

Although the water chemistry reached a steady state in the simulation, this was not the case for the minerals which went on dissolving or precipitating, even after 582 hours simulated reaction. This indicated that the steady state observed from fluid chemical analyses at the outlet end of the core did not correspond to an equilibrium state. Such a situation cannot be understood without considering coupled chemistry and transport phenomena. The results of the simulations showed that calcite, dolomite and quartz dissolved in the inlet region (Figure 7.30), whereas feldspars dissolved and illite precipitated throughout the length of the core (Figure 7.31). This concurs well with the SEM mineralogical observations (see section 7.4.3.1.). The dolo-

mite cement was corroded particularly close to the inlet end of the core, K-feldspar grains were corroded in the inlet and outlet regions, and authigenic illitic clay had developed in both regions. There was less evidence regarding the behaviour of quartz, albite and calcite. This could have been due to point counting determinations not being precise enough to detect small variations in abundance, and being biased by natural variations in sample mineralogy. For this particular experiment, the limitations in the use of point counting data have already been discussed (see section 7.4.3.1). The simulation predicted an increase in porosity at the inlet end of the core as a result of carbonate dissolution (Figure 7.32), whilst point counting data suggested that porosity enhancement occurred all along the core.

The agreement between experimental and modelled results could be improved by refining the model with the introduction of new mineral phases, and by careful consideration of the available kinetic and thermodynamic data. Such an approach would help in the interpretation of the experimental results as well as validating the coupled model and providing greater confidence in its predictive capacities.

7.4.3.3 CONCLUSIONS

It is interesting to compare the results of the core flood experiments with the results of the sandstone batch experi-

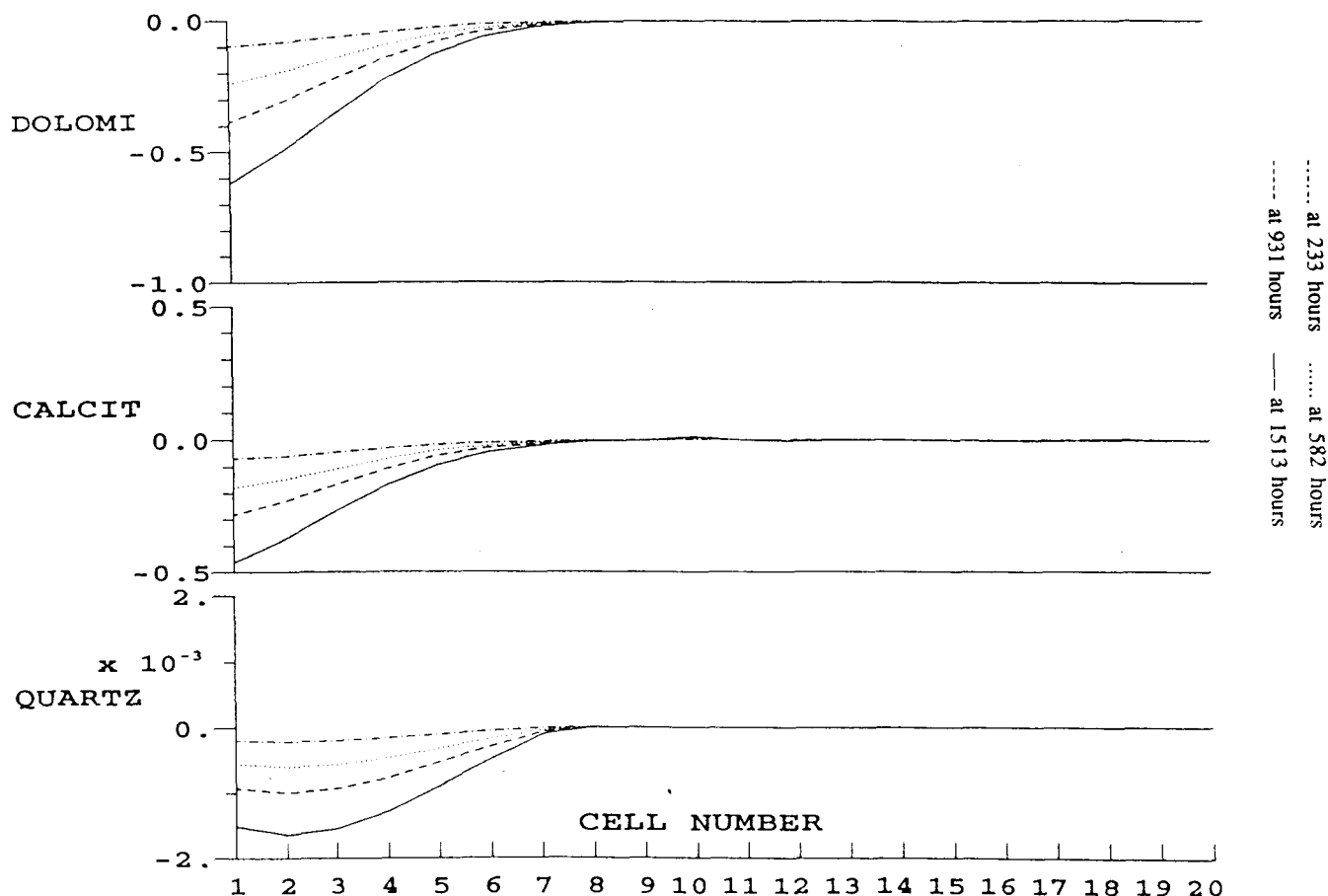


Figure 7.30 Changes in the numbers of moles of disordered dolomite, calcite and quartz during the simulation of the core flood experiment using 0.55 M NaCl solution equilibrated with SC CO₂.

ments, especially with those using the JMP8 subarkose which was the material used in the core flood experiments.

Observations revealed that there was no significant difference between the scale or extent of mineral dissolution and precipitation. However, the open systems did appear to cause more reaction compared to closed systems. This tended to be masked by the duration of the experiments, which was longer for the batch experiments (8 months) compared to the core flood experiments (2 months with CO₂-saturated seawater, 1 month with dry SC CO₂).

Secondly, the core flood experiments confirmed the results obtained from the sandstone batch experiments. The same trends in mineralogical transformations were observed, either in contact with CO₂-saturated water or in contact with SC CO₂. The experiments showed the dissolution of feldspars and dolomite cement, with the latter precipitation of secondary clays such as illite and another Na-K-Ca aluminosilicate (probably smectite).

However, some differences between the core flood and the batch experiments were noted. Feldspars continued to dissolve in the core flood experiment, whereas equilibrium appeared to have been reached in the batch experiments. There was more evidence for illite precipitation in the core flood experiments compared to the batch experiments. There was no calcite precipitation in the core flood experiments (indeed, calcite might have dissolved), whereas secondary calcite was described at the SC CO₂-water interface and occasionally over the rest of the external surfaces in the batch experiments. Secondary calcite was only observed developing within the JMP10 sandstone sample which contained anhydrite cement, but this sample was not

used for the core flood experiments. Precipitation of halite was not detected in the core flood experiment with dry SC CO₂, whereas it was extensive in the batch experiments. This was probably due to most of the initial synthetic seawater having been removed from the core by SC CO₂, thus preventing halite precipitation. No evidence for ion exchange reactions was detected in the core flood experiments, though this process may have been obscured by the complexity of the coupled chemical, flow and transport phenomena.

The overall effect of these mineral reactions on porosity is still a little unclear. For experiments using the same rock type (JMP8 subarkose), the batch experiments indicated a decrease of porosity whilst the core flood experiments gave more ambiguous results.

It should be noted that these experiments were conducted over relatively short timescales (compared to a real disposal situation) and that other dissolution/precipitation reactions may become more important over longer, more realistic timescales.

7.4.4 The kinetics of mineral dissolution

7.4.4.1 ANHYDRITE

The full analytical data can be found in Table 7.19. Figure 7.33 shows the variation of pH and flowrate with time for anhydrite dissolution experiment (run 423). It can be seen that pH remains fairly constant with time. Figure 7.34 shows the variation of Na and Cl concentrations with time, with the concentrations of both elements remaining rea-

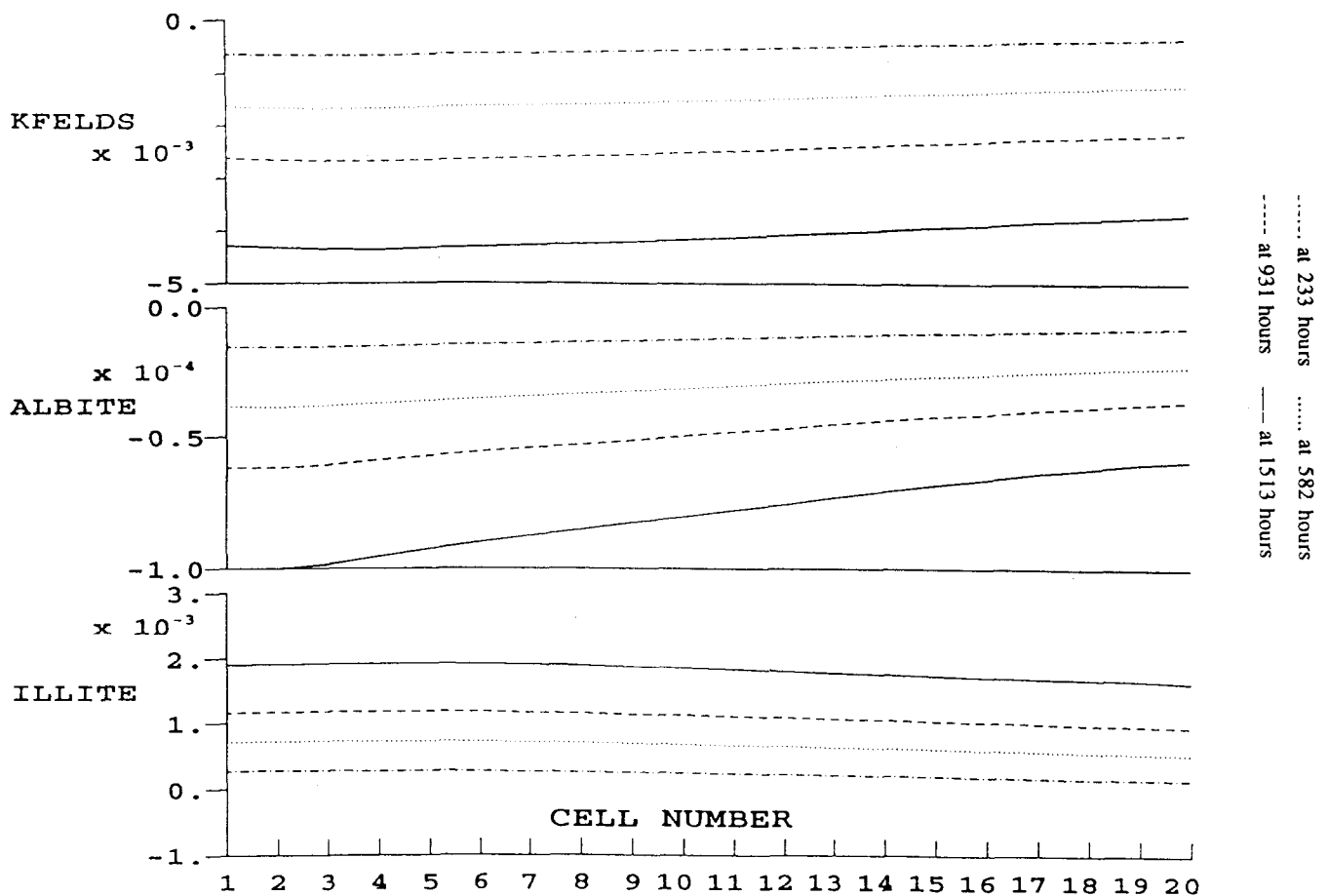


Figure 7.31 Changes in the numbers of moles of K-feldspar, albite and illite during the simulation of the core flood experiment using 0.55 M NaCl solution equilibrated with SC CO₂.

sonably constant. Figure 7.35 shows the variation of Ca and SO₄ concentrations with time, which like Na and Cl, were reasonably constant throughout the experiment at $\approx 1200 \text{ mg.l}^{-1}$ and $\approx 2700 \text{ mg.l}^{-1}$ respectively. The Ca and SO₄ data were used to calculate the rate constant for dissolution of anhydrite under the experimental conditions (200 bar, 80°C), which gave an average $\log k$ of $-12.5 \text{ mol.cm}^{-2}.\text{s}^{-1}$. This is much lower than the rate determined by Barton and Wilde (1971) for anhydrite dissolution of $\log k_{\text{Ca}} = -7.7 \text{ mol.cm}^{-2}.\text{s}^{-1}$. Since the Ca and SO₄ concentrations in the output fluids were somewhat higher than expected, the saturation state of the output fluids was examined. Anhydrite was found to be near saturation, and as a result did not fulfill 'far from equilibrium conditions'. However, the rate data could be useful when studying 'near-equilibrium dissolution'.

Mineralogical examination showed no evidence for corrosion in the anhydrite column either at the start, or end, of the column. The anhydrite grains remained fresh. This lack of corrosion was probably due to fluid being near saturation with respect to anhydrite.

7.4.4.2 QUARTZ

The full analytical data are presented in Table 7.20. Figure 7.36 shows the variation of pH and flowrate with time for quartz dissolution experiment (run 446). It can be seen that pH remained fairly constant with time, though was higher than the blank value ($t=0$). Figure 7.37 shows the variation of Na and Cl concentrations with time, here the

levels of both elements remained reasonably constant. Figure 7.38 shows the variation of SiO₂ concentration with time, as with pH the concentration remained fairly constant with time, though was higher than the blank value ($t=0$). The SiO₂ concentration data were used to calculate the rate constant for dissolution of quartz under the experimental conditions (200 bar, 80°C) of $\log k_{\text{SiO}_2} = -14.9 \text{ mol.cm}^{-2}.\text{s}^{-1}$. This compares with a rate of $\log k_{\text{SiO}_2} \approx -15.3 \text{ mol.cm}^{-2}.\text{s}^{-1}$ using the data of Rimstidt and Barnes (1980) at 80°C in the pH independent region ($4 \leq \text{pH} \leq 6$), and is in agreement with that calculated using the data of Knauss and Wolery (1988) for quartz dissolution when extrapolated to 80°C, of $\log k_{\text{SiO}_2} \approx -14.9 \text{ mol.cm}^{-2}.\text{s}^{-1}$, in the pH independent region ($\text{pH}_{25^\circ\text{C}} < 6$). Thus there is very good agreement with previous studies, which suggests that the presence of dissolved CO₂ has little effect on the rate, and hence mechanism, of quartz dissolution.

In general, no difference was observed between the inlet and outlet ends of the column with only very limited evidence for corrosion observed. Less than 5% of the grains had corrosion features on them. This corrosion was restricted to small-scale pitting along grain edges and at corners. The pits were up to 10 μm across and probably less than 5 μm deep. However, at the outlet end, although the proportion of grains suffering corrosion appeared similar, the corrosion features appeared better developed and slightly more extensive, covering larger areas up to 20 to 30 μm across.

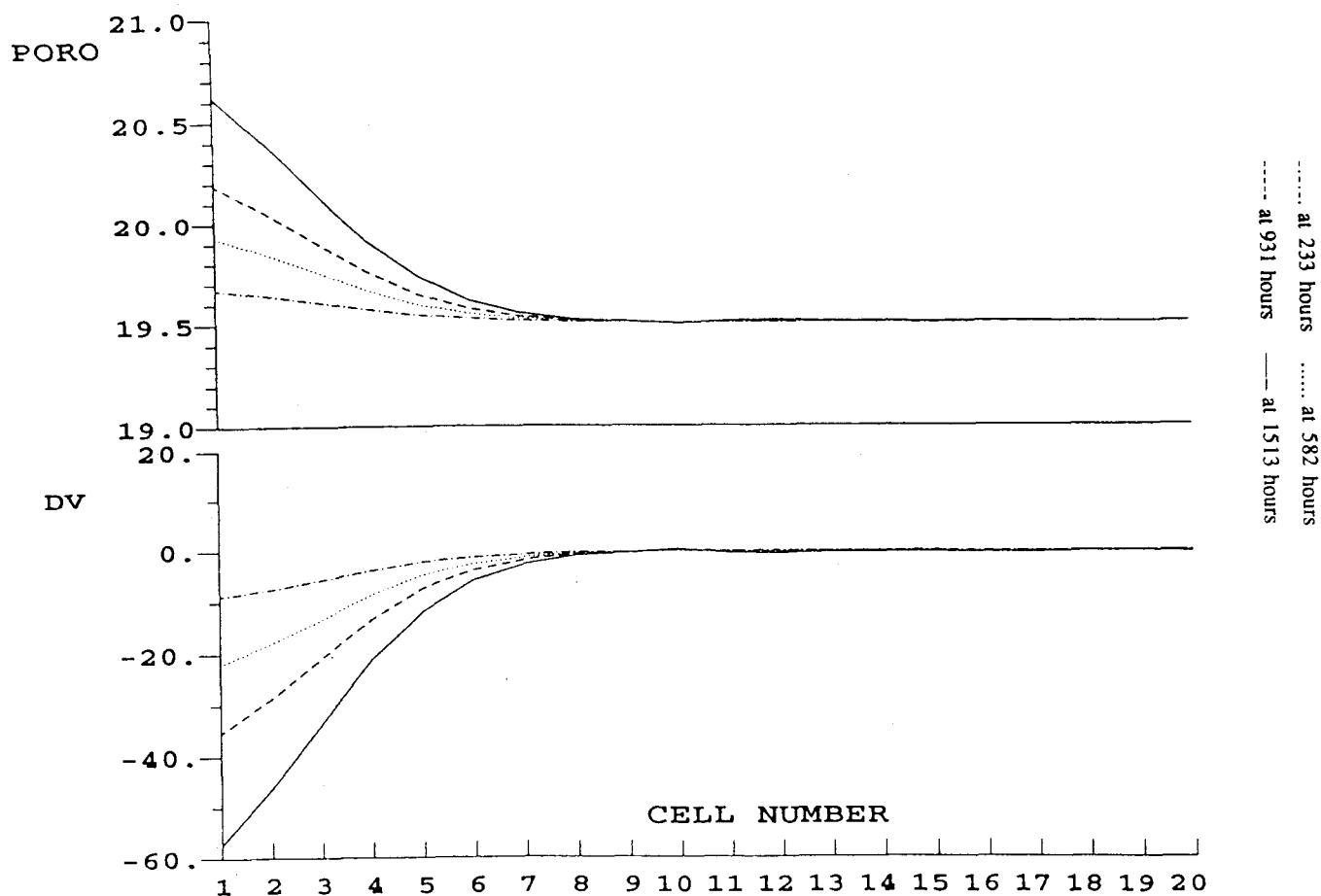


Figure 7.32 Variation of porosity (PORO, %) and mineral volume (DV, cm³) during the simulation of the core flood experiment using 0.55 M NaCl solution equilibrated with SC CO₂.

Table 7.19 Chemical analytical data for the kinetic experiment with anhydrite.

RUN 423: 80°C, 20 MPa							
Anhydrite — CO ₂ /Synthetic seawater							
Initial solid + PEEK column wt = 29.749 g							
Initial PEEK column wt = 27.5987 g							
Initial solid wt = 2.1503 g							
Surface Area = 0.9792 m ² .g ⁻¹							
Surface Area — Total = 2.106 m ²							
Sample Code	423/Blk	423/1	423/2	423/3	423/4	423/5	
Time (hours)	0.0	26.3	42.1	66.8	74.7	90.7	
Sample volume (ml)	16.0	16.0	17.0	20.0	7.0	12.0	
Flow rate (ml.hr ⁻¹)		0.61	1.07	0.81	0.88	0.75	
pH		7.66	7.84	7.87	7.90	7.98	
Ca	0.11	1200	1150	1140	1160	1170	
Mg	0.00	0.10	0.08	0.09	0.10	0.11	
Na	12600	12300	12200	12200	12100	12500	
K	<2.00	<2.00	<2.00	<2.00	<2.00	<2.00	
SiO ₂	<0.17	0.40	0.41	0.38	1.34	1.22	
Total Fe	<0.04	<0.04	<0.04	0.05	0.33	1.35	
Al	<0.10	0.42	0.41	0.30	0.33	0.39	
Cl	19100	18800	18500	18400	18500	17800	
SO ₄	<20.00	2850	2730	2710	2650	2570	
All concentrations quoted as mg.l ⁻¹							
Dissolution rate (mol.cm ⁻² .s ⁻¹)						Mean	
log k _{Ca}		-12.6	-12.4	-12.5	-12.5	-12.5	-12.5
log k _{SO₄}		-12.6	-12.4	-12.5	-12.5	-12.6	-12.5

Figure 7.33 pH and flowrate versus time for anhydrite dissolution experiment.

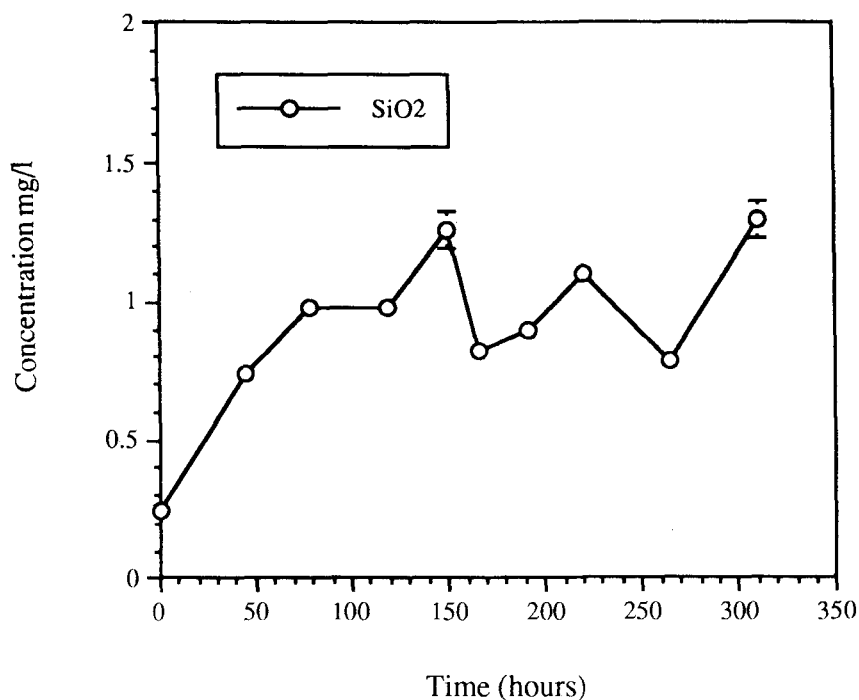
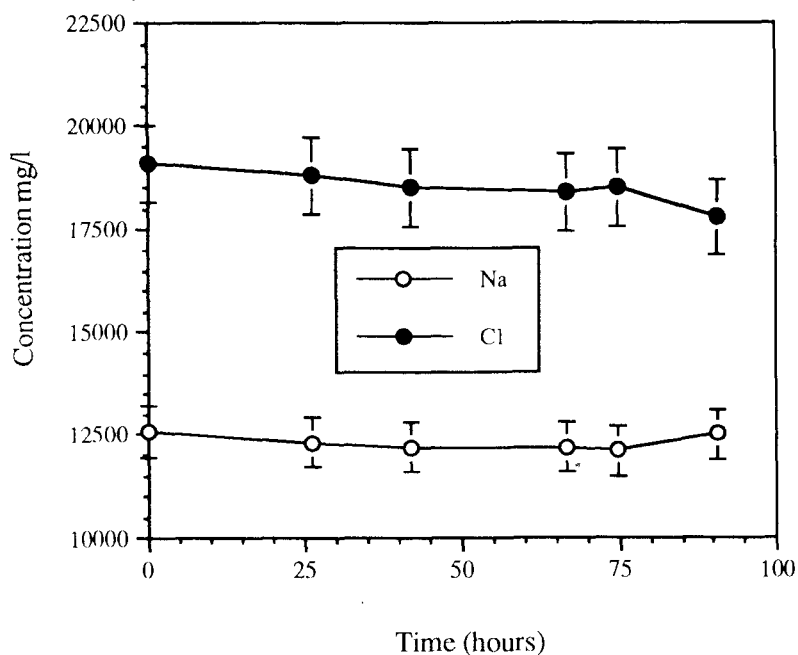


Figure 7.34 Na and Cl concentrations versus time for anhydrite dissolution experiment.



7.4.4.3 MICROCLINE

The full analytical data are presented in Table 7.21. Figure 7.39 shows the variation of pH and flowrate with time for the microcline dissolution experiment (run 447). It can be seen that pH remained fairly constant with time though was higher than the blank value ($t=0$). Figure 7.40 shows the variation of Na and Cl concentrations with time, here the levels of both elements remain reasonably constant throughout the experiment once Na concentrations had stabilised. Figure 7.41 shows the variation of SiO₂ and K concentrations with time. The SiO₂ concentration data were used to calculate the rate constant for dissolution of microcline under the experimental conditions (200 bar, 80°C) of $\log k_{\text{SiO}_2} = -14.3 \text{ mol.cm}^{-2}.\text{s}^{-1}$. This compares with a rate of $\log k_{\text{SiO}_2} = -14.8 \text{ mol.cm}^{-2}.\text{s}^{-1}$ as determined by Busenberg and Clemency (1976) extrapolated to 80°C, and a rate of $\log k_{\text{SiO}_2} = -14.5 \text{ mol.cm}^{-2}.\text{s}^{-1}$ using the data of Helgeson et al. (1984) combined with Murphy and Helgeson (1987), also extrapolated to 80°C. There was good agreement with the previous studies which, as for quartz, suggests that the presence of dissolved CO₂ had little effect on the rate, and hence mechanism, of microcline dissolution.

In this sample no significant differences were observed between grains from the start and end of the column. Up to approximately 50% of the grains were corroded in this sample. Corrosion typically occurred as small-scale pits or trails of pits developing along cleavage plains (Plate 47). Dissolution also occasionally occurred at grain corners and along grain edges. In approximately 1–3% of grains, this

corrosion was sufficiently developed to lead to significant grain shape modification. Pits are up to 10 μm^2 and are probably up to 10 μm deep at the deepest. Very occasionally, dissolution pits coalesced to form elongate channels oriented along the cleavage (Plate 48). There may have been a slight increase in the density of pits at the end of the column.

7.4.4.4 ALBITE

The full analytical data are presented in Table 7.22. Figure 7.42 shows the variation of pH and flowrate with time for the albite dissolution experiment (run 449). pH remained fairly constant with time, though was higher than the blank

Figure 7.35 Ca and SO₄ concentrations versus time for anhydrite dissolution experiment.

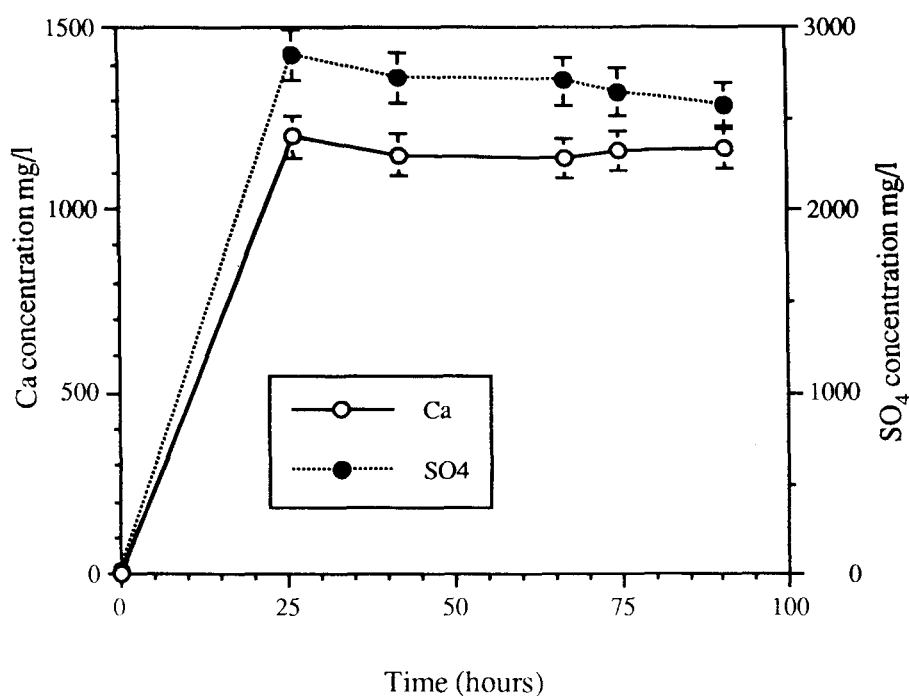


Table 7.20 Chemical analytical data for the kinetic experiment with quartz.

RUN 446: 80°C, 20 MPa											
Quartz — CO ₂ /Synthetic seawater											
Initial solid + PEEK column wt = 30.0687 g											
Initial PEEK column wt = 27.7234 g											
Initial solid wt = 2.3453 g											
Surface Area = 0.0827 m ² .g ⁻¹											
Surface Area - Total = 0.1940 m ²											
Sample Code	446/Blk	446/1	446/2	446/3	446/4	446/5	446/6	446/7	446/8	446/9	
Time (hours)	0.0	44.2	78.8	118.5	149.7	165.6	191.1	219.4	263.9	309.9	
Sample volume (ml)	—	16.89	22.82	31.21	18.94	18.51	21.69	18.86	58.40	18.76	
Flow rate (ml.hr ⁻¹)	—	1.07	0.66	0.79	0.61	1.16	0.85	0.67	1.31	0.41	
pH	—	6.5	6.9	7.7	7.8	7.82	7.74	7.79	7.67	—	
Ca	0.17	3.16	0.47	0.36	4.24	4.59	4.67	4.67	4.62	4.99	
Mg	0.02	0.36	0.08	0.07	4.51	5.47	5.35	5.34	5.41	6.13	
Na	12100	12200	13200	13100	12300	12600	12500	12000	12600	14000	
K	<2.00	<2.00	<2.00	<2.00	3.87	<2.00	2.09	2.07	<2.00	3.36	
SiO ₂	0.25	0.74	0.98	0.98	1.26	0.82	0.90	1.10	0.79	1.30	
Total Fe	<0.04	<0.04	0.11	<0.04	<0.04	<0.04	<0.04	<0.04	<0.04	0.11	
Al	<0.10	<0.10	0.18	<0.10	<0.10	<0.10	<0.10	<0.10	<0.10	<0.10	
Cl	18400	18900	19700	20300	19000	18700	18500	18600	18200	22000	
All concentrations quoted as mg.l ⁻¹											
Dissolution rate (mol.cm ⁻² .s ⁻¹)										Mean	
log k _{SiO₂}		-14.9	-14.9	-14.9	-14.8	-14.8	-14.9	-14.9	-14.8	-15.0	-14.9

value ($t = 0$). Figure 7.43 shows the variation of Na and Cl concentrations with time, the apparent scatter in the data probably being due to sampling problems. Figure 7.44 shows the variation of SiO₂ concentration with time. The SiO₂ concentration data were used to calculate an average rate constant for dissolution of albite under the experimental conditions (200 bar, 80°C) of $\log k_{\text{SiO}_2} = -13.8$ mol. cm⁻².s⁻¹. This compares with a rate of $\log k_{\text{SiO}_2} = -14.9$ mol. cm⁻².s⁻¹ calculated at 80°C, 0.1 MPa using the data Knauss and Wolery (1986), and $\log k_{\text{SiO}_2} = -13.9$ mol.

cm².s⁻¹ as determined by Busenberg and Clemency (1976) using their data from 25°C extrapolated to 80°C. There is good agreement with the extrapolated data of Busenberg and Clemency (1976), but not with the data of Knauss and Wolery (1986). Possible reasons for this were the differences in the fluids used in the experiments. Those used by Knauss and Wolery were pH buffers of low ionic strength, whereas Busenberg and Clemency used de-ionised water with CO₂ gas bubbling through it. This study used a 0.55 M NaCl fluid saturated with supercritical CO₂.

Figure 7.36 pH and flowrate versus time for quartz dissolution experiment.

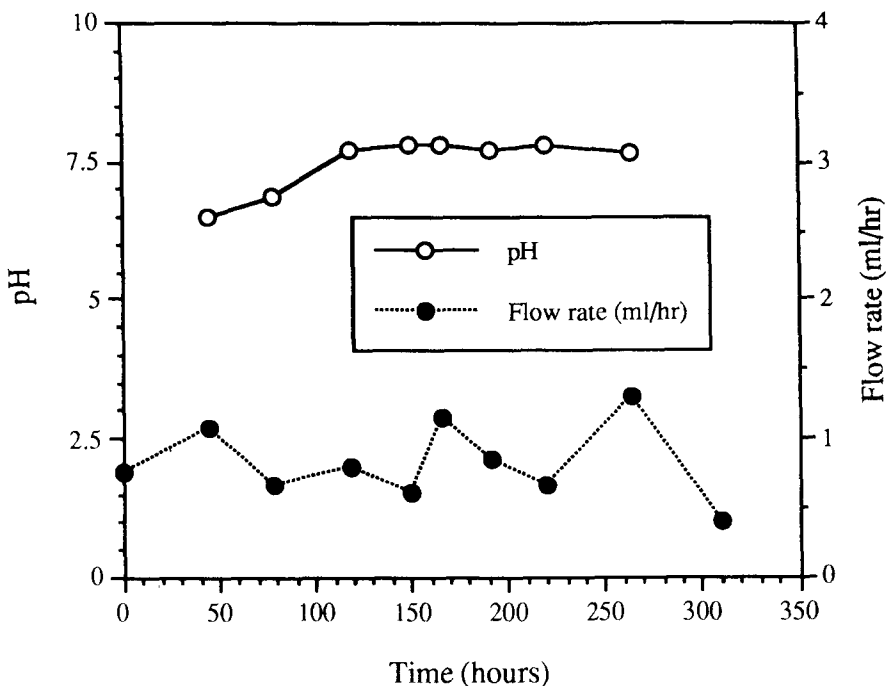
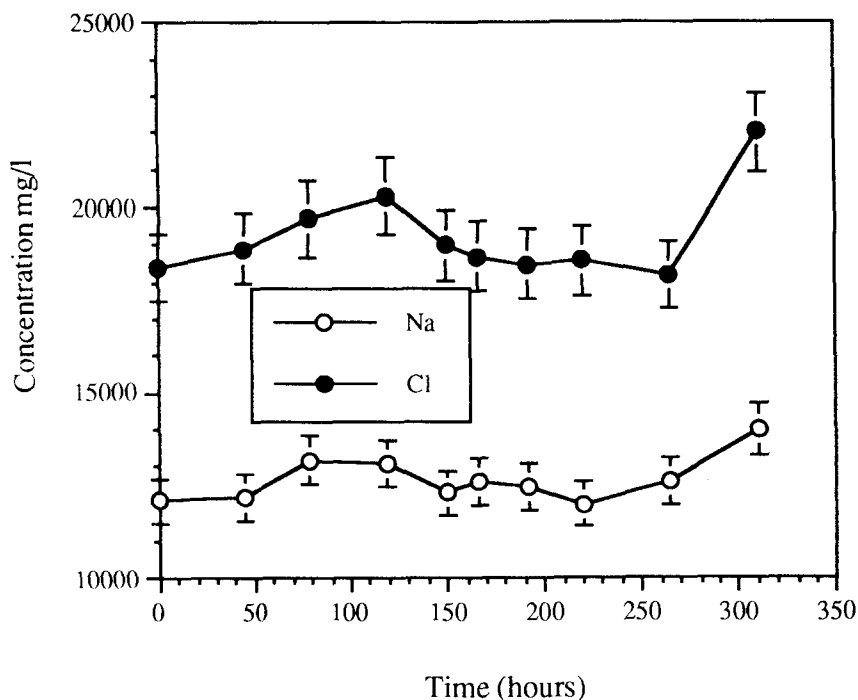


Figure 7.37 Na and Cl concentrations versus time for quartz dissolution experiment.



It may be that the presence of Na or CO₂ causes a change in reaction mechanism of albite dissolution, though the nature of this is not clear.

Corrosion of the albite column occurred as minor localised pitting and very limited channelling which follows cleavage (Plate 49). The proportion of corrosion was possibly less than that observed on the microcline sample described above. Roughly less than 5% of grains developed corrosion features in the albite sample.

7.4.4.5 CONCLUSIONS

Table 7.22 gives a summary of the experimentally determined rate constants (at 80°C, 200 bar). There was good

agreement with the literature values for quartz and microcline. However, the rate determined for albite dissolution was an order of magnitude faster than that determined by Knauss and Wolery (1986). It seems likely that this was due to a change in the reaction mechanism of albite dissolution, although it was not clear what form this took. However, the data were close to that determined by Busenberg and Clemency (1976). The anhydrite dissolution experiment reached approximate equilibrium in the first 25 hours of the experiment. As anhydrite dissolution is thus very rapid, it can be assumed to be at saturation for the purposes of modelling the reactions between CO₂-rich fluids and reservoir sandstones.

Figure 7.38 SiO₂ concentration versus time for quartz dissolution experiment.

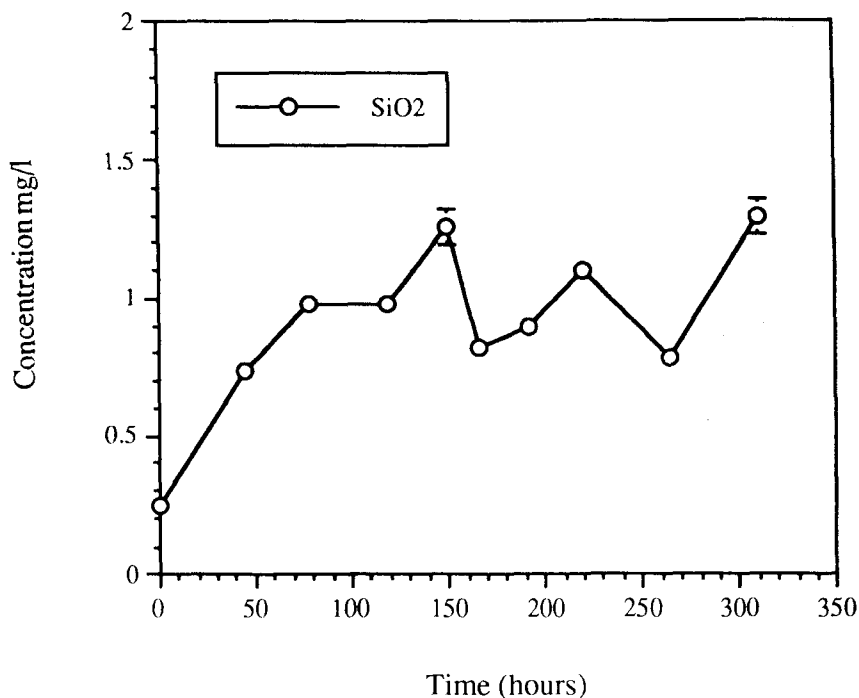


Table 7.21 Chemical analytical data for the kinetic experiment with microcline.

RUN 447: 80°C, 20MPa Microcline — CO ₂ /Synthetic seawater Initial solid + PEEK column wt = 31.908 g Initial PEEK column wt = 29.55 g Initial solid wt = 2.358 g Surface Area = 0.1519 m ² .g ⁻¹ Surface Area — Total = 0.3582 m ²									
Sample Code	447/blk	447/1	447/2	447/3	447/4	447/5	447/6	447/7	
Time (hours)	0.0	52.0	76.0	170.3	220.3	260.3	315.5	361.8	
Sample volume (ml)	—	21.12	10.16	25.26	14.84	11.53	18.88	24.16	
Flow rate (ml.hr ⁻¹)	—	0.41	0.42	0.27	0.30	0.29	0.34	0.52	
pH	5.95	7.49	7.79	7.81	7.53	7.51	7.55	7.36	
Ca	0.62	0.90	0.65	0.68	0.62	0.62	0.94	0.63	
Mg	0.24	0.26	0.26	0.29	0.26	0.26	0.30	0.26	
Na	11800	12800	12800	13900	13300	13000	13100	12800	
K	<2.00	<2.00	<2.00	2.02	2.06	<2.00	3.63	<2.00	
SiO ₂	0.26	4.70	3.45	2.42	3.71	3.64	3.34	2.91	
Total Fe	0.38	<0.04	<0.04	<0.04	<0.04	<0.04	<0.04	<0.04	
Al	<1.00	<1.00	<1.00	<1.00	<1.00	0.34	<1.00	<1.00	
Cl	20500	19600	16500	21800	19700	19400	19900	19500	
All concentrations quoted as mg.l ⁻¹									
Dissolution rate (mol.cm ⁻² .s ⁻¹)									
log kSiO ₂		-14.1	-14.2	-14.6	-14.4	-14.4	-14.3	-14.2	Mean -14.3

Figure 7.39 pH and flowrate versus time for microcline dissolution experiment.

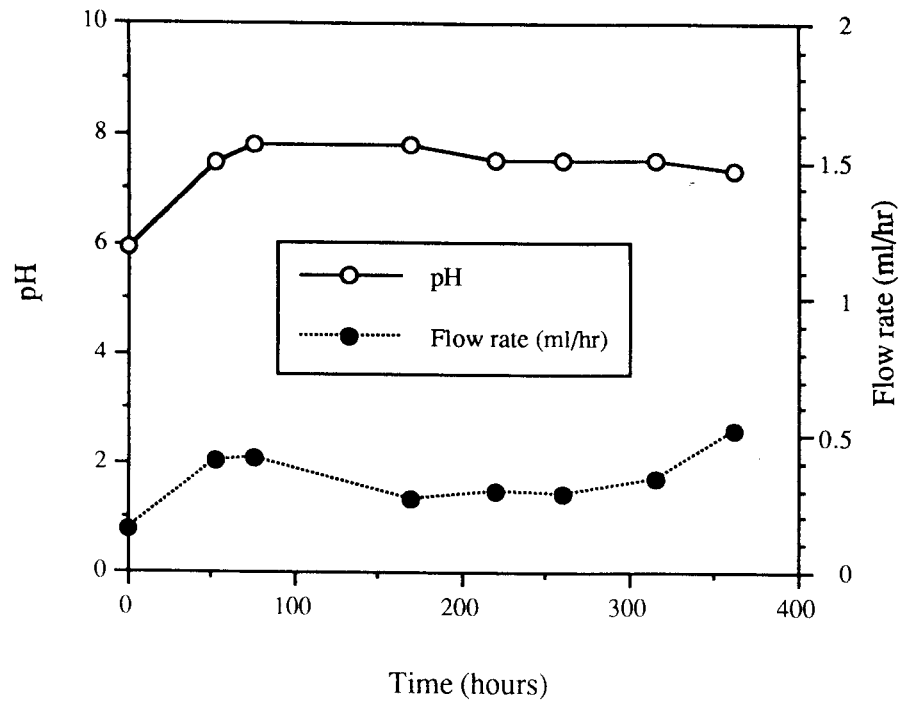


Figure 7.40 Na and Cl concentrations versus time for microcline dissolution experiment.

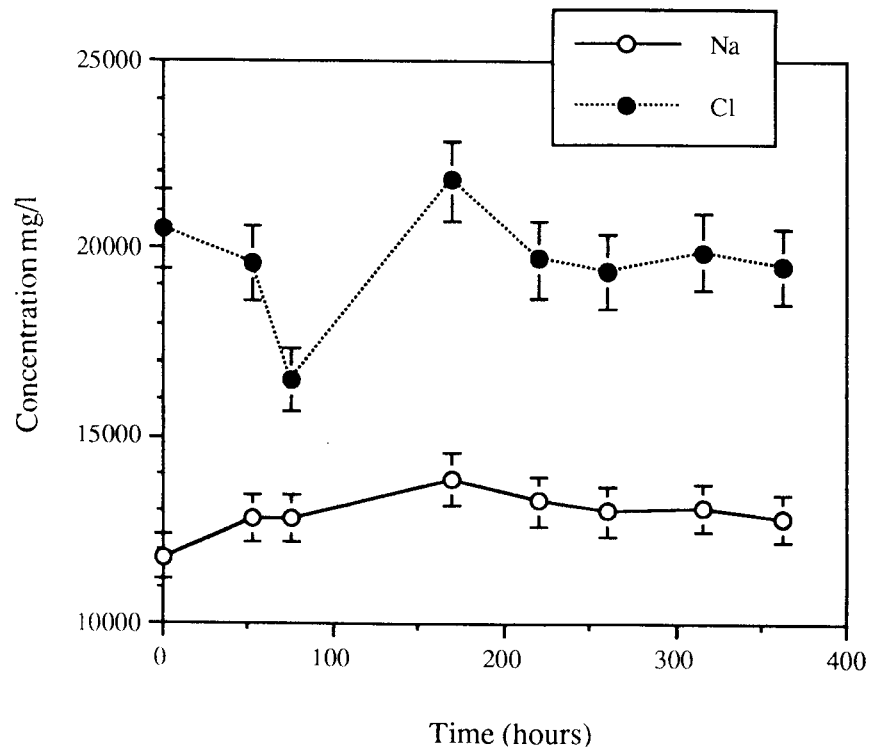


Figure 7.41 SiO₂ and K concentrations versus time for microcline dissolution experiment.

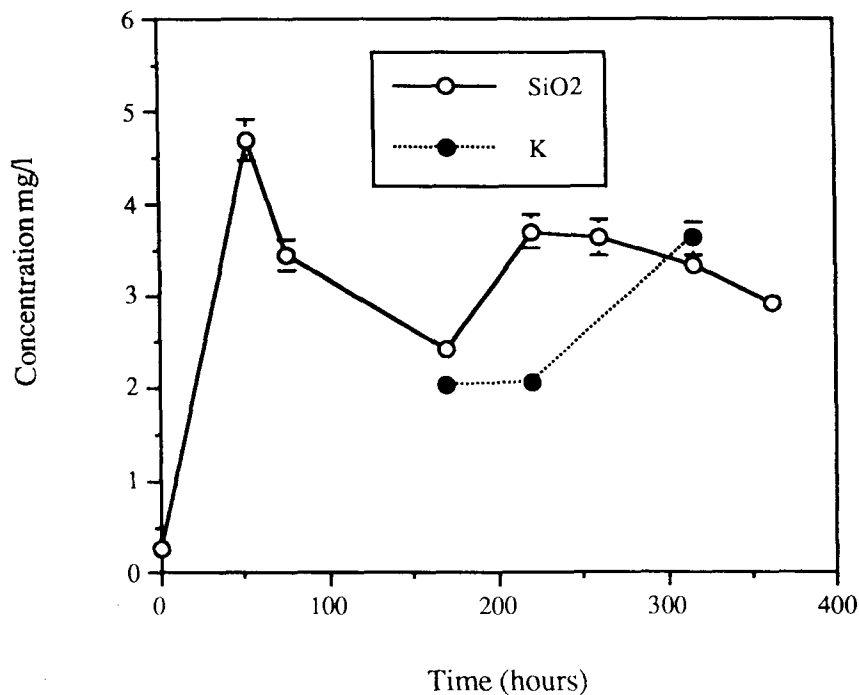


Table 7.22
Chemical analytical data for the kinetic experiment with albite.

RUN 449: 80°C, 20 MPa										
Albite — CO ₂ /Synthetic seawater										
Initial solid + PEEK column wt = 32.0034 g										
Initial PEEK column wt = 29.5386 g										
Initial solid wt = 2.4648 g										
Surface Area = 0.1674 m ² .g ⁻¹										
Surface Area — Total = 0.4126 m ²										
Sample Code	449/blk	449/1	449/2	449/3	449/4	449/5	449/6	449/7	449/8	
Time (hours)	0.0	166.2	195.8	220.5	237.5	244.1	261.8	286.8	316.34	
Sample volume (ml)	—	11.39	20.78	11.61	8.14	11.81	29.25	12.00	7.27	
Flow rate (ml.hr ⁻¹)	—	0.07	0.70	0.47	0.48	1.81	1.64	0.48	0.25	
pH	6.00	6.91	6.96	7.23	7.38	7.42	7.08	6.63	6.91	
Ca	0.36	83.8	2.14	3.92	1.32	3.45	3.79	1.44	3.36	
Mg	0.091	0.418	0.281	0.288	0.427	0.089	0.105	0.049	0.126	
Na	12800	14200	13500	13900	23200	13200	13200	3140	12900	
K	<10.0	<10.0	<10.0	<10.0	<10.0	<10.0	<10.0	<10.0	<10.0	
SiO ₂	<0.86	3.36	3.36	7.98	<0.86	9.50	7.38	<0.86	3.08	
Total Fe	<0.20	<0.20	<0.20	<0.20	<0.20	<0.20	<0.20	<0.20	<0.20	
Al	<0.40	<0.40	<0.40	<0.40	<0.40	<0.40	<0.40	<0.40	<0.40	
Ba	<0.020	0.154	0.342	0.105	0.194	0.086	0.101	0.130	0.202	
Sr	<0.020	0.290	0.057	0.105	0.034	0.076	0.103	0.040	0.110	
Mn	0.331	0.342	0.841	0.785	1.320	0.212	0.300	0.105	0.429	
Ni	162	171	328	293	517	100	143	52	199	
Cl	18200	20800	20400	20600	22800	13800	25400	n.s.	17900	
All concentrations quoted as mg.l ⁻¹										
Dissolution rate (mol.cm ⁻² .s ⁻¹)									Mean	
log kSiO ₂		-15.2	-14.2	-13.9	-	-13.2	-13.4	-	-14.7	-13.8

Figure 7.42 pH and flowrate versus time for albite dissolution experiment.

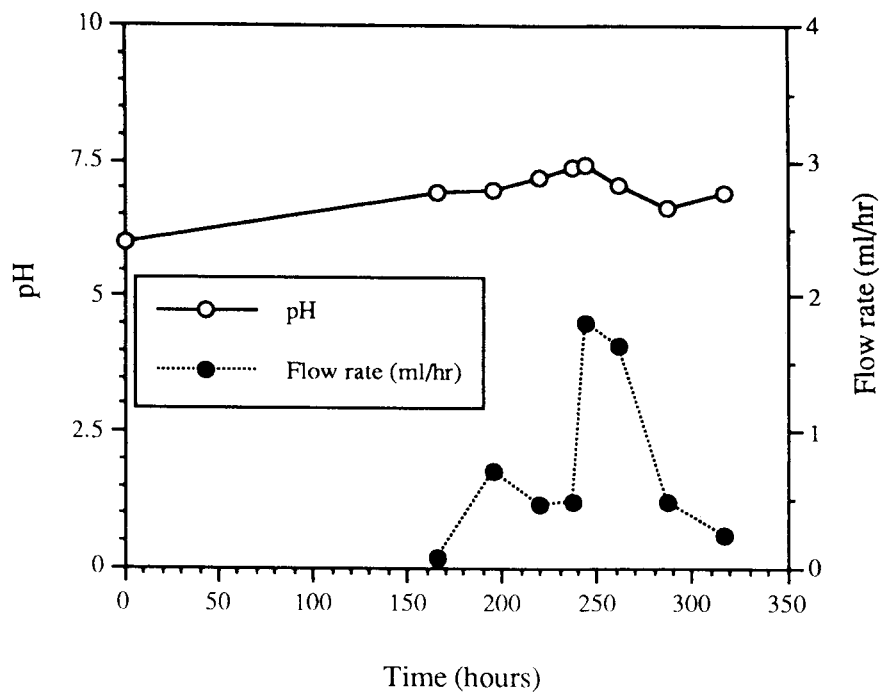


Figure 7.43 Na and Cl concentrations versus time for albite dissolution experiment.

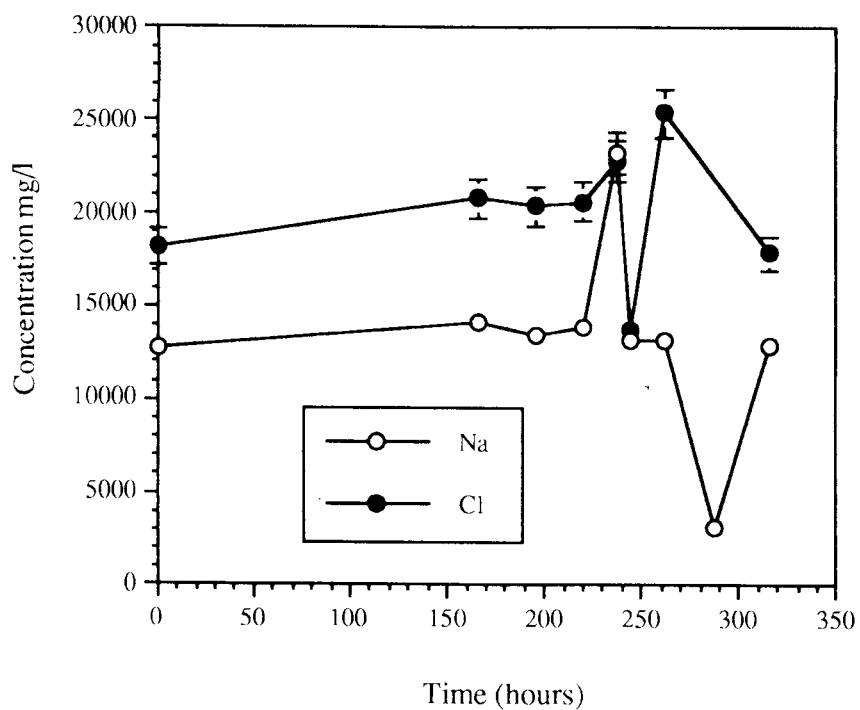


Figure 7.44 SiO₂ concentration versus time for albite dissolution experiment.

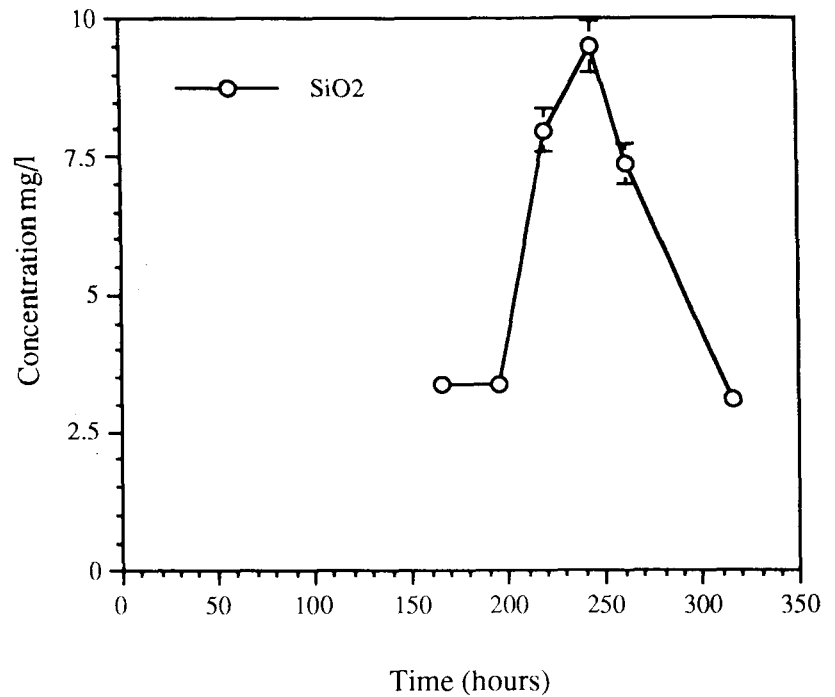


Table 7.23 Summary of the experimentally determined rate constants of mineral dissolution into a CO₂/NaCl fluid at 80°C and 20 MPa (see text).

Run number	Starting material	Rate of dissolution (mol.cm ⁻² .s ⁻¹) @ 80°C
Run 423	Anhydrite	Fluid saturated with respect to Anhydrite
Run 446	Quartz	$k_{\text{SiO}_2} = 1.26 \times 10^{-15}$ $\log k_{\text{SiO}_2} = -14.9$
Run 447	Microcline	$k_{\text{SiO}_2} = 5.01 \times 10^{-15}$ $\log k_{\text{SiO}_2} = -14.3$
Run 449	Albite	$k_{\text{SiO}_2} = 1.58 \times 10^{-14}$ $\log k_{\text{SiO}_2} = -13.8$

7.5 THE BRAVO DOME CO₂ FIELD (USA): A NATURAL ANALOGUE OF CARBON DIOXIDE DISPOSAL

7.5.1 Bravo dome carbon dioxide gas unit

The following description is based on information supplied by, and discussions with, Herb Wacker (Amoco Production Company) and Ron Broadhead (New Mexico Bureau of Mines) and published literature. The Bravo Dome field lies to the southeast of the Sierra Grande uplift in northeastern New Mexico. It is bounded by the Tucumcari Basin and the Dalhart Basin and separated from these by large-scale faults. This area of New Mexico was subjected to uplift as a series of faulted blocks during Pennsylvanian time (Broadhead, 1989). The Bravo dome area is one of many fault-bounded basins in the region. The Bravo Dome is so-called because of the surficial radial drainage pattern and does not relate to any geological structure. By Middle Pennsylvanian time, the Mississippian and Lower Pennsylvanian strata had been removed and the underlying granitic basement was being eroded to form the Early Permian arkosic sandstones of the Tubb — described below. These sandstones were then covered by evaporites of the Yeso Formation during the Middle Permian marine transgression from the adjacent Palo Duro basin. The overlying Triassic, Jurassic and Cretaceous rocks were

gently folded by Laramide (Late Cretaceous to Early Tertiary) compressive deformation. This resulted in a southeast plunging nose connecting the Sierra Grande Uplift with the Amarillo Uplift. This provides the structure, reservoir and seal for the carbon dioxide (Wacker, 1994). Tertiary basaltic volcanism followed Laramide deformation with volcanic centres apparently located along the northwest trending faults.

The source of the CO₂ is unclear with several hypotheses being proposed. The petroleum industry appears to accept a limestone decomposition mechanism as the CO₂ source, brought about by volcanic thermal metamorphism. The ¹²C/¹³C isotopic ratio for CO₂ in the Bravo Dome is isotopically heavy (Lang, 1959) and was therefore proposed by that author to be from marine limestones. However, Galimov (1968) suggested that juvenile CO₂ from mantle degassing could have a similar isotopic signature. Xenon and helium, associated in trace quantities with the CO₂, have isotopic signatures which indicate a juvenile magmatic origin (Phinney, et al., 1978) although this does not necessarily prove that the CO₂ is from the same source. In addition there has been only small-scale volcanic activity within the Bravo Dome area and there are very few significant limestone sources in the vicinity, either above or below the Tubb reservoir. It is likely that, whatever the source of CO₂, migration of the gas will have taken place along either Early Pennsylvanian faults in the underlying

Precambrian basement or Tertiary faults. Limited diagenetic evidence for gas migration in the northwest trending Tertiary faults is discussed below.

The reservoir rocks are continental red beds of the Permian Wolfcampian-Leonardian Abo/Tubb Sandstones which rest unconformably on Precambrian granite, rhyolite and diorite (Broadhead and King, 1988). Current depth to the top of the Tubb varies between 1900 to 2950 ft with an average thickness of 120 ft and maximum thickness of 300 ft. During early Permian, the Bravo Dome area was bounded to the west by the Sierra Grande Arch and to the east/southeast by the Palo Duro Basin (May, 1982). The Tubb Sandstone reservoir and overlying Cimarron Anhydrite caprock were deposited in a semi-arid to arid, bajada environment with gravel and debris from the topographic high of the Sierra Grande. These sandstones formed by alluvial deposition from a northwest source, initially as coarse grained alluvial fans. This was followed by the formation of a braidplain with subsequent reworking of increasingly finer grained sediments (Nelis, 1994). The Tubb has been informally divided by Wacker and Nelis on the basis of the depositional environments of each sandstone. The Lower Tubb consists of poorly sorted coarse grained arkoses formed in alluvial fans and braided stream environments. The Middle Tubb consists of medium to coarse grained arkoses deposited in a braided stream environment and the Upper Tubb consists of very fine to fine grained, well sorted subarkose to arkose formed in wadi environments or from reworked earlier sandstones. Towards the centre of the basin are local playa lake deposits and evaporitic sequences. The Cimarron represents a marine transgression into the area from the Palo Duro Basin.

Structurally the Tubb/Abo thickens to the southeast. It is dissected by a Tertiary fault or flexure that trends ESE/NNW with a downthrow to the north of ~200 ft. Close to the Sierra Grande uplift the Tubb is less than 100 ft thick and steadily thickens to the southeast to a thickness of over 500 ft. The Upper Tubb is not present close to the Sierra Grande uplift and only develops 25–40 miles down dip. The Middle Tubb is the main pay zone. Gamma ray logs easily identify the main geological units with the Cimarron anhydrite giving low signals, the Tubb sequence giving higher signals with high spikes indicating the presence of mudstone intervals. The granite wash gives very high signals.

The following summary of Tubb petrography and diagenesis is almost entirely based on a study carried out for Amoco Production Company by M. K. Nelis. Nelis (1994) has divided the Tubb Sandstone into five microfacies based on extensive and very detailed petrographic examination of 250 thin sections from 22 cored wells. The different microfacies represent varying textural maturity from microfacies I which includes all mature, very fine grained and very well sorted arkoses, to microfacies V which consist of coarse-grained, poorly-sorted arkoses with abundant detrital clay and silt. The sample maturity was found by Nelis (1994) to be related to the depositional environment. For example, the coarse grained sands of microfacies IV and V are the most feldspathic and are more common in the Lower Tubb. This was a result of deposition in an alluvial fan environment close to a granitic source where extensive reworking did not take place. Quartz content ranges from 50% to 75% (Nelis, 1994) and is most abundant in the texturally mature microfacies I. Feldspar content varies from 25% to 50% with the most feldspathic samples belonging to microfacies

III, IV and V. Plagioclase and K-feldspar are present in variable amounts in most samples with plagioclase showing the greatest corrosion and K-feldspar showing less corrosion and greater authigenic overgrowth development. Lithic grains, comprising granite, highly altered volcanics, diorite, and polycrystalline quartz of probably metamorphic origin, account for only a few percent of the Tubb sandstones. In addition, sedimentary lithic fragments such as mud intraclasts, dolomitic and dolomitised shales are common in these deposits. Detrital clay and silt and infiltrated clay are common in many samples, and in some coarser samples can lead to a matrix-supported fabric. The infiltrated clay tends to occlude porosity.

Dissolution of feldspars and ferromagnesian minerals during early burial lead to formation of hematite in cleavage cracks and as grain coatings. The Tubb is red in colour throughout the field due to this hematite. Illite has been detected by XRD analyses (Nelis, 1994) associated with this hematite. In addition, syntaxial quartz and K-feldspar overgrowths developed at an early stage in the burial history. Also at this stage anhydrite and gypsum were precipitated. Three fabrics could be recognised which reflected the different genesis of each type. These were primary evaporite, burial cements that formed during transformation of the primary evaporite, and 'contact cementation' by communication with the overlying Cimarron anhydrite. Dolomite occurs as lithoclasts described above and also as an early poikilotopic cement with ferroan dolomite overgrowths. The dolomite infills intergranular porosity and secondary dissolution porosity within feldspars. Calcite only occurs in a few samples as intergranular cement. Later cements include intergranular pore-filling chlorite in coarse-grained samples to the north of the field. Kaolinite occurs in partially-corroded plagioclase crystals, and vermicular shaped pores in detrital quartz indicates removal of earlier kaolinite. Laumontite occurs as a late cement in moldic pores, primary and secondary intergranular pores. The samples containing zeolite are spatially associated with the northwest trending fault/flexure. Fault control of diagenetic minerals has also been noted in the Rotliegende gas fields of Germany (Gaupp et al., 1993). The best reservoir sandstones are formed as a result of dissolution of early evaporites, carbonates and of detrital plagioclase.

Nelis (1994) suggests that the paragenetic sequence described above results from an evolving porefluid chemistry. The initial depositional environment produced alkaline and oxidising conditions. With increasing burial and the marine transgression conditions became more reducing. Acidic conditions are intimated by the extensive dissolution of evaporites and carbonates and is attributed by Nelis to the introduction of CO₂.

An estimated 12 TCF CO₂ is thought to have been originally present in the Bravo Dome Unit (Amoco, 1990) with the amount of ultimate recoverable gas estimated at 5300 to 9800 bcf (Broadhead, 1989). Annual production in 1989 was 127 bcf. CO₂ within the Bravo Dome is regionally underpressured. The regional pressure is 380 psi. Flow rates in the wells vary systematically across the field with the lowest rate to the northwest (e.g. 34 MCFGPD) and the highest rates to the southeast (3800 MCFGPD). The regional pressure variation has been modified by the Tertiary fault which has led to leakage of CO₂ from the southern upthrown side across to the downthrown northern side. This further migration of CO₂ has led to diagenetic haloes forming around the fault. However, a detailed examination of the pressures measured in wells across the

field reveals that the region can be further subdivided into areas of similar pressures (Broadhead, 1994). Each area of similar pressure appears to correspond almost exactly with the underlying faulted blocks of the Precambrian granitic basement. Broadhead therefore suggests that these faults are controlling, at least in part, CO₂ flow within the field. Interestingly, the underlying aquifers are at normal geopressures suggesting that a pressure difference is being maintained with the underpressured CO₂ above. In addition, the CO₂-water boundary is at different depths in each area. The reasons for this are not known, but Broadhead maintains that it is not a stratigraphic control and assumes that it must therefore be a diagenetic control. In other words, at the CO₂-water boundary precipitation of some phase has allowed the pressure difference to remain. No samples are available from this region and hence petrographic evidence can not be acquired.

The Bravo Dome was developed as a CO₂ producing field for enhanced oil recovery operations in the West Texas oilfields during the 1980s (Broadhead, 1989). The number of wells increased from 16 in 1982 to 425 productive wells as of July 1994 and now uses 500 miles of CO₂-grade fibreglass pipe and steel pipe. The average well deliverability is 1.5 MMCFGPD initial rate. The CO₂ producing wells and collection system consists of eight collection areas. These have been developed in three chronological phases. All wells are connected to a single 66 000 HP compressor station recently brought online during Phase III of the development that compresses the gas from 125 psi inlet pressure to 1900 psi outlet pressure. The main producing area is in the southeast quadrant of the unit where flow rates are the highest. Annual CO₂ production increased from 1 bcf in 1982 to 101 bcf in 1985 with total sales now 1078 bcf. Operation of the plant cost approximately \$125m in 1988 (prior to Phase III being online). Current price is 30¢ per 1000 cf. Porosity ranges in the gas-bearing zones vary from about 12% up to 35%. Pay quality permeability is 20 to 40 mD on average but some zones reach over 100 mD. The lower porosity sandstones do not appear to gas-bearing due to water retention by capillary action. The CO₂ is wet and has to be dried before and during compression using glycol scrubbers.

7.5.2 Petrography of Bravo Dome samples

Six samples were obtained from two boreholes within the Bravo Dome CO₂ field. These were three from the Culbertson well and three from the Nikkel Well. The Culbertson well is situated in the middle of the field and has moderate flow. The Nikkel Well is situated towards the southeast corner of the field where pressures are highest and production greatest. The samples were selected to provide a range of samples including pay zones and non-pay zones. Core from the two wells were briefly examined. The following additional information was obtained:

Nikkel N^o1:

Gamma ray, permeability and porosity log

Annotated core description sheets

Porosity and permeability data for 63 samples over ~100ft of core with brief descriptions of lithology

Gamma ray and neutron-density (CNL/DHL) logs for whole well, with cored intervals, pay zones and poroperm plug depths marked

Three samples were taken:

Nikkel 4–2147 ft. Pay zone, very fine grained, parallel laminated, red sandstone

Nikkel 6–2282 ft. Non-pay zone, muddy siltstone with syndepositional deformation

Nikkel 5–2230 ft. Pay zone, very fine grained, red parallel laminated sandstone with reduction spots.

Culbertson N^o1

Gamma ray, permeability and porosity log

Gamma ray and neutron-density (CNL/DHL) logs

Three samples were taken from this well:

Culbertson 3–2256 ft. Caprock, anhydrite and mudstone interlayered

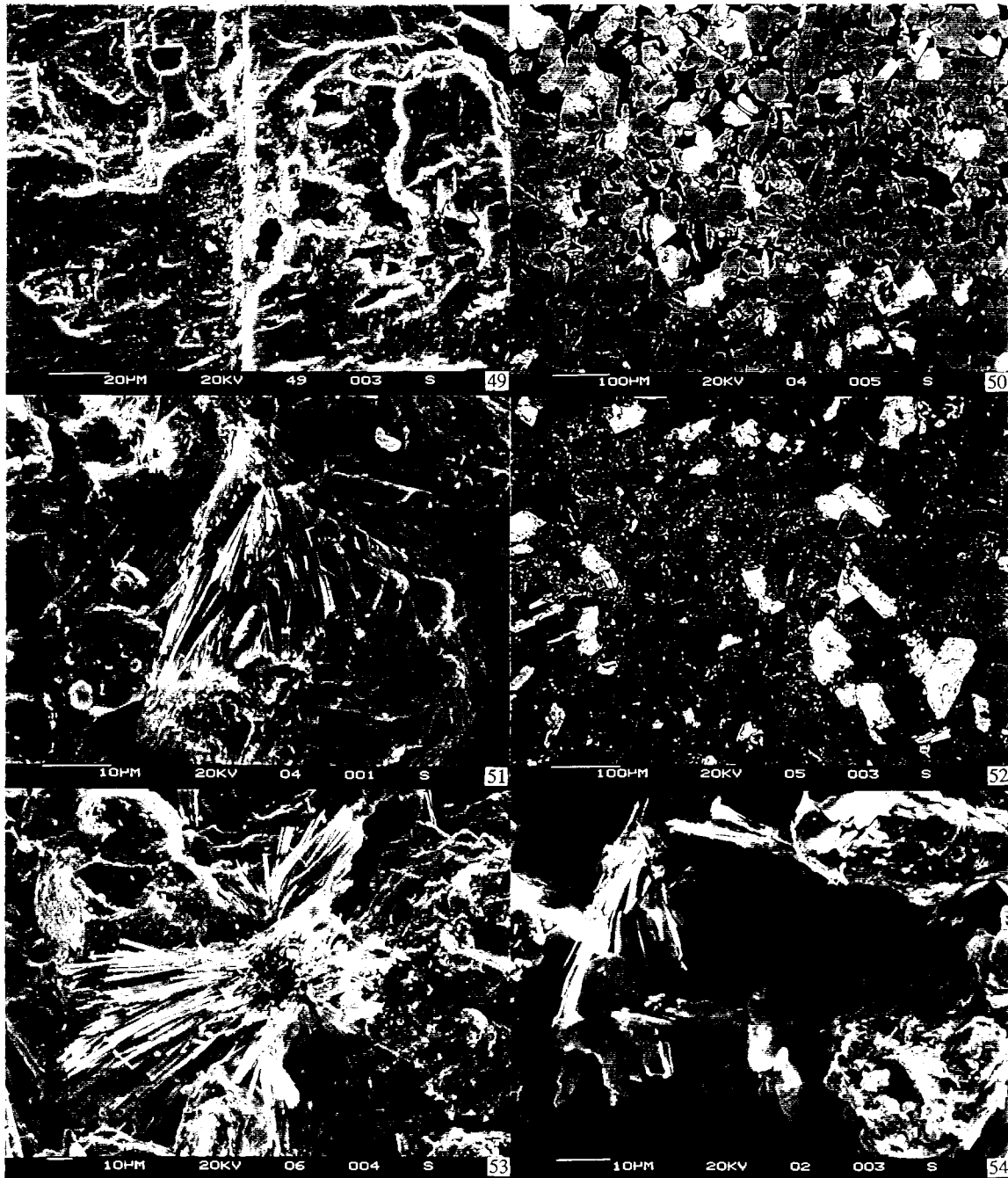
Culbertson 2–2284 ft. Non-pay zone (?), dense, bleached light pink/grey, very fine grained sandstone with extensive anhydrite cement

Culbertson 1–2296 ft. Pay zone sample, parallel laminated, aeolian, medium grained sandstone with anhydrite cement

7.5.2.1 NIKKEL N^o1

Nikkel 4, Pay zone (2147 ft) This is a light red, poorly laminated, bioturbated quartz arenite. It is a very fine grained (4.0–3.5 Ø), mature sandstone with detrital, angular quartz, K-feldspar and minor albite grains. Minor micas are splayed along basal cleavage and altered to hematite and possible illite-smectite clay. Heavy minerals mainly comprised zircon and magnetite. K-feldspar grains were corroded and twinned plagioclases were also corroded — especially K-feldspar twins. It is weakly cemented with a high proportion of very well connected secondary(?) porosity (Plate 50). Porosity at this depth is 15.2% with permeability very low at 0.9 mD. K-feldspars have developed some authigenic overgrowths which tend to be less corroded than detrital cores. Quartz overgrowths were patchily developed as isolated euhedral crystals lining pore walls. Authigenic ferroan calcite clasts also occurred throughout the sandstone partially infilling secondary pores. Very occasionally some areas were cemented by largely structureless to aggregates of radiating needles gibbsite (Plate 51) which was observed to post-date mica alteration. Generally authigenic clays were rare. In a few isolated areas relict, highly corroded gypsum cement occurred. Porosity is oversized in some areas due to extensive framework grain dissolution.

Nikkel 5, Pay zone (2230 ft) This is a light red, very fine grained (4.0–3.5 Ø), moderately sorted, parallel laminated quartz arenite with low angle cross-lamination comprising mainly angular quartz and K-feldspar grains. As in Nikkel 4, small areas are cemented by gibbsite although the majority of pore space is uncemented which results in a high proportion of well-connected porosity - some of which is oversized (Plate 52). Lenses of clay-rich matrix were also present forming locally matrix-supported fabric. EDXA indicated that the clay is Fe-rich illitic-smectitic in composition. Poikilotopic and occasionally expansive barite forms an early cement in patches up to several millimetres across. These cemented patches do not follow the lamination but appear to be associated with irregular muddy lenses, millimetre-scale open voids and significant secondary porosity enhancement. The gibbsite, more



- Plate 49 Secondary electron SEM photomicrograph of corrosion pits on albite at outlet end of dissolution column (9-10 cm). Run 449.
- Plate 50 Backscattered electron SEM photomicrograph of typical view of quartz arenite sample Nikkel 4. Note well connected secondary porosity, including moldic pores outlined by relict K-feldspar overgrowths and occasional gibbsite patches (dark grey centre top).
- Plate 51 Secondary electron SEM photomicrograph of radiating acicular gibbsite lining pore wall on detrital quartz surface. Nikkel 4.
- Plate 52 Backscattered electron SEM photomicrograph of typical view of quartz arenite sample Nikkel 5. Note well connected secondary porosity and occasional gibbsite patches (dark grey centre top).
- Plate 53 Secondary electron SEM photomicrograph of radiating acicular gibbsite lining pore wall on detrital quartz surface. Nikkel 6.
- Plate 54 Secondary electron SEM photomicrograph of euhedral hexagonal kaolinite plates lining pore wall in Culbertson 2.

common in this sample than Nikkel 4, post-dates the barite. Lamellae contain heavy mineral concentrations comprising zircon, magnetite, xenotime, rutile and anatase. No authigenic clays were observed in this sample. Some K-feldspar grains were corroded with occasional moldic pores outlined in euhedral relict K-feldspar overgrowths. Occasional skeletal grains developed with possible secondary clay alteration products. This secondary clay was Fe-rich illitic in composition with minor Ti possibly present as intimately mixed anatase although not resolved specifically. Permeability is 36 mD and porosity is 22.0%.

Nikkel 6, Non-pay zone (2282 ft) This is a light red, very fine grained (4.0–3.5 Ø), moderately sorted, parallel laminated quartz arenite with low angle cross-lamination comprising mainly angular quartz and K-feldspar grains. The porosity in this sample is still relatively high although it is now partially filled by dolomite cement. Gibbsite was again present in this sample occasionally developing a radiating acicular texture infilling oversized porosity (Plate 53). The gibbsite encloses and therefore post-dates chlorite. EDXA indicated that the chlorite is Fe-rich. Chlorite is relatively common in this sample and may be one reason for non-production at this interval. Micas are partially altered to hematite and chlorite. Detrital K-feldspar cores are again corroded to leave moldic pore spaces outlined by relict, euhedral K-feldspar overgrowths. The gibbsite formation may post-date K-feldspar dissolution. Heavy mineral bands tend to be less porous as they contain more chlorite matrix. Very rare kaolinite occurred as platelets developing from pore walls.

7.5.2.2 CULBERTSON N^o1

Culbertson 1, Pay zone (2296 ft) This is a very fine grained sandstone comprising angular quartz and angular to subrounded K-feldspar grains. Rare micas show minimal compaction and no alteration. Heavy minerals comprised predominantly zircon and magnetite and typically occur in thin lamellae. The sandstone is moderately well cemented by minor gibbsite, kaolinite and major gypsum. Quartz grains were initially cemented by euhedral to subhedral quartz overgrowths. Gibbsite occurred as relatively early cement and as subangular clasts post-dated by kaolinite. Kaolinite formed in extensive patches infilling much of porosity locally. In this sample porous zones graded into zones with much reduced porosity. The porosity may be minus cement porosity due to extensive removal of carbonate cements which were generally rare in the more porous zones. There was also a reduction in the proportion of gypsum cement in these areas. The porosity was often oversized and moderately well connected. Porous and non-porous zones alternate on a millimetre scale. Occasional patches of calcite cement were typically corroded and post-dated by kaolinite. The calcite was post-dated by gypsum which also post-dated the quartz overgrowths. Gibbsite was generally rare in this sample and associated with the more porous zones. Detrital K-feldspar surfaces were pitted in a very similar manner to that seen in the experimental reaction products. Structureless iron oxides were intimately associated with kaolinite (which post-dated it) in many areas in this sample.

Culbertson 2 Non-pay zone(?) (2284 ft) This is a very fine grained (4.0–3.5 Ø), texturally mature and massive sandstone. Angular quartz grains with much reduced, generally subangular K-feldspar. Kaolinite was still present although now predominantly confined to pore lining as

opposed to pore filling (Plate 54). Occasional micas showed alteration and splaying along basal cleavage with replacement by kaolinite. Subspherical patches were cemented by ferroan (±manganous) dolomite. Porosity in this sample was intergranular primary and secondary and, although the sample was porous, permeability will probably be low due to many pore throats being blocked by kaolinite. Major secondary porosity is likely to be minus cement porosity due to loss of carbonate and gypsum cements. Kaolinite post-dates dolomite and calcite cements. No gibbsite was observed in this sample.

Culbertson 3 Cap rock (2256 ft) This is a siltstone to muddy siltstone with angular quartz and K-feldspar grains in matrix-supported fabric. Heavy minerals comprised rare monazites, rutile, ilmenite, magnetite, zircon and trace chalcopryrite. Generally, K-feldspar was fresh although moldic pores evenly distributed throughout the matrix suggest that dissolution of some grains, probably plagioclase grains, had taken place. Porosity generally, however, was very low. Micas were slightly altered with kaolinite precipitation along slightly splayed basal cleavages. Authigenic structureless to slightly platy kaolinite infilled secondary porosity. Rare, ferroan calcite clasts were less than 10 µm across. Also, authigenic euhedral adularia occurred in some pores as isolated crystals less than 10 µm across. These were post-dated by the kaolinite. Occasional millimetre-scale gypsum lenses enclosed isolated quartz grains and were associated with ferroan dolomite and ankerite.

7.5.3 Other information

A general underlying concept to CO₂ injection held by most oilfield geologists involved in CO₂ injection operations, was the increased porosity and permeability obtained. This is due to the dissolution of carbonate cements and possibly feldspars in most sandstone reservoirs. In nearly all cases scale problems were experienced as a result of previous water-flooding operations prior to CO₂ injection. However, once CO₂ injection was initiated it was generally found that the build-up of carbonate and sulphate scales decreased rapidly in production wells. Where scale build-up was still a problem it was considered by the field managers that this was due to previous water-flooding. Even during water-alternating-gas (WAG) operations scale build-up was not considered a problem. In some cases, it is now thought more beneficial to initiate CO₂ injection before waterflooding, as opposed to after secondary recovery is complete. Some predictions suggest that over the life of an oilfield more oil would be obtained in this manner. However, due to the historical nature of oilfields in Texas and the relatively new CO₂ EOR procedure this had not been tried on a large scale.

One problem encountered was in a very old field that had been producing since the early part of this century. In this field, which was at relatively low temperatures (~65°F) severe and insurmountable problems were experienced with the precipitation of solid asphaltenes. This is because the crude oil present within the field is unusually heavy. Although CO₂ is not miscible with crude oil when injected above the minimum miscibility pressure (MMP) it becomes miscible with the light hydrocarbon fraction, up to C₁₂ (Taber, 1993). The process of multiple-contact miscibility, whereby hydrocarbon-enriched CO₂ repeatedly comes into contact with fresh reservoir oil results in progressively heavier crude oil remaining and the

precipitation of asphaltenes. These solid products significantly reduce porosity around production wells and the rate of production decreases. No solution to this problem has been found.

Due to the age of most of the oilfields and the injection wells within them, it was generally considered that most wells were now open-hole, i.e. any casing material originally present had completely corroded away. All pipelines for the CO₂-injection system were made of plastic piping obtained routinely through normal suppliers. In new injection wells resin-lined steel casing was used since the great depths to the reservoirs prevented plastic or asbestos being used as it is unable to support its own weight.

When questioned, most field operators thought it would be technically feasible to create artificial reservoirs of CO₂ in Europe, including the North Sea, for future use in EOR operations if the price of oil and declining production make it economic.

CO₂-reservoir interactions have also been studied using fluid chemistry data in order to understand potential scaling problems (Smith, 1993). Dissolution of carbonates occurred during injection of gaseous CO₂ (12 000 psi) and heat into a Tensleep Formation reservoir in Wyoming. Injection and oil production were from the same well with the well being sealed for a month between to allow equilibrium to be achieved. Scale build-up was significant during this process, mainly carbonates and sulphates. No solid samples were examined and so no evidence was obtained for the precipitation of phases within the reservoir itself. Apart from high Ca and Mg in solution, high concentrations of most major cations were also observed, most notably Al and Si. No evidence was found for precipitation of Al and Si as any solid phases such as clays. The formation of scales was attributed to the pressure drop during production

7.5.4 Core Research Centre, USGS, Denver

Core material has been obtained from some of the lithologies in which CO₂ reservoirs are located in the United States. However, no actual material from these fields was available. Core material from six wells were examined and logged graphically at the Core Research Centre and a total of 22 samples were taken for petrographic and mineralogical analysis. Samples are listed in Table 7.24.

7.5.5 The Bravo Dome field as analogue for hydrothermal experimentation and CO₂ disposal

The reactions observed in the hydrothermal experiments performed in this study can also be invoked to explain the later diagenetic history of the Permian Wolfcampian-Leonardian Tubb Sandstones of the Bravo Dome CO₂-field. Detailed comparisons are possible between the reacted Sherwood Sandstone samples from the hydrothermal experiments and the Tubb Sandstones because both are continental red bed sandstones with similar detrital mineralogies. Reactions observed in the hydrothermal experiments were principally dissolution of dolomite, feldspars and anhydrite with secondary precipitation of halite, illitic and possibly smectitic clay (although the latter was only very tentatively identified). The possible precipitation of calcite was controversial. Similarly, the Tubb Sandstone in the Bravo Dome has been subjected to dissolution of early anhydrite, dolomite and detrital plagioclases (Nelis, 1994). This dissolution occurred as a result of reaction with acidic groundwaters which Nelis (1994)

attributed to the introduction of dissolved CO₂ possibly via Early Pennsylvanian and/or Tertiary faults. In addition, the CO₂ in the Bravo Dome field is regionally underpressured whereas the underlying aquifers are at normal geopressures, suggesting that a pressure difference is being maintained. Although the reasons for this are not known it has been suggested (Broadhead, 1994) that a diagenetic seal may be preventing equilibration. The precipitation of halite and calcite, as seen in some of the hydrothermal experiments, may contribute to this seal. However, it must be stressed that there is no geological evidence for this in the Bravo Dome.

The Cimmarron Anhydrite forms an effective seal for the CO₂ in the Bravo Dome area, despite evidence for anhydrite cement dissolution both in the Tubb Sandstone and in the Sherwood Sandstones. The conclusions from the anhydrite batch experiments were that the addition of CO₂ had a negligible effect on the dissolution of anhydrite (see section 7.4.2.3.). Hence, it appears unlikely that an evaporite seal would be breached.

No kaolinite, laumontite or gibbsite was observed during the hydrothermal experiments, though these do form late-stage cements in the Bravo Dome field. The occurrence of these minerals indicates reaction with acidic groundwaters such as those that would develop during the introduction of CO₂ into the field. Further evidence for their association with CO₂ interaction is their apparent spatial proximity to Tertiary faults through which the CO₂ may have migrated. The precipitation of these minerals will most likely cause a decrease in the permeability of the aquifer.

Hence the Bravo Dome CO₂ field may be regarded as being at a more advanced stage of reaction than the hydrothermal experiments. As such, it could be studied further to help predict likely longer term reactions that are difficult to simulate during laboratory-scale experiments. It could also provide useful information on porosity and permeability changes that may occur in aquifers used for CO₂ storage.

7.5.6 Acknowledgements

Herb Wacker & staff, Amoco. Joe Studlick, Roger Shew, Shell. Ron Broadhead, New Mexico Bureau of Mines and Mineral Resources. Staff at Core Research Centre, USGS, Denver, US. Tony Milodowski and Dave Jones for core supply.

7.6 RESERVOIR-WIDE PREDICTIONS

Deep-seated aquifers are of two main types, carbonate aquifers and sandstone aquifers. Both types of aquifers could be potential host formations for CO₂ disposal. However, as previously noted by Gunter et al. (1993), their chemical response to reaction with CO₂ will be very different due to their different mineralogical make-up. In order to assess the main trends of chemical reactions for each type of reservoir, a typical carbonate reservoir and a typical sandstone reservoir have been selected.

The Dogger aquifer in the Paris basin was chosen to be representative of a carbonate formation. The two main minerals within it are calcite and a disordered dolomite. In the selected area of the formation, the salinity of the formation water is about 0.4 molar NaCl, while the reservoir temperature is 78°C and depth is 1600 m. An oil-bearing reservoir from the North Sea was chosen to be representative of a sandstone formation. Six minerals were considered important for the calculations; quartz,

Table 7.24 Samples investigated during the study of the Bravo Dome CO₂ field.

Operator	Well Name	Location	Depth	Formation	Sample description
Hamon Jake	#8-1 USA Federal	Emery Co., Utah	5091'2"	Coconino	Light grey green, very fine grained limestone with pyrite patches up to 1 mm across. Muddy flakes?
			5097'7"	Coconino	Mottled limestone with dark grey cores as rounded irregular patches and pale green outer zones. Pyrite patches up to 10 mm across.
			5111'6"	Coconino	Massive limestone with hydrocarbon speckling. Spotted with lighter grey, slightly coarser matrix.
			5132'8"	Coconino	Parallel, irregular lamination on 1–2 mm scale, dark grey limestone.
			5165'5"	Coconino	Massive, light grey limestone — typical lower core.
Energetics Inc.	41X-11 Federal	Emery Co., Utah	3375'8"	Kaibab	Conglomerate with chalky limestone clasts 7–30mm in diameter. Clasts have corroded edges and are occasionally vuggy. Enclosed in limestone with dark grey, irregular laminae.
			3377'6"	Kaibab	Pale grey, recrystallised limestone speckled with dark grey limestone, black h/c and/or clay.
Energetics Inc.	23X-7 Federal	Emery Co., Utah	~3028'	Kaibab	Fine grained, massive limestone with dark brown colour due to extensive hydrocarbon staining.
			~3066'7"	Kaibab	Dark brown to black, heavily h/c. stained limestone, porous with pores 2.5–1.5f. Occasional vuggy 2° pores are lined with vitreous bitumen.
			~3086'	Kaibab	Pale grey limestone with stylolite. Occasional secondary vugs are lined with vitreous bitumen.
Brownlie Wallace ET.	4-1 Orangeville Federal	Emery Co.,	~8407'2"		
			84037'3"	Kaibab	Pale grey very fine grained, recrystallised limestone with samples taken from well developed stylolite, mineralised by pyrite and ?h/c. Stylolite forms around calcite nodules.
			~8410'6"	Kaibab	Pale grey, massive limestone with speckled, vitreous h/c. mineralisation.
			~8418'	Kaibab	Mottled dark grey and light grey limestone with unusual steep angle bands of light grey limestone. H/c. staining well developed.
			~8425'	Kaibab	Very fine grained limestone with extensive pyrite mineralised muddy layer, h/c mineralised.
Rainy River	Utah State #1-2	Emery Co., Utah	1460'10"	Sinbad	Parallel laminated limestone with extensive pyrite in ~1 mm thick layers. H/c. mineralisation
			1461'	Sinbad	Recrystallised limestone, saccharoidal texture with 20–30% porosity. Extensive pyrite and h/c.
			1462'11"	Sinbad	Porosity ~50%, limestone stained orange brown by iron oxides from pyrite oxidation. Fresh pyrite in laminae associated with h/c.
			1464'9"	Sinbad	Cross-stratified limestone stained patchily orange brown by iron oxides. H/c is ~10%. No pyrite
			1466'7"	Sinbad	Limestone with orange Fe oxide stained bands.
			1476'9"	Sinbad	Pale grey, very fine grained limestone with unusual "deformation" structures.
			1477'2"	Sinbad	Orange-brown stained, recrystallised limestone with ~50% 2° porosity and much shell debris.
			1477'5"	Sinbad	Relatively coarse, recrystallised limestone stained with iron oxide and h/c. Reduced shell debris. Pyrite with iron oxide and h/c.

potassium and sodium feldspars, kaolinite, illite and calcite. The salinity of the formation water is about 0.7 molar NaCl, while the reservoir temperature is 98°C and depth is 2500 m.

The chemical response of both aquifers to CO₂ injection was assessed by combining two modelling approaches. The first was based on purely geochemical modelling. For this, the reservoir was assumed to be a closed system into which increasing amounts of CO₂ were progressively added. The results of the calculations, carried out at thermodynamic equilibrium, should highlight the final geochemical state of the reservoir depending on the particular partial pressure of CO₂ attained. Such an approach should give long term predictions of the behaviour of both types of reservoir once CO₂ injection has ceased. The second approach was based on coupled single phase reaction-transport modelling and concerned the injection period itself. Such an approach should highlight the time-dependent evolution of mineralogical transformations along a flow path where all the injected CO₂ is assumed to dissolve entirely and instantaneously into the formation water. This situation is applicable to the injection of CO₂ into large deep aquifers which have no structural traps but having low regional flow, what Gunter et al. (1993b) and Bachu et al. (1994) referred to as 'hydrodynamic trapping'. This situation would also represent processes occurring at the periphery of the storage volume, outside the two-phase region.

7.6.1 PREDICTIONS Based on geochemical considerations

Calculations were carried out with the CO₂ROCK simulator (see section 7.3.2.1.) with two sets of operating instructions. The first was dedicated to the Dogger carbonate formation. The masses of silicate and aluminosilicate minerals were set to zero, the temperature set at 78°C, the pressure was assumed to be 160 bar (16 MPa, corresponding to a depth of 1600 m), and the CO₂ fugacity coefficient was set to 0.59 (at 78°C, 160 bar). The second was dedicated to the North Sea sandstone formation. The mass of dolomite was set to zero, the temperature set at 98°C, the pressure was assumed to be 250 bar (25 MPa, corresponding to a depth of 2500 m), and the CO₂ fugacity coefficient was set to 0.56 (at 98°C, 250 bar).

Initially, prior to injection, both reservoirs were assumed to have thermodynamic equilibrium between the formation fluid and the selected minerals. Injection was simulated by adding increasing amounts of CO₂ from the SC CO₂ phase into the water phase. In these calculations, the reservoirs were assumed to be closed systems, normalised to 1 kg of water, with all homogeneous and heterogeneous chemical reactions occurring at thermodynamic equilibrium.

Figures 7.45 to 7.47 compare the trends in the main chemical variables for both types of reservoir. Assuming that dissolved gases, except CO₂, are negligible in the formation water, the maximum amount of CO₂ that will be

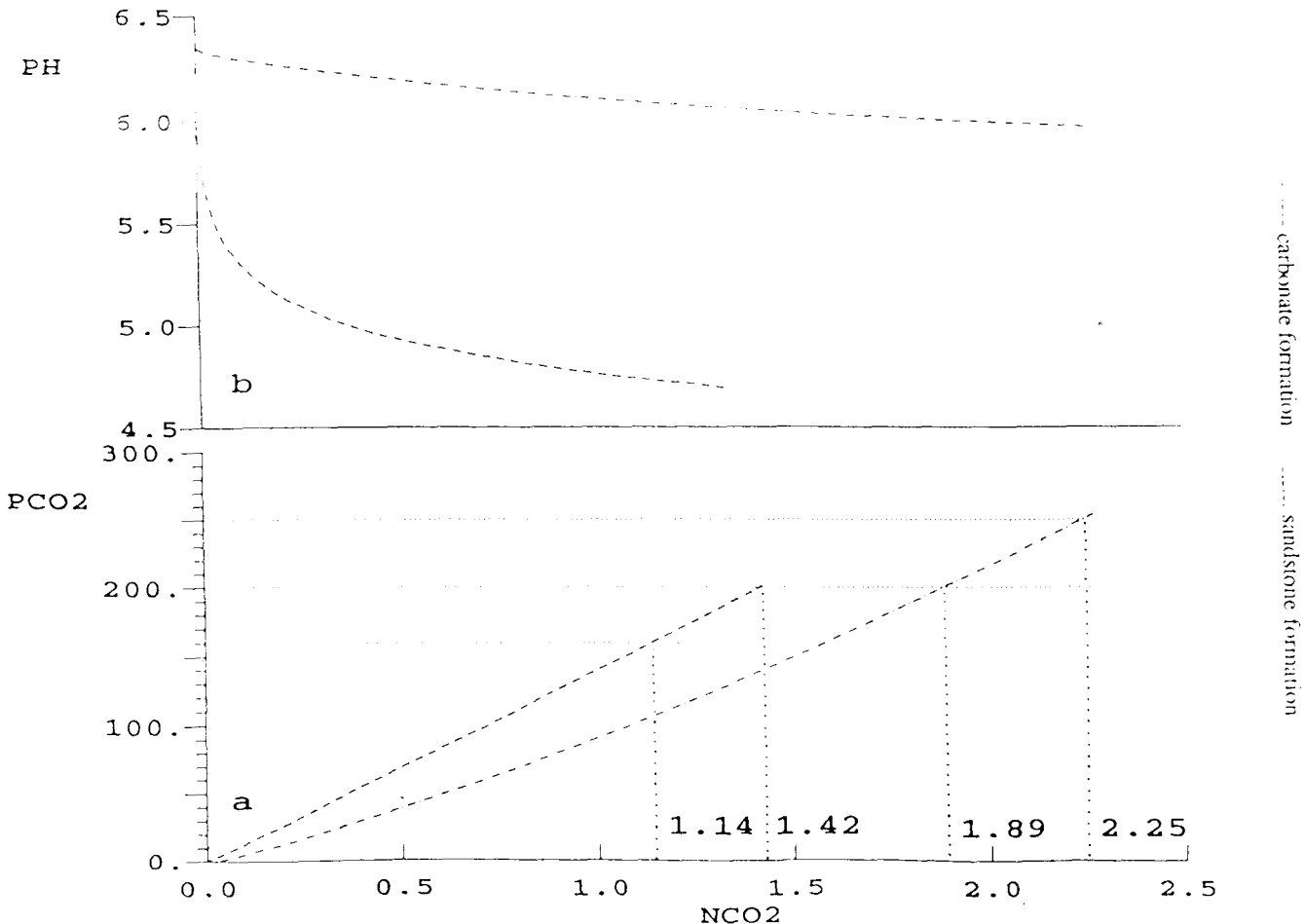


Figure 7.45 Variation in CO₂ partial pressure (PCO₂, bar) and pH with the number of moles of CO₂ added into a carbonate and a sandstone formation, normalized to 1 kg of solvent water.

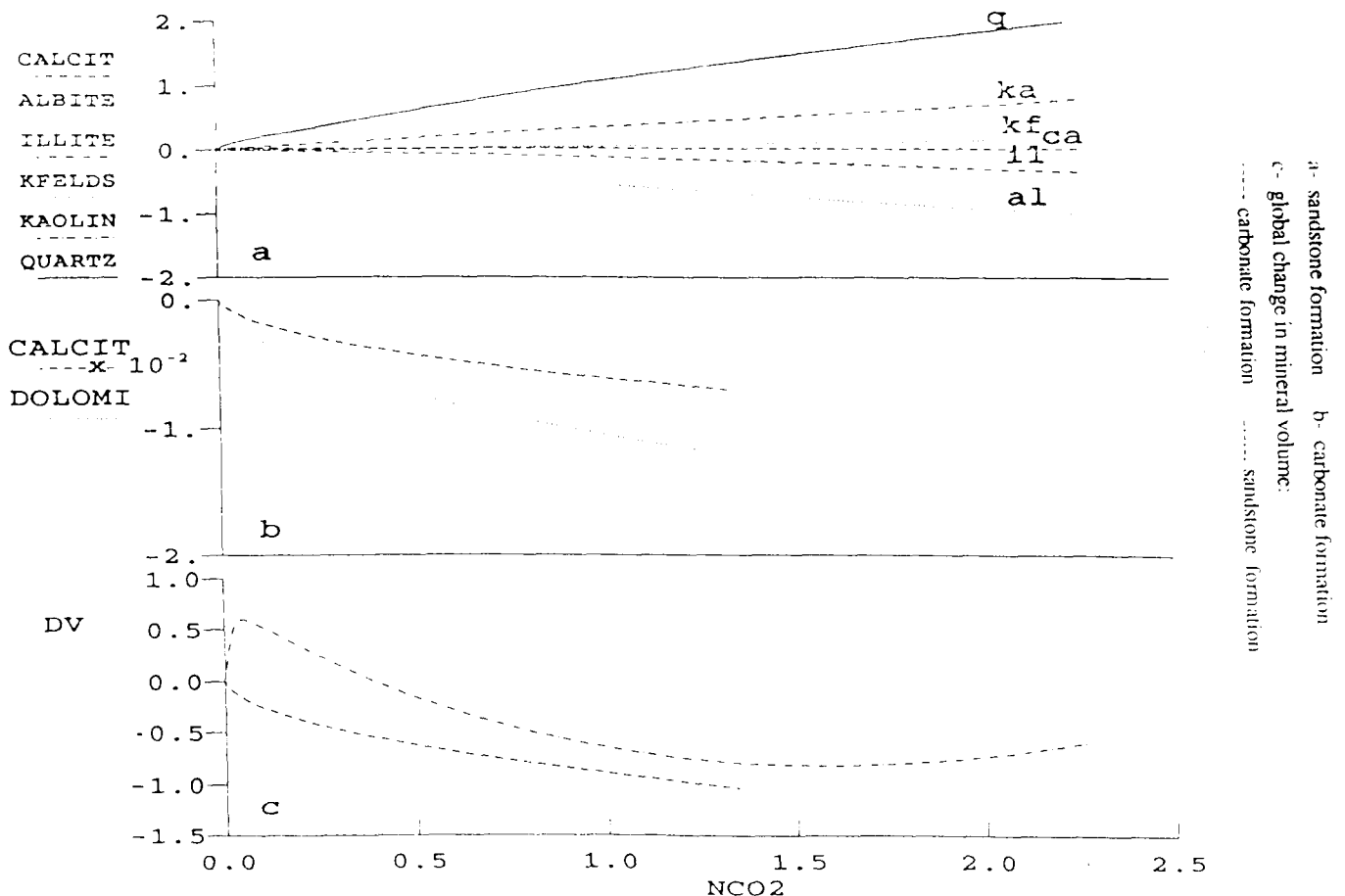


Figure 7.46 Changes in the numbers of moles of minerals and in mineral volume (DV, cm³) with the number of moles of CO₂ added into a carbonate and a sandstone formation, normalized to 1 kg of solvent water.

taken up by the formation water and mineral reactions will be reached when the partial pressure of CO₂ equals the formation pressure. This maximum amount is equal to 1.14 mol.kg⁻¹ H₂O or 50 g of CO₂ per kg H₂O in the case of the carbonate formation (78 °C, 160 bar, 0.4 M NaCl). Similarly, it is equal to 2.25 mol.kg⁻¹ H₂O or 100 g CO₂ per kg H₂O in the case of the sandstone formation (98 °C, 250 bar, 0.7 M NaCl). Without mineral reactions, the corresponding CO₂ solubility in water is 1.12 mol.kg⁻¹ H₂O or 49 g CO₂ per kg H₂O for the carbonate formation, and 1.31 mol.kg⁻¹ H₂O or 58 g CO₂ per kg H₂O for the sandstone formation.

Clearly, from a chemical thermodynamics standpoint, the sandstone reservoir would have a better storage capacity than the carbonate reservoir. This is surprising since the higher temperature and salinity of the sandstone reservoir should limit the dissolution of CO₂ into water, because CO₂ solubility decreases with increasing temperature and salinity. The higher pressure of the sandstone formation is not sufficient to explain the difference of behaviour between both types of reservoir. For instance, Figure 7.45a shows that if both reservoirs were at 200 bars pressure, the maximum amount of trapped CO₂ would have been 1.42 mol.kg⁻¹ H₂O or 62 g.kg⁻¹ H₂O for the carbonate reservoir, and 1.89 mol.kg⁻¹ H₂O or 83 g.kg⁻¹ H₂O for the sandstone reservoir. The explanation for these differences between carbonate and sandstone reservoirs lies in their different mineral reactions.

The complex set of mineral reactions in the sandstone formation (Figure 7.46a) has a greater buffering capacity

(Figure 7.45b) and favours the dissolution of CO₂. For this rock type all the injected CO₂ is distributed among aqueous CO₂, bicarbonate ions and bicarbonate complexes (Figure 7.47a). The uptake of CO₂ in mineral form is negligible as only very small amounts of calcite precipitate until there is no dissolved calcium left in the formation water. Conversely, the carbonate reservoir has a low buffering capacity. The solution of CO₂ into water causes the dissolution of carbonate minerals and a decrease in pH (Figures 7.46b and 7.45b), resulting in an increase in the dissolved calcium content of the fluid. Such mineral reactions do not significantly increase CO₂ uptake. Nearly all the injected CO₂ is converted into aqueous CO₂ (Figure 7.47b).

The balance between the molar volumes of product and reactant minerals (from data available at 25 °C in the DATA.COM.R10 database of EQ3/6) shows that the porosity of both reservoirs tends to increase when CO₂ is injected (Figure 7.46c).

7.6.2 PREDICTIONS Based on coupled chemistry and transport considerations

Coupled modelling was carried out in order to investigate how the front of dissolved CO₂ and chemical reactions would propagate within an open reservoir during injection operations. Limitations of the modelling were: i) mineral reactions were considered to occur at thermodynamic equilibrium, ii) the injection rate of pure CO₂ was assumed to be low compared to regional flow, so that all the injected

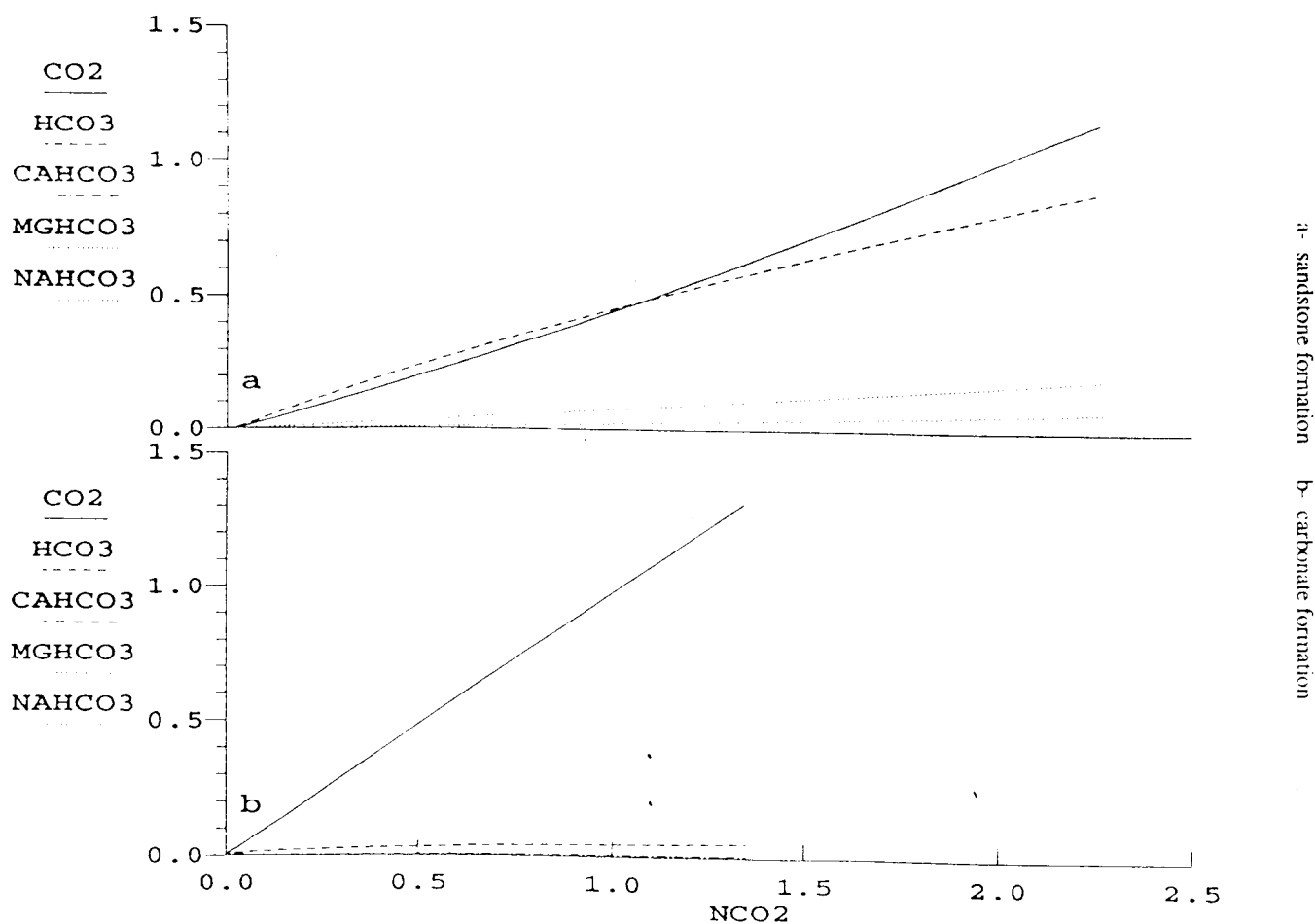


Figure 7.47 Aqueous distribution of carbonate species ($\text{mol.kg}^{-1} \text{H}_2\text{O}$) with the number of moles of CO_2 added into a carbonate and a sandstone formation, normalised to 1 kg of solvent water.

CO_2 would be able to dissolve instantaneously in the formation water and not disturb the regional flow.

The simulations focus on the typical North Sea sandstone aquifer. As well as the previous mentioned characteristics (6 basic minerals, 98°C , 250 bar, 0.7 M NaCl), the porosity was assumed to be 14.1%. The regional darcy flow was set to 1.1 m per year, which is considered a representative value for open aquifers. It also corresponds to the darcy flow of the core flooding experiment with water saturated with CO_2 . Two cases were considered for the calculations:

- Case A — There are sufficient quantities of all 6 basic minerals within the aquifer to ensure that none of them will completely dissolve during the calculations.
- Case B — The quantities of the 6 basic minerals within the aquifer correspond to actual values for this aquifer, i.e. 86.2% Quartz, 5.9% K-feldspar, 0.6% Albite, 3.5% Kaolinite, 1.3% Illite, 0.5% Calcite and 2.0% minor minerals (not considered in this modelled system).

Calculations were carried out with the CATCO₂ single phase reaction-transport code (see section 7.3.2.2.). One-dimensional transport of CO_2 was simulated from the point of injection to 150 m down the regional flow path. This

portion of the reservoir was divided into 20 cells of 7.5 m long and 4.5 m wide. Pure CO_2 was injected at a flow rate of 2.76 kg CO_2 per day (1007.4 kg per year). This was the maximum injection rate that ensured that all the injected CO_2 dissolved in the formation water (given the regional flow), as the solubility of CO_2 in such a reservoir was 1.31 moles CO_2 per kg H_2O (see section 7.6.1.). The time step was 350.7 days and was calculated so that the Courant number is equal to 1. The dispersivity was set to 1 m.

The results of the calculations for Case A and Case B are presented on Figures 7.48 to 7.56. Profiles are given along the 20 grid blocks as a function of the number of iterations which are directly related to the elapsed time from the beginning of injection. Figures 7.48a and 7.51a show the progression of the front of dissolved CO_2 and the corresponding increase in CO_2 partial pressure. Figures 7.49 and 7.52 to 7.54 describe the variations of the number of moles of each mineral in comparison with the numbers of moles initially present in the aquifer. The resulting overall change in mineral volume lead to variation of porosity as shown in Figures 7.50a and 7.56a. The evolution of pH is represented in Figures 7.50b and 7.56b.

Case A agrees with previous calculations for a closed system (see section 7.6.1). The set of mineral reactions acts as a buffer that maintains the pH at 6.07 and the partial pressure of CO_2 at the maximum level of 130 bars. Given the limitations of the model, this means that higher CO_2 injection rates could be operated in order to reach the

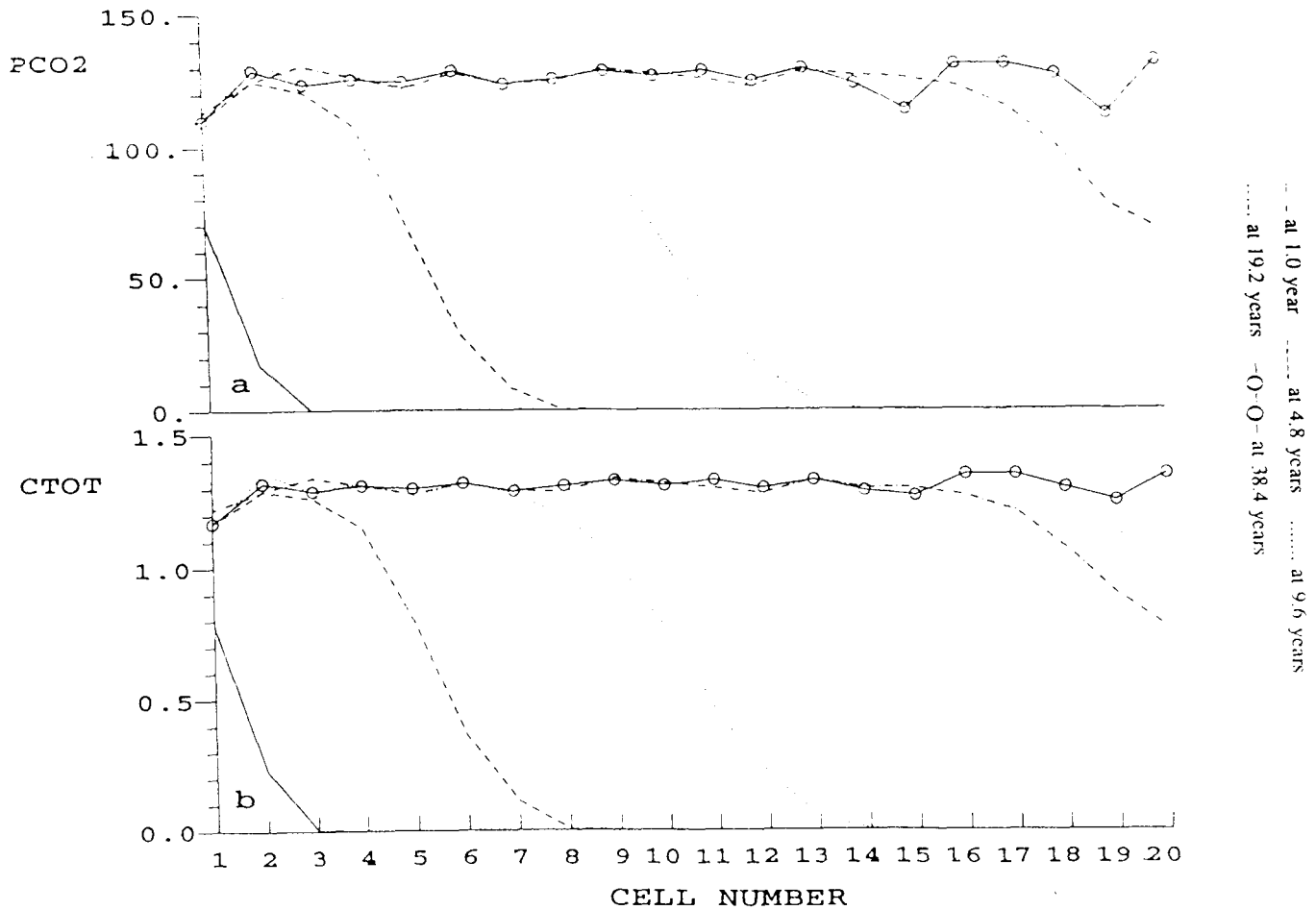


Figure 7.48 Progression of the fronts of CO₂ partial pressure (PCO₂, bar) and total dissolved carbon (CTOT, mol.kg⁻¹ H₂O) during injection of CO₂ into a sandstone formation — Case A (see text).

maximum allowed partial pressure, equal to the aquifer pressure (250 bar) if no other dissolved gases were present. However, in order to ensure that a supercritical CO₂ phase will not form, the rates of mineral reactions have to be investigated because they will effect the efficiency and reaction time of the buffer system. The constant values reached behind the chemical front by CO₂ partial pressure, pH and dissolved CO₂, are in agreement with the calculations carried out for a closed system (see section 7.6.1.). However, the scale of mineral reactions and the increase in porosity are far more important since the system is open. Aquifer porosity increased from 14.1% up to 14.3% in the injection zone. Simulations were carried out for a period of 38.4 years (40 iterations), after which all of the selected portion of the reservoir was in a stationary state whilst the chemical front was moving farther out in the reservoir. During this period of time, about 39 tonnes of CO₂ were injected into the reservoir. They were distributed quasi-exclusively between aqueous CO₂ and bicarbonate ions.

With Case B, the situation was very different because albite, followed by illite, completely dissolved. Here the 'buffering system' was modified and was far less efficient. The final value of pH at the stationary state was 5.0. The partial pressure of CO₂ reached 230 bars, which was slightly below the reservoir pressure. This meant that in this case mineral reactions barely enhance the CO₂ storage capacity of the reservoir. As shown on Figure 7.55, the

front of albite removal was ahead of the front of illite removal. The region between these two fronts was a transition zone between a forward zone where illite precipitated and kaolinite/K-feldspar dissolved, and a back zone with progressive removal of illite and consequent kaolinite/K-feldspar precipitation. The overall trend in aquifer porosity was a reduction from 14.10% to 14.01%. The front of dissolved CO₂ was slightly ahead the pCO₂ front because bicarbonate ions and complexes account for 35% of the dissolved CO₂. However, behind the chemical front aqueous CO₂ represents nearly all of the dissolved CO₂. Simulations were carried out for a period of 48 years (50 iterations), after which all of the selected portion of the reservoir was in a stationary state while the chemical front was moving farther out in the reservoir. During this period of time, about 48 tonnes of CO₂ were injected into the reservoir and were in the form of aqueous CO₂ only.

7.7 CONCLUSIONS-RECOMMENDATIONS

In order to assess the technical feasibility of the underground disposal of carbon dioxide, it was necessary to investigate in detail the chemical reactions between CO₂, formation water and reservoir rocks. The main issues were to study whether such reactions could; enhance the storage capacity, guide the design of the storage operations, or

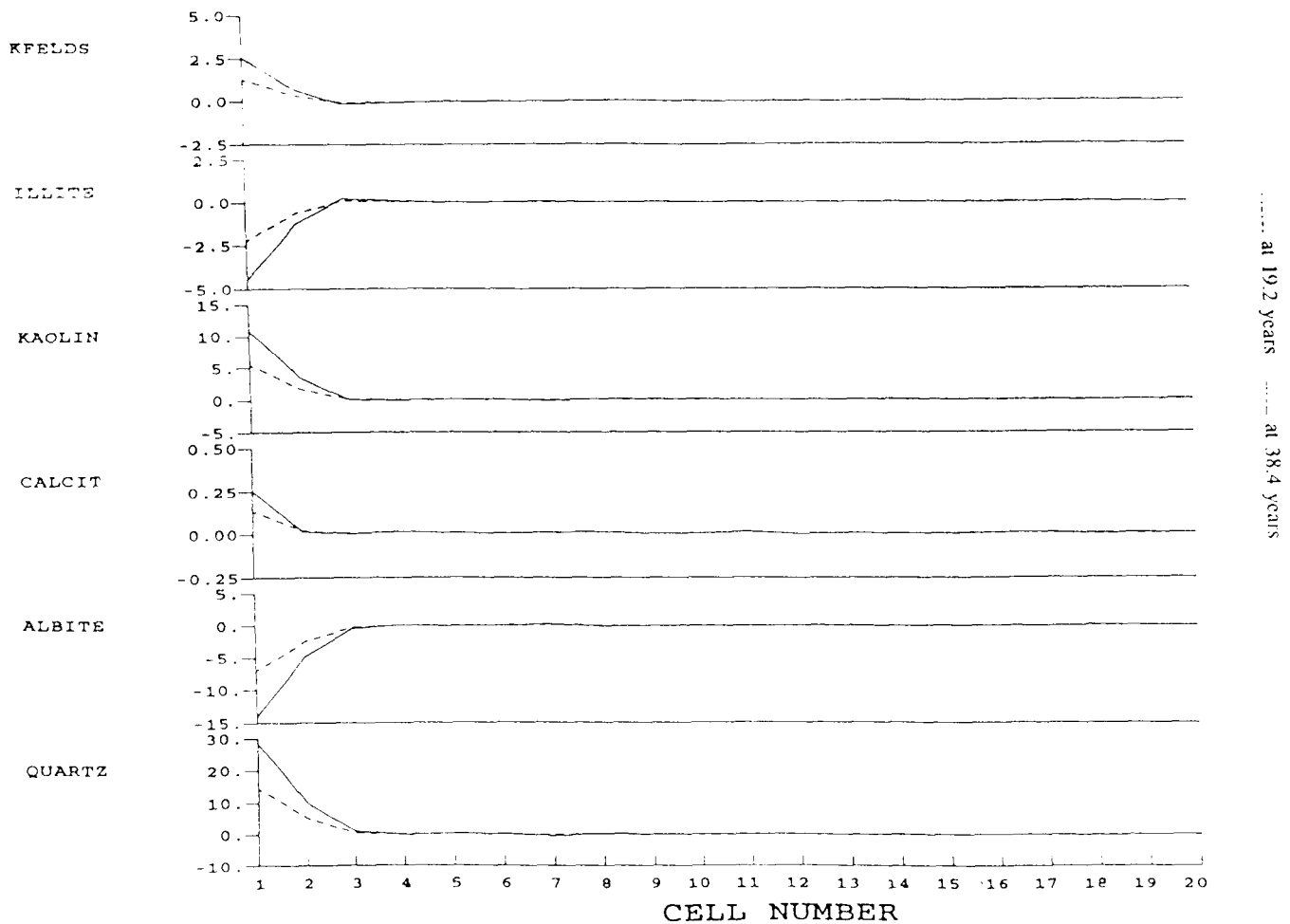


Figure 7.49 Changes in the numbers of moles of minerals during injection of CO₂ into a sandstone formation — Case A (see text).

have consequences on the safety and stability aspects of disposal sites. Laboratory experiments and numerical modelling, combined with an extensive literature review, led to the following conclusions.

Dissolution of CO₂ into formation water

CO₂ will dissolve very rapidly into formation water up to the mean value of approximately 50 g CO₂ per kilogram of water in the temperature range of 30–100°C. However, this is a mean value and may vary by 50% depending on temperature, pressure and salinity of the formation water. The amount of CO₂ able to dissolve into the formation water is proportional to increasing pressure, but inversely proportional to salinity. This effect is much more pronounced above 100°C. The pH of the formation water will decrease as a consequence of CO₂ dissolution, but this effect will be in part buffered by mineral reactions.

Theoretical calculations for a potential reservoir (dimensions: 100 km long, 5 km wide, 100 m thick; porosity: 10%) indicate that about 0.25 Gt of CO₂ could dissolve in the entire pore volume of the reservoir. This is a significant figure compared to the annual CO₂ emissions by power plants in Europe (see Chapter 4). Therefore, it could be beneficial for the injection operations to be designed in order to favour the dissolution of CO₂ into the entire reservoir. Several injection wells with low injection rates would be more efficient for this than a single injection well

with a high flowrate, due to the low volumetric sweep efficiency of CO₂ (see Chapter 4).

Mineral reactions

Two main types of deep-seated aquifers were investigated, carbonate aquifers and sandstone aquifers. Data based on chemical thermodynamics, the numerical simulations used in this study, as well as work by Gunter et al. (1993a,b), have shown that mineral reactions in carbonate formations would not significantly increase CO₂ uptake. However, such reactions would enhance the CO₂ storage capacity for a sandstone formation. The complex set of mineral reactions in a sandstone formation have a greater buffering capacity and favour the dissolution of CO₂ into water by the formation of bicarbonate ions and bicarbonate complexes. However, this process could be slow (though still fast on a geological timescale) as the efficiency and reaction time of the buffer system will depend on the reaction rates of aluminosilicate minerals, and might take several years or decades to achieve steady-state.

Disposal of CO₂ in carbonate formations

Although disposal in carbonate formations would be less efficient than in sandstone formations, the technical feasibility is easier to assess because the reactivity of the host formation is only controlled by carbonate minerals.

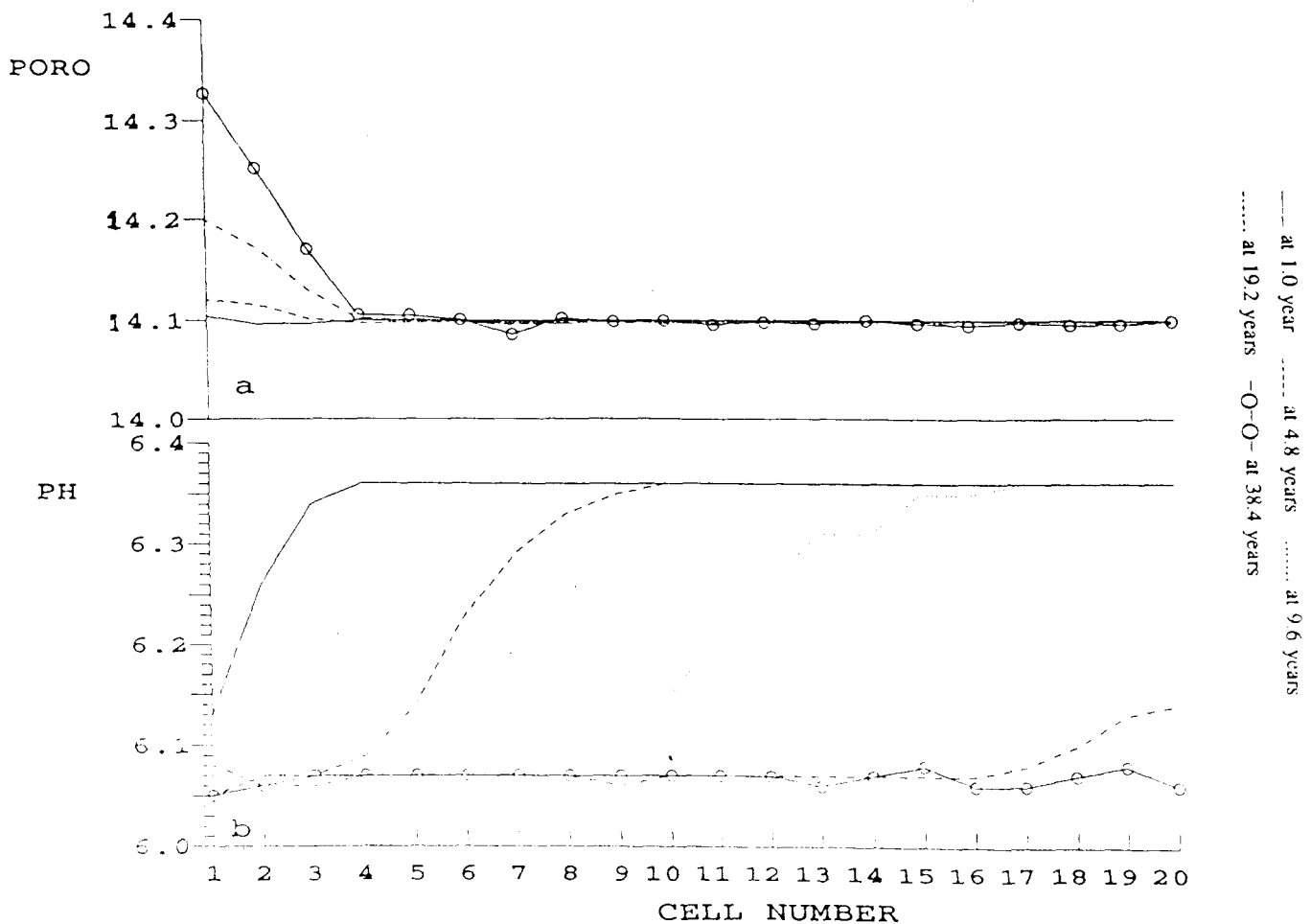


Figure 7.50 Variation of porosity (PORO, %) and pH during injection of CO₂ into a sandstone formation — Case A (see text).

Moreover, the reaction rates for such minerals are fast compared to silicate minerals and may only take hours or days to achieve steady-state.

Carbonate minerals will dissolve in the vicinity of the injection wells, with subsequent enhancement of porosity, permeability and injectivity. However, such minerals could precipitate farther away in the reservoir if the formation water, which has become saturated with respect to carbonate minerals, reaches zones of lower pressure or higher temperature. Temperature and pressure within the disposal site are thus crucial parameters to monitor in order to optimize the storage processes in carbonate formations.

Disposal of CO₂ in sandstone formations

Due to the variety and variability of mineral assemblages in sandstone formations, it is more difficult to give exact predictions for this type of reservoir. The chemical reactions that will take place in any host formation will be highly reservoir specific, and will depend on the mineralogy and physical nature of the rock, the temperature and pressure in the reservoir, flow rates and the timing of the reactions. However, general trends can be given.

Laboratory experiments and studies of natural CO₂ fields have shown that the injection of CO₂ into sandstone reservoirs would lead to the dissolution of feldspar grains, dolomite and anhydrite cements, and to the precipitation of clay phases. However, there was little evidence for calcite

precipitation, except where anhydrite was present. The present study has shown that a potentially large increase of CO₂ uptake through mineral trapping (calcite precipitation) could be achieved in sandstones rich in anhydrite cement. A similar mechanism would occur if the sandstone rocks contained Ca-feldspar, as proposed by Gunter et al. (1993a). However, host sandstone formations are unlikely to contain appreciable Ca-feldspar as this is readily altered during rock diagenesis. Anhydrite cement is more common in potential host sandstone formations. Formation waters rich in dissolved calcium could also favour mineral trapping. Further investigation would be required to confirm whether ion exchange reactions within clays could lead to calcite precipitation.

It appears from the data gained during enhanced oil recovery and from the core-flooding experiments that rock porosity should increase in the vicinity of the injection wells, with improvement of injectivity. This results from calcite and dolomite cements tending to dissolve initially, due to their higher reaction rates and their location along preferential flowpaths, which in turn depends on the texture of the rock.

Safety and stability aspects

The caprock properties of anhydrite and mudstone layers appear not to be significantly altered as a result of CO₂ injection. Laboratory experiments have shown that both

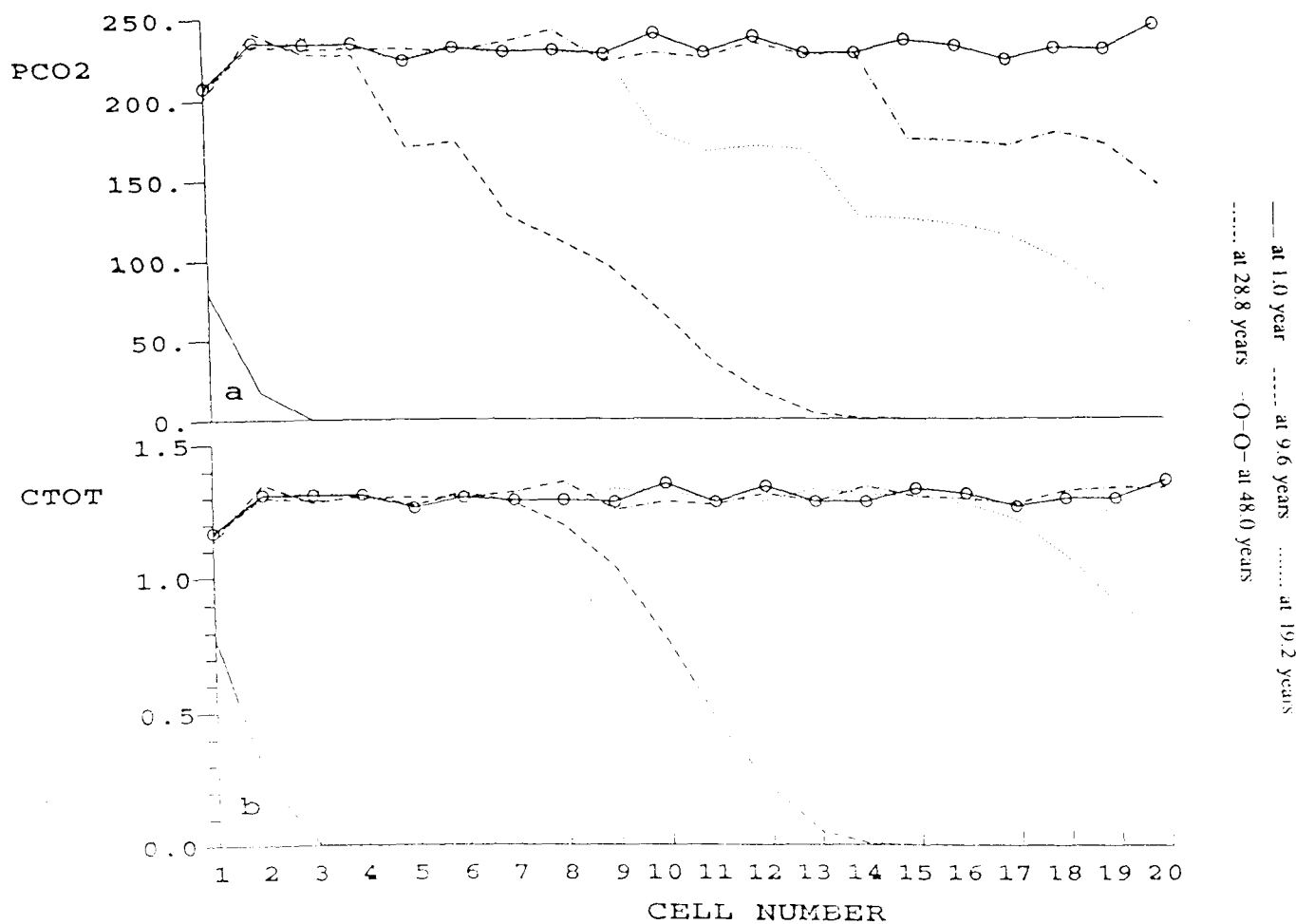


Figure 7.51 Progression of the fronts of CO₂ partial pressure (PCO₂, bar) and total dissolved carbon (CTOT, mol.kg⁻¹ H₂O) during injection of CO₂ into a sandstone formation - Case B (see text).

anhydrite and mudstone remained unaltered in contact with supercritical CO₂ alone. However, when in contact with CO₂-rich waters, laboratory experiments have revealed corrosion of the mudstone, or mudstone lenses included within anhydrite samples. However, it does appear that large CO₂-rich water/rock ratios would be needed to cause intensive alteration of the caprock. The presence of natural CO₂ fields in the US, together with large-scale enhanced oil recovery schemes using CO₂, suggest that the caprock properties of anhydrite and mudstones are not severely affected.

The underground storage of CO₂ may result in the mobilization of trace elements from residual oils or heavy minerals encountered in the reservoir, due to the complexing power of bicarbonate and thiocarbonate ions and to the solvent properties of supercritical CO₂. However, deposition of base metals is likely to occur at the edges of the reservoir due to CO₂ degassing when the pressure is reduced.

Perspectives

The present study has shown that large quantities of CO₂ are able to dissolve in formation waters, provided that CO₂ migration paths are not restricted to a limited part of the host formation, and that CO₂ could be trapped by calcite precipitation in sandstone formations containing anhydrite cements or Ca-rich formation waters. Thus, under these conditions, a structural trap would not be a prerequisite. According to the terminology used by Bachu et al. (1993)

and Gunter et al. (1993b), three mechanisms are available for the capture and long term storage of CO₂, i.e. structural trapping, hydrodynamic trapping and mineral trapping. Depending on the characteristics of the disposal site and on the quantities of CO₂ to be disposed of, these three mechanisms should be considered and possibly combined. Structural trapping would be useful if a part of the CO₂ was to be stored as a supercritical phase. Hydrodynamic trapping would be possible if most of the CO₂ was to be stored in a dissolved state when the extent and regional flow of the host aquifer allowed for long residence or travel times, in the order of thousands of years. Mineral trapping would ensure permanent storage and would only be possible in aquifers with very specific chemical and mineralogical characteristics.

Further investigations on the feasibility of underground disposal of CO₂ should be carried out on a site-to-site basis. Once a site has been preselected, laboratory experiments and numerical simulations should be undertaken by considering the specific mineralogical characteristics (nature and quantities of minerals, texture) of the reservoir rock, the chemical composition of the formation water, temperature, pressure, and flowrate of the formation water. Consideration of coupled phenomena including geochemical reactions, transport and single/two phase flow should enable the prediction of the storage capacity of the reservoir and optimisation of the design and operating conditions of the disposal operations for the selected site.

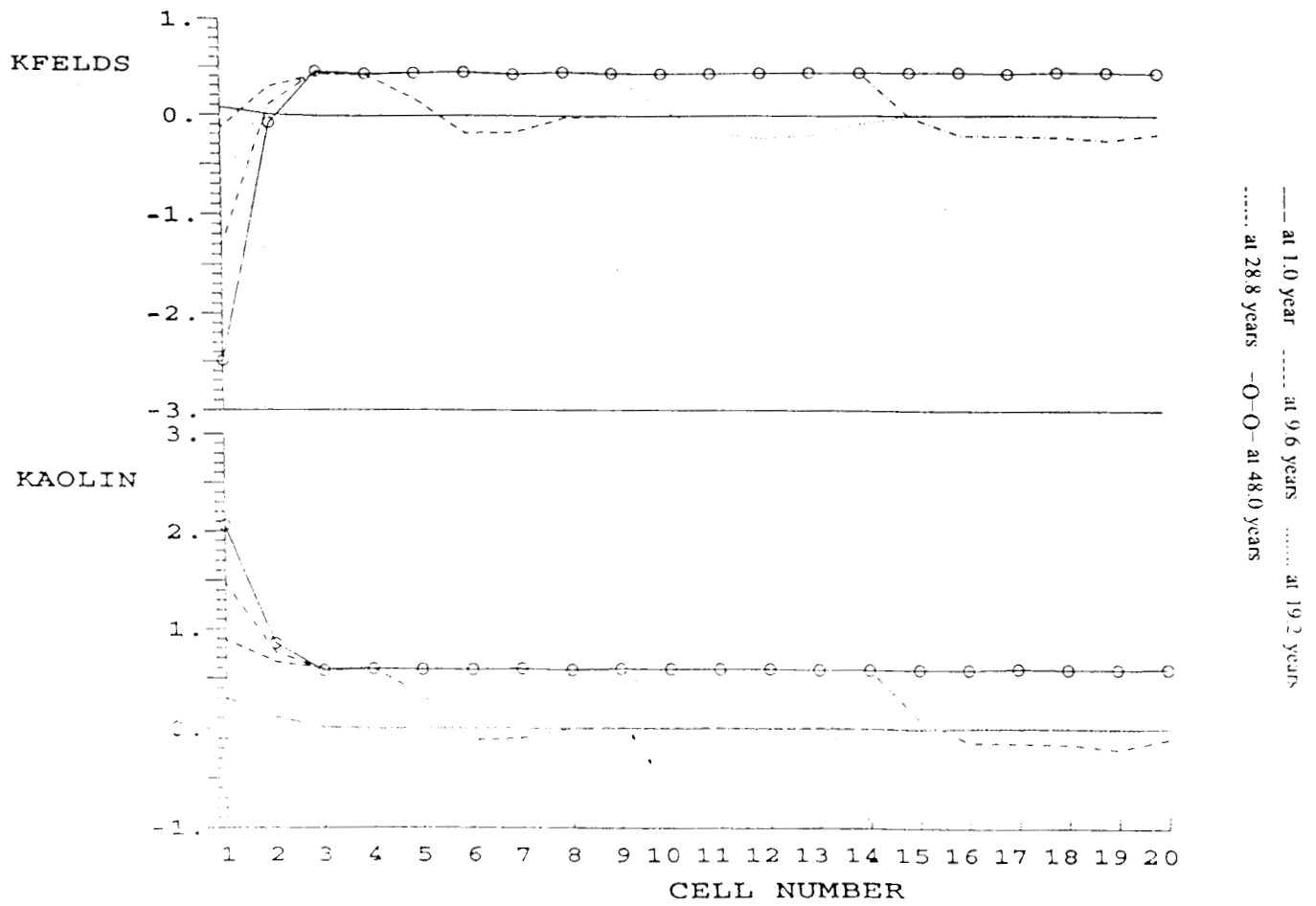


Figure 7.52 Changes in the numbers of moles of K-feldspar and kaolinite during injection of CO₂ into a sandstone formation - Case B (see text).

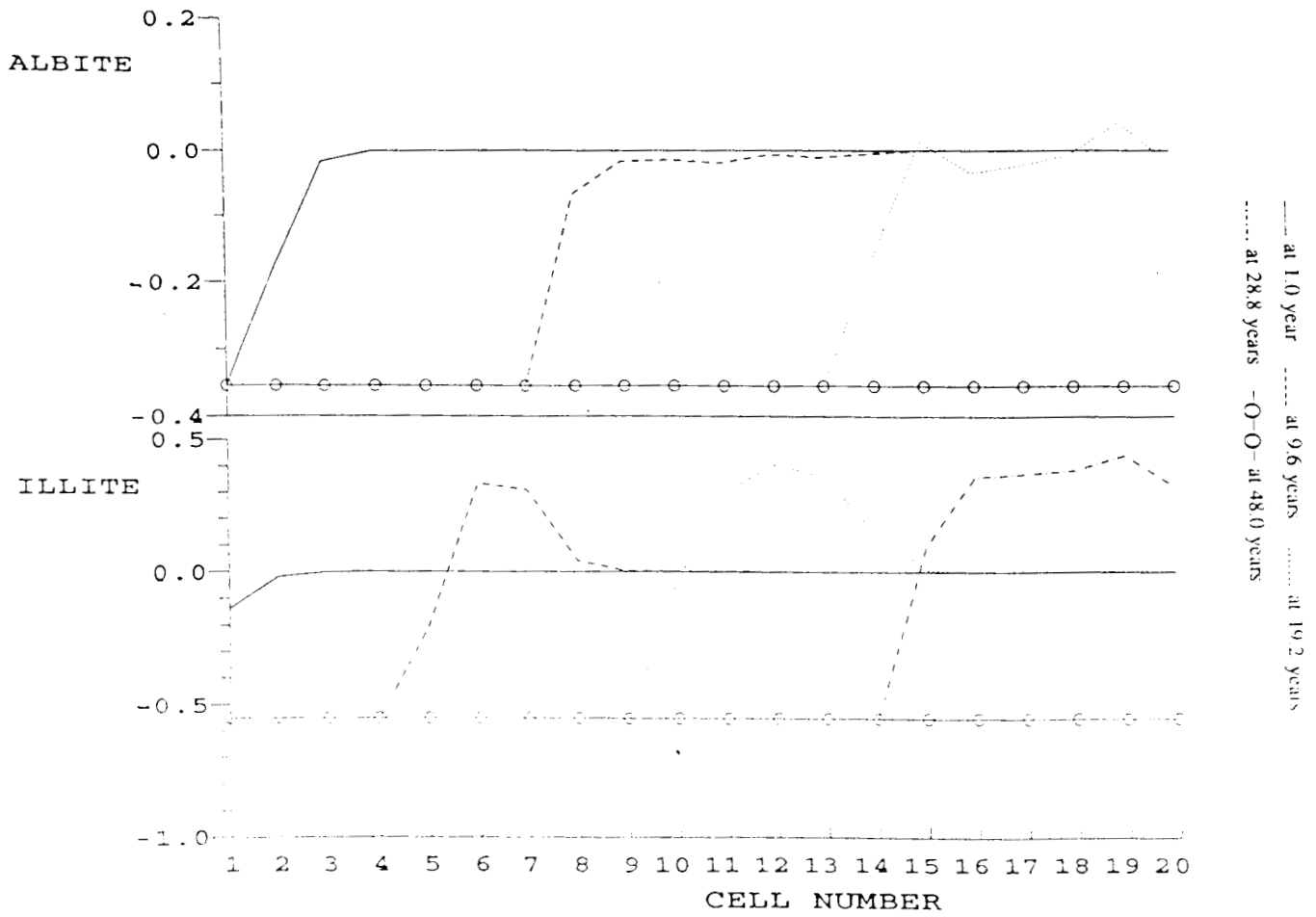


Figure 7.53 Changes in the numbers of moles of albite and illite during injection of CO₂ into a sandstone formation — Case B (see text).

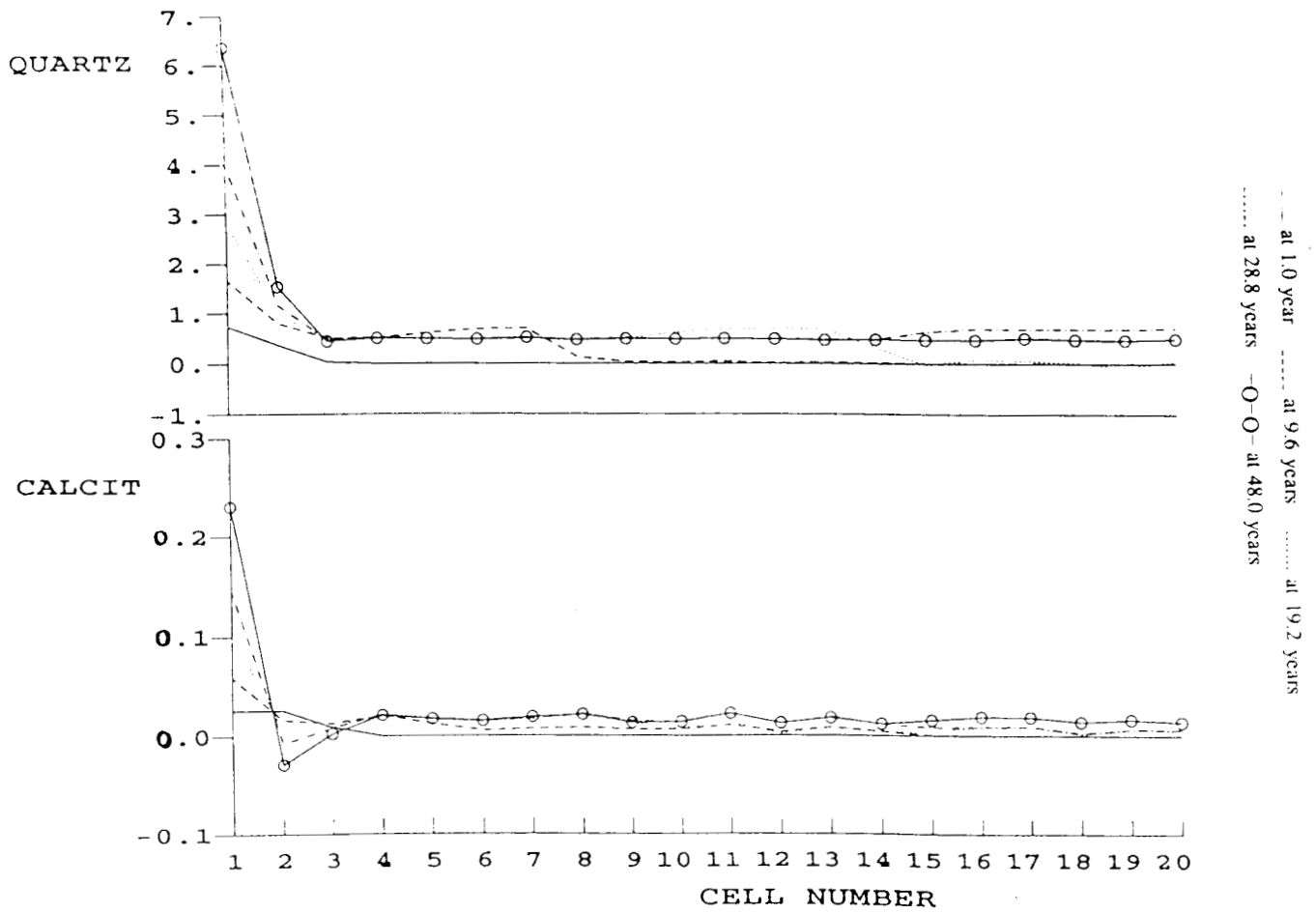


Figure 7.54 Changes in the numbers of moles of quartz and calcite during injection of CO₂ into a sandstone formation — Case B (see text).

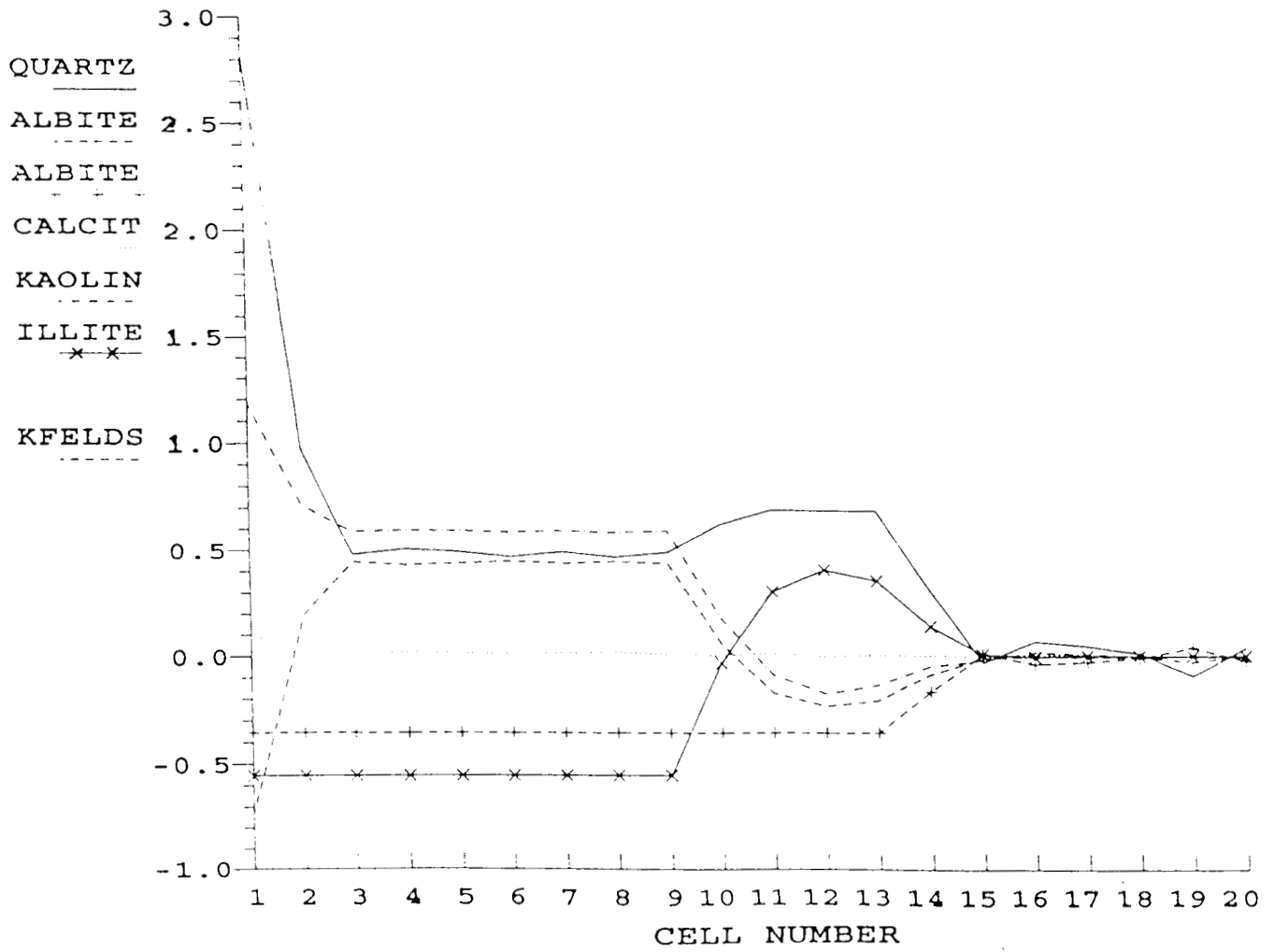


Figure 7.55 Changes in the numbers of moles of minerals at 19.2 years during injection of CO₂ into a sandstone formation — Case B (see text).

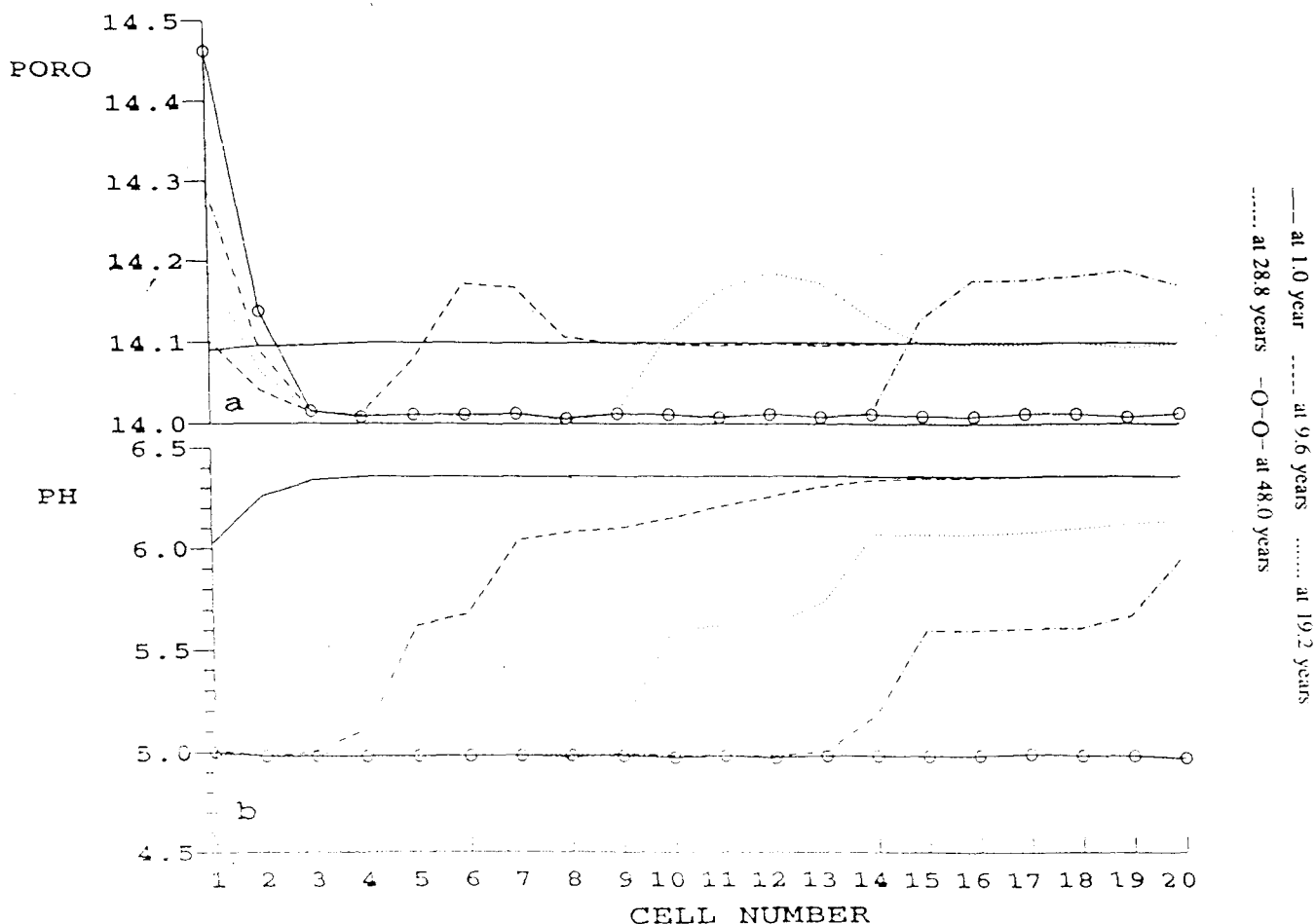


Figure 7.56 Variation of porosity (PORO, %) and pH during injection of CO₂ into a sandstone formation — Case B (see text).

7.8 REFERENCES

- ABBOTTS, I L. 1991. United Kingdom oil and gas fields, 25 years commemorative volume. *Geological Society of London Memoir*, 14.
- ANGINO, E E. 1984. Unconventional recovery of heavy oil and tar sands. In: "Exploration for heavy crude oil and natural bitumen" (R.F. Meyer, editor), *AAPG studies in geology*, 25, 603-643.
- AMOCO, P C. 1990. Bravo Dome Update — Carbon dioxide production in New Mexico. *Bravo Dome Operations Center, Amoco Production Company*.
- AZAROUAL, M. 1994. Modelisation des interactions solutions hydrothermales-granite, Application au futur echangeur geothermique de type roches chaudes seches de Soultz-sous-Forets, Alsace (France). These de Doctorat de l'Universite Paris VII, *Document du BRGM*, 232, 233p.
- BACHU, S, GUNTER, W D, and PERKINS, E H. 1994. Aquifer disposal of CO₂: hydrodynamic and mineral trapping. *Energy Convers. Mgmt.*, in press.
- BARTON, A F M, and WILDE, M M. 1971. Dissolution rates of polycrystalline samples of gypsum and orthorhombic forms of calcium sulphate by a rotating disc method. *Transactions of the Faraday Society*, 67, 3590-3597.
- BEN RHAJEM, H, TESSIER, D, and PONS, C H. 1986. Comportement hydrique et evolution structurale et texturale des montmorillonites au cours d'un cycle de dessiccation-humectation: Partie I. Cas des montmorillonites calciques. *Clay Minerals*, 21, 9-29.
- BEN RHAJEM, H, PONS, C H, and TESSIER, D. 1987. Factors affecting the microstructure of smectites: role of cation and history of applied stresses. *Proceedings of the International Clay Conference, Denver, 1985*, (L.G. Schultz, H. van Olphen, and F.A. Mumpton, eds.). The Clay Minerals Society, Bloomington, Indiana, 292-297.
- BLOOMFIELD, J P, and WILLIAMS, P J. 1994. Special study permeability and porosity results. *Technical Report, Hydrogeology Series British Geological Survey, WD/94/59C*.
- BLOUNT, C W, and DICKSON, F W. 1969. The solubility of anhydrite (CaSO₄) in NaCl-H₂O from 100 to 450°C and 1 to 1000 bars. *Geochim. Cosmochim. Acta*, 33, 227-245.
- BLOUNT, C W, and DICKSON, F W. 1973. Gypsum-anhydrite equilibria in systems CaSO₄-H₂O and CaSO₄-NaCl-H₂O. *Amer. Mineral.*, 58, 323-331.
- BOCK, E. 1961. On the solubility of anhydrous calcium sulfate and of gypsum in concentrated solutions of sodium chloride at 25°C, 30°C, 40°C and 50°C. *Can. J. Chem.*, 39, 1746-1751.
- BONDOR, P L. 1992. Applications of carbon dioxide in enhanced oil recovery. *Energy Convers. Mgmt.*, 33(5-8), 579-586. Pergamon Press, Oxford.
- BOWKER, K A, and SHULER, P J. 1991. Carbon dioxide injection and resultant alteration of the Weber sandstone, Rangely field, Colorado. *Bulletin of The American Association of Petroleum Geologists*, 75(9), 1489-1499.
- BRANTLEY, S L. 1992. Kinetics of dissolution and precipitation - Experimental and field results. In: *Water-Rock Interaction*, (Y.K. Kharaka and A.S. Maest, editors), Balkema, Rotterdam, 3-6.

- BRIGGS, C. C. 1978. *Ph.D. Thesis*, University of Sheffield, Sheffield, England.
- BROADHEAD, R. F. 1989. Bravo Dome CO₂ Field — U.S.A. New Mexico. *Treatise of Petroleum Geology, Atlas of Oil and Gas Fields The American Association of Petroleum Geologists*. A-011.
- BROADHEAD, R. F. 1994. Pers. Comm.
- BROADHEAD, R. F., and KING, W. E. 1988. Petroleum geology of Pennsylvanian and Lower Permian strata, Tucumcari Basin, east-central New Mexico. *New Mexico Bureau of Mines and Mineral Resources Bulletin*, 119.
- BRUNAUER, S., EMMET, P. H., and TELLER, E. 1938. Adsorption of gases in multimolecular layers. *Journal of the American Chemical Society*, 60, 309–319.
- BUSENBERG, and CLEMENCY 1976. The dissolution kinetics of feldspars at 25°C and 1 atm CO₂ partial pressure. *Geochim Cosmochim Acta*, 40, 41–49.
- CAPUANO, R. M. 1990. Hydrochemical constraints on fluid-mineral equilibria during compaction diagenesis of kerogen-rich geopressed sediments. *Geochim. Cosmochim. Acta*, 54, 1283–1299.
- CHARLES, R. W., and BAYHURST, G. K. 1983. Rock-fluid interactions in a temperature gradient: biotite granodiorite + H₂O. *J. Volcanol. Geotherm. Res.*, 15, 137–166.
- CHARLES, R. W. 1978. Experimental geothermal loop: 1, 295°C study. *Los Alamos Scientific Laboratory Report LA-7334-MS*, 1–44.
- CURIALE, J. A., BLOCH, S., RAFALSKA-BLOCH, J., and HARRISON, W. E. 1983. Petroleum-related origin for uraniferous organic-rich nodules of Southwestern Oklahoma. *AAPG Bull.*, 67(4), 588–608.
- CZERNICHOWSKI-LAURIOL, I., and FABRIOL, R. 1992. A new geochemical computer tool for the prediction of reservoir quality based on an integrated simulator generation system. *Proc. 2nd Lerkendal Petroleum Engineering Workshop*, Trondheim, Norway, 1992, 31–42.
- DAVELER, S. A., and WOLERY, T. J. 1992. EQPT, a data file preprocessor for the EQ3/6 software package: user's guide and related documentation (version 7.0). *Report UCRL-MA-110662 PT II*, Lawrence Livermore National Laboratory, CA, 89p.
- DELANY, J. M. 1985. Reaction of Topopah spring tuff with J-13 water: a geochemical modeling approach using EQ3/6 reaction path code. *Report UCRL-53642*, Lawrence Livermore National Laboratory, Livermore, CA, 44p.
- DIBBLE, W. E., and POTTER, J. M. 1982. Effect of fluid flow on geochemical processes. *Society of Petroleum Engineers 57th Annual Meeting*, New Orleans, 8pp.
- DOWNING, R. A., ALLEN, O. J., BIRD, M. J., GALE, I. N., KAY, R. L. F., and SMITH, I. F. 1985. Cleethorpes No. 1 Geothermal Well - A preliminary assessment of the resource. *Technical Report of the British Geological Survey*, Geothermal Resource Programme.
- DRUMMOND, S. E., Jr. 1981. Boiling and mixing hydrothermal fluids: chemical effects on mineral precipitation. Ph.D. thesis, The Pennsylvania State University, University Park, Pennsylvania.
- DUAN, Z., MOLLER, N., and WEARE, J. H. 1992. An equation of state for the CH₄-CO₂-H₂O system: I. Pure systems from 0 to 1000°C and 0 to 8000 bar. *Geochim. Cosmochim. Acta*, 56, 2605–2617.
- ELLIS, A. J., and GOLDING, R. M. 1963. The solubility of carbon dioxide above 100°C in water and in sodium chloride solutions. *American Journal of Science*, 261, 47–60.
- FABRIOL, R., and CZERNICHOWSKI-LAURIOL, I. 1992. A new approach to geochemical modelling with an integrated simulator generation system. In: *Water-Rock Interaction* (Y.K. Kharaka and A.S. Maest, eds.), 213–216. Balkema, Rotterdam.
- FABRIOL, R., SAUTY, J. P., and OUZOUNIAN, G. 1993. Coupling geochemistry with a particle tracking transport model. *Journal of Contaminant Hydrology*, 13, 117–129. Elsevier, Amsterdam.
- FARMER, R. E. 1965. Genesis of subsurface carbon dioxide. *American Association of Petroleum Geologists Mem.* 4, 378–385.
- FOUILLAC, C., and MICHARD, G. 1981. Sodium/lithium ratio in water applied to geothermometry of geothermal reservoirs. *Geothermics*, 10, 55–70.
- FOURNIER, R. O. 1979. A revised equation for the Na/K geothermometer. *Geoth. Res. Council Trans.*, 3, 221–224.
- FOURNIER, R. O., and POTTER, R. W. 1979. Magnesium correction to the Na-K-Ca chemical geothermometer. *Geochim. Cosmochim. Acta*, 43, 1543–1550.
- FOURNIER, R. O., and ROWE, J. J. 1966. Estimation of underground temperatures from the silica content of water from hot springs and wet-steam wells. *Amer. J. Sci.*, 264, 685–697.
- FOURNIER, R. O., and TRUESDELL, A. H. 1973. An empirical Na-K-Ca geothermometer for natural waters. *Geochim. Cosmochim. Acta*, 37, 1255–1275.
- FRANKS, S. G., and FORESTER, R. W. 1984. Relationships among carbon dioxide, pore-fluid chemistry and secondary porosity, Texas Gulf Coast. *Bulletin of The American Association of Petroleum Geologists*, 68(4), p.478.
- GALIMOV, E. M. 1968. Isotopic composition in carbon in gases of the crust. *International Geology Review*, 11, 1092–1104.
- GAUPE, R., MATTER, A., PLATT, J., RAMSEYER, K., and WALZEBUCK, J. 1993. Diagenesis and fluid evolution of deeply buried Permian (Rotliegende) Gas reservoirs, northwest Germany. *American Association of Petroleum Geologists Bulletin*, 77, 1111–1128.
- GIGGENBACH, W. F. 1988. Geothermal solute equilibria. Derivation of Na-K-Mg-Ca geothermometers. *Geochim. Cosmochim. Acta*, 52, 2749–2765.
- GIZE, A., and MACDONALD, R. 1993. Generation of compositionally atypical hydrocarbons in CO₂-rich geologic environments. *Geology*, 21, 129–132.
- GOLDSTEIN, J. I., NEWBURY, D. E., ECHLIN, P., JOY, D. C., FIORI, C., and LI-FSHIN, E. 1981. *Scanning Electron Microscopy and X-Ray Microanalysis*. Plenum Press, New York.
- GUNTER, W. D., PERKINS, E. H., and MCCANN, T. J. 1993a. Aquifer disposal of CO₂-rich gases: reaction design for added capacity. Proceedings of the IEA Carbon Dioxide Disposal Symposium (Oxford, England), 29–31 March 1993. *Energy Convers. Mgmt.*, 34, 941–948. Pergamon Press, Oxford.
- GUNTER, W. D., PERKINS, E. H., BACHU, S., LAW, D., WIWCHAR, B., ZHOU, Z., and MCCANN, T. J. 1993b. Aquifer disposal of CO₂-rich gases. Phase I. In the vicinity of the Sundance and Genesee power plants. Report of the Alberta Research Council, C-1993-5, March 1993.
- HARVIE, C. E., and WEARE, J. H. 1980. The prediction of mineral solubilities in natural waters: the Na-K-Mg-Ca-Cl-SO₄-H₂O system from zero to high concentration at 25°C. *Geochim. Cosmochim. Acta*, 44, 981–997.
- HAWTHORNE, S. B. 1990. Analytical-Scale Supercritical Fluid Extraction. *Analytical Chemistry*, 62, 633A–642A.
- HAYNES, F. M., and KESLER, S. E. 1986. Sphalerite deposition by CO₂ pressure release and acid neutralization. *Abstracts and Programs of the Geological Society of America*, 18(6), p.632.
- HEDRICK, J. L., and TAYLOR, L. T. 1990. Supercritical fluid extraction strategies of aqueous based matrices. *Journal of High Resolution Chromatography*, 13, 312–316.
- HELGESON, H. C., DELANY, J. M., NESBITT, H. W., and BIRD, D. K. 1978. Summary and critique of the thermodynamic properties of rock forming minerals. *Amer. J. Sci.*, 278A, 1–229.
- HELGESON, H. C., MURPHY, W. M., and AAGAARD, P. 1984. Thermodynamic and kinetic constraints on reaction rates among minerals and aqueous solutions, ii: Rate constants, effective

- surface area and the hydrolysis of feldspar. *Geochim Cosmochim Acta*, **48**, 2405–2432.
- HELLMANN, R, and CRERAR, D A. 1986. Theory and application of flow systems to mineral-water interactions. *Proceedings of Fifth International Symposium On Water-Rock Interactions*, Reykjavik, Iceland, 258–261.
- HEM, J D. 1985. Study and interpretation of the chemical characteristics of natural water. *United States Geological Survey Water-Supply Paper 2254*.
- HENNET, R J C, CRERAR, D A, and SCHWARTZ, J. 1988. The effect of carbon dioxide partial pressure on metal transport in low-temperature hydrothermal systems. *Chemical Geology*, **69**, 321–330.
- HILL, C G. 1977. *An introduction to chemical engineering kinetics and reactor design*. John Wiley and Sons, New York.
- HOLLOWAY, S, et al. 1993. The underground disposal of carbon dioxide, *First interim report of JOULE II project No. CT92-0031*, 165–224. Commission of the European Communities.
- HOLM, L W. 1959. Carbon dioxide solvent flooding for increased oil recovery. *Trans. AIME*, **216**, 225–231.
- JOHNSON, J W, OELKERS, E H, and HELGESON, H C. 1991. SUPCRT92: a software package for calculating the standard molal thermodynamic properties of minerals, gases, aqueous species and reactions from 1 to 5000 bars and 0° to 1000°C. *Computers and Geosciences*, **18**, 899–947.
- KAY, A, and STRONG, D F. 1983. Geologic and fluid controls on As-Sb-Au mineralization in Moreton Harbour Area, Newfoundland. *Economic Geology*, **78**, 1590–1604.
- KEMP, S J. 1992. Clay minerals and their importance in reservoir characterisation. *Technical Report British Geological Survey. WG/92/79R*.
- KERVEVAN, C, FABRIOL, R, GUILLEN, A, and SAUTY, J P. 1994. A sequential-parallel approach for coupling chemistry and transport in groundwater quality modelling. In "High-Performance Computing and Networking" (W. Gentzsch and U. Harms, editors), Lecture notes in computer science 796, 335–339. Springer Verlag, Berlin.
- KHARAKA, Y K, LICO, M S, and LAX, L M. 1982. Chemical geothermometers applied to formation waters, Gulf of Mexico and California basins. *Am. Assoc. Petrol. Geol. Bull.*, **66**, 588.
- KHARAKA, Y K, and MARINER, R H. 1989. Chemical geothermometers and their application to formation waters from sedimentary basins. In: *Thermal history of sedimentary basins: methods and case histories* (N.D. Naeser and T.H. McCulloch, editors). Springer-Verlag, New York, 99–117.
- KNAUSS, K G, and WOLERY, T J. 1986. Dependence of albite dissolution kinetics on pH and time at 25 °C and 70 °C. *Geochim. Cosmochim. Acta*, **50**, 2481–2497.
- KNAUSS, K G, and WOLERY, T J. 1988. The dissolution kinetics of quartz as a function of pH and time at 70°C. *Geochim Cosmochim Acta*, **52**, 1493–1501.
- KNAUSS, K G, and WOLERY, T J. 1989. Muscovite dissolution kinetics as a function of pH and time at 70°C. *Geochim. Cosmochim. Acta*, **53**, 2481–2497.
- KUK, M S, and MONTAGNA, J C. 1983. Solubility of oxygenated hydrocarbons in supercritical carbon dioxide. In: *Chemical Engineering at Supercritical Fluid Conditions*, Ann Arbor Science, Ann Arbor, MI, USA, 101–111.
- LANE, D L, RAWSON, S A, ALLEN, C C, and BURNELL, J R. 1986. The distribution of alteration phases during basalt-groundwater interactions: Preliminary insights from flow-through experiments. *Proceedings of Fifth International Symposium On Water-Rock Interactions*, Reykjavik, Iceland.
- LANG, W B. 1959. The origin of some natural carbon dioxide gases. *Journal of Geophysical Research*, **64**, 127–131.
- LASAGA, A C. 1981. Rate laws of chemical reactions. In: 'Kinetics Of Geochemical Processes' (A.C. Lasaga and R.J. Kirkpatrick, eds.), Mineralogical Society Of America. *Reviews In Mineralogy*, **8**, 1–68.
- LASAGA, A C. 1984. Chemical kinetics of water-rock interactions. *J. Geophys. Res.*, **89**, 4009–4025.
- LEVENSPIEL, O. 1972. *Chemical reaction engineering*. John Wiley and Sons, 1–578.
- LEVENSPIEL, O, and BISCHOFF, K B. 1963. Patterns of flow in chemical process vessels. In: 'Advances In Chemical Engineering', **4**, (T.B. Drew, J.W. Hooper and T. Vermeulen, eds.), 95–198. Academic Press.
- LOUCKS, R G, DODGE, M M, and GALLOWAY, W E. 1984. Regional controls on diagenesis and reservoir quality in lower tertiary sandstones along the Texas Gulf Coast, In: "Clastic Diagenesis", (D.A. McDonald and R.C. Surdam, editors). *Amer. Assoc. Petrol. Geol. Mem.*, **37**, 15–45.
- LUNDEGARD, P D, and LAND, L S. 1986. Carbon dioxide and organic acids: their role in porosity enhancement and cementation, Paleogene of the Texas Gulf Coast. In: "Roles of organic matter in sediment diagenesis" (D.L. Gautier, editor), *Special publication Society of economic paleontologists and mineralogists*, **38**, 129–146.
- MARSHALL, W L, SLUSHER, R, and JONES, E V. 1964. Solubility and thermodynamic relationships for CaSO₄ in NaCl-H₂O solutions from 40°C to 200°C, 0 to 4 molal NaCl. *J. Chem. Eng. Data*, **9**, 187–191.
- MATTHEWS, C S. 1989. Carbon dioxide flooding. In: "Enhanced Oil Recovery, II - Processes and operations", (E.C. Donaldson, G.V. Chilingarian and T.F. Yen, editors), 129–156. Elsevier, Amsterdam.
- MAY, B I. 1982. Geologic and petrophysical study of the Tubb interval, Bravo Dome Carbon Dioxide Gas Unit. *Research Memo Amoco*, **CF 4266**.
- MCGOWAN, D B, and SURDAM, R C. 1990. Carboxylic acid anions in formation waters, San Joaquin Basin and Louisiana Gulf Coast, U.S.A. — Implications for clastic diagenesis. *Applied Geochemistry*, **5**, 687–701.
- MCHUGH, M A, and KRUKONIS, V J. 1986. *Supercritical Fluid Extraction — Principles and Practice*, Butterworths, ISBN 0-409-90015-X.
- MICHARD, G. 1979. Géothermomètres chimiques. *Bull. BRGM (2) III*, n°2, 183–189.
- MICHARD, G. 1983. Recueil des données thermodynamiques concernant les équilibres eaux-minéraux dans les réservoirs hydrothermaux. *Rapport EUR 8590 FR*, Commission of the European Communities, 155p.
- MICHARD, G. 1989. *Equilibres chimiques dans les eaux naturelles*, 357p. Editions Publisud, Paris.
- MICHARD, G. 1990. Behaviour of major elements and some trace elements (Li, Rb, Cs, Fe, Mn, W, F) in deep hot waters from granitic areas. *Chem. Geol.*, **89**, 117–134.
- MILLIKEN, K L, LAND, L S, and LOUCKS, R G. 1981. History of burial diagenesis determined from isotopic geochemistry, Frio Formation, Brazoria County, Texas. *Amer. Assoc. Petrol. Geol. Bull.*, **65**, 1397–1413.
- MOLLER, N. 1988. The prediction of mineral solubilities in natural waters: A chemical equilibrium model for the Na-Ca-Cl-SO₄-H₂O system, to high temperature and concentration. *Geochim. Cosmochim. Acta*, **52**, 821–837.
- MOTOJIMA, K. 1957. Geochemical studies of natural gas accumulation in the vicinity of Isobe-Machi, Gunma Prefecture. *Japan Geol. Surv. Bull.*, **8(1)**, 23–40. (in Japanese).
- MULREADY, J. 1977. The Caroline carbon dioxide field and associated carbon dioxide occurrences, Gambier Embayment, South Australia. *Journal of The Australian Petroleum Exploration Association*, **17(1)**, 121–127.
- MURPHY, W M, and HELGESON, H C. 1987. Thermodynamic and kinetic constraints on reaction rates among minerals and aqueous solutions. III. Activated complexes and the pH-

- dependence of the rates of feldspar, pyroxene, wollastonite and olivine hydrolysis. *Geochim. Cosmochim. Acta*, **51**, 3137–3153.
- NELIS, M K. 1994. Bravo Dome II petrographic study. *Report Amoco Production Company*.
- NICHOLSON, K. 1993. *Geothermal fluids. Chemistry and Exploration Techniques*. Springer-Verlag, 261p.
- ODOM, I E. 1984. Smectite clay minerals: properties and uses. *Philosophical Transactions of the Royal Society of London*, **A311**, 391–409.
- OMOLE, O, and OSOBA, J S. 1983. Carbon dioxide-dolomite rock interaction during CO₂ flooding process. *Annual meeting of the Petroleum Society of the Canadian Institute of mining and metallurgy*, paper 83-34-17, 1–13.
- PARNELL, J. 1985. Uranium / rare earth enriched hydrocarbons in Devonian sandstones, northern Scotland. *N. Jb. Miner. Mh.*, **H.3**, 132–144.
- PARNELL, J, and EAKIN, P. 1987. The replacement of sandstones by uraniumiferous hydrocarbons: significance for petroleum migration. *Mineralogical Magazine*, **51**, 505–515.
- PARNELL, J, and EAKIN, P. 1989. Thorium-bitumen mineralisation in the Silurian sandstones, Welsh Borderland. *Mineralogical Magazine*, **53**, 111–116.
- PEABODY, C E, and EINAUDI, M T. 1992. Origin of petroleum and mercury migration in the Culver-Baer Cinnabar deposit, Mayacamas District, California. *Economic Geology*, **87**, 1078–1103.
- PHILLIPS, S L, IGBENE, A, FAIR, H, OZBEK, H, and TAVANA, M. 1981. A technical databook for geothermal energy utilization. *Report LBL-12810*, Lawrence Berkeley Laboratory, CA, 46p.
- PHINNEY, D, TENYSON, J, and FRICK, V. 1978. Xenon in CO₂ well gas revisited. *Journal of Geophysical Research*, **83**, 2313–2319.
- PITZER, K S. 1973. Thermodynamics of electrolytes: I. Theoretical basis and general equations. *J. Phys. Chem.*, **77**, 268–277.
- POHL, D C, and LIU, J G. 1983. Flow-through basalt glass-seawater reactions from 200–300 °C, 250 bars pressure. *Proceedings of The Fourth International Symposium On Water-Rock Interactions*, Misasa, Japan, 389–392.
- PONADER, H B, and LIU, J G. 1985. A flow-through apparatus for the study of rodinigitisation. *EOS*, **18**, p.423.
- POSEY-DOWTY, J, CRERAR, D, HELLMANN, R, and CHANG, C D. 1986. Kinetics of mineral-water reactions: Theory, design and application of circulating hydrothermal equipment. *Amer. Mineral.*, **71**, 85–94.
- POTTER, J M. 1981. Experimental rock/water interactions at temperatures to 300°C: implications for fluid flow, solute transport, and silicate mineral zoning in crustal geothermal systems. Unpublished Ph.D thesis, Stanford University, USA.
- POTTER, J M, and DIBBLE, W E. 1986. Experimental calibration of the na-k geothermometer: flow-through studies. *Proceedings of Fifth International Symposium On Water-Rock Interactions*, Reykjavik, Iceland, 444–447.
- RIMSTDT, J D, and BARNES, H L. 1980. The kinetics of silica-water reactions. *Geochim. Cosmochim. Acta*, **44**, 1683–1699.
- RIMSTDT, J D, and DOVE, P M. 1986. Mineral/solution reaction rates in a mixed flow reactor: Wollastonite hydrolysis. *Geochim Cosmochim Acta*, **50**, 2509–2516.
- ROSS, G D, TODD, A C, and TWEEDIE, J A. 1981. The effect of simulated CO₂ flooding on the permeability of reservoir rocks, In: "Enhanced Oil Recovery" (F.J. Fayers, editor), 351–366. Elsevier, Amsterdam.
- ROSS, G D, TODD, A C, TWEEDIE, J A, and WILL, A G S. 1982. The dissolution effects of CO₂-brine systems on the permeability of U.K. and North Sea calcareous sandstones. *Society of Petroleum Engineers/U.S. Department of Energy Third Joint Symposium on Enhanced Oil Recovery*, paper SPE/DOE 10685, 149–154.
- SAVAGE, D, BATEMAN, K, MILODOWSKI, A E, CAVE, M R, HUGHES, C R, GREEN, K, REEDER, S, and PEARCE, J. 1989. Geochemistry in relation to Hot Dry Rock development in Cornwall: Volume 6 Experimental investigation of granite-water interaction. *British Geological Survey Research Report*, SD/89/2.
- SAYEGH, S G, KRAUSE, F F, GIRARD, M, and DEBREE, C. 1990. Rock/fluid interactions of carbonated brines in a sandstone reservoir: Pembina Cardium, Alberta, Canada. *Society of Petroleum Engineers Formation Evaluation*, paper SPE19392, v. 5, 399–405.
- SCHMIDT, V, and McDONALD, D A. 1979. The role of secondary porosity in the course of sandstone diagenesis. In: "Aspects of Diagenesis" (P.A. Scholle and P.R. Schluger, editors), *Soc. Econ. Paleontol. Mineral., Spec. Publ.*, **26**, 185–207.
- SCHREMP, F W, and ROBERSON, G R. 1975. Effect of supercritical carbon dioxide (CO₂) on construction materials. *Soc. of Petroleum Engineers Journal*, June edition, 227–233.
- SIEBERT, R M, MONCURE, G K, and LAHANN, R W. 1984. A theory of framework grain dissolution in sandstones. In: "Clastic Diagenesis", (D.A. McDonald and R.C. Surdam, editors), *Amer. Assoc. Petrol. Geol. Mem.*, **37**, 163–175.
- SMITH, L K. 1993. Aspects of oilfield water chemistry: Part A. Induced diagenetic alteration and Part B. The effect of organic alkalinity on cation ratios. *Ph.D. University of Wyoming*.
- SMITH, J T, and EHRENBERG, S N. 1989. Correlation of carbon dioxide abundance with temperature in clastic hydrocarbon reservoirs: relationship to organic chemical equilibrium. *Marine and Petroleum Geology*, **6**, 129–135.
- STEWART, P B, and MUNJAL, P K. 1970. The solubility of carbon dioxide in pure water, synthetic sea water and synthetic sea-water concentrates at -5 to 25°C and 10 to 45 atm pressure. *Journal of Chemical and Engineering Data*, **15**(1), 67–71.
- STUDLICK, J R J, SHEW, R D, BASYE, G L, and RAY, J R. 1990. A giant carbon dioxide accumulation in the Norphlet formation, Pisgah Anticline, Mississippi. In: "Sandstone petroleum reservoirs" (J. Barwis, McPherson and J.R.J. Studlick, editors), p. 181–203. Springer Verlag, New York.
- TABER, J J. 1993. The use of supercritical CO₂ for enhanced oil recovery. In: *International Conference on Carbon Dioxide Utilisation*, University of Bari, Bari, Italy.
- TALMAN, S J, and GUNTER, W D. 1992. In: *Water-Rock Interaction*, (Y K Kharaka and A S Maestri, editors), Balkema, Rotterdam, 119–122.
- TALMAN, S J, Wiwchar, B, GUNTER, W D, and SCARFE, C M. 1990. Dissolution kinetics of calcite in the H₂O-CO₂ system along the steam saturation curve to 210 °C. In: *Fluid-mineral Interactions; A tribute to H.P. Eugster* (R J Spencer and I-Ming Chou, editors). *The Geochemical Society Special Publication*, **2**, 41–55.
- VAN ELDIK, R, and PALMER, D A. 1982. Effects of pressure on the kinetics of the dehydration of carbonic acid and the hydrolysis of CO₂ in aqueous solution. *Journal of Solution Chemistry*, **11**(5), 339–346.
- VAN GENUCHTEN, M T H, and ALVES, W J. 1982. Analytical solutions of the one-dimensional convective-dispersive solute transport equation. *US Dept of Agriculture Technical Bulletin*, **1661**, 149pp.
- VOGEL, A. 1978. *Textbook of Quantitative Inorganic Analysis - Fourth Edition*, Longman Scientific and Technical Harlow England.
- WACKER, H. 1994. The Bravo Dome Carbon Dioxide Gas Field.
- WEAST, R C. 1972/1973. *Handbook of Chemistry and Physics*, 53th edition. Published by The Chemical Rubber Co.
- WENCLAWIAK, B. 1992. *Analysis with supercritical Fluids: Extraction and Chromatography*. Springer - Verlag, New York.

WHITE, A F, and PETERSON, M L. 1990. Role of reactive-surface-area characterization in geochemical kinetic models. In: *Chemical Modeling of Aqueous Systems II* (D.C. Melchior and R.L. Bassett, editors), *ACS Symposium Series*, **416**, 461-475.

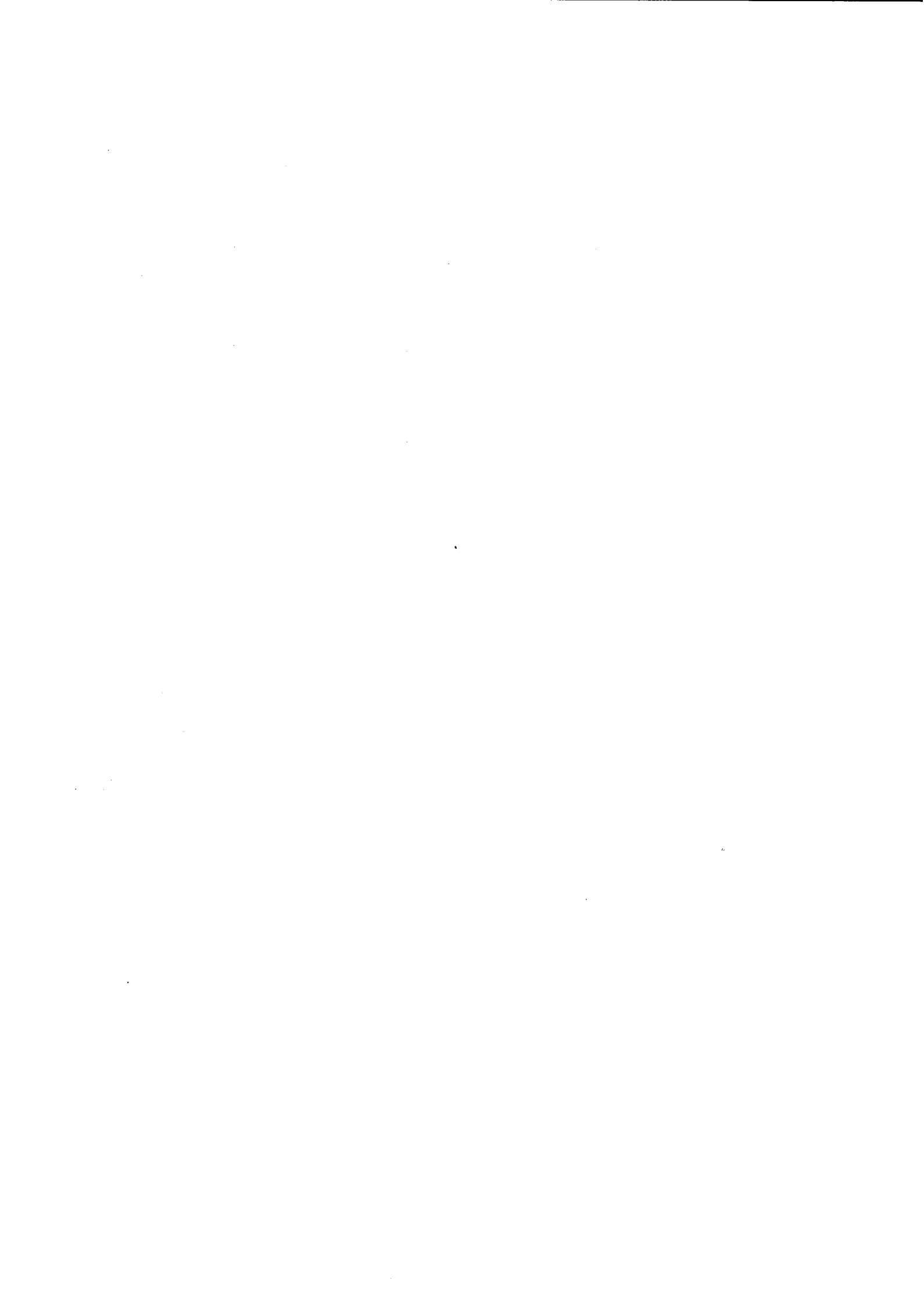
WIEBE, R. 1941. The binary system carbon dioxide-water under pressure. *Chemical Reviews*, **29**, 475-481.

WIEBE, R, and GADDY, V L. 1941. Vapour phase composition of carbon dioxide-water mixtures at various temperatures and at pressures up to 700 atmospheres. *Journal of the American Chemical Society*, **63**, p.475.

WILLIAMS, D F. 1981. Extraction with Supercritical Gases, *Chemical Engineering Science*, **36**, 1769-1788.

WOLERY, T J. 1992a. EQ3/6, a software package for geochemical modeling of aqueous systems: package overview and installation guide (version 7.0). *Report UCRL-MA-110662 PT I*, Lawrence Livermore National Laboratory, CA, 66p.

WOLERY, T J. 1992b. EQ3NR, a computer program for geochemical aqueous speciation-solubility calculations: theoretical manual, user's guide and related documentation (version 7.0). *Report UCRL-MA-110662 PT III*, Lawrence Livermore National Laboratory, CA, 246p.



CHAPTER 8

Area 6 Techno-economics of underground disposal

Prince Doherty and Bob Harrison (Renewable Energy Centre, University of Sunderland)

8.1 INTRODUCTION

The main objective of area 6 was to develop a techno-economic cost model and use it to investigate the costs of removing CO₂ from fossil fuel fired power plants and disposing of it safely in underground storage reservoirs.

8.1.1 The concept

The concept of CO₂ recovery and disposal can be broken down into three main stages as follows:

CO₂ recovery

CO₂ can be recovered from a variety of different power plant types using a variety of different methods; there are many different power plant/separation plant options. Following separation, the CO₂ is compressed into a supercritical liquid at the power station prior to transport.

CO₂ transport

This is the pipeline system required for transporting the CO₂ in the form of a supercritical liquid from source to the disposal site.

CO₂ disposal

CO₂ can be disposed of into a variety of underground reservoirs, namely aquifers, depleted gas fields and oil fields. In the latter case disposal is likely to be combined with enhanced oil recovery.

8.1.2 Costs and parasitics

The costs and energy requirements (parasitics) of the CO₂ recovery, transport and disposal systems determine the overall economics of the disposal routes. There are many options, which gives a large number of possible combinations, but these contain many common elements.

The costs and energy requirements of the CO₂ recovery system will be common to all transport and disposal options and depend only upon the choice of power plant type and recovery system option.

The costs and energy requirements of the CO₂ transport system are common to all methods of CO₂ recovery and disposal, but also depend upon the geographical relationship between the CO₂ source and the disposal site.

The costs and energy requirements of the CO₂ disposal option site specific conditions may vary over a wide range, and this presents major difficulties in the economics of the implementation of different disposal sites. The energy requirements at the injection well will limit the feasibility of CO₂ injection to those aquifers which have transmissivities above some limiting value. Previous studies have taken limiting values of 2.5–30 Dm [Van der Meer (1992)], and 5.44 Dm [Van der Burgt et al. (1992)].

8.2 ECONOMIC METHODOLOGY

The methodology of the calculation of the unit costs of CO₂ avoided from the power plant is summarised in equation 8.1: for an unmodified plant

CO₂ avoided costs (ECU/tonne) 'PP' at the power plant are given by

$$PP = \frac{\frac{P_1}{P_2} C_2 - C_1}{\left\{ T_1 - (1-r) T_2 \frac{P_1}{P_2} \right\}} \quad (8.1)$$

- where C = total annualised system costs (ECU/year)
P = net plant output (MW)
T = total annual CO₂ emission (tonnes/year)
r = fraction of CO₂ recovered
1 = base case power plant without CO₂ recovery
2 = power plant with CO₂ recovery.

The annualised system costs $C = I \times CRF(n,d) + O$

- where I = total investment costs (ECU)
O = operating and maintenance costs (ECU/year)
CRF(n,d) = capital recovery factor

$$CRF(n,d) = \frac{d(1+d)^n}{(1+d)^n - 1} \quad (8.2)$$

- where d = discount rate
n = system lifetime in years.

The term $\frac{P_2}{P_1}$ takes account of the parasitic losses by adjusting the costs of the modified power plant to make the net electrical output equal to that of the unmodified plant.

The term

$$T_w = \left\{ T_1 - (1-r) T_2 \frac{P_1}{P_2} \right\} \quad (8.3)$$

is the net CO₂ avoided by modifying the plant, after taking account of the fact that the electrical output is reduced. The net CO₂ avoided by CO₂ recovery at the modified plant is smaller than the total amount of CO₂ recovered at the plant. Typically the CO₂ recovered at the modified power plant is 90% of the emission and the CO₂ avoided is about 60% of the CO₂ emission; this is about 85% of the CO₂ emission from an unmodified plant with the same electrical output.

Transport of CO₂ to disposal sites, and disposal into underground reservoirs incurs capital and operating costs. Also, electricity may be consumed operating compressors and pumps. Strictly, these electrical losses should be included along with the power plant parasitic losses in calculating the CO₂ avoided at the power plant. However, if it is assumed that the downstream electrical consumption is always small in comparison with the power plant losses then a valuable simplification of the methodology is to include the electricity consumption as a cost and to ignore the small effect which this has on the CO₂ avoided. With this approach the calculations of the contribution of the transport and disposal costs to the overall costs can then be carried out independently of the plant costs. The overall costs can then be obtained by adding the separate contributions. This simplification does not introduce errors which are any larger than the other uncertainties in the calculations. The contribution to the costs of the CO₂ transport 'L' is given by

$$L = \frac{C_p}{T_{av}} \quad (8.4)$$

where C_p = total annualised costs associated with the pipeline including electricity (ECU/year). The contribution to the costs of CO₂ avoided 'D' is given by

$$D = \frac{C_d}{T_{av}} \quad (8.5)$$

where C_d = total annualised costs at the disposal site including electricity (ECU/year).

The total cost of CO₂ avoided 'A' is then given by

$$A = PP + L + D. \quad (8.6)$$

8.3 CARBON DIOXIDE RECOVERY AT THE POWER STATION

The recovery and disposal of CO₂ from fossil-fuelled power plants is currently the subject of major international interest and a number of important recent studies have been carried out on the performance and costs of implementing such systems [Brown et al. (1993), EPRI (1991a, 1991b), Goldthorpe (1993), Goldthorpe et al. (1992a, 1992b), Hendriks et al. (1989, 1991, 1992), IEA Greenhouse Gas (1992, 1993a, 1993b), Summerfield et al. (1993)].

A wide range of combinations of power plant options and CO₂ recovery systems are conceivable. However, in order to limit the study to those options which may be technically feasible and least expensive in the short to medium term, the following have been chosen to form the basis of calculations in this study.

Fuel	Power plant	CO ₂ recovery
Coal	PFFGD	Chemical scrubbing (MEA)
Coal	IGCC	Physical scrubbing (Sclexol)
Coal	O ₂ /CO ₂ recycle	Cryogenic distillation
N.Gas	GTCC	Chemical scrubbing (MEA)

Where:

PFFGD — Pulverised coal combustion with flue gas desulphurization

IGCC — Integrated gasification combined cycle

O₂/CO₂ recycle — Combustion of coal in a mixture of oxygen and recycled flue gas

GTCC — Natural gas, gas turbine combined cycle

MEA — Monoethanolamine solution

Recovery of CO₂ from the power station exhausts incurs additional investment and operating costs, and also there are electrical parasitic and thermal loads which reduce the power station output. These performance penalties are very important. A review of a number of major studies cited above for the selected power plant and CO₂ recovery options is included below. The results from this review are used in the estimation of the likely performance penalties and costs of CO₂ recovery from fossil-fuelled power plants.

8.3.1 Pulverised fuel plants with flue gas desulphurisation (PFFGD)

A number of major studies on the performance and costs of CO₂ recovery from pulverised fuel with flue gas desulphurization power plants have been published [EPRI (1991a), Goldthorpe (1993), Hendriks et al. (1989), IEA Greenhouse Gas (1992)]. In this section a comparative assessment of the main assumptions of these studies is carried out.

The main constituent of coal is carbon, with some additional hydrogen, nitrogen, sulphur, oxygen, mineral matter (ash), and moisture. Coal combustion therefore releases significant amounts of sulphur, nitrogen and carbon dioxide into the atmosphere. Sulphur and nitrogen oxides combine with water in the air to produce acids which are brought to earth in rainfall (the so-called "acid rain"). Desulphurization and denitrification of the exhaust flue gases of power plants is currently routinely carried out in power stations in some countries (e.g. Germany). However the removal of CO₂ from power plant flue gas exhausts is as yet a novel concept. It is assumed here that the basic coal fired plant will be fitted with flue gas desulphurization equipment, hence this cost is not attributable to CO₂ removal.

Carbon Dioxide Recovery

Figure 8.1 shows a block flow diagram of the PFFGD power plant. In conventional coal fired power plants the exhaust gases contain about 10%–15% CO₂ at near atmospheric pressure. A number of processes can be

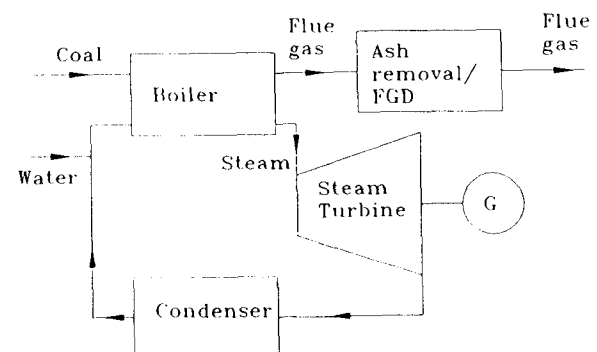


Figure 8.1 Block diagram of a PFFGD power plant.

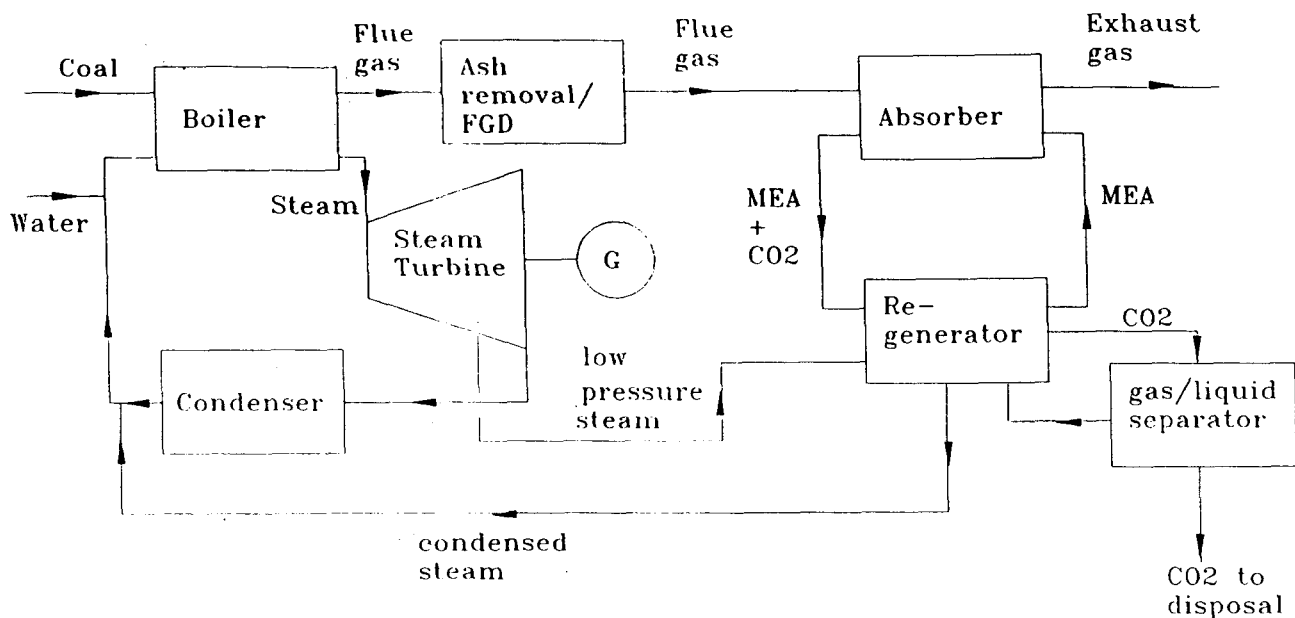


Figure 8.2 Block diagram of a PFFGD plant with modifications for CO₂ recovery.

considered for recovering the CO₂ but, because of the low CO₂ concentrations and the low partial pressures, chemical solvent scrubbing gives better separation and lower plant performance penalties than other removal schemes [Goldthorpe et al. (1992a)]. The process, however, requires large amounts of heat for solvent regeneration which can be met by extracting low pressure steam from the steam turbine (see Figure 8.2).

A block flow diagram for the PFFGD plant with chemical scrubbing is shown in Figure 8.2. Monoethanolamine (MEA) is considered to be a typical, commercially available, chemical solvent for CO₂ scrubbing. The process mainly involves the chemical absorption of CO₂ in MEA solution in an absorber column, and the regeneration of the MEA solvent in the stripper column using low pressure steam from the steam turbine.

After recovery the CO₂ gas is dehydrated (to prevent corrosion in the transport pipelines), liquefied and compressed to pipeline pressures (about 120 bar) ready for transport and disposal.

The Costs of CO₂ Recovery from PFFGD Plants

Figure 8.3 shows the comparative performance and costs of CO₂ recovery from PFFGD power plants for the studies which have been reviewed. In order to make the comparison the results have been normalised for the same thermal input (1000 MWt), plant capacity (85%), CO₂ recovery (90), lifetime (25 years), discount rate (10) and fuel costs (ECU 2.21 per GJ). In all cases CO₂ removal by chemical scrubbing has been considered. Table 8.1 below shows the percentage decrease and increase in the overall plant efficiency and costs respectively when comparing the

plant with CO₂ recovery with the unmodified plant in the individual studies.

The Hendriks et al. (1989) and the IEA (1992) studies give low plant performance penalties for CO₂ recovery, resulting in an average 28 decrease in the overall thermal efficiency of the power plant. The plant capital and operating costs for the IEA (1992) study increase by about 10 and 40 percent respectively giving an overall increase in the electricity production costs of approximately 54. The normalised cost of CO₂ recovery is estimated at ECU 35 per tonne when compared with the unmodified plant. In the study by Hendriks et al. (1989), the plant capital and operating costs increases by about 34 and 73 percent respectively giving an overall increase in the electricity production costs of approximately 65. The normalised cost of CO₂ recovery is estimated at ECU 35 per tonne. These two studies are optimistic possibly because a mature technology is assumed.

In the studies by Goldthorpe (1993) and by EPRI (1991a) efficiency penalties of about 28% and 35% respectively result when CO₂ recovery is taken into account. For the Goldthorpe (1993) study, the initial capital and operating costs of the PFFGD plant without recovery is higher than the other three studies possibly because a bolt-on rather than an integrated CO₂ recovery plant is assumed. CO₂ recovery increases these cost items by 42 and 93 respectively. The electricity production costs increase by about 85 and the normalised cost of CO₂ recovery is estimated at ECU 59 per tonne. For the EPRI (1991a) study, the plant capital and operating costs increase by about 66 and 100 percent respectively giving an overall increase in the electricity production costs of

Table 8.1 Percentage decrease in efficiency and increase in costs.

Cost studies	Efficiency	Capital costs	Operating costs	Electricity costs
Goldthorpe (1993)	-28	+42	+93	+85
EPRI (1991a)	-35	+66	+100	+110
IEA (1992)	-29	+10	+40	+54
Hendriks et al. (1989)	-27	+34	+73	+65

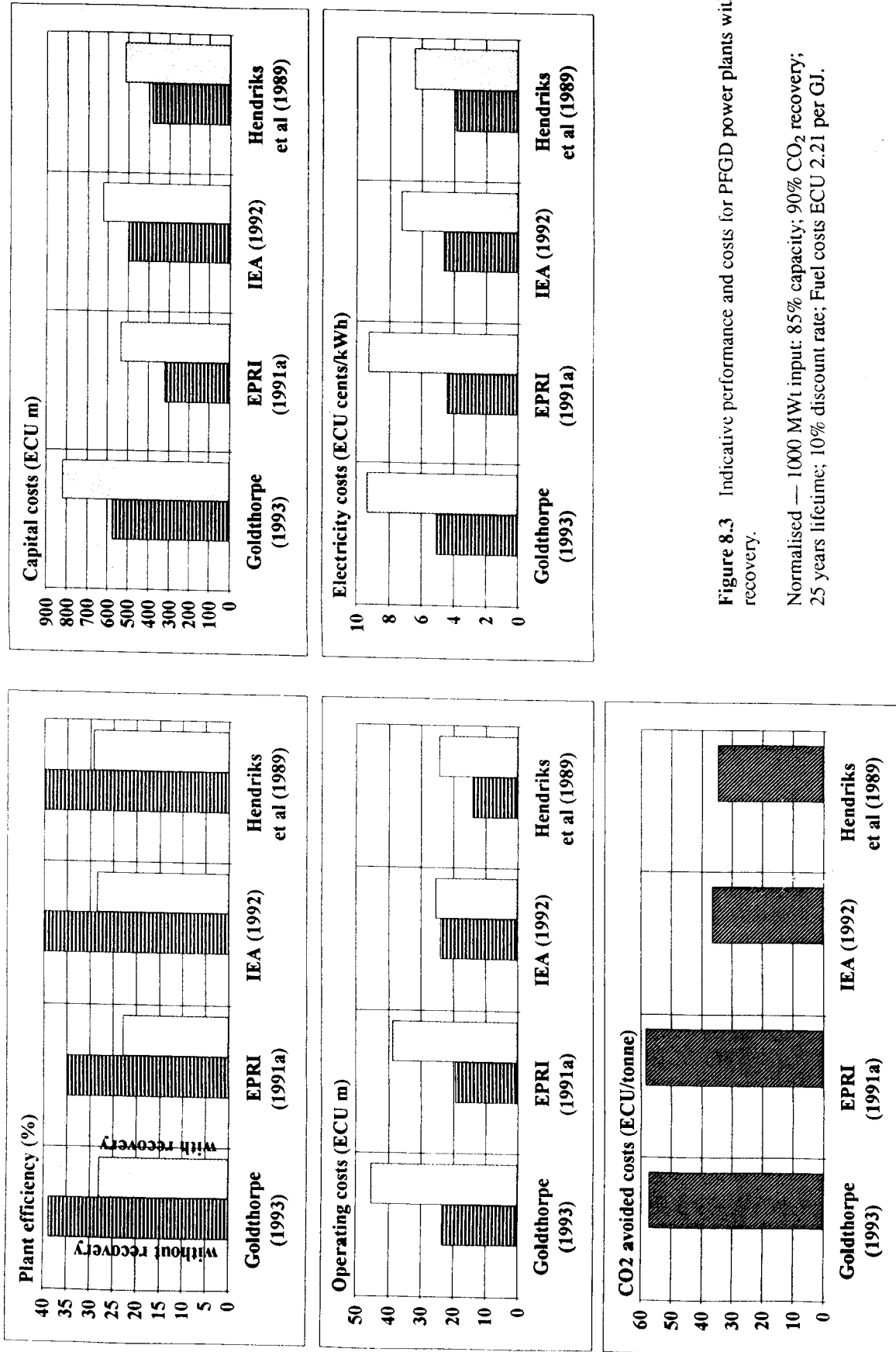


Figure 8.3 Indicative performance and costs for PFGD power plants with CO₂ recovery.

Normalised — 1000 MWt input; 85% capacity; 90% CO₂ recovery; 25 years lifetime; 10% discount rate; Fuel costs ECU 2.21 per GJ.

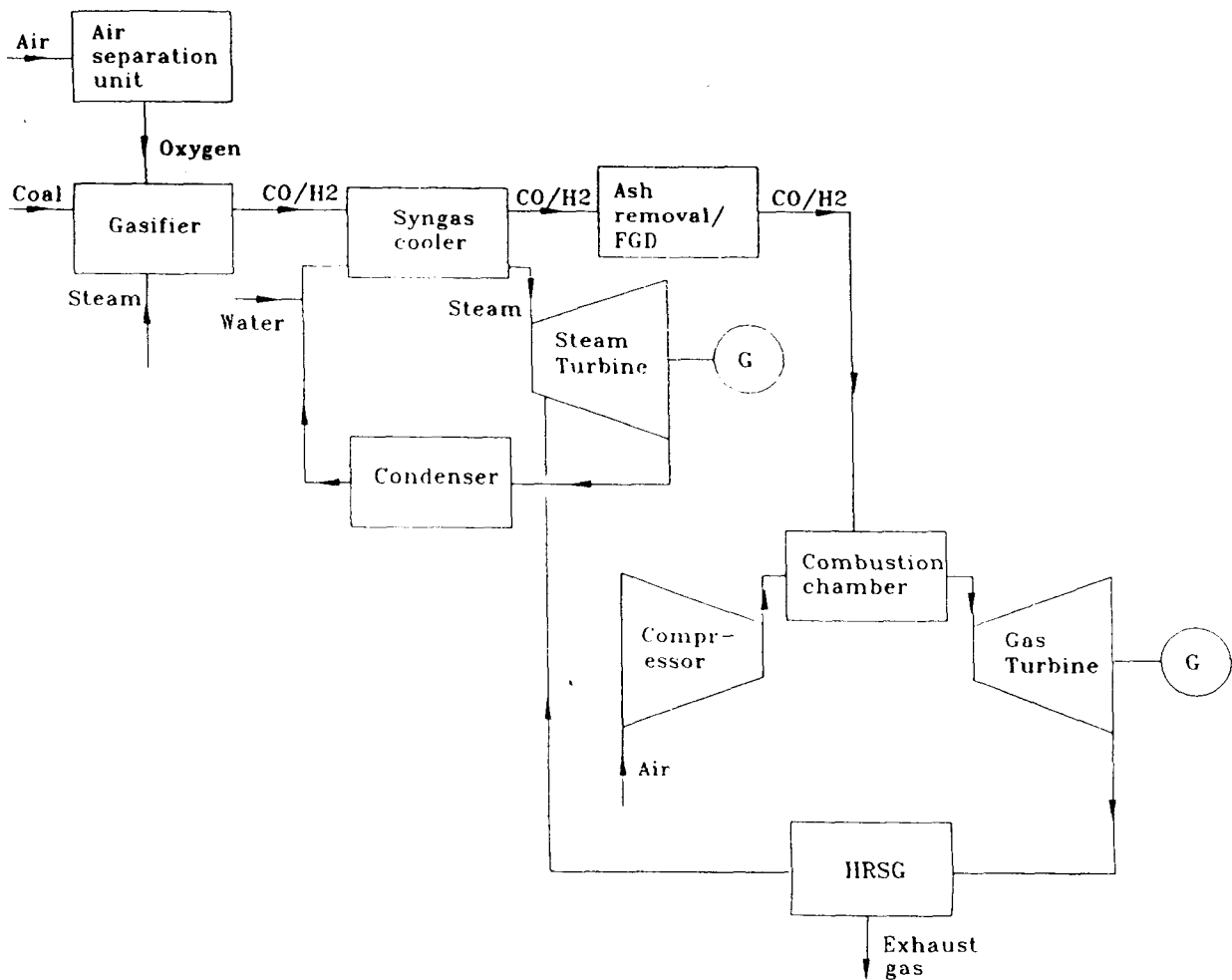


Figure 8.4 Block diagram of a coal gasification combined cycle power plant.

about 110. The normalised cost of CO₂ recovery is estimated at ECU 59 per tonne.

This review suggests that with CO₂ recovery the overall thermal efficiency of PFFGD power plants may decrease by 27–35, and the electricity production cost may increase by between 54–110 depending on whether a mature technology is assumed. The normalised cost of CO₂ recovery when compared with an unmodified plant may range from ECU 35–59 per tonne of CO₂ recovered.

8.3.2 Integrated coal gasification combined cycle (IGCC) power plants

A number of major studies on the performance and costs of CO₂ recovery from coal gasification combined cycle power plants have been published [Brown et al. (1993), EPRI (1991b), Goldthorpe et al. (1992b), Hendriks et al. (1991), IEA Greenhouse Gas (1993)]. In this section a comparative assessment of the main assumptions of these studies is carried out.

The basic concept of IGCC power plants is to feed coal into a gasifier unit together with oxygen and steam, at pressures ranging from 20–80 bar and at temperatures of 1500–1600°C [Hendriks et al. (1992)]. This produces a synthesis gas consisting mainly of carbon monoxide (CO), hydrogen (H₂) and heat. The heat evolved from the

gasification process is used to produce high pressure steam which drives a steam turbine. Any unburned carbon and molten ash in the synthesis gas is removed before the CO/H₂ gas is combusted with air in a gas turbine (see Figure 8.4). Heat recovered from the gas turbine exhaust is used to generate more steam which is also fed into the steam turbine to produce additional power.

Carbon Dioxide Recovery

Carbon from the gasified stream is removed by injecting the CO/H₂ mixture with steam in a shift reactor unit (Figure 8.5) thus converting the CO to CO₂ and H₂. Prior to the shift reaction process, sulphur contained in the syngas is removed. The gas mixture leaving the shift reactor contains a high concentration of CO₂ (40%) at partial pressures of about 20–30 bar [Summerfield (Private communications), Goldthorpe et al. (1992b)].

A number of technologies exist for removing the CO₂ gas. These include physical solvents (e.g. Selexol) scrubbing, chemical solvent (e.g. MEA) scrubbing and membrane separation [Goldthorpe et al. (1992b)]. Schutz et al. (1992) have shown that physical absorption processes give lower plant performance penalties when the CO₂ gas concentration and partial pressure is high in the exhaust gas mixture. The process involves the solubility of CO₂ at high pressures and low temperatures. Regeneration of the

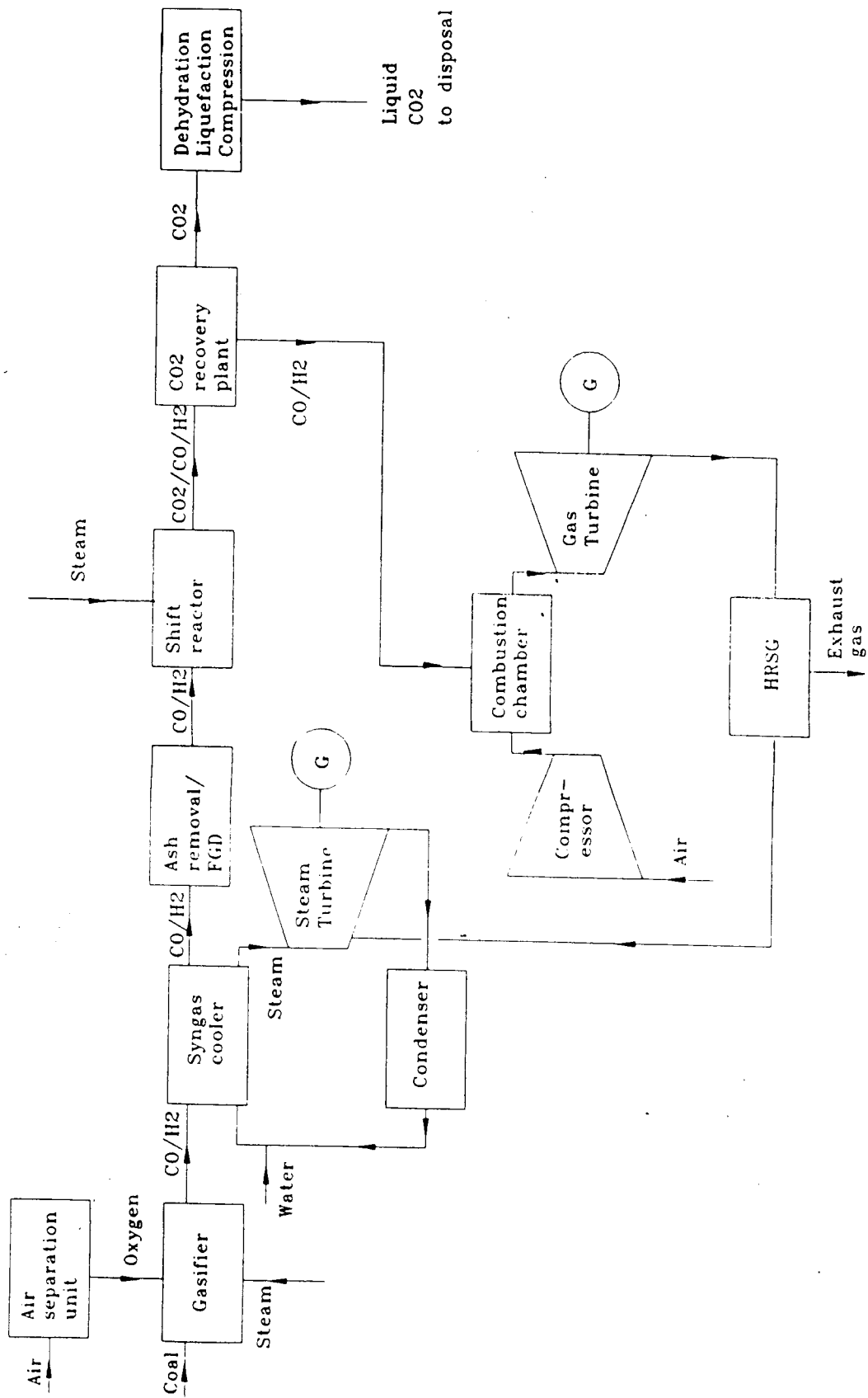


Figure 5.8 Block diagram of a coal gasification combined cycle plant modified for CO₂ recovery.

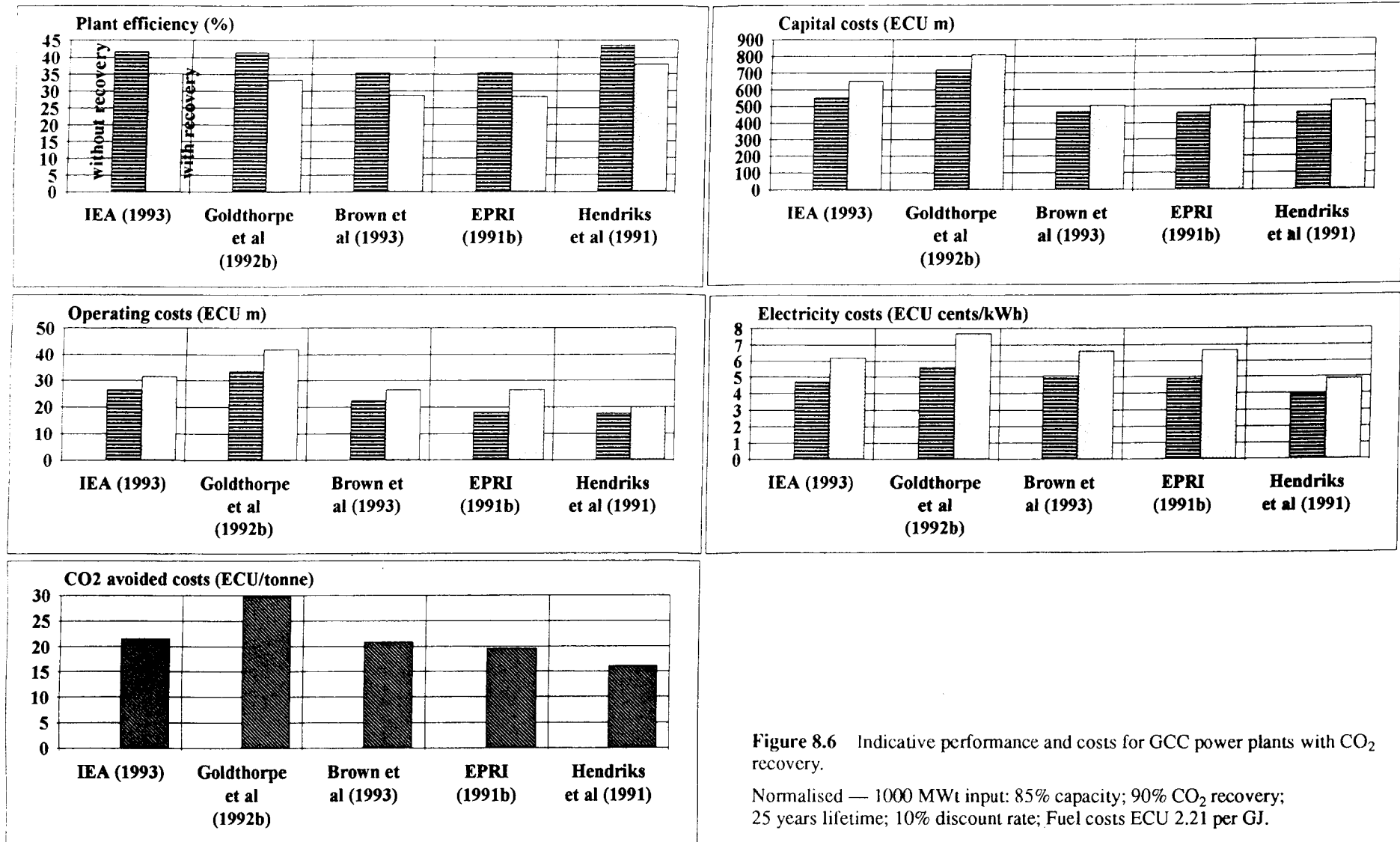


Figure 8.6 Indicative performance and costs for GCC power plants with CO₂ recovery.

Normalised — 1000 MWt input; 85% capacity; 90% CO₂ recovery; 25 years lifetime; 10% discount rate; Fuel costs ECU 2.21 per GJ.

solvent is achieved by reducing the partial pressure of CO₂.

After recovery the CO₂ gas is dehydrated (to prevent corrosion in the transport pipelines), liquefied and compressed to pipeline pressures (about 120 bar) ready for transport and disposal.

Costs of CO₂ Recovery from IGCC Plant

Figure 8.6 illustrates the performance and costs of CO₂ recovery from IGCC power plants for the studies which have been reviewed. They have been normalised for the same thermal input (1000 MWt), plant capacity (85), CO₂ recovery (90), lifetime (25 years), discount rate (10) and fuel costs (ECU 2.21 per GJ). In all cases CO₂ removal by physical scrubbing has been considered. The CO₂ recovery cost is calculated in comparison with the unmodified plant. Table 8.2 below gives the percentage decrease in electrical efficiency and the increase in costs when compared with an unmodified plant.

The study by Hendriks et al. (1991) gives the lowest plant performance penalties for CO₂ recovery, resulting in a 13 decrease in the overall thermal efficiency of the power plant. The plant capital and operating costs increase by about 15 and 14 percent respectively giving an overall increase in the electricity production costs of 24. The normalised cost of CO₂ recovery is estimated at ECU 16 per tonne.

The studies by the IEA (1993) and Goldthorpe et al. (1992b) give higher efficiency penalties of about 16% and 20 respectively. For the study by Goldthorpe et al. (1992b) the initial capital and operating costs of the IGCC plant without recovery are higher than the other four studies and with CO₂ recovery these cost items increase by 12 and 25 respectively. The electricity production costs increase by 38% and the normalised cost of CO₂ recovery is estimated at ECU 30 per tonne. For the IEA (1993) study the capital and operating costs increases by about 20% each, giving an increase in the electricity costs of 31% and an estimated cost of CO₂ recovery of ECU 22 per tonne. The studies by Brown et al (1993) and EPRI (1991b) give similar results.

This review therefore suggests that, with CO₂ recovery, the overall thermal efficiency of IGCC power plants may decrease by 13–20, the electricity production cost may increase by 24–38, and the normalised cost of CO₂ recovery when compared with an unmodified plant may range from ECU 16–30 per tonne of CO₂ recovered.

8.3.3 Pulverised coal combustion in a mixture of O₂ and recycled flue gas

Only one detailed study on the performance and costs of CO₂ recovery from coal-fired power plants with combustion in a mixture of oxygen and recycled flue gas has been identified [IEA Greenhouse Gas (1992)]. In this section an assessment of the main results from the study is carried out.

Coal Combustion in Oxygen and Recycled Flue Gas

The concept of coal combustion in a mixture of oxygen and recycled flue gas is to replace the nitrogen in air with recycled flue gas. Thus the combustion medium is oxygen produced from an air separation unit (ASU) and recycled flue gas (Figure 8.7). A ratio of recycled flue gas to oxygen can be obtained to give similar characteristics to combustion in air [Goldthorpe et al. (1992a)]. This type of combustion results in a flue gas containing high concentrations of CO₂ at the exhaust end ($\cong 85\text{--}90\%$ CO₂).

Carbon Dioxide Recovery

A number of technologies are possible for treating the CO₂ in the exhaust flue gases for this power plant option. Goldthorpe et al. (1992a) have shown that cryogenic processes will give lower efficiency penalties than other processes such as physical or chemical solvent scrubbing. The main energy consumption is due to the electrical requirement of the air separation unit which produces the oxygen for combustion.

The cryogenic process is operated at low temperatures and high pressures. Carbon dioxide in the exhaust gas is treated by compression, dehydration and cooling. This converts the CO₂ into the liquid phase. At this stage the single stage flash, distillation, and controlled freezing methods [IEA (1992)] may be used to recover up to 98 percent of high purity liquid CO₂.

After recovery the liquid CO₂ is further dehydrated and compressed to pipeline pressures (about 120 bar) ready for transport and disposal.

Performance and Costs of CO₂ Recovery

Figure 8.8 illustrates the performance and costs of CO₂ recovery from power plants with coal combustion in oxygen and recycled flue gas [IEA (1992)]. These results have been normalised for the same thermal input as the previous cases (1000 MWt), plant capacity (85), lifetime (25 years), discount rate (10) and fuel costs (ECU 2.21 per GJ). The amount of CO₂ removal in this case is considered to be 98%.

The only purpose of burning coal in a mixture of oxygen and recycled flue gas is to make it easier to recover CO₂ from the exhaust. Thus there is no comparable base case system which does not recover CO₂.

8.3.4 Natural gas turbine combined cycle (GTCC) power plants

Only one detailed study on the performance and costs of CO₂ recovery from gas turbine combined cycle power plants has been identified [IEA Greenhouse Gas (1992)]. In this section an assessment of the main results from the study is carried out.

Gas Turbine Combined Cycles

GTCC power plant consist of one or a number of natural gas turbines which produce power. Heat is recovered from

Table 8.2 Percentage decrease in efficiency and increase in costs.

Cost studies	Efficiency	Capital costs	Operating costs	Electricity costs
IEA (1993)	-16	+18	+19+	31
Goldthorpe et al. (1992b)	-20	+12	+25	+38
Brown et al. (1993)	-19	+8	+18	+31
EPRI (1991b)	-20	+10	+46	+37
Hendriks et al. (1991)	-13	+15	+14	+24

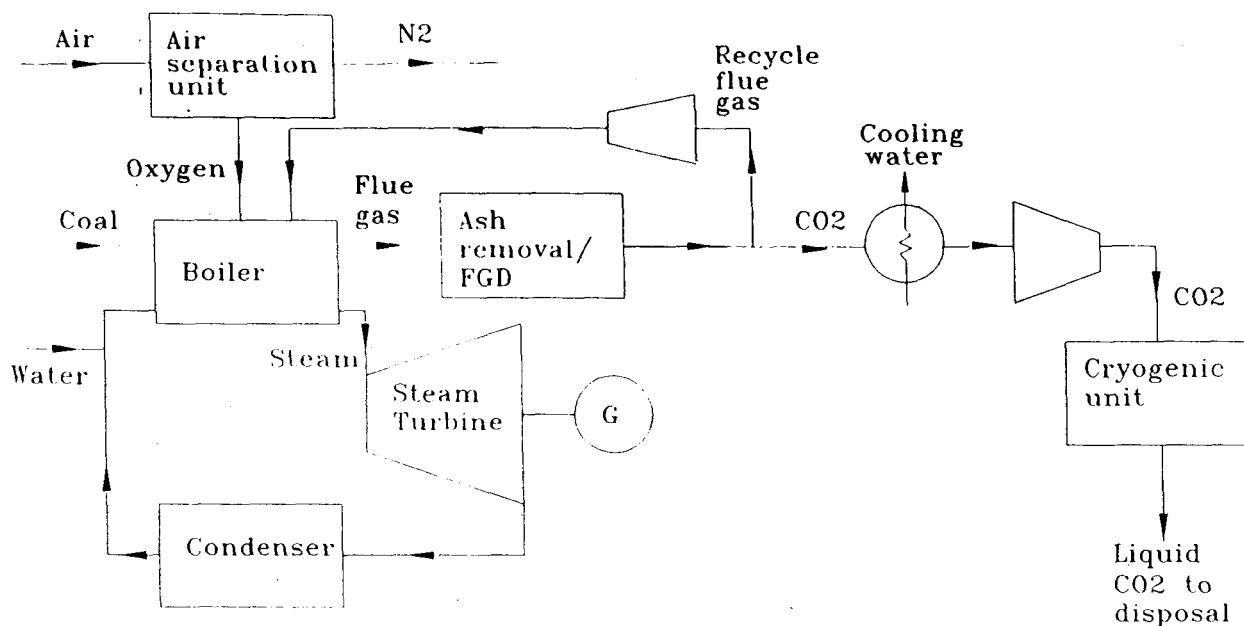


Figure 8.7 Block diagram of a plant in which coal is burnt in a mixture of oxygen and recycled flue gas and CO₂ is recovered.

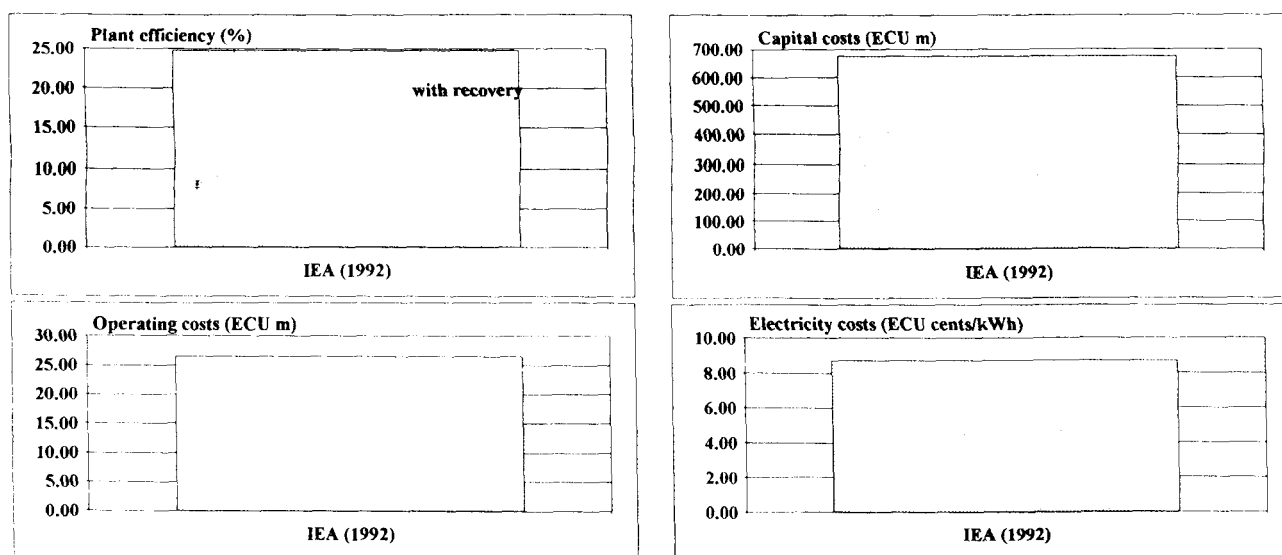


Figure 8.8 Indicative performance and costs for coal combustion in oxygen and recycled flue gas with CO₂ recovery.

Normalised — 1000 MWt input; 85% capacity; 90% CO₂ recovery; 25 years lifetime; 10% discount rate; Fuel costs ECU 2.21 per GJ.

the exhaust of the gas turbines and is used to generate steam, which is fed into a steam turbine to produce additional power (Figure 8.9). The high operating temperature of the gas turbine together with the recovery of heat from the exhausts gives a high overall thermal efficiency.

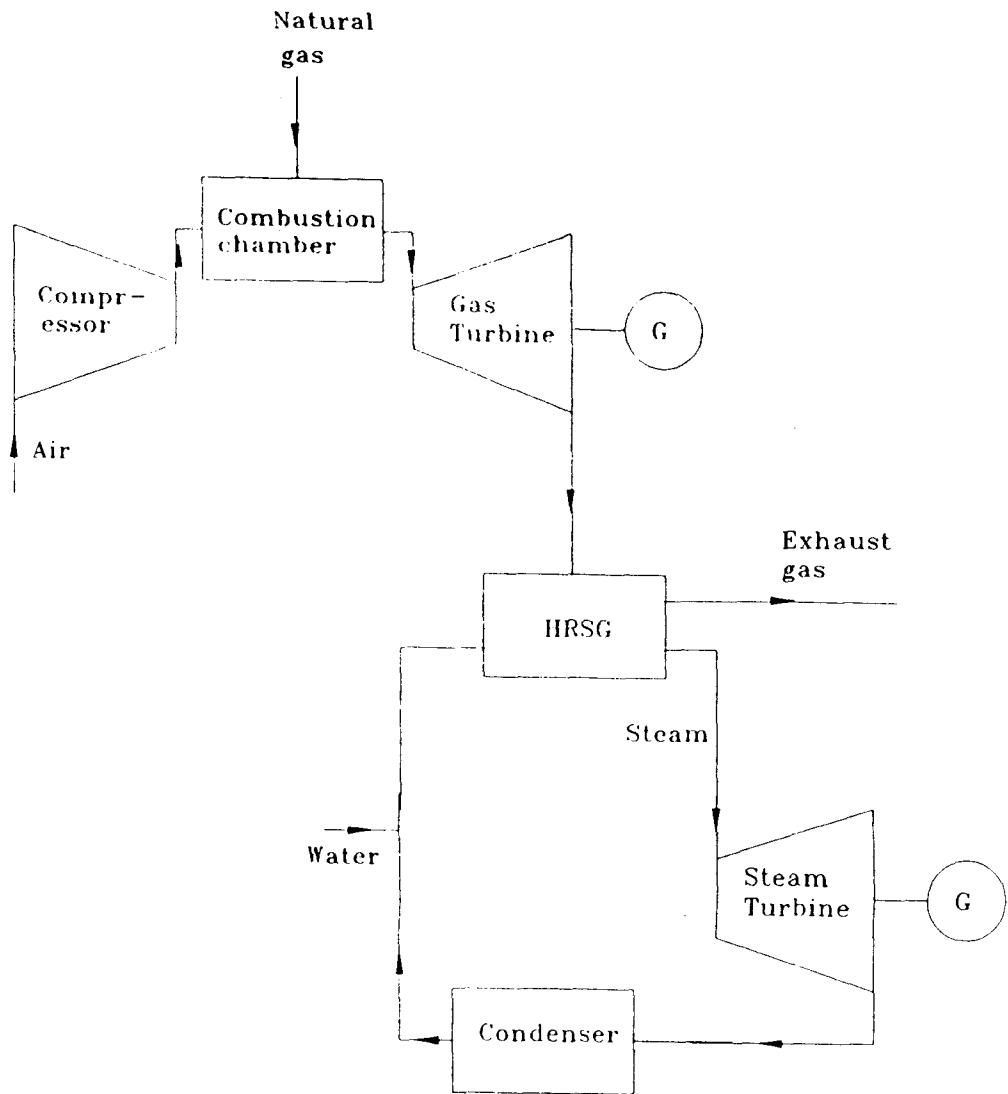
Carbon Dioxide Recovery

The exhaust from natural gas turbine combined cycle power plants have CO₂ concentrations typically in the range of 3–3.5% [IEA Greenhouse Gas (1992)]. Because of these low concentrations chemical solvent scrubbing seems the most suitable technology for CO₂ recovery. A number of other technologies have been considered in the

IEA study [IEA Greenhouse Gas (1993b)] but these require further development of the basic GTCC power plant to allow the combustion of natural gas in a mixture of oxygen and recycled flue gas. This method increases the CO₂ concentration in the exhaust flue gas. This study only considers the basic GTCC power plant with chemical absorption of CO₂.

Figure 8.10 shows a block flow diagram for the GTCC plant with chemical scrubbing. The carbon dioxide recovery process mainly involves the absorption of CO₂ in a chemical solvent (e.g. MEA) in an absorber column, and the regeneration of the solvent in the stripper column using low pressure steam extracted from the steam turbine.

Figure 8.9 Block diagram of a natural gas turbine combined cycle power plant.



After recovery the CO₂ gas is dehydrated (to prevent corrosion in the transport pipelines), liquefied and compressed to pipeline pressures (about 120 bar) ready for transport and disposal.

Costs of CO₂ Recovery

Figure 8.11 illustrates the performance and costs of CO₂ recovery from GTCC power plants for the IEA (1992) study. These results have been normalised for the same thermal input (1000 MWt), plant capacity (85%), CO₂ recovery (90%), lifetime (25 years), discount rate (10%) and fuel costs (ECU 3.32 per GJ). CO₂ removal by chemical scrubbing is considered. Table 8.3 below gives the percentage decrease and increase in the overall plant efficiency and costs respectively.

Table 8.3 Percentage decrease in efficiency and increase in costs

Cost study	Efficiency	Capital costs	Operating costs	Electricity costs
IEA (1992)	-21	+52	+82	+53

Plant performance penalties for CO₂ recovery result in a decrease of 21% in the overall efficiency. The plant capital and operating costs increase by about 52 and 82 percent respectively giving an overall increase in the electricity production costs of approximately 53%. The normalised cost of CO₂ recovery is estimated at ECU 53 per tonne when compared with the unmodified plant.

8.4 COSTS OF CO₂ AVOIDED AT POWER STATIONS

It is clear from the methodology outlined in Section 8.2 above that the costs of CO₂ avoided in each case will depend upon the type of basic plant without CO₂ recovery against which the CO₂ recovery option is being compared. While it seems obvious to compare two plants of the same type (i.e. one with and one without CO₂ recovery) it is equally valid to compare, for instance, a GTCC with CO₂ recovery with a PFFGD without CO₂ recovery. This would give the costs of CO₂ recovery when replacing PFFGD plant with new GTCC plant fitted with CO₂ recovery. This is a perfectly rational option. Thus in the calculation of the costs of CO₂ avoided it becomes important to decide which type of unmodified power plants are being replaced by modified plants which incorporate CO₂ removal. A

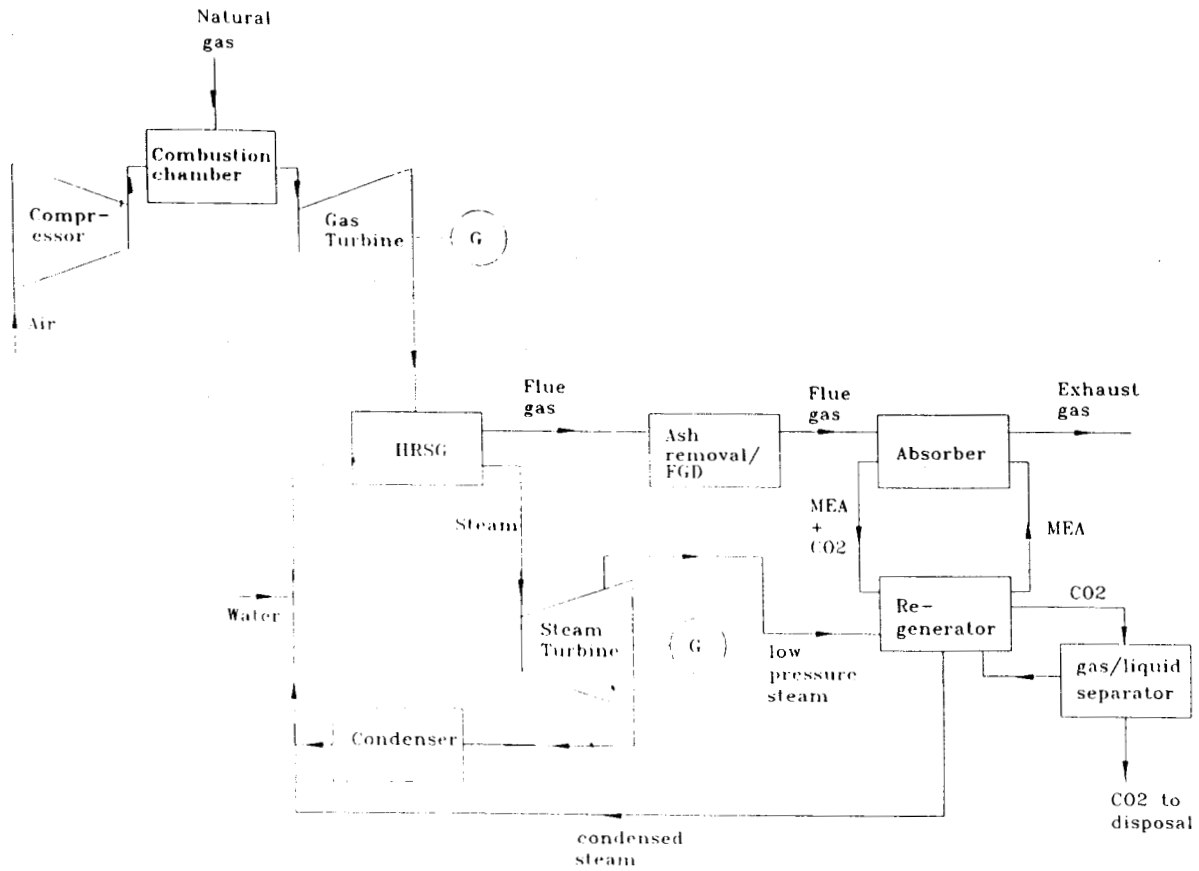


Figure 8.10 Block diagram of a natural gas turbine combined cycle power plant with modification for CO₂ recovery.

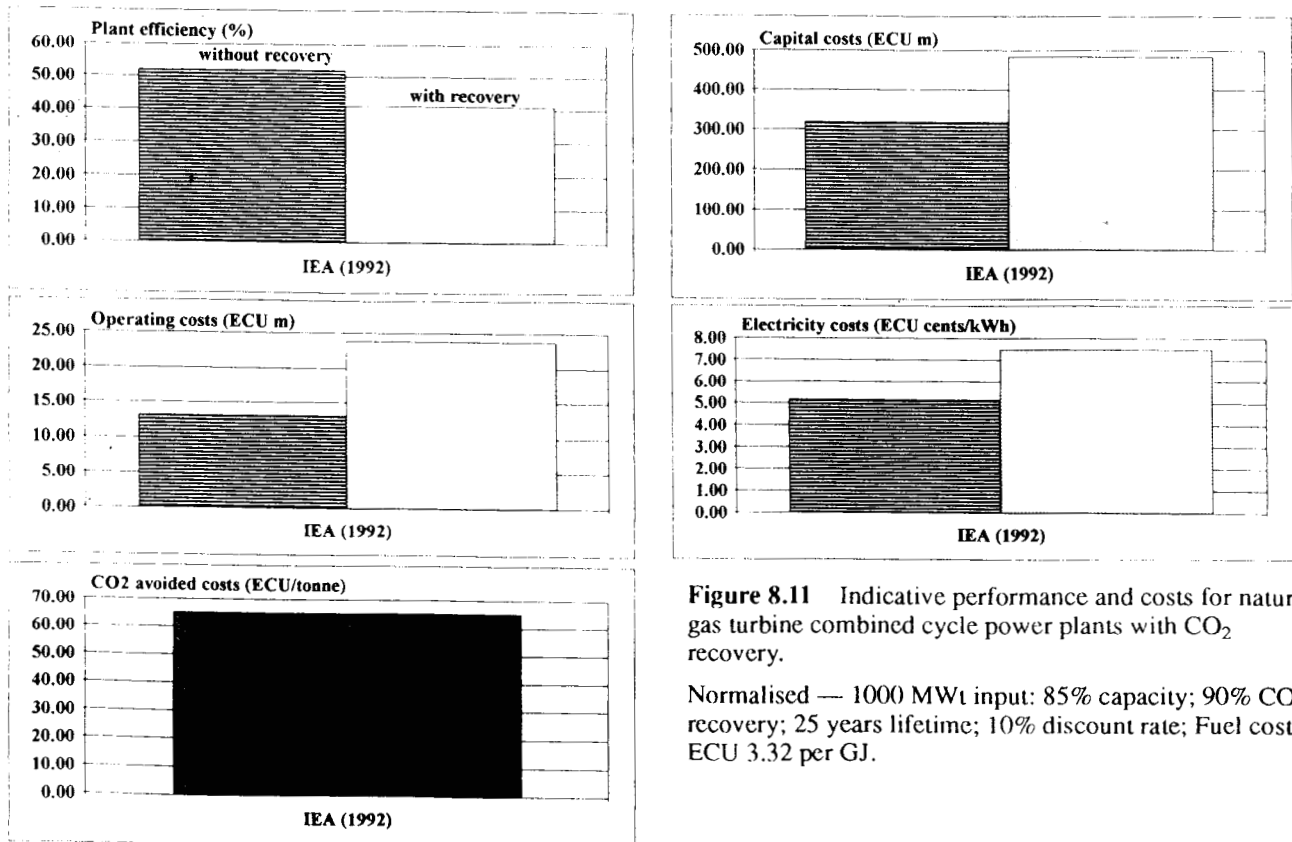


Figure 8.11 Indicative performance and costs for natural gas turbine combined cycle power plants with CO₂ recovery.

Normalised — 1000 MW_t input; 85% capacity; 90% CO₂ recovery; 25 years lifetime; 10% discount rate; Fuel costs ECU 3.32 per GJ.

Table 8.4 Summary of electricity costs and costs of CO₂ avoided from power stations.

	Power station types								
	OFFFGD(1)	PFFGD(2)	IGCC(3)	IGCC(4)	IGCC(5)	O ₂ /CO ₂ (6)	GTCC(7)	GTCC(8)	GTCC(9)
Electricity costs (ECU cents/kWh)	5.06	9.35	5.06	6.95	6.95	8.59	5.06	7.34	7.34
CO ₂ avoided costs (ECU/tonnes)		57.35	-0.27	26.68	24.53	41.96	-0.1	64.37	27.93

Column (1) shows an unmodified pulverised fuel plant with flue gas desulphurisation (PFFGD). Column (2) shows the electricity costs and costs of avoided CO₂ when compared with the plant in column (1). Column (3) shows an unmodified integrated coal gasification plant. The costs of CO₂ avoided are in comparison with the PFFGD plant in column (1). Column (4) shows the costs of CO₂ avoided when compared with the plant in column (3) and column (5) shows the costs when compared to the PFFGD plant in column (1). Column (6) shows the costs of an O₂/CO₂ recycle plant when compared with the PFFGD plant in column (1). Column (7) show the costs of an unmodified Gas turbine combined cycle plant. The costs of CO₂ avoided are in comparison with the PFFGD plant in column (1). Column (8) shows the costs of CO₂ avoidance when compared with the unmodified plant in column (7) and column (9) shows the costs of CO₂ avoidance when compared with the PFFGD plant in column (1).

Table 8.5 Pulverised fuel with flue gas desulphurisation; costs of CO₂ avoided at the power plant.

	PFFGD (1)	PFFGD + CO ₂ Recovery (2)
Scale factor	1.00	1.39
Thermal input (MW)	1289.00	1785.31
Gross output (MW)	N/A	N/A
Net output (MW)	500.00	500.00
Efficiency (%)	38.79	28.01
Plant capacity (%)	85.00	85.00
CO ₂ emission (t/h)	434.00	60.11
CO ₂ recovery (%)		90.00
Lifetime (years)	25.00	25.00
Discount rate (%)	10.00	10.00
Capital recovery factor	0.11	0.11
CAPITAL COSTS (ECU m)		
Plant	741.00	1462.04
ANNUAL COSTS (ECU m)		
Operating and maintenance	30.29	81.02
Fuel costs	76.58	106.06
ANNUAL CHARGE (ECU m)		
Electricity costs (ECU cents/kWh)	5.06	9.35
CO ₂ avoided (tonnes per hour)		373.89
CO ₂ avoided costs (ECU/tonne)		57.35

Data taken from 'Technical and Economic Assessment of CO₂ Abatement Technologies based on PFGD with MEA Scrubbing'.
S H Goldthorpe (1993)

CO₂ recovery costs are calculated with reference to the unmodified plant (1)

Table 8.6
Integrate
gasification
combined cycle:
costs of CO₂
avoided at the
power plant.

	IGCC (1)	IGCC + CO ₂ Recovery (2)	IGCC + CO ₂ Recovery (3)
Scale factor	0.85	0.96	0.96
Thermal input (MW)	1207.69	1501.94	1501.94
Gross output (MW)	560.68	620.43	620.43
Net output (MW)	500.00	500.00	500.00
Efficiency (%)	41.40	33.29	33.29
Plant capacity (%)85.00	85.00		85.00
CO ₂ emission (t/h)	403.42	50.17	50.17
CO ₂ recovery (%)		90.00	90.00
Lifetime (years)	25.00	25.00	25.00
Discount rate (%)	10.00	10.00	10.00
Capital recovery factor	0.11	0.11	0.11
CAPITAL COSTS (ECU m)			
Plant	691.11	965.80	965.80
ANNUAL COSTS (ECU m)			
Operating and maintenance40.56	63.00		63.00
Fuel costs	71.74	89.23	89.23
ANNUAL CHARGE (ECU m)	188.44	258.62	258.62
Electricity costs (ECU cents/kWh)	5.06	6.95	6.95
CO ₂ avoided (tonnes per hour)	30.58	353.25	383.83
CO ₂ avoided costs (ECU/tonne)	-0.27	26.68	24.53

Basic data taken from 'Economic Assessment of CO₂ Abatement Technologies based on IGCC with Physical Scrubbing or Membrane Separation'.

S H Goldthorpe and D R Exelby (1992). Some adjustments have been made to make the IGCC plant identical with the PFFGD plant in Table 8.5 column (1).

The CO₂ recovery costs (2) are calculated with reference to the unmodified plant in column (1) and those in column (3) are calculated with respect to the unmodified PFFGD plant in Table 8.5).

rational way to choose this base case is to take the unmodified option or options which produce electricity at the lowest unit costs. The basic PFFGD plant has the lowest capital and fuel costs. The integrated coal gasification combined cycle (IGCC) plant is more expensive but the higher thermal efficiency compensates for this with the result that the electricity costs are very close to those of the PFFGD plant. The data which have been used in this study have been adjusted to make the unit costs of the PFFGD and IGCC plant identical. The natural gas fired gas turbine combined cycle plant GTCC uses a more expensive fuel than the PFFGD plant but again this is compensated for by

a higher cycle efficiency with the result that the unit costs are almost identical with the PFFGD plant. With appropriate choice of fuel costs it is possible to make the unit costs of electricity production for these three basic plant nearly equal. This device greatly simplifies the interpretation of the results and still lies within the limits of the uncertainty of the calculations.

The results are shown in Tables 8.5–8.8 and summarised in Table 8.4. It is possible to avoid CO₂ at almost zero cost by simply switching from PFFGD to IGCC or GTCC plant without CO₂ recovery. This is because the IGCC and GTCC plant have higher thermal efficiency than the

Table 8.7 Oxygen/CO₂ recycle, costs of CO₂ avoided at the power plant.

	O ₂ /CO ₂ + CO ₂ Recovery
Scale factor	1.00
Thermal input (MW)	2020.00
Gross output (MW)	824.00
Net output (MW)	500.00
Efficiency (%)	24.75
Plant capacity (%)	85.00
CO ₂ emission (t/h)	13.20
CO ₂ recovery (%)	98.00
Lifetime (years)	25.00
Discount rate (%)	10.00
Capital recovery factor	0.11
CAPITAL COSTS (ECU m)	
Plant	1340.30
ANNUAL COSTS (ECU m)	
Operating and maintenance	52.32
Fuel costs	120.00
ANNUAL CHARGE (ECU m)	319.98
Electricity costs (ECU cents/kWh)	8.59
CO ₂ avoided (tonnes per hour)	420.80
CO ₂ avoided costs (ECU/tonne)	41.96

Data taken from 'Carbon Dioxide Capture: An examination of potential Cryogenic Technologies for the collection of CO₂ and other Greenhouse Gases arising from Power Generation using Fossil Fuel'.
IEA Greenhouse Gas R&D Programme — IEA/92/OE7 (1992)

The CO₂ recovery costs are calculated with respect to the unmodified PFFGD plant in Table 8.5.

PFFGD and because burning the hydrocarbon gas produces less CO₂ than the burning of coal. More CO₂ can be avoided by recovering CO₂ from the IGCC or GTCC plant. The costs of this further recovery are high because of the investments required and the additional fuel which must be burnt to compensate for the reduced thermal efficiency of the modified plant. The costs of further CO₂ recovery by modifying the GTCC plant are particularly high because of the high fuel costs. The costs of the savings in the different stages can be seen by comparing a

PFFGD plant with a GTCC plant with and without CO₂ recovery.

- A PFFGD plant generating 500 MW (net) releases 434 tonnes of CO₂ per hour.
 - A GTCC plant generating 500 MW (net) releases 203 tonnes of CO₂ per hour.
 - A GTCC plant with CO₂ recovery generating 500 MW (net) releases 26 tonnes of CO₂ per hour.
- Thus 434 - 203 = 231 tonnes of CO₂ per hour are avoided at zero cost when the PFFGD plant is replaced by the GTCC plant.

203 - 26 = 177 tonnes per hour are avoided at a cost of 64.37 ECU/tonne when the GTCC plant is replaced by a GTCC plant with CO₂ recovery generating 500 MW net.

Overall in replacing a PFFGD plant with a GTCC plant with CO₂ recovery generating 500 MW (net) the total CO₂ avoided is 408 tonnes.

$$\frac{231}{408} \times 100 = 57\% \text{ is avoided at zero cost.}$$

$$\frac{177}{408} = 43\% \text{ is avoided at 64.37 ECU/tonne}$$

hence the weighted cost of CO₂ avoided is;

$$64.37 \times 0.43 = 28 \text{ ECU/tonne.}$$

8.5 CO₂ TRANSPORT

It is assumed that CO₂ is collected from a group of power stations as a supercritical liquid using a collection system of pipes and is then fed into a single large pipe to transmit it to the disposal site. All of the initial compression costs and parasitics are included in the power plant calculations. It is further assumed that the collection and transport of CO₂ is carried out with the CO₂ as a supercritical liquid and that the pressure in the system does not fall below 80 bars in either onshore or offshore cases. Dynamic friction losses in the pipeline reduce the pressure of the CO₂ and this may need to be restored at some intervals by further compression. Because of the expense of the compensations it is normal to avoid compression so far as possible offshore. Low velocities are assumed (about 1 m/s) and pipe diameters are chosen so that compression stations are at least 250 km apart.

In general, the carrying capacity of pipelines offshore is higher than it is onshore. This is for two reasons:

- there is usually a higher static head gradient in the pipelines offshore which compensates for the dynamic head loss leading to an increase in design velocities.
- fluid temperatures are lower and average pressures are higher hence overall densities are higher.

Overall, in these calculations the carrying capacity onshore is about 75% what it would be offshore, and, as pipeline costs are broadly comparable onshore and offshore, the unit costs of CO₂ transport offshore are lower than they are onshore. This, together with the environmental and other problems associated with major pipe

laying projects onshore, gives an advantage to offshore disposal options.

8.6 CO₂ UNDERGROUND DISPOSAL

A number of important cost and physical calculations are carried out in relation to the disposal site. The cost calculations fall into two groups; onshore and offshore.

8.6.1 Onshore costs

The main onshore cost is the cost of drilling the injection wells. Here it is assumed that costs vary with depth only using the relationship shown in Figure 8.12.

8.6.2 Offshore costs

The offshore cost calculations are more complex because a variety of solutions are possible. With existing or exhausted oil and gas fields it may be possible to renovate and use the existing platforms. These platforms are all either at the end or close to the end of their design lifetimes and re-use would require reclassification, some renovation and possibly significant operation and maintenance costs to extend their life for another 25 years. Opinion within the industry is that this is a risky and possibly expensive option and that it is safer to assume that new facilities would be installed for CO₂ injection. This is the assumption which has been made in this study. The only exceptions to this are the enhanced oil recovery cases, where it has been assumed that CO₂ re-injection can be incorporated along with the normal platform activities on oil production platforms which have a significant remaining productive life.

For new facilities the main choice lies between subsea completions and simple wellhead platforms. Discussions with the industry have led to the formulation of a set of

rules by which the options can be chosen, and costing functions have been defined in each case. Wellhead platforms are used for water depths of less than 150 metres and subsea completions are assumed in deeper water.

Jack-up drilling rigs are used in water depths of less than 150 metres and semi-submersibles in deeper water.

8.6.3 Disposal volume

Different calculations are required for each option.

- **Aquifers.** The calculation determines the total pore volume in the formation in the area under consideration. This is corrected to determine the pore volume within 'closed' structures ie. above any overflow points and corrected again to take account of the proportion of the formation fluid which the injected CO₂ can displace; the 'storage efficiency'.
- **Gas fields.** The calculation determines the total pore volume vacated by the produced gas and it is assumed that all of this is available for CO₂ disposal.
- **Oil fields.** The calculation determines the total pore volume vacated by the produced oil during primary and tertiary recovery and it is assumed that the majority of this is available for CO₂ disposal. A special oil field case is that of enhanced recovery of oil this is described below.

8.6.4 Disposal system lifetime

This is calculated from the disposal volume and the rate of disposal of CO₂ from the power stations. The disposal lifetime is used in the calculation of the capital recovery factor for the repayment of the investment costs (see equation 8.2) above and it is a very important parameter. Short lifetimes give high annual payments for the recovery

Figure 8.12 Onshore and offshore well costs.

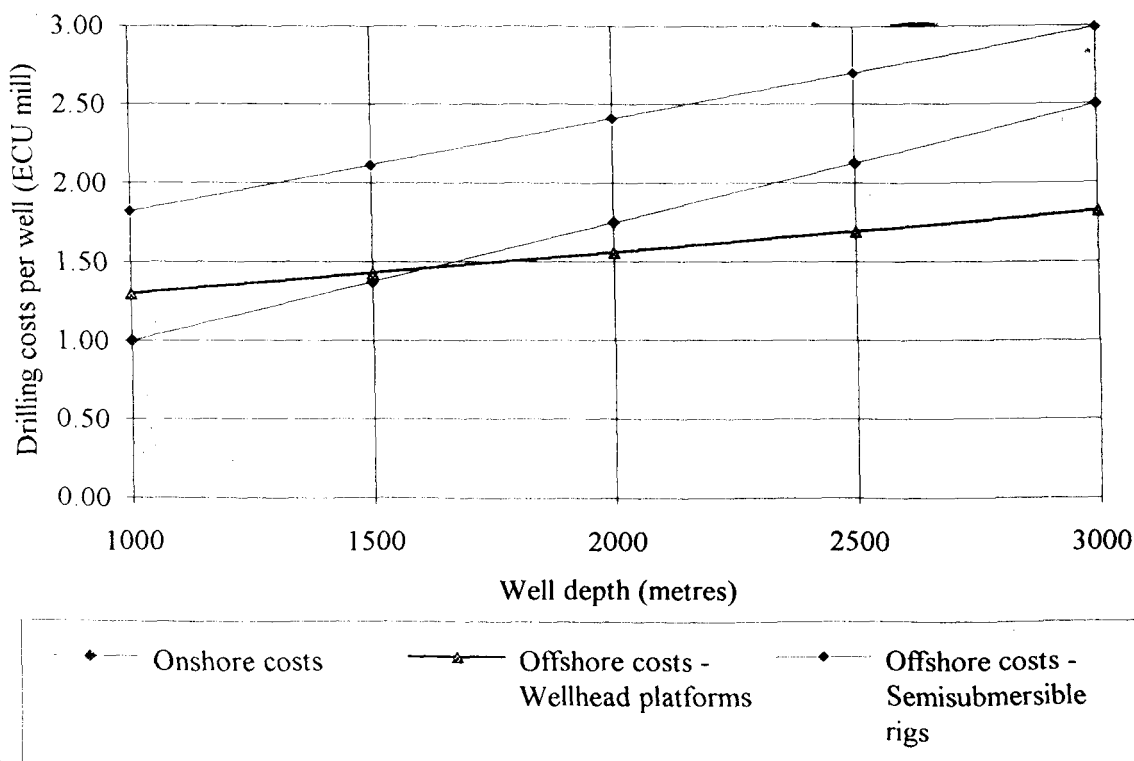


Table 8.8 Gas turbine combined cycle costs of CO₂ avoided at the power plant.

	GTCC (1)	GTCC + CO ₂ Recovery (2)	GTCC + CO ₂ Recovery (3)
Scale factor	1.08	1.36	1.36
Thermal input (MW)	962.37	1217.40	1217.40
Gross output (MW)	506.45	640.67	640.67
Net output (MW)	500.00	500.00	500.00
Efficiency (%)	51.96	41.07	41.07
Plant capacity (%)	85.00	85.00	85.00
CO ₂ emission (t/h)	203.23	25.71	25.71
CO ₂ recovery (%)		90.00	90.00
Lifetime (years)	25.00	25.00	25.00
Discount rate (%)	10.00	10.00	10.00
Capital recovery factor	0.11	0.11	0.11
CAPITAL COSTS (ECU m)			
Plant	306.13	587.59	587.59
ANNUAL COSTS (ECU m)			
Operating and maintenance	12.58	29.02	29.02
Fuel costs	142.02	179.66	179.66
ANNUAL CHARGE (ECU m)			
	188.33	273.41	273.41
Electricity costs (ECU cents/kWh)	5.06	7.34	7.34
CO ₂ avoided (tonnes per hour)	230.78	177.52	408.29
CO ₂ avoided costs (ECU/tonne)	-0.10	64.37	27.93

Data taken from 'Carbon Dioxide Capture: An experience of potential absorption technologies for the collection of CO₂ and other Greenhouse Gases arising from Power Generation using fossil fuel'. IEA Greenhouse Gas R&D Programme — IEA/92/OE4 (1992)

The costs of CO₂ avoidance in (1) and (3) are calculated with respect to the unmodified PFFGD plant in Table 8.5. The costs of CO₂ avoidance in (2) are calculated with respect to GTCC plant in column (1).

of investment capital and hence high unit costs of CO₂ disposal. The scheme lifetime is also limited ultimately by the physical lifetime of the facilities — pipeline, etc. In these calculations, if the disposal lifetime is less than 25 years then this lifetime is taken as the system lifetime. If the disposal lifetime is greater than 25 years then 25 years is taken as the system lifetime.

(8.7)

8.6.5 Numbers of wells required to inject the CO₂ supercritical liquid

Following Hendriks and Blok (1993), the injectivity of the wells 'q' is calculated from:

Where q = CO₂ flow rate under standard conditions (m³/s)
 K = reservoir permeability (m²)
 h = reservoir thickness (m)
 ΔP = overpressure of injection fluid above reservoir pressure (Pa)
 ρ_r = density of CO₂ in reservoir (kg/m³)

- ρ_s = density of CO₂ under standard conditions (kg/m³)
- r_e = radius of influence of the injection well (m)
- r_w = radius of the well (m)
- μ_r = viscosity of CO₂ in reservoir (Pa.s)

An upper limit on well flow of 2500 tonnes/day of CO₂ is assumed.

Hence if the injectivity is <2500 tonnes/day per well then the number of wells is calculated from

$$\frac{\text{disposal rate of CO}_2 \text{ (tonnes/day)}}{\text{injectivity per well}}$$

If the injectivity is >2500 tonnes/day per well then the number of wells is calculated from

$$\frac{\text{disposal rate of CO}_2 \text{ (tonnes/day)}}{2500}$$

Very low transmissivities are required for injectivities to fall below 2500 tonnes/day.

The CO₂ is delivered to the wellheads at above 80 bars, well flow rates are low and dynamic pressure losses in the wells are also low. Thus at shallow depths there is an excess of pressure at the well bottom over and above what is required to inject the CO₂ into the aquifer. At greater depths the difference in density between water and CO₂ means that the excess pressure becomes progressively reduced and pumping of the CO₂ is required. CO₂ injection is normally self-pumping at shallow depths down to about 3 km. It is assumed here that all of the cases studied in this work are shallow enough to be self-pumping at the pressures and injection flows assumed.

8.7 SIMULATION OF ENHANCED OIL RECOVERY

The use of CO₂ in enhanced oil recovery has been suggested by a number of authors as a practical method of disposing of CO₂ recovered from power stations. The reservoir voids left by both the primary and tertiary recovery could accommodate significant volumes of CO₂ and the sale of the oil produced during the tertiary recovery phase will defray some of the costs of CO₂ disposal.

The main methodological problem associated with this case is the treatment of the CO₂ produced during the burning of the tertiary oil production fractions. Two limiting cases can be identified.

- The oil produced during enhanced oil recovery is offered on world markets in a way which expands demand and increases CO₂ production. In this case the benefits of CO₂ disposal would be negated by the additional production of CO₂ from the oil which is sold.
- The oil produced during enhanced oil recovery is offered on world markets in such a way that demand does not expand; hence it replaces oil produced by primary or secondary recovery from other fields. In this case no net additional CO₂ is released to the atmosphere as a consequence of the enhanced oil recovery.

The calculations here are carried out using the assumptions of the second case i.e. production of oil by

enhanced oil recovery does not lead to the net release of CO₂ to the atmosphere.

8.7.1 The model of enhanced oil recovery

Storage Capacity

Oil production from an oil reservoir typically is carried out in three phases:

- primary production when oil is produced under reservoir pressure alone
- secondary production where reservoir pressure is maintained by water flooding or gas injection
- tertiary production - enhanced recovery where, when liquid CO₂ is used trapped oil dissolves in the injected CO₂.

It is assumed here that storage capacity of the reservoir is the sum of the primary and the tertiary production, and can be calculated as follows. The CO₂ disposal capacity is given by

$$DC = (P + E) Q \quad (8.7)$$

- where
- Q = Original oil in place (OOIP) (m)³
 - P = Primary production fraction
 - S = Secondary production fraction
 - E = Tertiary production fraction

CO₂ Recycling

Additional costs during enhanced oil recovery using CO₂ are associated with the recycling of CO₂ which is produced along with the oil during the tertiary production phase. If the production rate of oil during enhanced oil recovery is R tonnes/hr the quantity of CO₂ recycled is kR tonnes/hr (k may be in the region of 1 or above). This produced CO₂ is recovered from the CO₂ oil mixture by separation at atmospheric pressure and must be compressed to the injection pressure of about 80 bars before re-injection into the field. Thus CO₂ is being injected at rates which are in the region of twice the oil production rates and additional wells may be needed for this.

The enhanced oil recovery concept

It is assumed that CO₂ disposal commences at the start of water flooding and that during this phase the CO₂ is disposed of in the voids left during primary production. CO₂ injection continues beyond the water flooding phase when enhanced oil recovery takes place. In order to simplify the calculations it is assumed that CO₂ is disposed of within the reservoir at a constant rate during these different phases.

If the rate of CO₂ disposal is C tonnes/yr and the disposal takes place in two phases then for a single oil field (Figure 8.13a) during Phase 1 CO₂ disposal into primary voids with no enhanced recovery then the lifetime of phase 1 'L₁' is given by

$$L_1 = \frac{PQ}{C} \text{ yrs} \quad (8.8)$$

During phase 2 CO₂ disposal and enhanced recovery occur together and the lifetime 'L₂' is given by

$$L_2 = \frac{EQ}{C} \quad (8.9)$$

The concept is shown in Figure 8.13.

If the CO₂ which is disposed of directly replaces produced oil from within the reservoir pore spaces then the oil production rate R is identical with the CO₂ disposal rate.

Then the lifetime of the CO₂ disposal L is given by

$$L = (P + E) \frac{Q}{C} \quad (8.10)$$

and the oil sales last between L₁ and L years.

If a group of oil fields (Figure 8.13b) in varying stages of production are linked together at the end of the transmission pipeline, then it may be possible to manage the distribution of CO₂ to the fields in such a way that the overall rate of disposal is constant and the overall rate of oil production is constant.

Then by the same token, if taking all of the fields together, 'Q_t' is original oil in place, 'P_{ave}' is the average fraction of primary production and 'E_{ave}' is the average fraction of tertiary production;

Then the lifetime for CO₂ disposal L is given by

$$L = \frac{(P_{ave} + E_{ave})}{C_t} Q_t \text{ yrs} \quad (8.11)$$

where Q_t = total OOIP for fields (tonnes)
P_{ave} = average fraction of primary production
E_{ave} = average fraction of tertiary production
C_t = total rate of CO₂ disposal (tonnes/yr)

The average rate of oil production from tertiary production 'R_{ave}' is given by

$$R_{ave} = \frac{E_{ave} Q_t \times C_t}{(P_{ave} + E_{ave}) Q_t} \text{ tonnes/yr} \quad (8.12)$$

$$= \frac{E_{ave} C_t}{(P_{ave} + E_{ave})} \text{ tonnes/yr} \quad (8.13)$$

8.8 CO₂ DISPOSAL TEST CASES AND SENSITIVITY STUDIES

In order to test the economic model and generate some typical estimates of disposal costs a number of test cases have been identified. One of the main issues affecting the economics of CO₂ disposal is the lifetime of the disposal reservoir. Small reservoirs quickly become filled with CO₂ and the investments associated with their use become redundant. This results in very high disposal costs. In order to avoid this the test cases have been chosen with reservoirs which are large enough to accept the CO₂ from a number of power stations over a significant lifetime, i.e. at least 25 years.

Although data from the inventories and other formation data have been used as the bases of these cases no special significance should be attached to this. These cases are

illustrative only of the range of costs of CO₂ disposal and should not be seen as detailed costings of prototype developments.

Aquifers

Three cases have been examined, one onshore; the Bunter Sandstone Formation in Denmark, and two offshore; the Bunter Sandstone in the UK sector of the Southern North Sea, and the Utsira Formation in the Norwegian sector of the Central North Sea.

The Bunter case in Denmark is based upon information for the Thisted Dome. While this no longer appears in the theoretical inventory because its crest is above 800 metres, it does provide an example of a large onshore case. The fact that its crest is above 800 metres simply means that storage in the top part of the dome will be at subcritical conditions.

Gas fields

Two cases have been chosen. One onshore; the Groningen gas field in the Netherlands, and one offshore; the Leman gas field in the UK sector of the Southern North Sea. Real field data have been used as the bases of these cases but once again no special significance should be attached to this.

Oil field disposal with Enhanced Recovery

Two conceptual cases have been considered. A large field similar to the Forties field in the central North Sea, which accommodates all of the CO₂ from a group of power stations and where the enhanced oil production is delayed due to the production profile of the field. Secondly, a group of smaller oil fields which are at different stages of development where CO₂ can be supplied to different fields at different times and hence disposal and oil production can take place more or less continuously and without delay.

The CO₂ is collected from power station groups which are representative of typical groups in Northern Europe and the UK. The location of the cases are shown in Figure 8.14.

The results from the model runs of these test cases are given in the Appendix 8A spreadsheets.

Sensitivity studies

Sensitivity studies have been carried out for two main reasons:

- to illustrate the behaviour of the model
- to investigate the sensitivity of the results of the cases to the important assumptions

Three main aspects of the model have been examined:

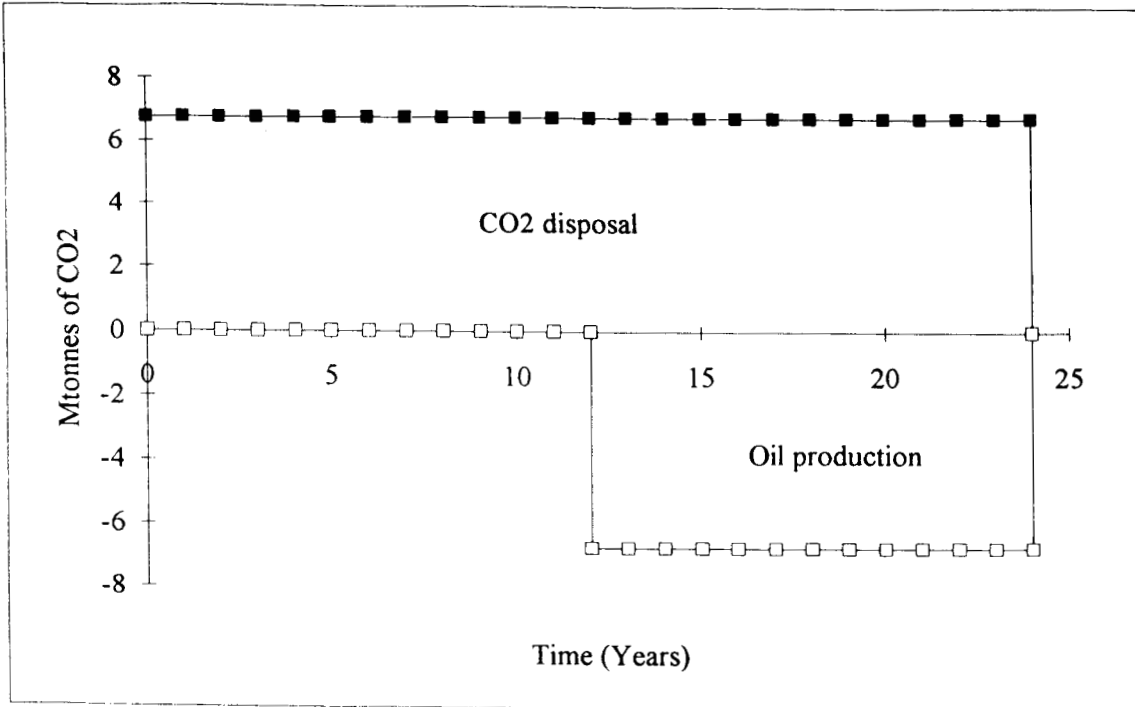
- pipeline calculations
- reservoir parameters
- enhanced oil recovery

Pipeline calculations

Figure 8.15 shows how pipeline sizes vary with the volume of CO₂ carried; the carrying capacity offshore is higher than that onshore for the reasons outlined above (Section 8.5). This produces a significant difference in the specific costs of CO₂ transport (Figure 8.16) between the onshore

Figure 8.13 Schematic profiles of CO₂ and oil production in enhanced oil recovery cases.

(a) Single oil field



(b) Group of small fields

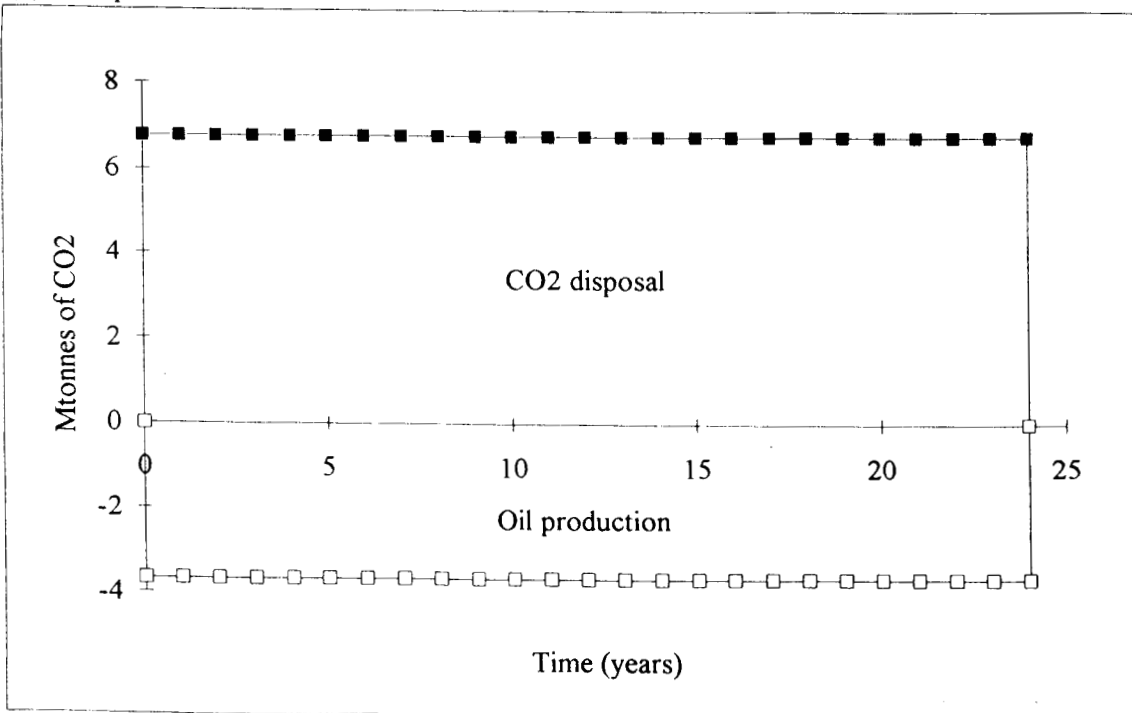
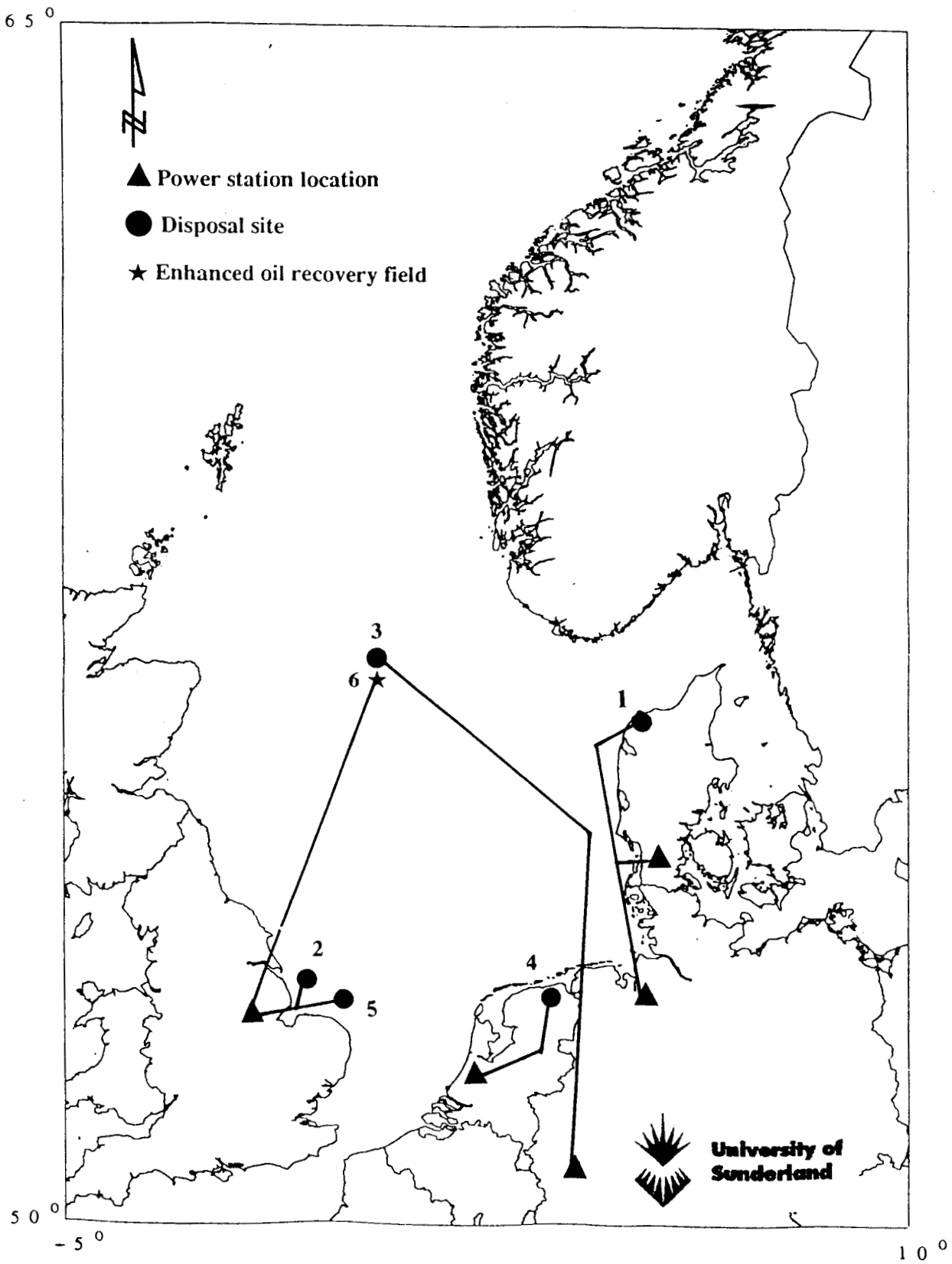


Figure 8.14 Indicative locations of economic model test cases.



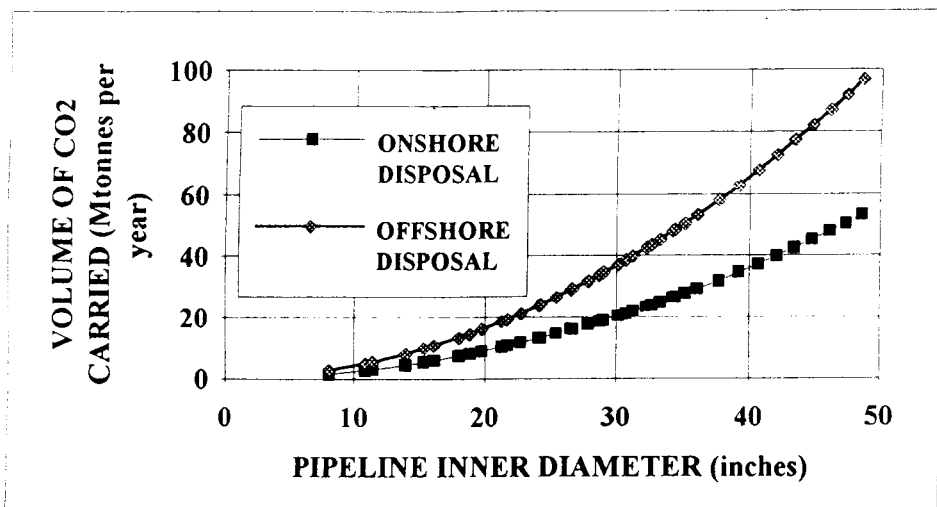


Figure 8.15 Pipeline flow capacities.

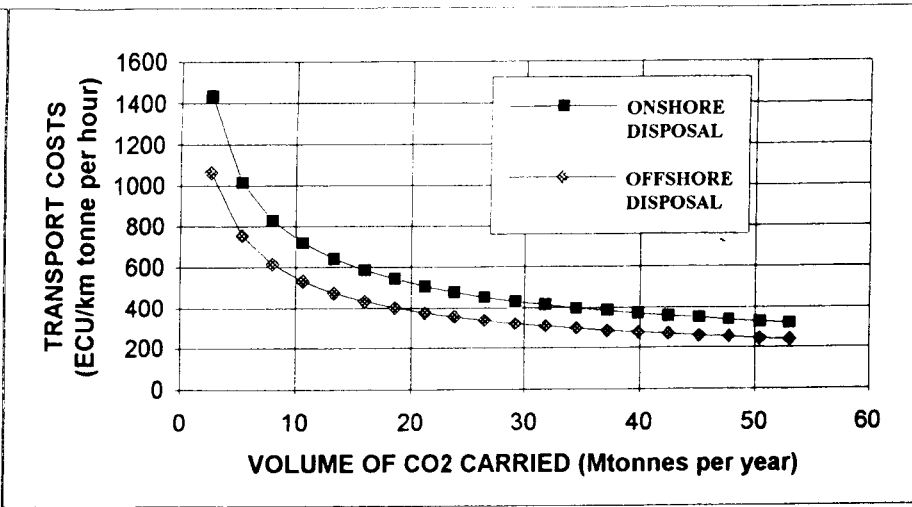


Figure 8.16 Variation in pipeline capital costs with CO₂ volume flow.

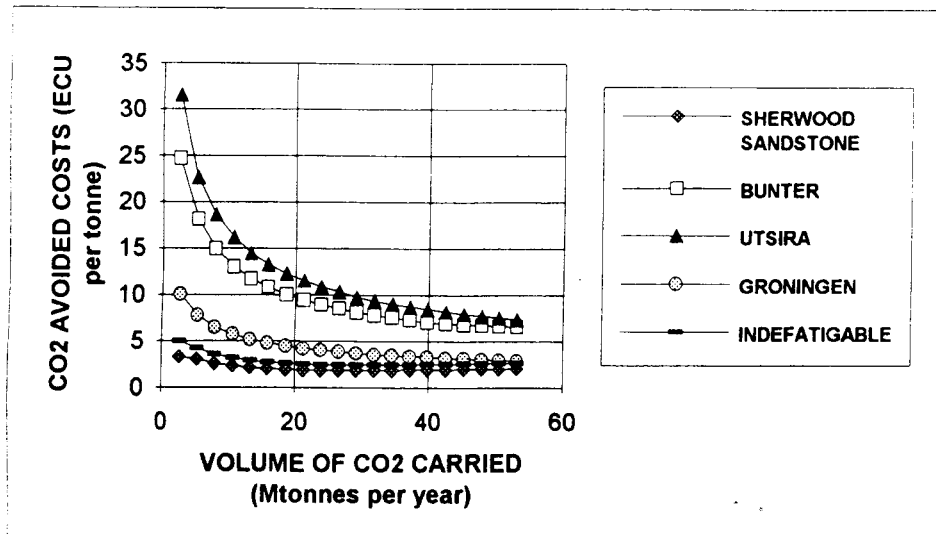


Figure 8.17 Variation in CO₂ transport costs with CO₂ volume flow.

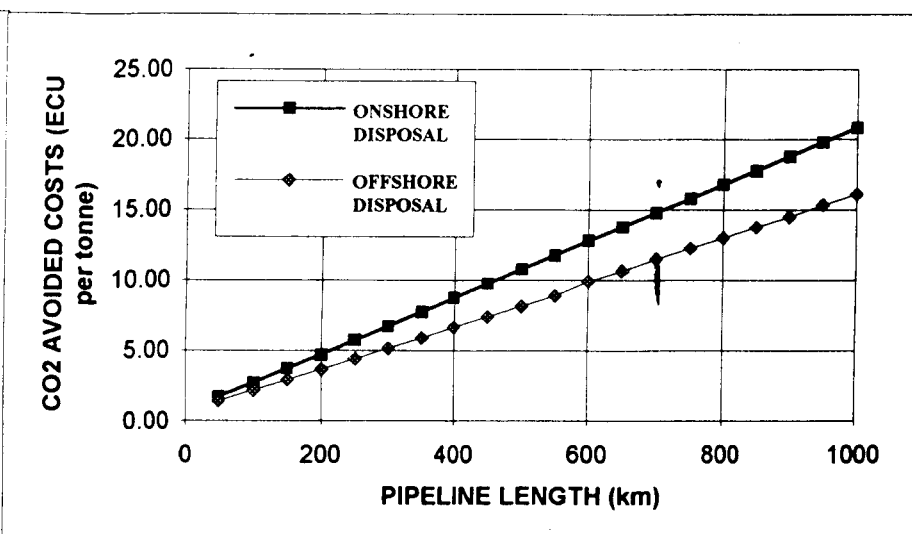


Figure 8.18 Variation in CO₂ transport costs with distance to disposal.

and offshore cases. The sensitivities show significant economies of scale in the specific transport costs. Figure 8.17 shows the contribution of the CO₂ transport costs ('L' above, section 8.2) to the overall costs of CO₂ avoidance. Economies of scale are reproduced but the major effect is the length of the pipeline. The cases with the longest pipeline — Bunter and Utsira — have the highest costs. Figure 8.18 shows the sensitivity of the costs of CO₂ avoidance to pipeline length; costs are linear with pipeline length as would be expected.

Reservoir parameters

Figures 8.19 and 8.20 show the effect of reservoir disposal capacity on the reservoir contribution to the costs of CO₂ avoidance ('D' above, section 8.2). Reservoir disposal capacity affects the lifetime of the CO₂ disposal system, small capacities give small lifetimes and this in turn gives high unit costs of CO₂ avoidance. The disposal cases have all been chosen to give disposal lifetimes of 25 years or above. Smaller reservoirs or traps have been ignored in these calculations.

Figures 8.21 and 8.22 show the effect reservoir permeability on injectivity and on the reservoir contribution to the costs of CO₂ avoidance ('D'). An upper ceiling of 2500 tonnes of CO₂ per day is placed upon injectivity per well, this corresponds to a reservoir permeability of about 5 Darcy-metres. Lower permeabilities give lower injectivities per well and this increases the numbers of wells required and hence the costs of CO₂ avoidance.

Enhanced oil recovery

The sensitivities here show the effect on the total overall costs of CO₂ avoided ('A' above, see equation 8.6). The tertiary recovery fraction (Figure 8.23) determines the amount of oil which can be produced and sold to defray the costs of CO₂ disposal and it also affects the lifetime of the CO₂ disposal system. Increasing the fraction reduces the overall costs of CO₂ avoidance. The recycle ratio (Figure 8.24) determines the parasitic loads required to recompress and reinject the CO₂ recovered with the oil during tertiary recovery. Increasing the recycle ratio increases the costs of CO₂ avoidance.

One of the most important parameters in this case is the value of the oil which is produced during tertiary recovery (Figure 8.25). A value of 70 ECU per tonne equates to about \$10 per barrel. If it is assumed that tertiary recovery of oil temporarily avoids oil production from other North Sea fields then an appropriate figure for this parameter would relate to oil production costs in the North Sea and a value of 50 ECU per tonne may be realistic. Clearly the market for oil has a major effect on the economics of this case.

8.9 CONCLUSIONS

The costs of the disposal cases are dominated in all cases by the costs of recovery of CO₂ at the power station. The costs of pipeline transport and underground disposal are both small in comparison with the recovery costs. Transmitting CO₂ 900 km to dispose of it in the Utsira Formation in the central North Sea — the most remote of the cases considered, gives a transport cost in the order of 15 ECU per tonne of CO₂ avoided with a disposal rate of 11 M tonnes of CO₂ per year. The costs of final disposal into the underground reservoir are in the region of 1 to 2 ECU per tonne of CO₂ avoided. These figures indicate that if it is

economically acceptable to recover CO₂ from power stations at costs of between 30 to 60 ECU per tonne avoided then the additional costs of transporting CO₂ to disposal sites and disposing of it in underground formations are either of the same order or are substantially lower. The costs of transport to and disposal of CO₂ in underground formations are not likely to be significant arguments against underground disposal of CO₂.

The enhanced oil recovery results indicate that if large volumes of CO₂ can be used in major enhanced oil recovery operations displacing oil which would be produced in other locations then this could totally defray the costs of CO₂ recovery at power stations, resulting in CO₂ avoidance at zero cost.

8.10 REFERENCES

- BROWN, D R, HUMPHREYS, K K, and VAIL, L W. 1993. 'Carbon Dioxide Control Costs for Gasification Combined Cycle Plants in the United States'. Pacific Northwest Laboratory, Richland, Washington 99352. Contract DE-AC06-76RLO 1830.
- ELECTRIC POWER RESEARCH INSTITUTE IE-7365. 1991. 'Engineering and Economic Evaluation of CO₂ Removal from Fossil-Fuel-Fired Power Plants'. Project RP2999-10, Research Reports Centre, Box 50490, Palo Alto, CA94303, (415). 965-4081. (a) Volume 1: Pulverized-Coal-Fired Power Plants (b) Volume 2: Coal-Gasification-Combined-Cycle Power Plants.
- GOLDTHORPE, S H, CROSS, P J I, and DAVISON, J E. 1992a. 'System Studies on CO₂ Abatement from Power Plants. *Energy Conversion and Management*', Vol. 33, No. 5-8.
- GOLDTHORPE, S H, and EXELBY, D R. 1992b. 'Economic Assessment of CO₂ Abatement Technologies based on IGCC with Physical Scrubbing or Membrane Separation' — Confidential.
- GOLDTHORPE, S H. 1993. 'Technical and Economic Assessment of CO₂ Abatement Technology based on PF + FGD with MEA Scrubbing' — Confidential.
- HENDRIKS, C A, BLOK, K, and TURKENBURG, W C. 1989. 'The Recovery of Carbon Dioxide from Power Plants. In: *Climate and Energy: The Feasibility of Controlling Carbon Dioxide Emissions*'.
- HENDRIKS, C A, and BLOK, K. 1991. 'Technology and Cost of Recovering and Storing Carbon Dioxide from an Integrated Gasifier Combined Cycle Plant. *Energy*, Vol. 16, No. 11/12.
- HENDRIKS, C A, and BLOK, K. 1992. 'Carbon Dioxide Recovery using a Dual Gas Turbine IGCC Plant. *Energy Conversion and Management*', Vol. 33, No. 5-8.
- HENDRIKS, C A, and BLOK, K. 1993. 'Underground Storage of Carbon Dioxide'. In: Proceedings of the International Energy Agency Carbon Dioxide Disposal Symposium, Oxford 29-31 March 1993. Pergamon Press, ISSN 0196-8904.
- IEA GREENHOUSE GAS R&D PROGRAMME. 1992. Technical Reports.
- IEA GREENHOUSE GAS R&D PROGRAMME. 1993a. 'Carbon Dioxide Capture: Alternatives for the Capture of CO₂ produced in an Integrated Gasification Combined Cycle System'.
- IEA GREENHOUSE GAS R&D PROGRAMME. 1993b. 'Carbon Dioxide Capture: Alternatives for the Capture of CO₂ produced from Natural Gas Combined Cycle Systems'.
- SCHUTZ, M, DAUN, M, WEINSPACH, P M, KRUMBECK, M, and HEIN, K R G. 1992. 'Study on the CO₂ Recovery from an IGCC Plant. *Energy Conversion and Management*', Vol. 33, No. 5-8.
- SKOVHOLT, O. 1993. 'CO₂ Transportation System'. In: Proceedings of the International Energy Agency Carbon Dioxide Disposal Symposium, Oxford 29-31 March 1993. Pergamon Press ISSN 0196-8904.

SUMMERFIELD, I R, GOLDTHORPE, S H, WILLIAMS, N, and SHEIK, A. 1993. '*Costs of CO₂ disposal options*'. In: Proceedings of the International Energy Agency Carbon Dioxide Disposal Symposium. 29-31 March 1993. Pergamon Press ISSN 0196-8904.

VAN DER BURGT, M J, and CANTLE, J. 1992. 'Carbon Dioxide disposal from coal based IGCC's in depleted gas field. *Energy Conversion and Management*', Vol. 33, No. 5-8.

VAN DER MEER, L G H. 1992. 'Investigations Regarding the Storage of Carbon Dioxide in Aquifers in the Netherlands. *Energy Conversion and Management*', Vol. 33, No. 5-8.

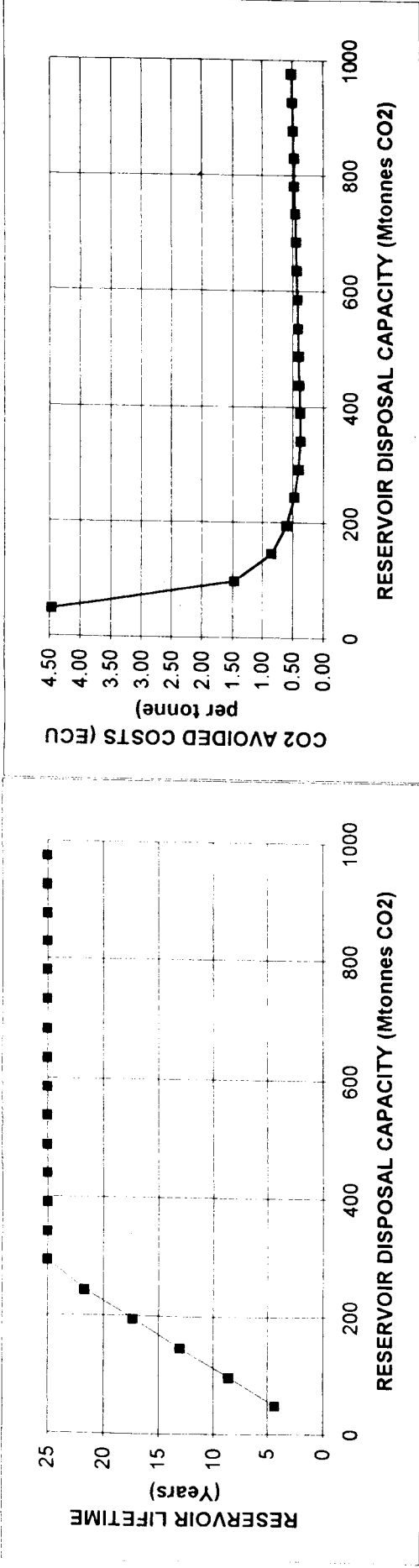


Figure 8.19 Change in reservoir lifetime with disposal capacity.

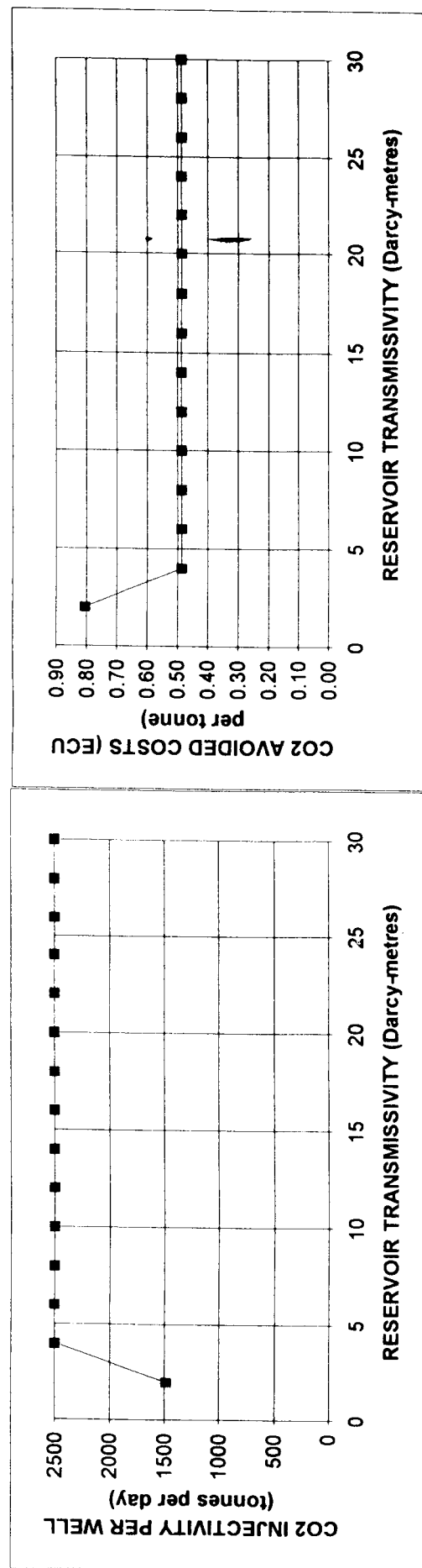


Figure 8.21 Variation in injectivity with changes in reservoir permeability.

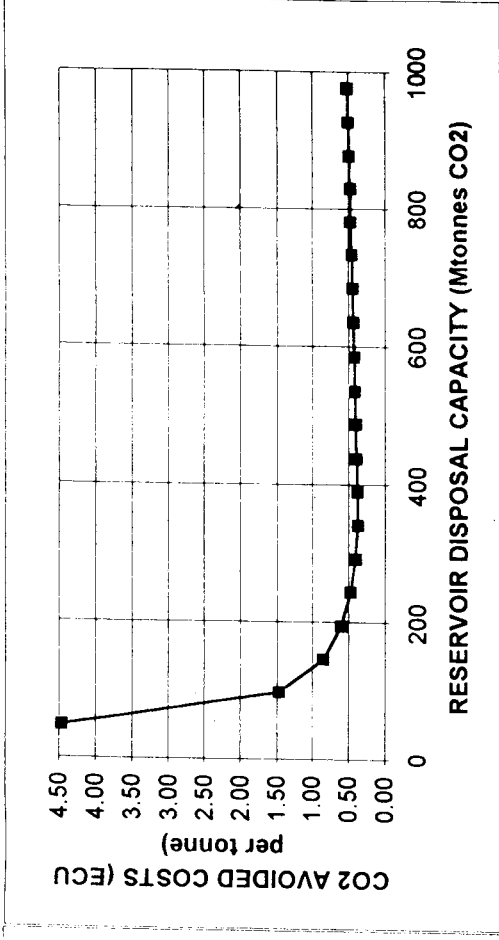


Figure 8.20 Variation in disposal costs with reservoir capacity.

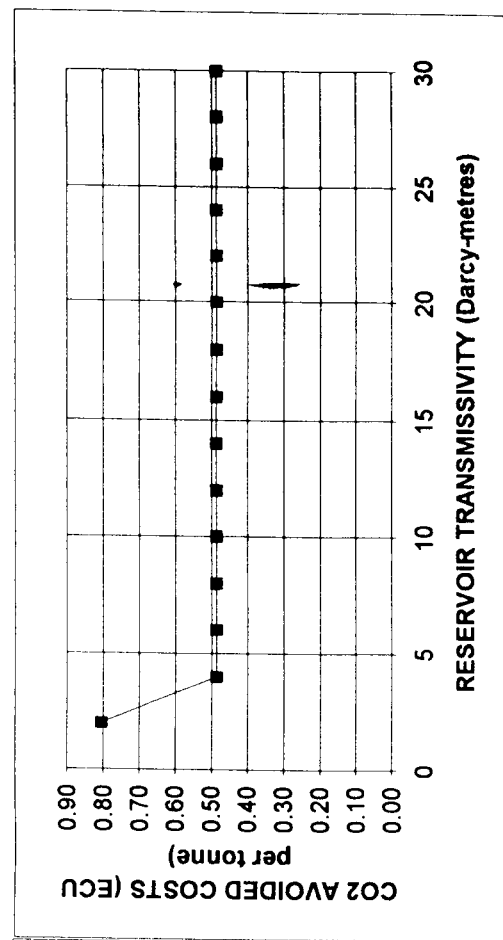


Figure 8.22 Variation in reservoir costs with changes in reservoir permeability.

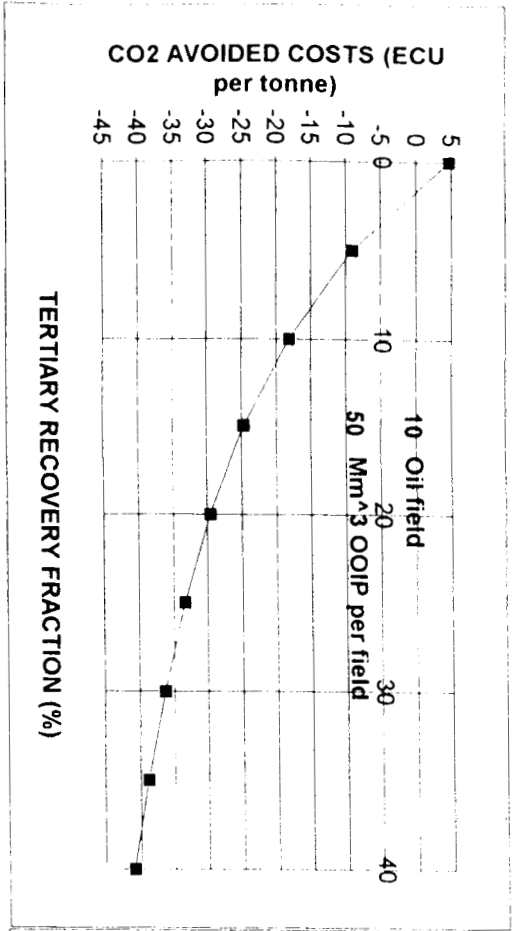


Figure 8.23 Variation in enhanced oil recovery costs with changes in the tertiary recovery fraction.

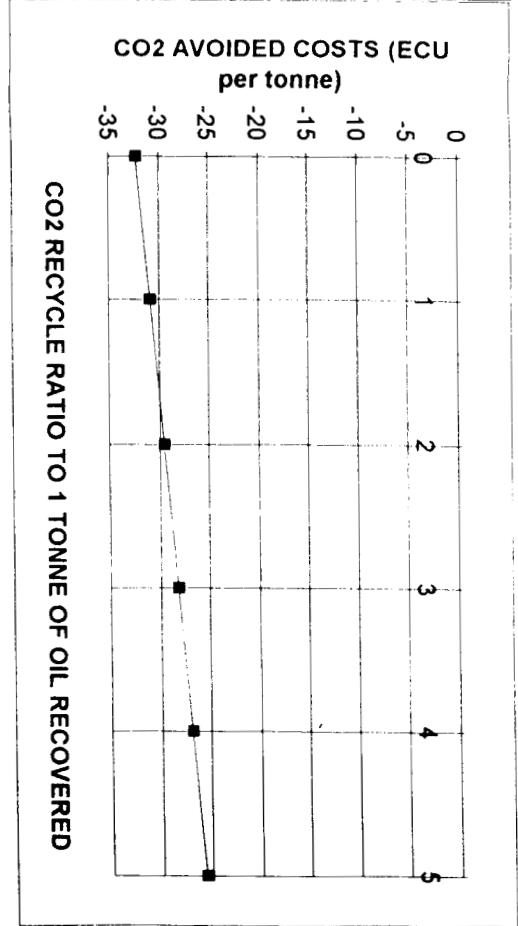


Figure 8.24 Variation in enhanced oil recovery costs with changes in CO2 recycle ratio.

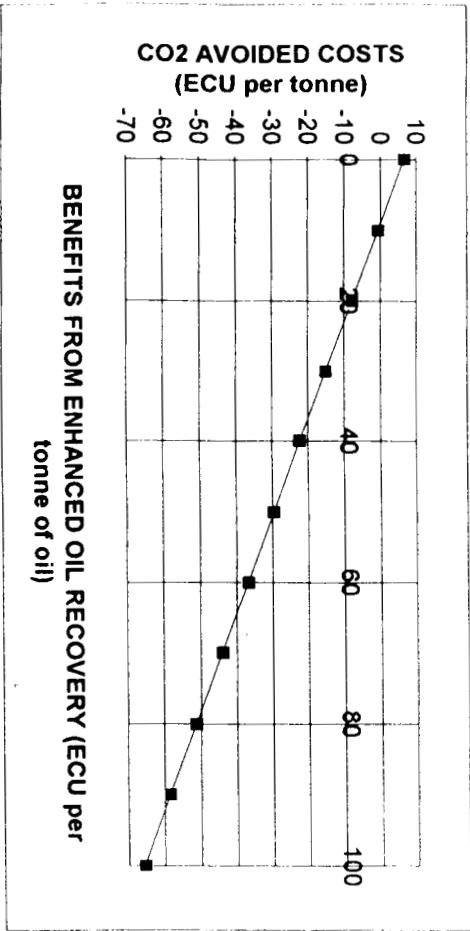


Figure 8.25 Variation in enhanced oil recovery costs with changes in oil prices.

APPENDIX 8A

ECONOMIC COST MODELLING UNDERGROUND DISPOSAL OF CO2

1

INPUT SUMMARY

CASE NAME = BUNTER (SHERWOOD SANDSTONE - OFFSHORE AQUIFER)

ECONOMIC PARAMETERS

Discount rate = percent
 ECU equivalent to £ = Ecu

POWER PLANT PARAMETERS

Power plant type = (PFGD, CGCC, O2/CO2, GTCC)
 Single plant thermal input = MW
 Number of power plants =

PIPELINE PARAMETERS

Total transport distance = km
 Pipeline temperature = degC

RESERVOIR PROPERTIES (AQUIFER + OIL & GAS FIELD DISPOSAL)

Reservoir depth (top) = metres
 Reservoir thickness = metres
 Ground surface temperature = degC
 Temperature gradient = degC/m
 Pressure gradient = bar/m
 Reservoir permeability = metres²

AQUIFER STORAGE PARAMETERS

Areal extent of the aquifer = km²
 Porosity = %
 Net:Gross ratio =
 Storage efficiency = %
 Correction factor for closure = %

OFFSHORE PARAMETERS

Water depth to sea bed = metres
 Cumulative oil production = m³
 Surface density of oil = kg/m³
 Oil FVF =

OIL AND GAS FIELD STORAGE PARAMETERS

Cumulative gas production = m³
 GEF =

ENHANCED OIL RECOVERY PARAMETERS

Number of oil fields = [REDACTED]
Average field OOIP = [REDACTED] Mm³

Average field parameters

Primary production of OOIP = [REDACTED] %
Sec. production of OOIP = [REDACTED] %
Tertiary production of OOIP = [REDACTED] %

EOR benefit = [REDACTED] ECU per tonne oil

Recycle ratio of CO₂ to Oil recovered = [REDACTED] to 1

CASE NAME = BUNTER (SHERWOOD SANDSTONE - OFFSHORE AQUIFER)

CALCULATIONS SUMMARY

POWER PLANT

Type of Power plant =	PFGD	
CO ₂ disposal =	11.28	Mtonnes per year
CO ₂ avoided =	7.80	Mtonnes per year
CO₂ avoided costs =	57.35	ECU/tonne CO₂

PIPELINE TRANSPORT

Pipeline diameter =	18	inches
CO₂ avoided costs =	2.18	ECU/tonne CO₂

RESERVOIR

OFFSHORE
AQUIFER

Site name = SHERWOOD SANDSTONE

Reservoir temperature =	55	degC
Reservoir pressure =	167.75	bars
CO ₂ density =	698	kg/m ³
CO ₂ injectivity per well =	2500	tonnes per day
Number of wells drilled =	15	
Storage capacity =	2714	Mtonnes CO ₂
Storage years =	241	years
Economic lifetime =	25	years
Storage over scheme lifetime =	282	Mtonnes CO ₂
CO₂ avoided costs =	1.58	ECU/tonne CO₂

Total costs of CO₂ avoided =	61.11 ECU/tonne CO₂
--	---------------------------------------

CASE NAME = **BUNTER (SHERWOOD SANDSTONE - OFFSHORE AQUIFER)**

COSTS SUMMARY

	Base case	Plant + CO2 rec.	
<u>POWER PLANT</u>	<u>ECU m</u>	<u>ECU m</u>	<u>ECU/t</u>
Plant capital costs =	574.86	818.93	28.53
Capital charge =	63.33	90.22	
** Fuel costs =	59.41	59.41	10.59
Operating costs =	23.50	45.38	18.22
Annual costs =	146.24	195.01	

Cost of CO2 avoided (Ecu/tonne) = 57.35

*** Base case and plant with CO2 recovery have identical thermal capacities*

	<u>ECU m</u>	<u>ECU/t</u>
<u>PIPELINE TRANSPORT</u>		
Collection system =	33.55	0.47
Pipeline costs =	72.11	1.02
Compressor costs =	0.00	0.00
Management + Contingency =	15.85	0.22
Total transport capital =	121.50	
Capital charge =	13.39	
Electricity costs =	0.00	0.00
Operating costs =	3.65	0.47
Annual costs =	17.03	

Cost of CO2 avoided (Ecu/tonne) = 2.18

	<u>ECU m</u>	<u>ECU/t</u>
<u>RESERVOIR DISPOSAL</u>		
Wellhead platform	37.14	0.52
Drilling (Jack-up rig)	22.13	0.31
Subsea completion	0.00	0.00
Drilling (Subsea compl.)	0.00	0.00
Management + Contingency =	8.89	0.13
TOTAL CAPITAL	68.16	
Capital charge	7.51	
Operation and Maintenance	4.77	0.61
	12.28	

Cost of CO2 avoided (Ecu/tonne) = 1.58

ECONOMIC COST MODELLING UNDERGROUND DISPOSAL OF CO₂

2

INPUT SUMMARY

CASE NAME = **BUNTER - ONSHORE AQUIFER**

ECONOMIC PARAMETERS

Discount rate = percent
 ECU equivalent to £ = Ecu

POWER PLANT PARAMETERS

Power plant type = (PFGD, CGCC, O₂/CO₂, GTCC)
 Single plant thermal input = MW
 Number of power plants =

PIPELINE PARAMETERS

Total transport distance = km
 Pipeline temperature = degC

RESERVOIR PROPERTIES (AQUIFER + OIL & GAS FIELD DISPOSAL)

Reservoir depth (top) = metres
 Reservoir thickness = metres

 Ground surface temperature = degC
 Temperature gradient = degC/m
 Pressure gradient = bar/m
 Reservoir permeability = metres²

AQUIFER STORAGE PARAMETERS

Areal extent of the aquifer = km²
 Porosity = %
 Net:Gross ratio =
 Storage efficiency = %
 Correction factor for closure = %

OFFSHORE PARAMETERS

Water depth to sea bed = metres

 Cumulative oil production = m³
 Surface density of oil = kg/m³
 Oil FVF =

OIL AND GAS FIELD STORAGE PARAMETERS

Cumulative gas production = m³
 GEF =

ENHANCED OIL RECOVERY PARAMETERS

Number of oil fields = [redacted]
Average field OOIP = [redacted] Mm³

Average field parameters

Primary production of OOIP = [redacted] %
Sec. production of OOIP = [redacted] %
Tertiary production of OOIP = [redacted] %

EOR benefit = [redacted] ECU per tonne oil

Recycle ratio of CO₂ to Oil recovered = [redacted] to 1

CASE NAME = **BUNTER - ONSHORE AQUIFER**

CALCULATIONS SUMMARY

POWER PLANT

Type of Power plant =	PFGD	
CO ₂ disposal =	11.28	Mtonnes per year
CO ₂ avoided =	7.80	Mtonnes per year
CO₂ avoided costs =	57.35	ECU/tonne CO₂

PIPELINE TRANSPORT

Pipeline diameter =	24	inches
CO₂ avoided costs =	11.75	ECU/tonne CO₂

RESERVOIR

**ONSHORE
AQUIFER
BUNTER**

Site name =

Reservoir temperature =	24	degC
Reservoir pressure =	88	bars
CO ₂ density =	797	kg/m ³
CO ₂ injectivity per well =	2500	tonnes per day
Number of wells drilled =	15	
Storage capacity =	878	Mtonnes CO ₂
Storage years =	78	years
Economic lifetime =	25	years
Storage over scheme lifetime =	282	Mtonnes CO ₂
CO₂ avoided costs =	0.49	ECU/tonne CO₂

Total costs of CO₂ avoided =	69.58 ECU/tonne CO₂
--	---------------------------------------

CASE NAME = BUNTER - ONSHORE AQUIFER

COSTS SUMMARY

	Base case	Plant + CO2 rec.	
<u>POWER PLANT</u>	<u>ECU m</u>	<u>ECU m</u>	<u>ECU/t</u>
Plant capital costs =	574.86	818.93	28.53
Capital charge =	63.33	90.22	
** Fuel costs =	59.41	59.41	10.59
Operating costs =	23.50	45.38	18.22
Annual costs =	146.24	195.01	

Cost of CO2 avoided (Ecu/tonne) = 57.35

** Base case and plant with CO2 recovery have identical thermal capacities

<u>PIPELINE TRANSPORT</u>	<u>ECU m</u>	<u>ECU/t</u>
Collection system =	33.55	0.47
Pipeline costs =	534.71	7.56
Compressor costs =	0.00	0.00
Management + Contingency =	85.24	1.20
Total transport capital =	653.50	
Capital charge =	71.99	
Electricity costs =	0.00	0.00
Operating costs =	19.61	2.51
Annual costs =	91.60	

Cost of CO2 avoided (Ecu/tonne) = 11.75

<u>RESERVOIR DISPOSAL</u>	<u>ECU m</u>	<u>ECU/t</u>
Initial Studies	0.46	0.01
Distribution System	0.98	0.01
Injection Wells	22.88	0.32
Injection Pumps	0.00	-0.00
Management + Contingency =	3.65	0.05
TOTAL CAPITAL	27.95	
Capital charge	3.08	
Electricity costs	0.00	0.00
Operation and Maintenance	0.72	0.09
	3.79	

Cost of CO2 avoided (Ecu/tonne) = 0.49

ECONOMIC COST MODELLING UNDERGROUND DISPOSAL OF CO2

3

INPUT SUMMARY

CASE NAME = UTSIRA - OFFSHORE AQUIFER

ECONOMIC PARAMETERS

Discount rate = percent
 ECU equivalent to £ = Ecu

POWER PLANT PARAMETERS

Power plant type = (PFGD, CGCC, O2/CO2, GTCC)
 Single plant thermal input = MW
 Number of power plants =

PIPELINE PARAMETERS

Total transport distance = km
 Pipeline temperature = degC

RESERVOIR PROPERTIES (AQUIFER + OIL & GAS FIELD DISPOSAL)

Reservoir depth (top) = metres
 Reservoir thickness = metres
 Ground surface temperature = degC
 Temperature gradient = degC/m
 Pressure gradient = bar/m
 Reservoir permeability = metres² 300 Darcy-metres

AQUIFER STORAGE PARAMETERS

Areal extent of the aquifer = km²
 Porosity = %
 Net:Gross ratio =
 Storage efficiency = %
 Correction factor for closure = %

OFFSHORE PARAMETERS

Water depth to sea bed = metres
 Cumulative oil production = m³
 Surface density of oil = kg/m³ 850.00
 Oil FVF =

OIL AND GAS FIELD STORAGE PARAMETERS

Cumulative gas production = m³
 GEF = 143

ENHANCED OIL RECOVERY PARAMETERS

Number of oil fields = [redacted]
Average field OOIP = [redacted] Mm³

Average field parameters

Primary production of OOIP = [redacted] %
Sec. production of OOIP = [redacted] %
Tertiary production of OOIP = [redacted] %

EOR benefit = [redacted] ECU per tonne oil

Recycle ratio of CO₂ to Oil recovered = [redacted] to 1

CASE NAME = UTSIRA - OFFSHORE AQUIFER

CALCULATIONS SUMMARY

POWER PLANT

Type of Power plant =	PFGD	
CO ₂ disposal =	11.28	Mtonnes per year
CO ₂ avoided =	7.80	Mtonnes per year
CO ₂ avoided costs =	57.35	ECU/tonne CO ₂

PIPELINE TRANSPORT

Pipeline diameter =	18	inches
CO ₂ avoided costs =	14.48	ECU/tonne CO ₂

RESERVOIR OFFSHORE
Site name = AQUIFER
UTSIRA

Reservoir temperature =	28	degC
Reservoir pressure =	88	bars
CO ₂ density =	756	kg/m ³
CO ₂ injectivity per well =	2500	tonnes per day
Number of wells drilled =	15	
Storage capacity =	49546	Mtonnes CO ₂
Storage years =	4392	years
Economic lifetime =	25	years
Storage over scheme lifetime =	282	Mtonnes CO ₂
CO ₂ avoided costs =	2.25	ECU/tonne CO ₂

Total costs of CO ₂ avoided =	74.08 ECU/tonne CO ₂
--	---------------------------------

CASE NAME = UTSIRA - OFFSHORE AQUIFER

COSTS SUMMARY

	Base case	Plant + CO2 rec.	
<u>POWER PLANT</u>	<u>ECU m</u>	<u>ECU m</u>	<u>ECU/t</u>
Plant capital costs =	574.86	818.93	28.53
Capital charge =	63.33	90.22	
** Fuel costs =	59.41	59.41	10.59
Operating costs =	23.50	45.38	18.22
Annual costs =	146.24	195.01	

Cost of CO2 avoided (Ecu/tonne) = 57.35

*** Base case and plant with CO2 recovery have identical thermal capacities*

	<u>ECU m</u>	<u>ECU/t</u>
<u>PIPELINE TRANSPORT</u>		
Collection system =	33.55	0.47
Pipeline costs =	648.95	9.17
Compressor costs =	12.00	0.17
Management + Contingency =	104.18	1.47
Total transport capital =	798.68	
Capital charge =	87.99	
Electricity costs =	0.97	0.12
Operating costs =	23.96	3.07
Annual costs =	112.92	

Cost of CO2 avoided (Ecu/tonne) = 14.48

	<u>ECU m</u>	<u>ECU/t</u>
<u>RESERVOIR DISPOSAL</u>		
Wellhead platform	65.45	0.92
Drilling (Jack-up rig)	19.31	0.27
Subsea completion	0.00	0.00
Drilling (Subsea compl.)	0.00	0.00
Management + Contingency =	12.71	0.18
TOTAL CAPITAL	97.47	
Capital charge	10.74	
Operation and Maintenance	6.82	0.88
	17.56	

Cost of CO2 avoided (Ecu/tonne) = 2.25

ECONOMIC COST MODELLING UNDERGROUND DISPOSAL OF CO₂

4

INPUT SUMMARY

CASE NAME = **GRONINGEN - ONSHORE GAS FIELD**

ECONOMIC PARAMETERS

Discount rate = percent
 ECU equivalent to £ = Ecu

POWER PLANT PARAMETERS

Power plant type = (PFGD, CGCC, O₂/CO₂, GTCC)
 Single plant thermal input = MW
 Number of power plants =

PIPELINE PARAMETERS

Total transport distance = km
 Pipeline temperature = degC

RESERVOIR PROPERTIES (AQUIFER + OIL & GAS FIELD DISPOSAL)

Reservoir depth (top) = metres
 Reservoir thickness = metres
 Ground surface temperature = degC
 Temperature gradient = degC/m
 Pressure gradient = bar/m
 Reservoir permeability = metres²

AQUIFER STORAGE PARAMETERS

Areal extent of the aquifer = km²
 Porosity = %
 Net:Gross ratio =
 Storage efficiency = %
 Correction factor for closure = %

OFFSHORE PARAMETERS

Water depth to sea bed = metres
 Cumulative oil production = m³
 Surface density of oil = kg/m³
 Oil FVF =

OIL AND GAS FIELD STORAGE PARAMETERS

Cumulative gas production = m³
 GEF =

ENHANCED OIL RECOVERY PARAMETERS

Number of oil fields = [REDACTED]
Average field OOIP = [REDACTED] Mm³

Average field parameters

Primary production of OOIP = [REDACTED] %
Sec. production of OOIP = [REDACTED] %
Tertiary production of OOIP = [REDACTED] %

EOR benefit = [REDACTED] ECU per tonne oil

Recycle ratio of CO2 to Oil recovered = [REDACTED] to 1

CASE NAME = GRONINGEN - ONSHORE GAS FIELD

CALCULATIONS SUMMARY

POWER PLANT

Type of Power plant =	PFGD	
CO2 disposal =	11.28	Mtonnes per year
CO2 avoided =	7.80	Mtonnes per year
CO2 avoided costs =	57.35	ECU/tonne CO2

PIPELINE TRANSPORT

Pipeline diameter =	24	inches
CO2 avoided costs =	5.22	ECU/tonne CO2

RESERVOIR

ONSHORE
GAS FIELD
GRONINGEN

Site name =

Reservoir temperature =	90	degC
Reservoir pressure =	308	bars
CO2 density =	726	kg/m ³
CO2 injectivity per well =	2500	tonnes per day
Number of wells drilled =	15	
Storage capacity =	7993	Mtonnes CO2
Storage years =	708	years
Economic lifetime =	25	years
Storage over scheme lifetime =	282	Mtonnes CO2
CO2 avoided costs =	0.79	ECU/tonne CO2

Total costs of CO2 avoided =	63.35 ECU/tonne CO2
------------------------------	---------------------

CASE NAME = GRONINGEN - ONSHORE GAS FIELD

COSTS SUMMARY

	Base case	Plant + CO2 rec.	
	<u>ECU m</u>	<u>ECU m</u>	<u>ECU/t</u>
POWER PLANT			
Plant capital costs =	574.86	818.93	28.53
Capital charge =	63.33	90.22	
** Fuel costs =	59.41	59.41	10.59
Operating costs =	23.50	45.38	18.22
Annual costs =	146.24	195.01	

Cost of CO2 avoided (Ecu/tonne) = 57.35

*** Base case and plant with CO2 recovery have identical thermal capacities*

PIPELINE TRANSPORT	<u>ECU m</u>	<u>ECU/t</u>
Collection system =	33.55	0.47
Pipeline costs =	218.75	3.09
Compressor costs =	0.00	0.00
Management + Contingency =	37.84	0.53
Total transport capital =	290.14	
Capital charge =	31.96	
Electricity costs =	0.00	0.00
Operating costs =	8.70	1.12
Annual costs =	40.67	

Cost of CO2 avoided (Ecu/tonne) = 5.22

RESERVOIR DISPOSAL	<u>ECU m</u>	<u>ECU/t</u>
Initial Studies	0.46	0.01
Distribution System	0.98	0.01
Injection Wells	36.88	0.52
Injection Pumps	0.06	0.00
Management + Contingency =	5.76	0.08
TOTAL CAPITAL	44.12	
Capital charge	4.86	
Electricity costs	0.13	0.02
Operation and Maintenance	1.14	0.15
	6.13	

Cost of CO2 avoided (Ecu/tonne) = 0.79

ECONOMIC COST MODELLING UNDERGROUND DISPOSAL OF CO2

5

INPUT SUMMARY

CASE NAME = INDEFATIGABLE - OFFSHORE GAS FIELD

ECONOMIC PARAMETERS

Discount rate = percent
 ECU equivalent to £ = Ecu

POWER PLANT PARAMETERS

Power plant type = (PFGD, CGCC, O2/CO2, GTCC)
 Single plant thermal input = MW
 Number of power plants =

PIPELINE PARAMETERS

Total transport distance = km
 Pipeline temperature = degC

RESERVOIR PROPERTIES (AQUIFER + OIL & GAS FIELD DISPOSAL)

Reservoir depth (top) = metres
 Reservoir thickness = metres
 Ground surface temperature = degC
 Temperature gradient = degC/m
 Pressure gradient = bar/m
 Reservoir permeability = metres²

AQUIFER STORAGE PARAMETERS

Areal extent of the aquifer = km²
 Porosity = %
 Net:Gross ratio = %
 Storage efficiency = %
 Correction factor for closure = %

OFFSHORE PARAMETERS

Water depth to sea bed = metres
 Cumulative oil production = m³
 Surface density of oil = kg/m³
 Oil FVF =

OIL AND GAS FIELD STORAGE PARAMETERS

Cumulative gas production = m³
 GEF =

ENHANCED OIL RECOVERY PARAMETERS

Number of oil fields = [REDACTED]
Average field OOIP = [REDACTED] Mm³

Average field parameters

Primary production of OOIP = [REDACTED] %
Sec. production of OOIP = [REDACTED] %
Tertiary production of OOIP = [REDACTED] %

EOR benefit = [REDACTED] ECU per tonne oil

Recycle ratio of CO₂ to Oil recovered = [REDACTED] to 1

CASE NAME = INDEFATIGABLE - OFFSHORE GAS FIELD

CALCULATIONS SUMMARY

POWER PLANT

Type of Power plant =	PFGD	
CO ₂ disposal =	11.28	Mtonnes per year
CO ₂ avoided =	7.80	Mtonnes per year
CO ₂ avoided costs =	57.35	ECU/tonne CO ₂

PIPELINE TRANSPORT

Pipeline diameter =	18	inches
CO ₂ avoided costs =	2.93	ECU/tonne CO ₂

RESERVOIR

OFFSHORE

GAS FIELD

Site name = INDEFATIGABLE

Reservoir temperature =	90	degC
Reservoir pressure =	286	bars
CO ₂ density =	701	kg/m ³
CO ₂ injectivity per well =	2500	tonnes per day
Number of wells drilled =	15	
Storage capacity =	393	Mtonnes CO ₂
Storage years =	35	years
Economic lifetime =	25	years
Storage over scheme lifetime =	282	Mtonnes CO ₂
CO ₂ avoided costs =	1.69	ECU/tonne CO ₂

Total costs of CO₂ avoided =	61.97 ECU/tonne CO₂
--	---------------------------------------

CASE NAME = INDEFATIGABLE - OFFSHORE GAS FIELD

COSTS SUMMARY

	Base case	Plant + CO2 rec.	
<u>POWER PLANT</u>	<u>ECU m</u>	<u>ECU m</u>	<u>ECU/t</u>
Plant capital costs =	574.86	818.93	28.53
Capital charge =	63.33	90.22	
** Fuel costs =	59.41	59.41	10.59
Operating costs =	23.50	45.38	18.22
Annual costs =	146.24	195.01	

Cost of CO2 avoided (Ecu/tonne) = 57.35

** Base case and plant with CO2 recovery have identical thermal capacities

<u>PIPELINE TRANSPORT</u>	<u>ECU m</u>	<u>ECU/t</u>
Collection system =	33.55	0.47
Pipeline costs =	108.16	1.53
Compressor costs =	0.00	0.00
Management + Contingency =	21.26	0.30
Total transport capital =	162.96	
Capital charge =	17.95	
Electricity costs =	0.00	0.00
Operating costs =	4.89	0.63
Annual costs =	22.84	

Cost of CO2 avoided (Ecu/tonne) = 2.93

<u>RESERVOIR DISPOSAL</u>	<u>ECU m</u>	<u>ECU/t</u>
Wellhead platform	37.37	0.53
Drilling (Jack-up rig)	26.24	0.37
Subsea completion	0.00	0.00
Drilling (Subsea compl.)	0.00	0.00
Management + Contingency =	9.54	0.13
TOTAL CAPITAL	73.15	
Capital charge	8.06	
Operation and Maintenance	5.12	0.66
	13.18	

Cost of CO2 avoided (Ecu/tonne) = 1.69

ECONOMIC COST MODELLING UNDERGROUND DISPOSAL OF CO2

6

INPUT SUMMARY

CASE NAME = EOR - GROUP OF 10 SMALL OILFIELDS

ECONOMIC PARAMETERS

Discount rate = percent
 ECU equivalent to £ = Ecu

POWER PLANT PARAMETERS

Power plant type = (PFGD, CGCC, O2/CO2, GTCC)
 Single plant thermal input = MW
 Number of power plants =

PIPELINE PARAMETERS

Total transport distance = km
 Pipeline temperature = degC

RESERVOIR PROPERTIES (AQUIFER + OIL & GAS FIELD DISPOSAL)

Reservoir depth (top) = metres
 Reservoir thickness = metres

 Ground surface temperature = degC
 Temperature gradient = degC/m
 Pressure gradient = bar/m
 Reservoir permeability = metres²

AQUIFER STORAGE PARAMETERS

Areal extent of the aquifer = km²
 Porosity = %
 Net:Gross ratio = %
 Storage efficiency = %
 Correction factor for closure = %

OFFSHORE PARAMETERS

Water depth to sea bed = metres

 Cumulative oil production = m³
 Surface density of oil = kg/m³
 Oil FVF =

OIL AND GAS FIELD STORAGE PARAMETERS

Cumulative gas production = m³
 GEF =

ENHANCED OIL RECOVERY PARAMETERS

Number of oil fields =
Average field OOIP = Mm³

Average field parameters

Primary production of OOIP = %
Sec. production of OOIP = %
Tertiary production of OOIP = %

EOR benefit = ECU per tonne oil

Recycle ratio of CO₂ to Oil recovered = to 1

CASE NAME = FORTIES - OFFSHORE OIL FIELD

CALCULATIONS SUMMARY

POWER PLANT

Type of Power plant =	PFGD	
CO ₂ disposal =	6.77	Mtonnes per year
CO ₂ avoided =	4.68	Mtonnes per year
CO₂ avoided costs =	57.35	ECU/tonne CO₂

PIPELINE TRANSPORT

Pipeline diameter =	14	inches
CO₂ avoided costs =	10.98	ECU/tonne CO₂

RESERVOIR OFFSHORE
OIL FIELD
Site name = FORTIES

Reservoir temperature =	56	degC
Reservoir pressure =	244.2	bars
CO ₂ density =	809	kg/m ³
CO ₂ injectivity per well =	2500	tonnes per day
Number of wells drilled =	9	
Storage capacity =	162	Mtonnes CO ₂
Storage years =	24	years
Economic lifetime =	24	years
Storage over scheme lifetime =	162	Mtonnes CO ₂
CO₂ avoided costs =	-29.59	ECU/tonne CO₂

Total costs of CO₂ avoided = 38.74 ECU/tonne CO₂

CASE NAME = FORTIES - OFFSHORE OIL FIELD

COSTS SUMMARY

	Base case	Plant + CO2 rec.	
POWER PLANT	ECU m	ECU m	ECU/t
Plant capital costs =	574.86	818.93	28.53
Capital charge =	63.33	90.22	
** Fuel costs =	59.41	59.41	10.59
Operating costs =	23.50	45.38	18.22
Annual costs =	146.24	195.01	

Cost of CO2 avoided (Ecu/tonne) = 57.35

*** Base case and plant with CO2 recovery have identical thermal capacities*

PIPELINE TRANSPORT	ECU m	ECU/t
Collection system =	20.13	0.48
Pipeline costs =	284.85	6.78
Compressor costs =	9.19	0.22
Management + Contingency =	47.13	1.12
Total transport capital =	361.30	
Capital charge =	40.25	
Electricity costs =	0.29	0.06
Operating costs =	10.84	2.32
Annual costs =	51.38	

Cost of CO2 avoided (Ecu/tonne) = 10.98

DISPOSAL+EOR	ECU m	ECU/t
Wellhead platform	0.00	0.00
Drilling (Jack-up rig)	0.00	0.00
Subsea completion	64.35	1.53
Drilling (Subsea compl.)	23.33	0.56
CO2 Recompression	11.40	0.27
Management + Contingency =	14.86	0.35
TOTAL CAPITAL	113.94	
Capital charge	12.69	
Operation and Maintenance	7.98	1.70
Annual electricity costs	10.11	2.16
Annual EOR sales	-169.22	-36.17
	-138.44	

Cost of CO2 avoided (Ecu/tonne) = -29.59

CHAPTER 9

Conclusions and recommendations

S Holloway, J P Heederik, L G H van der Meer, I Czernichowski-Lauriol, R Harrison, E Lindeberg, I R Summerfield, C Rochelle, T Schwarzkopf, O Kaarstad and B Berger

9.1 CONCLUSIONS

9.1.1 Feasibility

Underground disposal is a perfectly feasible method of disposing of very large quantities of carbon dioxide, such as are produced by fossil fuel fired power plant. All the necessary technological steps are commercially proven and thus could be implemented today. Furthermore, the study of large naturally occurring CO₂ accumulations indicates that CO₂ can be retained in underground reservoirs for millions of years.

The concept is so well established that large scale commercial underground CO₂ disposal will begin in 1996, when Statoil start to dispose of approximately 1 million tonnes of CO₂ a year into the Utsira Formation aquifer above the Sleipner Vest gas field in the centre of the North Sea.

The main obstacle to the implementation of the underground disposal of carbon dioxide from fossil fuel fired power stations is its high cost. Most of the cost is incurred by the necessity to separate the CO₂ from the flue gas before disposing of it.

9.1.2 Requirement for CO₂ separation

Flue gas from today's power plant contains a maximum of about 16% CO₂. It would be both undesirable and impractical to dispose of this flue gas in an untreated state. Firstly, the available storage space would not be big enough to cope with the vast quantities of untreated flue gas. Secondly, it would be undesirable to dispose of the harmless or beneficial atmospheric components, such as nitrogen, which is the largest component by volume of flue gas. There is also an overriding thermodynamic argument that prohibits the deep underground storage of untreated flue gas containing only around 15% CO₂. Due to the large volume of the flue gas, the work needed to compress it would be 65% or more of the total work that could be obtained from the coal fired power plant. At best, this would make it a far more expensive option than CO₂ separation. Therefore we believe the CO₂ would have to be separated from, or concentrated in, the flue gas. The energy required to separate CO₂ from power station flue gas decreases the efficiency of the power plant, meaning that more fuel is required to generate the same amount of electricity. This increases the gross amount of CO₂ generated, such that if 90% of the gross amount of CO₂ generated could be separated and disposed of underground, there would be a net CO₂ avoidance of around 85%.

9.1.3 Potential impact on global CO₂ emissions

It is generally accepted that a reduction in anthropogenic CO₂ emissions of around 60% is needed to stabilise atmospheric CO₂ levels. If CO₂ separation and disposal were implemented on all fossil fuel fired power stations

tomorrow, annual global anthropogenic CO₂ emissions would be reduced by approximately 20%. Thus other measures will also have to be taken if global CO₂ emissions are to be stabilised.

9.1.4 Preferred storage concepts

Shallow subsurface storage of CO₂ as a gas or liquid is considered impractical. There is insufficient gas tight man made void space to store significant quantities of CO₂. The alternative method of shallow storage, disposing of the CO₂ in traps in shallow porous and permeable reservoir rocks, is not practical because they generally have a more important use — for groundwater supply.

Storage in deep porous and permeable reservoir rocks, capped by very low permeability seals, such as clays or shales, is practical. These reservoirs have few present uses and, at typical subsurface conditions, free CO₂ would be in a dense, supercritical phase at depths of around 800 metres or more. This would vastly increase the storage per unit volume of reservoir rock compared to storage at shallow depths. Storage could take place in structural or stratigraphic traps, such as oil and gas fields (which have the advantage of a proven trap and well known geology) or analogous traps on aquifers. However, modelling suggests that fluid traps of this type would not always be necessary; CO₂ could simply be injected into certain large, essentially horizontal aquifers, for example in the centre of the North Sea, where it would dissolve into the surrounding formation water before it migrated more than a few kilometres towards the basin margins. It should be emphasised that all the deep storage concepts outlined above are thought to be valid, and different options may be preferred, depending on the case specifics and priorities of a particular disposal scheme.

9.1.5 Space available for underground disposal

We estimate that there is space available in the European Union and Norway to store approximately 800 Gt CO₂. This estimate is highly provisional — in reality the storage capacity of each reservoir is case specific and requires individual modelling, so only gross generalisations can be made for the European Union and Norway as a whole. Nonetheless, it is clear that there would be adequate storage space to cope with the annual supply of CO₂ from power generation in Europe (currently 0.95 Gt p.a.) for the foreseeable future. The bulk of this storage space is offshore, mostly under the North Sea. 800 Gt CO₂ is more than a quarter of the CO₂ presently in the atmosphere.

9.1.6 Risks to man and the environment

Deep underground disposal has the significant advantage that the CO₂ will be deposited in the geosphere, where it cannot interact with surface terrestrial or oceanic

ecosystems unless it escapes from its storage reservoir. Nonetheless, there are some risks to man and the environment attached to the underground disposal of CO₂. These could be minimised by appropriate design and monitoring of all stages of the CO₂ transport and disposal process, using best oilfield practice, as is used in the enhanced oil recovery industry in the USA and elsewhere today. Pipeline ruptures, or leaks from surface facilities, are possible, although CO₂ is classed as a low hazard material for pipeline transport in the USA today.

The other main risks are associated with the storage reservoir. A slow but persistent leak from an unidentified migration pathway out of a storage reservoir is a possibility. This could be a danger or pollutant at the point where the leak reached the surface, or could pollute potable water above or up dip from the storage reservoir. There might be a danger of asphyxiation from the highly unlikely event of a catastrophic release of CO₂ from an onshore storage reservoir. Risks to man and terrestrial ecosystems would be much reduced if storage took place offshore.

9.1.7 Geochemical effects of injecting CO₂ into underground reservoirs

The injection of CO₂ into a carbonate reservoir will lead to the dissolution of carbonate minerals in the vicinity of the injection wells and the formation water thereabouts will become saturated with respect to carbonate. As the formation water moves away from the injection wells, carbonates could be precipitated as pressure reduces or temperature rises. Thus permeability is likely to be increased significantly around the injection site, but may decrease further away, towards the reservoir margins. There is the possibility that dissolution of carbonate by prolonged injection of CO₂ into a purely limestone reservoir could eventually cause subsidence around the injection site, particularly when the reservoir pressure around the injection well declines. Injection of CO₂ into sandstone reservoirs is unlikely to cause subsidence.

Injection of CO₂ into a sandstone reservoir will cause dissolution of feldspars and subsequent precipitation of clays, carbonates and quartz (or another silica phase). The buffering power of aluminosilicate reactions will favour CO₂ uptake in the formation water by the formation of bicarbonate ions and complexes. Calcite precipitation could ensure (permanent) fixing of carbon via reaction of CO₂ with Ca-rich minerals or formation fluids.

Shale and anhydrite caprocks sealing the storage reservoirs are not likely to be greatly affected by CO₂/water/rock reactions.

The underground storage of CO₂ may result in the mobilisation of trace elements from oils or heavy minerals encountered in the reservoir, due to the complexing power of bicarbonate and thiocarbonate and to the solvent properties of supercritical CO₂.

9.1.8 Costs of CO₂ separation, transport and disposal

The costs of CO₂ separation are about 27 to 65 Ecu/tonne of CO₂ avoided. Thus CO₂ separation is likely to increase the cost of electricity by between 40% and 88%. In our opinion this is the main obstacle to the practical implementation of the underground storage of CO₂ from fossil fuel fired power plant. Nonetheless, the costs of electricity generation from thermal power plant with CO₂ recovery are broadly similar to the costs of electricity generation from wind power.

The costs of CO₂ transport and storage underground are small compared to the costs of CO₂ separation. Transport costs are variable depending principally on the length and diameter of the pipeline selected. They range up to about 14.5 Ecu/tonne of CO₂ avoided in our modelled scenarios. The costs of the underground disposal process alone are around 1 to 2.25 Ecu per tonne of CO₂ avoided. Modelling of CO₂ disposal combined with enhanced oil recovery indicates that if large volumes of CO₂ can be used to recover oil which would otherwise be produced in other locations, then cost credits from the sale of the produced oil could totally defray the costs of CO₂ recovery at power stations, resulting in CO₂ avoidance at near zero cost.

9.1.9 Level of CO₂ tax required to make underground disposal of CO₂ from fossil fuel fired power plant economically attractive

If a CO₂ tax was to be used as an incentive to reduce CO₂ emissions to the atmosphere, it would have to be set at a level of at least 30 Ecu/tonne of CO₂ to make the separation and underground disposal of carbon dioxide from fossil fuel fired power plant an economically attractive option.

This can be compared to the CO₂ taxes operating in certain countries shown in table XI.1 below:

Table XI.1 CO₂ taxes (Source: The Norwegian Parliament report No. 41, 94-95, page 84)

Country	Specification	Ecu/tonne CO ₂
Netherlands	5.16 NGL/tonne of CO ₂	2.6
Finland	28 FIM/tonne CO ₂	4.5
Denmark	Household 100 DKK/tonne CO ₂ Industry 50 DKK/tonne CO ₂	13.5 6.8
Sweden	Household and transport, average, can vary 9% Industry, average, can vary 9%	36.8 9.2
Norway	Transport and offshore 0.83 NOK/l gasoline or Sm ³ gas Heating (light mineral oil) 0.415 NOK/l	43.3 19.0

9.2 RECOMMENDATIONS

The next major step in implementing CO₂ disposal from power plant should be the demonstration and monitoring of large scale disposal. Any demonstration project which started from scratch would be extremely expensive. At a minimum it would require a dedicated source of carbon dioxide, probably a separation plant, a pipeline, a disposal site and accompanying infrastructure and injection wells. On top of this would be the requirements of the research and monitoring programme. The Sleipner Vest and Natuna Sea projects are essentially large scale demonstrations of the practicality of the underground disposal of carbon dioxide. As such they present an unparalleled opportunity for further research into underground disposal. Any form of collaborative research with the operators of these schemes would be extremely valuable scientifically and a cost-effective way to verify the findings of this report.

Our first recommendation is that DG XII of Commission should approach Statoil and Exxon with a view to collaborating scientifically on the Sleipner Vest and Natuna Sea CO₂ disposal projects.

Our second recommendation is that further research be conducted in the following areas:

1. Geochemical modelling and reservoir simulation of the disposal of carbon dioxide into offshore formations, preferably in the North Sea, without the need for a conventional fluid trap (see section 4.4.4). This would require detailed geological data from the chosen formations. It would lead to a refined estimate of the storage potential of the North Sea and a more detailed concept of disposal into such formations.
2. Further geochemical experiments and modelling to determine more precisely the effects of CO₂ on the permeability, porosity and stability of reservoir and cap rocks.
3. Construction of a two-phase flow reaction-transport reservoir simulator. This could be achieved by coupling a two phase flow reservoir simulator with the geochemical reaction-transport simulator developed for this project. It would enable simulation of the migration of supercritical CO₂ and water through a carbonate or sandstone reservoir and prediction of the geochemical changes that will occur with their effect on porosity and permeability. This will allow us to predict, for example, the amount of CO₂ which will dissolve in the formation water of the modelled reservoir and the amount of CO₂ which will be fixed by carbonate-precipitating CO₂/water/rock reactions. Such a code should also enable optimisation of the design and operating conditions of the disposal operations.

APPENDIX A

Technical and economical optimization of CO₂-removal in an IGCC power plant

Jochen Putter and Matthias Krumbek, RWE AG, Germany

CONTENTS

1 SUMMARY	324
2 TARGETS OF THE STUDY	324
3 THE BASIC IGCC POWER PLANT	324
4 CO₂ REMOVAL PROCESSES (RECOVERY AND LIQUEFACTION)	325
4.1 General	325
4.2 Considered CO₂ removal concepts	327
4.3 CO₂ removal without CO-shift	331
4.3.1 Rectisol wash unit	331
4.3.1.1 <i>General process description</i>	331
4.3.1.2 <i>Process description of the Rectisol wash</i>	331
4.3.1.3 <i>Comments</i>	331
4.3.2 NMP wash unit	331
4.3.2.1 <i>General process description</i>	331
4.3.2.2 <i>Process description of the NMP wash</i>	331
4.3.2.3 <i>Comment</i>	336
4.3.3 aMDEA wash unit	336
4.3.3.1 <i>General process description</i>	336
4.3.3.2 <i>Process description of the aMDEA wash</i>	336
4.3.3.3 <i>Comments</i>	336
4.4 CO₂ removal after CO-shift	336
4.4.1 Rectisol wash unit	336
4.4.1.1 <i>General process description</i>	336
4.4.1.2 <i>Process description of the Rectisol wash</i>	340
4.4.1.3 <i>Comments</i>	340
4.4.2 NMP wash unit	340
4.4.2.1 <i>General process description</i>	340
4.4.2.2 <i>Process description of the NMP wash</i>	340
4.4.2.3 <i>Comments</i>	344
4.4.3 aMDEA wash unit	344
4.4.3.1 <i>General process description</i>	344
4.4.3.2 <i>Process description of the aMDEA wash</i>	344
4.4.3.3 <i>Comments</i>	344
4.4.3.4 <i>Process option</i>	344
4.4.3.5 <i>Sulpherox plant for H₂S-removal from sour gas from the aMDEA wash unit (alternative 2b)</i>	344
4.5 Behaviour of trace components	348
4.6 CO₂-Liquefaction	348
5 INVESTMENT AND OPERATING COSTS	350
5.1 Assumptions	350
5.2 Comparison of the alternatives examined	350
6 CONCLUSIONS	354
7 LITERATURE	354
8 ENCLOSURE	354

FIGURES

1 IGCC-plant for brown coal	326
2 IGCC-plant for brown coal with CO ₂ -removal	328
3 Alternative concepts for CO ₂ -removal	329
4 CO-conversion	330
5 CO ₂ -removal concept with Rectisol wash	332
6 Rectisol wash unit	333
7 CO ₂ -removal concept with NMP wash	334
8 NMP wash unit	335
9 CO ₂ -removal concept with AMDEA wash	337
10 aMDEA wash unit	338
11 CO ₂ -removal concept with Rectisol wash	339
12 Rectisol wash unit	341
13 CO ₂ -removal concept with NMP wash	342
14 NMP wash unit	343
15 CO ₂ -removal concept with AMDEA wash	345
16 aMDEA wash unit	346
17 S-recovery unit (Sulferox)	347
18 Dependence of the efficiency of CO ₂ -liquefaction on the purity of the raw CO ₂	349
19 CO ₂ -liquefaction plant	351

TABLES

1 Investment and operating costs for CO ₂ -removal	352
2 Investment and operating costs for CO ₂ -removal	353
3 Investment and operating costs for CO ₂ -removal	355

APPENDIX A

Technical and economical optimization of CO₂-removed in an IGCC power plant

Jochen Putter and Matthias Krumbeck

1 SUMMARY

The present study examines the technical and economic optimization of CO₂ removal (separation and liquefaction) in an IGCC power plant. A combined-cycle power plant (3 × 300 MW) with integrated lignite gasification (HTW gasification) was chosen as a reference plant. Due to the low H₂S partial pressure in the raw gas, various absorptive scrubbing processes were applied for CO₂ removal (Rectisol, Purisol and aMDEA). All of the process types were examined on the condition that they remove the same amount of CO₂ with respect to the entire power plant. This was either accomplished by means of a simultaneous CO₂ removal in all three trains (3 × 26%) or by a CO₂ removal in only one train (1 × 78%), requiring an additional CO conversion. Moreover, maximum CO₂ removal was considered for each train of the power plant.

The comparative, technical and economic analysis of the different process concepts led to the following results:

- It is more economic to remove the same amount of CO₂ in one train than simultaneously in all three trains.
- For an economic CO₂ removal, extremely high separation rates (>90%) are indispensable.
- In view of a desired CO₂ reduction by 25%, it is more economic to carry out a complete CO₂ removal in combined-cycle power plants than to retrofit every single power plant in the existing power plant portfolio.
- The measures for CO₂ separation and liquefaction under investigation involve drastic cost increases. The specific investment costs are raised by approx. 25% to 30%, the additional electricity generating costs by approx. 30% to 40%. The specific costs for the recovery of 1 ton of CO₂ range between 40 DM/t and 50 DM/t.

The study did not take the costs for transport and storage of the liquefied CO₂ into account.

2 TARGETS OF THE STUDY

The main target of this study is to find out the technical and economic optimum of CO₂-removal (recovery and liquefaction) in an IGCC power plant. Additionally the sulphur of the fuel gas has to be removed to a level of 5 vpm.

Starting out from a brown coal-fired combined cycle power plant of approximately 900 MWe consisting of three trains it will be examined how additional steps for removing CO₂ from the gas can be integrated into the process.

To analyse the technical and economic applicability of the CO₂-removal, and according to the statement of the German Government to reduce CO₂-emissions in Germany by 25% up to the year 2005, several possible

acid gas removal processes are tested to separate 25% of the total CO₂ which is present in the flue gas downstream of the gas turbine. Additionally, the application of a CO-shift unit has to be discussed. Requested are both minimum investment and operating costs for the whole plant as well as maximum efficiency. The net electrical output of the original power plant should be preserved.

As the IGCC power plant consists of three trains the influence of the amount of CO₂-removal in one train (1 × 78%) or three trains (3 × 26% or 3 × 78%) has to be examined.

For all alternatives examined in the study the CO₂ produced is compressed, dried and liquefied in the refrigerant unit and then compressed to 50 bar. For the liquefied CO₂ no specifications are available at present. Therefore, the following assumptions have been made:

sulphur content (H ₂ S + COS)	max. 50 vppm
water dew point	-25°C at 50 bar
concentration of inerts	no vapor phase (50 bar, <15 °C)

No effort was made to remove higher hydrocarbons, as long as they are completely dissolved in the liquid CO₂ and solidification can not occur.

3 THE BASIC IGCC POWER PLANT

The characteristics of an IGCC power plant based on brown coal are:

- drying the brown coal down to 12 percent residual moisture
- complete gasification of the dried coal (e.g. HTW gasification)
- efficient purification of the product fuel gas under pressure
- gas and steam turbine process with unfired HRSG (heat recovery steam generator)
- extensive utilization of the heat obtained by cooling the fuel gas in the power generation process
- utilization of the calorific value of the residual coke from gasification (gasifier bottom product) and of the dry dust by fluidized-bed combustion.

Compared with conventional power plant technology, the IGCC power plant concept permits the net efficiency to be raised by approximate 30% to more than 45%. In addition, the emission of the pollutions SO₂, NO_x and dust is drastically reduced, for beyond due to the increase of efficiency.

The IGCC power plant, shown in Fig. 1 will have a gross electric output of about 320 MWe. Of this, the gas turbine accounts for some 200 MWe and the steam turbine for 120 MWe.

The essential elements of the IGCC power plant concept with HTW-gasifier are [1]:

— coal preparation and drying

The raw brown coal with a water content of approximately 50% is crushed to <6 mm size and subsequently dried to a residual moisture content of 12%

— gasification

The HTW-gasifier is designed for a dried coal throughput of 150 t/h at a gasification pressure of 27 bar. Coal is supplied to the gasifiers by lock hopper systems at 27 bar. The withdrawn bottom product is cooled to 60°C and conveyed to an outside combustion chamber.

In the gasifier, the brown coal is converted with oxygen and steam into a fuel gas which contains about 40% CO, 20% CO₂, 35% H₂, 4% CH₄, 0,2% H₂S and some trace gases [2].

— raw gas cooling

The sensible heat of the raw gas is utilized in two heat exchangers of the fire tube type for generating saturated high — and intermediate — pressure steam.

Most of the steam is sent to the HRSG downstream of the gas turbine for superheating, the minor portion being used to preheat the purified gas. The high dust content of the raw gas and the H₂S content in conjunction with the high operating temperature constitute stringent requirements for the design of the components with regard to erosion, corrosion and fouling behavior.

— dust separation

In consideration of the requirements of gas turbine operation, the dust content of the raw gas must be reduced to less than 5 mg/m³. This is performed in a hot filter unit with ceramic filter elements.

— wet scrubbing

In the wet scrubbing unit the residual dust and the trace substances such as NH₃, HCN, HCl and HF are removed. The required waste water pretreatment unit essentially consists of multi-stage stripping for removing the dissolved acid components (H₂S, CO₂ etc.) and NH₃. In the water scrubber the raw gas is cooled by direct contact with the water to 140°C. In the following cooling steps the gas is cooled to the inlet temperature of the desulphurization unit.

— desulphurization and sulphur recovery

In the gasifier, most of the sulphur contained in the feed coal is transferred to the gaseous phase, the minor portion is bound by the alkaline ash of the dust and the bottom product. The sulphur is present in the raw gas mainly in the form of H₂S and to a minor content in the form of COS.

In view of the fact that scrubbing out COS in the

desulphurization unit is problematic and expensive, the COS is first converted catalytically to H₂S.

For the selective H₂S-removal from the raw gas resulting from the gasification, a FLEXSORB-SE plus wash unit was selected due to the low H₂S-concentration in the gas and the high CO₂-content. Such a system works optimal at low H₂S partial pressure with, at the same time, a relatively low CO₂ coabsorption. As solvent a special sterically hindered amine is used.

Together with all of the H₂S about 10% of the CO₂ present in the fuel gas is absorbed resulting in an acid gas containing approx. 10 mol% H₂S. Such a gas cannot be processed in an usual Claus plant, but it is possible to convert the H₂S to elementary sulfur in a Clinsulf plant.

The Clinsulf unit allows to recover more than 90% sulphur from a gas which contains less than 10% H₂S. It is a catalytic direct oxidation process with an optional downstream sodium caustic scrubber for trace removal. The heart of the process is an internally cooled reactor. It contains a coiled heat exchanger submerged in the catalyst bed. Thus the outlet temperature can be lowered close to the sulphur dew point.

— fuel gas wetting and preheating

The power output of the gas turbine is improved and the formation of NO_x in the combustion chamber is reduced by humidifying the purified gas.

The purified gas is then further heated by a gas-gas heat exchanger using the raw gas downstream of the hot filter unit.

— gas turbine and air separation unit

The product fuel gas is burned in the gas turbine for electricity generation. The gasification oxygen is formed in an air separation unit (ASU) by using the boosted air of the gas turbine compressor.

— heat recovery steam generator (HRSG) and water/steam cycle.

As the temperature of the gas turbine exhaust gas is about 550°C, it is used for steam generation in the HRSG and for electricity production in the steam turbine.

4 CO₂ REMOVAL PROCESSES (RECOVERY AND LIQUEFACTION)

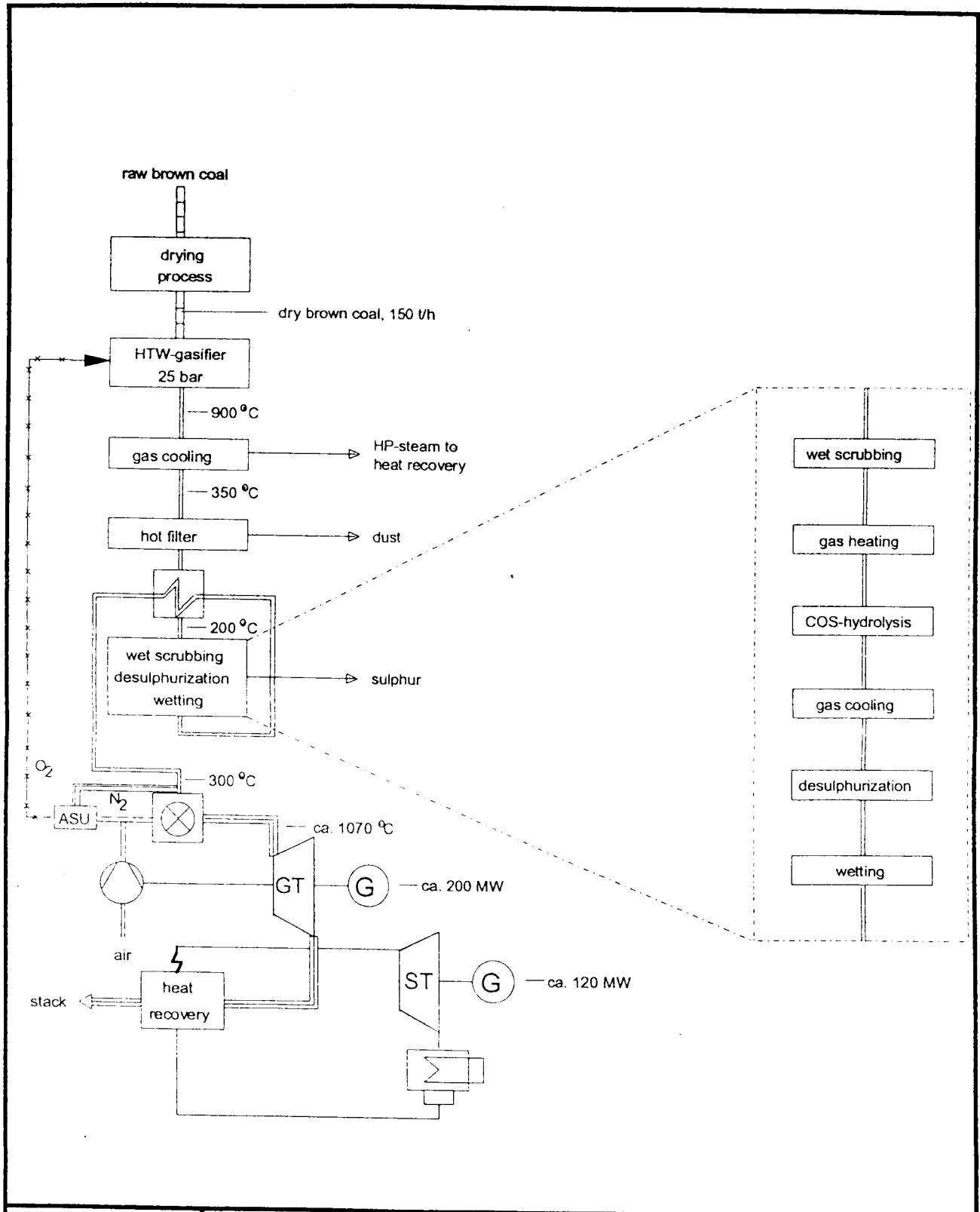
4.1 General

There are four basic techniques to capture CO₂: Adsorption, Absorption, Cryogenics and Membranes.

Processing techniques for the capture of CO₂ are significantly influenced by the concentration of partial pressure or the gas to be captured.

A number of studies pointed out that absorption processes are optimal for IGCC power plants. These normally continuous scrubbing systems use different kinds of solvents.

chemical solvent: The CO₂ reacts with the solvent to form a weakly bonded intermediate compound which is then broken down by



RWE
Aktiengesellschaft

fig. 1: IGCC-plant for brown coal

the application of heat regenerating, the original solvent and producing a CO₂-stream. Typical solvents are amine or carbonate based, such as MDEA (MEA, DEA, ammonia and hot potassium carbonate) and Flexsorb SE.

physical solvent: The CO₂ is physically absorbed in the solvent according to Henry's law and then regenerated using either heat or pressure reduction or both. Typical solvents are Rectisol and Purisol.

hybrid solvents: Such solvents combine the best characteristics of both the chemical and physical solvent and are usually composed by a number of complementary solvent. Typical solvents is aMDEA.

All the processes operate usually the same manner by scrubbing the flue gas in absorption columns to collect the CO₂ and then regenerating the solvent and releasing the CO₂.

4.2 CONSIDERED CO₂ REMOVAL CONCEPTS

The IGCC power plant with CO₂-removal (see fig. 2) consists of three parallel trains with a capacity of 300 MW each.

Six different variants were examined (see fig. 3) The alternatives 1a and 1c are designed to remove 33.333 Nm³/hr CO₂ in each train while the alternatives 2a and 2b remove 100.000 Nm³/hr CO₂ only in one train (with CO-shift).

Basic fired data:

alternatives 1 a and 1 b

H ₂	35	mole-%	total	200.000 Nm ³ /hr
CO	40	mole-%	pressure	24.0 bara
CH ₄	4	mole-%	temperatur	40°C
CO ₂	20	mole-%	H ₂ O-saturated at these conditions	
H ₂ S	0,25	mole-%		

alternatives 2 a and 2 b (downstream CO-shift)

H ₂	52,56	mole-%	pressure	23.0 bara
CO	3,00	mole-%	temperatur	40°C
CH ₄	2,94	mole-%	total	272.641 Nm ³ /hr
CO ₂	41,31	mole-%	H ₂ O-saturated at these conditions	
H ₂ S	0,19	mole-%		
COS	4	vpm		

In all alternatives two trains of CO₂-liquefaction are presumed (for 100.000 Nm³/hr).

Trace components will not be considered in this study; its influences are mentioned in chapter 4.5.

In order to compare the different alternatives, it is necessary to consider also the COS-hydrolysis, CO-shift, Flexorb SE Plus, Clinsulf and CO₂-liquefaction, whenever required COS-hydrolysis. In principle a COS-hydrolysis is necessary in fuel gas trains, where no CO-shift or Rectisol wash unit (a selective H₂S-removing amine wash does not remove the COS sufficiently) is implemented.

COS-hydrolysis

COS is a component which is normally present in fuel gases produced by partial oxidation. For a rough estimate about 5% of the total sulfur is present as COS.

COS is chemical neutral and therefore reacts only in a minor degree with amines. In physical acting solvents the solubility is smaller than that of H₂S. If a physical wash has to be designed in order to remove COS, the solvent flow rate has to be increased considerably with the consequence, that the selectivity between CO₂ and H₂S is decreasing.

The normal way to remove COS from fuel gases is a catalytic conversion of COS according to the formula



Such a hydrolysis step is performed in a catalytic reactor working in a temperature range between 150 and 170°C. The reaction requires water, but due to the stability of the catalyst the water dew point should be approx. 20°C below the operation temperature. In an optimal designed hydrolysis reactor the COS content can be reduced to a concentration of 5–10 vppm. Lower concentrations are possible, depending on the equilibrium of the components COS, H₂S, CO₂ and H₂O and on the operating conditions (temperature, pressure).

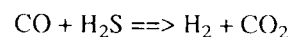
Flexsorb SE-plus wash unit for selective H₂S-removal

For the selective H₂S-removal from the raw gas from the gasification a FLEXSORB-SE plus wash unit was selected due to the low H₂S-concentration in the gas and the high CO₂-content. Such a system works optimal at low H₂S partial pressure having simultaneously a relative low CO₂ coabsorption. As solvent a special sterical hindered amine is used.

Together with all of the H₂S about 10% of the CO₂ present in the fuel gas is absorbed resulting in an acid gas containing approx. 10mol% H₂S. Such a gas cannot be processed in a usual Claus plant, but it is possible to convert the H₂S to elementary sulfur in a Clinsulf plant.

CO-shift conversion

In a CO-shift conversion (see fig. 4), CO is converted together with water to H₂ and CO₂ according to the relation



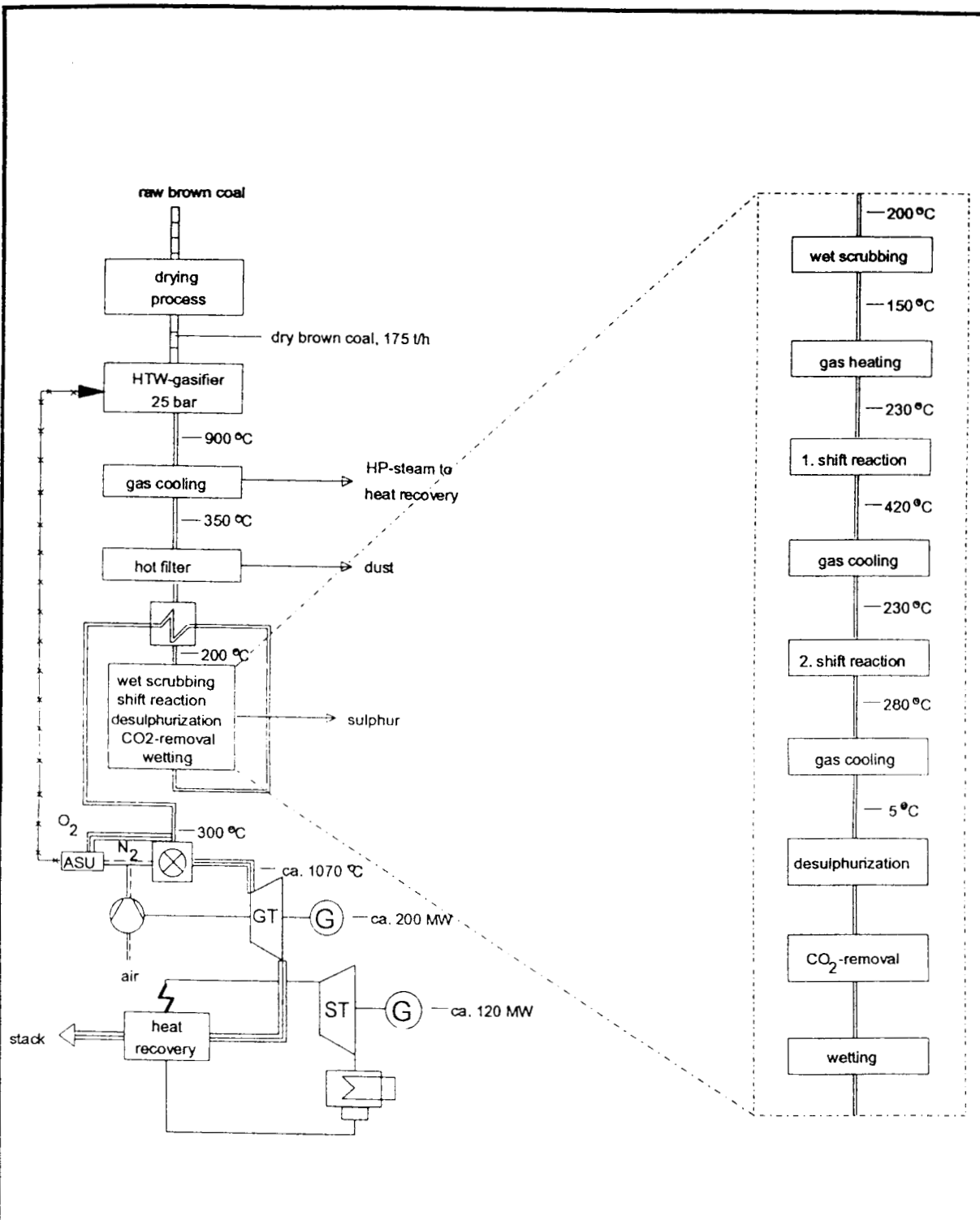
This process is carried out at a elevated temperature in the presence of a catalyst. Just in case of a sulfur containing feed gas the catalyst K8-11 from BASF is recommended and normally used for CO-conversion in ammonia plants based on partial oxidation of oil or coal.

The incorporation of the shift depends mainly on the heat recovery system of the hot fuel gas from the burner and the heat recovery after shift.

The CO-conversion unit is integrated between the wet scrubbing unit and the gas purification unit. The COS-hydrolysis will be abmitted and the CO₂-removal unit will be connected with the desulphurization unit.

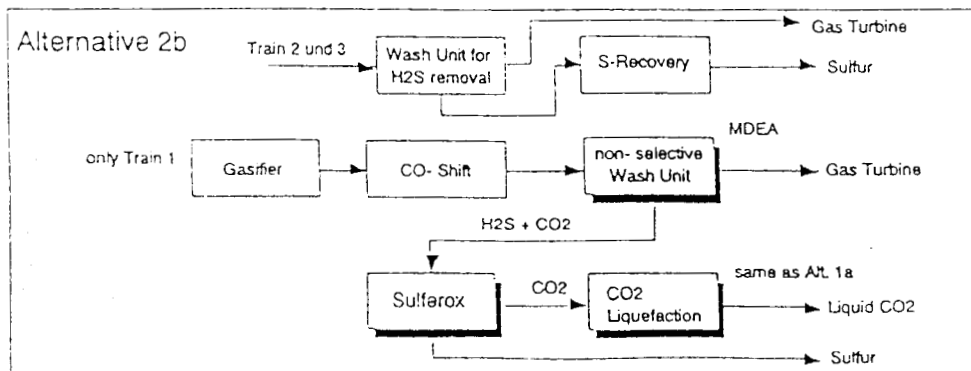
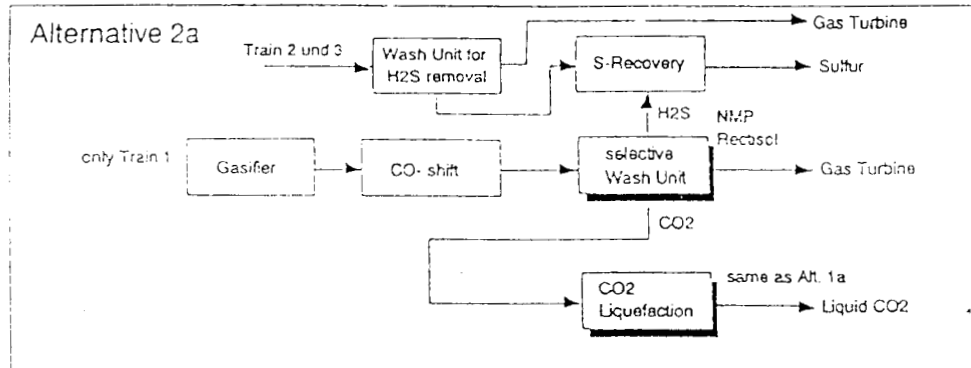
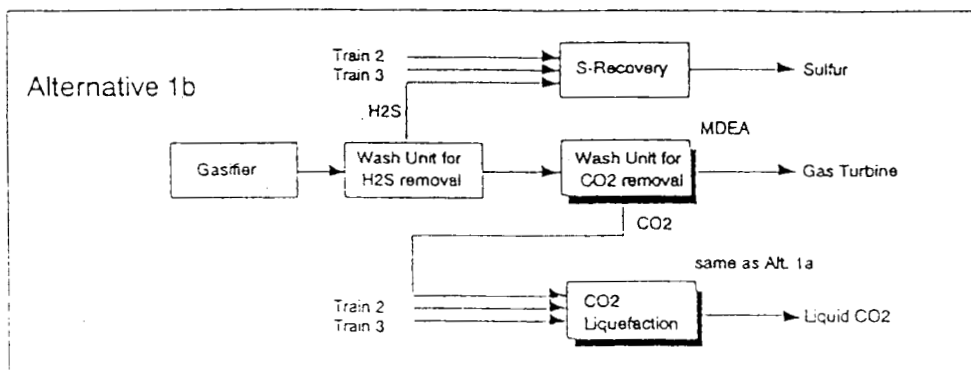
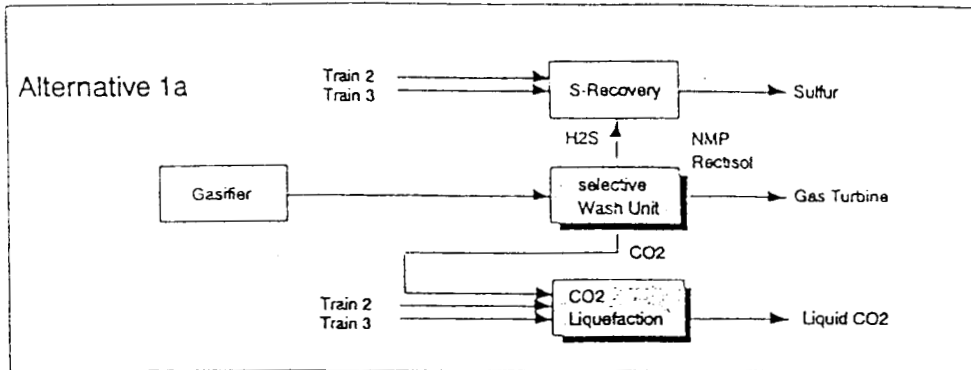
In an earlier study [3] it was carried out that the amount of CO-conversion has to be more than 90% to achieve on optimal CO₂-removal. Therefore several other concepts with lower amounts of CO-conversion and CO₂-recovery were tested. The results of the economical analysis pointed out that the optimal CO₂-removal presumed a high CO-conversion of more than 90%. The graduated variants are not suitable.

To convert more than 90% of the CO₂ to CO the conversion unit will comprise two shift reactors.



RWE
Aktiengesellschaft

fig. 2: IGCC-plant for brown coal with CO₂-removal



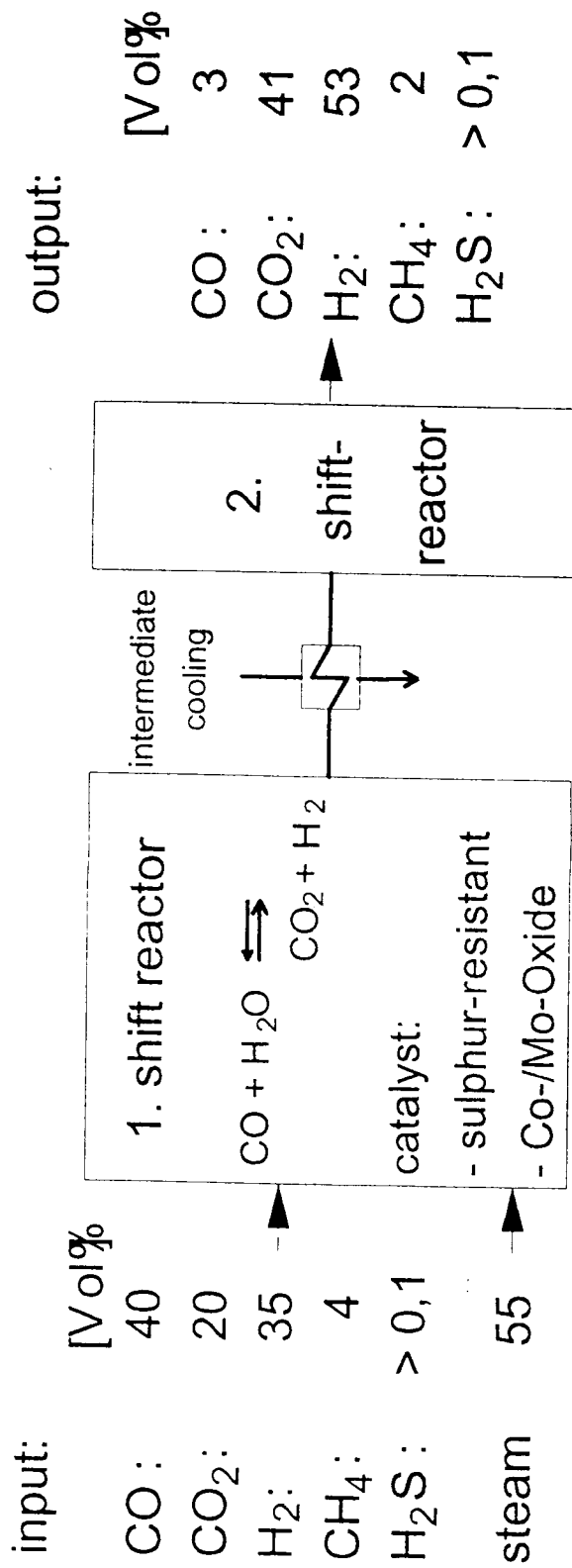
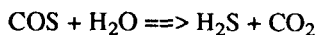


fig.4: CO-conversion

In the CO-shift also COS is converted according



Therefore after shift no COS-hydrolysis is required even in the cases where COS has to be removed to achieve the sulfur purity in the fuel gas.

4.3 CO₂ removal without CO-shift

4.3.1 Rectisol wash unit

for selective H₂S and CO₂ removal (alternative 1 a)

4.3.1.1 General process description (see fig. 5)

After corresponding cooling and pretreatment systems the raw gases of three trains of gasifiers are fed for selective H₂S- and CO₂-removal into three trains of a Rectisol wash unit. The purified gases downstream the Rectisol units are routed to the gas turbines (three trains).

In the Rectisol wash CO₂, H₂S and COS is removed from the gas by methanol as physical solvent. The absorption takes place at temperatures below 0°C; an external refrigeration is required.

The Rectisol units are recovering pure CO₂-streams, which are combined to be liquefied in only one train. The liquefaction takes place at about fuel gas pressure to Rectisol, so that the non liquefied portion from the liquefaction (tail gas) can be recycled upstream the wash units.

The H₂S-rich streams from the Rectisol units are also combined and routed to one train of S-recovery unit where the H₂S is recovered as elementary sulfur.

4.3.1.2 Process description of the Rectisol wash (see fig. 6)

The following process description is related to the most important process steps according to the attached process sketch.

- (1) After injection of methanol the feed gas is cooled down against cold product gases. The condensed methanol/water mixture is separated from the feed gas, the feed gas is routed to the wash sections of the absorber.
- (2) In the lower section of the wash column H₂S and COS are completely removed by the cold methanol, the CO₂ is removed in the upper section. The heat of solution is covered partly by warming up the methanol, partly by a cooling stage (external refrigeration). As the solubility of CO₂ in methanol is less than the one of H₂S, the methanol flow in the CO₂ removal section is greater than in the H₂S removal section. The methanol surplus from the CO₂ removal section is taken off from the middle of the column, this methanol is only loaded with CO₂. The other methanol from the sump of the column is loaded with CO₂ and H₂S.
- (3) Both methanol streams are expanded to an intermediate pressure in order to recover dissolved H₂ and CO. The flash gases (mainly H₂ and CO) are compressed and recycled into the feed gas to the Rectisol wash unit.
- (4) CO₂-production by expansion of both methanol streams to about ambient pressure into the CO₂ production column and rewash with sulfur free methanol routed to the top of this column.
- (5) The total solvent from the bottom of this column is further expanded for an increased CO₂-recovery rate. Flashed CO₂ is recompressed into the CO₂-production column also to be washed with S-free methanol.
- (6) The cold loaded methanol from the last expansion step is warmed up and fed into the regeneration column. The regenerated methanol is cooled down before reuse in the wash column.
- (7) In the hot regeneration column all yet dissolved acid gases are stripped off by means of methanol vapor, generated in a reboiler heated by steam. The lean solvent from the bottom of the column is pumped back to the wash column. Methanol vapor is condensed from the H₂S-fraction leaving the top.
- (8) The methanol/water mixture from (1) is separated in the methanol/water distillation column to methanol (top) and waste water (bottom). The column is heated by steam, as reflux lean methanol is used. The methanol from the top supports the warm regeneration, the waste water is routed to B.L.

4.3.1.3 Comments

A COS-hydrolysis in the feed gas before entering the Rectisol unit is not required, because the COS is completely removed in the Rectisol wash unit.

It is assumed that one third of the tail gas from the CO₂-liquefaction is recycled to each Rectisol unit.

The CO₂-content in the treated gas from the Rectisol unit is adjusted in order to recover totally the 100 000 Nm³/hr of CO₂.

4.3.2 NMP wash unit

for selective H₂S and CO₂-removal (alternative 1a)

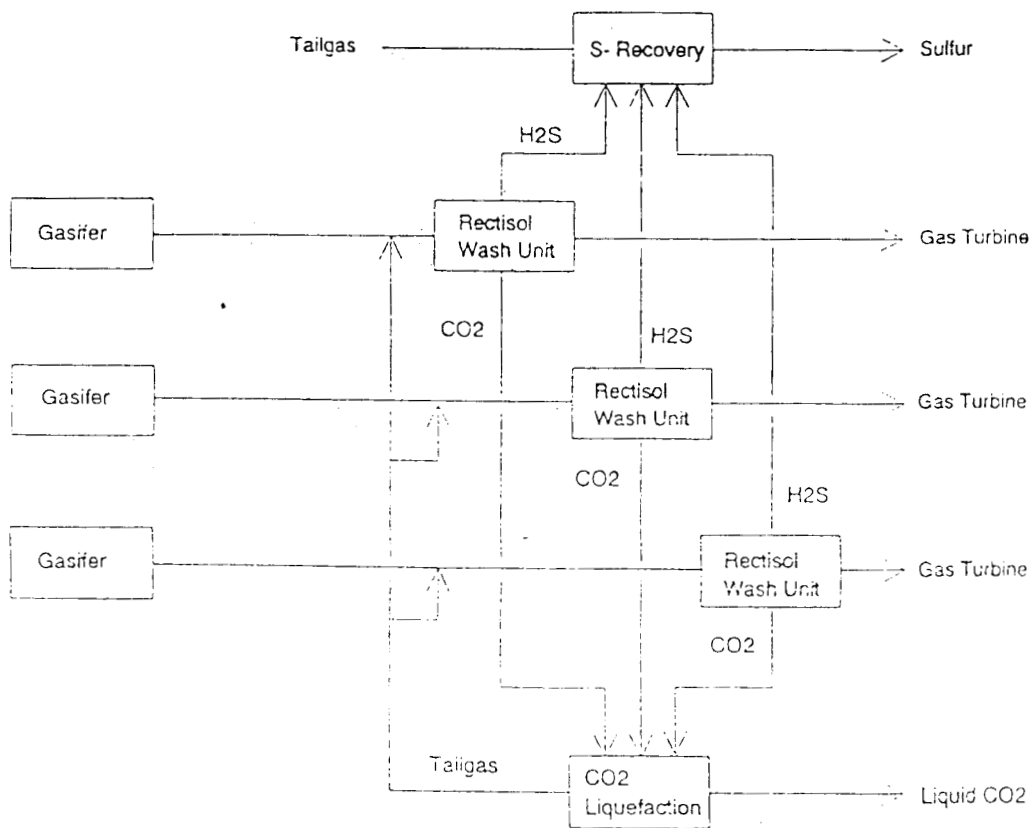
4.3.2.1 General process description (see fig. 7)

The process configuration is the same as for the Rectisol wash unit (chapter 4.3.1). The only difference is the requirement of a COS-hydrolysis step (one per train) upstream the NMP-wash in the scope of the fuel gas cooling system.

In the NMP (n-methyl-pyrrolidone) wash CO₂ and H₂S are removed from the gas by physical solvent. The absorption takes place at temperatures slightly above 0°C; an external refrigeration is required.

4.3.2.2 Process description of the NMP wash (see fig.8)

- (1) The feed gas is cooled down against cold product gases. The condensed water is separated from the feed gas, the feed gas is routed to the wash sections of the absorber.
- (2) In the lower section of the wash column H₂S is completely removed by the solvent, the CO₂ is removed in the upper section. The heat of solutions is covered partly by warming up of the NMP, partly by a cooling stage (external refrigeration). As the solubility of H₂S in NMP is much higher than the one of CO₂, the solvent flow required for the H₂S-removal section is only a small part of the NMP flow in the CO₂-removal section. Most of the solvent therefore can drawn off from the middle of the column, this NMP is only loaded with CO₂. The other NMP stream from the sump of the column is loaded with CO₂ and H₂S.



RWE 23200417
RECTISOL WASH UNIT
ALTERNATIVE 1A

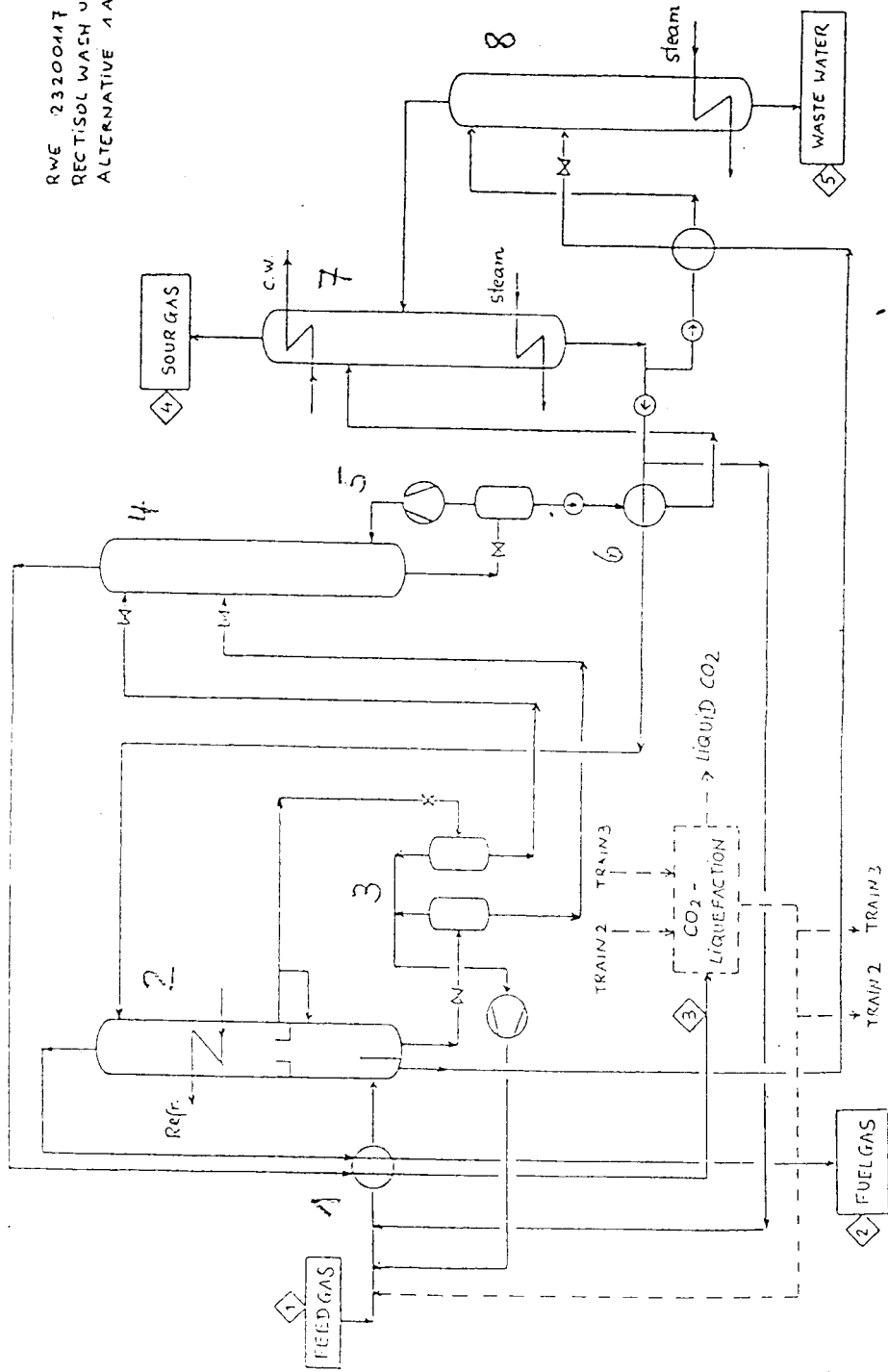
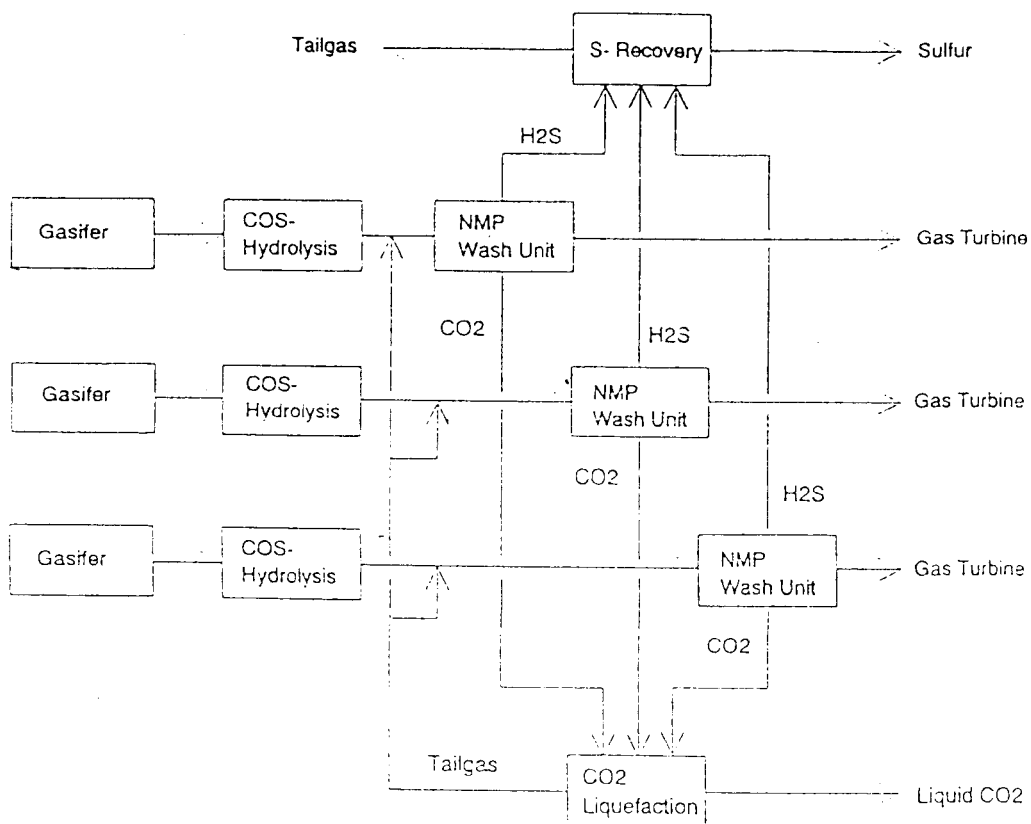


fig.6: Rectisol wash unit (alternative 1a)

RWE
Aktiengesellschaft



**fig. 7: CO₂-removal concept with NMP wash
(alternative 1a; 3 * 26%)**

- (3) Both solvent streams are expanded to an intermediate pressure in order to recover dissolved H₂S and CO. The flash gases (mainly H₂S and CO) are compressed and recycled into the feed gas to the NMP wash unit.
- (4) The H₂S-free NMP is expanded to about ambient pressure. After separation of flashed CO₂ in this vessel a big part of the solvent (which is not required for rewashing in the following CO₂-production column) can be pumped back to the middle of the absorber as semi-lean solvent and need not to be fed to the hot regeneration system.
- (5) Further CO₂-production by expansion of the CO₂- and H₂S-loaded NMP stream also to about ambient pressure into the CO₂ production column and rewash with sulfur free NMP routed to the top of this column coming from the vessel (4).
- (6) The total solvent from the bottom of this column is further expanded for an increased CO₂-recovery rate. Flashed CO₂ is recompressed into the CO₂-production column also to be washed with S-free solvent.
- (7) The cold loaded NMP from the last expansion step is warmed up and fed into the regeneration column. The regenerated NMP is cooled down before reuse in the wash column.
- (8) In the hot regeneration column all yet dissolved acid gases are stripped off by means of steam, reboiled out from the solvent (reboiler heated by steam). The NMP-solvent contains some percent of water. The lean solvent from the bottom of the column is pumped back to the wash column. Stripping vapor is condensed from the H₂S-fraction leaving the top.

4.3.2.3 *Comment*

A COS-hydrolysis in the fuel gas before entering the NMP wash is required, because the COS is only partially removed in the H₂S-section of the absorber by the NMP liquor.

It is assumed that one third of the tail gas from the CO₂-liquefaction section is recycled to each NMP unit.

The CO₂-content in the treated gas from the NMP unit is adjusted in order to recover totally the 100 000 Nm³/hr of CO₂.

4.3.3 *aMDEA wash unit*

for CO₂-removal downstream a selective H₂S-removal (Alternative 1b)

4.3.3.1 *General process description (see fig. 9)*

In this alternative (1b) the H₂S-removal and the CO₂-removal is done in two separate wash units with different solvents. There are three trains of this series of two wash units (one in each raw gas trains from the three trains of gasification section).

The H₂S-removal is assumed to be a highly selective wash process, e.g. a chemical wash using the Flexorb liquor (EXXON license) as solvent. Because such a wash system does remove the COS only partially every train needs an upstream COS-hydrolysis step again.

For the remaining CO₂-removal the activated MDEA-wash unit (BASF license) is installed as the most suitable process.

The three H₂S-rich acid gas streams from the H₂S-wash units are gathered and routed to only one S-recovery unit

(Clinsulf); the three CO₂-streams from the aMDEA wash units are distributed to two CO₂-liquefaction plants. The tail gases from the liquefaction plants are recycled upstream the aMDEA units.

4.3.3.2 *Process description of the aMDEA wash (see fig. 10)*

- (1) CO₂-removal in the absorber by means of lean solvent to the upper bed of the column and semi-lean solvent to the lower bed of the column.
Solvent traces from the purified gas are removed by a water wash cycle on the top of the column.
- (2) The loaded solvent is expanded to about ambient pressure in an expansion turbine (reverse running pump) in order to save electric energy for pumping the semi-lean solvent back to the absorber.
- (3) A big portion of the CO₂ is flashed in the desorption column. Flashed steam is recovered in the overhead condenser. The majority of the solvent can be recycled to the absorber (semi-lean), only a small part has to be routed to the hot regeneration.
- (4) The cold loaded MDEA solvent from the desorber is warmed up and fed into the regeneration column. The hot lean solvent is cooled down before reuse in the wash column.
- (5) In the hot regeneration column all yet dissolved CO₂ is stripped off by steam reboiled out from the solvent (reboiler heated by steam). The lean solvent from the bottom is pumped back to the absorber. The overhead vapor is directly routed to the desorption column to support the flashing of CO₂.

4.3.3.3 *Comments*

It is assumed that one third of the tail gas from the CO₂-liquefaction system is recycled to each aMDEA unit.

The CO₂-content in the treated gas from the aMDEA unit is adjusted in order to recover totally the 100 000 Nm³/hr of CO₂.

4.4 CO₂ removal after CO-shift

4.4.1 Rectisol wash unit

for selective H₂S and CO₂ removal (alternative 2a)

4.4.1.1 *General process description (see fig. 11)*

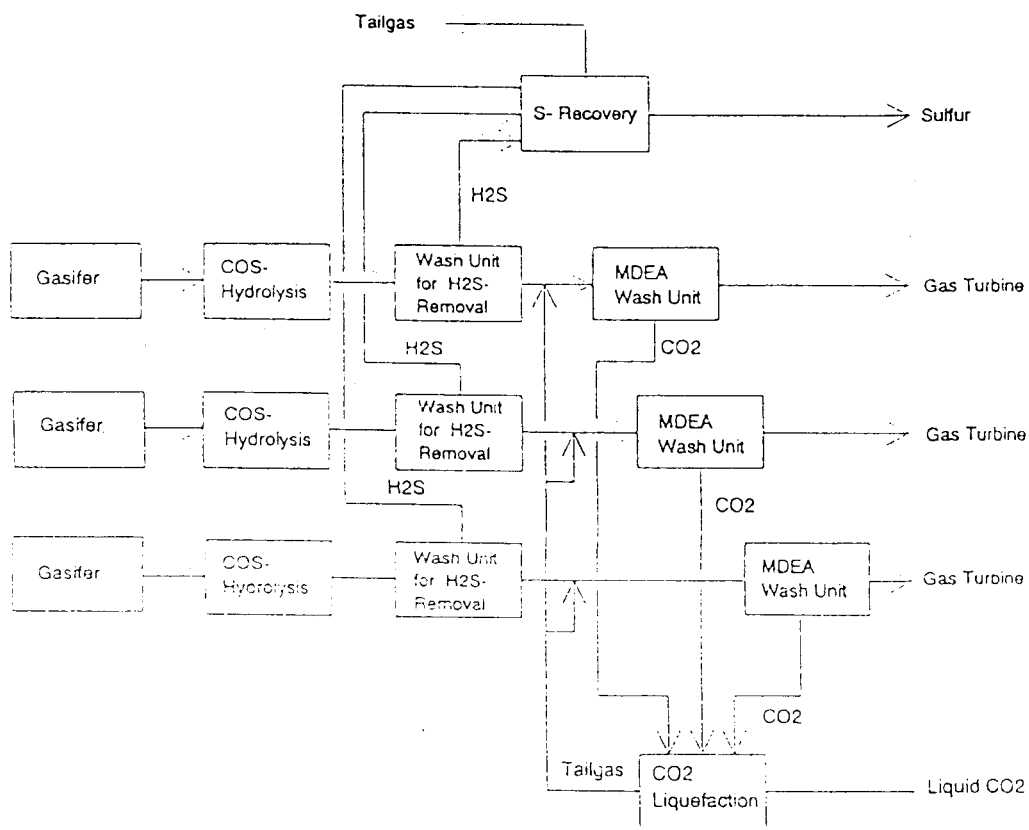
Only one train of the three trains of raw gases from the gasification sections is processed for CO₂-recovery.

In order to achieve the required CO₂-quantity in one fuel gas stream a CO-shift is passed upstream the Rectisol wash unit. The CO-content after the CO-shift is about 3 mole-%.

In the Rectisol wash CO₂, H₂S and COS are removed from the gas by methanol as physical solvent. The absorption takes place at temperatures below 0°C; an external refrigeration is required.

The Rectisol units are recovering pure CO₂-streams, which are combined to be liquefied in only one train. The liquefaction takes place at about feed gas pressure to Rectisol, so that the non liquefied portion from the liquefaction (tail gas) can be recycled upstream the wash units.

The other two trains of raw gases from the gasification sections have only to be desulfurized in a wash unit for selective H₂S-removal. The H₂S-rich streams from these



RWE
Aktengesellschaft

fig. 9: CO₂-removal concept with an MDEA wash
(alternative 1b; 3 * 26%)

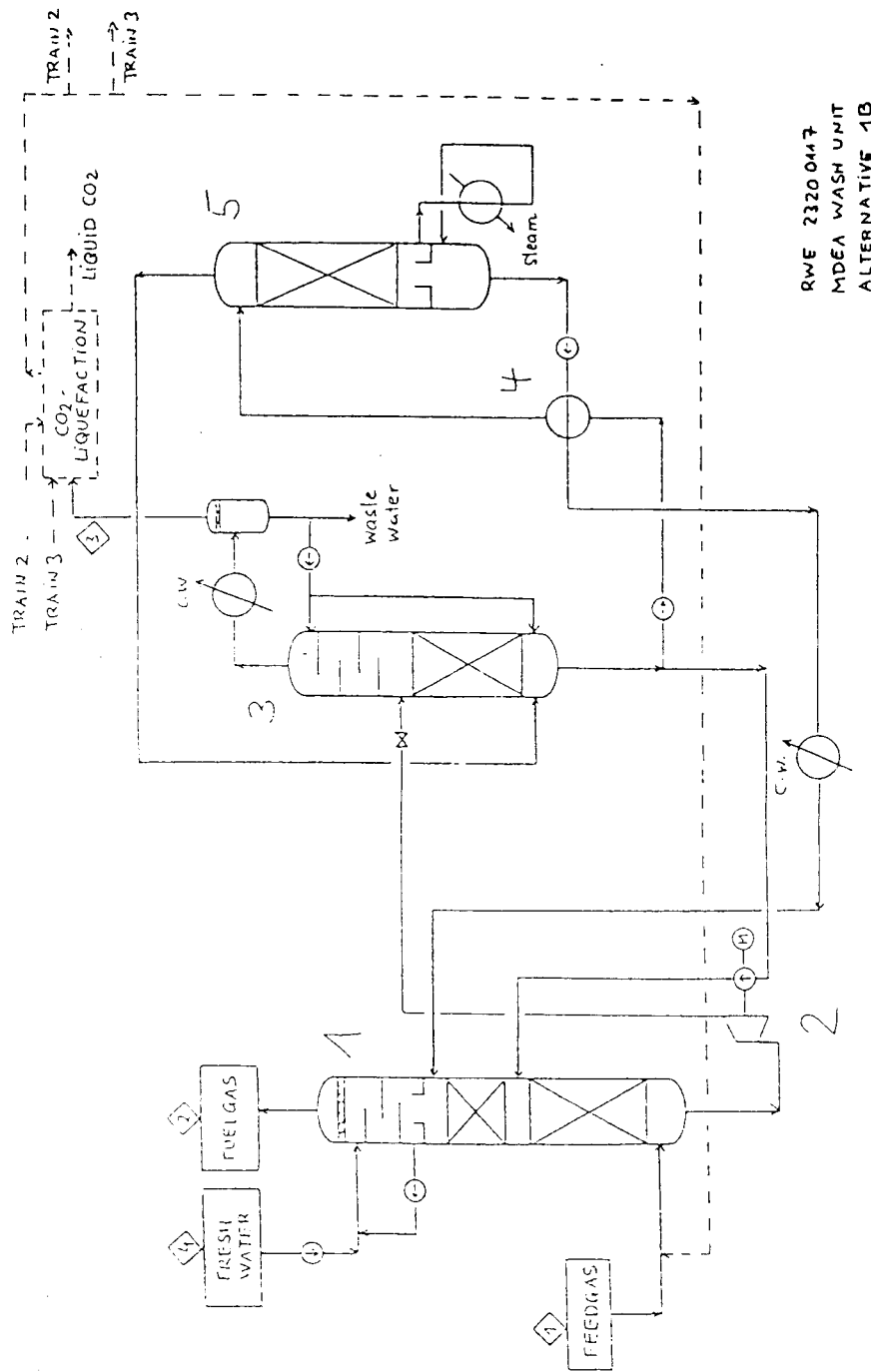
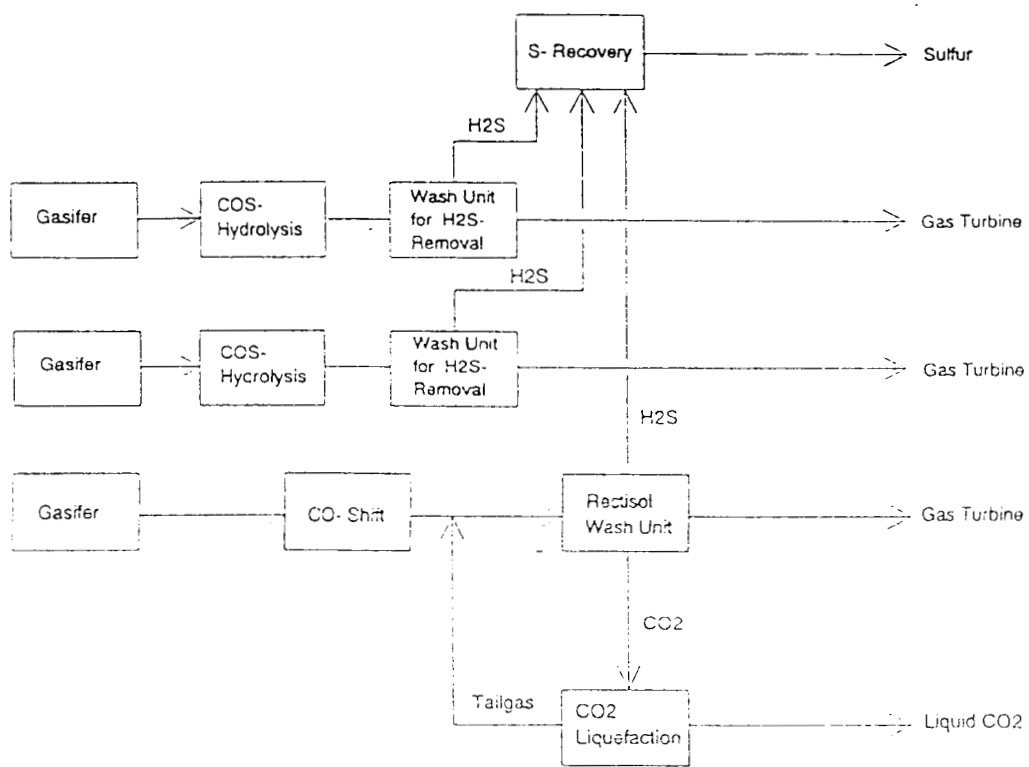


fig.10: aMDEA wash unit (alternative 1b)

RWE
Aktiengesellschaft



RWE
Aktiengesellschaft

fig. 11: CO₂-removal concept with Rectisol wash
(alternative 2a; 1 * 78%)

two wash units and from the Rectisol unit are combined and routed to one train of S-recovery unit (e.g. a Clinsulf process), where the H₂S is recovered as elementary sulfur.

4.4.1.2 Process description of the Rectisol wash (see fig. 12)

- (1) After injection of methanol the feed gas is cooled down against cold product gases. The condensed methanol/water mixture is separated from the feed gas, the feed gas is routed to the wash sections of the absorber.
- (2) In the lower section of the wash column H₂S and COS are completely removed by the cold methanol, the CO₂ is removed in the upper section. The heat of solution is covered partly by warming up the methanol, partly by a cooling stage (external refrigeration). As the solubility of CO₂ in methanol is less than the one of H₂S, the methanol flow in the CO₂ removal section is greater than in the H₂S removal section. The methanol surplus from the CO₂ removal section is taken off from the middle of the column, this methanol is only loaded with CO₂. The other methanol from the sump of the column is loaded with CO₂ and H₂S.
- (3) Both methanol streams are expanded to an intermediate pressure in order to recover dissolved H₂ and CO. The flash gases (mainly H₂ and CO) are compressed and recycled into the feed gas to the Rectisol wash unit.
- (4) CO₂-production by expansion of both loaded methanol streams to about ambient pressure into the CO₂ production column and rewash with sulfur free methanol routed to the top of this column. An intermediate warming-up step of the methanol against lean solvent supports the flashing of CO₂.
- (5) The total solvent from the bottom of this column is further expanded for an increased CO₂-recovery rate. Flashed CO₂ is recompressed into the CO₂-production column also to be washed with S-free methanol.
- (6) The cold loaded methanol from the last expansion step is warmed up and fed into the regeneration column. The regenerated methanol is cooled down before reuse in the wash column.
- (7) In the hot regeneration column all yet dissolved acid gases are stripped off by means of methanol vapor, generated in a reboiler heated by steam. The lean solvent from the bottom of the column is pumped back to the wash column. Methanol vapor is condensed from the H₂S-fraction leaving the top.
- (8) The methanol/water mixture from (1) is separated in the methanol/water distillation column to methanol (top) and waste water (bottom). The column is heated by steam, as reflux lean methanol is used. The methanol from the top supports the warm regeneration, the waste water is routed to B.L.

4.4.1.3 Comments

A COS-hydrolysis is only required for the two trains not incorporated in the CO₂-recovery.

The tail gas from the CO₂-liquefaction system is recycled upstream the Rectisol wash unit.

The CO₂-content in the treated gas from the Rectisol unit is adjusted in order to recover totally the 100 000 Nm³/hr of CO₂.

4.4.2 NMP wash unit

for selective H₂S and CO₂ removal (alternative 2a)

4.4.2.1 General process description (see fig. 13)

The block flow diagram is the same as for chapter 4.3.2.1; the only difference is the solvent for the gas wash unit downstream the CO-shift.

4.4.2.2 Process description of the NMP wash (see fig. 14)

- (1) The feed gas is cooled down against cold product gases. The condensed water is separated from the feed gas, the feed gas is routed to the wash sections of the absorber.
- (2) In the lower section of the wash column H₂S is completely removed by the solvent, the CO₂ is removed in the upper section. The heat of solutions is covered partly by warming up of the NMP, partly by a cooling stage (external refrigeration). As the solubility of H₂S in NMP is much higher than the one of CO₂, the solvent flow required for the H₂S-removal section is only a small part of the NMP flow in the CO₂-removal section. Most of the solvent therefore can be drawn off from the middle of the column, this NMP is only loaded with CO₂. The other NMP stream from the sump of the column is loaded with CO₂ and H₂S.
- (3) Both solvent streams are expanded to an intermediate pressure in order to recover dissolved H₂S and CO. The flash gases (mainly H₂S and CO) are compressed and recycled into the feed gas to the NMP wash unit.
- (4) The H₂S-free NMP is expanded to a pressure of about 4 bara. The flashed CO₂ is directly given to the CO₂-compressor of the CO₂-liquefaction section. The recovery of part of the required CO₂-quantity at increased pressure saves electric energy for CO₂-compression.
- (5) The H₂S-free NMP from (4) is expanded to about ambient pressure. After separation of flashed CO₂ in this vessel a big part of the solvent (which is not required for re-washing in the following CO₂-production column) can be pumped back to the middle of the absorber as semi-lean solvent and need not to be fed to the hot regeneration system.
- (6) Further CO₂-production by expansion of the CO₂- and H₂S-loaded NMP stream also to about ambient pressure into the CO₂ production column and rewash with sulfur free NMP routed to the top of this column coming from the vessel (5).
- (7) The total solvent from the bottom of this column is further expanded for an increased CO₂-recovery rate. Flashed CO₂ is recompressed into the CO₂-production column also to be washed with S-free solvent.
- (8) The cold loaded NMP from the last expansion step is warmed up and fed into the regeneration column. The regenerated NMP is cooled down before reuse in the wash column.

RWE 23200447
RECTISOL WASH UNIT
ALTERNATIVE 2A

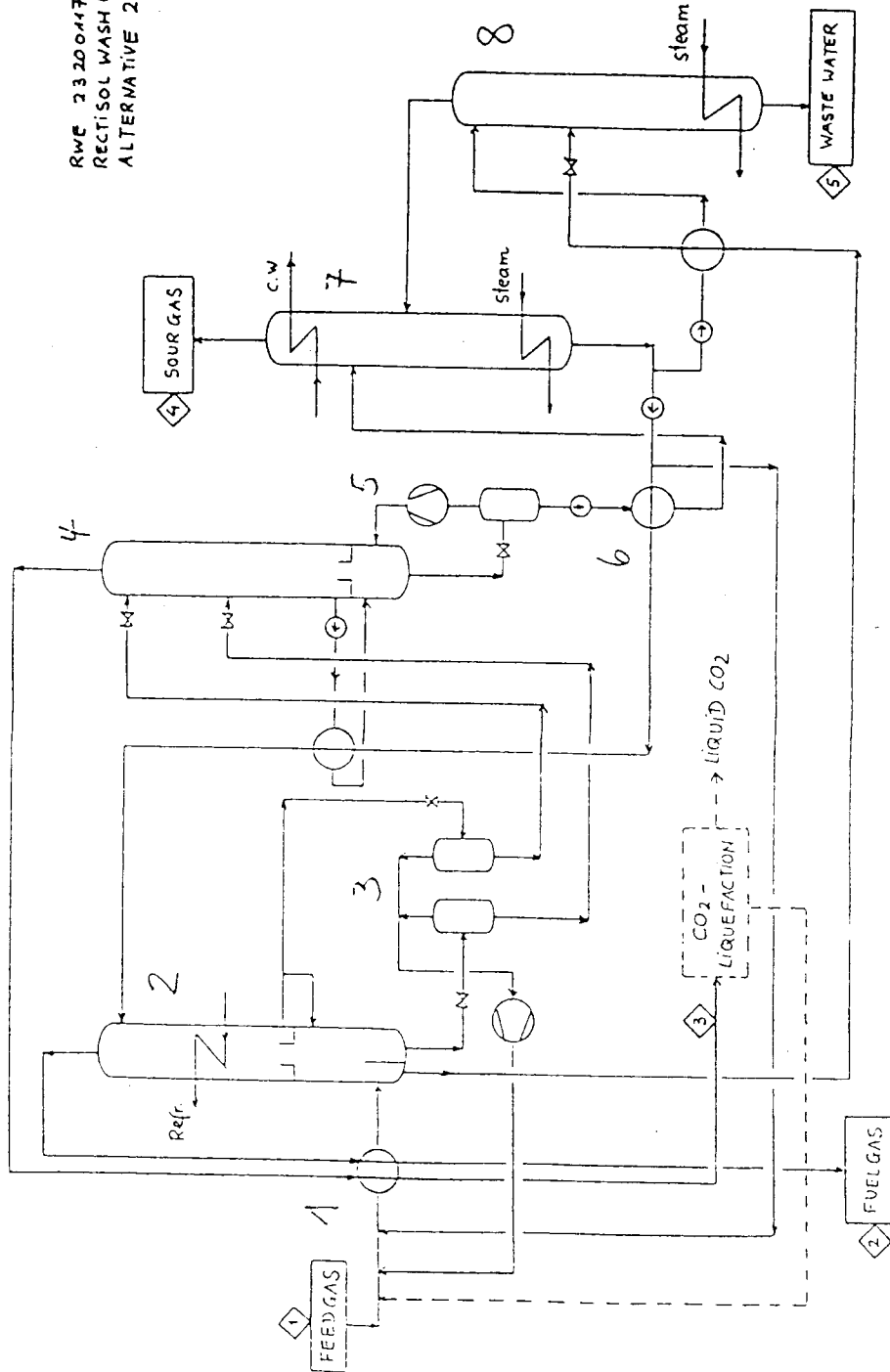


fig.12: Rectisol wash unit (alternative 2a)

RWE
Aktiengesellschaft

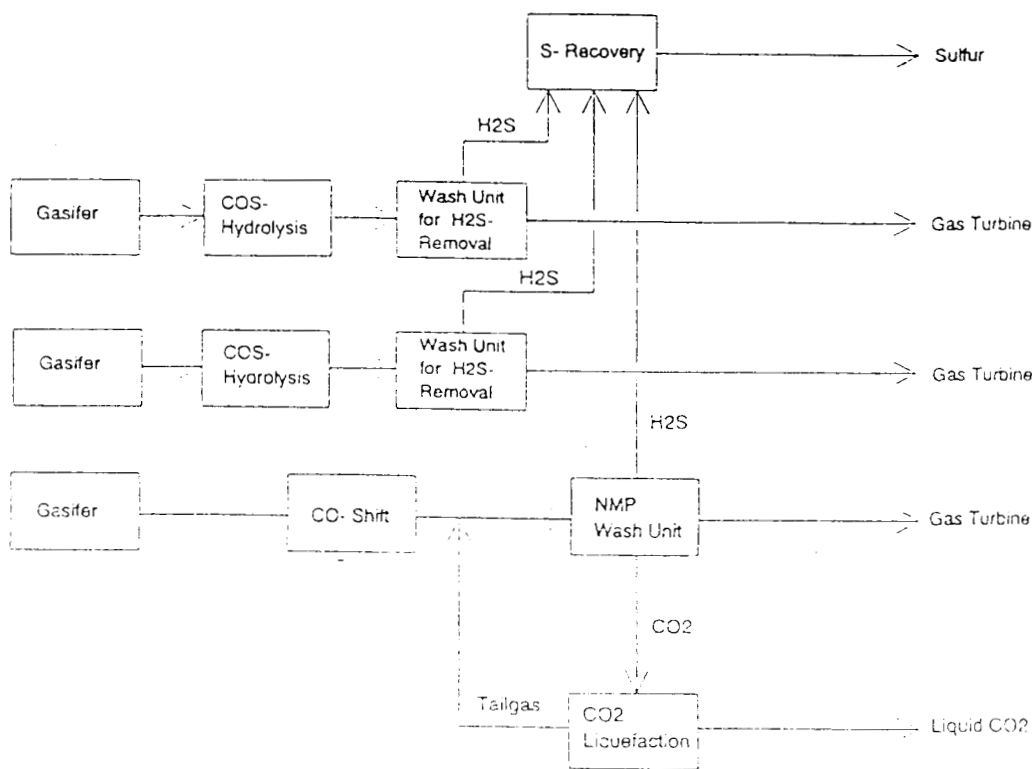


fig. 13: CO₂-removal concept with NMP wash
(alternative 2a; 1 * 78%)

RWE 232004M7
 NMP WASH UNIT
 ALTERNATIVE 2A

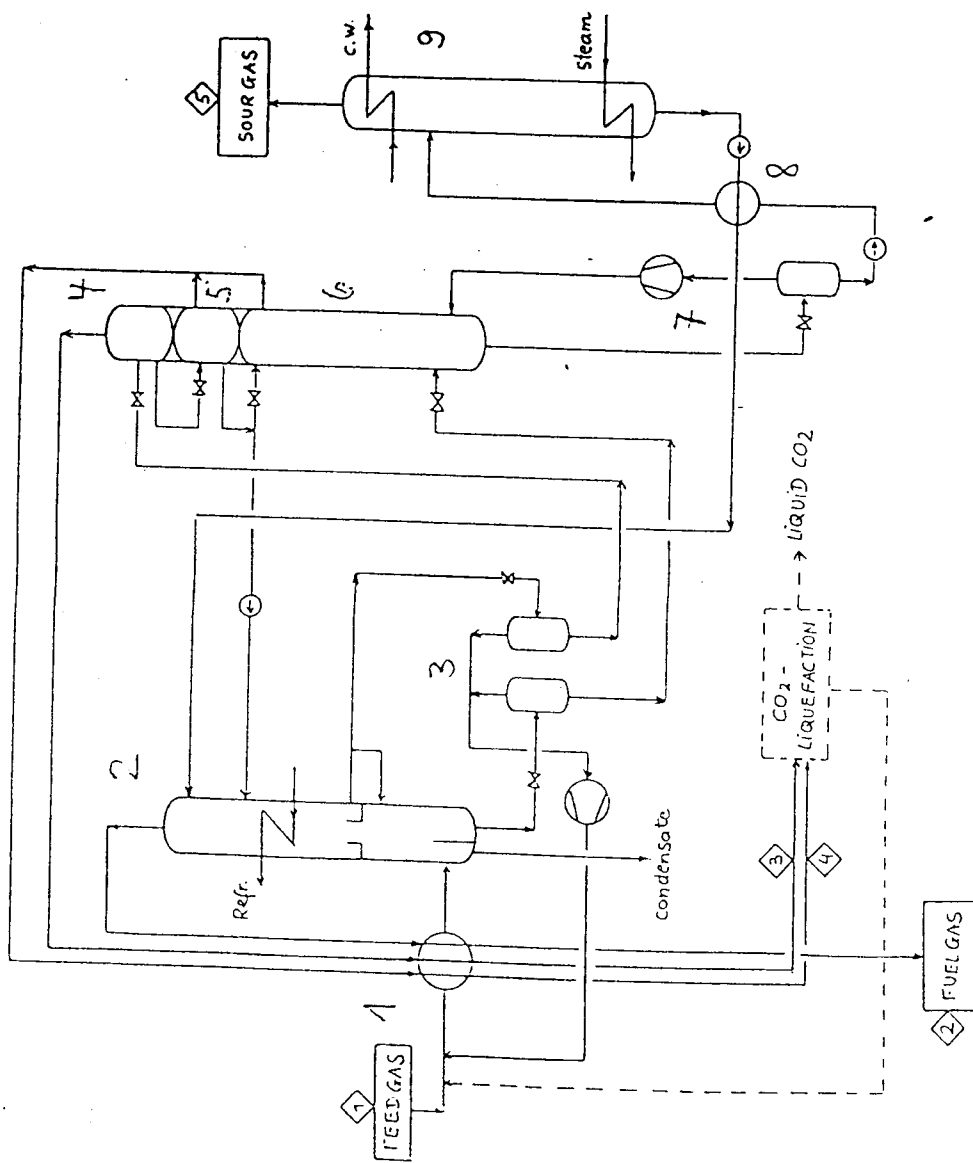


fig.14: NMP wash unit (alternative 2a)

RWE
 Aktiengesellschaft

(9) In the hot regeneration column all yet dissolved acid gases are stripped off by means of steam, reboiled out from the solvent (reboiler heated by steam). The NMP-solvent contains some percent of water. The lean solvent from the bottom of the column is pumped back to the wash column. Stripping vapor is condensed from the H₂S-fraction leaving the top.

4.4.2.3 Comments

A COS-hydrolysis in the fuel gas before entering the NMP wash unit is not required, because the CO₂-content of the feed gas is reduced sufficiently during the CO-shift conversion.

The tail gas from the CO₂-liquefaction is recycled upstream the NMP wash unit.

The CO₂-content in the treated gas from the NMP unit is adjusted in order to recover totally the 100 000 Nm³/hr of CO₂.

4.4.3 aMDEA wash unit

for simultaneous H₂S- and CO₂ removal (alternative 2b)

4.4.3.1 General process description (see fig. 15)

Only one train of the three trains of raw gases from the gasification sections is further processed for CO₂-recovery.

In order to achieve the required CO₂-quantity in one fuel gas stream a CO-shift is passed upstream the aMDEA wash unit. The CO-content after the CO-shift is about 3 mole-%.

In the downstream aMDEA wash CO₂ and H₂S is removed simultaneously from the gas. The acid gas stream leaving the aMDEA unit contains all removed H₂S and CO₂ and is given to a Sulpherox plant (see 4.4.3.4). In the Sulpherox unit the H₂S is removed out of the CO₂ and recovered as elementary sulfur. The remaining CO₂-stream is fed to the CO₂-liquefaction.

The other two trains of raw gases from gasification sections have only to be desulfurized in a wash unit for selective H₂S-removal. The H₂S-rich streams from these two wash units have to be routed to one train of S-recovery unit (e.g. a Clinsulf-process), where the H₂S is recovered as elementary sulfur.

4.4.3.2 Process description of the aMDEA wash (see fig. 16)

- (1) CO₂-removal in the absorber by means of lean solvent to the upper bed of the column and semi-lean solvent to the lower bed of the column. Solvent traces from the purified gas are removed by a water wash cycle on the top of the column.
- (2) The loaded solvent is expanded to a pressure of about 4 bara in an expansion turbine (reverse running pump) in order to save electric energy for pumping the semi-lean solvent back to the absorber.
- (3) The CO₂ flashed during solvent expansion is separated and directly given to the CO₂-compressor of the CO₂-liquefaction section. The recovery of part of the required CO₂-quantity at increased pressure saves electric energy for CO₂-compression.
- (4) The loaded solvent from (3) is expanded into the desorption column for further flashing of CO₂. Flashed steam is recovered in the overhead condenser. The majority of the solvent can be recycled to the absorber (semi-lean), only a small part has to be routed to the

hot regeneration.

(5) The loaded aMDEA solvent from the desorber is warmed up and fed into the regeneration column. The hot lean solvent is cooled down before reuse in the wash column.

(6) In the hot regeneration column all yet dissolved CO₂ is stripped off by steam reboiled out from the solvent (reboiler heated by steam). The lean solvent from the bottom is pumped back to the absorber. The overhead vapor is directly routed to the desorption column to support the flashing of CO₂.

4.4.3.3 Comments

A COS-hydrolysis in the feed gas before entering the aMDEA wash unit is not required, because the COS-content of the feed gas is reduced sufficiently during the CO-shift conversion.

The tail gas from the CO₂-liquefaction is recycled upstream the aMDEA wash unit.

The CO₂-content in the treated gas from the aMDEA unit is adjusted in order to recover totally the 100 000 Nm³/hr of CO₂.

4.4.3.4 Process option

In principle in this study the further processing of the tail gas from the S-recovery unit is not especially investigated. For this alternative the possibility of feeding this off-gas additionally to the Sulpherox plant should be mentioned (dashed line in the block flow diagram).

4.4.3.5 Sulpherox plant for H₂S-removal from sour gas from the aMDEA wash unit (alternative 2b)

The Sulpherox process (see fig. 17) was developed by Shell and Dow to recover H₂S and convert it to elementary sulfur. The process is a successor of the Stretford process. The main advance is the use of an iron chelate instead of a vanadium salt. The result of this change is a more effective H₂S-removal and the use of a non poisonous solvent.

The Sulpherox process is applicable for the H₂S-removal from diluted gases, but only for small sulfur production rate (1–20 t/d of sulfur). The process is really economic in relation to a Claus or similar plants, but often difficult in operation.

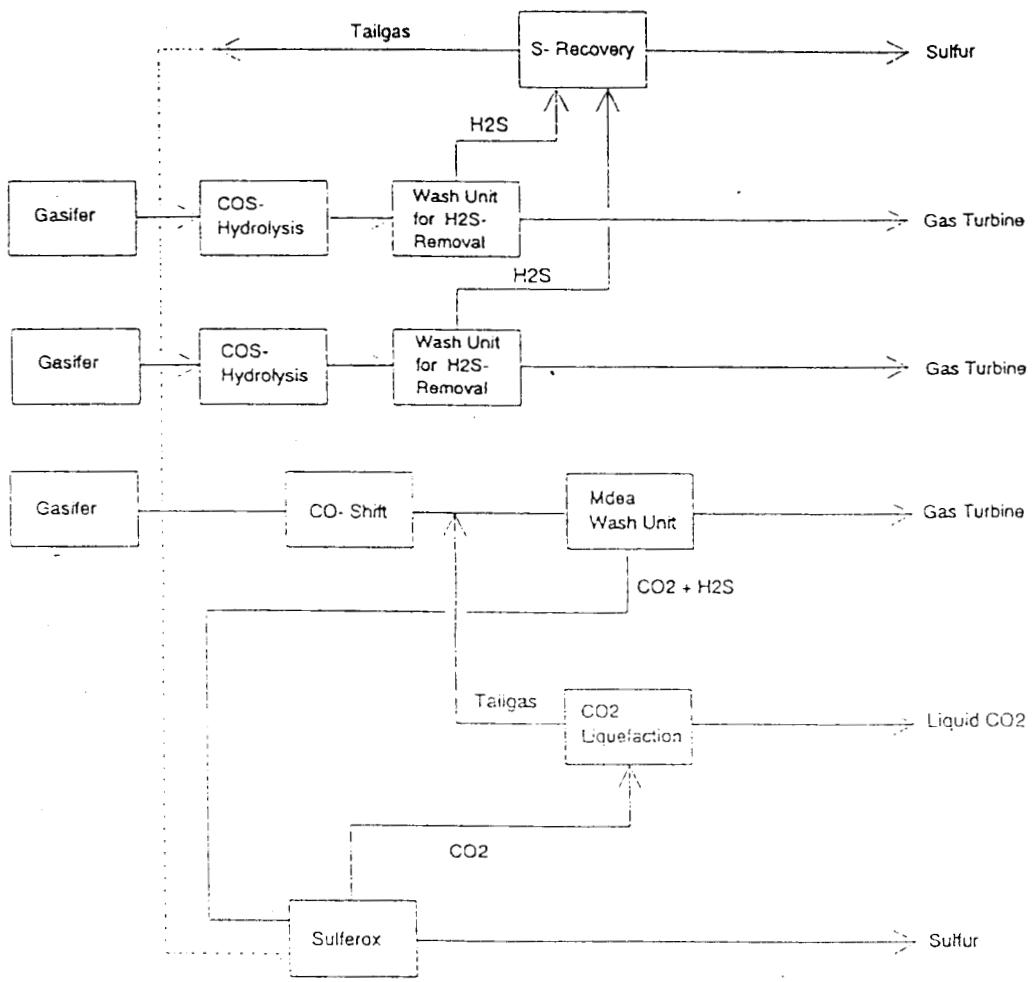
The main advantage is the simple process flow sheet, the main disadvantage is the loss of chemicals.

A rough estimate indicates, that the Sulpherox process is of interest for the H₂S-removal from the acid gas fraction from the aMDEA wash unit after shift. In this special case the H₂S concentration in the sour gas is so low, that the use of a Claus- or Clinsulf-process is not reasonable. In the case of a H₂S-removal from unshifted gas however, the total H₂S amount is too high for a Sulpherox plant.

In order to reduce the dimensions of the contractors, the Sulpherox plant is installed after the first stage of the CO₂ compressor. The layout of the purified gas will be 50 vppm, but a better H₂S-removal is possible at all.

In order to increase the CO₂-recovery, it is possible to feed the tail gas from the Clinsulf plant after hydration also to the Sulpherox plant. By such a configuration the additional utilities will increase only by a small amount; as the utilities are mainly proportional to the sulfur production. The only requirement would be to use oxygen in the Clinsulf process instead of air to reduce the amount of inerts.

The process involves three basis steps: absorption, regeneration and sulfur recovery



RWE
Aktiengesellschaft

fig. 15: CO₂-removal concept with aMDEA wash
(alternative 2b; 1 * 78%)

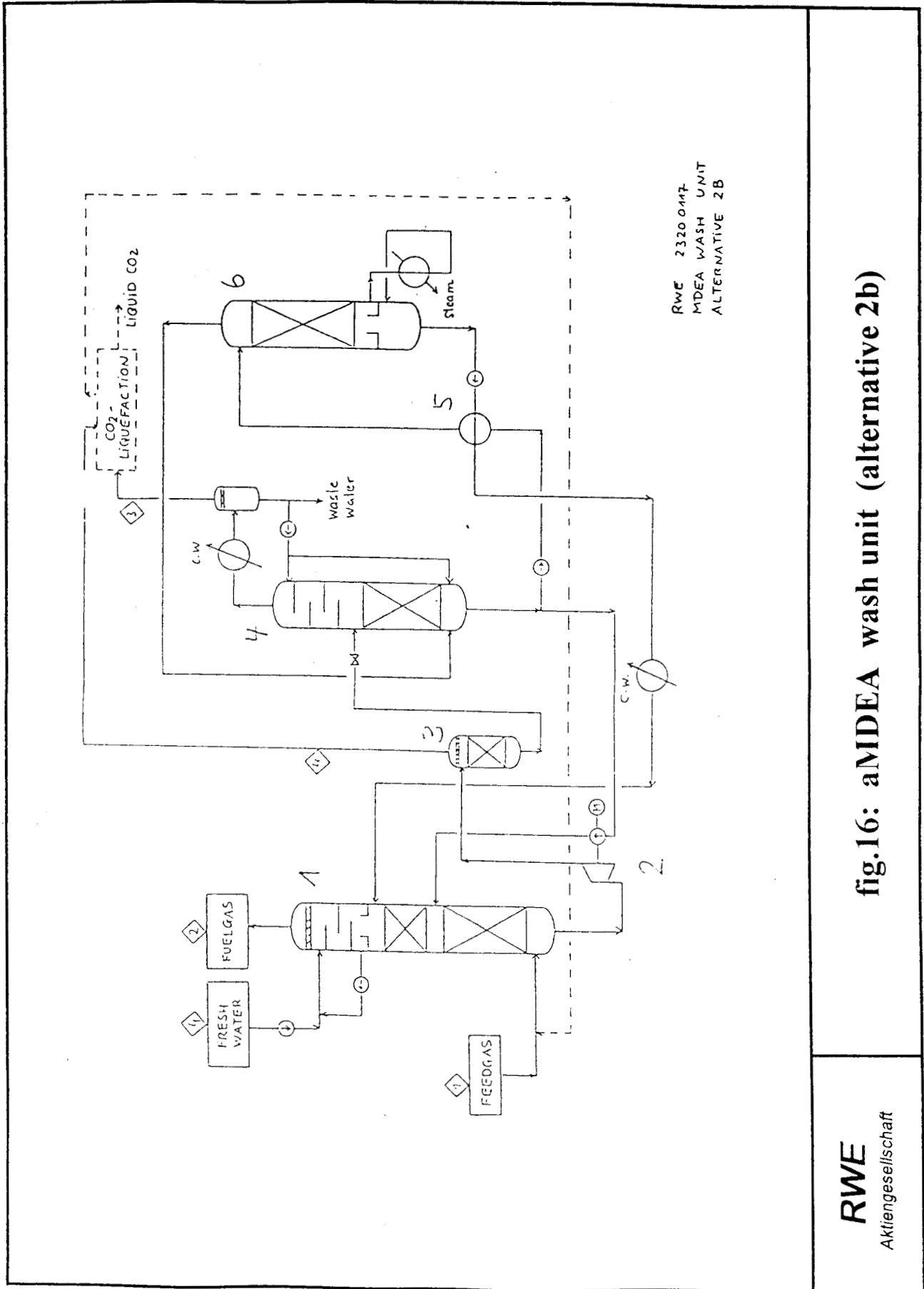


fig.16: aMDEA wash unit (alternative 2b)

RWE
Aktiengesellschaft

Absorption

The sour gas stream containing H₂S comes in contact with a liquid containing a soluble ferric chelate Fe(III). The H₂S is selectively oxidized to form elemental sulfur and the ferric chelate Fe(III) is reduced to the corresponding ferric chelate Fe(II).

Regeneration

In order to continually supply the absorption section with a fresh supply of iron in active Fe(III) form, the operation solution is sent to a regeneration section where the Fe(II) is reoxidized with air back to Fe(III). It is sent back to the absorption section to be reused.

Sulfur recovery

Elemental sulfur formed in the first reaction is concentrated, then filtered from the solution. The moist cake can then be reslurried and fed into a sulfur melter to produce a yellow, molten sulfur. In comparison to the sulfur product from a Claus or Clinsulf unit, the sulfur from the Sulpherox plant is of lower quality.

Feed gas flow	100 000–110 000 Nm ³ /h
H ₂ S-content in feed gas	0,48 mol%
Feed gas pressure	about 3 bara
Feed gas temperature	40°C
H ₂ S-content in CO ₂ -stream	50 vppm, max
Elementar sulfur	about 750 kg/h yellow, molten sulfur

4.5 Behaviour of trace components

In a feed gas produced by partial oxidation of oil or coal besides the noted components a lot of other trace components are present. The concentration of these components depends on the type of gasification and the used feed stock.

In regard to the acid gas removal normally the chemical active components are of importance. Among these ammonia, organic acid (formic acid), HCN and halogenes are the most critical components. But also components with a high boiling point, e.g. benzene and naphthalene can cause problems. The required removal steps and the tolerable levels are depending mainly on the used process for H₂S and CO₂-removal.

NH₃

NH₃ has a very good solubility in water and nearly all used solvents. As a result, NH₃ is removed from the fuel gas, but there would be an enrichment of ammonia or salts in the solvent and in the acid gas. Usually NH₃ is not tolerated in high concentrations in the feed gas to the sulfur recovery plants.

Therefore a water wash is installed in front of the acid gas removal wash.

HCN

In all types of amine wash units HCN reacts with the amine forming a heat stable cyanide. These heat stable salts are blocking the activity of the used amine (reaction with H₂S and CO₂), that means they reduce the capacity of the solvent to remove H₂S and CO₂. The removal of these heat stable salts requires the installation of a reclaiming

resulting in an increased steam requirement and a higher amine loss. Besides this HCN can react with elementary sulfur to HCNS (thiocyanic acid), which is even a stronger acid than HCN.

In physical wash units HCN has a better solubility in the used solvents than H₂S and is completely removed. The regeneration of the solvent however is designed for H₂S resulting in an enrichment of HCN in the solution.

The removal of HCN from the fuel gas is possible by catalytic conversion or by a pre-wash system. The catalytic conversion of HCN requires a higher temperature than the COS-hydrolysis. In the meantime a new catalyst is in the test phase converting HCN and COS at the same temperature.

The removal of HCN by a water wash is a common process, but the regeneration of the loaded wash water needs an own regeneration step. The handling of the resulting HCN-containing vapor stream is very expensive due to the high poisonsness of HCN.

Organic acids

Organic acid, mainly formic acid and halogenes (mainly HCl) are usually present in the gas leaving the reactor. Normally all these components are removed by the condensed water and are no real problem for the acid gas removal.

Benzene and naphthalene

Benzenes and naphthalenes have a very good solubility in all physical acting solvents (methanol, NMP, Selexol, ...) combined with the tendency of enrichment in the solvent circulation.

In a chemical wash benzene is not critical due to the low solubility in water and amine solutions. Naphthalene is more critical, if the melting point is 81°C and therefore blocking of pipes by solid naphthalene has to be expected.

The removal of benzene and naphthalene in a physical wash system is done by a small pre-wash section using the same solvent as in the main wash. The separation of the aromatics from the loaded solvent is done by extraction or by liquid-liquid separation achieved by adding of water. Although the requested solution flow rate to the pre-wash is relatively low, the investment and operation cost are considerable.

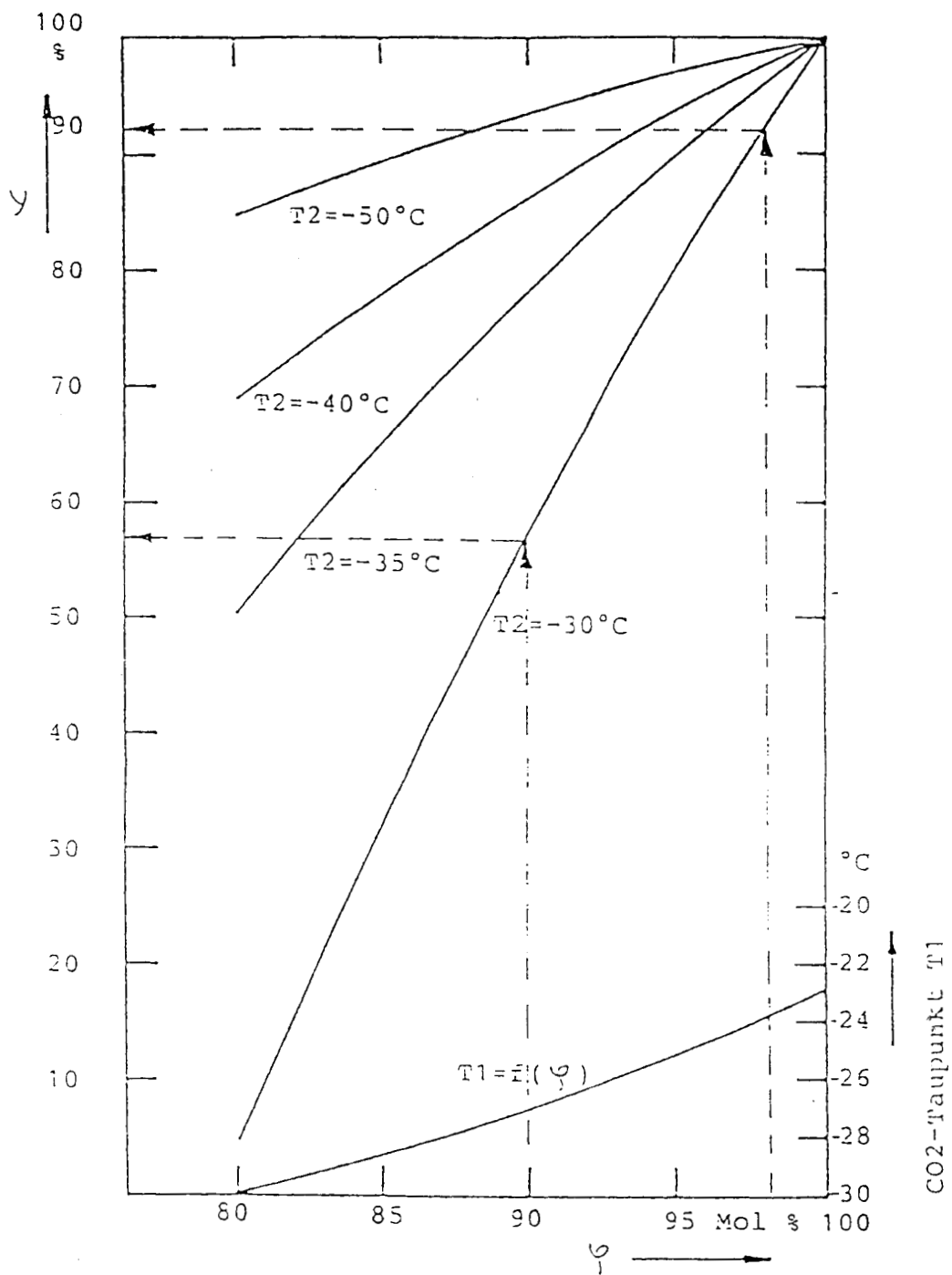
Using chemical wash systems the type of benzene and naphthalene removal depends on the concentration of these trace components and on the tolerable concentration of these components in the liquified CO₂.

4.6 CO₂-Liquefaction

Due to the critical point of CO₂ (T_K = 31 °C, P_K = 74 bara) the liquefaction must be performed at temperatures below 31°C. The CO₂ must be compressed to such a high pressure that the liquefaction can be performed either by means of a refrigeration unit or by cooling water.

The purity of the raw CO₂ to be liquefied is very essential on the process. If the raw CO₂ contains other gases, too, i.e. N₂ it has to be considered that these gases must also be compressed and that the efficiency of liquefaction will be reduced. Therefore if CO₂ must be liquefied, a high purity of the raw CO₂ is advantageous. Fig. 18 shows the dependance of the efficiency of CO₂ liquefaction on the purity of the raw CO₂.

With respect to investment cost, liquefaction efficiency, selection of refrigerant and the advantages of storage and



RWE
Aktiengesellschaft

fig. 18: dependance of the efficiency of CO_2 -liquefaction on the purity of the raw CO_2

transport, the liquefaction nowadays is performed at pressures between 15 and 25 bars and corresponding low temperatures (-30°C to -10°C).

At a lower liquefaction temperature the compression energy for the raw CO_2 is becoming smaller but of course the refrigeration unit consumes more energy. The total energy consumption of the CO_2 liquefaction unit which consists mainly of the compression energy for the raw CO_2 and the compression energy of the refrigeration unit is nearly independent from the selected liquefaction pressure.

For this study the preferred liquefaction pressure is 25 bara because then the not liquefied tailgas can be routed to the fuel gas.

In the flow sheet (see fig. 19) the main process steps of the CO_2 liquefaction are shown. They consist of

- compression of the raw CO_2 i.e. by means of a turbo compressor (2 stages for 18 bara, 3 stages for 25 bara)
- drying of the compressed raw CO_2 by means of an adsorptive process step (molsieve). The regeneration of the adsorbers can be done with the tailgas from the liquefaction or by recycling of the regeneration gas to the 2. stage of the compressor.
- liquefaction of the CO_2 by means of vapourizing refrigerant i.e. ammonia or propylene. Storage of the liquefied CO_2 and transport. The not liquefied tailgas is routed to the fuelgas.
- process data

CO_2 product:	100 000 Nm^3/h (200 t/h)
Raw CO_2 pressure	1.3 bar
Raw CO_2 purity	98 mol%
Liquefaction pressure	25 bara (18 bara)
Liquefaction temperature	-30°C
Liquefaction efficiency	92%

5 INVESTMENT AND OPERATING COSTS

5.1 Assumptions

To compare the different CO_2 -removal processes examined the cost estimation is based on the following assumptions.

A more or less turnkey supply has been assumed, including

- basic and detail engineering, license,
- supply of equipment and materials
- supply of the refrigeration unit
- erection of the units, including insulation and painting
- civil works

German and European Codes have been presumed for the design of the equipment, piping, instrumentation and electrical equipment. For pumps and compressors manufacturer standard shall apply. No special standards and requirements of power utilities have been considered or regarded. All compressors are supplied single without a spare machine.

All costs are based on the present cost situation with a degree of accuracy of 25%. It has been assumed that a fictitious contract is awarded on June 30, 1994, and consequently 50% of the engineering services and of the procurement can be performed in 1994, the other 50% are

to be performed in 1995. The delivery time ex works will be 15 months, the erection time will be approximately 8 months.

For such alternatives where an equipment list has been established, the price for equipment was estimated according to this list. The prices for materials like piping, instrumentation, electrical equipment, steel structure have been calculated by using a factor, which includes the prices for engineering and supply.

The price for the CO_2 -liquefaction unit is based on the investment costs of a 90 t/h CO_2 -liquefaction unit investigated and updated according to the present cost situation and then transformed to a 100 t/hr unit.

The price for the Sulpherox unit is based on a budget information from the licensor and supplemented according to the other price estimations.

5.2 Comparison of the alternatives examined

All the studied processes and alternatives yield different investment costs and different utility consumption figures which are due at different times.

For the comparison of the alternatives, investment costs alone are not sufficient, i.e. a process with low investment costs may have high utility consumption figures which can overcompensate for the lower investment costs within a limited time period and vice versa.

In order to get a more reliable comparison of the alternatives the additional annual total costs are determined. Therefore, the additional annual costs of capital, operation, personnel and maintenance are added. In addition the enlargement factor, designed by the different internal consumptions, considers the additional power requirement for producing the basic electric power of 300 MWe of each train (depending on the efficiency losses: 1.12–1.15). This factor has to be used for each train where a CO_2 -removal unit is integrated to get a constant electrical output, equal to the output of the basic design. This includes the reduction of efficiency from 45% to 38–40%. The additional annual capital costs include an interest rate of 7% within twenty years.

On the following tables (see tab. 1 and tab. 2) the calculation for the different processes is shown. To get an overall comparison the investment and operating costs of the basic IGCC power plant are reduced by those units which are modified or left out in an IGCC power plant concept with CO_2 -removal.

Additional the specific costs per t removed CO_2 , the spec. investment costs and the operating cost are presented.

Looking only upon the selective wash unit in alternative 1a the Rectisol process is significantly more favourable in the annual total costs versus the NMP wash process (90 Mio. DM instead of 109 Mio. DM). A comparison between alternative 1a Rectisol and 1b MDEA show a difference of 3 Mio. DM.

The comparison between Rectisol wash and NMP wash in alternative 2 (see Tab.2) again shows the Rectisol process as the more favourable process; the difference in total cost favouring the Rectisol wash in comparison with alternative 1 however, rather small (86 Mio. DM instead of 88 Mio. DM).

In the next step alternative 2a/Rectisol wash, has to be compared with the combination 2b/MDEA wash plus Sulftrox unit. The result is a slight advantage to the Rectisol wash (85 Mio. DM versus 89 Mio. DM).

For the final comparison of the best alternative the Rectisol cases 1a and 2a should be compared. Given the

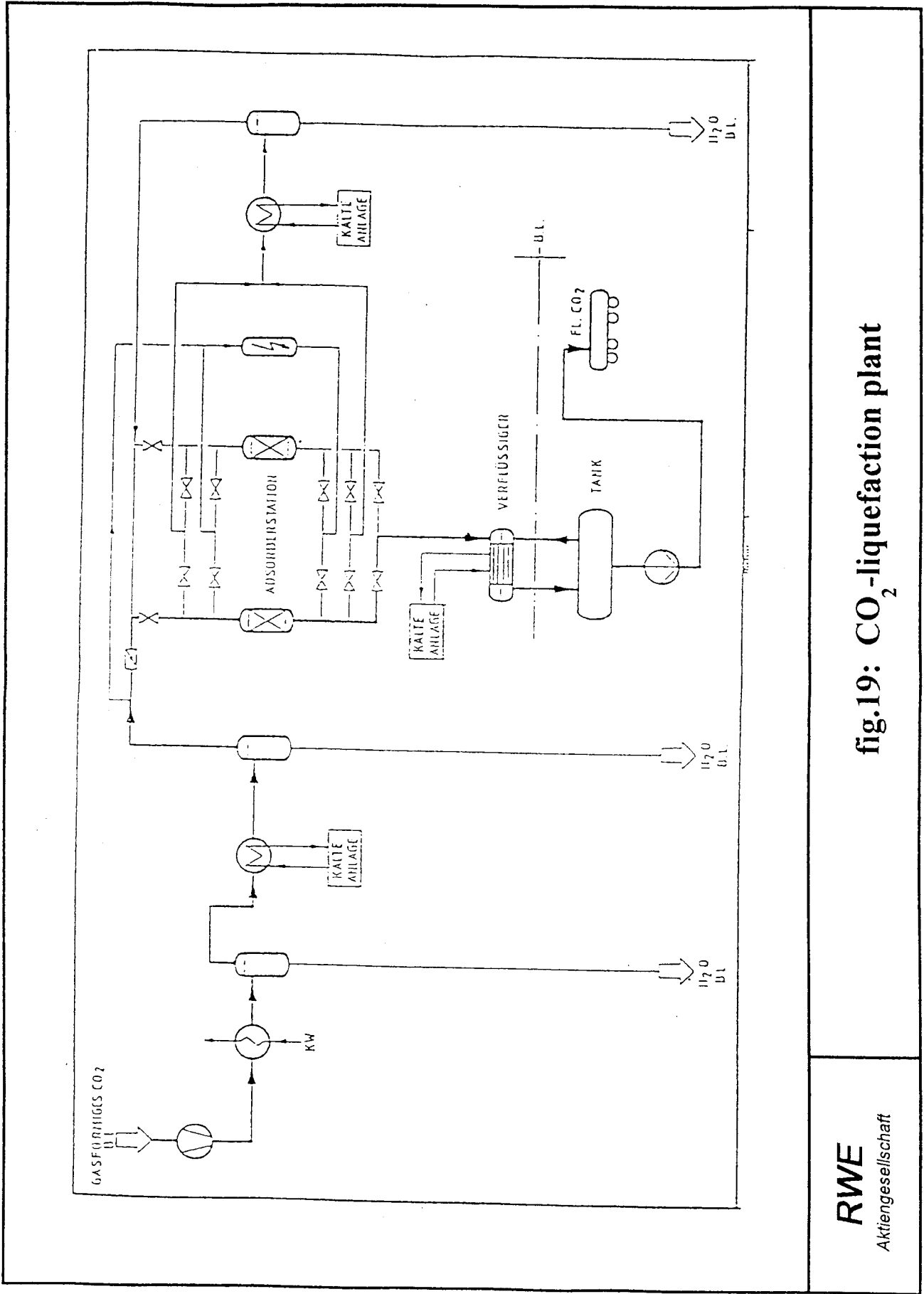


fig.19: CO₂-liquefaction plant

RWE
Aktiengesellschaft

tab. 1: investment and operating costs for CO₂-removal

(alternatives 1 without CO-shift; 3 * 26% CO₂-removal; *) with a degree of accuracy of ±25%)

alternative basic presumed CO ₂ -recovery	1a: NMP wash unit		1a: Rectisol wash unit		1b: MDEA wash unit	
	IGCC-900 MW 3 * 26 % (1,6 * 10 ⁶ [t/a])		IGCC-900 MW 3 * 26 % (1,6 * 10 ⁶ [t/a])		IGCC-900 MW 3 * 26 % (1,6 * 10 ⁶ [t/a])	
	investment costs *10 ⁶ [DM]	operating costs *10 ⁶ [DM/a]	investment costs *10 ⁶ [DM]	operating costs *10 ⁶ [DM/a]	investment costs *10 ⁶ [DM]	operating costs *10 ⁶ [DM/a]
reduction due to CO ₂ -removal (H ₂ S-wash unit, COS-hydrolysis, S-recovery)	64	11	84	12	0	0
additions						
Wash unit	218	35	192	28	86	11
S-Recovery						
CO ₂ -liquefaction	55	23	55	23	55	23
Δ CO-Shift						
total	210	47	163	40	141	35
additional annual capital costs	20 *10 ⁶ [DM]		15 *10 ⁶ [DM]		13 *10 ⁶ [DM]	
additional annual personal costs	2 *10 ⁶ [DM]		2 *10 ⁶ [DM]		2 *10 ⁶ [DM]	
additional annual maintenance costs	11 *10 ⁶ [DM]		9 *10 ⁶ [DM]		8 *10 ⁶ [DM]	
enlargement factor	1,12 [-]		1,10 [-]		1,15 [-]	
additional annual power requirement	29 *10 ⁶ [DM]		24 *10 ⁶ [DM]		36 *10 ⁶ [DM]	
additional annual total costs	109 *10 ⁶ [DM]		90 *10 ⁶ [DM]		93 *10 ⁶ [DM]	
costs per t CO ₂	68 [DM/t]		56 [DM/t]		58 [DM/t]	
costs per t CO ₂	*) 50 - 85 [DM/t]		*) 40 - 70 [DM/t]		*) 45 - 75 [DM/t]	
additional spec. investment costs	597 [DM/kW _e]		479 [DM/kW _e]		600 [DM/kW _e]	
additional spec. investment costs	*) 450 - 750 [DM/kW _e]		*) 350 - 600 [DM/kW _e]		*) 450 - 750 [DM/kW _e]	
additional costs of electricity (COE)	0,015 [DM/kWh]		0,013 [DM/kWh]		0,013 [DM/kWh]	
additional costs of electricity (COE)	*) 0,010 - 0,020 [DM/kWh]		*) 0,010 - 0,015 [DM/kWh]		*) 0,010 - 0,015 [DM/kWh]	

tab.2: investment and operating costs for CO₂-removal

(alternatives 2 with CO-shift; 1 * 78% CO₂-removal; *) with degree of accuracy of ±25%)

alternative basic presumed CO ₂ -recovery	2a: NMP wash unit		2a: Rectisol wash unit		2b: MDEA wash unit	
	IGCC-900 MW 1 * 78 % (1,6 * 10 ⁶ [t/a])		IGCC-900 MW 1 * 78 % (1,6 * 10 ⁶ [t/a])		IGCC-900 MW 1 * 78 % (1,6 * 10 ⁶ [t/a])	
	investment costs *10 ⁶ [DM]	operating costs *10 ⁶ [DM/a]	investment costs *10 ⁶ [DM]	operating costs *10 ⁶ [DM/a]	investment costs *10 ⁶ [DM]	operating costs *10 ⁶ [DM/a]
reduction due to CO ₂ -removal (H ₂ S-wash unit, COS-hydrolysis, S-recovery)	30	4	30	4	39	5
additions						
Wash unit	100	14	98	13	79	8
S-Recovery					19	11
CO ₂ -liquefaction	55	23	55	23	55	23
Δ CO-Shift	18	2	18	2	18	2
total	143	35	142	34	131	38
additional annual capital costs	13 *10 ⁶ [DM]		13 *10 ⁶ [DM]		12 *10 ⁶ [DM]	
additional annual personal costs	2 *10 ⁶ [DM]		2 *10 ⁶ [DM]		2 *10 ⁶ [DM]	
additional annual maintenance costs	8 *10 ⁶ [DM]		8 *10 ⁶ [DM]		7 *10 ⁶ [DM]	
enlargement factor	1,13 [-]		1,12 [-]		1,12 [-]	
additional annual power requirement	31 *10 ⁶ [DM]		29 *10 ⁶ [DM]		29 *10 ⁶ [DM]	
additional annual total costs	89 *10 ⁶ [DM]		85 *10 ⁶ [DM]		88 *10 ⁶ [DM]	
costs per t CO ₂	56 [DM/t]		53 [DM/t]		55 [DM/t]	
costs per t CO ₂	*) 40 - 70 [DM/t]		*) 40 - 70 [DM/t]		*) 40 - 70 [DM/t]	
additional spec. investment costs	538 [DM/kW _e]		512 [DM/kW _e]		499 [DM/kW _e]	
additional spec. investment costs	*) 400 - 700 [DM/kW _e]		*) 400 - 650 [DM/kW _e]		*) 400 - 650 [DM/kW _e]	
additional costs of electricity (COE)	0,012 [DM/kWh]		0,012 [DM/kWh]		0,012 [DM/kWh]	
additional costs of electricity (COE)	*) 0,010 - 0,015 [DM/kWh]		*) 0,010 - 0,015 [DM/kWh]		*) 0,010 - 0,015 [DM/kWh]	

difference of 5 Mio. DM, alternative 2a seems to be the most economic process for the required CO₂-removal.

The comparison of the different processes is based on the production and liquefaction of 100 000 Nm³/hr CO₂. This is equal to a total CO₂ recovery rate of 26% as on three trains for a 300 MW power plant. In the case without CO-shift an increase of the CO₂-recovery rate is not possible. In the cases of CO-shift however only one of three trains is used for CO₂-recovery. By installation of two further CO-shift plants the total CO₂-recovery rate can be increased to approx. 78%. This means 90% of the CO₂ in the fuel gas. Still a higher CO₂-recovery rate makes no sense, as the residual CO₂ is produced in the gas turbine by burning the unshifted CO and the hydrocarbons.

To analyse this concept, the alternatives 2 are calculated with the aim of removing 4.8×10^6 t CO₂/a ($3 \times 78\%$). The corresponding costs are shown in Tab. 3. In comparison with the concepts discussed above the specific costs per t CO₂ decrease by nearly 25%. The additional costs of electricity for the whole power plant only increase by a factor of 2.3, although the amount of removed CO₂ is tripled.

6 CONCLUSIONS

In conclusion, it is possible to design an integrated coal gasification combined cycle power plant with very low emissions but also with significantly higher costs.

The results of the technical and economical optimization are:

- To optimize the removal process, the total C-content in the fuel gas must be considered.
- An optimal CO₂-removal requires a CO-conversion of nearly 90%.
- A graduated CO-conversion is not suitable.
- It is more economical to remove a higher amount of CO₂ in one train than a lower amount of CO₂ in three trains concerning the same recovered quantity of CO₂.
- Compared with a "conventional" IGCC power plant without CO₂-removal, the specific costs for a concept with nearly total CO₂-removal are drastically higher.
 - The specific investment costs increase by 700–900 DM/kW (25% to 30%).
 - The costs of electricity (COE) for the whole plant rise by about 0,03 DM/kWh (30% to 40%).
 - The specific costs per t removed CO₂ are approximately between 40 and 50 DM/t.
 - The specific costs per t removed CO₂ decrease by improving the CO₂-removal rate.
 - It is more economical to remove nearly the total amount of CO₂ in one power plant than to modify

some power plants with a lower CO₂-removal capacity.

The results of this study consider only the recovery and liquefaction of CO₂ in an IGCC power plant based on brown coal. The additional costs for transport and underground disposal of CO₂ were not examined.

For the development of the relevant techniques and the calculation of the costs involved the estimated technical data of this study can be used as a basis.

7 LITERATURE

- [1] KoBra - 300 MW Kombikraftwerk Goldenberg
Sonderdruck aus Modern Power Systems 2/93
- [2] Engelhard, J; Theis, K A
Inbetriebnahme der HTW-Demonstrationsanlage
Erdöl, Kohle, Gas 103 (1987) Nr. 3
- [3] Schütz, M; Daun, M; Weispach, P.-M; Krumbek, M;
Hein, KR G
Study on the CO₂-Recovery from an IGCC-Plant
Energy Convers. Mgmt Vol. 33, Nr. 5–8, 1992

8 ENCLOSURE

- fig. 1: IGCC-plant for brown coal
- fig. 2: IGCC-plant for brown coal with CO₂-removal
- fig. 3: Alternative concepts for CO₂-removal
- fig. 4: CO-conversion
- fig. 5: CO₂-removal concept with Rectisol wash unit (alternative 1a; $3 \times 26\%$)
- fig. 6: Rectisol wash unit (alternative 1a)
- fig. 7: CO₂-removal concept with NMP wash unit (alternative 1a; $3 \times 36\%$)
- fig. 8: NMP wash unit (alternative 1a)
- fig. 9: CO₂-removal concept with a MDEA wash unit (alternative 1b; $3 \times 26\%$)
- fig. 10: aMDEA wash unit (alternative 1b)
- fig. 11: CO₂-removal concept with Rectisol wash (alternative 2a; $1 \times 78\%$)
- fig. 12: Rectisol wash unit (alternative 2a)
- fig. 13: CO₂-removal concept with NMP wash unit (alternative 2a; $1 \times 78\%$)
- fig. 14: NMP wash unit (alternative 2a)
- fig. 15: CO₂-removal concept with aMDEA wash (alternative 2b)
- fig. 16: MDEA wash unit (Sulferox)
- fig. 17: S-recovery unit
- fig. 18: Dependence of the efficiency of CO₂ liquefaction on the purity of the raw CO₂
- fig. 19: CO₂-liquefaction plant
- tab. 1: investment and operating costs for CO₂-removal (alternatives 1 without CO-shift; $3 \times 26\%$)
- tab. 2: investment and operating costs for CO₂-removal (alternatives 2 with CO-shift; $1 \times 78\%$)
- tab. 3: investment and operating costs for CO₂-removal (alternatives 2 with CO-shift; $3 \times 78\%$)

tab. 3: investment and operating costs for CO₂-removal
 (alternatives 2 with CO-shift, 3*78% CO₂-removal; *) with a degree of accuracy of ±25%)

alternative	2a: NMP wash unit IGCC-900 MW		2a: Rectisol wash unit IGCC-900 MW		2b: MDEA wash unit IGCC-900 MW	
	investment costs *10 ⁶ [DM]	operating costs *10 ⁶ [DM/a]	investment costs *10 ⁶ [DM]	operating costs *10 ⁶ [DM/a]	investment costs *10 ⁶ [DM]	operating costs *10 ⁶ [DM/a]
basic presumed						
CO ₂ -recovery	3 * 78 % (4,8 * 10 ⁶ [DM/a])	8	3 * 78 % (4,8 * 10 ⁶ [DM/a])	8	3 * 78 % (4,8 * 10 ⁶ [DM/a])	12
reduction due to CO ₂ -removal (H ₂ S-wash unit, COS-hydrolysis, S-recovery)	64	8	64	8	85	12
additions						
Wash unit						
S-Recovery	215	30	212	27	171	17
CO ₂ -liquefaction	119	50	119	50	40	23
Δ CO-Shift	38	3	38	3	119	50
total	308	75	305	73	283	82
additional annual capital costs	29 *10 ⁶ [DM]		29 *10 ⁶ [DM]		27 *10 ⁶ [DM]	
additional annual personal costs	2 *10 ⁶ [DM]		2 *10 ⁶ [DM]		2 *10 ⁶ [DM]	
additional annual maintenance costs	17 *10 ⁶ [DM]		16 *10 ⁶ [DM]		15 *10 ⁶ [DM]	
enlargement factor	1,11 [-]		1,11 [-]		1,11 [-]	
additional annual power requirement	79 *10 ⁶ [DM]		79 *10 ⁶ [DM]		79 *10 ⁶ [DM]	
additional annual total costs	202 *10 ⁶ [DM]		199 *10 ⁶ [DM]		205 *10 ⁶ [DM]	
costs per t CO ₂	42 [DM/t]		41 [DM/t]		43 [DM/t]	
costs per t CO ₂	30 - 55 [DM/t]		30 - 50 [DM/t]		30 - 55 [DM/t]	
additional spec. investment costs	688 [DM/kW _e]		685 [DM/kW _e]		657 [DM/kW _e]	
additional spec. investment costs	500 - 850 [DM/kW _e]		500 - 850 [DM/kW _e]		500 - 850 [DM/kW _e]	
additional costs of electricity (COE)	0,028 [DM/kWh]		0,028 [DM/kWh]		0,028 [DM/kWh]	
additional costs of electricity (COE)	0,020 - 0,035 [DM/kWh]		0,020 - 0,035 [DM/kWh]		0,020 - 0,035 [DM/kWh]	

